Conference Proceedings of the Society for Experimental Mechanics Series

Carter Ralph · Meredith Silberstein
Piyush R. Thakre · Raman Singh *Editors*

Mechanics of Composite and Multi-functional Materials, Volume 7

Proceedings of the 2015 Annual Conference on Experimental and Applied Mechanics

Springer

Conference Proceedings of the Society for Experimental Mechanics Series

Series Editor

Kristin B. Zimmerman, Ph.D.
Society for Experimental Mechanics
Bethel, CT, USA

More information about this series at http://www.springer.com/series/8922

Carter Ralph • Meredith Silberstein • Piyush R. Thakre • Raman Singh
Editors

Mechanics of Composite and Multi-functional Materials, Volume 7

Proceedings of the 2015 Annual Conference on Experimental and Applied Mechanics

Springer

Editors
Carter Ralph
Southern Research Institute
Birmingham, Alabama, USA

Meredith Silberstein
Cornell University
Ithaca, New York, USA

Piyush R. Thakre
The Dow Chemical Company
Midland, Michigan, USA

Raman Singh
Oklahoma State University
Tulsa, Oklahoma, USA

ISSN 2191-5644 ISSN 2191-5652 (electronic)
Conference Proceedings of the Society for Experimental Mechanics Series
ISBN 978-3-319-21761-1 ISBN 978-3-319-21762-8 (eBook)
DOI 10.1007/978-3-319-21762-8

Library of Congress Control Number: 2015945111

Springer Cham Heidelberg New York Dordrecht London

Printed on acid-free paper

Springer International Publishing AG Switzerland is part of Springer Science+Business Media (www.springer.com)

Preface

Mechanics of Composite and Multifunctional Materials represents the one of nine volumes of technical papers presented at the 2015 SEM Annual Conference and Exposition on Experimental and Applied Mechanics organized by the Society for Experimental Mechanics and held in Costa Mesa, CA, June 8–11, 2015. The complete Proceedings also includes volumes on the following: *Dynamic Behavior of Materials; Challenges in Mechanics of Time-Dependent Materials; Advancement of Optical Methods in Experimental Mechanics; Experimental and Applied Mechanics; MEMS and Nanotechnology; Mechanics of Biological Systems and Materials; Fracture, Fatigue, Failure and Damage Evolution; and Residual Stress, Thermomechanics and Infrared Imaging, Hybrid Techniques and Inverse Problems.*

This volume presents early findings from experimental and computational investigations on an important area within Composite, Hybrid, and Multifunctional Materials.

Composites are increasingly the material of choice for a wide range of applications from sporting equipment to aerospace vehicles. This increase has been fueled by increases in material options, greater understanding of material behaviors, novel design solutions, and improved manufacturing techniques. The broad range of uses and challenges requires a multidisciplinary approach between mechanical, chemical, and physical researchers to continue the rapid rate of advancement.

New materials are being developed from natural sources or from biological inspiration, leading to composites with unique properties and more sustainable sources. Existing materials used in new and critical applications require a deeper understanding of their behaviors and failure mechanisms on multiple scales. In addition, the unique properties of composites present many challenges in manufacturing and in joining them with other materials. Testing needs to be performed on these materials to characterize their properties, and new test methods and technologies must be developed in order to perform these studies and to evaluate parts during manufacture and use.

Birmingham, Alabama, USA — Carter Ralph
Ithaca, New York, USA — Meredith Silberstein
Midland, Michigan, USA — Piyush R. Thakre
Tulsa, Oklahoma, USA — Raman Singh

Contents

Chapter 1
Mechanics of Multifunctional Wings with Solar Cells for Robotic Birds

Ariel Perez-Rosado, Satyandra K. Gupta, and Hugh A. Bruck

Abstract Inspired by nature, Flapping Wing Aerial Vehicles (FWAVs), also known as Robotic Birds, use flexible compliant wings that deform while flapping to generate the aerodynamic forces necessary for flight. These vehicles sustain short flights due to the limited payload for on-board energy storage. Using flexible solar cells, energy can be harvested during flight to extend the flight of the FWAV. By integrating flexible solar cells into the wing structure of the FWAV, more electrical power is produced but at a cost. The solar cells increase the overall mass of the vehicle while also altering the deformation of the wing. These changes to the wing ultimately have an effect on the performance of the FWAV. In this paper, three different wing designs were designed, built and tested. The Robo Raven platform was used for each wing design. The first design was the original wing design without solar cells. The second design hosted 12 solar modules integrated into the wings. The final design was composed of 22 solar modules integrated into the wings. The aerodynamic forces generated by each wing design were observed in a wind tunnel while the FWAV was attached to a six DOF load cell. To understand how the wings changed with respect to deformation each wing was also observed in the wind tunnel 3D using Digital Image Correlation (DIC). The results from DIC demonstrated a correlation between the lift and thrust forces produced by the wings and the biaxial and shear strains observed on the wings surface respectively. By observing the power output form the solar cells while flapping, the corresponding wave form correlated well to the thrust force measurements. This allows th solar cells to also behave as sensors while flying. The resulting platform, Robo Raven III, is the first ornithopter to fly while using energy harvested from solar cells.

Keywords Flexible solar cells • Flapping wing air vehicles • Wing deformations • Aerodynamic force sensing

1.1 Introduction

Unmanned Aerial Vehicles (UAVs) are emerging as an important tool in a wide variety of defense and civilian applications [1–3]. Flapping Wing Aerial Vehicles (FWAVs) have the potential to combine the positive aspects of both fixed-wing and rotary flight, while eliminating many of the negative aspects. Inspiration for flapping has been derived from bats, insects, and birds that's have been observed in flight for all of human history. Using this inspiration, many platforms that use a flapping motion to maintain flight have been designed, built, and modeled [2–25]. Though the design and size of each of these designs may differ, the wings are all made of stiff lightweight rods that support a thin membrane.

More recently, a highly maneuverable robotic bird named Robo Raven was developed in the Advanced Manufacturing Lab at the University of Maryland [26–28] and was used as the base platform for this research. Like most FWAVs Robo Raven has a limited flight time due to the small on-board lithium polymer battery used to power all of its components. With the limited flight time and large surface area provided by the wings, it's a perfect candidate for solar cell integration. The new wing designs do not only provide the lift and thrust forces necessary for flight but also provide electrical power making them multifunctional. This new functionality increases vehicle endurance and overall system efficiency.

Multi-functional structures combine multiple functional requirements into a single structural component to create better efficiency in the overall design [29, 30]. A Micro Air Vehicle (MAV) constructed with MEMS technology has a membrane made of a PVDF skin, allowing it to act as a real time load sensor to directly analyze flight performance [13, 14]. Ma et al. developed another MEMS-based insect-inspired flapping wing platform known as RoboBee uses artificial muscles to achieve novel controlled flight dynamics [31]. Thomas et al. described the combination of structure and battery in the design of an electric-propelled UAV as an example of a multi-functional material system [30, 32]. More recently at the

A. Perez-Rosado • S.K. Gupta • H.A. Bruck (✉)
Department of Mechanical Engineering, University of Maryland, College Park, MD 20742, USA
e-mail: bruck@umd.edu

C. Ralph et al. (eds.), *Mechanics of Composite and Multi-functional Materials, Volume 7*,
Conference Proceedings of the Society for Experimental Mechanics Series, DOI 10.1007/978-3-319-21762-8_1

University of Maryland, elastomeric strain gauges were placed on the wings of a flapping wing Micro Air Vehicle (MAV) [33]. These sensors captured deformations caused by flapping. The outputs from these sensors were directly correlated to thrust production which essentially made the wing into a skin-like structure. By integrating solar cells into the wings, the functionality of the wings increases improving the design of the wings. However, if this increase in functionality does not allow the vehicle to fly, the integration of solar cells would be pointless. Being able to understand not only how the performance changes but why is important.

In this investigation, we report the effects of integrating solar cells into compliant wings for robotic birds. The aerodynamic forces generated by the wing are characterized on a six DOF in a wind tunnel. The wing deformations are characterized using 3D Digital Image Correlation (DIC). The mechanics of various configurations of solar cells on wing designs are investigated, as well as their energy harvesting capability.

1.2 Wing Designs

The platform used to test all of these wings was the original Robo Raven design. Robo Raven weighs 289 g and has a wingspan of 114.3 cm. Unlike typical ornithopter that use a single motor to actuate both wings, Robo Raven uses two separate motors to actuate each wing separate. This allows the FWAV to perform aerobatic maneuvers other ornithopter cannot execute. Using two motors allows for varying flapping frequencies, flapping ranges, and flapping profiles to be explored.

The wing was adapted from a previous design developed in Advanced Manufacturing Lab for a smaller FWAV [23–26]. This wing design has proven to be effective in generating lift and thrust forces across various size scales. The wing is mostly comprised of a carbon fiber skeleton made up of four different rods all held together by a Mylar membrane. The wing design can be seen in Fig. 1.1. The parameters of the wing are as follows: S is the semi-span, C is the chord, and t_n are the diameters of carbon fiber stiffening rods. Figure 1.1 also presents the values for these parameters for the typical Robo Raven wing. The Mylar membrane is 0.025 mm thick and provides the wing with its shape, flexibility, and toughness while remaining lightweight. Figure 1.2 shows the actual completed wing with the spars highlighted. The red spar is the leading spar and is directly driven by the motor. The passive deformation of the wing through the flapping cycle allow for the aerodynamic forces to be generated.

The passive deformation of the wings is crucial to endurance, speed, maneuverability, climbing, gliding and other behaviors. Making alterations to wing design will somehow affect these capabilities of the vehicle. With that in mind, if solar cells are to be integrated to the wing structure, they should be as light as possible and flexible. The solar modules choden for integration were Powerfilm's© MPT6-75 flexible solar cell modules. These flexible 7.3 × 11.4 cm solar cells are reported by the manufacturer to produce 50 mA of current at 6 V. However, these commercial modules came with an encapsulation that was too thick and stiffened the cells. By removing the encapsulation, the solar modules were thinner and less stiff, making them more compatible with the Mylar membrane. For the first solar cell wing design, six modules were soldered

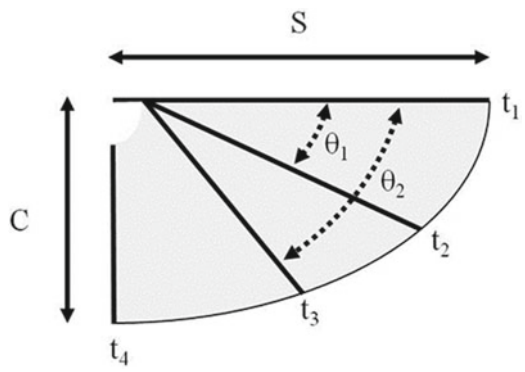

Parameter	Value	Units
S	605.8	Mm
C	362.0	Mm
t_1	3.18	Mm
t_2	1.63	Mm
t_3	1.63	Mm
t_4	1.63	Mm
θ_1	0.358	Rad
θ_2	0.750	rad

Fig. 1.1 Schematic of original Robo Raven wing design

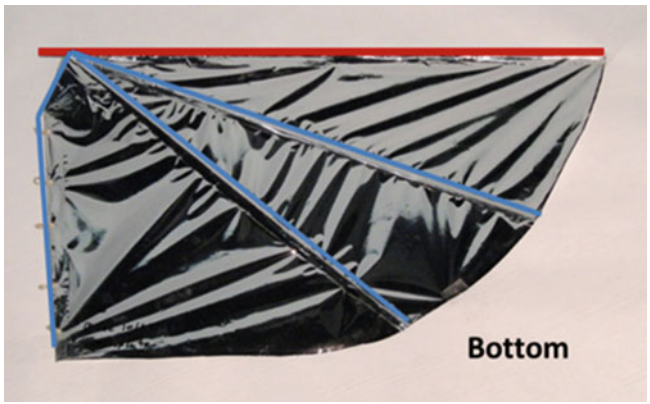

Fig. 1.2 Original fabricated Robo Raven wing

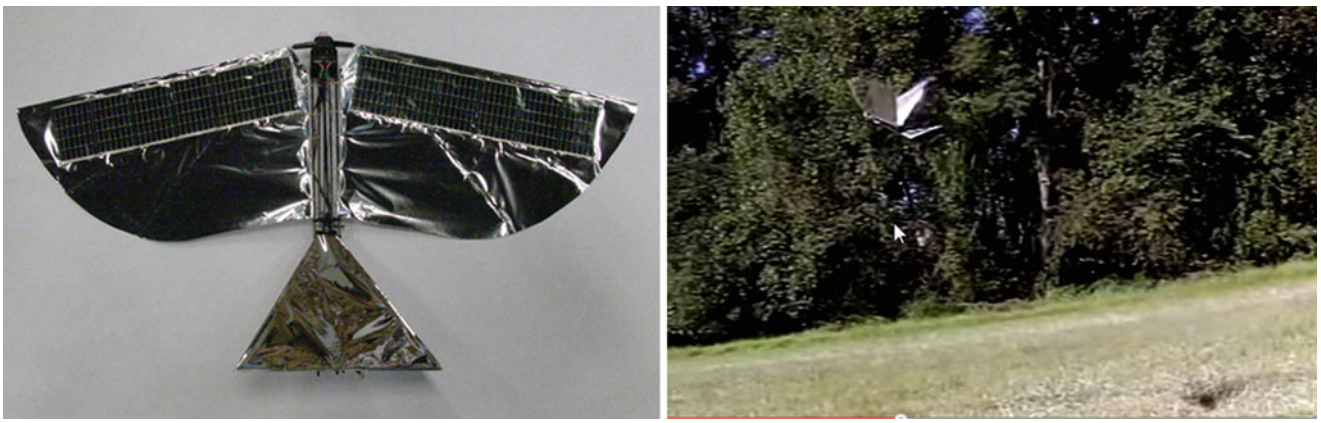

Fig. 1.3 (*Left*) Completed Robo Raven III design. (*Right*) Robo Raven III in flight (see Youtube videos at: https://www.youtube.com/watch?v = t1_mPe8Y0V4 https://www.youtube.com/watch?v=a8x8P5F3qTI)

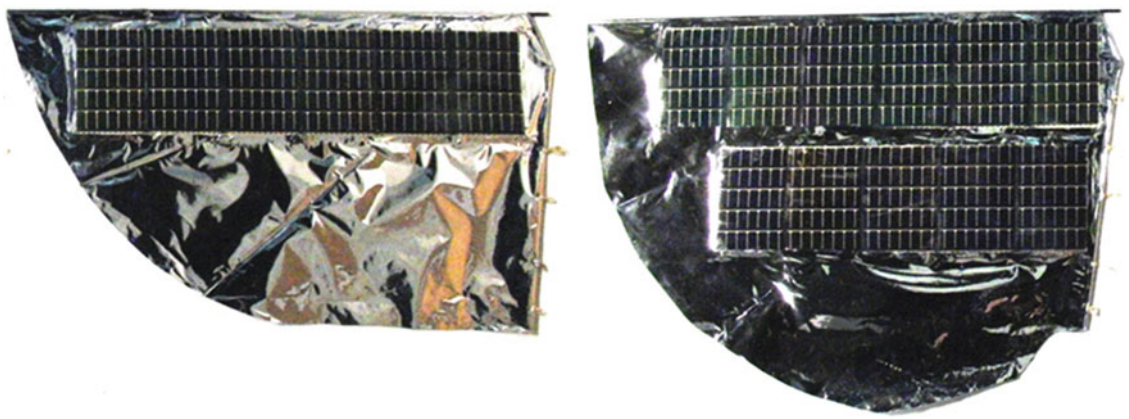

Fig. 1.4 11 module wing compared to the six cell wing

together to one panel for each wing. Each panel was integrated to the front most portion of the wing by cutting out a portion of the Myar and adhering the solar panel in its place. The FWAV would consist of 12 modules adding 20.2 g to the vehicle. This is a 60 % increase in mass for the wing; however, the wing can also produce 3.6 W (Fig. 1.3).

Once the 12 cell FWAV was completed, a flight test was conducted to determine if the vehicle would fly despite the changes that were made. The FWAV was able to sustain flight and climb, making the solar cell integration a success. To test the limits of solar cell integration, more solar modules were integrated to the wings. A second row of five modules was integrated just blow the first row. To achieve flight the wing had to be slightly modified to allow for more deformation to the wing. An additional section of Mylar at the trailing edge of the wing added the necessary compliance to achieve flight for the 22 module FWAV. The completed 11 module wing can be compared to the six module wing in Fig. 1.4. There are three main

differences between the new design and the previous. The first two involve extending carbon fiber tubes in the inside part of the wings to permit increase in wing area and compliance of the wing at the trailing edge. This was achieved by extending the tube closest to the front of the wing (t2) 3.81 cm and extending the lower tube (t3) 5.72 cm. The final modification involved changing the shape of the Mylar skin into a "teardrop".

1.3 Measurement of Lift and Residual Thrust Forces

To determine the change in performance caused by the integration of solar cells, the aerodynamic loads were directly measured in a wind tunnel. A new test stand was developed using a six DOF load cell that enables the lift and thrust forces to be measured simultaneously (Fig. 1.5). This test stand was comprised of an ATI Mini40 six degree of freedom transducer mounted on a wood/Delrin frame. The frame was built to hold the force transducer completely horizontal to the ground. This enabled the forces generated vertically to be collected as pure aerodynamic lift and the forces generated in the forward direction to be residual aerodynamic thrust. The test stand also allowed the UAV to be set to any angle of attack from 0 to 20°. Since the FWAV maintains flight at a 20° pitch, all load cell testing was done at 20°. An aluminum block is bolted to the frame to provide a smooth flat surface on which the load transducer is mounted. This six degree of freedom load cell is capable of measuring up to 40N of force with a resolution of 0.01N in the thrust direction and 120N of force with a resolution of 0.02N in the lift direction. The signal from the Mini40 is sent directly to a National Instruments PXI Data Acquisition Box. The raw signal is saved in National Instrument's Signal Express software. The data is then exported to Microsoft Excel for post-processing.

The FWAV was attached to the test stand and the test stand was placed inside of the wind tunnel. The wind tunnel was activated and the FWAV was flapped at 4 Hz with angular range of 60°. The actual lift and thrust data collected for each wing design can be seen in Fig. 1.6. These profiles were consistent with previous measurements and models of flapping wings for different compliant wing designs where the lift produces a sinusoidal profile consistent with aerodynamic drag while the residual thrust exhibits a double peak [34–36]. The peaks are out of phase which is expected with FWAVs. Because the solar cells stiffen the wings and reduce compliance in sections of the wing structure, it was predicted that the solar cell wings would underperform the regular wings. However, from the profiles it seems that the six module wings actually have slightly larger values for lift compared to the regular wings. The 11 module design had an increase in force generation compared to the original wings. The average values of lift and residual thrust load were found for each trial and can be seen in Table 1.1.

Ideally the residual thrust should average out to 0 g. The wind tunnel used creates a maximum velocity of 6 m/s. The actual flight velocity is 6.7 m/s. The actual payload was found experimentally to determine what the actual lift values were. The payload capacity for Robo Raven during steady-state flight was measured to be 40 g, from which the scaling factor was calculated to be 1.4×. The corrected forces were determined and are shown in Table 1.2.

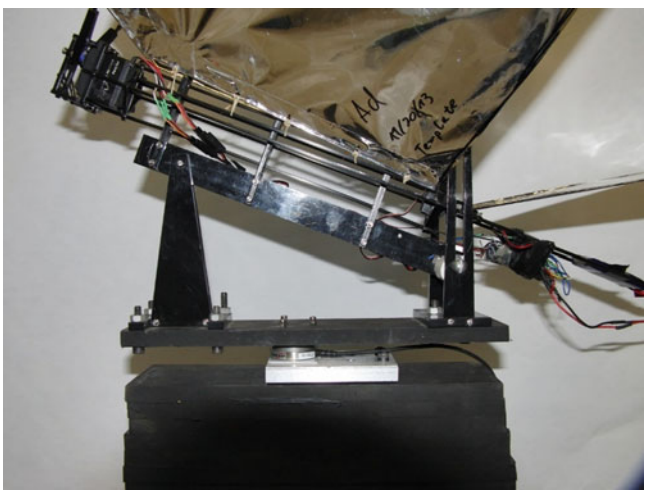

Fig. 1.5 Test stand with six DOF load cell

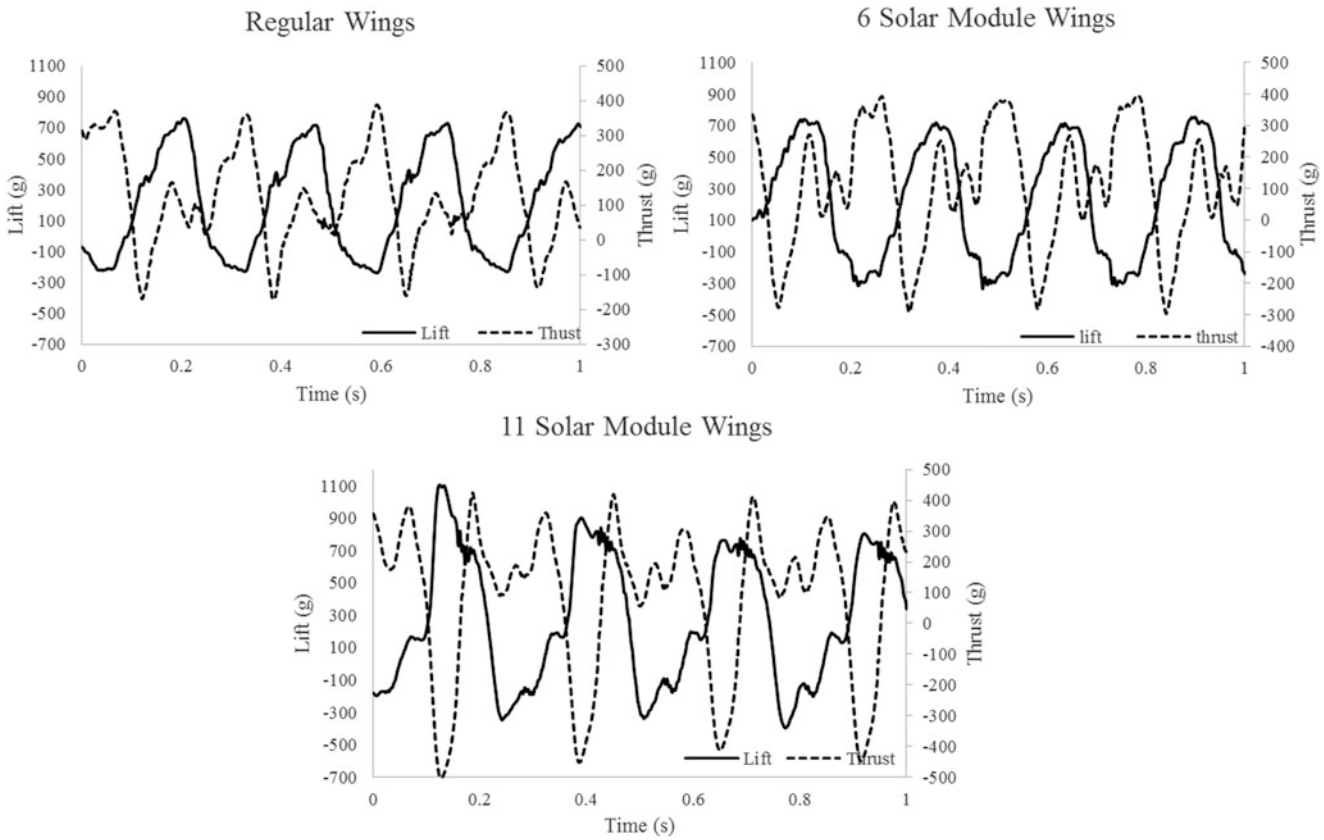

Fig. 1.6 Time resolved load cell results for the three wing designs

Table 1.1 Lift and Residual Thrust loads generated by each wing design

	Regular wings		12 Module FWAV		22 Module FWAV	
	Residual Thrust (g)	Lift (g)	Residual Thrust (g)	Lift (g)	Residual Thrust (g)	Lift (g)
Trial 1	111	208	111	201	81	247
Trial 2	100	208	99	206	74	229
Trial 3	111	207	93	230	82	268
Averages	107	208	101	212	79	248

Table 1.2 Weight and payload of each FWAV design

	Robo Raven	12 Module Robo Raven III	22 Module Robo Raven III
Weight of UAV (g)	290	317	346
Force Magnitude (g)	234	235	260.1
Total Flight Weight (g)	330	332	367
Payload (g)	40	15	21

1.4 Measurement of Deformation and Strain on Wing Surface

Digital Image Correlation (DIC) allows the surface of a body undergoing some deformation to be tracked, observed, and measured. DIC uses digital cameras to track many points on a speckled image and observe the displacement of these point in relationship to each other. Using 3D DIC on the wings allows the deformation of that wing to be observed over many flapping cycles. From these deformations, several strains can be calculated for each wing. This will help explain how the addition of solar cells affects the compliance of the wing.

3D Digital Image Correlation (DIC) using VIC-3D from Correlated Solutions (Columbia, SC) was employed during the wind tunnel testing. For our experiments, two Flea3 FL3-FW-03S1M cameras were used to acquire the high speed images for processing. The wings were recorded flapping at 80 fps allowing 20 images to be taken per flapping cycle at standard flapping frequency of 4 Hz used to achieve flight. The 3D data from each wing gives a better understanding of the differences in the lift and thrust loads acting on the wings. Representative data can be seen in Fig. 1.7. This shows the out of plane displacement (W) for each wing midway through the flapping cycle.

A comparison was made between the time-resolved resolved thrust and aerodynamic lift loads and the average shear strain and biaxial strain respectively of the wing. It was observed that lift force correlated very well with the biaxial strain (Fig. 1.8) where the thrust force correlated with the change in shear (Fig. 1.9) throughout the flapping cycle. As expected, the

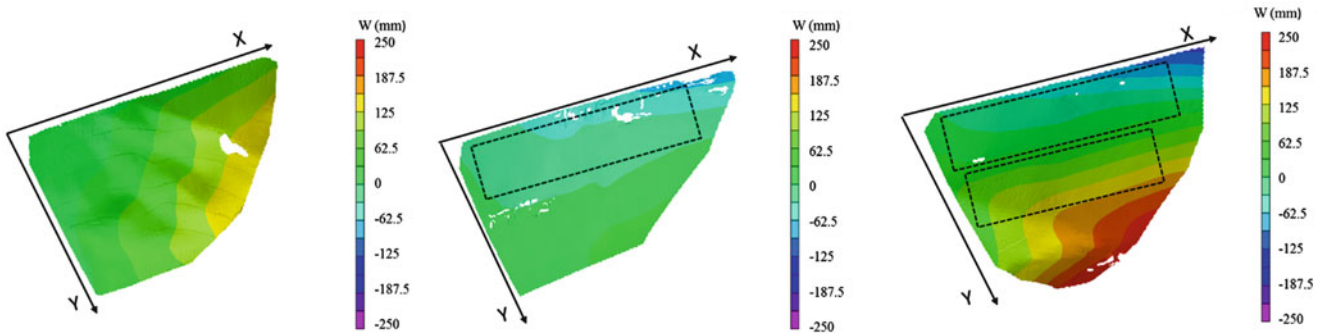

Fig. 1.7 Out of plane displacement (W) for each wing flapping downwards at the horizontal position: (*left*) regular wing, (*middle*) 6 module wing, (*right*) 11 module wing

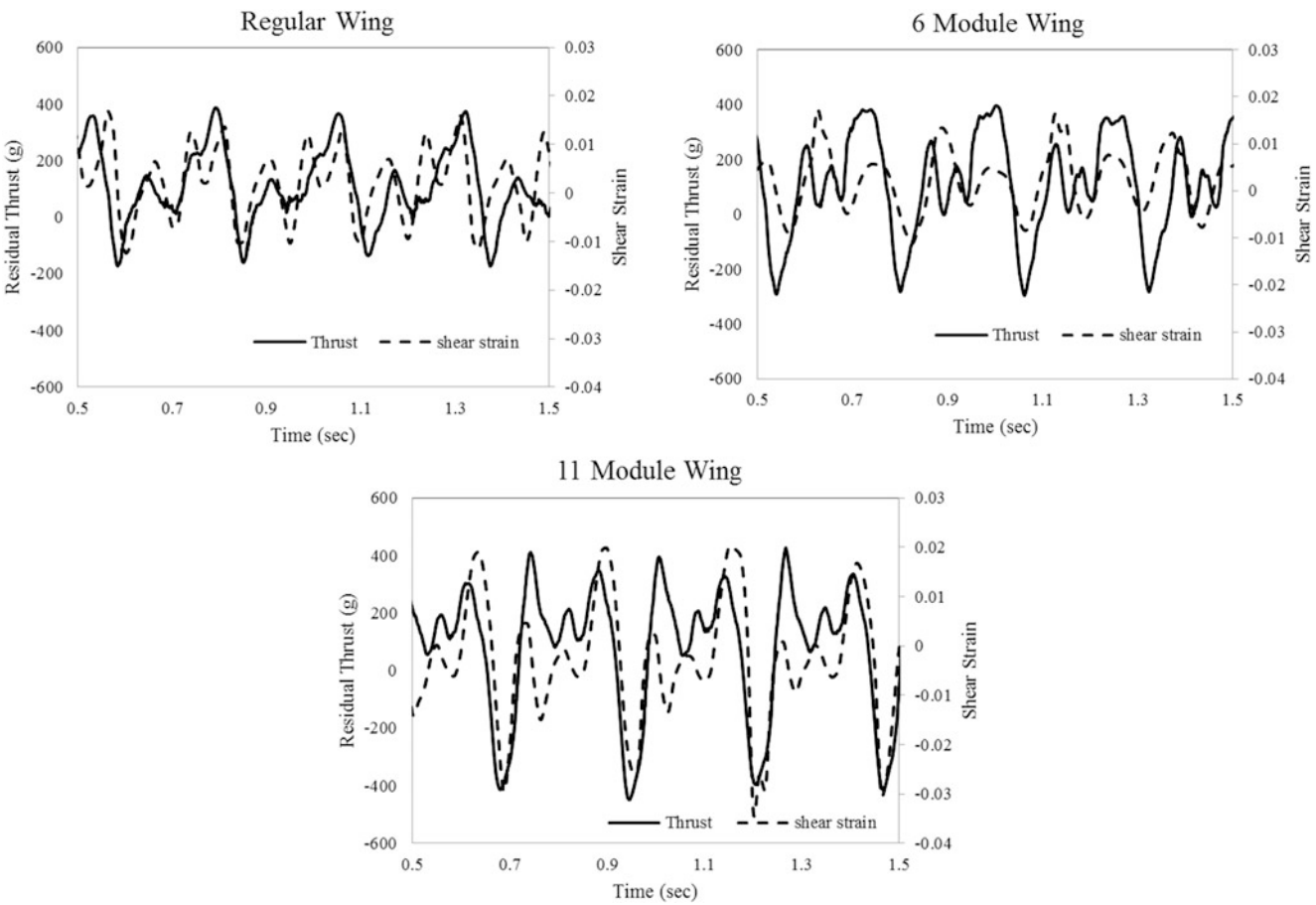

Fig. 1.8 Comparison of time resolved residual thrust and shear strain

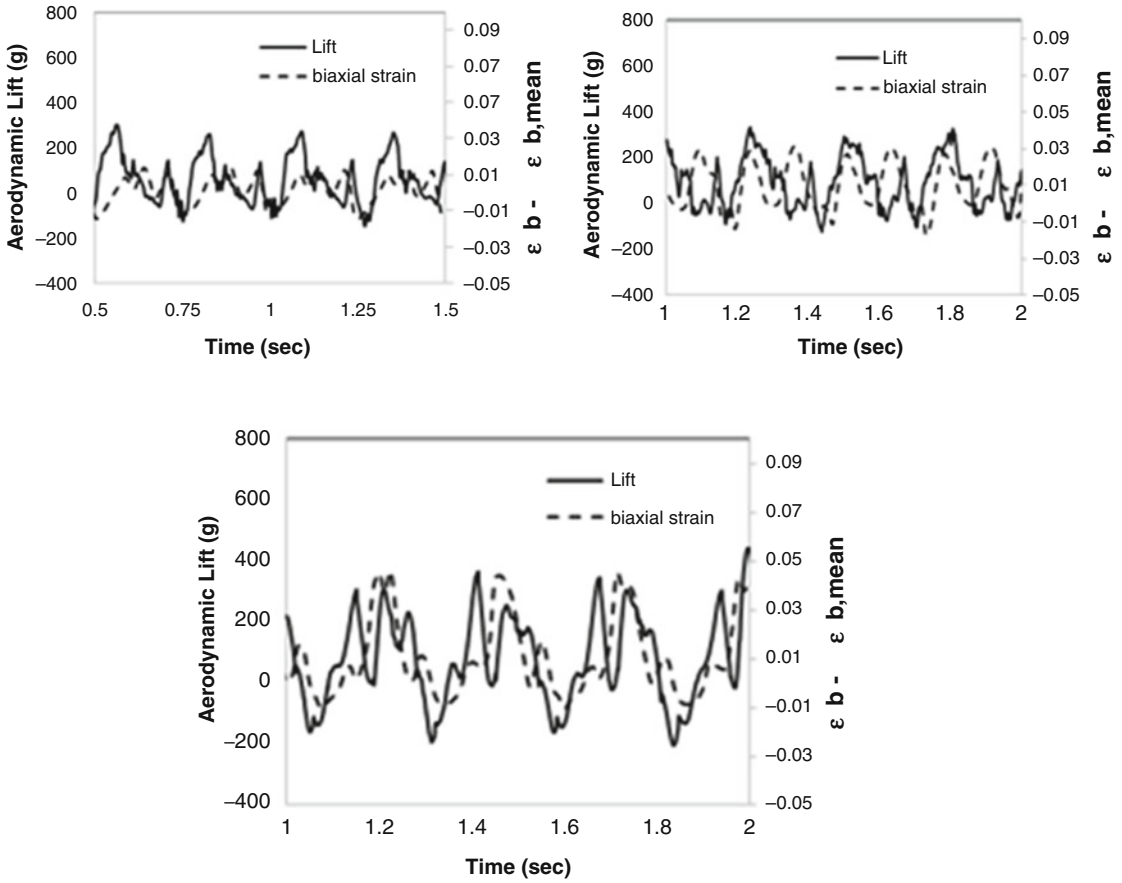

Fig. 1.9 Comparison of time resolved lift and biaxial strain relative to mean shear strain: (*top left*) regular wing, (*top right*) six module wing, (*bottom*) 11 module wing

integration of solar cells increased the stiffness of the wings since the solar cells are stiffer than the Mylar. This in turn reduces the amount of lift and thrust that can be generated; however, adding a larger are for compliance increases the deformation and can allow for these forces to be recovered.

As the majority of the wing becomes covered in solar cells, the deformation of the wing decreases. By observing the time resolved results from the 6 module wings, it is clear that the shear strain decreases as solar cells are added. By increasing the wing size and allowing for more deformation, a large increase in shear strain in the modified 11 module wing is observed. These results are also mirrored in the cyclic results. The shear strain for the six module wing have a much lower value than the regular wings. However, the modified 11 module wings have a much higher shear strain value. This increase in deformation is what allows the 22 module FWAV to maintain flight. The increase stiffness and weight of the solar cells is counteracted by the increase in overall wing deformation.

1.5 Sensing Using Solar Cells

An unexpected multifunctional aspect with the new wings was the new sensing capabilities. In observing the power production of the new solar celled wings, we observed the waveforms produced by the wings. Using a National Instrument's USB-6009 Data Acquisition card, the voltage and current were simultaneously collected while flapping in sunlight. Multiplying these two signals together, the power produced by each wing design was found. The 22 module FWAV produced on average 7.42 W while the 12 module FWAV produced 4.10 W.

By observing the percent change in power output, a double peak wave form was observed. This was similar to the thrust wave form observed from the load cell results. When the two signals were measured at the same time, the signals peaked in

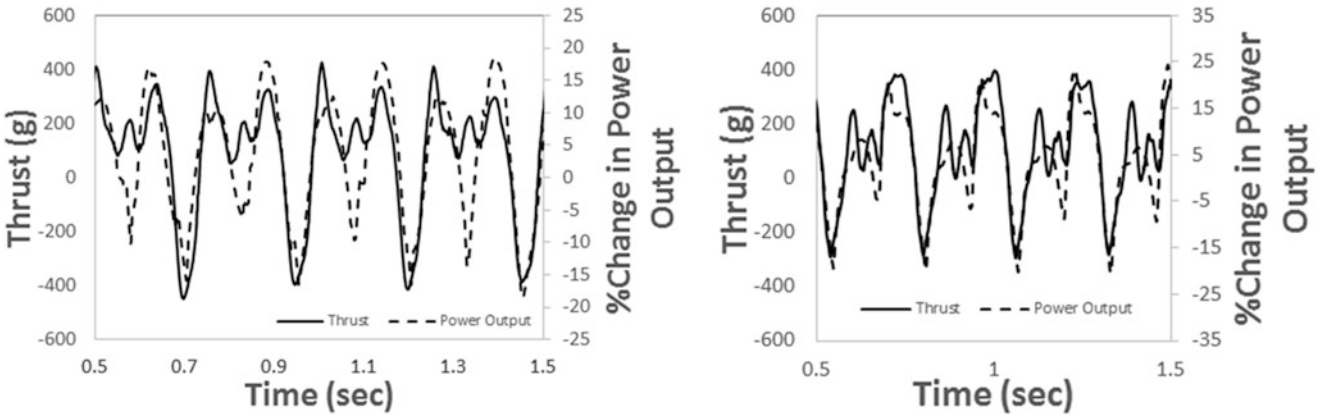

Fig. 1.10 Percent change in power output versus angular deviation in the wing normal vector for the 22 module FWAV

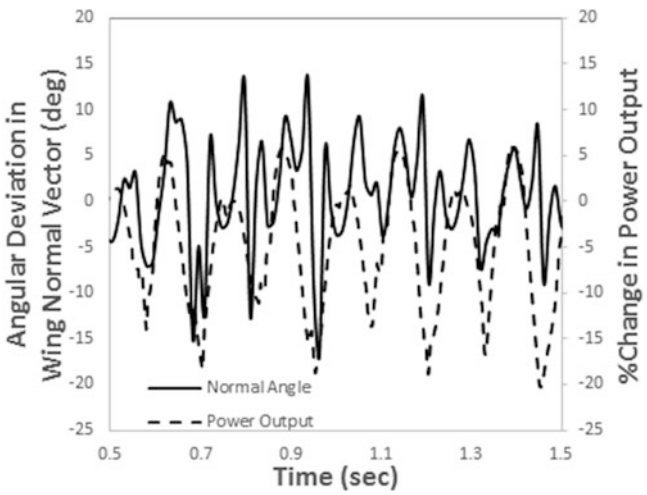

Fig. 1.11 Percent change in power output versus thrust (*left*) 22 module FWAV (*right*) 12 module FWAV

the same locations. This showed that the solar cells may be used to sense changes in thrust production. This change can be used to help with autonomous flight since the robot would be able to respond to changes quicker than the operator.

The mechanics associated with thrust generation have been previously associated with shear strains due to torsional deformations. However, for energy harvesting using solar cells, the primary effect of torsional deformations will be to affect the incidence of light upon the solar cell due to deviations in the angle of the normal vector for the wing. An advantage of using 3D DIC is the ability to directly determine the deviation of the normal vector across the wing. Therefore, the average angular deviations in the normal vector across the wing were compared to the percent change in power output from the solar cells for the 22 module FWAV (Fig. 1.11). It was observed that there was a similar correlation as observed with the thrust in Fig. 1.10. This provided additional confirmation of the relation of the power production of the solar cells to the deformation of the wings that may be used for sensing.

1.6 Conclusions

This paper investigates the effects of integrating flexible solar cells into the compliant wings of a robotic bird. The mechanics of the inherently change due to the increase in stiffness caused by the stiffer solar cells replacing the lightweight Mylar membrane. Adding solar cells makes these wings multifunctional and allows the wings to produce aerodynamic forces, produce electrical power, and sense changes in thrust during the flapping cycle.

Adding solar cells makes the wings less complaint. Adding complainant sections to the wings allows for the forces to be recovered. 12 module and 22 module wings were constructed flown and tested. Load cell tests were conducted to show the

aerodynamic forces being produced by the wings. The increase in mass from the solar cells was still overcome by the amount of lift produced by the FWAVs. To understand the change in deformation, 3D DIC was used to dynamically measure the full-field deformations of the wings during flapping. Using the 3D DIC strain measurements, a correlation between the thrust force produced and the shear strain on the surface of the wings was determined. Similarly, a correlation between lift and biaxial strain was also determined. The power output from the solar cells also correlated to the thrust force produced, as well as the angular deviation in the normal vector of the deformed wing determined using 3D DIC. Thus, these multifunctional wings are also capable of sensing changes in wing deformations and associated aerodynamic forces in real time. The platform produced by this work was named Robo Raven III, and was the first flying robot bird capable of harvesting solar energy harvesting during flight for power.

Acknowledgments This research has been supported by Dr. Byung-Lip "Les" Lee at AFOSR through grant FA95501210158. Opinions expressed in this paper are those of the authors and do not necessarily reflect opinions of the sponsors.

References

1. Gerdes, J.W., Gupta, S.K., Wilkerson, S.: A review of bird-inspired flapping wing miniature air vehicle designs. ASME J. Mech. Robot. **4** (2), 021003.1-021003.11(2012)
2. Kumar, V., Michael, N.: Opportunities and challenges with autonomous micro aerial vehicles. Int. J. Robot. Res.**31**(11), 1279-1291 (2012)
3. Pines, D.J., Bohorquez, F.: Challenges facing future micro-air-vehicle development. J. Aircr. **43**(2), 290–305 (2006)
4. Sane, S.P., Dickinson, M.H.: The aerodynamic effects of wing rotation and a revised quasi-steady model of flapping flight. J. Exp. Biol. **205**, 1087–1096 (2002)
5. de Croon, G.C.H.E., de Clerq, K.M.E., Ruijsink, R., Remes, B., de Wagter, C.: Design, aerodynamics, and vision-based control of the delfly. Int. J. Micro Air Vehicles **1**(2), 71–97 (2009)
6. Muijres, F.T., Johansson, L.C., Barfield, R., Wolf, M., Spedding, G.R., Hedenstrom, A.: Leading-edge vortex improves lift in slow-flying bats. Science **319**, 1250–1253 (2008)
7. Zhao, L., Huang, Q., Deng, X., Sane, S.: Aerodynamic effects of flexibility in flapping wings. Interface, **7**(44):485-97 (2009)
8. Arabagi, V., Hines, L., Sitti, M.: Design and manufacturing of a controllable miniature flapping wing robotic platform. Int. J. Robot. Res. **31** (6), 785–800 (2012)
9. Mahjoubi, H., Byl, K.: Trajectory tracking in the sagittal plane: decoupled lift/thrust control via tunable impedance approach in flapping-wing MAVs. American Control Conference (ACC). (2013)
10. Keennon, M., et al.: Development of the nano hummingbird: a tailless flapping wing micro air vehicle. Presented at 50th AIAA aerospace sciences meeting, Nashville, Tennessee 2012
11. Pornsin-Sirirak, T., Tai, Y., Ho, C., Keennon, M.: Microbat: a palm-sized electrically powered ornithopter. In: Proceedings of the NASA/JPL Workshop on Biomorphic Robotics, Pasadena, CA 2001
12. Mueller, T.J.: Fixed and flapping wing aerodynamics for micro air vehicle applications. American Institute of Aeronautics and Astronautics, Reston, VA (2001)
13. Yang, L.J., Hsu, C.K., Ho, J.Y., Feng, C.K.: Flapping wings with PVDF sensors to modify the aerodynamic forces of a micro aerial vehicle. Sens. Actuators, A (2007)
14. Hsu, C.K., Ho, J.Y., Feng, G.H., Shih, H.M., Yang, L.J.: A flapping MAV with PVDF-parylene composite skin. In: Proceedings of the Asia-Pacific Conference of Transducers and Micro-Nano Technology (2006)
15. Tsai, B.J., Fu, Y.C.: Design and aerodynamic analysis of a flapping-wing micro aerial vehicle. Aerosp. Sci. Technol. **13**(7), 383–392 (2009)
16. Hsu, C.K., Evans, J., Vytla, S., Huang, P.: Development of flapping wing micro air vehicles—design, CFD, experiment and actual flight. In: 48th AIAA Aerospace Sciences Meeting, Orlando, FL (2010)
17. Cox, A., Monopoli, D., Cveticanin, D., Goldfarb, M., Garcia, E.: The development of elastodynamic components for piezoelectrically actuated flapping micro-air vehicles. J. Intell. Mater. Syst. Struct. **13**, 611–615 (2002)
18. Yan, J., Wood, R.J., Avadhanula, S., Sitti, M., Fearing, R.S.: Towards flapping wing control for a micromechanical flying insect. In: Proceedings ICRA. IEEE International Conference on Robotics and Automation (2001)
19. Fenelon, M.A.A., Furukawa, T.: Design of an active flapping wing mechanism and a micro aerial vehicle using a rotary actuator. Mech. Mach. Theory (2009)
20. Jones, K.D., Bradshaw, C.J., Papadopoulos, J., Platzer, M.F., Improved performance and control of flapping-wing propelled micro air vehicles. In: Proceedings of the AIAA 42nd Aerospace Sciences Meeting and Exhibit, Reno, NV (2004)
21. Zdunich, P., Bilyk, D., MacMaster, M., Loewen, D., DeLaurier, J., Kornbluh, R., Low, T., Stanford, S., Holeman, D.: Development and testing of the mentor flapping-wing micro air vehicle. J. Aircr. **44**(5), 1701–1711 (2007)
22. Madangopal, R., Khan, Z., Agrawal, S.: Biologically inspired design of small flapping wing bird vehicles using four-bar mechanisms and quasi-steady aerodynamics. J. Mech. Des., **127**(4), 809-817 (2005)
23. Bejgerowski, W., Ananthanarayanan, A., Mueller, D., Gupta, S.K.: Integrated product and process design for a flapping wing drive-mechanism. J. Mech. Des., **131**(6), 061006 (2009)
24. Mueller, D., Gerdes, J.W., Gupta, S.K.: Incorporation of passive wing folding in flapping wing miniature air vehicles. ASME Mechanism and Robotics Conference, San Diego, CA (2009)

25. Bejgerowski, W., Gupta, S.K., Bruck, H.A.: A systematic approach for designing multifunctional thermally conducting polymer structures with embedded actuators. J. Mech. Des., **131**(11), 111009-111009-8 (2009)
26. Gerdes, J., Holness, A., Perez-Rosado, A., Roberts, L., Greisinger, A.J.G., Barnett, E., Kempny, J., Lingam, D., Yeh, C.H., Bruck, H.A., Gupta, S.K.: Design, manufacturing, and testing of Robo Raven. Advanced Manufacturing Lab Technical Report, University of Maryland, College Park, MD (2014)
27. Perez-Rosado, A., Griesinger, A.J.G., Bruck, H.A., Gupta, S.K.: Performance characterization of multifunctional wings with integrated solar cells for miniature air vehicles. In: ASME 2014 International Design Engineering Technical and Computers and Information in Engineering Conference, Buffalo, NY, 2014
28. Gerdes, J.W., Holness, A., Perez-Rosado, A., Roberts, L., Greisinger, A., Barnett, E., Kempny, J., Lingam, D., Yeh, C.H., Bruck, H.A., Gupta, S.K.: Robo Raven: a flapping-wing air vehicle with highly compliant and independently controlled wings. Soft Robot., **1**(4), 275-288 (2014)
29. Nemat-Nasser, S., Plaistead, T., Starr, A., Amirkhizi, A.: Multifunctional materials. In: Bar-Cohen, Y. (ed.) Biomimetics: biologically inspired technologies. CRC Press, Boca Raton, FL (2005)
30. Thomas, J.P., Qidwai, M.A.: The design and application of multifunctional structure-battery materials systems. JOM **57**(3), 18–24 (2005)
31. Ma, K.Y., Chirarattananon, P., Fuller, S.B., Wood, R.J.: Controlled flight of a biologically inspired, insect-scale robot. Science **340**, 603–607 (2013)
32. Thomas, J.P., et al.: Multifunctional structure-plus-power concepts., 43rd AIAA/ASME/ASCE/AHS/ASC Structures, Structural Dynamics, and Materials Conference, Denver, CO (2002)
33. Wissman, J., Perez-Rosado, A., Edgerton, A., Levi, B.M., Karakas, Z.N., Kujawski, M., Phillips, A., Papavizas, N., Fallon, D., Bruck, H.A., Smela, E.: New compliant strain gauges for self-sensing dynamic deformation of flapping wings on miniature air vehicles. Smart Mater. Struct., **22**(8), 085031 (2013)
34. Mueller, D., Bruck, H.A., Gupta, S.K.: Measurement of thrust and lift forces associated with drag of compliant flapping wing air micro air vehicles using a new test stand design. Exp. Mech. **50**(6), 725–735 (2010)
35. Gerdes, J.W., Roberts, L., Barnett, E., Kempny, J., Perez-Rosado, A., Bruck, H.A., Gupta, S.K.: Wing performance characterization for flapping wing air vehicles. ASME Mechanism and Robotics Conference, Portland, OR (2013)
36. Gerdes, J.W., Cellon, K.C., Bruck, H.A., Gupta, S.K.: Characterization of the mechanics of compliant wing designs for flapping-wing miniature air vehicles. Exp. Mech. **53**(9), 1561–1571 (2013)

Chapter 2
Optimization of Magnetic and Electrical Properties of New Aluminium Matrix Composite Reinforced with Magnetic Nano Iron Oxide (Fe_3O_4)

L.-M.-P. Ferreira, E. Bayraktar, M.-H. Robert, and I. Miskioglu

Abstract The utility of new permanent magnetic materials and their continual improvement became an attractive area for the academic and industrial partners. In the modern technology, there is no scene of permanent magnet applications decaying in near future. Naturally, there are optimistic prospects for innovative applications, especially if the properties of cost-effective magnetic pieces can be manufactured to new requirements such as corrosive and wear stability and/or high temperature applications, etc. Today, permanent magnets are unique in their capability to deliver magnetic flux into the air gap of a magnetic circuit without any continuous expenditure of energy. Aluminium matrix composite materials are used in aeronautical, aerospace, defence and automotive applications especially in the thermal management areas. Aluminium Matrix Composites (AMCs) reinforced with Nano Iron Oxide (Fe_3O_4) exhibit good physical and mechanical behaviour (electrical conductivity and magnetic permeability), which makes it an excellent multifunctional lightweight material. In the frame of this present work, low cost-effective permanent magnetic composites are proposed by using Aluminium Matrix Composites (AMCs) reinforced basically with Nano Iron Oxide (Fe_3O_4) and also addition of other reinforcement alloying elements such Nickel Oxide (NiO) have stabilized the structure. As for magnetic iron oxide, it is very easy to produce as nanoscale particles that were presented in the former papers. Magnetic iron oxide nanoparticles (Fe_3O_4) with a lattice parameter 0.8397 nm are very adaptable for new electromagnetic applications. Cost reduction can be obtained by reducing the total raw material cost as well as more efficient manufacturing and assembly. Electromagnetic applications such as electric motors, fast switching actuators or inductor cores for power electronics. As well-known pulse transformers (e.g. ignition systems) operate in high and transient magnetic fields. High resistivity products have specifically been developed to maintain low eddy-current losses in large cross-sections. Owing to the good magnetic and electrical properties, magnetite iron oxide (Fe_3O_4) is one of the favored and paramount characterized filler materials. The present paper is based on low cost manufacturing of light and efficient materials for aeronautical and automotive applications by creating these new type of composites based on aluminium matrix (AMCs) reinforced with Magnetic Nano Iron Oxide.

Keywords Aluminium matrix composites • Magnetic oxide • Electrical conductivity • Magnetic permeability

2.1 Introduction

The utility of new permanent magnetic materials and their continual improvement became an attractive area for the academic and industrial partners. In the modern technology, there is no scene of permanent magnet applications decaying in near future [1–3]. Naturally, there are optimistic prospects for innovative applications, especially if the properties of cost-effective magnetic pieces can be manufactured to new requirements such as corrosive and wear stability and/or high temperature applications, etc. Today, permanent magnets are unique in their capability to deliver magnetic flux into the air gap of a magnetic circuit without any continuous expenditure of energy [4–11].

L.-M.-P. Ferreira • M.-H. Robert
Mechanical Engineering Faculty, University of Campinas, UNICAMP, Campinas, Brazil

E. Bayraktar (✉)
Mechanical Engineering Faculty, University of Campinas, UNICAMP, Campinas, Brazil

Supmeca – Paris, School of Mechanical and Manufacturing Engineering, Saint-Ouen, France
e-mail: bayraktar@supmeca.fr

I. Miskioglu
ME-EM Department, Michigan Technological University, Houghton, MI, USA

C. Ralph et al. (eds.), *Mechanics of Composite and Multi-functional Materials, Volume 7*,
Conference Proceedings of the Society for Experimental Mechanics Series, DOI 10.1007/978-3-319-21762-8_2

In the frame of this present work, low cost-effective permanent magnetic composites are proposed by using Aluminium Matrix Composites (AMCs) reinforced with Nano Iron Oxide (Fe_3O_4) that has good electrical conductivity and magnetic permeability. As for magnetic iron oxide, it is very easy to produce as nanoscale particles that were presented in the former papers [3]. Magnetic iron oxide nanoparticles (Fe_3O_4) with a lattice parameter 0.8397 nm are very adaptable for new electromagnetic applications. Cost reduction can be obtained by reducing the total raw material cost as well as more efficient manufacturing and assembly. Electromagnetic applications such as electric motors, fast switching actuators or inductor cores for power electronics. As well-known pulse transformers (e.g. ignition systems) operate in high and transient magnetic fields. High resistivity products have specifically been developed to maintain low eddy-current losses in large cross-sections [9–17]. Owing to the good magnetic and electrical properties, magnetite (Fe_3O_4) is one of the favored and paramount characterized filler materials.

The present paper is based on low cost manufacturing of light and efficient materials for aeronautical applications by creating the composites based on aluminium matrix (AMCs) reinforced with Magnetic Nano Iron Oxide.

2.2 Experimental Conditions

The preparation of Fe_3O_4 magnetic nano-particles was exclusively adapted from our simple low-cost method that was carried out at the chemical processing laboratory in Paris [1–3].

Low Cost Manufacturing of the Composite Samples. A simple tubular ceramic oven was used to prepare sintering as an effective method. The compact geometry was prepared from aluminium and iron oxide (Fe_3O_4) powders. Aluminium with a purity of 99.7 % was used as the base material (Merck Co, France) with a grain size of <2 μm. The purity level of Fe_3O_4 was found to be 99.62 %. Distributions of the particle size are variable (45–70 nm). The mixtures were blended homogeneously in ball milling (4000–6000 rpm) during 2 h.

These Al matrix composites have given higher mechanical properties and homogeneous microstructure as indicated in the former reports [1, 2]. Then, blended powders were compacted by cold isostatic pressing (CIP) with a green compact pressure of 250 MPa, intending to produce an initial green density ranging from 85 % to 95 %. The aspect ratio of this geometry was 0.85. Sintering conditions were carried out under argon atmosphere to prevent the oxidation during the sintering. Sintering temperature was fixed for all the specimens as 600 °C in ceramic tubular oven. Three basic compositions were prepared for this present work. They are called AF-10A, AF-20A and AF-30A, respectively depending on the increasing amount of the magnetic nano iron oxide. All of the compositions contain 2 % Nickel powder and only one composition (AF20A) is compared regarding to two different nickel percentages (2 % and 4 %); they are called AF20A-2 and AF-20A-4 respectively. All of the measurements of the density and porosity of the specimens were carried out by pycnometer (digital density meters, Webb and Orr, 1997 work with helium gas) before and after sintering and the results were then compared. Measurements of magnetic properties essentially magnetization and hysteresis loop of the specimens were performed at room temperature using a special type commercial GMW vibrating sample magnetometer VSM 3474-140. This supplies the coercive force, remanence, saturation magnetization, etc. and also gives information about the magnetization process. Microstructures of the composites processed here were observed by using Optical (OM) and Scanning Electron Microscopy (JOEL-SEM) adapted with EDS and XRD (X-Ray-Diffraction) Analyses.

2.3 Results and Discussion

Microstructural Evaluation. Magnetic iron oxide powder obtained by chemical process and interface with Al matrix in different percentage, it means that depending on the magnetic nano iron oxide is given in the Fig. 2.1 as AF-10, AF-20 and AF-30 indicated as increasing amount of iron oxide, respectively. In general way, the process of these composites should be doped with certain elements before making mixture. Here, doping of iron oxide with certain elements at the first stage of alloying aluminium resulted in a more homogenous composite. Mixture and fusion of the iron oxide and aluminium after 2 h and microstructures of the three composites were indicated in the Fig. 2.2.

In reality homogenous distribution is related to the well-mixture of the composite powders. Even if there is a homogenous distribution of iron oxide in the matrix, it is worth to mix carefully due to fast heating of the powder (pure aluminium and Fe_3O_4). In the three compositions designed here, one may observe that iron oxide was dispersed homogeneously and continuously in the aluminium matrix, mainly around the grain boundaries of aluminium (Fig. 2.3). Also addition of zinc

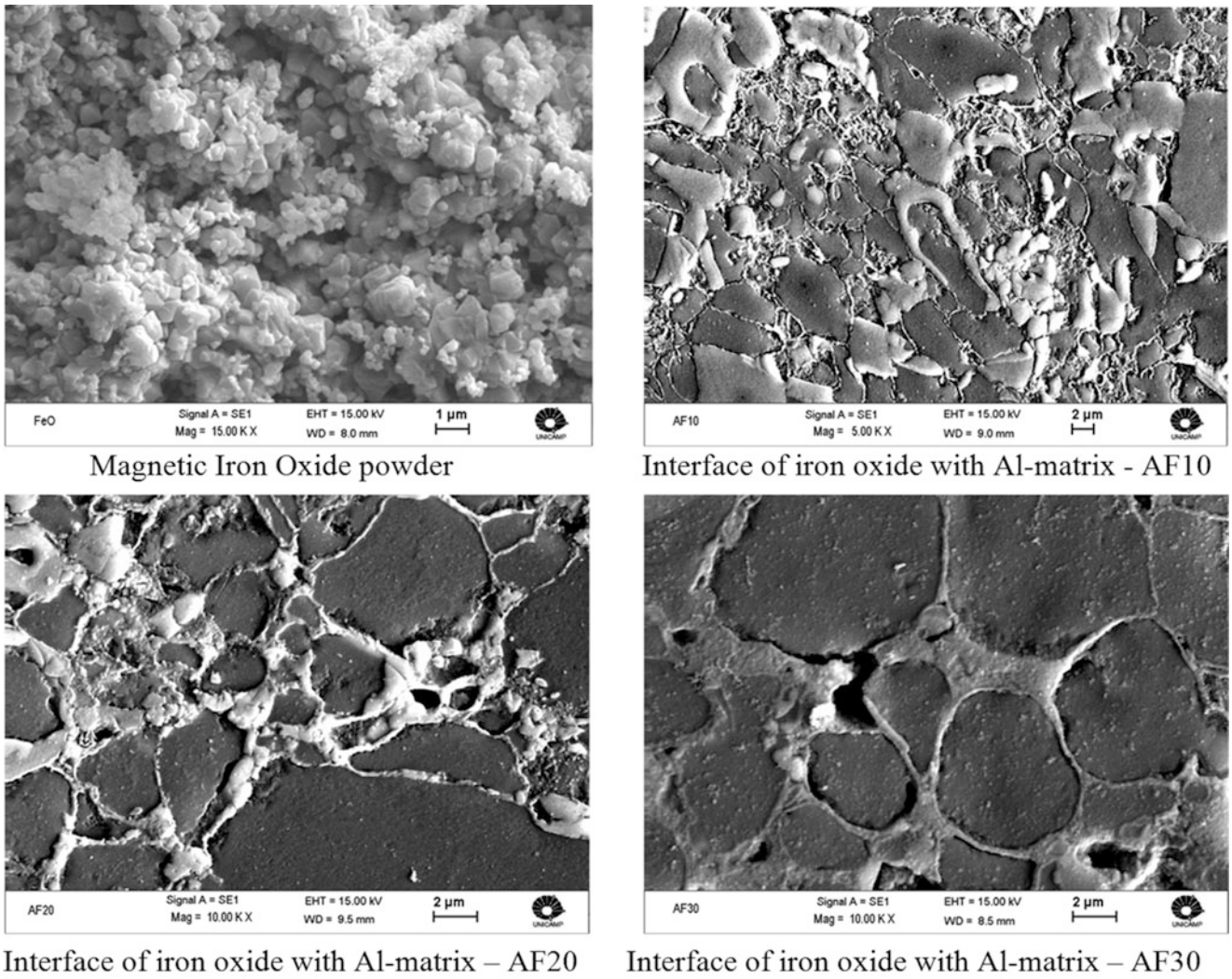

Fig. 2.1 Magnetic Iron Oxide powder obtained by chemical process and interface with Al matrix in different percentage

stearate during ball milling has prevented the joining and agglomeration phenomena and helped to improve the distribution of the alloying elements in the structure.

Even mixture and sintering process were made under carefully laboratory conditions, micro porosities were appeared between the matrix and the reinforcement particles. It is necessary to carry out the sintering process under vacuum and argon gas applications (Fig. 2.4).

X-Ray Diffraction (XRD) Analysis was made for the three composites of AF. Here, only an example, distribution of iron oxide on the fracture surface and XRD analysis taken from the same composite of AF10A were indicated in the Fig. 2.5. Under the laboratory conditions carried out here, all of the three composites show the same intensity level. In the same way, Density measurements have been done by means of "He" gas pycnometer (digital density meters):

All of the three composites have given almost the same density; the density value is lightly variable from 2.5 to 3 g/cm^3 with increasing of Fe_3O_4 contents, as reinforcements, AF10A, AF20A and AF30A, respectively.

Measurements of Electrical Properties. Electrical properties (resistivity and conductivity) were measured by means of a measurement device called "The Agilent 4338B". Five specimens were measured for each composition and the values were given as a mean value in the Table 2.1. For measurements, DC were regulated power supply voltage and current as 20V and 20A respectively. Acquisition Card "NI9234" was connected in parallel with the output of the power to outcome the acquisition of the voltage (voltage input accuracy was 24 bites). A high precision multi-meter "Agilent U1253N" was connected in series for measuring the intensity (A). All the measurements were displayed as the final data by means of with

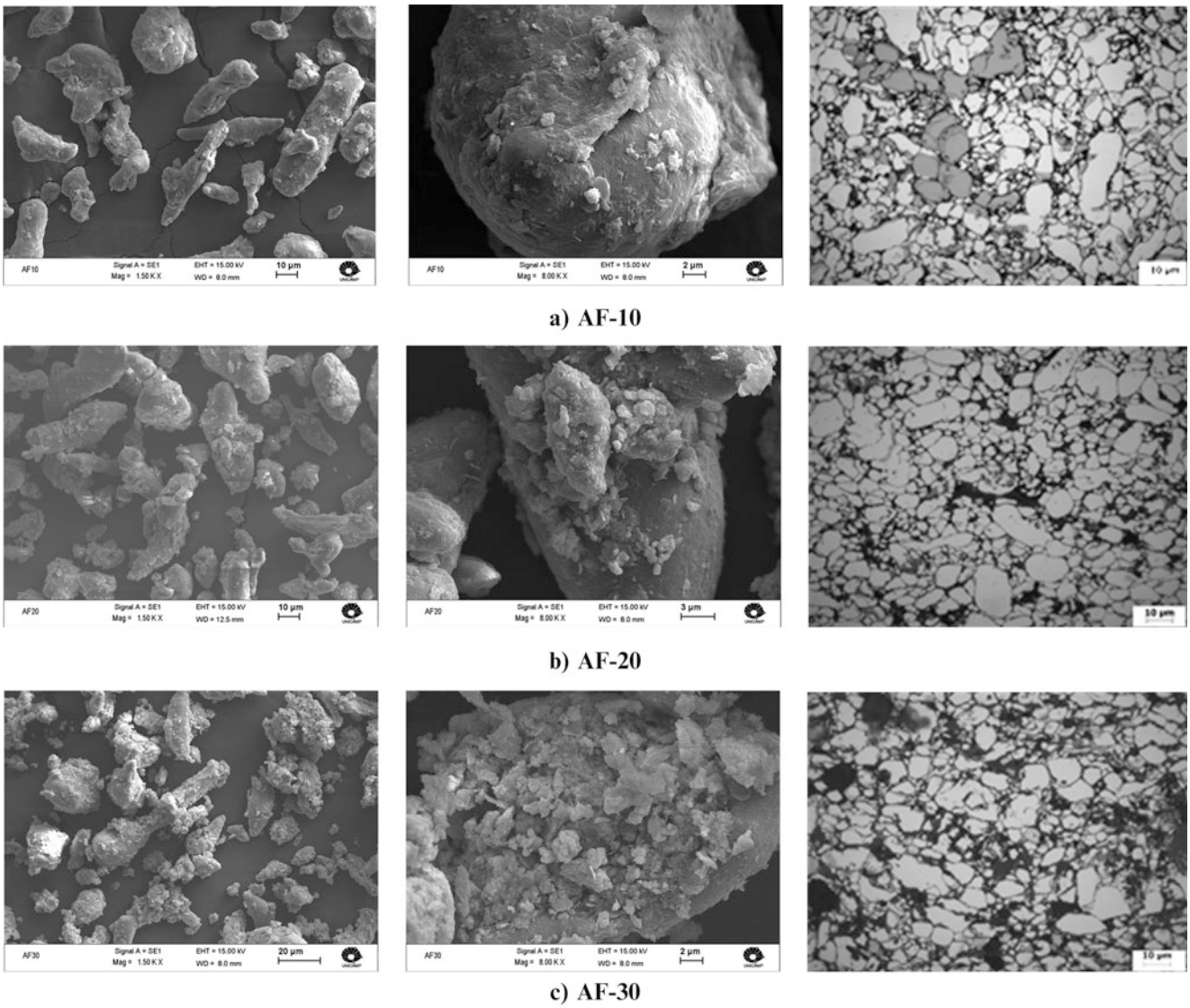

Fig. 2.2 Mixture and fusion of the iron oxide and aluminium after 2 h and microstructures of the three composites

the "Lab view". It is worth to remark that these results were given under laboratory conditions used in the present work. Naturally, the composites given here as three compositions were prepared carefully according the standard given in the notice of the measurement device but the form, micro porosity and surface conditions of the each sample can easily influence the measurements. That is the reason that all the specimens were produced in the same conditions and polished carefully both of the surfaces to keep a parallelism. Five specimens were also prepared for pure aluminium alloy without iron oxide in order to make a comparison under laboratory conditions. These results evidently should be considered as indicative results and it seems that form and surface conditions should be improved again.

Magnetic Property of Aluminium/Fe_3O_4 Composites. In general meaning, magnetic properties of the structures can be improved with small grain size especially in the nanoscale [5–9, 13–17]. As shown in the Fig. 2.6, the increase in the percentage of particles (Fe_3O_4) increased the magnetic properties of the composite studied.

The field dependence of magnetization measured was presented in the Fig. 2.6a, b and c depending on the percentage amount of magnetic iron oxide reinforcements. Magnetic properties; magnetic saturation and the normalized curve and comparison of the composites containing different amount of magnetic iron oxide (in increment of the percentages) were presented in Fig. 2.6d and e, respectively.

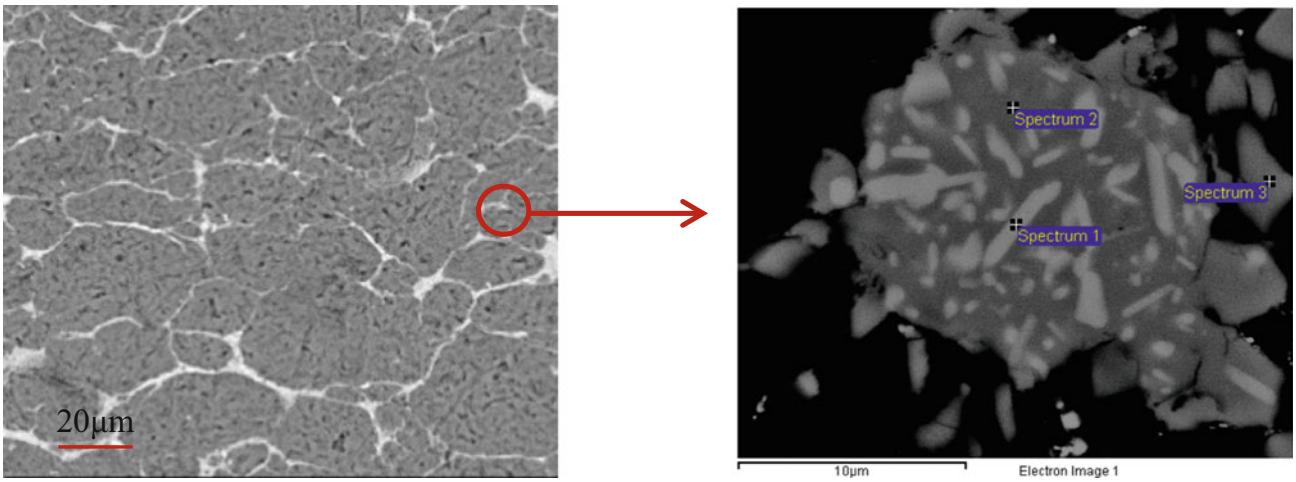

a) AF-10 b) Detail of AF-10

Spectrum AF10	O	Al	Fe	Ni	Cu	Total
Spectrum 1	1.62	63.19	26.09	7.22	1.88	100
Spectrum 2		68.05	19.03	11.55	1.38	100
Spectrum 3	4.42	70.62	14.24	8.91	1.81	100

Fig. 2.3 Distribution of iron oxide in the matrix for the samples of AF-10 and a detail of distribution of iron oxide at matrix (EDS results are also given taken from 3 spectrums, SEM)

As indicated in the former papers [3, 9–17], a basic and important parameter in the characterization of soft magnetic materials is the power loss; this kind of power gives a measure of the energy density available in the material for a specific application.

Data from the analysis of the hysteresis curve as the saturation magnetization (M_s), remanence magnetization (M_r), coercive field (H_c), the relationship between M_r and M_s and susceptibility (X_m) are presented in Table 2.2.
Figure 2.6f and g indicate the effect of the nickel amount on the variation of magnetization (M_s) and coercivity (H_c) with together Fe_3O_4 content. As known, the value of M_s must be maximized as much as possible to confirm a better response under the application of the pieces. In this work the highest saturation magnetization was presented by the composite with AF30A (at the level of 25–30 % Fe_3O_4). But one may remark here on the AF-20; the values obtained for AF-20 and AF30 should be similar if the sintering conditions are improved and also more homogeneous distribution should be required for making more detail comparison between AF20 and AF30. As for the nickel effect, it seems there is not so remarkable effect on the variation of magnetization (M_s) and coercivity (H_c) with together Fe_3O_4 content. As indicated at the experimental conditions, a short comparison with nickel was made only on one composition called AF20A. As indicated just above, all of the compositions prepared here contain 2 w% Ni. Only one additional composition was prepared with AF20A that contains two different amount of nickel, 2 w% and 4 w% respectively. All of these values are indicative, that should be required more experimental work.

As summary from general interpretation of the results given in the Figures from 2.6a to g show a short evolution of magnetization (M_s) and coercivity (H_c) with Fe_3O_4 content. The coercivity (H_c) decreases very keen with increase in the percentage of Fe_3O_4. In the other hand, magnetization (M_s) increases with increase in the percentage of Fe_3O_4. It means that H_c is inversely proportional to M_s. One may remark from these curves that the H_c values do not change for low content of iron oxide (10 and 20) as expected.

All of these results present a similar behaviour and the maximum H_c value is near 200G. This behaviour should be expected because the structure does not show so high purity homogeneous and the distribution of magnetic iron oxide particles in the matrix (even if they are in the grain boundaries in the regular way) is not so perfect, they are locally agglomerated as in the small islets. It should be considered also the role of the copper particles added in the structure even if its percentage is too low. Starting from a demagnetized state of the hysteresis loop, the inclination of the initial curve is

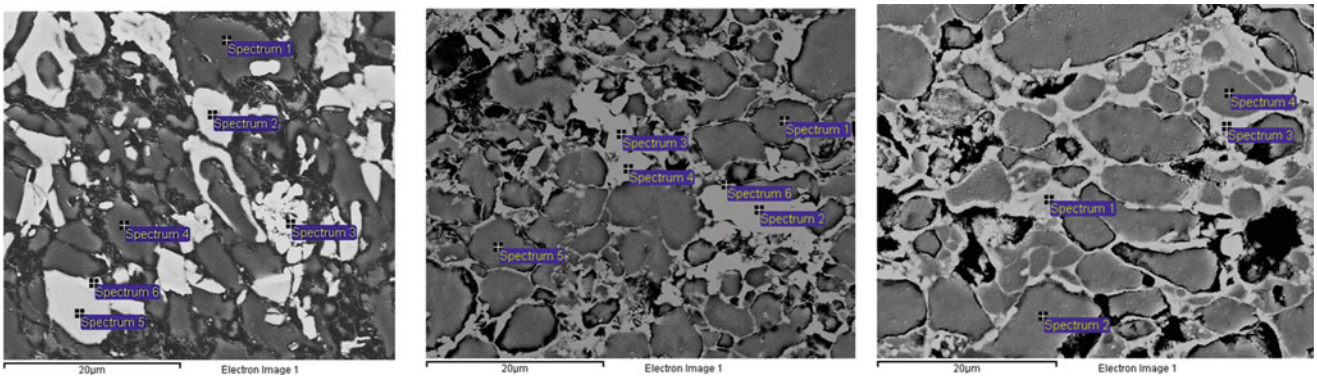

AF10 AF20 AF30

Spectrum AF10	O	Al	Si	Fe	Ni	Cu	Zn	Total
Spectrum 1	0.85	94.95		0.62		1.72	1.86	100
Spectrum 2		67.85		17.70	12.78	1.67		100
Spectrum 3	1.90	50.41	0.40	13.30	3.49	30.49		100
Spectrum 4		96.13				1.98	1.89	100
Spectrum 5		68.03		17.95	14.02			100
Spectrum 6	6.05	49.85	0.47	8.88	4.34	30.41		100

Spectrum AF20	O	Al	Si	Fe	Ni	Cu	Zn	Total
Spectrum 1	1.06	96.18		0.63		2.13		100
Spectrum 2	0.84	61.80		3.19	27.49	6.68		100
Spectrum 3	7.59	41.54		2.13	13.96	34.78		100
Spectrum 4	0.99	61.32		2.54	27.87	7.28		100
Spectrum 5	1.09	95.61		0.83		2.47		100
Spectrum 6	15.65	64.13	0.39	3.92	4.03	7.85	4.02	100

Spectrum AF30	O	Al	Si	Fe	Ni	Cu	Zn	Total
Spectrum 1	26.26	6.77	0.55	63.90			1.42	100
Spectrum 2	2.47	94.09		1.32		2.12		100
Spectrum 3	19.77	6.04	1.07	68.24	1.77		1.77	100
Spectrum 4	3.19	93.19		1.46		2.16		100

Fig. 2.4 Distribution of iron oxide in the matrix for the samples of AF-10A, AF20A, AF30A, respectively and detail of distribution of iron oxide at matrix (EDS results are also given taken from different zones as spectrums, SEM)

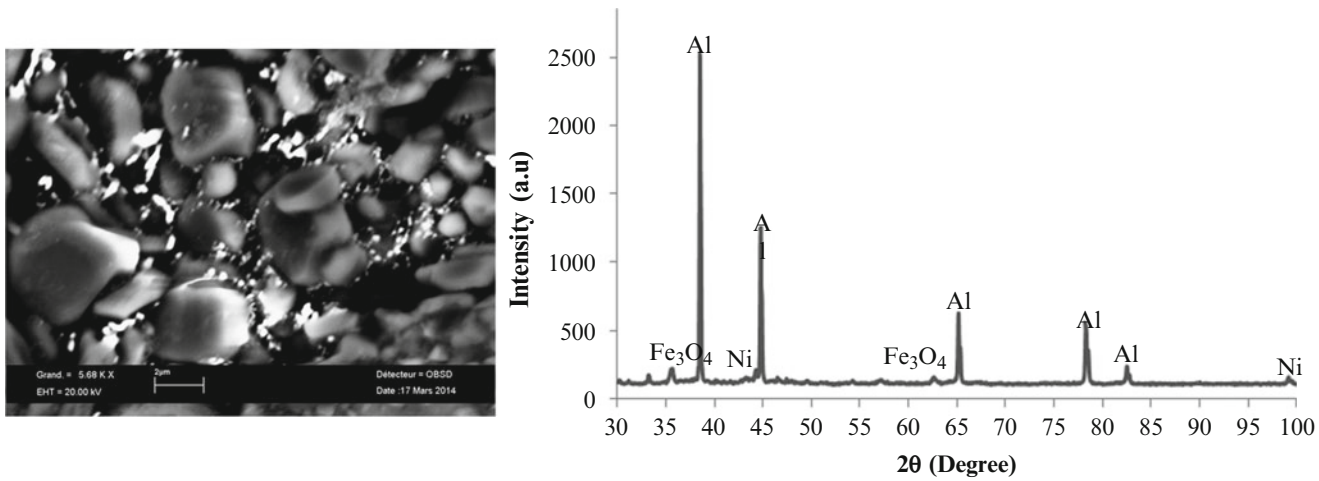

Fig. 2.5 Distribution of iron oxide on the fracture surface and XRD analysis taken from the same composite of AF10A

Table 2.1 Electrical properties (resistivity and conductivity) measured for three compositions

Composition	Resistivity (ohm-m)	Conductivity (S/m)
Pure Aluminium	0.000192	11,997
AF-10A	0.000281	3999
AF-20A	0.001028	1042
AF-30A	0.001036	1157
AF-20A-4Ni	0.001216	1031

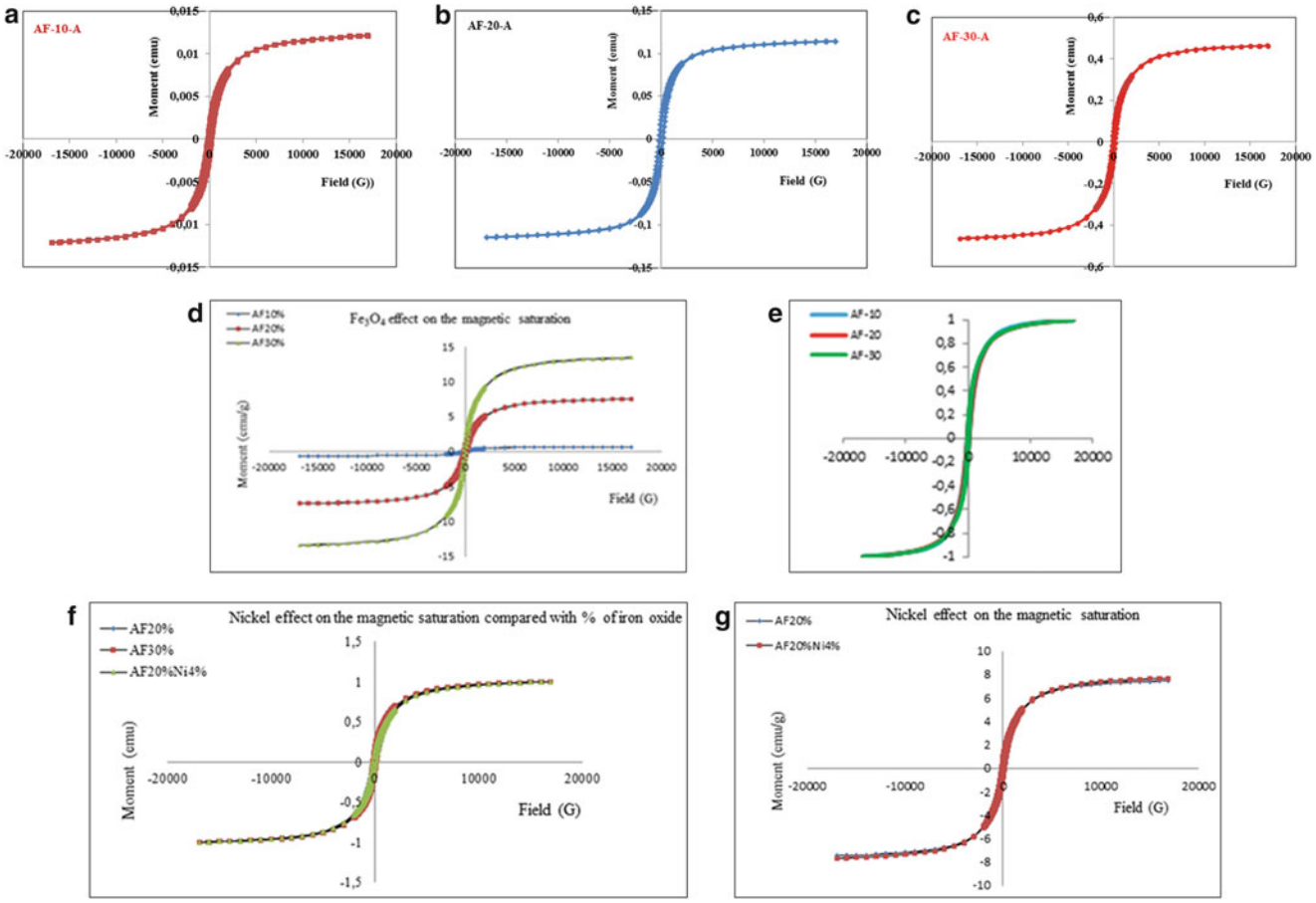

Fig. 2.6 Magnetic properties; magnetic saturation and the normalized curve and comparison of the composites containing different amount of magnetic iron oxide and Nickel, respectively

Table 2.2 Hysteresis parameters of the composite Aluminium/Fe_3O_4

Sample	M_s (emu/g)	M_r (emu/g)	H_c (G)	M_r/M_s	X_m
AF-10-A	0.55 ± 0.02	0.0880 ± 0.0003	199.446 ± 50.03	0.160 ± 0.023	7.18E-4
AF-20-A	7.45 ± 0.05	1.0697 ± 0.001	199.422 ± 50.09	0.1433 ± 0.051	7.66E-4
AF-30-A	13.44 ± 1.01	2.108 ± 0.07	149.42 ± 50.82	0.1569 ± 0.090	1.02E-3
AF20-A-4Ni	7.66	1.005	149.39	0.1310	8.16E-4

called the initial susceptibility. In the same way, the measurement of the initial susceptibility is important in a field which should be compared with the coercivity as a function of temperature. This point requires more detail precisions that will be given in the next work that is going on. Here, only limited measurements at room temperature were presented as they are indicative on the effect of reinforcements on the optimization of the magnetic and electrical properties of the aluminium based composites.

2.4 Conclusions

New designed aluminium based metal matrix composites reinforced with nano iron oxide magnetic particles gives much hope for aircraft and automotive applications. Optimizations of the certain parameters require much more experimental work to create magnetic pieces in industrial scale. In the same way, the measurements of the initial susceptibility are important in a field which should be compared with the coercivity as a function of temperature. This point requires more detail precisions that will be given in the next work that is going on. Here, only limited measurements at room temperature were presented as they are indicative parameters for better understanding the effect of reinforcements on the optimization of the magnetic and electrical properties of the aluminium based composites. Another aspect is that a comprehensive study with modelling is needed when rigidity and toughness are important. Final stage of this study will be completed after optimization of electrical and magnetic properties of these future multiferroïques composites.

Acknowledgements Authors want to thank financial support from CNPq—Conselho Nacional de Desenvolvimento Científico e Tecnológico (Brazil); Program French Catedra UNICAMP/French Embassy in Brazil

References

1. Bayraktar, E., Katundi, D.: Development of a new aluminium matrix composite reinforced with iron oxide (Fe_3O_4). J. Achiev. Mater. Manuf. Eng., JAMME **38**(1), 7–14 (2010)
2. Katundi, D., Bayraktar, E., Tan, M.-J., Tosun, A.: Design of aluminum matrix composites reinforced with nano iron oxide (Fe_3O_4). AMPT, 15th International Conference on "Advanced Materials Processing Technologies", vol. 1, pp. 1–12. Australia, 23–26 September 2012
3. Bayraktar, E., et al.: Manufacturing of aluminum matrix composites reinforced with iron oxide (Fe_3O_4) nanoparticles: microstructural and mechanical properties. Metall. Mater. Trans. B **45**(2), 352–362 (2014)
4. Coey, J.M.D.: Permanent magnet applications. J. Magn. Magn. Mater. **248**, 441–456 (2002)
5. Fang, B., Wang, G., Zhang, W., Li, M., Kan, X.: Fabrication of Fe_3O_4 nano-particles modified electrode and its application for voltammetric sensing of dopamine. J. Electroanal. **17**(9), 744–748 (2005)
6. Yan, Z.X., Deng, J., Luo, Z.M.: A comparison study of the agglomeration mechanism of nano and micrometer aluminum particles. J. Mater. Charact. **61**(2), 198–205 (2009)
7. Zhong, Y., et al.: Agglomeration/defluidization in a fluidized bed reduction of Fe_2O_3 particles by Co: influences of iron precipitation on particle cohesiveness. Powder Technol. **256**, 13–19 (2014)
8. Ismail, I., et al.: Crystallinity and magnetic properties dependence on sintering temperature and soaking time of mechanically alloyed nanometer-grain Ni0.5Zn0.5Fe_2O_4. J. Magn. Magn. Mater. **333**, 100–107 (2013)
9. Herzer, G.: Grain structure and magnetism, of nanocrystalline ferromagnet. IEEE Trans. Magn. **1**(25), 3327–3329 (1989)
10. Coey, J.M.D.: Permanent magnet applications. J. Magn. Magn. Mater. **248**, 441–456 (2002)
11. Du, S., Ramanujan, W.-R.V.: Mechanical alloying of Fe-Ni based nanostructured magnetic materials. J. Magn. Magn. Mater. **293**, 286–298 (2004)
12. Eichholz, C., et al.: Investigations on the magnetization behavior of magnetic composite particles. J. Magn. Magn. Mater. **368**, 139–148 (2014)
13. Ferreira, L.M.P., Bayraktar, E., Robert, M.H., Miskioglu, I.: Magnetic and electrical properties of new aluminium matrix composite reinforced with magnetic nano iron oxide. AMPT, 17th International Conference on "Advanced Materials Processing Technologies", vol. 1, pp. 1–12. Dubai, 16–26 November 2014
14. Laurent, S., Forge, D., Port, M., et al.: Magnetic iron oxide nanoparticles: synthesis, stabilization. Chem. Rev. **108**(6), 2064–2110 (2008)
15. Wu, W., Jiang, C., Roy, V.A.L.: Recent progress in magnetic iron oxide–semiconductor composite nanomaterials as promising photo catalysts. J. Nanoscale **7**, 38–58 (2015)
16. Baron, R.P., Jones, C., Wawner, F.E., Wert, J.A.: Mechanical properties of aluminium matrix composites reinforced with sintered ferrous compacts. Mater. Sci. Eng. **A259**, 308–313 (1999)
17. Wu, W., He, Q., Jiang, C.: Magnetic iron oxide nanoparticles: synthesis and surface functionalization strategies. Nanoscale Res. Lett. **3**, 397–415 (2008)

Chapter 3
Manufacturing and Characterization of Anisotropic Membranes for Micro Air Vehicles

Josh Wilcox, N. Brent Osterberg, Roberto Albertani, Mattia Alioli, Marco Morandini, and Pierangelo Masarati

Abstract This paper presents a solution for the production process of a anisotropic polymeric membrane developed for micro air vehicle (MAV) wings, and validates numerical models of the composite membrane with mechanical testing. The anisotropic properties of the membrane are achieved through consideration of material selection, fiber ratio, fiber pretension, and void formation in a spandex-fiber reinforced silicone-matrix. Direct analysis and composites micromechanics equations are used to model the composite membrane with the ability to predict material properties and response under various loading conditions including pressure distributions. Digital image correlation is used in conjunction with tensile tests and "hydrostatic" pressure differential tests to characterize the response of the membrane to various loading conditions. The non-isotropic properties of the composite membrane result in deflection fields that vary with respect to direction under a uniform pressure gradient across the membrane. With further development of the manufacturing process, spandex reinforced silicone membranes yield promising results as a future MAV membrane material.

Keywords Micro air vehicles • Membrane wing • Bio-inspiration • Non-isotropic • Digital image correlation

3.1 Introduction

Bat wings are intricate structures with a membrane skin and a muscular-skeletal configuration working in conjunction to achieve desirable flight characteristics. The membrane characteristics of bats in flight has been carefully studied and used as a benchmark model in the design of membrane wing fliers [1, 2]. As researchers continue to develop wing designs inspired by natural flyers, the availability of bio-inspired materials similar to the structure of these animals is important. Studies have shown that bat skin is an anisotropic membrane with different a stiffness in the chord and span directions which suggests similar characteristics might be needed to duplicate such flight [3].

Micro Air Vehicles (MAV), such as the one seen in Fig. 3.1, were defined by the Defense Advanced Research Projects Agency (DARPA) as aircraft with wingspan less than 15 cm and a maximum speed less than 15 m/s. These aircraft can be utilized for a variety of missions, carrying payload such as surveying and sensing equipment at a low operational cost [5]. In micro air vehicle designs, much like natural fliers, compliant membranes are used to passively enhance flight characteristics [6]. Historically, the membrane material has been an isotropic material due to its commercial availability. Methods such as pre-tension have been developed to alter flight characteristics [7], but may not give researchers the custamization they need to effectively mimic natural fliers. By developing a non-isotropic elastic membrane material capable of being tailored to an applicable stiffness range for membrane-based wings, researchers might be able to better replicate the successful characteristics of natural fliers.

Previous research on polymer-based reinforcements, such as the crane fly inspired micro-electro-mechanical system (MEMS) composite wings [8] has used the composite as the structural component of the membrane. The non-isotropic membrane developed in this work is designed as a pseudo-homogenous membrane material intended to be supported by a separate frame with a larger platform than the 3.6 cm wingspan, developed in Bao et al. Isolating the structural reinforcement and membrane reinforcement allows stiffer materials to be used as the supporting structure around the membrane similar to the function of bines and tendons in natural fliers. A non-isotropic membrane should respond differently to pressure loading

J. Wilcox • N.B. Osterberg • R. Albertani (✉)
School of Mechanical, Industrial and Manufacturing Engineering, Oregon State University, Rogers Hall, 2000 SW Monroe Ave, Corvallis, OR 97331, USA
e-mail: wilcoxjo.100@gmail.com; osterben@onid.oregonstate.edu; Roberto.Albertani@oregonstate.edu

M. Alioli • M. Morandini • P. Masarati
Dipartimento di Scienze e Tecnologie Aerospaziali, Politecnico di Milano, via La Masa 34, 20156 Milano, Italy
e-mail: mattia.alioli@polimi.it; marco.morandini@polimi.it; pierangelo.masarati@polimi.it

C. Ralph et al. (eds.), *Mechanics of Composite and Multi-functional Materials, Volume 7*,
Conference Proceedings of the Society for Experimental Mechanics Series, DOI 10.1007/978-3-319-21762-8_3

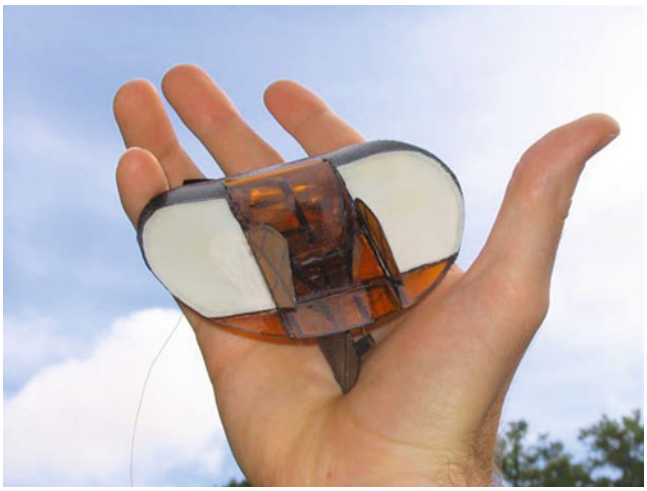

Fig. 3.1 Micro air vehicle from Dr. Peter Ifju's MAV lab at University of Florida [4]

between the longitudinal and transverse direction. This response could be used to vary designed flight characteristics of future membrane wings. The non-isotropic membrane exhibits properties similar to current silicone and latex membranes in membrane wing MAV research, allowing it to be tested as an alternative within existing MAV platforms [9].

The multi-step development process of this non-isotropic membrane involves implementing models to predict the behavior of a polymer-polymer composite membrane, manufacturing membrane samples based on the output of the theoretical models, and testing samples to validate models as predictors for the material properties. Challenges arose during the manufacturing process development due to the highly elastic nature of the materials used and the viscosity of the uncured matrix material.

A membrane finite element, implemented in a multibody formulation [10], is used in co-simulation with a fluid dynamics solver to predict the configuration of the system under static and unsteady loads [11, 12]. Analytical and numerical results, along with experimental measurements of actual membrane wing artifacts subjected to a variety of steady and unsteady flow conditions (this aspect will be the topic of future investigation), are used to validate the proposed formulation. Experimental data is based on digital image correlation in conjunction with a load cell and tensile test frame to measure stress and strain [13]. Measurements are further manipulated using moving least-squares (MLS) [14] to remap the displacements and the strains on the grid that is used for the analysis. The curvature of the membrane, obtained from the reconstructed shape, is used to estimate the surface loads, which are correlated with the values predicted by the coupled fluid-structure analysis.

A hydrostatic membrane pressure test was also conducted to characterize the behavior of the non-isotropic membrane under a constant and uniform pressure distribution. A non-isotropic and a silicone control sample were each secured over a frame and subjected to a pressure differential across the membrane. The membrane response to the pressure differential is used to predict the membrane behavior under aerodynamic loading. As researchers refine membrane wing designs, the availability of elastic, non-isotropic material similar to bat wings will provide another tool in the development of a functional MAV membrane design with potential for expanding their flight envelope.

3.2 Numerical Methods

The Rule of mixtures and Halpin-Tsai semi-empirical analysis were used as an initial micromechanics prediction method for the elastic modulus of the composite in the longitudinal and transverse directions while designing the non-isotropic elastic membranes [15]. Fiber diameter, fiber ratio, and the membrane thickness were inputs to the equation that were altered to find a material composition that would provide sufficient loads for the range of the load cell used for testing while also providing a sufficient anisotropy index defined by Eq. 3.1:

$$Anisotropy\ Index = \frac{Longitudinal\ Tensile\ Modulus}{Transvers\ Tensile\ Modulus} \tag{3.1}$$

Initial model results used estimations of the modulus of the fiber and matrix using common values found for both materials. The model was refined to match the tensile testing data of the matrix and fiber upon completion of material tests to provide a more representative comparison between the theoretical model and experimental results.

3.3 Direct Analysis

The direct analysis is performed using a tightly coupled fluid-structure co-simulation in which the structural problem is solved using the free general purpose multibody dynamics solver MBDyn1 [16] and the fluid problem is solved using a dedicated solver based on FEniCS2 [11, 12] where a collection of Python statements inherit the mathematical structure of the problem and automatically generate low level code. The fluid dynamics code is based on a stabilized finite element approximation of the unsteady Navier-Stokes equations (often referred to in the literature as G2 method [17]).

The multibody solver is coupled with the external fluid dynamic code by means of a general-purpose, meshless boundary interfacing approach based on Moving Least Squares with Radial Basis Function, as presented in [14]. This technique allows for an approximation of the field of the structural displacements, and velocities at the aerodynamic interface nodes. The membrane element, implemented in MBDyn as shown in [10], is formulated as a four-node isoparametric element based on second Piola-Kirchhoff type membranal resultants. The classical Enhanced Assumed Strains (EAS) method [18] is exploited to improve the response of the element: seven additional variables for each membrane element are added to the strain vector (see for example [19] for details). The stress tensor in vector form can be expressed as a function of the strain tensor, reorganized in the same manner, using the constitutive law of the membrane element, e.g.:

$$\begin{Bmatrix} \sigma 11 \\ \sigma 22 \\ \sigma 12 \end{Bmatrix} = \mathrm{D} \begin{Bmatrix} \varepsilon 11 \\ \varepsilon 22 \\ \varepsilon 12 \end{Bmatrix} \tag{3.2}$$

where

$$D = \frac{E}{1-v^2} \begin{bmatrix} 1 & v & 0 \\ v & 1 & 0 \\ 0 & 0 & (1-v)/2 \end{bmatrix} \tag{3.3}$$

In case of homogeneous constitutive properties, the forces per unit span are readily obtained by multiplying the stresses by the thickness h of the membrane (otherwise, thickness-wise integration is required). Generically anisotropic constitutive properties can be defined with a positive, symmetric D matrix, arbitrarily set by the user.

3.4 Experimental Data Re-sampling

Measurements provided by DIC [5] include: (i) the reference location in space of an arbitrary set of points on the surface, chosen by the DIC algorithm when the measurement system is activated, (ii) the displacements of the corresponding points in the current sample, and (iii) an estimate of the in-plane strains. Data preparation, for both the measured strains and the measured displacements used for correlation, requires re-sampling of unstructured measured fields onto the grid that is subsequently used for the analysis; for this purpose, a meshless mapping procedure is used. The mapping [14] produces a linear interpolation operator H, from the measurement domain $(\cdot)\mathrm{m}$, to the virtual sensing domain $(\cdot)\mathrm{v}$, namely $\mathrm{xv} = \mathrm{Hxm}$. Operator H is computed based on the initial positions of both domains; from that point on, it is used to map an arbitrary configuration of the measure domain onto the virtual sensing domain.

The participation of each component of a measure point's position to the mapping of the corresponding component of a virtual point is the same, i.e., the mapping is isotropic. As a consequence, any scalar field, as well as each component of any vector field, can be mapped separately using a subset of matrix H, obtained for example by extracting every one out of three columns and rows of matrix H

$$H = H(1:3:\text{end}, 1:3:\text{end}). \tag{3.4}$$

The re-sampled displacements, uv = Hum, are used to evaluate the quality of the reconstructed displacements. When a sufficiently large number of measurement points is required to interpolate the position of a virtual sensing point, the procedure also produces a smoothing of the input data, acting as a spatial filter. Thanks to the compact support used for the interpolation [6], the mapping matrix H is usually quite sparse, see [10]: it could be stored and handled exploiting such sparsity, thus drastically reducing the computational cost associated with field mapping.

3.5 Validation of the Hydrostatic Pressure Test Model

This section presents the validation of the direct analysis by comparing the direct predictions with experimental data for prestressed rectangular membranes subjected to hydrostatic pressure loads. Correlation is sought with respect to experimental results obtained in a test campaign performed at Oregon State University, where elastic deformations and strains were measured using DIC [13]. The experiments in [13] refer to a rectangular edge-clamped membrane wing, whose dimensions are 140 × 75 × 0.14 mm. The membrane, prestrained by a 9 % isotropic membrane strain ($\varepsilon x0 = \varepsilon y0 = 0.09, \gamma xy0 = 0$), was subjected to hydrostatic pressure difference between the lower and the upper surface ranging from 100 Pa to 500 Pa in steps of 100 Pa.

Summarizing the verification procedure: the displacement measurements, re-sampled onto the numerical grid that is subsequently used for the structural analysis, are used to evaluate the quality of the reconstructed displacements predicted using the tightly coupled fluid-structure co-simulation. Resampling is done by means of the previously discussed MLS procedure using radial basis functions initially developed for field interpolation [14]. Figure 3.2a and b compare the numerical results, for the problem with 300 Pa and 500 Pa of pressure difference, with the experimental ones re-sampled on the numerical mesh using the previously discussed moving least squares (MLS) procedure. The same domain mapping algorithm is used to exchange motion and loads at the nodes between MBDyn and the fluid solver implemented in FEniCS during the coupled fluid-structure solution when the interface nodes of the structure and fluid domains do not match.

The structural grid, implemented within the multibody simulation environment provided by MBDyn, consists of 8 × 16 four-node membrane elements, containing 153 structural nodes and 153 rigid body elements when a dynamic model needs to be used. Although not involved in the presented test cases, the mass lumped in each node is computed from the latex rubber sheet portion associated with the node, which is uniformly distributed. The membrane is made of latex rubber, with a tensile modulus E = 1.8e6 Pa, Poisson's modulus $\nu = 0.3$, and density $\rho = 1350$ kg/m^3. In [20, 21] a comparison of the direct solution for smaller and larger values of the prestrain is performed to study how much the problem is dependent on the value of the prestrain. In the experiments described in [13] the membrane prestrain was introduced as accurately as possible at the

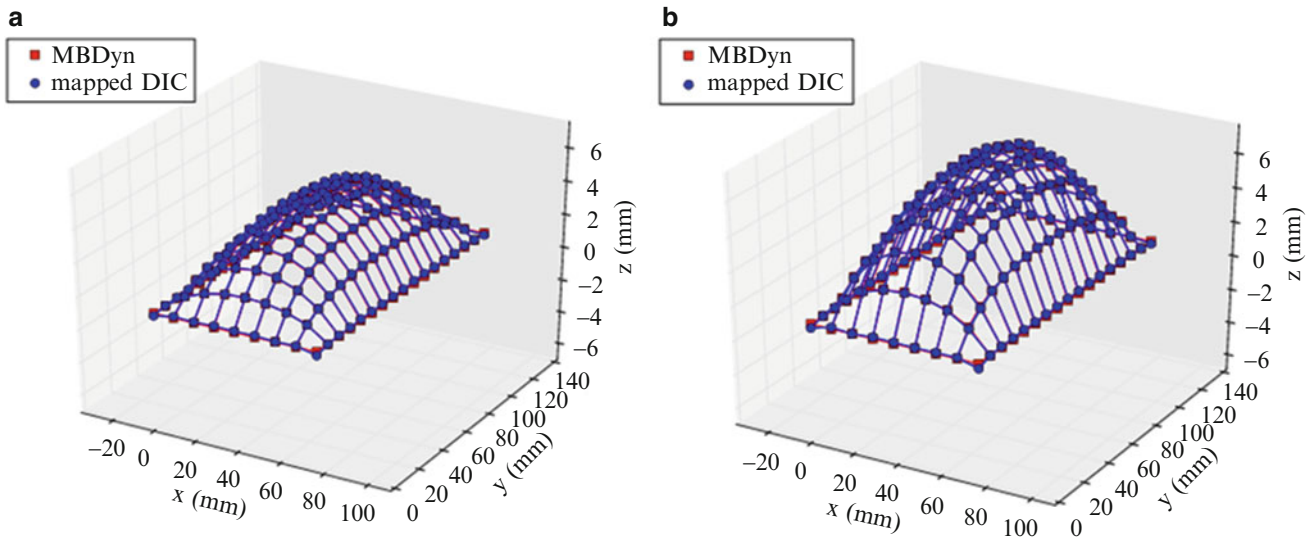

Fig. 3.2 Numerical/experimental correlation of hydrostatic pressure problem at 300 Pa (**a**) and 500 Pa (**b**)

nominal level, but could not be checked afterwards. The fact that the numerical solutions with nominal prestrain present a very good correlation with the experiments indicates that the actual prestrain in the experiments was in accordance with the expected value.

3.6 Non-isotropic Survey

A study case of non-homogeneous constitutive properties of the model was also investigated using the 100 % fiber modulus from experimental data and previously modeled latex rubber. The membrane dimensions, loading, boundary condition are the same as in direct analysis case discussed above. No prestress was introduced herein. A composite membrane was considered: the fibers, which are modeled as "rod" elements, are oriented parallel to the spanwise direction (i.e., y axis). The elastic modulus at 100 % strain was matched with experimental results of tensile tests. A corresponding model of the specimen with averaged membrane/fibers properties was also investigated, by defining orthotropic constitutive properties of the membrane. Figure 3.3a and b compare, for the problem with 100 Pa and 200 Pa of pressure difference, respectively, the deformed shapes obtained using a model of the specimen that directly models the fibers (the "fiber" model) with the results from a corresponding model with averaged membrane/fiber properties (the "average" model). As shown, the two models give consistent numerical results for hydrostatic pressure tests under controlled boundary conditions.

3.7 Manufacturing Method

Existing membrane-wing manufacturing techniques do not involve the inclusion of fibers within the membrane. Due to the lack of a suitable non-isotropic material, a manufacturing process was developed to address the deficiency. Platinum cure silicone offers desirable characteristics as a matrix material for this application due to its elastic properties when cured, its easy manufacturability and two-part liquid state before curing. Silicone is also currently used successfully as a membrane material in membrane wing research [7].

Spandex, an elastic polymer available in fiber form, has a 100 % elastic deformation modulus of 2.2 MPa. Spandex has a nonlinear stress/strain response and a 100 % elastic modulus approximately 1 order of magnitude higher than silicone, making it an ideal reinforcement material for optimum matching with matrix elastic properties. This relationship between the stiffness of the fibers and matrix allows the fiber to provide the necessary stiffness increase along the fiber direction without being excessively stiff, which could cause uneven deformations in the material under load. For the volume of production required for research, a simple mold with pins as seen in Fig. 3.4a was used to create the fiber structure by weaving a single fiber across the sample section of the mold and around each of the pins. The desired fiber ratio was achieved

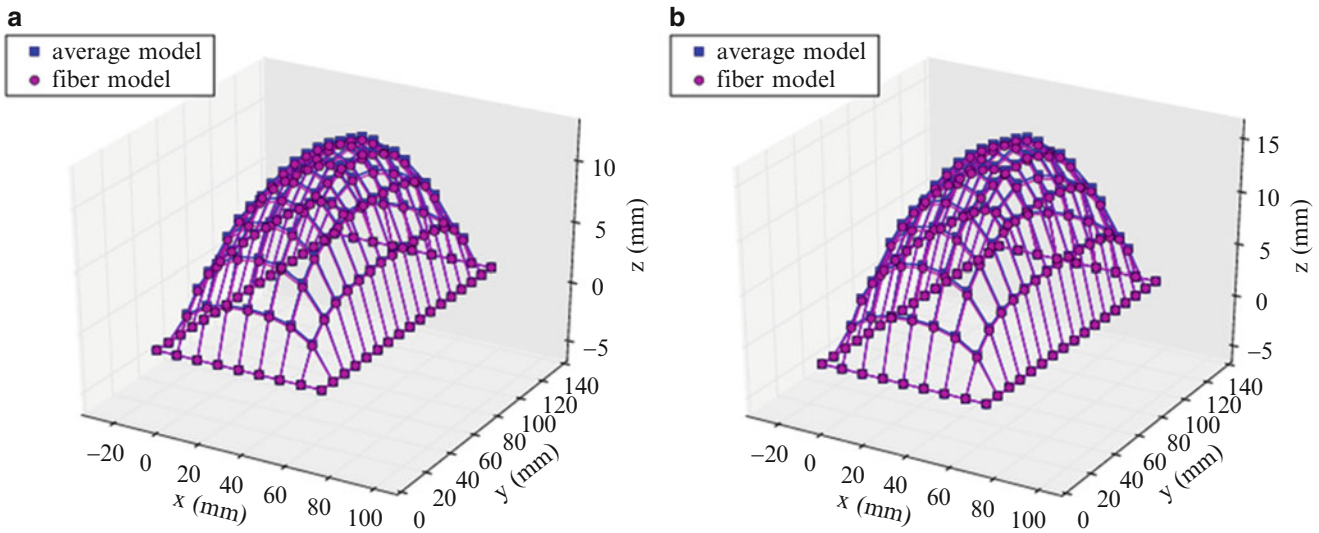

Fig. 3.3 Comparison of the "fiber" and "average" model, hydrostatic pressure problem at 100 Pa (**a**) and 200 Pa (**b**)

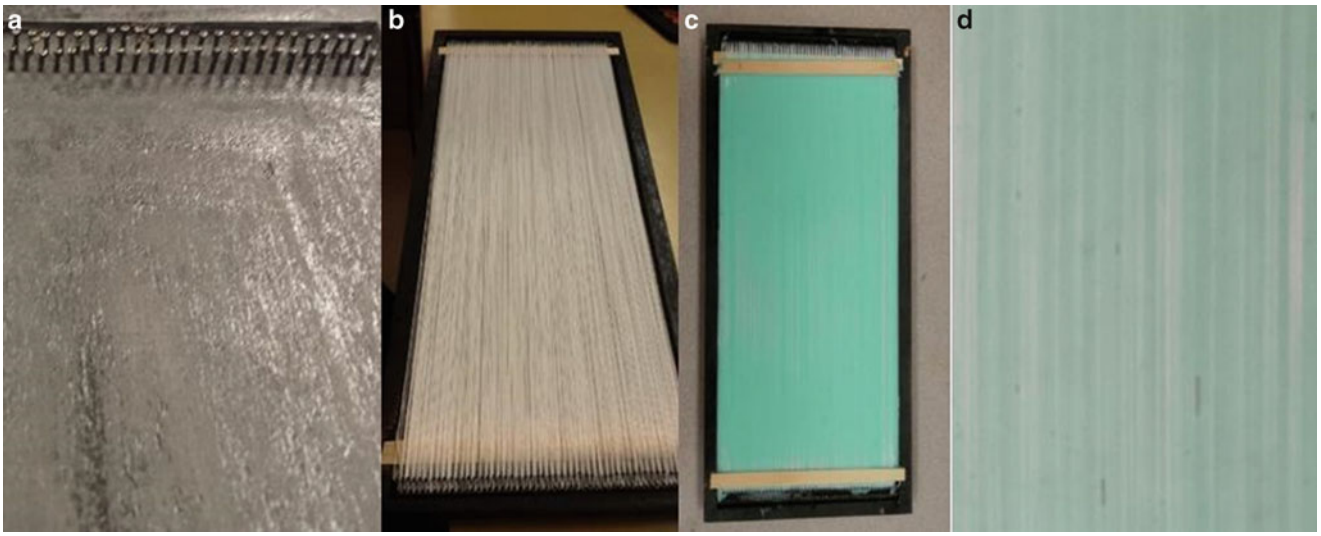

Fig. 3.4 Empty mold (**a**), dry fibers (**b**), completed sample in mold (**c**), and material surface (**d**)

by building multiple layers of fibers as illustrated in Fig. 3.4b within the membrane. Fibers were wound without intended pretension however, the elastic nature of the spandex fibers caused uncertainty of the fiber tension during the layup process introducing potential scatter in material characteristics. The membrane mold was designed to minimize variation in fiber pretension through the use of a continuous fiber wound across pins which allow the fiber to equalize across the sample.

Once the mold is properly prepared with fibers, the matrix is added to create the composite material seen in Fig. 3.4c. The viscosity of the matrix became an issue during wet-out process since the silicone, which has a viscosity of 12,500 Cps [22], would not easily flow through the fibers. The 50 min pot life of the matrix material allowed sufficient time to remove any voids in the material for full saturation of the fibers. Mold-Star platinum cure silicone, the formulation used as the matrix, did not require degassing in a vacuum chamber as is required for some silicones. One concern with a silicone matrix is the tendency for materials to not properly bond with silicone as shown in the results. Figure 3.4d shows the surface of the completed membrane material with some fibers visible through a thin layer of silicone.

The mold dimensions were designed to obtain four longitudinally reinforced and four transversely reinforced test specimens for tensile testing. Preparing each set of test specimens in the same sample removed manufacturing variance between samples as a possible source of error in testing the ratio between the longitudinal and transverse directions.

3.8 Testing Method

Tensile properties of the non-isotropic membranes were evaluated using the ASTM D412-06a testing method for rubber. Dogbone sample shapes according to the test standard were cut orthogonal from each full membrane which allowed isolation between the directional tests and possible variance in manufacturing between batches. DIC was used instead of the benchmark method listed in the standard to provide a more comprehensive set of strain information from the tests. The ability to measure local strains throughout the specimen without strain gauges or extensometers which might alter the results of the test make DIC an effective tool for measuring strain for this test. The fiber and matrix materials were characterized individually to validate the inputs of the numerical simulations and provide a more comprehensive understanding of their elastic response. The non-isotropic membrane was tested using multiple samples cut parallel and perpendicular to the fibers. The difference in elastic properties of the two directions was used to characterize the anisotropy index of the membrane.

During testing, the Instron testing machine in Fig. 3.5a, and the DIC system were synced to allow correlation between the two data sources. The Instron was used to measure the loads on the specimen, while the elastic deformation field was captured using the DIC system as seen in Fig. 3.5b. Each material and directional combination was tested three times with the results of each set averaged.

Hydrostatic membrane tests simulate the pressure loads seen by membrane wings in flight [13]. The membrane is stretched over a sealed frame seen at the bottom of Fig. 3.6a, creating a pressure chamber. The chamber is inflated to a specified pressure while 3-D DIC is used to measure the displacement the membrane to the pressure load using images such

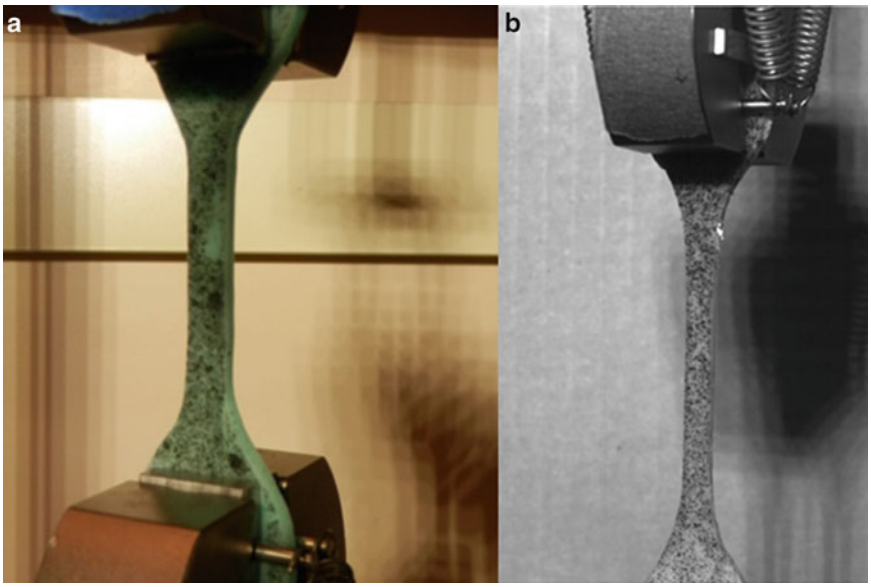

Fig. 3.5 Tensile testing with DIC (**a**) and DIC image of dogbone (**b**)

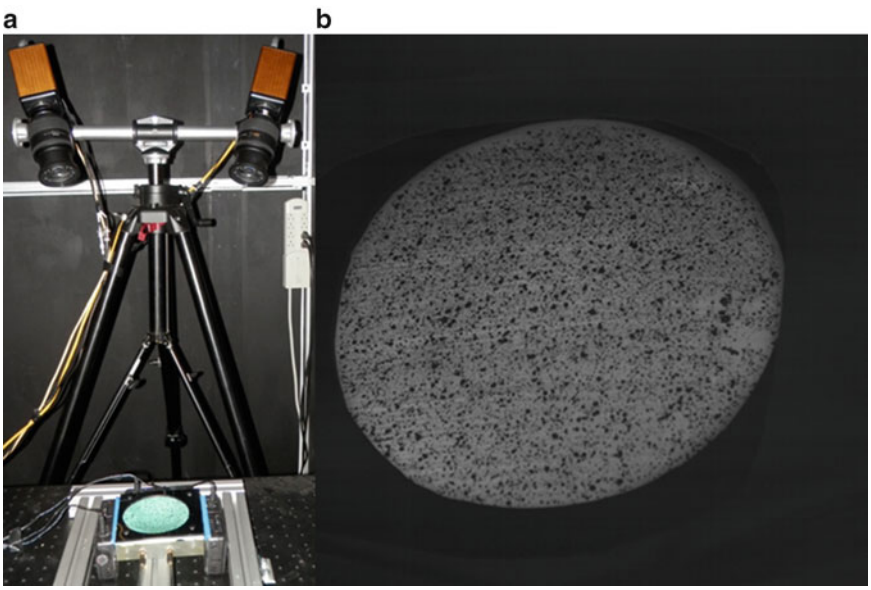

Fig. 3.6 "Hydrostatic" test setup (**a**) and DIC camera image of hydrostatic fixture (**b**)

as Fig. 3.6b. The tensile tests are useful for characterizing the global material properties of the membrane, but hydrostatic pressure tests allow researchers to better understand the behavior of the membrane under loading conditions similar to flight. A non-isotropic composite membrane was tested under the same parameters as an isotropic silicone control specimen to compare the response of the two membranes to pressure loads.

3.9 Mechanical Properties Characterization

The interfacial bond strength was a concern during early manufacturing development. Initial designs used a fiber diameter of 0.22 mm which maintained their bond during strain. Larger fibers with a diameter of .44 mm were used for the test samples used in the data analysis to achieve the 13 % fiber ratio. The .44 mm diameter fibers did not maintain a sufficient bond with the matrix, causing the tested values of the transverse modulus lower than the matrix control sample as seen in Fig. 3.7.

With E1 = 0.616 MPa, and E2 = 0.456 MPa at 100 % strain, the micromechanics analysis predicted an anisotropy index of 1.5 which is lower than the index of 4.4 experimental results of the manufactured specimen. The experimental results in

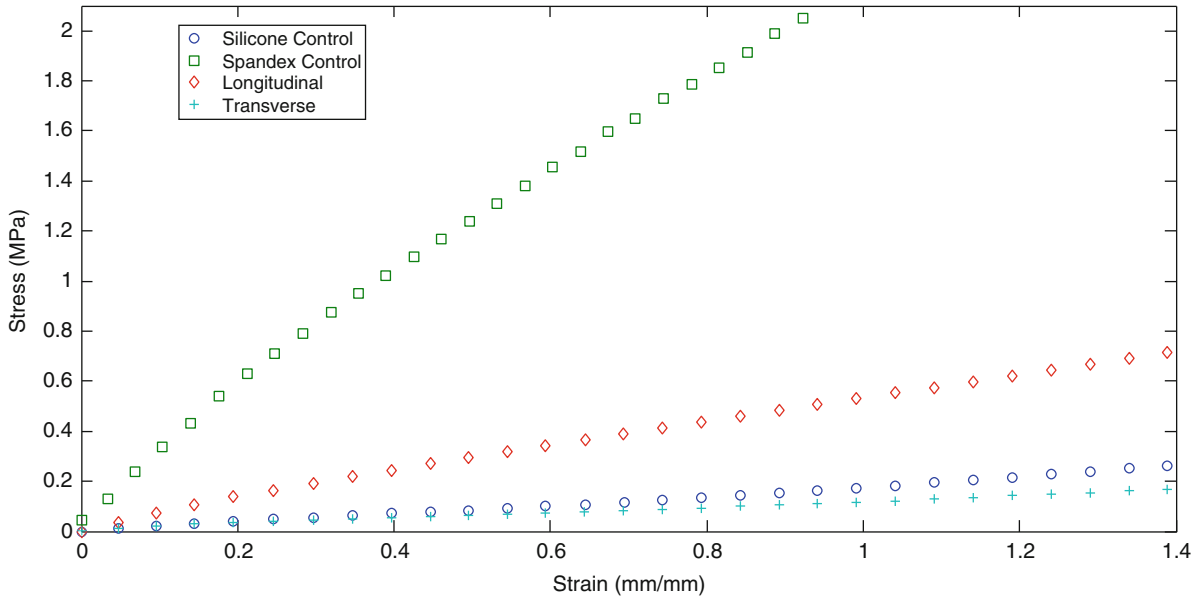

Fig. 3.7 Stress-strain curve of control samples and composite specimens

Fig. 3.7 show the 100 % strain moduli at E1 = 0.616 MPa, and E2 = 0.456 MPa. The E1 values are within 15 %, however, the predicted E2 value is 283 % greater than the experimental results.

The micromechanics equations assume a sufficient bond between the fiber and matrix. Variance in the anisotropy index could be attributed to the low transverse stiffness resulting from the poor bond between the fibers and matrix. This result shows a need for improving the interfacial bond between the matrix and fiber to create a more robust laminate. The anisotropy index was expected to remain nearly constant over the range of strain. At low strains, experimental results show a lower fiber ratio than the remaining strain region which is thought to be the result of slack in the fibers during production of the membrane. The presence of slack in the fibers reduces the effectiveness of the fibers in tension at low strain values. Since the fibers provide stiffness in the longitudinal direction, their ineffectiveness reduces the anisotropy index in the low strain region.

3.10 Numerical Model

A circular edge-clamped membrane was considered herein, whose diameter is 100 mm and with a thickness of 3 mm. The fiber ratio is 13 % fiber by volume, and the fibers were oriented parallel to the x-axis in 3 layers. The structural grid, implemented within the multibody simulation environment provided by MBDyn, consists of about 6800 structural nodes and 67,000 four-node membrane elements. The composite has spandex as the fiber, Ef = 2.2 MPa at 100 % strain, and silicone as the matrix, Em = 0.379 MPa at 100 % strain. The fiber diameter is 0.44 mm. A difference between the deflection in the fiber direction U (Fig. 3.8a) and transverse direction V (Fig. 3.8b) is observed in the maximum magnitudes displayed in the two plots.

Validation of the test was conducted using an isotropic membrane manufactured entirely of the matrix material. The U and V deflections of the matrix control sample resulted in a difference in average maximum magnitude δ_{ave} of deflection is within 4 % between the U and V directions.

$$\delta_{ave} = \frac{(|\delta_{max}| + |\delta_{min}|)}{2} \tag{3.5}$$

In Fig. 3.9a and b, a difference of 33 % is seen between δ_{ave} in the U and V directions. Larger displacements occur in V perpendicular to the fiber direction. This result matches the hypothesis that the non-isotropic membrane response to a pressure load would create a lower deflection in the fiber direction of the membrane than the transverse direction.

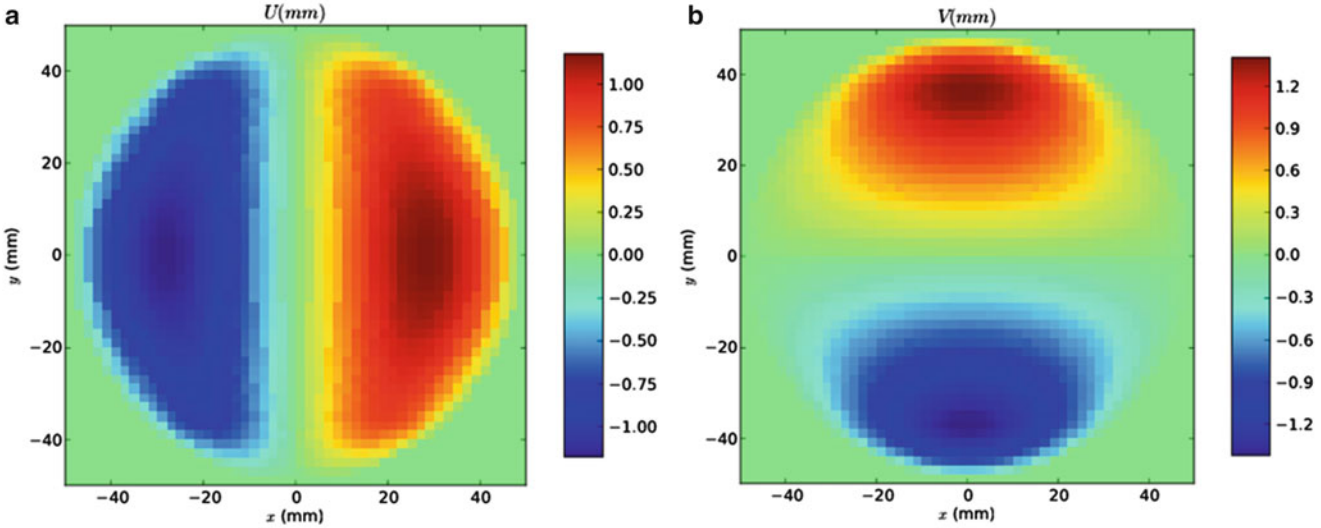

Fig. 3.8 FEA results of deflection parallel to the fiber direction (**a**), and transverse to the fiber direction (**b**) and of a clamped non-isotropic membrane subjected to a pressure load

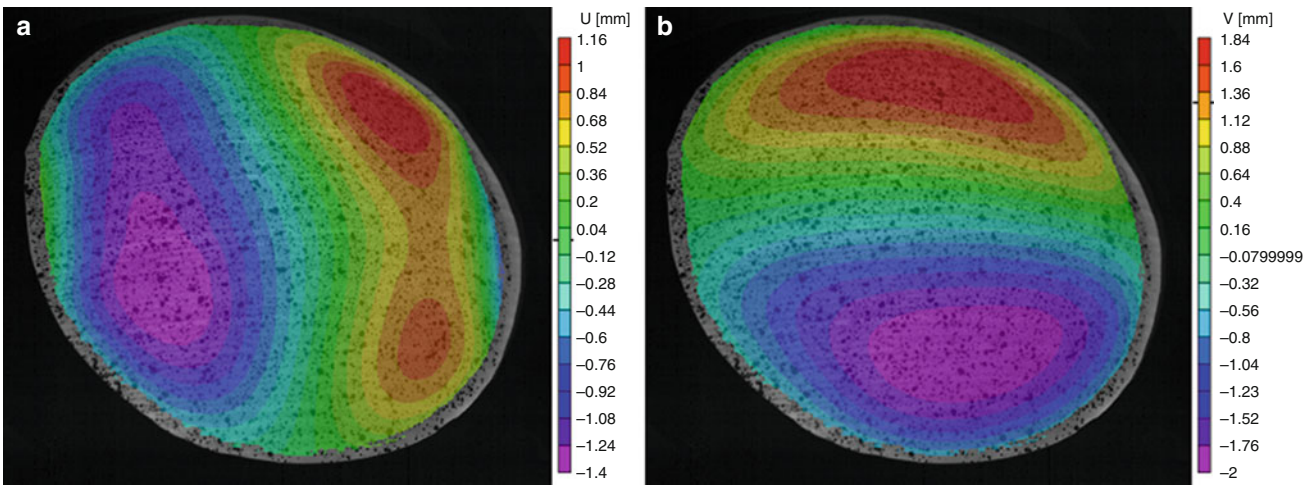

Fig. 3.9 Experimental results of deflection parallel to the fiber direction (**a**), and transverse to the fiber direction (**b**) of a clamped, non-isotropic membrane subjected to a pressure load

3-Dimensional DIC requires two cameras in stereo which causes each camera to be offset of the test fixture. This causes the skewed image of the circular test specimen seen in Fig. 3.9a and b. The variance in shape of the maximum deflection area, specifically the two isolated areas seen in Fig. 3.9a are likely due to a slight deviation from a truly flat surface in the membrane when the zero-image of the DIC analysis was captured. The deformation values are based off a zero-image captured at an unloaded state where any slack in the membrane would result in deviations from a flat surface.

3.11 Conclusions

A membrane with behavior to pressure distributions that varies with direction of deflection was created by drawing from bio-inspiration and existing membrane designs. A non-isotropic elastic membrane with an anisotropy index of 4.4 was manufactured using a fiber volume ratio of 13 % unidirectional polymeric fibers (spandex) reinforcing a silicone matrix. The fibers can be treated as voids in the material under transverse loading due to the lack of a bond between the fiber and matrix, which reduces the effective cross-sectional area of the membrane. This decreases the transverse modulus of the composite

membrane results in an increased anisotropy index of the membrane. Once the strength of the interfacial bond is resolved, silicone and spandex have ideal elastic properties for creating a composite material with an elastic response of a similar range to existing membrane wing platforms. Spandex is approximately 1 order of magnitude stiffer than silicone which is a closer range than the carbon fiber and fiberglass reinforcements used in other wings as stiffeners. When used in conjunction with higher stiffness support structures, the non-isotropic polymeric membrane could produce new wing characteristics not previously possible.

The current anisotropic membrane exhibits the varied response to pressure distributions as expected due to the directional stiffness of the fibers. Future development in manufacturing will seek to improve the transverse elastic properties by increasing the interfacial bond strength. Manufacturing development also revealed a maximum fiber volume ratio near 30 % fibers that resulted in the inability to fully wet the fibers with the matrix. The viscosity of the platinum cure silicone prevented easy flow of the silicone between fibers, causing the low maximum fiber ratio.

A four-node membrane element was implemented in a co-simulation analysis for the direct simulation of coupled fluid-structure problems. The direct analyses have been validated by comparing the direct prediction with experimental data for prestressed rectangular membranes subjected to hydrostatic pressure loads. The proposed analysis enables accurate and computationally efficient high-fidelity deformation solutions. It is therefore applicable to both static and dynamic problems. Further development and studies to this approach could provide higher accuracy estimates and the potential for offline estimation of time varying loads could be explored. Comparison of the direct simulation with experimental data for a non-isotropic membrane yields an accurate prediction in the fiber direction and a higher predicted value in the transverse direction. The difference in the transverse results can be attributed to the imperfect bond between the fiber and matrix which was not modeled.

Numerical models with experimental results from the manufactured membrane will allow future membrane designs to be refined using models before manufacturing and testing samples. Experimental data of tensile properties parallel to the fibers show behavior similar to traditional unidirectional composites with a resulting elastic modulus between the magnitudes of the fiber and matrix modulus. With refinements to the manufacturing process, fiber pretension, and the fiber ratio, a spandex reinforced silicone membrane shows promise as a future wing material on micro air vehicles. Spandex fibers will not replace the high stiffness composites currently used to maintain the wing shape, but they can complement the use of such materials in developing a more refined membrane wing design.

Acknowledgments Effort sponsored by the Air Force Office of Scientific Research, Air Force Material Command, USAF, under grant number FA8655-12-1-2114, technical monitor Dr. Gregg Abate. The U.S. Government is authorized to reproduce and distribute reprints for Governmental purpose notwithstanding any copyright notation thereon.

References

1. Albertani, R., Hubel, T., Swartz, S.M., Breuer, K.S., Evers, J.: In-flight wing-membrane strain measurements on bats. In: SEM annual conference and exposition on experimental and applied mechanics 2010, Indianapolis, 2010
2. Goulbourne, N., Wang, Y., Son, S., Skulborstad, A.: Microstructure and material characterization of bat wing tissue for active skin composites. In: 18th International conference on composite materials, Jeju, 2011
3. Skulborstad, A.J., Goulbounrne, N.: Biaxial mechanical characterization of bat wing skin and development of biomimetic constructs. In: ASME 2013 conference on smart materials, adaptive structures and intelligent systems, SMASIS 2013, Snowbird, 2013
4. Ifu, P., Ettinger, S., Jenkins, D., Martinez, L.: Composite materials for micro air vehicles. In: 46th International SAMPE symposium and exhibition—2001 a materials and processes odyssey, Long Beach, 2001
5. Albertani, R., Stanford, B., Hubner, J., Ifju, P.: Aerodynamic coefficients and deformation measurements on flexible micro air vehicle wings. Exp. Mech. **47**(5), 625–635 (2007)
6. Stanford, B., Ifu, P., Albertani, R., Shyy, W.: Fixed membrane wings for micro air vehicles: experimental characterization. Prog. Aerosp. Sci. **44**(4), 258–294 (2008)
7. Abudaram, Y.J., Ifu, P.G., Hubner, J.P., Ukeiley, L.: Controlling pre-tension of silicone membranes on micro air vehicle flexible wings. J. Strain Anal. Eng. Design. **49**(3), 161–170 (2014)
8. Bao, X., Bontemps, A., Grondel, S., Cattan, E.: Design and fabrication of insect-inspired composite wings for MAV application using MEMS technology. J. Micromech. Microeng. 21(12), (2011)
9. Albertani, R., Stanford, B., Hubner, J.P., Ifju, P.: Aerodynamic characterization and deformation measurements of a flexible wing micro air vehicle. In: 2005 SEM annual conference and exposition on experimental and applied mechanics, Portland, 2005
10. Solcia, T., Morandini, M., Masarati, P.: A membrane element for micro-aerial vehicle fluid-structure interaction. In: 2nd Joint international conference on multibody system dynamics, Stuttgart, 2012
11. Aliol, M.: Coupled fluid-structure simulation of flapping wings. Master's thesis, Politecnico di Milano (2011)
12. Alioli, M., Masarati, P., Morandini, M.: Coupled multibodyfluid dynamics simulation of flapping wings. In: Proceedings of ASME IDETC/CIE, Portland, 2013

13. Carpenter, T., Albertani, R.: Aerodynamic load estimation: pressure distribution from virtual strain sensors for a pliant membrane wing. In: 54th AIAA/ASME/ASCE/AHS/ASC structures, structural dynamics, and materials conference, Boston, 2013
14. Quaranta, G., Masarati, P., Mantegazza, P.: A conservative mesh-free approach for fluid structure interface problems. In: Coupled Problems, Santorini, 2005
15. Daniel, I.M., Ishai, O.: Engineering mechanics of composite materials. Oxford University Press, New York, NY (2006)
16. Masarati, P., Morandini, M., Paolo, M.: An efficient formulation for general-purpose multibody/multiphysics analysis. J. Comput. Nonlinear Dyn. **9**(4), 041001 (2014). doi:10.1115/1.4025628
17. Hoffman, J., Johnson, C.: Computational turbulent incompressible flow. Appl. Math. Body Soul **4** (2007). doi: 10.1007/978-3-540-46533-1
18. Simo, J., Rifai, M.: A class of mixed assumed strain methods and the method of incompatible modes. Int. J. Numer. Methods Eng. **29**(8), 1595–1638 (1990)
19. Andelfinger, U., Ramm, E.: EAS-elements for two-dimensional, threedimensional, plate and shell structures and their equivalence to HR-elements. Int. J. Numer. Methods Eng. **36**(8), 1311–1337 (1993)
20. Alioli, M., Morandini, M., Masarati, P., Carpenter, T., Roberto, A.: Nonlinear membrane direct and inverse fem analysis. In: ASME IDETC/CIE 2014, Bufflao, 2014
21. Alioli, M., Morandini, M., Masarati, P., Carpenter, T., Albertani, R.: Nonlinear membrane inverse finite element model for pliant wings. In: AIAA SCITECH, Kissimmee, 2015
22. Smooth-On. Mold Star 15, 16, and 30 [Online]. http://www.smooth-on.com/tb/files/MOLD_STAR_15_16_30_TB.pdf (2015). Accessed 2 Mar 2015

Chapter 4
Compliant Artificial Skins to Enable Robotic Sensing and Training by Touch

Hugh A. Bruck, Elisabeth Smela, Miao Yu, James Tigue, Oleg Popkov, Gokhan Ocel, and Ying Chen

Abstract Co-robotics is interested in understanding how robots interact with other structures, such as humans, for the purpose of decision-making. Robots are currently designed to execute programmed actions to satisfy specific commands and motions. If a robot could be taught to perform an action by a guiding touch from a human, rather than specific programmed actions, a single learning approach could be broadly applied to multiple robotic platforms. In order for a robot to learn from touch, the robot must have a sense of touch. To provide the robot with this sense of touch, an artificial skin was created by applying a conductive exfoliated graphite/latex mixture to a compliant latex substrate, resulting in a highly compliant skin conformable to a variety of structures. The skin was designed with an array of strain gauges on both sides of the substrate to form a grid capable of detecting localized forces through changes in skin resistance. Model experiments were used to characterize the mechanics of these skins when placed over compliant substrates. Surface strain was characterized directly with 3D DIC, and shown to correspond quantitatively to changes in skin resistance. The ability of the skin to sense touch has been demonstrated using a Braille target and a commercial robot arm with a finger designed with the sensing skin. Using these skins, it will be possible for robots to feel and sense features of their environment through touch, and to be trained via touch.

Keywords Tactile sensor • Strain gauge • Compliant • Robotic skin • Sensing skin • Exfoliated graphite • Robotic arm

4.1 Introduction

An effort to create a robotic skin has been conducted for over a decade, focused on both resistive and capacitive devices [1–5]. Both types have low cost and power consumption, wide working ranges, and simple electronics. The advantages of capacitive sensing include temperature immunity and good repeatability, but they are not compatible with the deformations that occur in a highly compliant structure, such as synthetic rubbers, foams, and soft tissues. Thus, they have difficulty maintaining continuous contact when interacting with these structures, and can induce large, highly localized contact forces which damage the surface of the structure or cannot conform to the surface to make an "impression". Therefore, our focus was on developing a highly compliant resistive sensing approach that is compatible with these structures to provide robots with a skin that has "nerves", similar to biological systems.

Resistive tactile sensors can be divided into two categories: piezoresistive and dimensional change. In general strain gauges are made of semiconducting or metallic materials, which are rigid. Strain gauges based on dimensional change are typically in the form of a long, thin, zig-zag pattern.

To overcome the disadvantage of rigidity in applications requiring large strain, efforts have been made to create peizoresistors with flexible polymers [1]. Many authors have reported embedding strain gauges in flexible substrates [1]. We will demonstrate that our process requires less effort and can withstand large deformations. Our tactile sensor comprises a piezoresistive composite thin film used in a grid. The composite consists of exfoliated graphite (EG) embedded in latex.

Only recently has EG been proven to be an effective component of compliant electrodes. Kujawski et al. demonstrated the mechanical properties and uses of a compliant EG/PDMS mixture [6]. Coupled with a polymer matrix, an effective EG piezoresistive strain gauge has been created and tested on a dynamic and static systems [7]. Wissman et al. demonstrated the use of an EG/latex strain gauge for measuring the highly dynamic deformation of a Micro Air Vehicle (MAV) wing. These tests showed that an EG composite is a relatively inexpensive alternative to other carbon-based composite strain gauges.

H.A. Bruck (✉) • E. Smela • M. Yu • J. Tigue • O. Popkov • G. Ocel • Y. Chen
Department of Mechanical Engineering, University of Maryland, College Park, MD 20742, USA
e-mail: bruck@umd.edu

C. Ralph et al. (eds.), *Mechanics of Composite and Multi-functional Materials, Volume 7*,
Conference Proceedings of the Society for Experimental Mechanics Series, DOI 10.1007/978-3-319-21762-8_4

In this paper, we studied a robotic skin made of a strain gauge grid using an EG and latex mixture. This skin has been previously proposed to provide a "nervous system" to various robotic platforms [8]. Therefore, a more rigorous characterization of the skin's response to forces and strains was performed. In order to directly validate the strain response, 3D DIC was used to measure the surface strains.

4.2 Experimental Procedure

4.2.1 Sample Fabrication

The strain gauges were made of a composite EG and latex mixture. Using the preparation methods described in [7], an EG/water solution was created. This solution was then mixed with latex in a 25 % wt mixture. A sample of latex sheet was masked using blue painter's tape (3M, 06818). On one side of a circular (10 cm diameter) latex sheet, eight vertical gauges were masked in a pattern (see Fig. 4.1). On the other side, eight horizontal gauges were masked. In this configuration, each gauge was isolated from the others. Each strain gauge was 0.5 cm wide. The uncovered areas were sprayed with the EG/latex mixture. Ten layers were applied, allowing each to dry for 10–20 min.

Wires were attached to the ends of each strain gauge using small drops of a two-part silver conductive epoxy (MG Chemicals, 8331-14G). Blue painter's tape was used to hold the wires in place during the setting time; the epoxy was allowed to set overnight. A foam substrate was used to support the skin. The skin over the foam allowed for large deformations of the surface, and the foam acts as a padding under the skin for the rigid robot arm.

4.2.2 Data Acquisition and Visualization

Each strain gauge in the grid was wired into identical circuits. Each gauge was powered with five VDC. In series with the gauge was a voltage divider resistor of 1000 ± 10 Ω. Voltage was measured across the fixed resistor in this voltage divider. A circuit diagram in given in Fig. 4.2.

A Labview program was created to collect the voltages from each voltage divider and process them for visualization. The program first measured 200 samples of voltage from each of the 16 voltage dividers at 6000 Hz. These values were saved as a Labview measurement file. These initial (homogeneous) voltages were used for comparison to all later measurements.

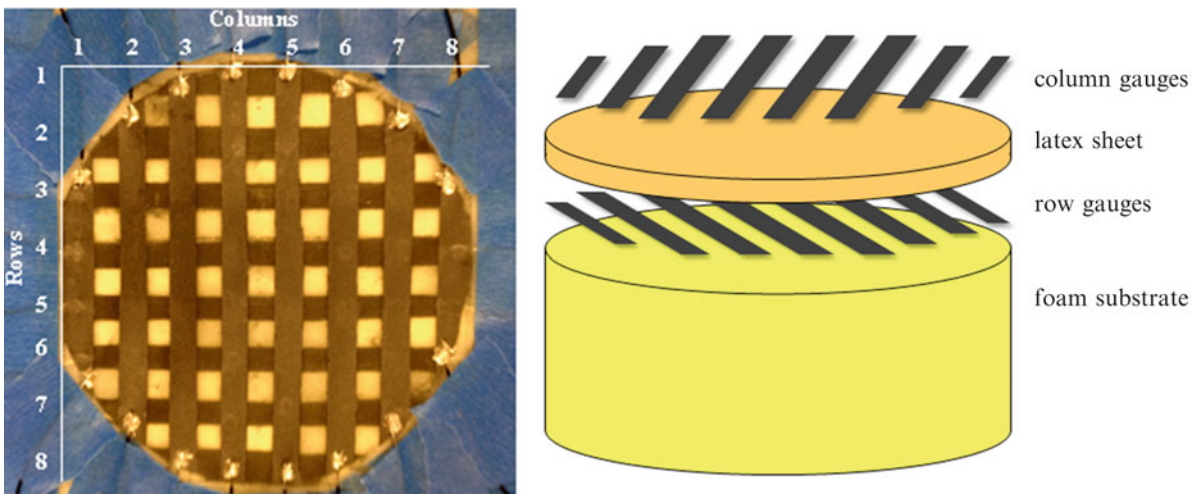

Fig. 4.1 (*Left*) Photograph of the strain gauge grid after final construction (numbers indicate row and column reference numbers). (*Right*) Schematic diagram showing the layering for the sensing skin on top of the foam substrate

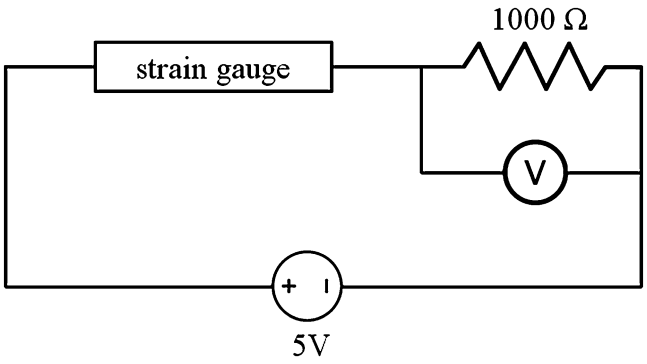

Fig. 4.2 Circuit for each strain gauge in the grid. Each gauge is independent of the other gauges

This step was preformed once at the beginning of the program with the skin under no strain. The program then began a loop to collect strain data. These sets of voltages (inhomogenous voltages) were also saved in the file, as was time.

The program ran a Matlab script to process the voltage measurements. First the script averaged both the 200 homogeneous voltages and the 200 inhomogeneous voltages. Then the voltages were converted into the resistance of the gauge using (4.1).

$$R_g = \left(\frac{V_s}{V} - 1\right) * R \tag{4.1}$$

R_g is the resistance of the gauge, V_s is the supply voltage, V is the voltage drop across the fixed resistor, and R is the resistance of fixed resistor. The homogenous resistances were saved as R_0 instead of R_g. The program then normalized the inhomogeneous resistances using (4.2).

$$\frac{dR}{R} = \frac{R_g - R_0}{R_0} \tag{4.2}$$

A Matlab function was written to take the 16 normalized resistances and return a 15 × 15 matrix of combined intersection resistances of the grid. The program separated the row and column normalized resistances and combined them at the intersections of row and column gauges using (4.3).

$$\Delta R(h, v) = \frac{dR}{R}(h) + \frac{dR}{R}(v) \tag{4.3}$$

$\Delta R(h, v)$ is the combined resistance change that is stored in a 15 × 15 matrix. $\frac{dR}{R}(h)$ is the resistance of row gauge h, and $\frac{dR}{R}(v)$ is the resistance of column gauge v. Since there are only 8 rows and 8 columns, the remaining indices of the 15 × 15 matrix are linearly interpolated. The corners of the matrix were appropriately set to zero to be consistent with the circular shape. The matrix values were plotted using the Matlab function colormap(). This created a color map of the change in resistance across the entire surface of the strain gauge grid. Figure 4.3 shows a sample output from the full data acquisition and visualization program.

This visualization technique provides users visual feedback as well as a comparison for further characterization of the resistance and strain relationships. This plot is the final step for the program loop. The loop repeats, measuring the inhomogeneous voltages.

4.2.3 Force Sensing

The goal of these tests was to develop an understanding of sensor response to forces applied perpendicular to the surface. Response from the tactile skin was tested using an Imada load frame (MX-500) with a 2.5 kg load cell. A 4–40 × 2 inch pan head machine screw was screwed into the load cell and used to produce a localized load. In order to prevent the possibility of grounding when the screw was in contact with the skin, it was covered with black electrical tape. A test fixture for the skin was also designed. The fixture kept the skin tight and stationary during testing. Two pieces of Delrin plastic were clamped around the edges of the sensor and foam substrate. After connecting the skin to the data acquisition circuit, the skin and fixture were placed on the load stand. A photo of the load stand force testing set-up with the skin in place can be seen in Fig. 4.4.

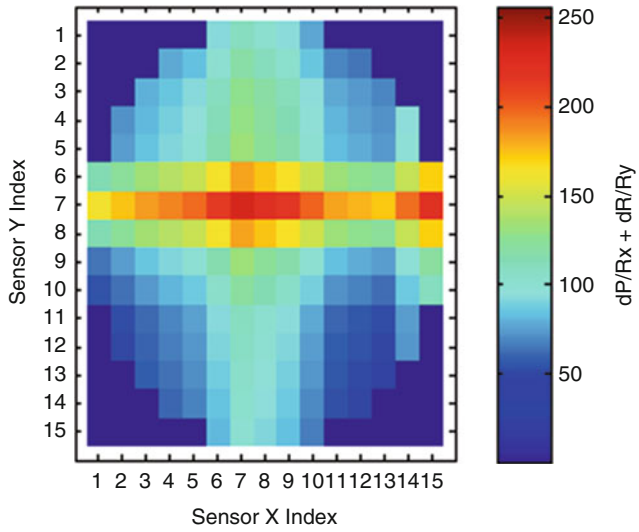

Fig. 4.3 Example output of the visualization program depicting a touch at row 4 and column 4. The color bar scale shows the normalized change in biaxial resistance

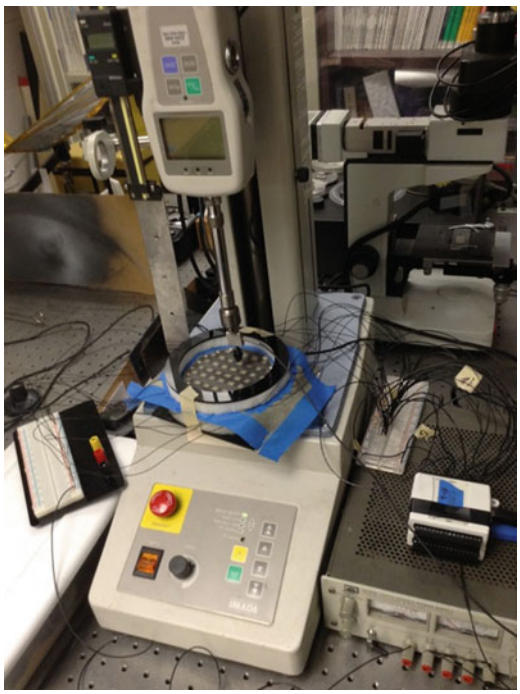

Fig. 4.4 Configuration for testing skin by applying a centralized load on the circular specimen shown in Fig. 4.1

4.2.4 3D Digital Image Correlation Characterization

Digital image correlation (DIC) is a full-field deformation measurement technique that has been applied to multiple length scales [9]. DIC was developed in the early 1980s [10]. It utilizes both optical imaging and numerical computing. DIC compares digitized images of an un-deformed specimen to multiple images of deformed specimens. Gray-scale speckle patterns are required for image reference during computation. The comparison of speckling in sequential imaging results in full-field deformation and strain. 3D DIC was developed in the 1990s [11]. 3D DIC employs two or more cameras to create a stereo vision system. 3D DIC is capable of calculating accurate surface deformations even under large three-dimensional deformations.

The 3D DIC measurement system used in this investigation consisted of two cameras to take stereo images of a surface. The cameras (Point Grey, FL2G-13S2M-C) were used with specific lenses (Tokina, SD 12–24 F4 (IF) DX). The two cameras were placed as close as possible to each other to create images that were as similar as possible. Additional lighting was added

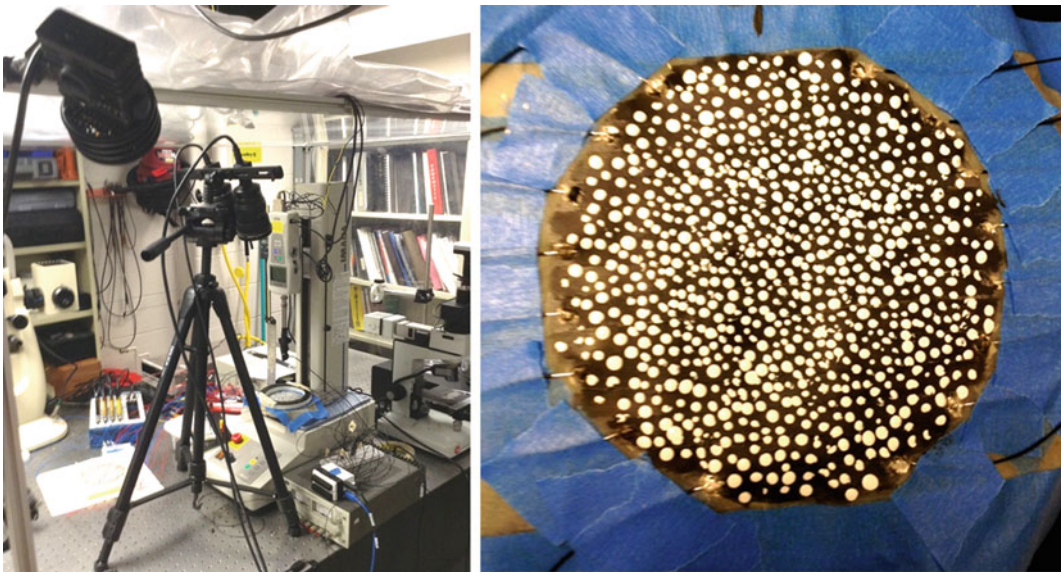

Fig. 4.5 (*Left*) 3D DIC cameras and lighting set-up around the Imada load frame. (*Right*) Skin with speckle pattern

to the area of interest (Lowel Pro, P2-10). The testing of the skin's surface and response took place on the Imada load frame. The set-up of the cameras and lighting for the 3D DIC measurements are shown in Fig. 4.5.

The surface to be deformed should have high contrast speckling. To accomplish this, black latex paint (Behr, UL203) was applied to the skin's surface to create a uniform dark background and white dots of latex paint (Behr, UL200) were manually applied to create the speckling (Fig. 4.5). This surface preparation allowed the processing software (VIC 3D, Correlated Solutions, Columbia, SC) to determine the shape of the surface. As the dots moved in each picture, the program determined the strain in the surface.

4.2.5 DIC Measurements

The Imada load frame was used to deflect the surface of the skin while the Labview program recorded data. The surface was deflected and then unloaded. Images were taken during this process using VIC Snap. After the deflection cycle was completed, the images were processed by 3D DIC. The program generated a 3D profile of the surface over which different variables can be displayed in gradients. A sample surface can be seen in Fig. 4.6. The data calculated for this surface image were exported into a csv (comma separated values) file. Data from 3D DIC and responses from the skin were compared for strain and resistance relationships.

The area of the surface plot that is missing was caused by obstruction between the camera and the speckle surface. Figure 4.6 also shows how the missing areas are caused by the load stand probe or lighting deficiencies. Areas with small holes in the surface reconstruction are caused by lighting insufficiencies. The large wedge of missing data was caused by the obstruction from the load stand probe and shadows.

4.3 Experimental Results and Discussion

4.3.1 3D DIC Surface Measurements

From the 3D DIC setup, measurements of surface deflection during loading were conducted. The load was applied at the center of the circular skin. This measurement was used to calculate the actual strain for comparison with the sensor response. This three dimensional representation of the skin surface shows nonlinear deflection across the radius of the circle. These data were used to calculate the strain of the surface.

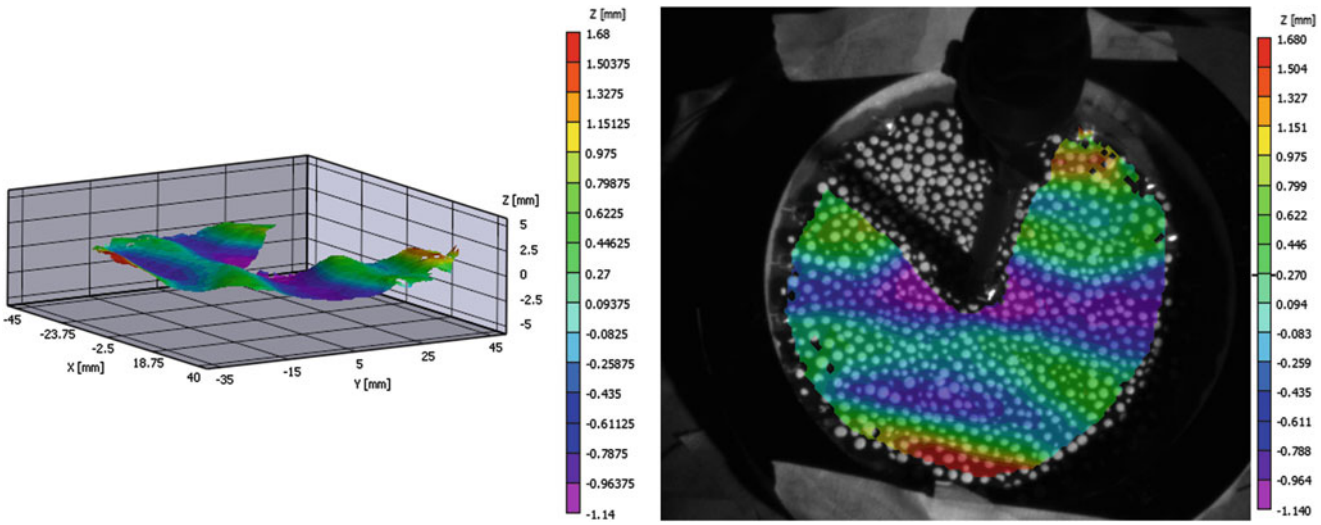

Fig. 4.6 (*Left*) Example output from 3D DIC for a skin without loading. Surface roughness of approximately 1 mm is evident over the 100 mm diameter skin (~1 % variation). (*Right*) Example of output of 3D DIC overlaid on surface image showing a missing area due to obstruction

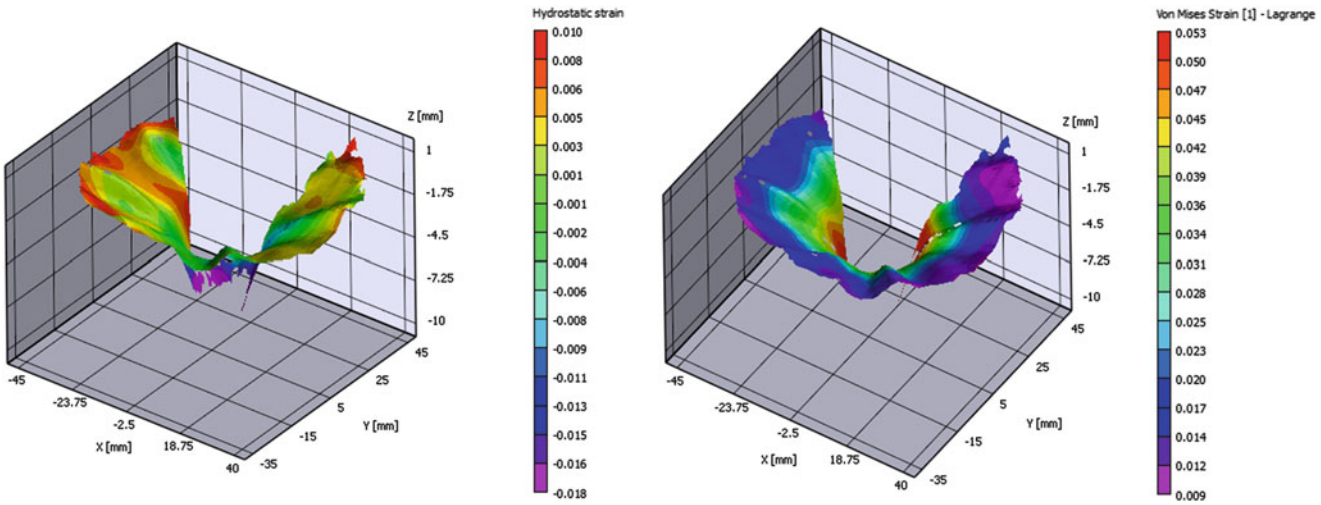

Fig. 4.7 Contour plot of 3D DIC strains on the sensor surface: (*Left*) hydrostatic and (*Right*) von Mises

When a material is under stress, the strain can be split into hydrostatic strain and deviatoric strain. Hydrostatic strain is the strain associated with volumetric deformation of the material, which is an invariant scalar quantity associated with pressure. Figure 4.8 shows the hydrostatic strain of the sensor surface. Deviatoric strain is associated with the distortion of the material. To visualize the deviatoric strain as a scalar, the Von Mises or "equivalent" strain is used. This strain is often used as a yield or failure criteria for a material. Figure 4.7 also shows the Von Mises strain of the skin surface at the maximum loading condition. Strain decreased radially from the center, as expected for axisymmetric deformations. By comparing this strain and deflection to the sensor response, an understanding of the sensor's tactile capabilities can be established.

4.3.2 Strain Response of Skin

The responses of multiple gauges are the first analyses of interest. For the skin to be an effective tactile sensor it should localize an external force. To a deformation of the gauge, it was expected that the skin would have a higher response at the center, where it was touched, and decreasing responses away from the center. Figure 4.8 shows the responses of the

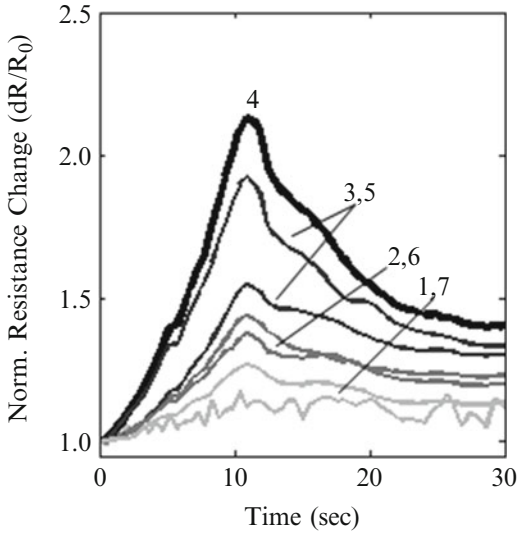

Fig. 4.8 Normalized resistance of individual column gauges to a load over the position of column 4. The *grayscale line* colors depict increasing distance from column 4

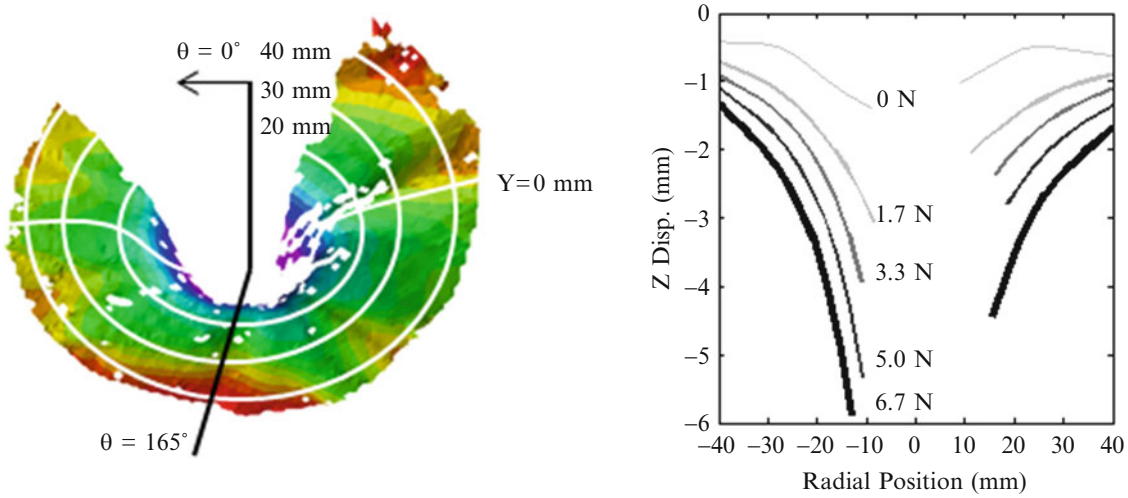

Fig. 4.9 (*Left*) Diagram of data taken from 3D DIC analysis (color contours represent Z deflections). White lines signify data sets used in further analysis. At an angle of 165°, there is a peak due to wrinkling. (*Right*) Deflection vs. radial position for varying force. Data were obtained along the horizontal white line shown on the left

column sensors. As hypothesized, the skin had its highest response at the center, at column gauge 4. The gauge responses decreased with distance from the center. This confirmed our expectations of force localization.

Using the 3D DIC and force testing set-up, measurements of sensor response and surface displacement were taken. The objective of these measurements was to characterize the response of the skin while under surface strain. The resulting shape of the surface measured by 3D DIC can be seen in Fig. 4.9. The black and white lines distinguish data sets of interest for further processing. Using these data sets, a characterization of skin response was conducted. The color gradient indicates the maximum Z displacement in purple and minimum in red. The forces required to deflect the surface are range from 0 to 6.7 N. The evolution of the shape of the skin is also seen in Fig. 4.9. At 0 N the surface is not completely flat. As force increases, the maximum deflection of the surface also increases. Deflections increased uniformly. (Again, data missing from the center of the plot were lost to obstructions in the 3D DIC imaging.) These data show that a correlation between surface strain and force could be made with further characterization.

Because this skin was not an idealized membrane under tension and experienced large deformations, the skin wrinkled when deflected. This wrinkling can contribute to variability in the strain signal associated with a given contact force. In order to better under this effect, an angular analysis of the surface displacement was conducted (Fig. 4.11). The wrinkling was largest furthest away from the center of loading. The radial pattern of this winkling was also consistent between specimens, and appears to be asymmetric. Therefore, the peak deformation for wrinkling was determined to be at 165° (Fig. 4.10).

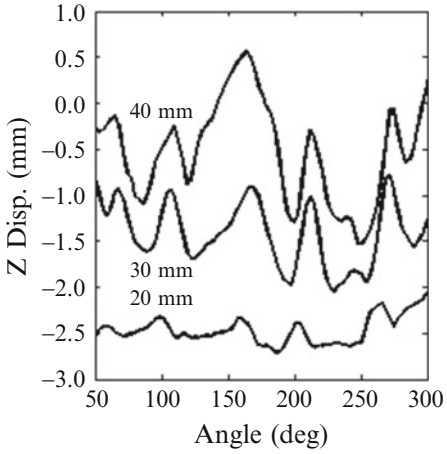

Fig. 4.10 Plot of surface position vs. angle around the midpoint of the surface. Labels indicate the radii of the circular data (Fig. 4.9)

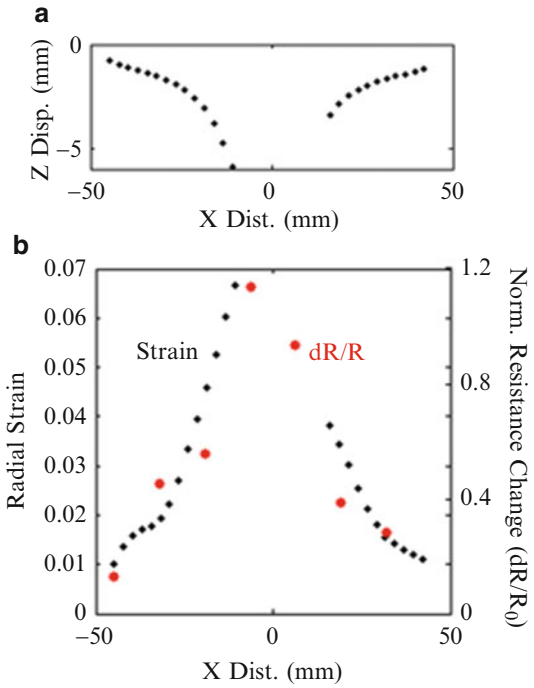

Fig. 4.11 (*Top*) Plot of displacement in the Z direction. These data were taken along the line shown in Fig. 4.9. (*Bottom*) Radial strain (3D DIC) along a radius of the sensor compared to the normalized resistance change of column gauges across the sensor surface

4.3.3 Comparison of Skin Response and 3D DIC Measurements

To accurately characterize the response of the gauges, direct comparisons were made with the DIC measurements. Figure 4.11 shows the shape of the cross-section and the relationship between strain and gauge response. The cross-sectional view of the surface shows non-linear deformation. The deformation is also symmetric. Because strain is related to surface deformation, strain should also be nonuniform. In Fig. 4.11, strain and normalized resistance change follow the same curve. This result indicates that the response of the skin sensor is proportionally related to the strain. This figure validates the imaging capabilities of the skin sensor. Further investigation into response and strain measurement will able to provide response and strain correlations.

4.3.4 Sensing Braille with a Robot Arm

To demonstrate the capability of the skin to enable robots to sense by touch, a finger was designed and attached to a Robot System Model 5150 arm from Festo Didactic (Eatontown, NJ). A skin with three parallel sensing strips 1 mm in width and 2 mm apart was designed for the finger. The finger with the skin attached can be seen in Fig. 4.12; the three strain gauges are

Fig. 4.12 (*Left*) Finger with sensing skin attached to the robot arm, (*center*) braille target, and (*right*) change in voltage from sensing skin raster over Braille target

oriented horizontally in the center of the image. The finger was used to sense a standard Braille target consisting of a pattern of semispherical bumps approximately 2 mm in diameter, also shown in Fig. 4.12. The finger was rastered by steps of 0.72 mm in the x and y directions over the target. The voltage output obtained from the finger is shown in the rightmost image of Fig. 4.12. From these results, it is clear that the new sensing skin is capable of resolving the features on the Braille target by touch.

4.4 Conclusions

The main purpose of the research was the development of a novel robotic skin capable of sensing loads to enable robots to sense and to be trained through touch. This skin was created with a compliant EG/latex strain gauge grid applied to a latex substrate. The skin was supported by a foam layer.

A 3D characterization of the skin's response was conducted. The skin was shown to accurately localize applied forces. Using 3D DIC, a strain analysis of the skin surface was conducted. As expected, strain and skin response were directly related. The pattern of gauge responses directly mimicked the strain of the surface. Further characterization of the skin's response to forces and strain must be conducted in order to fully understand the performance. The capability of using this skin to enable a robot to sense by touch was demonstrated using a Braille target.

Wrinkling was also observed during 3D DIC testing. The wrinkling of the surface was shown to be larger at the boundary, where the strain and subsequent tension ere the lowest. The wrinkling is relatively small in the areas of highest strain. Because of this characteristic, wrinkling is expected to have a minor impact on the surface response when detecting reasonable levels of force.

Acknowledgements This work was funded by the National Science Foundation (NSF) as a part of University of Maryland Miniature Robotics REU (award number 1062885). The work was also funded by NSF as a part of the project, NRI: Small: Compliant Multifunctional Robotic Structures for Safety and Communication by Touch (award number 1317913).

References

1. Stassi, S., et al.: Flexible tactile sensing based on piezoresistive composites: a review. Sensors **14**, 5296–5332 (2014)
2. Alvite, J.G.: Robotic skin. US Patent 4,694,231 A, 15 Sept 1987
3. Cheng, M.Y., et al.: An anthropomorphic robotic skin using highly twistable tactile sensing array. In: 5th IEEE Conference on Industrial Electronics and Applications, Taichung, pp. 650–655 (2010)
4. Vásárhelyi, G., et al.: Tactile sensing arrays—design and processing. Infocommun. J. **LXIII**, 22–27 (2008)
5. Engel, J.M., et al.: Multi-layer embedment of conductive and non-conductive PDMS for all-elastomer MEMS. In: The 12th Solid State Sensors, Actuator, and Microsystems Workshop, Hilton Head, SC, vol. 6, pp. 1–4 (2006)
6. Kujawski, M., et al.: Elastomers filled with exfoliated graphite as compliant electrodes. Carbon **48**, 2409–2417 (2010)
7. Wissman, J., et al.: New compliant strain gauges for self-sensing dynamic deformation of flapping wings on miniature air vehicles. Smart Mater. Struct. **22**, 085031 (2013)
8. Bruck, H.A., Smela, E., Yu, M., Dasgupta, A., Chen, Y.: Mechanics of Compliant Multifunctional Robotic Structures. In: Tandon, G. (ed.): Composite, Hybrid, and Multifunctional Materials, Volume 4: Proceedings of the 2014 Annual Conference on Experimental and Applied Mechanics, Conference Proceedings of the Society for Experimental Mechanics Series, pp. 1–8 (2015). doi 10.1007/978-3-319-06992-0_8
9. Haldar, S., Gheewala, N., Grande-Allen, K.: Multi-scale mechanical characterization of palmetto wood using digital image correlation to develop a template for biologically-inspired polymer composites. Exp. Mech. **51**, 575–589 (2010)

10. Bruck, H.A., McNeill, S.R., Sutton, M.A., Peters, W.H. III: Digital Image Correlation Using Newton-Raphson Method of Partial Differential Correction. Experimental Mechanics **29**, 261–267 (1989)
11. Sutton, M., et al.: The effect of out-of-plane motion on 2D and 3D digital image correlation measurements. Opt. Lasers Eng. **46**(10), 746–757 (2008)

Chapter 5
Electrical Impedance Spectroscopy for Structural Health Monitoring

Geoffrey A. Slipher, Robert A. Haynes, and Jaret C. Riddick

Abstract In-situ structural health monitoring systems on vehicles have the potential to enable on-demand material state awareness capability and eliminate the need for lengthy and costly down-times. Further, the information collected from a structural health monitoring system can be used to predict the remaining useful life of a structure or component. Electrical impedance spectroscopy is an emerging method of interrogating carbon fiber reinforced polymer composite materials subject to cyclic loading to determine the current damage state. This technique has the benefit of using the composite itself as the sensing material, thereby not requiring additional sensing material be placed into the composite. Information can be extracted from changes in both the phase and the impedance magnitude of the signal. Previous work found that special care must be taken to ensure that damage to the leads does not affect the results. In this work, a single interrogation path is examined to determine the usefulness of the single-path approach and the nature of the changes in impedance as they relate to fatigue life.

Keywords Electrical impedance spectroscopy • Structural health monitoring • Carbon fiber • Fatigue state • Damage state detection • Load state detection

5.1 Introduction

As composite materials gain prominence in the rotorcraft community, the need to characterize their damage state throughout the duration of their design life grows. Traditionally, the vehicle is taken out of service at regular conservative intervals, and Non-Destructive Evaluation (NDE) techniques are used to determine the damage state. This approach can be costly, and the vehicle cannot be used for extended periods of time. One emerging alternative is in-situ Structural Health Monitoring (SHM) systems. SHM systems are typically permanently attached to the structure and can be continuously operated to provide regular reports on the damage state of the structure. When combined with a characterization of the material for the particular SHM technique used, they can provide estimates of the remaining useful life of the structure.

There have been many investigations into self-sensing of damage in composite materials. The use of electrical resistance measurements to detect damage in conductive fiber-reinforced composites has been investigated, showing that the resistance changes when damage is incurred by flexure, tension, fatigue, and impact [1]. Changes in resistance can be associated with damage mode. For example, fiber breakage will increase the longitudinal resistance, and delamination will increase the through-thickness resistance. Embedded carbon nanotubes (CNTs) in glass-epoxy composites can create percolating electrical networks for sensing damage; this has been shown to work based on measuring the change in resistance due to cracking [2–5].

While electrical resistance is able to detect damage in fibrous composites, electrical impedance measurements can be more sensitive and selective for damage detection, quantification, and classification by using a full complex-plane analysis, considering both impedance magnitude and phase angle. Electrical resistance is equivalent to a zero-phase angle impedance. Electromechanical impedance spectroscopy has been demonstrated by using a piezoelectric patch [6]. Experimental measurements of carbon fiber composites with embedded piezoceramic patches have shown a close connection between mechanical properties and impedance [7]. Electrical conductivity measurements of embedded Carbon NanoTubes (CNT) thin films have been used to detect damage from low velocity impacts in glass fiber reinforced polymer composites [8]. The electrical impedance tomography response of the composite with the electrical conductive strain sensitive embedded

G.A. Slipher • R.A. Haynes (✉) • J.C. Riddick
Vehicle Technology Directorate, U.S. Army Research Laboratory, 4603 Flare Loop, Aberdeen Proving Ground, MD 21005, USA
e-mail: robert.a.haynes43.civ@mail.mil

C. Ralph et al. (eds.), *Mechanics of Composite and Multi-functional Materials, Volume 7*,
Conference Proceedings of the Society for Experimental Mechanics Series, DOI 10.1007/978-3-319-21762-8_5

thin film was measured by recording current-voltage measurements at the periphery of the composite. More recent work has shown the effectiveness of using piezoelectric patches to monitor the health of adhesive joints in composites subjected to various environmental conditions using electro-mechanical impedance [9].

In this work, direct electrical impedance spectroscopy (EIS) is used to estimate the damage state of the carbon fiber reinforced polymers (CFRPs) without adding inclusions or inserts into the composite. EIS interfaces can be permanently attached or temporarily connected. Previous work [10] investigated multiple conductive paths, but some of the attachments were subject to damage from the cyclic loading, making it difficult to determine if the source of changes in the impedance were from damage in the material or damage in the lead connection. In this work, one conductive path is interrogated to demonstrate that lead failure is not an effect seen in the response and that the load sensitivity still exists. Finally, the specimens undergo fatigue cyclic loading to failure to identify trends in the impedance that could be related to damage progression.

5.2 Motivation

Ideally, an SHM system would be simple and readily implementable, involve minimal modification to the composite manufacturing process, operate in near real-time, have minimal cost, and have the potential to spatially resolve damage and/or damage precursor locations. The objective of this work is to establish that when both the real and imaginary components of electrical impedance are examined, information regarding the accumulation of irreversible damage can be measured. Part of the appeal of EIS is that only a simple connection is needed to complete the conductive circuit. As damage accumulates in a carbon fiber reinforced component undergoing cyclic loading, electrical properties change, and that change can be detected and correlated with the type and location of the damage. Fiber breakage is expected to manifest predominantly as variations in component resistivity as well as in higher frequency response characteristics due to variations in the effective antenna length paths within a component. Delamination is expected to manifest predominantly as variations in the capacitive reactivity of the specimen as the physical spacing between parallel layers varies. A method with the capability to simultaneously detect changes in resistivity, frequency response, and reactivity would thus be required to resolve as many damage modes as possible. Resistance measurement techniques provide only one dimension of information along the real axis of the complex plane to resolve damage in CFRP components. Impedance analysis techniques add two additional dimensions of information: reactance and phase, as shown in Fig. 5.1. We therefore propose the EIS method as a potential improvement in NDE methods for CFRP structural health monitoring in Army systems such as rotorcraft. This paper describes initial experimental efforts to validate these hypotheses.

5.3 Experimental Procedure

Five specimens were manufactured from a woven graphite/epoxy material system with a thickness of 3 mm and cut to dimensions of 25 mm by 300 mm. Insulating fiber glass tabs of dimension 38 mm by 75 mm were attached to both sides and both ends of the specimen. The tabs extended beyond the specimen on both sides and the end to ensure that the wire leads

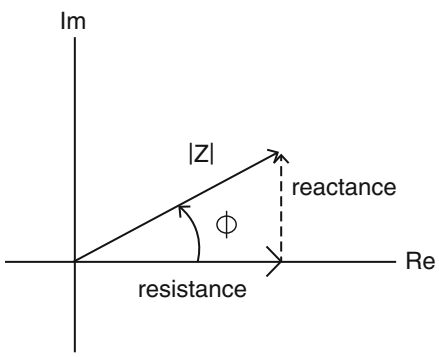

Fig. 5.1 Impedance complex plane

Fig. 5.2 Specimen configuration

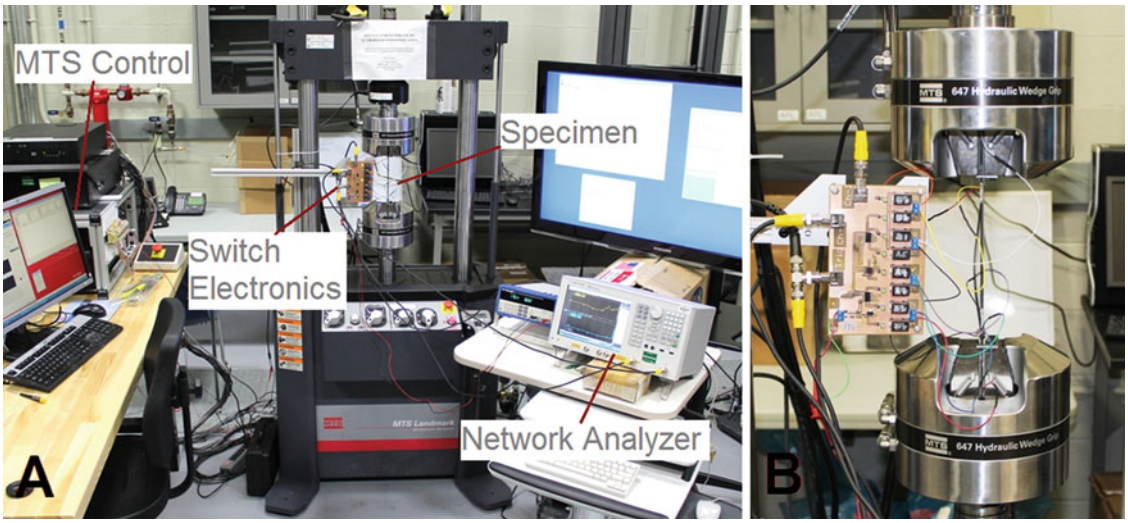

Fig. 5.3 Automated experimental setup: (**a**) wide view; (**b**) close-in specimen view with switching electronics

would touch the testing machine; see Fig. 5.2. All five specimens underwent cyclic loading with predefined pauses to record impedance measurements.

Silver epoxy was used to attach wire leads to the specimen in the configuration shown in Fig. 5.2. The electrical path that was interrogated was through the specimen from lead A1 to lead B1. Electrical impedance was measured using an Agilent E5061B-LF network analyzer (NA) using a port 1–2 thru series method. Prior to initiating sample characterization, a calibration procedure was executed on the NA that pushed the calibration plane out to the specimen. The A1 connection was used to inject the electrical signal through port 1, and the B1 connection was connected to port 2 for the NA return.

The cyclic loading was performed in an MTS 22-kip load frame with an MTS FlexTest 40 controller. An R-ratio of 0.1 was used with a maximum load of 55 kN and a frequency of 5 Hz. Cyclic loading was stopped periodically and a trigger signal was automatically sent from the controller to the NA and a switch that completed the electrical circuit. The NA performed logarithmic frequency scans from 1 kHz to 50 MHz for both statically loaded (55 kN) and unloaded states. Impedance magnitude and phase angle data were collected and saved. The electrical interrogation signal was a sine wave of varying frequency with power of 10dBm (707 mV @ 50 Ω). After the scan is complete, the controller automatically resumes the cyclic loading. The automated experimental setup is shown in Fig. 5.3.

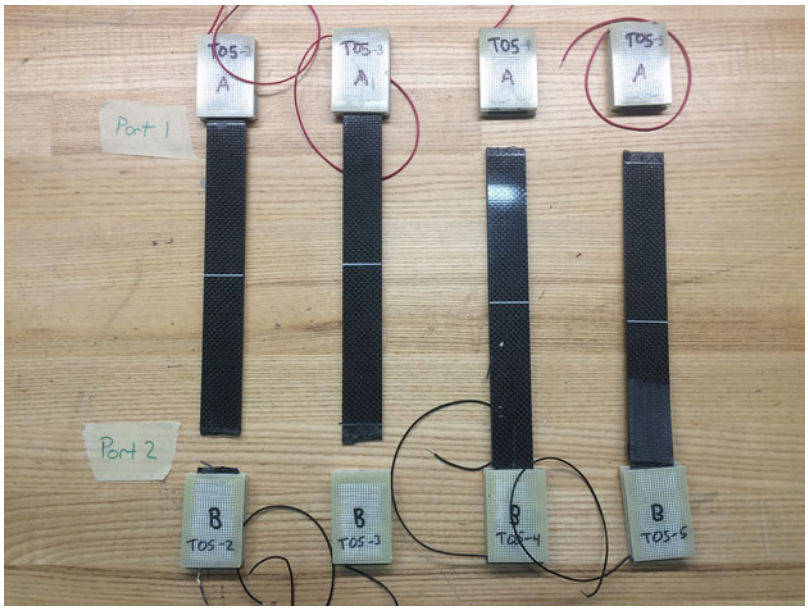

Fig. 5.4 Successfully tested specimens and lead configuration

5.4 Results and Discussion

Of the five specimens tested, the first specimen was discarded because the test stopped prematurely prior to the specimen failing; the remaining four specimens were successfully tested to failure. Specimens 2 through 5 failed after 141,000, 73,569, 13,907, 108,856 cycles, respectively. The failed specimens as well as the lead arrangement are shown in Fig. 5.4. Three broad results are examined in this work: first, that the use of only one interrogation path eliminates the effect of lead failure seen in previous work, second, that there still exists load sensitivity, and third, that there exists sensitivity to fatigue life. The network analyzer stores impedance magnitude and impedance phase as a function of frequency for every scan. As in previous work, the square of the change in the phase along the frequency dimension appeared to capture much of the relevant information, termed delta-phase-squared.

A. Elimination of Lead Failure Effects.
As mentioned previously, only one conductive path was interrogated in this work, meaning only two leads were attached. No lead detachment was observed during testing. Delta-phase-squared contour plots for specimens 2 through 5 in the loaded and unloaded states are shown in Figs. 5.5 and 5.6, respectively. Only frequencies up to 2.5 MHz are shown. For the reader's ease of comparison, Fig. 5.7 presents the delta-phase-squared contour plots from the previous work [10]. Note the elimination of the broadband frequency effects corresponding to lead detachment seen in the previous work. Finally, the frequency band at which the significant information is present regarding material state may vary for different electrical information. For example, Fig. 5.8 presents both delta-phase-squared and delta-magnitude-squared contour plots for specimen 4 while unloaded. Note that the significant material state information is present in the electrical phase data at in a relatively narrow band around 800 kHz versus in the case of the impedance magnitude data, where the material state information is present in a relatively broad band at much lower frequencies.

B. Detection of Specimen Load State.
Note the significantly different delta-phase-squared between Figs. 5.5 and 5.6, corresponding to when the specimen is loaded and unloaded, respectively. These differences are indicative of the sensitivity of the impedance to the load state in the specimen. This observation adds further confirmation to the hypothesis that the electrical state of the material and the material state are correlated, and that, therefore, interrogation of a material's current electrical state can yield useful information about the material's current material state.

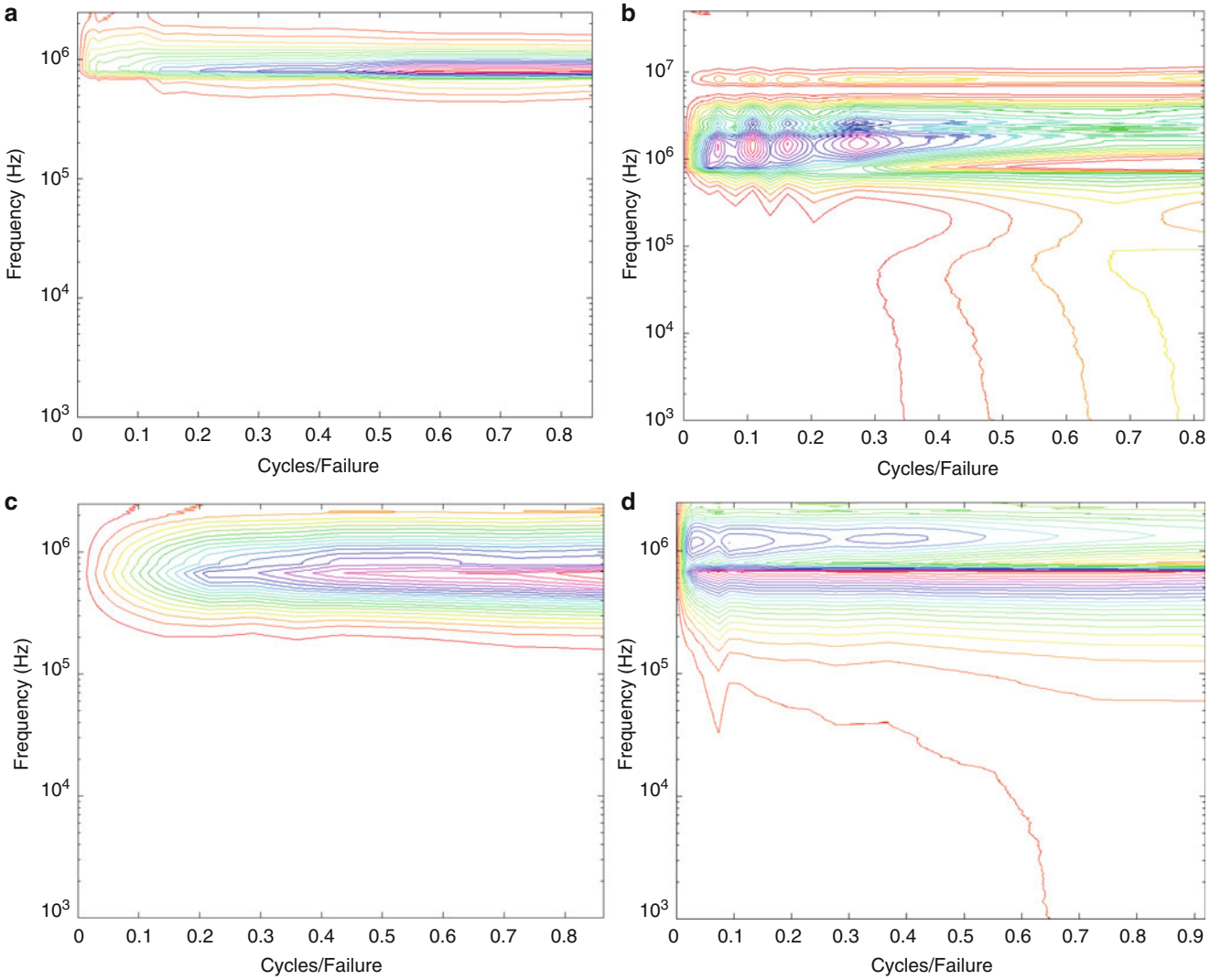

Fig. 5.5 Contour plots of the delta-phase-square for specimens in the loaded (55 kN) state (**a**, specimen 2; **b**, specimen 3; **c**, specimen 4; **d**, specimen 5)

C. Detection of Specimen Fatigue State.

A normalized 3-D contour plot of Fig. 5.5C is provided in Fig. 5.9 to illustrate the monotonic trend in peak delta-phase-squared observed in the specimen. The peak remains within a narrow frequency band throughout the course of the specimen's fatigue life. The data is normalized to a maximum value of 1. Figure 5.10 plots the normalized peak delta-phase-squared for all specimens. Specimens 2, 3, and 5 all show nearly monotonic increases in peak delta-phase-squared throughout fatigue life. It is unclear at this time why Specimen 3 does not show a monotonic trend.

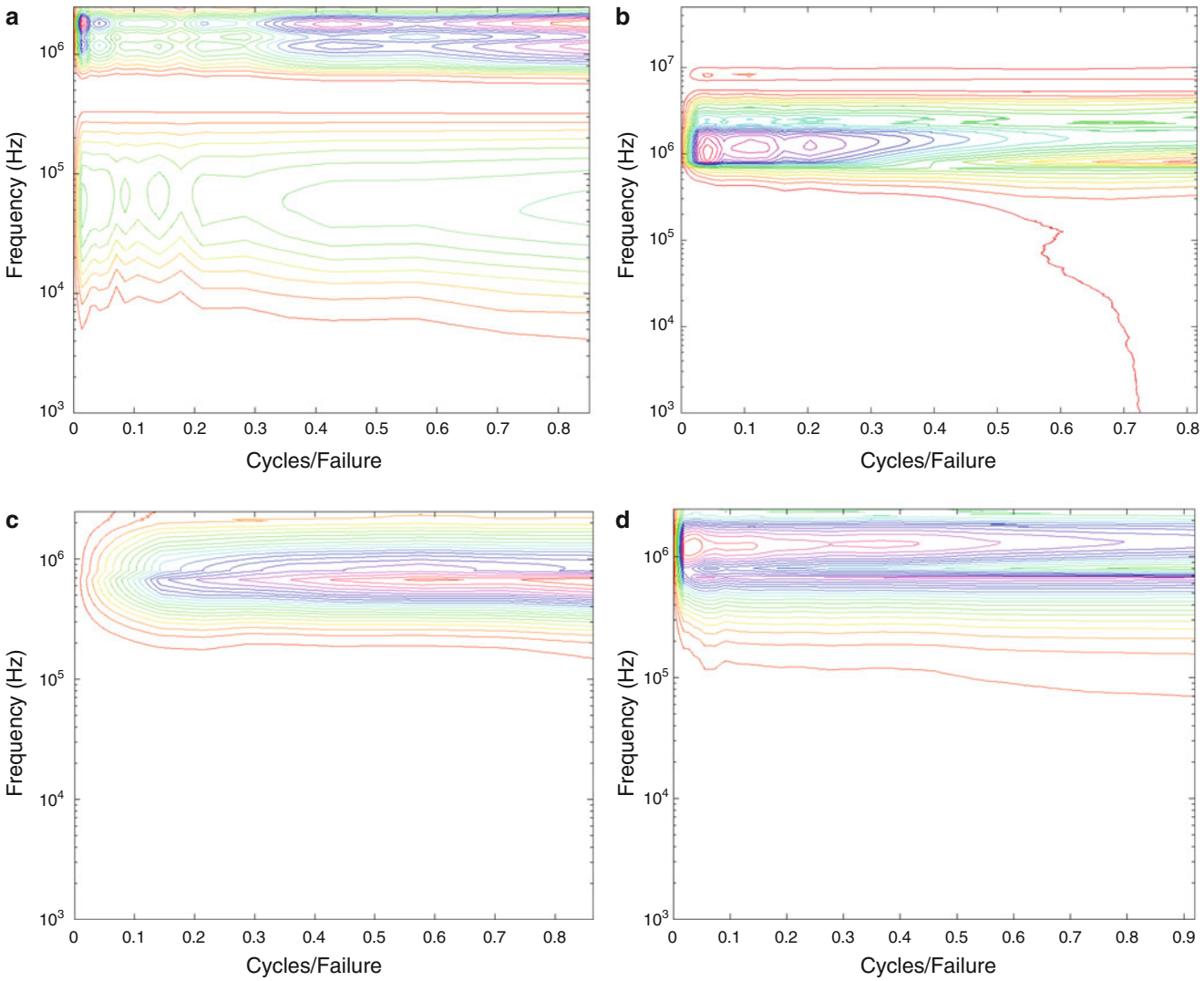

Fig. 5.6 Contour plots of the delta-phase-square for specimens in the unloaded (0 kN) state (**a**, specimen 2; **b**, specimen 3; **c**, specimen 4; **d**, specimen 5)

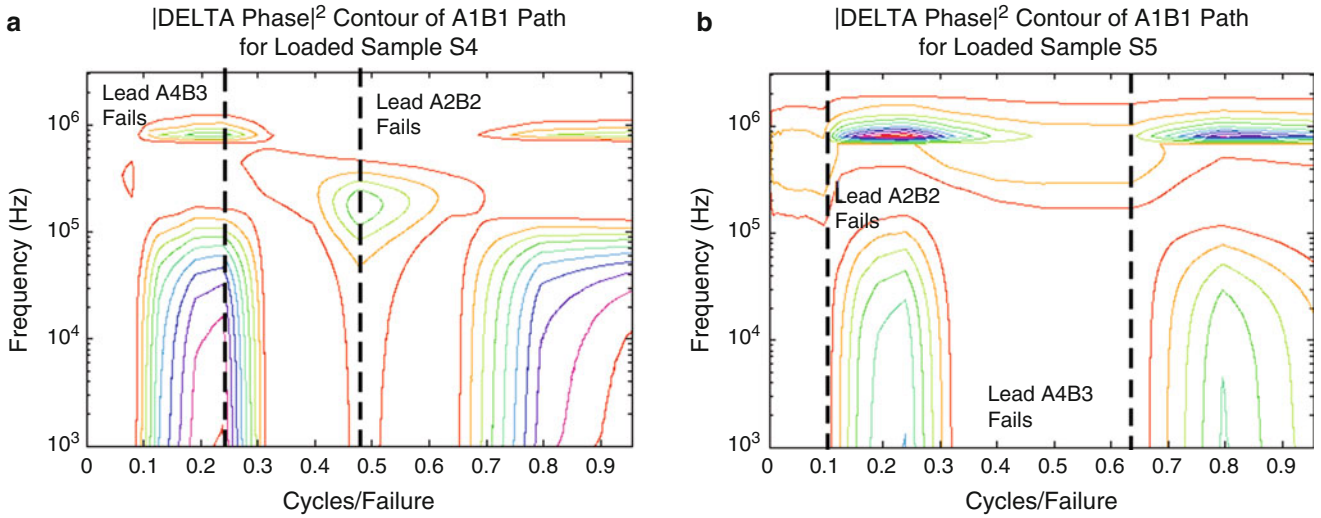

Fig. 5.7 Comparison of delta-phase-squared contours for two specimens from previous work, S4 (*left*) and S5 (*right*), with electrical lead damage indicated in the cycle/failure domain

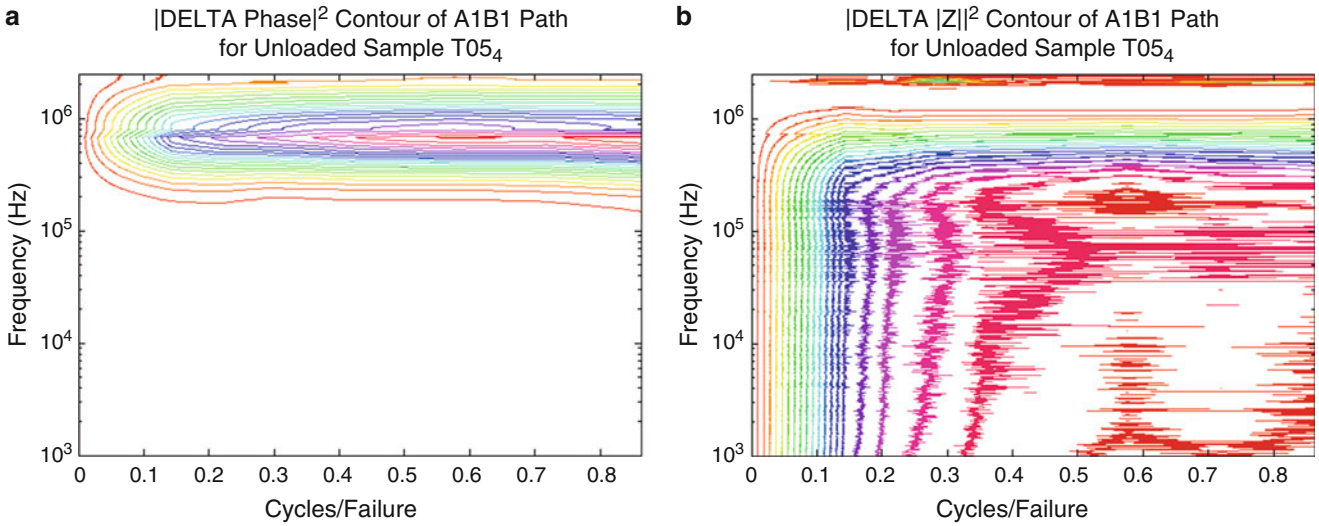

Fig. 5.8 Comparison of different frequency banding for delta-phase-squared data (*left*) versus delta-|Z|-squared data (*right*) for a representative data set, unloaded state of sample 4

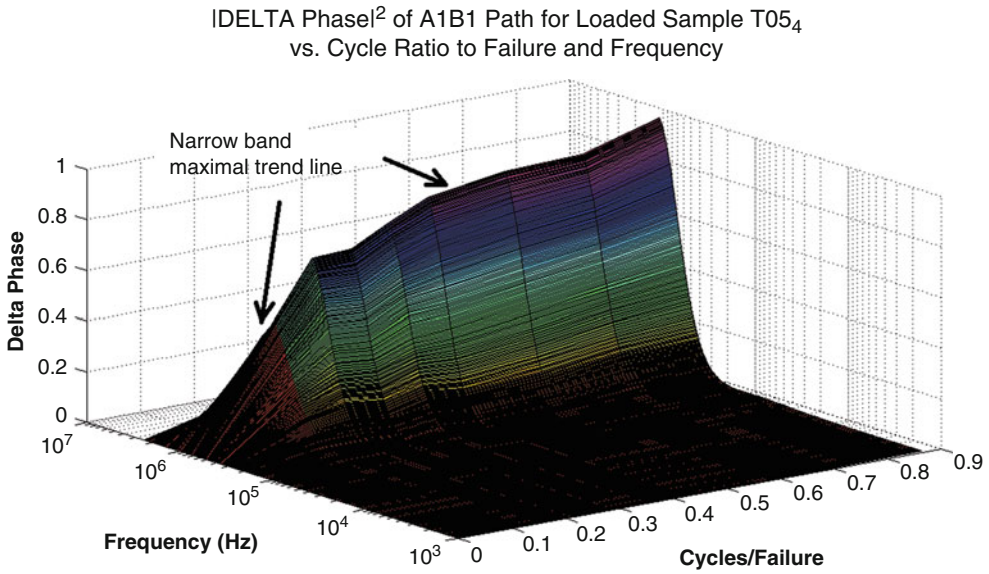

Fig. 5.9 Normalized square of delta-phase surface plot for loaded (55 kN) specimen showing peak trend line in narrow-band frequency (around 750 kHz)

5.5 Conclusions

Five specimens were subject to cyclic fatigue loading and were interrogated with an alternating current at predetermined intervals to determine how the specimens' electrical impedance varies throughout fatigue life. Three conclusions can be drawn. First, leads should not be attached to the gauge section of the specimen to prevent fatigue damage from affecting their integrity. This work demonstrates that placing the leads in the grip region away from the gauge section eliminates this issue. This finding can reasonably be expected to extend to any application of this system, wherein leads should be placed in locations experiencing minimum cyclic loading. Second, it has been confirmed that without the presence of lead failure, the impedance is sensitive to load changes in the specimen, meaning the electrical state of the specimen is coupled to its

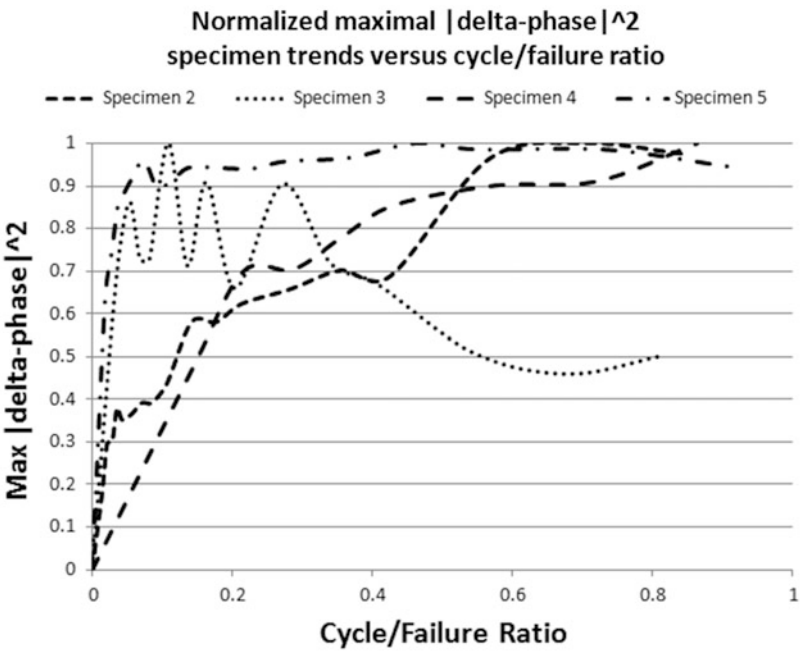

Fig. 5.10 Peak delta-phase-square trendlines for four loaded (55 kN) specimens

mechanical state. This effect is most readily seen in different frequency bands for different electrical information, i.e. magnitude or phase of impedance. Third, there is a possibility that changes delta-phase-squared are caused by changes in the damage state of the material. Deviations from the generally observed trend must be accounted for before this conclusion can made.

References

1. Chung, D.D.L.: Damage detection using self-sensing concepts. Proc. Inst. Mech. Eng. G J. Aerosp. Eng. **221**(4), 509–520 (2007)
2. Liu, A., Wang, K.W., Bakis, C.E.: Damage detection of epoxy polymer via carbon nanotube fillers and external circuitry. In: 18th International Conference on Composites or Nano Engineering, Anchorage, Alaska (2010)
3. Gao, L., Thostenson, E.T., Zhang, Z., Chou, T.-W.: Coupled carbon nanotube network and acoustic emission monitoring for sensing of damage development in composites. Carbon **47**(5), 1381–1388 (2009)
4. Thostenson, E.T., Chou, T.-.W.: Carbon nanotube networks: sensing of distributed strain and damage for life prediction and self healing. Adv. Mater. **18**(21), 2837–2841 (2006)
5. Chung, D.D.L.: Carbon materials for structural self-sensing, electromagnetic shielding and thermal interfacing. Carbon **50**(9), 3342–3353 (2012)
6. Ayres, J.W., Lalande, F., Chaudhry, Z., Rogers, C.A.: Qualitative impedance-based health monitoring of civil infrastructures. Smart Mater. Struct. **7**(5), 599 (1998)
7. Pohl, J., Herold, S., Mook, G., Michel, F.: Damage detection in smart CFRP composites using impedance spectroscopy. Smart Mater. Struct. **10**(4), 834 (2001)
8. Loyola, B.R., Briggs, T.M., Arronche, L., Loh, K.J., La Saponara, V., O'Bryan, G., Skinner, J.L.: Detection of spatially distributed damage in fiber-reinforced polymer composites. Struct. Health Monit. **12**(3), 225–239 (2013)
9. Na, S., Tawie, R., Lee, H.K.: Impedance-based non-destructive evaluation of the FRP adhesive joints in corrosive environment with re-usable technique. In: SPIE Smart Structures and Materials + Nondestructive Evaluation and Health Monitoring, pp. 79811B–79811B. International Society for Optics and Photonics (2011)
10. Slipher, G., Haynes, R., Riddick, J.: Electrical impedance spectroscopy for structural health monitoring. In: Proceedings of the Society for Experimental Mechanics Annual Conference, Greenville, SC, 2–5 June 2014

Chapter 6
Soliton-based Sensor/Actuator for Delamination and Weak Bond Detection in Laminated Composites

Eunho Kim, Taru Singhal, Brian Chang, Yong Han Noel Kim, and Jinkyu Yang

Abstract We design, fabricate, and test a new type of sensor/actuator device that uses stress wave solitons to detect the areas of delaminations and potentially weak adhesive bonds in laminated composites. In this technique, by injecting high energy solitons to a specific inspection area and measuring reflected waves simultaneously, we identify delaminations and characterize the quality of adhesive bonding interfaces in a fast and efficient manner. We also simulate the interaction between solitons and delaminations/weak bonds with the finite element method to understand the effect of composite damages on the scattering behavior of solitons. This proposed sensor technology can open a new way in conducting composite structures inspection, contributing to enhancing maintenance and inspection accuracy and efficiency.

Keywords Soliton • Granular sensor/actuator • Delamination • Weak bond • Damage evaluation

6.1 Introduction

Fiber reinforced polymer (FRP) composites are widely used for various vehicle structures (e.g., aircraft, launch vehicles, automotive, etc.), wind turbine blades, and pressure vessels owing to their high strength- and stiffness-to-mass ratios and corrosion resistance [1]. Moreover, we can tailor and enhance structural performance by changing various fabrication parameters of the composites, such as microstructures of fibers, fiber and matrix materials, stacking angles, and etc. However, their complex microstructures entail different types of damage modes, e.g., fiber breakage, matrix cracking and delamination, which are unprecedented in conventional metallic structures. Among these damage modes, delamination damage is the most common damage mode. In these days, delamination-related damage modes have received more attentions from the composite industry and research community due to the heavy reliance on adhesive bonding in composite structures' assemblies [2, 3]. Adhesive bonding is already adopted widely in large wind turbine blades to exploit their advantages, e.g., uniform stress concentration, reduced weight, and easy fabrication [4]. However, imperfect bonding conditions caused by voids in bondline or contamination at bond surfaces may result in bonding failure, which can potentially lead to structural failure during operation.

In this study, we propose a soliton-based granular sensor/actuator for delamination detection and adhesive bond quality assessment. A granular chain consisting of spherical beads can support the formation and propagation of nonlinear solitons (also called solitary waves), which are a type of highly localized and robust nonlinear waves [5]. Therefore it enables us to transmit a concentrated packet of energy over a long distance without distortion. Moreover, the characteristics of the solitons, e.g., its waveform and speed, are sensitive to the boundary and excitation conditions [6–10]. For the delamination detection, we inject a packet of soliton into a composite panel by using a prototype of granular sensor/actuator. The injected soliton interacts with the delamination present in the panel, thereby generating a unique pattern of wave backscattering. We diagnose the delamination by analyzing such reflected solitons. Likewise, if we inject the solitonic packet into a weak bond area, the transmitted energy breaks the weak bonding interface and induces disbond in a similar form of delamination mentioned above. With this approach we can detect the hidden weak bond and delamination in composite panels.

E. Kim • T. Singhal • B. Chang • Y.H.N. Kim • J. Yang (✉)
Department of Aeronautics and Astronautics, University of Washington, Seattle, WA 98195, USA
e-mail: jkyang@aa.washington.edu

C. Ralph et al. (eds.), *Mechanics of Composite and Multi-functional Materials, Volume 7*,
Conference Proceedings of the Society for Experimental Mechanics Series, DOI 10.1007/978-3-319-21762-8_6

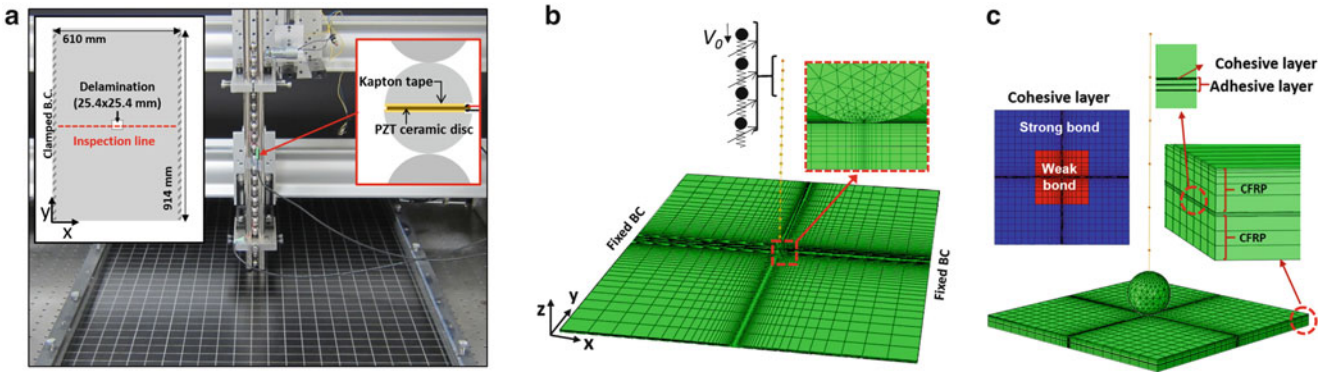

Fig. 6.1 (**a**) Photo of experimental setup for detecting hidden delamination in a composite panel with the granular sensor/actuator unit. *Left inset* shows geometry and dimension of the composite panel, and *right inset* is a schematic diagram of the sensor bead positioned in 7th bead from the top of the chain. (**b**) FE model of the composite panel and the granular sensor/actuator unit. (**c**) FE model for the weak bonding evaluation

6.2 Experiment Setup

Figure 6.1 shows an experimental setup for delamination detection using a soliton-based granular sensor/actuator. The granular sensor/actuator consists of 20 stainless steel spheres with an identical diameter 19.05 mm. They have an elastic modulus $E = 200$ GPa, Poisson's ratio $v = 0.26$ and density $\rho = 7800$ kg/m^3. The beads are supported by four steel rods and vertically aligned as shown in Fig. 6.1a. To generate a packet of soliton in the chain we drop a sphere (identical to the bead used in the sensor/actuator) on the top of the chain from a 5 mm drop height using a solenoid. We position an instrumented bead embedding a piezoelectric ceramic disk (see the right inset in Fig. 6.1a) on the 7th particle position from the top. This measures the compressive force when the soliton passes by this particle. The carbon FRP panel has a layup angle of $[5(0/90)]_s$ and dimensions of 914 mm $\times$ 610 mm $\times$ 4 mm. It has an artificial delamination at the panel's center with a size of 25.4 $\times$ 25.4 mm as shown in the left inset of Fig. 6.1a. We clamp long sides of the panel and scan the panel with the granular sensor along the middle inspection line. For a reference we also scan a pristine panel without delamination.

6.3 Numerical Approach

We use the finite element (FE) method to simulate the propagation of the soliton and its interaction with the carbon FRP panel using the commercial FE program ABAQUS. Figure 6.1b shows the FE model consisting of the composite panel and the spherical chain. We first describe the numerical model of the granular chain. For the efficient computation, we use a discrete element model for the sphere chain, where point masses connected with nonlinear springs representing the Hertizan contact interaction [5–7]. The force (F)-displacement (δ) relation of the Hertizan contact can be expressed as follows:

$$F = \beta[\delta]_+^{3/2}, \ \beta = \frac{2E\sqrt{R}}{3(1-v^2)} \tag{6.1}$$

where β is a contact coefficient depending on the geometry and material properties of the object in contact. We use solid element for the last bead to simulate interaction between the last bead and the panel accurately. To link the discrete element model with the last sphere consisting of 3D elements, we feed the displacement information of the last point mass into the central node of the last sphere. The FE model requires fine mesh at the contact region to simulate the Hertzian contact interaction as shown in the inset of Fig. 6.1b. For the efficiency of the numerical analysis, we use fine mesh only near the contact region. We use this granular chain model for the simulations of both delamination and weak bond detection.

Now we describe the FE model of the panel. For the delamination detection simulation, we build the numerical model as described in the previous section, using solid elements. For the weak bond detection, we use a composite panel having a layup of $[(0/90/45/\text{-}45)_{3s}/\text{adhesive}]_s$ and dimensions of 100 $\times$ 100 $\times$ 5 mm. We apply simply supported boundary conditions to four edges of the bottom surfaces. In between the upper composite panel and adhesive layer, we embed a cohesive element layer with no geometric thickness to simulate debonding. We separate the cohesive layer into two parts: a weak bond region at the central part and a strong bond region in the outer part, as shown in left inset of Fig. 6.1c.

For the elastic properties of the carbon FRP ply, we use $E_{11} = 143.4$ GPa, $E_{22} = E_{33} = 9.27$ GPa, $G_{12} = G_{13} = 3.8$ GPa, $G_{23} = 3.2$ GPa, $v_{12} = v_{13} = 0.31$, $v_{23} = 0.52$ where the subscript 1,2, and 3 represent the fiber-, transverse of the fiber- and the thickness-directions of the ply, respectively. Density of the composite panel is $\rho = 1850$ kg/m^3. For the cohesive layer, we use $t_I = 33$ MPa, $t_{II} = t_{III} = 54$ MPa, $G_I = 330$ N/m, $G_{II} = G_{III} = 800$ N/m, where t and G represent strength and fracture toughness, respectively, and subscripts I, II and III denote a normal mode and two shear mode, respectively [11]. We use 0.1 % of the strength and fracture toughness for weak bond area.

6.4 Results and Discussion

We first analyze the soliton propagation and its interaction with the pristine panel along the middle inspection line. Figure 6.2a shows spatio-temporal map of the soliton propagation in the chain. The impact excitation on the top of the chain generates a single soliton, which propagates through the chain and interacts with the composite panel. The interaction of the soliton with the composite panel generates multiple soliton reflections. Figure 6.2b shows force profile of the 7th particle (see the dashed line in Fig. 6.2a) at various inspection locations along the middle inspection line. The first pulse represents an incident wave, while the other pulses are ones reflected from the interface with the composite specimen. Inset in Fig. 6.2b shows reflected waves measured using the sensor bead in the experiment. The incident waves are identical through all inspections, while the reflected waves show difference depending on the inspection locations. This is because of the boundary effect of the plate. Once the soliton is injected into the composite panel, flexural waves form and propagate in the panel. These flexural waves are reflected back at the panel's boundary, therefore affecting the interaction of the last particle with the panel. Thus, the boundary effect on the soliton reflection depends on the distance of the inspection location from the boundary, the wave speed of the flexural wave, and the interaction time of the last particle with the panel. Figure 6.2b shows that if the inspection location is at least 160-mm apart from the boundary, the first wave reflection is free from the boundary effect. It is note that the second wave reflection to be free from the boundary effect the inspection location should be apart further from the boundary due to the longer time of the interaction after the soliton injected into the panel.

We also analyze and test the soliton interaction with the composite panel having artificial delamination at the panel's center and calculate the scattering of the reflected waves by comparing the signals from the pristine and damaged plates. To quantify the difference in the wave reflection between the two models, we define a damage index as follows:

$$DI = \left[\int \left[f_{r\_damage} - f_{r\_pristine} \right]^2 dt \Big/ \int f_{in}^2 dt \right]^{1/2} \tag{6.2}$$

where f_{r_damage} and $f_{r\_pristine}$ represents the force profiles of the soliton reflected from the damaged and pristine panels, and f_{in} is force profile of the incident soliton. As a result, Fig. 6.3 shows noticeable difference of this damage index at the position of the delamination in the center of the plate. The damage index from the experiment and the numerical simulation are also compared. We find a good agreements between them, both showing large peaks at the delamination location around $x = 305$ mm.

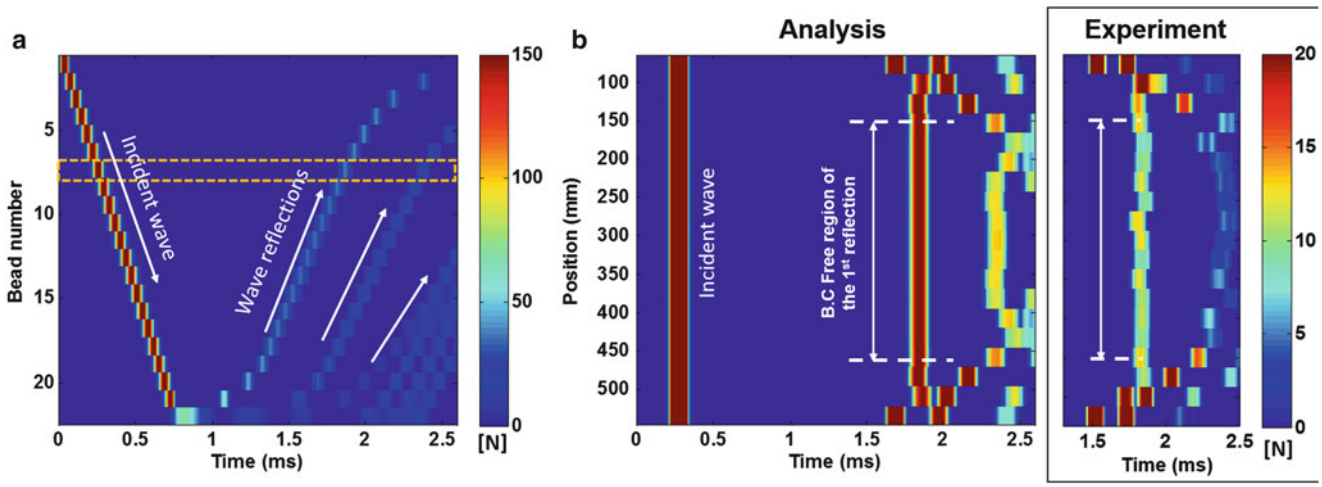

Fig. 6.2 (**a**) Spatio-temporal map of contact forces measured from the granular sensor/actuator unit. (**b**) Image map of the compressive force felt by the sensor bead at various inspection locations. *Inset* shows wave refection measured experimentally

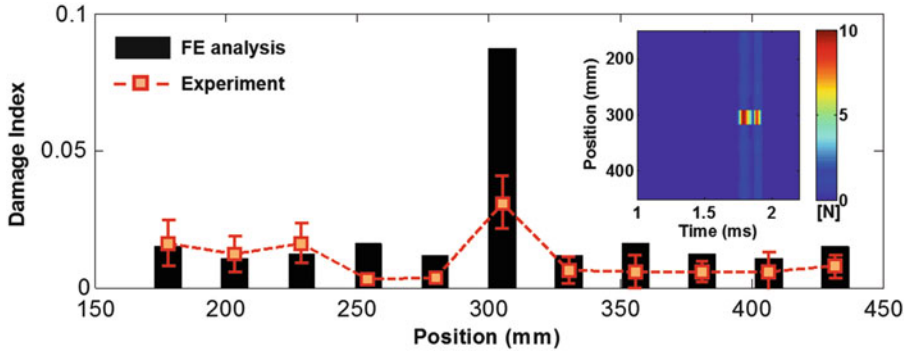

Fig. 6.3 Comparison of damage indexes between FE analysis and experimental results at various inspection locations. *Inset* shows scattered signals of the first wave reflection between the pristine and the damaged panels

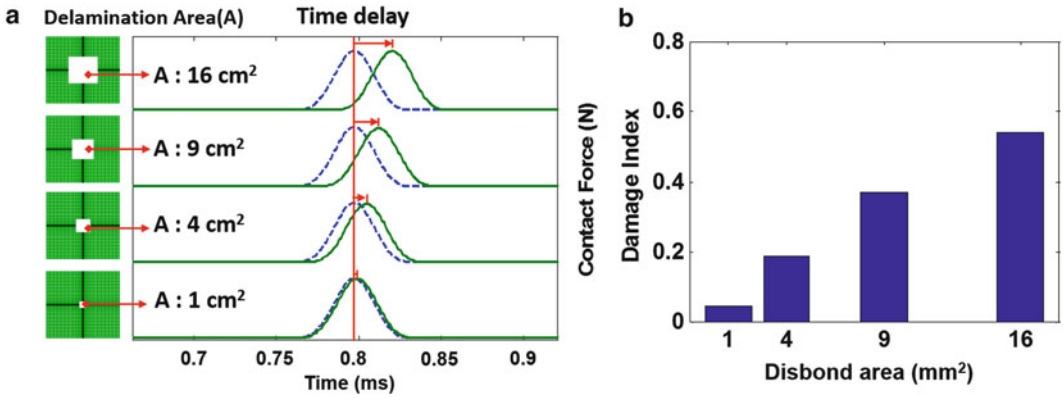

Fig. 6.4 (**a**) Comparison of the first wave reflection from the panels having various disbond sizes. *Blue dash line* shows the first wave reflection from the pristine panel without disbond and *green solid lines* show the reflected wave from the panels having various disbond sizes. (**b**) Change of the damage indexes with respect to disbond area

In the weak bond simulation, we apply an initial velocity of 2 m/s to the striker, which generates complete disbond in the weak bonding area. However, the first reflected wave does not show significant difference compared to the pristine case with no weak bond area. After the disbond generated, if we inject a soliton again, then the first wave reflection shows noticeable difference. We simulate several models having various disbond areas and compare the first wave reflection with the pristine case in Fig. 6.4a. As the disbond size increases the time delay of the first wave reflection increases, while the amplitude changes of the reflected wave are negligible. Figure 6.4b shows that the damage index increases as the disbond area increases. Experimental verifications of this weak bonding identification are currently in progress.

6.5 Conclusions

We experimentally and numerically demonstrate the delamination detection in the composite panel using soliton-based granular sensor/actuator. The impact excitation of the granular chain generates a soliton which interacts with a composite panel placed underneath the sensor. The interaction of the soliton with the composite panel is sensitive to the local stiffness of the inspection point, therefore resulting in the change of the wave's reflection patterns. The change of the local stiffness due to the delamination can be evidently distinguished by calculating the damage index. Moreover, we numerically identify that the high-intensity energy carried by the soliton can effectively generate disbond in weak bond regions. Once the weak bonding interface is disbonded, we can use the same approach to identify such disbonded regions. However, we find that the energy level should be carefully decided based on the structures geometry, boundary conditions, and the level of weak bond strength, which will be investigated in our future study.

Acknowledgements The experimental portion of this work has been conducted during J.Y.'s postdoctoral scholarship at Caltech. J.Y. acknowledges F. Restuccia and C. Daraio for the assistance and support of this work. The authors thank the support from the Royalty Research Fund at the University of Washington.

References

1. Hahn, H.T., Tsai, S.W.: Introduction to Composite Materials. Technomic Publishing, Lancaster, PA (1980)
2. Yang, S., Gu, L., Gibson, R.F.: Nondestructive detection of weak joints in adhesively bonded composite structures. Compos. Struct. **51**, 9 (2001)
3. Vijaya Kumar, R.L., Bhat, M.R., Murthy, C.R.L.: Evaluation of kissing bond in composite adhesive lap joints using digital image correlation: preliminary studies. Int. J. Adhes. Adhes. **42**, 60–68 (2013)
4. Ji, Y.M., Han, K.S.: Fracture mechanics approach for failure of adhesive joints in wind turbine blades. Renew. Energy **65**, 23–28 (2014)
5. Nesterenko, V.F.: Dynamics of Heterogeneous Materials. Springer, New York (2001)
6. Job, S., et al.: Solitary wave trains in granular chains: experiments, theory and simulations. Granul. Matter **10**, 13–20 (2007)
7. Yang, J., et al.: Interaction of highly nonlinear solitary waves with thin plates. Int. J. Solids Struct. **49**(13), 1463–1471 (2012)
8. Ni, X., et al.: Monitoring the hydration of cement using highly nonlinear solitary waves. NDT&E Int. **52**, 76–85 (2012)
9. Ni, X., Rizzo, P.: Highly nonlinear solitary waves for the inspection of adhesive joints. Exp. Mech. **52**(9), 1493–1501 (2012)
10. Yang, J., Restuccia, F., Daraio, C.: Highly nonlinear granular crystal sensor and actuator for delamination detection in composite structures. In: International Workshop on Structural Health Monitoring, Stanford, CA (2011)
11. Kim, E.-H., et al.: Composite damage model based on continuum damage mechanics and low velocity impact analysis of composite plates. Compos. Struct. **95**, 123–134 (2013)

Chapter 7
In Pursuit of Bio-inspired Triboluminescent Multifunctional Composites

David O. Olawale, Jin Yan, Divyesh H. Bhakta, Donovan Carey, Tarik J. Dickens, and Okenwa I. Okoli

Abstract In the last three decades, much research work has gone into efforts to utilize the triboluminescence properties of some crystals for damage monitoring in engineering structures such as bridges and aircrafts. The key challenge from practical application point of view has to do with integrating the sensor in opaque composite structures and successfully transmitting and characterizing the TL signals generated due to damage in these structures. To solve this problem, we have developed the bio-inspired in-situ triboluminescent optical fiber (ITOF) sensor that mimics the sensory neurons of the human nervous system with an integrated sensing and transmission system. The integration of the TL-based sensing component and the transmission component has greatly enhanced the efficiency of side-coupling making distributed sensing along the entire coated length of the polymer optical fiber possible. Our group is the first to apply TL-based damage sensing to cementitious composite systems such as concrete structures to create multifunctional composites with both load carrying and in situ damage monitoring capabilities. This work will highlight key results and advances made in the development of cementitious as well as fiber reinforced polymer composites with in situ damage monitoring capabilities.

Keywords Triboluminescence • Composites • Damage sensor • Structural health monitoring • In-situ sensing

7.1 Introduction

In the last three decades, much research work has gone into efforts to utilize the triboluminescence properties of some crystals for damage monitoring in engineering structures such as bridges and aircrafts. Although there are many nondestructive damage monitoring techniques and sensors for these structures, they suffer from many drawbacks that limit their effectiveness and application. These include imaging techniques such as ultrasonic C-scan, x-ray and thermography that are limited because they do not provide for in-situ sensing. This inhibits the real-time monitoring of the structure. The costs associated with the downtime required for periodic non-destructive inspections of these structures can be very high [1]. While acoustic emission technique is promising, it suffers from low-signal-to-noise ratio. On the other hand, surface-mounted resistive foil strain gages have potential for in-situ and continuous monitoring. They are however less effective in monitoring internal damage and are vulnerable to electromagnetic and electrical interference, as well as physical damage [2].

Triboluminescence-based sensor systems however have the potential to enable wireless, in-situ, real time and distributed (WIRD) structural health monitoring of composite structures [3]. Triboluminescence also known as fracto-[4], piezo-[5], or mechano-luminescence [6], is the emission of light by solid materials when they are stressed or fractured [7, 8]. It has been estimated that about 50 % of all crystal compounds exhibit a range of triboluminescence [9]. Triboluminescence was reportedly discovered in the sixteenth century by Sir Francis Bacon and serious research into the phenomenon began in the twentieth century. The main contribution of early nineteenth century research was the compilation of an extensive list of triboluminescent (TL) materials using highly subjective visual observation of the TL response as a function of time and quantity [9]. The development of the photomultiplier tube (PMT) in the 1930s and its application in triboluminescence studies in 1952 however introduced a quantitative technique for detecting, measuring, and comparing TL emissions objectively.

D.O. Olawale • T.J. Dickens • O.I. Okoli (✉)
High-Performance Materials Institute, FAMU-FSU College of Engineering, 2525 Pottsdamer Street, Tallahassee, FL 32310, USA

Nanotechnology Patronas Group Inc., Tallahassee, FL 32311, USA
e-mail: okoli@eng.fsu.edu

J. Yan • D.H. Bhakta • D. Carey
High-Performance Materials Institute, FAMU-FSU College of Engineering, 2525 Pottsdamer Street, Tallahassee, FL 32310, USA

C. Ralph et al. (eds.), *Mechanics of Composite and Multi-functional Materials, Volume 7*,
Conference Proceedings of the Society for Experimental Mechanics Series, DOI 10.1007/978-3-319-21762-8_7

There have been a number of attempts to apply the triboluminescence phenomenon for damage sensing in recent years [10–13]. A TL-based sensor system comprising highly efficient triboluminescent materials could allow simple, real time monitoring of both the magnitude and location of damage with minimal parasitic influence to the host structure [14, 15]. They have been proposed as stress, fracture, and damage sensors [16, 17]. They have also been demonstrated for visualizing the stress field near the crack-tip, stress distribution in solids, and quasi-dynamic crack-propagation in solids [11, 12, 16, 18–20]. In spite of all these research efforts, there is no information contained in the open literature that suggests commercial use of TL as a damage sensing mechanism [14].

A major challenge militating against the successful development and wide use of TL-based sensor systems is the inability to effectively capture and transmit the optical signal generated within opaque composites like concrete and carbon fiber reinforced polymers. To solve this problem, our team investigated different solution approaches. The first involved the direct dispersion of TL crystals, primarily Zinc Sulphide (ZnS) into unreinforced cementitious composite. The second approach involved the development of the bio-inspired in-situ triboluminescent optical fiber (ITOF) sensor. The ITOF sensor was used to demonstrate real time and distributed damage monitoring in cementitious composites as well as in fiber reinforced polymer composites.

7.2 Direct Dispersion of Zns:Mn Crystals in Cementitious Composite

The first approach investigated in developing a cementitious composite system with a triboluminescence-based damage detection system involved the direct dispersion of ZnS:Mn crystals in a mortar system [21]. The hypothesis is that as the system is loaded and crack formation occurs, the stress field developed around and along the crack path will cause the excitation of the crystals along the crack path. Such a system will exhibit ubiquitous damage detection. It will be able to detect any crack provided there is a TL crystal along the crack's path. To have an effective system, there is the need to determine the concentration level of the ZnS:Mn crystals required to ensure that any crack at any point in the system is detected without adversely affecting the mechanical properties of the cementitious composite.

7.2.1 Experimental

7.2.1.1 Sample Preparation

The cementitious optical sensor was prepared by physically mixing fly ash, water, cement, and ZnS:Mn crystals. The various properties of the constituents are given in Table 7.1. The ZnS:Mn was purchased from Phosphor Technology, UK. The thoroughly blended mixture was cured by adding water, and the resulting paste poured into a mold. The samples were then allowed to cure for predetermined number of days. The prepared molds had two plastic optical fibers already attached within, to allow for their embedment in the cured cementitious patch. The fibers pick up the triboluminescence signals emitted as the material is loaded, thereby indicating levels of internal damage. While the cement acts as the binder, the fly ash helps in improving the patch's properties by enhancing strength development, reducing voids and negating the effect of shrinkage. The samples produced had dimensions 50 × 50 × 6.25 mm (2 × 2 × 0.25 inch).

Table 7.1 Main constituents of the TL cementitious optical sensor [21]

Material	Bulk specific gravity	Particle size distribution (μm)	Proportion (by mass)
Type I/II Portland cement	3.15	1–50	
Boral class F fly ash	3.00	25	25 % of cement
ZnS:Mn	4.10	5–20	0, 5, 7.5, 10, 15, 20, 25 % of cementitious mixture
Water	1.00		Approx. 50 % of cement

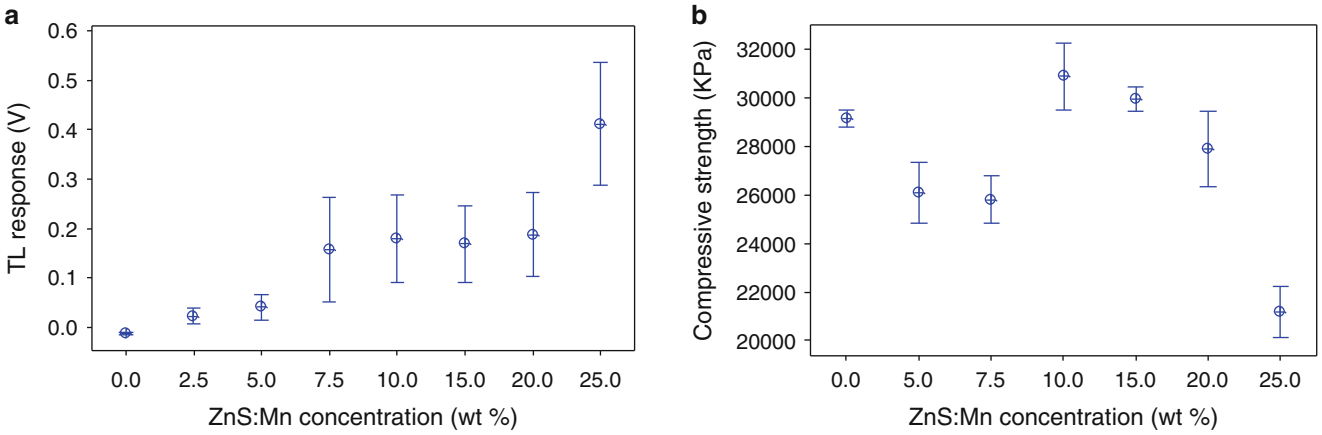

Fig. 7.1 Effect of ZnS:Mn concentration level on (**a**) TL output of composite, (**b**) Compressive strengths of 28 days-cured samples [21]

7.2.1.2 Mechanical Tests

The impact samples were loaded in a custom-built impact rig where they were impacted with a pneumatically-controlled piston at specific pressure values. The rig was fed by a compressed air line, and controlled with an adjustable pressure and release valve. The compressive strength of samples were determined using a CM-3000-DB compression rig from Test Mark Industries according to ASTM C109/C109M – 08 standard test methods for compressive strength of hydraulic cement mortars, using cube specimens of size 50 mm (2 inch). The operation of the impact rig and PMT was controlled using a MatLAB graphical user interface with a NI USB-6210 data acquisition device from National Instruments. The triboluminescent intensity was measured by connecting the plastic optical fibers (POF) from the cured samples to the PMT which converted the TL signals in to electrical signals (voltage).

7.2.2 Results and Discussion

There tends to be an increase in the TL response of the samples with increasing ZnS:Mn concentration levels (Fig. 7.1a). TL signals were obtained at concentration levels as low as 2.5 and 5 %. However, not all the samples tested at these low concentration levels yielded a triboluminescence response on impact. TL responses were obtained for all five samples tested at concentration levels of 7.5 % and higher.

Figure 7.1b shows the effect of ZnS:Mn concentration levels on the compressive strengths of 28 days-cured samples. The result shows that there was a reduction in the compressive strength of the pristine cementitious patch from about 29.5 MPa to about 26 MPa at ZnS:Mn concentrations of 5 and 7.5 % respectively. Enhancement of the compressive strength was however observed at ZnS:Mn concentration levels of 10 and 15 % with mean values of about 31 and 30 MPa respectively, compared to a mean value of about 29 MPa for the mortar system with no ZnS:Mn content. The TL crystals seem to provide some form of particle reinforcement at these concentration levels.

The work demonstrated the feasibility of utilizing a triboluminescence-based cementitious optical sensor for monitoring and detecting internal damage in concrete infrastructural systems. The ZnS:Mn crystals retained and exhibited their TL property in the high alkaline cementitious composite systems studied. A ZnS:Mn percolation level of 7.5 % weight percent will ensure that there is sufficient TL crystals in the system for damage to be well captured. A ZnS:Mn concentration level of 10–15 % gave high TL response without compromising the strength of the triboluminescence-based cementitious optical sensor system.

7.3 Bio-inspired In-Situ Triboluminescent Optical Fiber (ITOF) Sensor

Direct dispersion of TL materials in the host material however has a number of drawbacks, particularly in polymer composites [3]. Firstly, the concentration level (weight fraction) of the TL crystals in the host matrix required for good TL response is usually high. This introduces parasitic weight effect which is highly undesirable. The density differences

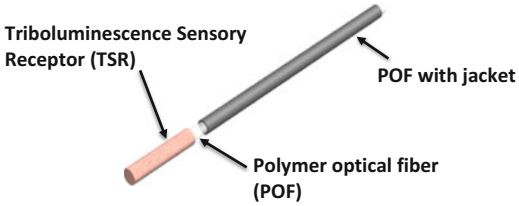

Fig. 7.2 A schematic of the ITOF sensor [24, 25]

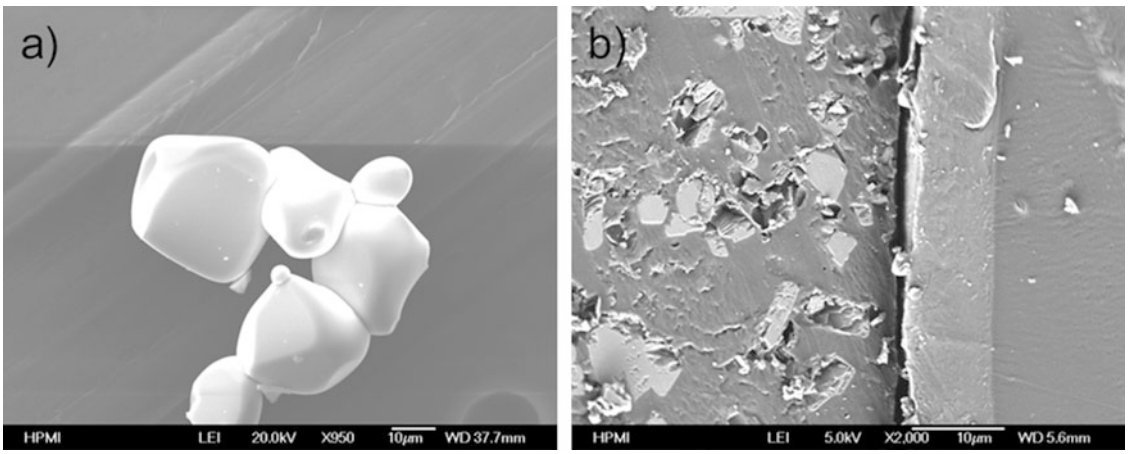

Fig. 7.3 Scanning electron micrographs (**a**) ZnS:Mn crystals (**b**) cross-section of an ITOF sensor showing the ZnS:Mn crystals loaded coating, interface between the coating and the smooth-surfaced POF

between the TL crystals and the host material, particularly resin in polymer composites, may also cause the settling of the crystals during curing. There will therefore be uneven dispersion of the crystals in the cured composite part or structure. In addition, filtration of the TL crystals by the fiber does occur during the resin infusion process.

The in-situ triboluminescent optical fiber (ITOF) sensor was developed to overcome these limitations. The ITOF sensor mimics the sensory receptor of the human nervous system (HNS) by converting the energy from damaging events like impact and fracture into optical signals that are indicative of the magnitude of damage. The ITOF sensor combines the highly desirable properties of optical fibers such as lightweight, small size, immunity to electromagnetic interference and capacity for distributed sensing [2, 22], with the TL property of ZnS:Mn.

The ITOF sensor (Fig. 7.2) consists of a polymer optical fiber (POF) with a highly sensitized section, the triboluminescent sensory receptor (TSR). The TSR is made by mechanically removing the jacket in that section along the length of the POF, and coating with epoxy containing dispersed ZnS:Mn crystals which is one of the most efficient TL materials known [23]. The ITOF sensor senses damage in the composite structure by converting the mechanical energy of the damage causing event like impacts and crack propagation into triboluminescent (TL) optical signals. The TL signals are then transmitted through the POF to a photodetector such as a photomultiplier tube (PMT) or a photodiode. The photodetector converts the TL optical signals into electrical signals that can be analyzed by a computer system for damage characterization.

Figure 7.3a shows some of the ZnS:Mn crystals used in this study. The ITOF coating, the interface between the coating and POF, and the POF are shown in Fig. 7.3b. The smooth morphology of the POF is easily distinguishable from the ZnS:Mn crystals-loaded ITOF coating. The size of the interface (~2 μm) between the coating and the POF permits effective side-coupling of TL emissions from the coating (vide infra) into the POF. The thin film coating of the ITOF made possible the placement of the TL crystals near to the surface of the transmission component (POF) for the successful coupling of the TL emissions into the POF. Effective side-coupling makes distributed sensing with the ITOF possible when the entire length of the POF is coated with this TL thin film.

7.4 Civil Infrastructure with In-Situ 'Pain' Sensing Capability

The development of the ITOF sensor can make it possible to create multifunctional cementitious composites with in-situ damage sensing capabilities. Such a system will mimic the human nervous system with the integrated ITOF sensors acting as the nerves with both sensing and signal transmission capabilities. Figure 7.4 is a schematic illustration of a triboluminescent

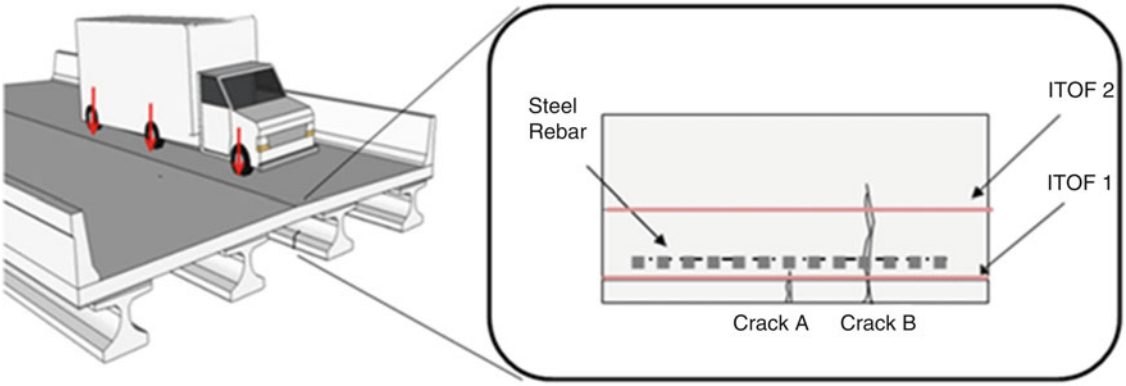

Fig. 7.4 Schematic of double layer sensor TMCC girder for early crack detection

Table 7.2 Constituents of triboluminescent multifunctional cementitious composite (mortar)

Ingredient	Proportion to cement content (by wt)
Portland cement	1.000
Fly ash	0.300
Sand	3.575
Plasticizer	0.012
Water	0.585

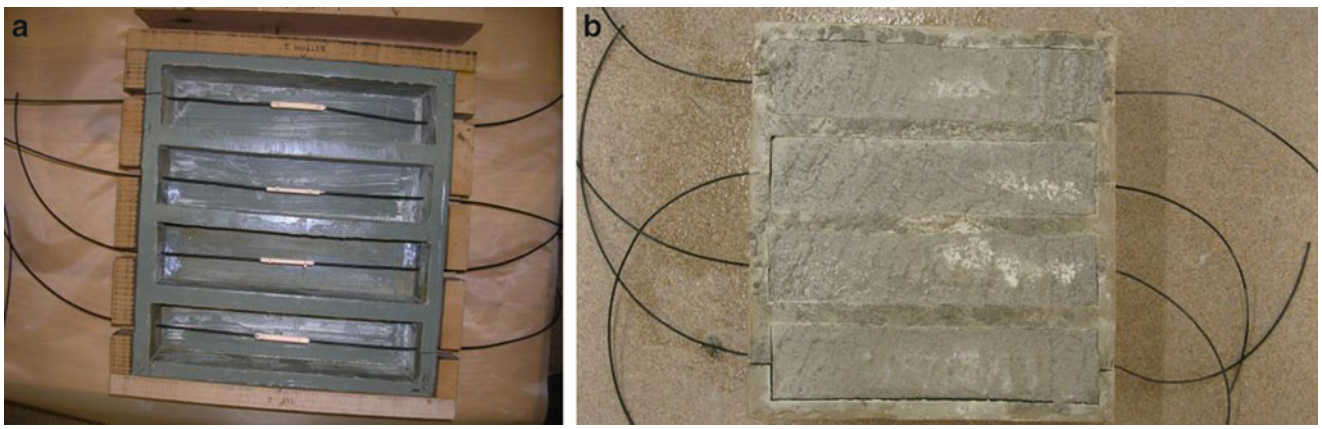

Fig. 7.5 (**a**) Silicon mold with single layer ITOF sensor ready for CC pouring, (**b**) fabricated TMCC beams ready for de-molding from silicon mold

multifunctional cementitious composite (TMCC) bridge girder with in-situ crack monitoring capabilities for protecting the steel reinforcement from corrosion through early crack detection.

7.4.1 Real-Time Failure Monitoring in Mortar Beams

7.4.1.1 Experimental

The mix design for the fabricated unreinforced triboluminescent multifunctional cementitious composite (TMCC) is as highlighted in Table 7.2. The appropriate constituents were measured and mixed thoroughly in an electric-powered concrete mixer. After thorough mixing in the electric-driven concrete mixer, the CC mix was poured into prepared silicon molds.

The ITOF sensors were then placed in the molds (Fig. 7.5a) before pouring the CC mix (Fig. 7.5b). The TMCC beams were de-molded after 24 h and immersed in water in a curing basin at room temperature to cure for 28 days. The dimension of the TMCC beams fabricated was 300 × 90 × 75 mm.

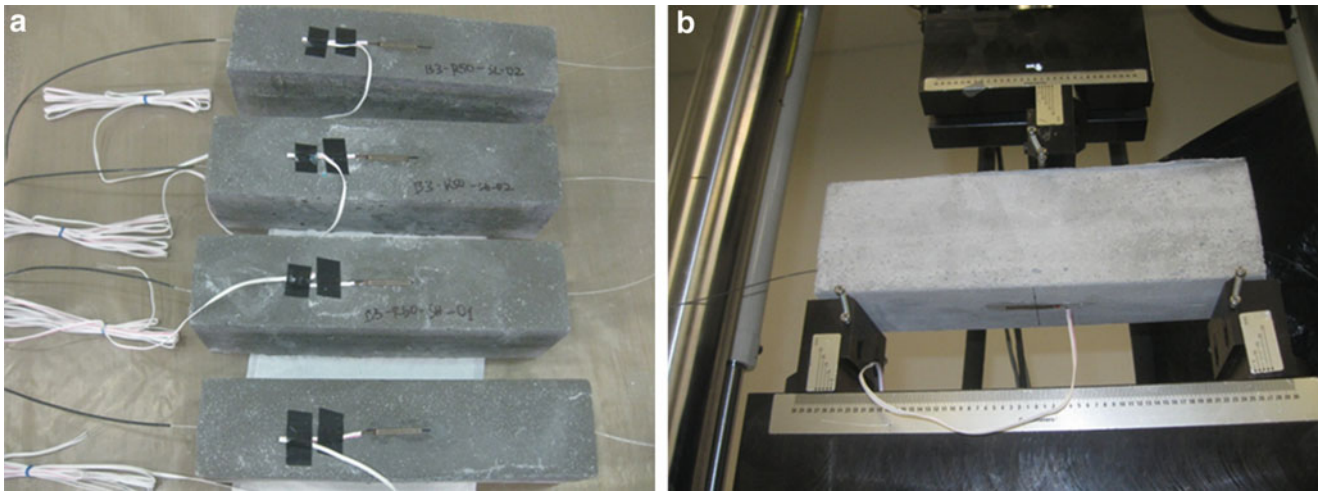

Fig. 7.6 (**a**) TMCC beams with strain gages installed (**b**) Three point bend tests (3PBT) set up

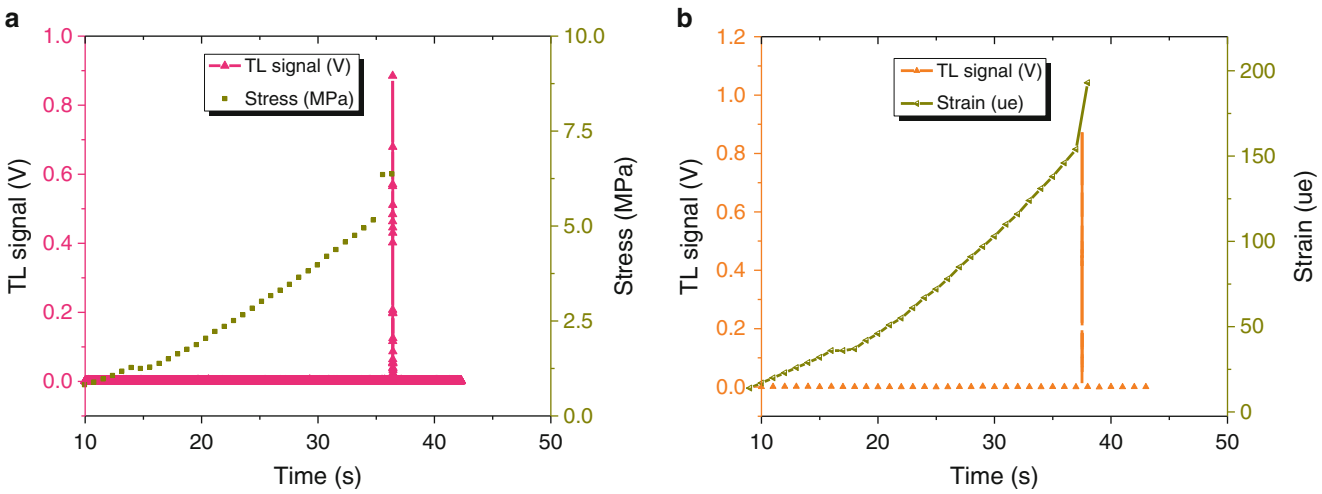

Fig. 7.7 (**a**) TL signal at instant of brittle failure of unreinforced mortar beam, (**b**) Large increases in strain value at instance of brittle failure corresponding to instance of TL signal generation

Three point bend tests (3PBT) were performed on the TMCC beams on a 25 kN MTS 858 mechanical testing machine. The TL signals generated by the ITOF sensor in the TMCC during crack propagation were transmitted to the photomultiplier tube (PMT) from Hamamatsu Corporation (H10722-01) where they were converted into electrical signals (voltage) and quantified. Some of the samples were instrumented with strain gages (by Kyowa Co, Japan) as shown in Fig. 7.6a before being tested (Fig. 7.6b).

7.4.1.2 Result and Discussion

The typical responses obtained at the instance of failure of the unreinforced cementitious beams are as shown in (Fig. 7.7a and b). To validate the effectiveness of the ITOF sensor to provide in-situ and real time damage monitoring in cementitious composites, four TMCC beams were instrumented with strain gages as shown earlier in Fig. 7.6. Damage was successfully detected in real time as can be seen by the coinciding of the time when the TL signal was detected with the time the sample failed as indicated by the loss in the load carrying capacity (Fig. 7.7a).

Similarly, the strain gage experienced a sudden increase in the strain value due to crack opening at the instance of brittle failure of the beam (Fig. 7.7b). At the same instance, a jump in the TL signal was observed (Fig. 7.7b). Unlike the ITOF sensor, a crack must come in contact with the strain gage before it can detect it. The ITOF sensor however offers the superior advantages of distributed and non-contact sensing as demonstrated earlier.

Table 7.3 Constituents of fabricated mortar and reinforced concrete beams

Ingredient	Proportion to cement content of RC (by wt)
Portland cement	1.000
Fly ash	0.23
Coarse aggregate	3.787
Sand	2.596
Plasticizer	0.004
Water	0.594

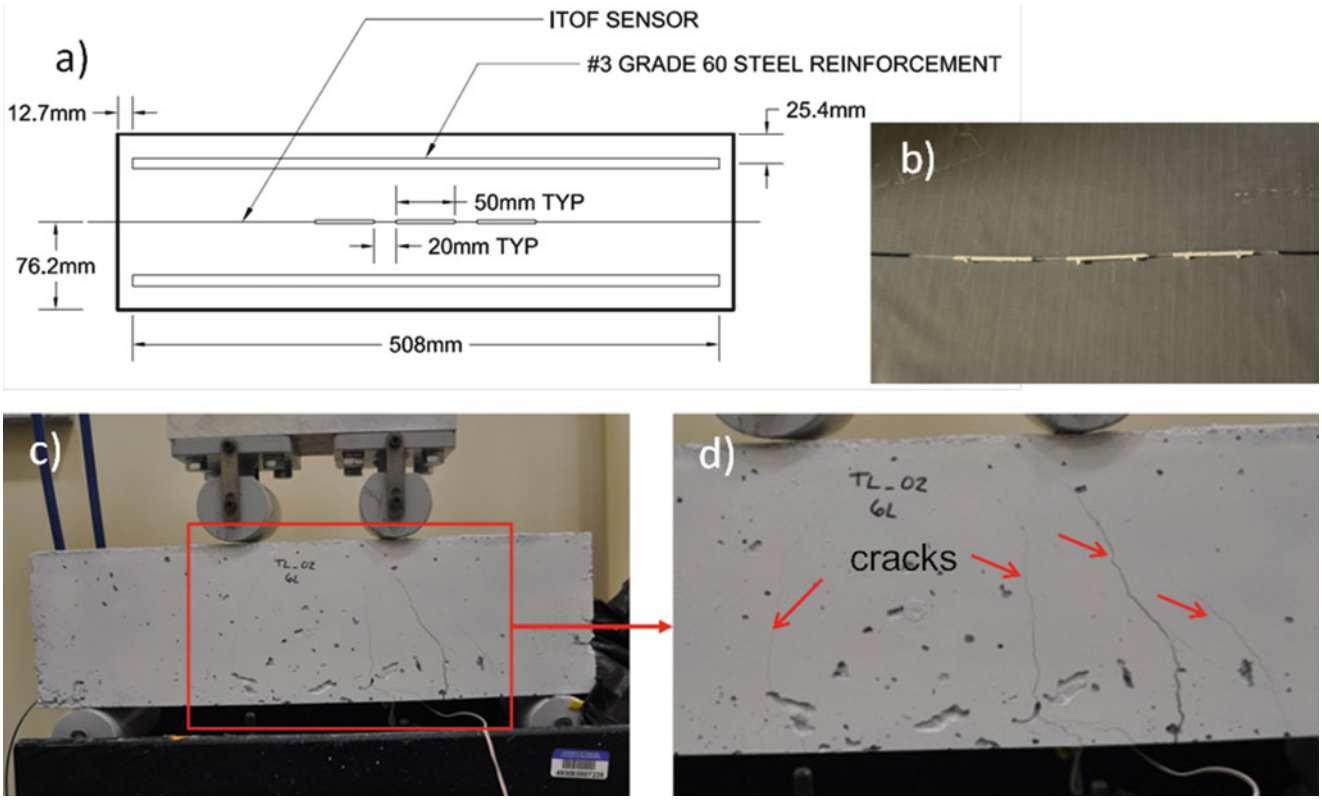

Fig. 7.8 (**a**) Schematic showing the location of the coated sections of the ITOF within the beam, (**b**) Fabricated ITOF sensor with three sections coated with TL composite for enhanced distributed damage sensing, (**c**) Multiple cracks from 4 point bend test, (**d**) Close view of multiple cracks on tested RC beam [26]

7.4.2 Real-Time Damage Monitoring in Reinforced Concrete Beams

7.4.2.1 Experimental

Table 7.3 shows the mix design for the fabricated RC beams. The configuration is as shown in Fig. 7.8a. For the reinforced concrete beams tested, three sections of the integrated ITOF sensors were coated with the triboluminescent (TL) film in an attempt to enhance distributed damage sensing along the length of the ITOF (Fig. 7.8a and b). The tension sides of the fabricated beams were marked to locate the position of the coated sections of the integrated ITOF.

7.4.2.2 Result and Discussion

Figure 7.8c and d highlight the multiple cracks formed in one of the tested beams during the flexural test. Figure 7.9a shows the TL and load profiles obtained during the flexural loading of the beam shown in Fig. 7.9d. Similar profiles were obtained

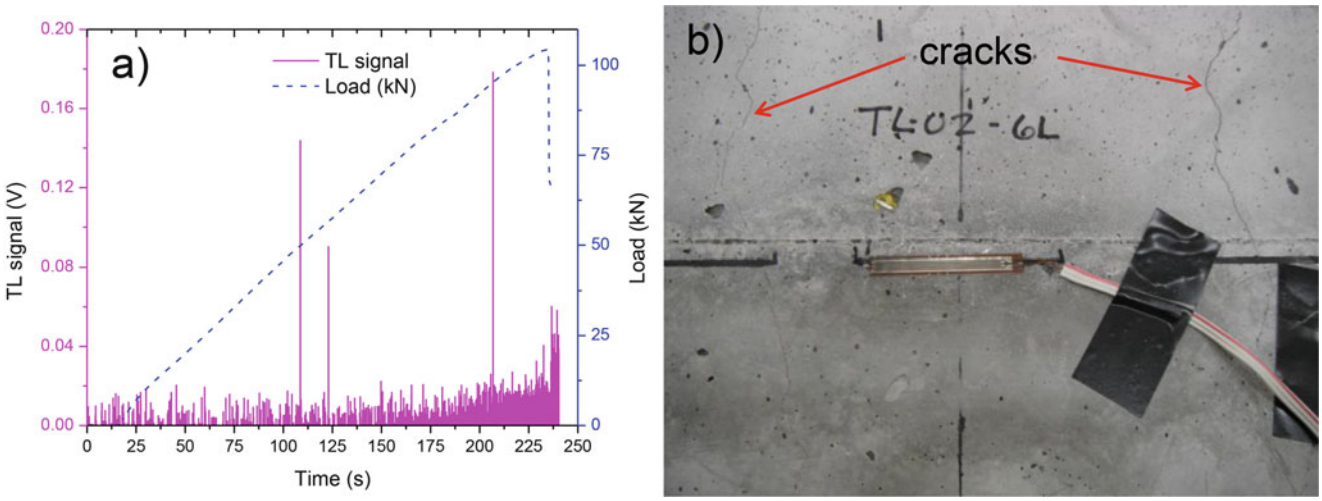

Fig. 7.9 (**a**) Multiple TL signals from multiple cracks providing early warning before structural failure of RC beam, (**b**) Base (tension side) of tested beam with cracks not being detected by strain gage but detected by integrated ITOF (*black horizontal lines* indicate position of integrated ITOF sensor) [26]

from other tested beams. Four cracks were observed on the tested beam but only three TL signal jumps were detected. The first TL signal (0.14 V) was observed at time 109 s when the beam was loaded to 50 kN (about half its strength). The second TL signal (0.09 V) was detected at time 123 s at a load value of 57 kN.

Shortly before failure at time 207 s and at a load of 95 kN, the highest TL signal value of 0.18 V was detected. The beam eventually failed 30 s later at time 236 s and at a load of 105 kN. The continued loading of the beam after the occurrence of the third TL signal resulted in increase in the crack width thereby permitting more ambient light to be detected as indicated by the gradual increase in the TL noise level from time 206 s (Fig. 7.9a). Visual inspection of the sample after the test showed that only two of the four cracks passed through the sensitized section of the integrated ITOF sensor (Fig. 7.9b). In addition, the second TL signal (with the least TL signal value of 0.08 V) must have been caused by the non-contact excitation of the ITOF sensor by a crack that propagated about 20 mm away from the end of the nearest coated section. The fourth crack generated no detectable TL signal because it propagated across the ITOF sensor about 81 mm from the end of the nearest coated section.

The above points to the viability of the ITOF sensor for structural health monitoring. Localized damage (cracks) that are indicators of the commencement of structural degradation were successfully detected as shown by the TL signals detected during loading. Furthermore, warning of impending structural failure was given by the integrated ITOF sensor. There was a big jump in the TL signal to 0.18 V at time 207 s before the failure of the beam. There was also an increase in the noise level indicative of crack opening that will lead to structural failure. This observation holds promise for crack width monitoring which is critical for corrosion prevention.

7.5 Fiber Reinforced Composites with In-Situ Damage Monitoring Capability

Fiber reinforced polymer (FRP) has many desirable properties such as high strength, high modulus, and low density [27]. These have fueled a steady growth in the use of these composites in critical engineering structures like air crafts and wind blades [28, 29]. FRP are however very prone to barely visible impact damage (BVID) and this necessitates the need for in-situ and distributed damage monitoring system.

7.5.1 Experimental

7.5.1.1 ITOF-CFRP Panel Fabrication and Low Velocity Impact Test

ITOF sensors with the entire length coated with TL materials were fabricated and used for this study. The ITOF sensors were then integrated into carbon fiber reinforced polymer during the composite fabrication to create the ITOF-CFRP composite parts as highlighted in Fig. 7.10. Six layers of carbon fiber 12 K plain weave (Fiber Glast Development Corp., USA) fabric

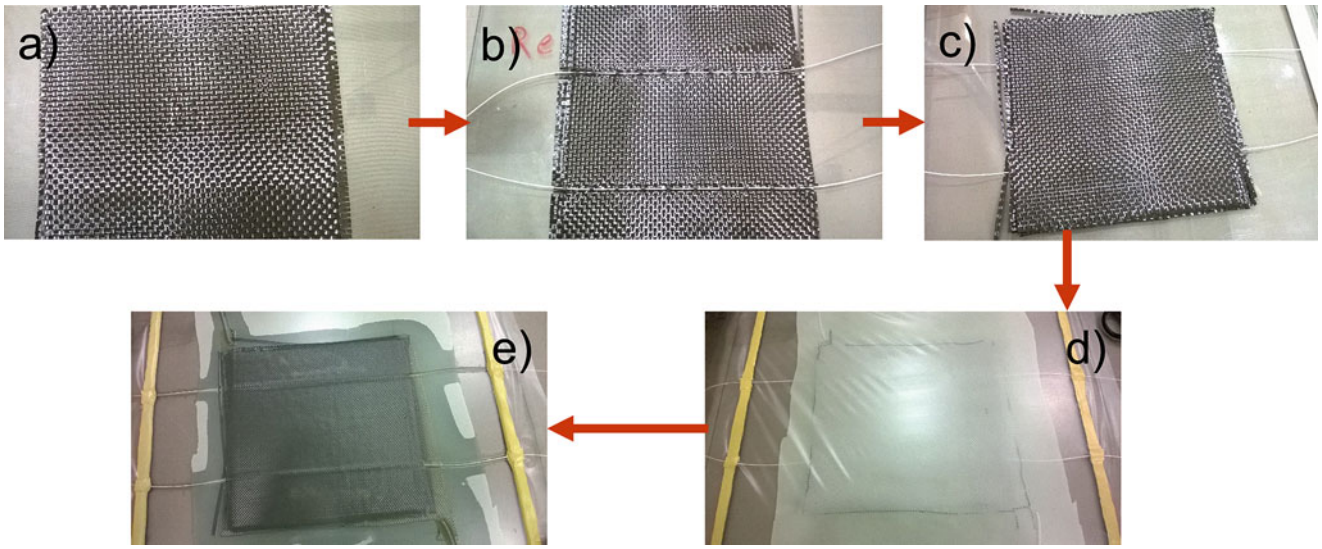

Fig. 7.10 ITOF-CFRP test panel fabrication (**a**) Fiber layup, (**b**) Integration of ITOF sensor using a weave method, (**c**) Completion of fiber layup, (**d**) Vacuum bagging, (**e**) Composite part fabrication with vacuum assisted resin transfer molding

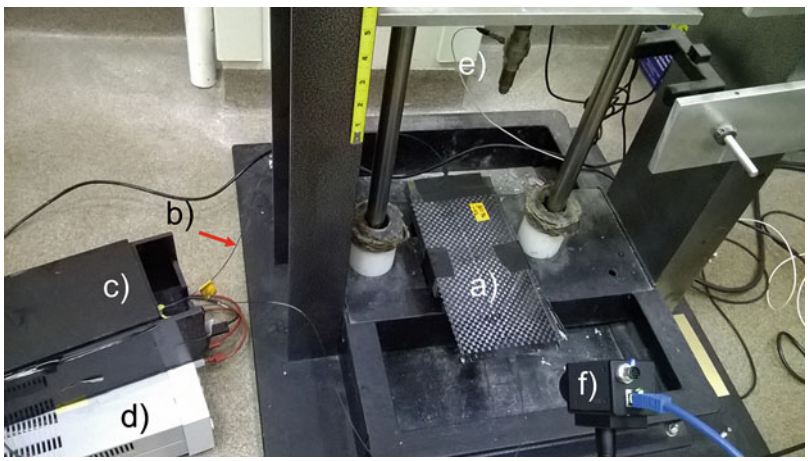

Fig. 7.11 Experimental setup for low velocity impact test on custom-built impact rig (**a**) ITOF-CFRP composite panel, (**b**) ITOF sensor from composite panel connected to PMT, (**c**) Black box housing photomultiplier tube (PMT), (**d**) Power supply, (**e**) Impactor with load cell, (**f**) Infrared camera (FLIR) system

were cut into rectangular size (127 by 254 mm). Three layers of carbon fiber fabric were laid on to the prepared mold surface. The fourth fabric layer had two ITOF sensors woven into it transversely to the longer edge and 63.5 mm from the shorter edges (Fig. 7.10b). The remaining two fabric layers were then laid (Fig. 7.10c) before vacuum bagging (Fig. 7.10d). Vacuum assisted resin transfer molding was used to fabricate the parts (Fig. 7.10e) using ArmorStar IVEX-C410 unsaturated polyester resin (Cook Composites & Polymers Co., USA). The parts were allowed to cure for 24 h before demolding and cutting into two panels, each with an ITOF sensor running centrally through it.

Figure 7.11 shows the experimental setup for the impact test conducted on the ITOF-CFRP samples. The integrated ITOF sensor was connected to a PMT for the detection of the impact-induced triboluminescent signals.

7.5.2 Results and Discussion

Impact test results show that the application of impact loads on the ITOF-CFRP samples resulted in the detection of distinct jumps in the TL signal. Figure 7.12 shows a typical TL signal from an ITOF-CFRP panel due to an impact load. The TL signal jumped to a value of about 4 AU (Fig. 7.12a) when an impact load of about 10 kN was applied to the ITOF-CFRP sample. The ITOF-CFRP exhibited in-situ impact sensing capability. Visual inspection revealed barely visible impact damage at the point of impact.

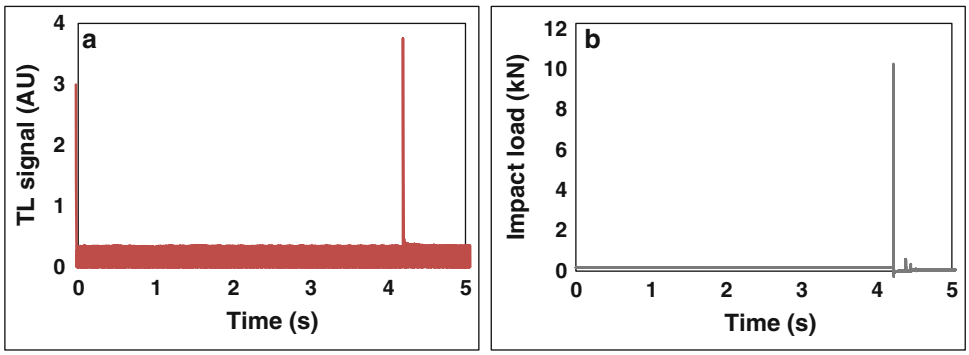

Fig. 7.12 ITOF-CFRP sample exhibiting in-situ impact sensing capability (**a**) TL signal from impact event, (**b**) Impact force level

7.6 Conclusion

TL-based sensor systems have been demonstrated to provide in-situ damage monitoring in both cement-based and polymer-based composites. The drawbacks associated with the direct dispersion of TL materials in the host structure material led to the development of the bio-inspired ITOF sensor. The ITOF sensor has been successfully demonstrated to enable real time failure monitoring in unreinforced cement-based composites and real time damage monitoring in reinforced concrete beams. These have great potential applications as early warning system in civil infrastructure such as bridges. In addition, preliminary results demonstrating the capability of the ITOF sensor as an integrated sensor system that can enable in-situ damage sensing in polymer based composites have been demonstrated with carbon fiber composites. Further work is ongoing to characterize the sensor's response under different loading conditions.

Acknowledgement The authors wish to acknowledge the support of the National Science Foundation (NSF) under NSF Awards No.: CMMI-0969413and EEC-1005016; and the Department of Energy under DOE Award No.: DE-NA0000728.

References

1. Chong, K.P., Carino, N.J., Washer, G.: Health monitoring of civil infrastructures. Smart Mater. Struct. **12**, 483–493 (2003)
2. Zhou, G., Sim, L.M.: Damage detection and assessment in fibre-reinforced composite structures with embedded fibre optic sensors—review. Smart Mater. Struct. **11**, 925–939 (2002)
3. Olawale, D.O., Dickens, T., Sullivan, W.G., Okoli, O.I., Sobanjo, J.O., Wang, B.: Progress in triboluminescence-based smart optical sensor system. J. Lumin. **131**, 1407–1418 (2011)
4. Kawaguchi, Y.: Fractoluminescence spectra in crystalline quartz. Jpn. J. Appl. Phys. Part 1 **37**, 1892–1896 (1998)
5. Reynolds, G.T.: Piezoluminescence from a ferroelectric polymer and quartz. J. Lumin. **75**, 295–299 (1997)
6. Chandra, B.P., Elyas, M., Majumdar, B.: Dislocation models of mechanoluminescence in [gamma]- and X-irradiated alkali halides crystals. Solid State Commun. **42**, 753–757 (1982)
7. Sweeting, L.M.: Triboluminescence with and without Air. Chem. Mater. **13**, 854–870 (2001)
8. Bergeron, N.P., Hollerman, W.A., Goedeke, S.M., Hovater, M., Hubbs, W., Finchum, A., Moore, R.J., Allison, S.W., Edwards, D.L.: Experimental evidence of triboluminescence induced by hypervelocity impact. Int. J. Impact Eng. **33**, 91–99 (2006)
9. Walton, A.J.: Triboluminesence. Adv. Phys. **26**, 887–948 (1977)
10. Womack, F.N., Goedeke, S.M., Bergeron, N.P., Hollerman, W.A., Allison, S.W.: Measurement of triboluminescence and proton half brightness dose for ZnS:Mn. IEEE Trans. Nucl. Sci **51**, 1737–1741 (2004)
11. Sage, I., Humberstone, L., Oswald, I., Lloyd, P., Bourhill, G.: Getting light through black composites: embedded triboluminescent structural damage sensors. Smart Mater. Struct. **10**, 332–337 (2001)
12. Xu, C.N., Watanabe, T., Akiyama, M., Zheng, X.G.: Preparation and characteristics of highly triboluminescent ZnS film. Mater. Res. Bull. **34**, 1491–1500 (1999)
13. Olawale, D.O., Dickens, T., Lim, A., Okoli, O., Wang, B., Sobanjo, J.O.: Characterization of the triboluminescence (TL) performance of ZnS: Mn under repeated mechanical loading for smart optical damage sensor system. Presented at the NDE/NDT for Highways and Bridges: Structural materials and Technology (SMT) 2010, New York, USA, 2010
14. Sage, I., Badcock, R.A., Humberstone, L., Geddes, N., Kemp, M., Bishop, S., Bourhill, G.: Squeezing light out of crystals: triboluminescent sensors. In: Smart Structures and Materials 1999: Smart Materials Technologies, Newport Beach, CA, USA (1999), pp. 169–179
15. Sage, I., Bourhill, G.: Triboluminescent materials for structural damage monitoring. J. Mater. Chem. **11**, 231–245 (2001)
16. Chandra, B.P., Zink, J.I.: Triboluminescence and the dynamics of crystal fracture. Phys. Rev. B **21**, 816–826 (1980)

17. Chandra, B.P., Baghel, R.N., Chandra, V.K.: Mechanoluminescenct glow curve of ZnS:Mn. Chalcogenide Lett. **7**, 1–9 (2010)
18. Xu, C.N., Zheng, X.G., Akiyama, M., Nonaka, K., Watanabe, T.: Dynamic visualization of stress distribution by mechanoluminescence image. Appl. Phys. Lett. **76**, 179–181 (2000)
19. Sohn, K.S., Seo, S.Y., Kwon, Y.N., Park, H.D.: Direct observation of crack tip stress field using the mechanoluminescence of $SrAl_2O_4$:(Eu, Dy, Nd). J. Am. Ceram. Soc. **85**, 712–714 (2002)
20. Kim, J.S., Kwon, Y.N., Shin, N., Sohn, K.S.: Mechanoluminescent $SrAl_2O_4$: Eu, Dy phosphor for use in visualization of quasidynamic crack propagation. Appl. Phys. Lett. **90**, 241916 (2007)
21. Olawale, D.O., Sullivan, G., Dickens, T., Tsalickis, S., Okoli, O., Sobanjo, J.O., Wang, B.: Development of a triboluminescence-based sensor system for concrete structures. Struct. Health Monit. **11**, 139–147 (2012)
22. Measures, R.M.: Structural monitoring with fiber optic technology. Academic, San Diego, CA (2001)
23. Bourhill, G., Pålsson, L.O., Samuel, I.D.W., Sage, I.C., Oswald, I.D.H., Duignan, J.P.: The solid-state photoluminescent quantum yield of triboluminescent materials. Chem. Phys. Lett. **336**, 234–241 (2001)
24. Olawale, D.O., Kliewer, K., Dickens, T., Uddin, M.J., Okoli, O.I.: Multifunctional cementitious composites with structural and damage monitoring capabilities for smart bridges. Presented at the SAMPE 2013, Society for the Advancement of Material and Process Engineering, Long Beach, CA, USA (2013)
25. Olawale, D.O., Kliewer, K., Dickens, T., Uddin, M.J., Okoli, O.I.: Triboluminescent optical nerves for smart concrete structures. Presented at the IWSHM 2013, The 9th International Workshop on Structural Health Monitoring—Stanford University, Stanford, CA, USA (2013)
26. Olawale, D.O., Kliewer, K., Okoye, A., Dickens, T.J., Uddin, M.J., Okoli, O.I.: Getting light through cementitious composites with in situ triboluminescent damage sensor. Struct. Health Monit. **13**, 177–189 (2014)
27. Chung, D.D.L.: Damage detection using self-sensing concepts. pp. 509–520, 19 April 2007
28. Hirano, Y., Katsumata, S., Iwahori, Y., Todoroki, A.: Artificial lightning testing on graphite/epoxy composite laminate. Compos. A: Appl. Sci. Manuf. **41**, 1461–1470 (2010)
29. Gagné, M., Therriault, D.: Lightning strike protection of composites. Prog. Aerosp. Sci. **64**, 1–16 (2014)

Chapter 8
Passive-Only Defect Detection and Imaging in Composites Using Diffuse Fields

Jeffery D. Tippmann and Francesco Lanza di Scalea

Abstract A wave-based passive approach is here presented to detect damage in composite materials subjected to diffuse wave fields. This is the case, for example, of wind turbine blades subjected to random air-structure interaction loads in operation. The known reconstruction of the Green's function from cross-correlations of diffuse fields is first performed. A first approach, based on wave reciprocity applied to the passively reconstructed Greens function, is first proposed to detect damage located along the straight path between two sensors. A second approach, based on matched field processing applied to the passively reconstructed Green's function, is then proposed to detect and locate damage anywhere in the structure. These techniques are suitable for structural health monitoring of structures subjected to random dynamic loads from operational environments such as wind turbines, aircraft, bridges, marine structures, etc.

Keywords Composites • Ultrasonic imaging • Matched field processing • Wind turbine blades • Structural health monitoring

8.1 Introduction

Passive damage detection is an increasingly popular option in Structural Health Monitoring (SHM) applications because of advances in technology for large data collection and the continued research of data processing methods required to make use large amounts of data. In SHM, passive systems are attractive because they limit the SHM data acquisition system design to passive sensors [1]. However, with a passive system, the excitation mechanism providing the system input can be limited and highly variable. This requires the thoughtful use of signal processing methods to extract a feature, or features, of interest that is used for damage detection.

It has been well known that the correlation between any two sensors provides unique information about the structural modal wave propagation properties. One of the first studies using correlations for passive SHM was applied to a bridge used for automobile vehicle traffic [2]. The long-time averaged correlations were created using vehicle traffic as an excitation and compared to modal dynamic properties. At about the same time period, significant research was being done in understanding how the average of several long-time correlations between two sensor pairs converges to impulse response between to two sensors recording signals in a diffuse field [3].

The use of extracting impulse response functions between two sensors in a diffuse field is very popular in ocean acoustics and seismology [4–6]. As a result of this work, a deeper understanding on the result of the long-time cross correlations has been developed from theoretical derivations and experimental comparisons. A significant finding showed the derivative of this cross correlation more closely matches the impulse response function, or the Green's function, as more widely known in wave physics [7].

More recently, the use of this method has been studied for wave propagation in elastic medium for the ultimate purpose of damage detection [8, 9]. The study of diffuse fields has also been popular for damage detection [10]. In elastic medium, the impulse response function contain more features than traveling acoustic waves in ocean and seismology due wave dispersion relationships of lamb waves [11]. For example, a broadband signal in a plate will contain a mixture of many symmetric and anti-symmetric modes depending on the type of excitation creating the diffuse field, as well as the possibility for many reflections due to the boundaries associated with structural features such as gussets, edges, material changes, etc.

The use of array signal processing methods is used widely in traveling wave detection, such as RADAR and SONAR. The conventional delay-and-sum beamforming methods enhance the signal by a gain due to the multiple element array [12]. In conventional beamforming applications, the time of arrival of the wave is detected and processed to obtain a position

J.D. Tippmann • F.L. di Scalea (✉)
University of California, San Diego, 9500 Gilman Drive, 92093 La Jolla, CA, USA
e-mail: flanza@ucsd.edu

C. Ralph et al. (eds.), *Mechanics of Composite and Multi-functional Materials, Volume 7*,
Conference Proceedings of the Society for Experimental Mechanics Series, DOI 10.1007/978-3-319-21762-8_8

based on the differences in arrival times to each element. This widely used method has been applied to damage detection methods in the active pitch-catch applications [13, 14]. However, the interference of reflections and dispersion are a major drawback in conventional time-of-arrival beamforming applications.

The same issue is observed in ocean acoustic applications where multiple arrivals are seen due to reflections off the surface and sea bottom. An alternate approach was developed. Instead of using one particular wave path, the entirety of the arrival structure is used in what is known as matched-field processing (MFP) [15–17]. In this method the look direction is constructed through a known full-field result. Because of the multiple arrival structure in the time domain it is more appropriate to work in the frequency domain.

Returning to the passive long-time correlations, the full-field impulse response function is simply the long-time averaged cross correlation function in a diffuse field. This powerful result means array signal processing methods can be used on the passive reconstructed impulse response function. This technique has been demonstrated in ocean acoustics [18]. This method is studied in this paper as applied to damage detection in a composite wind turbine blade. Rotor blades in utility sized wind turbines are a very attractive structure for passive monitoring because they see significant as well as stochastic loads and pressure waves during operation.

8.2 Background

8.2.1 Correlation Function in Diffuse Fields

The derivation of the extraction of the impulse response function from long-time averaged cross correlations can be found in literature [3, 7]. The basic result is expressed as a cross correlation function with two components, a causal and anticausal function (Eq. 8.1). The positive and negative time components correspond to the two directional impulse response functions between the two sensors. In a linear system, these two equal each other by the reciprocity principle. This similarity has been previously studied as a metric for damage detection in both an active-passive approach and a passive approach [9, 19]. In this experiment, each side represents the two impulse response functions for the sensor pair used in the array signal processing approach.

$$\frac{dC_{ij}(t)}{dt} h_{ji}(t) - h_{ij}(-t) \tag{8.1}$$

It is important to note that the forward and backward impulse response functions are only estimated to the degree that the noise sources are diffuse and broadband. A diffuse field requires spatially and temporally random sources. Because this is practically impossible to obtain in any application, care needs to be taken when observing the similarity between the forward and backwards portions of the cross-correlation function. For example, if noise sources are biased towards the side of one sensor then the two impulse response functions will differ by some amount. In addition to noise distribution, other factors to consider are frequency dependent attenuation in structure and sensor spacing.

8.2.2 Matched-Field Processing

The MFP method is the spatial representation of the plane-wave beamforming because it uses the full-field solution at a spatial point for determining the look direction [17]. The algorithms for improving the look-direction, such as the minimum-variance and a constraint on white-noise, can still be used [20, 21].

$$MFP(x, y,) = \left| w^*(x, y,)s() \right|^2 = \left| w^*(x, y,)s()s^*()w(x, y,) \right| \tag{8.2}$$

The MFP ambiguity output can be written as a function of spatial position, where the replica vector, w(x,y), is of length of the number of sensors in the array and the cross spectral density matrix (CSDM), K()=s()s*(), is simply the hermitian product of the data vector. The replica vector can be formed through numerical simulation or by experiment. In this paper, the replica vector is obtained through experiment. The benefits of obtaining a replica vector through an experiment is it is the most

accurate representation of the structure as it exists with all its boundary variations and uncertainties. In practical purposes, obtaining a replica vector experimentally can be difficult if there is wide variance between the structures being monitored.

8.2.3 *Dominant Source Null Operation*

In the most basic pulse-echo and pitch-catch nondestructive evaluation (NDE) approaches for detecting the presence of damage in a structure, the damage acts as a reflection, or wave scatterer. In the case where the damage does not exist between the direct path of the two sensors, a wave reflection can be tracked [14]. The addition of the damage results in a signal that is the sum of two principle signals in the total received signal. This sum can be represented in an eigenvalue decomposition of the cross spectral density matrix of the sparse sensor array. In the case of one dominant impulse response function, the dominant eigenvector can be found when only this excitation exists by using multiple snapshots to build a full rank matrix to give a full set of eigenvalues and eigenvectors [16]. The first eigenvalue will be related to the dominant impulse response while the rest should be zero if there is no correlation in the noise between two sensors.

$$z() = \left[I - U_m U^*{}_m\right] s() \tag{8.3}$$

$$P() = z() z^*() \tag{8.4}$$

When damage is introduced, another non-zero eigenvalue is added. The dominant impulse response function constructed through the long-time average of the cross-correlations can be removed from the data signal by simply subtracting out the dominant eigenvector from the signal space. The projection operation performed on the data vector including both signals results in a data vector with only the damage scatterer signal. This data vector can be used in the MFP output equation to locate and detect the presence of damage.

8.3 Experimental Setup

An array of accelerometers was placed on a composite wind turbine blade on a section of the blade midway between the root and tip. The rotor blade used in this experiment is the CX-100 design [22, 23]. The composite construction of the blade skin contains fiberglass outer layers and a balsa wood core. A picture of the blade experimental setup is shown in Fig. 8.1.

The grid boxes in Fig. 8.1b denotes the center of spatial locations of the replica vectors experimentally constructed that are used in the MFP output from Eq. 8.2. The sensors are placed as two vertical arrays with spaced 51 cm apart with internal spacing at about 15.2 cm. The array elements were PCB such and such accelerometers with an operating bandwidth of up to 10 kHz.

The accelerometers were connected to a signal conditioner box that was then connected to a data acquisition system for recording. The excitations were created by the data acquisition box and sent to an electrodynamic shaker. For this experiment, the excitation functions were white noise functions.

A 5-s excitation was created at each grid location to generate the replica field for the MFP output. The next step was to create the same excitation from the location of each sensor, representing the active source condition for that location. This produces the projection operator that is used to project out the dominant impulse response function between the two sensors in order to isolate the damage signal for localization and detection through the MFP method.

Finally, for simulating a diffuse field, signals were recorded from excitations and randomly placed positions on both sides of the vertical arrays. The estimates of the impulse response functions were created from the time-average of the correlation functions in 0.1 s window over the entire 5-s signal. This part of the experiment was repeated with damage simulated at a grid in the replica field. The damage was simulated in this experiment using modeling clay as shown in Fig. 8.1c. The modeling clay acted as an added mass to the system and provided the opportunity for an additional resonant source when the blade was excited by the shaker at various points.

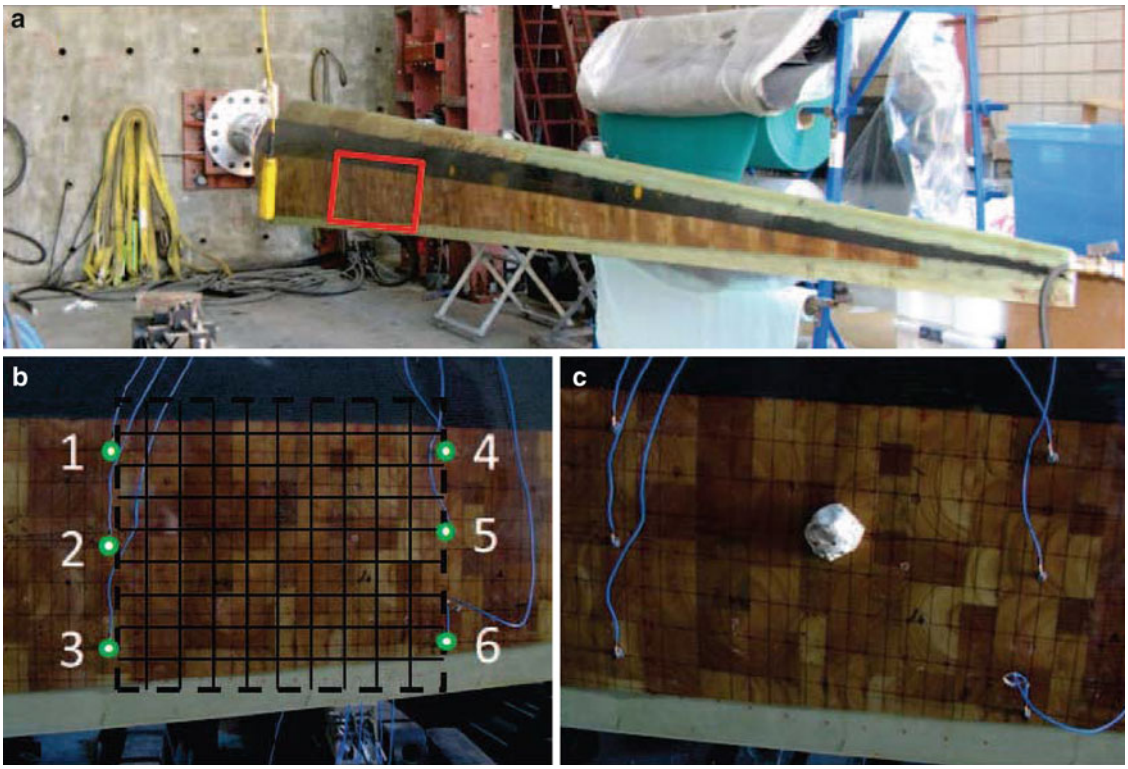

Fig. 8.1 (**a**) Experimental wind turbine blade at UCSD with highlight region the area of study (**b**) Experimental setup of the six accelerometer array with the MFP replica field grid drawn (**c**) Addition of single piece of clay added between sensors in grid box location of *row four* and *column six*

8.4 Experimental Results

The data produced results MFP ambiguity outputs for each of the four conditions when one sensor is the source and the remaining sensors are the receivers. The four conditions use a different data vector to compute the CSDM. The first uses the active excitation matched to the replica field. This can be seen in Fig. 8.2a for when sensor 1 is the excitation. The second is when the active excitation is removed from the undamaged data. This is shown in Fig. 8.2b, where the drop in signal is seen at the location of the sensor. The third condition, Fig. 8.2c, is when the impulse response function created in a damaged state is used. Here the damage cannot be seen in the ambiguity surface. The fourth condition is shown in Fig. 8.2d, when the dominant impulse response function eigenvector in an undamaged state is removed from the damaged data vector. Here, just for one sensor, the damage can be visually seen in the ambiguity surface.

This same procedure can be completed for remaining five sensor source and receiver combinations. Because each of the six combinations contains the same damage state, all six MFP can be averaged together to produce one output that further enhances detection of the damage. The average of all six outputs is shown in Fig. 8.3.

8.5 Discussion and Conclusions

In this paper, the MFP method was used to locate the simulated from data recorded in a noise field. The data was processed by taking long-time cross correlations between each sensor pairs to reconstruct the impulse response function between one sensor to the remaining sensors. Using the signal space of the impulse response function in an undamaged state, this signal was removed using a projection matrix in the damaged state. This new data vector was used in the MFP method to locate the simulated damage. The MFP result from all source and receiver combinations can be incoherently averaged to further improve the MFP ambiguity output.

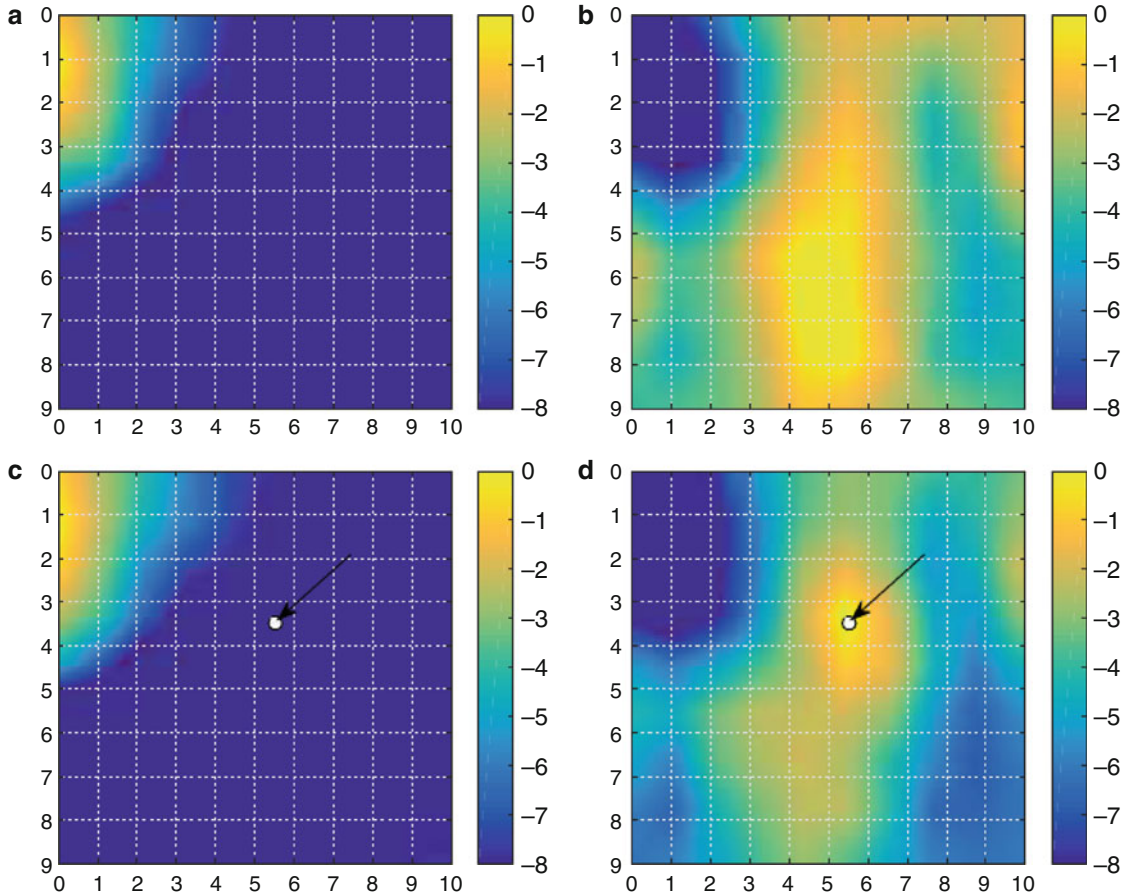

Fig. 8.2 MFP ambiguity output for (**a**) data with active excitation at sensor 1, (**b**) data with active excitation removed in undamaged condition, (**c**) data with reconstructed impulse response function at sensor 1, and (**d**) data with dominant response at sensor 1 removed. The colormap is in relative dB from maximum

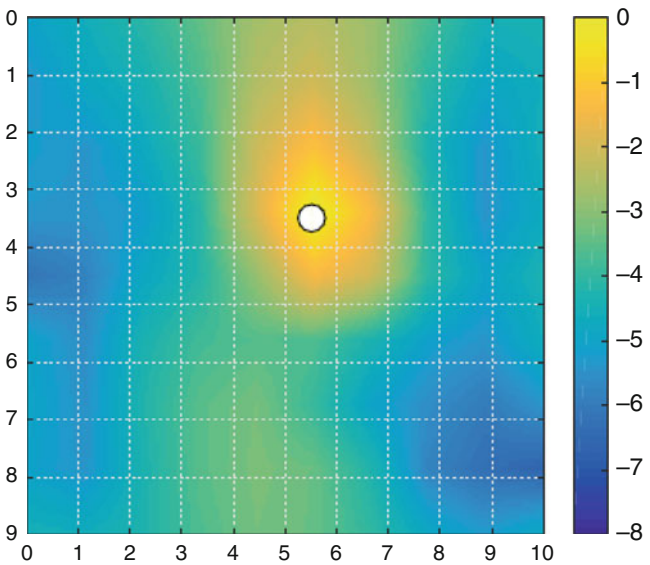

Fig. 8.3 Averaged MFP ambiguity output over all source and receiver combinations for replica grid data with dominant response at source position removed. The colormap is in relative dB from maximum

This approach was constructed with the idea of a passive damage detection of wind turbine blades. However, if an active system is available, the same array processing methods would produce similar results. Additionally, all array processing design considerations must be taken into account with particular frequency and wavelengths of interest.

In this experiment, damage was simulated using the modeling clay because it was a non-destructive approach. However, because the added mass of the clay behaves in the same way as the mass-loaded excitation mechanism of the electrodynamic shaker, the replica field was well suited for identifying the clay position. For practical damage detection purposes, such as identifying a hole or delamination, the source emitted from the damage must closely match the replica field. In this case, a numerical approach to generating a replica field may be more appropriate as one cannot move a delamination in the same way the shaker was moved from each grid point to grid point.

Acknowledgements We acknowledge the National Science Foundation for funding this work through Grant CMMI No. 1028365. Also, we thank Prof. William Kuperman of UCSD's Scripps Institution of Oceanography for his guidance and discussions on the passive reconstruction of the Green's functions and the MFP methods.

References

1. Farrar, C.R., Worden, K.: An introduction to structural health monitoring. Philos. Transact. A Math. Phys. Eng. Sci. **365**, 303–315 (2007)
2. Farrar, C., James III, G.: System identification from ambient vibration measurements on a bridge. J. Sound Vib. **205**, 1–18 (1997)
3. Weaver, R.L., Lobkis, O.I.: Diffuse fields in open systems and the emergence of the Greens function (L). J. Acoust. Soc. Am. **116**(5), 2731 (2004)
4. Roux, P., Kuperman, W.A.: Extracting coherent wave fronts from acoustic ambient noise in the ocean. J. Acoust. Soc. Am. **116**(4), 1995 (2004)
5. Sabra, K.G., Roux, P., Kuperman, W.A.: Arrival-time structure of the time-averaged ambient noise cross-correlation function in an oceanic waveguide. J. Acoust. Soc. Am. **117**(1), 164 (2005)
6. Sabra, K.G.: Surface wave tomography from microseisms in Southern California. Geophys. Res. Lett. **32**(14), L14311 (2005)
7. Roux, P., Sabra, K.G., Kuperman, W.A., Roux, A.: Ambient noise cross correlation in free space: theoretical approach. J. Acoust. Soc. Am. **117**(1), 79 (2005)
8. Sabra, K.G., Srivastava, A., Lanza di Scalea, F., Bartoli, I., Rizzo, P., Conti, S.: Structural health monitoring by extraction of coherent guided waves from diffuse fields. J. Acoust. Soc. Am. **123**, EL8–EL13 (2008)
9. Tippmann, J.D., Lanza di Scalea, F.: Passive-only damage detection by reciprocity of Green's functions reconstructed from diffuse acoustic fields with application to wind turbine blades. J. Intell. Mater. Syst. Struct. (2014). doi:10.1177/1045389X14538539
10. Michaels, J.E., Michaels, T.E.: Detection of structural damage from the local temporal coherence of diffuse ultrasonic signals. IEEE Trans. Ultrason. Ferroelectr. Freq. Control **52**, 1769–1782 (2005)
11. Rose, J.: Ultrasonic waves in solid media. Cambridge University Press, Cambridge (2004)
12. Johnson, D.H., Dudgeon, D.E.: Array Signal Processing: Concepts and Techniques. Simon & Schuster. New York, NY. (1992)
13. Michaels, J.E., Lu, Y., Michaels, T.E.: Methodologies for quantifying changes in diffuse ultrasonic signals with applications to structural health monitoring. In: Geer, R.E., Shull, P.J., Meyendorf, N., Kundu, T., Diaz, A.A., Aktan, A.E., Baaklini, G.Y., Gyekenyesi, A.L., Mufti, A. A., Michel, B., Wu, H.F., Doctor, S.R., Bar-Cohen, Y. (eds.) Proceedings of SPIE, vol. 5768, pp. 97–105 (2005)
14. Hall, J., Michaels, J.: Minimum variance ultrasonic imaging applied to an in situ sparse guided wave array. Ultrason. Ferroelectr. Freq. Control **57**(10), 2311–2323 (2010)
15. Baggeroer, A., Kuperman, W., Mikhalevsky, P.: An overview of matched field methods in ocean acoustics. IEEE J. Ocean. Eng. **18**(4), 401–424 (1993)
16. Corciulo, M., Roux, P., Campillo, M., Dubucq, D., Kuperman, W.A.: Multiscale matched-field processing for noise-source localization in exploration geophysics. Geophysics **77**, KS33–KS41 (2012)
17. Turek, G., Kuperman, W.: Applications of matched-field processing to structural vibration problems. J. Acoust. Soc. Am. **101**(May), 1430–1440 (1997)
18. Debever, C., Kuperman, W.A.: Robust matched-field processing using a coherent broadband white noise constraint processor. J. Acoust. Soc. Am. **122**, 1979–1986 (2007)
19. Park, H.W., Sohn, H., Law, K.H., Farrar, C.R.: Time reversal active sensing for health monitoring of a composite plate. J. Sound Vib. **302**, 50–66 (2007)
20. Capon, J.: High-resolution frequency-wavenumber spectrum analysis. Proc. IEEE **57**(8), 1408–1418 (1969)
21. Cox, H., Zeskind, R., Owen, M.: Robust adaptive beamforming. IEEE Trans. Acoust. Speech Signal Process. **35**, 1365–1376 (1987)
22. Berry, D., Ashwill, T.: Design of 9-meter carbon-fiberglass prototype blades: CX-100 and TX-100. Tech. Rep. September (2007)
23. Tippmann, J., Manohar, A., Lanza di Scalea, F.: Wind turbine inspection tests at UCSD. SPIE Smart Struct. **8345**, 7 (2012)

Chapter 9
Buckypaper-Cored Novel Photovoltaic Sensors for In-Situ Structural Health Monitoring of Composite Materials Using Hybrid Quantum Dots

Jin Yan, Deborah E. Daramola, Julian M. Antolinez, Nnamdi Okoli, Tarik J. Dickens, and Okenwa I. Okoli

Abstract This paper reports on work developing an efficient distributed photovoltaic (PV) sensor using Buckypaper (BP) as working electrodes (WEs). BP is a thin sheet made from an aggregate of carbon nanotubes (CNTs) with the advantages of good mechanical properties, high electrical conductivity and flexibility. These advantages enable sensor flexibility and significantly improve the charge transfer speed. In addition to BPs, quantum dots (QD) have recently drawn attention in photoconversion systems due to high absorption coefficient, tunable band gap and multiple exciton generation (MEG) effects. Herein, this work proposes to apply np-TiO_2/mp-TiO_2/CdS/CdSe/N719 hybrid structure to realize both MEG effects and multiple electron transmission paths. Previous research has confirmed that a liquid electrolyte and glass cladding were also components of the assembly process which additionally improve sensor efficiency. However, the reported efficiency (>5 %) of the solid state sensor is ten times that seen in previous work utilizing metal-cored wire-shaped liquid PV sensor. This article also discusses surface characterization of nanowires and the functionalization of solid-solid interfacial properties. Moreover, the distributed PV sensor construction is the basis of ongoing work towards embedded smart composites with intrinsic triboluminescent/mechanoluminescent (TL/ML) features.

Keywords Structural Health Monitoring • In-situ Monitoring • Photovoltaic • Buckypaper • Quantum Dots

9.1 Introduction

SHM Systems have been studied by engineers and researchers for years, with designations in various journals, etc. Current techniques are mostly based on acoustic emissions, thermography, x-rays, and strain gages. In practice, their application may be laborious, time consuming and expensive [1, 2]. New research based on the triboluminescent phenomenon may provide a relatively efficient and inexpensive way for ubiquitously monitoring the health of structures in real time [3]. SHM combines diverse sensing technologies with an embedded measurement controller to capture, log, and analyze real-time data. SHM systems are designed to reliably monitor and test the health and performance of structures such as bridges and dams, buildings and stadiums, vessels and platforms, airframes, wind turbines, large machinery and equipment. In 2007, Schulz et al. emphasized the problem of detecting damage in complex geometries and structural joints because damage often initiates at joints and locations where section properties change [4]. Triboluminescence (TL) is an optical phenomenon in which light is generated when material is pulled apart, ripped, scratched, crushed, or rubbed through the breaking of chemical bonds in the material [5]. Although there is some controversy, there are two common mechanism that lead to triboluminescence [6]. The first results from the storage of electrons which have been ejected by the penetrating gamma radiation of ^{40}K decay in lattice defects. A small mechanical shock is then sufficient for these electrons to overcome their energy barrier and cascade down to ground state. The second type results from the breaking of certain bonds, and this property is exhibited by materials such as calcium fluorite (CaF_2), sphalerite ((Zn, Fe)S), and wintergreen Life Savers™ [7]. This breakage creates free bonds, which immediately absorbs and ionize nitrogen from the atmosphere, producing a characteristic green or blue-green flash. It is also believed that TL emission is associated with an asymmetric crystal structure. Crystal bonds are broken along planes with opposing charge. When they re-connect, light is emitted as the charges pass through the gap created from the fracture [5, 8]. It is purported that 30 % of organic crystals and 50 % of inorganic

J. Yan • D.E. Daramola • J.M. Antolinez • N. Okoli • T.J. Dickens • O.I. Okoli (✉)
High Performance Materials Institute, FAMU-FSU College of Engineering, Florida State University,
2525 Pottsdamer Street, Tallahassee, FL 32310, USA
e-mail: ookoli@fsu.edu

C. Ralph et al. (eds.), *Mechanics of Composite and Multi-functional Materials, Volume 7*,
Conference Proceedings of the Society for Experimental Mechanics Series, DOI 10.1007/978-3-319-21762-8_9

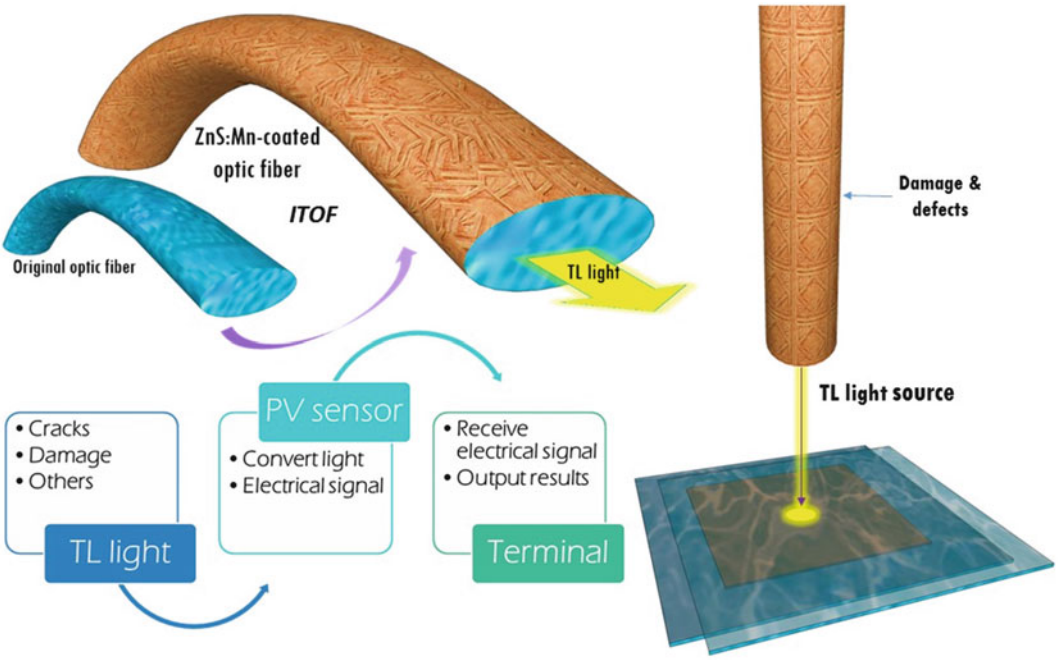

Fig. 9.1 Schematic illustration of TL-based SHM system

crystals are TL materials [5]. Therefore, a TL material embedded in or attached onto a composite structure will act as a real-time damage indicator, and therefore a sensor [9]. In this design (Fig. 9.1), TL crystals will be coated on the surface of optic fiber, and TL light will emit via the cross section of optic fiber when damages and defects happen. Then, PV sensor will receive the light and transmit it as an electrical signal which can be further analyzed by the terminal.

The continued interest in TL materials in SHM systems may be enhanced with the use of photovoltaic (PV) sensors (Fig. 9.1) within opaque composite structures. PV sensors may be able to convert the TL energy emission to electricity which can then be transmitted to logging devices. As such, the PV effect will be discussed here. The PV effect was observed initially by Becquerel in 1839 [10], as a method for converting solar radiation to electrical energy directly using semiconductor materials. The concept of photo-electricity was explained by Einstein in 1905 [11], and the first dye-sensitized PV cell (DSC) was reported in 1991 [12]. A PV sensor is a low-cost photoconversion device belonging to the group of thin-film solar cells, which accompany different fabrication techniques based on materials and application. The photoconversion efficiencies for DSCs have reached ~12 % using platinized FTO (fluorine doped tin oxide) [13–16]. However, rigid glass substrates result in limitations in engineering applications. To solve this problem, flexible PV cells have been investigated to show more advantages in detecting light [17] and in other engineering applications. The specially designed PV sensors with weaveable feature and low energy sensitivity are potentially applicable to intrinsic structural health monitoring (iSHM) systems. In recent years, research has focused on flexible PV sensors with emphasis on high efficiency and long-term stability akin to its conventional rigid 2D counterparts [18–21].

Buckypaper (BP) is a thin sheet made from an aggregate of carbon nanotubes [22]. The nanotubes are approximately 50,000 times thinner than a human hair. Originally, it was fabricated as a way to handle carbon nanotubes, but it is also being studied and developed into applications by several research groups, showing promise as vehicle armor, personal armor, and next-generation electronics and displays. Excellent properties such as light weight, highly flexibility and significant conductivity have been proved by scientists [23–33]. The idea of developing efficient sensitizer with BPs is to improve cell efficiency and realize distributed sensory system. Unlike wire-shaped PV sensor using CNYs, BPs can eventually form a sheet-like sensor. This sheet-like sensor can be treated as a single layer in the composite material and strengthen the composite in the meantime. In addition to BP, quantum dots (QD) have recently drawn attention in photoconversion systems due to their high photon absorption coefficient, tunable band gap, and multiple exciton generation (MEG) effects [34, 35]. In this report, CdS and CdSe QDs have been incorporated during post-hydrothermal process as an extra electron receiver for TiO_2 film. Herein, this report proposes to apply an np-TiO_2/mp-TiO_2/CdS/CdSe/N719 hybrid structure to realize both multiple excitons generation (MEG) effects and multiple electron transmission paths. N719 is known as one of the most efficient dyes to receive light, which here is used to minimize the cell band gap cooperating with two kinds of QDs.

This report will focus on the initial stage, in which FTO glasses will be used as counter electrodes (CEs) and help to form the sensor completely. After the optimal hybrid structure of sensitizer can be formed on the surface of BPs, FTO glasses will be removed and a novel structure of DSC will be proposed in the future to achieve excellent conductivity with highly flexibility.

9.2 Materials and Methods

Experimental Methods. The fabrication methods of distributed sensors will be partially adapted from the methods of wire-shaped sensors [20, 21]. When light hits the dye particles and other additives, electrons will be generated which will be further transmitted to BPs and FTO glasses via the hybrid sensitizer (QDs and TiO_2). The cycle will be completed when electrons finish their journey through the load and reach the other Pt coated FTO glass (CE).

Coating method used here is known as Doctor Blade Technique (DBT). Instead of scotch tape, Teflon sheet will be cut as coating screen (3 × 3 cm) (Fig. 9.2), which has high temperature resistance. Figure 9.2 shows the fabrication procedure for BP-based distributed sensor in detail, and the thickness of Teflon mode decides the thickness of TiO_2 coating. A basal-coating solution used titanium isopropoxide (TiP) as a precursor, which was applied before major sol-gel method and worked as a foundation for the main-coating [17, 36]. The preparation of major sol can be summarized as follows: Nano-water and 70 wt% HNO_3 were mixed together as solution A. Solution B consisted of Nano-Water, Acetic Acid Glacia, Triethylamine and TiP in same amount, Acetic Acid Glacia, Triethylamine and TiP. Solution A and B were prepared individually and mixed together after fully stirring. The mixture was heated in an autoclave at 240 °C, and 50 vol% of the solvent of resultant solution were evaporated at 75 °C. Polyethylene glycol was then added into the sol before coating. This sol was applied on the BPs (WEs) via DBT, and then BPs went through a heating process at 350 °C. This DBT-heating process was repeated several times to reach the height of Teflon screen (~20 μm). To fill the porous TiO_2 structure with as many as QDs, CdS and CdSe QDs were coated with chemical bath deposition (CBD) method. WEs were dipped into a 0.5 M $Cd(NO_3)_2$ ethanol solution, rinsed with ethanol and dried in the room temperature (RT). This step should be repeated twice before WEs are dipped into a 0.5 M Na_2S methanol solution and rinsed again with methanol. This whole cycle needed to be repeated twice for a mature coating. The preparation of CdSe QDs was similar except Na_2SeSO_3 solution needs refluxing at 70 °C for a longer time and a higher temperature was required during the dipping process. These treated electrodes were then sensitized overnight by immersing into N719 (N719 = [tetrabutylammonium] 2 [Ru (4-carboxylic acid-40-carboxy-late-2, 20-bipyridyl) 2(NCS)2]) dye (0.05 M N719 in the mixture of tert-Butanol and acetonitrile (volume ratio = 1:1)). The CEs were platinized using sputtering target at 1.5 KV and 5 mA for 60 s before twisting with WEs and finally were soaked in heated electrolyte. Solid electrolyte contained 0.5 M LiI, 0.05 I_2 and 0.5 tert-butyl pyridine in 3-methoxy propionitrile (3-MePRN). Poly(vinylidene fluoride-co-hexafluoropropene) (5 wt%) was added to confirm the solid state of the electrolyte media. All chemicals used in this experiment were purchased from Sigma-Aldrich. Two kinds of BPs (random and aligned) will be used in trials for comparison.

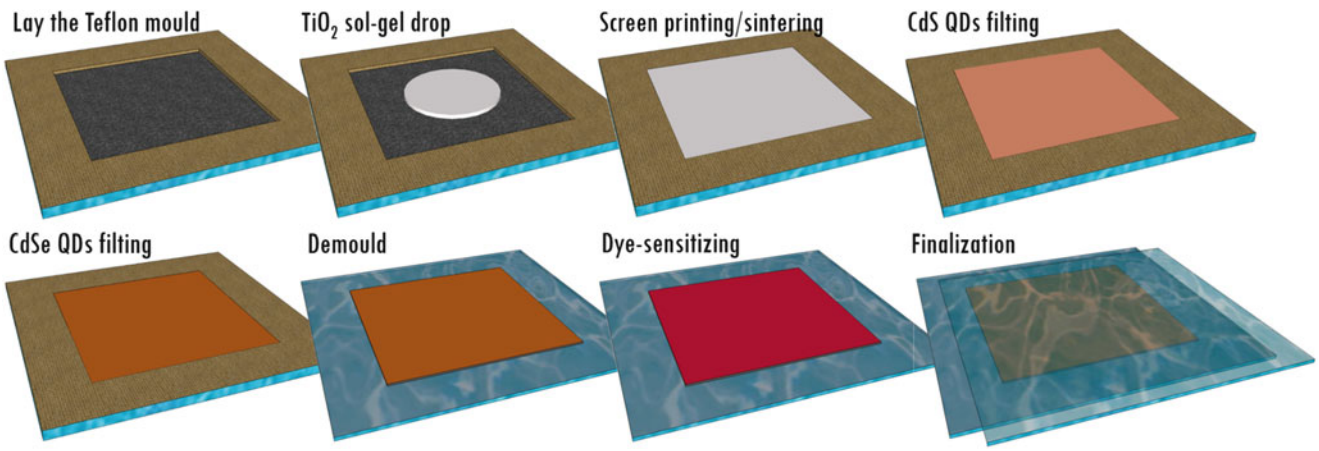

Fig. 9.2 Fabrication procedure for BP-based distributed sensor

Device Characterization. Cell performance was characterized by *J-V* curves which were measured with VersaSTAT3 (Electrochemical system with EIS capability, Princeton Applied Research, USA) with a solar simulator (Newport, Model 9129×, AM 1.5 illumination, light intensity 100 mW*cm^{-2}). To investigate the surface morphology and interface of electrodes, a field emission scanning electron microscope (SEM) (JOEL JSM-7410F) was used. Particularly, energy-dispersive X-ray spectroscopy (EDX) was also applied to finish elemental mapping and particle analysis/tracing.

9.3 Results and Discussion

Figure 9.3 shows the scheme of the TiO_2/CdS/CdSe/N719 hybrid structure and different particles dispersed well in iodide solid electrolyte. For example, when the DSCs receive low light from some special materials in the structure, small band gaps are needed to facilitate the electron transmission [37–39]. In this case, hybrid sensitizers may enhance cell performance to a large extent. When light hits dye particles on the cell surface, electrons are generated and transferred to either CdS or CdSe QDs [34, 35, 37]. Then, these electrons will be taken from QDs to nanoporous TiO_2 phase which has a larger band gap (3.2 eV). Simultaneously, the electrons will possibly be transferred from dye particles to TiO_2 phase directly. These two methods are utilized together to accomplish the hybrid electron transmission pass. This way, more charges were generated, and the multiple excitation effect was achieved. As shown in Fig. 9.3b, particular elements are detected using EDX spectroscopy combined with SEM. Ti element in the graph has the highest density, while other QD elements are shown much less on the surface. Figure 9.3c shows the SEM and EDX images for certain hybrid surface, in which the quantities are represented by the difference in density of various elemental dots. However, the QDs (CdSe and CdS) have been dispersed well in the hybrid structure, which can enhance the performance of the cell and help it to reach higher energy conversion efficiency.

The interface between BPs and sensitizer was also engineered. SEM images of two different kinds of BPs are shown in Fig. 9.4, from which individual carbon nanotubes with an average diameter of 20 nm is observed. BP treatment is necessary because the dispersed surface structure can be coated with more sensitizer particles to realize high energy conversion performance. Moreover, aligned BPs also have better electrical conductivity, which can enhance cell performance to a large extent.

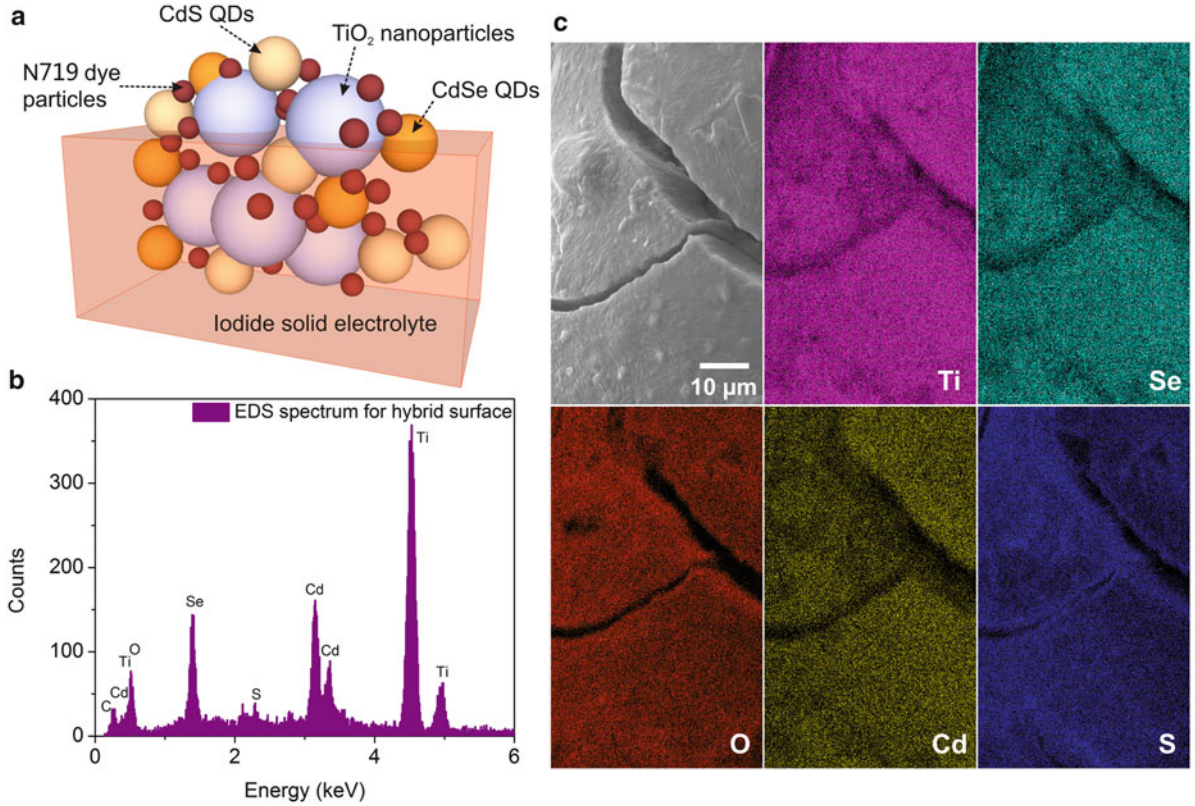

Fig. 9.3 (**a**) 3D sketch map of hybrid sensitizer; (**b**) EDX spectrum for hybrid surface; (**c**) SEM and EDX mapping images for hybrid surface [21]

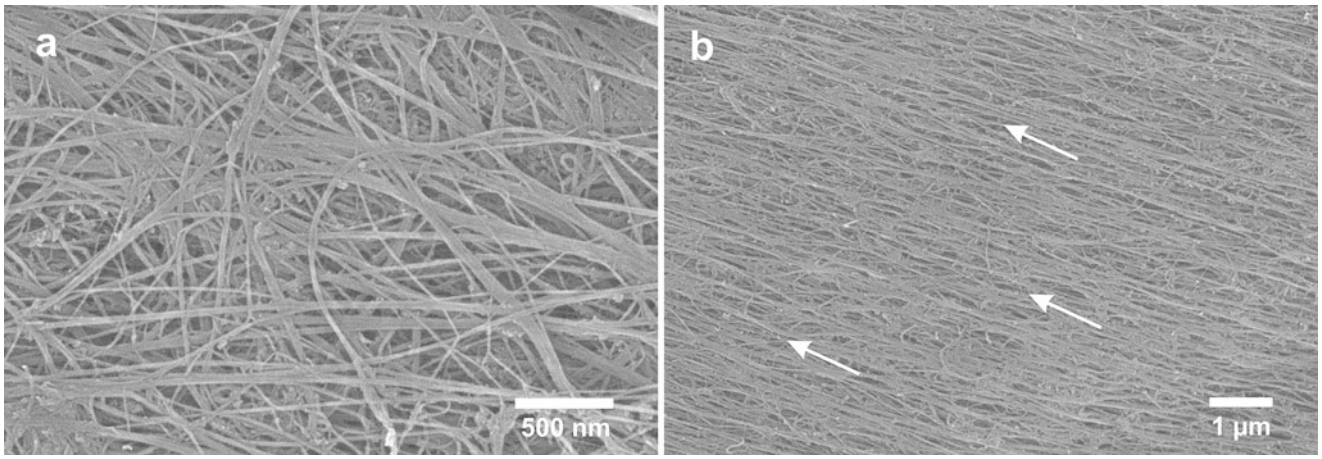

Fig. 9.4 SEM images of (**a**) random Buckypaper and (**b**) aligned Buckypaper

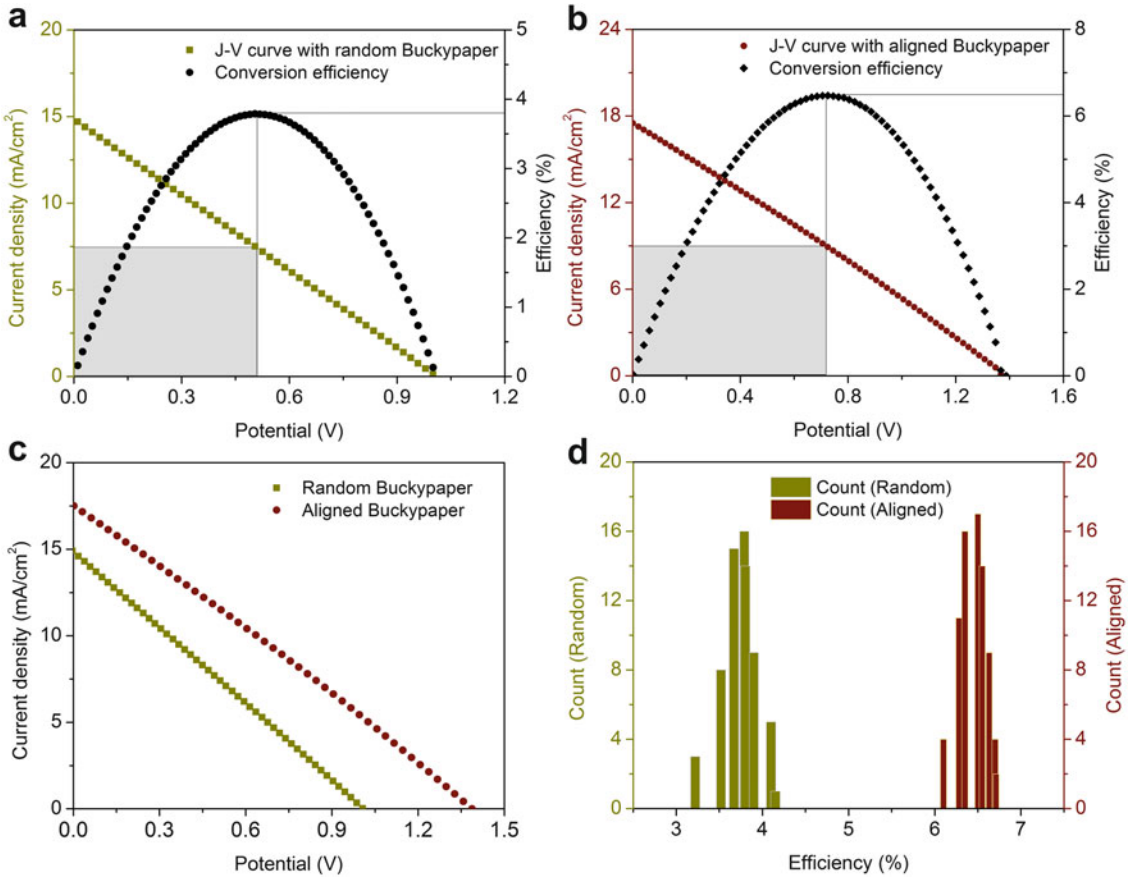

Fig. 9.5 *J-V* curves of distributed sensors using (**a**) random BP, (**b**) aligned BP and (**c**) comparison of random BP and aligned BP, (**d**) Counts of cell efficiency using random BP and aligned BP

To investigate the importance of BPs' surface treatment, a comparative test was conducted. In Fig. 9.5a and b, energy conversion efficiency (black dotted line) can be calculated from *J-V* curves, the maximum current density and maximum voltage can be related to the maximum cell current and voltage respectively. These relations are calculated at the maximum power point (connected point of *J-V* curves and shaded squares). In Fig. 9.5c, J_{sc} of the cell with random BP falls to 14.90 mA/cm^2 from 17.50 mA/cm^2 which is achieved by cell with aligned BP. With a decrease in V_{oc} ($\Delta = 0.38$ V), this cell

only gets an efficiency of 3.79 %. The cell with aligned BP achieves a higher energy conversion efficiency of 6.47 % and a higher open-circuit voltage of 1.39 V. From the statistical data of all sample efficiencies in Fig. 9.5d, the corresponding improvement in cell performance is significant, which proves the advantages of using aligned BPs.

9.4 Conclusion

The new distributed sensors were fabricated using Buckypaper (random and aligned) as WE and Pt-coated FTO glass as CE. The photosensitive TiO_2 film thickness has been set as 20 μm, which is comparable to Ito's work on 2D solar cells [40]. Sensor with aligned BP produces a 6.47 % energy conversion efficiency under standard AM 1.5 light intensity. Furthermore, compared to sensor with random BP, this kind of sensor enhances the applicability to triboluminescence based SHM system for damage detection by improving cell performance. Hybrid electron generation and transmission systems with QDs facilitate the cell performance to a certain degree. Sensor flexibility and stability will be realized in the future by replacing FTO glasses, and the on-going embedded tests for composite materials will prove the function of this novel in-situ TL-based SHM system.

Acknowledgement This work is supported by the U.S. National Science Foundation through grant ID CMMI-0969413 and Air Force Research Laboratory. The authors would also like to thank Dr. Zhiyong (Richard) Liang (High-Performance Materials Institute, Florida, USA) for providing both random and aligned Buckypapers.

References

1. Farrar, C.R., Worden, K.: An introduction to structural health monitoring. Philos. Trans. R. Soc. A Math. Phys. Eng. Sci. **365**, 303–315 (2007)
2. Worden, K., Farrar, C.R., Manson, G., Park, G.: The fundamental axioms of structural health monitoring. Proc. R. Soc. A Math. Phys. Eng. Sci. **463**, 1639–1664 (2007)
3. Sage, I., Badcock, R., Humberstone, L., Geddes, N., Kemp, M., Bourhill, G.: Triboluminescent damage sensors. Smart Mater. Struct. **8**, 504–510 (1999)
4. Kirikera, G.R., Shinde, V., Schulz, M.J., Ghoshal, A., Sundaresan, M., Allemang, R.: Damage localisation in composite and metallic structures using a structural neural system and simulated acoustic emissions. Mech. Syst. Signal Process. **21**, 280–297 (2007)
5. Walton, A.J.: Triboluminescence. Adv. Phys. **26**, 887–948 (1977)
6. http://scienceworld.wolfram.com/physics/Triboluminescence.html
7. Chandra, B.P., Chandra, V.K., Jha, P.: Models for intrinsic and extrinsic fracto-mechanoluminescence of solids. J. Lumin. **135**, 139–153 (2013)
8. Chandra, B.P., Zink, J.I.: Triboluminescence and the dynamics of crystal fracture. Phys. Rev. B **21**, 816–826 (1980)
9. Aggarwal, M.D., Penn, B.G., Miller, J., Sadate, S., Batra, A.K.: Triboluminescent materials for smart optical damage sensors for space applications. In: CASI, NASA, (eds.) NASA/TM-2008-215410, M-1230 (2008)
10. Becquerel, A.E.: Mémoire sur les effets électriques produits sous l'influence des rayons solaires. Comptes Rendus des Séances Hebdomadaires **9**, 561–567 (1839)
11. Einstein, A.: The Photoelectric Effect. Annalen der Physik, Wiley-VCH Verlag GmbH & Co. KgaA, Berlin (1905)
12. Oregan, B., Gratzel, M.: A low-cost, high-efficiency solar-cell based on dye-sensitized colloidal Tio2 films. Nature **353**, 737–740 (1991)
13. Gao, F., Wang, Y., Shi, D., Zhang, J., Wang, M.K., Jing, X.Y., Humphry-Baker, R., Wang, P., Zakeeruddin, S.M., Gratzel, M.: Enhance the optical absorptivity of nanocrystalline TiO(2) film with high molar extinction coefficient ruthenium sensitizers for high performance dye-sensitized solar cells. J. Am. Chem. Soc. **130**, 10720–10728 (2008)
14. Yu, Q.J., Wang, Y.H., Yi, Z.H., Zu, N.N., Zhang, J., Zhang, M., Wang, P.: High-efficiency dye-sensitized solar cells: the influence of lithium ions on exciton dissociation, charge recombination, and surface states. ACS Nano **4**, 6032–6038 (2010)
15. Sauvage, F., Chen, D.H., Comte, P., Huang, F.Z., Heiniger, L.P., Cheng, Y.B., Caruso, R.A., Graetzel, M.: Dye-sensitized solar cells employing a single film of mesoporous TiO2 beads achieve power conversion efficiencies over 10%. ACS Nano **4**, 4420–4425 (2010)
16. Nazeeruddin, M.K., Baranoff, E., Grätzel, M.: Dye-sensitized solar cells: a brief overview. Sol. Energy **85**, 1172–1178 (2011)
17. Uddin, M.J., Dickens, T., Yan, J., Chirayath, R., Olawale, D.O., Okoli, O.I.: Solid state dye-sensitized photovoltaic micro-wires (DSPMs) with carbon nanotubes yarns as counter electrode: synthesis and characterization. Sol. Energy Mater. Sol. Cells **108**, 65–69 (2013)
18. Fan, X., Chu, Z.Z., Wang, F.Z., Zhang, C., Chen, L., Tang, Y.W., Zou, D.C.: Wire-shaped flexible dye-sensitized solar cells. Adv. Mater. **20**, 592–595 (2008)
19. Zhang, S., Ji, C.Y., Bian, Z.Q., Liu, R.H., Xia, X.Y., Yun, D.Q., Zhang, L.H., Huang, C.H., Cao, A.Y.: Single-wire dye-sensitized solar cells wrapped by carbon nanotube film electrodes. Nano Lett. **11**, 3383–3387 (2011)
20. Yan, J., Uddin, M.J., Dickens, T.J., Daramola, D.E., Olawale, D.O., Okoli, O.I.: Tailoring the efficiency of 3D wire-shaped photovoltaic cells (WPVCs) by functionalization of solid-liquid interfacial properties. Phys. Status Solidi A **210**, 7 (2013)
21. Yan, J., Uddin, M.J., Dickens,T.J., Daramola, D.E., Okoli, O.I.: 3D wire-shaped dye-sensitized solar cells in solid state using carbon nanotube yarns with hybrid photovoltaic structure. Adv. Mater. Interfaces **1**, (2014)

22. Future planes, cars may be made of 'buckypaper'. Yahoo! Tech News. 2008-10-17. Retrieved 2008-10-18
23. Yoshida, H., Sugai, T., Shinohara Fabrication, H.: Purification, and characterization of double-wall carbon nanotubes via pulsed arc discharge. J. Phys. Chem. C **112**, 19908–19915 (2008)
24. Kukovecz, A., Smajda, R., Oze, M., Schaefer, B., Haspel, H., Konya, Z., Kiricsi, I.: Multiwall carbon nanotube films surface-doped with electroceramics for sensor applications. Phys. Status Solidi B Basic Solid State Phys. **245**, 2331–2334 (2008)
25. Simien, D., Fagan, J.A., Luo, W., Douglas, J.F., Migler, K., Obrzut, J.: Influence of nanotube length on the optical and conductivity properties of thin single-wall carbon nanotube networks. ACS Nano **2**, 1879–1884 (2008)
26. Pham, G.T., Park, Y.B., Wang, S.R., Liang, Z.Y., Wang, B., Zhang, C., Funchess, P., Kramer, L.: Mechanical and electrical properties of polycarbonate nanotube buckypaper composite sheets. Nanotechnology **19**(32), 325705 (2008)
27. Park, J.G., Li, S., Liang, R., Zhang, C., Wang, B.: Structural changes and Raman analysis of single-walled carbon nanotube buckypaper after high current density induced burning. Carbon **46**, 1175–1183 (2008)
28. Zhu, H.W., Wei, B.Q.: Assembly and applications of carbon nanotube thin films. J. Mater. Sci. Technol. **24**, 447–456 (2008)
29. Whitby, R.L.D., Fukuda, T., Maekawa, T., James, S.L., Mikhalovsky, S.V.: Geometric control and tuneable pore size distribution of buckypaper and buckydiscs. Carbon **46**, 949–956 (2008)
30. Enyashin, A.N., Ivanovskii, A.L.: Structural, elastic, and electronic properties of new superhard isotropic cubic crystals of carbon nanotubes. JETP Lett. **87**, 321–325 (2008)
31. Wang, D., Song, P.C., Liu, C.H., Wu, W., Fan, S.S.: Highly oriented carbon nanotube papers made of aligned carbon nanotubes. Nanotechnology **19**(7), 075609 (2008)
32. Han, J.T., Jeong, H.J., Lee, G.W.: Buckypaper from thin multiwalled carbon nanotubes. Proc. SPIE **7037**, 703717 (2008)
33. Zhu, W., Zheng, J.P., Liang, R., Wang, B., Zhang, C., Walsh, S., Au, G., Plichta, E.J.: Highly-efficient buckypaper-based electrodes for PEMFC. Proton Exchange Membrane Fuel Cells 8, Pts 1 and 2 **16**, 1615–1626 (2008)
34. Lee, Y.-L., Chi, C.-F., Liau, S.-Y.: CdS/CdSe co-sensitized TiO2 photoelectrode for efficient hydrogen generation in a photoelectrochemical cell. Chem. Mater. **22**, 922–927 (2009)
35. Lee, Y.-L., Huang, B.-M., Chien, H.-T.: Highly efficient CdSe-sensitized TiO2 photoelectrode for quantum-dot-sensitized solar cell applications. Chem. Mater. **20**, 6903–6905 (2008)
36. Uddin, M.J., Davies, B., Dickens, T.J., Okoli, O.I.: Self-aligned carbon nanotubes yarns (CNY) with efficient optoelectronic interface for microyarn shaped 3D photovoltaic cells. Sol. Energy Mater. Sol. Cells **115**, 166–171 (2013)
37. Yan, J., Uddin, M.J., Dickens, T.J., Okoli, O.I.: Carbon nanotubes (CNTs) enrich the solar cells. Sol. Energy **96**, 239–252 (2013)
38. Olawale, D.O., Sullivan, G., Dickens, T., Tsalickis, S., Okoli, O.I., Sobanjo, J.O., Wang, B.: Development of a triboluminescence-based sensor system for concrete structures. Struct. Health Monit. **11**, 139–147 (2012)
39. Olawale, D.O., Dickens, T., Uddin, M.J., Okoli, O.O.: Triboluminescence multifunctional cementitious composites with in situ damage sensing capability. Proc. SPIE **834538** (2012)
40. Ito, S., Ha, N.L.C., Rothenberger, G., Liska, P., Comte, P., Zakeeruddin, S.M., Pechy, P., Nazeeruddin, M.K., Gratzel, M.: High-efficiency (7.2%) flexible dye-sensitized solar cells with Ti-metal substrate for nanocrystalline-TiO_2 photoanode. Chem. Commun. **38**, 4004–4006 (2006)

Chapter 10
Viscoelasticity of Glass-Forming Materials: What About Inorganic Sealing Glasses?

Robert S. Chambers, Mark E. Stavig, and Rajan Tandon

Abstract Glass forming materials like polymers exhibit a variety of complex, nonlinear, time-dependent relaxations in volume, enthalpy and stress, all of which affect material performance and aging. Durable product designs rely on the capability to predict accurately how these materials will respond to mechanical loading and temperature regimes over prolonged exposures to operating environments. This cannot be achieved by developing a constitutive framework to fit only one or two types of experiments. Rather, it requires a constitutive formalism that is quantitatively predictive to engineering accuracy for the broad range of observed relaxation behaviors. Moreover, all engineering analyses must be performed from a single set of material model parameters. The rigorous nonlinear viscoelastic Potential Energy Clock (PEC) model and its engineering phenomenological equivalent, the Simplified Potential Energy Clock (SPEC) model, were developed to fulfill such roles and have been applied successfully to thermoplastics and filled and unfilled thermosets. Recent work has provided an opportunity to assess the performance of the SPEC model in predicting the viscoelastic behavior of an inorganic sealing glass. This presentation will overview the history of PEC and SPEC and describe the material characterization, model calibration and validation associated with the high Tg (~460 °C) sealing glass.

Keywords Nonlinear • Viscoelasticity • Polymers • Modeling • Glasses

10.1 Introduction

Glassy polymers exhibit behavior quite different from metals and ceramics. They undergo nonlinear, time-dependent relaxations in volume and stress that define a glass transition when heating or cooling between the rubbery and glassy state of the material. During that transition, properties can change significantly. It is not uncommon for the effective thermal expansion coefficient to experience a threefold change in magnitude while the shear modulus changes by a couple orders of magnitude. This is particularly important in electronic packaging where polymers often are used to encapsulate or underfill printed wiring board components. There the mismatch in thermal strains and material stiffness across bonded interfaces can generate high stresses leading to cohesive cracking, adhesive debonding or thermal fatigue in critical solder joints. Modeling provides a means to avoid premature component failures through systematic analyses guiding the development of robust designs and manufacturing processes. However, this requires an accurate material model capable of predicting the full range of polymeric behavior under general thermal-mechanical environments.

10.2 Potential Energy Clock (PEC) Model

A physically based polymer model must meet certain well-defined criteria drawn from experimental observations. The intrinsic time dependence arises from an underlying relaxation mechanism that has been shown to conform to the time-temperature hypothesis of Leaderman [1]. Dissipation, history dependence with fading memory, glass transition, a sensitivity to temperature and a "yield-like" behavior producing highly nonlinear relaxations under excessive stress or strain all strongly favor a nonlinear viscoelastic modeling approach over elasticity or plasticity. The thermorheologically simple behavior [2] is captured readily with a material clock described by the WLF equation [3] in the small strain regime for

R.S. Chambers (✉) • M.E. Stavig • R. Tandon
Sandia National Laboratories, P. O. Box 8500, Albuquerque, NM 87185-0346, USA
e-mail: rtandon@sandia.gov

C. Ralph et al. (eds.), *Mechanics of Composite and Multi-functional Materials, Volume 7*,
Conference Proceedings of the Society for Experimental Mechanics Series, DOI 10.1007/978-3-319-21762-8_10

the equilibrated material above glass transition. However, a nonlinear, thermodynamically consistent formalism is needed to predict properly the acceleration in relaxation rates under finite strains.

To meet these requirements, Caruthers et al. [4] developed a nonlinear viscoelastic formalism whereby the Helmholtz free energy was represented by a second order Frechet series expansion in the temperature and strain histories for a material undergoing finite deformations with fading memory employing a material clock. The proposed Helmholtz free energy served as a potential function from which the stress constitutive equation was derived along with other thermodynamic quantities of interest (e.g., entropy, internal energy). The success of the constitutive framework was secured by two important findings. The first was the identification of the Hencky strain as the appropriate strain measure for the second order expansion. This requirement arose from the need for the first invariant of the strain tensor to be a function of volume only to achieve the incompressibility limit as the material transitioned from the glass into the rubber. The second critical aspect of the model was determining the driving force for the material clock. That was found to be the potential part of the internal energy.

The PEC model was shown to predict a broad range of relaxation phenomena for both thermosets and thermoplastics including temperature and time dependence of stress-strain through "yield", volume and enthalpy relaxation and stress relaxation during multi-step loading histories [5]. Moreover, this was accomplished using a single set of PEC material parameters for each material. There are, however, intrinsic difficulties associated with the use of the PEC model. First, being formulated in terms of the Hencky stress-strain relations, the finite element implementation of the model requires a fourth order tensor transformation to map the logarithmic stress-strain equations into the Cauchy space. This is computationally taxing. Second, there are single and double hereditary integrals requiring four independent relaxation functions stemming from the entropy definition and the volume, shear, and temperature terms in the definition of stress. Although the model is populated exclusively from linear viscoelastic properties using no phenomenological tuning parameters, these viscoelastic functions, properties and all the associated temperature/volume dependencies must be measured accurately and consistently. That requires an extensive experimental characterization that is time consuming and prohibitively expensive for most engineering applications.

10.3 Simplified Potential Energy Clock (SPEC) Model

To ease the experimental and computational burdens imposed by the PEC formalism, a simplified potential energy clock (SPEC) model [6] was developed. This was accomplished by a combination of steps intended to reduce the complexity of the numerical computations, avoid some of the higher order temperature and volume dependencies and make the material clock more phenomenological by introducing "fitting" parameters. To bypass the calculations of a logarithmic strain and the fourth order tensor transformation needed to compute the Cauchy stress, the Hencky strain rate was approximated by the unrotated rate of deformation tensor, d. Although the integral of the rate of deformation tensor does not yield a true strain measure, it does provide a very close approximation to the Hencky strain for strain levels that would be reasonable for a glassy polymer. The resulting SPEC approximation for the Cauchy stress, σ, is

$$\begin{aligned}\underline{\underline{\sigma}}(t) \;=\; & \frac{\rho}{\rho_{ref}}\left[\Delta K(T)\int_0^t ds\, f_v\left(t^*-s^*\right)\frac{dI_1}{ds}-\Delta A(T)\int_0^t ds\, f_v\left(t^*-s^*\right)\frac{dT}{ds}\right]\underline{\underline{I}} \\ & +\frac{2\rho\Delta G(T)}{\rho_{ref}}\int_0^t ds\, f_s\left(t^*-s^*\right)\left[\underline{\underline{R}}(t)\cdot\underline{\underline{d}}_{dev}(s)\cdot\underline{\underline{R}}^{-1}(t)\right] \\ & +\frac{\rho}{\rho_{ref}}\left[K_\infty(T)I_1(t)-A_\infty(T)\{T(t)-T(0)\}\right]\underline{\underline{I}} \\ & +\frac{2\rho G_\infty(T)}{\rho_{ref}}\left[\underline{\underline{R}}(t)\cdot\underline{\underline{\varepsilon}}_{dev}(t)\cdot\underline{\underline{R}}^{-1}(t)\right] \end{aligned} \tag{10.1}$$

In this equation, ρ and ρ_{ref} are the densities at the current state and reference state, f_v and f_s are normalized volumetric and shear relaxation spectra which decay from 1 to 0, R is the rotation tensor, I is the identity tensor, ε is the strain computed from the integral of the rate of deformation tensor, I_1 is the trace of the strain tensor, T is temperature, and the "dev" subscript denotes the deviatoric part of the designated tensor. The prefactors in the above equations are parameters that must be determined for each specific material. In general, they are related but not identically equal to the more commonly recognized

bulk and shear moduli, K and G, and thermal expansion coefficient, α, as follows. A temperature dependence in these prefactors, denoted by (T) in the equations below, is allowed.

$$\Delta K(T) = K_g(T) - K_\infty(T) \tag{10.2}$$

$$\Delta G(T) = G_g(T) - G_\infty(T) \tag{10.3}$$

$$\Delta A(T) = \left[K_g\alpha_g - K_\infty\alpha_\infty\right](T) \tag{10.4}$$

The subscripts "∞" and "g" are applied to designate the "equilibrium" and "glassy" values of a designated parameter. The material clock is defined by a shift factor, "a", based on a re-definition of the potential energy found in the PEC model.

$$t^* = \int_0^t \frac{dw}{a(w)} \tag{10.5}$$

$$\log[a(t)] = -\frac{C_1 N(t)}{C_2 + N(t)} \tag{10.6}$$

$$\begin{aligned} N(t) \quad = & \left\{ \left[T(t) - T_{ref}\right] - \int_0^t ds\, f_v\left(t^* - s^*\right) \frac{dT}{ds}(s) \right\} \\ & + C_3 \left\{ I_1(t) - \int_0^t ds\, f_v\left(t^* - s^*\right) \frac{dI_1}{ds}(s) \right\} \\ & + C_4 \left\{ \int_0^t ds\, f_s\left(t^* - s^*\right) \underline{\underline{d}}_{dev}(s) \right\} : \left\{ \int_0^t ds\, f_s\left(t^* - s^*\right) \underline{\underline{d}}_{dev}(s) \right\} \end{aligned} \tag{10.7}$$

The coefficients C_1 through C_4 are phenomenological and must be fit to data. For an equilibrated material undergoing free thermal expansion/contraction above the glass transition temperature, the integrals are identically zero and the material clock depends on temperature and volume only.

Although the experimental characterization and model calibration process is easier for the SPEC model than the PEC model, the performance predictions are quite comparable. The SPEC approximations have been shown to be entirely suitable for engineering applications [6] having been applied to unfilled thermosets and thermoplastics as well as epoxies with particulate fillers that were characterized as an isotropic homogeneous continuum. An example of the latter is shown in Fig. 10.1 where

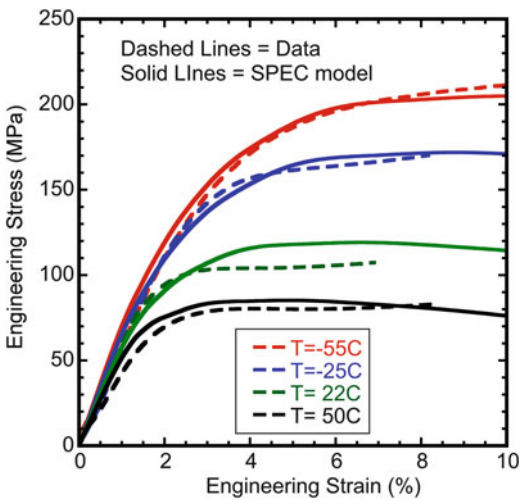

Fig. 10.1 SPEC model predictions of stress-strain behavior at four different temperatures for Epon 828/D230 filled with 30 vol% alumina particulates

stress-strain data at four different temperatures are compared to the SPEC predictions for an EPON 828 resin reacted with Jeffamine D230 and filled with 30 vol.% alumina. The glass transition temperature of this filled epoxy is ~80 °C.

10.4 Material Characterization and SPEC Model Calibration

Perhaps the most formidable challenge of viscoelastic modeling arises from the time, expense and difficulty in performing the requisite material characterization and model calibration. In general, the SPEC model requires data to define the two relaxation spectra, the decaying prefactors for the hereditary integrals and the corresponding equilibrium parameters. This leads naturally to three classes of experiments involving shear, temperature and volume.

The shear tests are relatively straightforward. The glass transition temperature (Tg) and modulus temperature dependence can be obtained with a Dynamic Mechanical Analyzer (DMA) measuring the storage and loss moduli during torsion at fixed frequency while sweeping the temperature at a constant rate from the glassy to the rubbery states. The shear master curve is built following the conventional approach for thermorheologically simple materials. Here, the DMA test protocol is changed to measure dynamic properties across a range of frequencies during isothermal tests conducted at different temperatures taken around glass transition. At each temperature, the shear storage and loss moduli, G' and G'' respectively, are measured and tan delta is computed as the ratio of the two values (tan delta $= G''/G'$). These data then are plotted versus the logarithm of frequency producing a family of curves, one for each test temperature. The master curve is generated from the tan delta plots by first choosing a reference temperature (Tref) curve and horizontally shifting all remaining curves on the log frequency axis to obtain a smooth, continuous, composite representation of the function. By performing the horizontal shifts with the tan delta curves, the modulus temperature dependence cancels out and the need for vertical shifts is removed. Once the horizontal shift factors have been defined from the tan delta curves, the master curves for storage and loss moduli are constructed by applying the same horizontal shifts. In this case, some vertical shifts may be necessary to accommodate small changes in moduli with temperature. Although this produces master curves in the frequency domain, viscoelastic analyses utilize relaxation functions in the time domain. That requires an additional mapping facilitated by an exponential series expansion (Prony series) providing a convenient representation for the shear relaxation spectrum as follows:

$$G(t) = G_\infty + \Delta G \sum_{i=1}^{N} f_i \exp(-t/\tau_i) = G_\infty + \Delta G f_s(t) \tag{10.8}$$

The values f_i and τ_i are fitting constants. When the exponential series is substituted into the linear viscoelastic shear hereditary integral and the stress is computed for a sinusoidal, constant amplitude shear strain history, $\gamma_o \sin(\omega t)$, expressions are obtained for the storage and loss moduli in terms of the exponential series parameters and the frequency, ω:

$$G'(\omega) - G_\infty = \Delta G \sum_{i=1}^{N} f_i (\omega\tau_i)^2 / \left[1 + (\omega\tau_i)^2\right] \tag{10.9}$$

$$G''(\omega) = \Delta G \sum_{i=1}^{N} f_i (\omega\tau_i) / \left[1 + (\omega\tau_i)^2\right] \tag{10.10}$$

The latter two equations are suitable for fitting the shear storage and loss master curves in the frequency domain. When the fitting constants are defined, the relaxation spectrum in the time domain is computed directly from Eq. 10.8.

The bulk modulus and its temperature dependence can be measured with a pressure-dilatometer. This often is achieved by applying strain gauges to a protected sample pressurized in a fluid bath. Mapping the bulk relaxation spectrum, f_v, directly by measuring the time dependence of the decaying pressure following step changes in volume at different temperatures is much more cumbersome. Fortunately, there is an alternative resulting from the fact that the SPEC model uses a single relaxation function for both the bulk and temperature hereditary integrals. Thermal strain data collected with a Thermal Mechanical Analyzer (TMA) provide another means of calibrating the model. Since the location and shape of the glass transition are determined by the prescribed temperature history, a properly calibrated constitutive equation must be able to predict the heating and cooling strains from an analysis of the actual test conditions. That suggests the possibility of using an iterative modeling approach to deduce the prefactors and relaxation function required to minimize the error between predictions and data. Starting from an assumed property set, the SPEC model is used to predict the thermal strain response during a

temperature history cycling through glass transition at prescribed rates. The resulting strain-temperature curves are compared to the measured data, and model parameters are adjusted to minimize the error. The slopes of the glassy and rubbery response contribute to the definition of the prefactors in Eqs. 10.2 and 10.4. The parameterization of the relaxation function is facilitated by simplifying the functional form to a stretched exponential. This allows the minimization of error from the relaxation function to be controlled through the specification of only two parameters, λ and β:

$$f_v(t) = \exp\left(-(t/\lambda)^{\beta}\right) \tag{10.11}$$

In general, the stretched exponential still must be converted to a Prony series for ease of constitutive computations. However, by specifying a fixed distribution of relaxation times, the Prony prefactors are solved readily from a linear set of equations. Surprisingly, the iterative process of parameterization works very well and is easily executed with a finite element analysis in a one-element problem.

Through a judicious choice of C_1 and C_2, the material clock equation for the logarithm of the shift factor can be reduced to the familiar WLF form for an equilibrated material. The C_3 parameter defines the pressure dependence of the glass transition temperature while C_4 governs the nonlinear relaxations producing "yield-like" behavior under loading. The C_4 parameter is chosen to reproduce stress-strain data like that illustrated in Fig. 10.1.

10.5 Inorganic Glasses

The material characterization and SPEC calibration procedures described in the previous section have been applied to epoxies for viscoelastic analyses designing a wide variety of adhesively bonded joints and encapsulated components. However, the interest in modeling the viscoelasticity of glass-forming materials is not confined to organic materials. Inorganic sealing glasses exhibit similar relaxation behaviors in volume and stress. Historically, this led Narayanaswamy [7] to develop a viscoelastic model with structural relaxation for analyzing glass tempering and annealing. Since similar modeling attributes are found in both classes of materials, it seems logical to question whether the SPEC model might be more generally applicable. To investigate that possibility, the Schott 8061 inorganic sealing glass was selected. Some preliminary work has been performed incorporating the proposed tests and model calibration procedures. A few key results are summarized in the remainder of this paper. In general, the applications driving inorganic glass modeling focus on two areas: minimizing tensile stresses to avoid fracture and predicting structural relaxation to maintain/control dimensional stability. This requires a capability to predict accurately the solidification through glass transition along with the accompanying thermal strain changes produced by arbitrary temperature histories. It is the shear and volume relaxation behaviors that govern these phenomena.

Shear data were collected from torsion tests conducted with the TA ARES rheometer on samples taken from the bulk glass. The test coupons were 55 mm long with a rectangular cross-section 11 mm × 1 mm having flat, parallel faces. The storage and loss moduli were measured at frequencies from 0.1 to 16 Hz at 10° temperature increments from 300 to 600 °C.

A plot of the raw tan delta versus frequency data for a sampling of temperatures is shown in Fig. 10.2.

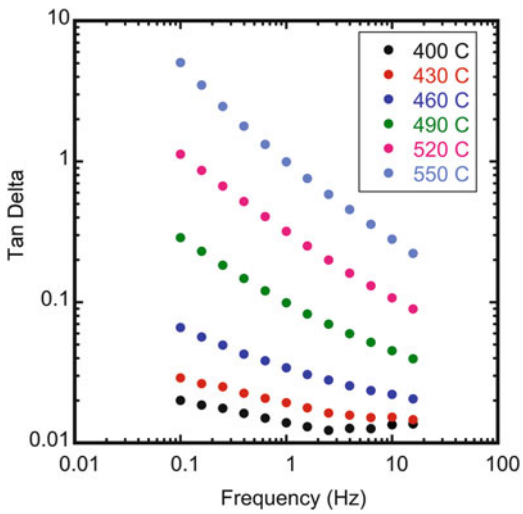

Fig. 10.2 Tan delta versus frequency data from dynamic torsion tests on S8061 glass conducted at several temperatures used for the master curve construction

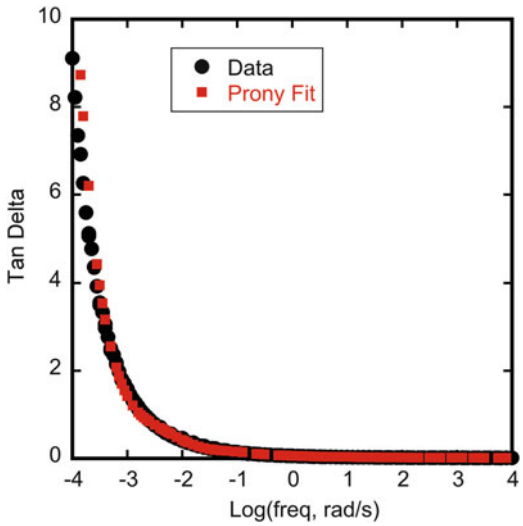

Fig. 10.3 Tan delta master curve data and Prony series fit for S8061 glass at a reference temperature 460 °C

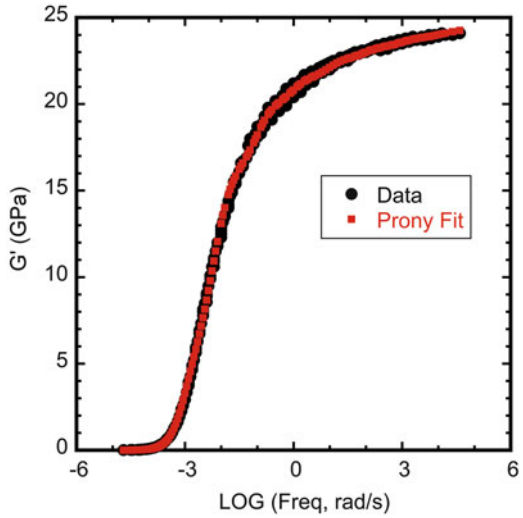

Fig. 10.4 Shear storage modulus master curve data and Prony series fit at reference temperature 460 °C

To assess the validity of thermorheological simplicity, a reference temperature of 460 °C (733 K) was selected and the tan delta curves were shifted in log frequency space relative to the reference temperature to construct a smooth master curve. That resulted in a shift factor defined by the WLF equation:

$$\log[a(T)] = -17\left(T - T_{ref}\right)/\left(350 + T - T_{ref}\right) \tag{10.12}$$

Using these shift factors, the master curves were constructed for G′ and G″, and a Prony series was fit simultaneously to the storage and loss moduli. The master curves for tan delta and the shear storage modulus are plotted in Figs. 10.3 and 10.4 along with the Prony series fits to the data. With these Prony coefficients, the shear relaxation function, $f_s(t)$, was defined. It is plotted in Fig. 10.5 along with a second function obtained by repeating the test on another sample. Although these curves differ slightly, the spectra differences appear to be within the margin of error deemed suitable for engineering accuracy.

The thermal strain data were collected in a DIL 402 C Netzsch dilatometer using samples 25 mm long with a square cross-section 5 mm × 5 mm. Data were recorded for two thermal strain histories. The first annealed the glass at 500 °C and then thermal cycled between 100 and 500 °C at 0.5 °C/min. Using the iterative approach, the shape of the volume relaxation spectrum, $f_v(t)$, was deduced by analyzing the experiment to minimize the error between thermal strain data and predictions across the temperature range of the experiment. This relied on the slopes of the expansion/contraction curves in the glassy and liquid regimes as well as the shape through glass transition. The initial estimates of bulk moduli and thermal expansion

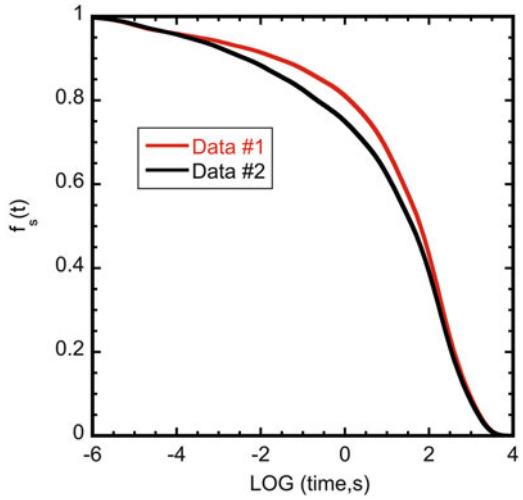

Fig. 10.5 Normalized shear relaxation spectra for S8061 glass constructed from two data sets with reference temperature 460 °C

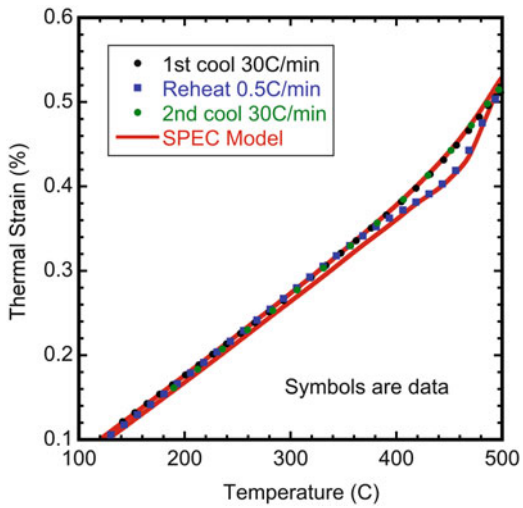

Fig. 10.6 S8061 glass thermal strain data and SPEC model predictions during cooling at 30 °C/min and reheating at 0.5 °C/min

coefficients were obtained from literature data (glassy Young's modulus and Poisson's ratio 68.5 GPa and 0.22). To add to the fidelity and check the quality of the model calibration, a second sample was subjected to a different thermal history. The second sample was cooled at 30 °C/min but heated at 0.5 °C/min generating a hysteresis created by the additional structural relaxation during heating. The thermal strain data and SPEC model predictions for the latter test are plotted in Fig. 10.6. A stretched exponential (time in seconds) was found to capture the volume relaxation function quite well:

$$f_v(t) = \exp\left(-(t/30)^{0.3}\right) \tag{10.13}$$

The numerical details and model comparisons to additional test data will be documented in a subsequent publication.

10.6 Summary

The viscoelastic behavior of glass-forming materials is an important consideration for the durability and life-time performance of many applications ranging from encapsulated components to hermetic glass-to-metal seals. Accurate material modeling enables analysts to anticipate and avoid many design flaws and to tailor material selection and manufacturing

processes to achieve higher quality. To be practical, this requires a high fidelity, physically based material model that can be calibrated routinely from a standard set of experiments that are relatively inexpensive to perform. The simplified potential energy clock (SPEC) nonlinear viscoelastic model is being used to fulfill this role. Current work is providing further evidence of the broad applicability of the SPEC model extending to the inorganic glasses.

Acknowledgements Sandia National Laboratories is a multi-program laboratory managed and operated by Sandia Corporation, a wholly owned subsidiary of Lockheed Martin Corporation, for the U.S. Department of Energy's National Nuclear Security Administration under contract DE-AC04-94AL85000. Special thanks are offered to Nicholas B. Wyatt for measuring the stress-strain curves and collecting other data characterizing the Epon 828/D230 alumina-filled epoxy.

References

1. Leaderman, H.: Elastic and Creep Properties of Filamentous Materials, p. 175. Textile Foundation, Washington, DC (1943)
2. Schwarzl, F., Staverman, A.J.: Time-temperature dependence of linear viscoelastic behavior. J. Appl. Mech. **23**(8), 838–843 (1952)
3. Williams, M.L., Landel, R.F., Ferry, J.D.: The temperature dependence of relaxation mechanisms in amorphous polymers and other glass-forming liquids. J. Am. Chem. Soc. **77**(14), 3701–3707 (1955)
4. Caruthers, J.M., Adolf, D.B., Chambers, R.S., Shrikhande, P.: A thermodynamically consistent, nonlinear viscoelastic approach for modeling glassy polymers. Polymer **45**(13), 4577–4597 (2004)
5. Adolf, D.B., Chambers, R.S., Caruthers, J.M.: Extensive validation of a thermodynamically consistent, nonlinear viscoelastic model for glassy polymers. Polymer **45**(13), 4599–4621 (2004)
6. Adolf, D.B., Chambers, R.S., Neidigk, M.A.: A simplified potential energy clock model for glassy polymers. Polymer **50**(17), 4257–4269 (2009)
7. Narayanaswamy, O.S.: A model of structural relaxation in glass. J. Am. Ceram. Soc. **54**(10), 491–498 (1971)

Chapter 11
Unified Creep Plasticity Damage (UCPD) Model for Rigid Polyurethane Foams

Michael K. Neilsen, Wei-Yang Lu, William M. Scherzinger, Terry D. Hinnerichs, and Chi S. Lo

Abstract Experiments were performed to characterize the mechanical response of several different rigid polyurethane foams to large deformation. In these experiments, the effects of load path, loading rate, and temperature were investigated. Results from these experiments indicated that rigid polyurethane foams exhibit significant damage, volumetric and deviatoric plasticity when they are compressed. Rigid polyurethane foams were also found to be extremely strain-rate and temperature dependent. These foams are also rather brittle and crack when loaded to small strains in tension or to larger strains in compression. Thus, a phenomenological Unified Creep Plasticity Damage (UCPD) model was developed to describe the mechanical response of these foams to large deformation at a variety of temperatures and strain rates. This paper includes a description of recent experiments and experimental findings. Next, development of a UCPD model for rigid, polyurethane foams is described. Finite element simulations with the new UCPD model are compared with experimental results to show behavior that can be captured with this model.

Keywords Polyurethane foam • Cellular solid • Constitutive model • Fracture • Unified Creep Plasticity

11.1 Introduction

Polyurethane foams are often used in packaging to protect sensitive components from accidental impact events. These foams are designed to absorb energy during impact events by undergoing large inelastic deformation. Thus, constitutive models that describe foam response to large deformation at various rates and temperatures are needed for use in finite element analyses of impact events.

Rigid, closed-cell, polyurethane foam consists of nearly spherical voids (Fig. 11.1) with a typical diameter of 100–300 μm. The closed cells are separated by a polymer matrix that forms cells. Voids are less spherical and walls between neighboring cells are often very thin or even ruptured in rigid polyurethane foams with densities of 192 kg/m^3 (12 pcf) or less. In higher density foams with densities of 320 kg/m^3 (20 pcf) or greater, cells are more spherical and walls between neighboring cells are typically intact.

11.2 Experimental Observations

When rigid, closed-cell polyurethane foam is compressed, it exhibits an initial elastic regime followed by a plateau regime in which the load needed to compress the foam remains nearly constant (Fig. 11.2). In the elastic regime, the foam sample is uniformly deformed. In the plateau regime, cell walls are plastically deformed and large permanent volume changes are generated. When additional load is applied, cell walls are compressed against neighboring cell walls (Fig. 11.3), and the stiffness and strength of the foam increases. In Fig. 11.2, uniaxial stress and strain are plotted as positive for both compression and tension. When rigid polyurethane foam is loaded in tension, it exhibits only a very small amount of plastic deformation before it fractures. Fracture surfaces generated by uniaxial tension are oriented such that the loading axis is normal to the fracture surface (Fig. 11.4). The mechanical response of polyurethane foam is also very sensitive to changes in either loading rate or temperature. The plateau strength of rigid polyurethane foam subjected to uniaxial compression

M.K. Neilsen (✉) • W.M. Scherzinger • T.D. Hinnerichs • C.S. Lo
Sandia National Laboratories, P.O. Box 5800, Albuquerque, NM 87185, USA
e-mail: mkneils@sandia.gov

W.-Y. Lu
Sandia National Laboratories, P.O. Box 969, Livermore, CA 94551, USA

C. Ralph et al. (eds.), *Mechanics of Composite and Multi-functional Materials, Volume 7*,
Conference Proceedings of the Society for Experimental Mechanics Series, DOI 10.1007/978-3-319-21762-8_11

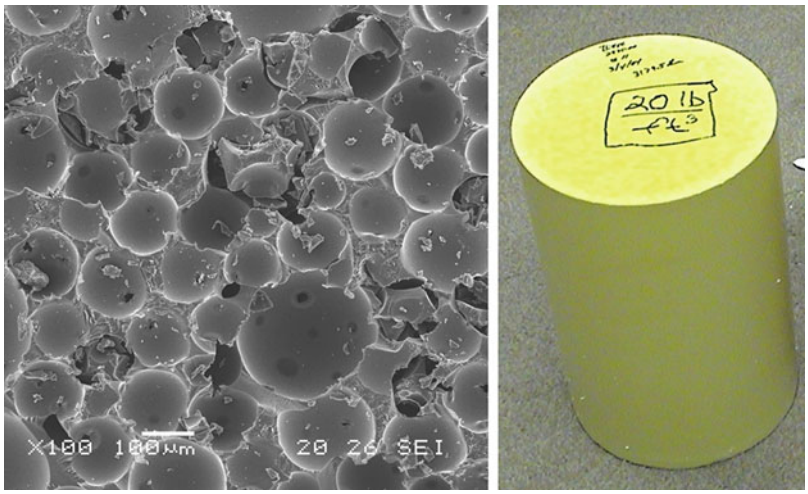

Fig. 11.1 320 kg/m^3 (20 pcf) rigid polyurethane foam cell geometry and 12 inch tall billet

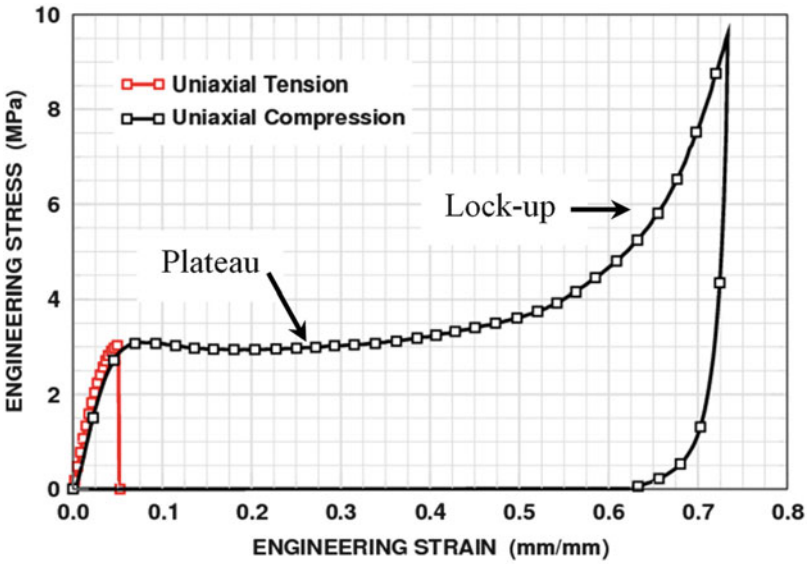

Fig. 11.2 Typical stress-strain curves for 176 kg/m^3 (11 pcf) polyurethane foam subjected to either uniaxial compression or uniaxial tension

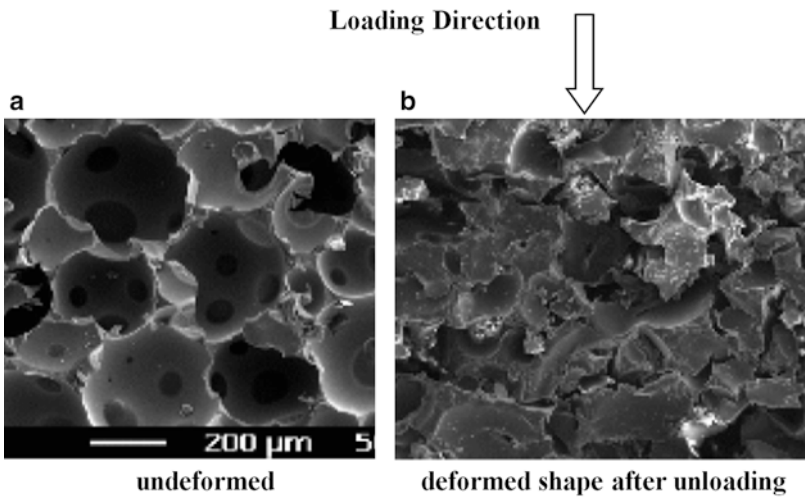

Fig. 11.3 Cell walls compressed against neighboring cell walls when 176 kg/m^3 (11 pcf) polyurethane foam is compressed into the lock-up regime and then unloaded

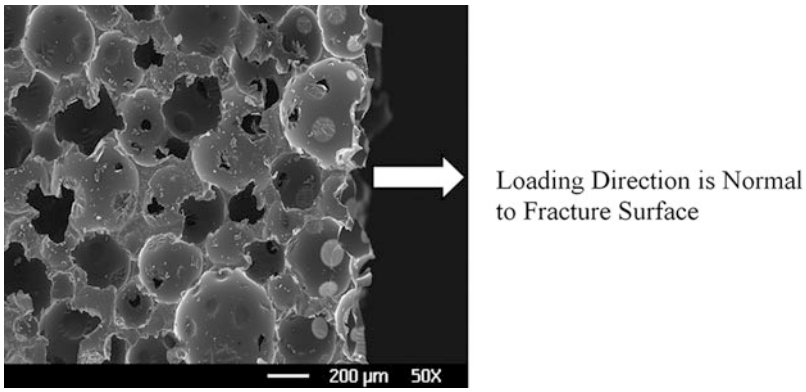

Fig. 11.4 Tensile failure surface generated by uniaxial tension of 176 kg/m^3 (11 pcf) polyurethane foam in the indicated direction

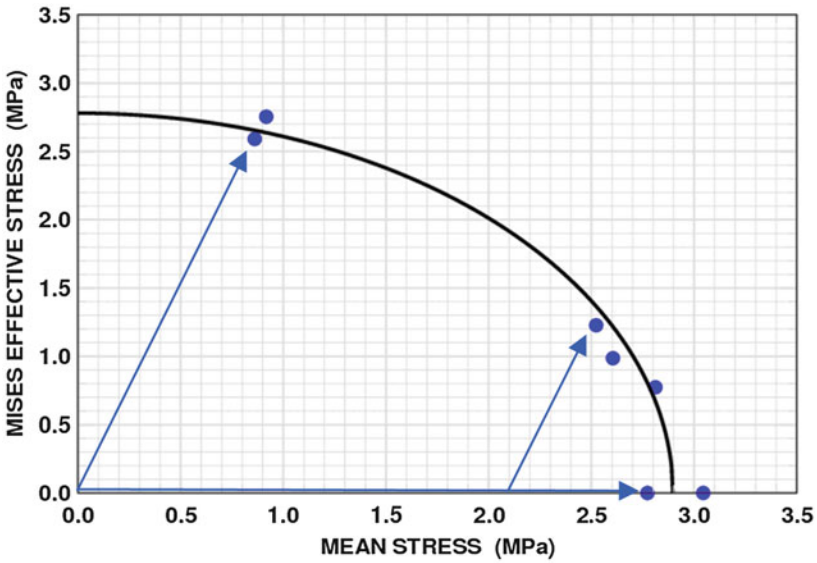

Fig. 11.5 Yield surface obtained from a series of uniaxial compression, hydrostatic compression and triaxial compression experiments on 192 kg/m^3 (12 pcf) FR3712 foam. Each blue symbol represents the result from one experiment

decreases significantly with increases in temperature. The plateau strength is also observed to increase significantly with increases in loading rate. When rigid polyurethane foam is subjected to hydrostatic compression, it exhibits a pressure versus volume strain curve that is similar in shape to its uniaxial stress-strain curve (Fig. 11.2). There is again an initial elastic regime followed by a plateau regime and finally a lock-up regime.

In addition to uniaxial and hydrostatic compression, FR3712 rigid polyurethane foam was also subjected to a variety of triaxial compression load paths in which the sample was initially subjected to hydrostatic compression and then the confining pressure was maintained while additional stress was applied in the axial direction only. Results from this series of triaxial compression experiments were then used to generate a plot of the initial yield surface for the foam in a von Mises effective stress versus mean stress space (Fig. 11.5). The experimental results (blue symbols in Fig. 11.5) indicate that the initial yield surface for the FR3712 foam could be described as an ellipse in this two dimensional space (solid line in Fig. 11.5) or as an ellipsoid about the hydrostat in three-dimensional principal stress space.

11.3 Unified Creep Plasticity Damage (UCPD) Model

From the experimental results presented in the previous section, it is clear that a metal plasticity model which includes only deviatoric (shape-changing) plasticity would not be adequate for describing the mechanical behavior of rigid polyurethane foams. Constitutive models for foams were previously developed by a number of researchers [e.g. 1–6]. Neilsen et al. [1] developed a plasticity model for polyurethane foams with a yield surface that has a cubic shape based on the use of a principal stress yield criterion. Deshpande and Fleck [2] developed a plasticity model for metal foams with a yield surface

that is an ellipsoid about the hydrostat. Deshpande and Fleck [3] subsequently developed a yield surface for polymeric foams with a yield surface that is the inner envelope of the ellipsoidal surface previously developed for metal foams and a surface based on a minimum (compressive) principal stress criterion.

The model developed here is similar to many existing foam models [e.g. 1–6]. Our current implementation in SIERRA [7], a framework for finite element codes, uses the unrotated Cauchy stress, $\boldsymbol{\sigma}$, and unrotated deformation rate, $\dot{\boldsymbol{\varepsilon}}$ [8, 9]. For small elastic strains, the total strain rate, $\dot{\boldsymbol{\varepsilon}}$, can be additively decomposed into elastic, $\dot{\boldsymbol{\varepsilon}}^{e}$, and inelastic, $\dot{\boldsymbol{\varepsilon}}^{in}$, parts as follows

$$\dot{\boldsymbol{\varepsilon}} = \dot{\boldsymbol{\varepsilon}}^{e} + \dot{\boldsymbol{\varepsilon}}^{in} \tag{11.1}$$

We also assume that the elastic response is linear and isotropic such that the stress rate is given by the following equation

$$\dot{\boldsymbol{\sigma}} = \mathbf{E}{:}\dot{\boldsymbol{\varepsilon}}^{e} = \mathbf{E}{:}\left(\dot{\boldsymbol{\varepsilon}} - \dot{\boldsymbol{\varepsilon}}^{in}\right) \tag{11.2}$$

where $\mathbf{E}$ is the fourth-order isotropic elasticity tensor. Based on the experimental results shown in Fig. 11.5, the initial yield surface is an ellipsoid about the hydrostat described by the function

$$\varphi = \frac{\overline{\sigma}^2}{a^2} + \frac{p^2}{b^2} - 1.0 \tag{11.3}$$

where a and b are state variables that define the current deviatoric and volumetric strengths of the foam. $\overline{\sigma}$ is the von Mises effective stress, a scalar measure of the deviatoric stress and is given by

$$\overline{\sigma} = \sqrt{\frac{3}{2}\,\mathbf{s}{:}\mathbf{s}} \tag{11.4}$$

p is the pressure or mean stress and is given by

$$p = \frac{1}{3}\,\boldsymbol{\sigma}{:}\mathbf{i} \tag{11.5}$$

where $\boldsymbol{\sigma}$ is the Cauchy stress and $\mathbf{i}$ is the second-order identity tensor. $\mathbf{s}$ is the second-order deviatoric stress tensor

$$\mathbf{s} = \boldsymbol{\sigma} - p\,\mathbf{i} \tag{11.6}$$

Puso and Govindjee [5] and Zhang et al. [6] developed strain rate dependent models for foam that have the foam's inelastic rate given as a power-law function of stress. For the model developed here, we start with the yield function, Eq. (11.3), rewritten as follows

$$\varphi = \sigma^{*} - a \tag{11.7}$$

where the effective stress, σ^{*}, is given as a function of the vonMises effective stress, $\overline{\sigma}$, and pressure, p, as follows

$$\sigma^{*} = \sqrt{\overline{\sigma}^2 + \frac{a^2}{b^2}p^2} \tag{11.8}$$

Next, using a Perzyna-type formulation, the following expression for the inelastic rate, $\dot{\boldsymbol{\varepsilon}}^{in}$, is developed

$$\dot{\boldsymbol{\varepsilon}}^{in} = \begin{cases} e^{h}\left\langle \dfrac{\sigma^{*}}{a} - 1 \right\rangle^{n} \mathbf{g} & \text{when} \quad \dfrac{\sigma^{*}}{a} - 1 > 0 \\ \mathbf{0} & \text{when} \quad \dfrac{\sigma^{*}}{a} - 1 \leq 0 \end{cases} \tag{11.9}$$

where **g** is a symmetric, second-order tensor that defines the orientation of the inelastic flow. This type of model is sometimes referred to as an overstress model because the inelastic rate is a power-law function of the overstress (distance outside the yield surface). For associated flow, **g** is simply normal to the yield surface and is given by

$$\mathbf{g}_{associated} = \frac{\frac{\partial \varphi}{\partial \boldsymbol{\sigma}}}{\left|\frac{\partial \varphi}{\partial \boldsymbol{\sigma}}\right|} = \frac{\frac{3}{a^2}\mathbf{s} + \frac{2}{3b^2}p\mathbf{i}}{\left|\frac{3}{a^2}\mathbf{s} + \frac{2}{3b^2}p\mathbf{i}\right|} \tag{11.10}$$

When lower density foams are subjected to a simple load path like uniaxial compression, the inelastic flow direction, at least prior to lock-up, is nearly uniaxial. In other words, the flow direction is given by the normalized stress tensor as follows

$$\mathbf{g}_{radial} = \frac{\boldsymbol{\sigma}}{|\boldsymbol{\sigma}|} = \frac{\boldsymbol{\sigma}}{\sqrt{\boldsymbol{\sigma}:\boldsymbol{\sigma}}} \tag{11.11}$$

This type of flow is referred to as radial flow. The UCPD model has a parameter, β, which allows for the flow direction to be prescribed as a linear combination of associated and radial flow directions as follows

$$\mathbf{g} = \frac{(1-\beta)\,\mathbf{g}_{associated} + \beta\,\mathbf{g}_{radial}}{|(1-\beta)\,\mathbf{g}_{associated} + \beta\,\mathbf{g}_{radial}|} \tag{11.12}$$

Rigid polyurethane foams have little ductility when they are subjected to tensile stress and behave more like elastic brittle materials for this load path. Even for uniaxial compression, these foams often exhibit cracking. The damage surfaces for the UCPD model are simply three orthogonal planes with normals given by the positive principal stress axes in principal stress space as shown in Fig. 11.6 and are described by the following equation

$$\varphi^{i}_{Damage} = \sigma^{**i} - c(1-w) = 0, \quad i = 1,3 \tag{11.13}$$

where σ^{**i} is a principal stress, c is the initial tensile strength which is a material parameter, and w is a scalar measure of the damage. Damage has an initial value of 0.0 and is limited to a maximum value of 0.99. As damage occurs, the damage surface will collapse toward the origin and the foam will have very little tensile strength. The foam will, however, still have compressive strength. Foam that is completely damaged can be removed using element death based on the damage variable reaching a value equal to 0.99 but removal of fully damaged elements is not required.

Damage is given as a monotonically-increasing, user-prescribed function of damage strain, ε_{dam}, and damage strain is a function of the maximum tensile strain, $\varepsilon_{\max}$, and the plastic volume strain, ε^{p}_{vol} as follows

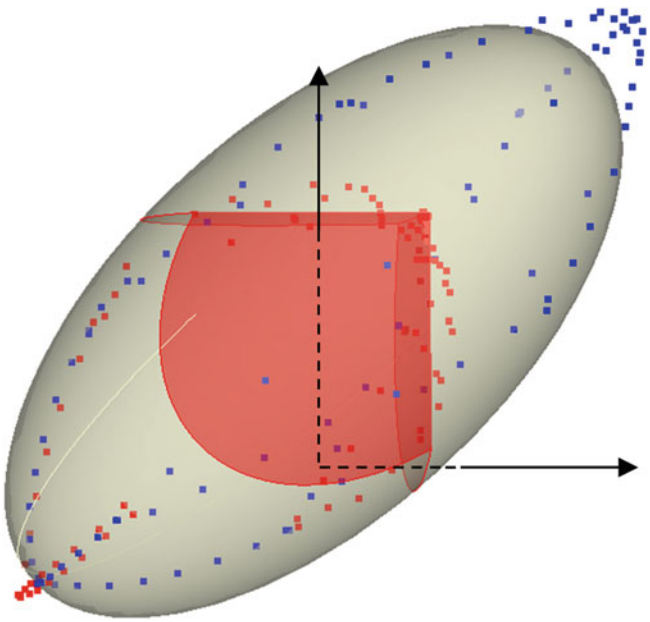

Fig. 11.6 Yield (*white*) and damage (*red*) surfaces in principal stress space. Symbols represent results from either experiments or cell-level simulations on a representative volume of foam

$$w = w(\varepsilon_{dam}) = w\left(a_{dam}\varepsilon_{\max} + b_{dam}\,\varepsilon_{vol}^{p}\right) \tag{11.14}$$

where a_{dam} and b_{dam} are positive material parameters which allow the user to control the rate at which damage is generated in tension and compression. Note that in compression the plastic volume strain obtains a negative value so the maximum tensile strain needed to generate damage is larger. Damage is never allowed to decrease even if the maximum tensile strain or plastic volume strain decrease which means that once foam is damaged, healing is not allowed.

To fully capture temperature, strain-rate, and lock-up effects several material parameters are no longer simply material constants but are instead functions of temperature, θ, and/or the maximum volume fraction of solid material obtained during any prior loading, ϕ, which depends on the volume strain. Material parameters defining the foams elastic response, Young's modulus and Poisson's ratio, are functions of both temperature, θ, and ϕ. To be more specific, the current Young's modulus and Poisson's ratio used in a simulation are given by

$$\begin{aligned} E &= E(\theta) \cdot E(\phi) \\ v &= v(\theta) \cdot v(\phi) \end{aligned} \tag{11.15}$$

The natural log of the reference flow rate, h, and the power law exponent, n, in Eq. 11.9 are also functions of temperature

$$\begin{aligned} h &= h(\theta) \\ n &= n(\theta) \end{aligned} \tag{11.16}$$

State variables that define current deviatoric and volumetric strengths, a and b, are user-prescribed functions of ϕ. Also in the UCPD model, the parameter β which defines the fraction of associated and radial flow is a user-prescribed function of ϕ.

Material parameters for a 192 kg/m^3 (12 pcf) FR3712 foam at temperatures between −53.9 °C and 73.9 °C, and quasi-static (0.001 per second) to dynamic (200 per second) strain rates are given in Table 11.1 and Fig. 11.7. The first step in the generation of these material parameters was to determine the initial volume fraction of solid material in the foam. Since the foam has a density of approximately 192 kg/m^3 and solid rigid polyurethane has a density of 1200 kg/m^3, the foam has an initial volume fraction of solid material, ϕ_0, equal to 0.16 (0.16 = 192/1200).

The next step in the fitting process was to plot the crush strength measured during uniaxial and hydrostatic compression experiments as a function of the current volume fraction of solid material. If we assume that the change in volume of the solid material is negligible compared with the change in volume of the foam, then the current volume fraction of solid material, ϕ, is related to the initial volume fraction, ϕ_0, of solid material as follows

$$\phi = \frac{\phi_0 V_0}{V} \tag{11.17}$$

where V_o is the initial volume of foam and V is the current volume of foam. Note that equations that are function of ϕ actually use maximum volume fraction of solid material obtained during any prior loading in simulations; however, for monotonic compressive loading the current volume fraction of solid material is the maximum value obtained during any prior loading. The consequence of this assumption in simulations is that once the foam is compressed it cannot be re-expanded to have the same mechanical properties it had prior to compression. Material parameter functions which were found to provide a good fit to the experimental data are shown in Fig. 11.7.

Table 11.1 Foam damage model parameters for 192 kg/m^3 (12 pcf) foam, FR3712

Parameter	Units	Value	Value	Value
Temperature	C	−53.9	18.3	73.9
Young's modulus $E(\theta)$	MPa	79.7	79.6	63.7
Poisson's ratio v	–	0.250		
Initial volume fraction solid ϕ_0	–	0.160		
Flow Rate $h(\theta)$	–	−10.0	2.60	7.50
Power exponent $n(\theta)$	–	18.0	14.0	6.00
Tensile strength c	MPa	1.931		
Adam a_{dam}	–	1.00		
Bdam b_{dam}	–	1.00		
Thermal expansion coefficient	1/C	60.0×10^{-6}		

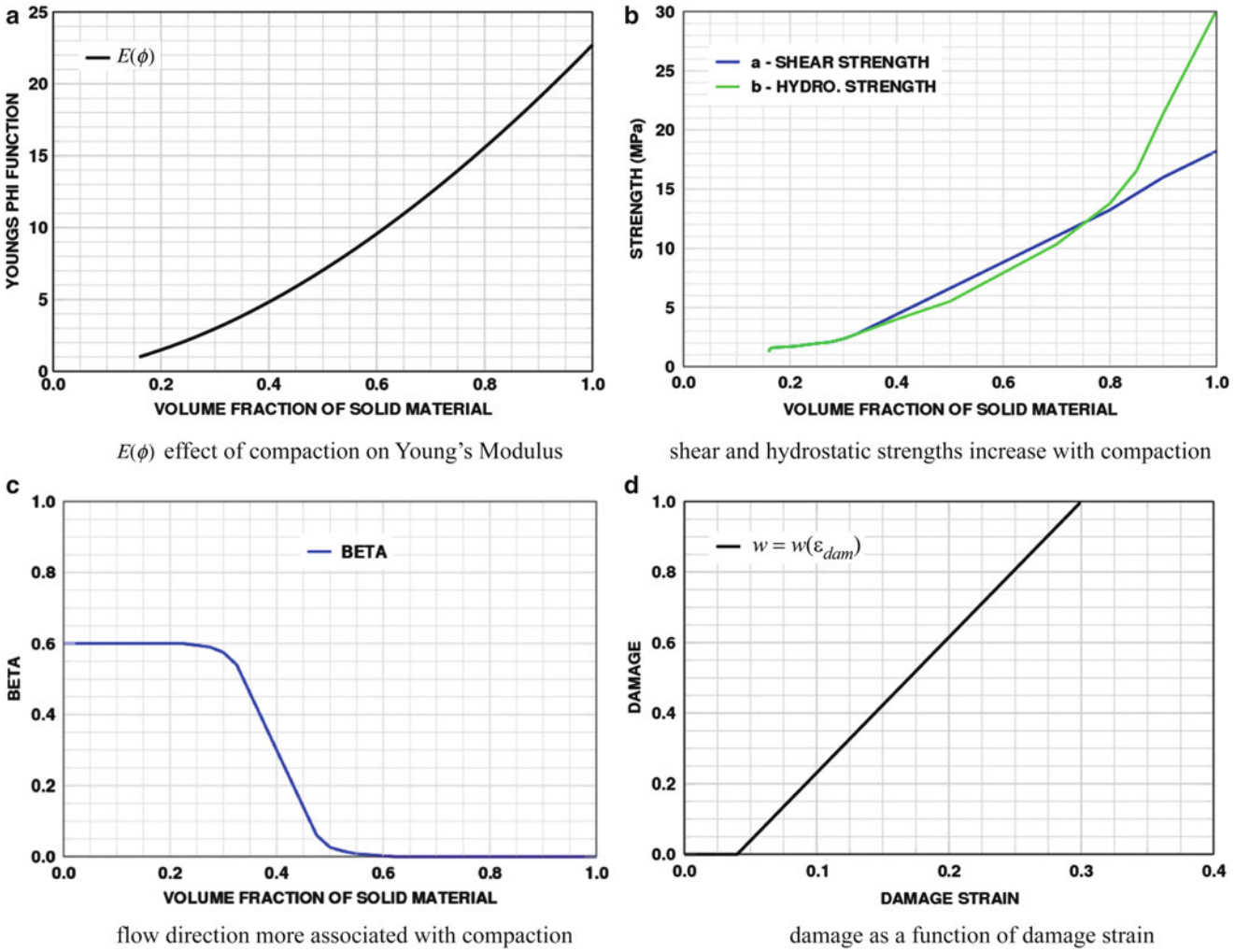

Fig. 11.7 Material parameter functions for FR3712

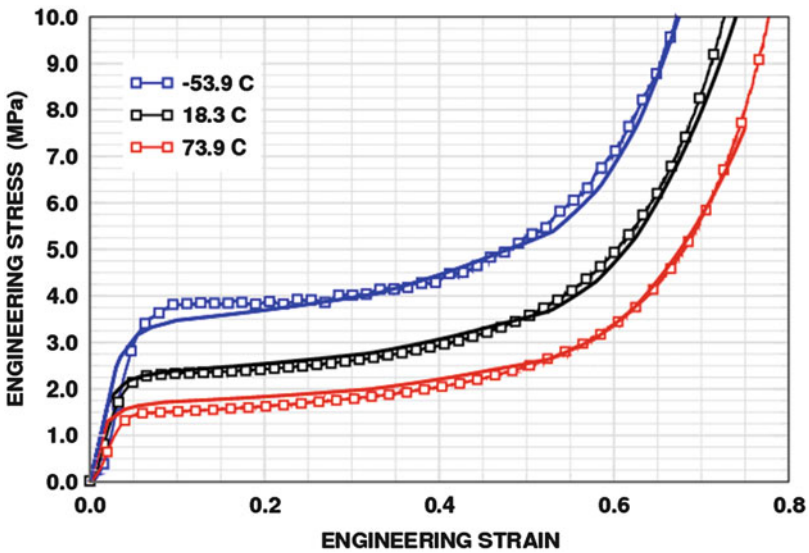

Fig. 11.8 FR3712 uniaxial compression experiments (*symbols*) and simulations (*solid lines*) at three different temperatures and a constant engineering strain rate of 0.001 per second

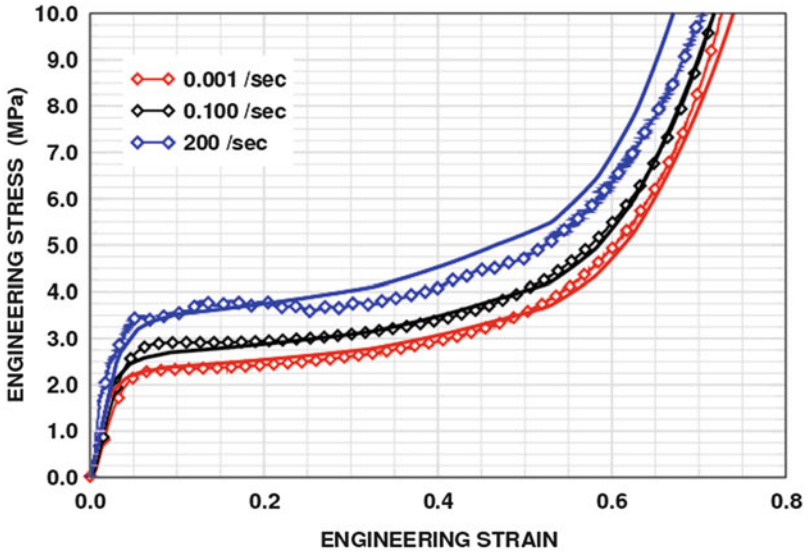

Fig. 11.9 FR3712 uniaxial compression experiments (*symbols*) and simulations (*solid lines*) at three different engineering strain rates and a constant temperature of 18.3 °C

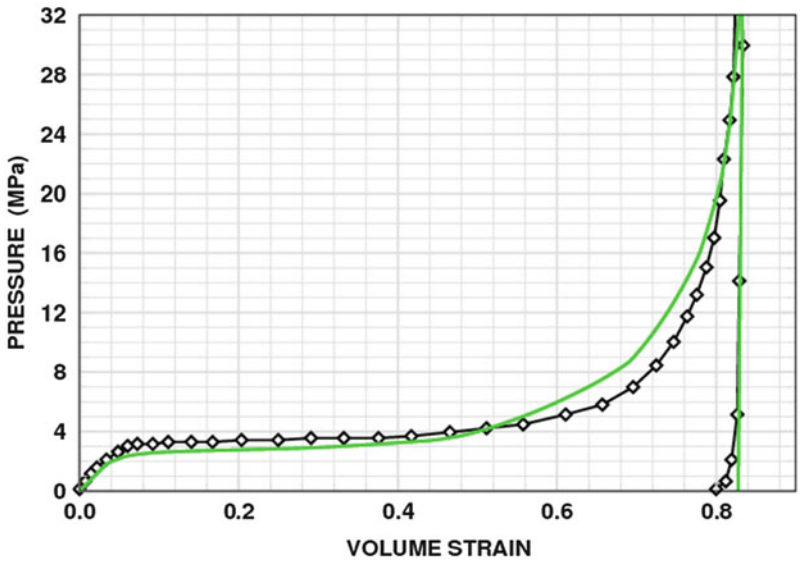

Fig. 11.10 FR3712 hydrostatic compression experiment (*symbols*) and simulation (*solid green line*) at room temperature

Uniaxial and hydrostatic compression experiments on FR3712 were simulated. The stress-strain curves generated by these simulations are compared with the experimental data in Figs. 11.8 and 11.9. For all temperatures and strain rates the fit is good. The hydrostatic compression experiment was then simulated. Pressure applied to the finite element model was increased at a constant rate of 0.1 MPa/s (14.5 psi/s) to match the experiment. The UCPD Model prediction matched the experiment well (Fig. 11.10). Unfortunately, there was no uniaxial tension data available for this foam so the damage parameters selected for FR3712 were simply based on experience with other rigid polyurethane foams with similar density.

Parameters were also generated for other foams and the experiments used to generate those parameters were then simulated to show that the model could capture both the inelastic deformation and cracking exhibited by the foam. For example, Fig. 11.11 shows a comparison of experiments and deformed model shapes from simulations of uniaxial tension and compression of a 320 kg/m^3 (20 pcf) foam. The model is able to predict cracking from both uniaxial tension and uniaxial compression.

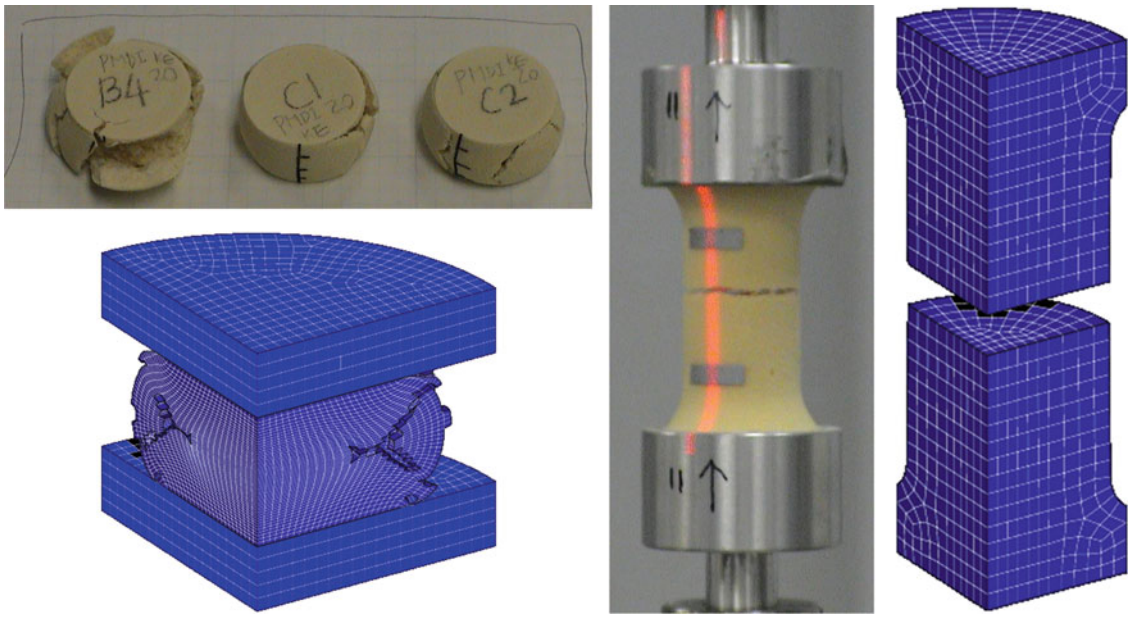

Fig. 11.11 Additional simulations showing UCPD models ability to capture foam cracking exhibited during uniaxial compression and uniaxial tension experiments on a 320 kg/m^3 (20 pcf) foam

11.4 Summary

A new UCPD model was developed to describe the mechanical response of rigid polyurethane foams to loading experienced during accidental impact events. This model captures the effects of load path, strain rate, and temperature on mechanical response. A series of experiments were performed to characterize the mechanical response of several different rigid polyurethane foams to large deformation. In these experiments, the effects of load path, loading rate, and temperature were investigated. Results from these experiments indicated that, as expected, these foams exhibit significant volumetric and deviatoric plasticity when they are compressed. Mechanical response of these foams is also significantly affected by changes in either loading rate or temperature. The new UCPD model captures both temperature and strain rate effects. This model also captures cracking exhibited by these rather brittle foams subjected to either uniaxial tension or compression. Investigation of the models ability to capture inelastic deformation and fracture for any load path are in progress.

Acknowledgments The authors are thankful for early experimental studies of polyurethane foam response to hydrostatic and tri-axial compression performed by Dr. W.A. Olsson and Dr. S.J. Bauer, Sandia National Laboratories, which were very informative. Sandia National Laboratories is a multi-program laboratory managed and operated by Sandia Corporation, a wholly owned subsidiary of Lockheed Martin Corporation, for the U.S. Department of Energy's National Nuclear Security Administration under contract DE-AC04-94AL85000.

References

1. Neilsen, M.K., Krieg, R.D., Schreyer, H.L.: A constitutive theory for rigid polyurethane foam. Polym. Eng. Sci. **35**(5), 387–94 (1995)
2. Deshpande, V.S., Fleck, N.A.: Isotropic constitutive models for metallic foams. J. Mech. Phys. Solids **48**, 1253–83 (2000)
3. Deshpande, V.S., Fleck, N.A.: Multi-axial yield behaviour of polymer foams. Acta Mater. **49**, 1859–1866 (2001)
4. Gibson, L.J., Ashby, M.F.: Cellular Solids—Structural and Properties. Pergamon, New York, NY (1988)
5. Puso, M.A., Govindjee, S.: A phenomenological constitutive model for rigid polymeric foam. In: Proceedings of the ASME Mechanical Congress and Exposition, MD-Vol. 68/AMD-Vol. 215, Mechanics of Plastics and Plastic Composites, ASME, pp. 159–176, 1995
6. Zhang, J., Kikuchi, N., Li, V., Yee, A., Nusholtz, G.: Constitutive modeling of polymeric foam material subjected to dynamic crash loading. Int. J. Impact Eng. **21**(5), 369–386 (1998)
7. Sierra Solid Mechanics Team, 'Sierra/Solid Mechanics 4.22 User's Guide,' SAND2011-7597, Sandia National Laboratories, 2011
8. Johnson, G.C., Bammann, D.J.: A discussion of stress rates in finite deformation problems. Int. J. Solids Struct. **20**(8), 725–737 (1984)
9. Flanagan, D.P., Taylor, L.M.: An accurate numerical algorithm for stress integration with finite rotations. Comput. Methods Appl. Mech. Eng. **62**, 305–320 (1987)

Chapter 12
Mechanical Behavior Characterization of Polyurethane Used in Bend Stiffener

G.L. Oliveira, A.G. Ariza, M. Caire, M.F. Costa, and M.A. Vaz

Abstract Bend stiffeners are structures employed in the offshore oil and gas industry designed to restrict curvature of flexible lines and umbilical cables connected to floating production units. They are conically shaped and fabricated in polyurethane (PU), an elastomeric material whose properties can be largely modified by the multiplicity of resins available in the market. Therefore, detailed polyurethane characterization is important to define the properties of the materials as well as to evaluate its stability in marine environment. In this work, a bend stiffener grade polyurethane was exposed to synthetic sea water and to the weather for 6 months. The material was characterized by infrared spectroscopy, tensile and stress relaxation tests. It was found that the mechanical characteristics are affected by sea water with a drop in tensile strength when material is tested on the same day that the final ageing time is completed. Relaxation and stress-strain curve fittings were performed using hyperviscoelastic and hyperelastic models, respectively. Among several hyperelastic models used, Alexander, Polynomial and Yamashita-Kawabata were found to successfully describe the experimental behavior. The hyperviscoelasticity model was compared with hyperelastic models considering the same strain rate.

Keywords Polyurethane • Ageing • FTIR • Hyperelastic and hyperviscoelasticity

12.1 Introduction

Polyurethane elastomers are very versatile polymeric materials which may exhibit excellent properties, such as high tensile strength and high elongation, when monomers used in their synthesis are chosen correctly. Once this step is successful, these materials become useful for several engineering applications among one of the most important is in the offshore industry where they are used as bend stiffeners.

A bend stiffener is an ancillary conical shaped component that locally supports the pipe to limit bending stresses and curvature of the pipe to acceptance levels [1]. This device is normally made of polyether polyurethane and is used to ensure a smooth stiffness transition between flexible riser and floating platform and thus to avoid riser damage due to the high cyclic loading promoted by waves and platform motions [2].

As in the offshore gas and oil industry the exploration has been performed at increasingly hostile environments and since bend stiffeners are exposed to sea water and weather, this work has as purpose to assess the effect of these environments in the chemical structure of a polyurethane elastomer and on its mechanical behavior by tensile and stress relaxation tests. Furthermore, hyperelastic and hyperviscoelastic models were used to suitably fit the experimental data found by the mechanical tests.

G.L. Oliveira • M.F. Costa
Metallurgical and Materials Engineering Program, Federal University of Rio de Janeiro, Rio de Janeiro, Brazil

A.G. Ariza • M.A. Vaz (✉)
Ocean Engineering Department, Federal University of Rio de Janeiro, Rio de Janeiro, Brazil
e-mail: murilo@oceanica.ufrj.br

M. Caire
Sintef Brasil, Rio de Janeiro, Brazil

C. Ralph et al. (eds.), *Mechanics of Composite and Multi-functional Materials, Volume 7*,
Conference Proceedings of the Society for Experimental Mechanics Series, DOI 10.1007/978-3-319-21762-8_12

12.2 Materials and Experimental Procedure

The materials used in this work were polyurethane of the same grade as employed for bend stiffener fabrication and artificial sea water synthesized according to ASTM D1141-98 [3] for material ageing. The samples were immersed in artificial sea water at 60 °C. Besides, samples were fixed on a stainless steel support and kept exposed to the weathering for 6 months.

In order to verify possible changes in the chemical structure of polyurethane elastomer occasioned by both environments, artificial sea water or weather, Fourier Transform Infrared Spectrometry (FTIR) was conducted at an Espectro 100 spectrometer with resolution of 4 cm^{-1} and 32 scans, in the range of 4000–550 cm^{-1}.

Tensile behavior of artificial sea water and weather aged and non-aged PU specimens was evaluated using a universal testing machine (Instron 5582) according to ASTM 412-06a [4]. At least five specimens of each material were tested at crosshead speeds of 50 mm min^{-1} at room temperature.

Tensile stress relaxation tests were also performed on the as-received sample and samples submitted to both aging protocols. Samples were stored under low temperature for at least 3 months prior the experimental tests. The relaxation time was kept at 480 min at room temperature using a universal testing machine (Instron 5567). At least three specimens were used for each strain value of 0.5% and 30 % and reached at a constant strain rate of 0.00625 s^{-1} and 0.075 s^{-1}, respectively. The strains were chosen in order to keep the loading time approximately constant.

12.2.1 Theoretical Background

Polymeric materials such as elastomers show nonlinear elastic behavior on stress-strain tests. These materials have hyperelastic mechanical behavior and can bear very high strain levels being able to return to their original configuration featuring a reversible behavior. A main relationship between stress-strain can be expressed using a Piola-Kirchhoff second tensor (S), strain energy density function (W) and Green's strain tensor (E), which are correlated by Eq. (12.1) [5],

$$\mathrm{S} = \frac{\partial W}{\partial \mathrm{E}} \tag{12.1}$$

The Cauchy stress for a three-dimensional case assuming isotropic and incompressible material and negligible influence of the third invariant is given by:

$$\sigma = -pI + 2\left(\frac{\partial W}{\partial I_1} + I_1 \frac{\partial W}{\partial I_2}\right)\mathrm{B} - 2\frac{\partial W}{\partial I_2}\mathrm{BB} \tag{12.2}$$

Where B is the Cauchy-Green strain tensor, I is the Identity matrix, I_1, I_2 are the first and second invariants of the tensor B, p is the hydrostatic pressure.

The relationship between the tensor B and strain gradient tensor (F) is defined by $B=FF^T$.

Where $F = \dfrac{\partial x}{\partial X}$.

The function W represents the stored energy due to the work necessary to deform the material and depends on the strain invariants.

Experimental tests such as tensile, compression, shear are treated as homogeneous strain problems. Thus, elongations are defined by:

$$\lambda_i = \frac{x_i}{X_i} \tag{12.3}$$

Where X_i is the position vector of the particle o in the initial configuration and x_i is position vector of the particle o' in the final configuration.

The invariants B can be represented using the main elongations:

$$I_1 = \lambda_1^2 + \lambda_2^2 + \lambda_3^2; \quad I_2 = \lambda_1^{-2} + \lambda_2^{-2} + \lambda_3^{-2} \tag{12.4}$$

Considering incompressible material, I_3=1, then $\lambda_3=(\lambda_1\lambda_2)^{-1}$.

Substituting the Eqs. (12.4) and (12.2) and assuming a constant hydrostatic pressure (p_0), stresses at the main directions are defined by:

$$\sigma_{11} = -p_0 + 2\lambda_1^2 \frac{\partial W}{\partial I_1} - \frac{2}{\lambda_1^2}\frac{\partial W}{\partial I_2}; \quad \sigma_{22} = -p_0 + 2\lambda_2^2 \frac{\partial W}{\partial I_1} - \frac{2}{\lambda_2^2}\frac{\partial W}{\partial I_2} \quad \sigma_{33} = -p_0 + \frac{2}{\lambda_1^2\lambda_2^2}\frac{\partial W}{\partial I_1} - \lambda_1^2\lambda_2^2 \frac{\partial W}{\partial I_2} \tag{12.5}$$

Tensile or compression tests are considered uniaxial tests. Assuming test with thin sheets, the elongations are expressed by:

$$\lambda_1 = \lambda; \quad \lambda_2 = \lambda_3 = \lambda^{-0.5} \tag{12.6}$$

Substituting Eq. (12.6) in Eq. (12.4) strain invariants are obtained:

$$I_1 = \lambda^2 + 2\lambda^{-1}; \quad I_2 = 2\lambda + \lambda^{-2} \tag{12.7}$$

The stresses σ_{22} σ_{33} are considered zero at tensile and compression tests, however, stress σ_{11} is represented by developing Eq. (12.5):

$$\sigma = \sigma_{11} = 2\left(\lambda^2 - \frac{1}{\lambda}\right)\left(\frac{\partial W}{\partial I_1} + \frac{1}{\lambda}\frac{\partial W}{\partial I_2}\right) \tag{12.8}$$

It should be noted that Eq. (12.8) is valid for tensile and compression tests.

12.2.2 Alexander Model

In the model developed by Alexander [6], stored energy is obtained by combination between Rivlin [7] and Hart-Smith [8] models. Thereby, deformation energy is defined as:

$$W = c_1 \int e^{c_2(I_1-3)^2} dI_1 + c_3 \ln\left(\frac{I_2 - 3 + \gamma}{\gamma}\right) + c_4(I_2 - 3) \tag{12.9}$$

Where c_1, c_2, c_3, c_4 and γ are constitutive constants of the material.
The uniaxial stress is defined substituting Eq. (12.9) in Eq. (12.8). So,

$$\sigma = 2\left(\lambda^2 - \frac{1}{\lambda}\right)\left[c_1 e^{c_2(I_1-3)^2} + \frac{1}{\lambda}\left(\frac{c_3\gamma}{I_2 - 3 + \gamma} + c_4\right)\right] \tag{12.10}$$

12.2.3 Yamashita-Kawabata Model

Yamashita-Kawabata model [9] is used to describe mechanical properties of rubber from industrial use. The equations were determined based on biaxial tests and W is defined by:

$$W = c_1(I_1 - 3) + c_2(I_2 - 3) + \frac{c_3}{n+1}(I_1 - 3)^{n+1} \tag{12.11}$$

Where, c_1, c_2, c_3 and n are constants of the material determined by experimental tests.
The stress σ_{11} is obtained substituting Eqs. (12.11) and (12.8) has:

$$\sigma = 2\left(\lambda^2 - \frac{1}{\lambda}\right)\left[c_1 + c_3(I_1 - 3)^n + \frac{c_2}{\lambda}\right] \tag{12.12}$$

12.2.4 Polynomial Model

The polynomial type function of the deformation energy W was elaborated through observation of existent models based on incomplete polynomials. This model employs first and second strain invariants with Eq. (12.13):

$$W = \sum_{i+j=1}^{N} c_{ij}(I_1 - 3)^i (I_2 - 3)^j \tag{12.13}$$

Where c_{ij} is a material's parameter.

Several hyperelastic models are simplifications of the polynomial model and a correct choice of the coefficients are associated to the described models in the literature. Finite elements' software uses this equation to describe an energy function.

When N = 3, Eq. (12.13) is simplified to:

$$W = c_{10}(I_1 - 3) + c_{01}(I_2 - 3) + c_{11}(I_1 - 3)(I_2 - 3) + c_{20}(I_1 - 3)^2 + c_{02}(I_2 - 3)^2 + c_{21}(I_1 - 3)^2(I_2 - 3) + c_{12}(I_1 - 3)(I_2 - 3)^2 \tag{12.14}$$

Substituting Eq. (12.14) in Eq. (12.8) and accurately rearranging it, the uniaxial stress is defined by:

$$\sigma = 2\left(\lambda^2 - \frac{1}{\lambda}\right)\left[a + \frac{b}{\lambda}\right] \tag{12.15}$$

Where:

$$a = c_{10} + c_{11}(I_2 - 3) + 2c_{20}(I_1 - 3) + 2c_{21}(I_1 - 3)(I_2 - 3) + c_{12}(I_2 - 3)^2$$
$$b = c_{01} + c_{11}(I_1 - 3) + 2c_{02}(I_2 - 3) + c_{21}(I_1 - 3)^2 + 2c_{12}(I_1 - 3)(I_2 - 3)$$

12.2.5 Hyperviscoelasticity

The hyperviscoelasticity uses hyperelasticity concept together with viscoelastic theory and this was used to fit stress relaxation curves. Figure 12.1 shows a schematic combination of elements where a hyperviscoelastic spring in parallel with a viscoelastic element [9, 10], for instance, Maxwell's element, represents the hyperviscoelasticity.

Total stress is represented by contribution of the elements,

$$\sigma = \sigma_{HE} + \sigma_{VE} \tag{12.16}$$

Where σ_{HE} and σ_{VE} are respectively the instant hyperelastic and viscoelastic stresses.

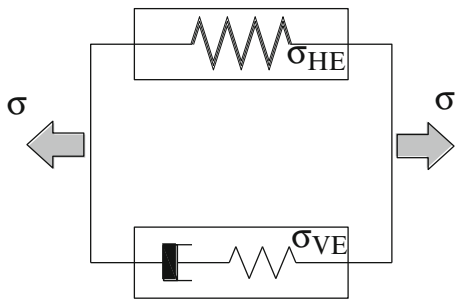

Fig. 12.1 Scheme of a hyperviscoelastic mechanical model

$$\sigma_{VE} = -p_{VE}\mathrm{I} + F \underset{s=-\infty}{\overset{t}{\Omega}} [\mathrm{C}(s)]F^T \tag{12.17}$$

Where p_{VE} is the hydrostatic pressure, Ω is a functional which describes effects of the strain history and F is the strain gradient which is time dependent.

$$\sigma_{11} = 2\left(\lambda^2 - \frac{1}{\lambda}\right)\left(\frac{\partial W_{HE}}{\partial I_1} + \frac{1}{\lambda}\frac{\partial W_{HE}}{\partial I_2}\right) + 2\left(\lambda^2 - \frac{1}{\lambda}\right)\int_{-\infty}^{t} \frac{\partial \mathrm{k}}{\partial I_1} ds + \left(4\lambda^2 - \frac{2}{\lambda}\right)\int_{-\infty}^{t} \frac{\partial \mathrm{k}}{\partial I_2}\lambda^{-1} ds - \frac{2}{\lambda}\int_{-\infty}^{t} \frac{\partial \mathrm{k}}{\partial I_2}\lambda^2 ds \tag{12.18}$$

Where W_{HE} is hyperelastic strain energy.

$$\frac{\partial \mathrm{k}}{\partial \mathrm{E}} = \frac{\partial W_{VE}}{\partial \mathrm{E}}\dot{\mathrm{E}}m(t-s) \tag{12.19}$$

Where W_{VE} is hyperviscoelastic strain energy, $m(t-s) = \sum m_i e^{\frac{-(t-s)}{\tau_i}}$ and $\sum m_i$=1.

12.3 Results and Discussion

12.3.1 FTIR Analysis

Infrared spectra of the artificial sea water and weather aged and non-aged polyurethane samples are showed in Fig. 12.2. It is possible to observe the characteristic urethane groups at 1526, 1693 and 3279 cm^{-1}, respectively [11, 12]. Other bands noted at 2940 and 2855 cm^{-1} are attributed to the asymmetric and symmetric stretching of CH_2 groups [11]. Furthermore, it is verified that this material presents a band around 1103 cm^{-1} related to the asymmetric stretching correspondent to the soft segment polyether polyol [13]. Nevertheless, there were no significant changes in the chemical structure of the material when

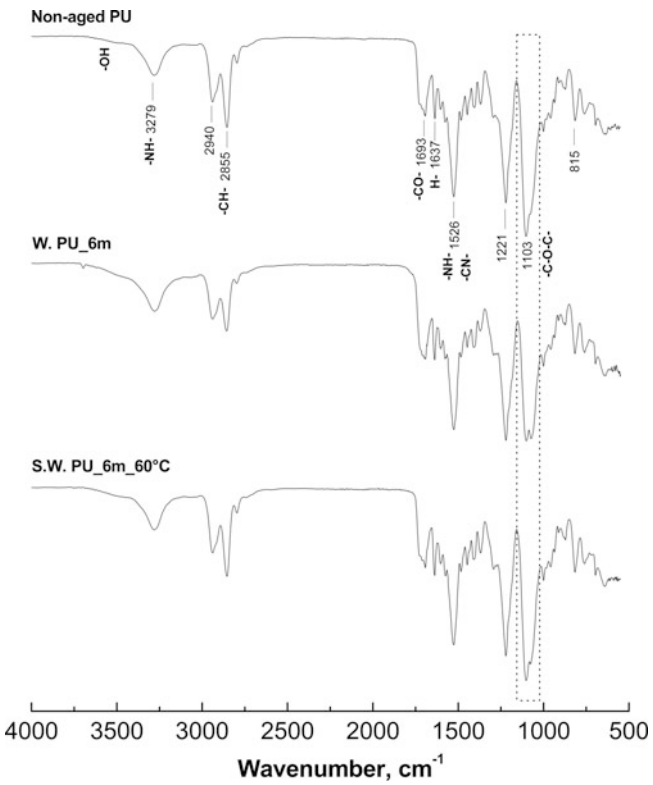

Fig. 12.2 FTIR spectra of the sea water and weather aged PU samples for 6 months

these were exposed to artificial sea water and to the weather during 6 months. Differently of the sea water aged and neat PUs spectra, a slight alteration at approximately 1103 cm^{-1} can be observed in the structure of weather aged PU where it is verified a decrease of the intensity of the peak indicating break of ether bonds. Moreover, it is also possible to note a second peak at 1072 cm^{-1} that also corresponds to the ether group and it becomes more visible with intensity reduction of the main peak at 1103 cm^{-1}. At the wavenumber range of 2850–2950 cm^{-1} it is observed peaks associated to CH_2 groups. It is also showed an intensity decrease which may be attributed to conformational changes in the chemical structure of the elastomer.

12.3.2 Tensile Test

The mechanical behavior of the artificial sea water and weather aged and as-received polyurethane samples were evaluated at 23 °C and the results can be observed in Fig. 12.3a. For sea water aged PU samples two different behaviors were found: one for the material tested on the same day they were removed from the reactor used for immersion in the fluid and other when the specimens were stored in a refrigerator for at least 3 months. All tests were carried out up to 200% since higher elongations led to slippery of the samples from grips.

As can be verified, the tensile curve of the weather aged samples is shifted to higher stress values compared to as-received material indicating an increase on the material's stiffness occasioned by ageing. Maybe this alteration can be justified by oxidation process which occasions chain scissions at short ageing time, but at high ageing time such as 6 months, molecular recombination or additional crosslinking may be formed [14]. On the other hand, sea water aged PU sample evaluated at the same day that they were removed from the ageing environment showed a drastic shift of the curve towards low resistance values. Meanwhile, when samples were kept at low temperature during a time period as previously stated, a partial recover of the tensile strength is obtained and for strains up to 100%, the behavior is closer to that one observed for the as-received samples. Since it has not been observed changes in the chemical structure of sea water aged PU as showed by FTIR analysis, these property changes are associated to physical alterations in the structure. It has been observed by other authors [15] that a plasticizer effect occasioned by fluid diffusion that causes decrease in the intermolecular forces and, consequently, lower tensile strength is observed for PU. Once the sample is removed from the immersion environment, the small water molecules will diffuse out of the sample. Since no chemical reaction is observed, the materials tend to recover their initial properties.

To describe the tensile behavior several models available in literature were used. Alexander, Polynomial and Yamashita-Kawabata models were found to best adjust the experimental data using least square method with support of the Mathcad Software. These data contributed for determining coefficients of the materials which were presented in Tables 12.1, 12.2 and 12.3, respectively. The determination of these coefficients presents advantages, such as their use at computational software and for analytic studies of structures which involves PU elastomers.

In Fig. 12.3a it is possible to observe that when a maximum strain of 200 % was considered, Alexander and Polynomial models perfectly adjusted the experimental data of the aged and non-aged materials. On the other hand, Yamashita-Kawabata

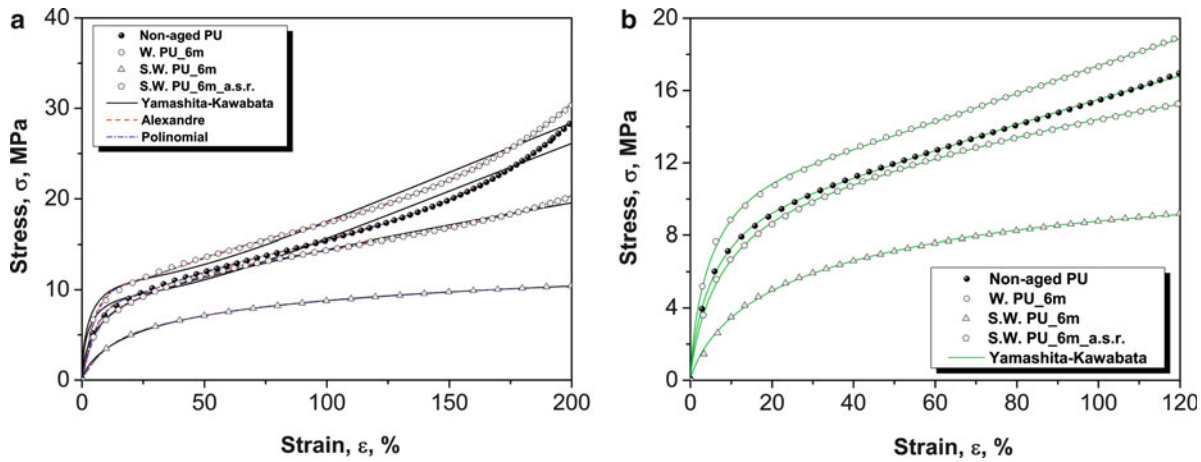

Fig. 12.3 Stress versus strain curves of the sea water and weather aged and non-aged PU samples during 6 months for strains of 200 % (**a**) and 120 % (**b**). S.W. PU_6m_a.s.r. (after stored in refrigerator)

Table 12.1 Coefficients of the Alexander model on different conditions

Samples	c_1 (MPa)	c_2 (MPa)	c_3 (MPa)	c_4 (MPa)	γ
Non-aged PU	1.93	0.013	15.77	4.387	0.034
S.W. PU_6m	0.535	-1.1×10^{-4}	3.652	3.742	0.074
S.W.PU_6m_a.s.r.	0.9835	9.73×10^{-3}	13.3227	5.8904	0.029
W. PU_6m	2.212	0.011	21.616	4.828	0.03

a.s.r. after stored in refrigerator

Table 12.2 Coefficients of Yamashita-Kawabata model on different conditions

Samples	c_1 (MPa)	c_2 (MPa)	c_3 (MPa)	n + 1
Non-aged PU	−34.81	−18.34	50.77	0.93
S.W. PU_6m	−129.64	−4.13	135.09	0.99
S.W.PU_6m_a.s.r.	−370.84	−18.93	386.94	0.99
W. PU_6m	−24.46	−20.86	42.54	0.91

Table 12.3 Coefficients of the Polynomial model on different conditions

Samples	c_{10} (MPa)	c_{01} (MPa)	c_{11} (MPa)	c_{20} (MPa)	c_{02} (MPa)	c_{21} (MPa)	c_{12} (MPa)
Non-aged PU	−149.98	175.16	984.53	−583.31	−294.63	2.14	132.46
S.W. PU_6m	−26.65	35.57	73.37	−45.74	−12.6	0.06	10.98
S.W.PU_6m_a.s.r.	−125.5	147.68	807.67	−479.94	−238.46	1.62	109.52
W. PU_6m	−201.17	233.05	1314.7	−780.22	−390.94	2.72	177.72

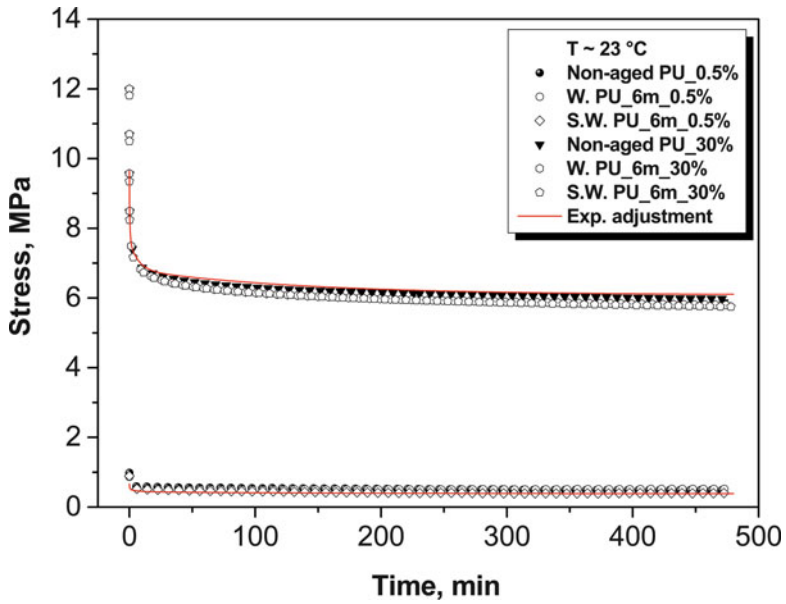

Fig. 12.4 Stress relaxation curves of the weather and sea water aged and non-aged samples during ageing time period of 6 months

model did not well describe the experimental behavior for elongations above 100%. However, when this model is used at moderate strain range, up to 120%, as shown in Fig. 12.3b, a very good agreement between experimental and theoretical data is observed.

12.3.3 Stress Relaxation Test

Stress relaxation behavior of polymers is of paramount importance to understand as these materials relax with time at constant strain. In order to investigate viscoelastic behavior of these materials and to assess ageing effects, two strain levels of 0.5 and 30 % were chosen arbitrarily. In Fig. 12.4 it is shown the stress relaxation versus time curves for aged and non-

Table 12.4 Coefficients of the Alexander models

	c_1 (MPa)	c_2 (MPa)	c_3 (MPa)	c_4 (MPa)	γ
W_{HE}	0.362	−285.953	8.576	5.015	0.013
W_{VE}	−0.682	−1957.528	5.527	1.338	0.02

Table 12.5 Coefficients of the Prony series

τ_i (s)	m_i (Pa/Pa)
3.4	0.546
31.7	0.212
410.6	0.129
8147.0	0.114

aged samples. As it can be seen, all materials present non-linear behavior and differently as observed on the tensile properties both weather and sea water exposure did not affect the relaxation response. Such fact can be corroborated by found results at the FTIR analysis. Furthermore, it is verified that sea water aged PU presented viscoelastic behavior as similar as to the one of the as-received PU. It is an indicative that storing of the samples in the refrigerator may minimize plasticizer fluid effect and, consequently, the differences between mechanical properties of sea water aged and non-aged materials.

The non aged materials were curve fitted using a hyperviscoelasticity model, a least square method was employed and a Mathcad software was developed. It was observed that this model describes well the experimental data as highlighted by Drapaca et al. [16]. The model coefficients are shown in Tables 12.4 and 12.5.

12.4 Conclusions

Though at offshore applications polyurethane bend stiffener is exposed to the weather during its use, when this elastomer was naturally aged on this environment no significant change was verified in the chemical structure of this material during ageing period of 6 months. Artificial sea water PU showed ageing susceptibility at 60 °C when it was submitted to tensile testing on the same day in which samples were removed from the reactor. Therefore, when samples were stored in the refrigerator, fluid plasticizer effect becomes less pronounced on the tensile strength.

Among several hyperelastic models found in literature and used in this work, Alexander and Polynomial models successfully described the experimental behavior in a full strain scale while Yamashita-Kawabata model was excellent for moderate strain scale. When nonlinear viscoelastic behavior of non-aged PU was assessed, it was noted that the hyperviscoelastic model rightly fitted experimental data within studied strain levels.

Acknowledgments The authors would like to thank to Finep and CNPq for financial support.

References

1. API: Specification 17J, specification for unbonded flexible pipe. American Petroleum Institute (2008)
2. Bazán, F.A.V., Lima, E.C.P., Siqueira, M.Q., Siqueira, E.F.N., Lemos, C.A.D.: A methodology for structural analysis and optimization of riser connection joints. Appl. Ocean Res. **33**, 344–365 (2011)
3. ASTM D1141: Standard practice for the preparation of substitute ocean water (1998)
4. ASTM D412: Standard test methods for vulcanized rubber and thermoplastic elastomers-tension (2006)
5. Patra, K., Sahu, R.K.: A visco-hyperelastic approach to modelling rate-dependent large deformation of a dielectric acrylic elastomer. Int. J. Mech. Mater. Des. **11**, 79–90 (2015)
6. Alexander, H.: A constitutive relaxation for rubber-like materials. Int. J. Eng. Sci. **6**, 549–563 (1968)
7. Rivlin, R.S., Saunders, D.W.: Large elastic deformations of isotropic materials VII. Experiments on the deformation of rubber. Phil. Trans. Roy. Soc Lond. A **243**, 251–288 (1951)
8. Hart-Smith, L.J.: Elasticity parameters for finite deformations of rubber-like materials. Z. Angew. Math. Phys. (ZAMP) **17**, 608–626 (1966)
9. Yamashita, Y., Kawabata, S.: Approximated form of the strain energy-density function of carbon-black filled rubbers for industrial applications. J. Soc. Rubber Ind. **65**(9), 517–528 (1992)

10. Anani, Y., Alizadeh, Y.: Visco-hyperelastic constitutive law for modeling of foam's behavior. Mater. Des. **32**, 2940–2948 (2011)
11. Silverstein, R.M., Webster, F.X., Kiemle, D.J.: Spectrometric Identification of Organic Compounds, 7th edn. Wiley, Hoboken, NJ. (2005)
12. Oprea, S.: Degradation of crosslinked poly (ester-urethanes) elastomers in distilled water: influence of hard segment. J. Appl. Polymer Sci. **124**, 1059–1066 (2012)
13. Bajsic, E.G., Rek, V., Sendijarevic, A., Sendijarevic, V., Frish, K.C.: The effect of different molecular weight of soft segments in polyurethanes on photooxidative stability. Polymer Degrad. Stabil. **52**, 223–233 (1996)
14. Boubakri, A., Guermazi, N., Elleuch, K., Ayedi, H.F.: Study of UV-aging of thermoplastic polyurethane material. Mat. Sc. Eng. A, **527**, 1649–1654 (2010.A)
15. Davies, P., Evrard, G.: Accelerated ageing of polyurethanes for marine applications. Polymer Degrad. Stabil. **92**, 1455–1464 (2007)
16. Drapaca, C.S., Sivaloganathan, S., Tenti, G.: Nonlinear constitutive laws in viscoelasticity. Math. Mech. Solid. **12**, 475–501 (2007)

Chapter 13
Effect of Pressure on Damping Properties of Granular Polymeric Materials

M. Bek, A. Oseli, I. Saprunov, N. Holeček, B.S. von Bernstorff, and I. Emri

Abstract Reduction of noise and vibration coming from the rail transport activities is an important objective of the environmental policy of the European Union, due to its impact on human and animal health. It has been identified that one of the major sources of noise and vibration in rail transport is from the interaction between the wheel and the rail, the so called rolling noise. One way to mitigate this noise is to attach polymeric damping elements to the rail. By modifying bulk properties of polymeric material we can modify its damping characteristics. In this chapter we demonstrated on the example of thermoplastic polyurethane (TPU) the effect of inherent hydrostatic pressure on the time- and frequency-dependent behavior of polymers. For the selected TPU material we found that increasing hydrostatic pressure from 1 to 2000 bar shifts frequency at which material exhibits its maximal damping properties ($G''max$) from 37 kHz to 235 Hz. It was also found that change of pressure changes values of storage modulus G' up to 3.5 times (depending on the frequency), while the values of loss modulus G'' are changed up to 5.5 times. Using this property of polymeric materials we developed new generation damping elements composed of glass fiber textile tubes filled with pressurized granulated polymeric materials. Granular material with properly selected multimodal particle size distribution acts as pressurizing agent. At the same time the generated hydrostatic pressure changes frequency dependence of the granular material bulk properties. By modifying material bulk properties we can modify damping characteristics of the new generation damping elements. Applying these damping elements to the rail can substantially reduce vibration amplitudes as well as sound pressure levels, thus reducing exposure of human and animal to noise and vibration.

Keywords Thermoplastic polyurethane • Dissipative granular materials • Effect of pressure • Viscoelasticity • Damping elements

13.1 Introduction

Sustainable economic development is one of the main objectives of the European Union (EU), which requires economic growth without additional environmental influences. Reductions in the emission of greenhouse gases, which are responsible for global warming and associated to climate change are nowadays a major concern. Around one quarter of all greenhouse gas emissions comes from transport activity [1–3] of which road transport takes the biggest share [4]. For this reason, the

M. Bek (✉)
Gorenje gospodinjski aparati, d.d., Velenje, Slovenia

Center for Experimental Mechanics, Faculty of Mechanical Engineering, University of Ljubljana, Pot za Brdom 104, Ljubljana, Slovenia
e-mail: marko.bek@fs.uni-lj.si

A. Oseli • I. Emri
Center for Experimental Mechanics, Faculty of Mechanical Engineering, University of Ljubljana, Pot za Brdom 104, Ljubljana, Slovenia

Institute for Sustainable Innovative Technologies, Pot za Brdom 104, Ljubljana, Slovenia

I. Saprunov
Center for Experimental Mechanics, Faculty of Mechanical Engineering, University of Ljubljana, Pot za Brdom 104, Ljubljana, Slovenia

N. Holeček
Gorenje gospodinjski aparati, d.d., Velenje, Slovenia

B.S. von Bernstorff
BASF Aktiengesellschaft, Ludwigshafen, Germany

C. Ralph et al. (eds.), *Mechanics of Composite and Multi-functional Materials, Volume 7*,
Conference Proceedings of the Society for Experimental Mechanics Series, DOI 10.1007/978-3-319-21762-8_13

goal of environmental policies is to minimize the current difference between road and railroad transport. However, problem of noise nuisance coming from railroads on population living near rail lines as well as impact on wildlife [5] remains.

Minimizing noise levels can be achieved by implementing different noise control measures: increased damping, reduction of excitations, acoustic shielding or absorption and vibration insulation. In order for noise-control measures to be successful, the dominant source of noise should be identified. It has been found that in many situations rolling noise is the dominant source of railway noise and is caused by wheel and rail vibrations induced at wheel/rail contact. Wheel and rail roughness generates movements of them relative to each other. This generates vibrations which are transmitted into both structures and from vibrating structures sound is radiated into the air [6].

Several reduction techniques for controlling rolling noise exist, among them are: grinding of rail surfaces, optimizing shape of rail wheels, replacing iron breaks with composite brakes, optimizing rail pads, sound barriers and tuned absorber systems. Currently soft rail pads are being used despite the fact that stiffer ones contribute to the reduction of rail noise. Soft rail pads increase decay rate of rails and it is necessary to apply damping treatments since reducing decay rate is important. For this reason tuned absorber systems were introduced, where cost benefit analysis performed in STAIRRS project showed that for moderate costs tuned absorber systems gives good results [7], leading to the conclusion that tuned absorber systems can be a very effective way in reducing the noise radiated by the rail.

As it will be shown on example of thermoplastic polyurethane (TPU) the inherent (hydrostatic) pressure changes frequency dependence of polymeric materials. Hence, by proper selection of damping material and a pressure to which material is exposed one can match the frequency range of its maximum damping properties with the resonance frequency of the vibrating structure (rail). In this way we fully utilize damping characteristics of the selected material and maximize the energy absorption properties of the damper.

Using this unique property of polymeric materials enabled us to design and build ultimate adaptive damping elements. For doing this we have additionally utilized patented finding [8] that viscoelastic granular materials with properly selected multimodal size-distribution exhibit fluid-like behavior, while maintaining behavior of the bulk material from which they were made. Hence, they may be used as "pressurizing media" to impose inherent hydrostatic pressure on itself and consequently change its own damping properties.

13.2 Materials and Methods

Within the framework of this chapter we show on the example of thermoplastic polyurethane (TPU) that by proper selection of the type of the material and proper selection of the hydrostatic pressure one can shift the maximum of the material damping properties to the frequency range of our interest. By doing this energy absorption properties of a damper could be increased several orders of magnitude. In the case of soft materials this would mean that stiffness of material is increased and at the same time damping capabilities of polymeric material is fully utilized.

We demonstrate that via storage modulus, $G'(\omega)$, and loss modulus $G''(\omega)$ measured at different pressures. Material functions in frequency domain were obtained through the process of interconversion from the shear relaxation modulus, G(t,T,P) measured on a specially designed apparatus known as CEM Measuring System—CMS [9, 10].

13.2.1 Shear Relaxation Measurements

The CMS apparatus [9–11] was developed to study the combined effects of temperature and hydrostatic pressure on behavior of polymers. The system can measure the volume and the shear relaxation moduli of solid polymer specimens simultaneously subjected to temperatures from −40 to +120 °C and pressures from atmospheric to 500 MPa [9, 10]. CMS apparatus consists of four main parts: hydraulic system, thermal system, data acquisition system and measuring inserts.

Hydraulic system includes hand pump for pressurizing silicone fluid to a pressure vessel. In thermal system, a circulator and thermal bath are used to regulate temperature of specimen. In order to process and record the signals from measuring inserts, i.e., relaxometer and dilatometer, data acquisition system is used which combines a carrier amplifier and computer.

13.2.2 Measuring Principle

CEM Measuring System measures four physical quantities: temperature, T(t), pressure, P(t), specimen length, L(t,T,P), and the decaying torque, M(t,T,P), resulting from the initially applied torsional deformation, θ_0, on the sample. Using these quantities measured at constant or varying temperature and pressure, other material functions can be calculated [9, 10]. In this particular case shear relaxation modulus is of our interest and is determined by measuring the decaying moment of a specimen exposed to selected constant temperature and pressure boundary conditions. The relaxation modulus curve usually extends over many decades of time, which are practically not possible to characterize at constant temperature or pressure. Keeping this in mind, experiments are performed within a certain time-interval—experimental window. A set of different shear relaxation modulus segments is obtained when experiments are carried out at different temperatures, and/or pressures. The segments are then shifted along the logarithmic time scale to produce master curves using the time-temperature t-T and time-pressure t-P superposition principles [12]. The final master curves represent the long-term behavior of the material, at the chosen reference conditions. The mastercurves of storage $G'(\omega)$ and loss modulus $G''(\omega)$ in frequency domain were then obtained from G(t, T, P) through the interconversion [11, 13].

13.3 Results and Discussion

For clarity reasons the results on storage $G'(\omega)$ and loss modulus $G''(\omega)$ are shown for two pressures, i.e., 1 bar and 2000 bar, only. The full symbols represent measurements done at lower pressure (P = 1 bar), whereas the empty symbols represent measurements done at higher pressure (P = 2000 bar). The results for storage modulus G′ are shown in Fig. 13.1 and for loss modulus G″ in Fig. 13.2.

As previously mentioned we utilize this property of polymers in construction of damping elements for railroad applications. Since the noise and vibration causing the most discomfort is located in frequency range between 1 and 1000 Hz, we will examine the effect of pressure on stiffness and damping properties of TPU within this frequency window.

From Fig. 13.3 we may clearly see that within the region of our interest (1–1000 Hz), changes of inherent (hydrostatic) pressure of TPU from 1 to 2000 bar cause material properties change for several orders of magnitude. Specifically, at frequency 1 Hz and pressure 1 bar the storage modulus (representing stiffness) is $G'(\omega = 1\ \text{Hz}, P = 1\ \text{bar}) = 2.99$ MPa, whereas at pressure 2000 bar the storage modulus increases to $G'(\omega = 1\ \text{Hz}, P = 2000\ \text{bar}) = 4.07$ MPa. Hence, material becomes 1.4 times stiffer. At the same frequency of 1 Hz the loss modulus (representing material damping characteristics) at pressure 1 bar is $G''(\omega = 1\ \text{Hz}, P = 1\ \text{bar}) = 0.29$ MPa, whereas at pressure 2000 bar it rises to $G''(\omega = 1\ \text{Hz}, P = 2000\ \text{bar}) = 0.92$ MPa. This means that at elevated pressure the materials ability to dissipate energy increases 3.15 times.

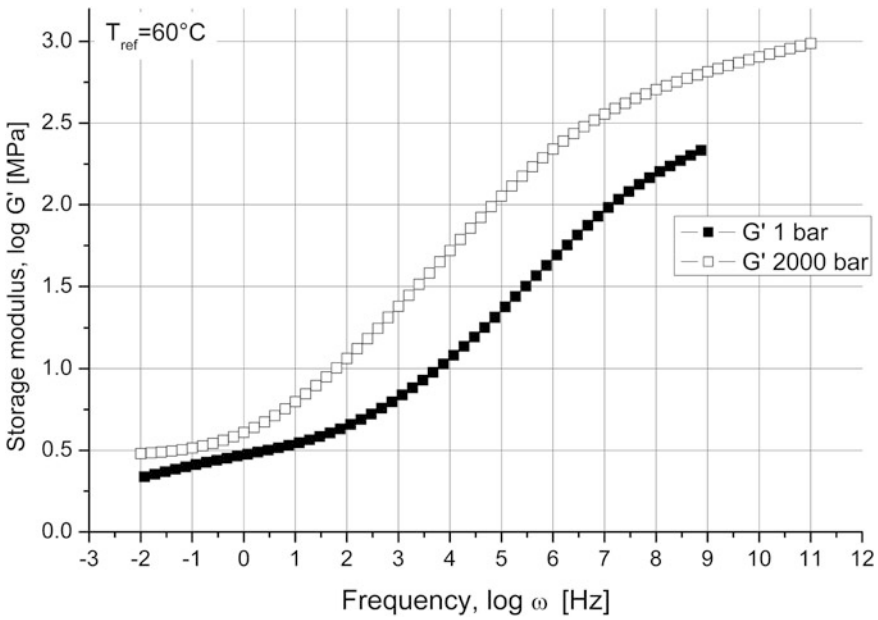

Fig. 13.1 Storage G′ at P = 1 bar and P = 2000 bar

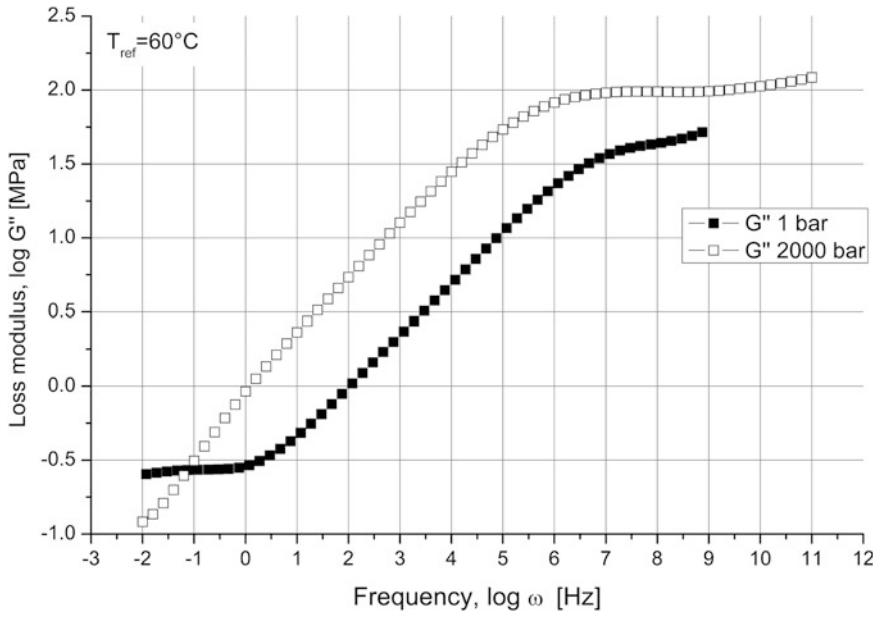

Fig. 13.2 Loss modulus G″ at P = 1 bar and P = 2000 bar

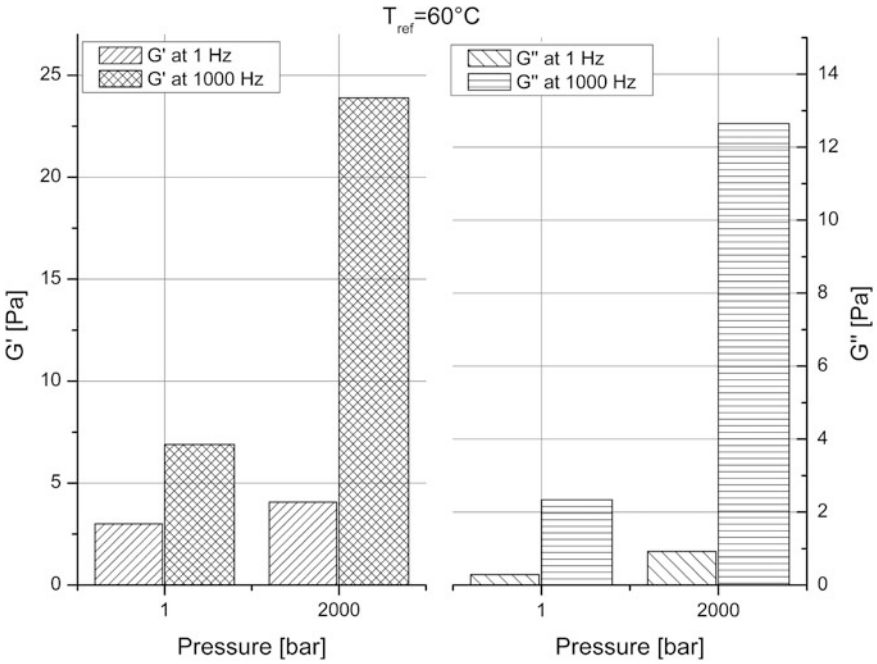

Fig. 13.3 Storage G′ and loss modulus G″ at P = 1 bar and P = 2000 bar

For the higher end of the frequency window, i.e., ω = 1000 Hz, we observe analogous trends. At 1 bar the storage modulus is G′(ω = 100 Hz, P = 1 bar) = 6.89 MPa, whereas at the pressure P = 2000 bar the storage modulus becomes G′(ω = 100 Hz, P = 2000 bar) = 23.89 MPa, meaning that material stiffness is increased 3.46 times. At the same time the loss modulus at pressure 1 bar is G″(ω = 100 Hz, P = 1 bar) = 2.33 MPa and at pressure 2000 bar it becomes G″(ω = 100 Hz, P = 2000 bar) = 12.65 MPa. Thus, the material ability to dissipate energy has increased 5.41 times.

From Figs. 13.1 and 13.2 one may easily see that by further increasing material inherent pressure we may increase the stiffness and damping properties of TPU up to 100 times!

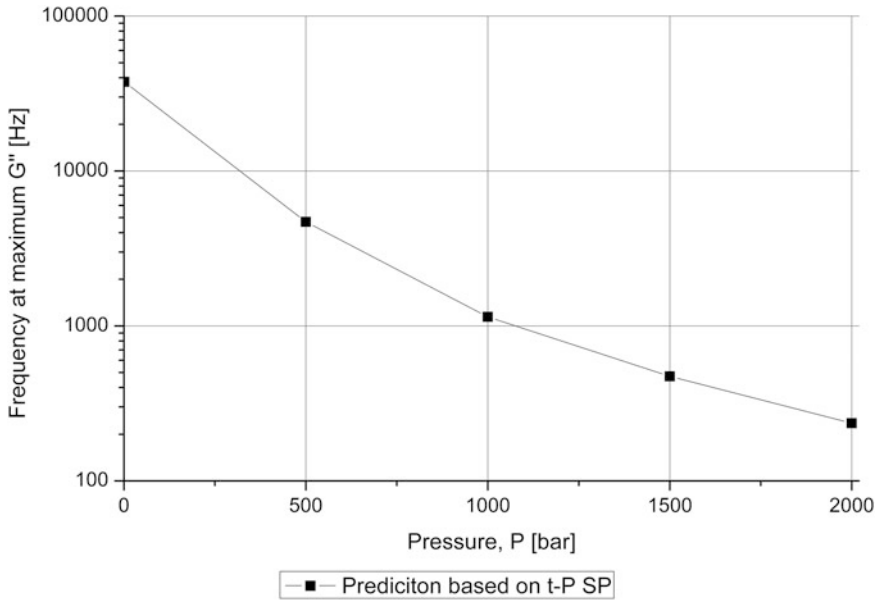

Fig. 13.4 Frequency at maximum damping

Using the time-pressure (t-P) superposition principle we can predict how frequency, at which TPU exhibit maximum damping properties (maximal value of loss modulus $G''(\omega)$) changes with pressure.

Figure 13.4 shows frequencies at which loss modulus has maximal values in dependence on pressure (from 1 to 2000 bar). We can see that higher pressure shifts maximal values of damping (maximal values of loss modulus G'') to lower frequencies. For example, frequency at which maximal value of damping at pressure $P = 1$ bar occurs is around $\omega = 37$ kHz, whereas at pressure $P = 2000$ bar it moves to as low as $\omega = 235$ Hz.

13.4 Damping Elements Based on Dissipative Granular Materials

Based on the presented results, where we showed that existing solutions for structural and vibration control do not and cannot fully utilize damping characteristics of time- and frequency-dependent materials, we developed the ultimate adaptive damping elements system, which we have called DGM System (DGM—Dissipative Granular Materials).

As we have showed, the inherent (hydrostatic) pressure changes frequency dependence of polymeric materials. Hence, by proper selection of damping material and a pressure to which material is exposed one can match the frequency range of its maximum damping properties with the resonance frequency of the building and/or structure exposed to earthquakes. In this way we fully utilize damping characteristics of the selected material and maximize the energy absorption properties of the damper.

Granular materials when excited beyond a certain level of stress flow similarly as liquids while maintaining all properties of a bulk material. The macroscopic flow of particles further expands the energy dissipation capability of granular materials. Hence, micro to macro-size multimodal elastomeric granular material may be used as a pressurizing media (similar as air in tires) to impose hydrostatic pressure on itself, and change frequency dependence of its own energy absorption properties. With proper adjustment of pressure we also adjust the stiffness of the damping element (again, similar as with air in tiers). The proposed particle-filled damping element will provide greater energy dissipation, since when granular materials are deformed there is relative motion of particles; such motion causes energy dissipation through friction. Our proposed solution consists of micro- and macro-sized particles. Smaller particles lead to more surface area per unit volume, which increases the magnitude of frictional dissipation energy caused by particle-particle interaction; while larger particles will allow macroscopic flow, as described above. Hence, our proposed solution utilizes all possible energy dissipation mechanisms and represents an optimal (ultimate) solution for the proposed novel damping system. Such patented damping elements [8] consist of elastomeric granular material, which is encapsulated in a flexible glass fiber tube, as shown in Fig. 13.5.

This design enables us to pressurize the granular material inside the damping element. At higher pressures properties of material shift to lower frequencies, compared to the reference values.

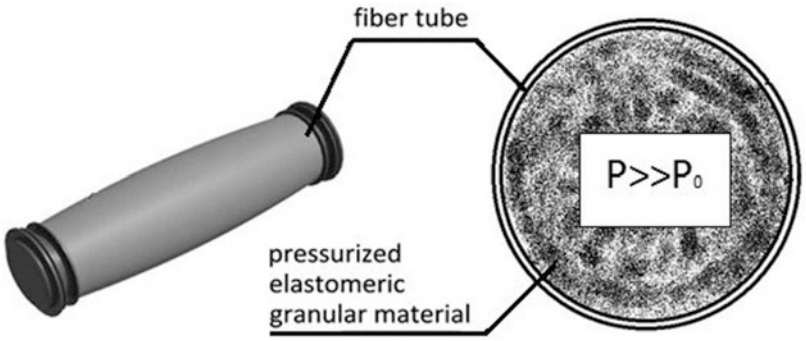

Fig. 13.5 Damping elements consisting of pressurized elastomeric granular material encapsulated by fiber tube

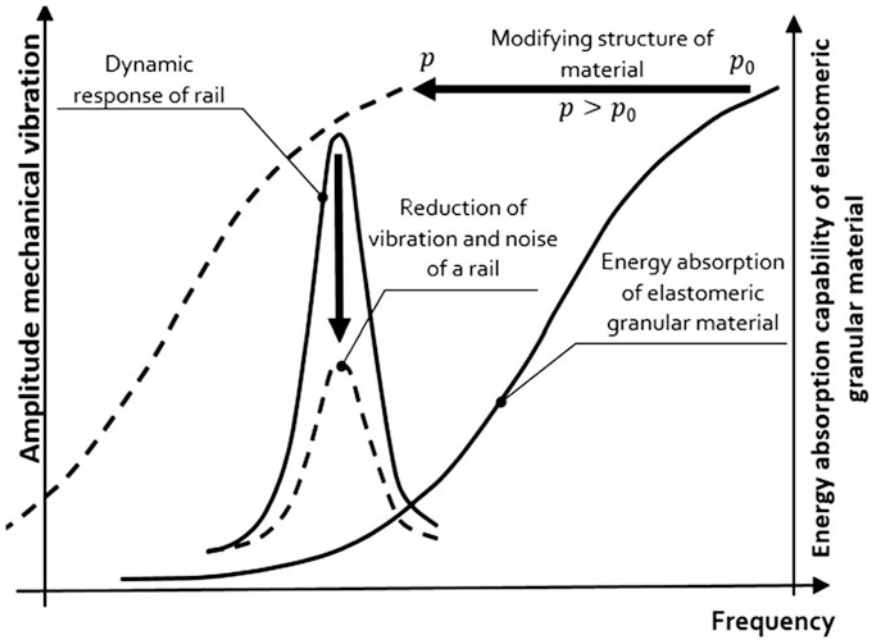

Fig. 13.6 Schematic presentation of working principle

Working principle of such damping element is explained in the diagram in Fig. 13.6, which shows the original dynamic response of the excited structure caused by earthquake and reduced dynamic response of the excited structure when damping elements are applied. The solid line on the right schematically shows damping characteristics of the selected granular viscoelastic material at atmospheric pressure. By self-pressurizing elastomeric granular material to properly selected hydrostatic pressure its frequency characteristic may be adjusted as required, to match the resonance frequency of the structure. This is schematically shown with an arrow showing that line in the right-hand side of Fig. 13.6 changes its frequency position to the dashed line. By modifying hydrostatic pressure to which elastomeric nano-sized granular material is exposed we can adjust the frequency, at which material exhibits maximum energy absorption, such so to match the frequency of the vibrating structure. By doing so, we observe substantial reduction of vibration amplitudes.

13.5 Conclusions

Minimizing noise levels from train–track interaction can be achieved by implementing different noise control measures. Among them, tuned absorber systems can be a very effective way in reducing the noise radiated by the rail. Tuned absorber systems consists of polymeric materials and as it was shown on example of TPU, existing solutions do not and cannot fully utilize damping characteristics of time- and frequency-dependent materials.

In this chapter we have demonstrated that by utilizing the basic knowledge on the effect of inherent hydrostatic pressure on the time- and frequency-dependent behavior of polymers it is possible to design and build the ultimate adaptive damping elements system for vibration control applications.

In this process we need an apparatus that allows determination of material functions, as functions of pressure and temperature in time or frequency domain, e.g., G(t). Presented CEM Measuring System is an example of such apparatus.

For the selected TPU material we found:

- By increasing pressure from 1 to 2000 bar the frequency at which material exhibits its maximal damping properties was shifted from 37 kHz, at P = 1 bar to 235 Hz at P = 2000 bar.
- The increase of inherent hydrostatic pressure from 1 to 2000 bar changes values of storage modulus G′ up to 3.5 times (depending on the frequency), while the values of loss modulus G″ are changed up to 5.5 times.

Acknowledgements Operation part financed by the European Union, European Social Fund.

References

1. EC-JRC/PBL. EDGAR version 4.2 [Online]. http://edgar.jrc.ec.europa.eu/ (2011). Cited 12 May 2012
2. International Transport Forum, OECD. Transport Outlook [Online]. http://www.internationaltransportforum.org/Pub/pdf/10GHGTrends.pdf (May 2010). Cited 10 May 2012
3. International Union of Railways: rail transport and environment, facts & figures [Online]. http://www.uic.org/homepage/railways&environment_facts&figures.pdf (2008). Cited 10 Jan 2012
4. European Commission Mobility and transport [Online]. http://ec.europa.eu/transport/publications/statistics/doc/2011/pocketbook2011.pdf (2011). Cited 22 Feb 2012. ISBN:978-92-79-19508-2
5. Habitat fragmentation due to transportation infrastructure, The European review [Online]. https://www.milieuinfo.be/productie/beheerplone/nietacm/iene/cost-341/SotA-COST341ER0318.pdf (2002). Cited 12 Jan 2011
6. Thompson, D.: Railway Noise and Vibration: Mechanisms, Modelling and Means of Control. Elsevier, Oxford (2009)
7. Strategies and tools to assess and implement noise—final technical report. Transport Research Knowledge Centre [Online]. http://www.transport-research.info/Upload/Documents/201003/20100310_134523_78957_Final%20Report%20V10_2_.pdf (2003). Cited 15 Jan 2012
8. Emri, I., Bernstorff, B.: Dissipative Bulk and Granular Systems Technology: Anmeldenummer 12006059.5 / EP 12006059–2012-08-24. Europäisches Patentamt, München (2012)
9. Emri, I., Prodan, T.: A measuring system for bulk and shear characterization of polymers. Exp. Mech. **46**(4), 429–439 (2006)
10. Kralj, A., Prodan, T., Emri, I.: An apparatus for measuring the effect of pressure on the time-dependent properties of polymers. J. Rheol. **45**(4), 929–943 (2001)
11. Knauss, W.G., Emri, I., Lu, H.: Mechanics of polymers: viscoelasticity. In: Sharpe, W.N., Sharpe, W.N. (eds.) Handbook of Experimental Solid Mechanics, pp. 49–95. Springer, New York (2008)
12. Tschoegl, N.W., Knauss, W.G., Emri, I.: The effect of temperature and pressure on the mechanical properties of thermo- and/or piezorheologically simple polymeric materials in thermodynamic equilibrium: a critical review. Mech. Time Depend. Mater. **6**(1), 53–99 (2002)
13. Tschoegl, N.W.: The Phenomenological Theory of Linear Viscoelastic Behavior: An Introduction. Springer, Berlin (1989)

Chapter 14
Wideband Material Characterization of Viscoelastic Materials

Hüseyin Gökmen Aksoy

Abstract In this study, non contact experimental method is proposed in order to determine the material properties in 20–400 kHz range. Diffraction correction is used to eliminate the spreading error due to the spherical wave generated by the hydrophone, which is used as a transmitter. Method is validated on polymethyl methacrylate (PMMA). Material properties of gelatine gel is also determined.

Keywords Material characterization • Viscoelastic materials • Through transmission technique • Spherical wave transmission • Broadband spectroscopy

14.1 Introduction

Determination of material properties is the most important issue of engineering science. Recent advances in material science and engineering technology requires data on frequency dependent material properties in wide range of frequencies and temperatures.

Dynamic material analysis (DMA) is the one of the methods used in determination of temperature and frequency dependent material properties [1]. In this method, test specimen is subjected to harmonic load of tension, compression, torsion or bending at a given frequency. Frequency dependent storage and loss modulus of the material is determined. This methodology allows one to determine material properties up to 100 Hz. On the other hand, characterization of soft matter is a challenging task due to high values of measurement uncertainties. Another methodology used in determination of elastic and viscoelastic material properties is resonant ultrasound spectroscopy (RUS) [2, 3]. In this method, prism like test specimen excited between two piezoelectric sensors and frequency response of the specimen is recorded. Material parameters are determined by solving inverse problem via computer simulations. This method allows one to determine the material properties between 10 and 300 kHz depending on the sensors and materials. One disadvantage of the method is experimental results are highly susceptible to user and specimen preparation. Both DMA and RUS have been widely used for materials with relatively high stiffness.

Determination of material properties of soft matter is also critical due to emerging technological applications. Rheometers are used in determination of viscoelastic material properties of gels [4]. When the loss modulus of material is high, rheometers can be used up to 100 Hz. Moreover rheometers can not be used for soft matter such as tissue or stiff materials like plastics and metals. In recent years, material characterization methods based on ultrasonic spectroscopy are well developed [5–7]. In long wavelength limit, waves interfere with the waves reflected from the surrounding environment or structural waves. This makes it difficult to use these methods for material characterization at lower frequencies. Moreover, most of the ultrasonic sensors has central frequency of 150 kHz or higher which makes it difficult to acquire data at lower frequencies. Ultrasonic methods are widely used in biomedical applications due to its nondestructive nature. One common approach in determination of material properties of soft matter is to use Rayleigh wave speed [8]. In many tissues and soft matter, shear wave speeds and surface wave speeds varies between 1 and 10 m/s [8–11] which limits the measured value of material properties to few hundred Hz. Acoustic radiation force is also used to predict the material properties of soft matter [12, 13]. In this method, acoustic force is applied to an object which is embedded in a soft matter. From the radiated waves from the obstacle or an interface and using the theory for the interaction between two media, material properties of soft matter are predicted. Atomic force microscopy [14] is also used in characterization of soft matter. Similar to the surface wave methods, atomic force microscopy can be used up to frequencies of few hundred Hz.

H.G. Aksoy
A Teknoloji, Ankara, Turkey
e-mail: hgaksoy@yahoo.com

C. Ralph et al. (eds.), *Mechanics of Composite and Multi-functional Materials, Volume 7*,
Conference Proceedings of the Society for Experimental Mechanics Series, DOI 10.1007/978-3-319-21762-8_14

In recent years, there has been an interest in development of instruments or methodologies for the characterization of tissues in order to be used in biomedical applications such as robotic surgery. One of the methodologies used is aspiration method [15]. In this method, cylindrical tube is placed on the tissue and air inside the tube is evacuated and tissue is deformed as a result of evacuation. During the deformation of the tissue, image of the deforming tissue is recorded in a computer by the help of fiberoptic cables, mirrors inside the tube and a camera. Strain in the tissue is calculated by using digital image correlation. Pressure in the tube is also measured during the deformation of the tissue. Material properties are estimated from stress-strain curve. This method has been successfully used during the surgical operations. On the other hand, reliability of the measured values depends on the operator. Another method used for tissue or soft matter characterization under dynamic or static loads is indentation test [16]. A sensor is indented to the tissue and force and displacement is measured. Reliability of the measured values depends on the operator. In addition, material properties only at low frequencies can be determined. Other than these, there are other characterization methods exist [17, 18].

Many of methods proposed in the literature are either for relatively rigid materials, invasive or has limited frequency range. In the proposed experimental setup, method based on acoustic through transmission technique is used for wideband material characterization of linear viscoelastic materials independent of its stiffness. Material properties are measured between 20 and 400 kHz. Method is validated on PMMA. Both longitudinal wave velocity and corresponding attenuation coefficient are in agreement with the previously measured values [2] which are in the range of 10–60 kHz. Material properties of 10 % w/w gelatine gel is also measured.

14.2 Experimental Method and Data Analysis

Through transmission technique is used for the determination of phase velocity and attenuation coefficient for which the measurement chain is shown in Fig. 14.1. This technique depends on the comparison of signals acquired with and without the specimen to obtain the transfer function of the specimen. From the transfer function, attenuation coefficient is obtained as given in [19]. PMMA with different thicknesses are used for the validation of the experimental method. Then attenuation coefficient of gelatine gel is measured.

Schematic drawing of the experimental setup and drawing of specimen is shown in Fig. 14.1. Experimental setup consists of CS1622 high speed digitizer from Gage Applied Technologies(Lockport, USA), AFG3021B signal generator from Tektronix (Beaverton, Oregon-USA), WMA 300 power amplifier from Falco Systems (Amsterdam, Netherlands), two hydropones TC4034 from Teledyne Reson(Slangerup, Denmark). Measurements are carried on PMMA and 10 % w/w gelatine gel. Custom built x-y scanning stage is used to scan the plane in front of the specimen. Gelatine specimens are prepared by using 300 bloom gelatine powder from Vyse Inc.(Schiller Park, Illinois-USA). 10 % by weight gelatine mixed with water at 65°C and stirred for 5 min. Specimens are prepared by using PMMA molds. After molding, specimens are remained to cool down to room temperature between 2 and 4 h. Then each specimen is placed in a refrigerator at 4°C for 12 h for complete gelation. Water filled box of 0.8 m $\times$ 0.8 $\times$ 1.2 m is used. Water temperature during the experiments are 20°C. Density of PMMA is measured to be 1180 kg/m^3 and density of gelatine gel is 1020 kg/m^3. Speed of sound in water is taken as 1496 m/s.

The distance between the transmitter and specimen is held fixed at 3 cm. Receiver is placed at 3 cm from the specimen. Acoustic center of the hydrophone is $d_f = 5.5$ mm from the tip of the transducer. In the experiments with PMMA, circular PMMA plates with $D = 30$ cm and thicknesses with $t = 2$ cm, $t = 3$ cm are used. In the case of a gelatine gel, diameter of test specimen is $D = 20$ cm. Transmitting transducer is excited with a single square wave with a width of 1.5 μs.

Methodology of calculating attenuation coefficient and phase velocity is given below for the readers convenience. Two signals received with and without specimen are

$$A_{\mathrm{sp}}(\omega) = A_T(\omega)A_1(\omega)T(\omega)A_s(\omega)D_s(\omega)A_2(\omega)A_R(\omega), \tag{14.1}$$

$$A_{\mathrm{wp}}(\omega) = A_T(\omega)A_1(\omega)A_w(\omega)D_w(\omega)A_2(\omega)A_R(\omega). \tag{14.2}$$

In Eqs. (14.1) and (14.2), $A_{sp}(\omega)$ is Fourier transform of the signal received with the specimen and $A_{wp}(\omega)$ is Fourier transform of the signal without specimen. $A_T(\omega)$ and $A_R(\omega)$ are the transfer functions of the transmitter and receiver. $A_s(\omega)$ is the transfer function of the specimen and $A_w(\omega)$ is the transfer function of the water replaced by the specimen. $A_1(\omega)$ is the

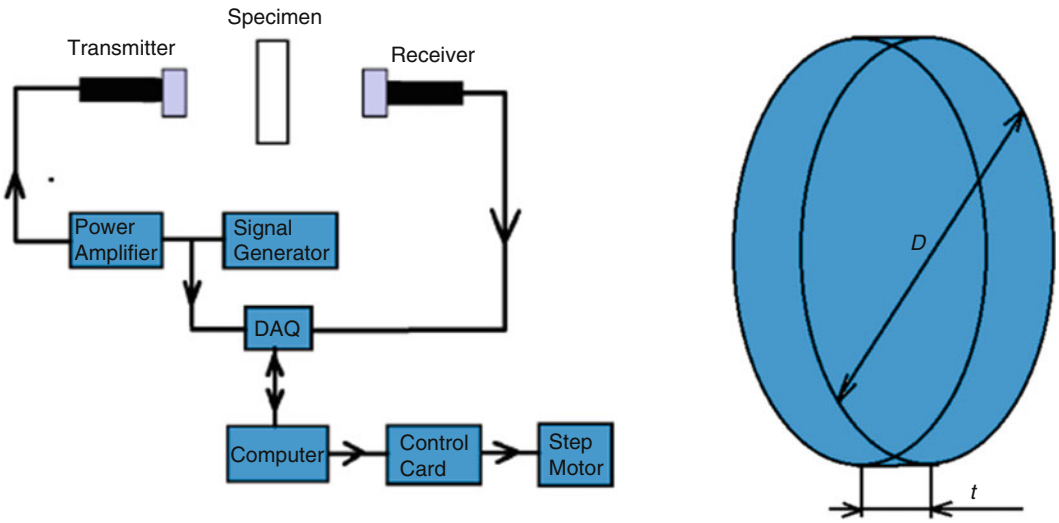

Fig. 14.1 Measurement chain and specimen. (**a**) Measurement chain. (**b**) Specimen

transfer function of the water between the transmitter and specimen. $A_2(\omega)$ is the transfer function of the water between the specimen and receiver. $T(\omega)$ is the transmission coefficient of the specimen. $D_s(\omega)$ and $D_w(\omega)$ are due to the spreading of waves in path with specimen and water only path respectively. Thus each transfer function can be represented as $B_a(\omega) = |B_a(\omega)|e^{i\varphi}$, where φ is the phase angle. Dividing Eq. (14.1) with Eq. (14.2), one obtains

$$A(\omega) = \frac{T(\omega)A_s(\omega)D_s(\omega)}{A_w(\omega)D_w(\omega)} = \frac{|T(\omega)||A_s(\omega)||D_s(\omega)|}{|A_w(\omega)||D_w(\omega)|} e^{i(\varphi_T+\varphi_s+\varphi_{Ds}-\varphi_w-\varphi_{Dw})}. \tag{14.3}$$

The frequency range which is of interest of this study is 20–400 kHz. Measurements are done in water. Therefore wavelengths vary between 0.35 and 30 cm, which are comparable to specimen dimensions. Moreover wave package is approximately 50 μs long. This causes interference of the wave with its self during the transmission through the specimen. In order to incorporate this phenomena, transmission coefficient which takes into account this phenomena is used [20].

$$T(\omega) = \frac{t_{ws}t_{sw}}{1 - r_{sw}^2 e^{-ik2d}} \tag{14.4}$$

In Eq. (14.4), t_{ws} and t_{sw} are the transmission coefficients of water-specimen and specimen-water interface. r_{sw} is the reflection coefficient of specimen-water interface [21].

Let us define the complex wave number as $k = \omega/c_p + i\alpha$, where ω is the circular frequency. c_p is the phase velocity and α is the attenuation coefficient.

Hydrophones behave as a point source and generates a spherical wave when it is used as a transmitter. Amplitude of spherical wave is inversely proportional with the radial distance from the point source and energy of the wave is spread. In through transmission experiments, wave is assumed to be plane and propagates in one dimension which means that problem is semi-infinite. Finite size of the transducer, which emits acoustic waves, taken into account by using diffraction correction [5, 20, 21]. Thus diffraction of emitted wave happens due to the energy flow in the radial direction in the ahead of a circular piston like transducers, which is perpendicular to the direction propagation, similar to that of energy decay in spherical waves. Spreading error due to the spherical wave is calculated via method used for diffraction correction [5, 20, 21]. Theoretical diffraction correction developed for focused transducers are used as represented in Fig. 14.2. Transfer function for diffracted wave is

$$D(s) = \left(1 - e^{-i2s}\right)(J_0(2\pi/s) + iJ_1(2\pi/s)), \tag{14.5}$$

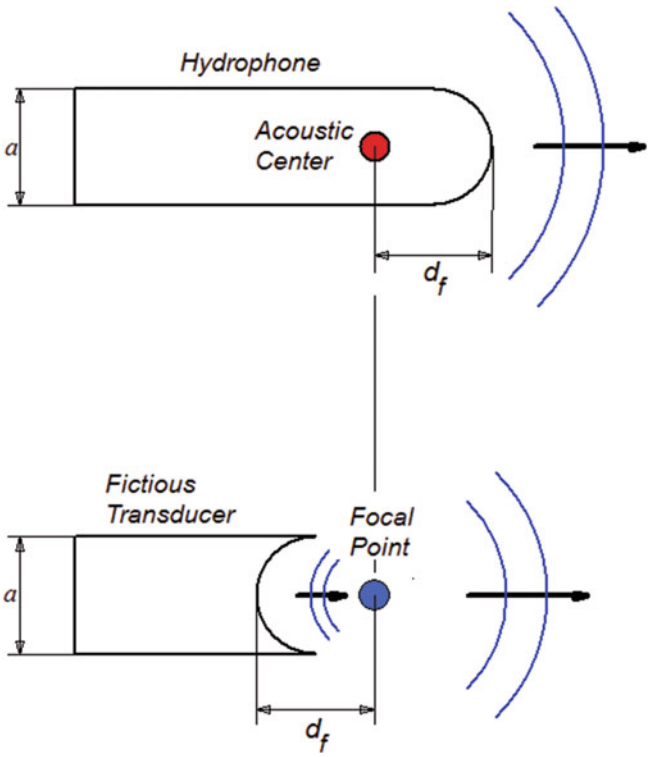

Fig. 14.2 Fictitious transducer used for correcting for spreading error

Where parameter s is defined as

$$s_w = \frac{4z_e c_w \gamma}{fa^2}, \tag{14.6}$$

$$s_s = \frac{4(z_e - t)c_w \gamma}{fa^2} + \frac{4tc_p \gamma}{fa^2}, \tag{14.7}$$

for water only path and path with specimen. In Eqs. (14.6) and (14.7), a is the aperture diameter. f is frequency. γ is correction parameter for the path for the focused transducer and defined as $\gamma = d_f / |z_e - d_f|$. z_e is the distance between the fictitious focused transducer and acoustic center of the receiver and $z_e = L + 2d_f$. c_w is the phase velocity of the water. L is the distance between two transducers and d_f.is the distance of the acoustic center of the transducer from its tip. t is the specimen thickness.

Signal of the path with specimen is shifted δt in time to avoid the phase ambiguity before taking the Fourier transform of the signal.

The attenuation coefficient is calculated as

$$\alpha = Log\left(\frac{|T(\omega)||A_s(\omega)||D_s(\omega)|}{|A_w(\omega)||D_w(\omega)|}\right)/t. \tag{14.8}$$

The phase velocity is calculated as

$$c_p = \frac{c_w}{1 - c_w \frac{(\varphi_s - \varphi_T - \varphi_w + 2\pi f \delta t)}{2\pi f t}} \tag{14.9}$$

Phase angle contribution of diffraction corrections to the phase velocity is assumed to be negligible.

14.3 Experimental Results

Spacetime plot of pressure at 3 cm from the specimen is shown in Fig. 14.3, when the specimen is PMMA. Phase velocity and attenuation coefficient of longitudinal wave are obtained from the measurement at $x = 0$ cm and phase velocity and attenuation coefficient of shear wave are obtained from the measurement at $x = 10$ cm where longitudinal wave becomes evanescent. Shear wave of soft materials are very low compared to longitudinal wave velocity and varies between 1 and 10 m/s [8–11]. Therefore it is not possible to determine the phase velocity and attenuation coefficient of shear wave in most soft materials. In this study, critical angle is not observed in the experiments with gelatine gel.

Longitudinal wave velocity and attenuation coefficient of PMMA is shown in Fig. 14.4. Decrease of thickness increases the uncertainty in the measurements. Both phase velocity and attenuation coefficient is in agreement with the previously reported values in the literature. Measured value of phase velocity is 2765 m/s and attenuation coefficient is 9.4 Np/m [22]. Longitudinal wave velocity is almost constant for a wide range of frequencies and goes up to 2726 m/s with an uncertainty of 40 m/s when the thickness is 3 cm. Attenuation coefficient increases with the increasing frequency. Maximum uncertainty

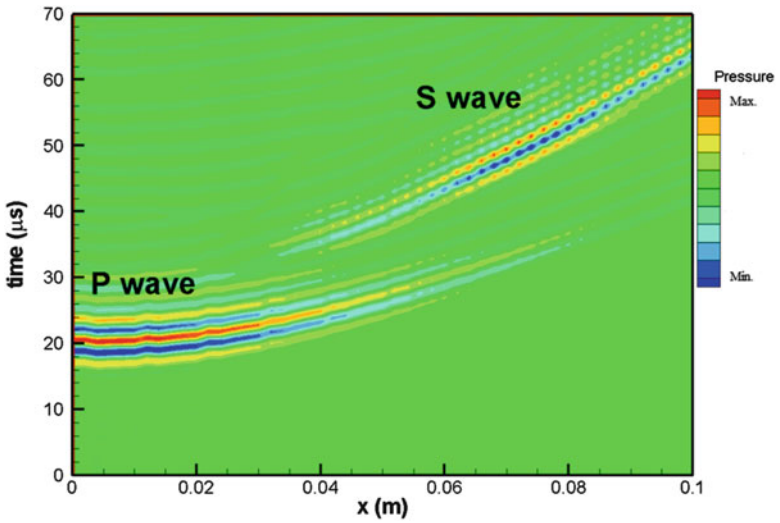

Fig. 14.3 Spacetime plot of pressure field when specimen is PMMA

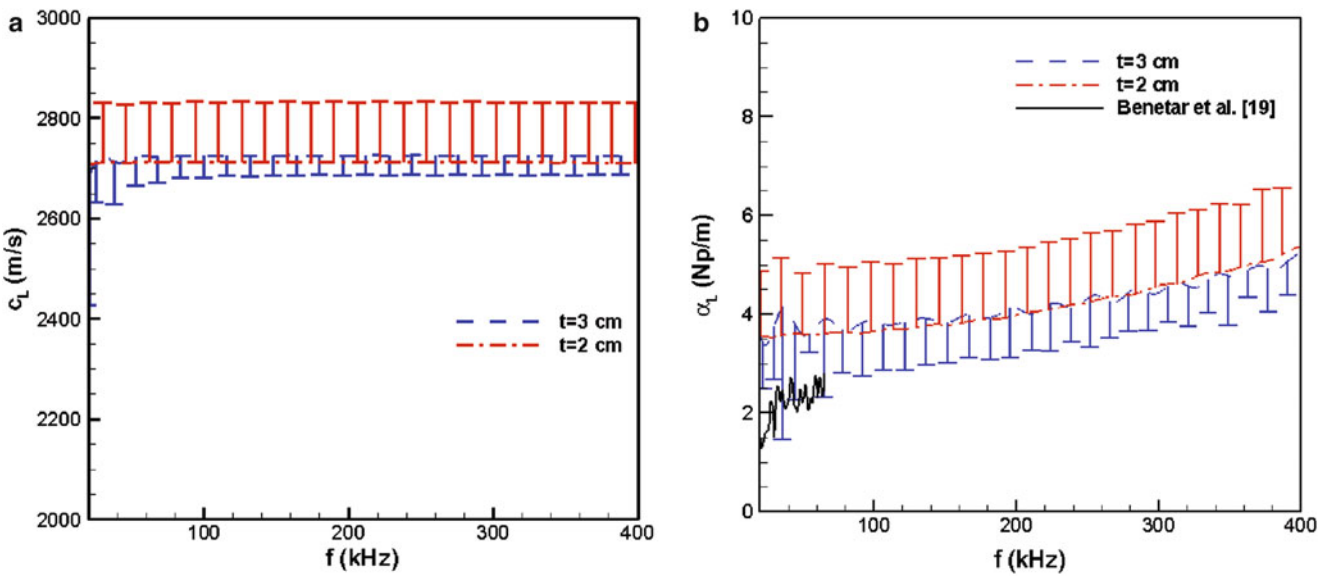

Fig. 14.4 Phase velocity and attenuation coefficient of longitudinal wave in PMMA. (**a**) Longitudinal wave velocity. (**b**) Attenuation coefficient of longitudinal wave

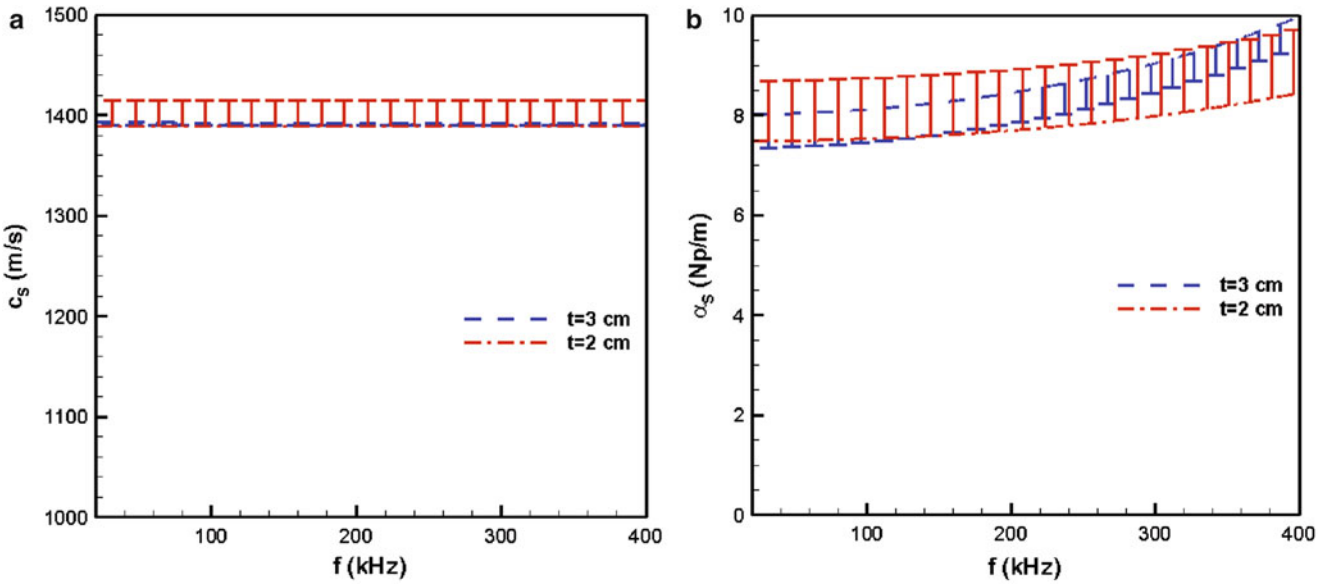

Fig. 14.5 Phase velocity and attenuation coefficient of shear wave in PMMA. (**a**) Shear wave velocity. (**b**) Attenuation coefficient of shear wave

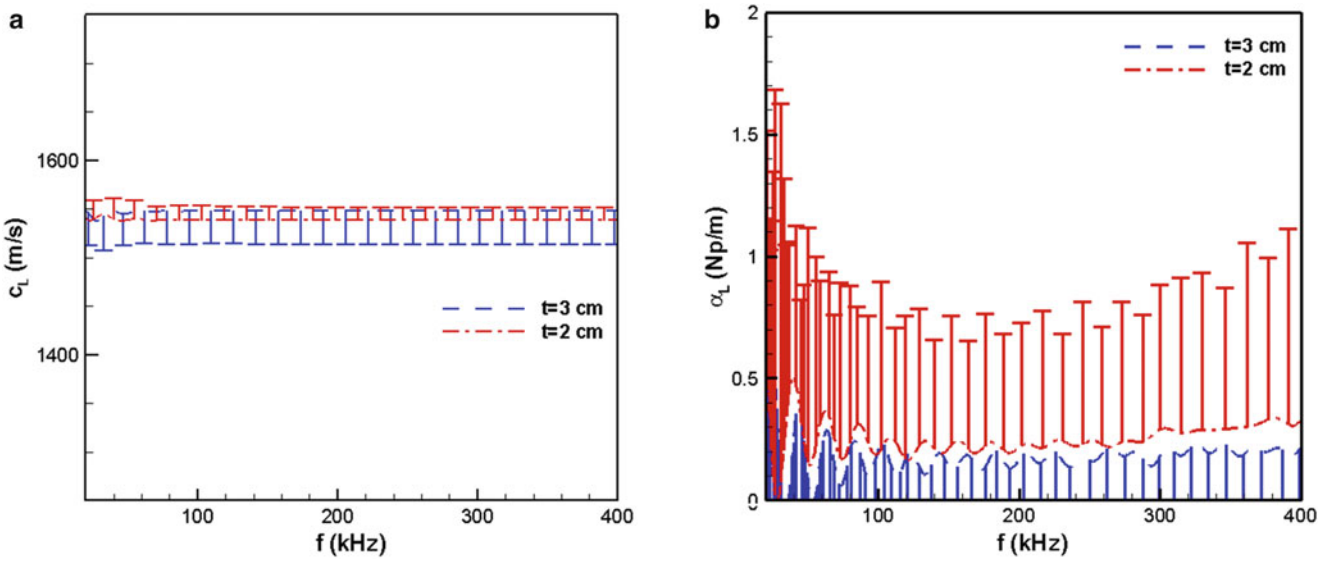

Fig. 14.6 Phase velocity and attenuation coefficient of longitudinal wave in gelatine gel. (**a**) Longitudinal wave velocity. (**b**) Attenuation coefficient of longitudinal wave

attenuation coefficient is 1 Np/m when thickness is 3 cm. Uncertainty in attenuation coefficient increases to 1.5 Np/m when the thickness of the specimen is 2 cm.

In Fig. 14.5, shear wave velocity and corresponding attenuation coefficient is presented. Shear wave velocity is 1390 m/s, measured by using contact transducers [22], which is in agreement with the results given in Fig. 14.5. On the other hand, attenuation coefficient varies between 7 and 9 Np/m, which is far below the reported value of 26.5 Np/m. Uncertainty in the attenuation coefficient of shear wave is around 1 Np/m for both thicknesses. Shear wave is found to be constant and nondispersive for wide range of frequencies. Shear wave speed is measured to be 1388 m/s with an uncertainty of 3 m/s when the specimen thickness is 3 cm.

Longitudinal wave velocity and attenuation coefficient of gelatine gel is presented in Fig. 14.6. Longitudinal wave velocity slightly increases with increasing frequency. Measured attenuation coefficient at around 0.5 Np/m. Uncertainty in the attenuation coefficient is 1 Np/m. One must note that uncertainty of the hydrophone is 0.35 Np/m. Increasing thickness

results in a decrease in the uncertainty in attenuation coefficient. Negative attenuation coefficient obtained in some measurement due to the very low values of attenuation coefficient.

14.4 Conclusions

Presented method allows wideband material characterization of linear viscoelastic materials between 20 and 400 kHz successfully. Therefore method is comparable to RUS method and it is less sensitive to specimen preparation and experience of operator compared to RUS and DMA. This method is a nondestructive and noncontact method which allows one to determine material properties of soft matter. Uncertainty in measurements are much lower than the previously reported values [22, 23]. In case of material characterization of aspiration method, measurement uncertainty can go up to 60 % [15]. Eventhough measurements are carried on at constant temperature, method allows one to determine the material properties between -40 and 130°C.

References

1. Menard, K.: Dynamic Mechanical Analysis: A Practical Introduction. CRC, Boca Raton, FL (2008)
2. Lee, T., Lakes, R.S., Lal, A.: Resonant ultrasound spectroscopy for measurement of mechanical damping: comparison with broadband viscoelastic spectroscopy. Rev. Sci. Instrum. **71**(7), 2855–2861 (2000)
3. Migliori, A., Maynard, J.D.: Implementation of modern resonant ultrasound spectroscopy for the measurement of the elastic moduli of small solid specimens. Rev. Sci. Instrum. **76**, 121301 (2006)
4. Mason, T.G., Weitz, D.A.: Linear viscoelasticity of colloidal hard sphere suspensions near the glass transition. Phys. Rev. Lett. **75**, 2770–2773 (1995)
5. Raisutis, R., Kazys, R., Mazeika, L.: Application of the ultrasonic methods for highly attenuating plastic materials. J. Acoust. Soc. Am. **59**, 1294–1298 (1974)
6. Mobley, J., Marsh, J.N., Christopher, S.H., Hughes, M.S., Brandenburger, G.H., Miller, J.G.: Broadband measurements of phase velocity in albunex suspensions. J. Acoust. Soc. Am. **103**, 2145–2153 (1998)
7. Krautkramer, J., Krautkramer, H.: Ultrasonic Testing of Materials. Springer (1990)
8. Zhang, X., Greenleaf, J.F.: Estimation of tissues elasticity with surface wave speed. J. Acoust. Soc. Am. **122**(5), 2522–2525 (2007)
9. Orescanin, M., Toohey, K.S., Insana, M.F.: Material properties from acoustic radiation force step response. J. Acoust. Soc. Am. **125**(5), 2928–2936 (2009)
10. Jacob, X., Catheline, S., Gennisson, J.L., Barriere, C., Royer, D., Fink, M.: Nonlinear shear wave interaction in soft solids. J. Acoust. Soc. Am. **122**(4), 1917–1926 (2007)
11. Sarvazyan, A.P., Urban, M.W., Greenleaf, J.F.: Acoustic waves in medical imaging and diagnostics. Ultrasound Med. Biol. **39**(7), 1133–1146 (2013)
12. Nightingale, K., Soo, M.S., Nightingale, R., Trahey, G.: Acoustic radiation force impulse imaging: in vivo demonstration of clinical feasibility. Ultrasound Med. Biol. **28**(2), 227–235 (2002)
13. Orescanin, M., Toohey, K.S., Insana, M.F.: Nonlinear shear wave interaction in soft solids. J. Acoust. Soc. Am. **122**(4), 1917–1926 (2007)
14. Kazemirad, S., Heris, H.K., Mongeau, L.: Experimental methods for the characterization of the frequency dependent viscoelastic properties of soft materials. J. Acoust. Soc. Am. **133**(5), 3186–3197 (2013)
15. Schiavone, P., Chassat, F., Boudou, T., Promayon, E., Valdivia, F., Payan, Y.: In vivo measurement of human brain elasticity using light aspiration device. Med. Image Anal. **13**, 673–678 (2009)
16. Ming, J., Zu, J.W., Hariri, A.: A new tissue resonator indenter device and reliability study. Sensors **11**, 1212–1228 (2011)
17. Markidou, A., Shih, W.Y., Shih, W.H.: Soft-matter elastic and shear moduli measurement using piezoelectric cantilevers. Rev. Sci. Instrum. **76**, 064302 (2005)
18. Baghani, A., Eskandari, H., Septimiu, S., Rohling, R.: Measurement of viscoelastic properties of tissue mimicking material using longitudinal wave excitation. IEEE Trans. Ultrason. Ferroelectr. Freq. Contr. **56**(7), 1405–1418 (2009)
19. Mobley, J., Marsh, J.N., Christopher, S.H., Hughes, M.S., Brandenburger, G.H., Miller, J.G.: Broadband measurements of phase velocity in Albunex suspensions. J. Acoust. Soc. Am. **103**, 2145–2153 (1998)
20. Rogers, P.H., Van Buren, A.L.: An exact expression for the Lommel diffraction correction integral. J. Acoust. Soc. Am. **55**, 724–728 (1974)
21. Kinsler, L.E., Frey, A.R., Coppens, A.B., Sanders, J.V.: Fundamentals of Acoustics. Wiley, New York (2000)
22. Bouzidi, Y., Schmitt, D.R.: A large ultrasonic bounded acoustic pulse transducer for acoustic transmission goniometry: modeling and calibration. J. Acoust. Soc. Am. **119**(1), 54–64 (2006)
23. Benatar, A., Rittel, D., Yarin, A.: Theoretical and experimental analysis of longitudinal wave propagation in cylindrical viscoelastic rods. J. Mech. Phys. Solid **51**(8), 1413–1431 (2003)

Chapter 15
On the Mechanical Response of Polymer Fiber Composites Reinforced with Nanoparticles

Addis Tessema, William Mitchell, Behrad Koohbor, Suraj Ravindran, Addis Kidane, and Michel Van Tooren

Abstract An experimental study was conducted on the effect of interply nanofiller on the mechanical response of fiber reinforced composite (FRC). Laminate samples were made by hot pressing of woven carbon fiber fabric prepregs. Two batches of samples are prepared, one using five plies of the basic prepreg, the other with silica nanofillers added between the plies during lay-up. Tensile specimen were cut from the laminate under 0, 15, 30, 45, 60, 75 and 90 degrees of fiber orientation are prepared from the laminate. DIC based tensile test is made and the effect of the nano fillers on the mechanical properties are analyzed. Appreciable improvement in strength and Modulus of Elasticity is obtained for fiber orientation of 75° and 60° and reversed response is observed for the fiber angle of 30° and 15°

Keywords Off-axis loading • Woven prepregs • Nano-silica • 3D-DIC • Full-filed

15.1 Introduction

The applications of carbon fiber reinforced composites (CFRC) are spreading at large, from automotive to aerospace and electronics industries. CFRC has possessed excellent in-plane strength and stiffness property when it is loaded along the fiber (weft or warp) directions. In such loading condition, the fiber is the main load barrier and the property of the composite is dominated by the fiber property, the fiber matrix interface strength has a major factor on failure mode [1]. Furthermore, the type of weave and amount of waviness plays a vital role on the elastic and fracture property of CFRC [2, 3]. However, during service time these CFRC's will be subjected to different loading directions, which can be along and off the axis of the fiber directions. It is found that, under uniaxial loading the tensile properties of these composites are highly dependent on the fiber orientation with respect to the loading direction [4, 5]. When the fibers and loading direction are aligned in the same direction, the load will be mainly carried by the fibers and the main failure mechanism would be fiber breakage. On the other hand in the off-axis loading (when fibers are not aligned with the loading direction), both the matrix and the fibers will carry the load and the main failure mechanism is at the interface of the fiber and matrix. In addition, the failure strength of the off-axis specimens are low compared with the specimen with fibers aligned with loading direction. In contrary, when the fiber is not aligned to the loading direction, the tensile strength reduces by half compared with the case where the fibers are in the loading direction [4].

In light of this, reinforcing the matrix with nano fillers is considered as promising approach to improve the mechanical property of the composite during off axis loading and it is getting more attention recently. It is reported that by addition of 45 % nanosilica has doubled the modulus of elasticity and increased the tensile strength by 10 %. Similarly, T. Mahrholz and Coworker [7] have found that inclusion of 2.5 % barium sulfate in the polymer matrix has increased tensile strength, impact strength and strain at break by 19, 73 and 82 % of the matrix respectively. Furthermore, they have added 10 and 20 % of Barium Sulphate but the result was decrement in the mechanical properties as the content of the filler increases. Mahrholz1 also have made GFRP with Silica Carbide addition by 20 % and they have seen an increment of tensile strength of 63 % and shear modulus of 72 %. In the other case where 3 % Carbon Nanotubes (CNT) is added in to aramid fiber/epoxy composites has increased the impact strength by 8 %, but no change has been observed for flexural modulus and tensile strength [11]. M. Tehrani et.al [2] also has discovered that for woven Carbon fiber prepregs with inclusion of 2 % CNT during impregnation has increased the impact energy by 21 % and strain to failure by 21 %. Different techniques are used to include nano-fillers within the composites, out of all Carbon fiber winding to make Prepreg in Silica Carbide (1.5 %) mixed matrix [9] has resulted a good dispersion of nanofiller within the composite. Improved results in mechanical properties is also obtained, the flexural modulus, strength, tensile strength and modulus have increased by 20, 32, 7.2 and 8 %

A. Tessema (✉) • W. Mitchell • B. Koohbor • S. Ravindran • A. Kidane • M. Van Tooren
Department of Mechanical Engineering, University of South Carolina, 300 Main Street, Columbia, SC 29208, USA
e-mail: atessema@email.sc.edu

C. Ralph et al. (eds.), *Mechanics of Composite and Multi-functional Materials, Volume 7*,
Conference Proceedings of the Society for Experimental Mechanics Series, DOI 10.1007/978-3-319-21762-8_15

respectively. Moreover, Vacuum Assisted Resin Transfer Mold (VARTM) [7] and Filament Winding [8] techniques have shown appreciable results.

The main objective of this paper is to quantify the mechanical response of off-axis loaded composites with and without nano fillers experimentally and understand the role of nano-fillers on the mechanical properties of the composites using 3D-DIC.

15.2 Sample Preparation and Test Method

15.2.1 Material Used and Sample Preparation

Two batches of materials are prepared using hot press molding machine, the first batch CFRP panel is made with raw prepreg only and for the second batch nanofillers are added as the third phase in addition to prepreg. The raw materials used are; as manufactured roll of 8H-Satin woven carbon fiber prepreg (TC350-1), which is obtained from Royal TenCate Cooperate. Silica nanopower (Silicon Dioxide) purchased from Sigma Aldrich is chosen as spherical filler, it has particle size of 10 to 20nm (BET) and 99.5 trace metal basis. For the first batch five 250mm × 250mm coupons of wet prepreg are cropped out of the roll and stacked with the same fiber orientation (0°) onto each other. The stack is vacuum bagged and placed inside the hot press machine. Using a vacuum pump the air trapped in the vacuum bag is removed, and then the prepreg is hot pressed at pressure of 3.5 ton and Temperature 125°F for 30 min and the temperature is raised to 325°F and kept for 3 h. The hot pressed material is then kept to cool for 16 h before the fully cured panel is taken out from the machine. The second batch materials is fabricated following the same basic procedure but in this case, before stacking the prepregs, the Silica nano-powders are uniformly dispersed between the prepreg layers using spray gun and compressed air. Finally, a panel size of 250m × 250mm, with four layers of prepreg reinforced with silica nanoparticles is prepared (Modified Prepreg (MP)).The prepared materials are then machined using CNC water jet to get rectangular tensile specimen (170mm × 25mm) at fiber angles of 0, 15, 30, 45, 60, 75 and 90.

15.2.2 Experiment Set-Up

Displacement controlled tensile experiment is conducted in both batches of materials using an MTS 810 testing machine at a displacement rate of 0.001in/min. Hydraulic grips with serrated platens are set to grip specimen, however flat aluminum pads were placed between the serrated platens and the specimen to prevent damage of carbon fiber due to the griping pressure. The specimen was clamped at both ends using the two grips as shown in Fig.15.2 and uniaxial tensile load is applied until the specimen fails. The full field in-plane strains are measured using 3D Digital Image Correlation (3D-DIC). In order to perform the DIC precisely, white flat paint is sprayed on the specimen surface and black speckles are patterned on the white painted surface (Fig. 15.1). Two Grasshopper 5M Pixels resolution camera systems with 35mm Nikon lenses are used to acquire pair of

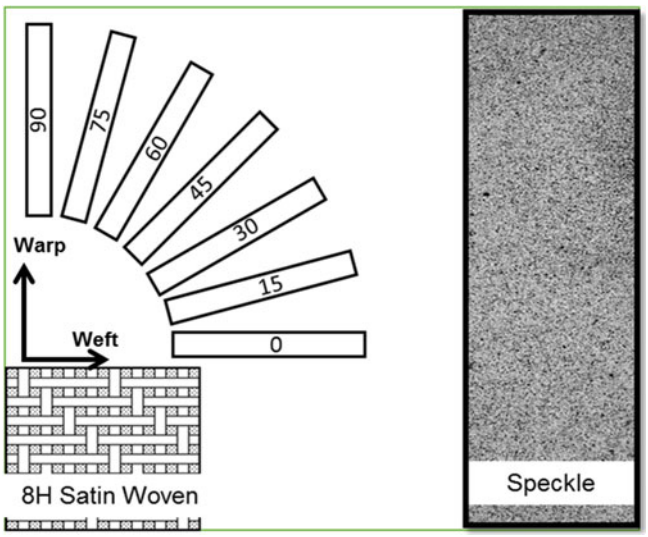

Fig. 15.1 Specimen cut out orientation and speckling

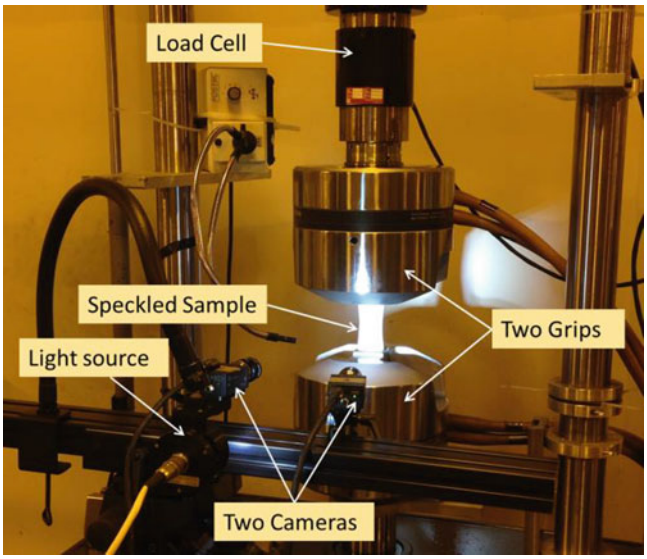

Fig. 15.2 Experimental set-up

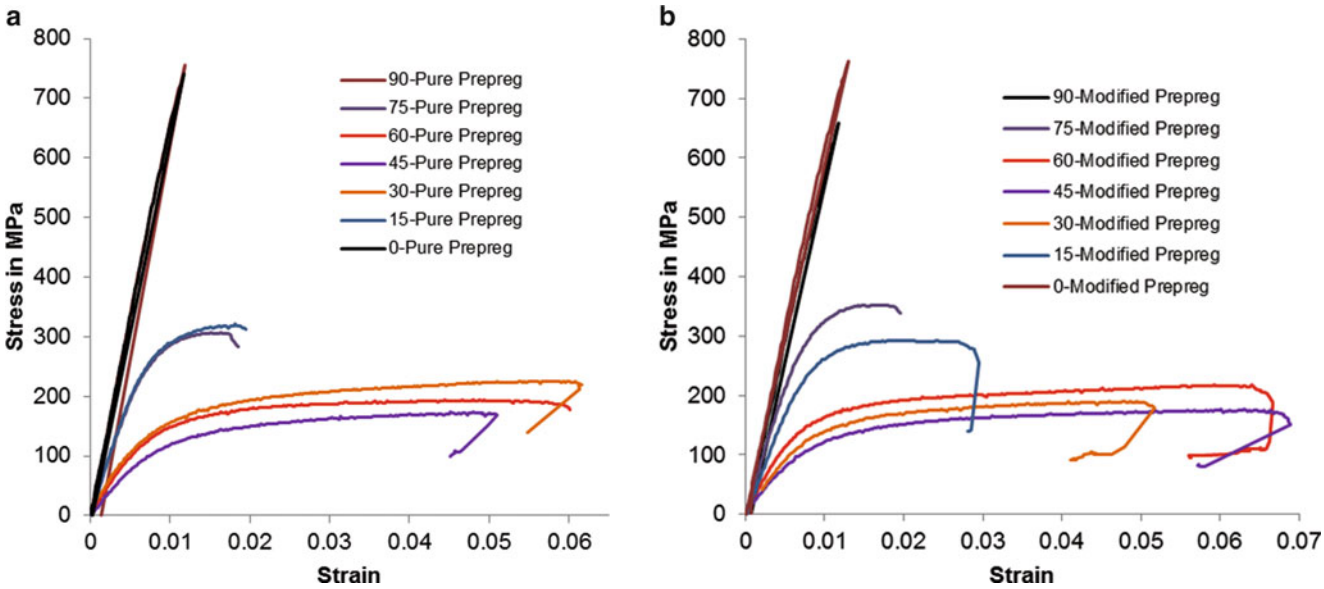

Fig. 15.3 Stress-strain diagram (**a**) Pure Prepreg and (**b**) Modified Prepreg

images at a rate of 1 frame per second. The recorded images are post processed using VIC-3D commercial software and the average full field normal and shear strain data are obtained. The Elastic Modulus and the strength of material are obtained for different of fiber orientation and the effects of nano-filler on these properties are discussed.

15.3 Results and Discussion

The stress- strain plot for pure prepreg and modified prepreg samples are shown in the Fig. 15.3. As it depicted in Fig. 15.3, for the on-axis (0° and 90°) loading, the strength and strain at failure for both pure very similar and decrease in strength is observed for modified prepreg samples. Since the fibers are the main load carrier members in the case of 0^o and 90^o samples, it is expected that the addition of nano-filler did not play a great roll.

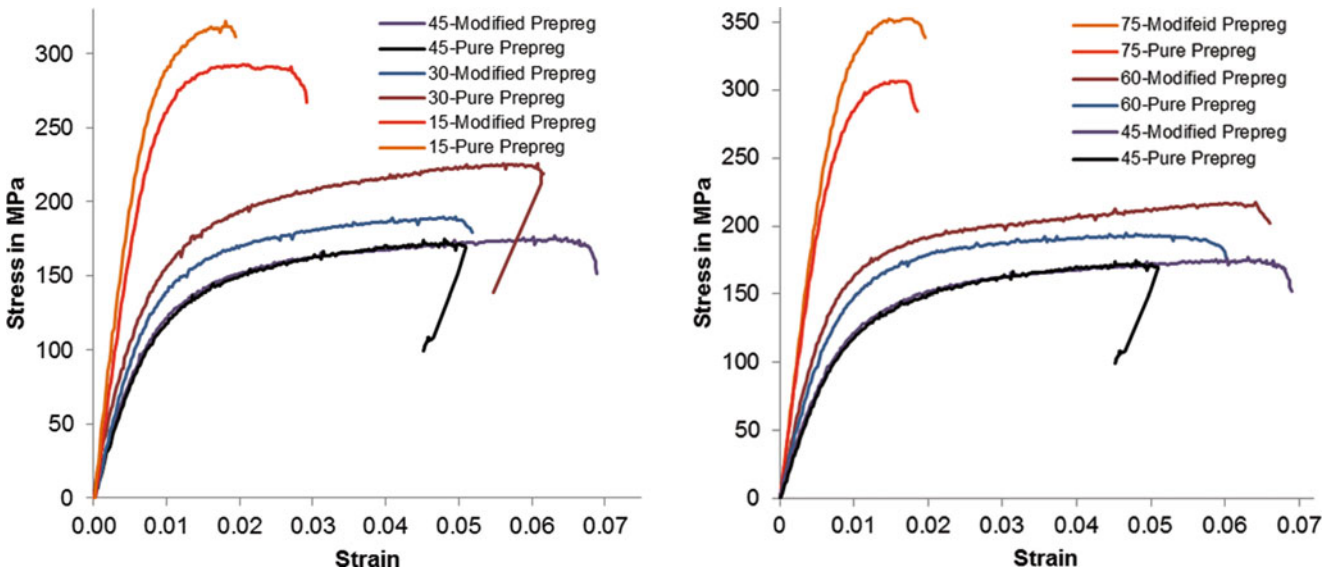

Fig. 15.4 Comparison of Stress-strain diagram for Pure and Modified prepregs

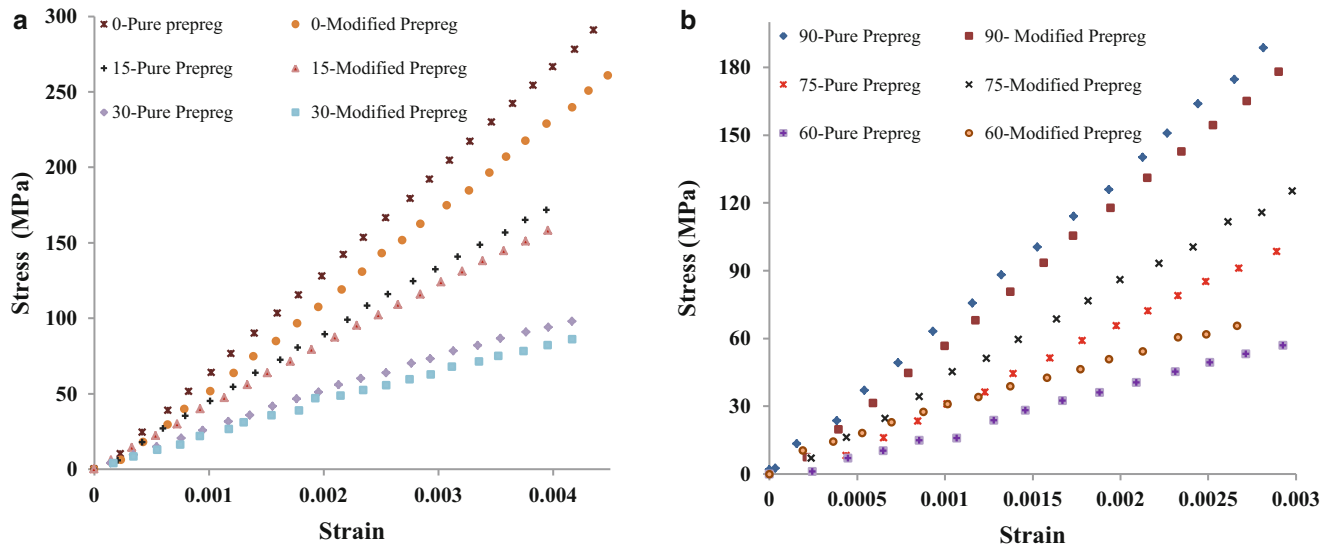

Fig. 15.5 Modulus of Elasticity for Modified and Pure prepregs (**a**) For fiber angle 0–30 degrees and (**b**) For fiber angle 60–90 degrees

However, as loading axis differs from 0° or 90°, the material characteristics become different for both materials. It can be seen from Fig. 15.3, the strength has reduced as the off-axis angle goes from 0° to 45° or 90° to 45° but strain at failure has increased. This designates that when the eccentricity of the load from the weft or warp axis increases the matrix start to engage in load bearing. Therefore, the material response will be dominated by the matrix and that is the reason we observe decrease in strength and increase in plastic deformation (Strain at failure). Concerning the changes observed because of adding nanofiller, as it is seen from the Fig. 15.4 for the angles 15° and 30° the modified prepreg has lower strength, which indicates that matrix has weakened due to the addition of the nanofiller. On contrary, from Fig. 15.4 (b) for the angles 60° and 75° the modified prepreg has shown enhancement in their strength and strain at failure.

Moreover, the Modulus of Elasticity is also affected by the addition of nanofillers. From Fig. 15.5, similar to the strength, for the groups 0°, 15°, 30° and 90° the Modulus of Elasticity has reduced for the modified samples relative to the pure prepreg. On the other side, for 60° and 75° samples the Modulus of Elasticity has improved for the modified prepreg. For 45 ° prepreg the Modulus of Elasticity and strength are the same for both materials. This can show that addition of nanofiller affects not only the matrix but the whole material network.

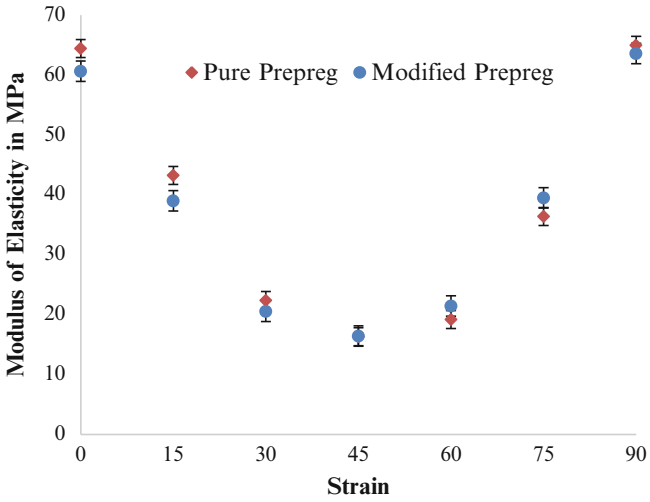

Fig. 15.6 Modulus of elasticity for different angle

As it seen from Fig. 15.6, the influence of nanofillers is different for angles less than and greater than 45°. And it was expected that the effect of nanofiller should be the same for 15° and 75° but that was not the situation. Therefore it is noticed that the nanofiller are not only affecting the matrix but it also affects the matrix fiber interaction.

15.4 Summary

Two different batches material are fabricated from carbon prepregs with and without nanofillers. Based on uniaxial tensile test incorporating with 3D-DIC technique, the off-axis elastic parameters of nano-silica filled prepreg is determined and is compared with pure prepreg. Though additional detail investigation is needed to come up with a solid conclusion, the following summary can be drawn from the current work;

- The inclusion of nanofillers has different effect on the strength and strain at failure for different off-axis specimen. For angle 15° and 30° the strength of nanoparticles modified sample is lower that the pure prepreg, but the effect is reverse for the 60° and 75°.
- The nano-fillers have small effect on the average Elastic Modulus (E) of the composites. The average elastic Modulus of the modified sample is slightly higher for 15° and 30° and slightly lower for 60° and 75° compared with pure prepreg samples.

Acknowledgment The financial support of the National Science Foundation under Grant No EEC-1342379 is gratefully acknowledged. Royal Tencate Corporate is also gratefully aknowledged for providing the materials.

References

1. Kotaki, M., Hamada, H.: Effect of interfacial properties and weave structure on mode I interlaminar fracture behavior of glass satin woven fabric composites. Compos. Part A **28A**, 257–266 (1997)
2. Tehrani, M., Boroujeni, A.Y., Hartman, T.B., Haugh, T.P., Case, S.W., Al-Haik, M.S.: Mechanical characterization and impact damage assessment of a woven carbon fiber reinforced carbon nanotube – epoxy composite. Compos. Sci. Technol. **75**, 42–48 (2013)
3. Kim, J., Shioya, M., Kobayashi, H., Kaneko, J., Kido, M.: Mechanical properties of woven laminates and felt composites using carbon fibers. Part 1: in-plane properties. Compos. Sci. Technol. **64**, 2221–2229 (2004)
4. Koohbor, B., Mallon, S., Kidane, A., Sutton, M.A.: A DIC-based study of in-plane mechanical response and fracture of orthotropic carbon fiber reinforced composite. Compos. Part B **66**, 388–399 (2014)
5. Pollock, P., Yu, L., Sutton, M.A., Guo, S., Majumdar, P., Gresil, M.: Full-field measurements for determining orthotropic elastic parameters of woven glass-epoxy composites using off-axis tensile specimens. Exp. Tech. **38**, 61–71 (2014)
6. Naik, N.K., Asmelash, A., Kavala, V.R., Veerraju, C.: Interlaminar shear properties of polymer matrix composites: strain rate effect. Mech. Mater. **39**, 1043–1052 (2007)
7. Nidal, A., Leif, A.C., Louis, B.: The effect of weave pattern and crack propagation direction on mode I delamination resistance of woven glass and carbon composites. Compos. Part B **29B**, 603–611 (1998)
8. Nelson, J.M., Hackett, S.C., Hine, A.M., Sedgwick, P., Lowe, R.H., Quinn, D., Goetz, D.P., Schultz, W.J.: Development of nanosilica-epoxy matrix resins for high temperature prepreg composites. Polym. Prepr. **52**(2), 91 (2011)

9. Mahrholz, T., Mosch, J., Röstermundt, D., Riedel, U., Herbeck, L.: New high-performance fibre reinforced materials with nanocomposites. In: Materials for Aerospace Applications, 24–26 Nov 2003
10. Zhou, Y., Baseer, M.A., Mahfuz, H., Jeelani, S.: Fabrication and evaluation on nano-phased unidirectional carbon fiber reinforced epoxy. J. Mater. Sci. **47**, 5002–5012 (2012)
11. Shih, C., Katoh, Y., Ozawa, K., Snead, L.: Interlaminar shear strength and trans-thickness tensile strength of CVI and NITE Sic/Sic composites. In: Fusion Reactor Materials Program DOE/ER-0313/52, vol. 52 (2012)
12. Song, Y.S.: Multiscale fiber-reinforced composites prepared by vacuum-assisted resin transfer molding. Polym. Compos. **28**, 459 (2007)
13. Suraj, R., Koohbor, B., Kidane, A.: On the meso-macro scale deformation of low carbon steel. In: Advancement of Optical Methods in Experimental Mechanics, vol. 3, pp. 409–414. Springer International Publishing (2015)

Chapter 16
Design of Al-Nb_2Al Composites Through Powder Metallurgy

E. Bayraktar, M.-H. Robert, and I. Miskioglu

Abstract The present study deals with a new design of aluminum alloy based composites reinforced with Nb_2Al particles and Glass Bubbles (GB) through powder metallurgy. The matrix for these composites was chosen as 1050 pure aluminum alloy powder. The composites were produced under solid state-liquid state sintering conditions to improve the interface between Nb_2Al and the aluminum matrix. Processing parameters were optimized and products were analyzed as a function of the content of reinforcing particles in the matrix, as their interfaces with matrix, etc. Mechanical properties were evaluated by means of compression tests. General results show the feasibility of producing composites by the proposed route economically. Products with good mechanical properties could be obtained. The process gives a new opportunity for the production of a novel material from recycled wastes. Microstructural evaluations were made by Optical and Scanning Electron Microscopes.

Keywords Recycling • Low cost engineering • MMC • Powder metallurgy • Composites

16.1 Introduction

Aluminium-matrix composites (AMC) reinforced with intermetallic compounds can be used instead of ceramics and/or ceramic oxides reinforced composites due to their suitable mechanical and chemical properties (very good cohesion of these particles with aluminium matrix, high corrosion resistance, etc.) [1–5].

The new design of light weight metal matrix composites reinforced with intermetallic particles such as Nb_2Al as we have proposed in this research can be a solution for special applications with suitable mechanical properties with high resistance capacity to corrosion under different environmental conditions [6–8].

In the literature, one can find many work carried out where "Ni–Al" intermetallic compounds were used as reinforcement in the light weight matrix such as aluminium based composites. However, very little work has been carried out with "Nb–Al" intermetallic compounds to reinforce aluminum matrix composites. Additionally, much information about the applications of the Nb_3Al type intermetallic is found for high temperature structural materials because of its high melting point and relatively lower density even if it has very low plastic workability at ambient temperature [4–12]. Today, development of next generation aircraft engines has intended the use of aerospace propulsion system exceeding the performance limits of high temperature super alloys and refractory alloys. In this research, we have used fresh scrap Nb_2Al intermetallic compounds as reinforcement to aluminum matrix composites for low cost production of high performance light weight composites. Additionally, we have also used glass bubbles, spherical hollow bubbles, with diameters that varied from 2 to 30 μm. Glass bubbles are very resistant to high temperatures (~750 °C) and improve the damping capacity of the composite parts up to certain percentages. Essentially we have chosen this intermetallic compounds due to their good interface with matrix. This case was studied by means of Scanning Electron Microscope (SEM).

E. Bayraktar (✉)
Supmeca-Paris, Mechanical and Manufacturing Engineering School, Paris, France

Mechanical Engineering Faculty, Materials Science Department, University of Campinas, Campinas, São Paulo, Brazil
e-mail: emin.bayraktar@supmeca.fr

M.-H. Robert
Mechanical Engineering Faculty, Materials Science Department, University of Campinas, Campinas, São Paulo, Brazil

I. Miskioglu
ME-EM Department, Michigan Technological University, Houghton, MI, USA

C. Ralph et al. (eds.), *Mechanics of Composite and Multi-functional Materials, Volume 7*,
Conference Proceedings of the Society for Experimental Mechanics Series, DOI 10.1007/978-3-319-21762-8_16

16.2 Experimental Conditions

Aluminium-matrix composites were produced using pure aluminum as metal matrix (with a fine grain size; d < 10 μm) and at the levels of 30, 40, 50 and 60 wt% Nb_2Al particles as reinforcement particles.

The reinforcement particles (Nb_2Al) were directly added in the aluminium matrix under two different milling conditions; ball milling was made for 2 h to obtain a homogeneous distribution with a ratio of ball/powder 20:1, and then blending and milling was made for 2 h with a conventional milling device for homogeneous distribution of glass bubbles in the structure.

Low cost manufacturing of the composite samples: A simple tubular ceramic oven was used to prepare sintering as an effective method. The aluminium matrix with a purity of 99.7 % was used as the base material (Merck Co, France) with a major grain size of <5 μm after ball milling. The purity level of Nb_2Al was found to be 95 %. Distributions of the Nb_2Al particle sizes are variable that was measured with Laser Granulometer (10–60 μm).

Then, blended powders were compacted by cold isostatic pressing (CIP) with a green compact pressure of 400 MPa, intending to produce an initial green density ranging from 85 to 95 %. The aspect ratio of this geometry was 0.85. Sintering conditions were carried out under argon atmosphere to prevent the oxidation during the sintering. Sintering temperature was fixed for all the specimens as 660–680 °C in the ceramic tubular oven.

Two different groups of composites were prepared: First group is without glass bubbles the second group is with a 5 vol% glass bubbles in order to compare the mechanical properties. Sintered products were then tested in compression under quasi-static loading conditions. Tests were carried out with a servo-hydraulic INSTRON Universal test system (model Instron 5500R, equipped with a load cell of 25,000 kgf) at a quasi-static loading rate (initial rate: 10 mm/min and second rate: 5 mm/min rate). Maximum load endpoint was 4500 N.

Microstructures of the composites processed here were observed by Scanning Electron Microscopy (JOEL-SEM).

16.3 Results and Discussions

In Fig. 16.1, binary phase diagram of Nb Aluminium couple was shown. Regarding to this diagram, the design of composites made in this work is found around certain intermetallic zone (Nb_2Al and Al_3Nb).

However, all of the chemical analyses and phase analyses have been carried out after sintering operations. Only, fresh scrap Nb_2Al compound were provided by the Brazilian Nb company and this compound was analyzed by XRD, X-ray

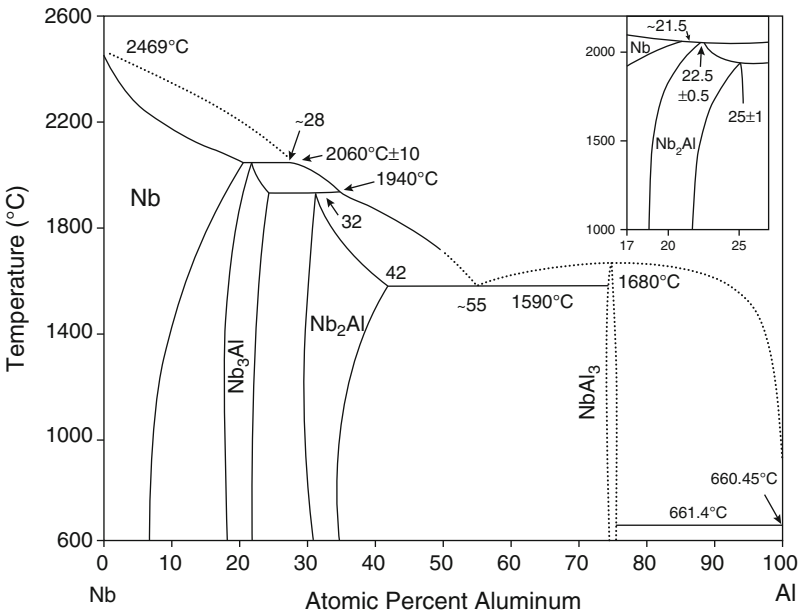

Fig. 16.1 Binary phase diagram for Nb-Al couple

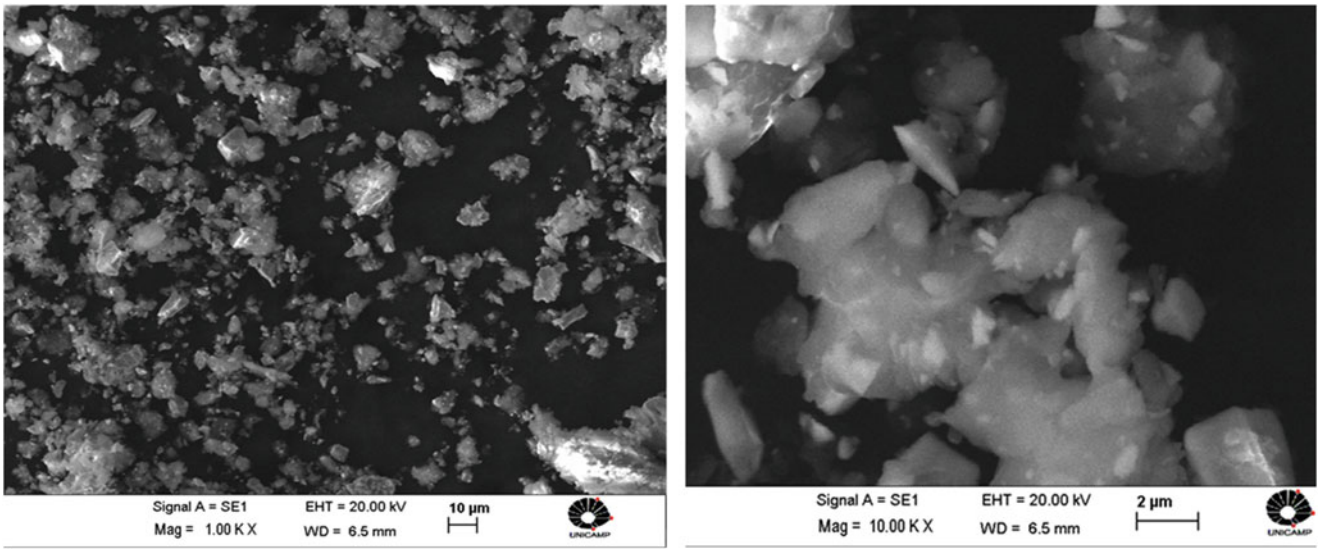

Fig. 16.2 Nb_2Al intermetallic powders before (*left column*) and after milling (*right column*)

diffraction in as received conditions. All the intermetallic compounds were cleaned carefully and then milled at high speed for 1 h before the mixing with aluminium powder (it also was high speed milled during 1 h before the blending stage). Fig. 16.2 shows the Nb_2Al intermetallic powders before (left column) and after milling (right column). By this way, very hard particles were milled by using high speed milling device (4000 rpm).

Results of differential thermal analysis of the Aluminum, Glass Bubbles (GB) powders are shown in Fig. 16.3. In the same Figure images of the powders obtained by SEM are also presented. The critical temperature-transformation points of the different raw materials can be observed in the DTA curves: a high energy transformation is observed for Al powders around 650 °C without mass loss, related to the melting point of the aluminum. For Glass Bubbles, it shows some reaction when heating from room temperature to 140 °C, with around 5 % of mass addition. This can be related to some chemical reaction in the glass material and must be further investigated. SEM images show aluminum powders with irregular, elongated shape, with average dimensions ranging from 16 to 300 µm. Hollow glass spheres are perfectly rounded, presenting diameters from 2 to 30 µm with very low density (0.20 g/cm^3).

Figure 16.4 shows the results of quasi-static compression tests for all of the compositions investigated. They contain 30, 40 50 and 60 wt% Nb_2Al intermetallic compounds respectively Evolution of the stress values depending on the deformation were compared with different parameters, for example, peak values (stress as MPa) are found very similar for the compositions containing 40, 50 and 60 wt% Nb_2Al intermetallics (200–250 MPa) for three compositions but only the specimens called 30Nb_2Al (containing 30 wt% Nb_2Al) have given much lower values, around 175 MPa.

The compositions discussed in Fig. 16.4 do not contain glass bubbles. Other test results carried out on the second series of the composites containing additionally 5 vol% glass bubbles. These two test series are summarized in Fig. 16.5 (because of the small scale of the axes, the compositions here indicated with shortened names, e.g. Nb30 means first series containing 30 wt% Nb_2Al and Nb30-5 is 30 wt% Nb_2Al with 5 vol% glass bubble added, and so on).

From the two sets of compression tests, it seems that the role of Glass Bubbles is relevant on the plasticity of the composites and they give better ductility if they are added in the matrix up to 5–10 vol%. Some of the test results not given here have shown that beyond these values (>10 vol% of Glass Bubbles) the effect is a decrease in ductility; the material becomes brittle at the higher percentages of this kind of additive. Figures 16.6, 16.7 and 16.8 shows all the details of the composites designed in this study with interface positions of matrix/reinforcements. The results showed that compacting and sintering at higher levels lead to the transformation of Nb_2Al particles to thin layers of Al_3Nb. It was also shown that the prolonged milling time to produce Al_3Nb intermetallic and the prolonged ball milling procedure for mixing the powders, both, promote the diffusion process at reinforcement/matrix interface.

In the same way, Fig. 16.8 indicate special zones taken from different compositions 30Nb_2Al, 50Nb_2Al-5 and 60Nb_2Al, and EDX analyses have been performed on the different regions of these special zones. Regarding to the Figs. 16.6, 16.7 and 16.8,

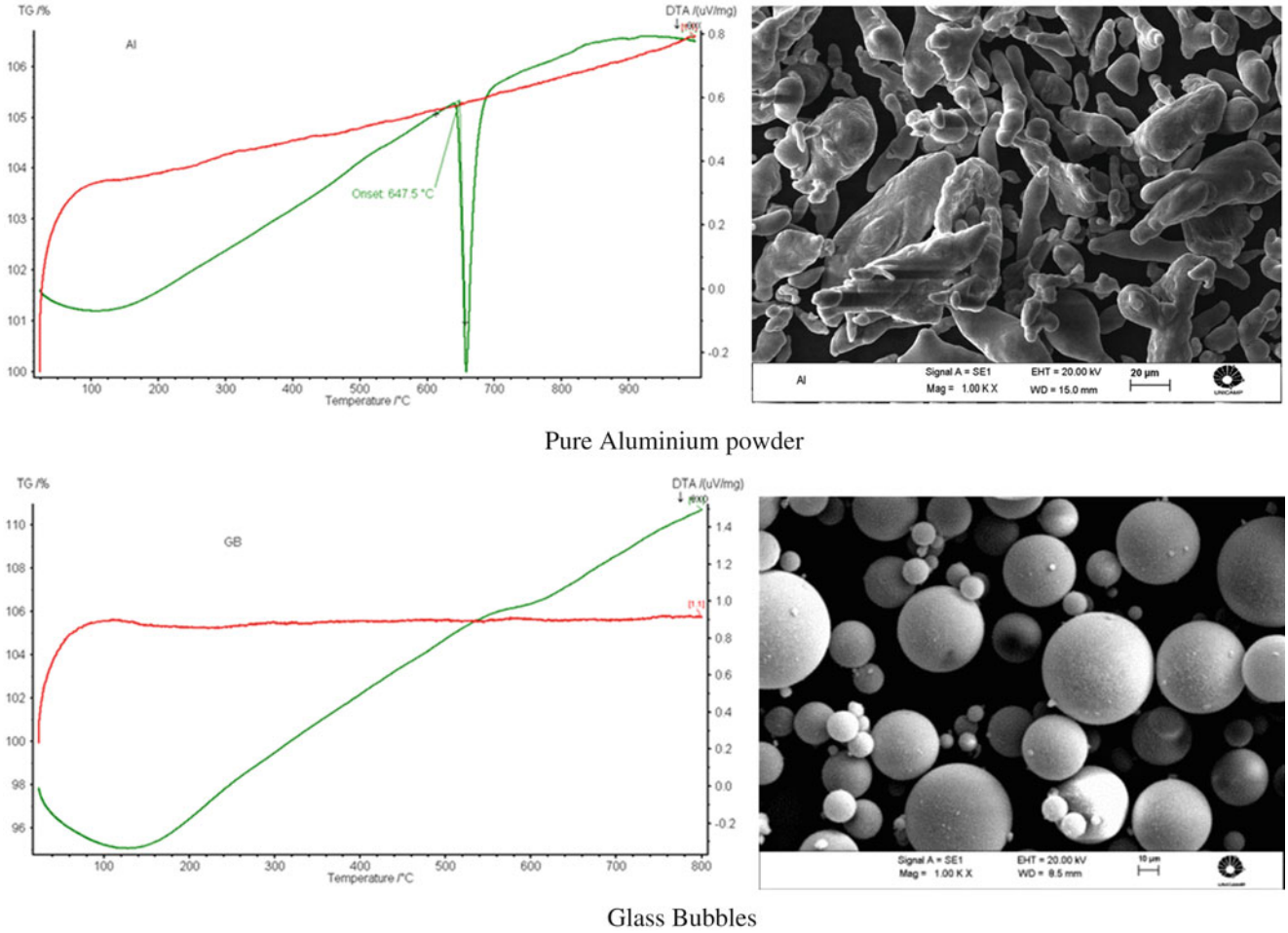

Fig. 16.3 Results of differential thermal analysis (DTA) and thermogravimetry (TG) of the powders used to produce composites *left column* and images obtained by SEM of the corresponding material, *right column*

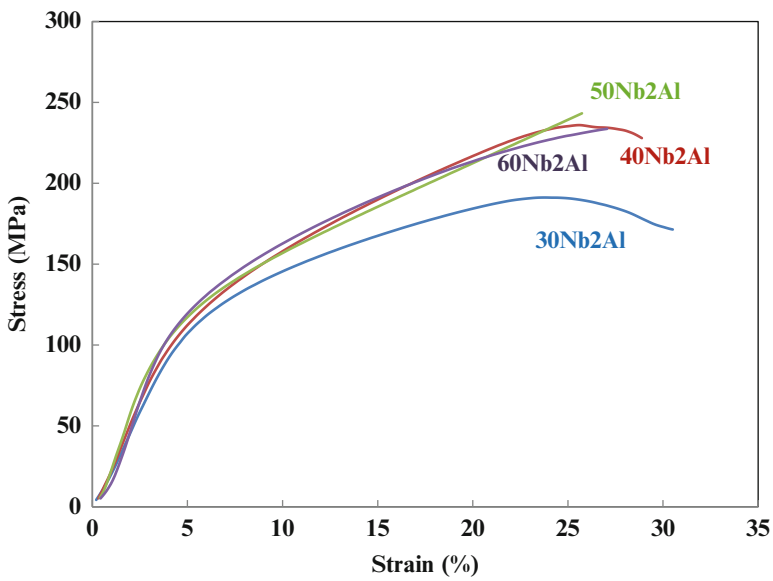

Fig. 16.4 Results of quasi-static compression tests for the composites produced

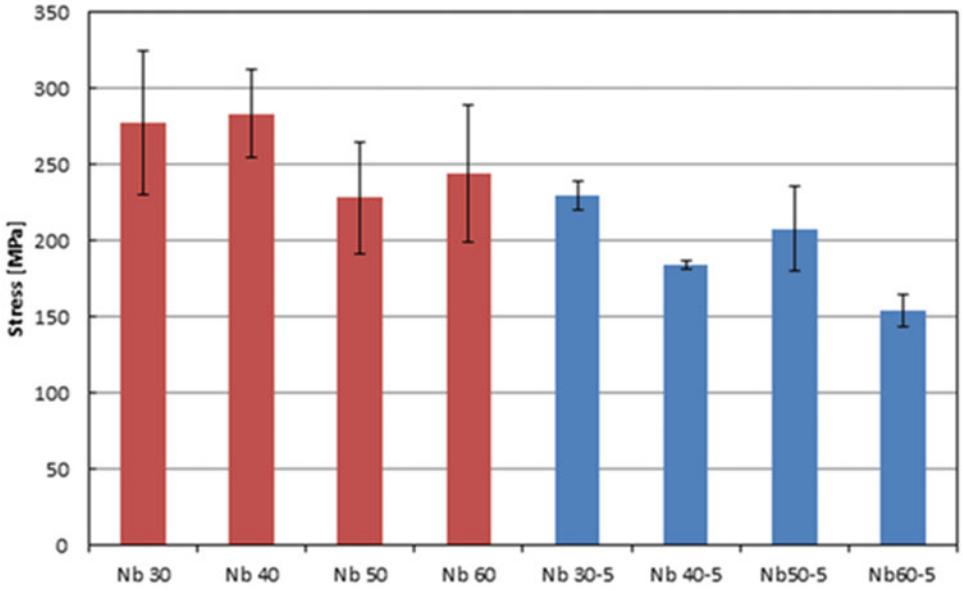

Fig. 16.5 Comparison of two series composites with only Nb_2Al and with Nb_2Al plus 5 vol% glass bubbles

very strong cohesion is observed at the interface of these compositions. However, the agglomerations in some areas in the structure are also observed due to the homogenization problem related to milling.

It is real that interfacial interactions at the matrix/reinforcement interface is considerably influenced by blending and mixture—milling time (mixing condition of Al and Nb_2Al powders), compacting pressure and most significantly sintering temperature.

Homogenous and fine distribution of reinforcement particles for the Al/Nb_2Al composites was achieved by ball milling. This apparently improved the mechanical properties of sintered composite and encouraged phase transformation of reinforcement.

All of the experimental data (in the frame of this research, 200 specimens were produced at the different compositions) have shown that a new chemical bonding occurs between light (soft particles (here aluminium as matrix) and hard particles (here Nb_2Al intermetallic) due to thermal reaction at the high temperatures. All of the experimental work carried out on these compositions have shown that low sintering temperature ($T_s < 630$ °C) can cause micro pores at the interface of matrix/intermetallic reinforcements. Very suitable cohesion at the interface can only be achieved at high sintering temperatures, i.e. between 660 and 680 °C.

By this way, a very stable vibrational chemical bonding between the matrix and intermetallic particles can be provided. For example, it should become a chemical bonding between light atoms (e.g. Aluminium) and heavy atoms (e.g. Nb and or Nb_2Al intermetallic particles) by application of high sintering treatment [2, 5, 7]. During the high sintering treatment a vibrational chemical bonding mechanism can occur between the two parts, namely the aluminum matrix and the Nb_2Al intermetallic reinforcement.

Microstructure of the composite sintered at 680 °C show that Nb_2Al particle reinforcements show quasi homogeneous interface. Increasing the sintering temperature can provide vibrational chemical bonding easily under the effect of thermal diffusion. Therefore, reaction phases at the interface matrix/intermetallic can be caused by a stable interface.

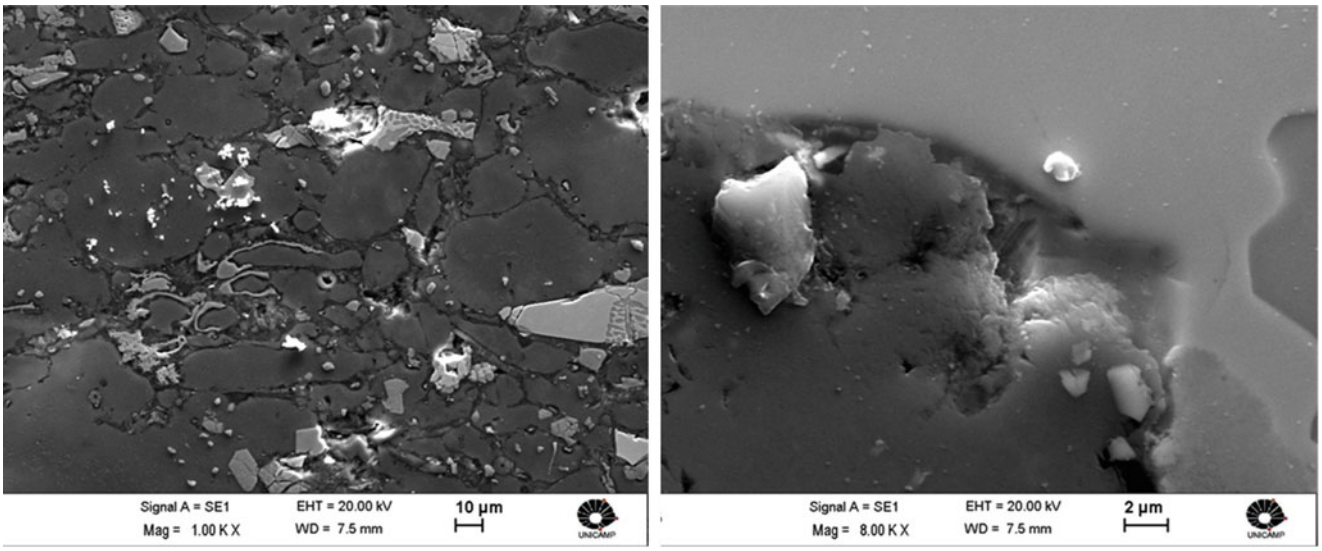

Fig. 16.6 Microstructure (*left column*) interface of matrix/reinforcement of the compositions called 30Nb_2Al and 40Nb_2Al (*right column*)

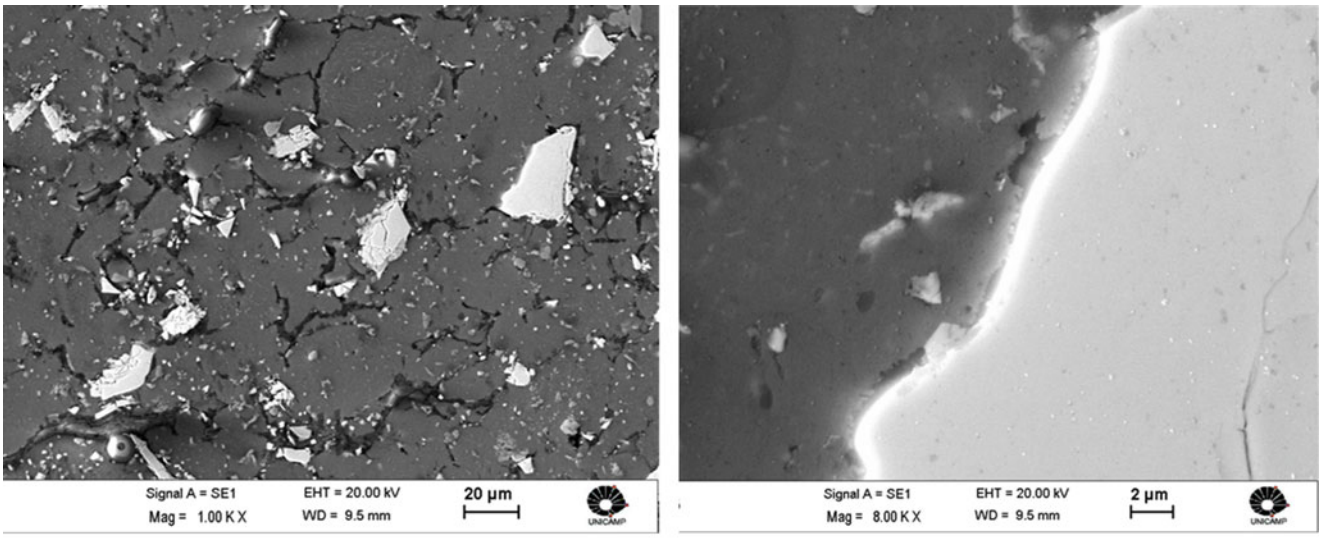

wt% 50-Nb_2Al

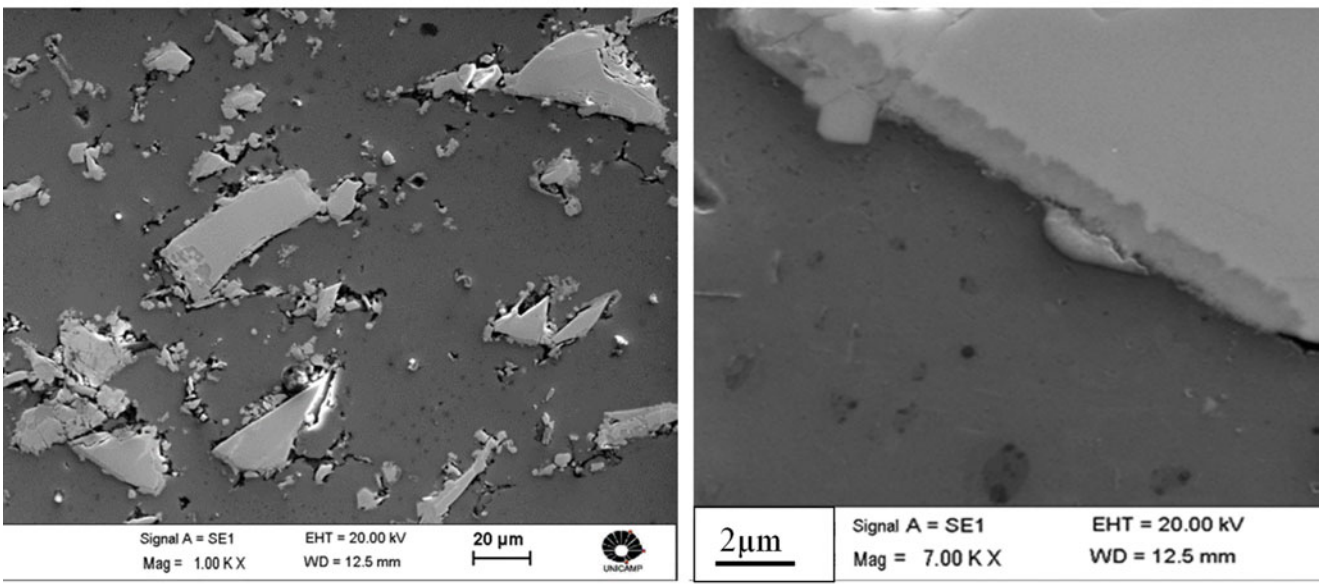

wt% 60-Nb_2Al

Fig. 16.7 Microstructure (*left column*) interface of matrix/reinforcement of the compositions called 50Nb_2Al and 60Nb_2Al (*right column*)

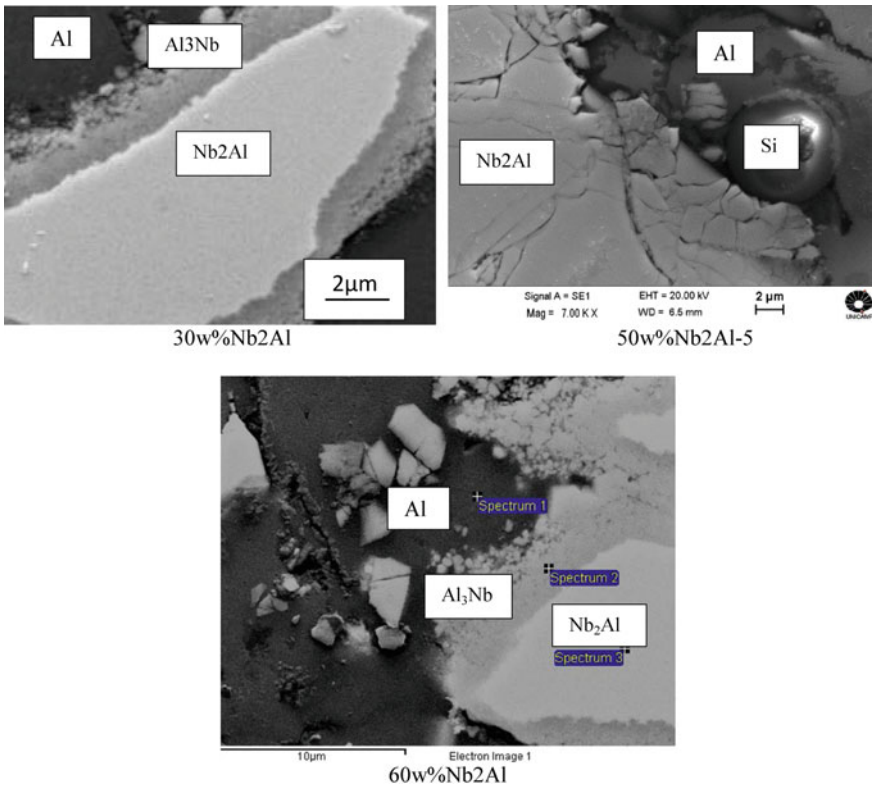

Fig. 16.8 Special zones taken from different compositions $30Nb_2Al$, $50Nb_2Al$-5 and $60Nb_2Al$ and EDX analyses have been made on the different parts of these special zones

16.4 Conclusions

Interfacial interactions at the matrix/reinforcement interface is considerably influenced by blending and mixture—milling time (mixing condition of Al and Nb_2Al powders), compacting pressure and most significantly sintering temperature.

Homogenous and fine distribution of reinforcement particles for the Al/Nb_2Al composites can be carried out efficiently by ball milling. This process apparently improved mechanical properties of the sintered composite and encouraged phase transformation of reinforcement.

Low sintering temperature (T_s < 630–640 °C) can cause regularly micro pores at the interface of matrix/intermetallic reinforcements. Good cohesion at the interface can only be achieved at high sintering temperatures, i.e. between 660 and 680 °C.

By this way, a very stable vibrational chemical bond between the matrix and intermetallic particles can be provided. Microstructure of the composite sintered at 680 °C shows that Nb_2Al particle reinforcements show quasi homogeneous interface. Increasing the sintering temperature can provide easily vibrational chemical bonding under the effect of thermal diffusion. Therefore, reaction phases at the matrix/intermetallic interface can be caused by a stable interface.

Acknowledgements Authors want to thank financial support from CNPq—Conselho Nacional de Desenvolvimento Científico e Tecnológico (Brazil); Program French Catedra UNICAMP/French Embassy in Brazil.

References

1. Velasco, F., da Costa, C.E., Rodero, B., Santamarta, C., Torralba, J.M.: Intergranular Corrosion Resistance of Fe_3Al/2014 Al Particulate MMC. J. Mater. Sci. Lett. **19**, 61–63 (2000)
2. Bayraktar, E., Ayari, F., Tan, M.-J., Tosun Bayraktar, A., Katundi, D.: Manufacturing of aluminium matrix composites reinforced with iron-oxide nanoparticles: microstructural and mechanical properties. Metall. Mater. Trans. B **45B**, 352–362 (2014)
3. Fogagnolo, J.B., Ruiz-Navas, E.M., Robert, M.H., Torralba, J.M.: The effects of mechanical alloying on the compressibility of aluminium matrix composite powder. Mater. Sci. Eng. A **355**(1), 50–55 (2003)

4. Lieblich, M., Gonzales-Carrasco, J.L., Garcia-Cano, F.: Asymmetrical phase growth in a PM Al/Ni_3Al composite. J. Mater. Sci. Lett. **18**, 905–908 (1999)
5. Ferreira, L.M.P., Robert, M.H., Bayraktar, E.: Production of aluminium/SiC/$NiAl_2O_4$ MMCs by thixoforming of recycled chips. Solid State Phenom. **217–218**, 286–293 (2015)
6. Sajjadi, M.: Evaluation of characteristics of interfacial phases produced in Al/Ni_3Al composite during manufacturing. Mater. Sci. Appl. **2**, 1340–1348 (2011)
7. Ferreira, L.M.P., Robert, M.H., Bayraktar, E., Zaimova, D.: New design of aluminium based composites through combined method of powder metallurgy and thixoforming, AMR. Adv. Mater. Res. **939**, 68–75 (2014)
8. Lu, L., Lap, M.D., Zhang, S.: Fabrication of Ni_3AI intermetallic compound using mechanical alloying technique. J. Mater. Process. Technol. **48**(1), 683–690 (1995)
9. Wang, Y.S., Tan, M.J., Chua, B.W., Bayraktar, E.: YSZ-reinforced Mg-based amorphous composites: processing, characterization and corrosion. Adv. Mater. Res. **939**, 122–129 (2014)
10. Velasco, F., da Costa, C.E., Candela, N., Torralba, J.M.: Fracture analysis of aluminium matrix composite materials reinforced with (Ni_3Al)p. J. Mater. Sci. **38**(3), 521–525 (2003)
11. Diaz, C., Gonzalez-Carrasco, J.L., Caruana, G., Lieblich, M.: Ni3Al intermetallic particles as wear-resistant for Al-based composites processed by powder reinforcement metallurgy. Metall. Mater. Trans. A **27**, 3259–3266 (1996)
12. Kusaka, K., Fujine, M., Okabe, M., Endo, H.: Mechanical properties of Nb3Al-based intermetallics prepared by a ceramic mold-HIP process. Mater. Trans. JIM **40**(7), 571–577 (1999)

Chapter 17
Influence of Heat Treatments on Microstructure and Mechanical Behaviour of Compressible Al Matrix, Low Density Composites

M.H. Robert, E.M. Nascimento, and E. Bayraktar

Abstract This work investigates the influence of solution/ageing treatments on mechanical properties under compression of a compressible, low-density composite based on AA7075 alloy as matrix, reinforced with porous ceramic particulates (foamed $SiO_2/Al_2O_3/Fe_2O_3$). Composites were produced by thixoforming and products were characterized related to mechanical behaviour under semi-static compression, in different conditions: as thixoformed and after solution/ageing treatments. Structure of thixoformed material requires particular heat treatment conditions due to coarser secondary phases, when compared to as-cast situation. Products presented relative density around 0.5 and compression behaviour characteristic of cellular metals, showing plastic deformation plateau due to collapse of porosity, which gives the composites potential applications as energy absorbers. Effect of heat treatments upon the properties showed increase in the order of 2× of the maximum strength required to start plastic deformation and 5× in the average plateau strength, with only 15 % reduction of plastic deformation.

Keywords Aluminium composites • Thixoforming • Low density composites • Aged structures • Compression behaviour

17.1 Introduction

The great majority of conventional metal matrix composites is related to Al alloys with ceramic particles such as SiC, Al_2O_3, SiO_2 or intermetallic particles such as AlN, Ni_3Al, $NbAl_3$ and others as reinforcing elements. More recent developments brought to light MMCs presenting low density, by using porous or compressible ceramic particles as reinforcement. Depending on the density of reinforcements and its relative amount in the metal matrix, this kind of composites can present very low relative density and can be called syntactic foams [1–3]. Besides presenting typical combination of properties of metallic matrix and ceramic constituents, can also present characteristics of cellular materials, such as low density and high plastic deformation under compression. Results on mechanical behaviour of Al alloys reinforced with porous ceramic particles were presented in previous works [4–6]. Processing of composites usually requires complex techniques to ensure proper incorporation and dispersion of reinforcing particles in the metal matrix. Sintering of isostatically compacted powders, friction stir processing, centrifugal casting, liquid infiltration under high pressure, *in situ* precipitation of phases, are among processing methods to produce MMCs with particulate reinforcements [7–12]. However, in the production area, obtaining materials with improved properties allied to low processing costs are issues to be pursed through the development of new manufacturing alternatives; in this scenario, the utilization of low cost raw material associated with low energy processing techniques as thixoforming has showed to be an interesting option of low cost processing of low density Al-MMCs, as shown in previous works by the authors [5, 6, 13]. Thixoformed structures present globular primary phase with homogeneous content of alloying elements in solution, and coarse eutectic in globules boundaries. Eutectic component can also be eventually present within globules of primary phase as consequence of entrapping of liquid, rich in alloying elements, during structure modification at the high temperatures required to produce the thixotropic semi-solid.

Prof. Bayraktar is visiting professor at UNICAMP/Campinas-SP-Brazil

M.H. Robert (✉) • E.M. Nascimento
Mechanical Engineering Faculty, University of Campinas, Campinas, São Paulo, Brazil
e-mail: helena@fem.unicamp.br

E. Bayraktar
Supmeca-Paris, Mechanical and Manufacturing Engineering School, Paris, France
e-mail: emin.bayraktar@supmeca.fr

C. Ralph et al. (eds.), *Mechanics of Composite and Multi-functional Materials, Volume 7*,
Conference Proceedings of the Society for Experimental Mechanics Series, DOI 10.1007/978-3-319-21762-8_17

The presence of coarse eutectic can result in poor mechanical behaviour of thixoformed products; therefore, solubilisation and ageing treatments shall be required to improve the material properties. This work investigates the effect of solubilisation and ageing treatments upon the composite AA7075/porous $SiO_2/Al_2O_3/Fe_2O_3$, produced by thixoforming.

17.2 Experimental Procedures

Aluminium AA7075 alloy (6.29 wt% Zn, 2.38 wt% Mg and 2.11 wt% Cu) was used as matrix; porous, foamed $SiO_2/Al_2O_3/Fe_2O_3$ particles (called cinasite) were used as reinforcement. Ceramic particles present density 0.85 g/cm^3, and sizes in the range 1–3 mm. Figure 17.1 shows typical internal structure of the foamed ceramic granulate used.

Composites containing 50 % vol (27 wt%) of cinasite were produced by thixoforming. A layer of loose porous particles was placed in a steel die and covered with a plate of the metal alloy. The assembly was heated to 627 °C to promote formation of the thixotropic semi-solid, followed by thixoforming.

Thixoforming temperature was defined to allow formation of 0.55 liquid fraction in the metallic alloy, according to data supplied by thermodynamic calculations using commercial software (Scheil conditions were considered for calculations). Applied pressure during thixoforming did not exceeded 3.5 MPa.

Samples produced were analysed by RX tomography to check internal quality and dispersion of particles in the matrix; density of product was measured by picnometry using He gas.

Thixoformed composites were submitted to solubilising followed by ageing heat treatments according to the thermal cycle presented in Fig. 17.2.

Samples from composites in the as-thixoformed, solubilised and aged conditions were prepared using conventional metallographic techniques for microstructure analysis by optical and electronic microscopy (OM and SEM). Indentations were made in the microstructures to establish lines for microprobe analysis, to evaluate the effect of heat treatment in the

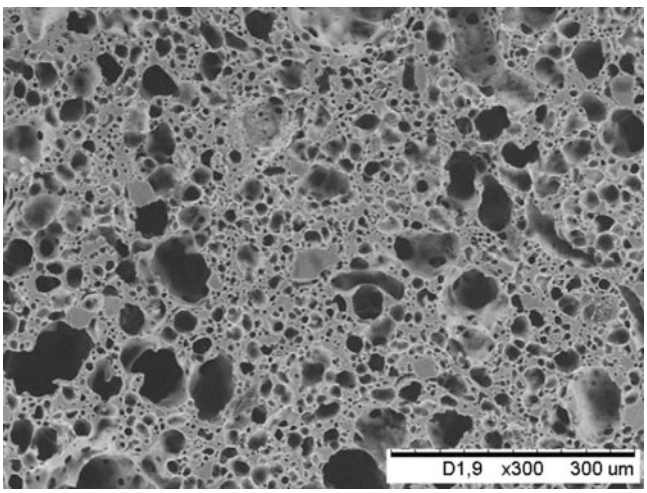

Fig. 17.1 Internal structure of foamed ceramic particles ($SiO_2/Al_2O_3/Fe_2O_3$) used as reinforcement (SEM)

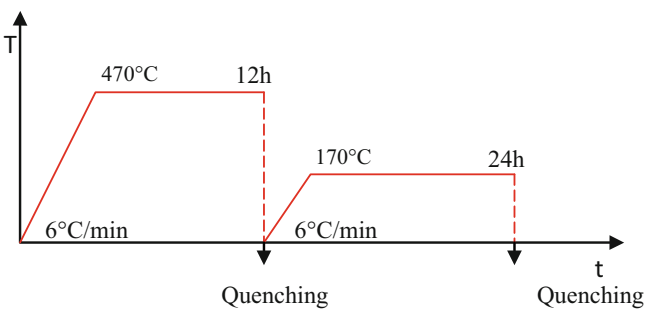

Fig. 17.2 Ageing thermal cycle for thixoformed AA7075/cinasite composites

distribution of main alloying elements in the matrix. Micro-hardness of the metallic matrix was also evaluated. Compression semi-static tests were performed in a conventional MTS machine, using punch speed of 0.15 mm/s [deformation rate $<$ (1/10)/s], at room temperature.

17.3 Results and Discussions

17.3.1 General Results: Typical Composite Product

Figure 17.3 shows typical AA7075/cinasite composite produced by thixoforming: it can be observed the general dispersion of the particles throughout the volume of the material. Tomography results, as shown in some typical slices, show good macro-distribution of the reinforcing particles within the material. Excellent forming behavior of the alloy was observed in the conditions employed; the thixotropic characteristic of the semi-solid required low pressure (around 3.5 MPa) to fill the mould and good reproduction of die cavity was achieved.

According to microstructures presented in Fig. 17.4, the matrix alloy shows globular structure typical of thixoformed material: globular primary phase (α) and eutectic constituent (mainly $MgZn_2$, AlCuMgZn and other complex intermetallics) in interglobular boundaries. It can be also observed the presence of pools of eutectic phases inside globules of the primary phase, due to liquid entrapment during coarsening of dendrites in liquid environment at the thixoforming temperature; heavy segregation is observed in the internal surface of the primary phase.

As observed in detail in (c), reinforcing particle/Al matrix interface can present good interaction, probably due to liquid metal penetration in the porosity of the ceramic particles. Unlike most of ceramic particle/metal matrix interfaces in conventional composites, were compact particles are used and poor interactions are the usual consequence, in the case of porous ceramic particles, some better result can therefore be expected. This apparently improved quality of interfaces shall result in better mechanical properties of composites and deserves further and more detailed investigation.

Measurements of density of obtained composites resulted in the value 1.58 $\pm$ 0.05 g/cm^3, which means a relative density of 0.56, taking 2.81 g/cm^3 as the density of bulk AA7075. This value is compatible with typical relative densities of syntactic cellular metals [14–16]. Therefore, characteristics of mechanical behavior of metallic foams can be expected in the produced composites.

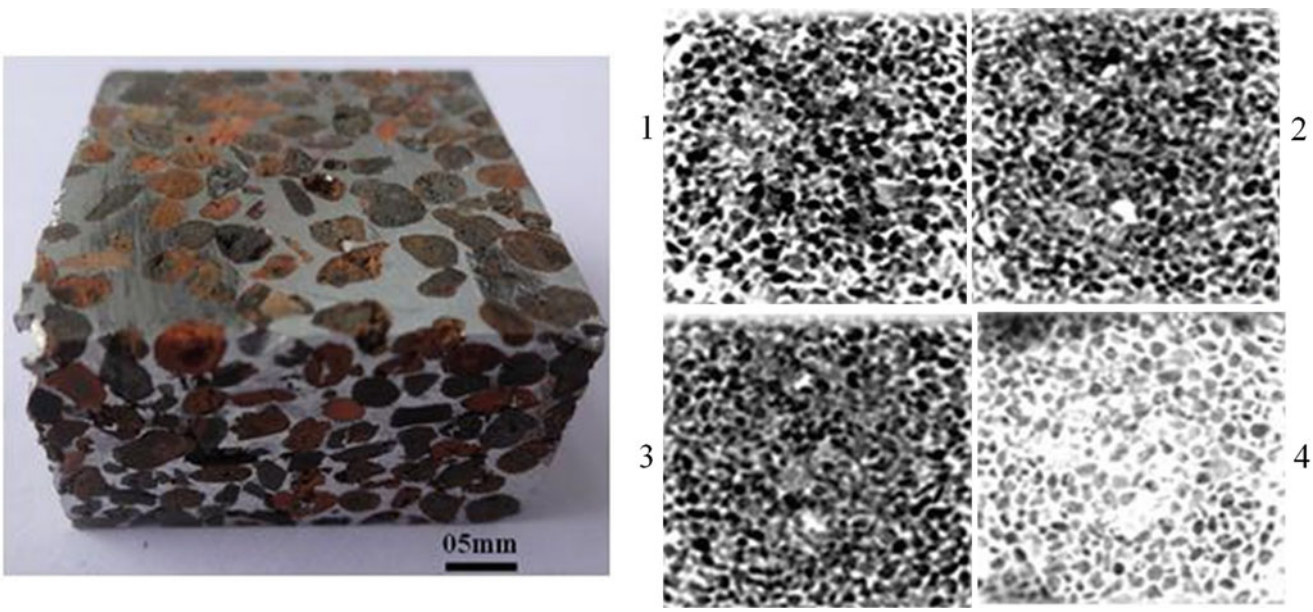

Fig. 17.3 Typical AA7075/cinasite composite produced by thixoforming: general view and example of tomography results (parallel slices 1–4 taken each 1.5 mm)

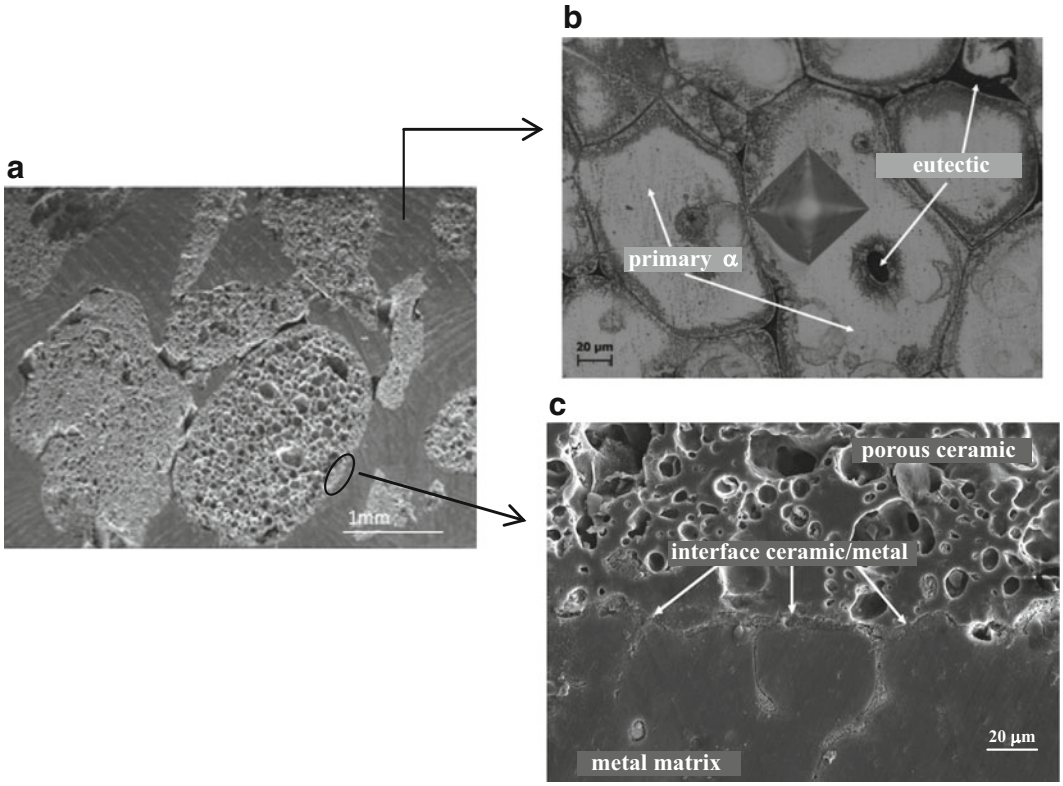

Fig. 17.4 AA7075/cinasite composite produced by thixoforming: (**a**) general view (OM); (**b**) microstructure of matrix (OM); (**c**) detail of matrix/reinforcement interface (SEM)

17.3.2 Effect of Heat Treatment on the Composite Microstructure

The influence of heat treatment on the microstructure of produced AA7075/cinasite composites is shown in Fig. 17.5.

In the thixoformed condition structure contains globular α phase and secondary phases in the globules boundary. Secondary phases constitution depends on the kinetics of the liquid solidification and are usually intermetallics with different compositions such as $MgZn_2$ (called phase η), $CuMgAl_2$ (phase S), $CuMg_4Al_6$, and AlCuMgZn, Mg_xZn_y, $Mg_xZn_yAl_z$ (phase M), $Mg_x(Al, Cu, Zn)_y$, whit different stoichiometry. For further information on equilibrium phases at different solidification conditions for AA7075 alloy, see [17, 18]. Most of these intermetallics are formed in the liquid around 476 °C, according to results obtained by thermodynamic simulations using commercial software. Primary α phase presents reduced and homogeneous content of the main alloying elements, Zn, Mg and Cu, in solution, as microprobe results shown in (a). This is a consequence of the heating and holding the structure at 627 °C for around 5 min required to promote the necessary liquid fraction and the spheroidisation of the structure, which promoted elimination of micro-segregation within the primary phase.

After solubilising, secondary phases tend to disappear by dissolution and diffusion of their constituents in the primary phase leads to the increase of Zn, Cu and Mg in solution in α phase, as observed in the results shown in (b). Eventual peaks of high content of specific element are related to the presence of intermetallics in the globules boundary or within the primary phase where liquid was entrapped in the spheroidisation process. One of such peak, with high Mg content, can be observed in point 5, corresponding to a globule boundary. Therefore, non dissolved intermetallics can still be present in the solubilising conditions employed.

Figure 17.5c shows microstructure and microanalysis results after ageing. The super-saturated solid solution produced by solubilisation drives towards equilibrium conditions at 150 °C promoting precipitation of phases within the primary α. As a result of this precipitation, aged material presents lower content of alloying elements in solution, as observed in (c), when compared to (b) and also to (a). Precipitated phases can be observed in the microstructure.

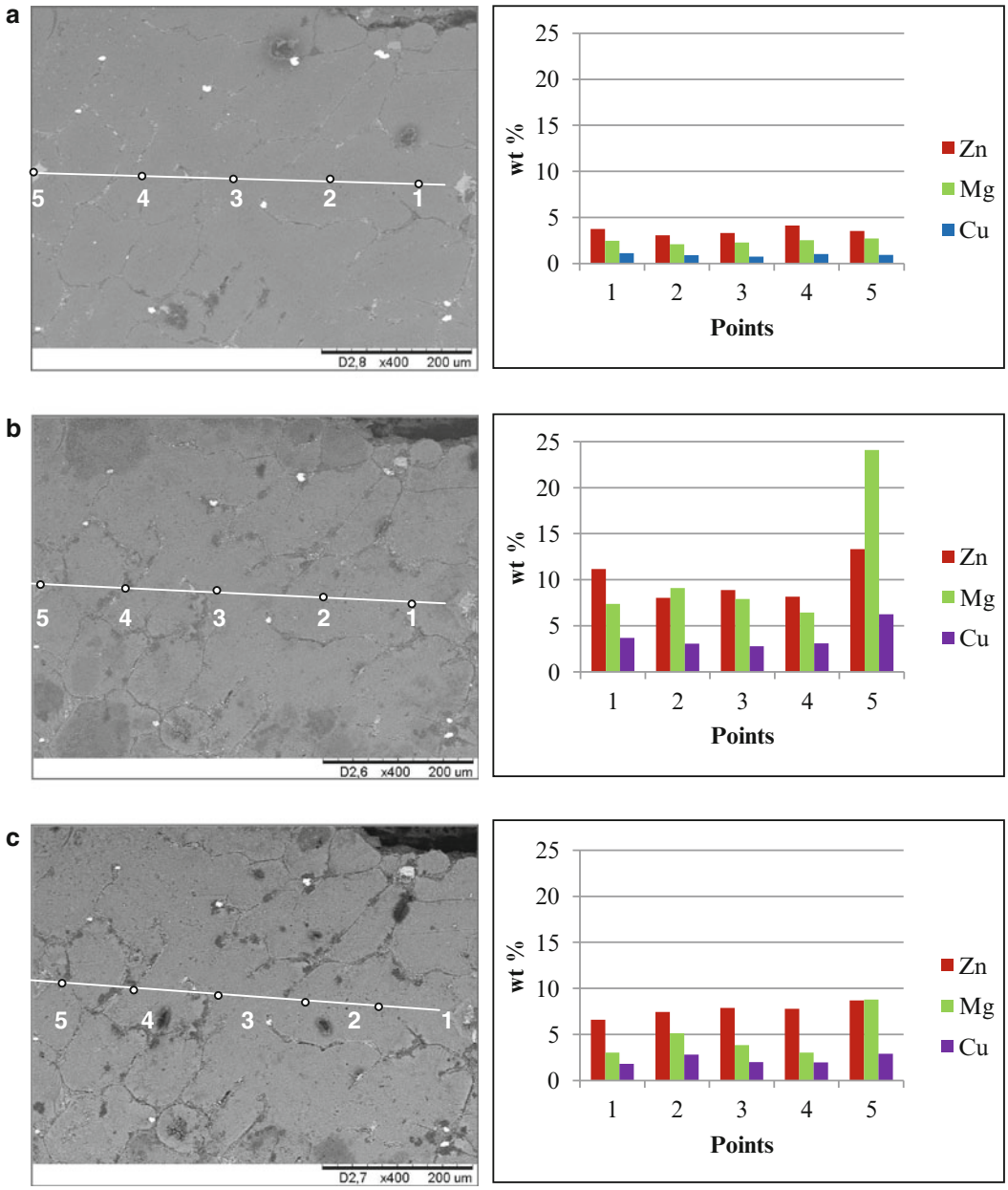

Fig. 17.5 Microstructures and results of microprobe analysis of AA7075/cinasite composites in different conditions: (**a**) as-thixoformed; (**b**) solubilised at 470 °C/12 h; (**c**) aged at 170 °C/24 h

17.3.3 Effect of Heat Treatment on Hardness and Mechanical Behaviour Under Compression

Micro hardness of the Al matrix increased as consequence of the heat treatment imposed to the thixoformed composites; values are presented in Table 17.1 and graphically in Fig. 17.6. When comparing thixoformed and aged conditions, the total increase in hardness is around 30 %. Solubilised condition presented slight higher (~5 % higher) due to probably incomplete dissolution of intermetallics in the Al matrix.

Results on semi-static compression tests of AA7075/cinasite composites are presented in Fig. 17.7. Some specific mechanical characteristics are presented quantitatively in Table 17.1. Stress × deformation curves for four samples in the same condition are presented, to evaluate the repeatability of results.

Table 17.1 Values of σ_{max}, σ_{pl} in semi-static compression tests of AA7075/cinasite composites, and micro hardness of the metallic matrix, in different conditions

	As-thixoformed (1)	Solubilised	Aged (3)	Quantitative effect (3)/(1)
HV (Al matrix)	128 ± 14	134 ± 15	169 ± 15	~1.3 (30 %)
σ_{max} (MPa)	37 ± 7	64 ± 10	74 ± 8	~2 (100 %)
σ_{pl} (MPa)	12 ± 7	44 ± 16	59 ± 19	~5 (400 %)
% d_D	58 ± 7	59 ± 7	50 ± 2	~0.86 (14 %)

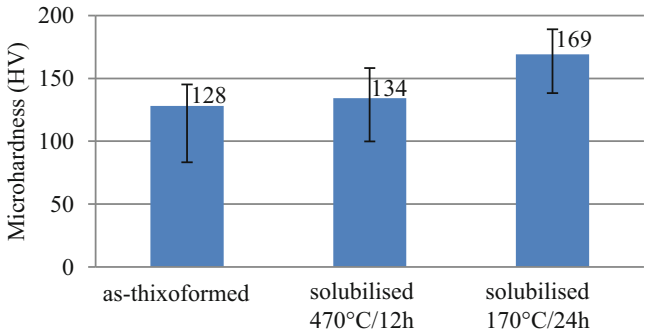

Fig. 17.6 Vickers micro hardness (HV) of the matrix structure in AA7075/cinasite composites, in different conditions

As a general observation for all conditions, it can be noted that stress × deformation curves show a initial elastic behavior kept at some significant deformation extent, followed by large deformation plateau under low stresses and, at the latest stage of deformation, increase in applied stresses is observed. This behavior is typical of cellular materials, where the wide plateau of plastic deformation at low stresses is related to the collapse of porous cells within the metallic matrix. Densification of the material leads to increase of the required stress to continue deformation in the final stages, as collapse of porous ceramic is no longer the main deformation mechanism and the role of the metallic matrix is now imposed in the material deformation behavior.

The significant area under the curve in the plastic deformation region states the ability of the composite to absorb high quantity of energy during deformation. Therefore, composites AA7075/cinasite not only present low density but also perspective application as energy absorbers.

It also can be observed, as a general result, some dispersion in the results of testing 4 different samples in the same condition. This dispersion can be understood under the light of the intrinsic heterogeneity of particulate composites and the structure of the foamed ceramic particles. However, results obtained for the distinct materials conditions analyzed is clearly differentiable.

In thixoformed condition, resulting stress × deformation behaviour as in Fig. 17.7a shows high plastic deformation (values around 60 %), low stress to initiate plastic zone (values of σ_{max} around 40 MPa) and deformation plateau at very low stresses (σ_{pl} around 12 MPa). Such low level of stresses to promote large plastic deformation ensures the high energy absorption ability of the composite.

Dissolution of secondary phases during solubilisation and enrichment of Zn, Mg, Cu in the α phase results in higher stresses in the elastic limit and in the plastic deformation plateau, when compared to thixoformed condition. Total plastic deformation, however, does not suffer a significant decrease (see Table 17.1). Results related to the aged condition, shown in Fig. 17.7c, show lower plastic deformation, and also higher stresses are required to promote deformation in this condition of the microstructure.

Therefore, solubilising and ageing treatments has significant effect over the material mechanical behaviour under compression, promoting increasing of around 100 % in σ_{max} and around 400 % in $\sigma_{pl.}$ On the other side, the effect of the treatments was not so effective in reducing the plastic deformation (overall reduction in the order of 14 %). Therefore, the material can keep absorption ability even at higher stress solicitations, without crashing at early deformation levels.

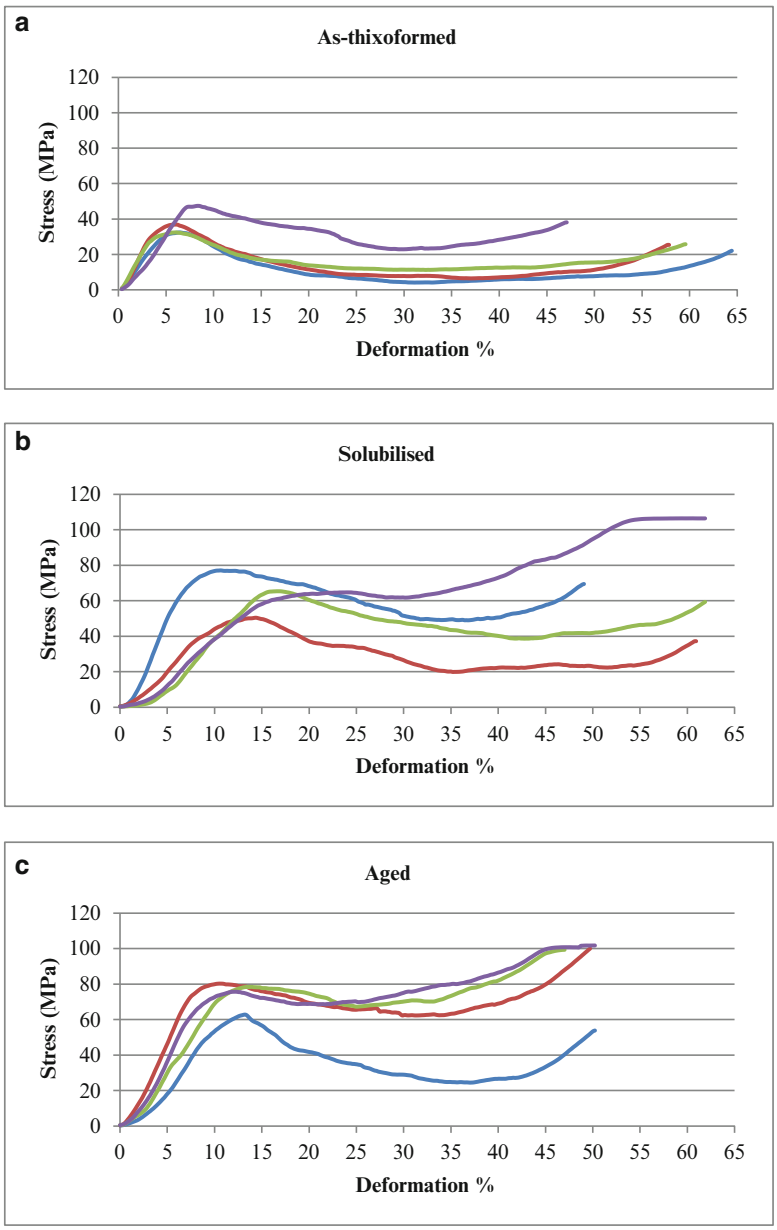

Fig. 17.7 Stress × deformation curves in semi-static compression tests of AA7075/cinasite composites in different conditions: (**a**) as-thixoformed; (**b**) after solubilising (470 °C/12 h); (**c**) after ageing (170 °C/24 h)

17.4 Conclusions

Composites AA7075/27 wt% of low density, foamed $SiO_2/Al_2O_3/Fe_2O_3$ particles, produced by thixoforming present wide plateau of plastic deformation under compression at low stresses, which gives the material ability to absorb energy in potential applications such as in impact situations.

Solubilising/ageing treatments can improve compression behaviour of the thixoformed composite, which presents in this condition coarse boundaries in the alloy microstructure. Results indicate that solubilising conditions investigated (470 °C/12 h) was not able to promote complete dissolution of secondary phases but even so significant increase in σ_{max} and σ_{pl} was reached. Micro hardness of the metal matrix and plastic deformation of the material were not so affected. Ageing conditions investigated (170 °C/24 h) promoted significant increase in σ_{max} (100 %) and σ_{pl} (400 %) when compared to thixoformed condition. Reduction of only around 14 % in plastic deformation was observed. This behaviour indicates high ability of energy absorption during mechanical solicitations under compression not only at low stresses.

Acknowledgments Authors want to thank financial support from CNPq—Conselho Nacional de Desenvolvimento Cientifico e Tecnológico (Brazil) and to Program French Catedra UNICAMP, Brazil/French Embassy for Prof. Bayraktar's visiting period at UNICAMP.

References

1. Balch, D.K., Dunand, D.C.: Load partitioning in aluminium syntactic foams containing ceramic micro-spheres. Acta Mater. **54**, 1501–1511 (2006)
2. Palmer, R.A., Gao, K., Doan, T.M., Green, L., Cavallaro, P.: Pressure infiltrated syntactic foams process development and mechanical properties. Mater. Sci. Eng. **464**(1–2), 358–366 (2007)
3. Tao, X.F., Zhao, Y.Y.: Compressive behaviour of Al matrix syntactic foams toughened with Al particles. Scr. Mater. **61**, 461–464 (2009)
4. Robert, M.H., Jorge, A.F.: Processing and properties of AA7075/porous SiO_2-MgO-Al_2O_3 composite. J. Achiev. Mater. Manuf. Eng. **3**, 1–5 (2012)
5. Robert, M.H., Jorge, A.F., Gatamorta, F., Silva, R.R.: Thixoinfiltration: a new approach to produce cellular and other low density metallic materials. J. Achiev. Mech. Eng. Manuf. **34**(2), 180–187 (2010)
6. Robert, M.H., Ferreira, L.M.P., Jorge, A.F., Bayraktar, E.: Production of metal matrix composites using thixoinfiltration techniques. In: Ventura, C.E. (ed.) Experimental and Applied Mechanics, vol. 4, pp. 157–164. Springer, New York (2013). ISBN 978-1-4614-4225-7
7. Gutierrez-Gonzalez, C.F., Fernandez-Garcia, E., Fernandez, A., Torrecillas, R., Lopez-Esteban, S.: Processing, spark plasma sintering, and mechanical behavior of alumina/titanium composites. J. Mater. Sci. **49**, 3823–3830 (2014). doi:10.1007/s10853-014-8095-5
8. Qian, J., Li, J., Xiong, J., Zhang, F., Lin, X.: In situ synthesizing Al_3Ni for fabrication of intermetallic-reinforced aluminum alloy composites by friction stir processing. Mater. Sci. Eng. A **550**, 279–285 (2012)
9. Song, C.J., Xu, Z.M., Li, J.G.: In-situ Al/Al_3Ni functionally graded materials by electromagnetic separation method. Mater. Sci. Eng. A **445–446**, 148–154 (2007)
10. Torralba, J.M., Da Costa, C.E., Velasco, F.: P/M aluminum matrix composites: an overview. J. Mater. Process. Technol. **133**(1–2), 203–206 (2003)
11. Bayraktar, E., Katundi, D.: New aluminium matrix composites reinforced with iron oxide. J. Achiev. Mater. Manuf. Eng. **38**(1), 7–14 (2010)
12. Ibrahim, I.A., et al.: Particulate reinforced metal matrix composites – a review. J. Mater. Sci. **26**, 1137–1156 (1991)
13. Ferreira, L.M.P., Robert, M.H., Bayraktar, E.: Production of Al/SiC/$NiAl_2O_4$ MMCs by thixoforming of recycled chips. Solid State Phenom. **217–218**, 286–293 (2015). doi:10.4028/www.scientific.net/SSP.218-286 (ISSN 1012-0394. ©Trans Tech Publications, Switzerland)
14. Kriszt, B.: Characterization of Cellular Metals. Handbook of Cellular Metals – Production, Processing, Applications. Wiley, Weinheim (2002)
15. Ashby, M.F., et al.: Metal Foams: A Design Guide. Butterworth-Heinemann, Boston (2000)
16. Gibson, L.J., Ashby, M.F.: Cellular Solids – Structure and Properties, 2nd edn. Cambridge University Press, Cambridge (1997)
17. Hatch, J.E. (ed.): Aluminum: Properties and Physical Metallurgy, pp. 351–378. American Society for Metals, Ohio (1993)
18. Yu, J., Li, X.: Modelling of the precipitated phases and properties of Al-Zn-Mg-Cu alloys. J. Phase Equilib. Diffus. 1547–7037. doi:10.1007/s11669-011-9911-0 (Published on line (26 May 201) @ASM International)

Chapter 18
Large Deformation of Particle-Filled Rubber Composites

Toshio Nakamura and Marc Leonard

Abstract Soft materials such as rubber may be stiffened by mixing with high modulus particles. In order to investigate their large behaviors at large deformation, particle-filled silicone rubber (RTV) specimens are fabricated. Although there have been numerous experiments for composites, a limited number of tests exists for finite deformation investigation of composites filled with uniformly shaped particles. In the tests, two types of particles are used. One is uniform glass beads with about 55 μm diameter and the other is spherical zirconia powder with diameters ranging from 30 to 80 μm. The former composites showed initial stiffening but the effects were limited as debonding of particles from matrix rubber occurs at large stresses. The latter composites showed better bonding as their surfaces are rough. Specimens are loaded multiple times in tension and compression. Their nonlinear behaviors as well as the Mullins effects are analyzed. The observed experimental results were compared with 3D finite element calculations as well as various nonlinear constitutive models and the rule of mixture.

Keywords RTV silicone • Finite strain • Incompressible materials • Rule-of-mixture • Soft materials

18.1 Introduction

Rubber has typically been used to make various products such as gloves, toys, boots, raincoats and tires. Due to its corrosion resistance properties, the chemical process industry found use for rubber in protecting storage tanks and process vessels [1]. As an engineering material rubber offers several benefits due to its corrosion, seal, damping, insulation and ablation properties. In engineering the term rubber refers to a specific class of materials called elastomer. Elastomers are amorphous polymers with their molecules in random motion. Polymers in turn are a high molecular compound formed by the addition of a small repeating unit, the monomer [1]. Usually in the form of a viscous liquid, rubber becomes usable through a process called vulcanization. The addition of curing agents creates cross-linking of the polymer chains and the material becomes a solid.

Rubber is a soft material which is capable of very large deformation without failure. However, the deformation of rubber is highly non-linear although the material essentially remains elastic. The material also exhibits viscoelastic properties. As a result several material models have been proposed to characterize the behavior of rubber. The Ogden and Mooney-Rivlin are ones among widely utilized models because they can be well-fitted to experimental data.

Recent advances in technology have created a need for high performance rubber with specific properties tailored to their end use. With advance manufacturing techniques, it is common to reinforce rubber with fillers made from elastic materials of high modulus. Most common fillers are carbon black and silica in fiber and particulate forms. The effect of particle volume concentration in rubber was first studied by Einstein on the effective viscosity for a dilute suspension of spheres. While it is well known that adding filler to the elastomer will increase its stiffness, the mechanics of such transformation still needs to be investigated. Often research is limited to small strain range for low filler concentration. Recently, Lopez-Pamies et al. [2, 3]. studied the effect of rigid particulate dilute inclusions in rubber.

T. Nakamura (✉) • M. Leonard
Department of Mechanical Engineering, Stony Brook University, Stony Brook, NY 11794-2300, USA
e-mail: toshio.nakamura@stonybrook.edu

C. Ralph et al. (eds.), *Mechanics of Composite and Multi-functional Materials, Volume 7*,
Conference Proceedings of the Society for Experimental Mechanics Series, DOI 10.1007/978-3-319-21762-8_18

18.2 Materials and Specimen Preparations

The rubber used as part of the investigation reported herein is the Bluesil RTV 3040 supplied from Freeman Manufacturing and Supply Company. It is a two part silicone elastomer commonly used in molding applications. Prior to making the samples, each component is weighted, then mixed in a 10:1 ratio in accordance to the material specification. The compound is mixed by hand and degassed under a vacuum at a pressure of 29 in of Hg for 30 min. Then the compound is poured into aluminum molds to make tension and compression specimens. Curing is done at an elevated temperature of 65 °C for 2 h. Tensile test coupons used in the experiment were made following the dimensions shown in Fig. 18.1. Note that for unfilled RTV, the mass density is 1.08 g/cm^3 and the reported tensile strength of 55.5 MPa. Following the testing of the unfilled RTV, reinforcing particles are added to the mixture to determine the effect on the particle-fill rubber. The particles are precision glass micro beads (diameter ranging from 53 to 63 μm with 2.52 g/cm^3 density) supplied by Corpuscular Inc., as shown in Fig. 18.1. They are added in volume fraction at 10.1 ± 3.5 %. To investigate the behavior under compression, a differently shaped specimens were prepared following the similar procedure. Here cylindrical specimens with uniform circular cross-section, as shown in Fig. 18.2, were made.

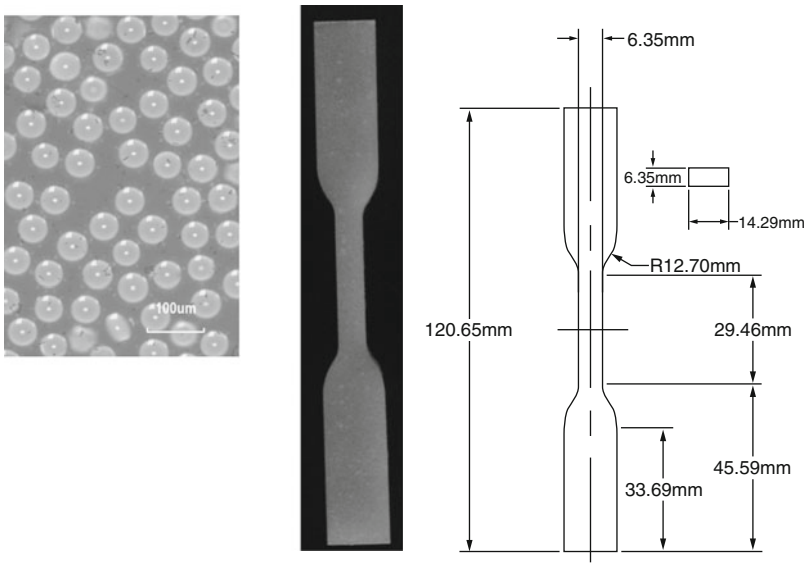

Fig. 18.1 Optical images of glass micro-beads, particle-filled tensile specimen and its dimensions

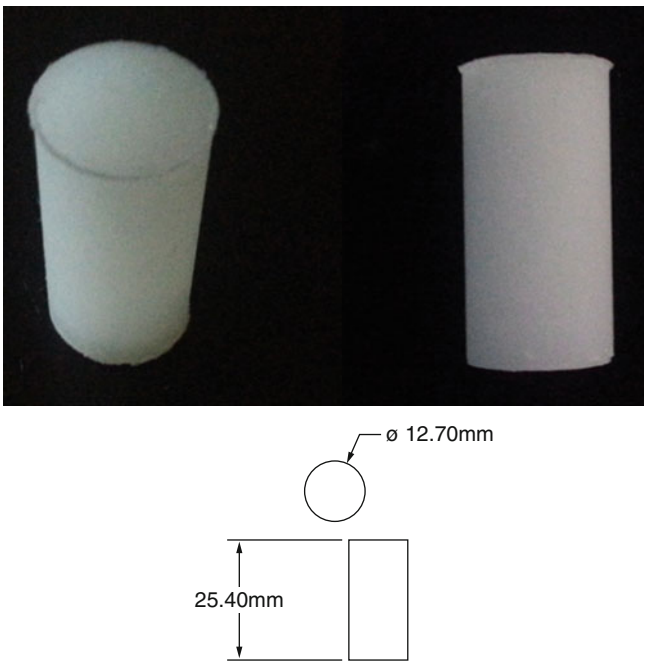

Fig. 18.2 Particle-filled compression specimen and its dimensions

18.3 Measured Stress and Deformation

The specimens were place in a loading machine (TiraTest 2 kN load cell) and cyclically loaded either in tension or in compression. The measured data is shown in Figs. 18.3 and 18.4. In the figures, the results of first three load cycles are shown. The amplitudes of load cycles are increased in each case. For both types of specimens with and without particles, they exhibit hysteresis. More precisely they show distinct Mullins effect where stress-deformation behavior depends on the maximum loading previously applied [4]. Various observations have concluded the Mullins effect to be the result of the physical and chemical interaction between the filled particles and the polymer matrix. There is continuous scission and cross-linking in the macromolecular network which leads to stress softening [5]. The Mullins effect may be also accompanied by crystallization, permanent set, anisotropy and recovery. In studying the Mullins effect, thermodynamic, macroscopic and microscopic models have been proposed and a number of constitutive models have been developed to describe this effect [6].

Since the purpose of this analysis to determine the effect of particle filler (i.e., micro-glass beads), the Mullins effect was minimized in the data interpretations. Essentially a steady-state stress-deformation without hysteresis may be obtained after repeating the load cycles with a constant amplitudes for 4–5 times. Comparing the specimens with and without particles, the ones with particle clearly shows the stiffer responses under both tension and compression. However the increases appear to somewhat less than that predicted by the rule-of-mixture for linearly elastic materials such as [7]. According to the theory, the raise should be about 30 % for 10 % volume fraction inclusion of glass-particles. In the present tests, although the stress ratio for a given stretch varies, the increase appears to be 10–20 % range. However if we compare the tangent modulus of first loading for strain less than 10 %, the increase in the modulus for particle-fill RTV is about 30 % over the unfilled RTV.

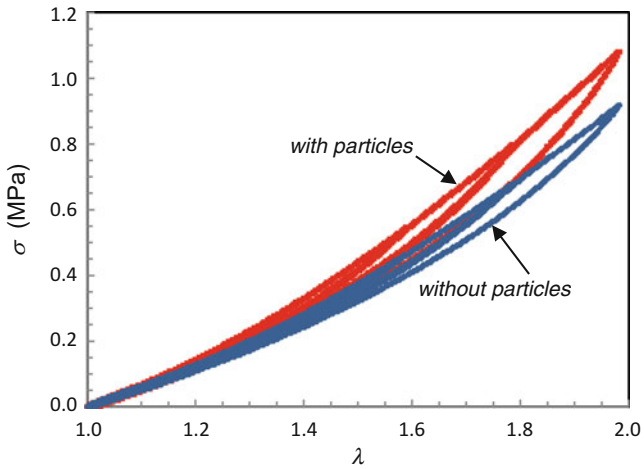

Fig. 18.3 Stretch vs. Cauchy stress of cyclic tensile loadings

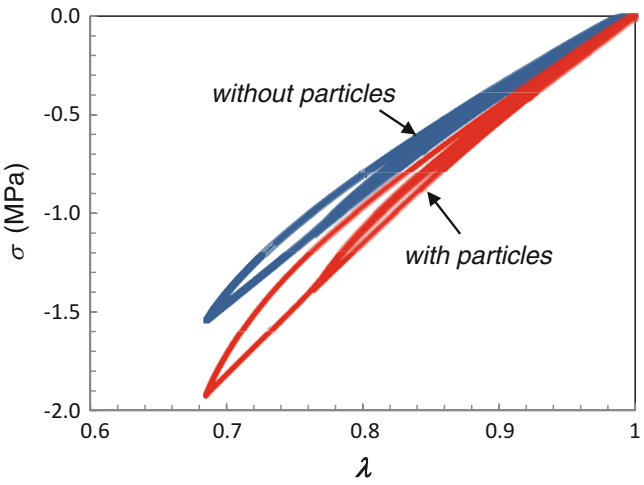

Fig. 18.4 Stretch vs. Cauchy stress of cyclic compression loadings

A possible cause of lower raise for larger stress and repeated loaded cases may be the debonding between the particles and the matrix RTV. Such phenomenon will cause a limited overall strengthening under large load. This aspect will be closely analyzed with the finite element models.

18.4 Finite Element Simulations

In order to understand the mechanical behavior of particle-filled soft materials, finite element model was constructed with discretely modeled spherical particles. Here, first the domain represented by a unit cube was considered. Then a program was developed to randomly place 30 spherical particles within the domain. Here the radius was assume to be uniform and the magnitude was determined by the set volume fraction of particles. Then using the mesh generator code (NETGEN), the 3D mesh was generated with ~65,000 10 hybrid noded tetrahedron elements. The elements were arranged so that the model can accommodate "periodic boundary conditions".

The property of matrix was modeled to follow that of Ogden. The material constants were fitted from the unfilled RTV results shown for tensile case. The particles were modeled as glass with $E = 60$ GPa, which is essentially identical to rigid with respect to the modulus of matrix. The model was gradually loaded with changing displacement along one directions while the other directions were constrained to following the periodic boundary condition. The average stress was determined from the division of reaction force with the cross-section area.

The computed stress contours are shown in Fig. 18.5 for tension and compression cases. For clarity, only the stress on the particles as well as the external boundary is shown. In both cases, they shown locally high stress concentrations. The magnitudes of these stresses are a few multiple of nominal (applied) stress. The high stress tends to occur where distances between particles are small. The resulting average stress and deformation for tension and compression loads are shown in Fig. 18.5. As predicted by the rule-of-mixture, the model with particles shows much higher stiffness as compared to that of

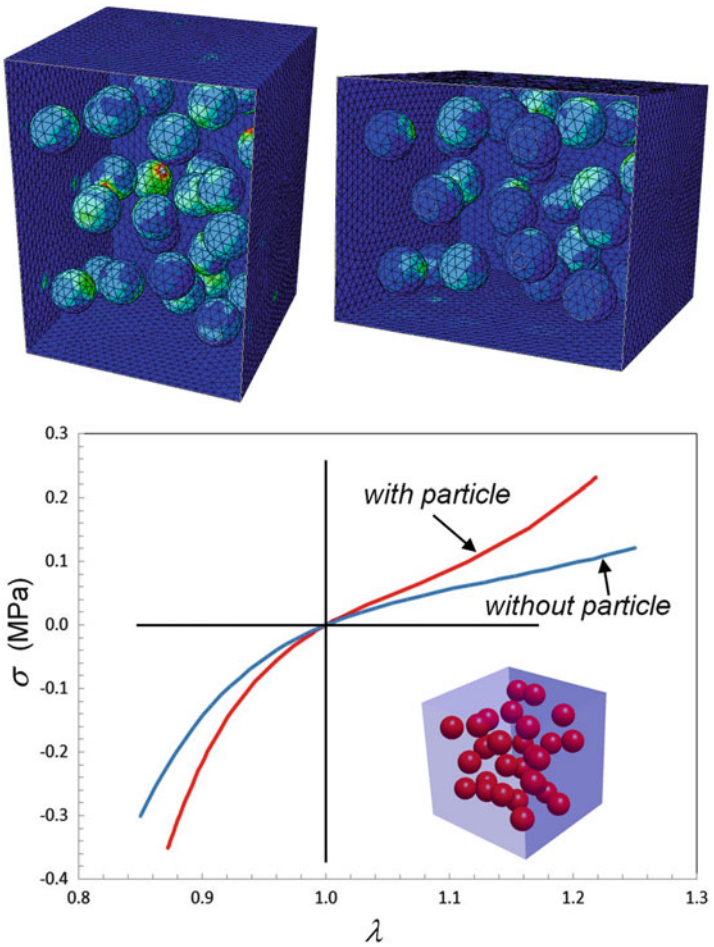

Fig. 18.5 Finite element simulation results. Von Mises stress contours under tensile and compressions loads. The resulting average stress and stretch

unfilled model. In fact the relative increase appears to rise under higher deformation. This contrasts with the experimentally observed data shown in Figs. 18.3 and 18.4. Most likely explanation lies in the debonding of particles from matrix under high stresses.

18.5 Conclusions

This work studies mechanical behavior of particle-filled RTV. The experimental data revealed that there can be debonding of particles and matrix which would lower the effective strengthening of particle-filled RTV. Another important phenomenon is the locally high stresses near the vicinity of two neighboring particles. They may induce local damage and/or delamination and potentially weakens the material. In order to closely investigate the effect of bonding between particles and matrix, additional analyses are underway. First to increase the bonding strength between the glass particles and matrix RTV, silane solutions are applied to the glass beads prior to the inclusion. They are soaked in the solution and dried which effectively add rough surfaces to the exterior of glass particles. A few silane solutions with different compositions are tested. Also too improve the decohesion resistance, YSZ particles are utilized instead of glass particles. Unlike glass spheres, YSZ particles contain edges and corners which should offer much stronger bonding strength due to the geometry. However unlike the glass particles, the sizes of particles range from 20 to 120 μm. These aspects are closely studied currently and will be report in the near future.

References

1. Chandrasekaran, V.C.: Essential Rubber Formulary: Formulas for Practitioners, 1st edn. Elsevier, New York (2007)
2. Lopez-Pamies, O., Goudarzi, T., Nakamura, T.: The nonlinear elastic response of suspensions of rigid inclusions in rubber: I—an exact result for dilute suspensions. J. Mech. Phys. Solids **61**, 1–18 (2013)
3. Lopez-Pamies, O., Goudarzi, T., Danas, K.: The nonlinear elastic response of suspensions of rigid inclusions in rubber: II—a simple explicit approximation for finite-concentration suspensions. J. Mech. Phys. Solids **61**, 19–37 (2013)
4. Mullins, L., Tobin, N.: Theoretical model for the elastic behavior of filler-reinforced vulcanized rubbers. Rubber Chem. Technol. **30**, 551–571 (1953)
5. De Tommasi, D.: A micromechanics-based model for the Mullins effect. J. Rheol. **50**, 495–512 (2006)
6. Dorfmann, A., Ogden, R.W.: A pseudo–elastic model for the Mullins effect in filled rubber. Int. J. Solids Struct. **41**, 1855–1878 (2004)
7. Hashin, Z., Shtrikman, S.: A variational approach to the theory of the elastic behavior of multiple materials. J. Mech. Phys. Solids **11**, 127–140 (1963)

Chapter 19
Advanced Structured Composites as Novel Phononic Crystals and Acoustic Metamaterials

Kathryn H. Matlack, Sebastian Krödel, Anton Bauhofer, and Chiara Daraio

Abstract We design and test new periodic materials that can reflect and prohibit the propagation of structural vibrations. These materials are engineered as periodic structures with resonant elements. We rely on recent advances in additive manufacturing to 3-D print composite materials that combine periodically embedded metal resonators within a periodic, truss-like polycarbonate lattice structure, functioning as a support matrix. The polycarbonate lattice geometry allows the matrix to be ultra-low density yet loadbearing, and have tunable density and tunable effective elastic modulus. The high acoustic impedance mismatch between this lattice and the metal resonators opens the possibility to create materials with low frequency and wide band gaps, or frequencies where acoustic propagation is forbidden, using a combination of Bragg scattering effects with effects due to the presence of local resonators. Finite element modeling is used to analyze various lattice geometries, lattice densities, and resonator locations to show materials with tunable acoustic properties.

Keywords Locally resonant acoustic metamaterial • Phononic crystals • Structural vibrations • Band gaps • 3D printing

19.1 Introduction

The design of phononic crystals and acoustic metamaterials has received considerable attention in the past decade. Stemming from unprecedented properties found in photonic materials, similar Bragg scattering mechanisms have been shown to exist for elastic waves in periodic structures. Physically, periodicity in material properties causes destructive interference of elastic waves, which forbids some frequencies from propagating in certain directions within the structure. Dynamic properties of a multitude of periodic lattice geometries have been explored—ranging from square, triangular, Kagome, and hexagonal 2D structures [1], to complex 3D geometries such as pentamode structures [2, 3], and auxetic geometries [4, 5], to name a few examples.

Locally resonant acoustic metamaterials contain resonators embedded in a matrix material. The advantage of locally resonant acoustic metamaterials is that wavelengths associated with resulting band gaps can be orders of magnitude longer than the periodicity of the metamaterial. So, small structures can be designed to absorb low frequency sound or vibrations, for applications such as passive frequency filters and acoustic shielding. Locally resonant acoustic metamaterials have been designed e.g. as materials of rigid inclusions surrounded by soft viscoelastic material that both acts as a soft spring against the inclusions and absorbs the vibration of the resonant modes of the inclusions to induce low frequency dips in the transmission spectrum [6, 7]. These systems have considered a variety of materials for inclusions (e.g. lead [6], gold [8], and tungsten [9], steel [7]), and in a variety of shapes and configurations [9, 10]. Other experimental designs have been explored, consisting of Helmholtz resonators [11], beams with periodic resonators [12, 13], embedded masses in a chiral lattice [14], among many others [15]. Low and wide frequency band gaps have been observed with the inertial amplification method studied in 2D [16] and 3D [17] mass-spring lattices. Local resonator concepts have also been utilized to engineer nanophononic metamaterials to reduce the thermal conductivity [18].

In this paper, we explore how to design locally resonant acoustic metamaterials that are coupled with periodic 3D geometric lattices. Instead of utilizing viscoelastic properties of coating material, we use the geometry of the structure to induce different locally resonant modes, considering structural modes within the designed materials. We study two representative 3D lattice geometries (square and auxetic) and investigate how these geometries can couple with local resonators to induce low frequency band gaps in structural vibrations. As a preliminary study, we consider quasi-1D lattice-resonator chains, containing a 3D lattice but with lattice-resonator periodicity in one dimension.

The original version of this chapter was revised. An erratum to this chapter can be found at DOI 10.1007/978-3-319-21762-8_56

K.H. Matlack (✉) • S. Krödel • A. Bauhofer • C. Daraio
Department of Mechanical and Process Engineering, ETH Zürich, Tannenstrasse 3, 8092 Zürich, Switzerland
e-mail: matlackk@ethz.ch

C. Ralph et al. (eds.), *Mechanics of Composite and Multi-functional Materials, Volume 7*,
Conference Proceedings of the Society for Experimental Mechanics Series, DOI 10.1007/978-3-319-21762-8_19

19.2 Wave Propagation Through Periodic Structures

Here, we briefly review the fundamental principles of wave propagation in a periodic elastic structure. The lattice constant is a, and for wave propagation over wavelengths, λ, on the order of or smaller than the lattice constant, the displacement can be assumed periodic. Neglecting attenuation, the Bloch theorem, or Floquet's principle in one-dimensional periodic structures, states:

$$u(x) = u(x_j)e^{(inka)} \tag{19.1}$$

where u is the displacement, $x = x_j + na$ is the position within the lattice, x_j is the position within the primitive unit cell, k is the wavenumber defined as $k = 2\pi/\lambda$, and n is the integer number of unit cells away from the primitive unit cell. This theorem states that the wave displacement within the lattice only depends on the location within the unit cell, and not within the periodic structure itself. This formalism, detailed much further in many other works [1, 5, 19], allows the analysis of the entire structure to be extracted from analyzing one primitive unit cell, resulting in large computational savings. Note that in the limit where the wavelength is much larger than the lattice constant, the bulk elastic wave properties of the material are recovered.

To further reduce the problem, wave propagation can be restricted to the edges of the first Brillouin zone [20, 21]. We assume plane harmonic waves, such that the wavenumber is periodic with period 2π. Thus the wavenumber defined over the space $k \in [-\pi/a, \pi/a]$. Due to symmetry about 0 within the dispersion relations, this space can further be reduced to $k \in [0, \pi/a]$.

19.3 Finite Element Modeling

Finite element modeling is used to numerically investigate the 3D lattice geometry coupling with locally resonant masses. This enables us to explore the wave propagation characteristics through complex geometries. The finite element modeling reported in this paper is computed with COMSOL Multiphysics, and by specifying Bloch periodic boundary conditions, a single unit cell can be analyzed but the full periodic solution can be extracted. We model the structure using the mechanical properties of polycarbonate, the material used in our experiments. Since polycarbonate is a viscoelastic material, we consider damping in our model. In a linear damped system, the FEM solver discretizes the set of matrix equations:

$$-\omega^2\mathbf{M}\mathbf{q} + i\omega\mathbf{C}\mathbf{q} + \mathbf{K}\mathbf{q} = 0 \tag{19.2}$$

where ω is the radial frequency, $\mathbf{M}$ is the mass matrix, $\mathbf{C}$ is the damping matrix, $\mathbf{K}$ is the stiffness matrix, and $\mathbf{q}$ represents the degrees of freedom in the unit cell [22]. To consider damping in the finite element analysis, we specify an isotropic loss factor that was determined experimentally.

Unit cells with resonators are meshed with tetrahedral elements, and have upwards of 100,000 elements, while unit cells for only the lattice geometries have 2200–4400 elements. A sufficiently fine mesh is used to resolve the wavelengths investigated: the maximum element size is less than 1/20 of the smallest wavelength calculated, both in terms of the maximum prescribed wave vector investigated and the maximum eigenfrequency based on the wave speed in bulk polycarbonate. Dispersion curves are calculated, relating the frequency to the wave vector of the propagating waves. In the analysis, the wave vector is varied either along the edge of the 2D irreducible Brillouin zone, or along the periodicity direction for the 1D chain structures.

Since we are combining the concepts of a periodic metamaterial with a locally resonant acoustic metamaterial, we assume periodicity throughout the structure. This is crucial since the location of the resonator within the unit cell induces different deformations and thus different modal properties of the lattice-resonator structure, as shown in the results section below. So, a homogenization analysis that only considers the different properties of the lattice and resonators separately would not be sufficient to capture the full modal properties of our structures (a lumped parameter model could likely capture some of the dynamics). Note that periodicity is generally not needed to realize low frequency transmission dips for locally resonant acoustic metamaterials [6, 23].

19.4 Fabrication of Lattice-Resonator Structures

For the experimental testing, the lattice-resonator structures were fabricated with advanced 3D printing techniques on a Fortus 400mc system. The lattice structures were printed with a polycarbonate material, with a reported Young's modulus of 2.3 GPa. However, tensile testing of 3D printed specimen revealed an actual Young's modulus of 1.78–2.16 GPa with slight anisotropy. Note that 3D printed material properties tend to be different than that of the bulk material due to influences from printing in layers and imperfections in the 3D printing process. Steel cubes, to be included in the lattice as resonating elements, were manufactured separately. A thin polycarbonate coating was attached to the top of the cubes to facilitate printing of subsequent layers. The lattice-resonator structure was printed, layer-by-layer, with holes replacing the steel cubes, and the printer was paused just before the layer above the hole. Then, the steel cubes were inserted into the structure manually, and then the remaining lattice layers were printed. A representative 3D printed lattice-resonator structure (with embedded metal cubes) is shown in Fig. 19.1. In this example, the lattice geometry is the square lattice described below, and the sample comprises a total of six unit cells.

19.5 Square Lattice Structures

As an initial study, we analyze a simple cubic lattice geometry, consisting of truss- or beam-like components forming a square geometry, with periodicity in three dimensions. The unit cell of this square lattice is shown in Fig. 19.2, along with the dispersion curves for wave propagation in the two dimensions. The irreducible Brillouin zone in 2D is superimposed on the unit cell to indicate the analyzed wave propagation directions, and dispersion curves are calculated with FEM. Units of frequency are in absolute units (Hz), to illustrate the applicable range of the fabricated structures. The lattice constant of the unit cell used in the square lattice is $2a$, where a $= 3.65$ mm, and the beams in all structures have a square cross-sectional area of 1.21 mm^2 (set as the limit of the 3D printer used for fabrication). The volume fraction (or relative density) of polycarbonate material in the unit cell is 0.22.

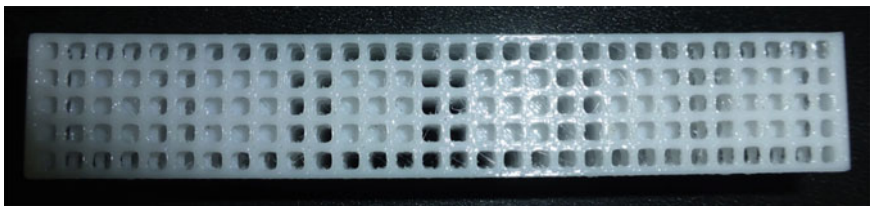

Fig. 19.1 3D printed lattice-resonator structure, consisting of six unit cells of polycarbonate square lattice matrix with embedded steel resonating masses. Note that the steel cubes are coated in a thin layer of polycarbonate to facilitate subsequent layer printing

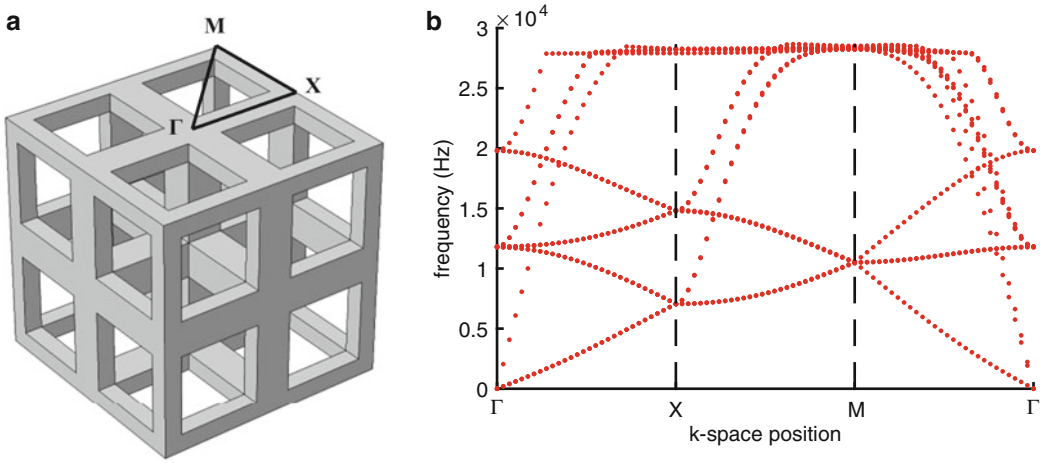

Fig. 19.2 Cubic unit cell (**a**) and corresponding dispersion curves (**b**). The irreducible Brillouin zone for a two-dimensional square lattice is superimposed on the unit cell, showing the Γ, X, and M edge points

19.5.1 1D Square Lattice-Resonator Chains

The lattice-resonator structures are modeled as 1D periodic chains, based on the unit cell in Fig. 19.2. The unit cell of the square lattice chain has a width of $5a$, and the cubic resonator centered within the unit cell has a side length slightly smaller than $3a$ (9.5 mm), as shown in Fig. 19.3. Note that the periodicity direction is along the x-axis. Dispersion curves for wave propagation in the 1D lattice-resonator chain are shown in Fig. 19.3. The modes of particular interest are those that induce resonant motion of the resonator. An example of one of these modes is shown in the representative unit cell in Fig. 19.3 (left), where the color map indicates *relative* modal displacements. This mode shows an in-plane motion of the local resonator, and is plotted at a frequency of 6429 Hz and wavenumber $k_x = a/\pi$. The dispersion curves show no band gap induced by the coupling of the local resonator with the periodic square lattice geometry.

We also explore the effect of a soft coating (E = 4 MPa) on the resonator, as depicted in Fig. 19.4 (right). This configuration is similar to those studied in other acoustic metamaterial locally resonant systems [6, 8], and has been shown to open up band gaps. The dispersion curves for a 1D square lattice-resonator with a soft coating are shown in Fig. 19.4 (left). These band structure shows a band gap centered around 2000 Hz, with a width of about 1000 Hz. Note that the

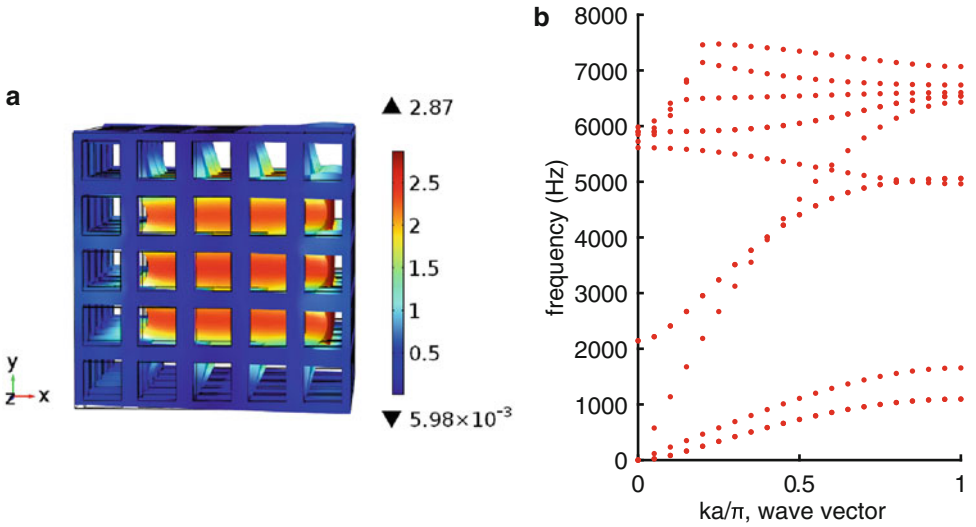

Fig. 19.3 Unit cell showing in-plane resonator mode (**a**) and calculated dispersion curves (**b**) for 1D square lattice-resonator chain, for both periodicity and wave propagation along the x-direction. The wave vector k is normalized by a/π, where a is the unit cell length. Note displacements in the unit cell are relative

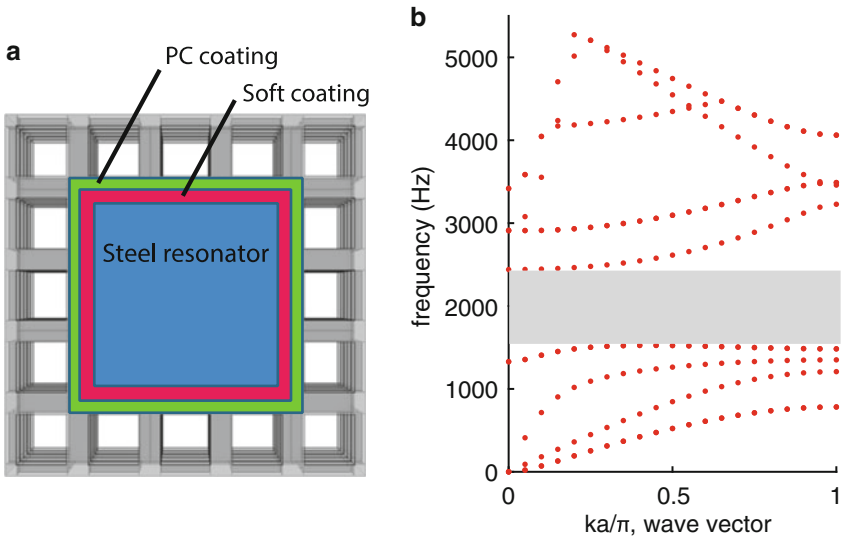

Fig. 19.4 1D chain of lattice-resonator structure with soft coating surrounding the local resonating mass, in pictorial representation (**a**), and resulting dispersion curves (**b**). The soft coating facilities the opening of a band gap centered around 2000 Hz

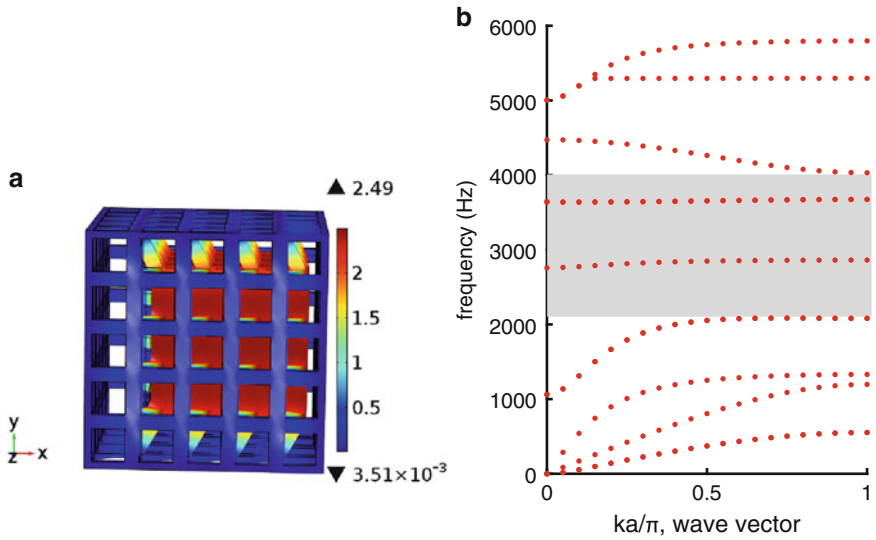

Fig. 19.5 Unit cell of 1D square lattice-resonator chain with beams under axial loading removed (**a**), and resulting band structure calculation (**b**). The removal of axially loaded beams decreases the stiffness of resonator-related modes to open up band gaps in the structure. Periodicity is in the *x*-direction

wavelengths corresponding to this frequency in air, $\lambda_{air} = 172$ mm, and in the bulk polycarbonate, $\lambda_{PC} = 637$ mm, are both over an order of magnitude larger than the lattice constant, $a = 18.25$ mm.

While the soft coating in the lattice-resonator opened a band gap, this approach has already been shown successful in many previous studies, e.g. [6, 8]. We want to avoid using a soft coating, and instead modify the geometry of the original square lattice-resonator to open up a band gap. As an example, we look at one of the modes of the original square lattice-resonator structure: the in-plane resonator mode in Fig. 19.3a. Next, we consider how to modify the lattice geometry to reduce the stiffness of this mode, since reducing the stiffness will reduce the frequency of the mode. Looking in more detail at the mode shape of this in-plane resonator mode, it is seen that the mode shape approximates a mass-spring system. The mass is the steel resonator (since it has the highest displacement), and the beams interfacing with the resonator act as springs in parallel. Looking closely at the beams, we see that some are in bending deformation (i.e. those in the *xz* and *xy* planes), and some are in axial deformation (i.e. those in the *yz* plane). Since beams are generally much stiffer under axial deformation than bending, it is likely that the stiffness of this mode will be greatly reduced if the beams under axial loading are removed. So, we design a new square lattice-resonator chain where we remove the beams that were in axial deformation. The resulting unit cell for this structure is shown in Fig. 19.5a, with the resulting in-plane mode shown. The dispersion curves for this new square lattice-resonator chain are shown in Fig. 19.5b.

The band structure shows an ultra wide band gap centered around 3000 Hz with a width of about 2000 Hz, with two highly localized modes in the middle that will not propagate due to their near-zero group velocity. Note that the modes surrounding the lowest band gap are not the in-plane mode, but a rotational mode of the local resonator (lower mode), and a mode with only deformation within the lattice (upper mode). The wavelengths corresponding to the band gap center frequency in air and bulk polycarbonate are both an order of magnitude larger than the lattice constant. So, the local resonators induce band gaps at lower frequencies than possible with Bragg scattering given the lattice periodicity.

A more important finding here is the width of this band gap—it is twice as wide as the band gap induced with the soft coating. This is unusual because band gaps resulting from local resonators are typically extremely narrow due to the localized nature of the resonators. Our results show that wide band gaps are in fact possible with local resonators embedded in a geometric lattice.

19.6 Auxetic Lattice Structures

Auxetic lattice geometries are characterized by a negative Poisson's ratio, such that compression in one dimension causes compression in the other dimensions. While materials and synthetic structures exhibiting this effect have been studied for some time and for a variety of applications [4, 24–26], wave propagation properties of these structures have only been studied in a few cases [5, 19, 27]. We study a cubic auxetic lattice geometry in the shape of a "bowtie", as shown in the designed unit cell in Fig. 19.6, which is based off previously explored designs for mechanical metamaterials [4]. The unit cell was designed to have a density equal to that of the square unit cell shown in Fig. 19.2, and periodicity in all dimensions.

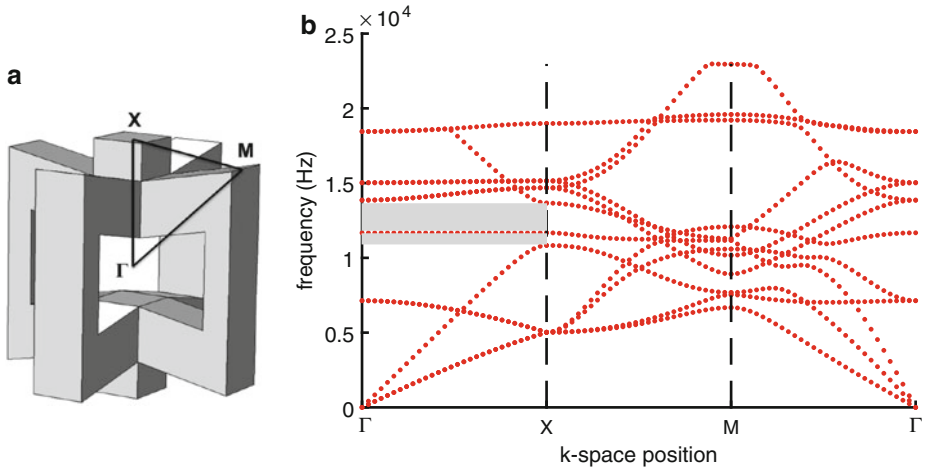

Fig. 19.6 Unit cell (**a**) and dispersion curves (**b**) for auxetic lattice geometry, with periodicity in all dimensions. *Grey boxes* indicate the directional band gaps in the ΓX direction

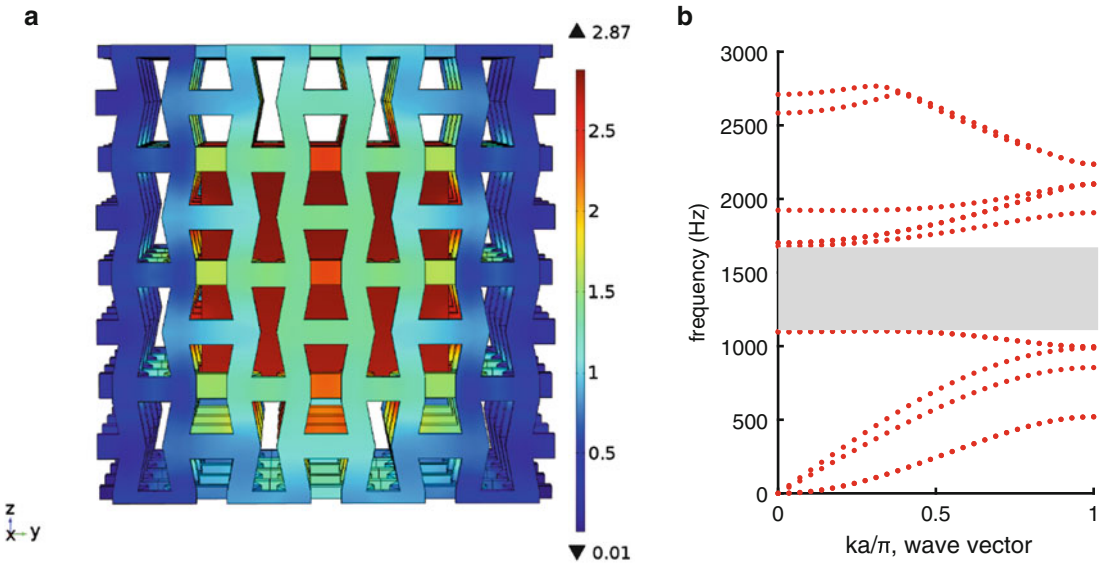

Fig. 19.7 Unit cell for 1D auxetic lattice-resonator chain (**a**), and resulting dispersion relations (**b**). The resulting band gap is centered at 1400 Hz. Periodicity is along the *y*-direction. Note that the mode displacements are not shown on the unit cell to more clearly see the geometry

The resulting structure contained square beams also of the same size as the square lattice (1.21 mm^2), with a unit cell length of slightly larger dimension, at 4.6 mm. The dispersion curves along two dimensions are also shown in Fig. 19.6.

While no full band gap is seen, there are two directional band gaps along the Γ-X direction. Given this result, we focus on 1D lattice-resonator chains with periodicity in this direction, to exploit current band gaps from Bragg scattering mechanisms in potential band gaps due to local resonances. It is interesting to point out that the mode below the first band gap at the X point resembles an in-plane motion of the unit cell sides, which is similar to cases with the lattice-resonator shown later.

19.6.1 1D Auxetic Lattice-Resonator Chains

The unit cell for the 1D auxetic lattice-resonator chains are modeled as $4 \times 4 \times 4$ lattice unit cells from Fig. 19.6 made of polycarbonate material, with inserted steel locally resonating masses, the same size as those in the square lattice-resonator chains. The 1D periodicity is in the $\Gamma - X$ direction (indicated as the *y*-direction in Fig. 19.7), since this is the wave

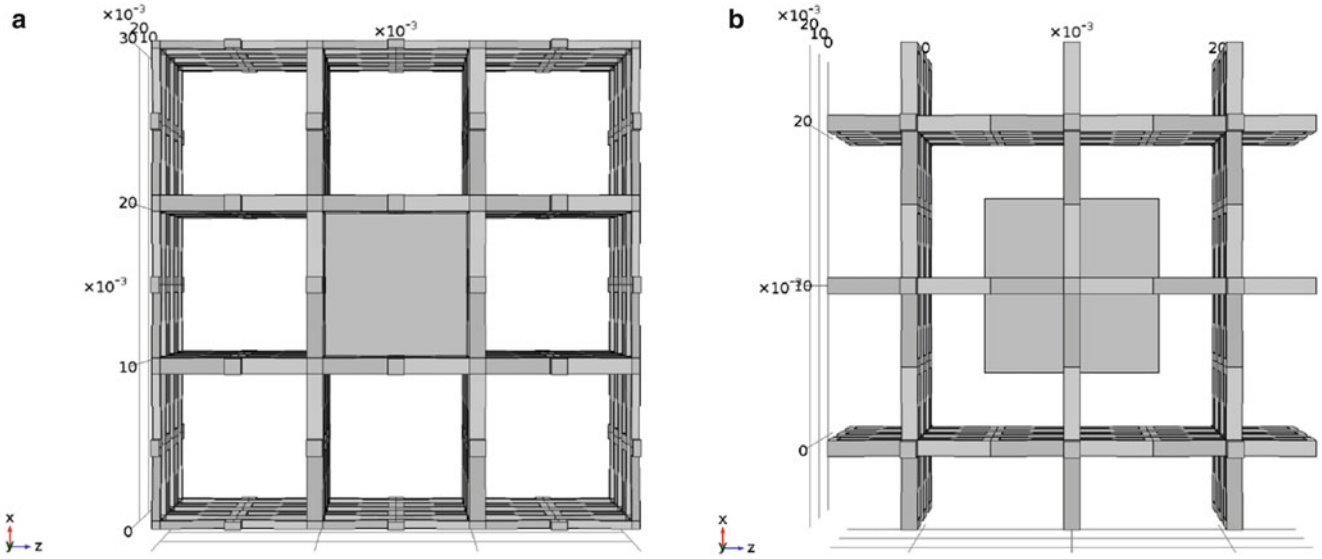

Fig. 19.8 Top view of the ultralight auxetic lattice with resonator in the embedded location (**a**), and exposed location (**b**). Periodicity is out of the plane

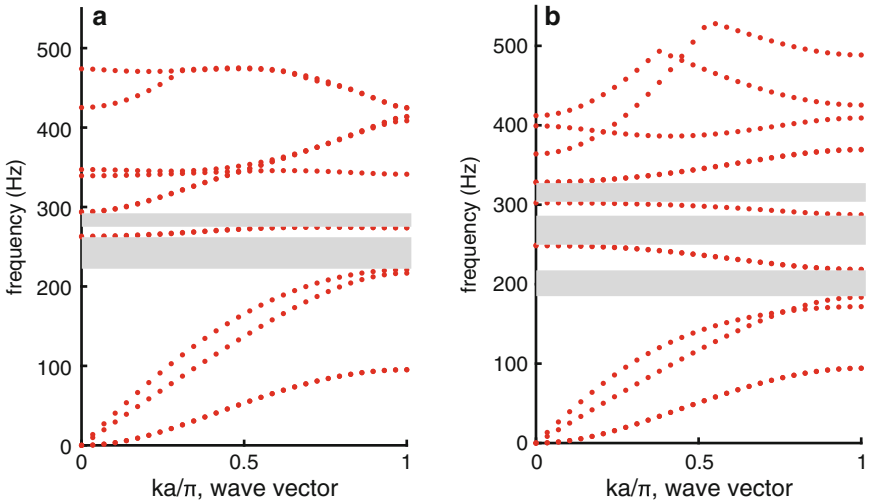

Fig. 19.9 Dispersion curves of 1D auxetic lattice-resonator chains, in the embedded (**a**) and exposed (**b**) configurations

propagation direction in which the direction band gaps were seen in Fig. 19.6. An example unit cell and resulting dispersion relation is shown in Fig. 19.7. Results show a band gap centered at 1400 Hz, with a bandwidth of 604 Hz. The absolute frequencies of the structural modes and band gaps are an order of magnitude lower than those of the pure lattice.

To explore more of the design space within the lattice-resonator concept, we investigate the effect of lattice density by considering ultralight auxetic lattices. This ultralight auxetic lattice has a density of about 25 % of the unit cell in Fig. 19.6, and has unit cell dimensions of 10 mm on all sides. The 1D lattice-resonator chain consists of $3 \times 3 \times 3$ unit cells with the same size steel resonator. Numerical simulations show that the location of the resonator within the lattice induces different band gaps at different frequencies, and thus induces different mode couplings of the resonator and lattice. Two resonator locations within the lattice, referred to as "embedded" and "exposed", are shown in Fig. 19.8, where the matrix is composed of $3 \times 3 \times 3$ unit cells of the ultralight auxetic lattice. The resulting dispersion curves for 1D chains with these two resonator locations are shown in Fig. 19.9. In the exposed configuration, three band gaps are present below 400 Hz, and the lowest band gap is lower than the embedded configuration. This suggests that materials with broad range of band gaps could be designed by varying the position of the resonator within the lattice.

19.7 Conclusions

In this paper, locally resonant acoustic metamaterial designs are studied, with the goal to induce low frequency band gaps in structures consisting of periodic lattice geometries with embedded masses. The possibility of mode coupling between the lattice and the local resonator was explored with two different lattice geometries—a square lattice and an auxetic "bow-tie" lattice. These composite acoustic metamaterials are designed as 1D chains of a polycarbonate lattice matrix with embedded steel resonating masses. Fabrication of these materials is made possible with advanced 3D printing techniques.

Low-frequency band gaps were found in some metamaterial designs that corresponded to coupling of lattice and resonator modes. Band gaps were not seen in the 1D square lattice-resonator chain, however upon removal of lattice beam elements under axial loading, band gaps opened due to a greater reduction of stiffness of the in-plane resonator mode. These results also show that it is possible to achieve wide band gaps with local resonators. Results show that band gaps in the auxetic lattice-resonator structure can be tuned by varying both the density of the surrounding lattice, along with the location of the resonator within the lattice.

Acknowledgement This research was funded by the ETH Postdoctoral Fellowship Program.

References

1. Phani, A.S., Woodhouse, J., Fleck, N.A.: Wave propagation in two-dimensional periodic lattices. J. Acoust. Soc. Am. **119**, 1995 (2006)
2. Kadic, M., Bückmann, T., Stenger, N., Thiel, M., Wegener, M.: On the practicability of pentamode mechanical metamaterials. Appl. Phys. Lett. **100**, 191901 (2012)
3. Bückmann, T., Thiel, M., Kadic, M., Schittny, R., Wegener, M.: An elasto-mechanical unfeelability cloak made of pentamode metamaterials. Nat. Commun. **5**, 4130 (2014)
4. Bückmann, T., Stenger, N., Kadic, M., Kaschke, J., Frölich, A., Kennerknecht, T., Eberl, C., Thiel, M., Wegener, M.: Tailored 3D mechanical metamaterials made by dip-in direct-laser-writing optical lithography. Adv. Mater. **24**, 2710–2714 (2012)
5. Krödel, S., Delpero, T., Bergamini, A., Ermanni, P., Kochmann, D.M.: 3D auxetic microlattices with independently controllable acoustic band gaps and quasi-static elastic moduli. Adv. Eng. Mater. **15**, 1–7 (2013)
6. Liu, Z., Zhang, X., Mao, Y., Zhu, Y.Y., Yang, Z., Chan, C.T., Sheng, P.: Locally resonant sonic materials. Science **289**, 1734–1736 (2000)
7. Zhao, H., Wen, J., Yu, D., Wen, X.: Low-frequency acoustic absorption of localized resonances: experiment and theory. J. Appl. Phys. **107**, 023519 (2010)
8. Goffaux, C., Sanchez-Dehesa, J.: Two-dimensional phononic crystals studied using a variational method: application to lattices of locally resonant materials. Phys. Rev. B **67**, 144301 (2003)
9. Krushynska, A.O., Kouznetsova, V.G., Geers, M.G.D.: Towards optimal design of locally resonant acoustic metamaterials. J. Mech. Phys. Solids **71**, 179–196 (2014)
10. Meng, H., Wen, J., Zhao, H., Wen, X.: Optimization of locally resonant acoustic metamaterials on underwater sound absorption characteristics. J. Sound Vib. **331**, 4406–4416 (2012)
11. Cheng, Y., Xu, J.Y., Liu, X.J.: Broad forbidden bands in parallel-coupled locally resonant ultrasonic metamaterials. Appl. Phys. Lett. **92**, 2006–2009 (2008)
12. Nouh, M., Aldraihem, O., Baz, A.: Vibration characteristics of metamaterial beams with periodic local resonances. J. Vib. Acoust. **136**, 061012 (2014)
13. Raghavan, L., Phani, A.S.: Local resonance bandgaps in periodic media: theory and experiment. J. Acoust. Soc. Am. **134**, 1950–1959 (2013)
14. Baravelli, E., Ruzzene, M.: Internally resonating lattices for bandgap generation and low-frequency vibration control. J. Sound Vib. **332**, 6562–6579 (2013)
15. Hussein, M.I., Leamy, M.J., Ruzzene, M.: Dynamics of phononic materials and structures: historical origins, recent progress, and future outlook. Appl. Mech. Rev. **66**, 040802 (2014)
16. Yilmaz, C., Hulbert, G., Kikuchi, N.: Phononic band gaps induced by inertial amplification in periodic media. Phys. Rev. B **76**, 054309 (2007)
17. Taniker, S., Yilmaz, C.: Phononic gaps induced by inertial amplification in BCC and FCC lattices. Phys. Lett. A **377**, 1930–1936 (2013)
18. Davis, B.L., Hussein, M.I.: Nanophononic metamaterial: thermal conductivity reduction by local resonance. Phys. Rev. Lett. **112**, 055505 (2014)
19. Ruzzene, M., Scarpa, F., Soranna, F.: Wave beaming effects in two-dimensional cellular structures. Smart Mater. Struct. **12**, 363–372 (2003)
20. Kittel, C.: Introduction to Solid State Physics. Wiley, New York (1996)
21. Brillouin, L.: Wave Propagation in Periodic Structures. Dover Publications, New York (1953)
22. Hussein, M.I.: Theory of damped Bloch waves in elastic media. Phys. Rev. B: Condens. Matter Mater. Phys. **80**, 1–4 (2009)
23. Sheng, P., Zhang, X.X., Liu, Z., Chan, C.T.: Locally resonant sonic materials. Phys. B Condens. Matter **338**, 201–205 (2003)
24. Lakes, R.: Foam structures with a negative Poisson's ratio. Science **235**, 1038–1040 (1987)
25. Bezazi, A., Scarpa, F.: Mechanical behaviour of conventional and negative Poisson's ratio thermoplastic polyurethane foams under compressive cyclic loading. Int. J. Fatigue **29**, 922–930 (2007)
26. Spadoni, A., Ruzzene, M.: Elasto-static micropolar behavior of a chiral auxetic lattice. J. Mech. Phys. Solids **60**, 156–171 (2012)
27. Ruzzene, M., Scarpa, F.: Directional and band-gap behavior of periodic auxetic lattices. Phys. Status Solidi Basic Res. **242**, 665–680 (2005)

Chapter 20
Low-Cost Production of Epoxy Matrix Composites Reinforced with Scarp Rubber, Boron, Glass Bubbles and Alumina

E. Bayraktar, I. Miskioglu, and D. Zaimova

Abstract Operating efficiency and economy with passenger comfort are paramount in commercial transport aircraft. Reduced airframe weight pays off in fuel economy and, therefore, reduces Direct Operating Costs for the operators. The composite parts combined with other design efficiencies led to reduced fuel consumption—a major attraction for the airlines. Currently, in Europe-French aeronautical applications, the different type of airframe (A300-600) is about 4.5 % composites by weight.

In the frame of this research programme, four different epoxy based composites have been prepared reinforced with boron, alumina for the commercial aeronautical applications. The aims of the present work are an improvement of mechanical properties of epoxy matrix composites containing reinforcements (especially boron & alumina) and a low cost production process of epoxy matrix composites containing recycled elements.

Mechanical properties have been evaluated by impact tests, bending test, etc. and also viscoelastic properties were analyzed by nano-indentation technique. Surface wear resistance were measured under different parameters.

Keywords Recycled composites • Epoxy-rubber • Creep-wear nanoindentation • Ceramic reinforcements

20.1 Introduction

Polymer composites or polymer matrix composites are used increasingly for engineering applications. Epoxy resin based thermosetting polymers are considered as the matrix in the composite materials for most engineering applications in aeronautical and automotive industries, etc. They show strong chemical resistance after curing process (low shrinkage on cure, absence of volatile solvents and low creep, etc.) and improved mechanical and thermal properties. It means that they are able to increase the strength under certain load conditions, but in certain applications they have detrimental effects and show brittleness and low toughness. For this reason, depth-sensing indentation is a technique used to measure mechanical properties of small volumes of materials [1–5]. Routine indentation data analysis yields time-independent elastic modulus and hardness values. Additionally, a number of efforts have been made to measure time-dependent mechanical properties on polymeric materials using indentation with some success [6–8]. However, comparisons to measurements made at the macroscale is an important check of such microscale measurements to ensure that macroscale properties, may be adequately characterized using indentation techniques. Creep compliance is a useful metric that measures a unique mechanical response of time-dependent materials. The analysis of contact creep compliance experiments to quantify the mechanical response of polymers is conceptually direct but includes several important experimental and analytical qualifications [8–14].

Manufacturing epoxy resin based composites for engineering applications to resist high mechanical and tribological loads, reinforcement of the matrix with certain fillers is absolutely necessary. In literature, usually certain fillers are chosen for the sake of simplicity of the processing during manufacturing. However, light weight high performance new composites need special fillers in the matrix in order to increase ductility and stiffness of the matrix materials. In reality, scrap rubber particles can be used easily as reinforcements for increasing toughness of epoxy based composites. However, for the

E. Bayraktar (✉)
Supmeca-Paris, School of Mechanical and Manufacturing Engineering, Paris, France
e-mail: bayraktar@supmeca.fr

I. Miskioglu (✉)
ME-EM Department, Michigan Technological University, Houghton, MI, USA
e-mail: imiski@mtu.edu

D. Zaimova
Supmeca-Paris, School of Mechanical and Manufacturing Engineering, Paris, France

University of Chemical Technology and Metallurgy, Sofia, Bulgaria

C. Ralph et al. (eds.), *Mechanics of Composite and Multi-functional Materials, Volume 7*,
Conference Proceedings of the Society for Experimental Mechanics Series, DOI 10.1007/978-3-319-21762-8_20

compatibility of the scrap rubber with epoxy matrix, a simple chemical treatment is needed in order to change surface properties for stable adhesion to matrix. In literature [5–14] methods such as plasma surface modification and other de-vulcanizations were proposed for chemical surface treatments that are long and expensive for the recycling process. In this research, low cost epoxy resin based composites were designed with certain recycled scrap reinforcements. After the research of the compatibility of different reinforcements with epoxy matrix, addition of fine scrap rubber powder after simple chemical treatment with silane, and addition of boron, alumina and glass bubbles were observed to be the most suitable reinforcements to toughen epoxy resin for aeronautical engineering applications. For this purpose, dielectric properties (permittivity and loss index) were measured and microstructural and fracture surface analysis were made by means of Scanning Electron Microscopy (SEM). Also, creep and wear tests have been carried out by nano indentation method.

20.2 Experimental Conditions

20.2.1 Materials Processing

A new design of an epoxy based composite reinforced with fine scrap rubber powder, boron, alumina and glass bubbles was prepared in two stages. At the first stage, dry very fine epoxy resin and scrap rubber (10 wt%) was mixed and chemically treated by using toluene and acrylic acid and vinyltriethoxysilane (2 %) dried after treatment in the oven to eliminate entirely the trace of the chemicals. Fresh scrap rubber has been milled into fine rubber powder. The powder preparation was done in a fast rotating toothed-wheel mill. The advantage of this technique is that one can obtain a fine elastic rubber powder. The mixture of epoxy resin and rubber powder was then milled 2 h to make a homogenous compound, and then heated at 80 °C for 2 h. At the second stage, dry boron and alumina in fine micro size was doped by mixing and placed in the oven for 2 h at 110 °C to eliminate any moisture in the mixture.

All of these compounds were then mixed in a blender and milled for 4 h. At the final stage, glass bubbles (GB-hollow glass microspheres produced by 3 M (St Paul, MN, USA) with a density of 0.227 g/cm^3, specified as S38HSS and K1) were added and mixed for homogenous distribution (ultrasound) for 2 h again. The specimens were then obtained by hot compacting (double uniaxial action) under pressure of 50 kN at the temperature of 180 °C for 15 min. All of the specimens (30 mm diameter) were cooled slowly. The post curing was concluded under isothermal conditions at 80 °C for 48 h.

20.2.2 Mechanical Tests and Microstructural Analysis

Compression tests were performed on all of the products with a servo-hydraulic INSTRON Universal Tester (model Instron 5500R, equipped with a load cell of 25,000 kgf) at quasi-static loading rate (initial rate: 10 mm/min and second rate: 5 mm/min rate).

Maximum load endpoint was set as 4500 N. All testing parameters are given in the Table 20.1. All of the static compression tests have been carried out under same conditions to evaluate damage behaviour of this composite. Total of 12 samples were used for damage analysis.

Microstructure and surface damage evaluations were made by means of optical (OM) and scanning electron microscopy (SEM). The accurate composition of this new designed material is given in Table 20.2 as wt%.

Table 20.1 General conditions for compression tests of produced composites

Initial speed (mm/min)	10	10	10	10
Load endpoint (N)	4500	4500	4500	4500
Outer loop rate (Hz)	100	100	100	100
Secondary speed (mm/min)	5	5	5	5
Strain endpoint (%)	80	80	80	80

Table 20.2 Composition of the epoxy-rubber based composites

Epoxy-rubber based composition →		I	II	III	IV
Reinforcements (wt%)	Boron	5	5	10	5
	Alumina	5	5	5	10
	Glass bubbles	–	5	5	5

20.2.3 Measurements of the Density of the Specimens

All of the measurements of the density of the specimens were carried out by pycnometer (digital density meters, Webb and Orr, 1997 work with helium gas) after post curing and the results were then compared.

20.2.4 Measurements of Dielectric Properties

Dielectric properties: Values of capacitance and dissipation factor (Permittivity (ε') and dielectric loss angle tangent ($\tan\delta$) were investigated using a Dielectric Thermal Analyzer (Rheometric Scientific) at three different frequencies (1, 10 and 100 kHz) in the temperature range from room temperature up to 300 °C. The temperature was increased at a rate of 1 °C/min. Data were collected at temperature intervals of 5 °C.

The samples used for these tests had a diameter of approximately 30 mm and were 1.5 mm thick.

20.2.5 Nanoindentation: Creep and Wear Tests

Creep tests using a nanoindenter were performed on the four composites manufactured. On each sample 20 indents were performed on a 5 × 4 grid with a Berkovich indenter. The indents were spaced 50 μm along the 5 indent side and 75 μm along the 4 indent side. The load was increased at a rate of 1 mN/s to the max load and kept at the maximum load for 500 s then unloaded. Two maximum loads of 20 and 50 mN were used in these tests.

Scratch testing capability of a nanoindenter is utilized to perform relatively fast wear tests to compare the wear behavior of the different samples. In the wear tests conducted a conical tip with a 90° cone angle was used. Wear tests were run under a normal load of 20 mN applied over a linear track of 500 nm for 50 cycles.

20.3 Results and Discussions

20.3.1 Microstructure and Fracture Surfaces of the Compositions

Measurements of the density for four different compositions are given in the Table 20.3. First of all, addition of glass bubbles to the structure slightly influences the density. Overall the densities of the four compositions do not vary from one another too much. The changes observed, although very slight, follow the increase in boron and alumina in the compositions.

The influence of the reinforcements on the mechanical behaviour of four compositions is shown in Table 20.4. Based on these results EBAL III exhibits higher compression resistance with respect to the other compositions. It appears that synergistic effect of boron and alumina is resulting in higher resistance to compression as evidenced by the compositions EBAL III and EBAL IV. With this limited testing, it is difficult to make a clear interpretation on the influence of reinforcements on the resistance of the composition. However, addition of glass bubbles tends to decrease density and increase plastic deformation of the material. These values should be necessitating supplementary tests. More efficient effect of boron reinforcement is observed on the compression resistance.

General microstructures in the transverse direction of the four compositions are shown in Fig. 20.1 (left column). All of the compositions have shown a homogenous distribution of the reinforcements in the structure. Essentially, all of the microstructures show that the adhesion of the rubber to the epoxy matrix is very successfully carried out after the simple chemical treatment.

Table 20.3 Measurements of the density by "He" gas pcynometer (digital density meters)

Composition	Density (g/cm^3)
EBAL-I	1.823 ± 09
EBAL-II	1.810 ± 05
EBAL-III	1.841 ± 04
EBAL-IV	1.838 ± 07

Table 20.4 General mechanical characteristics of the four compositions obtained in quasi-static compression tests

Sample	Peak load, F_{max} (N)	Peak stress (MPa)
EBAL-I	286.25	12.18
EBAL-II	295.16	14.40
EBAL-III	534.89	27.46
EBAL-IV	374.33	17.94

Distribution and cohesion of the all other reinforcements with epoxy are similar. Some small local agglomerations are observed in the structure due to the mixture process; homogenous distributions of the reinforcements need more mixture process.

Fracture surfaces of the four compositions are given in the Fig. 20.1 in the right column. All of the fracture surfaces of the specimens taken from four compositions indicate the regular fracture deviations due to the effect of added reinforcements. Even if some local agglomerations are observed in the structure; they function as strong barriers against crack propagation. The fracture surface of the composition n° 4 (EBAL-IV) is observed to be of more brittle in nature than the other three compositions. All of the SEM observations on the fracture surfaces of the four compositions indicate that no pullout of the reinforcement particles is detected on the specimens.

20.3.2 Dielectric Response of the Composite Structure

Dielectric properties (Permittivity (ε′) and dielectric loss angle tangent (tanδ) were investigated using a Dielectric Thermal Analyzer (DETA-Rheometric Scientific) at four different frequencies (1 kHz, 10 kHz, 100 kHz, 1 MHz) over a large temperature range, from room temperature up to 300 °C. The sample used for this type of test had a diameter of approximately 30 mm and was 1.5 mm thick. It is important to know dielectric response of the composite with different filler contents at room temperature. At the first stage, some preliminary results were plotted in Fig. 20.2a, b.

Dielectric permittivity and also dielectric loss angle tangent (tanδ) for the four composites are compared as a function of temperature. It can be observed that the dielectric permittivity was strongly dependent on the frequency and the concentration of the fillers. Higher values were obtained at low frequencies because of the low resistivity of magnetite, which generated electric charge conversion. The peaks obtained for 4 frequencies give different temperature values [these values are around 200 °C for 1 kHz and for 10 kHz and around 175 °C for 100 kHz and 1 MHz (Fig. 20.2a)]. The same observation is seen in Fig. 20.2b, dielectric loss angle tangent (tanδ) is found similar results mainly these values found at lower frequencies are very close. These peaks corresponded to a relaxation process and started to be evidenced at high temperatures [5, 12, 13].

Although the presented results are indicative of the dielectric response of the composite discussed in this work, additional testing will continue to get more detailed information in terms of certain parameters such as temperature interval and increasing of the number of the frequency etc.

All of the samples have shown a not so high permittivity (it means that they are in medium level of permittivity) and medium dielectric loss.

An interfacial effect is visibly evident and the additional elements effectively, filler effect of boron and alumina are significant; this is considerably important as parts of an aircraft can experience rather high and very low temperatures in service.

20.3.3 Creep Testing by Nanoindentation

Creep tests using a nanoindenter were performed on the four composites manufactured. On each sample 20 indents were performed on a 5 × 4 grid with a Berkovich indenter. The indents were spaced 50 μm along the 5 indent side and 75 μm along the 4 indent side. The load was increased at a rate of 1 mN/s to the maximum load and kept at the maximum load for

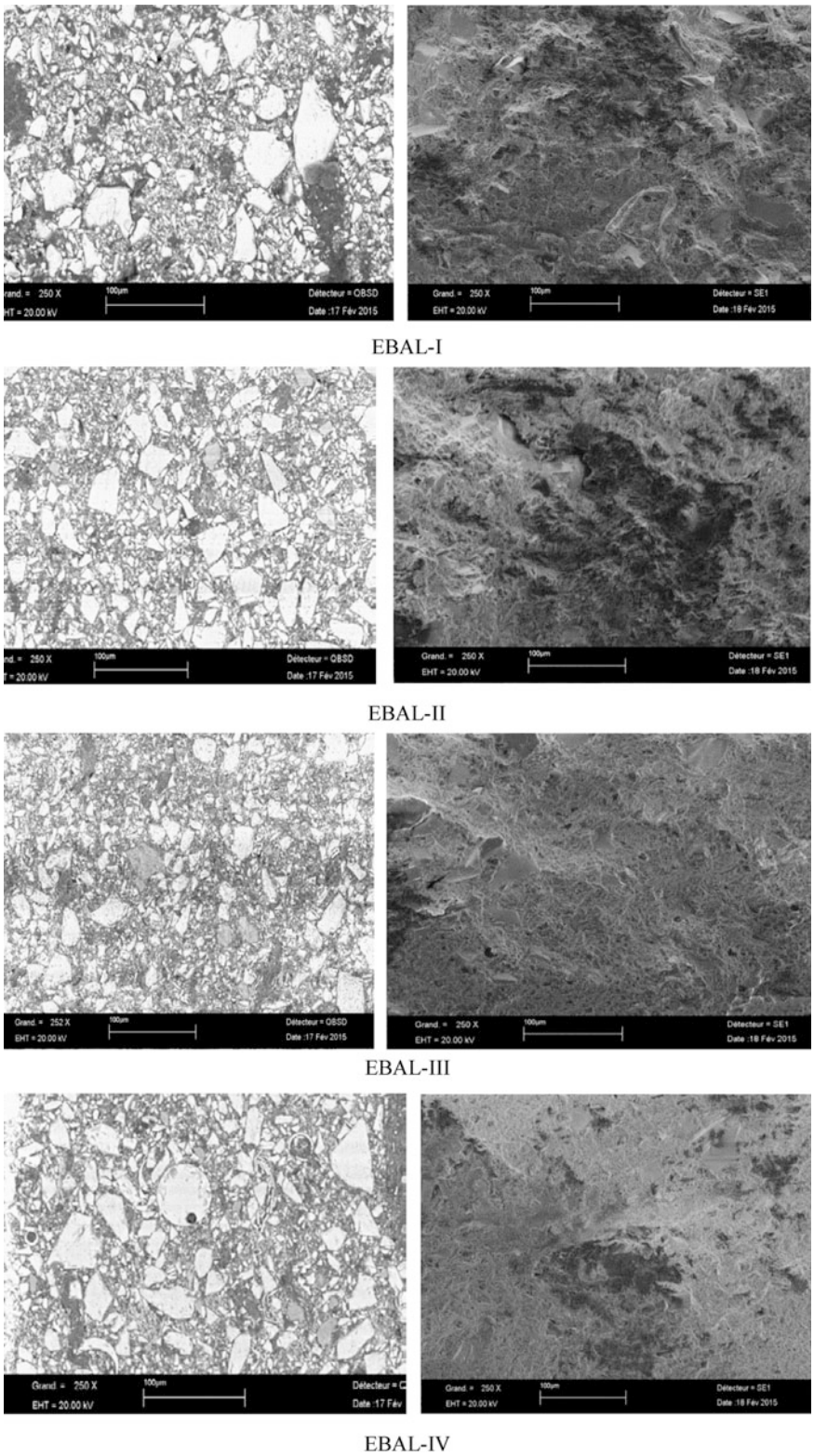

Fig. 20.1 Microstructural (*left column*) and fracture surfaces of the compositions (*right column*)

500 s then unloaded. A typical load-on-sample vs displacement-into-sample graph is shown in Fig. 20.3. Two maximum loads of 20 and 50 mN were used in these tests.

During each test data collected was used to calculate the creep compliance and the stress exponent defined by the relationships as follows [6]

$$\varepsilon(t) = \sigma_0 J(t) \tag{20.1}$$

where σ_0 is the constant stress applied and $J(t)$ is calculated using

$$J(t) = A(t)/(1-\nu)P_0 \tan\theta \tag{20.2}$$

In Eq (20.2) $A(t)$ is the contact area, P_0 constant applied load, θ is the effective cone angle which is 70.3° for a Berkovich indenter and the Poisson's ratio ν is assumed to be 0.3. A typical creep compliance graph is shown in Fig. 20.4a.

The strain versus time behavior during creep is characterized by a high strain rate $\dot{\varepsilon} = d\varepsilon/dt$ in the primary stage of creep and then in the secondary, steady state stage of creep, the strain rate can be written as

$$\dot{\varepsilon} = K\sigma^n \tag{20.3}$$

where K is a constant and n is the stress exponent. The strain rate is calculated in the software and in turn n is obtained from the log-log plot of strain rate versus stress in the secondary stage of creep.

The materials under consideration are heterogeneous in nature and the fact that the nanoindenter testing is carried out over a small area/volume, a large scatter in the data is observed. To illustrate this selected displacement-into-surface versus time-on-sample curves are shown in Fig. 20.4b.

The average stress exponent from the 20 indentations performed under 20 and 50 mN constant loads is presented in Fig. 20.5a with error bars showing ± one standard deviation. It is seen that increase in boron and alumina content after glass bubbles were added resulted in more favorable creep response (EBAL III and EBAL IV).

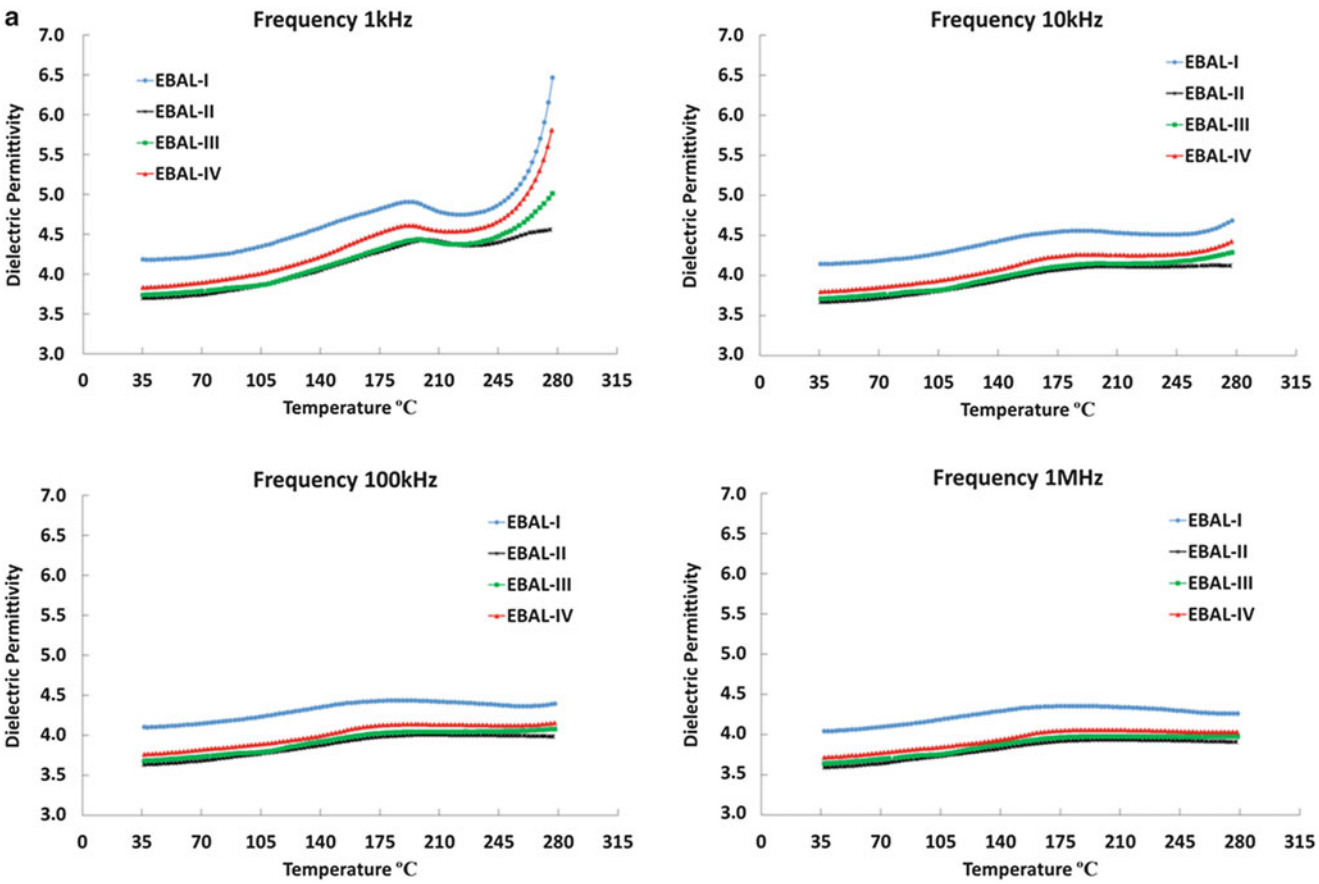

Fig. 20.2 (**a**) Evolution of dielectric permittivity as a function of temperature measured at the different frequencies variable as 1 kHz, 10 kHz, 100 kHz and 1 MHz. (**b**) Evolution of dielectric loss angle tangent (tanδ) as a function of temperature measured at the different frequencies variable as 1 kHz, 10 kHz, 100 kHz and 1 MHz

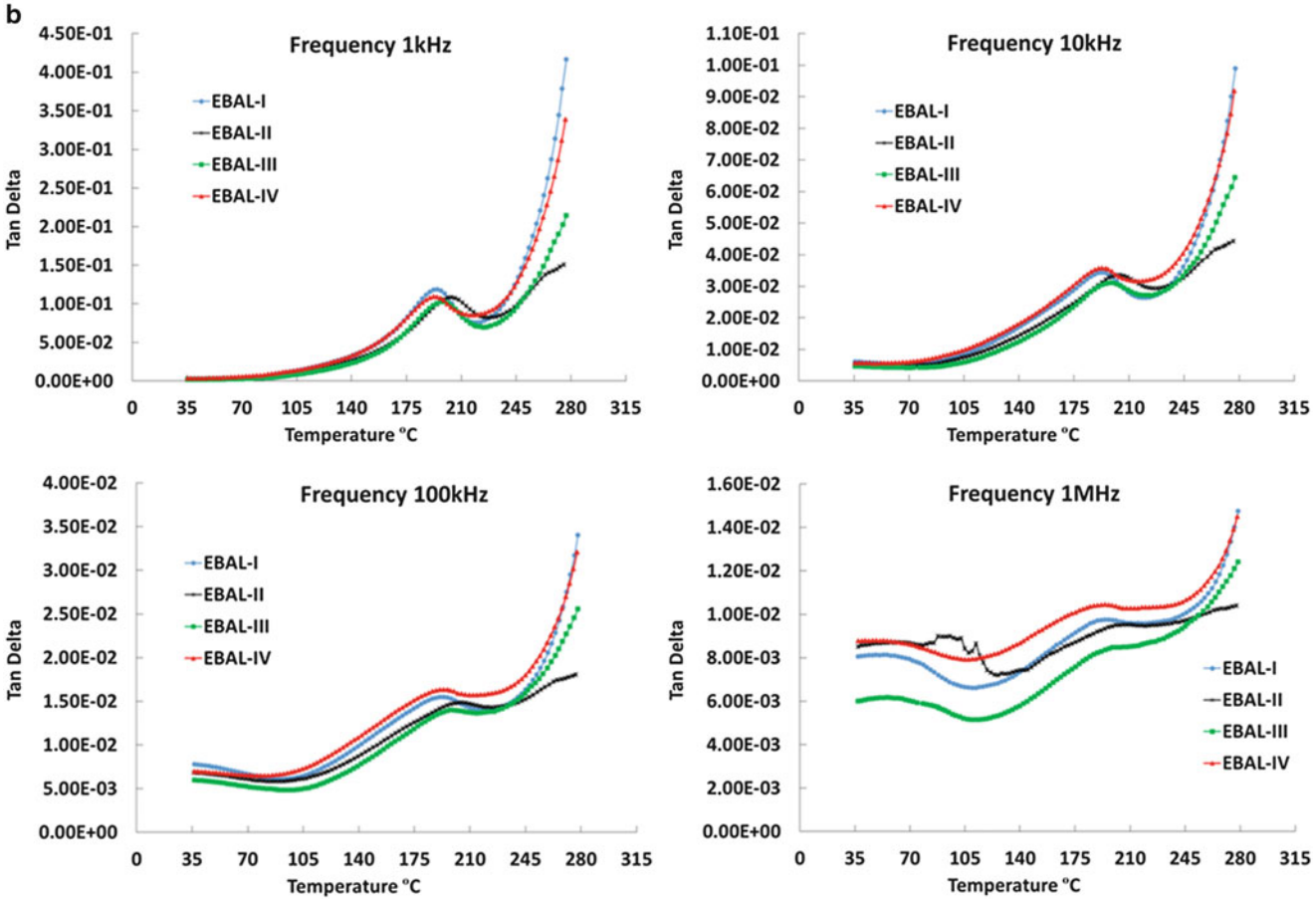

Fig. 20.2 (continued)

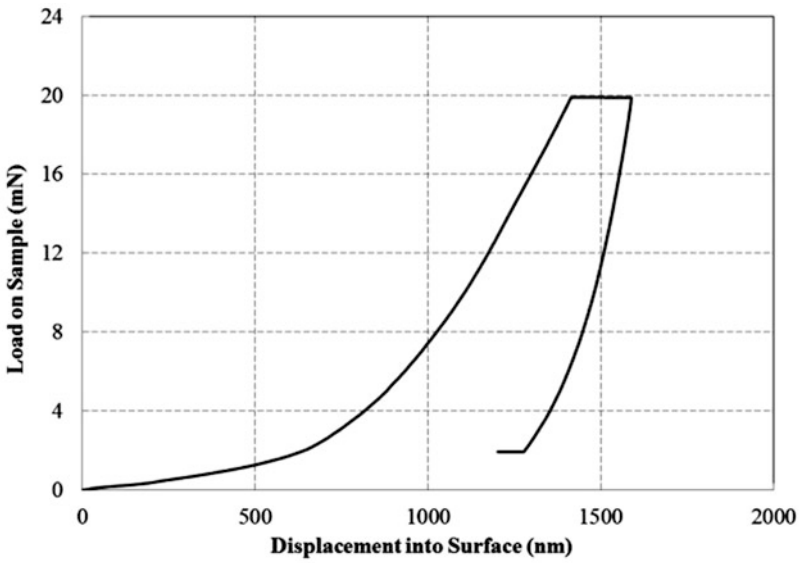

Fig. 20.3 Typical Load-displacement curve during the creep test; Data is from sample EBAL4, test 9

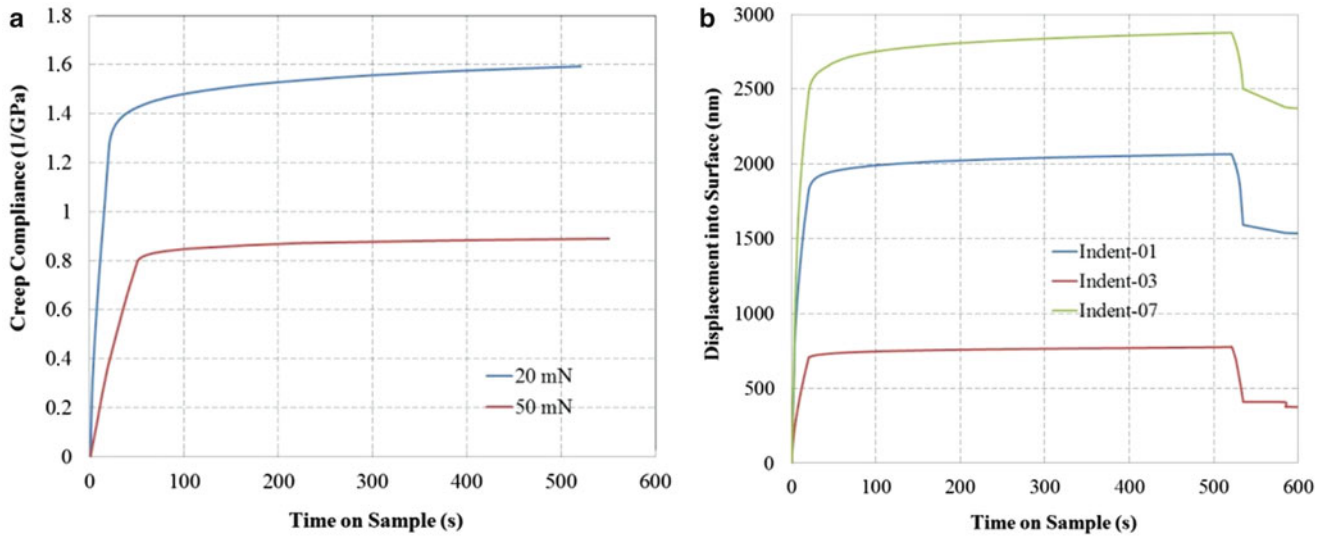

Fig. 20.4 (**a**) Creep Compliance curves for sample EBAL4, under 20 and 50 mN load and (**b**) Displacement into surface curves at different indent location on sample EBAL4, under 20 mN load

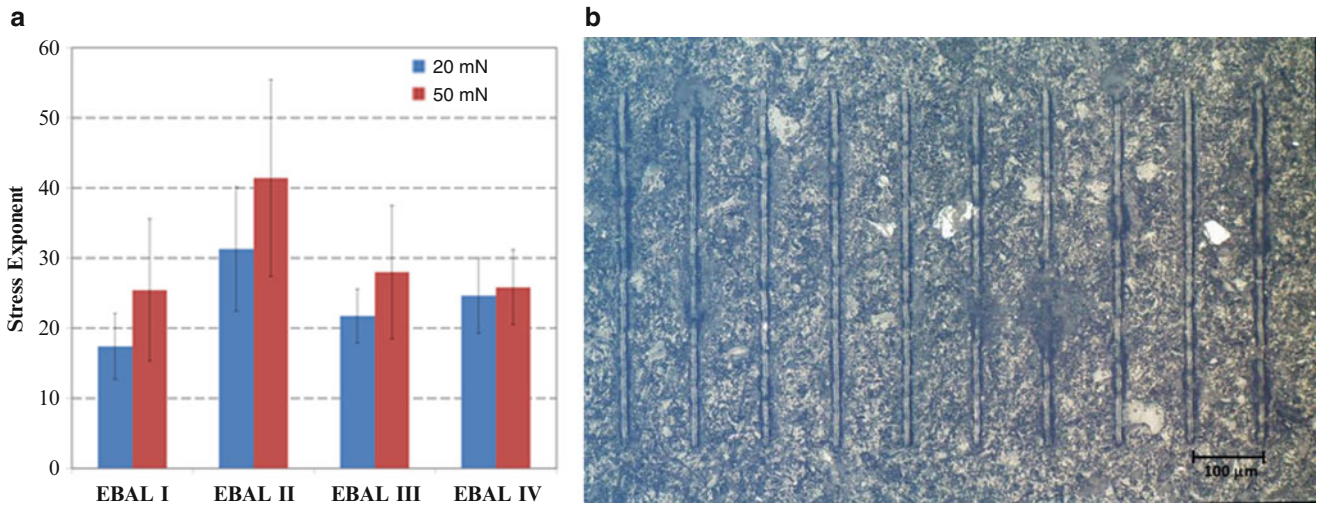

Fig. 20.5 (**a**) Stress exponent for the four composites under 20 and 50 mN load and (**b**) Wear tracks obtained on the specimen called EBAL-1 under 20 mN load application

20.3.4 Wear Testing by Nanoindentation

Scratch testing capability of a nanoindenter is utilized to perform relatively fast wear tests to compare the wear behavior of the different samples. In the wear tests conducted conical tip with a 90° cone angle was used. Wear tests were run under a normal load of 20 mN applied over a linear track of 500 nm for 50 cycles. One cycle is defined as a pass and return over the track, so the total distance covered for one wear test was 0.050 m. Speed of the tip during wear tests was 50 µm/s.

Total of 10 wear tests for each sample were performed under the two normal loads. The residual wear tracks on EBAL I under 20 mN force are shown in Fig. 20.5b. The wear in a track is characterized as the area between the initial profile and the residual profile of the wear track.

Figure 20.6a shows the initial and residual tracks for wear track 1 of sample EBAL I. Note that the normal load is applied between 100 and 600 µm along the Scratch Distance axis.

In the same way, the averages of the wear track deformation are shown in Fig. 20.6b.

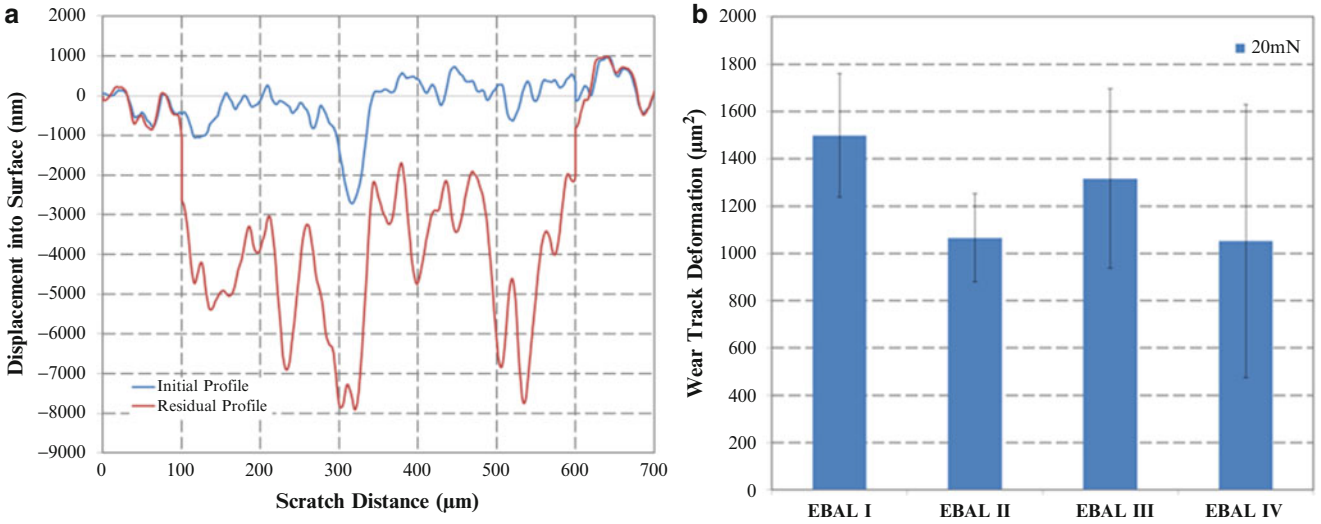

Fig. 20.6 (**a**) Example initial and residual profiles used in the calculation of wear track deformation and (**b**) Comparison of wear track deformation for the four composites

20.4 Conclusions

Microstructural observations of the four compositions show very successfull adhesion to rubber after a simple chemical treatment and also the cohesions of the other reinforcements with the epoxy matrix. The addition of glass bubbles tend to promote decrease in density and to increase plastic deformation of the material.

Fracture surfaces of the specimens taken from four compositions indicate regular fracture deviations due to the effect of added reinforcements even if some local agglomerations observed in the structure; play strong role as barriers against the propagation of the fracture surface.

Creep compliance is a useful metric that measures a unique mechanical response of time-dependent materials.

Measurements of dielectricity of the samples from four compositions have shown very little dependence on the reinforcements under our experimental conditions. Only small differences may come from the particle's sizes.

Scratch testing capability of a nanoindenter is utilized successfully to perform relatively fast wear tests to compare the wear behavior of the different samples.

Regarding to the results may be there are some variances for the composition of EBAL-II III and IV due to the glass bubbles and alumina reinforcements that necessitate supplementary tests.

Acknowledgments The authors would like to thank Dr. H.-A. Alhas and Mr. Carlo Nizam, of Airbus-Helicopter—France for their help in providing materials and for their valuable discussions.

References

1. Juliano, T.F., VanLandingham, M.R., Tweedie, C.A., Van Vliet, K.J.: Multiscale creep compliance of epoxy networks at elevated temperatures. Exp. Mech. **47**, 99–105 (2007)
2. Oliver, W.C., Pharr, G.M.: Measurement of hardness and elastic modulus by instrumented indentation: advances in understanding and refinements to methodology. J. Mater. Res. **19**, 3–20 (2004)
3. Briscoe, B.J., Fiori, L., Pelillo, E.: Nano-indentation of polymeric surfaces. J. Phys. D: Appl. Phys. **31**, 2395–2405 (1998)
4. Berthoud, P.G., Sell, C., Hiver, J.M.: Elastic-plastic indentation creep of glassy polymethyl methacrylate and polystyrene: characterization using uniaxial compression and indentation tests. J. Phys. D: Appl. Phys. **32**, 2923–2932 (1999)
5. Nelson, J.K., Fothergill, J.C., Dissado, L.A., Peasgood, W.: Towards an understanding of nanometric dielectrics. IEEE conference, electrical insulation and dielectric phenomena, pp. 295–298, Mexico, Oct 2002
6. Tehrani, M., Safdari, M., Al-Haik, M.S.: Nanocharacterization of creep behavior of multiwall carbon nanotubes/epoxy composite. Int. J. Plast. **27**, 887–901 (2011)
7. Wood, L.A., Roth, F.L.: Creep of pure-gum rubber vulcanizates from indentation-time measurements. In: Proceedings of 4th Rubber Technologies Conference, London, p. 328 (1962)

8. Wood, L.A., Roth, F.L.: Institution of rubber industry London 1963. Rubber Chem. Technol. **36**(611), 1963 (1963)
9. Wernik, J.M., Meguid, S.A.: Multiscale modeling of the nonlinear response of nano-reinforced polymer. Acta Mech. **217**(1–2), 1–16 (2011)
10. Psarras, G.C.: Hopping, conductivity in polymer matrix – metal particles composites. Compos. A **37**, 1545–1553 (2006)
11. Ultracki, L.A.: Polymer Alloys and Blends: Thermodynamic and Rheology. Hanser, New York (1990)
12. Psarras, G.C., Manolakaki, E., Tsangaris, G.M.: Electrical relaxations in polymeric particulate composites of epoxy resin and metal particles. Compos. A **33**, 375–384 (2002)
13. Findley, W.N.: Creep characteristics of plastics. In: ASTM Symposium on Plastics, Philadelphia 1944; American Society for Testing Materials, Philadelphia, USA, pp. 118–127 (1944)
14. Catherine Tweedie, A., Krystyn Van Vliet, J.: Contact creep compliance of viscoelastic materials via nanoindentation. J. Mater. Res. **21**(6), 1576–1589 (2006)

Chapter 21
Prediction of Flexural Properties of Coir Polyester Composites by ANN

G.L. Easwara Prasad, B.S. Keerthi Gowda, and R. Velmurugan

Abstract In the present study flexural strength of coir fiber reinforced polyester composite is predicted by using Artificial Neural Network. Randomly oriented coir fibers of length 10 mm were used to cast 3 mm, 5 mm and 6 mm thick specimens with fiber volume fraction of 10 %, 15 %, 20 % and 25 % respectively. The flexure tests were conducted as per ASTM D7264. From the experimental results it is observed that the flexural strength increased up to 20 % fiber volume fraction and then it decreased. Further flexural strength is found to increase with increase in the thickness of composite specimens also. Composite specimen of 5 mm thickness with 20 % fiber volume fraction recorded the highest flexural strength of 141.042 MPa. An Artificial Neural Network is adopted with supervised training approach to fix the optimum weighted matrix. Predicted results of flexural strength are also presented. Both the experimental and predicted results of flexural strength depict the similar trend. The error between predicted and experimental results is less than 5.00 %, hence Artificial Neural Network can be effectively adopted to prognosticate the flexural strength of coir fiber reinforced polyester matrix composites; which reduces the expensive manual involvement and its related errors during conduction of experimental programme. Artificial Neural Network results can be obtained quickly than the experimental results.

Keywords Coir • Flexural strength • ANN • Prediction • Polyester

21.1 Introduction

In spite of having low density and weight, natural Fiber Reinforced Polymer (FRP) composites are tough and have acceptable specific strength, good thermal properties and reduced dermal and respiratory irritation. Natural FRP composites are also biodegradable, economical, environmental friendly and impermeable to electromagnetic radiations. Compared to the artificial fibers natural fibers are easily (locally) available, requires less chemical treatment, requires lesser expenditure for fabrication setup. Hence in the present study one of non-wood natural fibers like coir is used as reinforcement with polyester resin. Cobalt naphthenate and methyl ethyl ketone peroxide are used as catalyst and hardener while casting the polyester resin matrix composites.

Earlier researchers have reported extensive studies on composites by using natural fibers as reinforcement among them Ghosh et al. [1] have reported that banana fiber having high specific strength makes a light weight composite material and can be used to make light weight automobile interior parts. Lu et al. [2] have reported that the sisal/phenol formaldehyde composites made by the synthesizing method have shown an increase of 17.61 %, 7.16 % and 12.25 % in impact strength, bending strength and bending modulus respectively as compared to conventional physical blending method. Ali [3] has reported that coconut fibers are ductile and energy absorbent. Zaman et al. [4] have shown that mechanical properties of coir fiber reinforced composites have a strong association with their dynamic characteristics. Sathiyamurthy et al. [5] have reported that Artificial Neural Network (ANN) models can be used effectively for predicting the mechanical properties of inorganic fillers impregnated coir—polyester composites. Gowda et al. [6] have reported that the tensile strength of coir fiber

G.L.E. Prasad (✉)
Department of Civil Engineering, MITE-VTU, Moodabidri, Karnataka, India
e-mail: principal@mite.ac.in

B.S.K. Gowda
Department of Structural Engineering, VTU PG Studies, Mysore, Karnataka, India
e-mail: keerthiresearch@yahoo.com

R. Velmurugan
Department of Aerospace Engineering, IIT Madras, Chennai, Tamil Nadu, India

C. Ralph et al. (eds.), *Mechanics of Composite and Multi-functional Materials, Volume 7*,
Conference Proceedings of the Society for Experimental Mechanics Series, DOI 10.1007/978-3-319-21762-8_21

reinforced polyester composite is relatively high when compared to sisal fiber reinforced polyester composites; and that natural fiber reinforced composites can be regarded as a useful light weight engineering material. Easwara Prasad et al. [7] have reported that the feed forward ANN model could be a very good mathematical tool for prediction of properties of coir fiber reinforced epoxy resin composites.

Further, Verma et al. [8] have reported that several natural fiber composites have shown mechanical properties akin to glass fiber composites and are being used in furniture and other related industries. Karthik et al. [9] have studied the surface roughness value of composites using boiled egg shell and rice husk particulate (15 %) and coir fiber (10 %). The study has revealed that higher surface roughness values are recorded when fibers of 10 mm length are used when compared with the values obtained using fiber of 30 mm length. Li et al. [10] have reported in their study that natural fibers can be a potential replacement for an artificial fiber in composite materials. Kuriakose et al. [11] have reported that adhesion at fiber—matrix interface can be improved by sodium hydroxide treatment—mercerization of the fibers. This treatment creates porous surface leading to a rough surface texture which allows coir fibers to reinforce strongly with polyester matrix. Idicula et al. [12] have reported the mechanical performance of short randomly oriented banana and sisal hybrid fiber reinforced polyester composites. With reference to the relative volume fraction of those two fibers, at a constant total fiber loading of 0.40 volume fractions, keeping banana as the skin material and sisal as the core material, the impact strength of the composites were increased with fiber loading. The tensile and flexural properties of respective composite were found to be better at 0.40 volume fraction. Girisha et al. [13] have reported that natural fibers (sisal and coconut coir) reinforced epoxy composites were subjected to water immersion tests in order to study the effects of water absorption on mechanical properties. Natural fibers like coconut coir (short fibers) and sisal fibers (long fibers) were used in hybrid combination and the fiber weight fraction of 20, 30 and 40 % for the fabrication of the composite. Water absorption tests were reported by immersing specimens in a water bath at 25 and 100 °C for different time durations. The tensile and flexural properties of water immersed specimens subjected to both aging conditions were evaluated and compared with dry composite specimens. The percentage of moisture uptake was found to increase along with increase in fiber volume fraction due to the high cellulose content of the fiber. The tensile and flexural properties of natural fiber reinforced epoxy composite specimens were found to decrease with increase in percentage moisture uptake. Moisture induced degradation of composite samples was observed at elevated temperature.

Additionally, Sen et al. [14] have depicted that the materials chosen for structural up-gradation must be functionally efficient, qualitatively superior and sustainable. The application of composites in structural facilities is at present mostly concentrated on increasing the strength of the structure with the help of artificial fibers and does not address the issue of sustainability of the raw materials used. Sisal is an abundant source of natural fiber used for making ropes, mats, carpets and as reinforcement with cement. In developing countries, sisal fibers are used as roofing materials in houses. Thomas et al. [15] have studied the mechanical properties of hybrid lingo-cellulosic fiber reinforced natural rubber composites. The objective of their study was to investigate the effect of the ratios of sisal and oil palm fibers on tensile properties of natural rubber composites. The mechanical properties were found to be more dependent on sisal fiber than oil palm. A positive hybrid effect was observed for the tensile properties. The extent of fiber alignment was found to be more when sisal and oil palm was present in equal amounts. Bujang et al. [16] have studied the effect of coir fibers volume on mechanical properties and dynamic characteristic of composite. They reported that the mechanical properties have a strong association with the dynamic characteristic. Both the properties are highly dependent on the volume percentage of fibers. The tensile strength of composite was found to be linearly proportional to the natural frequency. Moreover, the damping ratio was found to be increased by incorporation of coir fibers which giving an advantage to the structure in reducing the high resonant amplitude. Riedel et al. [17] reported that the fibers serve as a reinforcement and show high tensile strength and stiffness, while the matrix holds the fibers together, transmits the shear forces, and also functions as a coating. Further criteria for the choice of suitable reinforcing fibers include: elongation at failure; thermal stability; adhesion of the fibers and matrix; dynamic behavior; long-term behavior; and price and processing costs. Sabah et al. [18] depicts that natural fibers, when used as reinforcement, compete with such technical fibers as glass fiber. Till date, the most important natural fibers used in composites are Jute, flax, sisal and coir. Natural Fibers are renewable raw materials and they are recyclable.

ANN are a family of statistical learning algorithms inspired by biological neural networks and are used to estimate or approximate functions that can depend on a large number of inputs and are generally unknown. ANN are generally presented as systems of interconnected "neurons" which can compute values from inputs, and are capable of machine learning as well as pattern recognition. A significant reports and papers have been published in application of ANN for the prediction of future events in Civil engineering problems. Various studies reported are, Artificial Neural Network Applications in geotechnical Engineering [19], Neural networks for profiling stress history of clays from PCPT data [20], Reducing prediction error by transforming input data [21], A fuzzy-Neuro Model for Normal Concrete mix design [22], to predict optimized parameters of earth retaining wall [23, 24], to prognosticate concrete mix proportion of ingredients [25, 26],

From the literature survey it is observed that more detailed study is necessary in the area of predictive study of mechanical strength of natural fiber reinforced polymer matrix composites. Hence the present study aims to predict the flexural strength of coir fiber reinforced polymer matrix composite by using ANN.

21.2 Materials and Methods

21.2.1 Materials

In the present study raw (untreated) coir fiber is used as reinforcement, polyester resin as matrix, cobalt naphthenate as catalyst and methyl ethyl ketone peroxide as curing agent. Fabrication of specimen is carried out using hand operated simple compression molding machine.

21.2.2 Specimen Casting

The knotted fibers are obtained from coconut spathes and are cleaned up. These fibers are passed through a Knot Separating Machine to remove the knots and separate individual fibers. The fibers obtained from knot separating machine are dried in sunlight for a period of 48 h to remove the moisture content. Fibers are cut to a length of 10 mm to be used in randomly oriented fiber mats. In this stage, the spacers are used for casting composite panels of size 300 mm $\times$ 300 mm with varying thicknesses (3, 5, and 6 mm). These are placed on the base plate and a thick Mylar (a non sticky) sheet is placed in between spacers and base plate for the easy removal of composite specimen after fabrication. Resin, catalyst and hardener are mixed in a proportion of 50:1:1 that is 1000 ml:20 ml:20 ml in ratio and stirred well. A 10 mm long coir fiber of required fiber volume fraction (10, 15, 20 and 25 %) is weighed and distributed uniformly at the bottom of the mould inside the spacers. Compression load is then applied for 15 min on mould containing the fibers. Resin is then applied uniformly on this. Another releasing Mylar sheet is spread over as the top surface with a steel plate and then the specimen is compressed for 1 h for uniform distribution of matrix and elimination of entrapped air bubble if any. The composite is removed from the mould and left for curing at room temperature for 24 h after which the desired composite specimens were cut from the casted composite panels.

21.2.3 Flexure Test

The flexure strength of each specimen in the present study was carried out as per American Society for Testing and Materials (ASTM) standard D7264 [27]. As per the standards the support span-to-depth ratio is 32:1, the standard specimen thickness should be 4 mm and standard width is 13 mm with specimen length being 20 % longer than the support span. It also reveals that if the standard specimen thickness cannot be obtained in a given material system, an alternate specimen thickness shall be used while maintaining the support span-to-thickness ratio and specimen width. Optimal support span-to-thickness ratios of 16:1, 20:1, 40:1, and 60:1 may also be used. So in the present study the each specimens of thickness 3 mm, 5 mm and 6 mm of different percentages of fiber content were tested by using the optimal support span-to-thickness ratio of 20:1 respectively.

21.3 Results and Discussions

From the experimental results reported in Table 21.1 we can observe that the flexural strength of the coir fiber reinforced polyester matrix composite specimen is found to increase with increase in thickness of the specimens. Further it is also observed that the flexural strength of the specimens is found to increase with increase in the fiber volume fraction up to 20 % of fiber volume fraction and then it decreased. Figure 21.1 shows the variation of flexural strength with respect to fiber volume fraction as obtained from the experimental studies.

Table 21.1 Flexural strength of coir polyester composite (MPa)

Fiber volume fraction (%)	Thickness of composite specimen (mm)		
	3	5	6
10	20.102	55.923	68.253
15	28.934	63.862	67.157
20	67.652	141.042	116.611
25	38.216	60.348	54.592

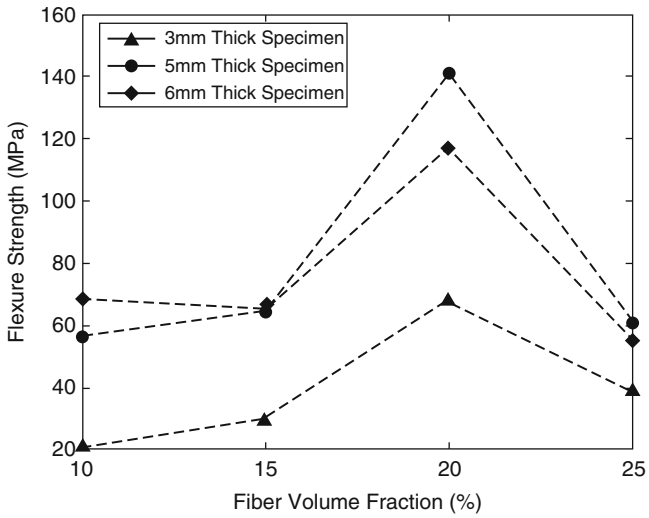

Fig. 21.1 Variation of flexural strength with fiber volume fraction

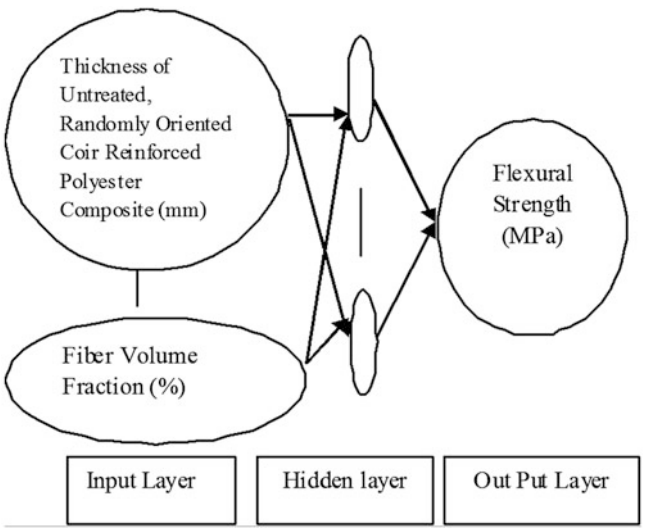

Fig. 21.2 Topology to predict flexural strength of untreated coir reinforced polyester composite (2-14-1)

Figure 21.2 represents the topology adopted to fix the optimal weighted matrix to prognosticate the flexural strength of coir polyester composites. Figure 21.3 shows the training convergence curve developed during the supervised training process of ANN and Fig. 21.4 depicts the variation of mean square error (MSE) between experimental data and predicted data (by using ANN) during the ANN training process. This graphical variation shows that as number of epoch increases MSE decreases. Table 21.2 represents the predicted flexural strength of coir polyester composites by using ANN. Here flexural strength of 3, 4, 5 and 6 mm thick coir polyester composite of fiber volume fraction from 10 to 25 % is predicted.

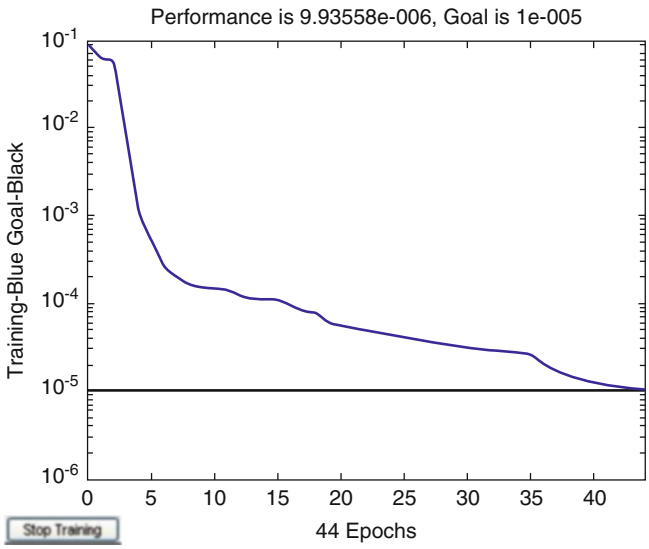

Fig. 21.3 ANN convergence curve

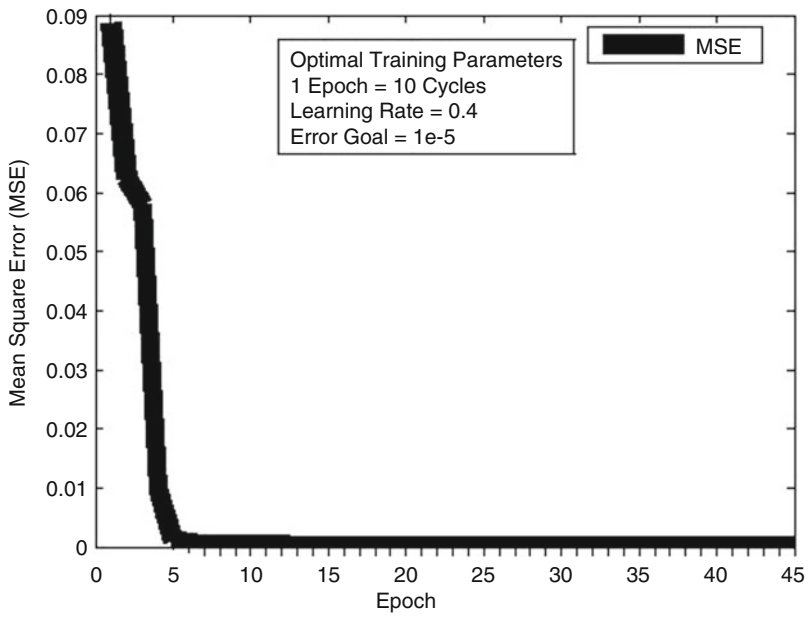

Fig. 21.4 Variation of mean square error with epoch

Value in the parenthesis is the experimental results. Here all the values follow the same trend as experimental data. The difference between experimental values and predicted values of flexural strength is less than 5.00 % and its correlation co-efficient is estimated as 0.999.

21.4 Conclusion

From the experimental results obtained (see Table 21.1), it can be observed that untreated coir fiber reinforced polyester matrix composite specimens of 5 mm thickness have given highest flexural strength at its 20 % fiber volume fraction. In general it can also be observed that the flexural strength of coir fiber reinforced polyester matrix composite specimens is found to increase with increase in thicknesses. Further it can be observed from the Table 21.2 and Fig. 21.5, when the fiber volume fraction increases above 21 % a decrease in flexural strength is observed. From the above observations it can be

Table 21.2 Predicted flexural strength of untreated randomly oriented coir reinforced polyester matrix composite

	Thickness of composite specimen (mm)			
Fiber volume fraction (%)	3	4	5	6
10	20.160 (20.102)	37.298	55.219 (55.923)	67.555 (68.253)
11	15.856	26.778	41.335	56.625
12	13.874	25.297	36.275	50.464
13	15.876	27.762	39.542	52.034
14	20.899	34.559	49.602	59.015
15	28.452 (28.934)	48.248	63.937 (63.862)	68.050 (67.157)
16	37.917	64.869	80.602	77.876
17	47.082	79.883	98.796	88.958
18	55.295	95.248	117.266	101.056
19	62.671	108.161	131.359	111.216
20	67.762 (67.652)	116.173	140.08 (141.042)	116.371 (116.611)
21	69.455	120.391	144.820	117.779
22	68.913	118.140	140.817	114.032
23	62.559	105.095	125.552	103.304
24	51.292	83.118	99.99	84.102
25	38.816 (38.216)	47.065	62.872 (60.348)	54.196 (54.592)

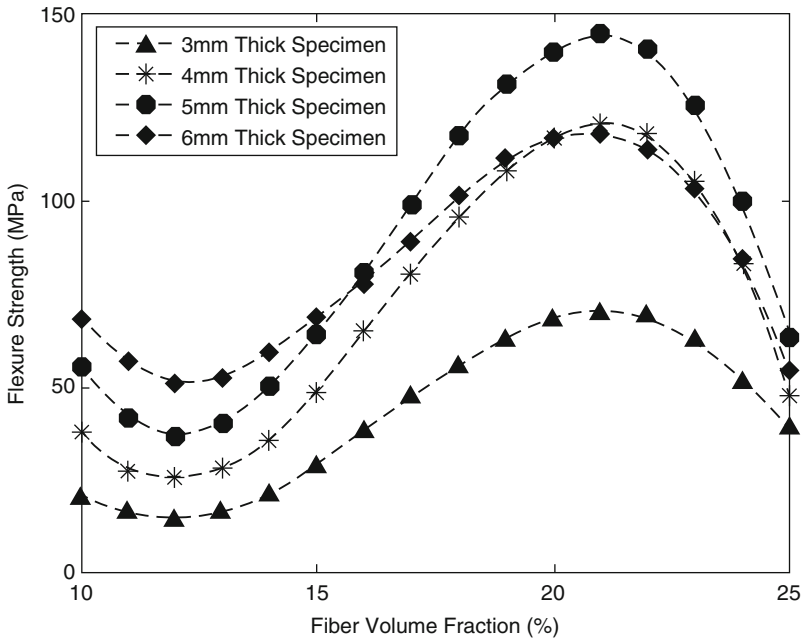

Fig. 21.5 Prediction of flexural strength with fiber volume fraction

concluded that with higher volume of fibers the availability of matrix for bonding gets reduced leading to reduction in flexural strength of the specimen. Figure 21.6 shows the comparison of flexural strength obtained from experimental study and ANN is found to match well (see Fig. 21.6).

Predicted values of flexural strength (see Table 21.2 and Fig. 21.5) shows that ANN can be authentically adopted as predicting tool to forecast the flexural strength of untreated coir polyester matrix composites of the required strength. The correlation co-efficient between experimental data and predicted data strongly supports the suitability of ANN for prediction process of flexural strength of coir polyester composites. This soft computing technique effectively minimizes the manual involvement in the experimental process of flexural strength of coir polyester composites and reduces its related manual error with less time consumption.

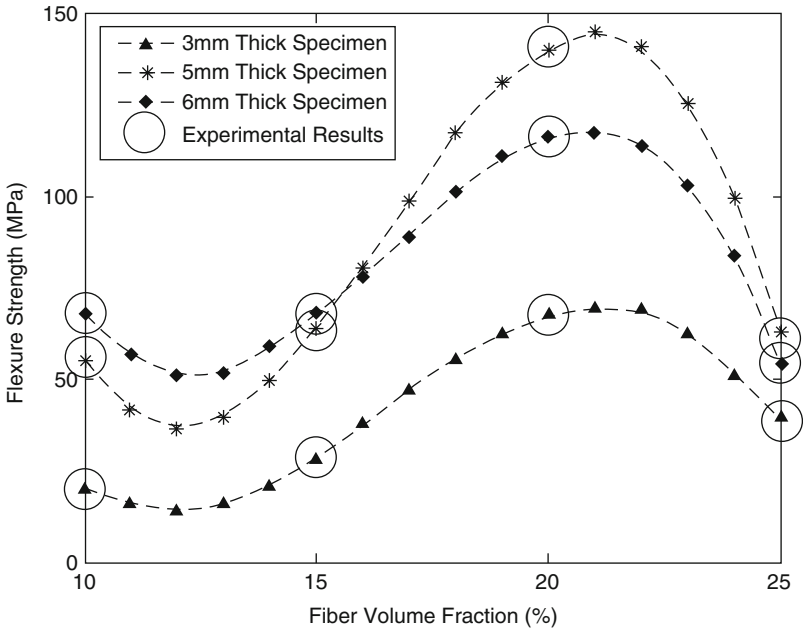

Fig. 21.6 Comparison of flexural strength obtained from experimental study and ANN

References

1. Ghosh, R., Krishna, A.N.R., Reena, G., Raju, B.H.L.: Effect of fiber volume fraction on the tensile strength of banana fiber reinforced Vinyl Ester resin composites. Int. J. Adv. Eng. Sci. Technol. **4**(1), 89–91 (2011). ISSN: 2230-7818
2. Lu, J., Zhong, J.-B., Wei, C.: Studies on the properties of sisal fiber/phenol formaldehyde resin in-situ composites. Res. J. Text. Appar. **10**(3), 51–58 (2006)
3. Ali, M.: Coconut fiber – a versatile material and its applications in engineering. Second international conference on sustainable construction materials and technologies, 28–30 June 2010
4. Zaman, I., Ismail, A.E., Awang, M.K.: Influence of fiber volume fraction on the tensile properties and dynamic characteristics of coconut fiber reinforced composite. J. Sci. Technol. **1**(1), 55–71 (2011)
5. Thaheer Satiyamurthy, S., Abu, A.S., Jayabal, S.: Prediction and optimization of mechanical properties of particles filled coir – polyester composites using ANN and RSM algorithms. Indian J. Fiber Text. Res. **38**(1), 081–086 (2013)
6. Gowda, B.S.K., Prasad, G.L.E., Velmurugan, R., Akshay, N.K.: Comparative study of tensile strength of coir and sisal fiber reinforced composites. Proceedings of the Indo Russian workshop on tropical problems in solid and applied mechanics, Chennai, 12–16 Nov 2013
7. Prasad, G.L.E., Gowda, B.S.K., Velmurugan, R.: Prediction of properties of coir fiber reinforced composites by ANN. In: Experimental Mechanics of composites, Hybrid and Multifunctional Materials, vol. 6, pp. 1–7. Springer International Publishing (2014)
8. Verma, D., Gope, P.C., Shandilya, A., Gupta, A., Maheswari, M.K.: Coir fiber reinforcement and application in polymer composites: a review. J. Mater. Environ. Sci. **4**(2), 263–276 (2013). ISSN: 2028-2508
9. Karthik, R., Sathiyamurthy, S., Jayabal, S., Chidambaram, K.: Tribological behaviour of rice husk and egg shell hybrid particulated coir-polyester composites. IOSR J. Mech. Civil Eng. 75–80, E-ISSN: 2278-1684, p-ISSN: 2320-334X (2014)
10. Li, X., Lope, G.T., Panigrahi, S.: Chemical treatments of natural fiber for use in natural fiber – reinforced composites: a review. J. Polym. Environ. **15**(1), 25–33 (2007)
11. Kuriakose, S., Varma, D., Vaisakh, V.G.: Mechanical behaviour of coir reinforced polyester composites – an experimental investigation. Int. J. Emerg. Technol. Adv. Eng. **2**(12), 751–757 (2012). ISSN: 2250-2459
12. Idicula, M., Neelakantan, N.R., Oommen, Z., Joseph, K., Thomas, S.: A study of the mechanical properties of randomly oriented short banana and sisal hybrid fiber reinforced polyester composites. J. Appl. Polym. Sci. **96**(5), 1699–1709 (2005)
13. Girisha, C., Sanjeevamurthy, Gunti, R.S.: Sisal/coconut coir natural fibers – epoxy composites: water absorption and mechanical properties. Int. J. Eng. Innov. Technol. **2**(3), 166–170 (2012)
14. Sen, T., Reddy, H.N.J.: Application of sisal, bamboo, coir and jute natural composites in structural upgradation. Int. J. Innov. Manag. Technol. **2**(3), 186–191 (2011)
15. Thomas, S., Varughese, K.T., John, M.J.: Green composites from natural fibers and natural rubber: effect of fiber ratio on mechanical and swelling characteristics. J. Nat. Fibers **5**(1), 47–60 (2008)
16. Bujang, I.Z., Awang, M.K., Ismail, A.E.: Study on the dynamic characteristic of coconut fiber reinforced composites. Regional conference on engineering mathematics, mechanics, manufacturing & architecture, noise, vibration and comfort research group, pp. 184–202 (2007)
17. Riedel, U., Nickel, J.: Applications of natural fiber composites for constructive parts in aerospace, automobiles, and other areas. Biopolymers. Online 15 Jan 2005. DOI: 10.1002/3527600035.bpola001(2005)

18. Reem, S.M., Ansari, M., Mohannad, S.H.: A study on mechanical, thermal and morphological properties of natural fibre/epoxy composite. J. Purity Util React Environ **1**(5), 237–266 (2012)
19. Shahin, M.A., Jaksa, M.B., Maier, H.R.: Artificial neural network applications in geotechnical engineering. Aust. Geomech. **36**(1), 49–62 (2001)
20. Kurup, P.U., Dudani, N.K.: Neural networks for profiling stress history of clays from PCPT data. J. Geotech. Geoenviron. Eng. **128**(7), 569–578 (2002)
21. Bhattacharya, B., Solomatine, D.P.: Machine learning in soil classification. Neural Netw. **19**(2), 186–195 (2006)
22. Nataraja, M.C., Jayaram, M.A., Ravikumar, C.N.: A fuzzy-neuro model for normal concrete mix design. Eng. Lett. **13**(2), 98–107 (2006)
23. Gowda, B.S.K., Chethan, V.R., Rao Sri Rama, T.A.: Optimization of counterfort retaining wall using artificial neural network. In: A Proceedings of National Conference on Contemporary Civil Engineering Research and Practices, MIT Manipal (2012)
24. Gowda, B.S.K., Prasad, G.L.E., Velmurgan, R.: Prediction of optimized cantilever earth retaining wall using ANN. Int. J. Emerg. Trends Eng. Dev. **6**, 328–333 (2012)
25. Gowda, K., Prasad, G.L.: Prognostication of concrete mix proportion by ANN approach. Adv. Mater. Res. **261**, 426–430 (2011)
26. Prasad, G.L.E., Gowda, B.S.K., Velmurugan, R., Yashwanth, M.K.: Prediction of properties of CRPCSC particulate composite by ANN. In: Experimental Mechanics of Composite, Hybrid, and Multifunctional Materials, vol. 6, pp. 17–22. Springer International Publishing (2014)
27. ASTM D7264: The standard test method for tensile properties of polymer matrix composite materials. The American Society for Testing and Materials committee on Standards, 100 Barr Harbor Drive, West Conshohocken, PA 19428 (1995)

Chapter 22
Filler-Reinforced Poly(Glycolic Acid) for Degradable Frac Balls Under High-Pressure Operation

Shinya Takahashi, Masayuki Okura, Takuma Kobayashi, Hikaru Saijo, and Takeo Takahashi

Abstract The mechanical strength and degradability of chopped glass fiber (GF)- and glass powder (GP)-reinforced poly (glycolic acid) (PGA) were investigated. A loading of 30 wt% GF improved the tensile and compressive strength of PGA by 20–100 %. The reinforcement depended on the interface adhesion between the GF and PGA matrix, and the aspect ratio and orientation of the fibers. The GP did not improve the tensile strength of PGA, whereas the composite containing 30wt% GP exhibited 20–40 % higher compressive strength than PGA. The ball made of PGA/GP composite showed a higher pressure capability than PGA, and the improvement appeared to be related to the increase in the compressive strength of the material. The degradability of the PGA/GP composite is similar to that of PGA, and the rate of the degradation is predictable in the same manner as PGA. These findings suggest that frac balls consisting of GF or GP-reinforced PGA are suitable for high-pressure high-temperature operations.

Keywords Mechanical properties • Fibers • Degradable polymers • Interfacial adhesion • Aspect ratio

22.1 Introduction

The pursuit of cost-effective completion for horizontal wells in unconventional reservoirs has resulted in an increase in the stage count of hydraulic fracturing. A typical system used for multistage fracturing is the ball-activated sleeve system (Fig. 22.1). This system consists of an outer sleeve with frac ports, inner sliding sleeves covering the frac ports, and ball seats with different internal diameters linked to the sliding sleeves. The fracturing process with the sleeve system is as follows. A small frac ball is inserted into the sleeve system installed in a wellbore. The ball passes through ball seats with larger internal diameters than the ball's outer diameter, and finally lands on the ball seat with a smaller internal diameter. Subsequently, hydraulic pressure is applied to the wellbore so that the inner sliding sleeve moves downstream and the frac ports of the outer sleeve are opened. The pressurized fluid flows out of the frac ports and creates fractures that are propagated inside the formation. This procedure is repeated from the toe to the heel of the wellbore with a series of balls that gradually increase in diameter. Many frac balls that are being used for well completions to fracture formations and produce oil and gas efficiently are made of non-degradable thermosetting polymers or metals.

One of the disadvantages of the sleeve systems with the conventional balls is the cost and risk of the post-fracturing process to remove the frac balls from a wellbore after use. Milling out with coiled tubing is often used to remove the balls and secure the flow path to recover the oil and gas production rate [1], because ball stacking often occurs at the seat and can permanently isolate the stages behind it. Milling out can damage the wellbore and is usually time-consuming and costly. The cost of milling out can easily reach $100,000–200,000, and this can double or triple if the process is not effective [2]. In addition, milling out can extend the schedule, delaying well completion. For example, it takes 86 h to mill out 29 seats with 20,000 ft of 2 in. coiled tubing [3]. Therefore, replacing conventional non-degradable materials with materials that can simplify the post-fracturing process and can significantly reduce the cost of well completions are in great demand.

Poly(glycolic acid) (PGA) is a semicrystalline polyester that consists of one methylene group and one ester group in a repeating unit. The simple molecular structure enables the molecular chains to pack densely in both the crystalline and amorphous phases, leading to its high mechanical strength, which is comparable to engineering plastics [4]. Moreover, PGA shows high degradability in the presence of water compared with other polyesters, such as polylactic acid and polyethylene terephthalate, because of the large numbers of hydrolysable ester groups per unit volume. These properties make this polymer an ideal material for many applications in oil and gas recovery that require both mechanical strength and degradability.

S. Takahashi (✉) • M. Okura • T. Kobayashi • H. Saijo • T. Takahashi
Kureha Corporation, 3-3-2 Nihonbashi-Hamacho, Chuo-ku, Tokyo 103-8552, Japan
e-mail: shinya-takahashi@kureha.co.jp

C. Ralph et al. (eds.), *Mechanics of Composite and Multi-functional Materials, Volume 7*,
Conference Proceedings of the Society for Experimental Mechanics Series, DOI 10.1007/978-3-319-21762-8_22

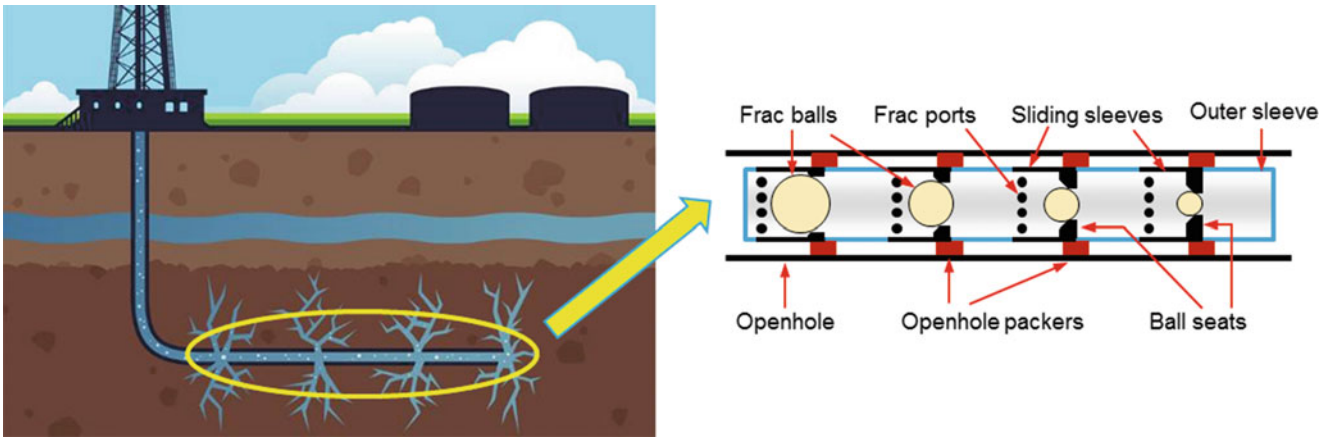

Fig. 22.1 Schematic of sleeve system for multi-stage fracturing

Vast numbers of patents have been granted around the use of degradable materials, including PGA, for downhole tools or drilling chemicals. For example, Erbstoesser et al. [5] patented the use of PGA ball sealers for sealing casing perforations to divert the flow direction of treatment fluid. The balls are used to block perforations temporarily, which are opened around the flow paths for recovering oil and gas. The balls are degraded by water in the wellbore; thus, the oil and gas can pass through the perforations and be recovered. Hodge et al. [6] reported the use of PGA for self-degradable lost circulation materials that can prevent drilling fluid leaking through natural fractures in a wellbore. They concluded that PGA powder can plug the fractures sufficiently to stop leaking of the fracturing fluids during drilling and that it does not inhibit the oil and gas recovery during production because it degrades in the presence of water and heat in subterranean formations. Despite the performance of PGA in diverter balls and diverting agents, the use of PGA had been limited because of the lack of a commercial supply of PGA.

Recent progress in the manufacturing processes for PGA resin has allowed industry to use PGA for various applications. In the 1990s, the manufacturing process for PGA resin was dramatically improved [7], because the efficient de-polymerization of glycolic acid oligomers allowed the large-scale production of the PGA monomer, glycolide. High molecular weight PGA can be obtained by the ring-opening polymerization of the glycolide because the generation of water molecules, which inhibit the polymerization of glycolide to PGA, can be strongly suppressed. Furthermore, suitable additives that enhance the thermal stability of PGA during the melt-molding process have been developed. Both these breakthroughs contributed to the decrease in the production cost of high molecular weight PGA with good melt-molding processability. Currently, a wide variety of PGA products is available at commercially acceptable prices.

PGA is one of the best materials for degradable frac balls owing to its high mechanical strength, high thermal stability, and rapid degradation in water. The balls are homogenous, and have sufficient structural integrity during fracturing operations because of the high strength of PGA (Fig. 22.2). This allows the balls to be used in the same manner as the conventional balls. The PGA frac balls degrade via a surface degradation mechanism [8], and thus gradually decrease in diameter in water in the typical temperature range found in shale formations (Fig. 22.3). The diameter change is predictable because the rate of the decrease is linear with respect to immersion time in water. The degraded PGA frac balls can easily leave the ball seat even if they have become stuck because of the hydraulic pressure during fracturing. The ball can return to the surface through flow back or completely degrade after further immersion in water, and do not inhibit the production of oil and gas. Although some metallic degradable frac balls with a high compressive stress have recently become available, PGA frac balls are still the most suitable for many sleeve systems because metallic degradable frac balls often require a trigger, such as an acid or a salt, to initiate degradation. Moreover, the degradation rate of PGA is faster than that of the other degradable polymers at low temperatures; therefore, it is a suitable material for shale gas plays in the US where the well temperature is relatively low. Indeed, PGA frac balls have been used since they became commercially available in 2012.

Despite the performance of PGA frac balls, it is necessary to improve the mechanical strength of PGA. This is because of the increase in fracturing stage count, and also to allow the PGA balls to be used in higher temperature and pressure wells. As the stage count increases, the increment between the adjacent seats becomes smaller and smaller, leading to a small ball-seat overlap of 3.175 mm or less. The balls need to have a higher tensile and compressive strength to hold the fracturing

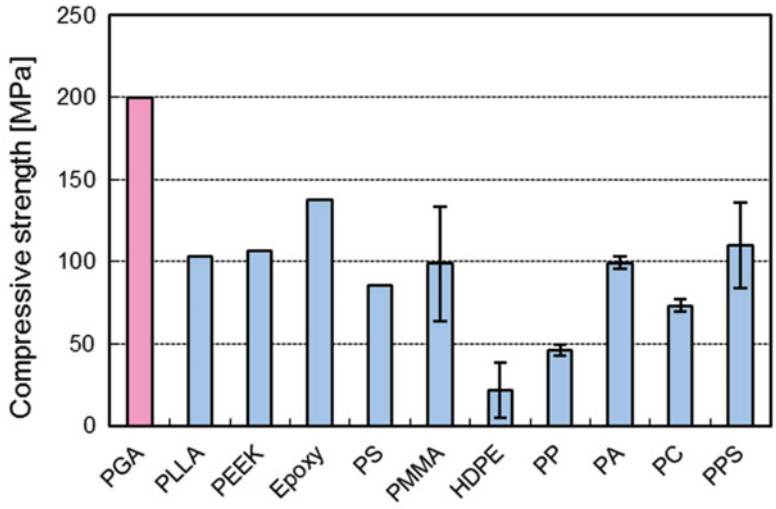

Fig. 22.2 Comparison of compressive strength of PGA with other ball materials at ambient temperature. *PLLA* poly-L-lactic acid, *PEEK* polyetheretherketone, *Epoxy* epoxy resin, *PS* polystyrene, *PMMA* poly(methyl methacrylate), *HDPE* high-density polyethylene, *PP* polypropylene, *PA* polyamide, *PC* polycarbonate, *PPS* poly (phenylene sulfide)

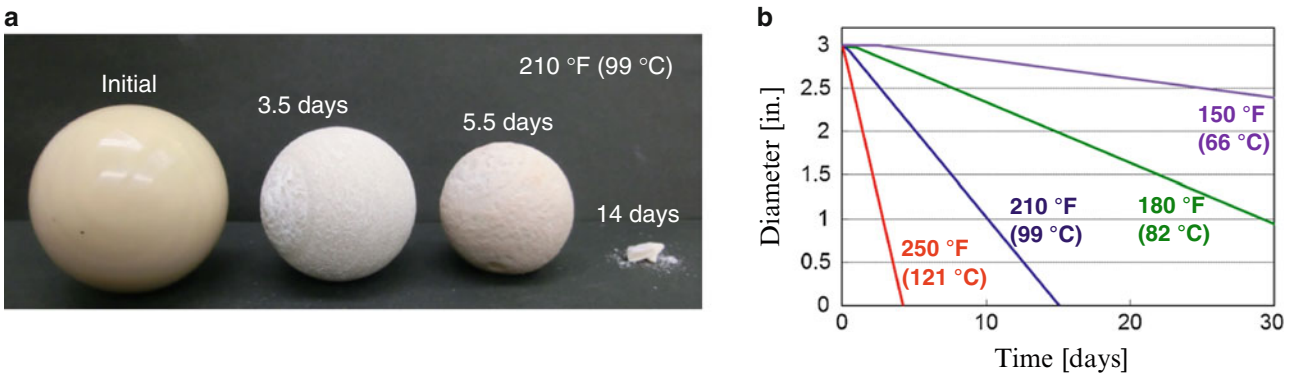

Fig. 22.3 (**a**) Photograph and (**b**) plot of the change in the diameter of PGA frac balls in water over time

pressure with such a small overlap. Moreover, as with other plastic materials, the mechanical strength of PGA depends on temperature; its mechanical strength is lower at higher temperatures. To broaden the range of conditions that PGA balls are suitable for, the mechanical strength of PGA must be increased.

Filler-reinforcement is a common method that has been used industrially to improve and optimize the mechanical properties of polymers for specific end use applications [9]. In particular, inorganic fillers afford beneficial properties when blended with polymers. There are many studies of polymer/inorganic filler composites, including particulates or fibers [10–12]. The effectiveness of reinforcement depends on their constituent properties, filler content, and the interfacial compatibility between the fillers and matrix polymers [13, 14].

In this chapter, we report the mechanical strength of filler-reinforced PGA and the pressure capabilities of the filler-reinforced PGA balls. Chopped glass fiber (GF) and milled glass powder were chosen as the fillers for improving the mechanical strength of PGA. The results are discussed in terms of the morphology of the composites and the interfacial compatibility between the fillers and PGA. The tensile and compressive strength of the composites was increased by 1.2–2.0 times, depending on the aspect ratio and the type of coupling agent coated on the filler surface. The filler-reinforced PGA balls showed a higher pressure capability than neat PGA balls, suggesting that the reinforced balls are suitable for high-pressure operations.

22.2 Experimental

22.2.1 Materials

Kuredux (Kureha Corporation) was used as the matrix PGA material. The melt viscosity measured by capillary rheometer was at around 900 Pa s at 122 s^{-1} and 270 °C. The moisture level in PGA was less than 50 ppm. The fillers used in this study are listed in Table 22.1. All GF originally had a length of 3 mm and a diameter of 10 μm; however, different sizing agents were used, which coat the fiber surface and work as a coupling agent between the fibers and matrix polymers. Rod-like glass powder (GP) with a length of 50 μm and a diameter of 10 μm was used.

22.2.2 Preparation of PGA Composites

PGA and the fillers were melt-blended in a co-rotating twin-screw extruder at 250 °C. The filler composition was fixed at 30 wt% for all the composites. Four types of screws were used to introduce low to high shear to the composites during blending. The composites were then injection molded to produce dumbbell-shaped test specimens for tensile testing and rectangular plates for three-point flexural measurements. The specimens were annealed at 120 °C for 2 h in a N_2 environment. Solid-state extrusion molding was also used to shape round bars of the composites. The bars were then machined to flat square plates for compressive testing, or to balls for pressure capability evaluation.

22.2.3 Measurements

Tensile testing was carried out with a Universal tester equipped with a 20 kN load cell (AG2000-E, Shimadzu Corporation) using a crosshead speed of 5 mm/min at 23, 93, 121, and 149 °C. The engineering tensile strength was calculated from the maximum tensile force and the original cross-section.

Three-point flexural measurements were also carried out with the Universal tester at 23 °C to evaluate adhesion between the fillers and the matrix PGA. The specimens were 18 mm long, 6.07 mm wide, and 3.17 mm thick. The crosshead speed was 1 mm/min. The distance between the two support points was sufficiently small (15 mm) to allow the adhesive strength to be measured before the bending fracture occurs. Interlaminar shear strength, τ, is defined as follows [15]:

$$\tau = 3F/4(W\,t) \tag{22.1}$$

Here, F is the maximum force, W is the width of tested specimens and t is the thickness.

Another universal tester (55R-4206, Instron) was used to measure the compressive strength of the PGA composites at 23 and 121 °C. The crosshead speed was 1 mm/min. Here, the compressive strength is defined as the engineering stress at the inflection point of the stress-strain curves.

The morphology of the composites and the lengths of the GF in the composites after blending were evaluated by scanning electron microscopy (SEM; JSM-6301F, JEOL). To evaluate the length, the composites were first incinerated in an oven at 800 °C to remove matrix PGA before the microscopic observation.

Pressure capability testing was performed for 76.2 mm balls on a 73.025 mm seat at 66 °C. The balls were tested with a conical seat of 30 ° and ball-seat overlap of 3.175 mm. After the ball was seated on the seat, a hydraulic pressure was applied to the ball. The pressure was subsequently increased until ball failure was observed.

The degradability was investigated by the decrease in thickness of the composite specimens. The specimens were 23 × 23 × 23 mm cubes cut from the round bars, and were immersed in distilled water at 121 and 149 °C. After a certain

Table 22.1 Characteristics of fillers used

Filler	Sizing agent	Diameter (μm)	Length (mm)
GF1	Epoxy	10	3
GF2	Urethane	10	3
GF3	PVAc	10	3
GP	Silane compound	10	0.05

amount of time, the specimens were removed from the water and dried for several hours at ambient temperature. Because the degradation of PGA proceeds via surface degradation, the embrittlement proceeds from the surface to the core of the specimens. The degraded brittle layer was peeled, and then the thickness of the core layer that had not degraded and maintained the original mechanical strength was measured. After the thickness measurement of the core, the specimens were immersed in water again. This procedure was repeated until the original specimen completely disappeared. All experiments were conducted under static conditions without stirring the water.

22.3 Results and Discussion

Figure 22.4 shows the tensile strength of PGA and the composites at the tested temperatures. The PGA/GF1 composite exhibited the highest tensile strength at all temperatures. The tensile strength of PGA/GF2 was also higher than that of neat PGA, PGA/GF3, and PGA/GP. It was assumed that with equivalent processing conditions and mold geometry, the fiber lengths of all the PGA/GF composites here should be identical. Indeed, the SEM results revealed that the fiber length of all the PGA/GF composites was around 220 μm, although only the data for PGA/GF1 is shown in Fig. 22.7. The difference in tensile strength may arise from the different sizing agents.

Compared with neat PGA and the other composites, the tensile strength of PGA/GF3 has a different temperature dependence. The tensile strength of PGA/GF3 is approximately 20 % higher than that of neat PGA and PGA/GP at ambient temperature; however, the difference disappears at higher temperatures. This can be explained by the effect of the sizing agent. The sizing agent for GF3, poly(vinyl acetate) (PVAc), interacts with GF and PGA below the melting temperature of PVAc (55 °C), and the interaction may be lost above the melting temperature.

The compatibility between fillers and matrix polymers affects the reinforcement strongly [13]. The sizing agent is a key to promoting the adhesion between the fillers and matrix polymers for which it is formulated. The testing load profiles (Fig. 22.5) were obtained by three-point flexural testing at 23 °C to evaluate the interlaminar shear strength for three

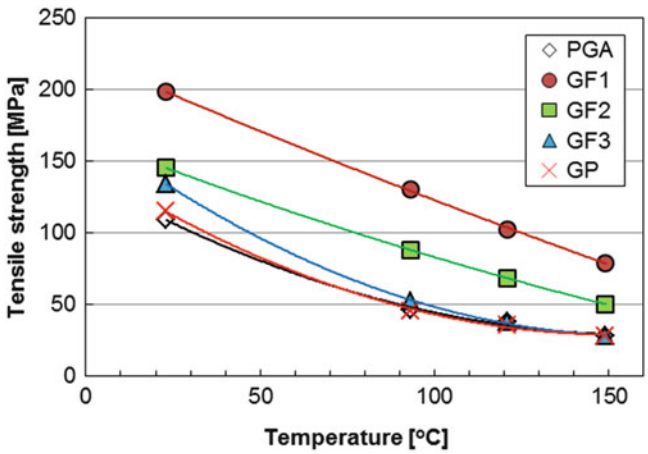

Fig. 22.4 Tensile strength of PGA and PGA composites

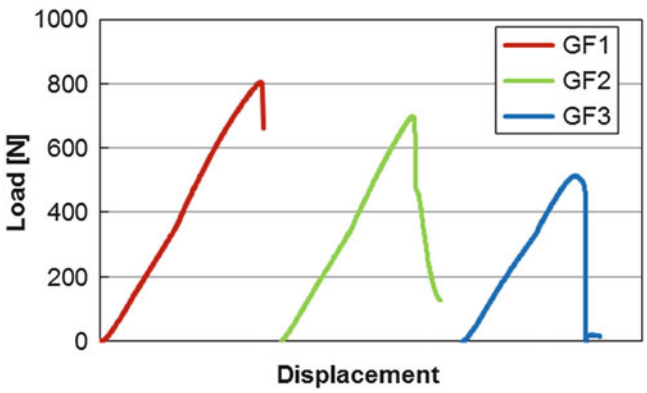

Fig. 22.5 Load profiles of PGA/GF composites during three-point flexural testing

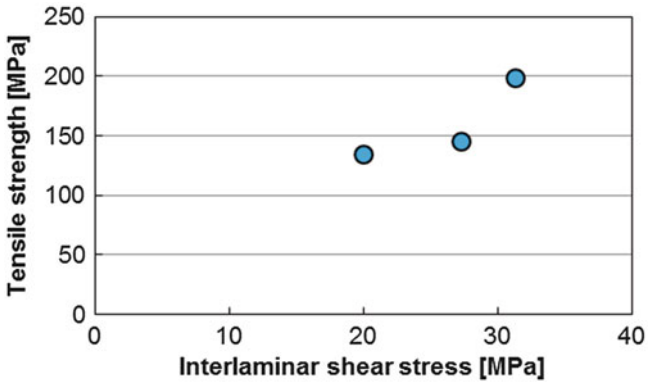

Fig. 22.6 Relationship between the tensile strength and interlaminar shear strength of the PGA/GF composites

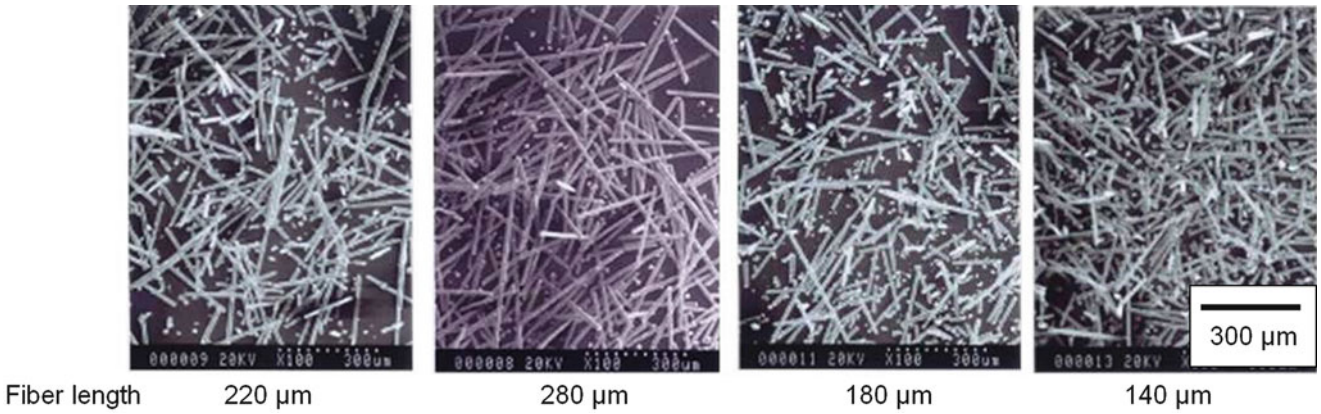

Fig. 22.7 SEM images of PGA/GF1 composites prepared under different blending conditions. The images are arranged in order of the shear rate during blending from the lowest (*left*) to highest (*right*)

PGA/GF composites to discuss the adhesion between fillers and matrix polymers. The load profiles indicate an abrupt decrease in the load force, suggesting that the delamination occurred at the interface between GF and matrix PGA. The maximum load of PGA/GF1 showed the highest value, followed by PGA/GF2 then PGA/GF3. This is consistent with the tensile strength measurement results. The tensile strength of the composites is plotted against interlaminar shear strength calculated by Eq. (22.1) in Fig. 22.6. Indeed, the tensile strength showed good correlation with the interlaminar shear strength.

This tendency can be explained as follows. The epoxy group may react with the PGA chain terminal groups and main chains, resulting in good adhesion between the GF and matrix PGA and high tensile strength. However, lower tensile strength for PGA/GF3 may arise from the poor compatibility of PVAc with PGA. Urethane coated GF (GF2) showed a lower tensile strength than epoxy coated GF (GF1). The thermal degradation temperature of the urethane compound was lower than the molding temperature in this study, at around 250 °C. Because a certain amount of urethane sizing agent degraded during blending and injection molding, the adhesion between PGA and GF2 was weak, leading to the lower tensile strength compared with PGA/GF1.

The GP has little effect on the tensile strength of PGA as shown in Fig. 22.4. The mechanism by which the tensile strength of polymers is increased by filler materials has been already reported [16]. The increase of tensile strength depends on the aspect ratio and orientation of filler materials. The small effect of GP can be explained by its small aspect ratio and poor orientation parallel to the tensile direction. The actual aspect ratio was not measured; however, it will be low (<5) because of the fracture of GP during melt blending. In addition, the small aspect ratio can also affect the orientation of GP. GF, which contains longer fibers, tends to align parallel to the flow direction when the dumbbell specimens are injection molded. This increases the tensile strength because the tensile direction is also parallel to the flow direction. For GP, the particles tend to have a random configuration, resulting in a smaller contribution to the increase in the tensile strength.

To clarify the effect of filler lengths on the tensile strength, four composites consisting of PGA and GF1 with different fiber lengths were prepared by changing the shearing conditions during blending. Figure 22.7 shows the SEM micrographs of the four composites after incineration of injection molded tensile test samples. The original fiber lengths were 3 mm

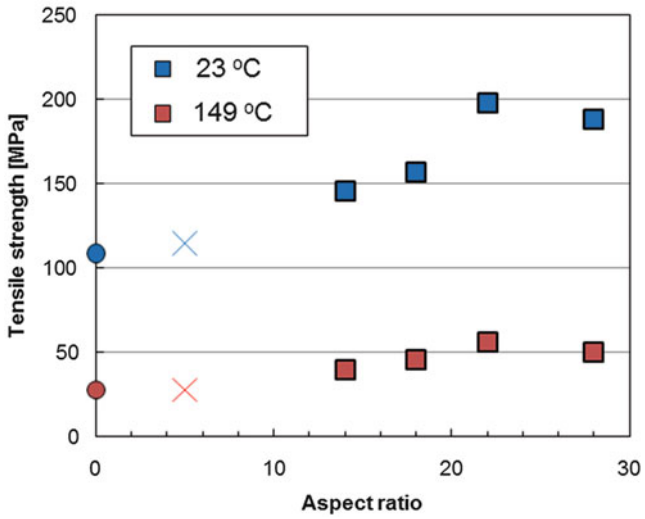

Fig. 22.8 Tensile strength of PGA composites with different filler aspect ratios. *Circle*: neat PGA, *cross*: PGA/GP composite, *square*: PGA/GF1 composites

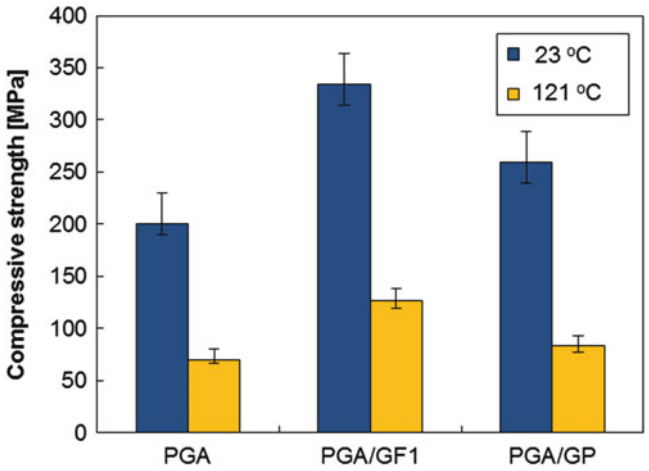

Fig. 22.9 Compressive strength of PGA, PGA/GF1, and PGA/GP composites at 23 and 121 °C

whereas the fiber lengths decreased after blending and subsequent injection molding. The higher shearing process during blending gave rise to greater fiber length attrition. The tensile strength of the composites was plotted against the aspect ratio calculated from the weight average fiber length, which was evaluated from the SEM observations and the fiber diameter in Fig. 22.8. The tensile strength increased with the aspect ratio. This may be attributed to the orientation of the fibers. The flow direction in the injection molding was consistent with the tensile direction; hence, the fibers should be aligned in the same direction. The load force introduced was held by the fibers, which have a higher tensile strength than PGA. However, short fibers may be randomly dispersed in the matrix PGA, resulting in less effective reinforcement. The tensile strength of the PGA/GP composite is also plotted in the figure. The data broadly follows the same trend as PGA/GF1 irrespective of the sizing agent.

The compressive strengths of neat PGA, PGA/GF1, and PGA/GP were also measured at 23 and 121 °C (Fig. 22.9). The compressive strength of the composites was increased by 1.7–1.8 times for PGA/GF1 and by 1.2–1.4 times for PGA/GP. Similar to the tensile strength, GF1 also showed better improvement of the compressive strength than GP. This can also be explained by the effect of the aspect ratio and orientation of the filler materials. GP improves the compressive strength, although it does not increase the tensile strength.

To determine how filler materials can improve the pressure resistance of PGA balls, pressure capability testing was performed. GF tends to be orientated in the flow direction during molding. The resultant heterogeneous structure may lead to the anisotropy of the mechanical strength of the molded specimens and the machined balls. The end result is the inconsistent performance of the ball [17]. Hence, PGA/GP was chosen as the ball material for pressure testing instead of PGA/GF composites. The pressure capability of the PGA/GP ball was 1.3 times greater than that of the PGA ball, which is similar to

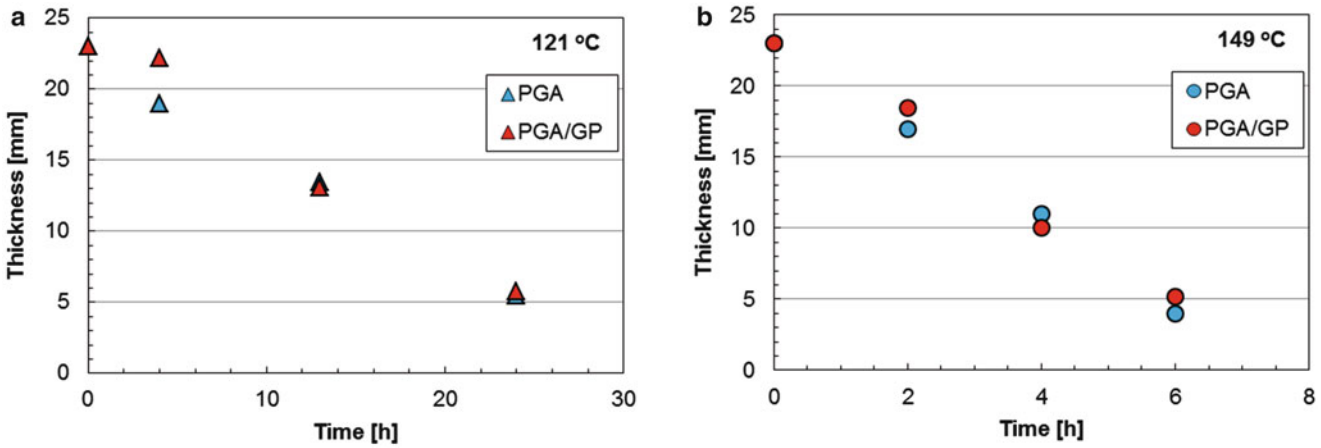

Fig. 22.10 Decrease in the thickness of PGA and PGA/GP composites at (**a**) 121 and (**b**) 149 °C

the improvement in the compressive strength. This suggests that the pressure capability of ball sealers depends strongly on the compressive strength of the material. Our unpublished work also indicates that the compressive stress is the main factor that determines the pressure capability of ball sealers.

Figure 22.10 shows the decrease in the thickness for neat PGA and PGA/GP composites in distilled water at 121 and 149 °C. The thickness of the neat PGA decreased with time because hydrolysis proceeded on the surface, and it completely disappeared after 30 h at 121 °C and 7 h at 149 °C, respectively. The composite also decreased its thickness at a similar rate compared with PGA. This indicates that the fillers and their sizing agent do not affect the degradation rate and the degradation mechanism of the PGA matrix. The decrease in the ball diameter consisting of PGA/GP composites can be predicted in the same manner as the PGA ball.

22.4 Conclusions

Blending GF and GP increased the mechanical strength of PGA. The tensile strength and compressive strength of the composites containing the GF was approximately 20–100 % higher than those of neat PGA. The tensile strength of the PGA/GP composites was equivalent to that of neat PGA, whereas the compressive strength was 30 % higher than that of neat PGA. The PGA/GP composite ball showed a pressure capability 1.3 times greater than that of PGA; thus, the composite frac balls should be suitable for high-pressure operations and high-temperature wells, in which the neat PGA frac balls are easily extruded from the seats.

Acknowledgement The authors would like to thank the management of KUREHA CORPORATION for allowing publication of this chapter.

References

1. Wozniak, G.: Frac sleeves: is milling them out worth the trouble? Paper SPE 138322 presented at the SPE tight gas completions conference, San Antonio, TX, USA, 2–3 Nov 2010
2. Tompkins, R., Smith, N., Wellhoefer, B., Yuyi, S., Stivers, P.: Factors affecting effective millout of multistage fracturing sleeves in horizontal wellbores. Paper SPE 163899 presented at SPE/ICoTA coiled tubing & well intervention conference & exhibition, The Woodlands, TX, USA, 26–27 Mar 2013
3. Griffin, J., Barraez, R., Campbell, S.: To mill or not to mill: a fully retrievable multistage fracturing system. Paper SPE 163936 presented at the SPE/ICoTA coiled tubing & well intervention conference & exhibition, The Woodlands, TX, USA, 26–27 Mar 2013
4. Okura, M., Takahashi, S., Kobayashi, T., Saijo, H., Takahashi, T.: Improvement of impact strength of polyglycolic acid for self-degradable tools for low-temperature wells. Paper SPE 172969 presented at the SPE Middle East unconventional gas conference and exhibition held in Muscat, Oman, 26–28 Jan 2015
5. Erbstoesser, S.R., Cooke, C.E., Sinclair, R.G., Epstein, M.: Use of degradable ball sealers to seal casing perforations in well treatment fluid diversion. US Patent 4,716,964 (1988)

6. Hodge, R.M., MacKinlay, W.M., Landnun, W.R.: The selection and application of loss control materials to minimize formation damage in gravel packed completions for a North Sea Field. Paper SPE 30119 presented at the European formation damage conference, The Hague, The Netherlands, 15–16 May 1995
7. Sato, H., Shigaki, Y., Sunagawa, K., Ichikawa, Y., Yamane, K.: Development of industrial production technology of high-molecular-weight polyglycolic acid. Polymer Preprint. Jpn. **61**, 34 (2012)
8. Okura, M.: Downhole tool member for hydrocarbon resource recovery. International (PCT) Patent WO2014092067 A1 (2012)
9. English, B., Chow, P., Bajwaz, D.S.: Processing Composites. CRC, New York (1997)
10. Mohr, J.G.: Fiberglass. In: Katz, H.S., Milewski, J.V. (eds.) Handbook of Fillers and Reinforcements of Plastics. Van Nostrand Reinhold, New York (1978). Chapter 26
11. Theberge, J.E., Goebel, C.V.: A review of the significant developments in glass fiber reinforced thermoplastics: 1966-1976. Polymer Plast. Tech. Eng. **11**, 27–39 (1978)
12. Titow, W., Lanham, B.: Reinforced Thermoplastics. Applied Science, London (1975)
13. Fu, S.Y., Feng, X.Q., Lauke, B., Mai, Y.W.: Effects of particle size, particle/matrix interface adhesion and particle loading on mechanical properties of particulate-polymer composites. Compos. B Eng. **39**, 933–961 (2008)
14. Mallick, P.K.: Fiber Reinforced Composites. Materials, Manufacturing and Design. Marcel Dekker, New York (1997)
15. Sideridis, E., Papadopoulos, G.A.: Short-beam and three-point-bending tests for the study of shear and flexural properties in unidirectional-fiber-reinforced epoxy composites. J. Appl. Polymer Sci. **93**, 63–74 (2004)
16. Okuzono, T.: Relationships of molecular weight, fiber length and fiber orientation versus mechanical strength and molding shrinkage of a glass-fiber reinforced polycarbonate. Polymer Preprint. Jpn. **39**(11), 4157–4159 (1990)
17. Baihly, J., Aviles, I., Johnson, J., Melenyzer, G.: Sleeve activation in open-hole fracturing systems: a ball selection study. Paper SPE 162657 presented at the 2012 SPE Canadian unconventional resources conference, Calgary, AB, Canada, 30 Oct–1 Nov 2012

Chapter 23
Characteristics of Elastomeric Composites Reinforced with Carbon Black and Epoxy

D. Zaimova, E. Bayraktar, and I. Miskioglu

Abstract In different industrial applications of the elastomeric composites, optimization of processing as well as performance requirements through variation in the mixture composition is one of the basic tools. Thus, various components taking part in a particular formulation play an important role on the final properties. The main focus of this work is based on the effect of additional elements on the mechanical properties of elastomeric composites based on a mixture of natural (NR) and butadiene (BR) rubber. Influence of accelerator-vulcanizing agent system was studied. In addition part of the conventional filler (carbon black) was replaced by epoxy resin in order to investigate the possibility of achieving new properties of the composites. Mechanical, physical and viscoelastic properties were investigated by different experimental techniques (swelling, tensile test, microindentation, DMTA, etc.). Damage analysis of the studied composites was made by using Scanning Electron Microscopy.

Keywords Elastomer composites • Mechanical properties • Chemical-Physical analysis • Epoxy

23.1 Introduction

Polymers are a versatile class of engineering materials because of their ability to be tailor-made to suit specific requirements. Fillers play a dominant role in modifying the properties of the base polymer. In rubber industry, a variety of fillers are used to improve and modify the physical properties of the elastomeric materials. As an important type of polymer material, rubber is widely used due to its high and reversible deformability. Since the essential modulus and strength of neat rubber are low, an additional reinforcing phase is necessary for practical uses of rubber materials [1]. The common method of reinforcement is to add dispersed fillers, such as carbon black or silica, into rubber thus the strong interactions between fillers and rubber take part in the complex networks which include sulfur crosslinks and chain entanglements as well as the carbon black bound rubber-carbon black networks [2–4]. The three kinds of networks interact with each other and cooperatively affect the properties of the vulcanizates. Early research on interactions between carbon black and rubber focused on the dispersion mechanism of carbon black [5] and the relationship of dynamic mechanical properties with interactions between carbon black aggregates as well as between carbon black aggregates and rubber chains [6]. The addition of fillers in the rubber matrix makes these interactions even more complicated. There is no available information about the use of epoxy powder as additional filler together with carbon black.

For this reason the aim of this study is to investigate the influence and reinforcing effect of epoxy powder in rubber composites filled with certain ratios carbon black/epoxy powder. Natural-butadiene based sulphur vulcanized rubber mixtures are investigated by several different methods such as swelling, tensile test, dynamic mechanical thermal analysis (DMTA), microindentation, nanoindentation, scanning electron microscopy (SEM), etc.

D. Zaimova (✉)
UCTM, University of Chemical Technology and Metallurgy, Sofia, Bulgaria

School of Mechanical and Manufacturing Engineering, Supmeca-Paris, Saint-Ouen, France
e-mail: diana.zaimova@gmail.com

E. Bayraktar (✉)
School of Mechanical and Manufacturing Engineering, Supmeca-Paris, Saint-Ouen, France
e-mail: bayraktar@supmeca.fr

I. Miskioglu
ME-EM Department, Michigan Technological University, Houghton, MI, USA

C. Ralph et al. (eds.), *Mechanics of Composite and Multi-functional Materials, Volume 7*,
Conference Proceedings of the Society for Experimental Mechanics Series, DOI 10.1007/978-3-319-21762-8_23

23.2 Experimental Conditions

Two blends were mixed in the laboratory of Polymer Department of UCTM—Sofia by using a two roll mixer. Both of the blends are based on a mixture of natural and butadiene rubber with different accelerator to sulphur ratios. Two accelerator to sulphur ratios were used for the preparation of the compounds also known as conventional vulcanization system (CV), where the quantity of sulphur is higher and efficient vulcanization system (EV), where the quantity of accelerator is higher. In addition part of the carbon black used as filler was replaced by epoxy powder. Two ratios carbon black to epoxy powder were used—25CB/25Epoxy and 15CB/35Epoxy parts per hundred rubber.

The moulding conditions and curing characteristics were determined from torque data using moving die rheometer MDR 2000 (Alpha Technologies) at 140 °C for all composites. Standard rectangular test sheets with 2 mm thickness were prepared by compression moulding. The moulding took place at 150 °C and at a pressure of 10 MPa. As a result four different composites were obtained E1 (CV+25CB/25Epoxy), E2 (CV+15CB/35Epoxy), E3 (EV+25CB/25Epoxy), and E4 (EV +15CB/35Epoxy).

The behaviors of these composites in detrimental environmental conditions were tested by means of swelling experiments. All the swelling tests were carried out by immersing the molded samples in toluene at room temperature. After these tests, the crosslink densities for each composite were calculated according to the molecular mass between two crosslinks. All of the crosslink densities were calculated according to Fory-Rehner relation [7]:

$$\frac{1}{2M_c} = \frac{1}{2\rho V_0}\left[\frac{\ln(1-V_r)+V_r+\mu V_r^2}{V_r^{1/3}-\frac{1}{2}V_r}\right] \tag{23.1}$$

$$\nu = \frac{1}{2M_c} \tag{23.2}$$

where;

M_c—molecular mass between crosslinks;
ρ—Density of the rubber;
V_0—molar volume of the solvent;
V_r—volume fraction of the swollen rubber;
μ—interaction parameter between the rubber sample and the solvent;
ν—Crosslink density.

The standard deviation of the method is ±5 % and all values which are not within this limit are not taken in account.

The measurements of mechanical properties were carried out in accordance with ASTM D 412a$^{\varepsilon 2}$ (2010) [8]. Hardness values (Shore A) were measured according to the standard—ASTM D 2240-05 (2010) [9]. The standard deviation is 3A.

Dynamic Mechanical Thermal Analysis (DMTA) was carried out on the Dynamic Mechanical Analyzer MK III system (Rheometric Scientific). As a mode of deformation, single cantilever bending was used at a heating rate of 2 °C/min, a frequency of 5 Hz and deformation 64 μm in temperature range from −80 to 80 °C. The size of the specimen was 10 mm width, 80 mm length and 2 mm thickness. CSM Micro Indentation Tester with a Vickers diamond indenter was used. Nine tests were performed for each composition and then averaged. The samples' thickness was approximately 2 mm. The maximum indentation load (F_{max}) was 250 mN, the rate for loading-unloading was 500 mN/min. The load was held at maximum for 50 s. The indentation hardness (H_{IT}) and indentation modulus (E_{IT}) were determined by using the Oliver and Pharr method [10].

Nanoindentation characterisation was carried out to determine the visco-elastic behaviour of these composite materials by creep phenomenon. For each specimen 16 indents are taken at four different loads—5, 10, 15 and 20 mN. Each indent is 50 μm away from its neighbouring indents. The load was increased from zero to the maximum at a rate of 1 mN/s. Then load was held at the maximum for 400 s then unloaded. During unloading the modulus and hardness were calculated using the Oliver-Pharr method [10]. A Berkovich indenter was used in all the tests. Poisson's ratio was assumed to be 0.36 for all samples. Using the data collected during a typical creep test the creep compliance $J(t)$ was calculated using [11]:

$$J(t) = \frac{A(t)}{(1-\nu)P_0 \tan\theta} \tag{23.3}$$

where:

$A(t)$ = Contact area

P_0 = Constant applied load

θ = 70.3° For a Berkovich indenter

ν = 0.36 (Assumed)

A multi-cycle wear test analysis was performed. The type of indenter tip was conical with 90° apex angle. The loads on sample were respectively 10 mN and 20 mN and wear distance for one wear cycle was 1000 μm. The wear test speed was 50 μm/s. Twenty wear cycles per wear set were performed. On one sample wear tests were performed along five different paths (parallel paths separated by 50 μm).

Scanning electron microscopy was used to study the microstructure of the fracture surfaces.

23.3 Results and Discussion

23.3.1 Vulcanization Characteristics

Table 23.1 shows the vulcanization characteristics of composites E1 to E4. The minimum torque M_L in a reograph measures the viscosity of the vulcanizates and maximum torque M_H is generally correlated with the stiffness. At first sight composites E1 and E2 are more viscous than E3 and E4. Both E3 and E4 have higher stiffness. The higher quantity of epoxy (E2 and E4) resulted in lower M_H and hence lower stiffness. This is probably due to the poor interaction between the matrix and epoxy. As it is well known there is good interaction between carbon black and rubber matrix so in the case of E1 and E3 we have higher values for M_H. Without the addition of special chemicals the epoxy-carbon black and epoxy-rubber links are most probably physical.

A quick look at ΔM tells us that composite E3 exceeds the other three composites regarding the crosslink density. This claim is also supported by the results obtained from the swelling test (Fig. 23.1).

In both cases (CV and EV) the higher content of epoxy is lowering the crosslink density. This again can be attributed to the poor interaction between the epoxy and the rubber matrix. The swelling test however cannot detect the type of the crosslinks so it is not possible to make a general conclusion about the properties of the examined composites.

The scorch time (T_{S2}) is shorter for CV (E1 and E2) due to the greater quantity of sulfur which increases the rate of vulcanization in the beginning. The greater quantity of accelerator used in E3 and E4 consumes the most of the sulfur very quickly slows down the vulcanization in the beginning. In addition sulfenamide type of accelerators (in our case TBBS) are characterized with delayed action in the beginning of vulcanization which makes them also very suitable for production of thick rubber parts.

There is no clear relation between the rate epoxy/carbon black and the optimal vulcanization time (T_{90}).When CV is used the higher quantity of epoxy decreases the vulcanization time but in the case of EV increase in T_{90} is observed.

Table 23.1 Vulcanization characteristics composites E1 (140 °C-25CB/25Epoxy) E2 (140 °C-15CB/35Epoxy), E3 (140 °C-25CB/25Epoxy) E4 (140 °C-15CB/35Epoxy)

	Blend no			
Characteristic	E-1	E-2	E-3	E-4
ML (dNm)	0.7	0.7	1.4	1.3
MH (dNm)	15.0	11.9	23.0	18.9
ΔM = (MH – ML)	14.3	11.1	21.7	17.7
T_{90} (min:s)	39:57	33:40	28:36	39:03
T_{s2} (min:s)	8:55	10:17	11:20	12:45
V (% min)	3.22	4.30	5.83	3.76

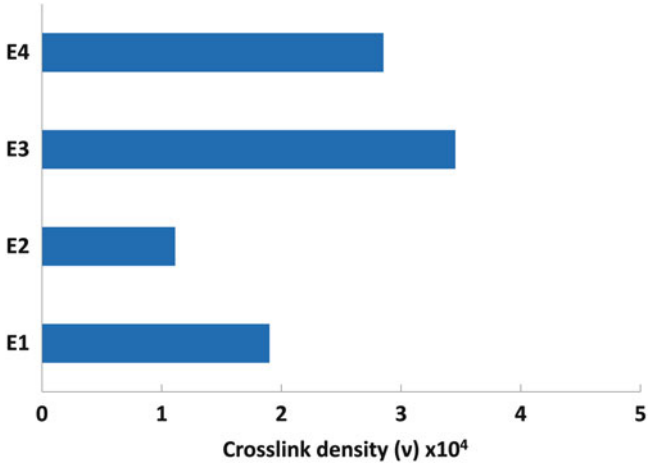

Fig. 23.1 Crosslink density determined by swelling of composites E1 (140 °C-25CB/25Epoxy) E2 (140 °C-15CB/35Epoxy), E3 (140 °C-25CB/25Epoxy) E4 (140 °C-15CB/35Epoxy)

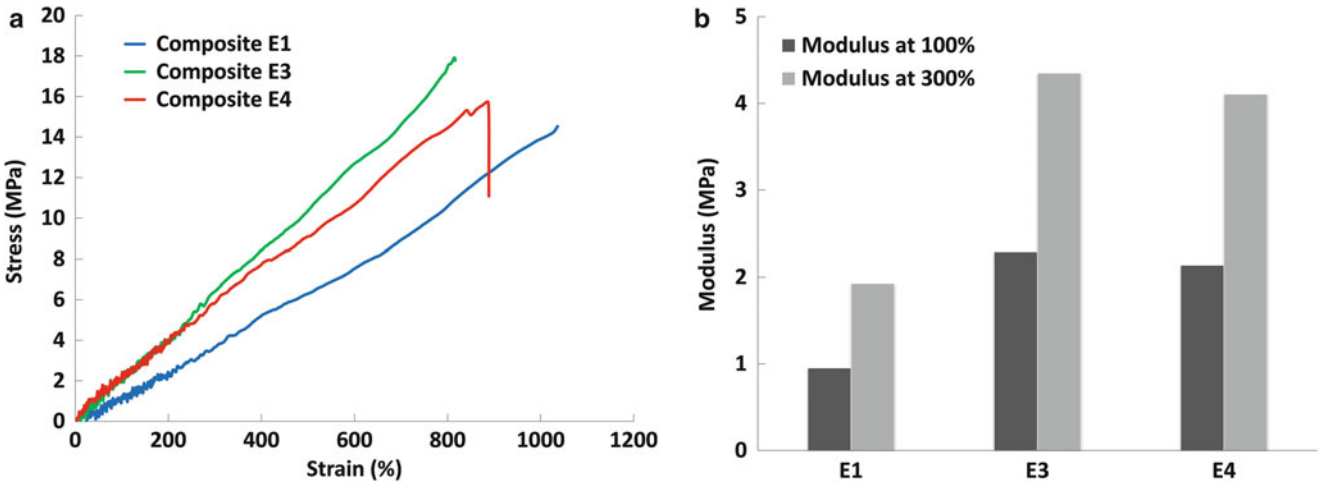

Fig. 23.2 Comparison of stress-strain curves (**a**) and M_{100} and M_{300} (**b**) for composites E1 (140 °C-25CB/25Epoxy) E2 (140 °C-15CB/25Epoxy), E3 (140 °C-25CB/25Epoxy) E4 (140 °C-15CB/35Epoxy)

If we take a look at the swelling test results it can be seen that regardless the rate of vulcanization the higher quantity of epoxy gives lower crosslink density.

23.3.2 Mechanical Properties

In Fig. 23.2a engineering stress-strain curves are presented. The displayed results are only for three of the composites (E1, E3, E4) because it was impossible to break the specimens cut from the test sheets made out of composite E2. Obviously there is a vulcanization problem with this composite.

In Fig. 23.2b modulus at 100 and 300 % deformation are displayed. It is clearly seen that both composites with EV give higher values, which corresponds to better stiffness, comparing to CV. This result is in accordance with the crosslink densities obtained by both rheometer and swelling tests.

Tensile strength of the composites is shown in Fig. 23.3a. In this figure the difference between CV and EV is almost absent suggesting that the crosslink density does not have significant effect on the tensile strength when epoxy/carbon black mixture is used as filler.

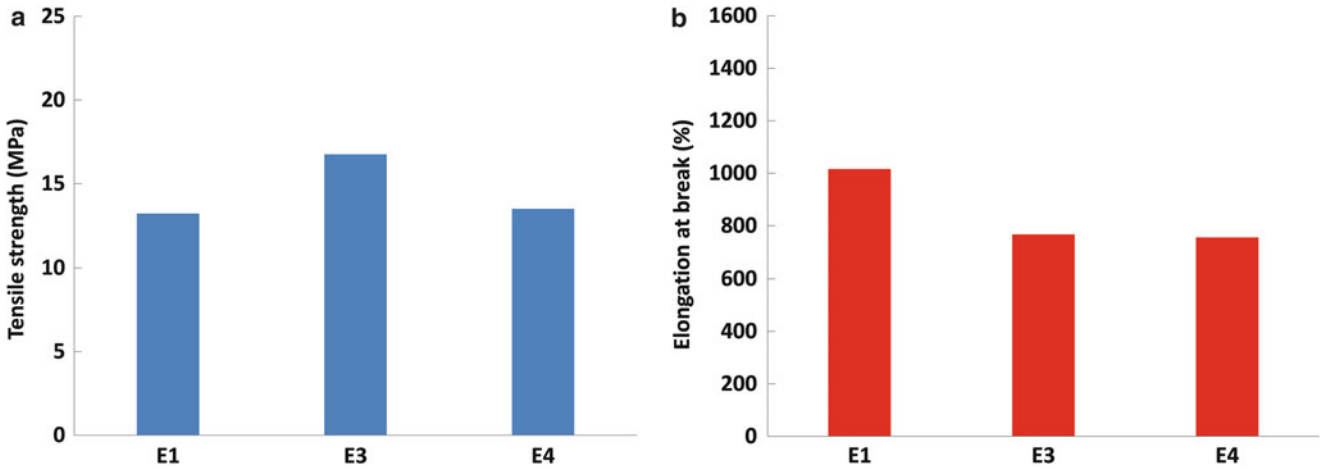

Fig. 23.3 Comparison of tensile strength (**a**) and elongation at break (**b**) for composites E1 (140 °C-25CB/25Epoxy) E2 (150 °C-15CB/25Epoxy), E3 (140 °C-25CB/25Epoxy) E4 (140 °C-15CB/35Epoxy)

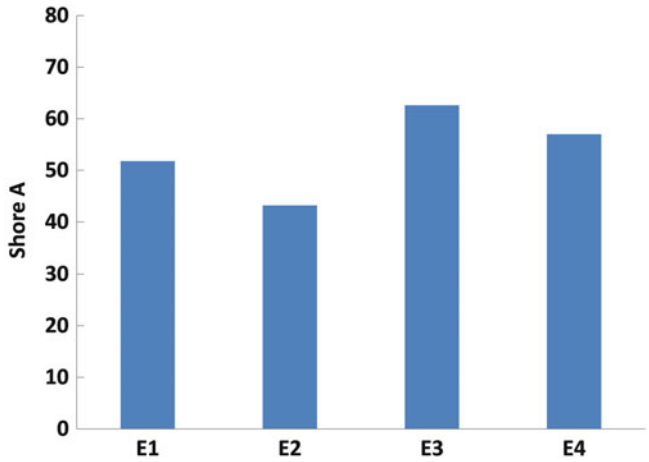

Fig. 23.4 Comparison hardness (shore A) for composites E1 (140 °C-25CB/25Epoxy) E2 (140 °C-15CB/35Epoxy), E3 (140 °C-25CB/25Epoxy) E4 (140 °C-15CB/35Epoxy)

The elongation at break is given in Fig. 23.3b. Here the effect of vulcanization system is visible. The superior value for composite E1 is expected because CV helps for forming of polysulphidic linkages which increases the elasticity hence gives better resistance to deformation. There is no effect observed regarding the quantity of epoxy.

23.3.3 Hardness-Shore A Test Evaluation

The results of the hardness (Shore A) tests obtained for the four composites are shown in Fig. 23.4. The higher quantity of epoxy (E2 and E4) has negative effect on the hardness. This is probably due to low interaction between the filler and the matrix. Concerning the effect of vulcanization system can be said that when EV is used the hardness is increasing. The domination of C-C and monosulphidic bonds is possible reason for these results.

23.3.4 Dynamic Mechanical Thermal Analysis

The dependence of storage modulus (Fig. 23.5a) and dynamic mechanical loss angle tangent (Fig. 23.5b) on the temperature of vulcanization and vulcanization system were studied in the temperature interval from −80 to +80 °C. In the temperature

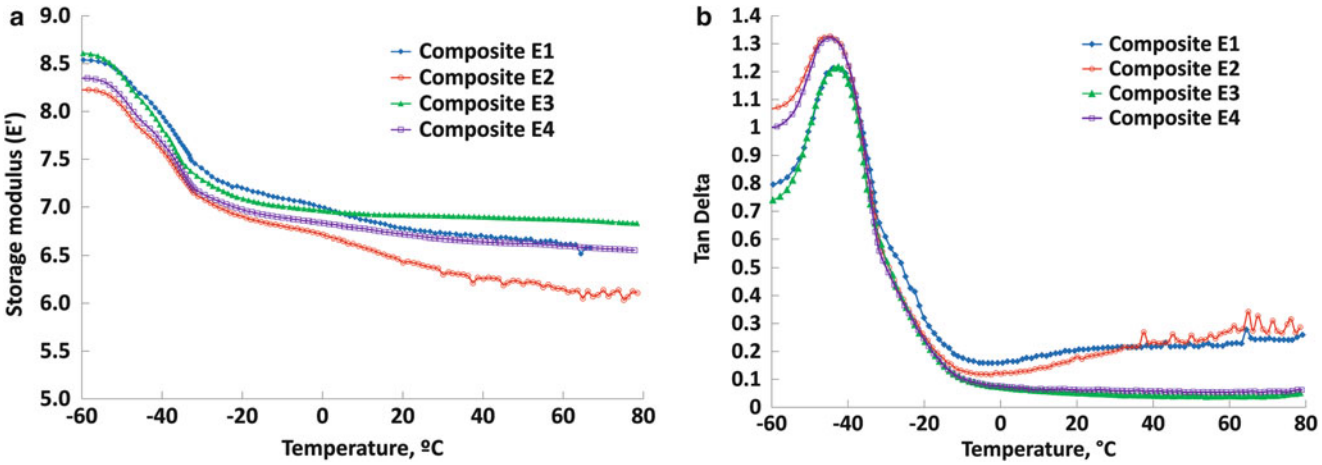

Fig. 23.5 Storage modulus (**a**) and Tan Delta (**b**) as a function of the temperature for Composites E1 (140 °C-25CB/25Epoxy) E2 (140 °C-15CB/35Epoxy), E3 (140 °C-25CB/25Epoxy) E4 (140 °C-15CB/35Epoxy)

interval from −60 to −40 °C the effect of the quantity of epoxy on the storage modulus can be seen clearly. Both composites—E1 and E3 provide higher values of E′. The higher values of E′ can be explained with the limited mobility of the rubber molecules being immobilized onto the surface of the filler. Accordingly this effect can be used as a measure of the filler reinforcing activity because the greater reinforcing activity of the filler the lesser mobility and higher storage modulus values are. Obviously the carbon black has stronger effect after the higher quantity of epoxy (composites E2 and E4) provides lower E′. After the transition from glassy into viscoelastic state there is no indication of any dependence on the filler quantity or vulcanization system.

The mechanical loss angle tangent (Tan delta) is given in Fig. 23.5b. It represents naturally the macromolecules' mobility of the chains and polymers phase transitions. It is accepted that the higher tan delta is the greater mechanical losses are. These losses are related to high energy input required for the motion of the molecular chains of the polymer as the transition is being approached [12]. The position of the tan delta peak in the loss factor versus temperature curve can be used to identify the Tg of the rubber materials. It is observed that Tg of the studied composites does not change considerably (within the limits of 2–3 °C). The intensity of the peak though is a bit higher for composites E2 and E4 which means that more energy is required to pass from glassy to the viscoelastic state. It is noted that in the interval from 0 to 80 °C there is a significant difference in the values of tan delta regarding the vulcanization system. Composites E1 and E2 (CV) show much higher values than composites E3 and E4 (EV). This could be a result of forming of additional crosslinks in composites E1 and E2 under the influence of elevated temperatures. In support of this claim come the results of swelling test and vulcanization characteristics according to which the crosslink density is low for both E1 and E2 and could be sign for vulcanization problems. Based on the discussion of the DMTA results it can be said that composites E3 and E4 possess better dynamic properties than composites E1 and E2.

23.3.5 Microindentation Analysis

The microindentation results are presented in Fig. 23.6a, b the effect of vulcanization system is clearly observed for both indentation hardness and indentation modulus. Composites E3 and E4 have higher indentation hardness and indentation modulus. Obviously at low deformation and load EV gives better results compared to CV. This is probably due to the higher strength of C-C and monosulphidic bonds (dominating in the composite structure thanks to EV). These results correlate with the results obtained for Shore hardness. The effect of the quantity of epoxy is absent hence the quantity of epoxy does not play a role when small loads and deformations are applied. Only the strength of the bonds is important for the properties of the studied vulcanizates.

This claim is supported by the results for the curves obtained at maximum load (Fig. 23.7). Composites E3 and E4 have better stiffness.

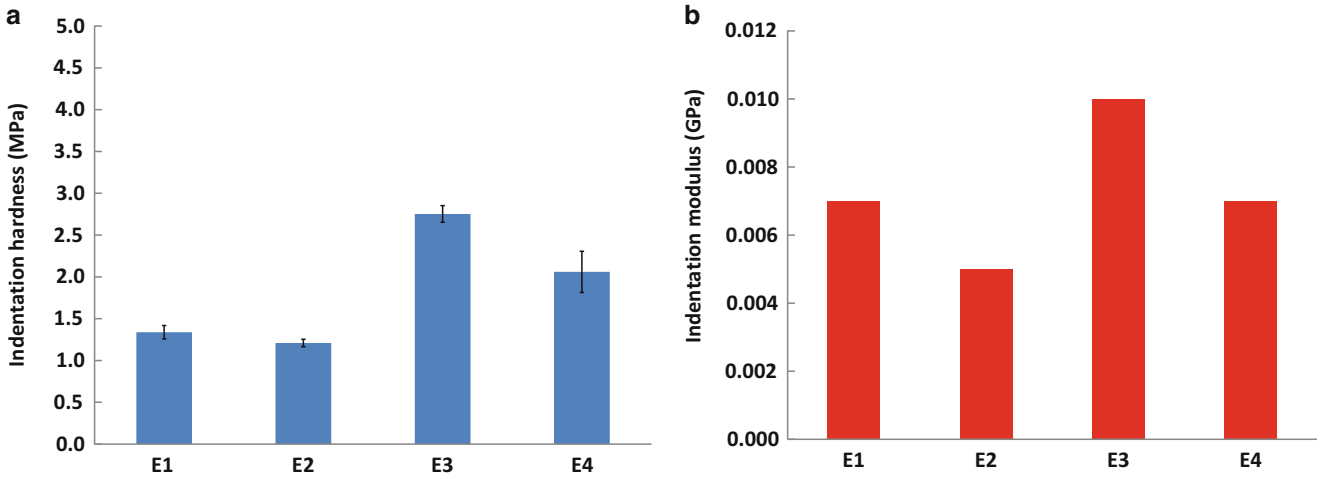

Fig. 23.6 Comparison of indentation hardness (**a**) and indentation modulus (**b**) obtained by microindentation for composites E1 (140 °C-25CB/25Epoxy) E2 (140 °C-15CB/35Epoxy), E3 (140 °C-25CB/25Epoxy) E4 (140 °C-15CB/35Epoxy)

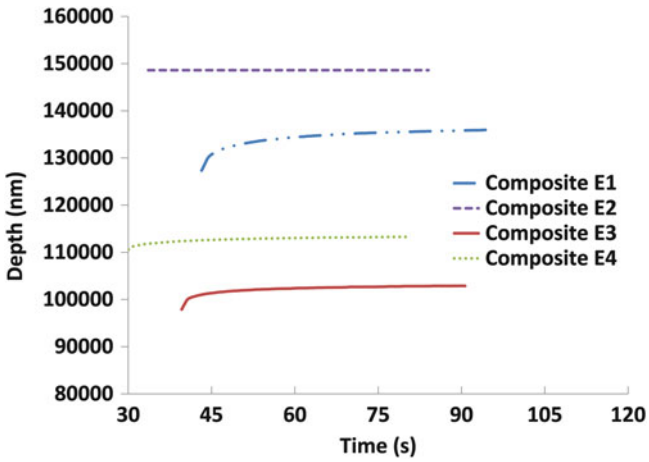

Fig. 23.7 Comparison of indentation depth at maximum load as a function of time for composites E1 (140 °C-25CB/25Epoxy) E2 (140 °C-15CB/35Epoxy), E3 (140 °C-25CB/25Epoxy) E4 (140 °C-15CB/35Epoxy)

23.3.6 Nanoindentation Analysis

The effect of maximum load size was observed by the means of nanoindentation test. The results are presented in Fig. 23.8. The four composites were examined separately in order to facilitate the understanding. As explained before four different loads were applied—5, 10, 15 and 20 mN. Some of the samples (E1 and E2) give fluctuating values at 20 mN which means that they don't support completely this load. The results are given though because they are important for seeing the difference between CV and EV. The higher quantity of epoxy plays negative role on the viscoelastic properties on both CV and EV vulcanizates under the different loads. This claim is supported with the results obtained by microindentation (Fig. 23.7) where the same dependence is observed even though the maximum load is much higher. Concerning the vulcanization system it is clearly seen that composites E3 and E4 have better resistance to deformation in time than E1 and E2 under all equivalent loads on nano and also microscale. This means that EV provides better bonding between the filler and the matrix.

Indentation hardness calculated from nanoindentation test data is given in Fig. 23.9a. Here is not possible to detect any relation between vulcanisation system or epoxy quantity and indentation hardness. Even the effect of the load is contradictory.

The indentation modulus is given in Fig. 23.9b. The effect of vulcanization system and epoxy quantity are very slight and only visible at maximum load of 5 mN. The indentation modulus is higher for EV vulcanizates and once again there is a correlation between nano and microindentation results. Regarding the quantity of epoxy could be said that the higher content of epoxy has a negative effect on indentation modulus. The value obtained for composite E2 at 20 mN is inadequate

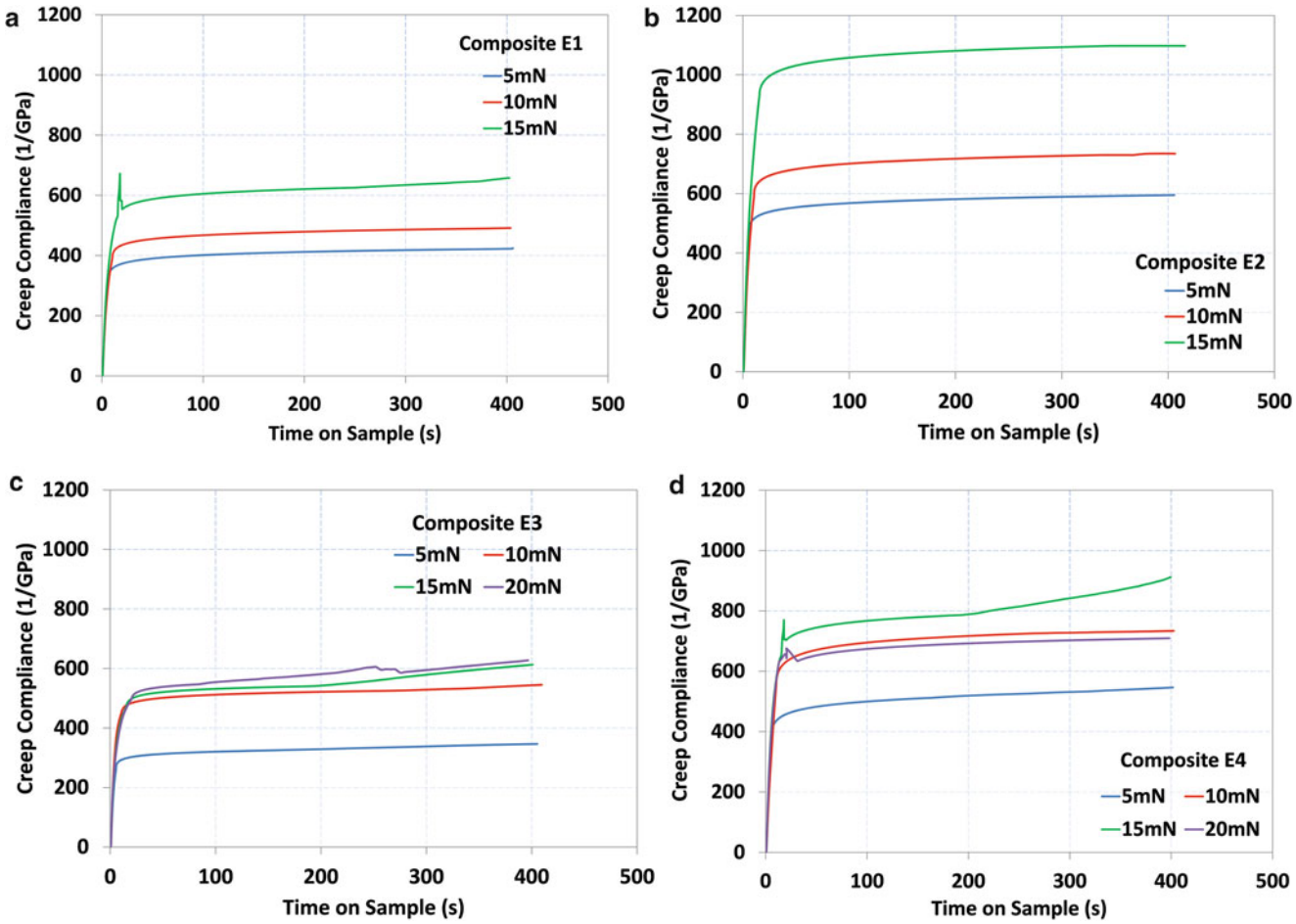

Fig. 23.8 Comparison of creep compliance evolution as a function of time for the composites (**a**) E1 (140 °C-25CB/25Epoxy), (**b**) E2 (140 °C-15CB/35Epoxy), (**c**) E3 (140 °C-25CB/25Epoxy) and (**d**) E4 (140 °C-15CB/35Epoxy) at four different maximum loads (5 mN, 10 mN, 15 mN, 20 mN)

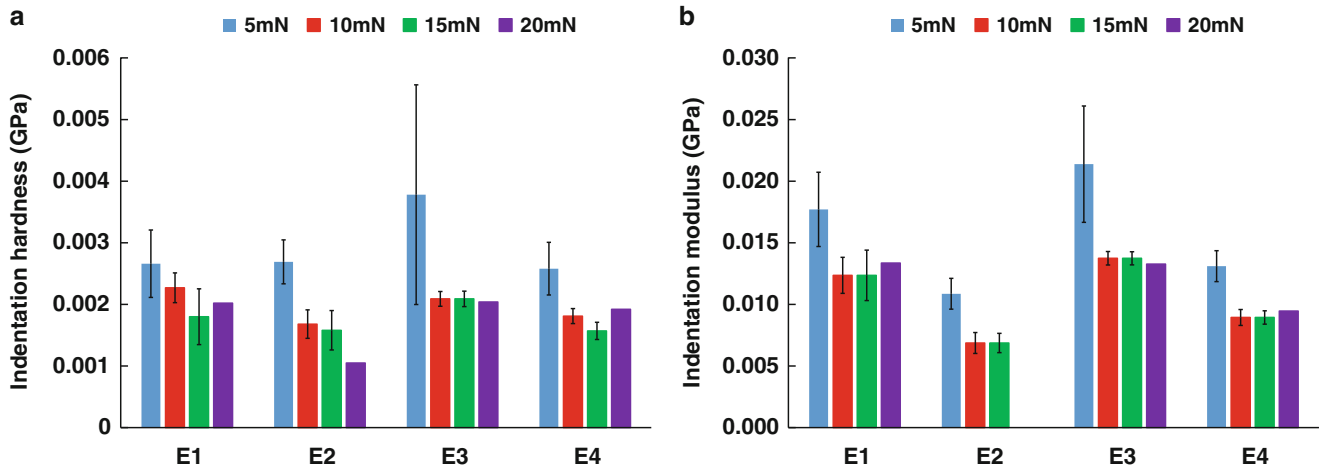

Fig. 23.9 Comparison of indentation hardness (**a**) and indentation modulus (**b**) obtained by nanoindentation test for composites E1 (140 °C-25CB/25Epoxy) E2 (140 °C-15CB/35Epoxy), E3 (140 °C-25CB/25Epoxy) E4 (140 °C-15CB/35Epoxy) at four different maximum loads (5 mN, 10 mN, 15 mN, 20 mN)

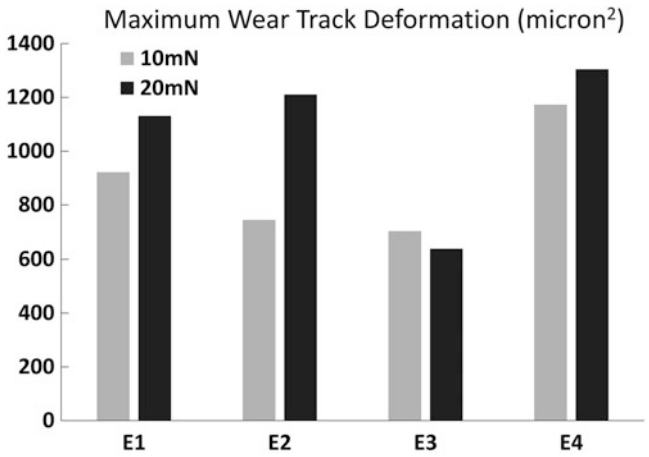

Fig. 23.10 Comparison of maximum wear track deformation of composites E1 (140 °C-25CB/25Epoxy) E2 (140 °C-15CB/35Epoxy), E3 (140 °C-25CB/25Epoxy) E4 (140 °C-15CB/35Epoxy) obtained by multi-cycle wear test at two different maximum loads; 10 and 20 mN

comparing to all other composites. This could be a result of single particle measurement which is completely possible because of heterogeneous content of all composites and the small area of the indenter.

The maximum wear track deformation obtained by multi-cycle wear test is given in Fig. 23.10. Two different loads were applied—10 and 20mN. The size of applied load does not play a role after the same dependence is observed for all composites. There is any clear effect of the quantity of epoxy or vulcanization system. Composite E3 has better resistance to deformation which is expected because of the high crosslink density of this composite. What is surprising is that composite E2 shows better wear resistance after it has the lowest crosslink density. This phenomenon occurs only at 10mN maximum load. At 20mN the results for composites E1, E2 and E3 are similar.

23.3.7 Damage and Fracture Surface Analysis by Means of Scanning Electron Microscopy

Surface images just under the fracture side of the tensile specimens observed by means of the Scanning Electron Microscopy (SEM). Evidently, this type of analysis should give more realistic information to understand the damage behaviour of these four composites. Because these observations show that the fracture energy and stability are exceedingly reliant on the composition and morphology of these new elastomeric composites. Figure 23.11 indicates surface images just under the fracture side for the four composites.

Actually, EDS, chemical analysis give the general appearance of these composites. In fact, all of the composites indicate more and less similar results that were not presented in this chapter due to the excessive volume of the other figures. In reality, elastomeric composites do not exhibit the same fracture type as metallic materials. It is always possible to see tearing deformation lines, occasionally one may see on each specimen.

These microstructures that are located in narrow stressed layers of the fracture surface give obvious information about the initiation peak and propagation and fracture directions. The failure initiates from a particles ("EDS" analysis gives basically a small metallic and/or metallic oxide such as Zn) and propagates from these particles after that, a failure occurs at the final stage very rapidly by showing regular tearing lines at the fracture surface. This behaviour can be observed very often in entire composites. Similar results carried out on the four composites designed here can be found in the literature [13–16].

23.4 Conclusion

The majority of the test results show that the higher quantity of epoxy in most cases plays negative role and lowers the properties of the investigated composites. This phenomenon is due to poor interaction between the epoxy and the rubber matrix and leads to mostly weak physical crosslinks which are destructed during testing. In most cases the vulcanizates where efficient vulcanization system (EV) is used have better properties than the ones where conventional vulcanization system is used. The overall results suggest that the surface of the epoxy powder should be treated with substances which can improve the interaction between epoxy powder and rubber matrix in order to improve the composite's properties.

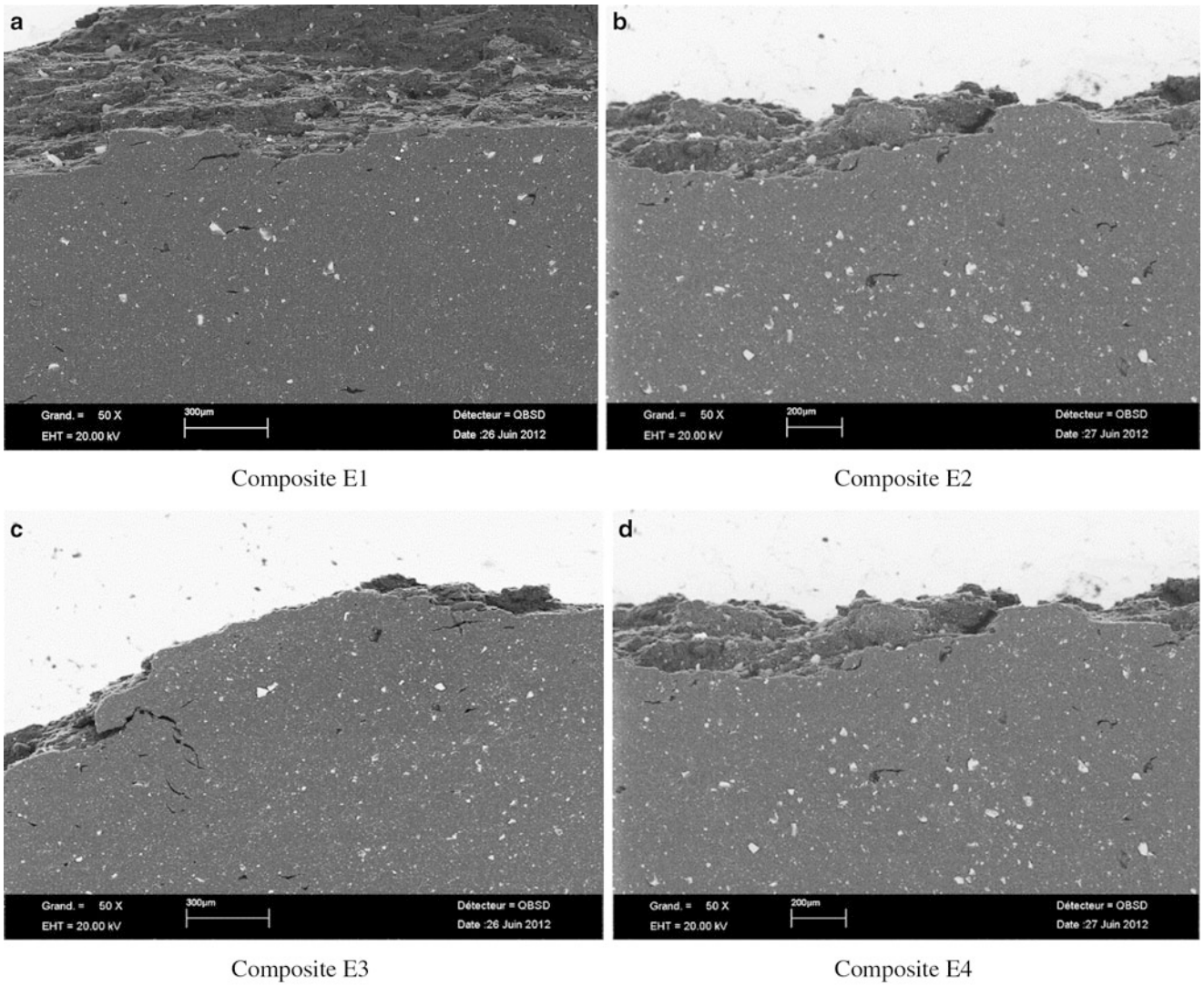

Fig. 23.11 Typical scanning electron microscopy (SEM) surface images just under the fracture side for the composites just under the fracture side for the composites E1, E2, E3, E4. (**a**) Composite E1. (**b**) Composite E2. (**c**) Composite E3. (**d**) Composite E4

References

1. Viswanathan, B., Murthy, V.R.K. (eds.): Ferrite Materials: Science and Technology, 1st edn. Narosa, New Delhi (1990)
2. Coran, A.Y.: Blends of dissimilar rubbers—cure-rate incompatibility. Rubber Chem. Tech. **61**(2), 281–292 (1988)
3. Choudhury, N.R., Bhowmick, A.K.: Studies on adhesion between natural rubber and polyethylene and the role of adhesion promoters. J. Adhes. **32**(1), 1–14 (1990)
4. Pal, P.K., De, S.K.: Effect of reinforcing carbon black on network structure, technical properties, and failure mode of EPDM rubber. J. Appl. Polymer Sci. **28**(11), 3333–3347 (1983)
5. Young, R.J., Al-Khudhairy, D.H.A., Thomas, A.G.: Characterization of filled rubbers using small-angle X-ray scattering. J. Mater. Sci. **21**(4), 1211–1218 (1986)
6. Ghoneim, A.M., Ismail, M.N.: Studies on Epdm/Nr blends. I. Dielectric and mechanical properties. Polymer Plast. Tech. Eng. **38**(5), 979–995 (1999)
7. Zaimova, D., Bayraktar, E., Miskioglu, I., Katundi, D., Dishovsky, N.: Manufacturing of new elastomeric composites: mechanical properties, chemical and physical analysis. In: Tandon, G. (ed.) Composite, Hybrid, and Multifunctional Materials, vol. 4, pp. 139–150. Springer, Cham (2015)
8. ASTM and D. 412aε2. Standard Test Methods for Vulcanized Rubber and Thermoplastic Elastomers—Tension. www.astm.org (2010)
9. ASTM and D. 2240-05. Standard Test Method for Rubber Property—Durometer Hardness. www.astm.org (2010)
10. Oliver, W.C., Pharr, G.M.: An improved technique for determining hardness and elastic-modulus using load and displacement sensing indentation experiments. J. Mater. Res. **7**(6), 1564–1583 (1992)

11. Tehrani, M., Safdari, M., Al-Haik, M.S.: Nanocharacterization of creep behavior of multiwall carbon nanotubes/epoxy nanocomposite. Int. J. Plast. **27**(6), 887–901 (2011)
12. Zaimova, D., Bayraktar, E., Berthout, G., Dishovsky, N.: Design of new elastomeric matrix composites: comparison of mechanical properties and determining viscoelastic parameters via continuous micro indentation. In: Patterson, E., Backman, D., Cloud, G. (eds.) Composite Materials and Joining Technologies for Composites, vol. 7, pp. 227–234. Springer, New York (2013)
13. Luong, R., Isac, N., Bayraktar, E.: Damage initiation mechanism in rubber sheet composites during the static loading. Arch. Mater. Sci. Eng. **28**(1), 19–26 (2007)
14. Botelho, T.D.S., Isac, N., Bayraktar, E.: Modelling of damage initiation mechanism in rubber sheet composites under the static loading. International journal of achievement in materials and manufacturing engineering, JAMME. **22**(2), 55-59 (2007)
15. Botelho T.D.S., Isac, N., Bayraktar, E.: Modeling of damage initiation mechanism in rubber sheet composites under the static loading. International journal of achievement in materials and manufacturing engineering, JAMME. **22**(2), 55–59 (2007)
16. Bayraktar, E., Isac, N., Bessri, K., Bathias, C.: Damage mechanisms in natural (NR) and synthetic rubber (SBR): nucleation, growth and instability of the cavitation. Fatig. Fract. Eng. Mater. Struct. **31**(2), 184–196 (2008)

Chapter 24
Mechanical Properties of Extensively Recycled High Density Polyethylene

P. Oblak, J. Gonzalez-Gutierrez, B. Zupančič, A. Aulova, and I. Emri

Abstract In the plastics industry it has been common practice to mechanically recycle waste material arising from a production. However, mechanical recycling affect material mechanical properties and consequently quality of the end products; therefore it needs to be quantified.

Mechanical recycling of high density polyethylene (HDPE) was simulated by one-hundred consecutive extrusions. After every cycle, portion of material was removed for the purpose of characterization. Solid mechanical properties of the material were characterized in terms of hardness and modulus measured with nanoindentation. Furthermore, shear creep compliance was measured to characterize the materials' time-dependent mechanical properties in solid state. In addition, differential scanning calorimetry (DSC) measurements were performed in order to study structural changes through the degree of crystallinity.

The results on hardness and modulus show deterioration of the material mechanical properties through the process of repeating recycling. This becomes increasingly evident after 10th extrusion. Similarly, shear creep compliance measurements show an unfavourable effect of mechanical recycling on the time-dependent mechanical properties. In this case, evident changes are visible in particularly after the 30th extrusion. After 100th recycling material mechanical properties reduces for about 20 %. All those changes are well supported by changes of the degree of crystallinity.

Keywords High density polyethylene • Mechanical recycling • Hardness and modulus • Creep compliance • Crystallinity

24.1 Introduction

In the second half of the twentieth century, plastics became one of the most universally-used multipurpose materials in the global economy. With continuous growth of plastic industry also amount of generated waste is increasing, not only as post-consumer waste but also as waste generated during the production process. Runners, sprues and off-specification products are common in production; they are easy to identify and are of high quality [1]. Instead of being rejected as waste they are granulated and reprocessed; this makes economic sense as it reduces both production waste and utilisation of raw materials. Reprocessing of production waste is particularly important in cases where amount of waste is high in respect to the product. As an extreme case, micro injection moulding can be exposed; in its case the volume of delivery system, i.e., sprue and runner systems, which represent the waste material, can exceed that of the injected part by a factor 100 or more [2]. Another example is extrusion blow-moulding technology where amount of the scrap during production can reach 40 % [3].

Reprocessing of production waste is also known as in-house or primary recycling and represents a type of mechanical recycling where plastics are grinded and then processed through a physical process [4]. In these cases material can be exposed to excessive number of reprocessing that may affect its processability and quality of end products.

Properties of mechanically recycled polymers do not remain the same because of degradation from heat, mechanical stresses and oxidation during their reprocessing. Degradation affects molecule structure and consequently material mechanical properties [5, 6] thus the quality is the main issue when dealing with mechanically recycled products [7]. Besides mechanical, also rheological properties are changed [8–10]. This has direct effect on the processability and needs to be considered during the following technological processes.

P. Oblak (✉) • J. Gonzalez-Gutierrez • B. Zupančič • A. Aulova
Faculty of mechanical engineering, Center for Experimental Mechanics, University of Ljubljana, Ljubljana, Slovenia
e-mail: pavel.oblak@fs.uni-lj.si

I. Emri
Faculty of mechanical engineering, Center for Experimental Mechanics, University of Ljubljana, Ljubljana, Slovenia

Institute for Sustainable Innovative Technologies, Ljubljana, Slovenia

C. Ralph et al. (eds.), *Mechanics of Composite and Multi-functional Materials, Volume 7*,
Conference Proceedings of the Society for Experimental Mechanics Series, DOI 10.1007/978-3-319-21762-8_24

In line with the information mentioned above, present work is focused to investigation of the mechanical properties of HDPE when exposed to extensive mechanical recycling, i.e., to one hundred (100) consecutive extrusions cycles. In this paper we focus on short-, and long-term material mechanical properties, determined through nano-indentation and creep experiments. In addition, this investigation supports changes of mechanical properties by observed structural changes presented through the changes of degree of crystallinity.

24.2 Materials and Methods

24.2.1 Material

For the purposes of the investigation, high density polyethylene (HDPE) LANUFENE®HDI-6507UV, produced by Ras Lanuf Oil & Gas Processing Co. was used. The material has density 0.965 g/cm^3 (23 °C) and melt flow index 7.5 g/10 min (190 °C and 2.16 kg) [11]. Furthermore, producer provides information on suitability of material for the manufacturing of crates, containers, trays and other similar injection moulded objects where good weather-ability and mechanical properties are needed. In addition, the producer gives information that the material contains UV light stabilizers and recommends its processing temperature to be 220–270 °C [11].

24.2.2 Simulation of Mechanical Recycling

The process of mechanical recycling was simulated by extensive extrusion. For this purpose, twin-screw extruder, PolyLab PTW 16/40 OS, produced by Thermo Scientific (Germany) was used. Extruder had installed horizontal rod die and a nozzle with diameter of 4 mm. Material was extruded at screw rotation of 150 min^{-1}, a processing temperature of 240 °C with a throughput between 1200 and 1300 g/h. After material was extruded, it was pelletized using a Thermo Haake pelletizer and a portion was removed for the purpose of afterwards characterization. The rest of material was submitted to a new extrusion cycle.

24.2.3 Nanoindentation

Measurements of hardness and modulus were performed with nanoindentation using G200 apparatus, produced by Agilent Technologies (USA). The measurements were carried using continuous stiffness measurement technique (CSM) [12] with a Berkovich indenter tip while oscillation frequency was 45 Hz and amplitude 2 nm. For virgin HDPE material as well for its recyclates measurements were repeated on three samples, with 40 indentations on each. In order to obtain reliable data and exclude unstable one caused by surface effects, data from each successful indentation curve was averaged thought the depth of penetration from 1000 to 1500 nm. Further values of elastic modulus and hardness were averaged for all the indents.

24.2.4 Shear Creep Compliance

Shear creep is a process of deformation change over time, $\gamma(t)$, occurring in a material loaded with constant step-like shear stress of magnitude $\tau(t) = \tau_0 \cdot h(t)$. The relation between the constant shear stress loading of magnitude τ_0, and the time-dependent shear strain response, $\gamma(t)$ is after integration expressed through the time-dependent shear creep compliance function, $J(t)$, as presented with the following equation:

$$J(t) = \frac{\gamma(t)}{\tau_0} \tag{24.1}$$

Shear creep measurements were performed on Shear Creep Torsiometer developed by our group [13]. Before performing creep measurements all samples were annealed to erase the residual stresses. HDPE samples were heated up and annealed at 100 °C over a period 7 h, and then gradually cooled to 30 °C over a period of 8 h. After annealing, the measurement continued with loading, unloading and conditioning of the sample at 30, 50, 65, 75 and 90 °C. Loading phase lasted 3 h at a constant temperature, then the torque was removed and the temperature was increased to the next measuring temperature

within 3 h. The specimen was again torque-loaded, and the procedure of exchanging the phases of loading, unloading and conditioning was repeated over the selected measuring temperature range. The stresses applied to each specimen were selected as to remain in the linear viscoelastic region for all materials and ranged from $\tau_0 = 9.6 \times 10^4$ Pa at 30 °C to 3.0×10^4 Pa at 90 °C. Two repetitions were performed at each condition for all materials.

24.2.5 Differential Scanning Calorimetry

Differential scanning calorimetry (DSC) analysis was performed on DSC7 instrument, produced by Perkin Elmer (USA). The measurements were carried out according to ISO 11357, in a nitrogen atmosphere. Mass of the specimens was 5.0 ± 0.1 mg. Heating and cooling rate was 20 °C/min. Heat (enthalpy) of fusion (ΔH_f) was evaluated from a second heating run. The degree of crystallinity (X_{cr}) was calculated based on next relation:

$$X_{cr} = \frac{\Delta H_f}{\Delta H \cdot 100\%}, \tag{24.2}$$

where $\Delta H \cdot 100\%$ is the heat of fusion for 100 % crystalline HDPE, which has been estimated to be 293 J/g [14]. Average values of six repetitions are presented in this study.

24.3 Results and Discussion

24.3.1 Hardness and Modulus

Mechanical properties of virgin HDPE as well its recyclates, i.e., hardness and modulus, were measured using nanoindentation technique. Results are presented in Figs. 24.1 and 24.2. It can be seen that both, hardness and modulus, exhibit similar trend. For both properties one observes four different regions: (Region I) Through the first 10 extrusion cycles, no significant changes are detected while further, (Region II) between 10th and 20th extrusion cycle, "quick" drop is evident. Afterwards (Region III), both values are gradually decreasing up to 70th extrusion cycle where (region IV) both properties stabilise. When taking into account first 10 extrusion cycles, we can say that our results are in line with those

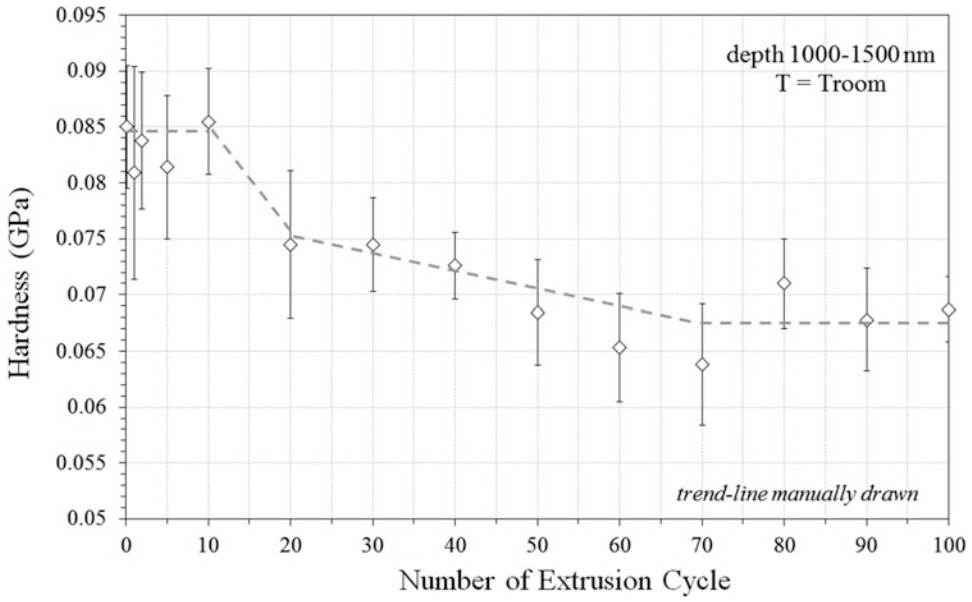

Fig. 24.1 Hardness in dependence of the number of extrusion cycles

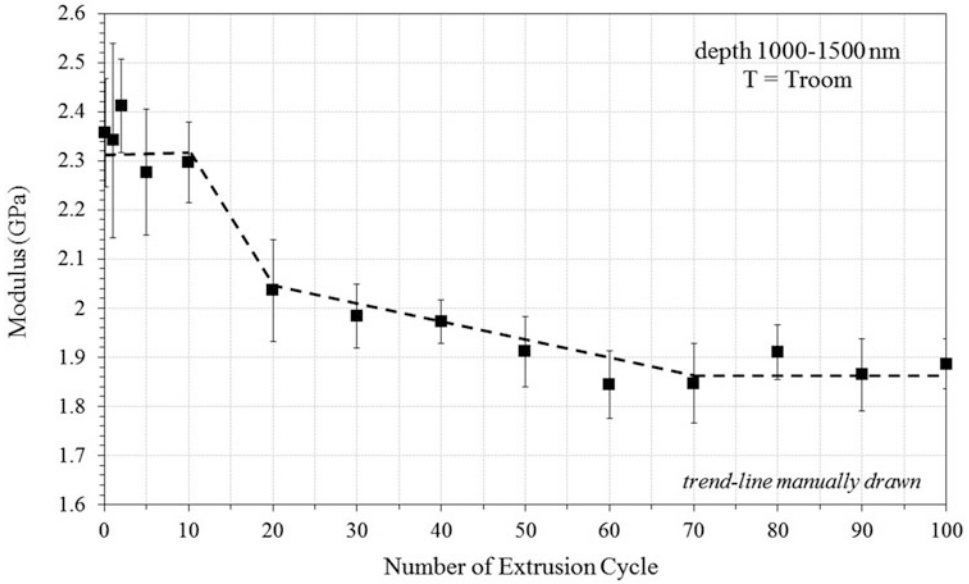

Fig. 24.2 Modulus in dependence of the number of extrusion cycles

reported by other authors [5, 15–17], while none of them extend their investigation above ten reprocessing cycles. Changes of hardness and modulus can be attributed to the changes in the degree of crystallinity presented in Fig. 24.4.

In practice, information on decreasing trend of hardness and modulus might be useful when designing products made from recycled HDPE; when using recycled material, lower performance in respect to a product made from virgin material can be expected when material recycled more than ten times is used.

However, we need to emphasize that even after 100 recycling material retains 80 % of its initial mechanical properties! Hence, if this fact is taken into account during the phase of structural part designing recycled HDPE may be used without any restrictions.

24.3.2 Shear Creep Compliance

Time-dependent (long term) properties of virgin HDPE and its recyclates were characterized performing shear creep compliance measurements. To present long-term product mechanical stability, first, master curves of virgin HDPE and its recyclates were generated and shifted to reference temperature 30 °C using the CFS methodology [18]. Further, isochronal values of creep compliance at time equal to 3 and 10 years were taken from individual master curves; results are presented in Fig. 24.3. It can be seen that extrusion did not significantly affect shear creep compliance through first 30 reprocessing cycles. Furthermore an increasing trend is evident in time of 3 years as well in 10 years. At 100th extrusion cycle, creep compliance rises for 16 % after 3years and 20 % after 10 years in comparison to virgin material. In addition we might say that difference in creep between 3 and 10 years remains more or less constant.

Since shear creep compliance is measured in solid state we can relate increasing shear creep with extrusion cycles to the degree of crystallinity, presented in Fig. 24.4, which shows the opposite, decreasing trend. We may conclude that products made of HDPE recycled more than 30 times, have lower long-term mechanical stability or in other words, using those materials represents the risk that a product will have lower performance. The reduction over 100 recycling is about 20 %.

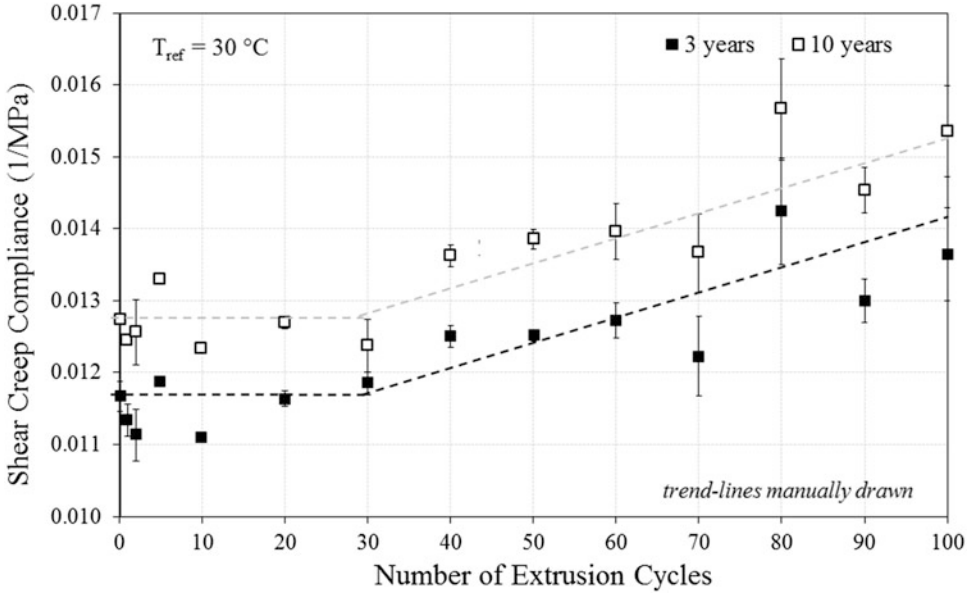

Fig. 24.3 Creep compliance in dependence of the number of extrusion cycles after 3 and 10 years

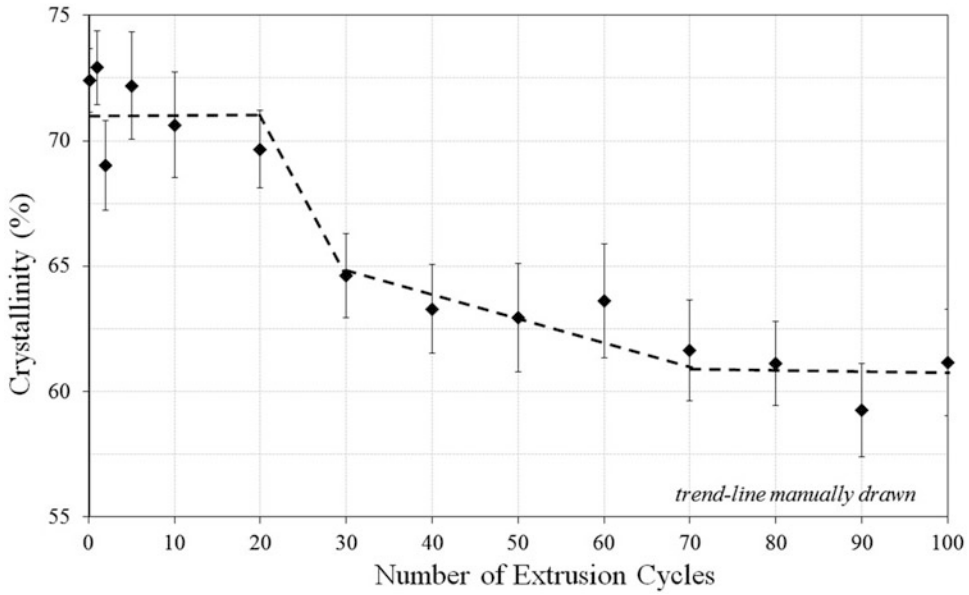

Fig. 24.4 Variation of crystallinity in dependence of the number of extrusion cycles

24.3.3 Differential Scanning Calorimetry

Curve, representing the degree of crystallinity is presented in Fig. 24.4. It shows that extrusion leads to noticeable decrease in a degree of crystallinity only after 20th reprocessing cycle. The evident leap was detected between 20th and 30th extrusion cycles while the largest drop of 18 % can be observed at 90th extrusion cycle. Similarly, several authors who investigated the effect of HDPE reprocessing on degree of crystallinity [5, 16, 19, 20], did not observe any significant change on crystallinity throughout 10 reprocessing cycles. This is in line with our findings from first 20 extrusion cycles. Decreasing of the degree of crystallinity shows the reducing of molecular ability to pack and form crystal regions. This might be consequence of crosslinking or chain branching process in the material, which is one of the mechanisms present at the degradation under processing conditions [21, 22]. Moreover, changes in the degree of crystallinity may result in changes of mechanical properties, i.e., hardness, modulus and creep compliance as previously presented in Figs. 24.1, 24.2, and 24.3.

24.4 Conclusions

In the current study, effect of extensive mechanical recycling on mechanical properties of HDPE was investigated. Decrease of hardness and modulus becomes increasingly evident after 10th extrusion cycle. Similarly, shear creep compliance measurements show an unfavourable effect of mechanical recycling on the time-dependent mechanical properties, while in this case, evident changes are visible in particularly after the 30th extrusion cycle. However, all those changes are well supported by the degree of crystallinity which does not show significant changes through the first 20 extrusion cycles while after, between 20th and 30th cycle, significant drop is recorded and gradual decreasing afterwards. It can be concluded that mechanical recycling causes deterioration of HDPE mechanical properties that becomes evident after 10th reprocessing cycle. This information should be taken into account when designing products from recycled HDPE. However, it needs to be emphasized that even after 100 recycling material retains 80 % of its initial mechanical properties and durability is reduced for about 20 %! Hence, if these facts are taken into account during the product-designing phase recycled HDPE may be often used without any restrictions.

Acknowledgements This work was conducted with the financial support of the Slovenian Research Agency—ARRS.

References

1. Lundquist, L., Leterrier, Z., Sunderland, P., Månson, J.A.E.: Life Cycle Engineering of Plastics Technology, Economy and Environment. Elsevier, New York (2000)
2. Jeggy, C.: Micro-Injection Moulding: From Process to Modelling. UCL Presses Universitaires. de Louvain, Leuven (2004)
3. Board, N.I.I.R.: The Complete Book on Biodegradable Plastics and Polymers (Recent Developments Properties, Analyses, Materials & Processes). Asia Pacific Business Press, Delhi (2006)
4. Goodship, V.: Introduction to Plastics Recycling, 2nd edn. Smithers Rapra Technology Limited, Shawbury (2007)
5. Abad, M.J.: Effects of a mixture of stabilizers on the structure and mechanical properties of polyethylene during reprocessing. J. Appl. Polym. Sci. **92**(6), 3910–3916 (2004)
6. Kotiba, H., Mosab, K., Fawaz, D.: Effect of recycling on rheological and mechanical properties of poly(lactic acid)/polystyrene polymer blend. J. Mater. Sci. **46**, 3013–3019 (2011)
7. Al-Salem, S.M., Lettieri, P., Baeyens, J.: Recycling and recovery routs of plastic solid waste (PSW): a review. Waste Manag. **29**, 2625–2643 (2009)
8. Dostal, J., Kašparkova, V., Yatloukal, M., Muras, J., Šimek, L.: Influence of the repeated extrusion on the degradation of polyethylene. Structural changes in low density polyethylene. Eur. Polym. J. **44**, 2652–2658 (2008)
9. da Costa, H.M., Ramos, V.D., Rocha, M.C.G.: Rheological properties of polypropylene during multiple extrusion. Polym. Test. **24**, 86–93 (2005)
10. Gonzalez-Gonzalez, V.A., Neira-Velazquez, G., Angulo-Sanchez, J.L.: Polypropylene chain scission and molecular weight changes in multiple extrusion. Polym. Degrad. Stab. **60**, 33–42 (1998)
11. Ras Lanuf Oil & Gas Processing Co, LANUFENE®HDI-6507UV technical specification. www.nascopolymers.com/PDF/HDPE/HDI%206507%20UV.pdf (2014). Accessed May 2014
12. Li, X., Bhushan, B.: A review of nanoindentation continuous stiffness measurement technique and its applications. Mater. Charact. **48**, 11–36 (2002)
13. Metlikovič, P., Emri, I.: Naprava za merjenje lezenja torzijsko obremenjehih polimernih preizkušancev. Strojniški vestn. **36**, 101–104 (1990)
14. Blaine, R.L.: Thermal Application Note, Polymer Heats of Fusion, TA Instruments. NewCastle, USA. www.tainstruments.com/library_download.aspx?file=TN048.pdf (2014). Accessed June 2014
15. Kartalis, C.N.: Mechanical recycling of postused high-density polyethylene crates using the restabilization technique. I. Influence of reprocessing. J. Appl. Polym. Sci. **73**(9), 1775–1785 (1999)
16. Stromberg, E., Karlsson, S.: The design of a test protocol to model the degradation of polyolefins during recycling and service life. J. Appl. Polym. Sci. **112**(3), 1835–1844 (2009)
17. Apone, S.: Effects of thermomechanical treatments on HDPE used for TLC ducts. Polym. Test. **22**(3), 275–280 (2003)
18. Gergesova, M., Zupančič, B., Saprunov, I., Emri, I.: The closed form t-T-P shifting (CFS) algorithm. J. Rheol. **55**(1), 1–16 (2011)
19. Altan, M.: Residual stresses determination in injection molded virgin and recycled HDPE blends: mechanical properties and morphology. E-Polymers **8**(1), 1937–1964 (2008)
20. Luzuriaga, S.: Degradation of pre-aged polymers exposed to simulated recycling: properties and thermal stability. Polym. Degrad. Stab. **91**(6), 1226–1232 (2006)
21. Epacher, E.: Two-step degradation of high-density polyethylene during multiple extrusion. J. Appl. Polym. Sci. **74**(6), 1596–1605 (1999)
22. Hamad, K.: Recycling of waste from polymer materials: an overview of the recent works. Polym. Degrad. Stab. **98**(12), 2801–2812 (2013)

Chapter 25
Mechanical Characterization and Preliminary Modeling of PEEK

Wenlong Li, Eric N. Brown, Philip J. Rae, George Gazonas, and Mehrdad Negahban

Abstract Poly-ether-ether-ketone (PEEK) is a high-performance semi-crystalline polymer with mechanical and thermal stability characteristics that are superior to most tough polymers. The mechanical characteristics of this polymer are modeled over a broad range of mechanical loading conditions using a thermodynamically consistent modeling process. This preliminary model, which ignores the thermal response and the possible recrystallization of this material during loading, shows an outstanding ability to capture the multidimensional nonlinear response of PEEK up to 60 % compression, with loading rates from 0.0001 to 3000 1/s at room temperature. The model includes the measured anisotropy in the wave response that develops with plastic flow, captures the evolution of the measured equilibrium stress, and correctly matches the evolution of the tangent modulus at equilibrium. This broad range of rates and experimental conditions are achieved by using a two-element nonlinear thermodynamically-consistent model.

Keywords Poly-ether-ether-ketone (PEEK) • Equilibrium stress • Plastic flow • Anisotropic elasticity • Mechanical modeling

25.1 Introduction

Poly(ether-ether-ketone) (PEEK) is a relatively expensive high-performance polymer used when its combination of thermal stability and mechanical properties cannot be achieved with other materials. It is also considered for use in medical implants [1]. Its superior properties and semi-crystalline structure have resulted in several investigations of its mechanical properties [2–4]. As commonly seen in polymers and metals, plastic flow of PEEK results in the development of elastic anisotropy that is dependent on the extent and characteristics of the plastic flow. The strength of this anisotropy depends on the extent of deformation [5], which is also a characteristic seen when processing metals [6].

Modeling the change in symmetry for deforming materials, and in particular for models for plasticity, has been studied in some detail for first gradient mathematical models [7–9]. The modeling of such changes in a nonlinear viscoelastic material can be done using a thermodynamically consistent modeling method [10, 11]. This modeling requires information on the changes in the equilibrium stress, the developing anisotropy, and the rate dependence of the material. The results presented in [4] on the dynamic response under monotonic loading are combined with additional results on the equilibrium stress, tangent modulus at equilibrium, and the developing anisotropic elastic response to build a preliminary model for the response of PEEK at room temperature.

An evaluation of the developing elastic anisotropy of polycarbonate (PC) after plastic flow was recently conducted using ultrasonic wave speed measurements along different directions in compressed samples and these results were used to show how to model the developing elastic anisotropy with plastic flow [12, 13]. A similar method is used to evaluate the speed of ultrasonic waves and to get the developing elastic anisotropy induced by plastic compression in PEEK samples after plastic compression at room temperatures. These are used to create a preliminary model for the development of anisotropic elastic response in PEEK.

W. Li • M. Negahban (✉)
Mechanical & Materials Engineering, University of Nebraska-Lincoln, Lincoln, NE 68588-0526, USA
e-mail: mnegahban@unl.edu

E.N. Brown • P.J. Rae
Los Alamos National Laboratory, Los Alamos, NM 87545, USA

G. Gazonas
U.S. Army Research Laboratory, Aberdeen Proving Ground, MD 21005, USA

C. Ralph et al. (eds.), *Mechanics of Composite and Multi-functional Materials, Volume 7*,
Conference Proceedings of the Society for Experimental Mechanics Series, DOI 10.1007/978-3-319-21762-8_25

A method for the evaluation of equilibrium stress in plastically deforming materials by cyclic loading has been shown and demonstrated for PC to provide both the equilibrium stress and equilibrium tangent modulus [14]. This method is used to evaluate the equilibrium stress in PEEK during plastic compression and evaluate the changing tangent modulus at equilibrium. This is used to characterize the back stress in the response of PEEK, and to identify the partition between the slow and fast response. These results, and those described in [15], are imbedded in a two-element model to capture both the slow and fast response of PEEK during room temperature loading.

25.2 Materials and Experimental Methods

The experimental results on PEEK were conducted on samples taken from a 12 × 12 inch^2 commercial sheets of 0.5 inch thick VICTREX 450G PEEK. Cylindrical samples were cut from the as-received sheet with the cylinder axis perpendicular to the sheet surface. No additional thermal conditioning was done on the samples. The cylindrical samples were compressed with an MTS 8500 universal testing machine to final nominal plastic strains of 0 % (unreformed), −15 %, −30 % and −45 %, and then left unloaded for at least 1 day before further testing.

25.2.1 Wave Moduli Measurement

The shear and longitudinal wave moduli were evaluated along the axis and perpendicular to the axis of compression using the equations

$$G = \rho v_s^2, \quad E = \rho v_l^2, \tag{25.1}$$

where G and E are, respectively, the shear and longitudinal wave moduli, ρ is the density, and v_s, v_l are, respectively, the shear and longitudinal wave speeds. To obtain the axial and transverse moduli, samples were cut from the initially compressed PEEK cylinders as shown in Fig. 25.1.

At room temperature, the density of plastically compressed samples were measured using a Mettler Toledo AT201 scale using the relation

$$\rho = \rho_w \times \frac{W_a}{W_a - W_w}, \tag{25.2}$$

where ρ_w is the density of the distilled water used, and W_a and W_w are the weight of the sample measured in air and in distilled water.

The velocity of ultrasonic wave traveling through the sample was determined by measuring the time of flight of the wave through the thickness of the sample using a standard pulse-echo setup. Normal incidence and shear wave contact transducers (Olympus 5 MHz; V155 and V109 RM) were used. To avoid interference from waves returning from the sample edges rather than the parallel surfaces, cylindrical samples with 5 mm height and 12.5 mm diameter were cut out along the axial direction (direction of original compression) and the transverse direction as shown in Fig. 25.1. As shown in the figure, E_a and E_t are

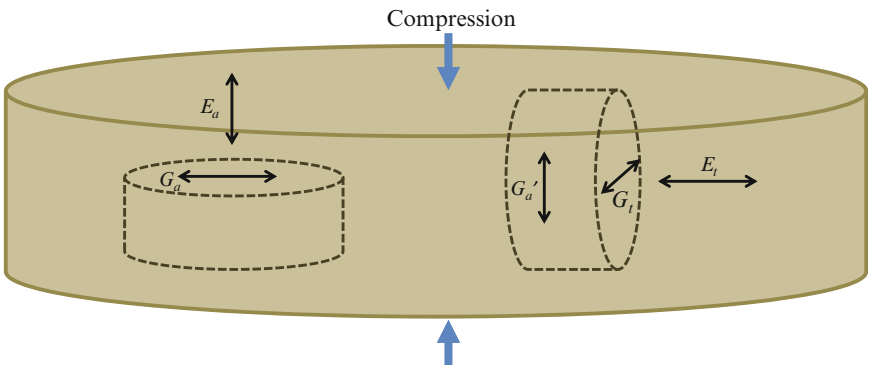

Fig. 25.1 Samples taken for the measurement of wave moduli after plastic flow

longitudinal wave moduli, respectively, along the direction of compression and perpendicular to it, and G_a and G_t are shear wave moduli, respectively, along the same directions. Since the compressed sample is transversely isotropic, G_a and $G_a^{'}$ are the same.

The errors were calculated using the error propagation from the error of each measurement and were consistent with the published values [4].

25.2.2 Equilibrium Stress Measurement

Cyclic compression tests were used to find the equilibrium state of the material. Following the procedure described in [14], the equilibrium state was determined from the point where the tangent modulus during loading and unloading are the same. This is shown to be the point at which the plastic strain rate is zero, describing a state of equilibrium stress.

The sample was cylindrical with a 6.35 mm (1/4 inch) diameter and a 6.35 mm (1/4 inch) length. The axial cyclic compression test was done in an MTS 8500 universal testing machine at room temperature. The unloading cycle was conducted at every 6–8 % axial strain during the compression. The unloading was to below 40 MPa to guarantee capturing of the equilibrium. The compression was continued to 50 % compression at a strain rate of 0.01 1/s.

25.3 Experimental Results and Discussion

Plastic flow resulted in a volume expansion of PEEK, thus reducing the density, as shown in Fig. 25.2a. As indicated in Fig. 25.2b, both the longitudinal and shear wave moduli along the direction of compression decrease as the samples undergo compression, while these same wave moduli in the transverse direction increase.

The equilibrium stress can be evaluated by measuring the tangent modulus for both the loading and the unloading segments, as shown in Fig. 25.3. The corresponding tangent modulus at equilibrium can be obtained during this test and is shown in Fig. 25.7. As indicated, the axial tangent modulus at equilibrium drops with compression.

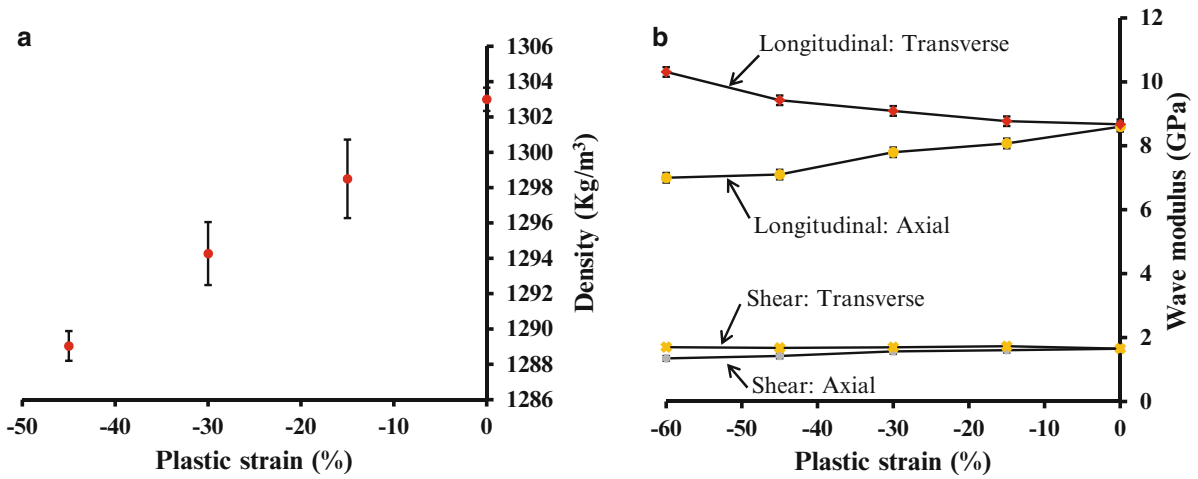

Fig. 25.2 Density (**a**) and anisotropic wave moduli (**b**) after plastic compression

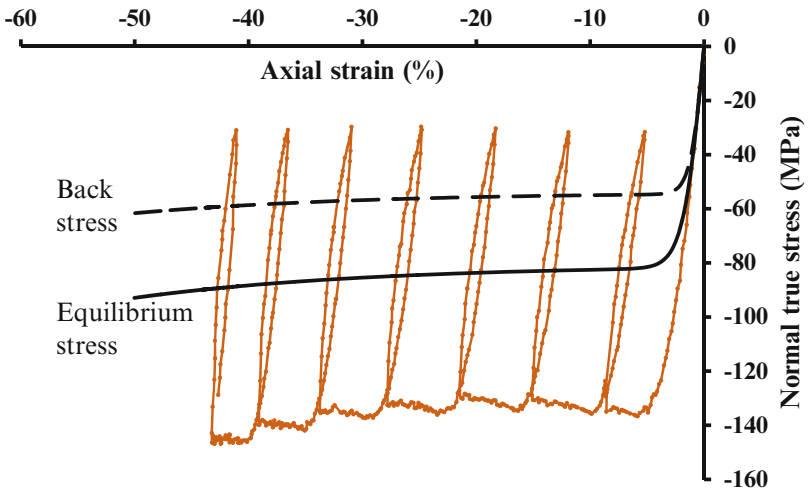

Fig. 25.3 Equilibrium stress in the cyclic uniaxial compression test

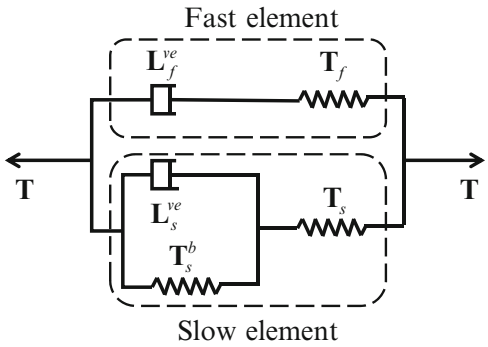

Fig. 25.4 Schematic of the two-element viscoelastic model developed

25.4 Modeling

The model used to capture the response of PEEK is based on the large deformation thermodynamic theory for viscoelastic and plastic flow as described in [10]. This is a thermodynamically consistent model that can be extended to non-isothermal response. For PEEK, a two-element model is proposed to describe the mechanical response. The schematic of the connection between the elements of this model is shown in Fig. 25.4. The model consists of slow and fast response elements. The components of the slow response element are designated by adding a subscript "s" to the variable, and the components of the fast response element are denoted by using a subscript "f". The slow response element consists of an elastic stress $\mathbf{T}_s$, a back stress $\mathbf{T}_s^b$, and a viscous component characterized by the viscoelastic velocity gradient $\mathbf{L}_s^{ve}$. The fast response element, only showing noticeable contribution during rapid loading, consists of components with elastic stress $\mathbf{T}_f$ and viscous flow characterized by the viscoelastic velocity gradient $\mathbf{L}_f^{ve}$. The effort of the modeling is to identify and model these elements.

The model assumes that the response of each element decomposes into elastic and viscoelastic parts that follow the standard multiplicative decomposition. The deformation gradient $\mathbf{F}$ is thus assumed to decompose into elastic and viscoelastic deformation gradients through the kinematic relation

$$\mathbf{F} = \mathbf{F}_s^e \mathbf{F}_s^{ve} \mathbf{F}_s^\theta = \mathbf{F}_f^e \mathbf{F}_f^{ve} \mathbf{F}_f^\theta, \tag{25.3}$$

where $\mathbf{F}_s^e$, $\mathbf{F}_s{}^{ve}$, $\mathbf{F}_s{}^\theta$, $\mathbf{F}_f^e$, $\mathbf{F}_f{}^{ve}$, and $\mathbf{F}_f^\theta$ are, respectively, the elastic, viscoelastic and thermal deformation gradients for, respectively, the slow and fast elements.

The free energy ψ is assumed to be a function ψ^+ of the elastic, viscoelastic, and thermal deformation gradients, and temperature (which we are leaving out for this paper). This is written as

$$\psi = \psi^+\left(\mathbf{F}_s^e, \mathbf{F}_s^{ve}, \mathbf{F}_s^\theta, \mathbf{F}_f^e, \mathbf{F}_f^{ve}, \mathbf{F}_f^\theta, \theta\right), \tag{25.4}$$

This results in models for elastic and back stress of the form

$$\begin{aligned} \mathbf{T}_s &= \rho\, \partial_{\mathbf{F}_s^e}(\psi)\mathbf{F}_s^{eT}, \quad \mathbf{T}_s^b = \rho\, \partial_{\mathbf{F}_s^{ve}}(\psi)\mathbf{F}_s^{veT}, \\ \mathbf{T}_f &= \rho\, \partial_{\mathbf{F}_f^e}(\psi)\mathbf{F}_f^{eT}, \quad \mathbf{T}_f^b = \rho\, \partial_{\mathbf{F}_f^{ve}}(\psi)\mathbf{F}_f^{veT}. \end{aligned} \tag{25.5}$$

The free energy is further assumed to separate into independent components for the slow and fast parts that depend on the Green-Lagrange strains

$$\mathbf{E}_s^e = \frac{1}{2}(\mathbf{C}_s^e - \mathbf{I}), \quad \mathbf{E}_s^{ve} = \frac{1}{2}(\mathbf{C}_s^{ve} - \mathbf{I}), \quad \mathbf{E}_f^e = \frac{1}{2}\left(\mathbf{C}_f^e - \mathbf{I}\right), \quad \mathbf{E}_f^{ve} = \frac{1}{2}\left(\mathbf{C}_f^{ve} - \mathbf{I}\right), \tag{25.6}$$

where $\mathbf{C} = \mathbf{F}^T\mathbf{F}$ in each case is the associated right Cauchy stretch tensor. A form of the free energy consistent with the schematic in Fig. 25.4 is given by

$$\psi = \psi_s^+\left(\mathbf{E}_s^e, \mathbf{E}_s^{ve}, \theta\right) + \psi_f^+\left(\mathbf{E}_f^e, \theta\right) + \psi_\theta^+(\theta). \tag{25.7}$$

Assumption of isotropy of the initial state gives the free energy of the slow component to be a function of the ten isotropic invariants

$$\begin{aligned} &I_1 = \det\left(\mathbf{F}_s^e\right), \quad I_2 = tr\left(\mathbf{E}_s^{e*}\right), \quad I_3 = tr\left(\mathbf{E}_s^{e*2}\right), \quad I_4 = \det\left(\mathbf{F}_s^{ve}\right), \quad I_5 = tr\left(\mathbf{E}_s^{ve}\right), \quad I_6 = tr\left(\mathbf{E}_s^{ve2}\right), \\ &I_7 = tr\left(\mathbf{E}_s^e\mathbf{E}_s^{ve}\right), \quad I_8 = tr\left(\mathbf{E}_s^e\mathbf{E}_s^{ve2}\right), \quad I_9 = tr\left(\mathbf{E}_s^{e2}\mathbf{E}_s^{ve}\right), \quad I_{10} = tr\left(\mathbf{E}_s^{e2}\mathbf{E}_s^{ve2}\right), \end{aligned} \tag{25.8}$$

and the free energy of the fast response to be a function of the three isotropic invariants

$$\bar{I}_1 = \det\left(\mathbf{F}_f^e\right), \quad \bar{I}_2 = tr\left(\mathbf{E}_f^{e*}\right), \quad \bar{I}_3 = tr\left(\mathbf{E}_f^{e*2}\right), \tag{25.9}$$

where a superscript "*" denotes that the volume part was removed from the associated deformation gradient so that

$$\mathbf{E}_s^{e*} = \frac{1}{2}\left(\frac{1}{J_s^{e2/3}}\mathbf{C}_s^e - \mathbf{I}\right), \quad \mathbf{E}_f^{e*} = \frac{1}{2}\left(\frac{1}{J_f^{e2/3}}\mathbf{C}_f^e - \mathbf{I}\right), \tag{25.10}$$

where $J_s^e = \det\left(\mathbf{F}_s^e\right)$ and $J_f^e = \det\left(\mathbf{F}_f^e\right)$ denote the volume ratios. For more details refer to [10].

Due to the assumed form of the free energy given in (25.7) and the assumption of initial isotropy for the PEEK before deformation, we get the models for elastic and back stress given by

$$\begin{aligned} \mathbf{T}_s^T &= \rho \sum \frac{\partial \psi}{\partial I_i}\, \partial_{\mathbf{F}_s^e}(I_i)\mathbf{F}_s^{eT}, \quad \mathbf{T}_s^{bT} = \rho \sum \frac{\partial \psi}{\partial I_i}\, \partial_{\mathbf{F}_s^{ve}}(I_i)\mathbf{F}_s^{veT}, \\ \mathbf{T}_f^T &= \rho \sum \frac{\partial \psi}{\partial I_i}\, \partial_{\mathbf{F}_f^e}(I_i)\mathbf{F}_f^{eT}, \quad \mathbf{T}_f^{bT} = 0. \end{aligned} \tag{25.11}$$

It also follows that the measured Cauchy stress $\mathbf{T}$ is given by

$$\mathbf{T} = \mathbf{T}_s + \mathbf{T}_f. \tag{25.12}$$

25.5 Anisotropic Elastic Response

As indicated in Fig. 25.2, the ultrasonic response is isotropic in the as-received sample and becomes anisotropic with plastic flow, the anisotropy growing continuously during the compression. The ultrasonic tests were done after the completion of compression, and complete relaxation so one can assume both the elastic stress elements have gone to zero stress, and the two viscoelastic strains are the same. The ultrasonic loading is assumed to be rapid and thus should not change the

viscoelastic flow elements. This allows one to assume $\mathbf{F}^e = \mathbf{F}_s^e = \mathbf{F}_f^e$ and $\mathbf{F}^p = \mathbf{F}_s^{ve} = \mathbf{F}_f^{ve}$ during the ultrasonic loading. The wave speeds measured are thus associated with combined elastic components of both the slow and fast elements. These can be evaluated from the elastic tangent modulus calculated from the total stress by

$$\mathbf{E} = \partial_{\mathbf{F}^e}(\mathbf{T}). \tag{25.13}$$

Considering the dependence of the slow and fast elements on the isotropic invariants, a model for free energy was selected that can fit the four measured ultrasonic moduli at each plastic compression. The selected free energy results in the model

$$\begin{aligned}\mathbf{T}^T = &\frac{\kappa}{J^\theta J^p}(J^e-1)\mathbf{I} + \frac{G}{J^\theta J^p}\frac{1}{J^{e5/3}}\left[\mathbf{B}^e - \frac{tr(\mathbf{C}^e)}{3}\mathbf{I}\right] \\ &+ \frac{C_1}{J^\theta J^p} tr(\mathbf{E}^e\mathbf{E}^p)\mathbf{I} + \frac{C_1}{J^\theta J^p J^e}(J^e-1)\mathbf{F}^e\mathbf{E}^p\mathbf{F}^{eT} + \frac{C_2}{J^\theta J^p J^e}\mathbf{F}^e(\mathbf{E}^e\mathbf{E}^p + \mathbf{E}^p\mathbf{E}^e)\mathbf{F}^{eT},\end{aligned} \tag{25.14}$$

where J^θ, J^p and J^e are, respectively, the determinant of $\mathbf{F}^\theta$, $\mathbf{F}^p$ and $\mathbf{F}^e$. This model has four material functions κ, G, C_1, and C_2 that are assumed to depend on the invariants of the permanent deformation. This results in the elastic tangent modulus at zero loading given by

$$\begin{aligned}\mathsf{E}_{ijkl}\big|_{\mathbf{F}^e=\mathbf{I}} = \frac{\partial \mathbf{T}_{ij}^T}{\partial \mathbf{F}_{kl}^e} = &J^\theta J^p \kappa\left[\delta_{ij}\delta_{kl}\right] + J^\theta J^p G\left[\delta_{ik}\delta_{jl} + \delta_{il}\delta_{jk} - \frac{2}{3}\delta_{ij}\delta_{kl}\right] + J^\theta J^p C_1\left[\delta_{ij}\mathbf{E}_{kl}^p + \mathbf{E}_{ij}^p\delta_{kl}\right] \\ &+ \frac{1}{2}J^\theta J^p C_2\left[\delta_{il}\mathbf{E}_{jk}^p + \delta_{ik}\mathbf{E}_{jl}^p + \mathbf{E}_{il}^p\delta_{jk} + \mathbf{E}_{ik}^p\delta_{jl}\right].\end{aligned} \tag{25.15}$$

The four material functions for this model were fit, shown in Fig. 25.5, to the ultrasonic response using the models

$$\kappa = 6.37 - 0.108I_5, \quad G = 1.17e^{-0.5I_5} + 0.5, \quad C_1 = 0.84\left(1 - 0.79e^{-15I_5}\right), \quad C_2 = 0.55e^{-12.5I_5} + 0.65, \tag{25.16}$$

where $I_5 = tr(\mathbf{E}^p)$. Figure 25.6 shows the fit of this model to the measured moduli.

25.6 Partition of the Cauchy Stress

The model for stress given in Eq. (25.14) assumes that both elastic elements deform identically. To get the slow and fast element elastic response models, we need to partition this model. This can be done by comparing the modulus from this model to that under conditions that would only induce motion in the slow elastic element. This was done by experimentally evaluating the tangent modulus at the equilibrium stress from cyclic loading, as shown in Fig. 25.3, to the modulus calculated from the stress described in Eq. (25.14) under equilibrium conditions. Figure 25.7 shows that these results are similar, but shifted by a fixed amount. As can be seen, 67 % of the predicted modulus from the ultrasonic model matches directly with the measured response at equilibrium, which is supposed to be associated only with the slow response. Since there is no back stress term in the fast response, we associate all terms with the plastic deformation gradient to the slow response and partition the balance based on the observed 67 %/33 % ratio. The thermal expansion is assumed to be the same for both so that the models are taken to be of the form

$$\begin{aligned}{\mathbf{T}_s}^T = 0.67\Bigg\{&\frac{\kappa}{J^\theta {J_s}^{ve}}({J_s}^e - 1)\mathbf{I} + \frac{G}{J^\theta {J_s}^{ve}}\frac{1}{{J_s}^{e5/3}}\left[{\mathbf{B}_s}^e - \frac{tr({\mathbf{C}_s}^e)}{3}\mathbf{I}\right]\Bigg\} \\ &+ \frac{C_1}{J^\theta {J_s}^{ve}} tr({\mathbf{E}_s}^e{\mathbf{E}_s}^{ve})\mathbf{I} + \frac{C_1}{J^\theta {J_s}^{ve} {J_s}^e}(J_e^e - 1)\mathbf{F}_s^e{\mathbf{E}_s}^{ve}{\mathbf{F}_s}^{eT} + \frac{C_2}{J^\theta {J_s}^{ve} {J_s}^e}\mathbf{F}_s^e(\mathbf{E}_s^e\mathbf{E}_s^{ve} + \mathbf{E}_s^{ve}\mathbf{E}_s^e)\mathbf{F}_s^{eT},\end{aligned} \tag{25.17}$$

$${\mathbf{T}_f}^T = 0.33\left\{\frac{\kappa}{J^\theta {J_f}^{ve}}({J_f}^e - 1)\mathbf{I} + \frac{G}{J^\theta {J_f}^{ve}}\frac{1}{{J_f}^{e5/3}}\left[\mathbf{B}_f^e - \frac{tr(\mathbf{C}_f^e)}{3}\mathbf{I}\right]\right\}. \tag{25.18}$$

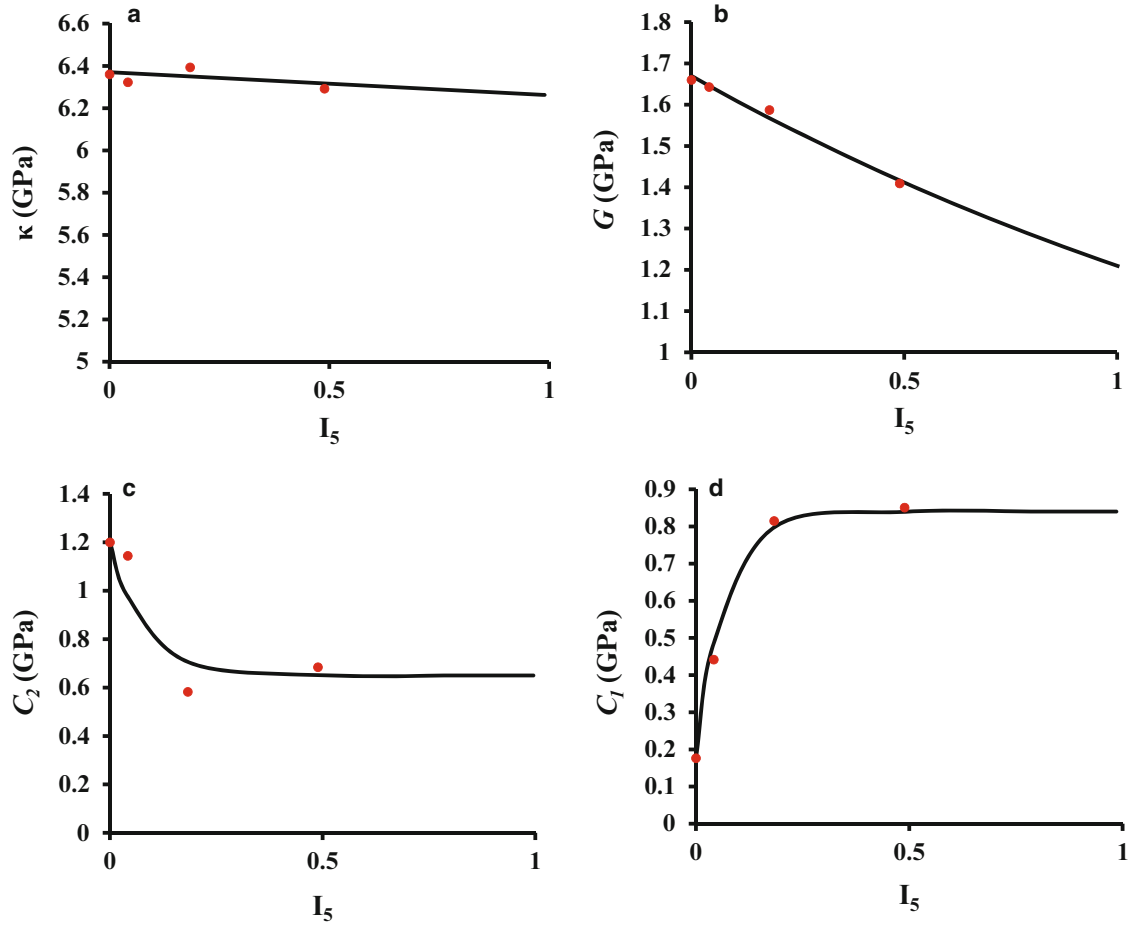

Fig. 25.5 Evaluation of material parameters for stress from the ultrasonic response after plastic compression

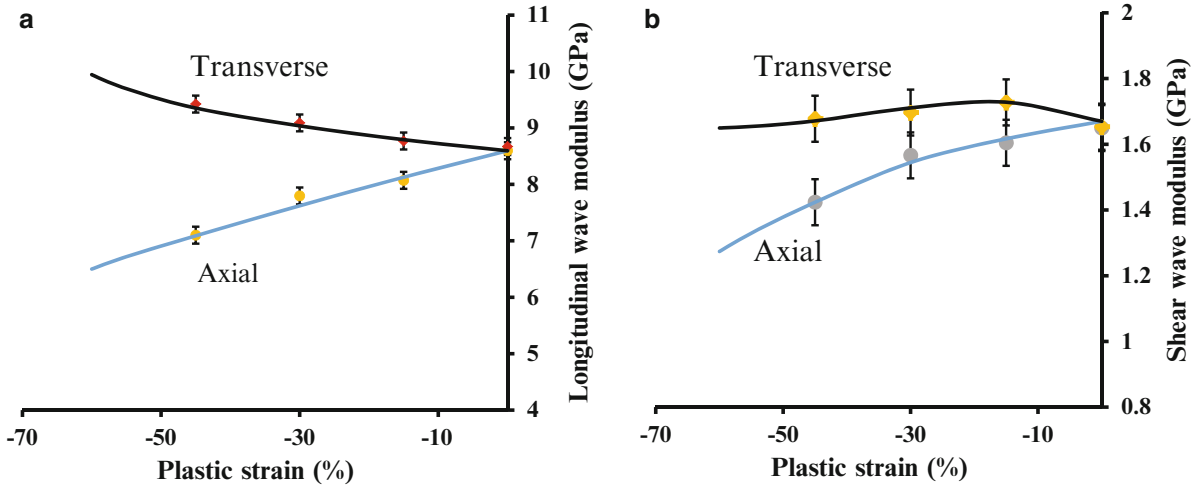

Fig. 25.6 The final model and the experimental results for the longitudinal (**a**) and shear (**b**) ultrasonic moduli after plastic compression

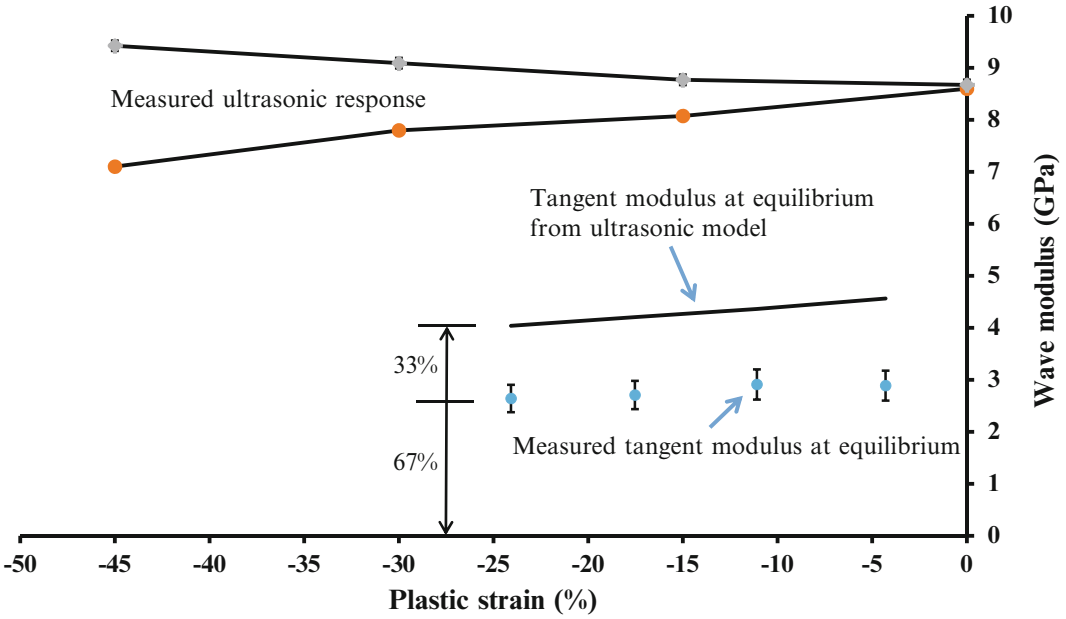

Fig. 25.7 Tangent modulus at equilibrium measured in cyclic testing and using ultrasonic model

25.7 Modeling Back Stress

Using the cyclic loading shown in Fig. 25.3, one can calculate the stress at the state of equilibrium by matching conditions of similar tangent modulus on adjacent loading and unloading sections [14]. This follows from the fact that the modulus becomes rate independent at equilibrium. The equilibrium response for PEEK was evaluated from this figure and then related to the back stress, which is approximately two third the equilibrium stress in compression.

The primary model for the back stress is described in [15]. This thermodynamically based model is primarily calculated from the viscoelastic deformation in the slow element, but also contains interaction terms that we introduced in the anisotropic elastic model for the slow elastic element. The primary terms that only depend on the slow viscoelastic deformation can be written as

$$\mathbf{T}_s^{b1} = \frac{1}{J_s^{ve}}\left\{ \left(G_o^b - G_{\infty 1}^b\right) \frac{\tanh\left[\sqrt{\left(G_o^b - G_{\infty 1}^b\right)^2 \tau_o^{b2}}\left[tr\left(\mathbf{B}_s^{ve}\right) - 3\right]\right]}{\sqrt{\left(G_o^b - G_{\infty 1}^b\right)^2 \tau_o^{b2}}\left[tr\left(\mathbf{B}_s^{ve}\right) - 3\right]} + G_{\infty 1}^b + G_{\infty 2}^b\left[tr\left(\mathbf{B}_s^{ve}\right) - 3\right] \right\} \left[\mathbf{B}_s^{ve} - \frac{tr\left(\mathbf{B}_s^{ve}\right)}{3}\mathbf{I}\right], \quad (25.19)$$

where, G_o^b, $G_{\infty 1}^b$, $G_{\infty 2}^b$ and τ_o^{b2}, respectively, are the initial shear modulus, the hardening shear modulus, the second hardening shear modulus and the initial yield stress. These four parameters are fitted to the data in Fig. 25.3 by

$$G_o^b = 3356.55 \text{ MPa}, \quad G_{\infty 1}^b = 10.49 \text{ MPa}, \quad G_{\infty 2}^b = 0 \text{ MPa}, \quad \tau_o^{b2} = 47.06 \text{ MPa}. \quad (25.20)$$

The interactions terms that come from the free energy (included to capture the anisotropy in the stress) result in the following additional terms

$$\mathbf{T}_s^{b2} = \frac{C_1}{J_s^{ve} J_s^e}\left(J_s^{ve} - 1\right)\mathbf{F}_s^e \mathbf{E}_s^{ve} \mathbf{F}_s^{eT} + \frac{C_2}{J_s^{ve} J_s^e}\mathbf{F}_s^e\left(\mathbf{E}_s^e \mathbf{E}_s^{ve} + \mathbf{E}_s^{ve} \mathbf{E}_s^e e\right)\mathbf{F}_s^{eT}. \quad (25.21)$$

The total expression for back stress in the slow element is the sum of the stresses in (25.19) and (25.21) to give

$$\mathbf{T}_s^b = \mathbf{T}_s^{b1} + \mathbf{T}_s^{b2}. \quad (25.22)$$

25.8 Modeling Flow Rule

In the proposed schematic of the model, described in Fig. 25.4, both the fast and slow elements need flow rules to capture the viscoelastic flow. These elements are also responsible for damping the system. Details of developing flow rules are given in [10]. The flow rule for the slow and fast elements are assumed to depend on the associated thermodynamic overstresses given, respectively, by

$$\Delta \mathbf{T}_s = F_s^{e-1} \mathbf{T}_s F_s^e - \mathbf{T}_s^b, \tag{25.23}$$

$$\Delta \mathbf{T}_f = F_f^{e-1} \mathbf{T}_f F_f^e. \tag{25.24}$$

The flow rules are described by the dependence of the viscoelastic velocity gradients on the overstresses. The assumed models are given as

$$\mathbf{L}_s^{ve} = \beta_s \Delta \mathbf{S}_s, \tag{25.25}$$

$$\mathbf{L}_f^{ve} = \beta_f \Delta \mathbf{S}_f, \tag{25.26}$$

where, $\Delta \mathbf{S}_s$ and $\Delta \mathbf{S}_f$ are, respectively, the deviatoric part of over stress in the slow and fast elements, and β_s and β_f are the functions selected to fit the response. The slow strain rate monotonic loading tests were used to construct the flow rule for the slow element. Using this model, the fast strain rate monotonic loading tests were used to construct the flow rule for the fast response element. In this way it was possible to fit the response of all monotonic loading tests for strain rates from 0.0001 to 3000 1/s, given by Rae et al. [4], using the flow rules

$$\beta_s = 7.3168 \times 10^{-13} e^{0.5819 \|\Delta \mathbf{S}_s\|}, \tag{25.27}$$

$$\beta_f = 0.3 e^{0.2383 \|\Delta \mathbf{S}_f\|}, \tag{25.28}$$

where $\|\Delta \mathbf{S}\| = \sqrt{0.5 \Delta \mathbf{S} : \Delta \mathbf{S}}$. Using these flow rules, and the models developed for the stresses, one can simulate the response for the monotonic loading given by Rae et al. et al. [4] and shown in Fig. 25.8. As can be seen, the model accurately predicts the yield over seven decades of strain rates, and the flow behavior for the slow rate. The model would need to include the thermal softening seen in high rate tests, which results from adiabatic heating, to capture the full loading range under high loading rates. This can be done, but is outside the scope of this paper.

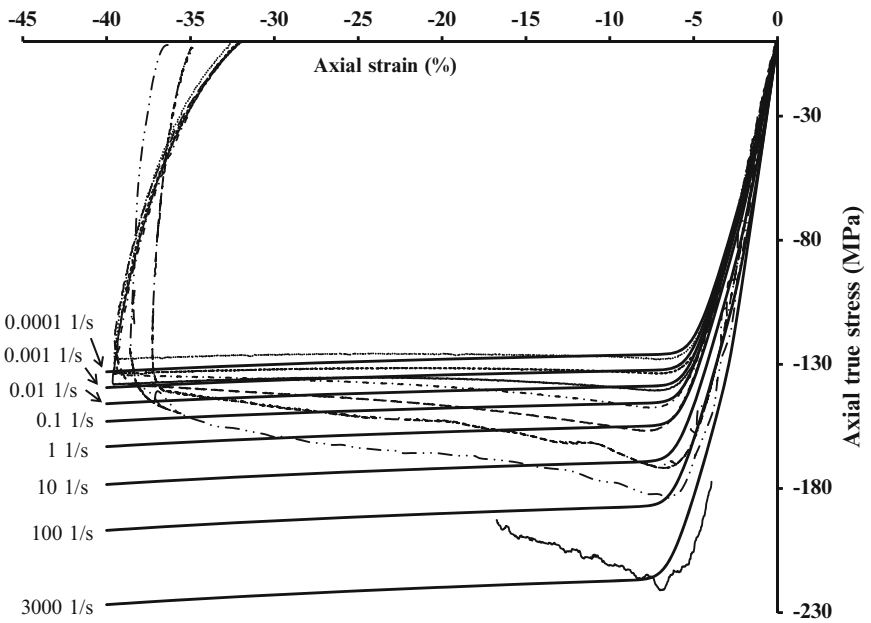

Fig. 25.8 Comparison of model and response under uniaxial compression at strain rates ranging from 0.0001 to 3000 1/s (data from [4])

25.9 Summary

Anisotropic ultrasonic wave moduli and cyclic loading in compression was measured for PEEK and used in combination with monotonic compression tests over a broad range of loading to mode the room temperature response of PEEK based on a thermodynamically consistent modeling method. The resulting model accurately captures the response over seven decades of loading rates in compression, and matches the stress and tangent modulus at equilibrium. In addition, the model captures the development of anisotropic ultrasonic response, properly describing the changing wave speed characteristics resulting from plastically compressing PEEK.

This preliminary model for room-temperature response is based on a slow and a fast responding element. It is capable of capturing the response of PEEK under a broad range of loadings. In addition, the model, without using rate dependent moduli, produces a varying tangent modulus that depends on the loading rate. The model, being based on a fully consistent thermodynamic structure, can be extended to non-isothermal response by adding the temperature dependence.

Acknowledgement The research has been partially supported by the US Army Research Laboratory through Contract Number W911NF-11-D-0001-0094. The experiments performed during this project were completed by utilizing the stress analysis center facility of the University of Nebraska-Lincoln.

References

1. Attwood, T.E., Dawson, P.C., Freeman, J.L., Hoy, L.R.J., Rose, J.B., Staniland, P.A.: Synthesis and properties of polyaryletherketones. Polymer **22**, 1096–1103 (1981)
2. Talbott, M.F., Springer, G.S., Berglund, L.A.: The effects of crystallinity on the mechanical properties of PEEK polymer and graphite fiber reinforced PEEK. J. Compos. Mater. **21**, 1056–1081 (1987)
3. Dahoun, A., Aboulfaraj, M., G'Sell, C., Molinari, A., Canova, G.R.: Plastic behavior and deformation textures of poly(ether ether ketone) under uniaxial tension and simple shear. Polym. Eng. Sci. **35**, 317–330 (1995)
4. Rae, P.J., Brown, E.N., Orler, E.B.: The mechanical properties of poly(ether-ether-ketone) (PEEK) with emphasis on the large compressive strain response. Polymer **48**, 598–615 (2007)
5. Ward, I.M.: Mechanical Properties of Solid Polymers, p. 294. Wiley, New York, NY (1979)
6. Bunge, H.J., Roberts, W.T.: Orientation distribution, elastic and plastic anisotropy in stabilized steel sheets. J. Appl. Crystallogr. **2**, 116–128 (1969)
7. Negahban, M., Wineman, A.S.: Material symmetry and the evolution of anisotropies in a simple material: II the evolution of symmetry. Int. J. Nonlinear Mech. **24**, 537–549 (1989)
8. Negahban, M., Wineman, A.S.: The evolution of anisotropies in the elastic response of an elastic–plastic material. Int. J. Plast. **8**, 519–542 (1992)
9. Negahban, M., Wineman, A.S.: The evolution of material symmetry in the elastic response of a fully strain space theory of plasticity. Appl. Mech. Div. Pub. AMD **158**, 19–24 (1993)
10. Negahban, M.: The Mechanical and Thermodynamical Theory of Plasticity, pp. 553–554. CRC, New York, NY (2012)
11. Goel, A.: Thermodynamically consistent large deformation constitutive model for glassy polymers. Engineering mechanics dissertations & thesis. University of Nebraska-Lincoln (2009)
12. Negahban, M., Goel, A., Zhang, L.: Evaluating the development of elastic anisotropy with plastic flow. Acta Mech. **208**, 259–267 (2009)
13. Goel, A., Strabala, K., Negahban, M., Turner, J.A.: Modeling the development of elastic anisotropy as a result of plastic flow for glassy polycarbonate. Polym. Eng. Sci. **49**, 1951–1959 (2009)
14. Negahban, M., Goel, A., Delabarre, P., Feng, R., Dimick, A.: Experimentally evaluating the equilibrium stress in shear of glassy polycarbonate. ASME J. Eng. Mater. Technol. **128**, 537–542 (2006)
15. Goel, A., Sherafati, A., Negahban, M., Azizinamini, A., Wang, Y.: A finite deformation nonlinear thermo-elastic model that mimics plasticity during monotonic loading. Int. J. Solids Struct. **48**, 2977–2986 (2011)

Chapter 26
Characterization of the Nonlinear Elastic Behavior of Chinchilla Tympanic Membrane Using Micro-fringe Projection

Junfeng Liang, Huiyang Luo, Don Nakmali, Rong Zhu Gan, and Hongbing Lu

Abstract A combined experimental and numerical approach was used to determine the mechanical properties of a chinchilla TM under quasi-static condition based on the response of the TM to static pressure. A chinchilla bulla was prepared and the intact TM was subjected to static pressures while its topography was measured using the micro-fringe projection technique. Images of the deformed TM were acquired and processed with a phase-shift method to reconstruct the surface profile and determine the volume displacement of the TM under pressures. Finite element method with the implementation of a hyperelastic model was employed. By solving the inverse problem with the model, the Young's moduli of chinchilla TMs from ten bullas were determined as ~19 MPa up to a strain level of 25 %, changing with stress or strain.

Keywords Chinchilla • Tympanic membrane • Micro-fringe projection • Static pressure • Hyperelastic model

26.1 Introduction

Eardrum or tympanic membrane (TM) separates the middle ear from the external ear and plays an important role to transmit the sound pressure from the ear canal into the cochlea. The function of the TM can be affected by ambient air pressure, which changes widely from a few of Pa to a few kPa. If the pressure level goes beyond the limit of the physiological pressure for TM (e.g., 2 kPa), it can cause significant alternation of hearing ability [1, 2]. In order to understand the effect of the ambient pressure upon the transmission function of TM, it is critical to accurately measure the TM mechanical properties as a function of pressure, for more accurate simulations.

In most of the early studies, mechanical properties were measured from either strip specimens cut from TM [3, 4] or TM separated from temporal bone [5]. Cutting a strip specimen from the TM may cause both radial and circumferential collagen fibers to shrink, which can affect the mechanical properties that are important for sound conduction [6]. Recently, there are some researches on measuring elastic [7] or viscoelastic properties [8] of TM. However, direct measurement of the effective mechanical properties of entire TM (pars tensa) under static pressure, has not yet been reported.

In this paper, a combined experimental and numerical investigation was made to measure the mechanical properties of chinchilla TM. The TM inside a bulla was applied pressures while its topography was determined by a full-field micro-fringe projection technique. Volume displacement was thus calculated from the topography. Finite element method (FEM) was then applied to model the TM to simulate pressure-volume displacement relation. Mechanical properties of TM under different static pressure were determined by solving an inverse problem through minimizing the error between the simulation results and measurement results.

26.2 Method

26.2.1 Micro-fringe Projection

A micro-fringe projection technique was used to capture the surface topography of the TM under a prescribed static pressure. In fringe projection, a grating (or fringe) is projected onto an object and image of the projected fringe on the surface of the

J. Liang • H. Luo • H. Lu (✉)
Department of Mechanical Engineering, The University of Texas at Dallas, Richardson, TX 75080, USA
e-mail: hongbing.lu@utdallas.edu

D. Nakmali • R.Z. Gan
School of Aerospace and Mechanical Engineering, University of Oklahoma, Norman, OK 73019, USA

C. Ralph et al. (eds.), *Mechanics of Composite and Multi-functional Materials, Volume 7*,
Conference Proceedings of the Society for Experimental Mechanics Series, DOI 10.1007/978-3-319-21762-8_26

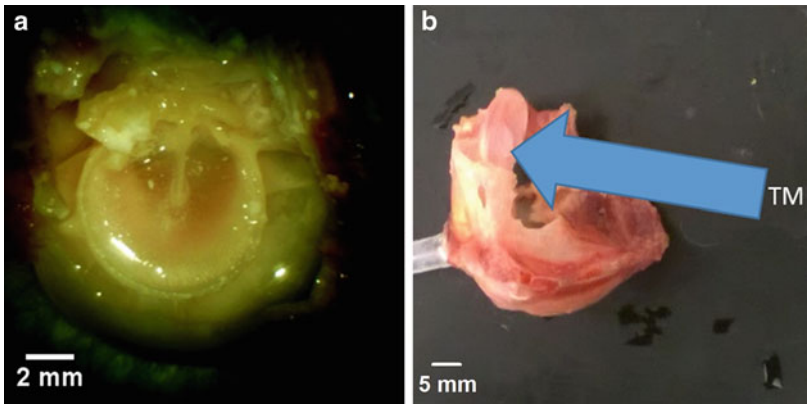

Fig. 26.1 Chinchilla bulla prepared for measurements: (**a**) The medial side of TM with intact malleus-incus immobilized (**b**) Typical sample with TM exposed and PVC tube inserted

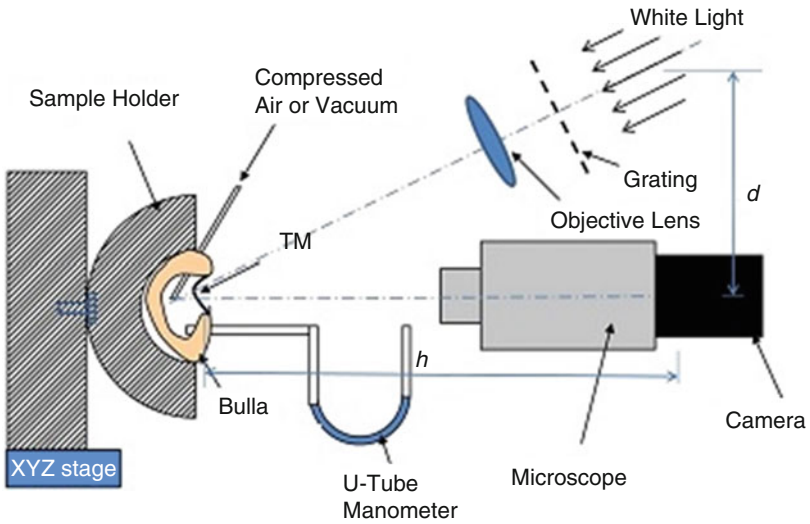

Fig. 26.2 Schematic of experimental setup of fringe projection system

object is acquired by a digital camera. The image of the projected fringe is subsequently digitally superimposed with the reference fringe to generate interferometry fringes. A virtual shifting was made by utilizing five phase-shifted images of the original image to calculate the phase; the quality bins algorithm was used to unwrap the phase map for surface profile reconstruction [9].

26.2.2 Sample Preparation

A adult chinchilla free of middle ear disease as evaluated by otoscopic examination were used in this study. After the examination, the chinchilla was euthanized with ketamine (100 mg/kg IM) and xylazine (10 mg/kg IM) and the temporal bones or bullas were harvested. The bullar wall was open from the middle ear side and both cochlea and stapes were removed until the medial side of TM was fully exposed (Fig. 26.1a). The malleus-incus complex was immobilized by applying superglue between the incus section and the petrous wall behind. A PVC tubes with 3/16″ inner diameter and 1/4″ mm outer diameter connected to the pressure source and monometer respectively were inserted into the ear canal and the gap between the tube and the ear canal was sealed with epoxy (Fig. 26.1b). The TM was dyed with thin layer of titanium oxide in saline solution (100 mg/ml) to provide good reflection so that images of the projected fringes on TM can be acquired by a digital camera.

A syringe was used to apply pressure to the sample, and a manometer connected to a three-way stopcock was used to measure pressure through the aforementioned PVC tube. Both positive pressure and negative pressures were applied to the bulla for the measurement of the response of the TM to the pressures to measure mechanical properties of the TM. Pressures were applied with a magnitude from 0 to 1.0 kPa with step of 0.125 kPa. For each step, the stopcock was closed to ensure that a constant pressure was maintained (Fig. 26.2).

Images of the TM in natural state without pressure and under pressure for each TM were acquired by the camera. For each image, reconstruction of TM surface was conducted using the method described in Sect. 26.2.1. The reconstructed TM surfaces were then used to calculate the volume displacement.

Figure 26.2 illustrates a schematic diagram of the experimental setup. The chinchilla bulla was placed on a rotatable sample holder, attached to a temporal bone bowl, in order to allow the direction of the TM surface adjusted for micro-fringe projection as well as for observation by a camera. A *XYZ* stage was used to hold the temporal bone bowl, to position the TM within the field of the projected fringe and view field of the camera. A micro-fringe projector, including a set of projection lenses, grating, and fiber light source was used to project fringes onto the TM in the bulla. A digital camera was attached to a surgical microscope, nearly perpendicular to the sample holder plane to acquire the images for the fringes on the TM under different static pressures.

26.2.3 Finite Element Simulations

The commercial finite element code ANSYS-15 was used for FEM simulation of chinchillaTM under quasi-static pressure. The surface topography reconstructed from micro-fringe projection was converted to a three-dimensional model using the computer-aided design (CAD) code SolidWorks 2013. Since the TM thickness is small compared with its major or minor diameters, TM is modeled as a shell with a thickness of 10 μm. The CAD model was then converted to a shell model for simulation in ANSYS. The boundary and the location of malleus were determined by the optical image of the TM sample. Malleus was constructed using SolidWorks as a part of the TM. The malleus was assigned with properties of a bone (with 10 GPa Young's modulus). The outer boundary (annulus tympanicus) of the TM was fixed for all degrees of freedom (no translation or rotation) and a uniform pressure was applied from the medial side or lateral side, at the same pressure used in experiments in the range of 0 kPa to 1 kPa.

The pressure-volume displacement response of TM shows behavior similar to an elastomer, including stiffening after reaching a certain pressure, the Ogden model was used to describe the mechanical properties of TM for large deformation. The uniaxial *N*-order Ogden model [10] is given as

$$T_U = \sum_{i=1}^{N} \frac{2\mu_i}{\alpha_i}\left(\lambda_U^{\alpha_i - 1} - \lambda_U^{-0.5\alpha_i - 1}\right), i = 1, 2, \ldots \mathrm{N} \tag{26.1}$$

where N is the number of terms in the Ogden model; T_U is the uniaxial stress; μ_i and α_i are constants of the hyperelastic model; λ_U is the uniaxial stretch ratio, and $\lambda_U = 1 + \varepsilon_U$, with ε_U being the uniaxial strain. Under uniaxial stretch, assuming incompressibility of the TM, the principal stretch ratios λ_i ($i = 1, 2, 3$) are given as $\lambda_1 = \lambda_U$, $\lambda_2 = \lambda_3 = \lambda_U^{-\frac{1}{2}}$. In this study, N was taken as 2. In order to determine the model parameters μ_i and α_i, an inverse problem-solving scheme was used by allowing the FEM simulated TM deformation data to match the measured values. The procedures are described as follows:

1. Give initial values for μ_i and α_i.
2. Generate a FEM model for the TM. The TM is assigned with hyperelastic properties (Ogden model). The out-of-plane displacement (i.e., displacement perpendicular to the image plane of the camera), and height Z of each node was obtained.
3. Interpolate nodal displacement obtained in Step 2 to the background grids with point density identical to the pixel density of images obtained in experiments using bilinear interpolation scheme [11].
4. Calculate the volume displacement from the out-of-plane displacement of the background grid, and compare with the experimental volume displacement experimental data which can be calculated as:

$$\Delta V = \iint_{\Omega} [z(x, y) - z_0(x, y)] dx dy \tag{26.2}$$

   where, $z(x, y)$ and $z_0(x, y)$ are the height profiles under finite pressure and zero pressure, respectively; Ω is the boundary of the annulus.
5. Modify μ_i and α_i in Step 1 and repeat Steps (1) through (4) until the volume displacement calculated from simulation agrees with the measured data.

26.3 Results and Discussion

The TM surface topographies under different pressure levels were obtained from the micro-fringe projection system. Figure 26.3a shows the TM image under projected micro-fringes before reconstruction of the surface. The four sections of TM, namely superior, posterior, inferior, anterior and umbo, are shown and marked as "**S**", "**P**", "**I**", "**A**" and "**U**", respectively. Figure 26.3b shows the typical height color contours of TM under natural state (0.0 kPa). Figure 26.3c, d show the z-displacement, U_3 contours under pressures. Under −1 kPa, the edge of TM close to inferior-posterior region has nearly zero displacement. The TM close to the umbo has displacement near zero mm. The umbo has a negative displacement near −0.09 mm. The complex boundary condition has contributed to the displacement field in this area near the umbo. In Fig. 26.3d under positive pressure of 1 kPa, there is also small negative displacement in the umbo. The displacement in the TM near the umbo is slightly negative as well, due to the complex boundary condition in this region.

Using Eq. (26.2), the pressure-volume displacement can be calculated from the Z-displacement U_3 profile. Figure 26.4a shows the pressure as a function of volume displacement, plotted in terms of the curves from the testing of 10 chinchilla TMs and the average curve. The error bar represents the standard deviation from 10 tests. Figure 26.4b shows a comparison of the average pressure-volume displacement curve between FEM results and experimental data for ten TM. The error is less than 2 % between FEM and experimental data, indicating that the hyperelastic model is appropriate to describe the TM mechanical behavior. The model parameters were obtained at both positive and negative pressure.

The Young's modulus is defined as the slope at the linear region of stress-strain curve under small deformations. The slope of the stress-strain curve at any point is the tangent modulus. The Young's modulus is also the tangent modulus at the initial, linear portion of a stress-strain curve. In the case of hyperelastic material, the tangent modulus can be obtained by taking derivative of stress with respect to strain from Eq. (26.1), which is given as

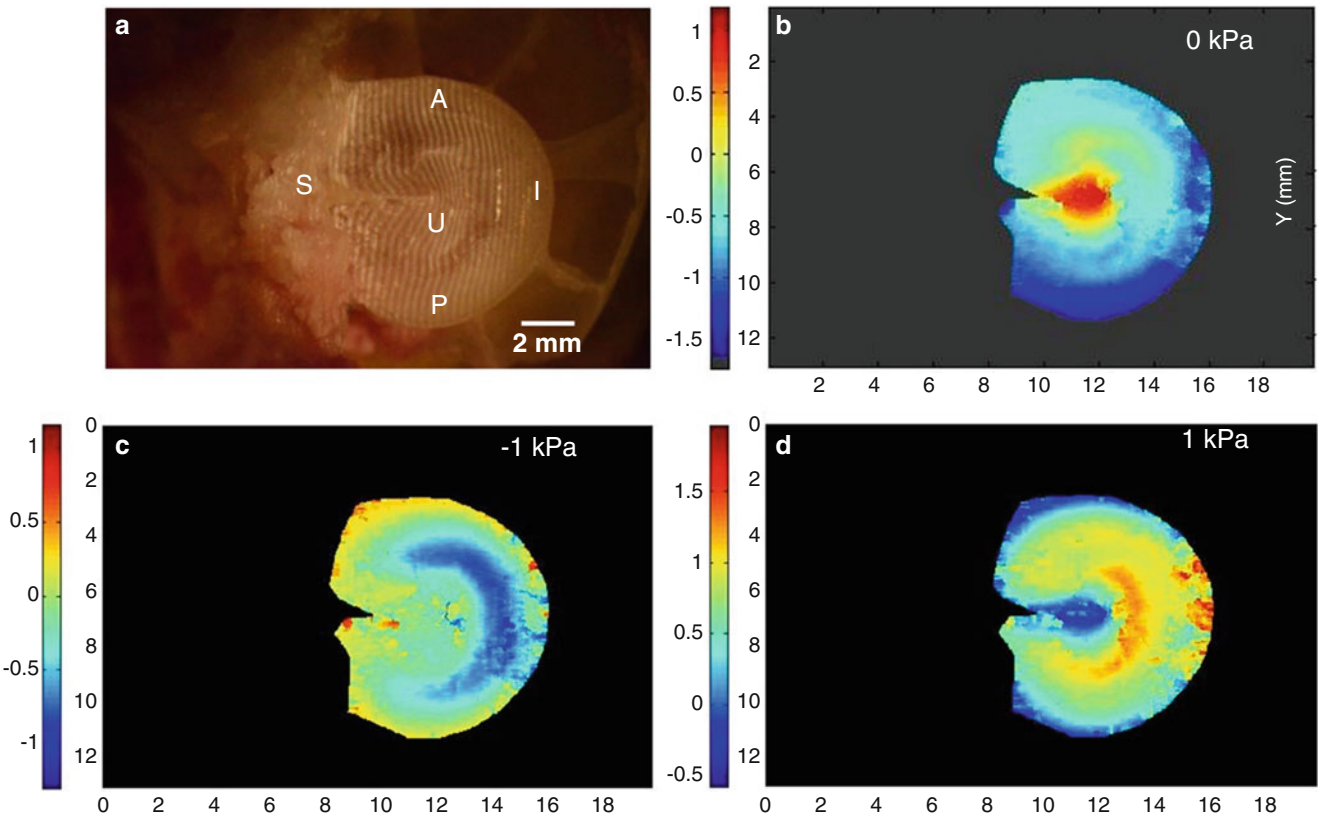

Fig. 26.3 TM images under micro-projected fringes for surface profilometry. (**a**) Micro-projected fringes on a guinea pig TM; (**b**) Height profile z (x, y) under zero pressure; (**c**) Z-displacement U_3 under 0.5 kPa pressure; (**d**). Z-displacement U_3 under 1.0 kPa pressure

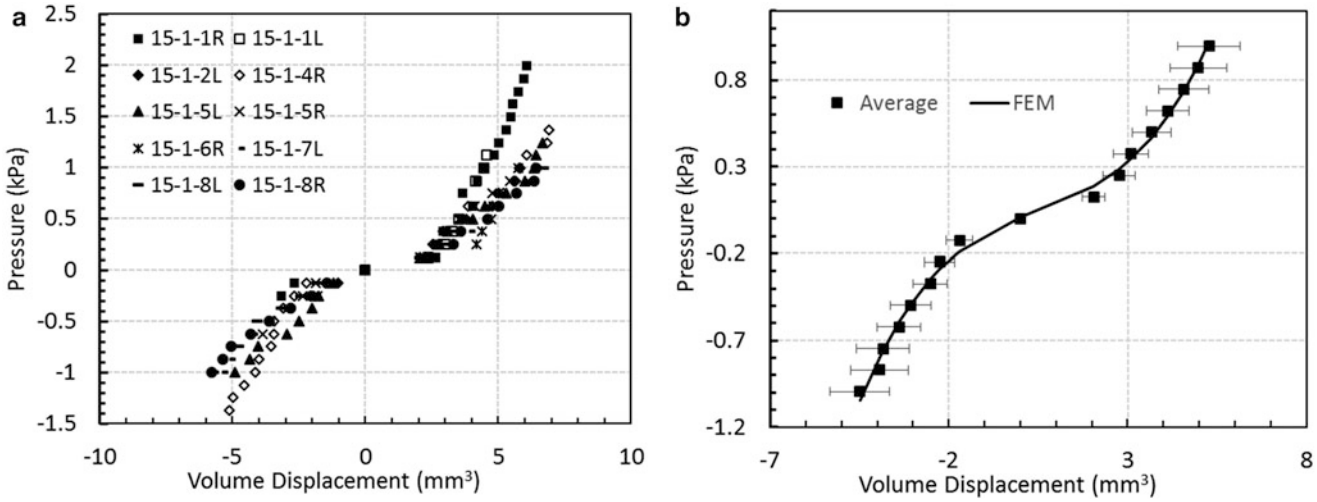

Fig. 26.4 Pressure-volume displacement relationships for chinchilla TMs under different pressures. (**a**) For 10 chinchilla TM samples. (**b**) A comparison of finite element simulation results with experimental data

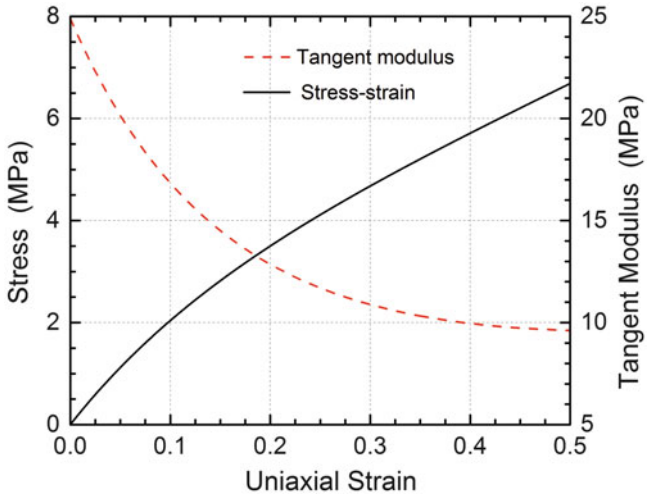

Fig. 26.5 Tensile stress-strain curves and tangent modulus of guinea pig TM determined from the Ogden model

$$\frac{dT_U}{d\varepsilon_U} = \sum_{i=1}^{2} \frac{2\mu_i}{\alpha_i} \left[(\alpha_i - 1)(1 + \varepsilon_U)^{\alpha_i - 2} + (0.5\alpha_i + 1)(1 + \varepsilon_U)^{-0.5\alpha_i - 2} \right] \tag{26.3}$$

The Ogden model parameters were best-fit solved as $\mu_1 = 1.2$, $\alpha_1 = 3.9$, $\mu_2 = 7.1$, $\alpha_2 = -4.3$. With known parameters, the Eqs. (26.1) and (26.3) were plotted into Fig. 26.5, respectively. Figure 26.5 shows the tangent modulus as a function of strain for 10 chinchilla TMs. The average Young's modulus was plotted with results obtained using average model parameters. The slope of stress-strain curve is not a constant: it changes slightly within a narrow range, showing a nonlinear relationship between stress and strain. At strain close to zero, the tangent modulus is 25 MPa then it decreases to 9.7 MPa at 50 % strain. The average tangent modulus less than 25 % strain is chosen as the representative Young's modulus. Therefore, the average value of 19 MPa was taken as the modulus.

26.4 Conclusion

Quasi-static air pressure was applied to a chinchilla TM inside the bulla, and a micro-fringe projection method was used to measure the volume displacement of the TM under the pressure. The surface topography of the TM was then used as an input in a finite element model for simulation. An Ogden hyperelastic model of order 2 was used to describe the TM constitutive behavior in FEM for simulations. An inverse problem solving scheme was used to allow the pressure-volume displacement relationship simulated by FEM to match with the corresponding experimental results, through tuning the model parameters. The model parameters were used to describe the mechanical behavior of chinchilla TM and the Young's modulus of the TM was estimated as 19 MPa, up to a strain level of 25 %.

Acknowledgments We acknowledge the support of NIH R01DC006632, R01DC011585, DOE NEUP 09-818, and NSF CMMI-1031829, CMMI-1132174, and ECCS-1307997. We also thank Zachary, Yokell, at University of Oklahoma for preparation of bullas. Lu acknowledges the Louis A. Beecherl Jr. Chair for additional support.

References

1. Volandri, G., Puccio, F.D., Forte, P., Carmignani, C.: Biomechanics of the tympanic membrane. J. Biomech. **44**(7), 1219–123 (2011)
2. Dirckx, J.J.J., Decraemer, W.F.: Human tympanic membrane deformation under static pressure. Hear. Res. **51**(1), 93–105 (1991)
3. Cheng, T., Dai, C., Gan, R.: Viscoelastic properties of human tympanic membrane. Ann. Biomed. Eng. **35**, 305–314 (2007)
4. Huang, G., Daphalapurkar, N.P., Gan, R., Lu, H.: A method for measuring linearly viscoelastic properties of human tympanic membrane using nanoindentation. Trans. ASME- J. Biomech. Eng. **130**(1), 014501 (2008)
5. Daphalapurkar, N.P., Dai, C., Gan, R., Lu, H.: Characterization of the linearly viscoelastic behavior of human tympanic membrane by nanoindentation. J. Mech. Behav. Biomed. Mater. **2**(1), 82–92 (2009)
6. O'Connor, K.N., Tam, M., Blevins, N.H., Puria, S.: Tympanic membrane collagen fibers: a key to high-frequency sound conduction. Laryngoscope **118**(3), 483–490 (2008)
7. Gaihede, M., Liao, D., Gregersen, H.: *In vivo* areal modulus of elasticity estimation of the human tympanic membrane system: modeling of middle ear mechanical function in normal young and aged ears. Phys. Med. Biol. **52**(3), 803–814 (2007)
8. Aernouts, J., Dirckx, J.J.J.: Viscoelastic properties of gerbil tympanic membrane at very low frequencies. J. Biomech. **45**(6), 919–924 (2012)
9. Heredia-Ortiz, M., Patterson, E.A.: Location and shape measurement using a portable fringe projection system. Exp. Mech. **45**(3), 197–204 (2005)
10. Wang, B., Lu, H., Kim, G.: A damage model for the fatigue life of elastomeric materials. Mech. Mater. **34**(8), 475–483 (2002)
11. Ghiglia, D.C., Pritt, M.D.: Two-Dimensional Phase Unwrapping: Theory, Algorithms, and Software. Wiley, New York (1998)

Chapter 27
Compression of Silicone Foams

Wei-Yang Lu

Abstract Silicone foams are used as cushions for impact protection. They are soft and will recover from very large deformation with little damage. Understanding their compression behaviors in high performance environments and providing necessary calibration and validation data for constitutive models are highly important. Characterizing these soft materials, however, is quite challenging. In this study, the foam deformation is carefully studied. With a new compression experimental setup, the force and displacement fields at the foam-platen interface are examined in detail. These additional data will be used to compute the compressive stress-stain behavior of the soft material. The experimental method and foams compression results are presented.

Keywords Silicone foam • Compression • Friction • Stress-strain • Soft materials

27.1 Introduction

In an ideal compression test, the specimen is allowed to slide with little friction at the specimen-platen interfaces and to deform uniformly. Unfortunately, for soft materials, part of the side surface of a specimen is often suspected to roll over and becomes in contact with the platen during compression. In such case, a uniform uniaxial state of stress or strain is not achieved. With non-uniform stress and strain distributions of the specimen, the results may be questionable when using surface or volume strain measurement to determine the material's stress-strain behavior. Lubricants are commonly applied to reduce the friction and improve the uniformity of deformation and pressure, but the effect of lubricants has not been investigated. This paper addresses the deformation and pressure distribution at the interface during a compression test.

27.2 Material and Specimen

Sheets of silicone foam of 50 % and 0 % porosity, shown in Fig. 27.1, were the materials used this investigation; the measured densities were about 0.577 and 1.153 g/cc (36 and 72 pcf), and the thickness of the sheets were approximately 7.061 and 1.930 mm (0.278 in. and 0.076 in.), respectively. Here, if the porosity is not mentioned, the term silicone foam denotes the 50 % porosity material and solid silicone refers to the 0 % porosity material.

Silicone foam is a flexible and open-cell type of foam. Figure 27.2a shows a scanning electron microscope image of the foam, the averaged cell size is about 550 μm (0.022 in.). Compressive specimens used in this investigation were punched out from the sheet. A typical specimen is shown in Fig. 27.2b. The edge of the flat surface was colored so the initial boundary between the flat and cylindrical surfaces could be identified during experiment.

W.-Y. Lu
Sandia National Laboratories, Livermore, CA 94551-0969, USA
e-mail: wlu@sandia.gov

C. Ralph et al. (eds.), *Mechanics of Composite and Multi-functional Materials, Volume 7*,
Conference Proceedings of the Society for Experimental Mechanics Series, DOI 10.1007/978-3-319-21762-8_27

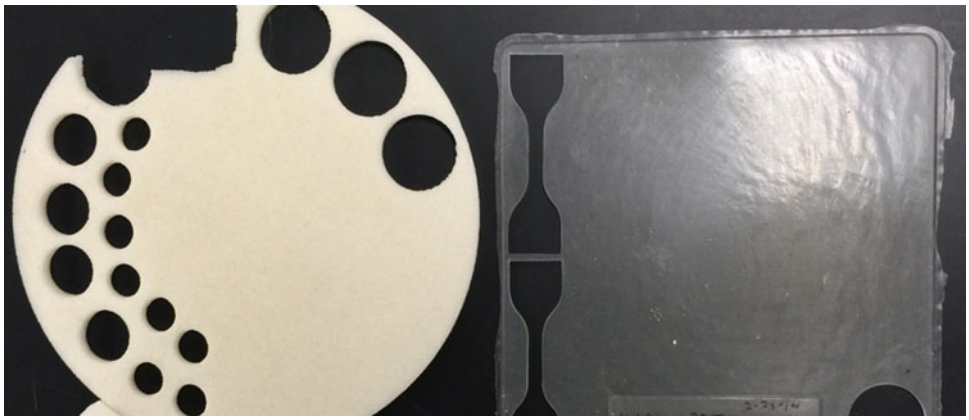

Fig. 27.1 Sheets of silicone foam of 50 % (*left*) and 0 % porosity (*right*)

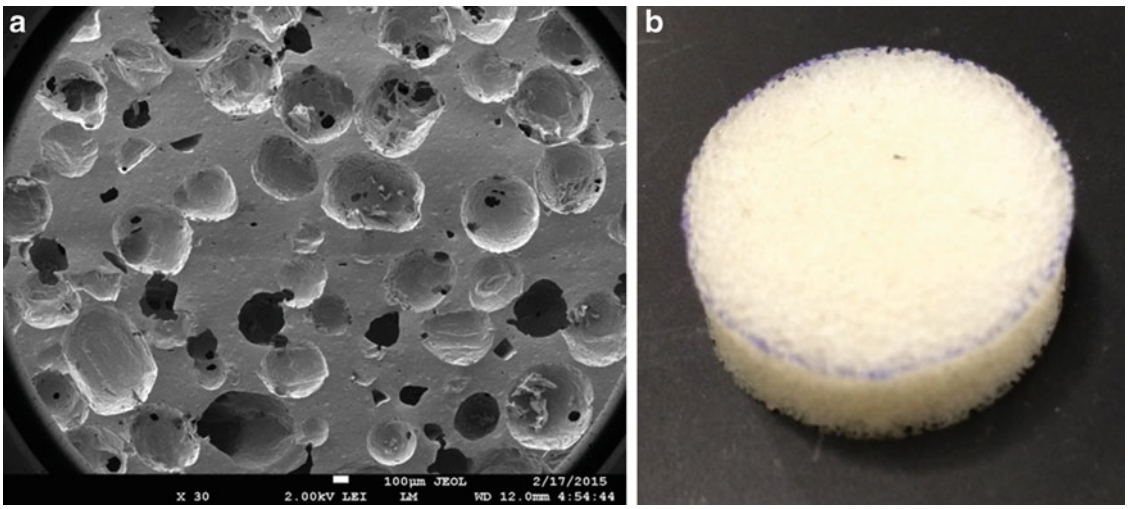

Fig. 27.2 A typical foam specimen and microstructure: (**a**) SEM image of the foam, and (**b**) compressive specimen

27.3 Experimental Setup

A new compression setup on MTS Bionic System was developed, Fig. 27.3a; a close-up of the testing area is shown in Fig. 27.3b. Between the top platen and the specimen is a thin layer of pressure sensor. It has an array of 44 × 44 sensing elements, which measures the pressure distribution over an area of 27.94 × 27.94 mm (1.1 × 1.1 in.) with a pressure range of 3.45 MPa (500 psi). The area of each sensing element is 0.403 mm^2 (0.000625 $in.^2$). The pressure sensor also estimates the contact area. Beneath the specimen is the bottom platen, which is a thick glass sits on a specially designed fixture. The rectangular shape fixture is hollow inside with two openings, one at the top and one at the side wall. By inserting a mirror at 45° angle, it allows the front viewing of the foam-glass interface through the glass platen. A digital camera was utilized to record the interface during compression.

27.4 Experiment

The compression tests were done under quasi-static loading at a rate of 0.0254 mm/s (0.001 in./s) to a very large strain, $\Delta L/L_o$ was greater than 60 %. The force and displacement were acquired at 10 Hz by the MTS system. Digital videos of the deformation and the pressure distribution at the bottom and top foam-platen interfaces, respectively, were both recorded at

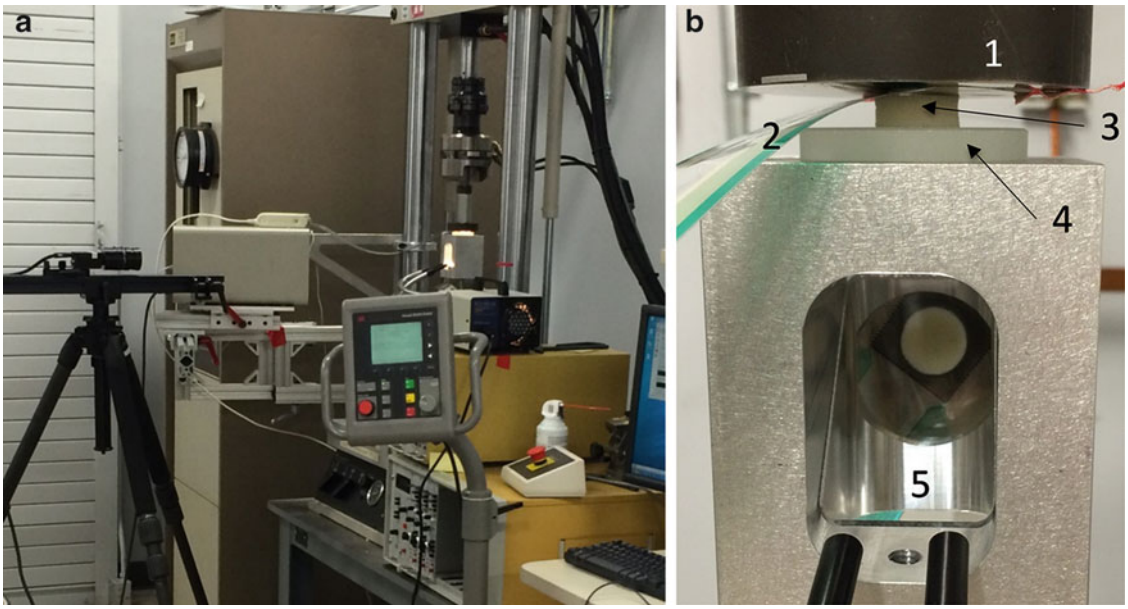

Fig. 27.3 New compression setup for silicone foams: (**a**) whole setup, (**b**) close-up of the testing area, 1-top platen, 2-pressure sensor array, 3-silicone foam specimen, 4-bottom platen and 5-mirror

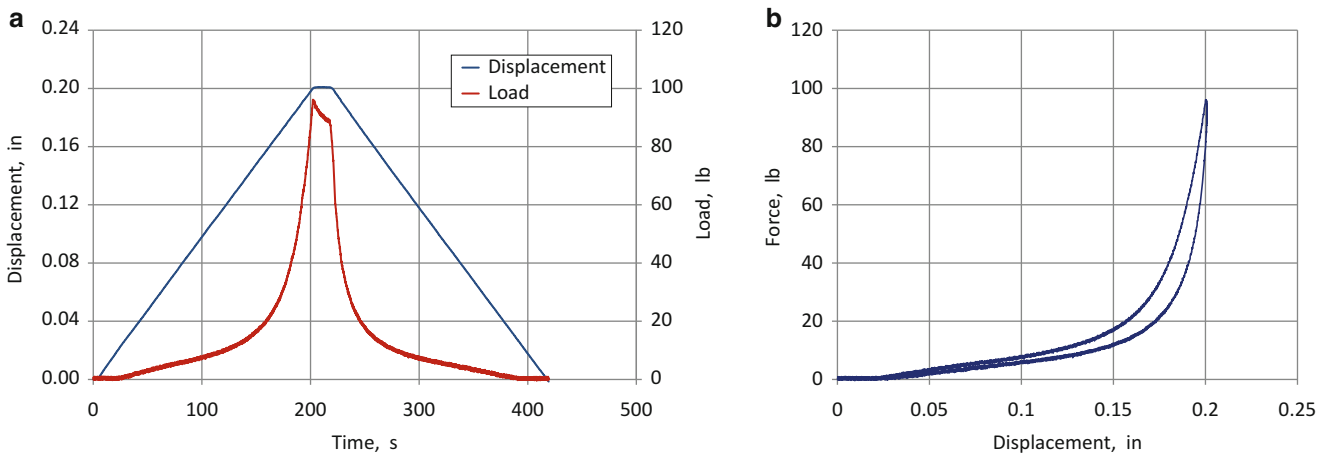

Fig. 27.4 Results of silicone foam Specimen 03 under dry compression, (**a**) loading history, and (**b**) load-displacement curve

0.5 Hz. All three systems, MTS, video, and pressure scan systems were synchronized. Two sizes of silicone foam, 19.05 and 12.7 mm (0.75 and 0.5 in.) in diameter, and three interface conditions, dry, grease and oil, were considered in this investigation. In this paper only the result of one test, Specimen 03, is discussed in detail; the others are briefly described.

Specimen 03, which had the initial dimension of 19.05 mm (0.75 in.) diameter and 7.06 mm (0.278 in.) height, was compressed under the dry contact condition, i.e. no lubricant was used. Figure 27.4a shows a typical displacement time history of the test, which has a constant speed of loading and unloading; it also includes the history of the corresponding force. The top platen was not in contact with the specimen initially. The force-displacement curve is depicted in Fig. 27.4b. The data indicates the loading begins at the displacement $z = 0.457$ mm (0.018 in.) or time $t = 25$ s. The specimen experienced a loading-unloading cycle and returned very close to its original shape at the end of the cycle. It recovered completely eventually.

A series of images taken by the optical digital camera was quantitatively analyzed to examine the deformation of the foam specimen at the bottom platen interface. Two parameters were of interest, which were the diameter of the specimen-platen contact surface, $d_{contact}$, and the diameter of the deformed bottom surface of the specimen, $d_{bottom\ face}$. The measurements were made at each recorded image. Since the boundary of the bottom surface was highlighted with dark color, it could be

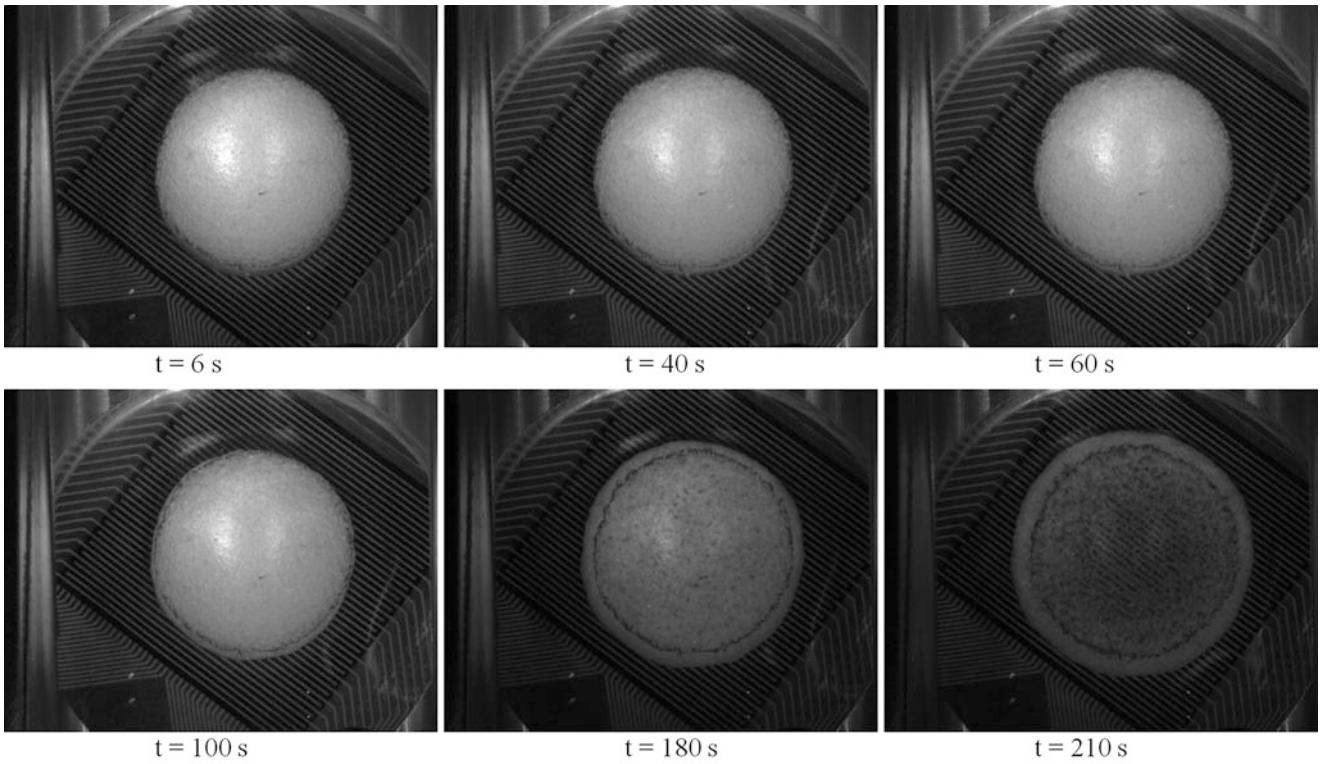

Fig. 27.5 Images of bottom specimen-platen interface during the compression of silicone foam Specimen 03

Table 27.1 Deformation at foam-platen interface for compression test of silicon foam specimen B3

Time	Displacement	Force	Diameter	Diameter
t (s)	Δz (in.)	F (lb)	$d_{contact}$ (in.)	$d_{bottom\ face}$ (in.)
6	0.002	~0	0.750	0.750
40	0.038	1.86	0.753	0.751
60	0.058	4.26	0.757	0.752
180	0.178	37.04	0.852	0.768
210	0.201	90.40	0.924	0.803

tracked easily for measuring $d_{bottom\ face}$. Focusing on the loading portion of the experiment, Fig. 27.5 displays a few selective images of the interface, at time $t = 6$, 40, 60, 180 and 210 s. Table 27.1 listed the corresponding values of displacement, load, and the diameters of interest. Initially, i.e. $t < 25$ s before the loading started, the diameter of the total contact $d_{contact}$ was the same as that of the bottom face $d_{bottom\ face}$. As the loading increased, both diameters grew bigger; $d_{contact}$ increased at a rate faster than $d_{bottom\ face}$. Take $t = 180$ s for example, $\Delta d_{contact} = 2.591$ mm (0.102 in.) and $\Delta d_{bottom\ face} = 0.457$ mm (0.018 in.).

Clearly, the bottom face did not enlarge much, the increase of the contact area was mostly due to the cylindrical side wall rolled over and got in contact with the platen; only a small portion was from the expending of the bottom surface of the specimen. From the measured diameters and the displacement, the contact area, specimen bottom face area, and the volume of the sample can be calculated for the whole loading cycle, which is shown in Fig. 27.6. The data show that the area of specimen bottom face changes gradually, but speeds up at the end of the loading; it behaves similarly for unloading, changes gradually at the beginning, but speeds up at the end of the unloading. The rate of volume change, on the other hand, gradually decreases as the loading increases. The vertical red line indicates the time that the displacement reaches the maximum. At that time, the axial deformation $\Delta L_{max}/L_o \approx 62.4$ %, the radial deformation $(\Delta d_{contact})_{max}/d_o \approx 21.9$ %, and the volume deformation $\Delta V_{max}/V_o \approx 43.0$ %. Further loading will cause the force to increase sharply and may exceed the capacity of the pressure sensor. To obtain the data for larger deformation, higher capacity pressure sensor needs to be used.

Figure 27.7 shows selected pressure distributions of the foam-platen interface, which correspond to the same compression states as those show in Fig. 27.6. Three charts are included for each discrete time: the legend (right), raw 2D pressure plot

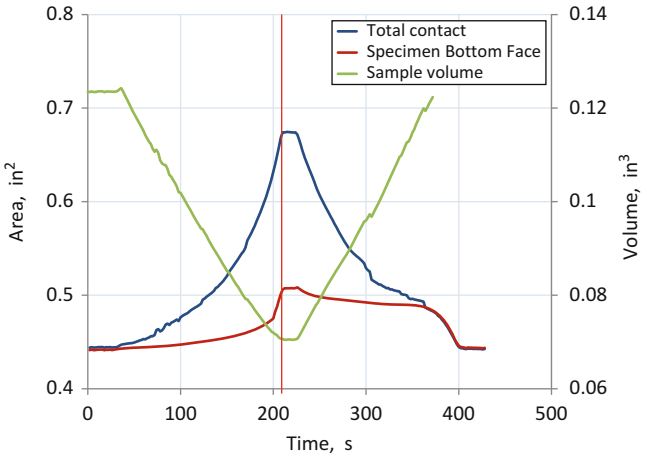

Fig 27.6 Contact areas and total volume during the compression cycle of Specimen 03

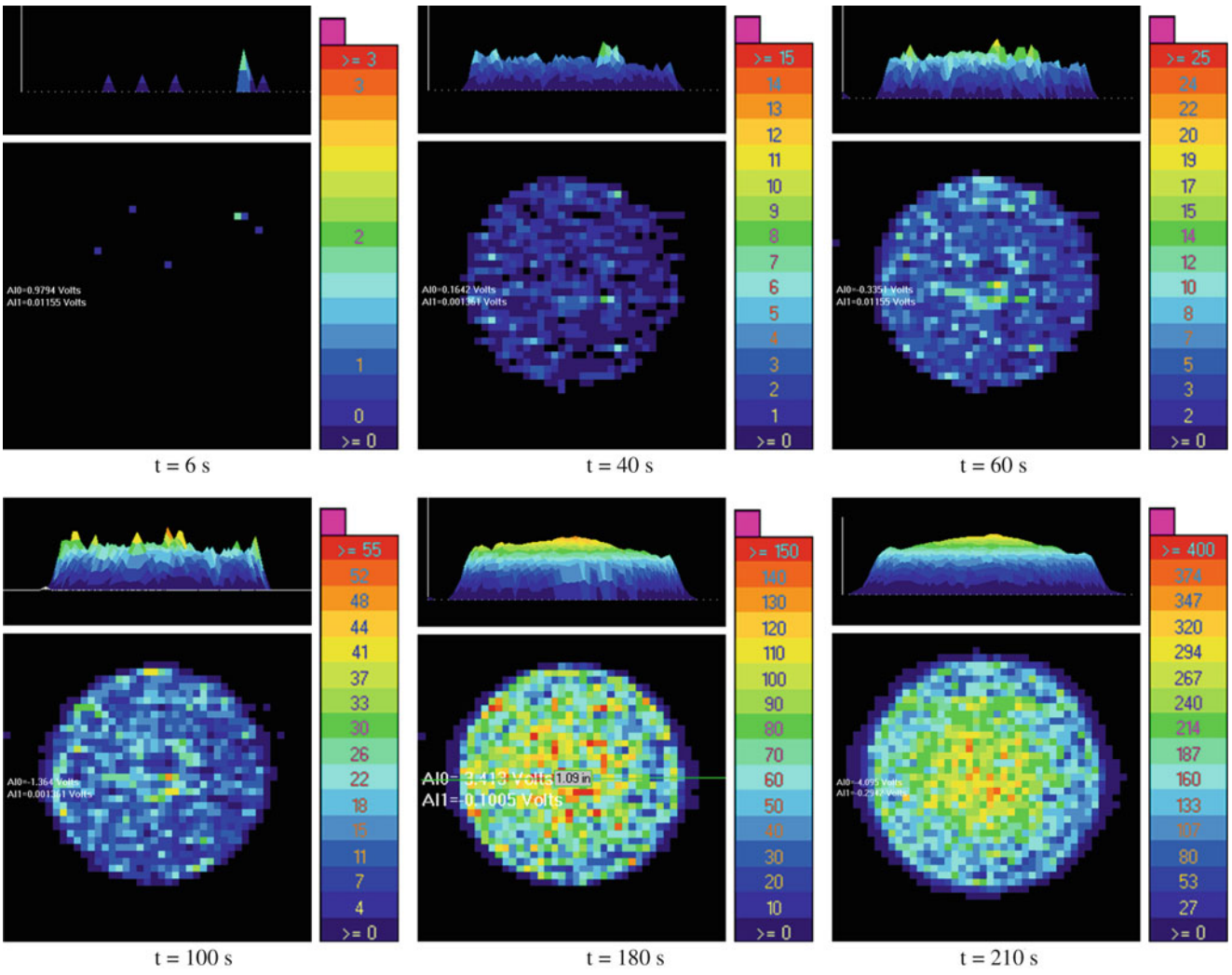

Fig. 27.7 Pressure distributions of top specimen-platen interface during the compression of silicone foam Specimen 03 measured by the pressure sensor

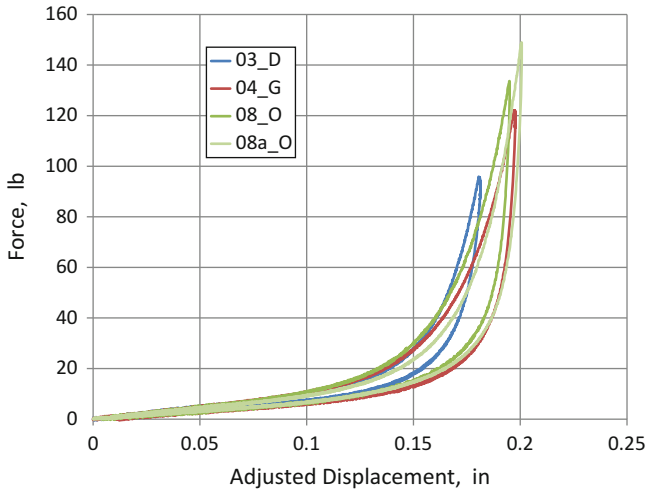

Fig. 27.8 Effects of lubricant on compression results of silicone foam

(bottom left), and 90° side view of the 3D contours plot (top left). The pressure scale is optimized for each compression state. The 2D plot shows that the raw pressure data is scattered widely from element to element. It is due to that the size of the pressure sensing element, 0.635 mm × 0.635 mm (0.025″ × 0.025″), and the foam void size, approximately 0.508 mm (0.020 in.) diameter, are about the same. Each sensing elements could have a very different degrees of contact with silicone or void. More data processing is needed to obtain homogenized results. Nonetheless, several qualitative behaviors can be observed. Since the sample is axisymmetric, the 90° side view plot illustrates the pressure distribution across the diameter. The pressure distribution appears to be somewhat uniform when $t \leq 100$ s; however, it is evident that the pressure is higher toward the center when $t \geq 180$ s. Also, there is a ring of relative high pressure close to the edge. Comparing this result to the optical images of Fig. 27.6, it seems the ring corresponding to the specimen bottom face boundary. More analysis is needed to confirm this result.

Compression tests of silicone foam under different friction conditions were also performed. A thin layer of vacuum grease was applied at top and bottom faces of Specimen 04, and a light lubricant household oil was applied for Specimen 08. Their load-displacement curves are shown in Fig. 27.8. In the figure, the displacements are adjusted so that force and displacement both start to increase from zero at the same time. Specimen 08 was tested for two compression cycles, 08 was the first cycle and 08a was the second cycle. These load-displacement curves are all different. Using different lubricants varies the friction at the interface and results in differences in load-displacement curves. It is not clear why the second cycle of Specimen 08 behaves slight differently from the first cycle, which is not seen in the other cases. It is possible that the oil infiltrates the open cell foam and modifies the behavior. Observing the foam-platen interface, dry surface has the most amount of side surface rolling over and oil lubricated surface is the least.

27.5 Conclusion

A new setup has designed to study the compression behavior of soft materials to very large deformation. Compression tests of silicone foam were performed using various lubricants to change the friction at specimen-platen interface. Depending on the friction, the side surface of the specimen has a different degree of roll over to contact the platen. In general, less roll over is observed for a lower friction interface. The pressure (or stress) distribution at the interface is determined by an array of pressure sensor elements. The pressure is not uniform, typically higher at the center. It is hard to achieve an ideal compression condition for material characterization. The experimental results presented in this paper provide quantitative boundary conditions at the interface, which can be used in numerical analysis to obtain the stress-strain relation of the silicone foam.

Acknowledgements Sandia National Laboratories is a multi-program laboratory managed and operated by Sandia Corporation, a wholly owned subsidiary of Lockheed Martin Corporation, for the U.S. Department of Energy's National Nuclear Security Administration under contract DE-AC04-94AL85000.

Chapter 28
Voltage Control of Single Magnetic Domain Nanoscale Heterostructure, Analysis and Experiments

Scott M. Keller, Cheng-Yen Liang, and Gregory P. Carman

Abstract Micromagnetic simulations of magnetoelastic nanostructures traditionally rely on either the Stoner-Wohlfarth model or the Landau-Lifshitz-Gilbert LLG model assuming uniform strain (and/or assuming uniform magnetization). While the uniform strain assumption is reasonable when modeling magnetoelastic thin films, this constant strain approach becomes increasingly inaccurate for smaller in-plane nanoscale structures. This paper presents analytical work verified with experimental data to significantly improve simulation of finite structures by fully coupling LLG with elastodynamics, i.e. the partial differential equations are intrinsically coupled.

28.1 Introduction

Electrical control of ferromagnetic elements represents an important and emerging area of study in multiferroics. Magnetic control has conventionally been accomplished using an applied magnetic field rather than an electric field. Recently a number of researchers have focused on electric field induced strain-mediated control of magnetic properties. While interesting, a robust modeling approach that accurately predicts the response of nanoscale structures magnetic response is unavailable.

The strain-mediated multiferroic approach consists of mechanically coupling magnetoelastic elements onto ferroelectric substrates [1], e.g. sputter deposition of composite heterostructures. In these composites, an electric field applied to the ferroelectric/piezoelectric substrate induces an anisotropic strain in the magnetoelastic material. The anisotropic stain induces a magnetic anisotropy via the converse magnetoelastic effect [2]. There exist fairly extensive studies containing both theoretical and experimental work on strain-mediated magnetization changes, coercivity changes [3], and strain-induced anisotropy in continuous magnetic thin films [4]. In all of the continuous film studies the strain is appropriately assumed to be uniform in the ferroelectric and ferromagnetic layers.

A relatively less studied area is the strain-mediated effect in multiferroic nanostructures [5]. For example, Bur et al. [6] reported strain-induced coercive field changes in patterned single-magnetic-domain nickel nanostructures deposited on Si/SiO_2 substrate. A few analytical studies also exist on uniform strain transfer and strain-induced change of magnetization in nanostructures [5, 7, 8]; however, as the thickness of the nanostructures increases or in-plane dimensions decrease, the validity of the uniform strain assumption becomes increasingly compromised. Recently, researchers have begun to investigate more sophisticated modeling techniques for coupling LLG with elastodynamics. These approaches include mathematical [9] and numerical [10, 11] methods for the solutions of coupled micromagnetic and elastodynamic equations. While a few sophisticated solutions have been presented, these presentations do not compare their data directly with experimental results and thus leaves the modeling accuracy questionable.

In this study, we develop a numerical method based on finite elements to fully-couple micromagnetic simulations with elastodynamics in finite size 3D structures. The analytical results are compared to both conventional analytical methods and experimental results. The validated model is used to guide the development of experimental tests and devices using nanoscale magnetoelastic structures.

S.M. Keller (✉) • C.-Y. Liang • G.P. Carman
Department of Mechanical and Aerospace Engineering, Translational Applications of Nanoscale Multiferroic Systems TANMS, University of California, Los Angeles, CA 90095, USA
e-mail: smkeller@ucla.edu; liang1982@ucla.edu; carman@seas.ucla.edu

C. Ralph et al. (eds.), *Mechanics of Composite and Multi-functional Materials, Volume 7*,
Conference Proceedings of the Society for Experimental Mechanics Series, DOI 10.1007/978-3-319-21762-8_28

28.2 Theory

The theoretical magnetoelastic framework for a problem between micromagnetics and elastodynamics reduces to seven coupled PDEs, which can be formulated in their weak form (i.e. referred to as LLG/EQ). Assumptions include small elastic deformations, linear elasticity, magnetostatics, and negligible electrical current contributions. The elastodynamic governing equations are

$$\rho \frac{\partial^2 \underline{u}}{\partial t^2} - \cdot \underline{\underline{\sigma}} = \underline{0} \tag{28.1}$$

where ρ is the density, σ is the stress tensor. The phenomenological Landau-Lifshitz-Gilbert (LLG) micromagnetic relations represent the second set of equations defined by

$$\frac{\partial \underline{m}}{\partial t} = -\mu_0 \gamma \left(\underline{m} \times \underline{H}_{eff} \right) + \alpha \left(\underline{m} \times \frac{\partial \underline{m}}{\partial t} \right) \tag{28.2}$$

Where γ is the Gilbert gyromagnetic ratio and α is the Gilbert damping constant. Substituting the appropriate constitutive relations and definitions including external field H_{ext}, magnetocrystalline anisotropy field H_{anis}, exchange field H_{ex}, demagnetization field H_d, and magnetoelastic field H_{me} reduces the set of equations to six partial differential equations relating the displacements $\underline{u}$ and the magnetization $\underline{m}$ defined as:

$$\rho \frac{\partial^2 \underline{u}}{\partial t^2} - \cdot \underline{\underline{C}} \left[\frac{1}{2} \left(\underline{u} + (\underline{u})^T \right) \right] + \cdot \underline{\underline{C}} \left(\underline{\underline{\lambda}}^m \underline{m} \underline{m}^T \right) = \underline{0} \tag{28.3}$$

$$\frac{\partial \underline{m}}{\partial t} = -\mu_0 \gamma \left(\underline{m} \times \left(\underline{H}_{ext} + \underline{H}_{ex}(\underline{m}) + \underline{H}_d(\phi) + \underline{H}_{anis}(\underline{m}) + \underline{H}_{me}(\underline{m}, \underline{u}) \right) \right) + \alpha \left(\underline{m} \times \frac{\partial \underline{m}}{\partial t} \right) \tag{28.4}$$

Equations (28.3) and (28.4) along with the Ampere's law $\underline{H}_d = -\nabla \phi$ represent seven equations as a function of seven unknowns defined by $\underline{u}$, φ, and $\underline{m}$. To solve this system LLG/EQ of coupled equations, the PDEs are formulated in their weak forms and solved numerically using finite elements.

28.3 Simulation and Results

Experimental tests have been conducted on 100 nm × 300 nm × 35 nm nickel single domain nanostructures subjected to mechanical loads. An illustration of the finite element model used to analyze the experimental data is shown in Fig. 28.1a. The structure is discretized using tetrahedral elements with a size on the order of nickel's exchange length (~8.5 nm). The nickel properties were derived from bulk values [12] and the Gilbert damping constant was chosen to be $\alpha = 0.5$ to improve stability and process time.

Figure 28.2a compares the coercive fields H_c as a function of effective applied strain ($\varepsilon_{yy} - \varepsilon_{xx}$) for the Stoner Wahlforth SW model, the micromagnetic LLG model assuming constant strain, the LLG/EQ model (described in this paper), and experimental data. The SW model shows significant disagreement with the experimental data by as much as 2350 Oe, while the LLG model and LLG/EQ model results have relatively better agreement but differ by as much as 200 Oe. Such inconsistencies in the analytical results are attributed to thermal issues, surface roughness, aspect ratio, or geometric smoothing in the nanostructure, which are not adequately represented in the numerical simulations. In Fig. 28.2b, the change in coercive field values (i.e., $\Delta H_c = H_c - H_c^0$) for the different curves are provided. The LLG/EQ model shows very good agreement with experiment data (less than 2 % deviation) while the SW model and the LLG-constant strain model show relatively poor agreement with errors as large as 60 %. These set of comparisons clearly indicate that non-uniform strain distributions must be considered when predicting the strain-mediated magnetic anisotropic effects in nanostructures. This is especially true when considering substantially stronger magnetoelastic materials such as Terfenol-D.

Figure 28.3 shows analytical LLG/EQ results of the relative strain distribution in the Ni nanostructure with an effective applied strain $\varepsilon_{yy} - \varepsilon_{xx} = -671$ με and zero applied magnetic field. Figure 28.3a shows the surface plot for strains

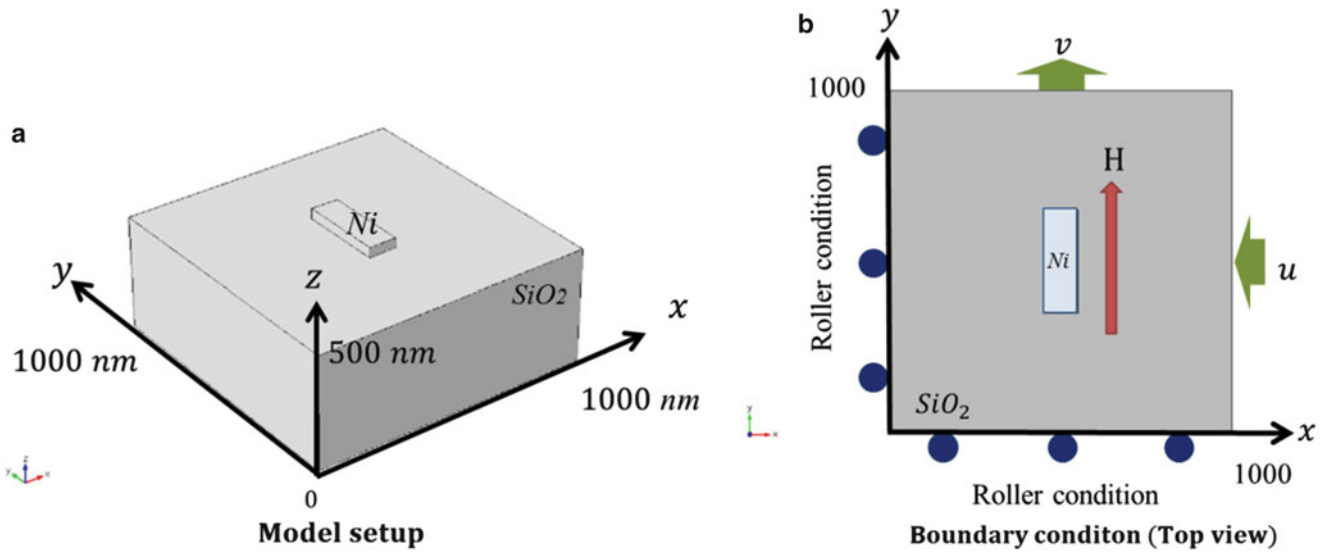

Fig. 28.1 Schematic diagram of the model and boundary conditions. (**a**) Model setup. (**b**) Boundary condition (*top view*)

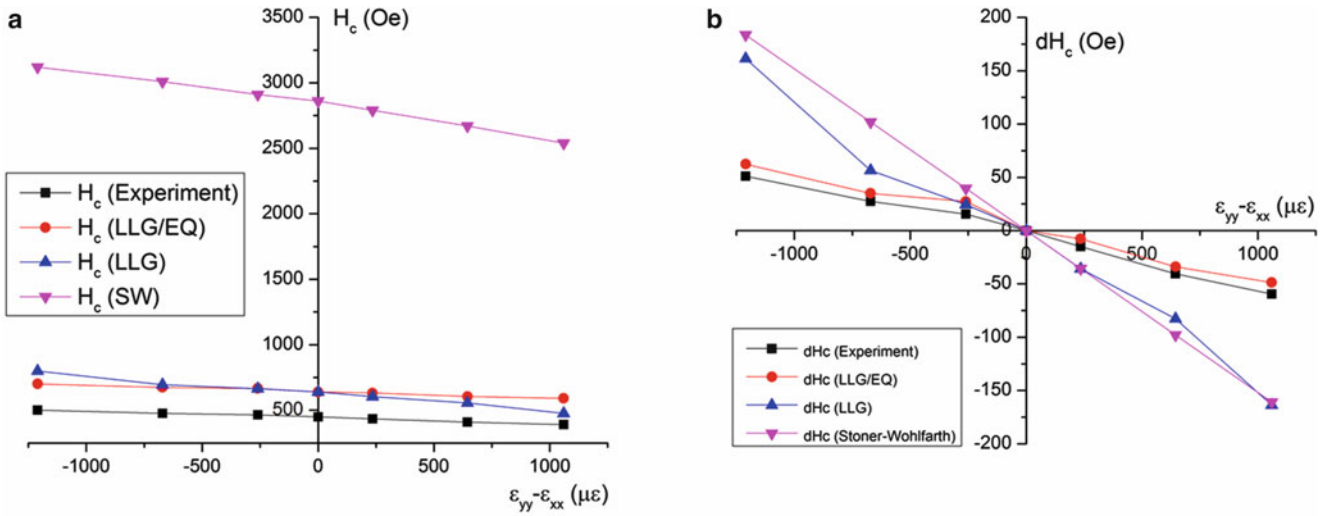

Fig. 28.2 Comparison of models for (**a**) coercive field H_c and (**b**) coercive difference ΔH_c, as a function of $(\varepsilon_{yy} - \varepsilon_{xx})$

($\varepsilon_{yy} - \varepsilon_{xx} = -671$ με) in the nickel nanostructure. The simulation results clearly show that the strain distribution is non-uniform throughout the nanostructure. The relative strain values vary substantially between -700 με and -80 με. Figure 28.3b plots the relative strain ($\varepsilon_{yy} - \varepsilon_{xx}$) as a function of y at $x = 50$ nm for four different z values. Large strain variations are observed near the nanostructure ends ($y = 0$ nm and $y = 300$ nm), while the strain in the middle ($y = 150$ nm) is relatively uniform. The volume-averaged strain ($\varepsilon_{yy} - \varepsilon_{xx}$) for the nickel nanostructure is -322 με and is 50 % less than the applied strain. The strain variation as a function of position occurs due to a well-known phenomenon, classically referred to as shear lag in the mechanics community. Therefore, one can clearly see that the assumption of constant strain present in SW and LLG is inappropriate for this structure.

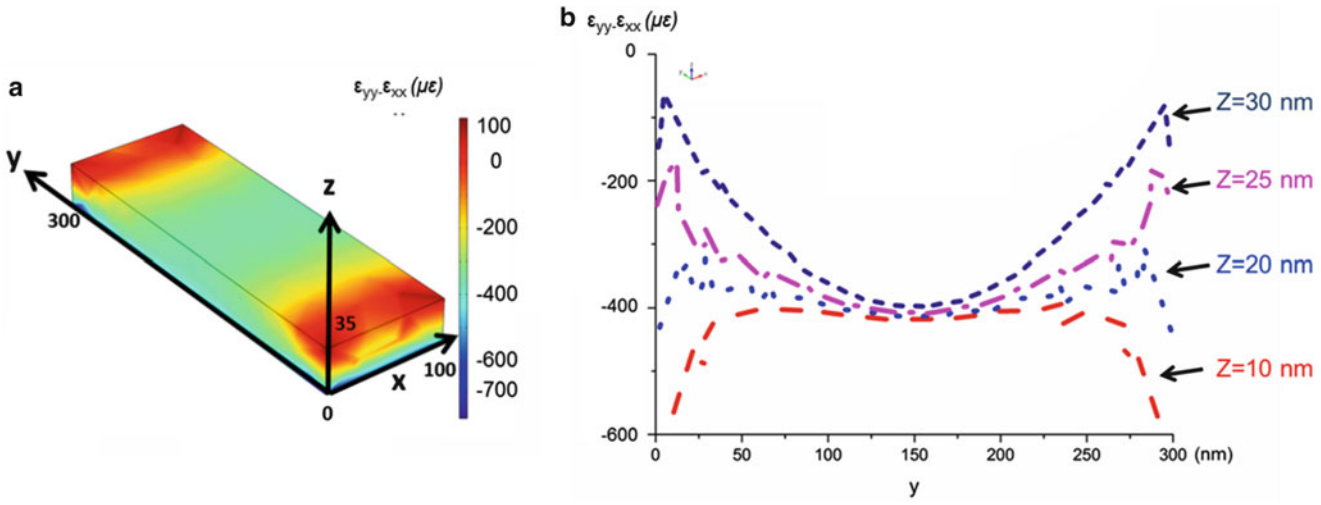

Fig. 28.3 The strain distributions with ($\varepsilon_{yy} - \varepsilon_{xx} = -671$ με) (**a**) contour plot and (**b**) as a function of y direction

28.4 Conclusion

In conclusion, we have developed a numerical approach based on a weighted residual formulation and finite elements for simulating magnetization states, magnetic hysteresis curves, and strain-induced coercive field changes in magnetic nanostructures by coupling the spatially-dependent strain state with micromagnetic simulation with elastodynamics (LLG/EQ model). This model provides substantially better predictive results than the LLG model and the conventional Stoner-Wohlfarth (SW) model and in some cases must be used to accurately predict the response of a nanoscale structure. The LLG/EQ coupled model was verified with existing experimental data validating its predictive capabilities. In general this work strongly encourages researchers to use coupled solutions when modeling the magnetoelastic response of finite size structures to accurately predict the magnetic response. This is important in a wide range of fields including memory, motors, and spin wave propagation.

Acknowledgments This work was supported by the NSF Nanosystems Engineering Research Center for Translational Applications of Nanoscale Multiferroic Systems (TANMS), under Cooperative Agreement Award EEC-1160504.

References

1. Ma, J., Hu, J.M., Li, Z., Nan, C.W.: Recent Progress in multiferroic magnetoelectric composites: from bulk to thin films. Adv. Mater. **23**, 1062–1087 (2011)
2. Zhu, B., Lo, C.C.H., Lee, S.J., Jiles, D.C.: Micromagnetic modeling of the effects of stress on magnetic properties. J. Appl. Phys. **89**, 7009–7011 (2001)
3. Hu, R.L., Soh, A.K., Zheng, G.P., Ni, Y.: Micromagnetic modeling studies on the effects of stress on magnetization reversal and dynamic hysteresis. J. Magn. Magn. Mater. **301**, 458–468 (2006)
4. Chen, Y.J., Fitchorov, T., Vittoria, C., Harris, V.G.: Electrically controlled magnetization switching in a multiferroic heterostructure. Appl. Phys. Lett. **97**, 052502 (2010)
5. Hu, J.M., Sheng, G., Zhang, J.X., Nan, C.W., Chen, L.Q.: Phase-field simulation of electric-field-induced in-plane magnetic domain switching in magnetic/ferroelectric layered heterostructures. J. Appl. Phys. **109**, 123917 (2011)
6. Bur, A., Wu, T., Hockel, J., Hsu, C.J., Kim, H.K.D., Chung, T.K., Wong, K., Wang, K.L., Carman, G.P.: Strain-induced magnetization change in patterned ferromagnetic nickel nanostructures. J. Appl. Phys. **109**, 123903 (2011)
7. Roy, K., Bandyopadhyay, S., Atulasimha, J.: Switching dynamics of a magnetostrictive single-domain nanomagnet subjected to stress. Phys. Rev. B **83**, 224412 (2011)
8. Atulasimha, J., Bandyopadhyay, S.: Bennett clocking of nanomagnetic logic using multiferroic single-domain nanomagnets. Appl. Phys. Lett. **97**, 173105 (2010)
9. Banas, L.: Numerical methods for the Landau-Lifshitz-Gilbert equation. Numer. Anal. Its Appl. **3401**, 158–165 (2005)
10. Shu, Y.C., Lin, M.P., Wu, K.C.: Micromagnetic modeling of magnetostrictive materials under intrinsic stress. Mech. Mater. **36**, 975–997 (2004)
11. Zhang, J.X., Chen, L.Q.: Phase-field microelasticity theory and micromagnetic simulations of domain structures in giant magnetostrictive materials. Acta Mater. **53**, 2845–2855 (2005)
12. O'Handley, R.C.: Modern Magnetic Material: Principles and Applications. Wiley, New York (2000)

Chapter 29
Active Damping in Polymer-Based Nanocomposites

Frank Gardea, Dimitris Lagoudas, and Mohammad Naraghi

Abstract In this research, we present the preliminary results related to our investigations on the potential of electrical signals through the network of nanoscale reinforcements and the consequent Joule heating in polymer-based nanocomposites as a means to augment damping in the material. The intended damping mechanism in this case is the creep and relaxation in the matrix phase, which is to be intensified via locally increased temperatures. The reinforcement of choice will be carbon nanotubes. The effectiveness of this method partly depends on rate and special uniformity at which the temperature of the matrix is increased, and as such it scales with the surface to volume ratio of the reinforcements. To demonstrate active damping augmentation experimentally, composites were then fabricated with the carbon nanotubes (CNTs) randomly distributed within an epoxy matrix. The active control of the damping behavior was pursued by joule heating the CNT reinforcements during the dynamic tensile testing on a Dynamic Mechanical Analyzer (DMA). Damping was quantified by the ratio of loss to storage modulus, equivalent to the ratio of dissipated mechanical energy to the elastic energy stored in the material during dynamic loading.

Keywords Active damping • Nanocomposites • Polymer relaxation • Variable stiffness • Carbon nanotubes

29.1 Introduction

Energy dissipation during oscillatory loads, also known as vibration damping, is an important function of structural components not only to enhance performance but also for reliability in the structural response. Traditionally, approaches to suppressing structural vibration consist of externally attached dampers in addition to any inherent damping capability in the structure, which can lead to issues of increased weight and physical space. The advancement of materials for damping is relying not only on achieving advanced structural performance but also on developing materials with multifunctional capabilities. An effective alternative to traditional approaches is to provide a means for the damping mechanism within the structural material itself, which could then be triggered by external means. Specifically, polymer composite structures are of interest. The focus on polymers comes from their low density, ease of manufacturability, and large range of applications [1–3]. In addition, polymers show significant enhancement in damping capability near the glass transition temperature [4]. One approach to enhancing the energy dissipation in polymers, while increasing effective stiffness, is by embedding these polymers with nanoparticles. This approach would be attractive to many applications due not only to the minimal increase in weight and lack of external components, but also the additional improvement in mechanical properties, such as elastic modulus, yield strength, electrical conductivity etc. For example, one can take advantage of the electrically conductive path formed by these fillers, and thus pursue an active damping technique. In this regard, Joule heating of these fillers can result in local heating of the matrix, to near the glass transition temperature where polymer damping is most effective, thus allowing for the viscoelastic properties of the matrix to additionally contribute to damping. The high surface to volume ratio of the nanoscale reinforcements will accelerate the damping mutation of the matrix by facilitating the heat transfer. However, interfacial thermal resistance must be taken into account as to not damage the composite with prolonged electrical signals.

Active damping consists of modulating the damping properties of a structure or structural material via external stimuli, mainly but not limited to electrical signals. Since the viscoelastic properties of the matrix, which is highly temperature-sensitive especially near glass transition temperature, can add to the energy dissipation of a structure, one approach to augment damping in polymer-based structures is by temperature control of the polymer via an external stimulus. Active heating of the polymer to exploit the thermomechanical coupling inherent to polymers has been shown to have potential in damping applications. Smith et al. developed a tuned-mass damper that could be continuously varied, and thus self-tune, by

F. Gardea • D. Lagoudas • M. Naraghi (✉)
Department of Aerospace Engineering, Texas A&M University, 3409 TAMU, College Station, TX 77843-3409, USA
e-mail: naraghi@tamu.edu

C. Ralph et al. (eds.), *Mechanics of Composite and Multi-functional Materials, Volume 7*,
Conference Proceedings of the Society for Experimental Mechanics Series, DOI 10.1007/978-3-319-21762-8_29

taking advantage of the temperature-sensitive viscoelastic properties of the polymer [5]. The polymer relaxation mechanism has also been shown to be effective in improving the impact response of carbon fiber polymer matrix composites [6]. Similar techniques have also been used to actively control the damping capabilities of carbon microfiber reinforced composites leading to reduced deflection and stresses in the composite [7]. Even though these results show that this mechanism is effective in improving the damping capabilities of microfiber composites, a more efficient activation of this mechanism is expected with the addition of nanoscale reinforcements. This is because the high surface to volume ratio of the fillers will facilitate the transfer of heat from the particle to the matrix.

The goal of the present research is to test the hypothesis that damping of a polymer based nanocomposite can be actively and controllably augmented via electrical signals. The potential of using joule heating of embedded nanoparticles in modulating the damping capabilities of nanocomposites is investigated. The intended damping mechanism is the relaxation of the matrix surrounding the nanoparticle. The relaxation of the polymer is enhanced by the local increase in temperature. The main parameter to control during this study is the magnitude and duration of the input heat flux to be controlled via electric signals.

29.2 Experimental

29.2.1 Processing

The epoxy resin, EPON™ 862, and curing agent, EPIKURE™ W, used in this study were both obtained from Hexion Specialty Chemicals, Inc. The CNTs, which contain mostly single-walled CNTs were purchased from Carbon Nanotechnologies, Inc. (Unidym, Incorporated) and were used as is with no surface functionalization. The composite fabrication was taken from [8], described as follows. Carbon nanotubes were first ground in 2 ml of ethanol with a mortar and pestle. The CNT bundles were then dispersed, in a flask, in a mixture of toluene and ethanol with an ultrasonicator bath for 1 h. The nanotube/solvent solution was added to the EPON™ 862 resin and magnetically stirred at 400 rpm and 60 °C under vacuum until all the solvent evaporated. The epoxy was pre-cured with 20 % of the total amount of the curing agent (100:26.4 by weight), at 120 °C for 200 min, after solvent evaporation. The solution was then cooled to increase its viscosity and the remaining amount of curing agent added. The CNT/epoxy solution was then poured into a mold with a curing cycle set to 8 h at 40 °C followed by 2 h at 120 °C and another 2 h at 175 °C. Composites with 1 wt% CNT concentration were fabricated.

29.2.2 Mechanical Characterization

Dynamic mechanical analysis (DMA) was performed using a TA Instruments RSAIII DMA. In order to obtain the dynamic response as a function of temperature on the neat polymer, a temperature sweep was performed by varying the chamber temperature from 25 °C to 180 °C at a rate of 10 °C/min. The dynamic strain amplitude was fixed at 0.1 % and the frequency at 1 Hz. The CNT/epoxy composite was tested at a fixed dynamic strain amplitude of 0.1 % and a frequency of 1 Hz. To investigate active damping, the temperature of the sample was varied via Joule heating of the composite using a voltage amplifier and a function generator. The voltage was applied via a two point probe formed by copper wires which were glued to the sample using high purity silver paint, thus minimizing any Joule heating at the electrodes. The testing set-up is shown in Fig. 29.1. The voltage was varied from 0 to 60 V as a means to control the heat flux and the temperature of the sample. The change in storage modulus and tan δ was recorded as a function of time. Thermal images were obtained using an infrared camera and the surface temperature of the sample was monitored during testing.The ratio of loss to storage modulus, tan δ, was reported as a measure of energy dissipation capability of the material.

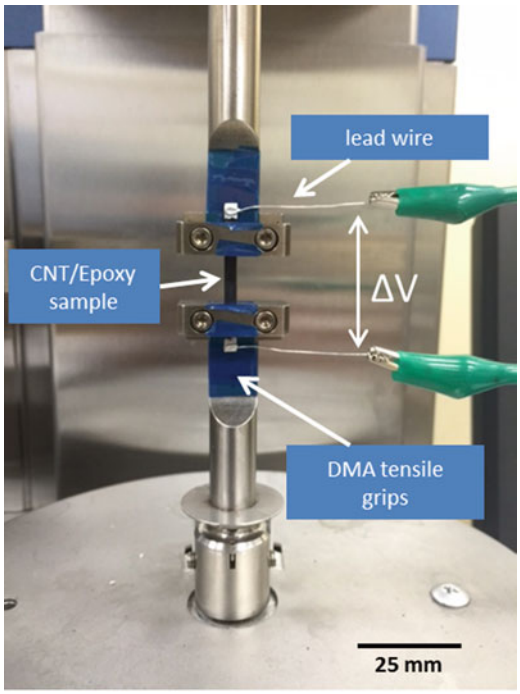

Fig. 29.1 Testing set-up showing the sample, gripped to the DMA testing machine, with the glued lead wires which are used to Joule heat the sample via a voltage amplifier and function generator

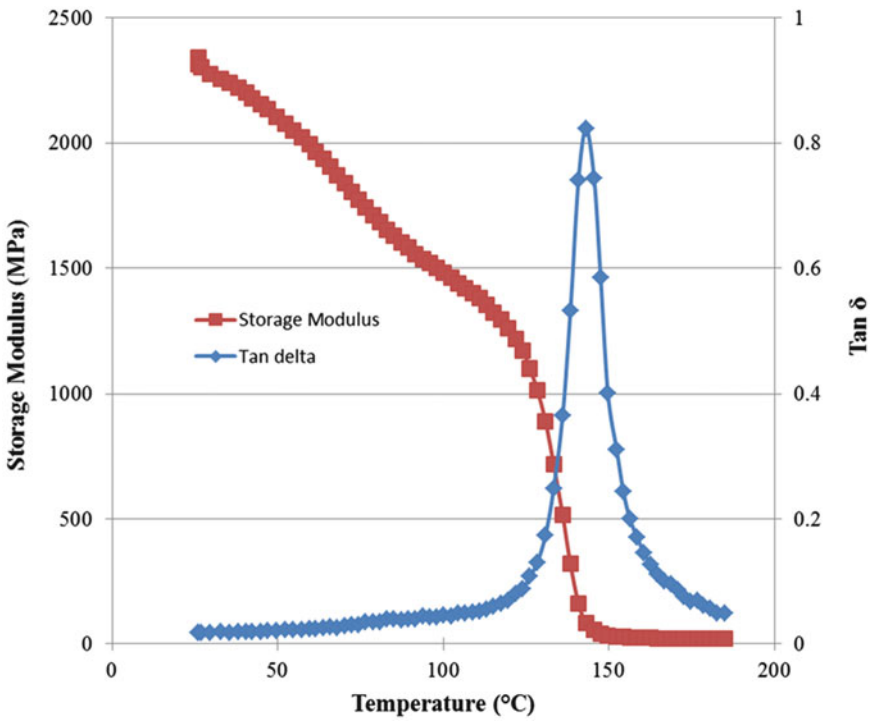

Fig. 29.2 Storage modulus and tan δ as a function of temperature for neat EPON 862 epoxy

29.3 Results and Discussion

The DMA response of epoxy as a function of temperature during the temperature sweep experiment (no Joule heating) is shown in Fig. 29.2. As observed in the plot, the maximum dissipation, tan δ, occurs around the glass transition temperature of the material, ~140 °C. The tan δ increases by up to a factor of 47, however this increase in damping comes at a cost of a significant decrease in storage modulus. Therefore, in order to maintain a considerable portion of the composite stiffness, joule heating was performed to temperatures just below the Tg of the epoxy.

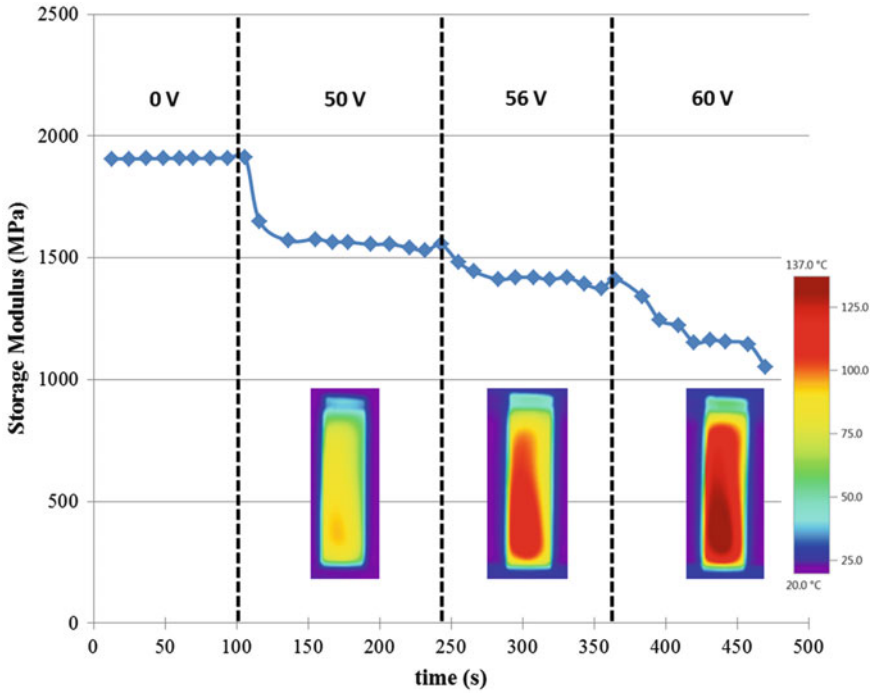

Fig. 29.3 Storage modulus variation with time for various applied voltages for a 1 wt% CNT/epoxy composite. Insets show the temperature distribution in the composite obtained from an infrared camera

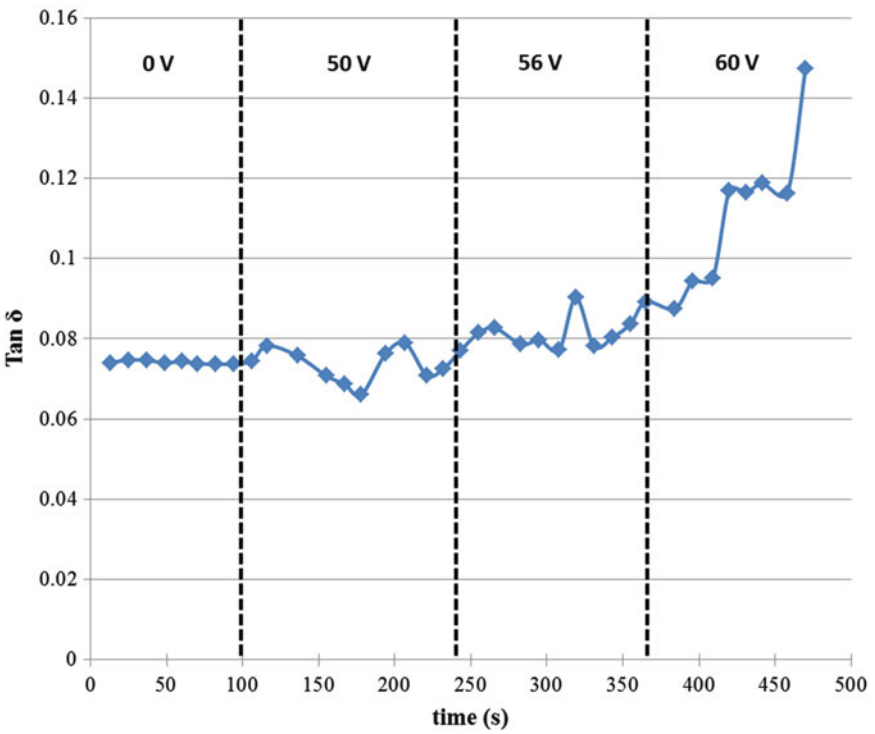

Fig. 29.4 Tan δ as a function of time with various applied voltages for a 1 wt% CNT/epoxy composite

The active damping performance of the composite via joule heating are shown in Figs. 29.3 and 29.4. The results show that as the voltage potential is applied to the sample, the damping capability of the structure increases while the storage modulus shows a sudden drop which correlates with an increase in tan δ. For instance, an applied voltage of ~60 V nearly doubles the tan δ, while the storage modulus is reduced by 40 %. This result points to polymer relaxation as the thermally activated mechanism to enhance the damping behavior of the composite material. In addition, the sudden change in storage modulus is an indication of effectiveness of the CNTs as volumetric heat sources, with the CNTs providing rapid heating of the sample. This rapid heating will allow for controllability of the active damping of the material.

By taking advantage of the polymer relaxation resulted from an increase in temperature, the composite shows the potential for damping enhancement. However, this enhancement in damping comes at a significant cost in decrease of storage modulus. While the loss of modulus may adversely affect the structural performance in some applications, it has been shown that a reduction in stiffness of structural components in civil structures has led to a decrease in absolute accelerations and related forces [9]. In addition, vibration suppression has been pursued by using variable-stiffness members [10]. However, in order to minimize or control the decrease in modulus, an alternative approach is to use semi-crystalline polymers instead of an amorphous polymer. With a semi-crystalline polymer, the storage modulus will decrease by a less relative amount at the glass transition temperature. That is because the crystalline structure will remain intact at Tg, since this temperature is below the crystal melt temperature. Therefore, the crystalline structure in the material will maintain some storage modulus while still allowing the polymer chains within the amorphous regions to have some relative movement, which will contribute to the energy dissipation in the material.

29.4 Conclusions

The active damping potential of CNT fillers in polymer matrix composites was investigated through experimental techniques. The thermomechanical response of the polymer was targeted and studied as a potential damping source within the nanocomposite. The nanoscale reinforcements were used as heat sources, via joule heating, to trigger the matrix relaxation. By taking advantage of the polymer relaxation resulted from an increase in temperature, the composite shows the potential for damping enhancement. The high surface to volume ratio of CNTs facilitated the heat flow from CNTs to matrix, resulting in rapid damping augmentation. Future research should be focused on semi-crystalline polymers, to minimize the undesired loss of storage modulus which accompanies the increase in damping capability.

References

1. Gangopadhyay, R., De, A.: Conducting polymer nanocomposites: a brief overview. Chem. Mater. **12**(3), 608–622 (2000)
2. Harris, P.: Carbon nanotube composites. Int. Mater. Rev. **49**(1), 31–43 (2004)
3. Schmitt, C., Lebienvenu, M.: Electrostatic painting of conductive composite materials. J. Mater. Process. Technol. **134**(3), 303–309 (2003)
4. Gong, Z., et al.: Investigation of the effects of temperature and strain on the damping properties of polycarbonate/multiwalled carbon nanotube composites. J. Phys. Chem. C **115**(38), 18468–18472 (2011)
5. Smith, K.E., Maly, J.R., Johnson, C.D.: Smart tuned mass dampers. In: Active Materials and Adaptive Structures: Proceedings of the ADPA/AIAA/ASME/SPIE Conference (1991)
6. Sierakowski, R.L., Telitchev, I.Y., Zhupanska, O.I.: On the impact response of electrified carbon fiber polymer matrix composites: effects of electric current intensity and duration. Compos. Sci. Technol. **68**(3), 639–649 (2008)
7. Barakati, A., Zhupanska, O.: Thermal and mechanical response of a carbon fiber reinforced composite to a transverse impact and in-plane pulsed electromagnetic loads. J. Eng. Mater. Technol. **134**(3), 031004 (2012)
8. Gardea, F., Lagoudas, D.C.: Characterization of electrical and thermal properties of carbon nanotube/epoxy composites. Compos. Part B **56**, 611–620 (2014)
9. Cimellaro, G.P.: Simultaneous stiffness–damping optimization of structures with respect to acceleration, displacement and base shear. Eng. Struct. **29**(11), 2853–2870 (2007)
10. Onoda, J., et al.: Vibration suppression by variable-stiffness members. AIAA J. **29**(6), 977–983 (1991)

Chapter 30
MWCNT and CNF Cementitious Nanocomposites for Enhanced Strength and Toughness

P.A. Danoglidis, M.G. Falara, M.K. Katotriotou, M.S. Konsta-Gdoutos, and E.E. Gdoutos

Abstract Cementitious nanocomposites reinforced with carbon fibers at the nanoscale were fabricated and tested, exhibiting remarkably improved mechanical and fracture properties. The cementitious nanocomposites were reinforced with well dispersed multiwall carbon nanotubes (MWCNTs) and carbon nanofibers (CNFs). A dispersion method involving the application of ultrasonic energy and the use of a superplasticizer was employed to prepare the nanoscale fiber suspensions. Flexural strength and Young's modulus were experimentally investigated and compared with similarly processed reference cement based mixes without the nano-reinforcement. The nanocomposites' fracture properties were also determined using the two parameter fracture model (TPFM). The excellent reinforcing capability of MWCNTs and CNFs is demonstrated by a significant improvement in flexural strength (87 % for MWCNTs and 106 % for CNFs reinforcement), Young's modulus (100 %), and fracture toughness (86 % for MWCNTs and 119 % for CNFs reinforcement).

Keywords Multi-walled carbon nanotubes • Carbon nanofibers • Mortars • Fracture mechanics • Young's modulus

30.1 Introduction

Cementitious materials suffer from low tensile strength and limited strain capacity, which gives rise to the formation of nanocracks under relatively low tensile loads. The use of new reinforcing materials like multiwall carbon nanotubes (MWCNTs) and carbon nanofibers (CNFs) makes it possible to produce cement based nanocomposites with revolutionary properties. These materials, with aspect ratios greater than 1000, have Young's modulus around 1 TPa [1] tensile strength of 65–93 GPa, and maximum strain of 10–15 %. However MWCNTs form agglomerates or bundles and adhere together with van der Waals forces, which make it particularly difficult to separate. Early attempts to add MWCNTs to cementitious materials have failed due to poor adhesion. Konsta-Gdoutos and coworkers [2, 3] developed a revolutionary method for effective dispersion of MWCNTs in cement pastes, mortars and concrete. The dispersion of different lengths of MWCNTs and CNFs in water was achieved by applying ultrasonic energy and using a surfactant. Recent and ongoing research by the same authors have focused on developing multifunctional cement paste nanocomposites with high strength and advanced strain detection ability that can be used as a novel self-sensing nanoreinforced cementitious structural material. The incorporation of highly dispersed MWCNTs and/or CNFs at low concentrations has been shown to effectively arrest the cracks at the nanoscale, imposing significant improvements in the mechanical properties of the nanocomposites [4–8]. While a few studies on the mechanical strength of cementitious systems containing MWCNTs and CNFs exist, there haven't been any studies on the fracture performance of MWCNT and CNF mortar nanocomposites. The incorporation of fibers at the nanoscale and their influence on the interfaces and the pore structure of the mortar matrix are likely to render significant differences to the fracture response of the nanoreinforced mortars as compared to conventional ordinary Portland cement (OPC) systems.

The objective of this study is to investigate the mechanical and fracture properties of MWCNT and CNF reinforced mortars. Mortar nanocomposites reinforced with well dispersed MWCNTs and CNFs at an amount of 0.1 wt% of cement were fabricated. A detailed investigation on the effect of the nanoscale fibers on the mechanical properties and fracture toughness of the mortar matrix was performed by conducting three-point bending and fracture mechanics experiments. Results compared with similarly fabricated reference mortars without the nano-reinforcement are clearly showing that the incorporation of MWCNTs and CNFs in the mortar matrix significantly improves the mechanical and fracture properties of the mortar matrix.

P.A. Danoglidis • M.G. Falara • M.K. Katotriotou • M.S. Konsta-Gdoutos • E.E. Gdoutos (✉)
Department of Civil Engineering, Democritus University of Thrace, 12 Vas. Sofias, 671 00 Xanthi, Greece
e-mail: egdoutos@civil.duth.gr

C. Ralph et al. (eds.), *Mechanics of Composite and Multi-functional Materials, Volume 7*,
Conference Proceedings of the Society for Experimental Mechanics Series, DOI 10.1007/978-3-319-21762-8_30

30.2 Experimental Program

30.2.1 Materials and Specimen Preparation

The material investigated was a cement-based composite with the matrix reinforced by MWCNTs or CNFs. Characteristic properties of MWCNTs and CNFs are seen in Table 30.1. Values of an estimated number of MWCNTs or CNFs per unit volume of the cementitious matrix are also included in Table 30.1, expressed as fiber count. Mortar specimens were prepared at a water to cement ratio (w/c) of 0.485 and standard sand according to EN 196-1 at a sand to cement ratio (s/c) of 2.75. Commercially available Type I ordinary Portland cement (OPC) was used for all mixes. To allow homogeneous dispersion of MWCNTs and CNFs, suspensions were prepared by adding the MWCNTs or CNFs in an aqueous surfactant solution and applying ultrasonication energy, following the method described in Konsta-Gdoutos and coworkers [2, 3]. The materials were mixed according to ASTM 305. Two types of specimens were prepared: 40 × 40 × 160 mm prisms for the flexural strength testing; and 20 × 20 × 80 mm notched beams for the determination of the fracture toughness. Following demolding, the samples were cured in lime-saturated water for 3, 7, and 28 days.

30.2.2 Mechanical and Fracture Testing

The mechanical and fracture performance of the nanocomposites was evaluated by three point bending and notched three point bending tests, respectively. Three point bending tests were conducted on 40 × 40 × 160 mm beams at the age of 3, 7 and 28 days, using a closed-loop MTS servohydraulic testing machine with a 25 kN capacity. The rate of displacement was kept at 0.1 mm/min. The ASTM C348 was followed to determine the average values of the flexural strength and Young's modulus. Fracture mechanics tests were conducted on notched 20 × 20 × 80 mm prismatic specimens at the age of 3, 7 and 28 days, by the aforementioned experimental procedure. A 6 mm notch was introduced into the prismatic specimens using a water-cooled band saw machine. To measure the crack mouth opening displacement (CMOD) a pair of knife edges is attached at the two sides of a performed notch on the lower surface of the specimen. The crack mouth opening displacement (CMOD) at the notch, set at a rate of 0.012 mm/min, was used as the feedback control signal for running the test. Young's modulus, and fracture toughness were calculated from the load-CMOD graphs as described in [9]. Specifically, the Young's modulus is expressed from the specimens' compliance as:

$$E = \frac{6Sa_0 g_2(a_0)}{C_i b^2 t} \tag{30.1}$$

where S, b, t and a_o are specimens' dimensions presenting in Fig. 30.1, C_i (mm/N) is the initial compliance calculated from the load-CMOD curve and $g_2(a_o)$ is the geometric function calculated as:

$$g_2(a_0) = 0.76 - 2.28a_0 + 3.87a_0^2 - 2.04a_0^3 + \frac{0.66}{(1 - a_0)^2} \tag{30.2}$$

Fracture toughness values were calculated using both the loading and unloading compliances according to the two-parameter fracture model (TPFM) developed by Jenq and Shah [10].

Table 30.1 Properties and fiber count of MWCNTs and CNFs

Fiber type	Diameter (nm)	Length (μm)	Purity (%)	Surface area (m^2/gr)	Bulk density (gr/cm^3)	Aspect ratio	Fiber count
MWCNTs	20–45	≥10	>98	>200	≤0.18	500	36.1×10^{10}
CNFs	50–200	30–100	–	43	0.016–0.048	650	2.11×10^{10}

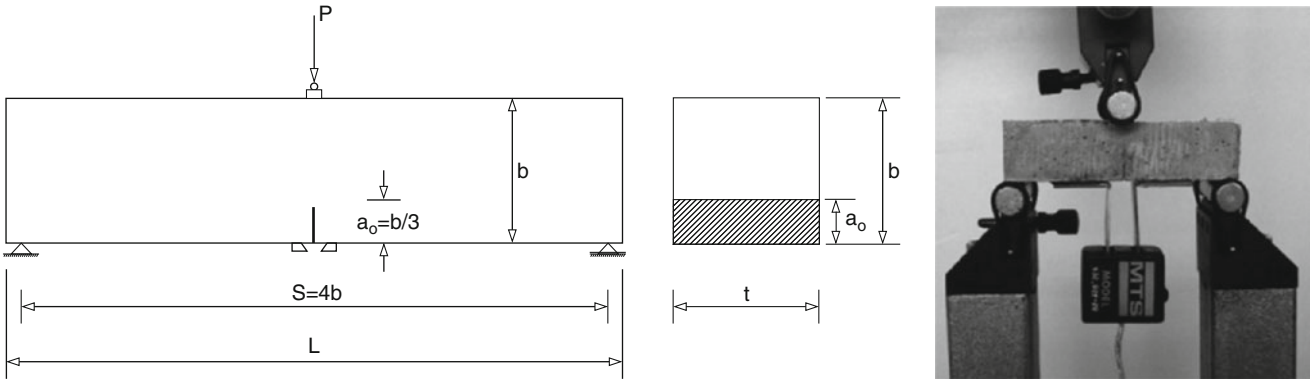

Fig. 30.1 Experimental setup of fracture mechanics test

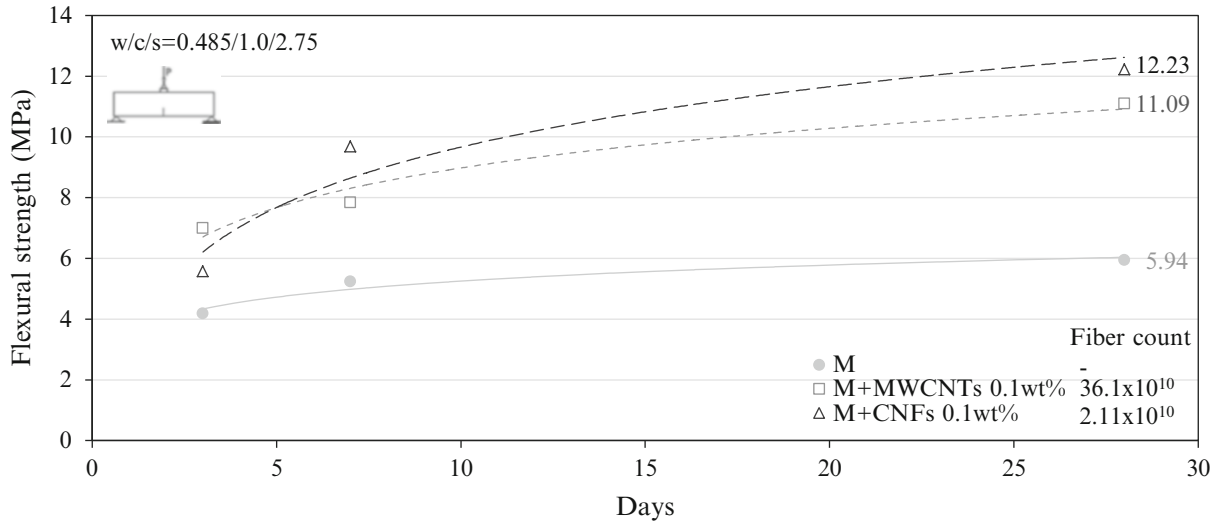

Fig. 30.2 Flexural strength of mortar nanocomposites reinforced at an amount of 0.1 wt% of cement MWCNTs and CNFs

30.3 Results and Discussion

Results of the flexural strength and Young's modulus of neat mortars and mortars reinforced with MWCNTs or CNFs at an amount of 0.1 wt% by weight of cement at the age of 3, 7 and 28 days are presented in Fig. 30.2 and Table 30.2 respectively. So far, results in the literature report either a decrease, or occasionally only a marginal increase in the flexural strength and Young's modulus of nanoreinforced cement pastes and mortars [11–14]. In our nanoreinforced mortars however, both the flexural strength and Young's modulus increase greatly, at all ages. More specifically, the 28 days nanocomposites reinforced with MWCNTs or CNFs at amounts of 0.1 wt% exhibit a 86.7 % and 105.9 % increase in flexural strength and 92.4 % and 94.3 % increase in Young's modulus, respectively. As it is depicted from Table 30.2 the Young's modulus values determined by the three point bending tests are consistent with the values determined by the fracture mechanics tests on notched specimens. It is also observed that despite the fact that the CNF fiber count is much lower than the MWCNT count, the flexural strength of the CNF nanocomposites is slightly higher than that of the MWCNT mixes. This can be explained by the CNFs' complex nanostructure. Their outer surface usually consists of conically shaped graphite planes canted with respect to the longitudinal fiber axis [15, 16]. These edges, which are present along the circumference of the fiber, can be used to help anchor the fiber in the matrix and prevent interfacial slip. Additionally, these edges provide the CNFs with a higher reinforcing efficiency. As a result the CNF cementitious composites demonstrate the ability for higher load transfer

Table 30.2 Young's modulus of MWCNT/CNF reinforced mortars

	Age	Young's modulus (GPa) 40 × 40 × 160 mm	Young's modulus (GPa) notched 20 × 20 × 80 mm
M	3	9.18	9.89
	7	10.83	12.00
	28	13.52	14.28
M + MWCNTs 0.1 wt%	3	16.01	16.68
	7	18.06	18.43
	28	27.13	27.47
M + CNFs 0.1 wt%	3	11.75	12.21
	7	16.98	16.86
	28	27.08	27.74

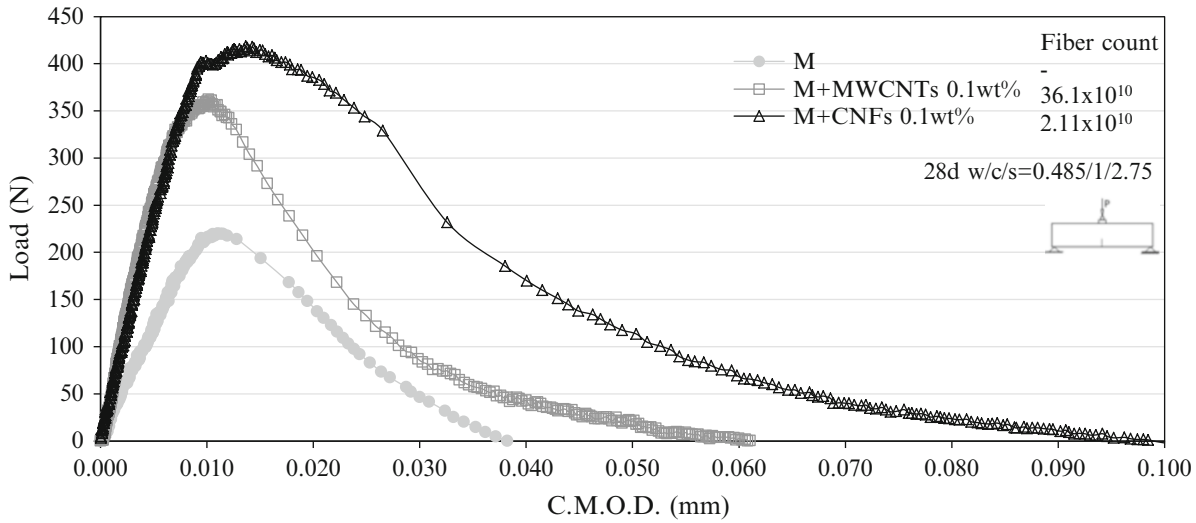

Fig. 30.3 Load-CMOD curves for 28 day neat mortar and mortar reinforced with MWCNTs or CNFs at amount of 0.1 wt% of cement (Linear elastic fracture mechanics)

efficiency, which is the key element that determines the mechanical response of the fiber nanocomposites. Typical load-CMOD curves (following the linear elastic fracture mechanics) of OPC mortar specimens and specimens reinforced with MWCNTs and CNFs at amount of 0.1 wt% of cement, are shown in Fig. 30.3. The load-CMOD response of the nanocomposite mortars revealed an increase of the peak load as much as 65 % for the MWCNT and 89 % for the CNF reinforced mortars compared to the neat mortar. Figure 30.4 shows the TPFM loading and unloading compliance curves for the neat mortar and mortar nanocomposites that are used to determine the fracture toughness, K_{IC}. The fracture toughness is the most important parameter for the characterization of a material's fracture properties. It gives a measure of the resistance of a material to the growth of existing cracks. From Fig. 30.5 it is observed that the K_{IC} values of both the MWCNT and CNF nanocomposites are higher than the values of the neat mortar at all ages. Compared to the neat mortar the 28 days MWCNT and CNF nanocomposites exhibited a 86.1 % and 119.4 % increase in fracture toughness, respectively.

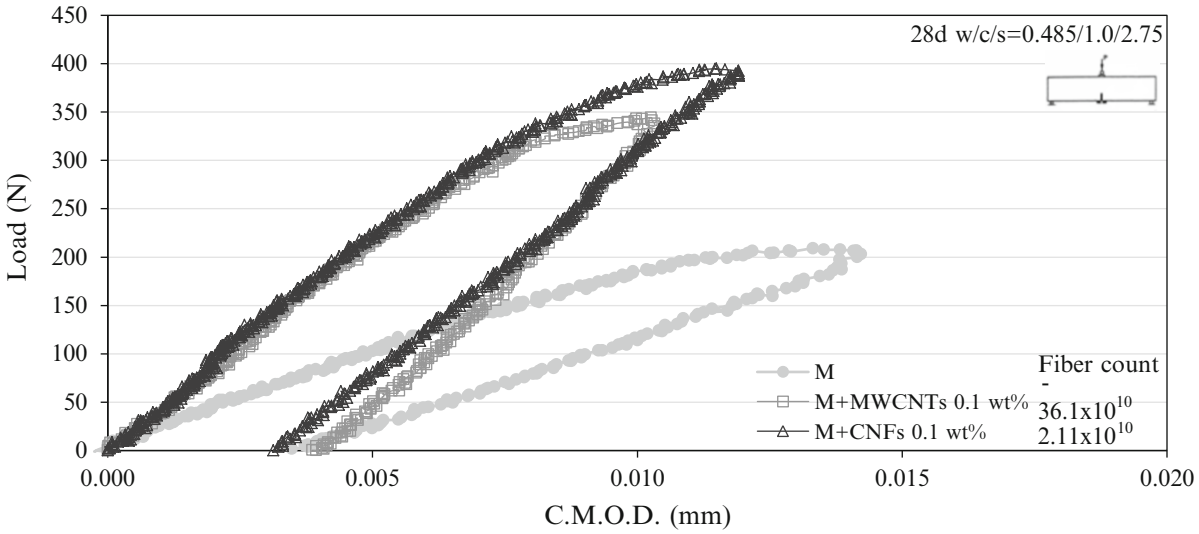

Fig. 30.4 Load-CMOD curves for 28 day neat mortar and mortar reinforced with MWCNTs or CNFs at amount of 0.1 wt% of cement (Two-parameter fracture model)

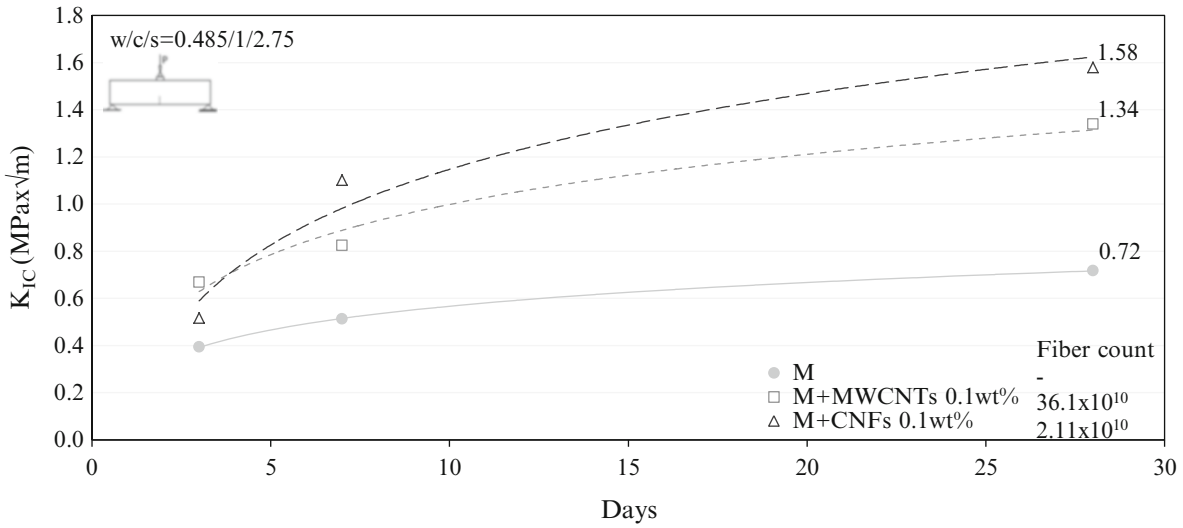

Fig. 30.5 Fracture toughness of OPC mortar and mortars reinforced at an amount of 0.1 wt% of cement MWCNTs and CNFs

30.4 Conclusions

A thorough investigation of the mechanical and fracture properties of cementitious nanocomposites reinforced with well dispersed multiwall carbon nanotubes (MWCNTs) and carbon nanofibers (CNFs) was performed. Flexural strength and Young's modulus and critical fracture toughness were investigated and compared with similarly processed reference cement based mixes without the nano-reinforcement. The excellent reinforcing capability of MWCNTs and CNFs is demonstrated by a significant improvement in flexural strength (87 % for MWCNTs and 106 % for CNFs reinforcement), Young's modulus (100 %), and fracture toughness (86 % for MWCNTs and 119 % for CNFs reinforcement).

Acknowledgements The authors would like to acknowledge the financial support of the National Strategic Reference Framework (NSRF) Research Funding Program "Thales-Democritus University of Thrace-Center for Multifunctional Nanocomposite Construction Materials" (MIS379496) funded by the European Union (European Social Fund—ESF) and Greek national funds through the Operational Program "Education and Lifelong Learning".

References

1. Belytschko, T., Xiao, S.P., Schatz, G.C., Ruoff, R.: Atomistic simulations of nanotube fracture. Phys. Rev. B **65**, 235430–235437 (2002)
2. Shah, S.P., Konsta-Gdoutos, M.S., Metaxa, Z.S.: Highly dispersed carbon nanotube-reinforced cement-based materials. US Patent and Trademark Office, United States Patent Application 20090229494, Publication number WO/2009/099640 (2009)
3. Hersam, M.C., Seo, J.-W.T., Shah, S.P., Konsta-Gdoutos, M.S., Metaxa, Z.S.: Highly Concentrated Carbon Nanotube Suspensions for Cementitious Materials and Method of Reinforcing Such Materials, Publication number US8865107 B2 and US20120042806 A1 (2014)
4. Konsta-Gdoutos, M.S., Metaxa, Z.S., Shah, S.P.: Highly dispersed carbon nanotubes reinforced cement based materials. Cem. Concr. Res. **40**, 1052–1059 (2010)
5. Metaxa, Z.S., Konsta-Gdoutos, M.S., Shah, S.P.: Carbon nanotubes reinforced concrete, American Concrete Institute. ACI Spec. Publ. **267 SP**, 11–20 (2009)
6. Metaxa, Z.S., Konsta-Gdoutos, M.S., Shah, S.P.: Mechanical properties and nanostructure of cement-based materials reinforced with carbon nanofibers and polyvinyl alcohol (PVA) microfibers, American Concrete Institute. ACI Spec. Publ. **270 SP**, 115–126 (2010)
7. Konsta-Gdoutos, M.S., Metaxa, Z.S., Shah, S.P.: Multi-scale mechanical and fracture characteristics and early-age strain capacity of high performance carbon nanotube/cement nanocomposites. Cem. Concr. Compos. **32**(2), 110–115 (2010)
8. Metaxa, Z.S., Konsta-Gdoutos, M.S., Shah, S.P.: Carbon nanofiber cementitious composites: effect of debulking procedure on dispersion and reinforcing efficiency. Cem. Concr. Compos. **32**(2), 110–115 (2010)
9. Gdoutos, E.E.: Fracture Mechanics: An Introduction, 2nd edn. Springer, Dordrecht (2005)
10. Jenq, Y., Shah, S.P.: Two parameter fracture model for concrete. J. Eng. Mech. **111**, 1227–1241 (1985)
11. Siddique, R., Mehta, A.: Effect of carbon nanotubes on properties of cement mortars. Constr. Build. Mater. **50**, 116–129 (2014)
12. Yazdani, N., Mohanam, V.: Carbon nano-tube and nano-fiber in cement mortar: effect of dosage rate and water-cement ratio. Int. J. Mater. Sci. **4**(2), 45–52 (2014)
13. Sobolkina, A., Mechtcherine, V., Khavrus, V., Maier, D., Mende, M., Ritschel, M., Leonhardt, A.: Dispersion of carbon nanotubes and its influence on the mechanical properties of the cement matrix. Cem. Concr. Compos. **34**, 1104–1113 (2012)
14. Esmaeili, J., Mohammadjafari, A.R.: Increasing flexural strength and toughness of cement mortar using multi-walled carbon nanotubes. Int. J. Nano Dimens. **5**(4), 399–407 (2014)
15. Lawrence, J.G., Berhan, L.M., Nadarajah, A.: Structureal transformation of vapor grown carbon nanofiber studied by HRTEM. J Nanoparticle. Res. **10**, 1155–1167 (2008)
16. Tibbetts, G.G., Lake, M.L., Strong, K.L., Rice, B.P.: A review of the fabrication and properties of vapor-grown carbon nanofiber/polymer composites. Compos. Sci. Technol. **67**, 1709–1718 (2007)

Chapter 31
Small Scale Thermomechanics in Si with an Account of Surface Stress Measurements

Yang Zhang, Ming Gan, and Vikas Tomar

Abstract Multiscale experiments and models have repeatedly shown that thermal and mechanical properties of materials are a strong function of the length scale of measurement. This work uses a newly established nanomechanical Raman spectroscopy approach to analyze creep deformation of microscale Si cantilevers as a function of temperature and mechanical strain. This research reports in-situ creep properties of silicon micro-cantilevers in this temperature range under uniaxial compressive stress. The experimental setup consists of micro-scale mechanical loading platform and localized heating module. The results reveal that in the stress range of 50–150 MPa, the strain rate of the silicon cantilever increases linearly as a function of applied stress. The strain rate also increases a function of temperature increase. However, the strain rate increase slows down with increase in temperature. The strain rate of the microscale silicon cantilever ($0.2–2.5 \times 10^{-6}$ s^{-1}) was comparable to literature values for bulk silicon reported in temperature range 1100–1300 °C but with only one tenth of the applied stress level. The relaxation of the near-surface atoms also contributes to the creep of the material. Analyses are also used to establish a surface stress relation in one dimensional nanostructures subjected to mechanical loading at high temperatures.

Keywords Surface stress • Silicon cantilever • Uniaxial creep • High temperature deformation mechanism • Creep exponent • Surface mechanics

With short-wavelength ultraviolet light and tip enhancement technology, the spatial resolution of Raman spectroscopy can be as high as 100 nm. For a laser wavelength of 244 nm, the penetration depth into silicon is about 6 nm. This implies that Raman spectroscopy can be used to measure the depth-sensitive stress distribution in silicon at the nanoscale. First in-situ measurements of the surface stress as a function of applied stress and as a function of temperature have only been recently reported by Tomar and co-workers, Gan et al. [1], Gan and Tomar [2–4], Gan et al. [5], in the case of silicon via development of Nanomechanical Raman Spectroscopy. The surface stress as a function of depth was determined. Microscale creep behavior of silicon cantilevers is investigated from room temperature to 100 °C.

The Nanomechanical Raman Spectroscopy experiments were carried out using an integrated nanomechanical loading Raman spectroscopy platform (Fig. 31.1a, b). The mechanical load was applied in the uniaxial direction (Fig. 31.1a) and the Raman spectroscopy apparatus approached the sample from the lateral direction (Fig. 31.1b). The sample used in this research was an AFM cantilever CT170 (Nanoscience Instruments, Inc., AZ), as shown in Fig. 31.1d. The size of the cantilever was 225 μm × 40 μm × 6.5 μm. The sample was highly-doped single-crystalline silicon, with the top surface having a [100] orientation. The laser used for Raman spectroscopy was a 514.5-nm Ar^+ laser (Modu-Laser Inc., UT) with a maximum output of 50 mW. The laser was focused and collected using a 40× objective. The Raman signals were sent to a spectrometer (Acton SP2500; Princeton Instruments Inc., NJ).

The stress inside the silicon cantilever specimens during measurements can be expressed in three different ways: σ_A—the applied stress (the applied force divided by the cross-sectional area); σ_S—the stress calculated from the measured strain and the compliance matrix; σ_R—the stress measured by Raman spectroscopy. The laser spot size in the Raman spectroscopy method used in the present work is on the micrometer length scale. Therefore, the stress obtained from Raman spectroscopy is the localized stress near the surface, which is in the vicinity of 4 μm. A comparison of σ_S and σ_R can validate the Raman deformation potentials. The comparison between the global stress (σ_A, σ_S) and the localized stress (σ_R) reveals the difference between the stress near the surface at the microscale and the applied Cauchy stress. All three stress measurements at the different temperatures are shown in Fig. 31.2 as a function of strain.

Y. Zhang • M. Gan • V. Tomar (✉)
Purdue University, West Lafayette, IN, USA
e-mail: tomar@purdue.edu

C. Ralph et al. (eds.), *Mechanics of Composite and Multi-functional Materials, Volume 7*,
Conference Proceedings of the Society for Experimental Mechanics Series, DOI 10.1007/978-3-319-21762-8_31

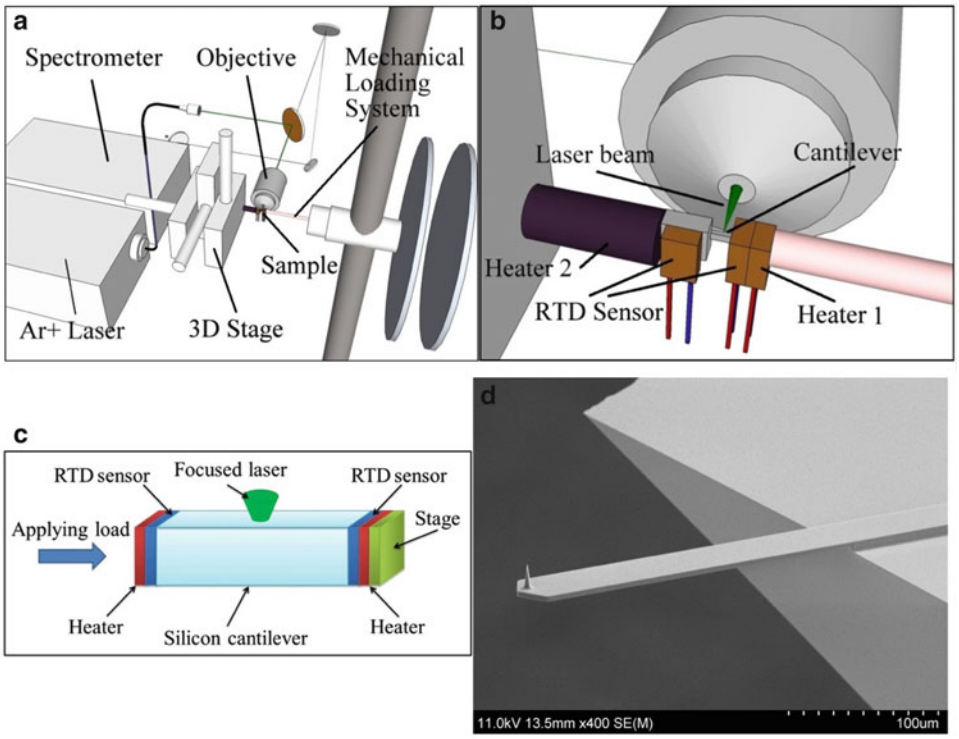

Fig. 31.1 (**a**–**c**) Diagrams of the combined mechanical loading and Raman spectroscopy setup: (**a**) overview; (**b**) detailed view; (**c**) schematic showing the directions of load application and Raman laser focus. (**d**) SEM image of a silicon cantilever sample

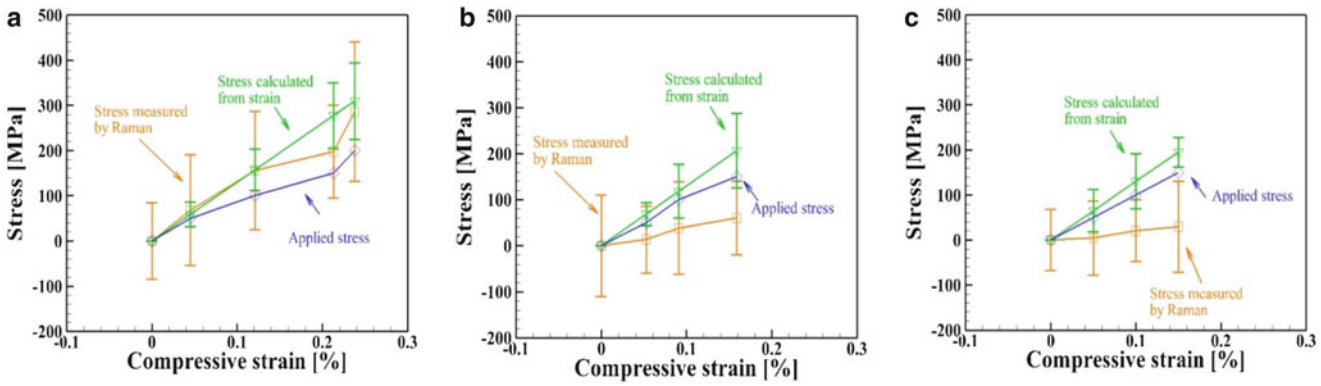

Fig. 31.2 Applied stress, stress calculated from the strain, and stress measured from Raman spectroscopy at (**a**) room temperature; (**b**) 50 °C; and (**c**) 100 °C

As pointed out in reference to Fig. 31.2, the surface stress is invariably lower than the applied stress. Based on this observation, a relationship between the two stresses can be obtained, which can be used to predict the stress at the surface, and to predict the bulk and applied stress as a function of distance from the surface as:

$$\sigma = \sigma_S \cdot \left(1 - Exp\left(-\alpha \frac{T_0}{T} \frac{d^2}{d_0^2}\right)\right). \tag{31.1}$$

Here, σ_S is the bulk stress (applied stress); d is the distance to the free surface; d_0 is the characteristic depth (constant for a given material and a fitting constant in this work), at which the stress approaches σ_S; α is a constant dependent on the

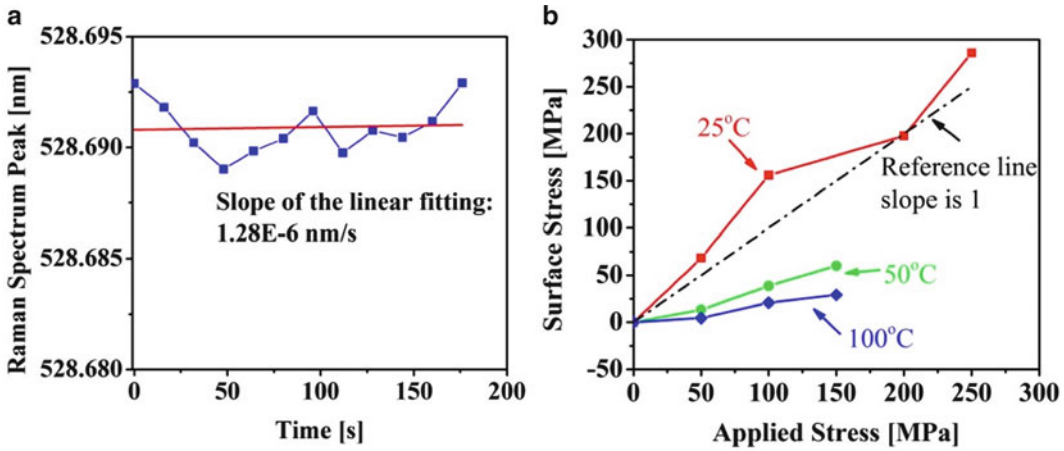

Fig. 31.3 (**a**) The effect of creep on Raman spectroscopy measurement; (**b**) comparison of near-surface stress and applied stress to the silicon cantilever

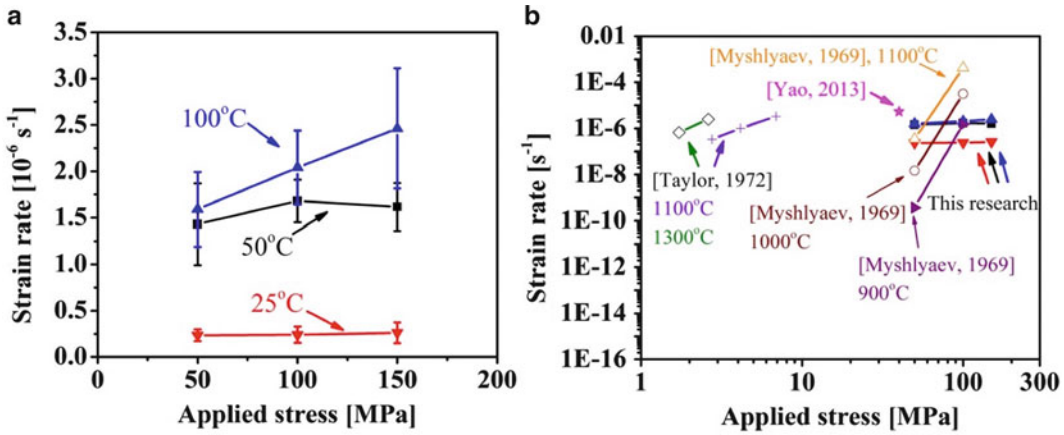

Fig. 31.4 (**a**) strain rate of the silicon cantilever as a function of applied stress at 25, 50 and 100 °C; (**b**) comparison with literature values, Yao et al. [6], Walters and Spearing [7], Taylor and Barrett [8]

geometry of the material; T is the absolute temperature in Kelvin at which the stress is being predicted; and T_0 is the room temperature. At a specific temperature, the stress at the surface is zero ($d = 0$). With increasing distance from the free surface, the stress increases rapidly to σ_S. The constant d_0 is taken as half the cross-section thickness.

The Raman shift from a single time interval of 200 s is shown in Fig. 31.3a. Considering the strain rate of the silicon cantilever is only 2.5×10^{-7} s^{-1}, for the time interval of 200 s, the strain change is 5×10^{-5}, or 0.005 %, which is at least one order of magnitude lower than the strain level in the Raman spectroscopy measurement of this research. Therefore, in the temperature range of 25–100 °C, and the stress level of ten to 100 s of MPa, the effect of creep on the Raman spectroscopy measurement is very limited during the exposure time of 200 s. The strain rate of the silicon sample measured in earlier research works was in the range of the 3×10^{-7}–3×10^{-6} s^{-1}, which is comparable to the strain rate observed in this research, Fig. 31.4.

A new analytical technology Nanomechanical Raman Spectroscopy has been developed to measure in-situ surface stress evolution at microscale and nanoscale in materials undergoing deformation as a function of temperature. Results are demonstrated in the case of silicon at microscale. Analyses show correlation between the surface stress and applied stress as a function of deformation at temperatures up to 100 °C.

References

1. Gan, M., Samvedi, V., Cerrone, A., Tomar, V.: Effect of microscale compression on nanoscale elastic modulus values of trabecular bone. Exp. Mech. **50**(6), 773–781 (2010)
2. Gan, M., Tomar, V.: An in-situ platform for the investigation of Raman shift in micro-scale silicon structures as a function of mechanical stress and temperature increase. AIP Rev. Sci. Instrum. **85**, 013902 (2014) (10 pp)
3. Gan, M., Tomar, V.: Surface stress variation as a function of applied compressive stress and temperature in microscale silicon. AIP J. Appl. Phys. **116**, 073502 (2014) (10 p)
4. Gan, M., Tomar, V.: Temperature dependent microscale uniaxial creep of silicon and surface dominated deformation mechanisms. ASME J. Nanotechnol. Eng. Med. **5**, 021004 (2014) (9 p)
5. Gan, M., Samvedi, V., Tomar, V.: A Raman spectroscopy based investigation of thermal conductivity of stressed silicon micro-cantilevers. AIAA J. Thermophys. Heat Transf. (2014). doi:10.2514/1.T4491
6. Yao, S.K., Xu, D.H., Xiong, B., Wang, Y.L.: The plastic and creep behavior of silicon microstructure at high temperature. In: Solid-State Sensors, Actuators and Microsystems (TRANSDUCERS & EUROSENSORS XXVII), 2013 Transducers & Eurosensors XXVII: The 17th International Conference on. (2013)
7. Walters, D.S., Spearing, S.M.: On the flexural creep of single-crystal silicon. Scr. Mater. **42**(8), 769–774 (2000)
8. Taylor, T.A., Barrett, C.R.: Creep and recovery of silicon single crystals. Mater. Sci. Eng. **10**, 93–102 (1972)

Chapter 32
Magnetorheological Elastomers: Experimental and Modeling Aspects

Laurence Bodelot, Tobias Pössinger, Kostas Danas, Nicolas Triantafyllidis, and Christian Bolzmacher

Abstract Magnetorheological elastomers (MREs) are active composite materials that deform under a magnetic field because they are made of a soft elastomer matrix filled with magnetizable micrometric particles. Along with short response times and low magnetic inputs, not only do MREs alter their viscoelastic properties and stiffness in response to external magnetic fields but they can also undergo very high deformation states. While the former effect can be exploited in controllable-stiffness devices, the latter is of interest for haptic devices such as tactile interfaces for the visually impaired. In the perspective of developing a persistent tactile MRE surface exhibiting reversible and large out-of-plane deformations, the first part of this work focuses on the fabrication of MREs that can sustain large deformations. In particular, we determine the critical strain threshold up to which the interfacial adhesion between particles and matrix is ensured. In the second part of this work, an experimental setup is developed in order to characterize MRE composites under coupled magneto-mechanical mechanical loading. The experiments conducted on this setup will eventually serve as an input for a continuum model describing magneto-mechanical coupling.

Keywords Magnetorheological elastomers • Active materials • Multiphysics couplings • Magneto-mechanical characterization • Constitutive modeling

32.1 Introduction

Materials whose properties can be tuned by the application of an external stimulus, or that can respond rapidly and reversibly to changes in their environment, belong to the specific class of active materials, also known as smart materials. More particularly, soft active materials encompass electroactive polymers (EAPs), magnetorheological fluids (MRFs) and magnetorheological elastomers (MREs). EAPs consist of a dielectric (polymer) that is sandwiched into two compliant electrodes and that deforms under an applied voltage [1]. The voltage required to reach large deformations is unfortunately on the order of kilovolts, which limits practical applications of such actuators, even more so by the risk of a dielectric breakdown of the polymer. MRFs are two-phase metallic particle suspensions, whose flow or shear properties can be changed by an externally applied magnetic field requiring rather low electrical input compared to the EAPs. Since the early 2000s, they have found their way into a wide variety of applications such as clutches, vibration dampers and shock absorbers for the high-end automotive industry [2]. However, MRFs suffer from the settling down of particles over time as well as a risk of leakage when the shell surrounding them wears out. This thus limits their range of possible applications to only mildly demanding environments in which parts can be replaced.

MREs, which are the subject of this study, are the solid counterparts of MRFs. They are composite materials made of two phases. One phase serves as the matrix and is an elastomeric material (e.g., silicone, rubber. . .). This matrix phase is non-magnetic but is rather soft such that it can carry large deformations without fracturing. The second phase is made of a magnetic material (e.g., iron or rare earth magnets) and usually is in the form of micrometric particles embedded in the soft elastomeric phase [3, 4]. By application of an external magnetic field on the cured composite, the particles re-arrange their positions in the solid in order to align with the applied magnetic field, thus inducing a deformation of the matrix phase and, overall, of the composite. Along with short response times (of the order of milliseconds) and low magnetic inputs, not only can MREs alter their viscoelastic properties and stiffness in response to external magnetic fields but they can also undergo very high deformation states. While the former effect is of interest for the next generation of haptic devices such as tactile

L. Bodelot (✉) • K. Danas • N. Triantafyllidis
Ecole Polytechnique, Laboratoire de Mécanique des Solides, Route de Saclay, Palaiseau Cedex 91128, France
e-mail: laurence.bodelot@polytechnique.edu

T. Pössinger • C. Bolzmacher
CEA LIST Sensorial and Ambient Interfaces Laboratory, Gif-sur-Yvette Cedex 91191, France

C. Ralph et al. (eds.), *Mechanics of Composite and Multi-functional Materials, Volume 7*,
Conference Proceedings of the Society for Experimental Mechanics Series, DOI 10.1007/978-3-319-21762-8_32

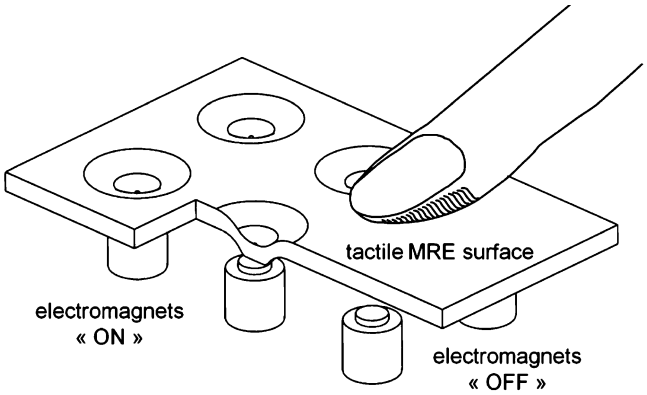

Fig. 32.1 Schematics of the working principle of a tactile MRE interface with patterns created by a matrix of electromagnets placed underneath a MRE layer

interfaces for the visually impaired, the latter can be exploited in controllable-stiffness devices for numerous advanced damping applications ranging from aircraft to prostheses as well as adaptive materials applications. They are indeed more energy-efficient than intrinsically stiffer EAPs that require high-voltage inputs. They are also more reliable than MRFs used so far in haptic applications since these fluids face a degradation of their properties over time.

In spite of such a potential, these materials have been seldom utilized in commercial applications because the design of MRE-based devices has been so far accomplished through an empirical approach, in contrast with the advanced numerical modeling methodology currently used in the design of standard elastomer components such as tires. The main difficulties in analyzing the response of MREs are the need for a dedicated multiphysics experimental characterization as well as coupled magneto-mechanical theories. In the perspective of developing a persistent tactile MRE surface exhibiting reversible and large out-of-plane deformations as sketched in Fig. 32.1, the next section of this paper focuses on the fabrication of MREs that can sustain large deformations. In particular, we determine the critical strain threshold up to which the interfacial adhesion between particles and matrix is ensured. In the third section, an experimental setup is developed in order to characterize MRE composites under coupled magneto-mechanical mechanical loading. These experiments will serve as an input for a continuum model describing magneto-mechanical coupling that is exposed in the fourth section. Finally, Section 32.5 concludes the paper.

32.2 Study of Interfacial Adhesion

An important aspect influencing the strength of a composite material, especially under large deformations, is the interfacial adhesion between the filler particles and the matrix [5]. Indeed, at a critical stress level, debonding acts as a distinct failure phenomenon in a polymer containing rigid inclusions due to stress concentrations at the weak particle-matrix interface [6]. After some studies showed the improved bond strength between many silane-primed metallic surfaces and addition-cured silicon elastomers [7], different kinds of silane primers and have been used in MREs [8] in order to modify the particle-matrix interactions and more precisely to improve their interfacial adhesion. A silane primer typically consists of two different reactive groups, one compatible with the filler particles and the other one with the elastomer matrix, and serves as an adhesion promoter between the two initially non-bonding surfaces.

Although the phenomenon of interfacial adhesion appears to be a key property for the behavior of filled soft elastomer composites, the interfacial adhesion at high tensile deformations in soft MREs has rarely been investigated in detail. In this section, we address the crucial question of interfacial adhesion between the particles and the elastomer for the MRE composites used in this work. We investigate how a pretreatment of the particles with a silane primer can modify the interfacial adhesion both from a microscopic and a macroscopic perspective and settle upon whether such pretreatment is needed in the rest of the study. More particularly, different MRE samples are prepared by modifying the surface of the CIP via silane primer treatment according to two procedures, prior to samples fabrication. These samples are then compared to a sample without particle treatment both under scanning electron microscope (SEM) and during mechanical testing.

In the perspective of obtaining optimal magneto-mechanical coupling, a very soft elastomer (Shore A hardness of 00–20), Ecoflex0020 from Smooth-On Inc, is used as the matrix material. Pure silicone samples are obtained by mixing Part A (the silicone) and Part B (platinum-based catalyzer) in equal proportions. The compound is then degassed to remove the air

entrapped during mixing, poured in a mold and cured at 100 °C during 30 min. For MRE composite samples, spherical Carbonyl Iron Particles (CIP) SM (average diameter of 3.5 μm) from BASF are added to Part A prior to the pouring of Part B. Following previous works [8], though they were focusing on small strains, tests were conducted with a silane-based primer, clear 1200 OS Primer from Dow Corning, in order to identify the optimal way to apply the primer onto the particles. Two techniques were used: (1) mixing the particles in primer, filtering the mix and letting the particles dry on a teflon plate for 45 min and (2) dispersing the particles in a plastic container, spraying the primer with an airbrush onto the particles while shaking the container and letting them dry for 45 min. The particles were then used in the fabrication procedure mentioned above and samples with a 20 % particles weight fraction were fabricated using the two primer application techniques. An additional sample with non-treated particles was also fabricated. All samples were then cut open with a scalpel, maintained under a tension of 140 % nominal strain and observed under SEM (Quanta 600 FEG SEM operated at 10 kV). While the matrix was cleanly detaching from the particles for the non-treated sample, treated samples showed adhesion of the matrix to the particles through matrix strands that remained attached to the particles. These strands were in greater number and much wider, covering nearly all the particle surface, in the case of the primer applied by airbrush, thus suggesting that method (2) was more appropriate to apply primer onto the particles.

The mechanical response under tension was then investigated for non-treated samples and samples in which the particles were spray-coated, for three different particles weight fractions: 20 %, 140 % and 170 %. In these preliminary experiments, samples are 24 mm × 24 mm × 4 mm in size and loaded with step motors equipped with load cells [9]. A uniaxial tensile test was conducted on each sample after a pre-conditioning of ten cycles. For elastomers, pre-conditioning consists in submitting the sample to cyclic loading prior to the actual test in order to attain a stabilized behavior after an initial cyclic softening known as Mullins effect [10]. The corresponding results are reported in Fig. 32.2. For the lowest particle weight fraction, the effect of the primer treatment is nearly negligible on the macroscopic mechanical response of the corresponding sample. For higher particle weight fractions, one observes a threshold in nominal strain above which the response of non-treated and primer treated (by spray-coating) is no longer the same, the primer-treated sample showing a significantly larger stiffness above the threshold, sign of an enhanced adhesion between the particles and the matrix. In the case of the highest weight fraction studied, this threshold is 80 % in nominal strain. In the present study, since we will use particles weight fractions below 170 % and remain under 80 % in nominal strain, particles will not be primer-coated in order to reduce the samples fabrication time.

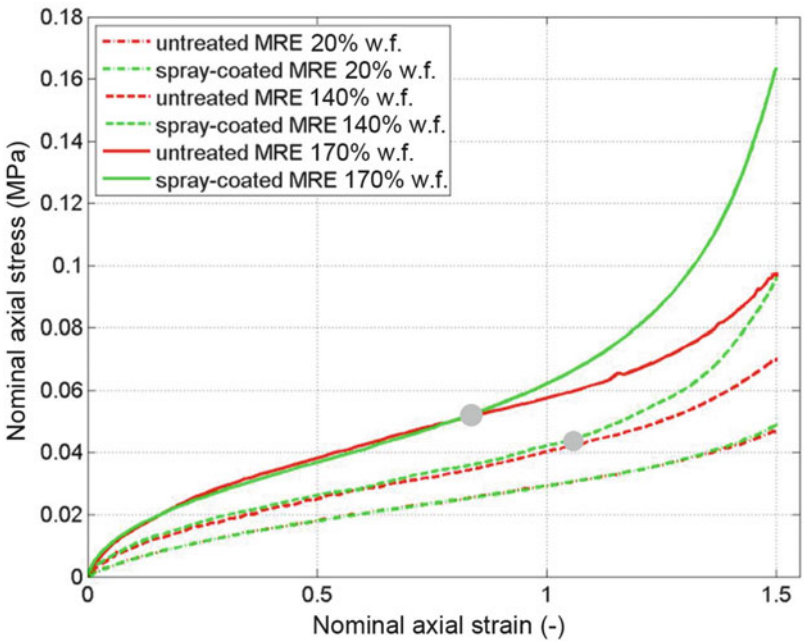

Fig. 32.2 Macroscopic uniaxial tensile behavior of non-treated and primer-treated MREs (by spray-coating technique) for different particles weight fractions

32.3 Magneto-Mechanical Experimental Characterization

In order to characterize experimentally the coupled magneto-mechanical behavior of MRE samples, a dedicated tensile setup has been developed and is presented in Fig. 32.3. The magnetic field is generated by a two-coil electromagnet that yields a homogeneous field, up to 0.8 T, within two 90 mm-diameter poles situated 82 mm apart from each other. The symmetric tension setup, installed at the center of the magnetic field, consists in two Piezo LEGS actuators from PiezoMotors mounted on 6 N-capacity OMEGA load cells and equipped with RENISHAW optical encoders allowing for closed-loop displacement control. Local strains are measured at the center of the specimen by optical extensometry. The setup is equipped with a mirror next to the sample to access deformations along the three principal axes of the sample at once. At the beginning of the test, Hall probes located behind and on the side of the sample (see Fig. 32.3b) give access to the applied magnetic field and the initial magnetization of the sample, respectively.

In order to validate the experimental setup and its optical diagnostics, a uniaxial tensile test was conducted on a pure elastomer cylindrical dog-bone-shaped sample after a pre-conditioning of ten cycles. Results in terms of nominal axial stress as a function of axial stretch ratio are presented in Fig. 32.4a. For this experiment, calculation of the transformation Jacobian from the three principal dilatations confirms (by equaling one) the incompressible behavior of the silicone and thus the proper alignment of the optical extensometry system. A second MRE composite cylindrical dog-bone-shaped sample (70 % in particles weight fraction) is then tested under pure mechanical tensile loading. The plot of its axial nominal stress as a function of axial stretch ratio (Fig. 32.4b) shows a stiffer behavior for the filled elastomer in comparison to the pure silicone. Finally, the previous sample initially at rest is submitted to a pure magnetic loading. In this case, the evolution of the three

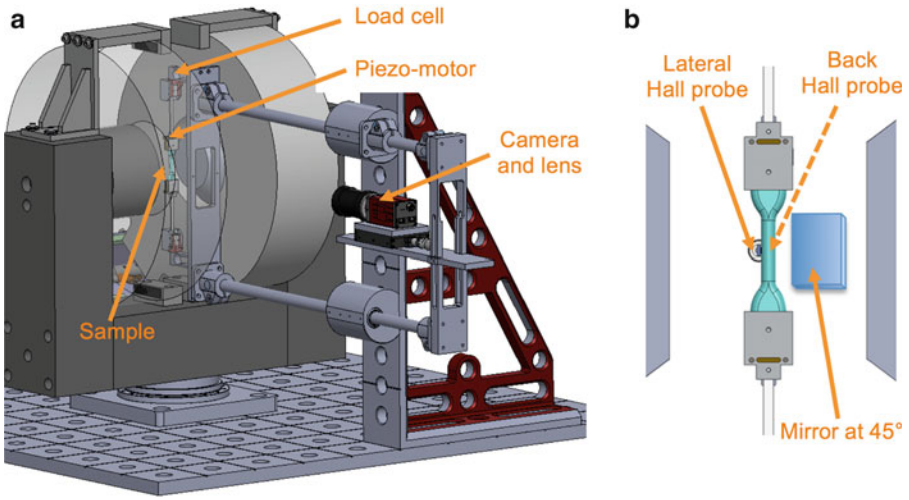

Fig. 32.3 (**a**) Schematics of the setup dedicated to the coupled magneto-mechanical characterization of MREs (**b**) Close-up schematics within the poles of the electromagnet

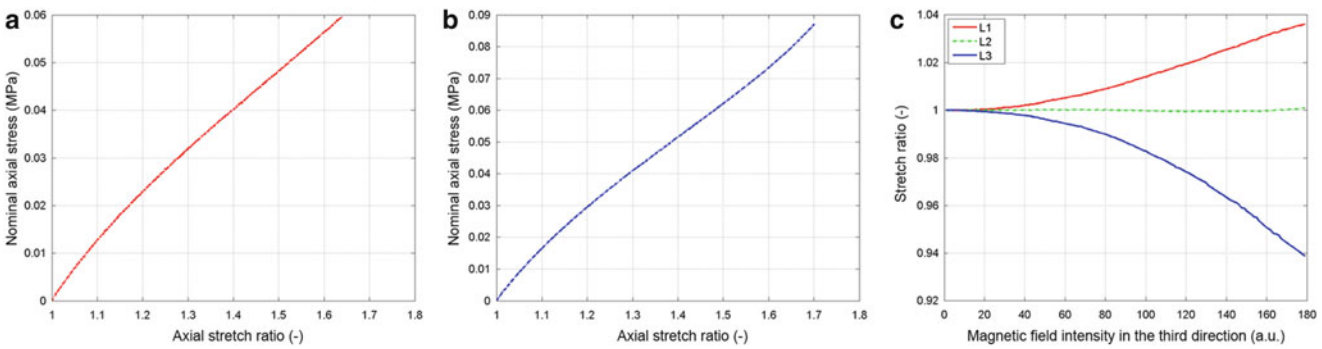

Fig. 32.4 (**a**) Behavior of pure silicone under mechanical loading (**b**) Behavior of MRE composite (70 % in particles weight fraction) under mechanical loading (**c**) Evolution of principal stretch ratios of MRE composite (70 % in particles weight fraction) under magnetic loading

principal stretch ratios is reported as the magnetic field intensity increases. In Fig. 32.4c, where L2 represents the axial stretch ratio whereas L1 and L3 correspond to the transverse stretch ratios, perpendicularly and along the field, respectively, one can infer the change undergone by the section of the sample: from circular, it becomes elliptic underneath the sole effect of the magnetic field (the major axis of the ellipse is along the magnetic field).

Following these preliminary results, a more complete characterization including different weight fractions of particles and coupled loading will be conducted and serve as an input to identify the parameters of the continuum model describing magneto-mechanical couplings.

32.4 Constitutive Modeling

The approach used in this work is based on the fully-coupled minimization variational principle proposed by Dorfmann and Ogden [11]. Since the interest here is the modeling of the behavior of MREs at finite strains, the most convenient framework is indeed the one using minimum variational principles and Lagrangian kinematics, in which the free energy of the solid under study is described by Lagrangian measures of the deformation and the magnetic field in the undeformed configuration. This approach is based on the minimization of the potential energy $\varepsilon(\mathbf{u}, \mathbf{M}, \mathbf{A})$ of the magnetoelastic solid, given by:

$$\varepsilon(\mathbf{u},\ \mathbf{M},\ \mathbf{A}) = \int_V \rho_0(\psi - \mu_0 \mathbf{h}_0 \bullet \mathbf{M} - \mathbf{b} \bullet \mathbf{u})\, dv \ + \frac{1}{2\mu_0}\int_{\mathbf{R}^3} \|\nabla \times \mathbf{A} \ - \mu_0 \rho_0 \mathbf{M}\|^2\, dv - \int_{\partial \mathbf{V}} \mathbf{t} \bullet \mathbf{u}\, da, \tag{32.1}$$

where $\boldsymbol{\psi}(\mathbf{C}, \mathbf{M})$ is the free energy plus magnetic dipole energy and is a function of $\mathbf{C}$ (right Cauchy-Green tensor) and of $\mathbf{M}$ the magnetization per unit mass. $\mathbf{u}$ is the displacement, $\mathbf{h}_0$ is the externally applied magnetic field, $\mathbf{b}$ is the externally applied non-magnetic body force (e.g., gravity) per unit mass, $\mathbf{A}$ is the vector potential for the magnetic field perturbation, ρ_0 is the reference mass density, μ_0 is the magnetic permeability of free space and $\mathbf{t}$ is the externally applied mechanical traction. Notice that the magnetic energy appears in the second integral over the entire space R^3 since the magnetic field also exists outside the solid under consideration, which occupies a volume V with boundary ∂V. The above potential energy is a functional of $\mathbf{u}$, $\mathbf{M}$, and $\mathbf{A}$, which are its independent variables. The Euler-Lagrange equations with respect to $\mathbf{A}$ are Ampere's equations and interface conditions (across an interface with reference normal $\mathbf{N}$), namely:

$$\varepsilon_{,\mathbf{A}}\ \delta\mathbf{A} = \ 0 \quad \Rightarrow \quad \nabla \times \mathbf{H} = \mathbf{0} \ \text{ in } \ \mathbb{R}^3, \qquad \mathbf{N} \times [\![\mathrm{H}]\!] = \mathbf{0} \quad \text{on } \ \partial V, \qquad \mathbf{H} = \mathbf{h} \bullet \mathbf{F} \ , \tag{32.2}$$

where $\mathbf{H}$ and $\mathbf{h}$ are the h fields in the reference and current configurations respectively and $\mathbf{F}$ the deformation gradient. Variation with respect to specific magnetization $\mathbf{M}$ gives the magnetic part of the constitutive response:

$$\varepsilon_{,\mathbf{M}}\ \delta\mathbf{M} = 0 \quad \Rightarrow \frac{\partial \psi}{\partial \mathbf{M}} = \mu_0 \mathbf{h}. \tag{32.3}$$

Variation with respect to displacement $\mathbf{u}$ gives the equations of mechanical equilibrium and corresponding interface conditions:

$$\varepsilon_{,\mathbf{u}}\ \delta\mathbf{u} = 0 \quad \Rightarrow \quad \nabla \bullet \mathit{\Pi} \ + \ \rho_0\ \mathbf{f} = \ 0 \ \text{ in } \ V, \qquad \mathbf{N} \bullet [\![\mathbf{\Pi}]\!] \ = \mathbf{T} \quad \text{on } \ \partial V \ , \tag{32.4}$$

where the first Piola-Kirchhoff stress $\mathbf{\Pi}$, is related to the total Cauchy stress $\boldsymbol{\sigma}$ by:

$$\mathbf{\Pi} = J\mathbf{F}^{-1} \bullet \ \boldsymbol{\sigma}, \qquad \boldsymbol{\sigma} = \rho_0 \left(2\mathbf{F} \bullet \frac{\partial \psi}{\partial \mathbf{C}} \bullet \mathbf{F}^T \ + \ \mu_0 (\mathbf{M}\mathbf{h} + \mathbf{h}\mathbf{M})\right) + \mu_0 \left(\mathbf{h}\mathbf{h} - \frac{1}{2}(\mathbf{h} \bullet \mathbf{h})\mathbf{I}\right). \tag{32.5}$$

Notice from (32.5) that the total Cauchy stress $\boldsymbol{\sigma}$ has a mechanical part (term in ψ, recognized from finite elasticity) plus a magnetic part termed Maxwell stress. It is worth noticing that even in the absence of material ($\rho_0 = 0$) the Maxwell stress component is nonzero, which is a bit strange for solid mechanics where the concept of stress is associated with the presence of a solid, but here the magnets exert a net force to each other resulting to the above stress measure.

Finally, the phenomenological characterization of an MRE as a continuum will require the determination of the free energy ψ (**C**, **M**). Following the formulation proposed by Kankanala and Triantafyllidis [12], this free energy can be expressed as a function of invariants linked to the deformation gradient **F** and the magnetization **M**. The coefficients appearing in the expression of the free energy will be identified on experimental data.

32.5 Conclusion

In the perspective of developing a persistent tactile MRE surface exhibiting reversible and large out-of-plane deformations, we studied the interfacial adhesion between carbonyl iron particles and the elastomer matrix in MREs submitted to large deformations. Coating the particles with a silane primer prior to sample fabrication does improve the macroscopic mechanical behavior, in terms of stiffness, though only above a critical strain threshold that depends on the particles weight fraction. Hence, in the deformation ranges targeted in this work, particles will not be primer-coated so as to reduce the samples fabrication time. In a second part of this work, an experimental setup was developed in order to characterize MRE composites under coupled magneto-mechanical mechanical loading. The experiments conducted on this setup will serve as an input for a continuum model describing magneto-mechanical coupling.

References

1. Pelrine, R., Kornbluh, R., Pei, Q., Joseph, J.: High-speed electrically actuated elastomers with strain greater than 100 %. Science **287**, 836–839 (2000)
2. Carlson, J.D., Jolly, M.R.: MR fluid, foam and elastomer devices. Mechatronics **10**, 555–569 (2000)
3. Ginder, J.M., Nichols, M.E., Elie, L.D., Clark, S.M.: Controllable-stiffness components based on magnetorheological elastomers. Proc. SPIE **3985**, 418–425 (2000)
4. Danas, K., Kankanala, S.V., Triantafyllidis, N.: Experiments and modeling of iron-particle-filled magnetorheological elastomers. J. Mech. Phys. Solids **60**, 120–138 (2012)
5. Dekkers, M.E.J., Heikens, D.: The effect of interfacial adhesion on the tensile behavior of polystyrene–glass-bead composites. J. Appl. Polym. Sci. **28**, 3809–3815 (1983)
6. Gent, A.N., Park, B.: Failure processes in elastomers at or near a rigid spherical inclusion. J. Mater. Sci. **19**, 1947–1956 (1984)
7. Peignot, P., Rhodes, K.: Choosing a silicone adhesive and treatment system. Med. Device Technol. **15**, 22–24 (2004)
8. Coquelle, E., Bossis, G., Szabo, D., Giulieri, F.: Micromechanical analysis of an elastomer filled with particles organized in chain-like structure. J. Mater. Sci. **41**(18), 5941–5953 (2006)
9. Pössinger, T., Bolzmacher, C., Bodelot, L., Triantafyllidis, N.: Interfacial adhesion between the iron fillers and the silicone matrix in magneto-rheological elastomers at high deformations. Proc. SPIE **8763**, 87631Y-11 (2013)
10. Mullins, L., Tobin, N.R.: Theoretical model for the elastic behavior of filler-reinforced vulcanized rubbers. Rubber Chem. Technol. **30**, 555–571 (1957)
11. Dorfmann, A., Ogden, R.: Magnetoelastic modelling of elastomers. Eur. J. Mech. A. Solids **22**, 497–507 (2003)
12. Kankanala, S.V., Triantafyllidis, N.: On finitely strained magnetorheological elastomers. J. Mech. Phys. Solids **52**, 2869–2908 (2004)

Chapter 33
Failure Criteria of Composite Materials Under Static and Dynamic Loading

I.M. Daniel

Abstract To facilitate and accelerate the process of introducing, evaluating and adopting new material systems, it is important to develop/establish comprehensive and effective procedures of characterization, modeling and failure prediction of structural laminates based on the properties of the constituent materials, e.g., fibers, matrix, and the single ply or lamina. A new failure theory, the Northwestern (NU-Daniel) theory, has been proposed for predicting lamina yielding and failure under multi-axial states of stress including strain rate effects. It is primarily applicable to matrix-dominated interfiber/interlaminar failures. It is based on micromechanical failure mechanisms but is expressed in terms of easily measured macroscopic lamina stiffness and strength properties. It is presented in the form of a master failure envelope incorporating strain rate effects. The theory was further adapted and extended to the prediction of in situ first ply yielding and failure (FPY and FPF) and progressive failure of multi-directional laminates under static and dynamic loadings. The significance of this theory is that it allows for rapid screening of new composite materials without very extensive testing and offers easily implemented design tools.

Keywords Mechanical characterization • Dynamic testing • Failure criteria • Failure envelopes • Strain rate effects

33.1 Introduction

Composite materials in service are exposed to severe loading and environmental conditions which pose new challenges to the designer. In many structural applications composite materials are exposed to high energy, high velocity dynamic loadings producing multi-axial dynamic states of stress. Under these conditions composites exhibit nonlinear and rate-dependent behavior. The process of fabrication, testing and modeling of these composites is costly and time consuming and impedes the introduction of new materials. To facilitate and accelerate the process of introducing and evaluating new composite materials, it is important to develop/establish comprehensive and effective methods and procedures of constitutive characterization and modeling of structural laminates based on the properties of the constituent materials, e.g., fibers, polymers and the basic building block of the composite structure, the single ply or lamina.

Failure of composite materials has been investigated extensively from the physical and phenomenological points of view, on microscopic and macroscopic scales. On the micromechanical scale, failure initiation and failure mechanisms vary widely with type of loading and are intimately related to the mechanical, physical and geometric properties of the constituent phases.

On the macromechanical lamina scale, numerous failure theories have been proposed for analysis of composites and reviewed in the literature [1–12]. The plethora of theories is accompanied by a dearth of suitable and reliable experimental data. A recent development is a new failure theory developed at Northwestern University (NU-Daniel theory) which has been proven very successful in predicting yielding and failure of a composite lamina under multi-axial states of stress and varying strain rates [13, 14]. This theory addresses a class of problems where other theories differ the most from each other. The challenge now is to adapt and extend this new theory to the analysis of progressive failure of multi-directional structural laminates under multi-axial static and dynamic loadings and offer easily implemented engineering design tools.

I.M. Daniel
Northwestern University, Evanston, IL, USA
e-mail: imdaniel@northwestern.edu

C. Ralph et al. (eds.), *Mechanics of Composite and Multi-functional Materials, Volume 7*,
Conference Proceedings of the Society for Experimental Mechanics Series, DOI 10.1007/978-3-319-21762-8_33

33.2 Characterization of Composite Lamina

Two unidirectional material systems were investigated, AS4/3501-6 and IM7/8552 carbon/epoxy composites. The first one displays quasi-brittle behavior, has been studied more extensively and there is a large body of data available for it. The second system has a higher strength carbon fiber and displays a higher degree of nonlinearity and ductility. Multi-axial experiments were performed by testing unidirectional carbon/epoxy specimens at various loading directions with respect to the principal fiber reinforcement. These experiments produced primarily stress states combining transverse normal and in-plane shear stresses.

Experiments were conducted at three strain rates. Quasi-static and intermediate rate tests were conducted in a servohydraulic testing machine at strain rates of 10^{-4} s^{-1} and 1 s^{-1}, respectively. High strain rate tests were conducted by means of a split Hopkinson (Kolsky) pressure bar at strain rates ranging from 180 to 400 s^{-1} using prismatic off-axis specimens (Fig. 33.1). Stress-strain curves were obtained for various off-axis loadings corresponding to different biaxial stress states at various strain rates (Fig. 33.2). The ultimate values provide failure data for various biaxial states of stress.

33.3 Strain-Rate-Dependent Failure Criteria

Most failure theories assume linear elastic behavior and are expressed in terms of macroscopic lamina stresses and strength parameters along the principal material axes. These theories in general can be divided into three categories: (1) *Limit or non-interactive theories*, such as the maximum stress and maximum strain theories, (2) *Fully interactive theories* such as the Tsai-Hill and the Tsai-Wu criteria, and (3) *Partially interactive or failure mode based theories*, such as the Hashin-Rotem, Puck, and NU-Daniel theories. The popular fully interactive Tsai-Wu criterion is expressed in the form of a failure polynomial involving all the stress components [1]. The Hashin-Rotem criteria are based on the premise that failure on any plane is only a function of the stress components acting on that plane. Furthermore, separate fiber and interfiber failure modes are considered. The Puck and Sh□rmann theory is based on the concept of internal friction and a modified Coulomb-Mohr criterion [6]. Sun et al. proposed an empirical modification of the Hashin-Rotem criterion for matrix compressive failure to account for the apparent increase in shear strength due to the transverse compressive stress [2]. Predictions of the various theories, even for a simple unidirectional lamina, can differ a great deal from each other. Failure theories deviate the most from each other for states of stress involving transverse compression and interfiber shear.

The Northwestern (NU-Daniel) interfiber/interlaminar failure theory is based on micromechanical matrix failure mechanisms but is expressed in terms of easily measured macromechanical properties. Three dominant failure mechanisms or modes are identified in a composite element consisting of fibers and interfiber matrix, compression, shear and tension dominated modes [10]. In the compression dominated case, the composite element is loaded primarily in transverse compression with a non-dominant shear component. Failure is assumed to be governed by the maximum (critical) elastic shear strain in the interfiber matrix while the strain along the fiber is constrained to be zero. In the shear dominated case, the composite element is loaded primarily in in-plane shear with a non-dominant compression component. Failure is assumed to be governed by the maximum (critical) elastic tensile strain in the interfiber matrix while constraining the strain component along the fibers. In the tension dominated case, the composite element is loaded primarily in tension with a non-dominant

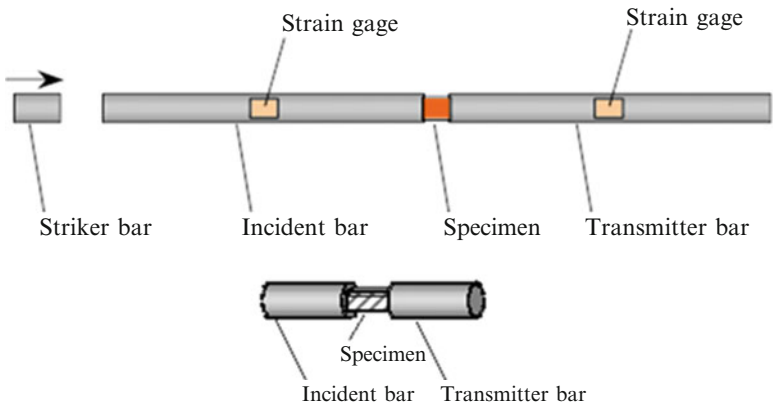

Fig. 33.1 High rate testing of composite specimens in Hopkinson bar

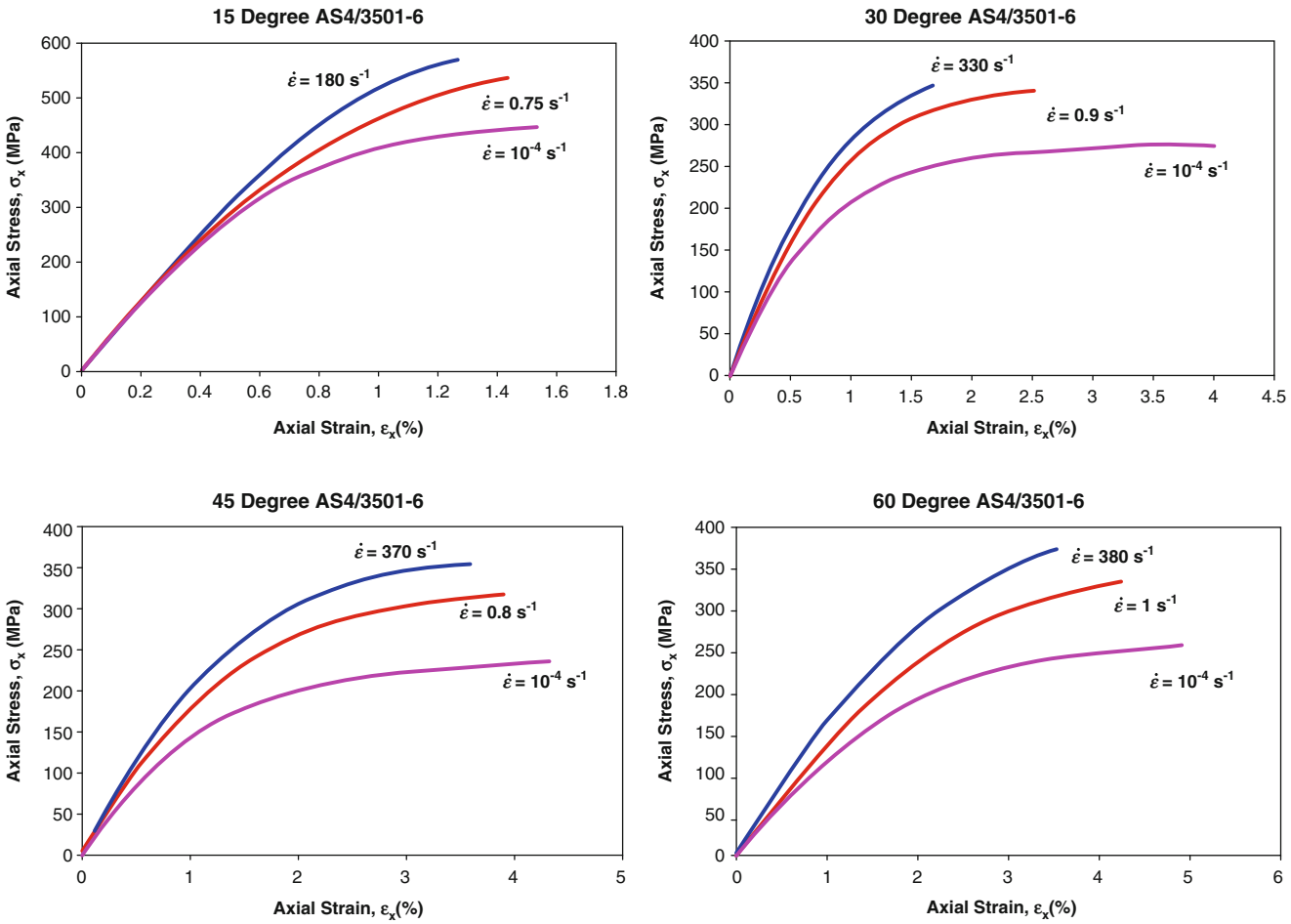

Fig. 33.2 Stress-strain curves for various states of stress at three strain rates

shear component. Failure is assumed to be governed by the maximum (critical) elastic tensile strain in the interfiber matrix while constraining the strain component along the fibers. These failure modes are expressed by the following failure criteria:

Compression dominated failure:

$$\left(\frac{\sigma_2}{F_{2c}}\right)^2 + \alpha^2\left(\frac{\tau_6}{F_{2c}}\right)^2 = 1 \tag{33.1}$$

Shear dominated failure:

$$\left(\frac{\tau_6}{F_6}\right)^2 + \frac{2}{\alpha}\frac{\sigma_2}{F_6} = 1 \tag{33.2}$$

Tension dominated failure:

$$\frac{\sigma_2}{F_{2t}} + \left(\frac{\alpha}{2}\right)^2\left(\frac{\tau_6}{F_{2t}}\right)^2 = 1 \tag{33.3}$$

where σ_2 and τ_6 are the transverse (to the fibers) normal stress and in-plane shear stress; F_{2t}, F_{2c} and F_6 are the transverse normal tensile and compressive strengths and in-plane shear strength, respectively; $\alpha = E_2/G_{12}$ is the ratio of the transverse Young's to the in-plane shear modulus.

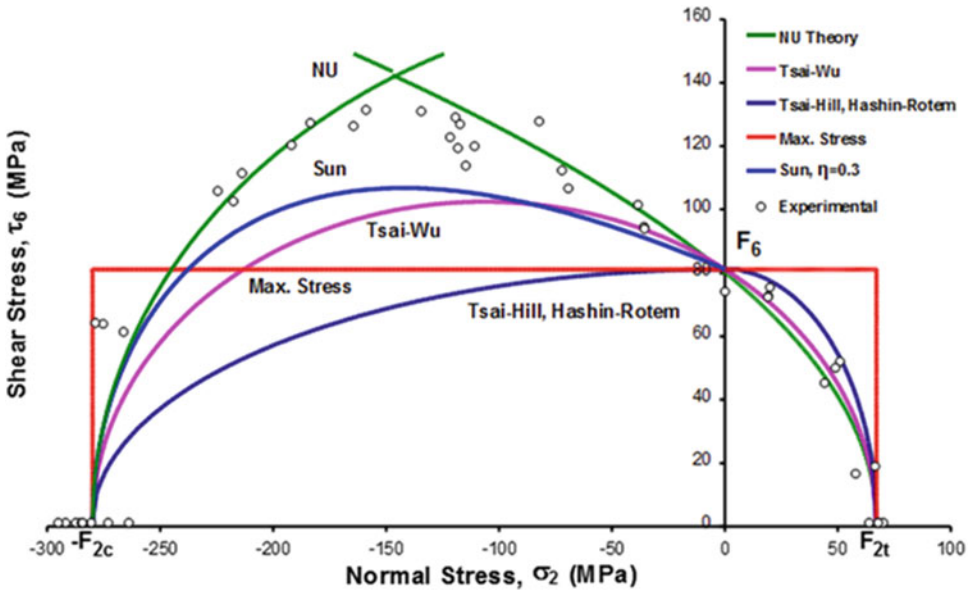

Fig. 33.3 Failure envelopes and experimental results for AS4/3501-6 unidirectional carbon/epoxy composite under in-plane shear and transverse normal loading [10]

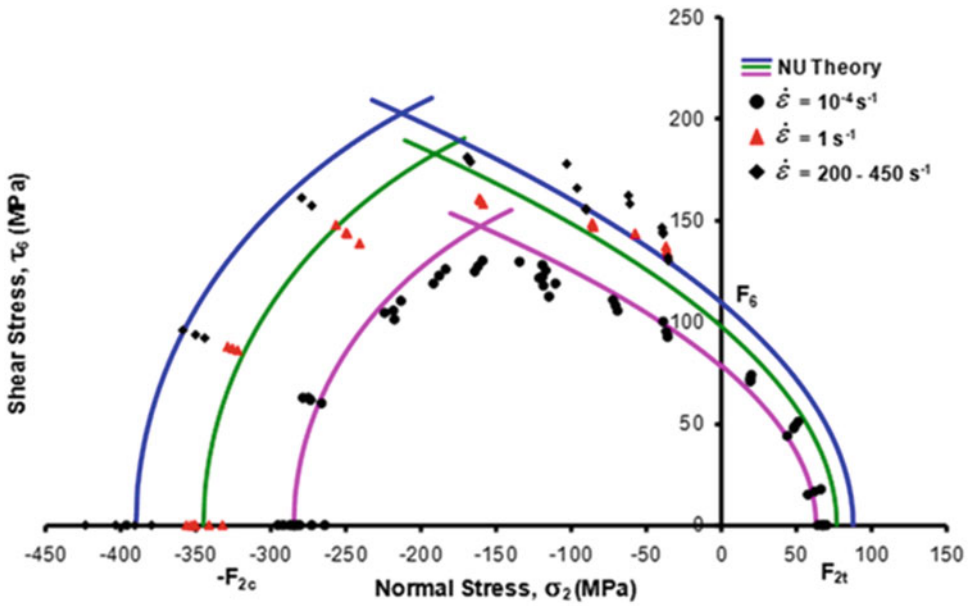

Fig. 33.4 Experimental results and failure envelopes predicted by the NU-Daniel theory for AS4/3501-6 carbon/epoxy composite at three strain rates [12]

Figure 33.3 shows failure envelopes for a carbon/epoxy composite (AS4/3501-6) under matrix dominated states of stress (transverse compression, transverse tension and in-plane shear). It is shown how the NU-Daniel theory is in very good agreement with experimental results. Similar results were obtained for IM7/8552 carbon/epoxy, which has a much more ductile matrix [12, 13]. The agreement with experimental results is very good. This attests to the robustness of the NU-Daniel theory which is governed by ultimate elastic strains irrespective of the nonlinear elastic and plastic behavior.

Stress-strain curves to failure of 90-deg and off-axis specimens of the carbon/epoxy composite were obtained as discussed before at three different strain rates (Fig. 33.2). The basic strength parameters at different strain rates were used in the failure criteria of Eqs. 33.1–33.3. Failure envelopes were plotted in Fig. 33.4 at three strain rates. The comparison between these failure envelopes predicted by the NU-Daniel theory and experimental results is very satisfactory.

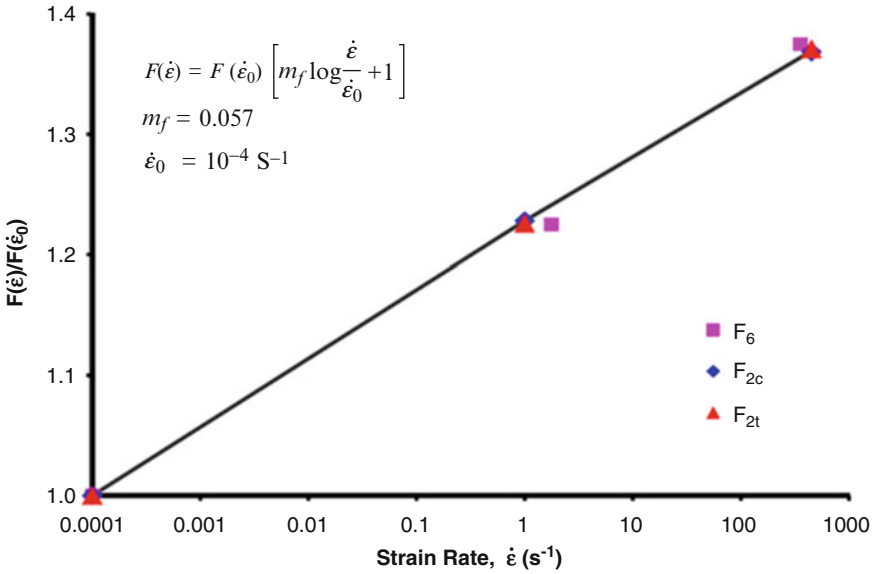

Fig. 33.5 Variation of transverse and shear strengths with strain rate

The basic matrix dominated properties of the composite, including the initial transverse and in-plane shear moduli, E_2 and G_{12}, the transverse tensile and compressive strengths, F_{2t} and F_{2c}, and the in-plane shear strength, F_6, were obtained from the tests at different strain rates. The strengths, normalized by their quasi-static values, were found to vary linearly with the logarithm of strain rate (Fig. 33.5). It appears that, for the range of strain rates considered, the variation with strain rate of the matrix dominated strengths can be described as

$$F(\dot{\varepsilon}) = F(\dot{\varepsilon}_o)\left(m\log_{10}\frac{\dot{\varepsilon}}{\dot{\varepsilon}_o} + 1\right) \tag{33.4}$$

where F = strength $(F_{2t},\ F_{2c},\ F_6)$
$m = 0.057$
$\dot{\varepsilon}_o$ = reference strain rate $= (\dot{\varepsilon}_o = 10^{-4}\ s^{-1}$ for quasi-static loading).

In view of the results of Fig. 33.5 and Eq. 33.4, the failure criteria of Eqs. 33.1–33.3 are recast in a normalized form incorporating the strain rate effects as follows [11]:

Compression dominated failure:

$$\left(\frac{\sigma_2^*}{F_{2c}}\right)^2 + \alpha^2\left(\frac{\tau_6^*}{F_{2c}}\right)^2 = 1 \tag{33.5}$$

Shear dominated failure:

$$\left(\frac{\tau_6^*}{F_6}\right)^2 + \frac{2}{\alpha}\frac{\sigma_2^*}{F_6} = 1 \tag{33.6}$$

Tension dominated failure:

$$\frac{\sigma_2^*}{F_{2t}} + \left(\frac{\alpha}{2}\right)^2\left(\frac{\tau_6^*}{F_{2t}}\right)^2 = 1 \tag{33.7}$$

where $\sigma_i^* = \sigma_i\left(m\log\frac{\dot{\varepsilon}}{\dot{\varepsilon}_o} + 1\right)^{-1}$, $\sigma_i = \sigma_2$, τ_6 and $\alpha = E_2/G_{12}$ (independent of strain rate).

Based on the above generalized criteria, the failure envelopes of Fig. 33.4 collapse into the normalized master envelope shown in Fig. 33.6.

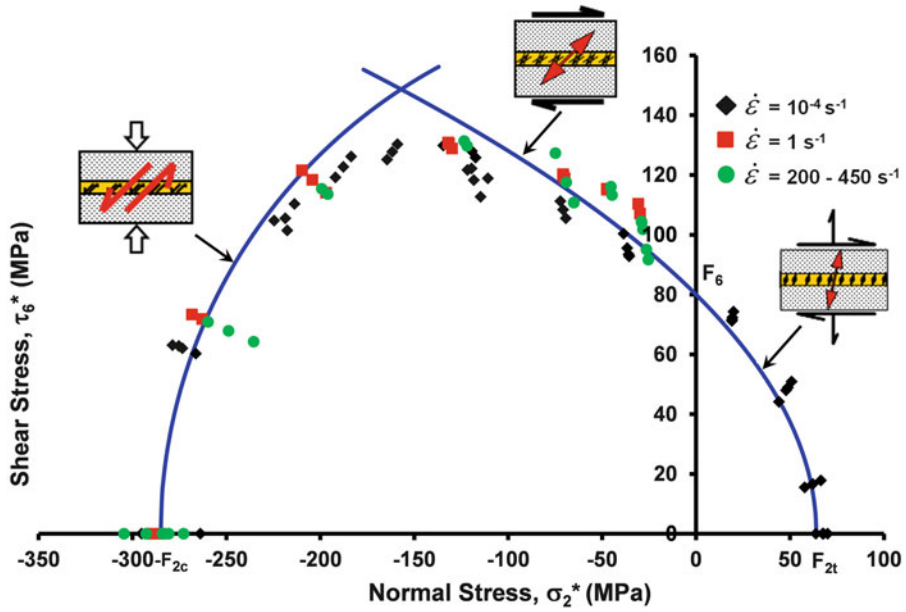

Fig. 33.6 Master failure envelope for AS4/3501-6 carbon/epoxy composite for strain rates in the range of 10^{-4}–450 s^{-1} [11]

33.4 Strain-Rate-Dependent Yield Criteria

Before undertaking an analysis of progressive damage in a multi-directional laminate, it is important to understand the initiation of yielding in a lamina, whether isolated or embedded in a laminate. The stress-strain curves of Fig. 33.2 show a quasi-linear behavior up to a point, yield point, and thereafter become very nonlinear due to plastic deformation. The normal and in-plane shear stress components at yield were fitted to the form of the NU-Daniel failure criteria of Eqs. 33.1–33.3 by substituting yield stresses for failure stresses [15]. NU yield envelopes and experimental results at three strain rates are shown in Fig. 33.7. The lamina yield stresses were normalized by their respective quasi-static values and found to vary linearly with the logarithm of strain rate as in the case of failure stresses before [12, 15]. The linear logarithmic variation is described as follows

$$F^y(\dot{\varepsilon}) = F^y(\dot{\varepsilon}_o)\left[m\log_{10}\left(\frac{\dot{\varepsilon}}{\dot{\varepsilon}_o}\right) + 1\right] \tag{33.8}$$

where F^y is the yield stress (F_{2c}^y, F_{2t}^y, F_6^y), m is 0.092, and $\dot{\varepsilon_o}$ is reference strain rate of 10^{-4} s^{-1}.

This allowed for transformation of stresses σ_2 and τ_6 at any strain rate into equivalent values at the reference strain rate as

$$\sigma_i^*(\dot{\varepsilon}_0) = \frac{\sigma_i(\dot{\varepsilon})}{f^y} \tag{33.9}$$

where $f^y(\dot{\varepsilon}) = \mathrm{m}\log_{10}\left(\frac{\dot{\varepsilon}}{\dot{\varepsilon}_o}\right) + 1$ and $\sigma_i = \sigma_2, \tau_6$

The NU yield criteria were generalized as follows to account for strain rate dependence:

Compression dominated yield:

$$\left(\frac{\sigma_2^*}{F_{2c}^y}\right)^2 + \left(\frac{E_2}{G_{12}}\right)^2\left(\frac{\tau_6^*}{F_{2c}^y}\right)^2 = 1 \tag{33.10}$$

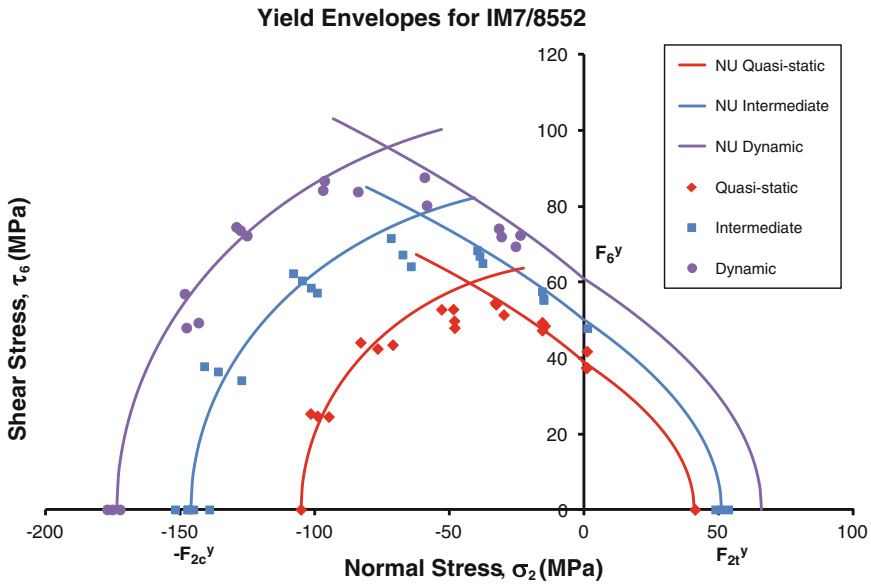

Fig. 33.7 Comparison of NU-Daniel yield envelopes with experimental results at three stain rates for IM7/8552

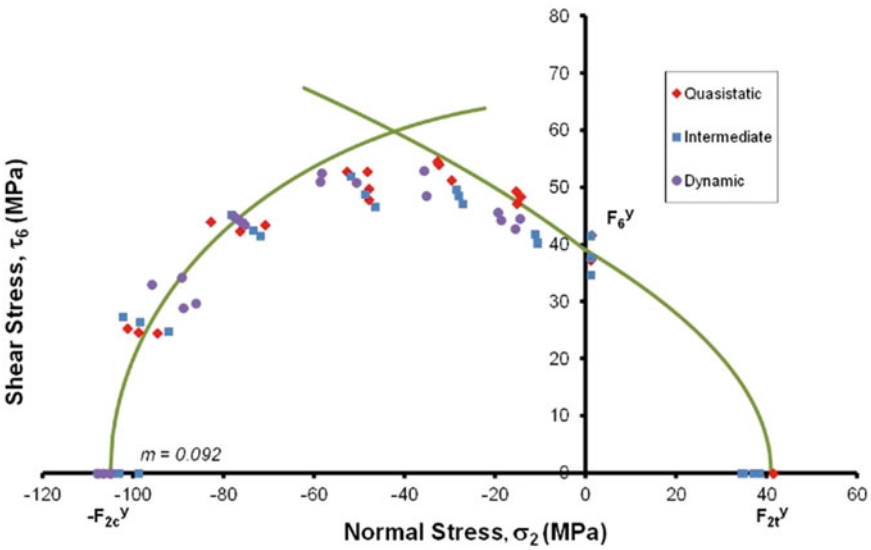

Fig. 33.8 Master yield envelope for IM7/8552 lamina and experimental results

Shear dominated yield:

$$\left(\frac{\tau_6^*}{F_6^y}\right)^2 + 2\left(\frac{G_{12}}{E_2}\right)\left(\frac{\sigma_2^*}{F_6^y}\right) = 1 \tag{33.11}$$

Tension dominated yield:

$$\left(\frac{\sigma_2^*}{F_{2t}^y}\right) + \frac{1}{4}\left(\frac{E_2}{G_{12}}\right)^2\left(\frac{\tau_6^*}{F_{2t}^y}\right)^2 = 1 \tag{33.12}$$

Based on the above, the yield envelopes of Fig. 33.7 collapsed into a master yield envelope at the reference strain rate, entirely analogously to the previously described failure envelopes (Fig. 33.8). Experimental results are in very good

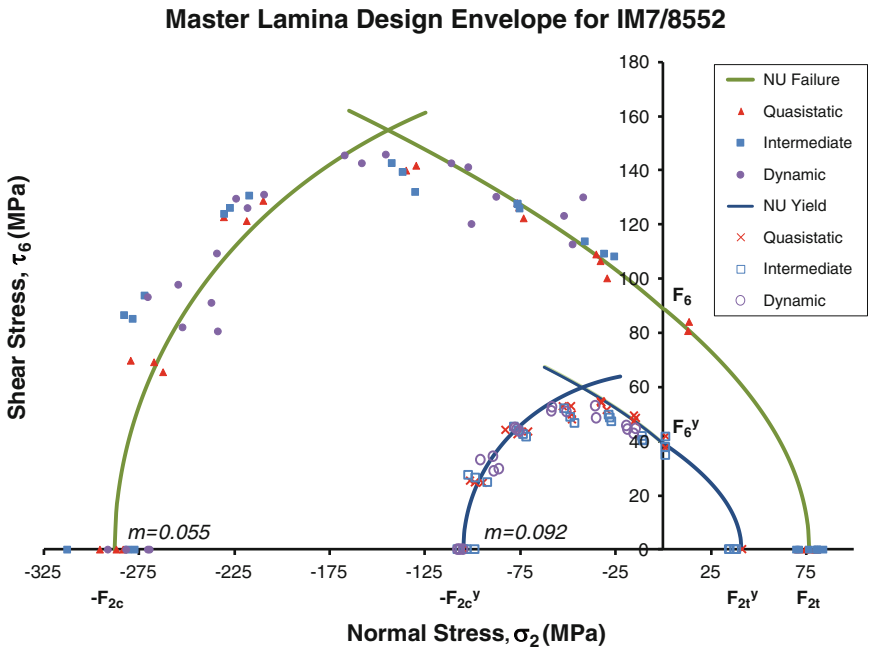

Fig. 33.9 Master NU-Daniel yield and failure envelopes and experimental results for IM7/8552

agreement with the yield criteria of Eqs. 33.10–33.12. The NU-Daniel master yield envelope combined with the previously obtained master failure envelope for this material [12] can serve as lower and upper bounds for design purposes as illustrated in Fig. 33.9.

33.5 Progressive Damage of Composite Laminates

33.5.1 Yielding of Lamina

For a given laminate under mechanical and hygrothermal loading, the first stage of damage is the first-ply-yielding (FPY), i.e., the load at which the first ply or group of plies will start yielding or behaving non-linearly. Prediction and characterization of FPY is a challenging task. First-ply-yielding is determined by linear lamination analysis and/or numerical methods, determining the state of stress in each individual layer, including fabrication residual stresses. This assumes that a layer or lamina within the laminate exhibits the same properties and behavior as an isolated unidirectional lamina. Residual stresses are calculated using hygrothermal lamination analysis based on the effective temperature difference, which can be estimated as the difference between the service temperature and the glass transition temperature of the matrix resin [8]. The calculated transverse normal and shear stresses in the lamina at yield are described by the same NU-Daniel failure criteria, as described before. Lamina yield envelopes were thus obtained for angle-ply laminates of $[\pm\theta]_{14s}$ layup at various strain rates and plotted in Fig. 33.10. After noting the linear variation of the normalized yield stresses with the logarithm of strain rate, the yield envelopes collapse into a master yield envelope which is combined with the yield envelope for the isolated lamina of Fig. 33.8 and shown in Fig. 33.11.

33.5.2 Failure Initiation and Characteristic Damage State

Following yielding, the lamina is expected to behave in a nonlinear fashion up to failure initiation. In a rigorous analysis a stiffness softening law, $E' = f(E)$, is required to track the behavior of the lamina (and laminae) from yielding up to failure initiation. This is usually in the form of onset of matrix cracking, which is predicted by the selected failure criterion.

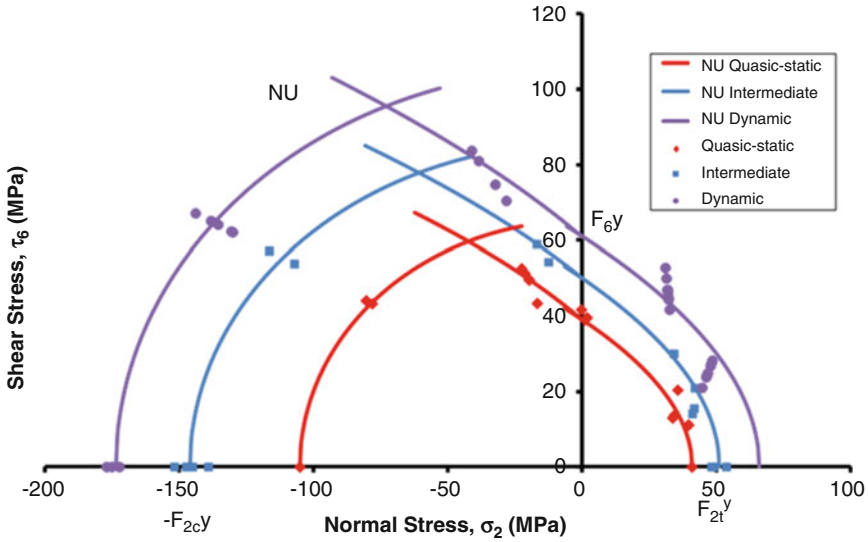

Fig. 33.10 Lamina yield envelopes and experimental results for IM7/8552 angle-ply laminates at three strain rates [15]

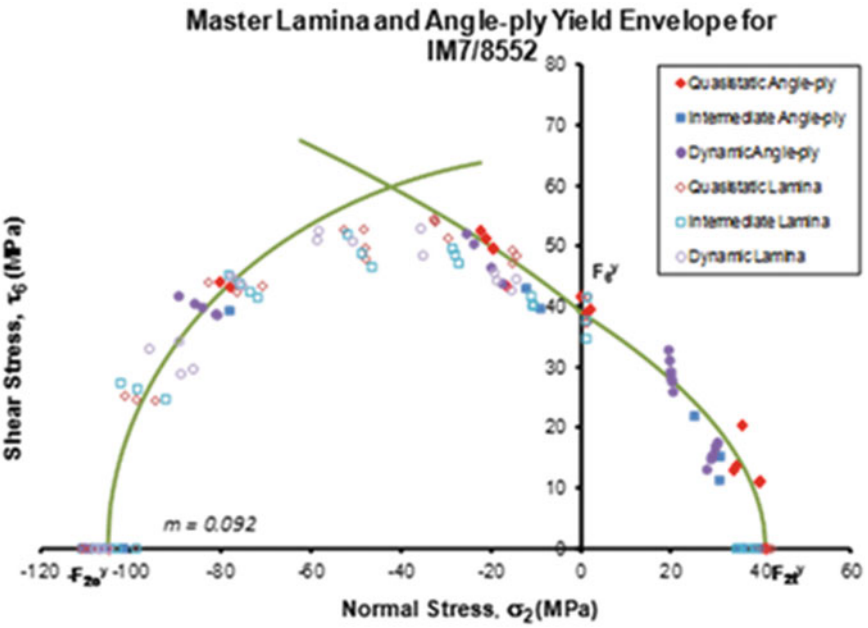

Fig. 33.11 Master yield envelope for lamina and angle-ply laminates [15]

Lamina failure within a laminate takes the form of dispersed damage (microcracking) rather than a major localized flaw or crack. This microcracking progresses up to a limiting state or maximum crack density, referred to as the characteristic damage state (CDS). This progressive microcracking is accompanied by lamina (and laminate) stiffness degradation. The stress level at this point is the characteristic damage state stress, $\sigma_{cds,}$ and corresponds to the maximum damage and minimum stiffness of the layer in the laminate. For the stress-strain curves shown in Fig. 33.2, the characteristic damage state stress can be determined as the laminate stress when the terminal modulus is reached as shown in Fig. 33.12. This characteristic damage state stress found experimentally for various angle-ply laminates was compared with predictions of the NU-Daniel failure theory. CDS stress envelopes were thus obtained for various angle-ply laminates at three strain rates as shown in Fig. 33.13. As before, these envelopes collapsed into one master envelope (Fig. 33.14). The agreement with experimental results is satisfactory.

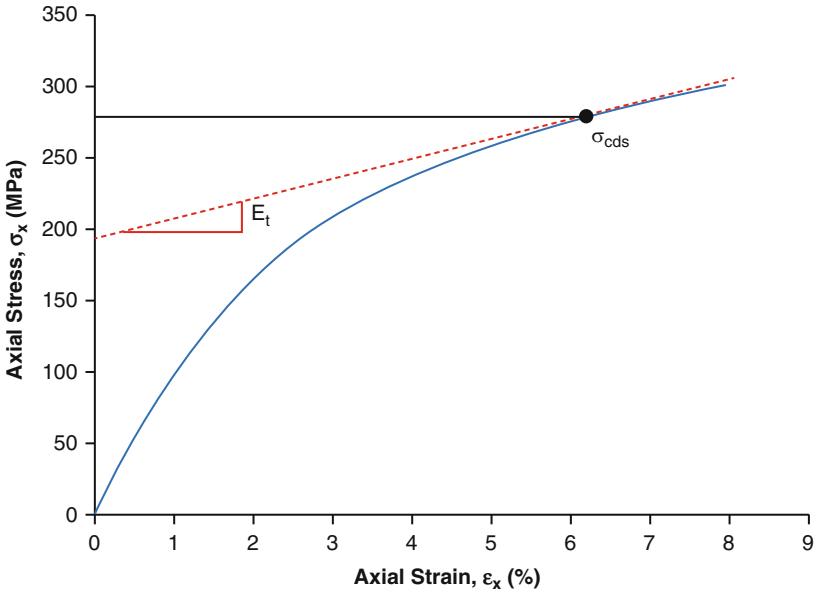

Fig. 33.12 Stress-strain behavior of lamina within a laminate illustrating the definition of characteristic damage state

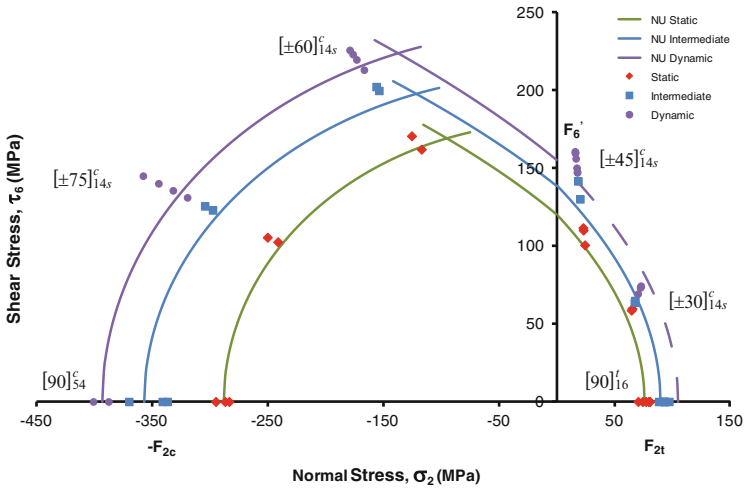

Fig. 33.13 Envelopes of characteristic damage state stresses in various angle-ply laminates at three strain rates

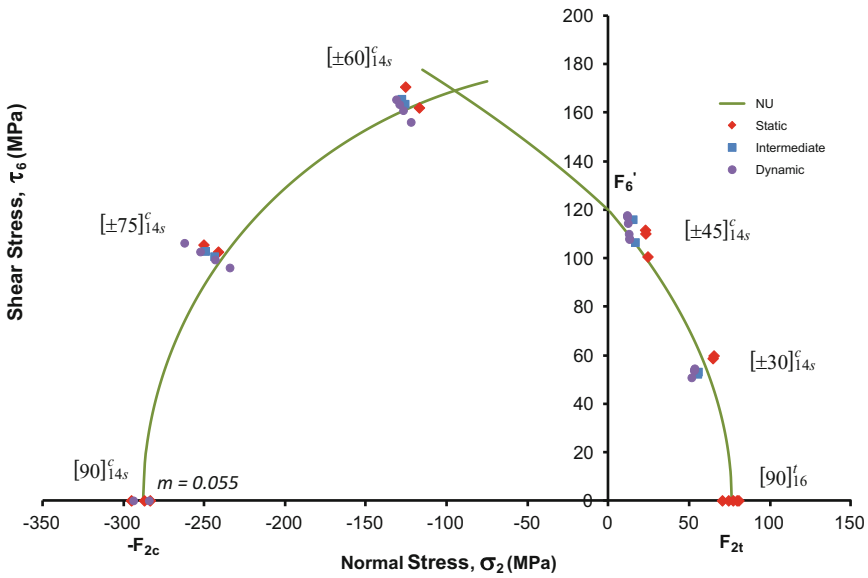

Fig. 33.14 Master envelope for characteristic damage state stresses in angle-ply laminates for various strain rates

33.6 Summary and Conclusions

A strain-rate-dependent failure theory (NU-Daniel theory) was described and demonstrated for composite materials. Failure of a composite lamina at various strain rates can be represented by a single master failure envelope. Theoretical predictions are in excellent agreement with experimental results.

An entirely analogous theory was described for yield criteria in a composite lamina under multi-axial states of stress at various strain rates. The onset of yielding for various states of stress and strain rates was represented by a single master yield envelope. Again, the predictions of the NU-Daniel yield theory were in very good agreement with experimental results.

The results for an isolated lamina were extended to the behavior of a lamina within a multi-directional laminate. Damage evolution in a laminate was studied using lamination theory and accounting for residual stresses. The state of stress at the onset of yielding and at the damage saturation state (characteristic damage state) was determined for a lamina within a laminate and fitted to the NU-Daniel theory format. Experimental results for various angle-ply laminates at various strain rates were in good agreement with theoretical predictions.

Acknowledgement This work was supported by the Office of Naval Research (ONR). We are grateful to Dr. Y. D. S. Rajapakse of ONR for his encouragement and cooperation.

References

1. Tsai, S.W., Wu, E.M.: A general theory of strength for anisotropic materials. J. Compos. Mater. **5**, 58–80 (1971)
2. Sun, C.T.: Strength analysis of unidirectional composites and laminates. In: Kelly, A., Zweben, C. (eds.) Comprehensive Composite Materials, pp. 641–666. Elsevier Science, Oxford (2000)
3. Christensen, R.M.: A survey of and evaluation methodology for fiber composite material failure theories. In: Aref, H., Phillips, J.W. (eds.) Mechanics for a New Millennium. Kluwer, Dordrecht (2001)
4. Hinton, M.J., Soden, P.D., Kaddour, A.S.: Failure Criteria in Fibre-Reinforced-Polymer Composites. Elsevier, Oxford (2004)
5. Hinton, M.J., Kaddour, A.S., Soden, P.D.: A comparison of the predictive capabilities of current failure theories for composite laminates, judged against experimental evidence. Compos. Sci. Technol. **62**, 1725–1798 (2002)
6. Puck, A., Sh□rmann, H.: Failure analysis of FRP laminates by means of physically based phenomenological models. Compos. Sci. Technol. **62**, 1633–1662 (2002)
7. Davila, C.G., Camanho, P.P., Rose, C.A.: Failure criteria for FRP laminates. J. Compos. Mater. **39**, 323–345 (2005)
8. Daniel, I.M., Ishai, O.: Engineering Mechanics of Composite Materials, 2nd edn. Oxford University Press, New York (2006)
9. Daniel, I.M.: Failure of composite materials. Strain **43**, 1–9 (2007)
10. Daniel, I.M., Luo, J.-J., Schubel, P.M., Werner, B.T.: Interfiber/interlaminar failure of composites under multi-axial states of stress. Compos. Sci. Technol. **69**, 764–771 (2009)
11. Daniel, I.M., Werner, B.T., Fenner, J.S.: Strain-rate-dependent failure criteria for composites. Compos. Sci. Technol. **71**(3), 357–364 (2011)
12. Schaefer, J.D., Werner, B.T., Daniel, I.M.: Strain-rate-dependent failure of a Toughened matrix composite. Exp. Mech. **54**(6), 1111–1120 (2014)
13. Daniel, I.M.: Constitutive behavior and failure criteria for composites under static and dynamic loading. Meccanica **50**(2), 429–442 (2015)
14. Werner, B.T., Schaefer, J.D., Daniel, I.M.: Deformation and failure of angle-ply composite laminates. In: G.P. Tandon et al. (eds.) Experimental Mechanics of Composite, Hybrid, and Multifunctional Materials, vol. 6, p. 19. Springer (2013). doi:10.1007/978-3-319-00873-8_19
15. Schaefer, J.D., Daniel, I.M.: Strain-rate-dependent yield criteria for composite laminates. 2015 SEM Annual Conference and Exposition on Experimental and Applied Mechanics, Costa Mesa, CA, 8–11 June 2015

Chapter 34
A Theory of Multi-Constituent Finitely-Deforming Composite Materials Subject to Thermochemical Changes with Damage

R.B. Hall

Abstract A mixture theory with arbitrary numbers of constituents of anisotropic solids and fluids, invoking the postulate of maximum rate of entropy production with coupled diffusion, reaction, deformation and thermal history, is briefly described. The model generalizes the 2-constituent theory of Hall and Rajagopal (2012) to include, in addition to the previously-described features, multiplicatively decomposed kinematics for thermal and chemical volume expansions and contractions. Applications of interest generally include the evolution of asymmetric material features involving finite-dimensional growth and recession, leading to local rotations important to the description of failure. An example process is the oxidation of SiC to form SiO_2 in SiC-based ceramic matrix composites (CMCs), which results in a 2.2× local volume increase.

A damage approach is described that relies on the decomposition of the internal energy into non-dissipative and dissipative parts applied within the principle of virtual power.

Keywords Mixture • Anisotropic • Anisothermal • Reaction • Damage

34.1 Introduction

The present theory considers an initial anisotropic scaffold of fibrous material (preform), into which are introduced additional anisotropic solid and fluid constituents which may interdiffuse and chemically react. Elements of previous studies by the authors [1, 2] are brought together to achieve a comprehensive framework suitable to complex problems such as the processing science and/or degradation of composite materials under harsh environments.

In the present study, directional reaction propagation is limited to following from the directional properties of the diffusivity which brings the reactants together throughout the body.

Superscript α ($\alpha = 1,2,\ldots N$) refers to all species, solid and fluid. The superscript γ ($\gamma = 1,2,\ldots,N_\gamma$) will be used to indicate solid constituents. Superscript η ($\eta = 1,2,\ldots N_\eta$) will be used to refer to the fluid species. These indices (α, γ, η) will not follow the summation convention, but will be summed explicitly using the customary operator. Other indices will generally follow the summation convention, and the correct summation interpretation should be evident from the context. The present paper is only an incomplete outline of some of the results.

34.2 Chemothermal Decomposition

The thermal and chemical changes relative to the constituent reference configurations associated with the solid preform are assumed to be transversely isotropic.

A multiplicative decomposition of the chemically reacting solid constituents is employed:

$$\mathbf{F}^{\gamma} = \mathbf{F}^{e\gamma}\mathbf{F}^{G\gamma}, \tag{34.1}$$

R.B. Hall (✉)
Materials and Manufacturing Directorate, Air Force Research Laboratory, AFRL/RXCC Bldg 654, WPAFB, OH 45433-7750, USA
e-mail: richard.hall.16@us.af.mil

C. Ralph et al. (eds.), *Mechanics of Composite and Multi-functional Materials, Volume 7*,
Conference Proceedings of the Society for Experimental Mechanics Series, DOI 10.1007/978-3-319-21762-8_34

$$\begin{aligned}\mathbf{F}^{G\gamma} &= \vartheta^{\gamma}[\theta]g^{\gamma}[n^{\gamma}]\mathbf{m}_{\kappa_p}\otimes\mathbf{m}_{\kappa_p} + \beta^{\gamma}[\theta]h^{\gamma}[n^{\gamma}]\left(\mathbf{n}_{\kappa_p}\otimes\mathbf{n}_{\kappa_p} + \mathbf{p}_{\kappa_p}\otimes\mathbf{p}_{\kappa_p}\right)\\ &= \mathbf{U}^{G\gamma}[\theta,n^{\gamma}] = \mathbf{U}^{\theta\gamma}[\theta]\mathbf{U}^{n\gamma}[n^{\gamma}],\ \ \frac{d}{dt}\mathbf{U}^{G\gamma} = \frac{d}{d\theta}(\mathbf{U}^{\theta\gamma})\mathbf{U}^{n\gamma}\frac{d\theta}{dt} + \mathbf{U}^{\theta\gamma}\frac{d}{dn^{\gamma}}(\mathbf{U}^{n\gamma})\frac{dn^{\gamma}}{dt}\end{aligned} \tag{34.2}$$

($\mathbf{F}^{\gamma}$, $\mathbf{F}^{e\gamma}$, $\mathbf{F}^{G\gamma}$) are respectively the total, elastic and chemothermal deformation gradients of species γ. θ is absolute temperature. n^{γ} is the molar volume density of γ. ($\vartheta^{\gamma}[\theta]$, $\beta^{\gamma}[\theta]$) and ($g^{\gamma}[n^{\gamma}]$, $h^{\gamma}[n^{\gamma}]$) are, respectively, thermal and chemical stretches of the γth constituent, and are assumed transversely isotropic in the reference configuration. $\mathbf{m}_{\kappa_p}$, $\mathbf{n}_{\kappa_p}$, $\mathbf{p}_{\kappa_p}$ are the reference directions of the underlying preform material, with $\mathbf{m}_{\kappa_p}$ the fiber axis direction.

The balance equations of mass, momentum, energy and entropy lead to the following result for the specific rate of entropy production γ:

$$\begin{aligned}&\sum_{\alpha=1}^{\mathrm{N}}\mathrm{tr}\left\{\left[\mathbf{T}^{\alpha} - \rho\mathbf{F}^{e\alpha}\left(\frac{\partial\psi}{\partial\mathbf{F}^{e\alpha}}\right)^{T} + \rho^{\alpha}\left(\frac{\mu^{\alpha}}{M^{\alpha}} + \sum_{\beta=1}^{N}\left[\frac{\rho^{\beta}}{\rho}\left(\psi^{\beta}-\psi^{\alpha}\right)\right]\right)\mathbf{I}\right]\mathbf{L}^{\alpha}\right\} - \rho\left(\frac{\partial\psi}{\partial\theta} + \eta - \sum_{\alpha=1}^{\mathrm{N}}\mathrm{tr}(\mathbf{P}^{\alpha}\mathbf{A}^{\alpha})\right)\frac{d\theta}{dt}\\ &+\sum_{\alpha=1}^{N}u_g^{\alpha}\left[\begin{array}{l}\dfrac{\mu^{\alpha}}{M^{\alpha}}\rho^{\alpha}_{,g} + F^{e\alpha}_{iN,g}F^{e\alpha-1}_{Nj}\left(\rho F^{e\alpha}_{jK}\left(\dfrac{\partial\psi}{\partial F^{e\alpha}_{Ki}}\right)^{T}\right) + \rho n^{\alpha}_{,g}\mathrm{tr}(\mathbf{P}^{\alpha}\mathbf{N}^{\alpha})\\ \quad -\displaystyle\sum_{\beta=1}^{N}\left[\frac{\rho^{\alpha}\rho^{\beta}}{\rho}\left(\psi^{\alpha}-\psi^{\beta}\right)\right]_{,g} + [\rho\mathrm{tr}(\mathbf{P}^{\alpha}\mathbf{A}^{\alpha}) - \rho^{\alpha}\eta^{\alpha}]\theta_{,g} - \dfrac{1}{2}\rho M^{\alpha}\dot{n}^{\alpha}u_g^{\alpha} - I_g^{\alpha}\end{array}\right]\\ &-\rho\sum_{\alpha=1}^{N}(\mu^{\alpha} - \mathrm{tr}(\mathbf{P}^{\alpha}\mathbf{N}^{\alpha}))\dot{n}^{\alpha} - \frac{\nabla\theta\cdot\mathbf{q}}{\theta} = \rho\theta\gamma = \xi\end{aligned} \tag{34.3}$$

where

$$\mathbf{P}^{\gamma} = \left(\frac{\partial\psi}{\partial\mathbf{F}^{e\gamma}}\right)^{T}\mathbf{F}^{e\gamma},\ \ \mathbf{A}^{\gamma} = \frac{d}{d\theta}(\mathbf{U}^{\theta\gamma})\mathbf{U}^{\theta\gamma-1},\ \ \mathbf{N}^{\gamma} = \frac{d}{dn^{\gamma}}(\mathbf{U}^{n\gamma})\mathbf{U}^{n\gamma-1}, \tag{34.4}$$

$$\mathbf{u}^{\alpha} \equiv \mathbf{v}^{\alpha} - \mathbf{v}. \tag{34.5}$$

ρ, ψ, η, $\mathbf{q}$ are respectively the total mass density, total specific Helmholtz energy, total specific entropy and total areal heat flux of the mixture. $\mathbf{T}^{\alpha}$, ρ^{α}, μ^{α}, M^{α}, ψ^{α}, $\mathbf{L}^{\alpha}$, $\mathbf{I}^{\alpha}$ are respectively the Cauchy stress, mass density, chemical potential, molecular weight, Helmholtz energy, velocity gradient, and interactive force per unit mixture volume of species α. d/dt and overdots denote material time derivatives. ξ is defined as $\rho\theta\gamma$.

34.3 Maximization of Entropy Production

The rate of entropy production objective function $\hat{\xi}$ is now introduced, which is constrained via Lagrange multipliers $\lambda, \widetilde{\lambda}_j$ to enforce its equality to the preceding results of the balance laws.

$$\begin{aligned}\Phi = \hat{\xi} &- \lambda\Bigg\{\sum_{\alpha=1}^{\mathrm{N}} \mathrm{tr}\Bigg\{\left[\mathbf{T}^{\alpha} - \rho\mathbf{F}^{e\alpha}\left(\frac{\partial\psi}{\partial\mathbf{F}^{e\alpha}}\right)^{T} + \rho^{\alpha}\left(\frac{\mu^{\alpha}}{M^{\alpha}} + \sum_{\beta=1}^{N}\left[\frac{\rho^{\beta}}{\rho}\left(\psi^{\beta} - \psi^{\alpha}\right)\right]\right)\mathbf{I}\right]\mathbf{L}^{\alpha}\Bigg\}\\ &-\rho\left(\frac{\partial\psi}{\partial\theta} + \eta - \sum_{\alpha=1}^{\mathrm{N}}\mathrm{tr}(\mathbf{P}^{\alpha}\mathbf{A}^{\alpha})\right)\frac{d\theta}{dt}\\ &+\sum_{\alpha=1}^{N} u_{g}^{\alpha}\left[\begin{array}{l}\dfrac{\mu^{\alpha}}{M^{\alpha}}\rho_{,g}^{\alpha} + F_{iN,g}^{e\alpha}F_{Nj}^{e\alpha-1}\left(\rho F_{jK}^{e\alpha}\left(\dfrac{\partial\psi}{\partial F_{Ki}^{e\alpha}}\right)^{T}\right) + \rho n_{,g}^{\alpha}\mathrm{tr}(\mathbf{P}^{\alpha}\mathbf{N}^{\alpha})\\ -\displaystyle\sum_{\beta=1}^{N}\left[\frac{\rho^{\alpha}\rho^{\beta}}{\rho}\left(\psi^{\alpha} - \psi^{\beta}\right)\right]_{,g} + [\rho\mathrm{tr}(\mathbf{P}^{\alpha}\mathbf{A}^{\alpha}) - \rho^{\alpha}\eta^{\alpha}]\theta_{,g} - \dfrac{1}{2}\rho M^{\alpha}\dot{n}^{\alpha}u_{g}^{\alpha} - I_{g}^{\alpha}\end{array}\right]\\ &-\rho\sum_{\alpha=1}^{N}(\mu^{\alpha} - \mathrm{tr}(\mathbf{P}^{\alpha}\mathbf{N}^{\alpha}))\dot{n}^{\alpha} - \frac{\nabla\theta\cdot\mathbf{q}}{\theta} - \hat{\xi}\Bigg\} + \rho\sum_{j=1}^{N-M'}\sum_{\alpha=1}^{N}\widetilde{\lambda}_{j}Y_{j\alpha}\dot{n}^{\alpha}.\end{aligned} \tag{34.6}$$

where $Y_{j\alpha}$ is a (N−M′) × N matrix [2, Eqs. 5.20b, 5.21] representing the constraint that only M′ reaction equations are independent, together with reflecting the stoichiometry.

The following dependence for the rate of entropy production objective function is therefore assumed, where the quantities to the left of the semicolon are the *fluxes* driving the entropy production, and $s[t]$ denotes the state variables $\{\mathbf{F}^{e\alpha}, \rho^{\alpha}, \theta\}$, upon which the constitutive coefficients may depend:

$$\xi = \hat{\xi}\left[\mathbf{L}^{\alpha}, \dot{\theta}, \mathbf{u}^{\alpha}, \nabla\theta, \mathfrak{n}^{\alpha}; s[t]\right] \tag{34.7}$$

The extrema of Φ are found by setting its first derivatives with respect to the fluxes equal to zero (of course, the second derivatives have to satisfy the appropriate conditions, and we ensure that they do).

The Lagrange function is rewritten as

$$\Phi = \hat{\xi} - \lambda\left(\mathbf{A}(\mathbf{J})\cdot\mathbf{J} - \hat{\xi}\right) + \rho\sum_{j=1}^{N-M'}\sum_{\alpha=1}^{N}\widetilde{\lambda}_{j}Y_{j\alpha}\dot{n}_{\alpha} \tag{34.8}$$

where

$$\mathbf{A}(\mathbf{J})\cdot\mathbf{J} = \xi \tag{34.9}$$

is a vectorial expression of Eq. (34.6), with flux vector $\mathbf{J}$ and corresponding thermodynamic force vector $\mathbf{A}(\mathbf{J})$.

The solution of the first Lagrange multiplier is

$$\overline{\lambda} = \frac{\hat{\xi} + \mathbf{J}\cdot\frac{\partial\mathbf{A}}{\partial\mathbf{J}}\cdot\mathbf{J}}{\frac{\partial\hat{\xi}}{\partial\mathbf{J}}\cdot\mathbf{J}} \tag{34.10}$$

where $\overline{\lambda} \equiv (1+\lambda)/\lambda$.

The extrema of Eq. (34.8), together with (34.10), can be used to find $\hat{\lambda}_{j}$ for a given matrix $Y_{j\alpha}$ reflecting a specific system of reactions.

34.4 Entropy Production Function

Define the entropy production (per unit mixture volume) function ξ_{v} as follows:

$$\xi_v = \sum_{\alpha=1}^{N} \rho^\alpha \xi_\rho^{\ \alpha},$$

where $\xi_\rho^{\ \alpha}$ is the entropy production per unit mass for constituent α:.

$$\xi_v = \frac{1}{2}\sum_{\gamma=1}^{N_\gamma} \frac{\rho^\gamma}{\rho_R^\gamma}\left[\dot{\mathbf{E}}^\gamma \cdot \mathbf{A}^{L0\boldsymbol{\gamma}} \cdot \dot{\mathbf{E}}^\gamma + \nabla_0^\gamma \theta \cdot \mathbf{l}^{\gamma 0} \nabla_0^\gamma \theta\right] + \frac{1}{2}\sum_{\eta=1}^{N_\eta} \frac{\rho^\eta}{\rho_R^\eta}\left[\mathbf{D}^\eta \cdot \mathbf{A}^{L\boldsymbol{\eta}} \cdot \mathbf{D}^\eta + \nabla\theta \cdot \mathbf{l}^\eta \nabla\theta\right] + \frac{1}{2}\frac{\rho}{\rho_R}\sum_{\alpha=1}^{N}\sum_{\beta=1}^{N} \dot{n}^\alpha \varsigma_{\alpha\beta}^n \dot{n}^\beta$$
$$+ \frac{1}{2}\sum_{\alpha=1}^{N} \frac{\rho^\alpha}{\rho_R^\alpha}\left(\mathbf{u}^\alpha \cdot \mathbf{A}^{\mathbf{v}\alpha} \cdot \mathbf{u}^\alpha + c_\theta^{\alpha 0}\dot{\theta}^2\right), \tag{34.11}$$

$$\nabla_0^\gamma \theta = \frac{\partial \theta}{\partial X_J^\gamma}\mathbf{e}_J \tag{34.12}$$

$\mathbf{E}^\gamma$, $\mathbf{A}^{\mathbf{L}0\gamma}$, $\mathbf{l}^{\gamma 0}$ are Lagrangian strain, viscosity and thermal conductivity tensors for the solid species γ. $\mathbf{D}^\eta$, $\mathbf{A}^{\mathbf{L}\eta}$, $\mathbf{l}^\eta$ are rate of deformation, and Eulerian viscosity and thermal conductivity tensors, for the fluid species η. $\mathbf{A}^{\mathbf{v}\alpha}$ is a tortuosity tensor and $c_\theta^{\ \alpha 0}$ is a material property tensor governing entropy production due to temperature rate.

Substitution of the entropy production objective function into the extremization results leads to the following constitutive expressions:

$$\mathbf{T}^\alpha = \rho \mathbf{F}^{e\alpha}\left(\frac{\partial \psi}{\partial \mathbf{F}^{e\alpha}}\right)^T - \rho^\alpha\left(\frac{\mu^\alpha}{M^\alpha} + \sum_{\beta=1}^{N}\left[\frac{\rho^\beta}{\rho}\left(\psi^\beta - \psi^\alpha\right)\right]\right)\mathbf{I} + \overline{\lambda}\frac{\rho^\alpha}{\rho_R^\alpha}\mathbf{A}^{L\boldsymbol{\alpha}} \cdot \mathbf{D}^\alpha \tag{34.13a}$$

($\mathbf{F}^{e\alpha}$ is employed only for solids.)

$$I_g^\alpha = -\overline{\lambda}\frac{\rho^\alpha}{\rho_R^\alpha}A_{gr}^{\mathbf{v}\alpha}u_r^\alpha + F_{iN,g}^{e\alpha}F_{Nj}^{e\alpha-1}\left(\rho F_{jK}^{e\alpha}\left(\frac{\partial \psi}{\partial F_{Ki}^{e\alpha}}\right)^T\right)$$
$$-\sum_{\beta=1}^{N}\left[\frac{\rho^\alpha\rho^\beta}{\rho}\left(\psi^\alpha - \psi^\beta\right)\right]_{,g} + [\rho \mathrm{tr}(\mathbf{P}^\alpha\mathbf{A}^\alpha) - \rho^\alpha\eta^\alpha]\theta_{,g} - \rho M^\alpha \dot{n}^\alpha u_g^\alpha + \frac{\mu^\alpha}{M^\alpha}\rho_{,g}^\alpha + \rho n_{,g}^\alpha \mathrm{tr}(\mathbf{P}^\alpha\mathbf{N}^\alpha) \tag{34.13b}$$

$$\rho\eta = -\rho\left(\frac{\partial \psi}{\partial \theta} - \sum_{\alpha=1}^{N}\mathrm{tr}(\mathbf{P}^\alpha\mathbf{A}^\alpha)\right) - \overline{\lambda}\sum_{\alpha=1}^{N}\frac{\rho^\alpha}{\rho_R^\alpha}c_\theta^{\alpha 0}\dot{\theta} \tag{34.14}$$

$$\frac{\overline{\lambda}}{\rho_R}\varsigma_{\alpha\beta}^n \dot{n}^\beta = -(\mu^\alpha - \mathrm{tr}(\mathbf{P}^\alpha\mathbf{N}^\alpha)) - \frac{1}{2}M^\alpha\mathbf{u}^\alpha \cdot \mathbf{u}^\alpha - \sum_{j=1}^{N-M'}\hat{\lambda}_j Y_{j\alpha} \qquad (\text{index } \beta \text{ is summed}) \tag{34.15}$$

$$\frac{\mathbf{q}}{\theta} = -\sum_{\alpha=1}^{N}\left[\overline{\lambda}\frac{\rho^\alpha}{\rho_R^\alpha}\mathbf{l}^\alpha\nabla\theta + (\rho^\alpha\eta^\alpha - \rho\mathrm{tr}(\mathbf{P}^\alpha\mathbf{A}^\alpha))\mathbf{u}^\alpha\right] \tag{34.16}$$

34.5 Definition of Strain Energy and Application to a Material with Evolving Damage

The previously-described framework can be joined to the evolution of damage. Consider a homogeneous material. The first law can be expressed as follows (cf. [3]):

$$\rho\dot{u} = (\mathbf{T}\text{:}\mathbf{D} - \theta\rho\sigma) + \theta\left(\frac{\dot{Q}}{\theta} + \rho\sigma\right) = (\mathbf{T}\text{:}\mathbf{D} - \theta\rho\sigma) + \theta\rho\dot{\eta}, \quad \dot{Q} = -\mathrm{div}\mathbf{q} + \rho r \tag{34.17}$$

u and σ are respectively the specific internal energy and rate of dissipation. A generalized strain energy rate function $\dot{\phi}$ can be defined for the non-dissipative/reversible work rate as:

$$\rho\dot{\phi} = \mathbf{T}:\mathbf{D} - \theta\rho\sigma \tag{34.18}$$

Thus Eq. (34.17) is re-expressed:

$$\dot{u} = \dot{\phi} + \theta\dot{\eta} \tag{34.19}$$

The interpretation of Eq. (34.19) is the first law can be re-expressed that, per unit mass or volume, the rate of internal energy is given by sum of the nondissipative/reversible work rate $\dot{\phi}$ and the total entropy rate multiplied by temperature.

In the case of isothermal processes, with zero energy values of integration constants,

$$\phi = \psi \equiv u - \theta\eta. \tag{34.20}$$

Consider a material with overall strain energy and Helmholtz energy described by:

$$\phi = \phi[\mathbf{F}, \theta, \boldsymbol{\alpha}] \quad \psi = \psi[\mathbf{F}, \theta, \boldsymbol{\alpha}] \tag{34.21}$$

where $\mathbf{F}$ is the deformation gradient and $\boldsymbol{\alpha}$ is an internal variable. Then

$$\dot{\phi} = \dot{u} - \theta\dot{\eta} = \dot{\psi} + \eta\dot{\theta} = \frac{\partial\psi}{\partial\mathbf{F}} : \dot{\mathbf{F}} + \left(\frac{\partial\psi}{\partial\theta} + \eta\right)\dot{\theta} + \frac{\partial\psi}{\partial\boldsymbol{\alpha}} : \dot{\boldsymbol{\alpha}} \tag{34.22}$$

It can be concluded from Eq. (34.22) that in general,

$$\eta \neq -\frac{\partial\psi}{\partial\theta}. \tag{34.23}$$

Stiffness properties may be strong functions of temperature and thus temperature is expected to affect the strain energy. Reference to Eq. (34.18) indicates that either temperature is integral to the definition of ϕ (Eq. (34.23) holds), or alternatively, the dissipation function must be homogeneous of degree one in θ^{-1} for Eq. (34.23) to hold as an equality. The latter requirement implies for example that increasing temperature has a diminishing influence on the rate of dissipation, while due to e.g. observed heightened expressions of viscous deformation effects as temperature increases, one actually expects the opposite. The conclusion Eq. (34.23) is consistent with the framework [1] underlying the developments described above.

Thus Eq. (34.22) has no non-zero terms in general, and

$$\frac{\partial\phi}{\partial\mathbf{F}} = \frac{\partial\psi}{\partial\mathbf{F}}, \quad \frac{\partial\phi}{\partial\theta} = \frac{\partial\psi}{\partial\theta} + \eta, \quad \frac{\partial\phi}{\partial\boldsymbol{\alpha}} = \frac{\partial\psi}{\partial\boldsymbol{\alpha}}. \tag{34.24}$$

Referring to Eq. (34.19), it is seen that in the present framework, the rate of the entropy function is given with inverse temperature as the integrating factor for the function h, where

$$h = u - \phi \tag{34.25}$$

$$\dot{\eta} = \frac{1}{\theta}\dot{h}. \tag{34.26}$$

The arguments of Hellan [4], slightly modified here, demonstrate that the principles of virtual power/work deliver the Griffith cracking criterion. The principle of virtual power (cf. [5]) can be stated, substituting the actual velocities for the virtual,

$$\int_{S_0} \overline{p}_i \frac{du_i}{dt} dS_0 + \int_{V_0} \rho_0 \left(b_i - \dot{v}_i\right) \frac{du_i}{dt} dV_0 = \int_{V_0} \tau_{ij} L_{ij} dV_0 \tag{34.27}$$

where $\overline{p}_i$ are the prescribed traction components per unit reference area, u_i are the displacement components, and τ_{ij}=$J\sigma_{ij}$ are the components of Kirchoff stress.

Let now the velocity gradient be split into elastic and inelastic parts L_{ij}=$L^e_{ij} + L^{in}_{ij}$, and following Hellan [4], the work on the continuum body under consideration derives in part from the work done on it by a small process zone of area S^p_0 bordered by/including the developing crack surface.

$$\begin{aligned} &\int_{S_0} \overline{p}_i \frac{du_i}{dt} dS_0 + \int_{V_0} \rho_0 b_i \frac{du_i}{dt} dV_0 - \frac{d}{dt} \frac{1}{2} \int_{V_0} \rho_0 v_i v_i dV_0 - \frac{d}{dt} \int_{V_0} \int_a^b \left(\tau_{ij} \frac{du^e_{i,j}}{dt} dt \right) dV_0 \\ &= \frac{d}{dt} \int_{V_0} \int_a^b \left(\tau_{ij} \frac{du^{in}_{i,j}}{dt} dt \right) dV_0 - \int_{S_0^p} \overline{p}_i \frac{du_i}{dt} dS_0. \end{aligned} \tag{34.28}$$

The time argument t of Eq. (49) is replaced by the evolving crack area A, with then d/dA replacing d/dt, making the result time-independent. The result can be expressed as the Griffith cracking criterion (generalized to include kinetic energy) [4]:

$$W - \frac{dT}{dA} - \frac{d\Phi}{dA} = D + C = \mathbf{G} \tag{34.29}$$

W corresponds to the overall work rate terms of Eq. (34.29), T to the overall kinetic energy, Φ to the overall elastic strain energy, D to the overall dissipation rate, and C to the separation work rate (last term of (49)). G is the potential energy release rate.

The principle of virtual power is now rewritten for a summation of p cracks within a local volume:

$$\int_S \bar{t}_i v_i dS + \int_V \rho b_i v_i dV - \int_V \rho v_i \frac{dv_i}{dt} dV - \int_V \rho \dot{\phi}\, dV = \int_V \theta \rho \sigma dV - \sum_p \int_{S^p} \bar{t}_i \frac{du_i}{dA_p} \dot{A}_p dS \tag{34.30}$$

Eq. (34.30) can be applied to a single crack or distributed damage via appropriate constitutive functions. $\sigma_{ij} L_{ij}{}^{in}$ in Eq. (34.28) was replaced by the continuum dissipation rate per unit volume $\theta\rho\sigma$ from Eqs. (34.17)–(34.18). Applying the divergence theorem and the equation of motion to Eq. (34.30) yields, in the limit as $V \to 0$,

$$\mathbf{T} \cdot \mathbf{D} - \rho \dot{\phi} = \theta \rho \sigma + \dot{d} \tag{34.31}$$

$$\dot{d} = -\lim_{V \to 0} \frac{1}{V} \sum_p \int_{S^p} \bar{t}_i \frac{du_i}{dA_p} \dot{A}_p dS \tag{34.32}$$

$\dot{d}$ represents work rate on the process zone by the continuum. Its appearance parallels that of the continuum dissipation and represents a loss of potential energy via the stress power. The stress power of the continuum must enlarge to make available the energy required for damage, above the expenditures on stored and dissipated energies of the continuum. The expression (34.32) suggests compatibility with cohesive zone traction models, such as employed e.g. by Iarve et al. [6].

Acknowledgement The author thanks K.R. Rajagopal for fruitful interactions.

References

1. Hall, R.B., Rajagopal, K.R.: Diffusion of a fluid through an anisotropically chemically reacting thermoelastic body within the context of mixture theory. Math. Mech. Solids **17**(2), 131–164 (2012). doi:10.1177/1081286511407754
2. Kannan, K., Rajagopal, K.R.: A thermodynamical framework for chemically reacting systems. ZAMP **62**, 331–363 (2011)
3. Truesdell, C.: Rational Thermodynamics. Springer, New York, NY (1984)
4. Hellan, K.: Introduction to Fracture Mechanics. McGraw-Hill, New York, NY (1984)
5. Malvern, L.E.: Introduction to the Mechanics of a Continuous Medium. Prentice-Hall, Englewood Cliffs, NJ (1969)
6. Iarve, E., Gurvich, M., Mollenhauer, D., Rose, C., Davila, C.: Mesh independent matrix cracking and delamination in laminated composites. Int. J. Numer. Methods Eng. **88**(8), 749–773 (2011)

Chapter 35
Pressurized In-Situ Dynamic Mechanical Thermal Analysis Method for Oilfield Polymers and Composites

Yusheng Yuan and Daniel Sequera

Abstract Oilfield downhole equipment uses engineered polymers and composites extensively in various operations. The capability of polymers and composites to resist high temperature in downhole hot-wet fluid and gas environment is critical. Dynamic mechanical thermal analysis (DMA) is known as the best analysis technique to determine this capability represented by glass transition temperatures (T_g) of polymeric materials. However, current commercially available DMA analyzers are commonly designed to perform a temperature sweep in a dry atmosphere—even for wet T_g determination of exposed wet samples, where a drying process associated with the analysis gives inaccurate results. Some recent DMA analyzers are equipped with an immersing test fixture; however, they are opened to ambient pressure with a low upper-temperature limit. There is no pressurized DMA analyzer commercially available.

This study presents an innovative and unique pressurized DMA analyzer using an in-house-developed HPHT in-situ mechanical testing system. The analysis can be conducted for a polymer or composite specimen in an immersed fluid condition up to 260 °C and 70 MPa under 3-point bending, compression and tension dynamic modes. This in-situ DMA method can determine accurately the dry and wet T_gs for polymers and composites and the true DMA curves in an immersed wet condition. Hydrostatic pressure-dependent T_gs of ABS and PEEK polymers were also determined up to 69 MPa.

Keywords Polymers • Composites • Hot-wet condition • Dynamic mechanical analysis (DMA) • Glass transition temperature (T_g) • Hydrostatic pressure-dependent T_g

35.1 Introduction

Oilfield downhole operations, including drilling, logging, completion, production and workover, require the service tools to perform in an extremely harsh environment in deep wells involving high-pressure, high-temperature (HPHT) and various corrosive fluids and gases. This requires the materials for building the downhole equipment to possess high strength with heat- and corrosion-resistance. Recently developed technologies in oil and gas exploration and production involve offshore deepwater and unconventional shale play extended-reach horizontal drilling, completion and hydraulic fracturing. These technologies further require the materials for downhole equipment to be lightweight, fatigue-resistant or easy to mill out. For these applications, in addition to using conventional metals and specialty heat- and corrosion-resistant metallic alloys, advanced high-temperature elastomers, plastics and high-performance fiber-reinforced polymer composites play important roles in sealing and some structural applications offering advantages in lightweight, corrosion resistance, long fatigue life and easy removal [1, 2]. However, in many cases of these applications, the materials are required to perform in a hot-wet downhole environment at temperatures above 204 °C and pressures above 70 MPa. These conditions present significant challenges to the applications.

High-temperature engineering polymers, including various advanced high-temperature thermosetting and thermoplastic polymers, have been used extensively in aerospace structures and critical industrial applications with relatively high-temperature and environmental-resistant capability. However, when moisture or a wet condition is associated with the high temperature, many of these polymers behave very differently from their original dry state due to hot-wet degradations from the high-temperature hot-wet environment. These involve a combination of temperature effect, moisture-induced thermomechanical degradation, hygrothermal structural damage and hydrolytic reactions [3–6]. Proper characterization and full understanding of the HPHT hot-wet thermomechanical properties of various high-temperature polymers and their composites based on an accurate, reliable, environmentally simulated thermomechanical testing and analysis method is

Y. Yuan (✉) • D. Sequera
Baker Hughes, 14990 Yorktown Plaza Dr., Houston, TX 77040, USA
e-mail: yusheng.yuan@bakerhughes.com

C. Ralph et al. (eds.), *Mechanics of Composite and Multi-functional Materials, Volume 7*,
Conference Proceedings of the Society for Experimental Mechanics Series, DOI 10.1007/978-3-319-21762-8_35

extremely important, including dynamic mechanical thermal analysis (DMA) in a fluid condition for polymers and composites.

Because of the limitations in testing technology, the conventional environmental-thermal-mechanical test methods for polymers and polymer composites based on the industrial test standards from ASTM, ISO, NACE, API and NORSOK separate the post-conditioning thermal and mechanical testing from the environmental conditioning procedure. The post-conditioning thermomechanical test condition in a conventional test setup is very different from the exposure condition. Testing is usually performed in an ambient condition or in heated dry air, where the conditioned wet test specimens are subjected to a drying process and the effect of the hydrostatic pressure is omitted. Furthermore, dry preheating in a high-temperature mechanical test can serve as a thermal impact and introduce additional structural damage to the wet specimens. All these problems with conventional environmental-mechanical test methods may result in inaccurate or incorrect test results. To eliminate all these problems, the authors developed a unique HPHT in-situ mechanical test system and the associated HPHT in-situ test methods during 2004–2007 [7, 8]. The new test methods combine the post-conditioning mechanical testing and the HPHT environmental exposure in one procedure and conducts the mechanical tests directly in a simulated HPHT fluid and gas condition after a period of HPHT environmental exposure. However, the HPHT in-situ DMA capability was not established.

In polymer and polymer composite oilfield downhole applications, the heat-resistant capability of the materials in downhole environmental conditions is critical. The glass transition temperature (T_g) of a polymeric material is as a major indication of this capability, and it is affected by hot-wet conditions to many polymers [5, 6]. Properly determining dry and wet T_gs of the polymers and polymer composites is essential. Methods for T_g determination of polymeric materials have been established for decades, including thermo-mechanical analysis (TMA), differential scanning calorimetry (DSC) and dynamic mechanical analysis (DMA) with different theories and analytical mechanisms. Various thermal analysis instruments for these analysis methods are commercially available. Among these analysis methods, the DMA method can measure the dynamic modulus transition of the sample material directly during the temperature sweep, and is the most reliable and meaningful method for determining the T_g of the polymers and polymer composites in engineering application point of view. However, current commercial DMA analyzers are commonly designed to perform a temperature sweep in a dry atmosphere. This procedure is acceptable for dry T_g determination, but for wet T_g determination of the exposed wet specimen, the drying process associated with the analysis will give inaccurate or incorrect analysis results. Some DMA analyzers made by TA and Perkin Elmer are equipped with an immersing fixture or a fluid bath. However, these are opened to ambient pressure with a low upper-temperature limit. There is no pressurized DMA analyzer commercially available.

After searching ASTM and ISO test standards for thermal analyses, we found only the ASTM D7028-07 that covers a DMA test procedure for determining wet T_gs of polymer composites. This test method runs the DMA for the conditioned wet specimen in a heated dry atmosphere with a conventional DMA analyzer. This DMA test standard sets a fast heating rate of 5 °C/min for fiber-reinforced composites to compromise the drying process to the wet specimens. This heating rate might be too fast for neat resin or nonconductive fiber-reinforced composites as ASTM E1640-09 sets the DMA heating rate of 1 °C/min for determining the dry T_g of polymer materials. D7028 recommends monitoring the weight changes of the conditioned wet specimens before and after the DMA testing to quantify the change of the moisture content. However, in many cases, the drying process is rapid if the specimen size is small and the sweep temperature is high. It is desirable to determine the wet T_g of a high-temperature polymer or polymer composite directly in an immersed fluid condition by using a pressurized in-situ DMA testing and analysis system.

The hydrostatic pressure effect on T_g of polymers has been a theoretical and experimental research topic for many years. Increasing hydrostatic pressure on an amorphous polymer increases the molecular crowding. This situation reduces the free volume in the context of the free-volume model or decreases the entropy of the polymer according to the entropy theory, and subsequently increases the T_g of the polymer [9]. A high-pressure dilatometry apparatus is commercially available and has been used mostly for determining the hydrostatic pressure-dependent T_g of polymers by measuring the sample specific volume as a function of temperature under a constant pressure (isobaric) based on the free-volume theory [10]. This apparatus was specially designed for pressure-volume-temperature (PVT) measurement and uses mercury as the containing fluid for the polymer samples [11]. This design is not flexible in use, and the effect of the application fluid environment cannot be included. Hydrostatic-dependent T_gs of early ICI Victrex PolyEtherEtherKetone (PEEK) G380 and the recent Victrex PolyArylEtherKetone (PAEK) polymers were determined by this method [10, 12]. The torsion pendulum has been a simple method with free oscillation for dynamic mechanical measurements of polymers [13]. A high-pressure torsion pendulum apparatus was developed in the 1970s and has been used to determine the effect of the hydrostatic pressure on dynamic mechanical properties of the polymers under a high pressure including nylons, PET, PVAC and PMMA [14]. The drawback of this method is that the frequency of the free oscillation depends on the stiffness of polymer test specimen and varies with the test temperatures. Nitrogen gas was used as the pressure medium to provide minimum viscous drag on the

inertial mass. This apparatus was designed for the temperature range from −30 °C to 140 °C only, and the effect of the application fluid could not be applied. Because of the limitations, this method was not commercialized.

In this paper, the authors introduce the recently developed HPHT in-situ thermomechanical testing and analysis system and the associated test methods for high-temperature polymers and composites. This HPHT in-situ test system is capable of performing standard and custom tensile, compression, shear and flexural tests directly in a simulated HPHT fluid and gas environment up to 260 °C and 70 MPa. Incorporated with an MTS dynamic actuator and a dynamic mechanical characterization code, the HPHT in-situ test system can be used in a dynamic oscillation mode as a DMA analyzer to determining the wet T_gs of the high-temperature polymers and composites in various fluid conditions under hydrostatic pressure. For illustration, in-situ DMA curves and the wet T_g degradations of a hot-wet exposed carbon/epoxy composite laminate and a hot-wet exposed rigid polymer foam were determined for the first time in a pressurized, immersed hot-wet conditions under 3-pint bending and compression dynamic modes, respectively. The measured in-situ DMA curves and the wet T_gs are compared with the measured dry and wet DMA curves and T_gs per current standard DMA procedure by a commercial TA DMA analyzer. Issues and limitations with the current DMA method for wet T_g determination of polymeric materials are addressed. Hydrostatic pressure-dependent T_gs of an amorphous acrylonitrile butadiene styrene (ABS) plastic and a semi-crystalline thermoplastic PEEK grade were determined by the in-house developed HPHT in-situ DMA system successfully up to 69 MPa for the first time in the industry. The test results of the hydrostatic pressure-dependent T_gs are presented and compared with the data from the literature.

35.2 Experimental

35.2.1 HPHT In-Situ Thermomechanical Testing System

The HPHT in-situ thermomechanical testing and analysis system was designed to contain the HPHT environmental chamber (autoclave) and the mechanical test load frame. This enables us to combine environmental conditioning and the post-conditioning mechanical testing in one test procedure and eliminate all the problems with the conventional environmental-mechanical test methods. As illustrated in Fig. 35.1, the HPHT in-situ thermomechanical testing and analysis system

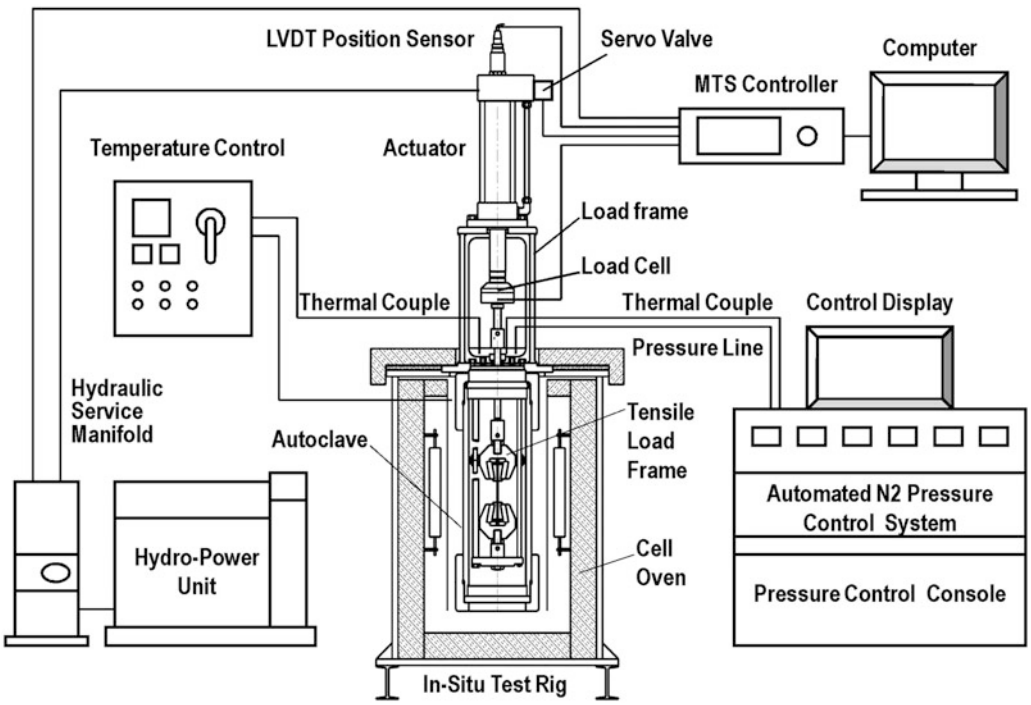

Fig. 35.1 Schematic illustration of the HPHT in-situ thermomechanical testing system with the associated hydraulic, gas pressure and control systems

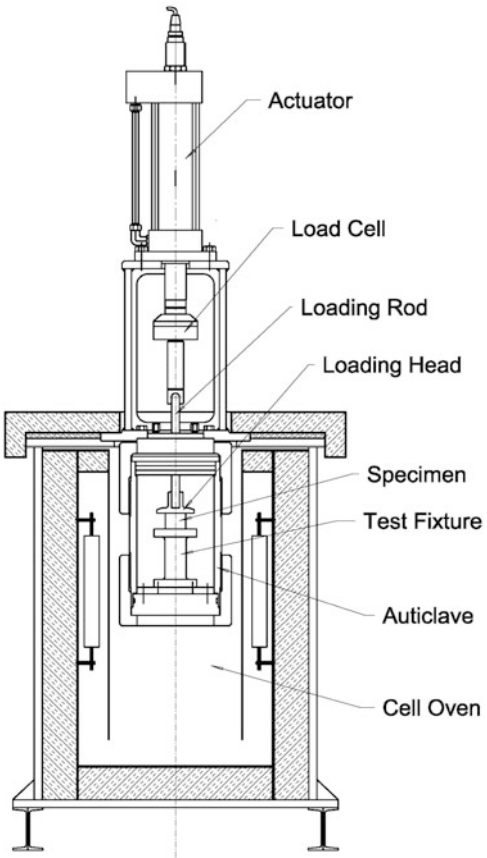

Fig. 35.2 Schematic of the HPHT in-situ compression test setup

consists of an HPHT autoclave, a controlled cell oven, a hydraulic driving system, a mechanical test load frame, a high-pressure gas source and a nitrogen pressure control system. The autoclave can accommodate the in-situ tensile load frame, applied standard test fixtures (compression, shear and flexural) and the environmental medium under high temperature and high pressure. In the compression, shear or flexural test setup, the test fixture is installed on the bottom plug of the autoclave. The autoclave casing serves also as a part of load frame, as shown in Fig. 35.2. All components exposed to the test environment are made of high-strength, corrosion-resistant alloys. The hydraulic driving system includes an actuator, a servo valve, a service manifold and a hydraulic power unit. The load frame connects the hydraulic actuator and the loading train that includes a load cell and a loading rod that passes through a high-temperature, low-friction reciprocating seal in the top plug of the autoclave. The hydraulic driving system and the mechanical test frame are controlled by a full-functional MTS controller for operation and data acquisition. The nitrogen pressure control system can control the autoclave pressure accurately within ±5 psi. The in-situ test system is rated to a 50 KN (11.2 kip) loading capacity and capable of running various standard and custom quasi-static, time-dependent and DMA tests for polymers and composites in an HPHT fluid and gas environment up to 260 °C and 70 MPa. A close look of the HPHT in-situ test rig is shown in Fig. 35.3. More detailed information on the HPHT in-situ thermomechanical testing and analysis system can be found from author's earlier publications [7, 8].

35.2.2 Test Materials

For illustration purposes, the in-situ DMA tests in 3-PB mode were conducted for the carbon/epoxy laminate specimens, in-situ DMA tests in compression mode were conducted for rigid polymer foam specimens, and for investigation in T_g hydrostatic pressure-dependence, the HPHT in-situ DMA tests were conducted in compression mode for ABS and PEEK specimens. For test specimen preparation, the carbon/epoxy laminates were wet-laminated with 3 k carbon fiber plain weave (PW) fabric and a high-temperature tetra-functional epoxy resin, and cured at 185 °C under pressure for four hours. The dry

Fig. 35.3 Overall view of a HPHT in-situ thermomechanical test rig with the control system and hydraulic power unit

T_g of the cured carbon/epoxy laminate is approximately 200 °C. The rigid polymer foam was made of a proprietary polymer formulation with a dry T_g ranging from 135 °C to 150 °C. The ABS amorphous thermoplastic was selected as the first trial material for the hydrostatic-pressure dependent T_g investigation because it has a clear T_g of approximately 105 °C and is readily available from plastic distributors. The commercial-grade extruded 2-in. diameter ABS solid bars were purchased for machining the DMA test specimens. The high-performance semi-crystalline thermoplastic PEEK possesses excellent high-temperature and corrosion resistance and is used extensively in oilfield downhole tools as sealing and insulation components. PEEK possesses a dry T_g approximately 143 °C in ambient conditions, and it is expected that a high hydrostatic pressure can improve its heat-resistant capability in a HPHT downhole condition. In this study, the Victrex unfilled PEEK 450G grade was selected and the 2-in. diameter extruded 450G PEEK solid bar was ordered for machining the DMA test specimens.

35.2.3 In-Situ wet T_g Determination

The HPHT in-situ DMA analyzer is equipped with a fatigue-rated hydraulic actuator and is controlled by MTS Multi-Purpose Testware (MPT) with a Dynamic Characterization Process program. This HPHT DMA analyzer is also supported by a high-pressure nitrogen pump, an accumulator, and a precision gas pressure control system so the analyzer can run a temperature sweep under a constant autoclave pressure. The test program requires the inputs of specimen geometry, specimen dimensions, oscillation frequency, displacement mean level, amplitude, the estimated total cycles and the number of cycles per data recording. In this study, the true in-situ DMA curves and the wet T_gs of the hot-wet exposed carbon/epoxy laminate and the rigid polymer foam were determined in the pressurized 3 % NaCl brine or deionized water under a constant low pressure slightly above the saturated steam pressure of the maximum sweep temperature. The purpose of using a low near-ambient autoclave pressure (2–3.5 MPa) is to minimize the friction between the loading rod and the reciprocating seal. In this case, the calibrated rod friction force under a sine weave rod movement is less than 27 N (6 lb) in most cases; with relatively larger sized 3-PB beam specimens and rigid polymer foam specimens this low rod friction force ensures an accurate calculation of the measured storage modulus. An in-situ 3-PB test fixture was specially designed with optional 50.8 mm and 38.1 mm span and optional 12.7 mm and 19.1 mm specimen width, as shown in the photo in Fig. 35.4. In the current 3-PB DMA analysis, the test specimens were cut from the carbon/epoxy composite laminate in a rectangular beam shape with dimensions of 76.2 mm × 19.1 mm × 3.2 mm for the 50.8 mm span in the test fixture. The compression mode

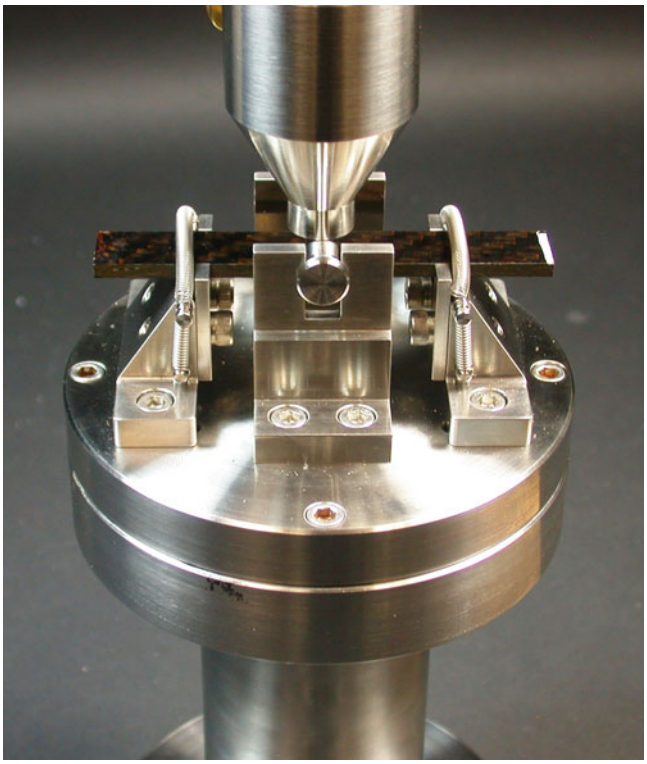

Fig. 35.4 A carbon/epoxy beam specimen mounted in the in-situ 3-PB test fixture

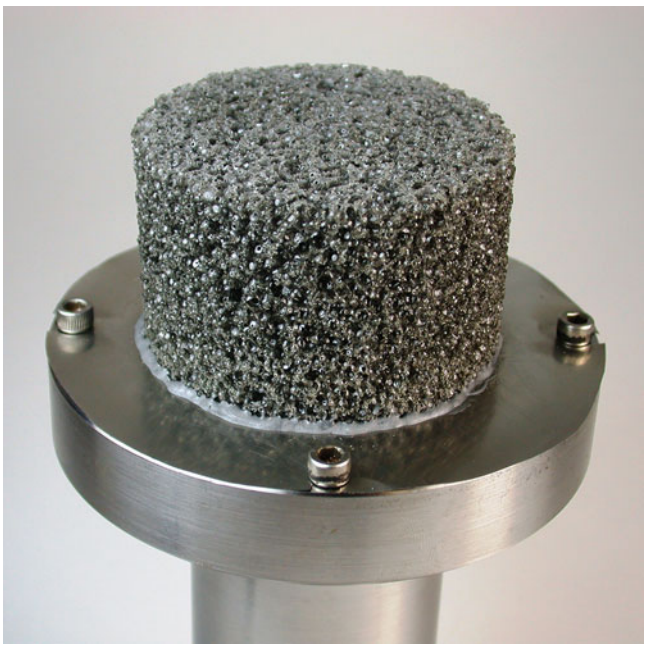

Fig. 35.5 A rigid polymer foam specimen mounted on the in-situ compression platen

was used for the rigid polymer foam cylinder and the hollow plastic cylinder specimens. Figures 35.5 and 35.6 show a foam cylindrical specimen and a plastic hollow cylinder specimen mounted on the in-situ compression test platen, respectively. The cylindrical rigid polymer foam test specimens were machined from the pre-processed foam billets with 64.8 mm diameter and 42.4 mm height. The hollow plastic cylinder design for hydrostatic pressure-dependent T_g determination will be discussed in the next section. The in-situ DMA sweeps under 3-PB or compressive oscillating mode were conducted in the similar in-situ testing setup as that for the regular in-situ compression tests, as shown in Fig. 35.2. The DMA runs were

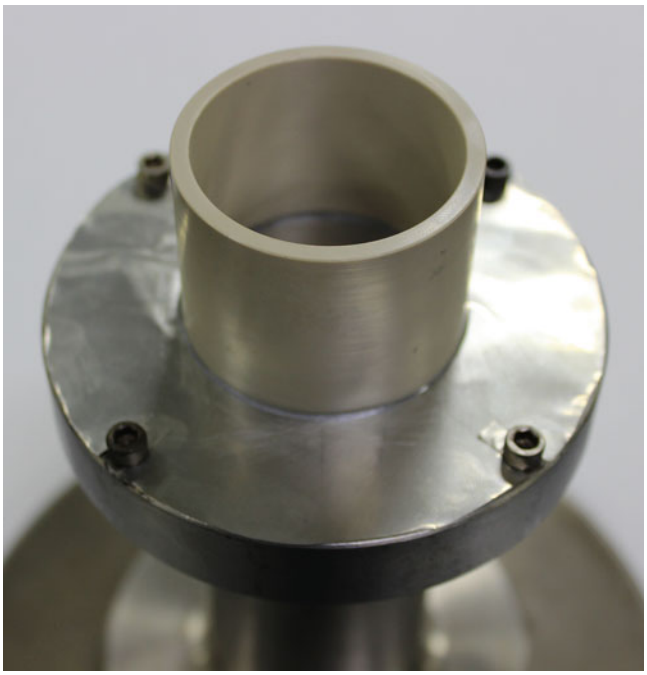

Fig. 35.6 A PEEK hollow cylinder specimen mounted on the in-situ compression platen

Table 35.1 Designed dimensions of hollow cylinder DMA specimens for ABS and PEEK G450

	OD (mm)	ID (mm)	Length (mm)
ABS	50.8	38.1	38.1
KEEK G450	50.8	44.45	38.1

conducted with 0.2 Hz frequency, approximately 0.94 mm mean deflection and 0.76 amplitude for the carbon/epoxy specimen 3-PB oscillation, while with 0.1 Hz frequency, approximately 2 % mean compressive strain and 1 % strain amplitude. Both DMA temperature sweeps were under approximately 1 °C/min heating rate.

35.2.4 Hydrostatic Pressure-Dependent T_g Determination

In the DMA for hydrostatic pressure-dependent T_g determination, a high autoclave pressure is involved. The rod friction force caused by the high autoclave pressure can be calibrated and adjusted easily in quasi-static tests, but it is very challenging to make a real-time calibration and correction during the DMA temperature sweep. Based on the rod friction calibration under different autoclave pressure, the friction forces were found within ~35 N (8 lb) under 3.4 MPa, ~155 N (35 lb) under 41.4 MPa and ~356 N (80 lb) under 69 MPa. By using full loading capacity of the HPHT in-situ test rig, we can design a special HPHT in-situ DMA specimen that is rigid enough to provide a high oscillating force so that the friction-induced force becomes relatively small compared to the specimen deformation-induced oscillating force. This is a simple approach as an alternative to this complicated and challenging HPHT DMA testing method development. Under this concept, the hollow cylinder geometry was selected for the compressive DMA specimen in determining the hydrostatic pressure-dependent T_gs of ABS and PEEK plastics. With a proper dimensional design, this simple geometry can provide the required high oscillating force, large heating area and easy specimen preparation. Considering the full loading capacity of the HPHT in-situ test rig, the oscillating compressive force was set in the range from 11.1 KN (2500 lb) to 20.5 KN (4500 lb). Based on the measured elastic modulus and the planned input of the compressive deformation of the test specimens, also a verification calculation on structural buckling of the hollow cylinder under compression according to Timoshenko [15], the designed dimensions of the hollow cylinder test specimens for ABS and PEEK grades are listed in Table 35.1. The hollow cylinder test specimens were machined accurately from the extruded ABS and PEEK G450 solid rods, respectively.

The HPHT in-situ DMA temperature sweeps for ABS specimens were conducted in de-ionized water from ambient temperature to 177 °C under 2.1, 41.4 and 68.9 MPa, respectively, while the DMA temperature sweeps for PEEK specimens

were conducted in de-ionized water from ambient temperature to 232 °C under 3.4, 41.4 and 68.9 MPa, respectively. This HPHT compressive dynamic characterization procedure set the oscillating frequency 0.1 Hz, and the mean compressive strain 1.5–1.7 % with 0.8 % amplitude. All the HPHT DMA temperature sweeps were under approximately 1.2 °C/min heating rate. The measured initial compressive oscillating loading ranges from the ABS and PEEK test specimens in the tests met the designed loading requirements.

35.3 Results and Discussion

35.3.1 Results of In-Situ Wet T_g Determination

In-situ DMA temperature sweeps were conducted in 3-PB oscillating mode in 3 % NaCl brine under 3.4 MPa autoclave pressure for the carbon/epoxy laminate specimens after exposure in the 3 % NaCl brine at 149 ° C and 7 MPa for 72 h. The measured in-situ DMA curves of the composite specimens in the pressurized wet condition are presented in Fig. 35.7, along with its dry DMA curves determined from an unexposed carbon/epoxy specimen by the same in-situ test setup in the dry condition. From the presented results we can see that the dry storage modulus curve shows an initial transition with a measured dry T_g of approximately 200 °C, and a second transition with a measured dry T_g of approximately 230 °C that might be caused by the drying and continuous curing process during the analysis at a high temperature above 200 °C. However, the measured in-situ wet storage modulus curve from the exposed specimen shows the first onset point at 134 °C and the second onset point at 160 °C. This defines the wet T_g of the carbon/epoxy composite in the range of 134 °C to 160 °C (a big shift from the dry T_g) with a deep modulus reduction after the transition. This in-situ DMA system conducted the temperature sweep directly in a pressurized hot-wet environment, provided the true hot-wet DMA curves to a high-temperature range above 100 °C and the true wet T_g values for the first time.

For validating and comparative purpose, the same DMA temperature sweeps were conducted at a commercial TA torsional rheometer ARES-G2 for the same composite specimens before and after the same hot-wet exposure as that applied to the in-situ DMA specimens. The measured dry and wet DMA curves of the composite specimens before and after the hot-wet exposure are presented in Fig. 35.8, where the dry and wet T_gs were determined from the measured dry and wet storage

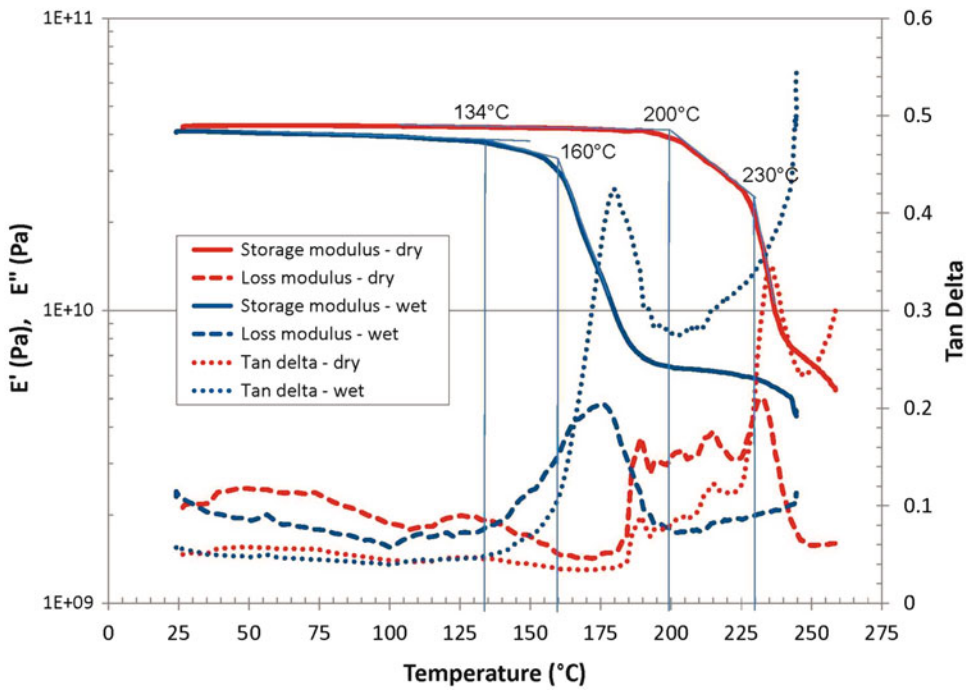

Fig. 35.7 In-situ 3-PB DMA curves of Carbon/Epoxy composite specimen in dry condition and in 3 % KCl brine after exposure in the brine at 300 °F for 72 h

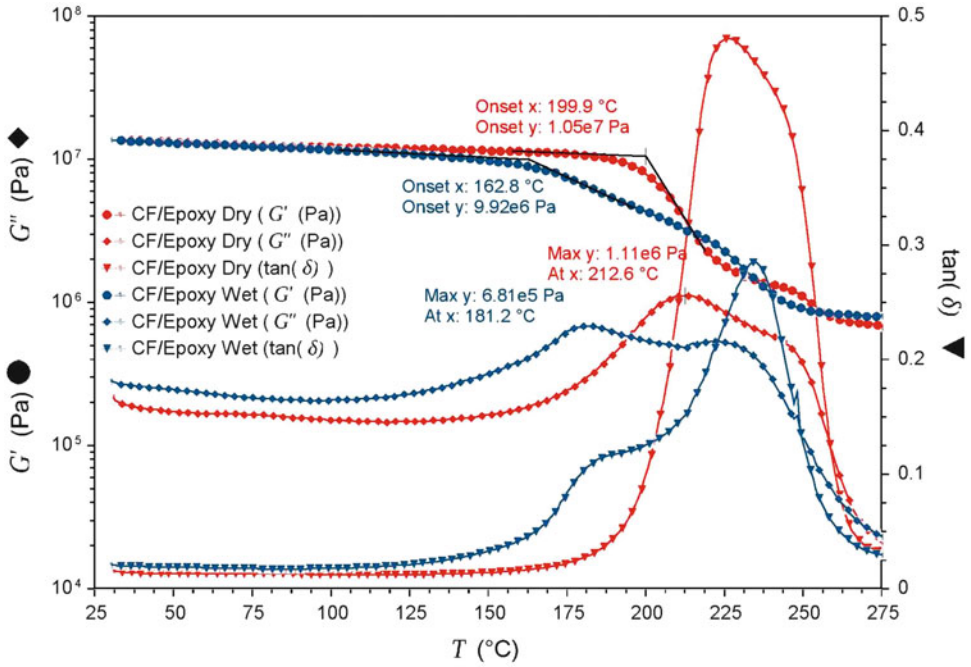

Fig. 35.8 Torsional DMA curves of Carbon/Epoxy composite specimen in dry condition and after exposure in 3 % KCl brine at 300 °F for 72 h determined by TA ARES-G2 rheometer

Table 35.2 Measured specimen weight of carbon/epoxy laminate specimens in unexposed condition and before and after DMA

	Unexposed	Exposed /before DMA	After DMA
Specimen weight #1 (g)	4.4466	4.4844	4.4328
Specimen weight #2 (g)	4.3932	4.4357	4.3779

modulus curves as 199.9 °C and 162.8 °C, respectively. Comparing the measured dry and wet T_gs determined from the commercial DMA analyzer with the in-situ DMA results, we found the two measured dry T_gs were identical, indicating a high accuracy of the in-situ DMA analyzer. However, for wet T_g measurement, the measured wet T_gs by the commercial analyzer were higher than the measured in-situ wet T_gs, and especially, the measured wet storage modulus curve after the transition flattened significantly; a very different result compared to the measured true in-situ wet storage modulus curve. These deviations are believed to be caused by the drying effect during the temperature sweep in the later portion of the analysis at higher temperatures. According to ASTM D7028, the procedure requires monitoring the moisture drying out in the exposed specimen in the wet T_g determination procedure by the regular DMA method. Table 35.2 lists the measured original dry weight of the two carbon/epoxy laminate specimens before the 72 h hot-wet exposure, after the hot-wet exposure (before DMA), and after the DMA procedure. We found from these data that the two DMA samples were dried out completely after the regular DMA procedure up to 275 °C.

Similarly, Fig. 35.9 presents the measured in-situ DMA curves for the rigid polymer foam specimens determined in unexposed dry condition and in de-ionized water after a two-hour exposure in the water at room temperature, respectively. From these results, we can see a major shift in wet T_g of the polymer foam. However, if we try to measure the wet T_g of the exposed foam specimen in a dry heating condition in a regular DMA analyzer, the exposed porous foam specimen would be dried out very quickly, and we could not even catch its wet T_g. This situation can be viewed clearly from Fig. 35.10 that presents the measured DMA curves for the rigid polymer foam specimens determined in unexposed dry condition and after exposure in the water at 150 °F for 3 h, respectively, in a TA ARES-G2 rheometer, where the measured "wet" DMA curves from the exposed wet foam specimen approached to the measured dry DMA curves from the unexposed dry foam specimen. Table 35.3 lists the measured original dry weight of the two rigid polymer foam specimens before the 3-h hot-wet exposure, after the hot-wet exposure (before DMA), and after the DMA procedure, where a complete drying out of the exposed specimens is also observed.

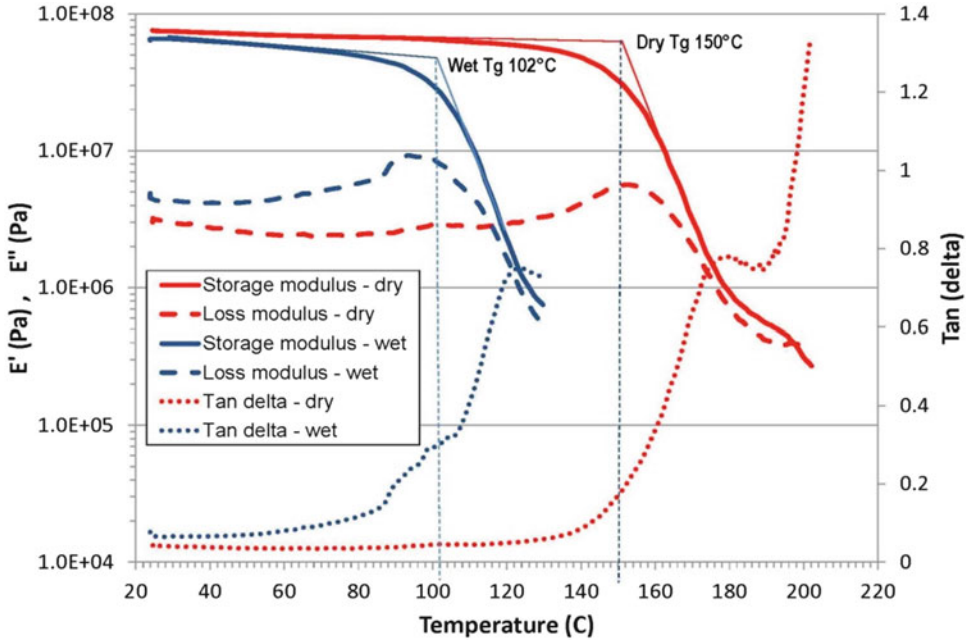

Fig. 35.9 In-situ compressive DMA curves of rigid polymer foam specimens in dry condition and in water after exposure in water at RT for 2 h

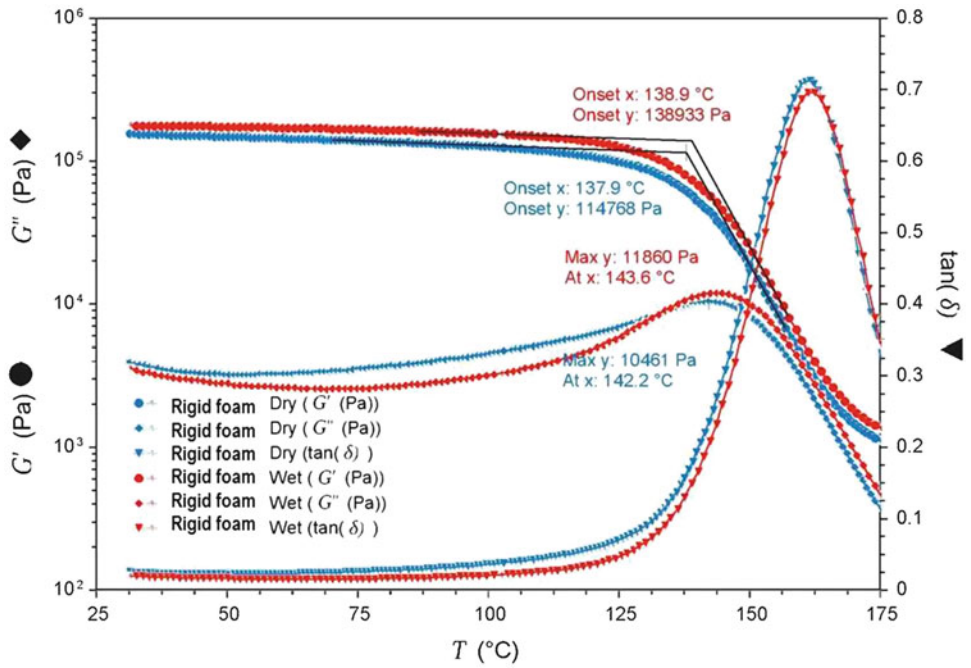

Fig. 35.10 Torsional DMA curves of rigid polymer foam sample in unexposed dry condition and after exposure in water at 150 °F for 3 h, determined at TA ARES-G2 rheometer

Table 35.3 Measured specimen weight of rigid polymer foam in unexposed condition and before and after DMA

	Unexposed	Exposed/before DMA	After DMA
Specimen weight #1 (g)	0.5077	0.8871	0.5033
Specimen weight #2 (g)	0.4931	0.9024	0.4897

It is agreed that by using the current standard DMA procedure with a relatively large-sized dense polymer or composite specimen, the analysis may still be able to catch the wet T_g of the exposed wet specimen closely in the early part of the temperature sweep starting from lower sweep temperatures if the wet T_g of the material is not very high. In the later part of the analysis under high sweep temperatures, however, the specimen drying out during the analysis could alter the analysis results, depending on the drying rates of the sample materials and the final sweep temperature.

35.3.2 Results of Hydrostatic Pressure-Dependent T_g Determination

Figure 35.11 presents the measured HPHT in-situ compressive DMA curves of ABS specimens determined in de-ionized water under 2.1, 41.4 and 68.9 MPa autoclave pressure, respectively. T_gs of ABS specimens under different hydrostatic pressures were determined by the onset points of each storage modulus curve as shown in Fig. 35.11, are 92.5 °C, 104 °C and 112.5 °C with respect to 2.1, 41.4 and 68.9 MPa hydrostatic pressure, respectively. A linear proportional relationship is observed between the measured T_gs and the applied hydrostatic pressure, as shown in Fig. 35.13. This linear relationship can be expressed as:

$$T_g(P) = 92.5 + 0.296\,P, \text{ where } T_g \text{ is in } ^\circ C \text{ and P is in MPa}$$

Figure 35.12 presents the measured HPHT in-situ compressive DMA curves of the PEEK specimens determined in de-ionized water under 3.4, 41.4 and 68.9 MPa autoclave pressure, respectively. T_gs of PEEK specimens under different hydrostatic pressures were determined by the onset points of each storage modulus curve as shown in Fig. 35.12, are 143 °C, 157 °C and 167 °C with respect to 3.4, 41.4 and 68.9 MPa hydrostatic pressure, respectively. A linear proportional relationship is observed between the measured T_gs and the applied hydrostatic pressure, as shown in Fig. 35.13. This linear relationship can be expressed as:

$$T_g(P) = 143 + 0.368\,P, \text{ where } T_g \text{ is in } ^\circ C \text{ and P is in MPa.}$$

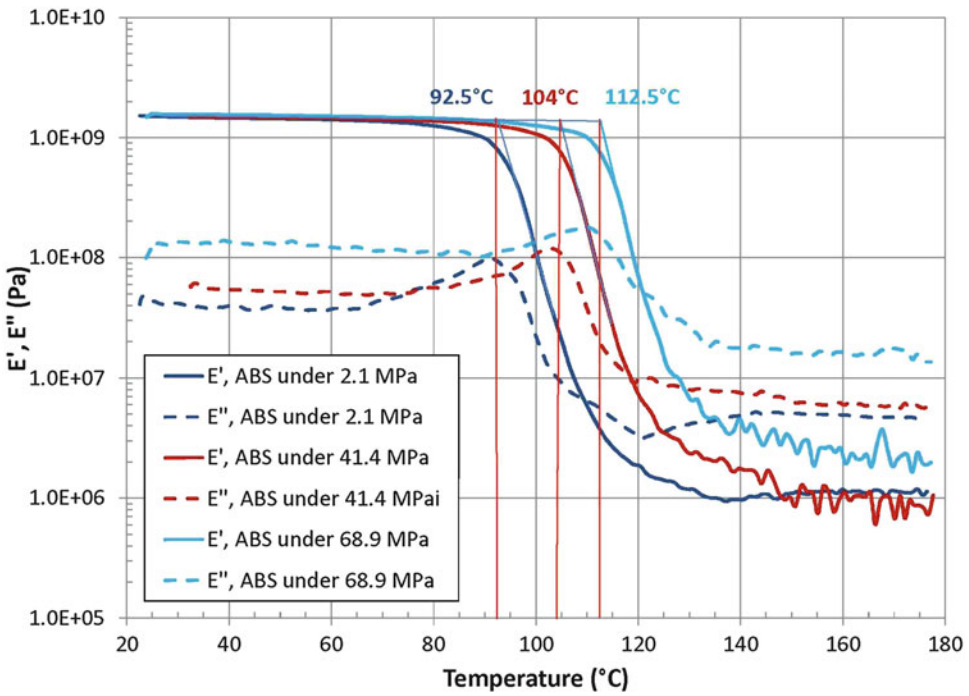

Fig. 35.11 HPHT in-situ compressive DMA curves of ABS specimens determined in deionized water under 2.1, 41.4 and 68.9 MPa autoclave pressure, respectively

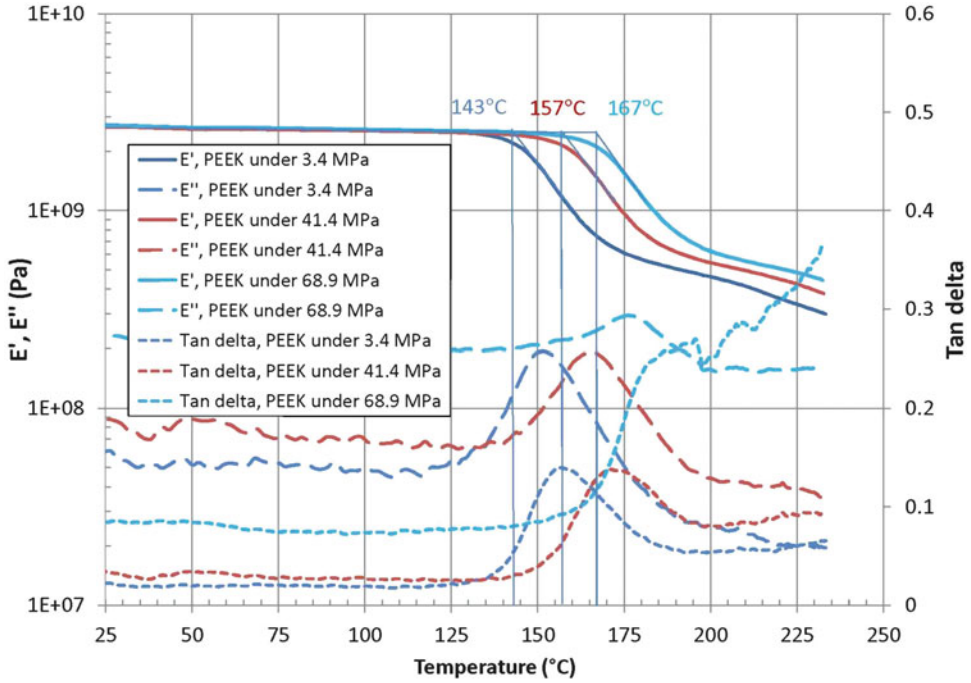

Fig. 35.12 HPHT in-situ compressive DMA curves of PEEK 450G specimens determined in deionized water under 3.4, 41.4 and 68.9 MPa autoclave pressure, respectively

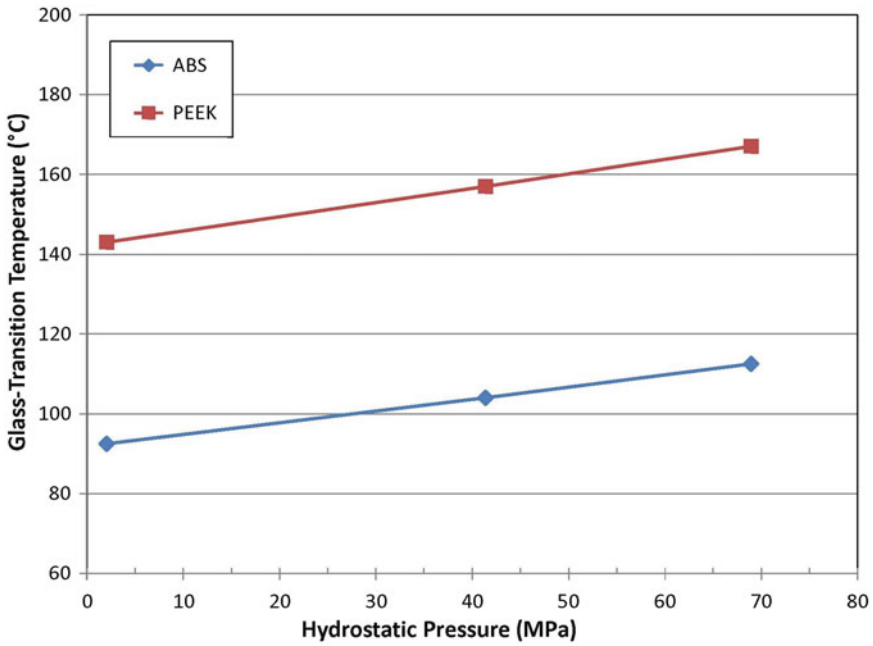

Fig. 35.13 Measured T_gs of ABS and PEEK G450 specimens as a function of hydrostatic pressure

In comparison of these results with the results reported for Victrex PEEK from the literature [10, 12], they reported a slope of 0.59 and 0.451, respectively. The major reasons causing this discrepancy are considered to be: (1) the different analysis mechanisms between the DMA method with current study and the dilatometry or PVT method with the two references; (2) the different containing fluids—in the current work, the de-ionized water was used that may give a possible degradation of the T_g of the PEEK specimen under a HPHT wet environment, while mercury was used in the dilatometry measurements; (3) the current HPHT in-situ DMA work had only three test points and tested only up to 69 MPa. However, the observed trend of increase in T_g of the polymers with increasing of the hydrostatic pressure is true.

Based on current HPHT in-situ DMA results from ABS and PEEK specimens, in addition to the verification of the hydrostatic pressure dependence of polymer T_g, we found no major effect of the hydrostatic pressure on storage modulus of the polymers in the glassy state before the transition under the current pressure range. However, the hydrostatic pressure may increase the modulus of the polymers in the rubbery state after the transition. This observation needs to be verified further.

35.4 Conclusions

(1) An innovative, industry-first HPHT in-situ DMA test system has been developed and established in-house based on the recently developed HPHT in-situ mechanical testing technology. This HPHT in-situ DMA analyzer is capable of performing DMA temperature sweep up to 260 °C in compression, 3-PB and tensile modes in a specified fluid and gas condition under a constant autoclave pressure up to 69 MPa (10,000 psi). This in-situ DMA analysis method can provide true wet DMA curves and wet T_gs of polymers, composites and polymer foam structures in a simulated HPHT hot-wet environment, and eliminates all the issues with the current DMA analyzers and the standard test procedures when analyzing the exposed wet specimens of the high-temperature polymers and composites.

(2) Hydrostatic pressure-dependent T_gs of ABS and PEEK polymers were determined by the in-house HPHT in-situ DMA analyzer in de-ionized water up to 69 MPa autoclave pressure. The in-situ DMA T_gs of the ABS and PEEK polymers increase with increasing of the hydrostatic pressure linearly with a slope of 0.296 and 0.368, respectively. No major effect of the hydrostatic pressure on storage modulus of the materials was observed in the glassy state of the polymers before the transition under current pressure range. However, the hydrostatic pressure may increase the modulus of the polymers in the rubbery state after the transition; this observation needs to be verified further.

Acknowledgement The authors would like to thank Baker Hughes Completions and Wellbore Intervention and Unconventional Multistage Completion Technology for their permission to publish this paper. The authors would like to express sincere appreciation to Bennett Richard, Director, Research and Technology, for his constant support, direction and encouragement to this research project and for his vision in expanding this HPHT in-situ testing capability in 2011. Thanks to Charley Tompkins, Testing & Automation Engineer at CTI Test Lab, for his fine work in creating the nitrogen pressure control system for the HPHT in-situ test system. Thanks also due to Shawn Young for his assistance to conducting HPHT in-situ tests for the projects.

References

1. Yuan, Y., Goodson, J.: Progress and challenges of composite applications in downhole operations. In: Proceedings of the third MERL Conference on Oilfield Engineering with Polymers, pp. 99–112. London, UK, Nov. 28–29, 2001
2. Yuan, Y., Goodson, J.: Hot-wet downhole conditions affect composite selection. Oil & Gas J. **105**(34), 52–63 (2007)
3. Ruffner, D.R.: Hygrothermal behavior. In: ASM Handbook, Vol. 21, Composites, pp. 246–251, ASM International (2001)
4. Browning, C.E.: The mechanisms of elevated temperature property losses in high performance structural epoxy resin matrix materials after exposure to high humidity environments. Ph.D. Dissertation, University of Dayton, Dayton, OH (Aug. 1976)
5. Yuan, Y., Goodson, J.: HP/HT hot-wet thermomechanical behavior of fiber-reinforced high-temperature polymer composites (Chapter 16). In: Tandon, G.P., et al. (eds.) Experimental Mechanics of Composite, Hybrid, and Multifunctional Materials. Conference Proceedings of the Society for Experimental Mechanics Series, vol. 6. Springer (2014)
6. Yuan, Y., Goodson, J., Fan, R.: HP/HT hot-wet resistance of thermoplastic PEEK and its composites (Chapter 18). In: Patterson, E., et al. (eds.) Composite Materials and Joining Technologies for Composites. Proceedings of the 2012 SEM Annual Conference on Experimental and Applied Mechanics, vol. 7. Springer, (2013)
7. Yuan, Y., Goodson, J.: HT/HP hot-wet thermomechanical properties and HT/HP in-situ mechanical test method of high-temperature polymer composites. In: Proceedings of The 52nd International SAMPE Symposium and Exhibition, Baltimore, MD, 3–7 June 2007
8. Yuan, Y., Goodson, J.: HTHP in-situ mechanical test rig and test method for high-temperature polymers and composites, SPE 113516. In: Proceedings of the 2008 SPE Europec/EAGE Annual Conference and Exhibition, Rome, Italy, 9–12 June 2008
9. Ngai, K.L.: The glass transition and the glassy state (Chapter 2). In: Physical Properties of Polymers, 3rd (edn.) Cambridge University Press (2004)
10. Zoller, P., Kenl, T.A., Starkweather, H.W., Jones, G.A.: The equation of state and heat of fusion of poly(ether ether ketone). J. Polym. Sci. **27**, 993–1007 (1989)
11. GNOMIX, Research, PVT apparatus description
12. Chaplin, A., Duckworth, C., Warmington, K.: Improved Temperature Performance PolyArylEtherKetone Polymers for use in HPHT Conditions, OTC-25212-MS. Presented at the Offshore Technology Conference, Houston, TX, USA, 5–8 May 2014
13. Ward, I.M., Sweeney, J.: The Mechanical Properties of Solid Polymers (Chapter 5), 2nd edn. Wiley, Chichester (2004)
14. Parry, E.J., Tabor, D.: A high-pressure torsion pendulum for viscoelastic studies on polymers. J. Phys. D: Appl. Phys. **6**, 1328–1335 (1973)
15. Timoshenko, S.P., Gere, J.M.: Theory of Elastic Stability (Chapter 11), 2nd edn. McGraw-Hill, New York (1961)

Chapter 36
HPHT Hot-Wet Resistance of Reinforcement Fibers and Fiber-Resin Interface of Advanced Composite Materials

Yusheng Yuan, Jiaxiang (Jason) Ren, and Christopher Campo

Abstract Advanced fiber-reinforced polymer-matrix composites are used extensively in oilfield downhole operations because of their performance, lightweight and easy-removal advantages. However, high-pressure/high-temperature (HPHT) corrosive borehole environments pose significant challenges to these materials. It is well known that a high-temperature hot-wet environment degrades most matrix resins. Effects of this environment on various advanced reinforcement fibers and the fiber/resin interfaces in composites, however, have not received enough attention.

In this study, E-glass, S2-glass, aramid and carbon fibers were studied in weaved tape and braided sleeve forms. Tape pull tests were conducted before and after hot-wet exposure in 3 % NaCl brine at room temperature, 66 °C, 121 °C, 204 °C under 34.5 MPa for 168 h. SEM, EDS, FTIR, TGA and DSC techniques were used to identify the degradation mechanisms of various fibers from the environmental exposure. Glass and aramid fibers were determined to be susceptible to severe hydrolytic degradations when immersed in a HPHT wet environment. The fiber-resin interfaces of the continuous and chopped glass and carbon fiber-reinforced thermoset and thermoplastic matrix composites were examined under microscopy after the hot-wet exposure and revealed major differentiations. The effects of the fiber-resin bonding strength and interface debonding after the environmental exposure on the mechanical properties of the composites were also evaluated.

Key words Composite materials • Reinforcement fibers • Fiber/resin interface • Interface debonding • HPHT • Hot-wet condition

36.1 Introduction

Advanced fiber-reinforced composite materials have been used extensively in aerospace and numerous critical industrial applications, including those in oilfield operations [1–3], where high-temperature performance and certain environmental-resistance capability are demanded. Recent technology advancements in deepwater drilling and completion and unconventional oil and gas recovery pushed the oilfield downhole operations into an extreme high-pressure and high-temperature (HPHT) environment where the bottom-hole temperature and pressure can reach 204 °C and 70 MPa or higher associated with a hot-wet environmental condition. This HPHT hot-wet borehole condition provides significant challenges to composite materials and their applications [4, 5].

Hygrothermal mechanical behavior and hygrothermal or hydrolytic degradation of composite materials has been a critical research subject for high-performance composite materials and their applications since the 1960s. This class of degradations in composite materials involves the degradations of matrix resins, reinforcement fibers and fiber/resin interface or interphase adhesion. A high-temperature hot-wet condition introduces major degradations to most high-temperature polymer resins, involving moisture-induced glass transition temperature (T_g) shift and high-temperature mechanical property loss [6, 7] and even destructive hydrolytic polymer chain scission or total polymer destruction in such a hot-wet environment [8, 9, 5].

Carbon, glass and Kevlar fibers are high-performance reinforcement fibers used commonly in advanced polymer matrix composites. Continuous glass fibers are produced by a drawn process from molten glass, contain 52–66 % silica and a host of other oxides, and designed with E-, S- and ECR-grades for various applications [10]. Carbon or graphite fibers are produced by converting polyacrylonitrile (PAN) or pitch-based polymer fiber precursors through a high-temperature carbonization or graphitization process under stretching. These fibers are designed and produced in different

Y. Yuan (✉) • J. Ren • C. Campo
Baker Hughes, 14990 Yorktown Plaza Dr., Houston, TX 77040, USA
e-mail: yusheng.yuan@bakerhughes.com

C. Ralph et al. (eds.), *Mechanics of Composite and Multi-functional Materials, Volume 7*,
Conference Proceedings of the Society for Experimental Mechanics Series, DOI 10.1007/978-3-319-21762-8_36

performance grades including "standard modulus," "high-strength" and "high-modulus high-strength" [11]. Kevlar or aramid fibers are made by an extrusion and drawing process through a spinneret from an aromatic polyamide liquid-crystalline solution (poly para-phenylene terephthalamide). Subsequent high-temperature heat treatment of the spun fibers under tension can increase the orientation of the crystalline structure and enhance the tensile modulus and tensile strength of the fibers [12, 13].

Kevlar fibers are organic aromatic polyamide fibers. Research in 1984 pointed out that the amide linkage in the aromatic polyamide macromolecule is susceptible hydrolytic chain scission [13]. Experimental studies on the tensile strength degradation rate of the Kevlar 49 fiber yarns aged in 100 % relative humidity at various temperatures under stress-free conditions indicated that the degradation rates were 12,426 % per year when aged at 200 °C for 2 days, 199 % per year when aged at 125 °C for 32 days and about 3 % per year when aged at 65 °C for 440 days [13]. However, DuPont researchers reported dry and hot-wet tensile modulus and strength data of the Kevlar 49 aramid yarn before and after aging in 95 % relative humidity at 180 °C for 21 days and found no major degradation when tested at 180 °C [12]. In all these studies, the Kevlar 49 fiber yarns were exposed in 95–100 % relative humidity, and no reliable hot-wet mechanical property data available from the fiber yarns aged in an immersed hot-water condition.

Glass fibers and carbon fibers are inorganic fibers with higher application temperatures. Engineers often have fewer concerns about hot-wet degradation of these fibers. Reports since the 1960s have indicated that humidity and water immersion led to continuous loss of strength of the glass fibers. The proposed major mechanism for this strength loss in an aqueous environment was alkali ion leaching/exchanging and the hydroxide forming process in the wet glass-fiber surface region. The hydroxyl ions broke further the siloxane bonds in the glass structure and eventually dissolved the silicate glass [14–16].

Fiber/resin interface or interphase and their effects on the performance of the composite materials have been important research topics in composite materials and mechanics for decades. Comprehensive review on these topics can be found from the review articles and reports [17, 18]. Extensive studies on environmental effects, especially moisture effects on interfacial properties have been conducted for glass fiber- and carbon fiber-reinforced composites, but focused more to the glass fiber-reinforced composites because glass fibers are more susceptible to moisture degradation [19–23]. Surface treatment techniques involving surface chemistry altering and surface topographical feature introduction, have been used successfully to treat the carbon fibers and improve their wettability and adhesion to the matrix resin [18]. Less-significant effects of humidity or seawater immersion on the interfacial properties of the carbon/epoxy or carbon/BMI composites were observed at ambient temperature conditions [18, 23]. A silane coupling agent was developed and applied to glass fibers to protect them from environmental corrosion in a wet condition [24, 17, 19]. However, this protection can only last at ambient or low temperatures when the glass fibers are used as reinforcement in a resin composite in a wet condition. Other reports have indicated that when the composite was exposed in water at 60–100 °C, the glass fibers de-bonded from the matrix resin quickly, even when the glass fibers were treated with silane coupling agent. This de-bonding was a result of the hot-water invasion, resin swelling, glass fiber surface corrosion and osmosis pressure buildup at the fiber/resin interface in the hot-wet condition [19, 20, 24]. In all the above-mentioned studies the tests were conducted at ambient temperature or a temperature below 100 °C; no test data have been reported under a HPHT hot-wet test condition. In addition, the test materials were mainly limited to carbon or glass fiber-reinforced epoxy or other thermosetting resins, where the advanced thermoplastic matrix composites such as PEEK matrix composites were not included except in the author's two publications [4, 5].

In this study, E-glass, S2-glass, aramid and carbon fibers were studied with weaved narrow tape forms. Tape pull tests were conducted before and after a hot-wet exposure in 3 % NaCl brine at RT, 66 °C, 121 °C and 204 °C under 34.5 MPa for 168 h. Scanning electron microscopy (SEM), energy-dispersive X-ray spectroscopy (EDS), Fourier-transform infrared (FT-IR), differential scanning calorimetry (DSC) and thermal gravity analysis (TGA) techniques were used to identify the degradation mechanisms of various fibers from the environmental exposure. Glass and aramid fibers were identified to be susceptible to hydrolytic breakdown when immersed in the HPHT wet environment. The fiber-resin interfaces of the continuous and chopped glass and carbon fiber-reinforced thermoset and thermoplastic matrix composites were examined under microscopy after the hot-wet exposure and revealed major differentiations. The effects of the fiber strength degradation and fiber-resin interface de-bonding after the environmental exposure on the mechanical properties of the composites were also evaluated.

36.2 Experimental

36.2.1 Reinforcement Fibers and Composite Laminates

E-glass, S-glass, carbon and aramid (Kevlar) fibers are advanced reinforcement fibers for structural composites that were selected for evaluation. To evaluate the hot-wet environmental-resistant capability of various fibers in a simulated HPHT hot-wet condition conveniently, fibers of each type were weaved into 25.4-mm wide and 0.25-mm thick continuous plain-wave fabric tapes by Carolina Narrow Fabric (CNF) Co. and Fabric Development Inc., respectively. Type of fiber, elastic modulus, weaving style, dimensions and manufacturer information are listed in Table 36.1. Pictures of various tapes are shown in Fig. 36.1.

To investigate the HPHT hot-wet degradations of various fibers and fiber/resin interfaces in various composite material systems and their effect on mechanical properties of the composite materials, E-glass, S2-glass and carbon fibers were used as reinforcements, and a high-temperature amine-cured tetra-functional epoxy resin (EP-1) and a thermoplastic PEEK resin (TP-1) were used as matrix resins to form cross-ply or bidirectional fabric composite laminates. In addition, Victrex chopped glass fiber- and chopped carbon fiber-reinforced PEEK molding compounds, 450GL30 and 450CA30, were also under investigation because these materials are used extensively in downhole equipment and applications. These molding compounds were used to mold the ASTM D638 Type 1 tensile specimens by injection molding. These composite systems, with descriptions on their resin and reinforcement systems, fiber architecture, processing method, cure or consolidation schedule, manufacturer and their measured dry T_g are listed in Table 36.2.

Table 36.1 List of fabric tapes weaved from various reinforcement fibers in study

Fabric tape	Fiber type	Elastic modulus (msi)	Weaving style	Width × Thick (mm)	Fiber manufacturer	Tape manufacturer
E-glass fiber tape	E-glass	10.5	PW	25.4 × 0.25	Owens-Corning	CNF
S-glass fiber tape	S-glass	12.4	PW	25.4 × 0.25	Owens-Corning	CNF
Aramid fiber tape	Kevlar 29	12.0	PW	25.4 × 0.25	Du Pont	CNF
Carbon fiber tape	AS4	34.0	PW	25.4 × 0.25	Hexcel	Fabric Development

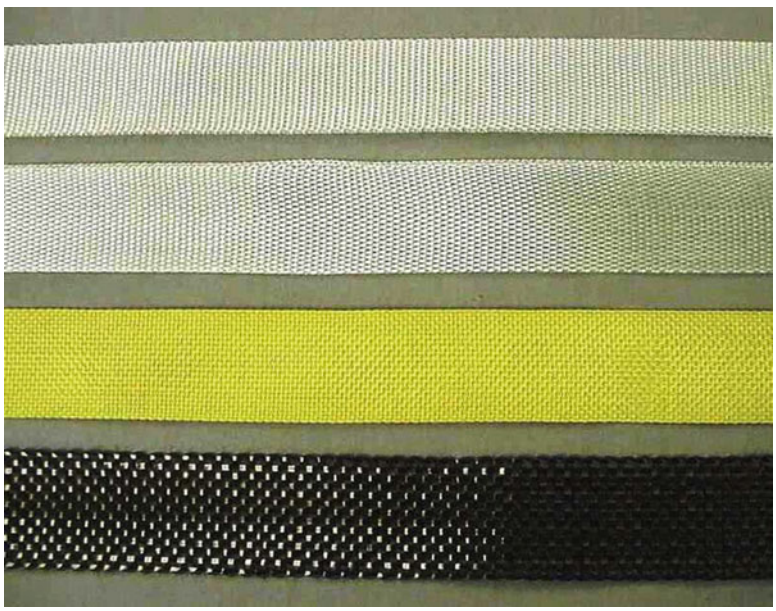

Fig. 36.1 E-glass, S2-glass, Kevlar and carbon fiber narrow fabric tapes (25.4 mm wide, 0.25 mm thick) from top to bottom for evaluation

Table 36.2 List of composite laminates and chopped short fiber-filled PEEK molding compounds in study

Composite system	Type of resin	Type of fiber	Fiber architecture	Processing method	Cure/consolidation schedule	V_f (%)	Dry T_g (°C)	Manufacturer A, B, C
EP-1/ 7781E	Tetra-f. epoxy amine cured	E-glass	7781 8HS fabric 51 %/ 49 %	Wet lamination	Cured at 191 °C for 3 h under 100 psi	54	228	Resin by A Laminate by B
EP-1/ 6781S	Tetra-f. epoxy amine cured	S2-glass	6781 8HS fabric 51 %/ 49 %	Wet lamination	Cured at 191 °C for 3 h under 100 psi	53	228	Resin by A Laminate by B
EP-1/T300	Tetra-f. epoxy amine cured	T300 carbon	284 PW fabric 50 %/50 %	Wet lamination	Cured at 191 °C for 3 h under 100 psi	54	221	Resin by A laminate by B
TP-1/AS4	Victrex PEEK 150G	AS4 carbon	UD tape [0/90] ns	Autoclave prepreg lamination	390 °C, 150 psi for 25 min; cooled under pressure	59	144[a]	Prepreg by Cytec Laminate by Cytec
TP-1/S2-G	Victrex PEEK 150G	S2-glass	UD tape [0/90] ns	Prepreg lamination	Manufacturer's proprietary	58	145[a]	Prepreg by Cytec Laminate by C
Victrex 450GL30	Victrex PEEK 450G	E-glass	~0.8 mm long in molding flow	Injection molding	Manufacturer's proprietary	17.7 30 % by wt.	143	Comp'd by Victrex Molded by Victrex
Victrex 450CA30	Victrex PEEK 450G	Carbon	~0.8 mm long in molding flow	Injection molding	Manufacturer's proprietary	23.8 30 % by wt.	143	Comp'd by Victrex Molded by Victrex
Victrex 450G	Victrex PEEK neat resin	None	_	Injection molding	Manufacturer's proprietary	_	143	Molded by Victrex

36.2.2 HPHT Hot-Wet Environmental Simulation

Hostile wellbores often involve high temperatures, high pressures and corrosive fluid and gas environments. Among various downhole fluid and gas conditions, one of the most commonly encountered and most destructive environment to polymeric resins and their composites are caustic water-based brine solutions. The current HPHT environmental exposure tests were designed to be conducted in 3 % NaCl brine in a high-pressure autoclave at 121 °C to 204 °C under 34.5 MPa for 3–10 days, simulating a class of short-term HPHT downhole applications [2, 3]. At the end of each HPHT exposure process, the autoclave temperature was first cooled to below 93 °C, and then the pressure was released at 0.34 MPa/min to 13.8 MPa and then at 0.14 MPa/min to the ambient pressure to avoid any rapid gas decompression (RGD) damage to the exposed test specimens. This environmental exposure design is an application-oriented, fixed-time conditioning scheme, where the effect of the specimen thickness on the water absorption is noted.

36.2.3 Hot-Wet Evaluation of Woven Fabric Tape

E-glass, S2-glass, Kevlar (Aramid) and carbon fiber woven fabric tape, as shown in Fig. 36.1, were used as the test specimens in this evaluation. The tape specimens were cut to 50 cm and rolled into small loose rolls for easy handling during the exposure procedure. The evaluation involved (1) hot-wet exposure of the tape specimens in 3 % NaCl brine at room temperature (RT) and 66 °C under ambient pressure for 168 h and at 121 °C and 204 °C under 34.5 MPa for 168 h, (2) visual inspection to the tape specimens after each hot-wet exposure procedure, and (3) tape pull tests, conducted on an MTS machine at RT before and after the hot-wet exposure using a set of roller tape grips, as shown in Fig. 36.2, under the displacement control mode with displacement rate of 12 in/min per ASTM D5035.

Fig. 36.2 Roller grips used for fabric tape pull tests on an MTS test machine

36.2.4 Composite Mechanical Tests

Standard tensile and compression tests were conducted for the selected composite laminates and the injection molded test specimens at room and elevated temperatures before and after the hot-wet environmental exposure. The purpose of conducting mechanical tests at room temperature (RT) before and after the hot-wet exposure was to identify the hot-wet-exposure-induced material structural damage and the structural damage caused mechanical degradation with the exposed test specimens because this comparative scheme excludes any other effects to the investigation in addition to the hot-wet-exposure-induced material structural damage. The tensile and compression tests were conducted on a 100 KN MTS servo-hydraulic testing machine with a controlled test oven, an alignment fixture, a set of tensile wedge grips and a regular or an advanced video extensometer for tensile tests, and a standard combined loading compression test fixture for compression tests according to ASTM standards D3039, D638 and D6641, respectively. The standard straight-side D3039 tensile specimens (254 × 25.40 × 3.20 mm) and D6641 compression specimens (140.0 × 12.70 × 3.20 mm) were cut and machined using diamond tools from the composite laminate panels. The laminate panels were supplied by the manufacturers, fabricated by wet or prepreg lamination process in symmetric cross-ply or balanced bi-directional woven-fabric lamination with thicknesses ranging from 2.50 to 3.20 mm. These laminates were further cured or consolidated in an autoclave or under a hot press per the manufacturer's specified cure or consolidating schedules. For short fiber-filled PEEK molding compounds, ASTM D638 Type 1 standard tensile specimens were prepared by an injection molding process by the compound manufacturer. The tensile and compression tests were conducted under displacement control mode with a loading rate of 1.5 mm/min for composite laminate specimens and 5 mm/min for short-fiber filled PEEK specimens, respectively, according to the applied ASTM test standards. In the high-temperature tests, the test specimens were heated at the test temperature for 20 min in the tensile grips or compression test fixture in the test oven prior to the mechanical testing. Four to six tests were conducted under each test condition.

36.2.5 Microstructure and Interface Examination

To study the hot-wet resistance of the fiber/resin interfaces in the selected continuous fiber-reinforced composite laminate specimens and the molded short fiber-reinforced composite specimens, microstructures of the laminated and the molded test specimens before and after the HPHT hot-wet exposure were examined with carefully polished cross-sectional composite samples under a Leica MDI 5000 M inverted optical microscope with magnifications in the range of ×100 to ×2000. The

laminate cross-sectional samples were cut along the symmetric planes of the cross-ply or bi-directional fabric laminate specimens. For the injection-molded short fiber-reinforced PEEK specimens, the cross-sectional samples were cut in longitudinal and transverse directions of the test specimens.

36.2.6 Thermal Mechanical Analysis

Glass transition temperatures (T_g) and the related dynamic viscoelastic behavior of the composite samples in study were analyzed and determined by dynamic mechanical analysis (DMA) using an TA ARES G2 analyzer with torsional oscillation mode per ASTM D4065 before and after the specified hot-wet environmental exposure. In the DMA analysis, a 0.05 % torsional strain was applied under 1 Hz frequency and a heating rate of 3–5 °C per minute. The T_g values were determined by the onset point of the storage modulus curves (G'). The torsional beam samples were about 51 × 12.7 × 3.2 mm in dimensions. This relatively large sample size is helpful to keep the absorbed moisture inside the exposed test samples during the DMA temperature sweep.

36.2.7 Analytical Methods for Fiber Degradation Mechanism Study

Fourier-transform infrared (FT-IR), thermal gravity analysis (TGA), and differential scanning calorimetry (DSC) measurements were performed on the Kevlar tapes before and after hot-wet exposure. FT-IR, energy-dispersive X-ray spectroscopy (EDS), and scanning electron microscopy (SEM) measurements were performed on the E- and S2-glass tapes before and after the exposure. The E-glass sleeve sample during the interim of the exposure was also included in the analysis. The FT-IR measurements were performed with a Thermofisher Nicolet 6700 instrument. The attenuated total reflectance (ATR) sampling technology was used with diamond crystal. The TGA measurements were performed with TA instrument TGA Q500 in nitrogen environment with 10 °C/min heating rate. The DSC measurements were performed with TA instrument DSC Q2000 in nitrogen environment with 10 °C/min heating rate up to 550 °C. The EDS and SEM measurements were performed with FEI Quanta 600 instrument.

36.3 Results and Discussion

36.3.1 Hot-Wet Resistance of Reinforcement Fibers

Visual Inspection and Pull Test Results. Visual inspection to E-glass, S2-glass, Kevlar and carbon fiber tape specimens after exposure in 3 % NaCl brine for 168 h at various temperatures indicated that (1) no major changes in appearance were found from all types of the tape specimens after exposure at RT and 66 °C for 168 h; (2) after exposure at 121 °C and 34.5 MPa for 168 h, the E-glass tape were distorted, Kevlar tape were discolored from yellow to brown, but no major changes in appearance were found from the S2-glass and the carbon fiber tape; (3) after exposure at 204 °C and 34.5 MPa for 168 h, the E-glass tape became thinner and fragile, the Kevlar tape became very fragile and could be torn by the fingers easily, and the S2-glass tapes were broken when the tapes were unrolled from their test rolls, as shown in Figs. 36.3, 36.4 and 36.5. This observation indicated a hydrolytic degradation occurred in the glass fibers and Kevlar fibers. Only the carbon fiber tape survived with no major changes in appearance, dimensions and flexibility. In addition to this, Fig. 36.6 shows a braided E-glass sleeve after repeated exposure in 3 % NaCl brine at 121 °C to 177 °C and 34.5 MPa for up to 80 days, where the E-glass sleeve became thinner and thinner during the hot-wet exposure. Eventually, the E-glass fibers lost their fiber form completely and became a very brittle and fragile substance.

The tape pull tests were conducted at room temperature (RT) after exposure in 3 % NaCl brine at RT, 66 °C, 121 °C and 204 °C for 168 h, respectively. By using the breaking force of each unexposed tape at RT as the base line, the normalized breaking force retention of various fabric tape after exposure in different temperature conditions for 168 h are summarized in the chart presented in Fig. 36.7. From these pull test results, the hot-wet environment induced mechanical degradation to the glass fibers and the Kevlar fibers are clearly visible. After exposure in 3 % NaCl brine at 204 °C and 34.5 MPa for 168 h, the

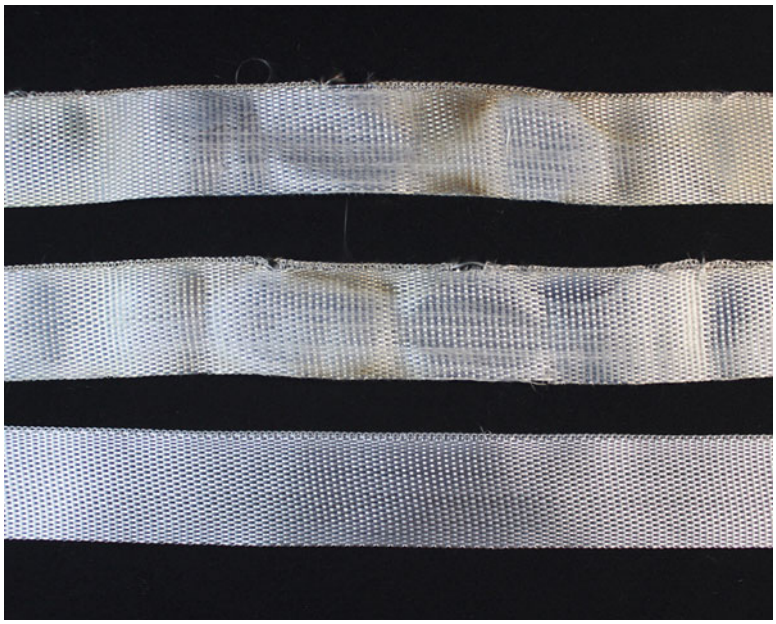

Fig. 36.3 E-glass fabric tape samples before (bottom) and after (top two) exposure in 3 % NaCl brine at 204 °C, 34.5 MPa for 168 h

Fig. 36.4 S2-glass fabric tape samples before (bottom) and after (top two) exposure in 3 % NaCl brine at 204 °C, 34.5 MPa for 168 h

glass fibers and aramid fibers lost their mechanical strength completely; only carbon fibers could retain close to it's full strength (>90 %).

Degradation Mechanism and Analysis Results. The Kevlar tape became very fragile with color change after HPHT hot-wet exposure. Figure 36.8 shows the FT-IR spectra of the Kevlar tape before and after the 168-h exposure in 3 % NaCl brine. The peak at wavenumber 3300 cm^{-1} is assigned to hydroxyl group and amine group while the peaks at wavenumber 1538 and 1508 cm^{-1} are assigned to phenyl group, and the phenyl group was stable in the brine environment. The peak area ratio at wavenumber 3300 cm^{-1} to that at wavenumber 1538, 1508 cm^{-1} increased after the exposure, which was likely due to the formation of more hydroxyl and primary amine groups during the hydrolysis process of the Kevlar tape. The FT-IR spectra of the other peaks changed little after the exposure. TGA measurement results in Fig. 36.9 show that the onset thermal degradation temperature of the fiber reduced from 485 °C to 467 °C after the exposure. The reduction of the thermal degradation temperature is likely due to the molecular weight reduction of the Kevlar tape after the exposure. The melting temperature was not detected up to 550 °C by DSC measurement for the sample before and after the exposure, which implies

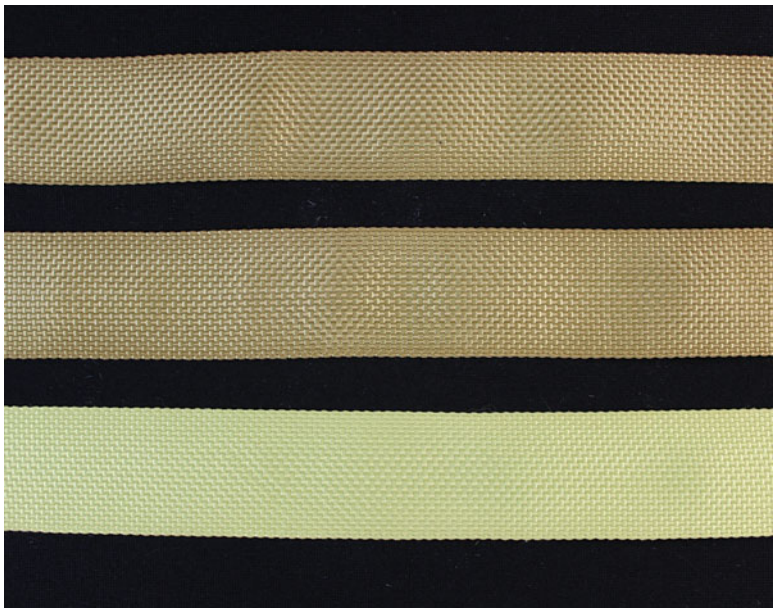

Fig. 36.5 Kevlar fabric tape samples before (bottom) and after (top two) exposure in 3 % NaCl brine at 204 °C, 34.5 MPa for 168 h

Fig. 36.6 Braided E-glass sleeves before (*left*) and after repeated exposure in 3 % NaCl brine at 121 °C to 177 °C, 34.5 MPa for about 50 days (interim) and for about 80 days (*right*)

that the melting temperature of the fresh and the exposed Kevlar tape is above 550 °C. The degradation of the Kevlar tape in the brine at 204 °C is due to the hydrolytically induced chain scission of amide linkage. The results of the study are consistent with the hydrolysis study of poly (p-phenylene tere-phthalamide) polymer by Morgan and coworkers [13].

Figures 36.10 and 36.11 show the SEM micrographs of the S2-glass and E-glass tape, respectively, before and after the hot-wet exposure in 3 % NaCl brine at 204 °C for 168-h, where we can see clearly that fresh sizing was applied on each individual fiber in the unexposed tape. However, after the hot-wet exposure only clean glass fibers can be observed with some precipitated or deposited material on the surface of the fibers.

Figure 36.12 shows the FT-IR spectra of the S2-glass tape before and after the 168-h hot-wet exposure. The peaks at wavenumber 3300 cm^{-1} and 1730 cm^{-1} of the unexposed S-glass fiber are very likely attributed to the coupling agent on the glass fibers. The wavenumber at 3300 cm^{-1} could be due the hydroxide group, which bonds coupling agent with Si-O group on the glass surface [20]. The peak at wavenumber 1730 cm^{-1} is likely due to the C=O group in the coupling agent [25]. The peaks at the two wavenumbers disappeared after the exposure, implying that the coupling agent was not stable in the brine at 204 °C and dissolved in the 168-h exposure. The wavenumber and area of the other main peaks that define the S2-glass structure did not change much after the exposure.

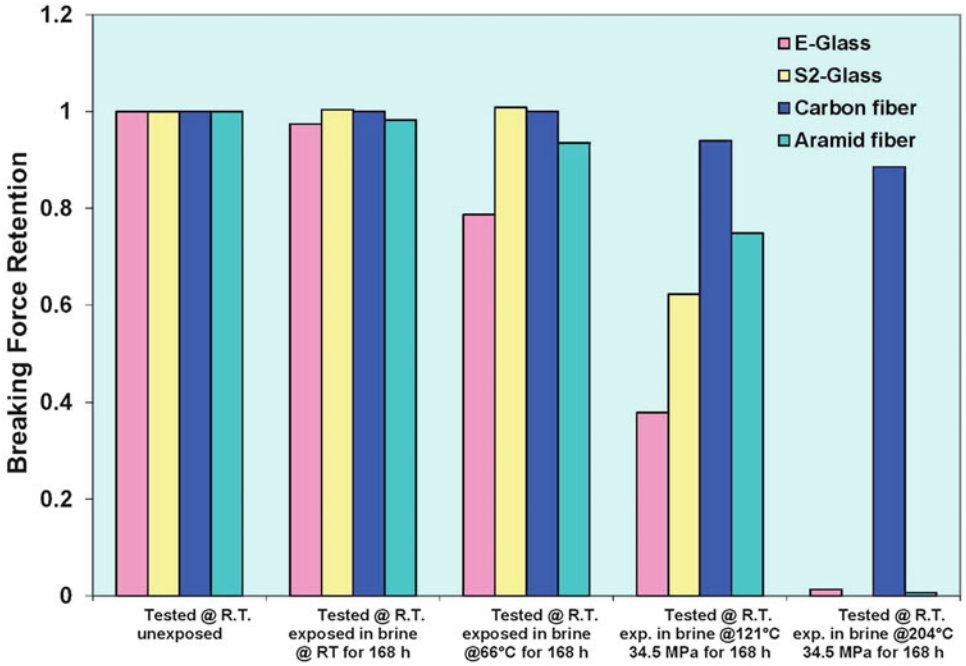

Fig. 36.7 Breaking force retention of various types of woven fabric tapes before and after the hot-wet exposure at different temperatures

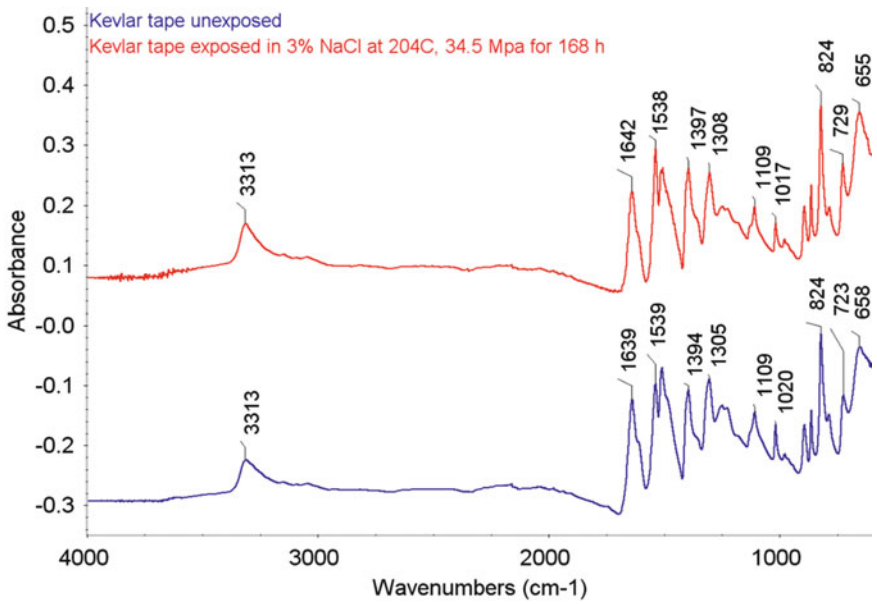

Fig. 36.8 FT-IR spectra of Kevlar tape before and after exposure in 3 % NaCl at 204 °C, 34.5 MPa for 168 h

EDS measurement spectra of the unexposed S2-glass tape show that Mg, Al, and Si are the major elements (oxygen is not included) in the S2-glass fibers. The weight concentrations of the elements were calculated based on the spectra and the results are consistent with the reported composition of S2-glass fiber in the literatures [10]. Table 36.3 summarizes the weight concentration of major elements of the S2-glass tape before and after the 204 °C hot-wet exposure. Mg had a major loss in weight concentration after the hot-wet exposure, which implies a leaching process of Mg ions out from the S2-glass fibers was associated with the hot-wet exposure. This observation is consistent with the early finding by Andrew Hsu and his coauthors [26]. These results agreed with early researchers [14–16, 20] on the degradation mechanisms of the glass fibers when immersed in a hot-wet condition that involved alkali ion leaching or exchanging, a reaction with the hydrogen ion from water and a hydroxide-forming process in the wet glass fiber surface region (Stage 1), and the formed hydroxyl ions breaking further the siloxane bonds in the glass structure and finally dissolving the silicate glass with formation of silicic acid

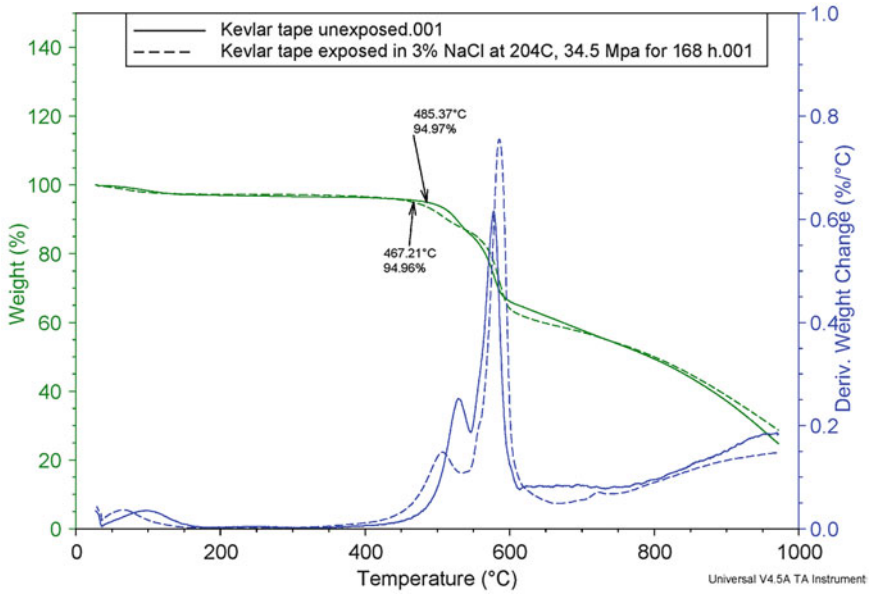

Fig. 36.9 TGA measurement results of Kevlar tape before and after exposure in 3 % NaCl at 204 °C, 34.5 MPa for 168 h

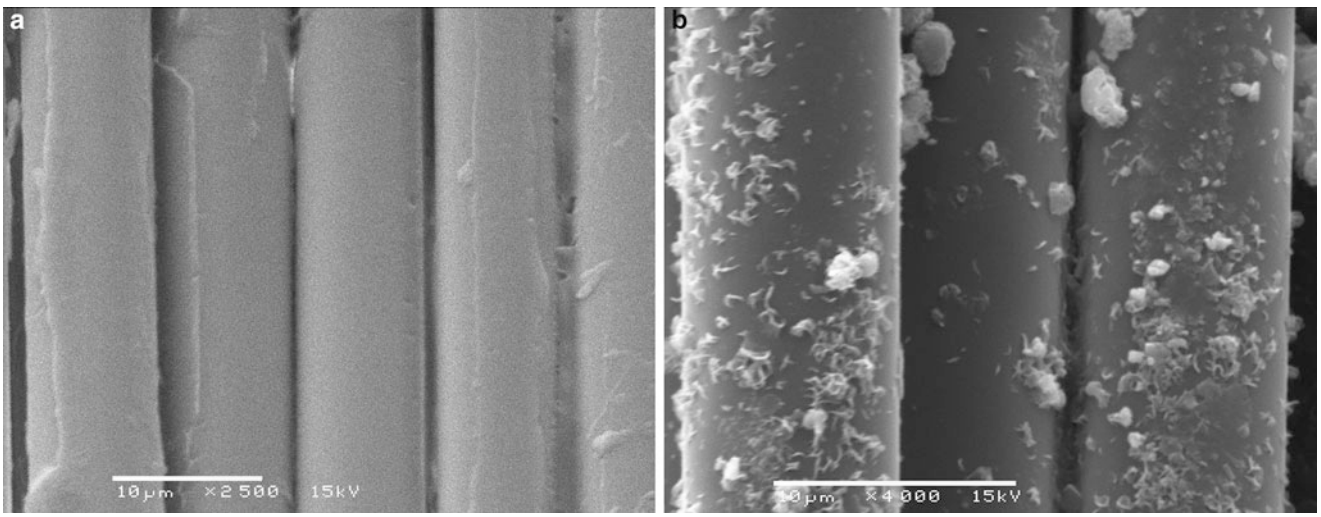

Fig. 36.10 SEM micrographs of S2-glass woven fabric tape before (**a**) and after (**b**) hot-wet exposure in 3 % NaCl brine at 204 °C, 34.5 MPa for 168 h

hydroxyls (Stage 2). In the current 168-h hot-wet exposure condition at 204 °C, the degradation is still considered to be limited in the surface region of the glass fibers, where the glass is still in fiber form but porosity and cracking were produced on the surface region. This structural degradation on the glass fiber surface eliminates the tensile strength of the glass fibers because the brittle glass fibers are very sensitive to their surface defects and cracking.

The FT-IR spectra of the E-glass tape before and after the 168-h hot-wet exposure are presented in Fig. 36.13, where the spectra show the main peak at wavenumber 911 cm^{-1} shifted to 979 cm^{-1} after the exposure. The peak at 911 cm^{-1} is assigned to a symmetric Si-O vibration in the alkali environment. The increase of the wavenumber of the peak could be due to the formation of SiO_2 film on the glass fiber surface by the preferential leaching of alkali ions and calcium ions into the solution during the exposure process. Other peaks at 3323 cm^{-1}, 1735 cm^{-1}, 1377 cm^{-1} are also observed for the unexposed E-glass tape. The peak at 3323 cm^{-1} is likely due to the hydroxide group formed between the coupling agent and the Si-O group on the glass surface with adsorbed moisture. The peak at 1735 cm^{-1} is likely attributed to the C=O group in the coupling agent and the peak at 1377 cm^{-1} is likely attributed to the vinyl group in the coupling agent. After aging, the peaks from the coupling agent did not disappear, but the wavenumber of the peaks shifted, indicating that the coupling agent on

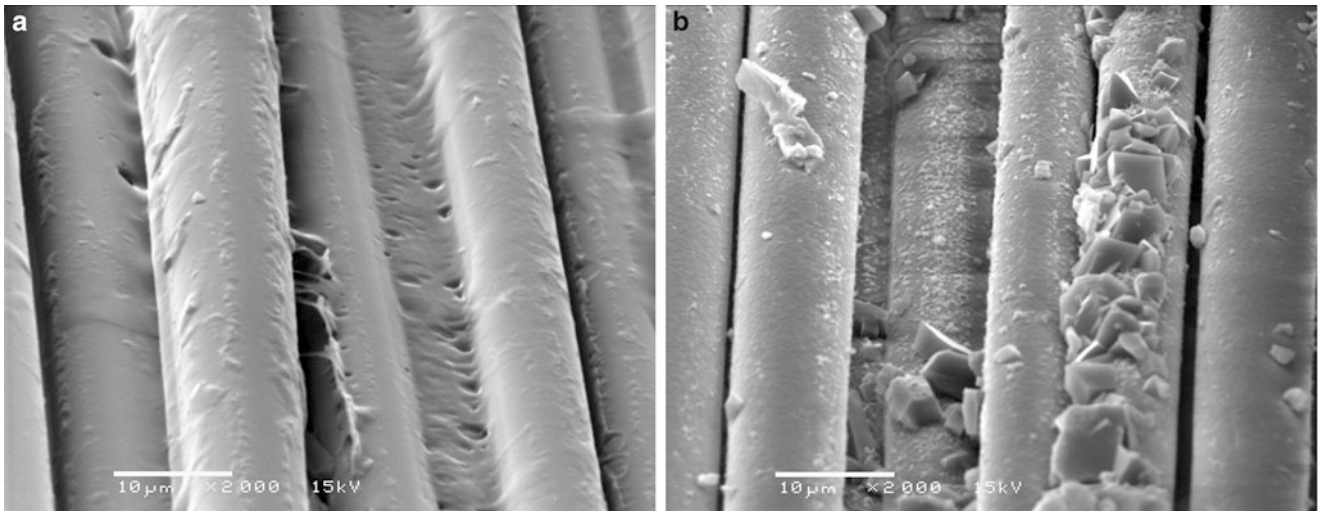

Fig. 36.11 SEM micrographs of E-glass woven fabric tape before (**a**) and after (**b**) hot-wet exposure in 3 % NaCl brine at 204 °C, 34.5 MPa for 168 h

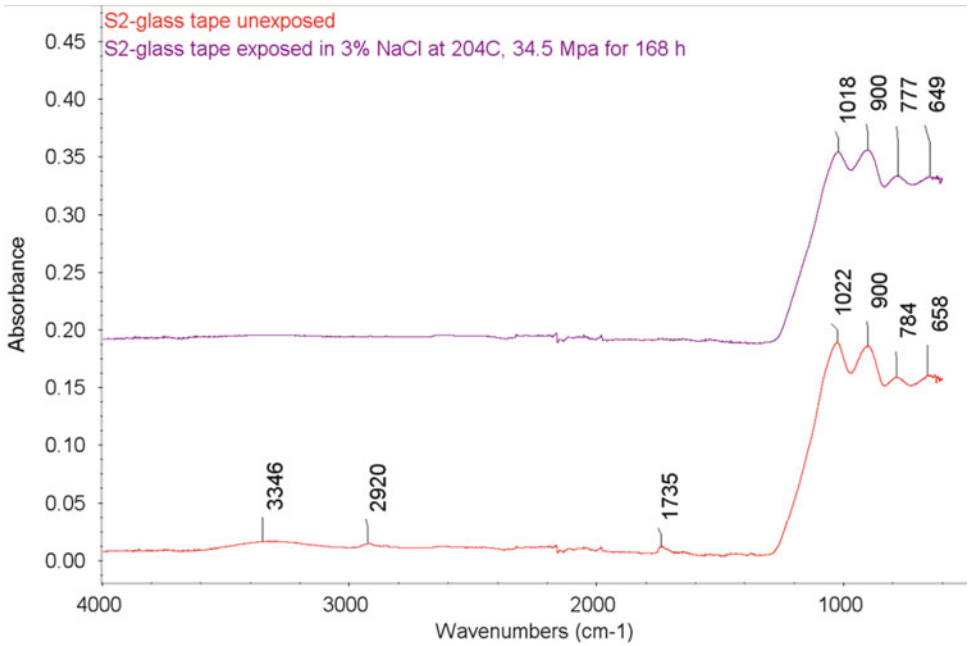

Fig. 36.12 FT-IR spectra of S2-glass tape before and after exposure in NaCl at 204 °C, 34.5 MPa for 168 h

Table 36.3 EDS results of S2-glass tape and E-glass tape before and after the specified hot-wet exposure

	Weight % of element			
Sample and analysis position	Mg	Al	Si	Ca
S2-glass tape Unexposed—at fiber surface	4.695	19.197	76.108	–
S2-glass tape exposed in 3 % NaCl at 204 °C, 34.5 MPa for 168 h—at fiber surface	3.883	18.352	77.765	–
E-glass tape Unexposed—at fiber surface	–	9.391	49.469	41.140
E-glass tape exposed in 3 % NaCl at 204 °C, 34.5 MPa for 168 h—at fiber surface	–	10.180	52.510	37.309

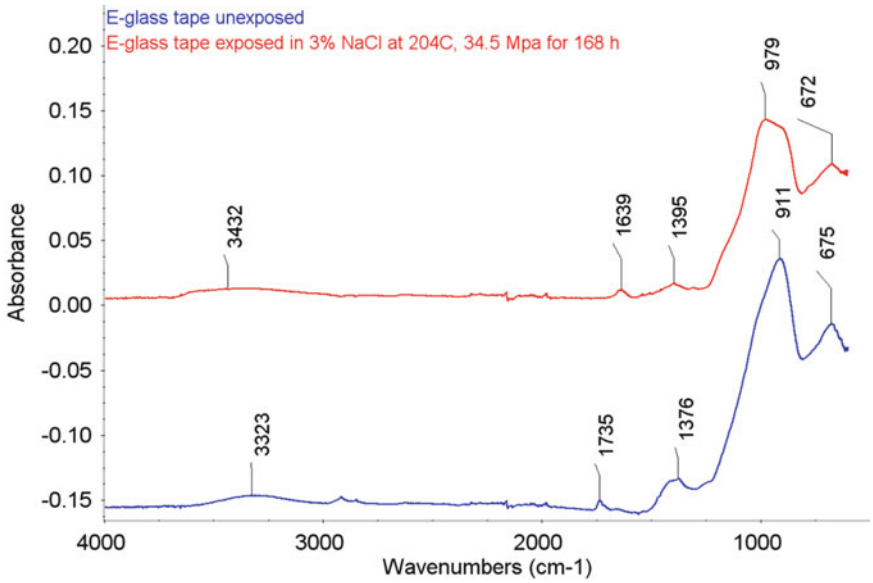

Fig. 36.13 FT-IR spectra of E-glass tape before and after exposure in NaCl at 204 °C, 34.5 MPa for 168 h

E-glass fibers was more stable than that on S2-glass fiber in the 3 % NaCl brine at 204 °C. The wavenumber of peak at 3323 cm^{-1} shifted to 3432 cm^{-1} after aging, which was likely due to hydrolysis breakdown of the siloxane linkage on the glass fiber surface and produced silicic acid hydroxyls [25]. The wavenumber of peak at 1735 cm^{-1} decreased to lower wavenumber at 1639 cm^{-1}, which could be due to that C=O group formed hydrogen bonding with OH group.

The measured EDS results for E-glass tape are also presented in Table 36.3 that show the weight concentration of the major elements in the E-glass fibers before and after the 168-h hot-wet exposure. Major elements Al, Ca and Si (oxygen is not included) were identified in the unexposed E-glass tape, and their weight concentrations are measured and presented in the table. It is found further from the measured data that a major loss in Ca concentration occurred in the E-glass tape during the hot-wet exposure, which implies a leaching process of Ca ions out from the E-glass fibers. The degradation mechanisms of the E-glass tape in the current hot-wet exposure condition are similar to those discussed for S-glass tapes. In the case of the E-glass tape, the major leached element is Ca instead of Mg in the S2-glass tape, and the amount of Ca leached from an E-glass tape is much higher than the amount of Mg leached from an S2-glass tape. In addition, E-glass fiber contain additional chemical species that could also be leached out from the E-glass fibers. This may be the reason why the E-glass tape became thinner after the 168-h exposure at 204 °C but S2-glass did not. However, in the current 168-h exposure condition the amount of leaching or reaction was still small and limited in a small depth from the fiber surface compared to the fiber diameter. In this case, although we can see the surface chemical changes by EDS (1.5 μm is the typical penetration depth of SEM election) after the current hot-wet exposure, the major chemical structure of the glass fibers was not altered.

This glass fiber hot-wet degradation mechanism can be confirmed further from a study on the E-glass sleeves with repeated hot-wet exposure. The E-glass fiber sleeves became thinner and weaker during a repeated hot-wet exposure in 3 % NaCl brine at 121–177 °C and 34.5 MPa and eventually lost their fiber form and became a very brittle and fragile solid substance after about 80 days, as shown in the pictures in Fig. 36.6. Figure 36.14 shows the FT-IR spectra of the three E-glass sleeve samples from the three different exposure stages: the unexposed, during the interim of the repeated exposure, and after 80 days of the repeated exposure. The main peak at 906 cm^{-1} of the unexposed sample is assigned to a symmetric Si-O vibration in the alkali environment. The peak wavenumber at 906 cm^{-1} shifted gradually to 952 cm^{-1} during the interim of the exposure, and then 972 cm^{-1} after repeated exposure for about 80 days, where the area of the peak increased too during the exposure process. These results suggest that a thicker SiO_2 layer formed on the E-glass fiber surface by the calcium and alkali ion leaching process during the repeated hot-wet exposure. In addition, a new peak at 3400 cm^{-1} was formed during the interim of the exposure, and the wavenumber of the peak shifted to a higher value further after the exposure for 80 days. This again indicates a hydrolytic breakdown of the siloxane linkage on the glass fiber surface and produced silicic acid hydroxyls $Si(OH)_4$, and the 3400 cm^{-1} peak was mainly attributed to the OH group from $Si(OH)_4$ [16, 25].

EDS analysis results for three E-glass sleeve samples from the three different exposure stages are presented in Table 36.4. From the analysis results we can see that the Ca weight concentration decreased from 24.4 % in unexposed sample quickly to 1.3 % in the interim sample, and eventually to 0 % in the sample after the repeated exposure for 80 days. This finding supports the observation and explanation on the shift of the wavenumber of the Si-O symmetric vibration peak to higher value in the FT-IR spectra for E-glass sleeve samples could be due to the preferential leaching of the

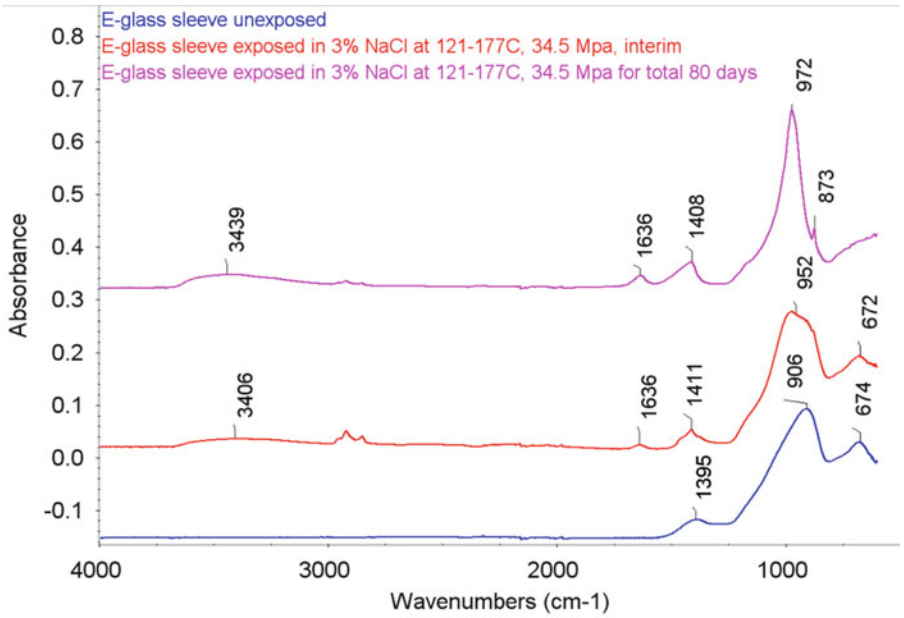

Fig. 36.14 FT-IR spectra of E-glass sleeve before and after repeated exposure in 3 % NaCl at 121–177 °C, 34.5 MPa for total 80 days

Table 36.4 EDS results of E-glass sleeve before and after the specified repeated hot-wet exposure

	Weight % of element						
Sample and analysis position	O	Mg	Al	Si	Ca	Na	Cl
E-glass sleeve unexposed—at fiber surface	25.2	0.5	10.4	39.3	24.4	0.2	0.0
E-glass sleeve repeatedly exposed in 3 % NaCl at 121–177 °C, 34.5 MPa (interim)—at fiber surface	25.6	0.4	13.9	56.5	1.3	2.3	0.0
E-glass sleeve repeatedly exposed in 3 % NaCl at 121–177 °C, 34.5 MPa for total 80 days—at particle surface	25.7	0.4	14.7	51.1	0.0	7.0	1.1

calcium and sodium ions from the glass fibers to the solution. The increase of the Na and Cl concentration during the aging process could be due to the deposition of NaCl to the surface of the glass fiber from the NaCl brine. Because of the repeated hot-wet exposure in the brine solution, the calcium and alkali ions continuously leached out from the E-glass fibers and reacted with water at elevated temperature, and the formed hydroxyl ions further reacted with glass and continuously broke the siloxane bonds in the glass structure deeper and deeper. Eventually, the calcium and alkali ions leached out from the glass fibers completely and the glass structure within the glass fibers was broken completely. At this time, the E-glass sleeves lost their fiber form and became a very brittle and fragile solid substance, the silica sand powder, as shown in the pictures in Figs. 36.6 and 36.15.

36.3.2 Fiber and Fiber/Resin Interface Degradation in Composites

To study the HPHT hot-wet resistance of fiber/resin interfacial bonding in various continuous fiber-reinforced composite laminates and the molded short-fiber composite specimens, microstructures were examined under a high-magnification optical microscope from the polished cross-sections of the various composite test specimens before and after the specified HPHT hot-wet exposure. Figures 36.16, 36.17 and 36.18 show the cross-sectional micrographs of the EP-1/7781E, EP-1/6781S and EP-1/T300 epoxy laminate specimens after exposure in 3 % NaCl brine at 177 °C, 34.5 MPa for 96 h, respectively. From these micrographs, severe fiber/resin interface debonding, glass-fiber weakness and epoxy resin phase cracking were observed in the E-glass and S2 glass fiber-reinforced EP-1/7781E and EP-1/6781S composite laminate specimens after the hot-wet exposure even though the glass fibers were protected by silane coupling agent and the epoxy matrix resin phase, while very minor fiber/resin interface debonding was identified in the carbon fiber-reinforced EP-1/T300

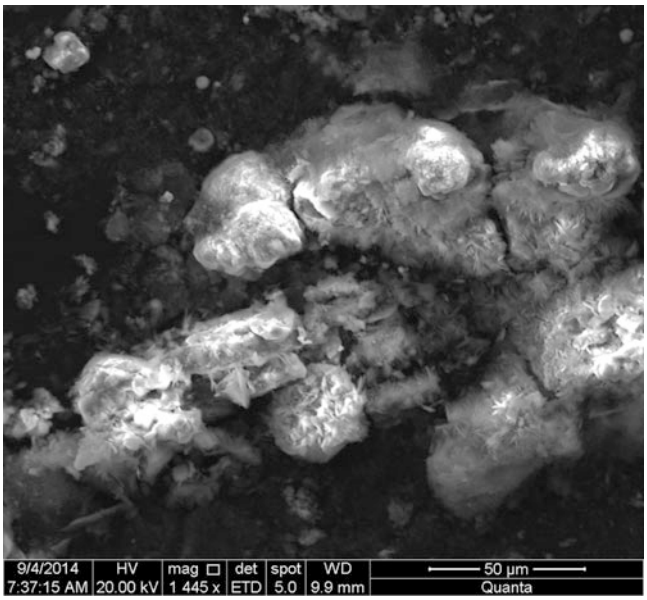

Fig. 36.15 SEM image of E-glass sleeve after repeated exposure in 3 % NaCl at 121–177 °C, 34.5 MPa for total 80 days

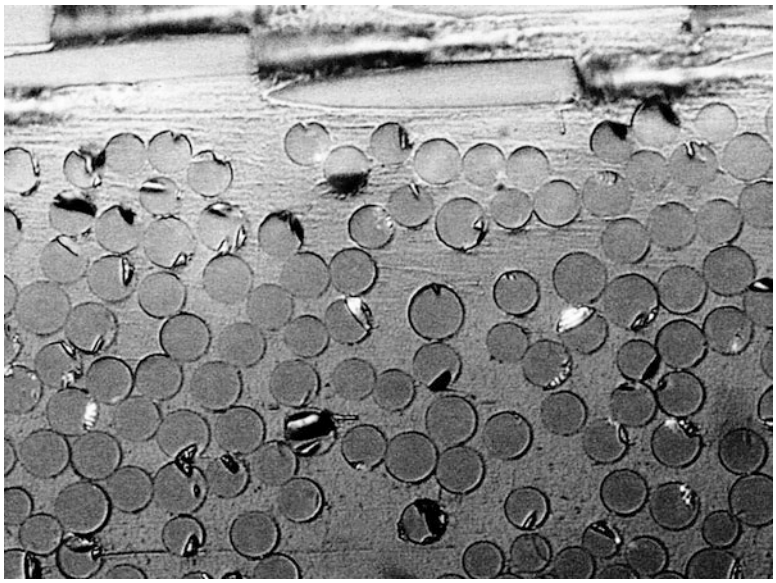

Fig. 36.16 Micrograph (×800) of a cross-section surface of an EP-1/7781E laminate sample after exposure in 3 % NaCl brine at 177 °C, 34.5 MPa for 96 h

composite laminate specimens after the same hot-wet exposure. As discussed previously in the introduction and fiber degradation mechanism sessions, the mechanisms causing this difference involved weak hot-wet resistance of the surface sizing and the hydrophilic nature of the glass fibers in such a high-temperature hot-wet condition. The osmotic pressure built up at the fiber/resin interfaces by dissolution of the surface sizing and leaching of chemical components, such as K_2O and Na_2O, from the glass fibers, especially from the E-glass fibers, and caused the fiber/resin interface debonding in the high-temperature aqueous environment [19]. This osmotic pressure could also generate micro-cracks in the hot-wet degraded epoxy resin phase surrounding the fibers, causing higher water absorption and thickness expansion as discussed in more detail in author's earlier publications [5]. These observations also proved further that the carbon fibers with proper surface chemical treatment provided excellent high-temperature hot-wet resistance and excellent interfacial adhesion with the epoxy matrix resin. By looking into the details of fiber/resin interface region in the micrograph of the EP-1/T300 laminate sample after HPHT hot-wet exposure in Fig. 36.18, we found that the miner "interphase" de-bonding sites were very localized small cracks with the same orientation in the epoxy matrix phase near the interfaces, and believe that they were initiated from epoxy matrix near the interfaces (not from the interface bonding) under certain internal localized stress, while the epoxy matrix

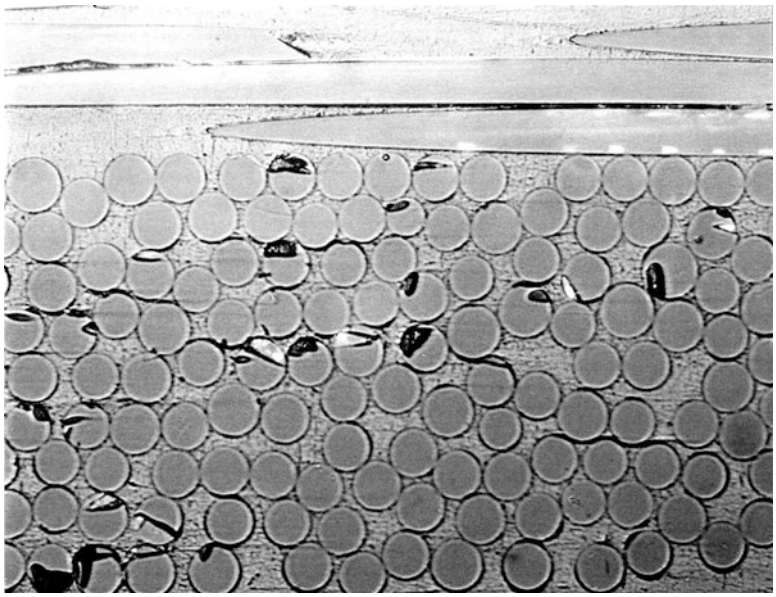

Fig. 36.17 Micrograph (×800) of a cross-section surface of an EP-1/6781S laminate sample after exposure in 3 % NaCl brine at 177 °C, 34.5 MPa for 96 h

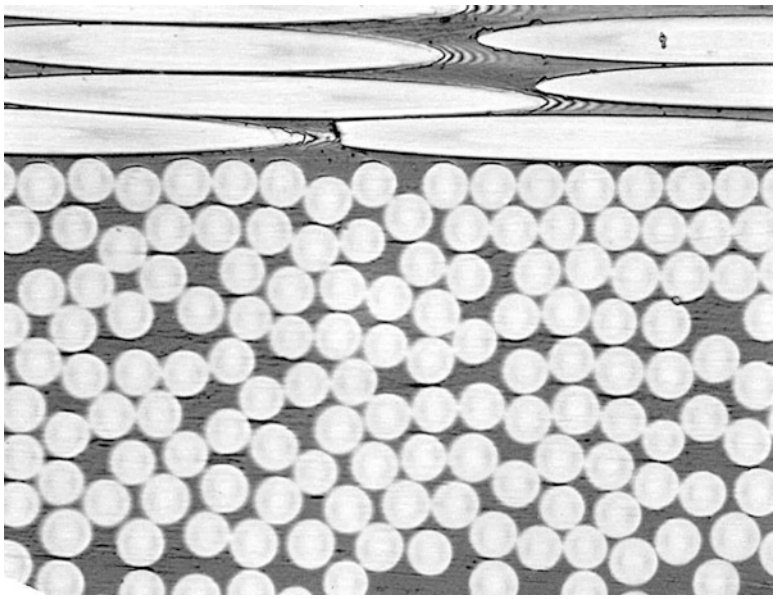

Fig. 36.18 Micrograph (×1000) of a cross-section surface of an EP-1/T300 laminate sample after exposure in 3% NaCl brine at 177 °C, 34.5 MPa for 96 h

phase in the EP-1/T300 laminate was weakened by the plasticization effect in the hot-wet environment as discussed in detail in reference [5].

Figure 36.19 presents the microstructure and fiber/resin interfacial condition in the continuous carbon fiber-reinforced thermoplastic PEEK composite laminate TP-1/AS4 after the HPHT hot-wet exposure in 3 % NaCl brine at 177 °C under 34.5 MPa for 240 h, and the Figs. 36.20 and 36.21 present the microstructure and fiber/resin interfacial condition in the continuous S2-glass fiber-reinforced PEEK composite TP-1/S2-G before and after the same HPHT hot-wet exposure for 240 h. These two laminates were fabricated by using the AS4/PEEK and S2/PEEK UD prepreg tape produced by the same manufacturer with the same PEEK resin. The micrograph of TP-1/AS4 sample after the HPHT hot-wet exposure presented in Fig. 36.19 showed perfect carbon-fiber/resin interfacial bonding and fiber integrity after the sample polishing process, indicating a good interfacial bonding between the carbon fibers and the PEEK resin and an excellent HPHT hot-wet resistance of the carbon fibers, PEEK matrix resin and their interface bonding. However, in the hot-wet exposed S2-glass reinforced PEEK laminate TP-1/S2-G, glass fiber fragility and full fiber/resin interface debonding between the S2-glass fibers and the PEEK matrix resin were identified as shown in Fig. 36.21 and compared with the micrograph of the unexposed

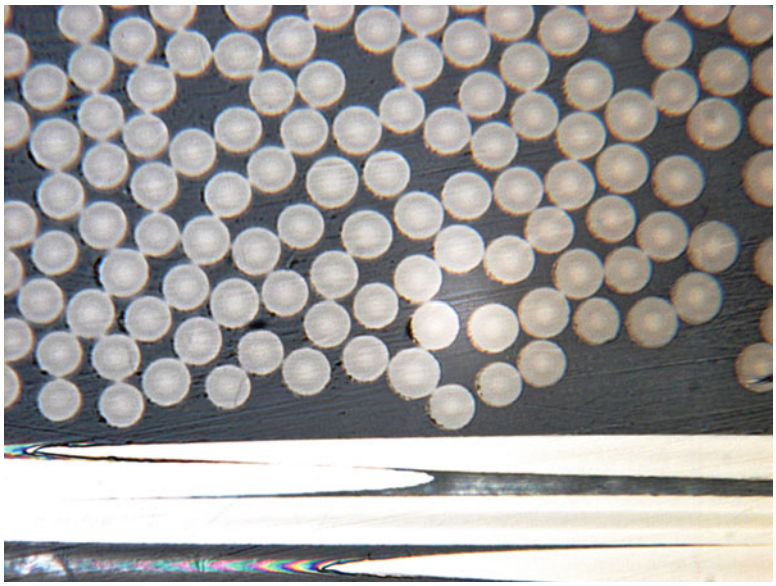

Fig. 36.19 Micrograph (×1000) of a cross-section surface of a TP-1/AS4 laminate sample after exposure in 3% NaCl brine at 177 °C, 34.5 MPa for 240 h

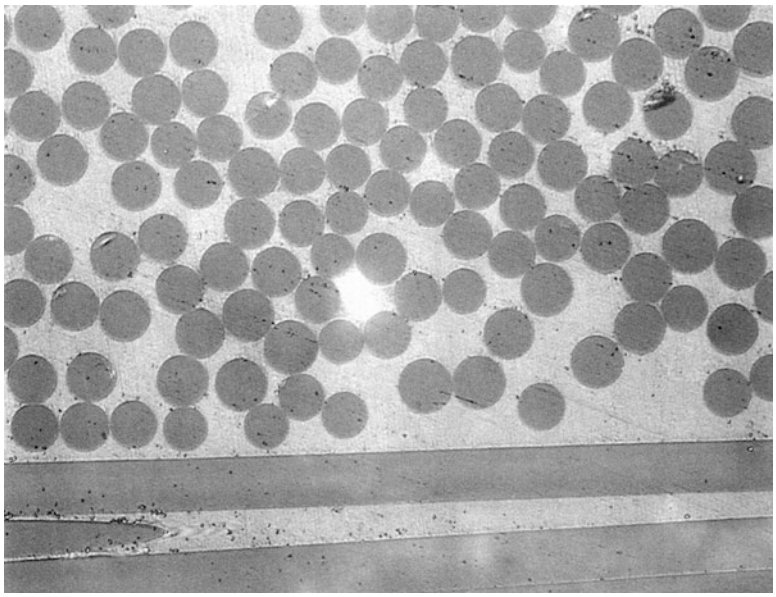

Fig. 36.20 Micrograph (×800) of a cross-section surface of a TP-1/S2-G laminate sample in the as-received condition

TP-1/S2-G sample, as shown in Fig. 36.20. Compared with the interfacial debonding in the S2 glass fiber-reinforced epoxy composite EP-1/6781S as shown in Fig. 36.17, less intensity, smaller debonding gaps and no matrix cracking were observed in S2-glass reinforced PEEK composite TP-1/S2-G. This was mainly attributed to the good HPHT hot-wet resistance and small water absorption and moisture diffusion rate of the semi-crystalline thermoplastic PEEK matrix [5]. However, in the case of TP-1/S2-G laminate system, even though the water diffusion through the PEEK matrix is slow, the water can also transport along the fiber/resin interface, and the rate of water penetration along the fiber can be much faster than through the resin phase [20]. This can cause further debonding of the glass-fiber/resin interface and the glass fiber surface corrosion.

Additional studies were conducted with the chopped E-glass and carbon fiber (~0.8 mm in length) filled PEEK composite molding compounds, Victrex 450GL30 and 450CA30, respectively. These two thermoplastic molding compounds and their standard tensile test specimens were compounded and molded by the same manufacturer with the same grade of PEEK resin and the same process. In these short fiber-reinforced molding compounds, the fiber/resin interfacial bonding strength and its hot-wet resistant capability are more critical in control of the mechanical properties and hot-wet resistant capability of the composite materials than those in the continuous fiber-reinforced composite materials. These studies further confirmed very

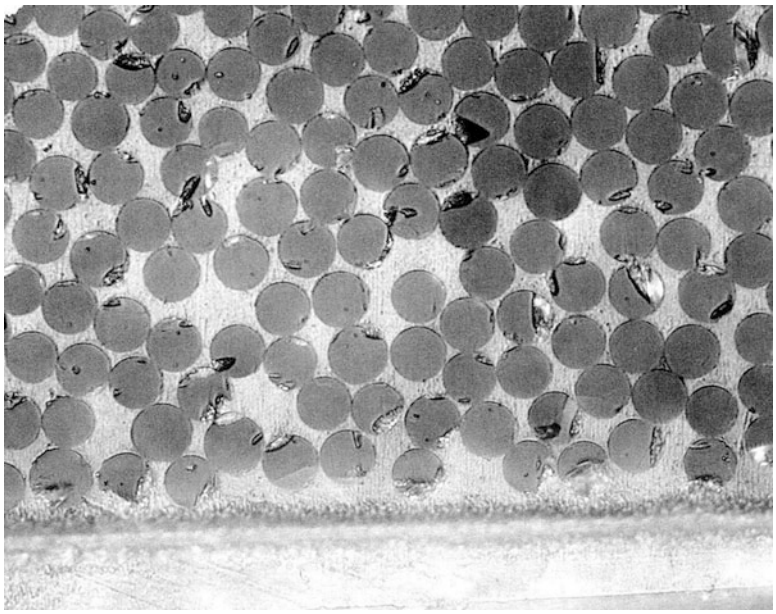

Fig. 36.21 Micrograph (×800) of a cross-section surface of a TP-1/S2-G laminate sample after exposure in 3 % NaCl brine at 177 °C, 34.5 MPa for 240 h

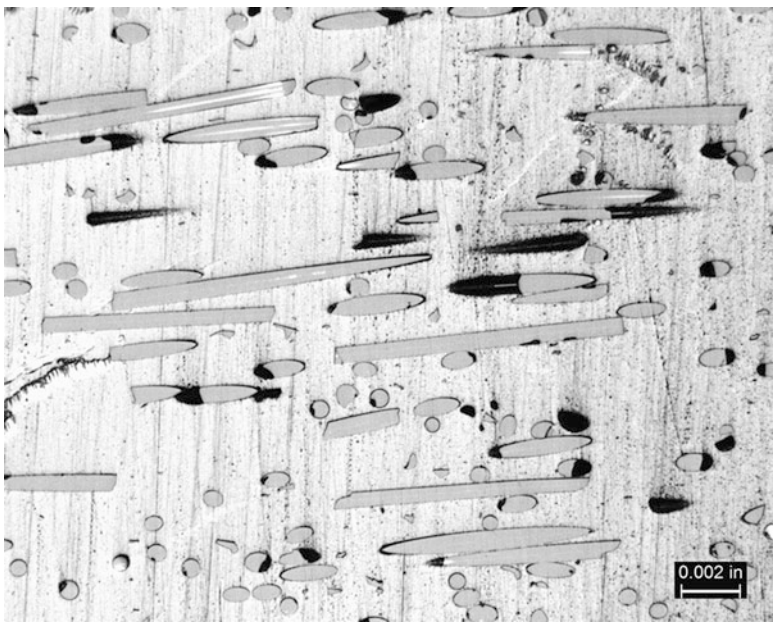

Fig. 36.22 Micrograph on longitudinal cross section of a 450GL30 specimen after exposure in 3 % NaCl brine at 149 °C, 34.5 MPa for 240 h (E149)

different fiber/resin interfacial bonding and its HPHT hot-wet resistant capability between the glass fiber-filled PEEK and the carbon fiber-filled PEEK compounds.

Micrographs in Figs. 36.22, 36.23, 36.24 and 36.25 present the microstructures and fiber/resin interfacial conditions in the molded chopped glass fiber-filled 450GL30 test samples after the hot-wet exposure in 3 % NaCl brine at 149 °C (E149) and 204 °C (E204) under 34.5 MPa for 240 h, respectively. From these micrographs, glass fiber fragility and fiber/resin interface debonding can be seen clearly in longitudinal and transverse cross sections of the 450GL30 samples after E149 and E204 hot-wet exposure. However, in the case of the chopped carbon fiber-filled 450CA30 molding compound, no evidence of degradation in carbon fibers and the carbon-fiber/resin interfacial bonding can be identified in longitudinal and transverse cross sections of the molded 450CA30 test samples after the hot-wet exposure in 3 % NaCl brine at 204 °C (E204) and even at 232 °C (E232) under 34.5 MPa for 240 h, respectively, as shown clearly in the micrographs presented in Figs. 36.26, 36.27, 36.28, and 36.29.

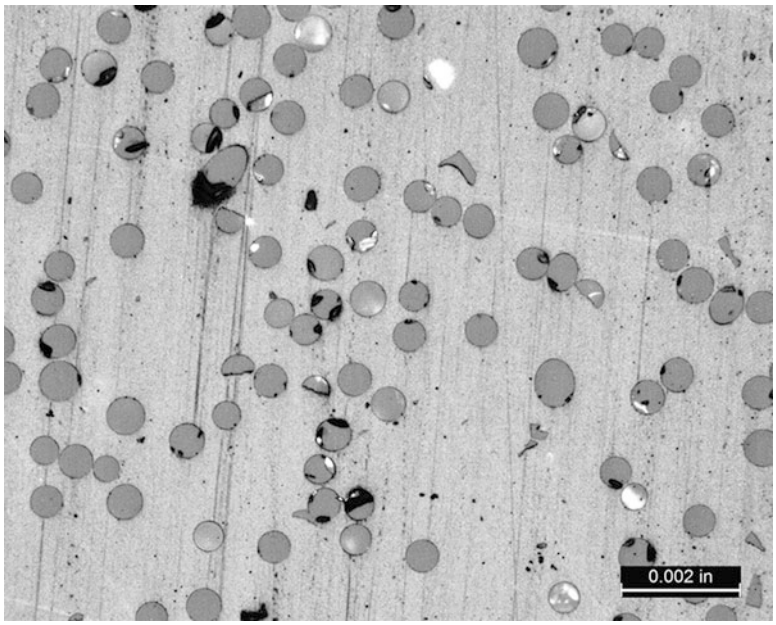

Fig. 36.23 Micrograph on transverse cross section of a 450GL30 specimen after exposure in 3 % NaCl brine at 149 °C, 34.5 MPa for 240 h (E149)

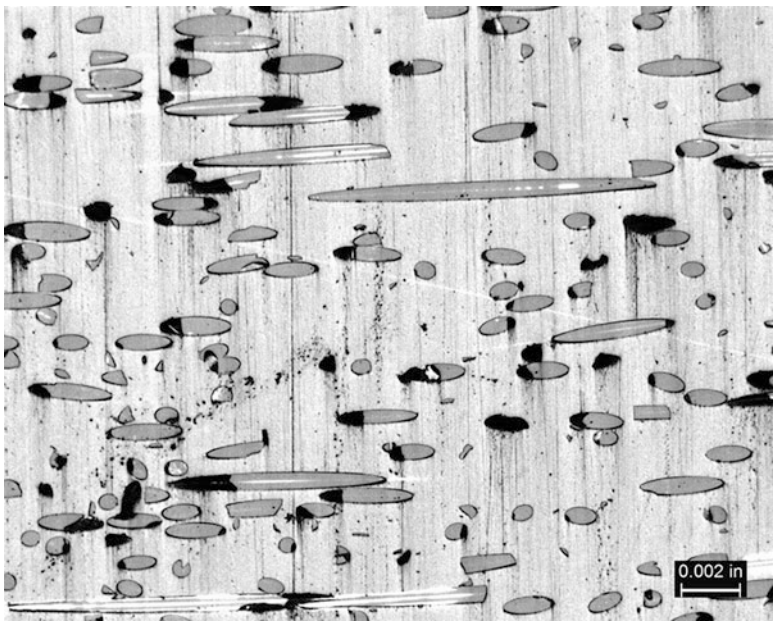

Fig. 36.24 Micrograph on longitudinal cross section of a 450GL30 specimen after exposure in 3 % NaCl brine at 204 °C, 34.5 MPa for 240 h (E204)

36.3.3 Fiber and Fiber/Resin Interfacial Effects on Mechanical Properties of Composites

36.3.3.1 Tensile Strength of Selected Continuous Fiber-Reinforced Composites

Measured tensile strength of the TP-1/AS4, TP-1/S2-G, EP-1/T300, EP-1/6781S and EP-1/7781E composites at RT, 177 °C and 204 °C before and after the HPHT hot-wet exposure in 3 % NaCl brine at 177 °C and 204 °C for 240/168 h, respectively, are plotted in Fig. 36.26. The test results indicate that: (1) The tensile strength retention of the carbon fiber-reinforced composites, TP-1/AS4 and EP-1/T300, are all very good at 177 °C and 204 °C before and after the HPHT hot-wet exposure. This is because the tensile strength in a principal fiber direction of a continuous fiber-reinforced composite is a fiber-dominated property, and the carbon fibers and their interface bonding with PEEK and epoxy resins possess excellent high-temperature and hot-wet environmental resistance as concluded in the previous sections. (2) There is one exception in above

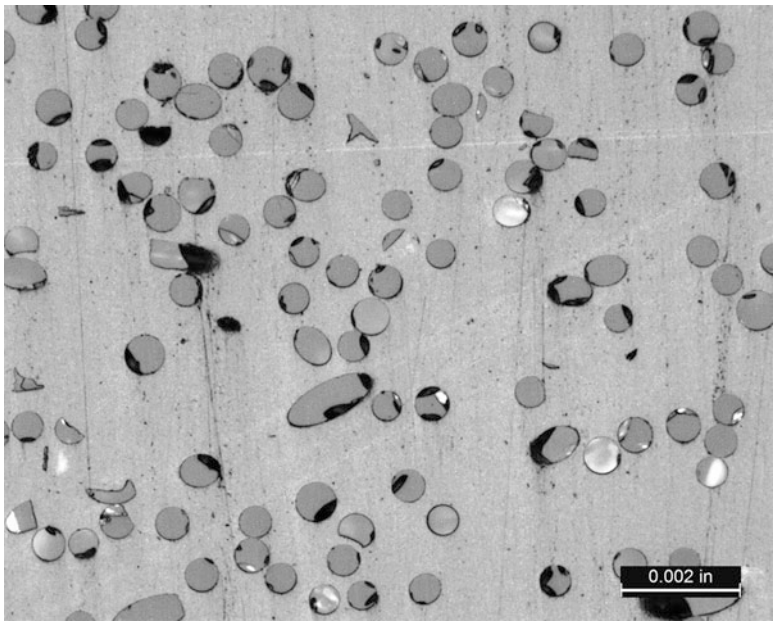

Fig. 36.25 Micrograph on transverse cross section of a 450GL30 specimen after exposure in 3 % NaCl brine at 204 °C, 34.5 MPa for 240 h (E204)

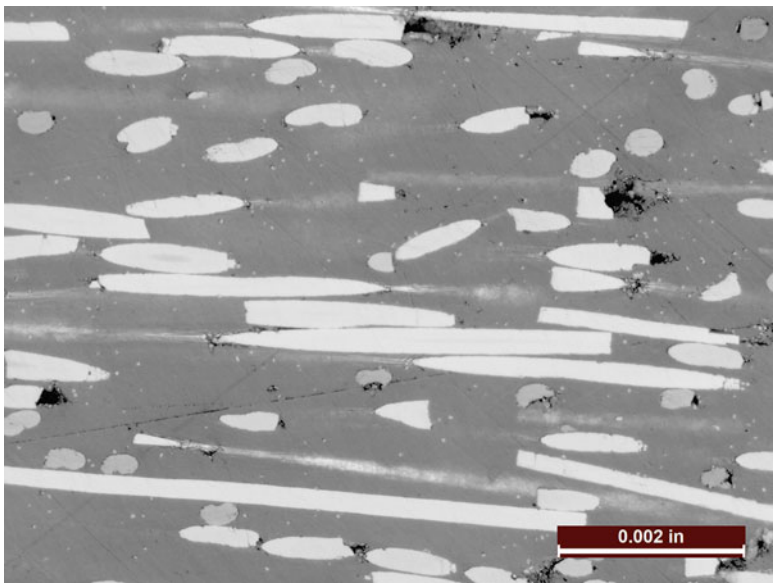

Fig. 36.26 Micrograph on longitudinal cross section of a 450CA30 specimen after exposure in 3 % NaCl brine at 204 °C, 34.5 MPa for 240 h (E204)

observation for the EP-1/T300 specimens when tested at 204 °C after the 204 °C hot-wet exposure. In this case, even though in a continuous fiber-reinforced composite, a functional matrix resin phase is still required for effectively bonding the fibers and transferring and distributing stresses. According to author's earlier studies [4, 5], after the 204 °C hot-wet exposure for 168 h, the TP-1 (PEEK) resin could still keep similar tensile properties at 204 °C as in unexposed condition, while the EP-1 (epoxy) resin lost its mechanical performance at 204 °C, involving wet T_g degradation/plasticization and possible resin blistering that caused further weakening or even losing the carbon-fiber/epoxy resin interface bonding. This was the reason for causing a substantial degradation in tensile strength of the EP-1/T300 composite at 204 °C after the 204 °C hot-wet exposure, as indicated in Fig. 36.26. (3) In contrast to the carbon fiber-reinforced EP-1 and TP-1 composites, tensile strengths of the glass fiber-reinforced EP-1 and TP-1 composites, EP-1/6781S, EP-1/7781E and TP-1/S2-G, dropped 70–80 % and 45–55 %, respectively, after the hot-wet exposure at 177 °C, 34.5 MPa for 240 h. This indicates the glass fibers, especially the E-glass fibers, and the glass-fiber/resin interfaces in EP-1 epoxy matrix and even in TP-1 PEEK matrix composites were attacked severely by the hot-wet environment through the resin phase diffusion and more quickly through fiber/resin interface capillary action, and consequently resulted in large degradation in tensile strength of the glass fiber-

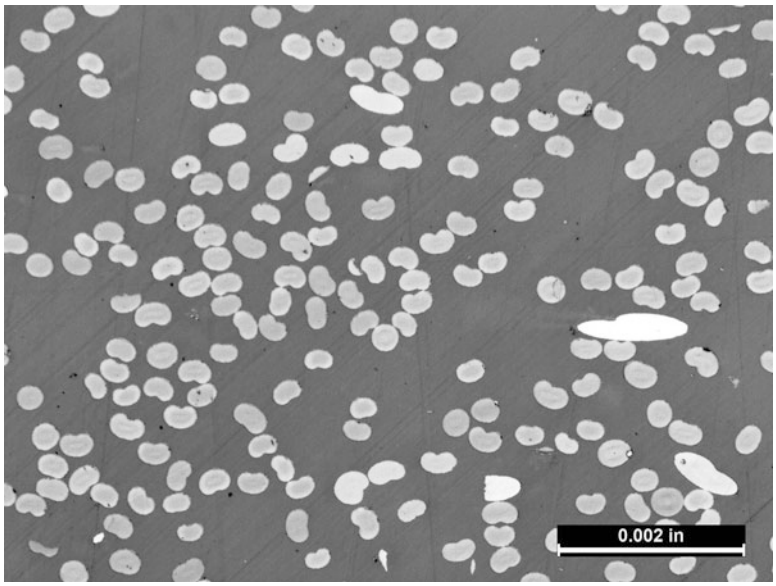

Fig. 36.27 Micrograph on transverse cross section of a 450CA30 specimen after exposure in 3 % NaCl brine at 204 °C, 34.5 MPa for 240 h (E204)

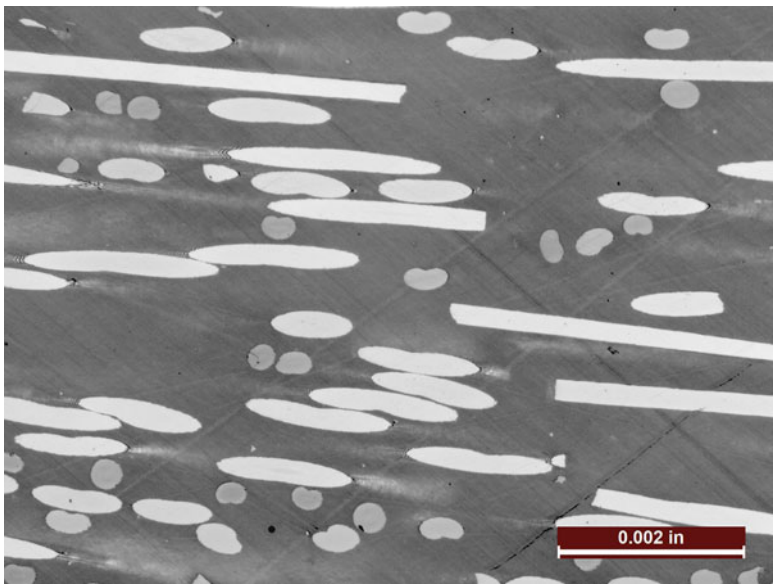

Fig. 36.28 Micrograph on longitudinal cross section of a 450CA30 specimen after exposure in 3 % NaCl brine at 232 °C, 34.5 MPa for 240 h (E232)

reinforced composites. The degradation mechanism of the glass fibers and glass-fiber/resin interfaces in HPHT hot-wet environment have been discussed thoroughly in previous sections. (4) It was also observed that the initial dry tensile strength of the S2-glass fiber-reinforced PEEK [0/90]ns laminate, TP-1/S2-G, is very low and even much lower than the tensile strength of the S2-glass fiber-reinforced epoxy laminate, EP-1/6781S, where a balanced bi-directional 6781 fabric was used in lamination with a lower fiber content than that of the TP-1/S2-G UD cross-ply laminate. The low initial tensile strength of the continuous S2-glass fiber-reinforced PEEK composite was also reported by other researchers [27, 28]. In author's opinion, the low initial tensile strength of the TP-1/S2-G laminate in its unexposed condition is due to an original weak glass/PEEK interfacial bonding [28].

36.3.3.2 Compression Strength of Selected Continuous Fiber-Reinforced Composites

In general, people consider that compressive properties of a continuous fiber-reinforced composite are matrix resin-dominated properties, especially when the composite is applied at an elevated temperature. If the matrix resin is softened

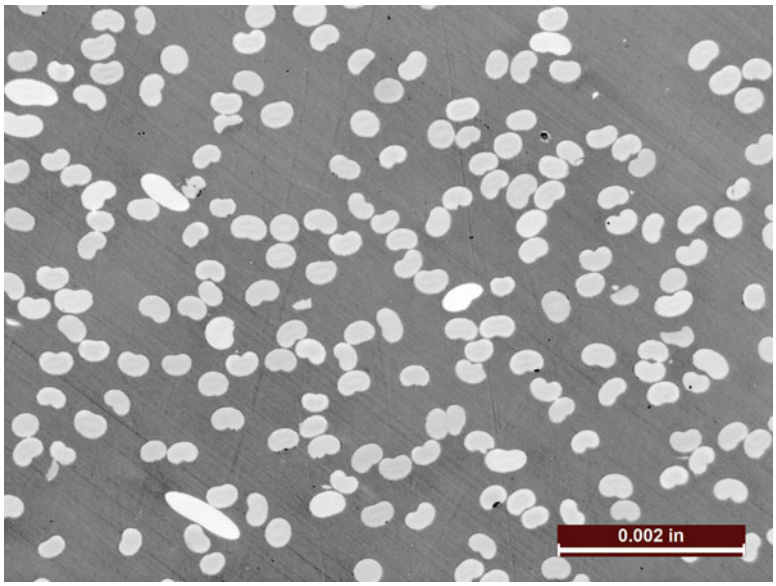

Fig. 36.29 Micrograph on transverse cross section of a 450CA30 specimen after exposure in 3 % NaCl brine at 232 °C, 34.5 MPa for 240 h (E232)

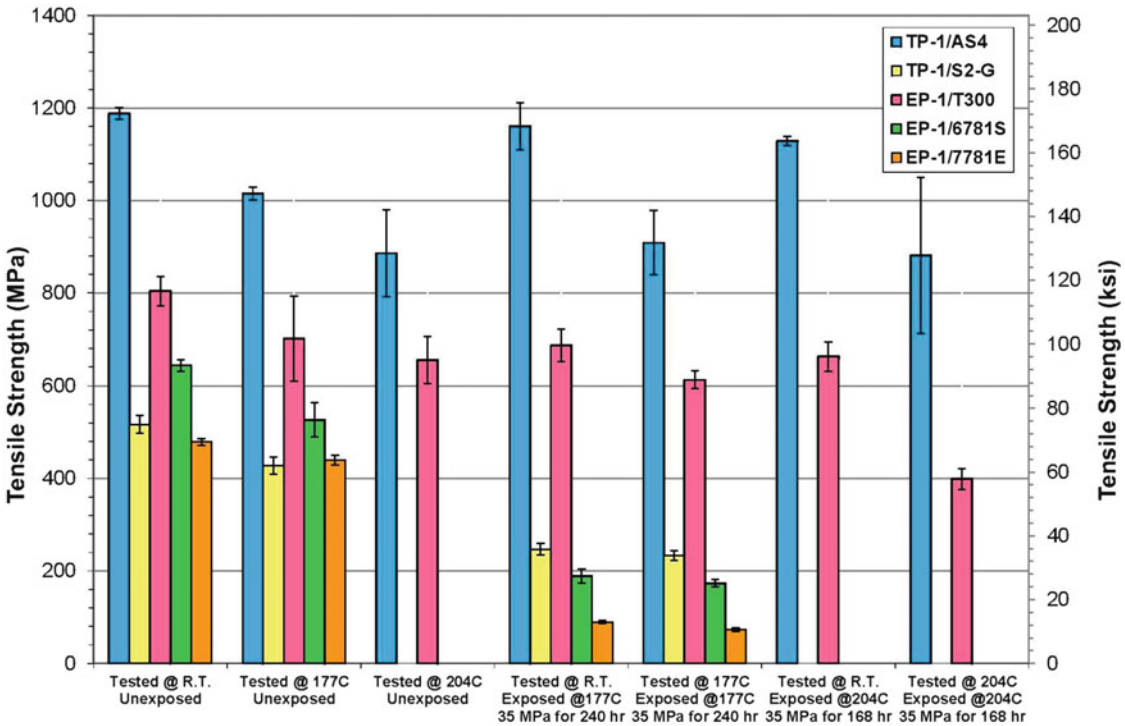

Fig. 36.30 Measured tensile strengths of the selected continuous fiber-reinforced composites at RT, 177 °C and 204 °C before and after the specified HPHT hot-wet exposure in 3 % NaCl brine

or plasticized by heat or certain environmental condition, the continuous fibers will buckle in the matrix phase (micro-buckling) under a compressive load, and the composite will lose its structural stability and fail in compression. On the other hand, if a high-temperature hot-wet condition is involved and degradation in reinforcement fibers and/or fiber/resin interface in a composite occur, the fiber strength and fiber/resin interfacial condition, in addition to matrix resin degradation, will also play important roles in determining the compressive strengths of the composites.

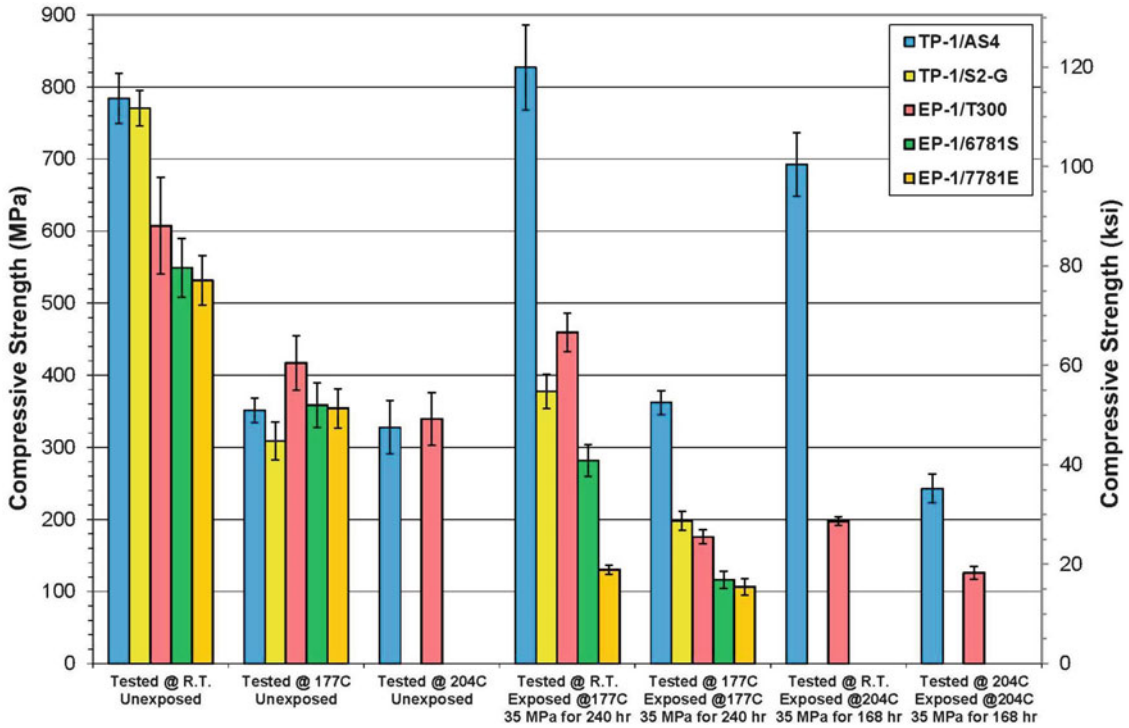

Fig. 36.31 Measured compressive strengths of the selected continuous fiber-reinforced composites at RT, 177 °C and 204 °C before and after the specified HPHT hot-wet exposure in 3 % NaCl brine

Measured compressive strengths are presented in Fig. 36.27 for the TP-1/AS4, TP-1/S2-G, EP-1/T300, EP-1/6781S and EP-1/7781E composites at RT, 177 °C and 204 °C before and after the HPHT hot-wet exposure in 3 % NaCl brine at 177 °C and 204 °C for 240/168 h, respectively. From the test data presented we can see that the temperature effect on compressive strengths of the composites are more significant than its effect on the tensile strength, and the effects are more dependent on the type of matrix resins when tested in unexposed dry condition. We can see also that the carbon fiber- and S2-glass fiber-reinforced PEEK composites, TP-1/AS4 and TP-1/S2-G, have higher initial RT compressive strength than the carbon fiber- and glass fiber-reinforced epoxy composites, EP-1/T300, EP-1/6781S and EP-1/7781E, because TP-1/AS4 and TP-1/S2-G are the UD tape laminated composites with a higher fiber content while EP-1/T300, EP-1/6781S and EP-1/7781E are woven fabric laminated composites.

It is noted that the room-temperature compressive-strength retention of the EP-1/T300 composite after the hot-wet exposure at 177 °C for 240 h, compared with its initial compressive strength at RT in unexposed dry condition, was as high as 76 % (460 MPa). However, when the exposed wet specimens were tested at 177 °C, the compressive strengths were reduced dramatically to only about 172 MPa (30 % retention) even if the composite is reinforced by carbon fibers. Mechanisms responding to this observation can be explained as (1) the moisture absorbed in the EP-1 epoxy resin phase in the exposed EP-1/T300 specimens reduced the T_g of the epoxy matrix resin or composite from 221 °C in dry condition to about 167 °C in wet condition [5]; (2) When tests were conducted at room temperature the test temperature was far below the wet T_g of the epoxy matrix composite, resulting in a high room-temperature property retention; however, (3) when tests were conducted at 177 °C, the test temperature was above the wet T_g of the exposed test specimens, where the epoxy matrix phase was plasticized and softened resulting in a significant loss of the compressive strength. This moisture-induced physical degradation mechanism in the carbon fiber-reinforced epoxy composite EP-1/T300 when exposed at 177 °C or a lower temperature is not related to fiber, fiber/resin interface as examined and discussed in the early sections.

However, in the case of the EP-1/7781E and EP-1/6781S composites after the hot-wet exposure at 177 °C for 240 h and the EP-1/T300 composite after the hot-wet exposure at 204 °C for 168 h, the room-temperature compressive-strength retentions were no longer high, only about 25 %, 50 % and 32 %, respectively. These indicate, in addition to the moisture-induced thermo-mechanical degradation, significant irreversible structural damage occurred in glass fibers, epoxy resin phase and at the fiber/resin interfaces as discussed and illustrated in the previous sections and in an early publication [5]. When these hot-wet exposed EP-1/7781E, EP-1/6781S and EP-1/T300 specimens were further tested at 177 °C and 204 °C, respectively, even lower compressive strengths were obtained, where a combined constituent and composite structural

damage and the moisture-induced thermo-mechanical degradation were imposed. The authors want to point out here that when the mechanical tests were conducted at 177 °C or 204 °C, the dry preheating to the exposed wet test specimens at the high temperatures could serve as a thermal impact and generate additional hygrothermal structural damage in the test specimens as identified and discussed in early publications [2, 5]. This is a test method issue associated with the current environmental-mechanical testing especially for thermosetting resins and their composites, which needs to be further resolved [29].

It is observed further form the chart in Fig. 36.23 that the carbon fiber-reinforced PEEK composite, TP-1/AS4, possesses a high initial compressive strength at room temperature and excellent hot-wet environmental resistance with no degradation in compressive strength at RT and 177 °C after the 177 °C exposure compared with the compressive strengths at RT and 177 °C, respectively, in unexposed dry condition and very limited degradation in compressive strength at RT and 204 °C after the 204 °C exposure compared with the compressive strengths at RT and 204 °C, respectively, in unexposed dry condition. This hot-wet mechanical performance is supported by the combined hot-wet resistance of PEEK resin, carbon fibers and their interfacial bonding, and the excellent thermal impact resistance of the tough PEEK matrix phase of the composite as identified in the early study [2]. Compressive strengths of the S2-glass reinforced PEEK composite, TP-1/S2-G, at RT and 177 °C in dry condition are very similar to those measured from the TP-1/AS4 composite. However, after the hot-wet exposure at 177 °C for 240 h, the compressive strength of the TP-1/S2-G composite at RT and 177 °C are only 49 % and 64 % of its initial dry compressive strength at RT and 177 °C, respectively. This major compressive strength degradation of the TP-1/S2-G composite after the hot-wet exposure is due to the weak hot-wet resistance of the glass fibers and the interfacial bonding between the glass fibers and PEEK matrix resin as illustrated and discussed in previous sections.

36.3.3.3 Tensile Properties of Short Fiber-Filled PEEK Composite Molding Compounds

Victrex 450GL30 and 450CA30 are 30 % (by weight) chopped short glass fiber- and carbon fiber-filled PEEK molding compounds, respectively. They were produced by the same manufacturer with the same PEEK resin and the same manufacturing process. All the tensile test specimens were made by the same injection molding process and with the same geometry and dimensions (ASTM D638 Type 1). Mechanical properties and HPHT hot-wet resistant capability of a chopped short-fiber filled composite material depend on the fiber volume fraction, fiber aspect ratio, fiber and resin stiffness, fiber/resin interfacial bonding and their hot-wet resistance, where the glass fibers and carbon fibers play an important role, but with quite different performances. Tensile properties of the molded 450GL30 and 450CA30 specimens were determined before and after the HPHT hot-wet exposure in 3 % NaCl brine at 149 °C (E149), 204 °C (E204) and 232 °C (E232) under 34.5 MPa for 240 h, respectively.

Room-Temperature Tensile Properties

Room-temperature (RT) tensile stress-strain curves of the unexposed (UE) and the E149, E204 and E232 exposed 450GL30 and 450CA30 specimens are presented in Fig. 36.32, and the measured RT tensile moduli and tensile strengths of the 450GL30 and 450CA30 specimens in UE condition and after the E149, E204 and E232 exposure are presented in the charts in Figs. 36.37 and 36.38, respectively. For comparative purpose, tensile properties of unfilled Victrex PEEK neat resin 450G are also presented in these two charts.

From the RT test data we can see that the initial RT tensile modulus and tensile strength of the carbon fiber-filled compound 450CA30 in unexposed condition are significantly higher than those of the glass fiber-filled compound 450GL30 (26.7 vs 11.8 GPa in modulus and 247.7 vs 148 MPa in strength). The reasons resulting in this big difference in tensile properties are (1) the 450CA30 contains much higher carbon fiber by volume than the glass fiber by volume in the 450GL30 (23.8 vs 17.7 %) though they have the same fiber content (30 %) by weight; (2) the carbon fiber possesses much higher elastic modules than the E-glass fiber (235 vs 74 GPa); (3) if the chopped carbon fibers and the chopped glass fibers have the same length then the chopped carbon fibers have higher aspect ratio since the carbon fibers have smaller diameters; (4) even in the unexposed condition, the carbon fibers may have stronger interfacial bonding with the PEEK matrix resin than the glass fibers, as discussed in the previous sections. In comparison with the tensile properties of the PEEK neat resin 450G, it can be seen that the RT tensile modulus of 450GL30 and 450CA30 is three times and eight times of the neat resin modulus, respectively, and the RT tensile strength of 450GL30 and 450CA30 is 158 % and 262 % of the neat resin tensile strength, respectively. These indicate the chopped carbon fibers and glass fibers provided very efficient reinforcement functions. However, on the other hand, a substantial brittleness was introduced by these fiber reinforcements since the tensile elongation dropped from typically 40 % for neat resin 450G to only around 1.6 % for 450CA30 and 2.4 % for 450GL30.

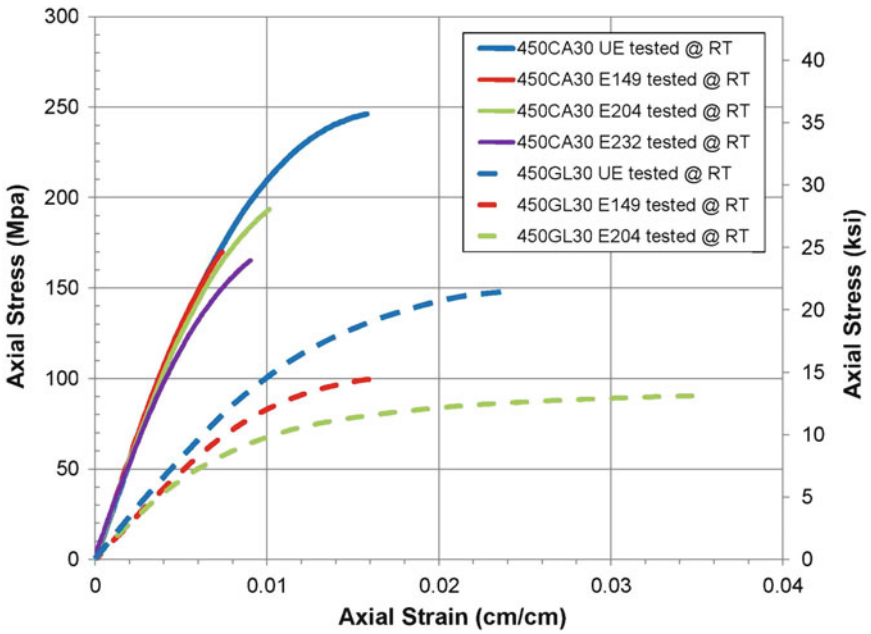

Fig. 36.32 Measured tensile stress-strain curves of 450CA30 and 450GL30 compounds at RT before and after the specified HPHT hot-wet exposure in 3 % NaCl brine

No degradation was observed in RT tensile modulus of the carbon fiber-filled 450CA30 compound after E149, E204 and E232 hot-wet exposure, compared with the initial RT tensile modulus in unexposed condition, because no fiber/resin interface debonding and resin phase structural degradation were observed after the HPHT hot-wet exposure. In the case of the glass fiber-filled 450GL30 compound, certain degradation in RT tensile modulus was observed after the E149 and E204 hot-wet exposure; however, this degradation was small (dropped from 11.8 GPa to 9.98–9.51 GPa) even though the glass fiber/PEEK resin interface debonding has been identified from the exposed 450GL30 specimens as shown in Figs. 36.22, 36.23, 36.24 and 36.25. In author's opinion, when the fiber/resin interfaces debonded in the 450GL30 test specimen in the high-temperature hot-wet condition and then cooled down to room temperature, the fiber/resin interfaces became frictional interfaces because of the resin phase thermal contraction, and these frictional interfaces could provide certain stress transfer capability between the fibers and resin phase and showed a high RT tensile modulus retention after the HPHT hot-wet exposure determined in the initial low-loading part of the tensile curve. When the tensile stress increased, the tensile curves showed more nonlinear and ductile deformation and higher elongation, as shown in Fig. 36.32. It is believed that in this late part of the tensile deformation, the glass-fiber/resin interface sliding occurred. However, this was not the case for the carbon fiber filled 450CA30 compound.

The RT tensile strength of the 450GL30 specimens after E149 and E204 hot-wet exposure dropped from ~148 MPa in unexposed condition to 103 and 95 MPa (28 and 36 % lower), respectively, and no ductile deformation until the specimens were exposed in E204 condition. The mechanism causing these strength degradations are obvious according to the early discussion on glass-fiber/resin interface debonding. This fiber/resin debonding process with further weakening of glass fiber mechanical strength during the HPHT hot-wet exposure created irreversible material structural damage or degradation.

Similarly, the RT tensile strength of the 450CA30 specimens after E149, E204 and E232 hot-wet exposure dropped from ~248 MPa in unexposed condition to 176, 194 and 162 MPa (29, 22 and 35 % lower), respectively. However, the degradation mechanism for this RT tensile strength reduction is not straight forward since no carbon fiber/resin interfacial debonding has been identified in the test specimens after the E149, E204 and E232 hot-wet exposure. As we can see from the RT tensile stress-strain curves of 450CA30 specimens after the E149, E204 and E232 hot-wet exposure, all these tests failed at a very low tensile elongation around or less than 1 % at RT. These indicate that a further embrittlement was introduced in the test material after the hot-wet exposure compared with the RT tensile elongation 1.6 % of the unexposed material. Based on this observation, we can explain further the degradation mechanism for the RT tensile strength reduction of the 450CA30 compound after the E149, E204 and E232 hot-wet exposure as follows: (1) in a high-modulus short fiber-reinforced composite material with perfectly bonded fiber/resin interfaces, a high stress concentration is introduced in the matrix resin phase at the ends of the short fibers when the composite is under a tensile load (as high as 0.6–0.8 of the applied tensile stress to the composite) [30]; (2) it has been identified by the authors that embrittlement can be introduced in the 450G neat resin with RT tensile elongation reduced from typically 40 % in unexposed condition to 18 % after the E149 exposure and to 22 % after the E204 exposure [4]. Under these circumstances, a lower tensile stress (than that applied to the unexposed 450CA30 specimen) applied to the exposed 450CA30 specimen could introduce microcracks in the matrix resin phase at the fiber ends, and consequently cause a brittle fracture of the composite specimen.

Elevated-Temperature Tensile Properties

Since the elevated-temperature mechanical properties of a PEEK compound depends on its glass transition temperature (T_g) and its degradation when exposed in certain environmental conditions. Detailed study on the T_gs and the effect of hot-wet condition on them for the PEEK neat resin and the 30 % glass fiber-filled PEEK compound 450GL30 was conducted and reported in an early publication [4]. For the 30 % carbon fiber-filled PEEK compound 450CA30, its T_gs were determined by the dynamic mechanical analysis (DMA) for the specimens in unexposed condition and after E149, E204 and E232 exposure. The measured DMA storage modulus (G′) and loss modulus (G″) curves and the determined T_gs by G′ onset and G″ peak for the 450CA30 samples in various exposure conditions are presented in Fig. 36.33. It can be seen from the analysis results that the measured onset dry T_g of the unexposed samples is about 145 °C, and the shifts of the T_g to lower levels by E149, E204 and E232 hot-wet exposure conditions were also determined.

Typical tensile stress-strain curves of the 450CA30 and 450G L30 specimens tested at 149 °C, 204 °C and 232 °C in unexposed (UE) condition and after the corresponding E149, E204 and E232 exposure, respectively, are presented in Fig. 36.34. RT tensile stress-strain curves of the 450CA30 and 450G L30 specimens tested in unexposed condition are also presented for referencing. The measured tensile moduli and tensile strengths of the 450GL30 and 450CA30 specimens at

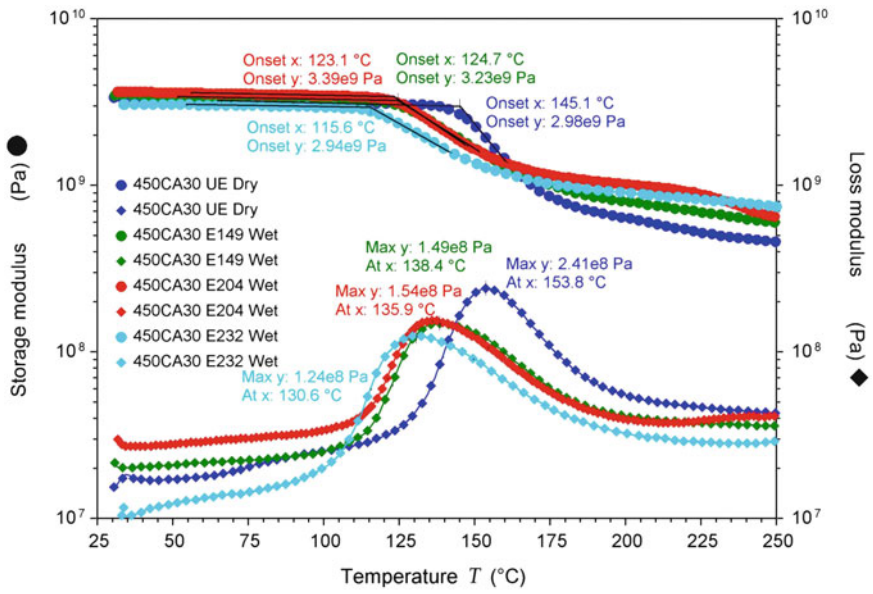

Fig. 36.33 Measured DMA curves of 450CA30 samples in unexposed condition and after E149, E204 and E232 hot-wet exposure in 3 % NaCl brine

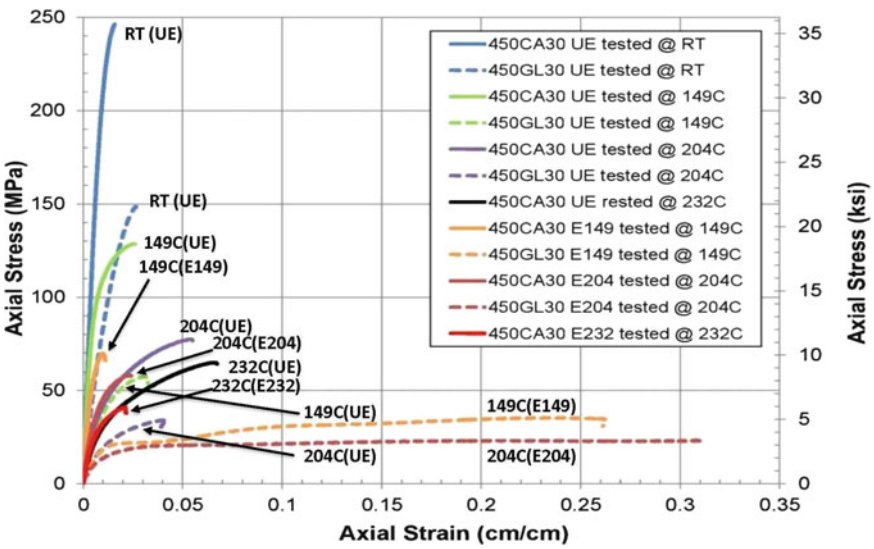

Fig. 36.34 Measured tensile stress-strain curves of 450GL30 and 450CA30 compounds at 149 °C, 204 °C and 232 °C before and after the specified HPHT hot-wet exposure in 3 % NaCl brine

Fig. 36.35 Failed unexposed 450CA30 specimens tested at 204 °C and 232 °C (from top down in the first two), and the failed E204 and E232 exposed 450CA30 specimens tested at 204 °C and 232 °C (from top down in the second two), respectively

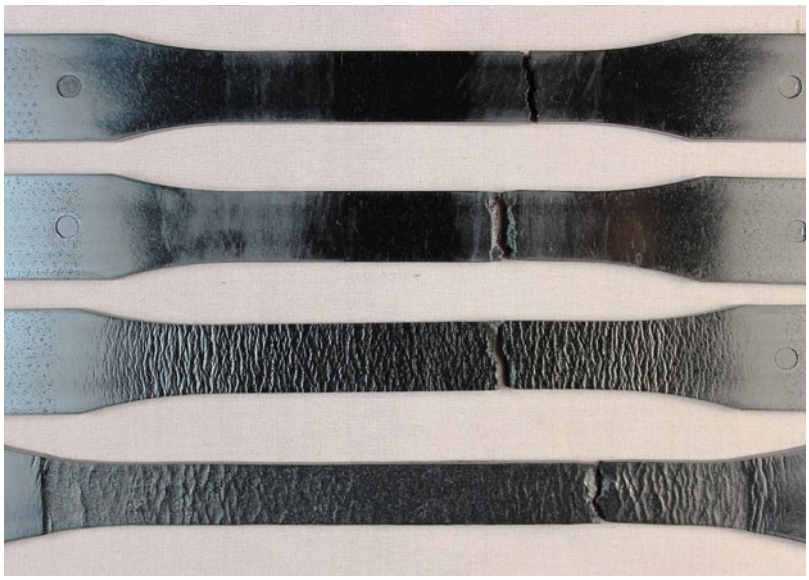

Fig. 36.36 Failed unexposed 450GL30 specimens tested at 149 °C and 204 °C (from top down in the first two), respectively, and the failed E149 and E204 exposed 450GL30 specimens tested at 149 °C and 204 °C (from top down in the second two), respectively

149 °C, 204 °C and 232 °C in unexposed and the E149, E204 and E232 exposed conditions are also presented in the charts in Figs. 36.37 and 36.38, respectively. From the stress-strain curves presented we can see different types of tensile deformation and failure modes from the two different PEEK compounds tested at different temperatures, including brittle fracture, ductile failure, necking and cold drawing. These failure modes can be viewed clearly in the photos, presented in Figs. 36.35 and 36.36, taken from the failed 450CA30 and 450GL30 tensile specimens tested at 149 °C, 204 °C and 232 °C, respectively, in unexposed (UE) and E149, E204 and E232 exposed conditions.

Carbon fiber-filled 450CA30: In unexposed (UE) condition, the carbon fibers in 450CA30 compound can provide a very effective reinforcement function to the PEEK matrix at elevated temperatures, and produce much higher tensile modulus and tensile strength for the 450CA30 compound at 149 °C, 204 °C and even 232 °C, as shown in the tensile stress-strain curves and the charts in Figs. 36.34, 36.37 and 36.38. In the exposed conditions at elevated temperatures, the carbon fibers can maintain good reinforcement function, and also the carbon fiber-filled compound 450CA30 can keep good or quite decent retentions in both tensile modulus and tensile strength at 149 °C, 204 °C and 232 °C, respectively, since the carbon fiber/resin interface bonding has excellent hot-wet resistance up to 232 °C. It is further noted that, compared with the tensile

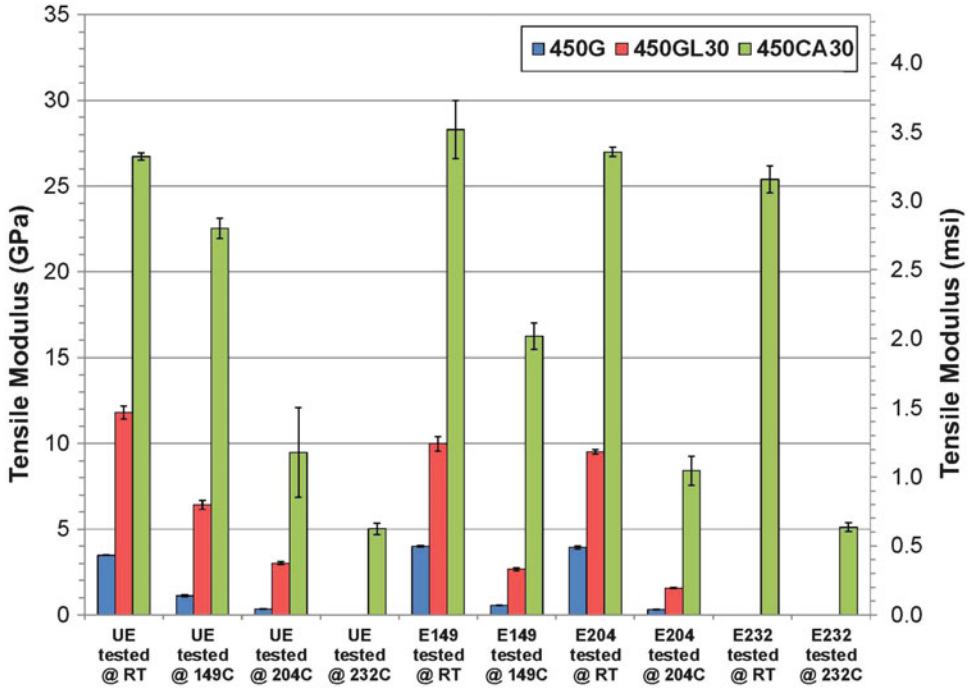

Fig. 36.37 Measured tensile moduli of 450G, 450GL30 and 450CA30 compounds at RT, 149 °C, 204 °C and 232 °C before and after the specified HPHT hot-wet exposure in 3 % NaCl brine

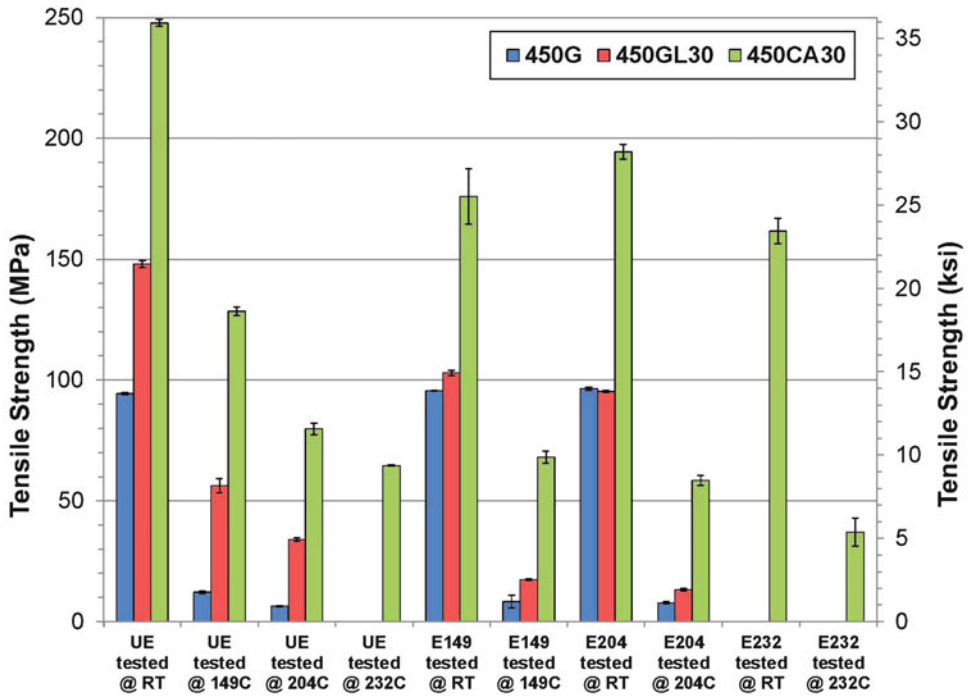

Fig. 36.38 Measured tensile Strengths of 450G, 450GL30 and 450CA30 compounds at RT, 149°, 204 °C and 232 °C before and after the specified HPHT hot-wet exposure in 3 % NaCl brine

properties in unexposed condition at the same test temperature, the tensile modulus retention of 450CA30 at 204 °C after E204 exposure and at 232 °C after E232 exposure were 89 % and 100 %, respectively, and the tensile strength retentions at 204 °C after E204 exposure and at 232 °C after E232 exposure were 73 % and 57 %, respectively. However, at 149 °C after E149 exposure, the tensile modulus and tensile strength retentions were only 72 % and 53 %, respectively. The reasons for

making these lower retentions at a lower temperature are: the test temperatures at 204 °C and 232 °C were far above both the dry T_g (145 °C) and the wet T_gs (123 °C and 115.6 °C) of the 450CA30 samples after the E204 and E232 exposure, which resulted in no major effect to the mechanical properties at 204 °C and 232 °C from the wet T_g shift. However, when tested at 149 °C, the test temperature was quite close to the dry T_g (145 °C) but far above the wet T_g (124.7 °C) of 450CA30 after the E149 exposure. This gave lower tensile property retention when testing the E149 exposed 450CA30 specimens at 149 °C. It can be seen further from the tensile stress-strain curves in Fig. 36.34 that even when the 450CA30 specimens were tested at 204 °C or 232 °C, the tensile elongations were found to be less than 7 % in unexposed condition and around 2.3 % in E204 and E232 exposed condition. This indicates that the carbon fiber-filled 450CA30 compound is even more brittle when tested at 204 °C or 232 °C after the E204 or E232 exposure. The brittle fracture failure molds of the 450CA30 test specimens at 204 °C and 232 °C before and after the corresponding hot-wet exposure are presented in the photo in Fig. 36.35.

Glass fiber-filled 450GL30: In unexposed (UE) condition, the glass fibers can provide quite effective reinforcement function to the PEEK matrix 450G at elevated temperatures, and produce much higher tensile modulus and tensile strength for the 450GL30 compound at 149 °C and 204 °C, as shown in the tensile stress-strain curves and the charts in Figs. 36.34, 36.37 and 36.38. Because of the hot-wet environment-induced degradation in the glass-fiber/resin interface adhesion and in glass fiber strength in the 450GL30 compound in the hot-wet exposed conditions, tensile properties of the 450GL30 specimens at various elevated temperatures decreased substantially. As presented in Figs. 36.37 and 36.38, the measured tensile modulus values of the E149 and E204 exposed 450GL30 specimens at 149 °C and 204 °C decreased from their unexposed values 6.41 GPa and 3.01 GPa to 2.66 GPa and 1.56 GPa, respectively, and the measured tensile strengths of the E149 and E204 exposed 450GL30 specimens at 149 °C and 204 °C decreased from their unexposed values 56.2 MPa and 34.0 MPa to 17.3 MPa and 13.2 MPa, respectively. Comparing the elevated-temperature test data of the exposed glass-fiber filled 450GL30 specimens to the test data measured from the exposed unfilled 450G specimens at the same temperatures and with the same exposure conditions, respectively, we found that (1) although the tensile modulus values of the E149 and E204 exposed 450GL30 specimens at 149 °C and 204 °C are about 5 times of those measured from the exposed 450G specimens, but the measured absolute values are only around 1.5–2.7 GPa at 204 °C and 149 °C, which are quite low; (2) tensile strengths of the E149 and E204 exposed 450GL30 specimens at 149 °C and 204 °C are only about twice of those measured from the exposed 450G specimens, and the measured absolute values are only around 13–17 MPa at 204 °C and 149 °C, respectively, which is very low, very close to the performance of the unfilled 450G specimens.

These elevated-temperature test results from the unexposed and the hot-wet exposed 450GL30 specimens can be further explained by their tensile failure modes. As shown in the photo in Fig. 36.36, when tested at 149 °C and 204 °C, the unexposed (UE) 450GL30 specimens showed a slight ductile deformation but fractured at a small strain (<4.5 %). We can see only very localized plastic deformation near the fracture surface when tested at 204 °C. In these tests, although the test temperature is higher or much higher than the dry T_g of the PEEK resin, the glass fibers in 450GL30 compound enhanced significantly its rigidity. For the E149 and E204 exposed specimens, when tested at 149 °C and 204 °C, the tensile failure modes became cold-draw with major plastic deformation and transverse ruptures as shown in Fig. 36.36. In these cases, the glass-fiber/resin interface debonding in the exposed test specimens released the restriction of the glass fibers to the plastic flow of the PEEK matrix resin in the 450GL30 specimens. Here, the test temperatures were above the wet T_g of the E149 and E204 exposed specimens that facilitated the cold-draw deformation of the PEEK matrix resin in the HPHT hot-wet exposed 450GL30 test specimens.

In summary, although the glass-fiber reinforcement enhanced the mechanical properties of the 450GL30 composite at room temperature and elevated temperatures quite efficiently to a high level in unexposed (UE) condition, after exposure in 3 % NaCl brine at 149 °C or 204 °C under 34.5 MPa for 240 h, respectively, mechanical properties of the 450GL30 composite at elevated temperatures degraded severely to a much lower level and became comparable to the mechanical properties of the unfilled virgin PEEK 450G in the same exposure condition, especially in mechanical strength. This indicates that after the HPHT hot-wet exposure the glass-fibers in the 450GL30 specimens lost their reinforcement functionality partially or completely at elevated temperature because of the fiber/resin interface debonding.

36.4 Conclusions

Based on the experimental studies on HPHT hot-wet exposure, fiber degradation mechanism, fiber and fiber/resin interface examination, dynamic mechanical thermal analysis and mechanical testing for various reinforcement fibers and composites, respectively, the following conclusions may be reached:

1. Glass fibers and aramid fibers were found to be susceptible to hot-wet degradation and hydrolytic attack when the hot-wet exposure temperature is above 66 °C. Degradation mechanisms were investigated and found to be consistent with the current literature. Glass fibers can be used as reinforcements in composites for downhole tool structural applications only for short-term at relatively low operating temperatures. Carbon fibers possess excellent HPHT hot-wet resistance capability, and are considered the best choice for composite extreme HPHT applications.
2. Continuous glass fibers and the fiber/resin interface bonding in both epoxy (thermoset) and PEEK (thermoplastic) matrix composites were found to be degradable in hot-wet environment, which consequently caused major degradation in mechanical properties of the composite materials, and the degree of the degradation depends on the exposure temperature.
3. Tensile strength retention of the continuous carbon fiber-reinforced PEEK and epoxy composites are all good in hot-wet environment up to 204 °C because the tensile strength in a principal fiber direction of a continuous fiber-reinforced composite is a fiber-dominated property and the carbon fibers and their interface bonding with PEEK and epoxy resins possess excellent high-temperature and hot-wet resistance. Compressive strength retentions of the continuous carbon fiber-reinforced PEEK and epoxy composites in hot-wet environment depend more on the temperature and hot-wet environmental resistant capability of the matrix resin phase, including plasticization effect.
4. 30 % (by weight) chopped glass fibers or carbon fibers provides significant reinforcement functions to the PEEK resin, and boost the mechanical properties of the filled 450GL30 and 450CA30 composite compounds to a much higher level at room and elevated temperature in unexposed dry condition. Because of the excellent hot-wet resistance of the carbon fiber and carbon fiber/PEEK resin interface bonding, good tensile property retention of the carbon fiber-filled 450CA30 compound has been identified while the embrittlement of the test specimens by the hot-wet exposure was also noted. However, after a short-term hot-wet exposure at 121 °C or above, the glass fibers in the 450GL30 specimen debonded from the PEEK resin, and the tensile properties of the glass fiber-filled 450GL30 composite degraded severely and became comparable to the tensile properties of the unfilled PEEK neat resin tested in the same environmental condition.
5. Elevated temperature only (tested in dry condition) or wet condition only (tested at RT) could give only partially the mechanical property degradation of the composite materials; a combined elevated temperature and hot-wet exposure condition will give the composites a full range of degradation involving temperature effect, moisture effect and the HPHT hot-wet-exposure induced structural damage of the materials.

Acknowledgement The authors would like to thank Baker Hughes Completions and Unconventional, Multi-Stage Completions for their permission to publish this paper. The authors would also like to express sincere appreciation to Bennett Richard, Director, Research and Technology, for his constant support and encouragement to the research projects. Special thanks due to Victrex plc for their kind support to this project by providing all the Victrex PEEK tensile test coupons.

References

1. Yuan, Y., Goodson, J.: Progress and challenges of composite applications in downhole operations. In: Proceedings of the third MERL Conference on Oilfield Engineering with Polymers, pp. 99–112, London, UK, 28–29 November 2001
2. Yuan, Y., Goodson, J.: Advanced composite downhole applications and HP/HT environmental challenges. In: Paper 04616, Corrosion-2004, NACE International 59th Annual Conference & Exposition, New Orleans, LA, 28 March–1 April 2004
3. Yuan, Y., Goodson, J.: Hot-wet downhole conditions affect composite selection. Oil Gas J. **105**(34), 52–63 (2007)
4. Yuan, Y., Goodson, J., Fan, R.: HP/HT hot-wet resistance of thermoplastic PEEK and its composites (Chapter 18). In: Patterson, E., et al. (eds.) Composite Materials and Joining Technologies for Composites, vol. 7, Proceedings of the 2012 SEM Annual Conference on Experimental and Applied Mechanics. Springer (2013)
5. Yuan, Y., Goodson, J.: HP/HT hot-wet thermomechanical behavior of fiber-reinforced high-temperature polymer composites (Chapter 16). In: Tandon, G.P., et al. (eds.) Experimental Mechanics of Composite, Hybrid, and Multifunctional Materials, vol. 6, Conference Proceedings of the Society for Experimental Mechanics Series. Springer (2014)
6. Browning, C.E.: The mechanisms of elevated temperature property losses in high performance structural epoxy resin matrix materials after exposure to high humidity environments. Ph.D. Dissertation, University of Dayton, Dayton, OH (August 1976)
7. Browning, C.E., Husman, G.E., Whitney, J.M.: Moisture effects in epoxy matrix composites. Compos. Mater. Test. Des. ASTM STP 617, 481–496 (1977)
8. Morgan, R.J., Shin, E.E., Lincoln, J.E., Zhou, J., Drzal, L.T., Wilenski, M.S., Lee, A., Curliss, D.: Durability characterization of bismaleimide and polyimide-carbon fiber composites. In: Proceedings of the 43rd International SAMPE Symposium, pp. 106–119. Anaheim, CA, 31 May–4 June 1998
9. Shin, E.E., Morgon, R.J., Zhou, J.: Hydrolytic degradation mechanisms and kinetics of polyimides for advanced composites. In: Proceedings of the 45th International SAMPE Symposium, Long Beach, CA, 21–25 May 2000
10. Wallenberger, F.T., Watson, J.C., Li, H.: Glass fibers. In: Composite, ASM Handbook, vol. 21. ASM International, pp. 27–34
11. Walsh, P.J.: Carbon fibers. In: Composite, ASM Handbook, vol. 21. ASM International, pp. 35–40 (2001)

12. Chang, K.K.: Aramid fibers. In: Composites, ASM Handbook, vol. 21, ASM International, pp 41–45 (2001)
13. Morgan, R.J., Allred, R.E.: Aramid fiber reinforcements (Chapter 8). In: Lee, S.M. (ed.) Reference Book for Composites Technology, vol. 1. Technomic Publishing (1989)
14. Gurney, C.: Sources of weakness in glass. In: Proc. Royal Soc. of London, A282, pp. 24–33 (1964)
15. Lowrie, R.E.: Glass fibers for high-strength composites (Chapter 11). In: Broutman, L.J., Krock, R.H. (eds.) Modern Composite Materials, pp. 270–323. Addison-Wesley, Reading, MA (1967)
16. Clark, D.E., Pantano Jr., C.G., Hench, L.L.: Corrosion of Glass. Books for Industry Publisher, New York, NY (1979)
17. Drzal, L.T.: Interfaces and Interphases. In: Composites, AMS Handbook, pp. 169–179
18. McMahon, P.E., Ying, L.: Effects of fiber/matrix interactions on properties of graphite/epoxy composites. NASA Contractor Report 3607 (1982)
19. Ashbee, K.H.G., Wyatt, R.C.: Water damage in glass fiber/resin composites. In: Proc. Royal Soc. of London, Series A, vol. 312, no. 1511, pp. 553–564 (1969)
20. Ishida, H., Koenic, J.L.: The reinforcement mechanism of fiber-glass reinforced plastics under wet conditions: a review. Polym. Eng. Sci. **18** (2), 128–149 (1978)
21. Drzal, L.T., Madhukar, M.: Fiber-matrix adhesion and its relationship to composite mechanical properties. J. Mater. Sci. **28**, 569–610H (1993)
22. Wagner, H.D., Lustiger, A., Ling, S.: Assessing glass epoxy interface after environmental exposure. In: Wang, S.S., Fitting, D.W. (eds.) Proceedings of the First International Workshop on Composite Materials for Offshore Operations, pp. 203–211. Houston, TX, 26–28 October 1993
23. Carlsson, L.A., Pomies, F.: Influence of seawater on transverse tensile properties of PMC. In: Wang, S.S., Fitting, D.W. (ed.), Proceedings of the First International Workshop on Composite Materials for Offshore Operations, pp. 213–225. Houston, TX, 26–28 October 1993
24. Plueddemann, E.A.: Silane Coupling Agents (Chapter 4). Plenum, New York, NY (1982)
25. Ishida, H., Koenic, J.L.: Fourier transform infrared spectroscopic study of the structure of silane coupling agent on E-glass fiber. J. Colloid Interface Sci. **64**(3), 565–576 (1978)
26. Hsu, A.C.T., Jemian, W.A., Wilcox, R.C.: Solvent effect of water on S-glass. J. Mater. Sci. **11**, 2099–2104 (1976)
27. Cytec Thermoplastic Composites Guide
28. Lou, A.Y., Murtha, T.P., O'Connor, J.E., Brady, D.G.: Continuous-fiber thermoplastic composites (Chapter 6). In: Carlsson, L.A. (ed.) Thermoplastic Composite Materials. Elsevier, New York, NY (1991)
29. Yuan, Y., Goodson, J.: HTHP in-situ mechanical test rig and test method for high-temperature polymers and composites, SPE 113516. In: Proceedings of the 2008 SPE Europec/EAGE Annual Conference and Exhibition, Rome, Italy, 9–12 June 2008
30. Agarwal, B.D., Broutman, L.J.: Analysis and Performance of Fiber Composites (Chapter 4), 2nd edn. Wiley, New York, NY (1990)

Chapter 37
Laboratory Testing on Composites to Replicate Oil and Gas Service

Sabine Munch, Glyn Morgan, Morris Roseman, and Barry Thomson

Abstract Oil and gas reserves are being explored and produced in ever more hostile operating conditions. These include high levels of hydrogen sulphide or carbon dioxide in the production or injection stream, operations in colder climates, deeper water or remote regions. All of these conditions are pushing polymers (and metals) to their operating limits. This has resulted in a surge in the development of high performance polymeric materials and the final acceptance of materials such as fibre reinforced composites as a viable solution for steel replacement and protection where the benefits overcome the unfamiliar. However, with the materials close to their operating limits, there is a need to develop robust and improved methods to evaluate them in these harsh conditions to ensure reliability, fitness for purpose, service life and satisfy the doubters. This chapter will present some of the current testing methods for composites.

Keywords Composite • Oil & Gas • Ageing • Visual assessment • Mechanical testing

37.1 Introduction

Even with the decline in oil prices, the Oil & Gas industry is looking towards exploiting reserves that are less easy to produce. These horizons include ultra-deep water, ultra-deep wells, Arctic conditions, highly sour reservoirs, or "unconventional oil" such as shale, bitumen and tar sands. Many operators produce from high pressure high temperature (HPHT) reservoirs and some anticipate having to develop technology to exploit fields, as yet untapped, where extreme conditions (XHPHT) exist. This may mean working with downhole temperatures in excess of 180 °C and pressures in excess of 20,000 psi (1400 bar, 140 MPa). Such developments place greater demands on materials in terms of their ability to withstand the operating conditions [1–4]. The sector will face situations where composite materials may be the only economically viable material available. Their main attributes, high stiffness and strength in the fibre direction, lower weight and corrosion resistance, will give them an edge over carbon steel. However, the implementation of composite materials and, more importantly, their qualification for long term performance, represents an opportunity and a technology gap.

The methods currently used to assess polymers such as thermoplastics, elastomers and thermosets can be used—to a certain extent—to start characterising degradation mechanisms in composites. Simple mechanical tests are associated with analytical tools to better understand what happens when these materials are subjected to high temperatures, high pressures and aggressive fluids.

37.2 Experimental Work

The ability to accurately estimate service life for polymers installed in systems where maintenance operations are difficult or very costly, is a definite asset. When materials age over time during exposure to a chemically-aggressive fluid at different temperatures, they usually display a change in magnitude of a performance property such as tensile modulus, as shown in Fig. 37.1. If a failure criterion is defined by whatever means possible (e.g. 50 % change in modulus for ISO 23936-2), then exposure testing can be conducted at three or more temperatures which are above that of service to increase reaction rate and promote chemical changes which correlate with a change in modulus with exposure time and temperature. In Arrhenius plots, the logarithm of reciprocal of the time to reach a certain change in property (50 % here) is plotted against reciprocal absolute temperature, with the slope of the plot divided by the gas constant (R) quantifying the activation energy for the

S. Munch (✉) • G. Morgan • M. Roseman • B. Thomson
Element Materials Technology, Hitchin, Wilbury Way, Hitchin, Herts SG4 OTW, UK
e-mail: sabine.munch@element.com

C. Ralph et al. (eds.), *Mechanics of Composite and Multi-functional Materials, Volume 7*,
Conference Proceedings of the Society for Experimental Mechanics Series, DOI 10.1007/978-3-319-21762-8_37

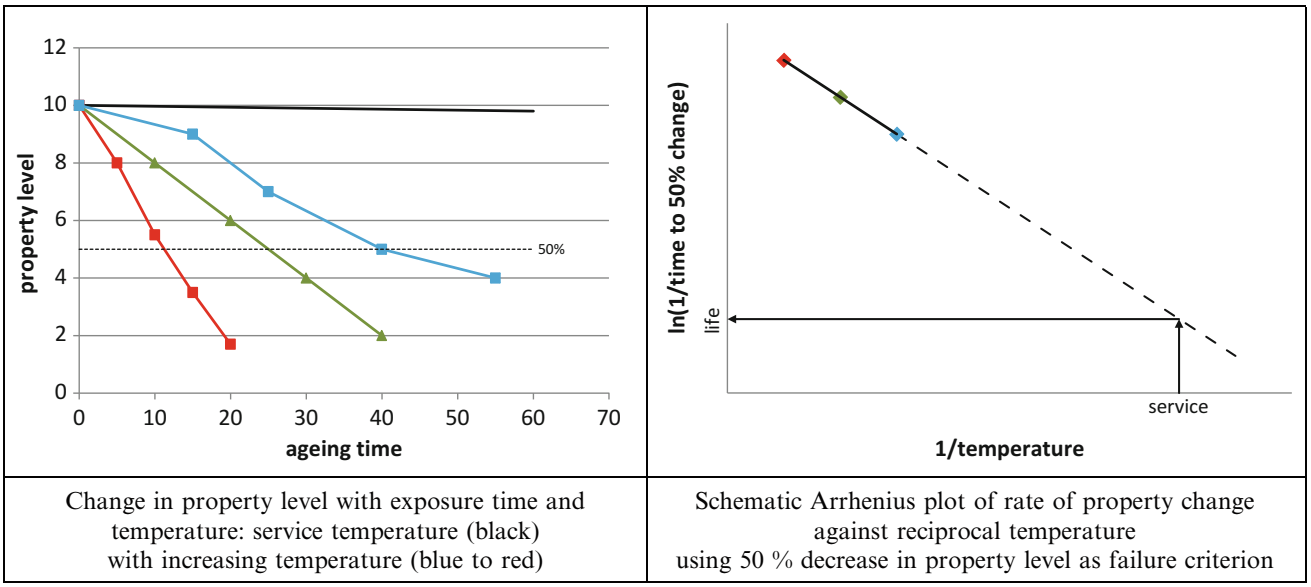

Change in property level with exposure time and temperature: service temperature (black) with increasing temperature (blue to red)

Schematic Arrhenius plot of rate of property change against reciprocal temperature using 50 % decrease in property level as failure criterion

Fig. 37.1 Arrhenius principal

process (E_a). This predicts material change with time when subjected to accelerated ageing: 'life' under service conditions can be extrapolated. The validity of this approach has been verified for nitrile rubbers by comparing long term degradation at temperatures just above service with short term, high temperature testing. In this instance, the results were comparable, giving confidence in the accelerating principle.

This technique is more difficult to apply to other polymers let alone composites; some may present limited changes in mechanical properties during exposure, making it impossible to use Arrhenius to extrapolate service life. An example is a carbon fibre filled thermoplastic subjected to exposure in a sour fluid containing a small amount of hydrogen sulphide and carbon dioxide in methane, oil and water at 380 bar (around 5500 psi). Samples were immersed in the oil phase of the test fluid at 180, 190 and 200 °C (356, 374 and 392 °F) and retrieved at four different sampling points per temperature.

Tensile (ASTM D3039M) and three point bend (ASTM D790M) testing was performed on unaged as well as exposed specimens. Tensile testing proved unreliable as the presence of an oily film on the surface of the samples meant that gripping was difficult and often led to slippage. The properties measured during the flexure tests were of much better quality; the data is summarised in Fig. 37.2. After an initial decrease in flexural modulus from time 0 at all temperatures, due to the absorption of the test fluid effectively plasticising the material, the property appears to remain stable over the test duration, even at the high test temperatures ranging from 180 to 200 °C (356–392 °F). The same can be said for the maximum strength and strain. They appear to both increase and then "stabilise" within one standard deviation from the mean. If a polymer appears to remain unaffected by the exposure fluid even after long times at elevated temperatures, it is not possible to establish a service life. In other words, for more chemically resistant materials test conditions may have to be so severe to initiate any material changes that this causes effects unlikely to be seen in service and so invalidates the approach of thermal acceleration.

In addition, fluid absorption in materials such as composites is even more complex than in elastomers, thermoplastics and thermosets alone. Fluid diffuses into the composite matrix, with the extent of the absorption depending on the chemistry and morphology of the polymer as well as the volume fraction and configuration of the fibres, whether bubbles and voids are present in the matrix and wicking occurs at the interface between fibres and resin. The combination of fluid absorption and elevated temperature will cause plasticisation of the matrix, which allows relaxation of the polymer chains. It also affects the residual stresses present within the composite and may allow micro-crack formation which could ultimately lead to increased water absorption and/or weakening of the fibre/matrix interface; physical processes not accounted for by an Arrhenius approach to ageing. The test fluid may also chemically attack fibres and/or resin, compromising the fibre/resin bond or even dissolving fibres and/or resin. The effects of fluid absorption tend to become more apparent the higher the exposure temperature. This is due to the fact that the higher the temperature the faster the rate of diffusion and ultimately the higher the level of absorption over a fixed time period.

It is clear from the above, that the tools to define service life for composite materials have not yet been fully developed. To help identify what mechanisms are involved in ageing, Element Materials Technology Hitchin is investigating different

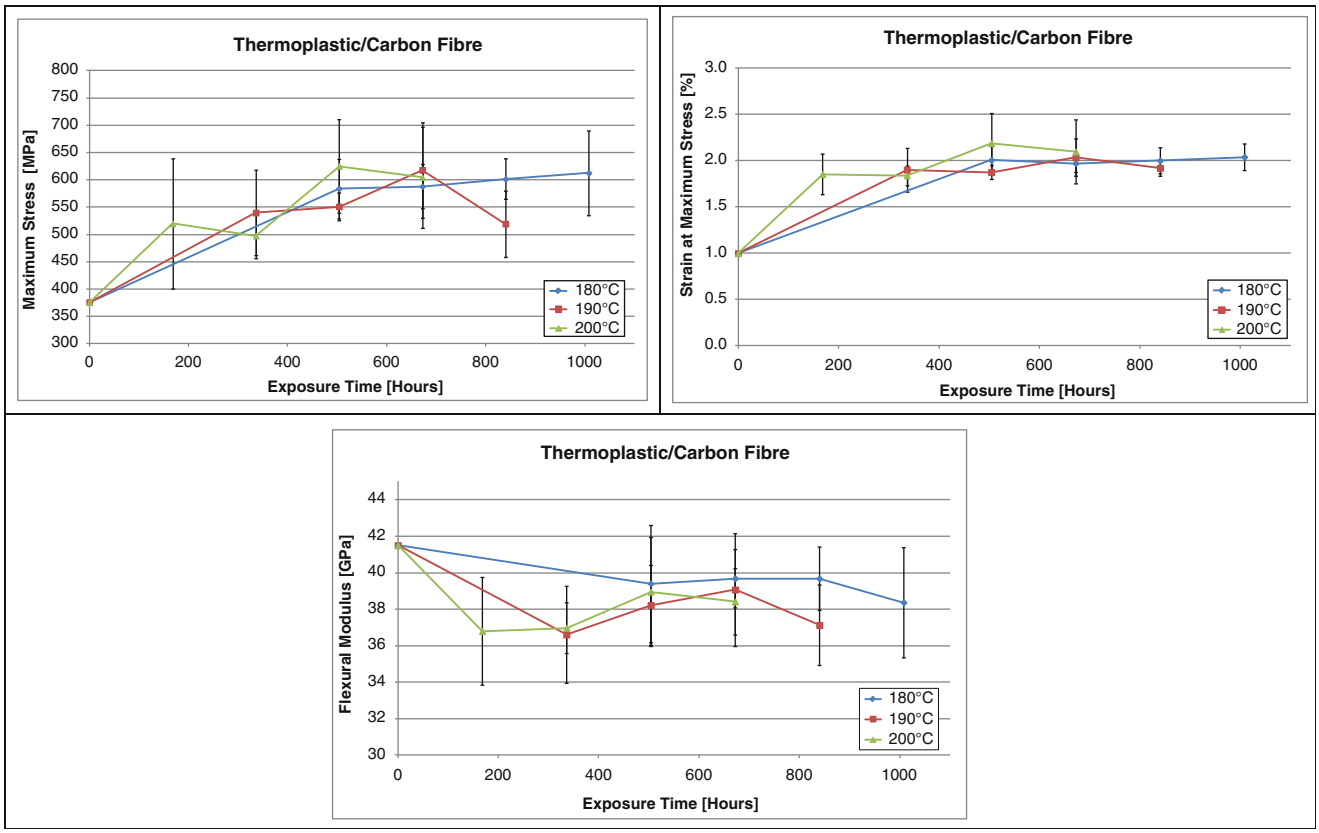

Fig. 37.2 Evolution of the flexural properties of a carbon fibre reinforced thermoplastic composite with exposure time and temperature in 380 bar (ca. 5500 psi) pressure sour fluid

analytical test methods. As an example, a long term ageing study was conducted on a glass fibre reinforced thermoset intended for offshore usage and subjected to seawater. In this case, the material was again immersed in the test fluid at temperatures above its normal operating conditions, i.e. 60, 80 and 100 °C (140, 176 and 212 °F) for up to 35 weeks. It is evident from Fig. 37.3, that temperature has an effect on fluid absorption. It appears that fluid uptake is faster and greater as temperature increases. Concentrating now on the highest temperature 100 °C (212 °F), after having reached saturation, the material exhibits a loss in mass from around 6 weeks (6.5^2 days). This could be due to several factors such as leachables escaping the composite, the dissolution of the resin or of the fibres. This behaviour is not visible at the two other temperatures. Does this mean that only the reaction rate of the processes at play increases or could other ageing mechanisms take place at the highest temperatures?

The samples were assessed visually for changes with exposure time and temperature. Following removal after 245 days, the samples displayed a slight increase in surface roughness accompanied by discoloration. Both were more noticeable as temperature increased (Fig. 37.4). The physical changes observed could be linked to the fact that some of the resin may have been dissolving over the course of the immersion test, which can also explain the loss in mass sustained by the samples having undergone exposure to the fluid at the highest temperature.

Three point bend (ASTM D790M) and short-beam shear (ASTM D2344M) testing was conducted following exposure, to monitor changes to the material properties with time in the test conditions. The test fluid does not seem to plasticise the material as maximum flexural strength decreases between dry and wet state at all temperatures (Fig. 37.5). As highlighted before, the loss in flexural properties could be due to residual stresses being relieved by micro-cracking. It appears that after the initial changes sustained due to fluid absorption, virtually no changes are seen over the 35 weeks of testing at the highest test temperature. The fibre dominated property—strain at maximum stress—does not exhibit much variation at 100 °C (212 °F). An overall decrease in maximum stress, strain at maximum stress and modulus is seen over the exposure period at both 60 and 80 °C (140 and 176 °F). This could mean that full saturation of the material may not have been reached by the time the first measurement is carried out after exposure. The fact that the flexural properties at the highest temperature are relatively stable seems to show that the material does not age.

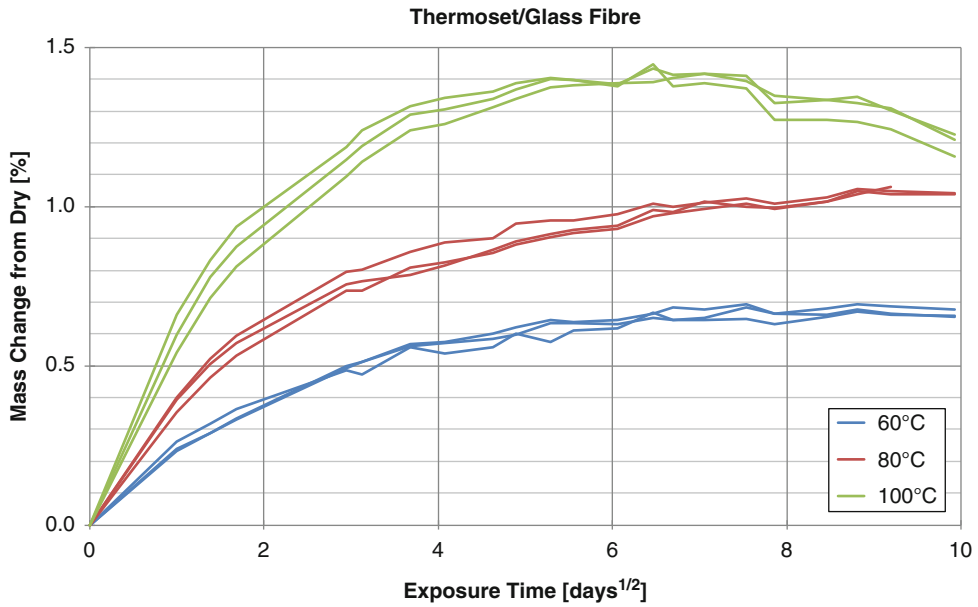

Fig. 37.3 Change in mass as a function of square root of time and temperature

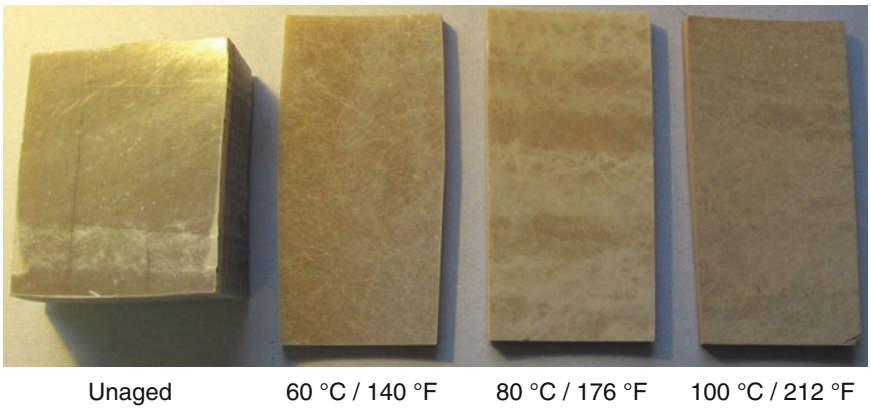

Fig. 37.4 Visual changes after 245 days exposure to synthetic seawater at vapour pressure and different temperatures; from left to right - Unaged, 60°C / 140 °F, 80 °C / 176 °F, 100 °C / 212 °F

The ILSS (Interlaminar short-beam shear) data, paints a different picture, with again a loss in property between dry and wet, but also a steady loss in strength with exposure time at all temperatures (Fig. 37.6). This behaviour ties in with the hypothesis that the thermoset resin may degrade and dissolve with exposure time.

As the material displayed a loss in short-beam strength, discoloration and greater surface roughness following exposure, samples having undergone exposure to seawater for 245 days at all three temperatures were observed at high magnification under an SEM and compared to an unaged test piece (Fig. 37.7). Scratches and pits were seen on the surfaces of all samples, and the glass fibres themselves were often visible. The increase in surface roughness with exposure time and temperature appears to be linked to non-reversible chemical ageing. An increasing level of degradation was seen at the interface between the fibres and the matrix accompanied by a loss of fibre integrity with increasing test temperature. No cracking of the matrix material was observed in any of the samples. Therefore, it continued to protect the glass fibres within the bulk material hence maintaining mechanical properties after saturation. Only those glass fibres that were at the surface have been degraded. It can be assumed that exposure for longer periods of time (beyond the scope of this project) would cause further fibre degradation as seawater slowly attacked the protected fibres within the material bulk.

For the above study, ILSS appears to be a good indicator of composite ageing. This mechanical method can be associated with other tools to produce a good picture of composite behaviour in aggressive fluids. However, reliable accelerated ageing methods and life prediction procedures are still not defined for these fascinating materials.

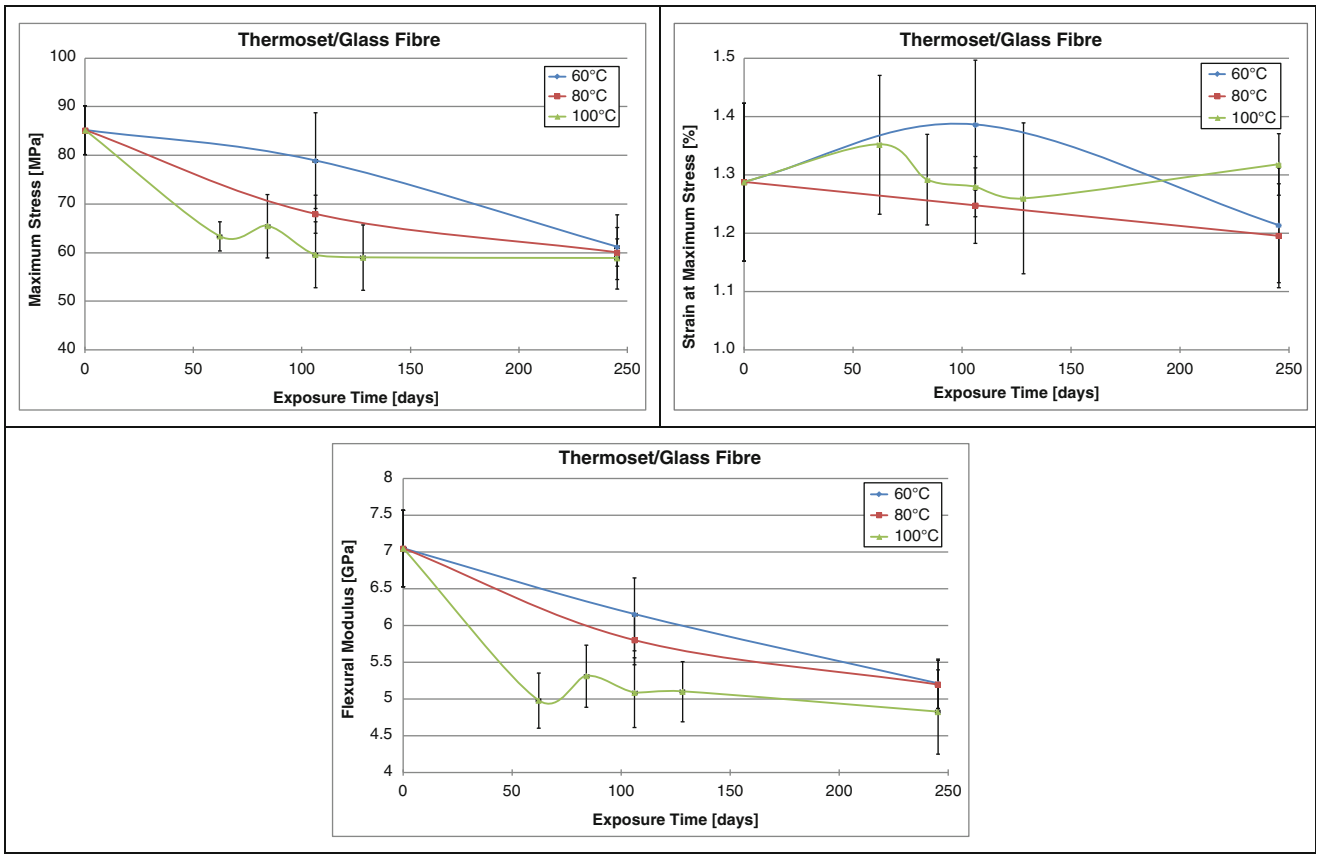

Fig. 37.5 Evolution of the flexural properties of a glass fibre reinforced thermoset composite with exposure time and temperature in synthetic seawater at vapour pressure

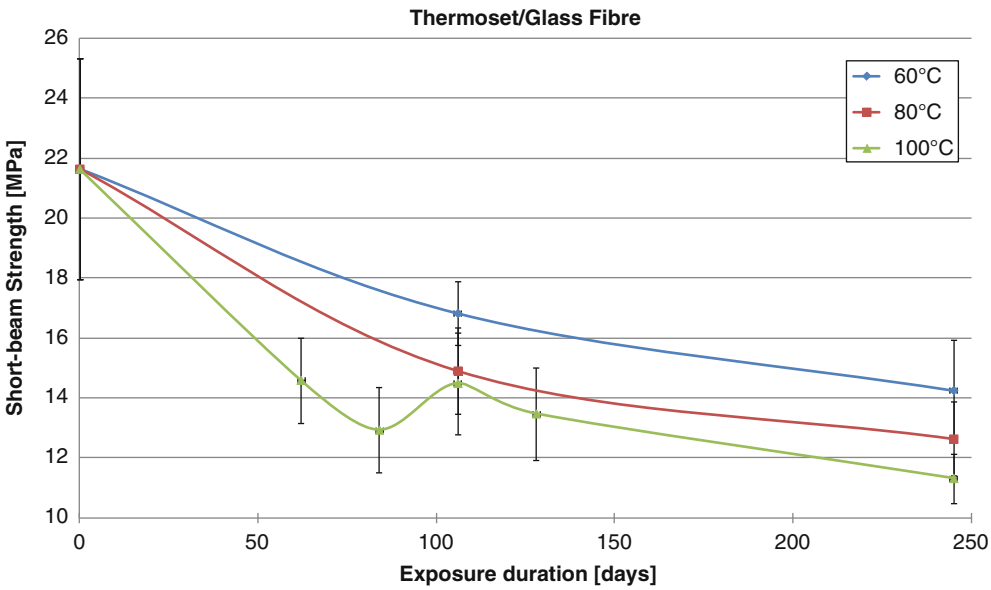

Fig. 37.6 Evolution of the short-beam strength of a glass fibre reinforced thermoset composite with exposure time and temperature in synthetic seawater at vapour pressure

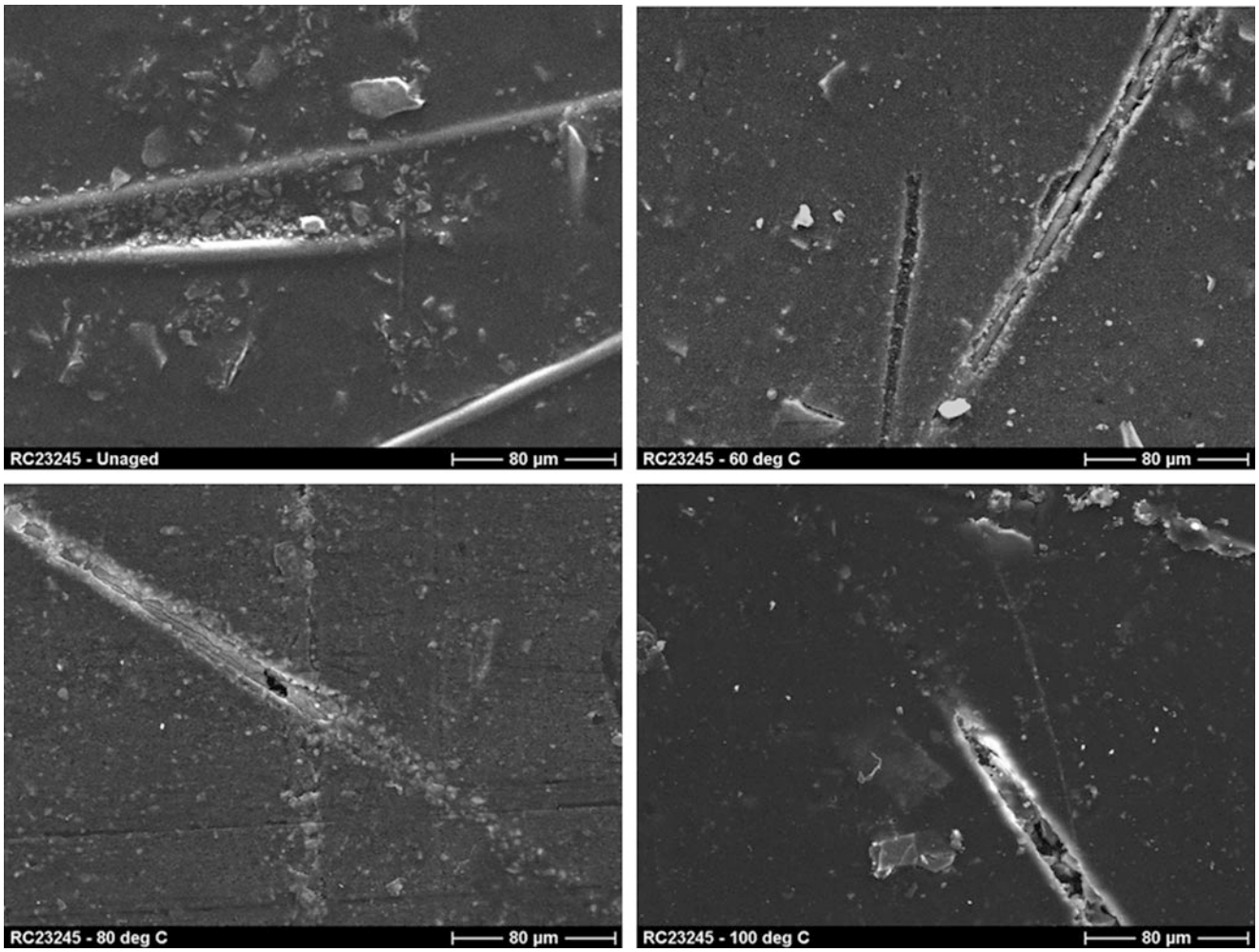

Fig. 37.7 SEM micrographs: surface state of unaged samples and specimens having been exposed to seawater for 245 days at 60, 80 and 100 °C (140, 176 and 212 °F)

37.3 Conclusion

Using mechanical testing to assess if ageing has taken place in composite materials is a good tool when associated with other analytical methods. It appears that ILSS in combination with flexure testing and visual assessment can give an insight in degradation. This can be associated to other techniques such as a study of the evolution of glass transition temperature with exposure time. Although ageing can be characterised in particular conditions, extrapolating the long term behaviour of composites does not appear to be possible at the moment. The different ageing mechanisms at play may need to be isolated and understood before being combined in FEA models to have a better picture of degradation mechanisms and extent.

In addition to ageing, Oil & Gas conditions present further challenges for composites. These materials, in contact with high solvation power fluids such as supercritical carbon dioxide may sustain rapid gas decompression damage. When equilibrium is reached between external gas pressure and dissolved gas concentration within a composite, the rapid release of external pressure—called rapid gas decompression (RGD)—triggers material expansion and may lead to the formation of cracks and delamination, which could help promote ageing and loss of structural properties. The avoidance of RGD in service situations is often not possible since slow depressurisation over a long period—one way to prevent fracture development—is not viable. Moreover, uncontrolled gas decompression may accidently occur. Composites in contact with fluids which may induce RGD damage (also called blistering) have to be assessed in conditions close to that of the field. Interestingly, some material may present good RGD resistance in their dry unaged state, but fair poorly when subjected to pressure cycling after exposure to fluids which may have affected the bond between fibres and resin or resin and/or fibre integrity. There are currently no standards available to define RGD resistance for composites in oilfield fluids.

Composite liners appear to be a good corrosion resistant solution; with products cheaper and lighter than CRAs. In this instance, manufacturing is of paramount importance. To maintain its good barrier properties, composites should present low permeation to the fluids contacting them. Again, permeation testing is a useful tool to determine how materials as well as structures behave. There are however no standard available to the industry to confidently measure and analyse these important properties.

A general observation about the majority of current standards is that information about testing of non-metallics and interpretation of data is very scarce and could be improved upon to provide better overall industry understanding and therefore raise confidence in design and test results. Composites have not seen such widespread use in safety critical applications such as offshore operations due to a lack of recognised standard test methods. A scarcity of experts in the field, and the shortage of field experience to give confidence in the use of these materials, result in a classic Catch 22 situation. To develop the full potential of composites requires improved methods to evaluate these materials which give data relevant to their applications and to implement these methods into suitable, robust industry standards. To qualify them for even more onerous future service conditions, several DNV documents provide a good starting point. To complete this effort, ISO standards are under development incorporating knowledge and methodologies acquired through project work and research ranging from ageing/chemical effects through permeation studies to mechanical strength, with the aim of establishing performance envelopes and long term durability assessment procedures.

Therefore, a pragmatic approach should be followed involving material testing in combination with component-specific testing which tests the robustness of the design and manufacturing process as much as the long term material suitability.

References

1. Martin, R., Roseman, M.: Composite Materials: An Enabling Material for Offshore Piping Systems. Offshore Technology Conference, Document ID: OTC-23925-MS, Houston, TX, USA, 6–9 May 2013
2. Gibson, A.G.: The Cost Effective Use of Fibre Reinforced Composites Offshore. University of Newcastle Upon Tyne for the Health and Safety Executive, HSE Books, Research Report 039 (2003)
3. Martin, R.: A Technology Gap Review of Composites in the UK Oil and Gas Industry. The UK National Composites Network, Document Number: MERL C1889-1 Rev B (2007)
4. Morgan, G., Roseman, M., Thomson, B.: Future evaluation requirements of composites and thermoplastics to meet the next level of operational challenges. In: High Performance Thermoplastics & Composites for Oil & Gas Applications 2011 Conference, Paper 19, Houston, USA, 11–12 Oct 2011

Chapter 38
Measurement of Thermal Deformation of CFRP Under Rapid Heating

J. Koyanagi, Y. Fukuda, K. Hirai, A. Yoshimura, T. Aoki, T. Ogasawara, and S. Yoneyama

Abstract CFRP which consists of carbon fiber/phenol resin is widely used for a thermal protection system in Aerospace field. Rapid-heating-induced thermal deformation of CFRP is measured using digital image correlation (DIC) technique in the present study. Specimen temperature is above 1200 K so that long wavelength radiation is significant and the DIC technique is not easy to apply. A heat resistance random pattern on the specimen surface, which is made by ceramic materials, and low pass filter allow to apply the DIC method. A complicated deformation including rapid-heat transfer and simultaneously occurring CFRP ablation is measured transitionally.

Keywords Optical Methods • Digital Image Correlation • CFRP • Rapid heating • IR lamp heating equipment • CTE

38.1 Introduction

In this study, we focused on the estimation of thermal deformation of CFRP, which are used for Solid Rocket Motor (SRM) nozzles. When the virgin CFRP which is consisted of carbon fiber and phenol resin are heated, the phenol resin causes pyrolysis, and it changes the virgin layer into charring layer. The current thermal analyses are able to reproduce the behavior of heat conduction and the progression of charring layer at the CFRP during heating process. But, we have never been able to estimate that the thermal deformation of CFRP during heating process. That's because the characteristic data of the thermal expansion which is the driving force of the thermal deformation behavior is not able to reproduce the reality of CFRP. The results of numerical model are expected because it is need for to estimate of behavior at the SRM nozzles and the warhead of rockets. The characteristic data of thermal expansion is based on typical thermal expansion test. It does not deal with the tape-wrap CFRP such as used in rocket nozzle. Understanding the phenomenon and making the numerical model of the behavior of thermal deformation of CFRP are essential to improve the reliability.

The heating environment, restraint states and situation of outflowing pyrolysis gases are considered the dominant factors of the behavior of thermal deformation of CFRP. These dominant factors are different at conventional heating test and real environment. Therefore, based on above, we have been conducting research as below.

1. Grasp the characteristic of thermal deformation of small size tape-wrap CFRP.

   Make the IR (infrared) lamp rapid heating equipment.
   Establish the method of measurement of thermal deformation of CFRP with Digital Image Correlation (DIC) method.
   Make the models of thermal deformation of tape-wrap CFRP

J. Koyanagi (✉) • Y. Fukuda
Department of Materials Science and Technology, Tokyo University of Science, 6-3-1 Niijuku, Katsushika-ku, Tokyo 125-8585, Japan
e-mail: Carry.pan0515@gmail.com

K. Hirai
Technologies Development Department, IHI Aerospace Co., Ltd, Fujiki 900, Tomioka, Gunma 370-2307, Japan

A. Yoshimura • T. Aoki • T. Ogasawara
Advanced Composite Research Center, Institute of Aeronautical Technology, Japan Aerospace Exploration Agency,
6-3-1, Ohsawa, Mitaka, Tokyo 181-0015, Japan

S. Yoneyama
Department of Mechanical Engineering, Aoyama Gakuin University, 5-10-1 Fuchinobe, Chuo-ku, Sagamihara, Kanagawa 252-5258, Japan

C. Ralph et al. (eds.), *Mechanics of Composite and Multi-functional Materials, Volume 7*,
Conference Proceedings of the Society for Experimental Mechanics Series, DOI 10.1007/978-3-319-21762-8_38

2. Validation of thermal deformation model of large size tape-wrap CFRP.

In this time, this study is still at the stage of establishing the measurement method of measurement of the thermal deformation of CFRP with DIC method under rapid heating with IR rapid heating equipment. In this chapter, we introduced the rapid heating test about SUS304 with IR lamp which went as the preliminary test [1–5].

38.2 Infrared Lamp Rapid Heating Equipment

In this study, we made a new test device. It has some IR lamps to heat rapidly. The quartz infrared heater lamp is made in Research Inc. One unit is consisted of six valves (external diameter: 10 mm, effective length: 250 mm, 5 kW). And this unit's body is made of aluminum alloy.

Figure 38.1 shows the quarts infrared heater lamp and the situation these lamps are operated. It can heat 90 kW with the infrared light irradiation by combining three units (30 kW $\times$ 3). The heating area size when these three units are combined is 320 $\times$ 245.1 mm^2. And it enables to heat rapidly above 100 kW/m^2 [6]. In this study, we heat CFRP rapidly. However, when the CFRP is heated, it generates the pyrolysis gas. Therefore, we need special chamber which is not sealed up unlike typical system. And, since we observe optically, we need an anti-fog system near the observation windows. So, the IR lamp rapid heating equipment which we made newly this time has the device which enables to avoid the pyrolysis gas flowing from specimen.

Figure 38.2 shows the whole picture of the newest equipment. And the details of the chamber are shown in Fig. 38.3.

These observation windows are provided on side of chamber every angle of 90°. These observation windows and heating window are made of silica glass. We measure the deformation of CFRP with DIC method through these observation windows. Near the observation windows, gas exhaust nozzles are provided. By emitting the N_2 gas from these nozzles, it can prevent adhesion of contamination. The surface temperature is measured with radiation thermometers. But the wave length is used under 2.5 μm because it through the silica glass.

Moreover, in this study, we measured the deformation of the specimen with the DIC method. However, the specimen's temperature is so high that it is conceivable that the effect of radiation from specimen occurs. To relieve the effect of radiation, we used an optical filter which enables to cut off the long wave length. We used the blue glass filter which made in Shibuya Optical Co., Ltd.

Figure 38.4 shows the transmitted light wave length of this blue glass. And in this study, we measure the deformation with DIC method. That method needs random pattern by paints. But, the pattern made by common paints normally burns out at temperatures above 250 °C. So, in this work, we used the ceramic bond (Asahi Chemical Co., Ltd, SUMICERAM®, S-301) to make random patterns [7].

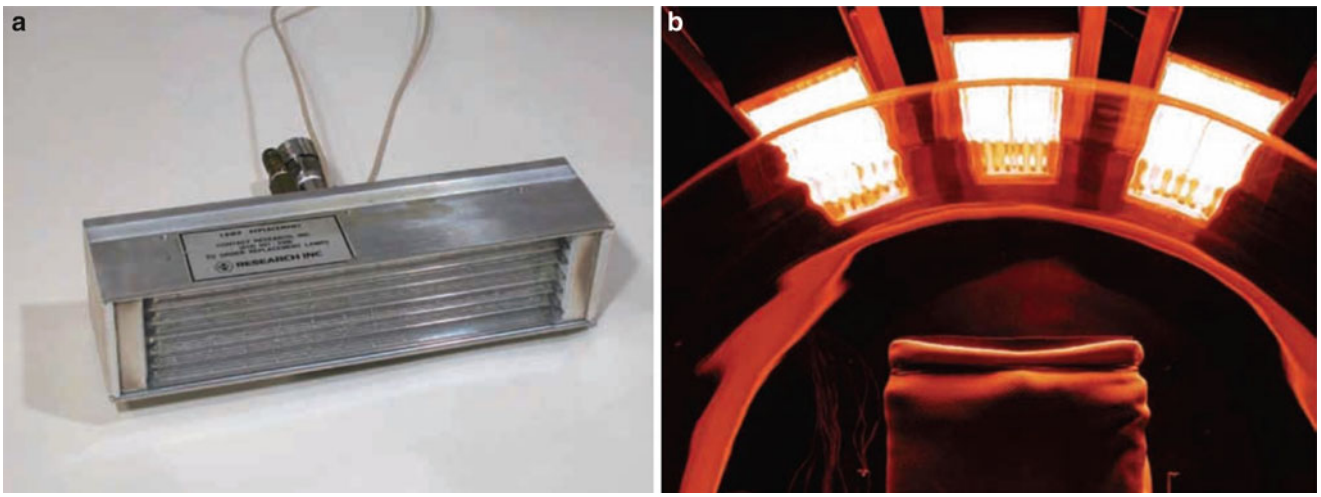

Fig. 38.1 (**a**) Quartz infrared heater lamp, (**b**) situation of heating by quartz IR heater lamp

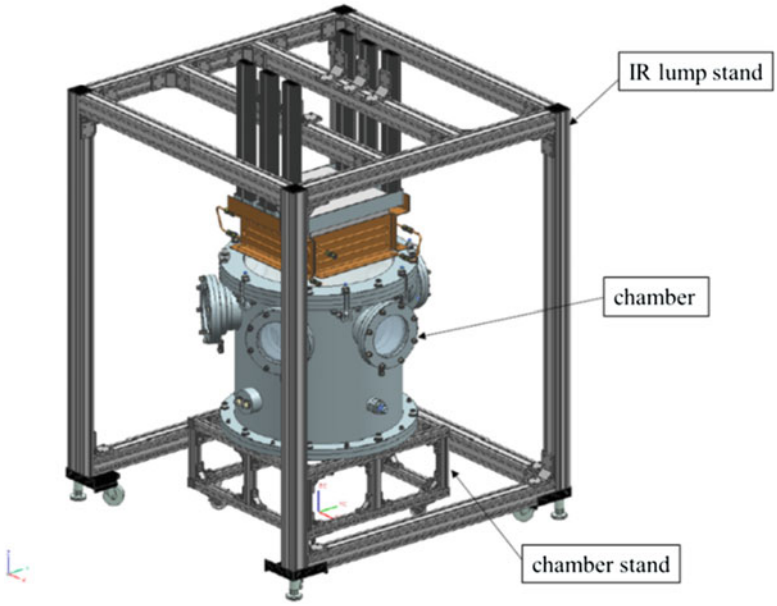

Fig. 38.2 IR lamp rapid heating equipment

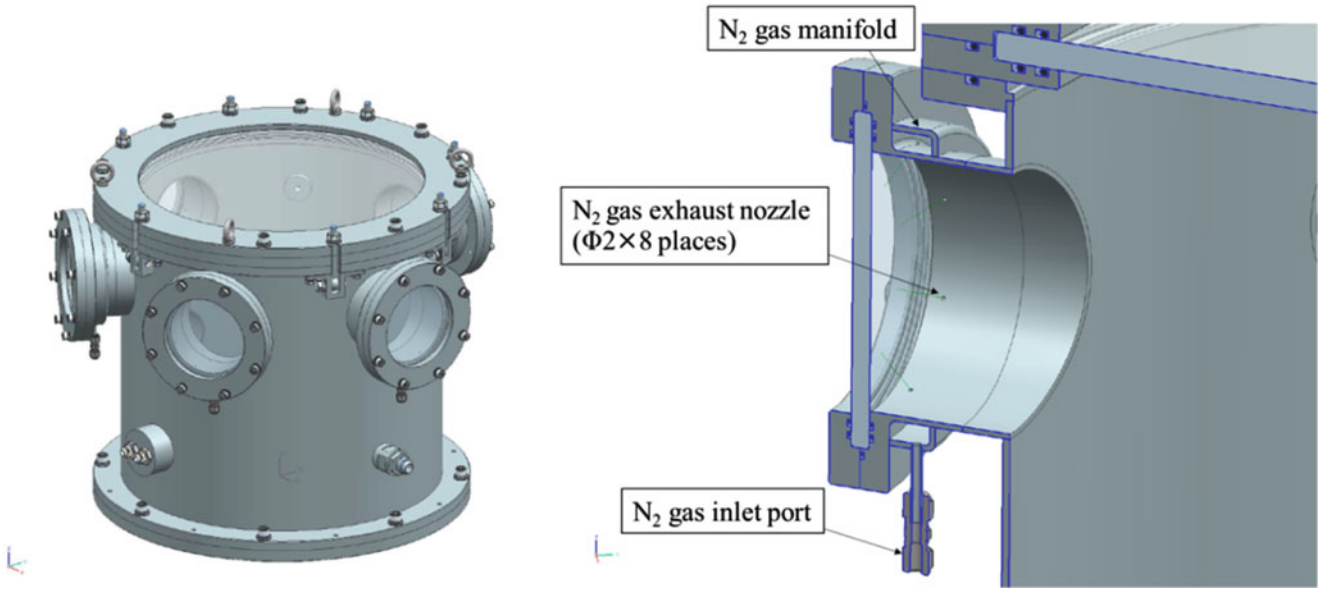

Fig. 38.3 Details of the chamber

38.3 Digital Image Correlation Method

Experimental techniques in solid mechanics rely heavily on surfaces displacement field measurements. Several optical methods, such as moiré interferometry, holographic interferometry or speckle pattern interferometry have long been used in experimental solid mechanics to study mechanical deformation of solids and the mechanics of fracture. Among them, digital image correlation technique, which can obtain the deformation of a surface by comparison of digital images of the undeformed and deformed configurations, is becoming popular and widely used. Since this method does not need a complicated optical system, the measurement can be performed easily. In addition, unlike other methods which utilize the interference of light waves, phase analysis of the fringe pattern and subsequent phase unwrapping process are not required.

In two-dimensional digital image correlation, displacements are directly detected from digital images of a specimen.

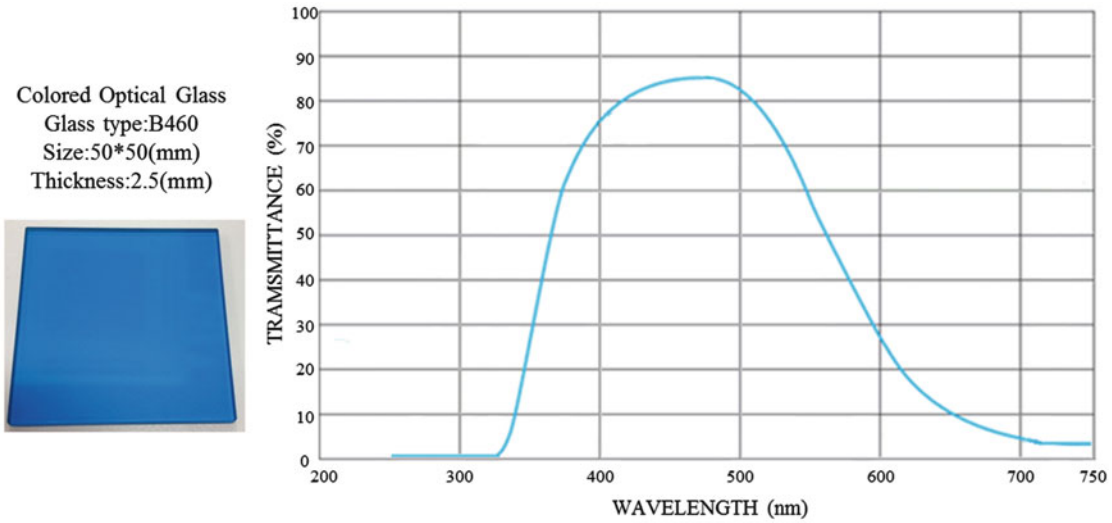

Fig. 38.4 Optical grass

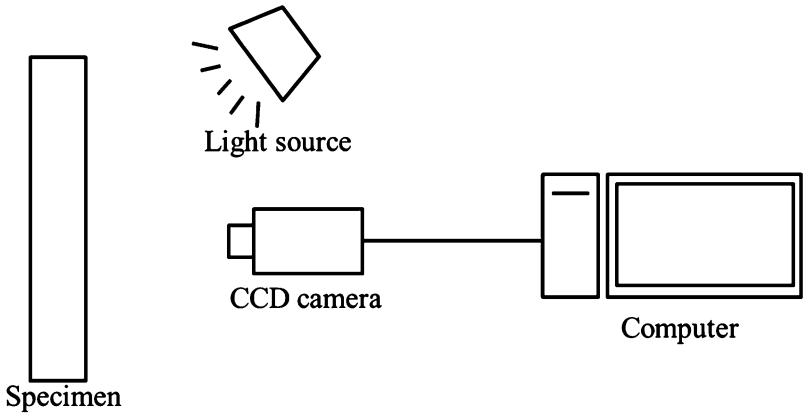

Fig. 38.5 Setup for displacement measurement using digital image correlation

Figure 38.5 shows a typical example of an experimental setup for two-dimensional digital image correlation. Then, the images on the surface of the object, one before and another after deformation, are recorded, digitized and stored in a computer as digital images. These images are compared to detect displacements by searching a matched point from one image to another. Here, because it is almost impossible to find the matched point using a single pixel, an area with multiple pixel points (such as 20 × 20 pixels) is used to perform the matching process. This area, usually called subset, has a unique light intensity distribution inside the subset itself. It is assumed that this light intensity distribution does not change during deformation.

Figure 38.6 shows the part of the digital images before and after deformation. The displacement of the subset on the image before deformation is found in the image after deformation by searching the area of same light intensity distribution with the subset. Once the location of this subset in the deformed image is found, the displacement of this subset can be determined. In order to perform this process, the surface of the object must have a feature that allows matching the subset. If no feature is observed on the surface of the object, an artificial random pattern must be applied. Based on the above basic concept, several functions exist to match the subset from one image to another. One is the magnitude of intensity value difference as

$$R(x, y, x^*, y^*) = \sum \left| F(x, y) - G(x^*, y^*) \right| \tag{38.1}$$

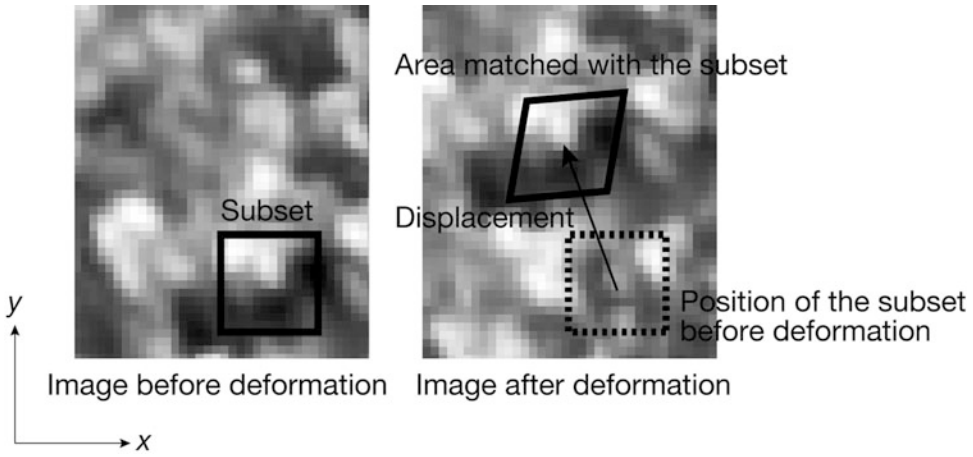

Fig. 38.6 Matching the subset before and after deformation

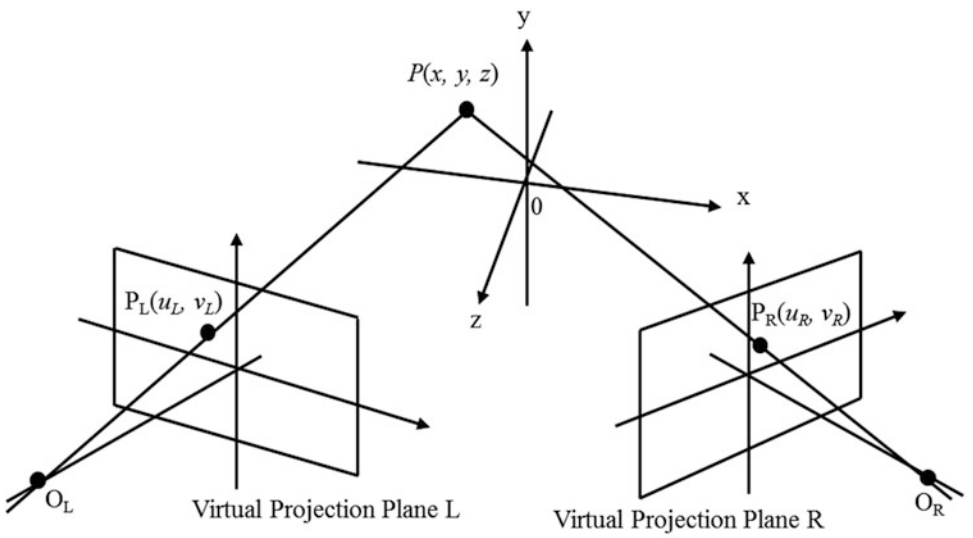

Fig. 38.7 Relationship of camera and specimen at stereovision techniques

And another is the normalized cross-correlation as

$$C(x, y, x^*, y^*) = \frac{\sum F(x, y)G(x^*, y^*)}{\sqrt{\sum F(x, y)^2 \sum G(x^*, y^*)^2}} \tag{38.2}$$

Where F(x, y) and G(x*, y*) represent the gray levels within the subset of the undeformed and deformed images, and (x, y) and (x*, y*) after deformation relates to the coordinate (x, y) before deformation. Therefore, displacement components are obtained by searching the best set of the coordinates after deformation (x*, y*) which minimize R(x, y, x*, y*) or maximize C(x, y, x*, y*). The normalized cross-correlation is widely used for matching the subset in digital image correlation. Furthermore, the strain is obtained from calculating the derivative of distribution of displacement.

By using the stereovision techniques that utilizes multiple cameras, we can measure the three-dimensional displacement and strain.

Figure 38.7 shows the situation of taking a photograph with two cameras. The coordinate space about the feature is represented as (x, y, z), and the virtual projection planes are represented as (u, v). P(x, y, z) is the point on the specimen. O_L and O_R are the each center of the projection of camera L and R. $P_L(u_L, v_L)$ and $P_R(u_R, v_R)$ are each images of P on the virtual projection plane. That is, P and P_L, P and P_R are in the conjugate relations. And the point on (x, y, z) focus into an image on the point (u_L, v_L) and (u_R, v_R). By using the pinhole camera model, the relationship of point (u, v) and (x, y, z) are represented as

Fig. 38.8 Random pattern at the specimen surface

$$u = \alpha \frac{r_{11}x + r_{12}y + r_{13}z + t_u}{r_{31}x + r_{32}y + r_{33}z + t_w} + \gamma \frac{r_{21}x + r_{22}y + r_{23}z + t_v}{r_{31}x + r_{32}y + r_{33}z + t_w} + u_0$$
$$v = \beta \frac{r_{21}x + r_{22}y + r_{23}z + t_v}{r_{31}x + ry_{32}^{32} + r_{33}z + t_w} + v_0 \tag{38.3}$$

where α, β, γ are the scale factor, and u_0, v_0 are the principal point position at the virtual projection surface. However, in reality, because of the distortion of the lens, the point (u, v) is obtained as the point (u′, v′) which is on the deformed image. These relationships are represented as

$$u' = u + k_1(u - u_0)\left\{(u - u_0)^2 + (v - v_0)^2\right\}$$
$$v' = v + k_1(v - v_0)\left\{(u - u_0)^2 + (v - v_0)^2\right\} \tag{38.4}$$

where k_1 is a coefficient of distortion which called internal parameters. On the other hand, r_{11}~r_{33} are the coefficient of pose of the camera. And t_u, t_v, t_w are the coefficient of location of the camera. There are called external parameters. These parameters are obtained by calibration. The point (u_L, v_L) and (u_R, v_R) are obtained by Eq. (38.3). Therefore, when these positions P_L and P_R are determined, the position of P is obtained as an intersection point on the extension line of O_LP_L and O_RP_R. By obtaining these points with DIC method, we could measure the three-dimensional shape and displacement. Furthermore, the three-dimensional strain is obtained from calculating the derivative of distribution of displacement [8, 9].

38.4 Preliminary Experiment

In this work, we experimented with the SUS304, as the preliminary experiment of heating test of CFRP. We use the SUS304 which is well known as the stainless steel. The specimen shaped cylinder. The internal diameter is 19 mm, and the external diameter is 20 mm. The height is 20 mm. We used the Infrared lamp heating equipment which is held by JAXA. It is the same lamp as that we have scheduled to use. The heating rate was set fixed. And we measured the surface temperature with radiation thermometers, and took the surface picture with digital camera every 10 s. In this study, we used the blue grass which is able to cut off the long wave length light to prevent the effect of surface radiation to the photo. The blue glass is as well as the aforementioned ones. We used the ceramics bond because it is needed to get the random pattern at the high temperature. The ceramics bond is SUMICERAM®, which made in Asahi Chemical Co., Ltd.

Figure 38.8 shows the random pattern at the specimen surface. We measured the thermal deformation from photo with DIC method. And we calculated the CTE from that experimental data. After that, we compared the calculated CTE data with the literature value. Figure 38.9 shows the experimental value and the literature value.

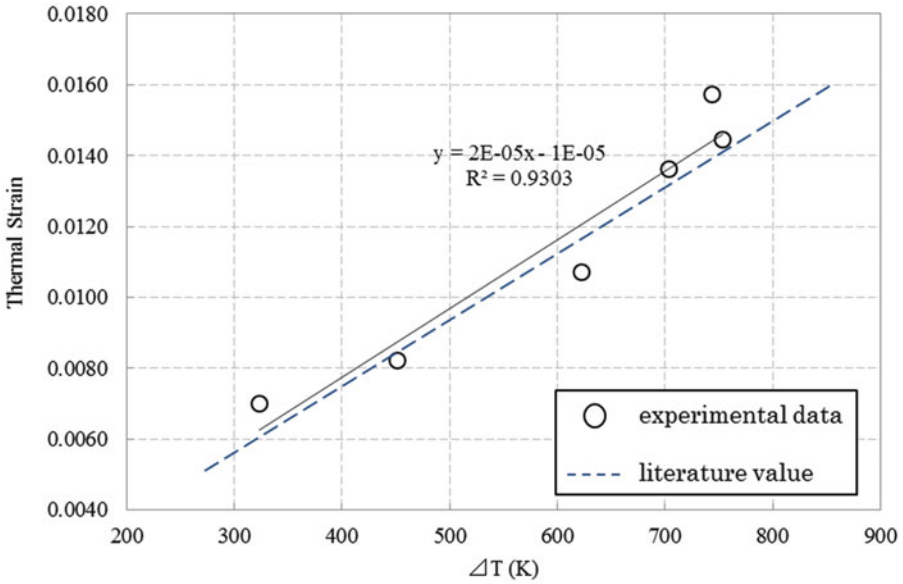

Fig. 38.9 Comparison of experimental data and literature value

As a result, the experimental data was value close to the literature value. So we determined that this method was effective to measure the thermal expansion at such as high temperature under rapid heating. But, in addition, we invented problem in this method. The brightness of the picture which took while the IR lamp isn't used are different from it took while the IR lamp are used. So we couldn't measure the deformation with DIC at that situation. According to that, we considered that we need to eliminate the visible lay or insert the light from outside.

38.5 Conclusion

We investigated how to measure the displacement with DIC method under rapid heating with IR lamp. According to the preliminary experiment, we verified that it is possible to measure the displacement with DIC method under rapid heating with IR lamp by using the optical glass and ceramic bond. At the same time, we proposed problems and improvements in this technique which was found by preliminary experiment. The luminosity value of the picture was different whether the IR lamp is operated. In this reason, we couldn't measure the displacement with DIC method. According to that, we considered that we need to eliminate the visible lay or insert the light from outside. In the future, based on this result, we intend to measure thermal displacement of tape-wrap CFRP by newest IR lamp rapid heating equipment.

References

1. Okuyama, I., Koyanagi, J., Arikawa, S., Yoneyama, S.: Dynamic and static failure behavior of notched CFRP laminate investigated by digital image correlation. Mech. Time Depend. Mater. **18**, 685–695 (2014)
2. Akinori, Y., Ryohei, H., Jun, K., Toshio, O.: X-ray computed tomography used to measure fiber orientation in CFRP laminates. Adv. Compos. Mater. In press (2015)
3. Yoneyama, S., Koyanagi, J., Arikawa, S.: Discontinuous displacement/strain measurement using mesh based digital image correlation. Adv. Compos. Mater. In press (2015)
4. Koyanagi, J., Adachi, Y., Arikawa, S., Yoneyama, S.: Time-dependent internal damage progress and residual strength in notched composite laminates. J. Solid Mech. Mater. Eng. **6**, 701–710 (2012)
5. Koyanagi, J., Watanabe, A., Kawabata, N., Ozaki, T., Higuchi, K., Ishimura, K., Kasaba, Y.: Long-term durability of tri-axial woven CFRP tube structure extended along the spin axis of spinning platforms for the SCOPE mission. Adv. Compos. Mater. **23**, 115–128 (2014)

6. Tanemura, T., Sato Y., Kai, T.: Functionality improvement and heating property evaluation of infrared lamp heating system for thermal resistive structure element tests. JAXA Research and Development Memorandum, JAXA-RM-06-012
7. Pang, B., Wu, D., Wang, Z., Xia, Y.: High-temperature digital image correlation method for full-field deformation measurement at 1200 degrees. Meas. Sci. Tech. **22**(1), 015701 (2011)
8. Yoneyama, S., Murasawa, G.: Experimental Mechanics. Eolss Publishers, Oxford (2009)
9. Yoneyama, S.: Computing strain distributions from measured displacements on a three-dimensional surface. JSEM **10**(special issue), 113–118 (2010)

Chapter 39
Performance of Patch and Full-Encirclement Bonded Composite Repairs

C.W. Burnworth and M.W. Keller

Abstract Composite repair systems offer the potential of changing the way engineers approach onsite pipeline repairs. Composite repair in pipeline and pressure equipment are a growing segment of the corrosion mitigation industry and have seen large expansions since the introduction of the technique in the early 1990s. Industry acceptance has widened since the initial products came on to the market and the capabilities of the repair have steadily increased. This chapter presents results comparing the performance of full encirclement repairs with patch-type repairs on 6-in. nominal diameter pipe specimens. Each pipe specimen has a 75 % wall loss defect simulating corrosion damage on a pipeline. Specimens were cycled from 0 to 75 % of maximum operating pressure until failure. Fatigue lives and substrate strain levels are compared for the patch and full-encirclement repairs. Design suggestions for patch repairs are also presented.

Keywords Pipeline • Composite Repair • Full-encircle Repair • Patch Repair • Fatigue Testing

39.1 Introduction

Fiber-reinforced polymeric composites, also called fiber-reinforced plastics (FRPs), have gained acceptance in many industries, including aerospace, automotive, infrastructure, and recently oil and gas. FRPs possess superior strength to weight ratios over traditional materials and their processing is well suited to many applications. A recent application that has recently seen significant growth, is the use of composite materials to repair damaged pressure equipment. The United States spends billions of dollars on the repair of corroded or damaged pipelines [1]. The bulk of this cost comes from the traditional repair methods used in the repair of these pipelines. Currently to repair a pipeline the system must be taken offline and the damaged section of pipe replaced resulting in a large amount of time and cost expenditure. Over the last 15 years advances in composite repair systems has made it possible to repair damaged pipelines with a composite wrap, for example see [2–6]. Composite overwraps are more cost-effective than replacements as they can be applied while the system is online and can be less labor intensive to install when compared to metallic repairs.

A typical composite repair consists of a thermosetting resin, such as epoxy or polyurethane, with continuous fiber reinforcement. Installation of a composite repair, consists of a surface preparation step, typically grit blasting, followed by the application of a dimensional restoration putty. This putty serves two purposes, the first purpose is to fill any damaged material and restore the outside profile of the pressure vessel to its original state. The second purpose is to provide load transfer from the damaged region to the composite repair. Finally, a primer is applied to the substrate pipe and the composite is wrapped around the damaged area and allowed to cure. Typically, the composite is installed by circumferentially wrapping the material around the exterior of the defective area on the pipe. This is known as a full encirclement repair and is shown schematically in Fig. 39.1a. This method has proven effective on smaller pipeline systems. As the diameter of the substrate increases both the material and labor also increase, which can significantly increase cost. Additionally, installing a full-encirclement repair can be cumbersome when the diameter of the pressure vessel becomes very large. In an attempt to reduce the cost associated with the repair of large diameter substrates, the use of patch-type repairs have been considered. Patch repairs are shown schematically in Fig. 39.1b and consist of a bonded "patch" of composite that does not completely encircle the pressure vessel. However, lack of critical performance data for these types of repairs has limited industry acceptance.

C.W. Burnworth • M.W. Keller (✉)
Department of Mechanical Engineering, The University of Tulsa, Tulsa, OK 74104, USA
e-mail: cwb196@utulsa.edu

C. Ralph et al. (eds.), *Mechanics of Composite and Multi-functional Materials, Volume 7*,
Conference Proceedings of the Society for Experimental Mechanics Series, DOI 10.1007/978-3-319-21762-8_39

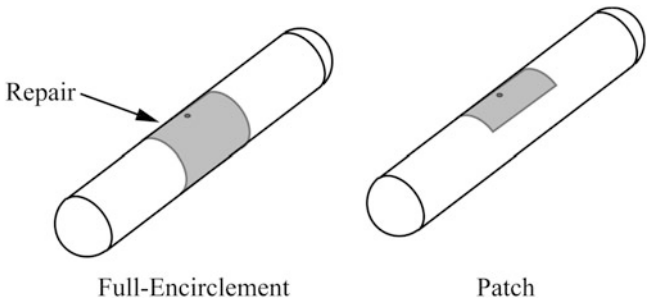

Fig. 39.1 Schematic representation of a full-encirclement and a patch repair type

In order to fill the gaps in understanding the differences between full-encirclement repairs and patch repairs, a combined set of computational and experimental studies were undertaken. Small-scale test specimens (6-in. ASTM A106b) were fabricated and then repaired. The repair samples were then pressure fatigue tested to compare patch and encirclement performance. A series of finite element analyses were performed to compare the behavior of patch and encirclement repairs and to parametrically study the components of the repair.

39.2 Experimental

39.2.1 Specimens Design and Manufacture

Performance of patch and full-encirclement repairs were compared using a small-scale pressure vessel. A simulated corrosion defect was machined into a 6-in. diameter schedule 40 ASTM A106b (x42) straight pipes. Dimensions of the simulated corrosion defect are shown below in Fig. 39.2. The defects were machined to a depth that approximated 75 % wall loss. Hemispherical end caps were welded onto the machined pipes. Composite repairs were then applied to the defects after the substrate material had been grit-blasted to a NACE 2 finish (near white-metal). Specimens were allowed at least a 48 h room temperature cure before pressure fatigue testing.

39.2.2 Pressure Fatigue Testing

A multi-vessel fatigue test system was used to pressure cycle the repaired pipe specimens. A schematic of this fatigue system is shown in Fig. 39.3. Specimens were filled with water and then cycled between 375 KPa (55 psi) and 14.6 MPa (2130 psi) pressure at a rate of 10.5 cycles per minute. Strain gages were applied at several locations on the base pipe, composite repair, and defect. A schematic indicating the location of the strain gages is shown in Fig. 39.4.

39.3 Finite Elemental Analysis

Full encirclement and patch specimen were simulated using finite element analysis (Abaqus). The material model for the steel substrate was based on quasi-static tensile tests performed using coupons cut from representative pipe sections. A multi-linear material model was then constructed using this data [7]. The composite material was modeled as a linear-elastic orthotropic material with material parameters taken from experimental data [8]. All repairs consisted of a 6.25 mm (0.25 in.) thick composite layer assumed to be perfectly bonded to the substrate. Repairs extended 88.9 mm (3.5 in.) in the axial direction beyond the end of the defect shown in Fig. 39.4, for the patch repairs, the composite extended 88.9 mm (3.5 in.) circumferentially around the pipe. An internal pressure load equivalent to the maximum allowed operating pressure (MAOP) was applied to the interior surfaces of the model. Each simulation was meshed using hexagonal elements globally seeded at

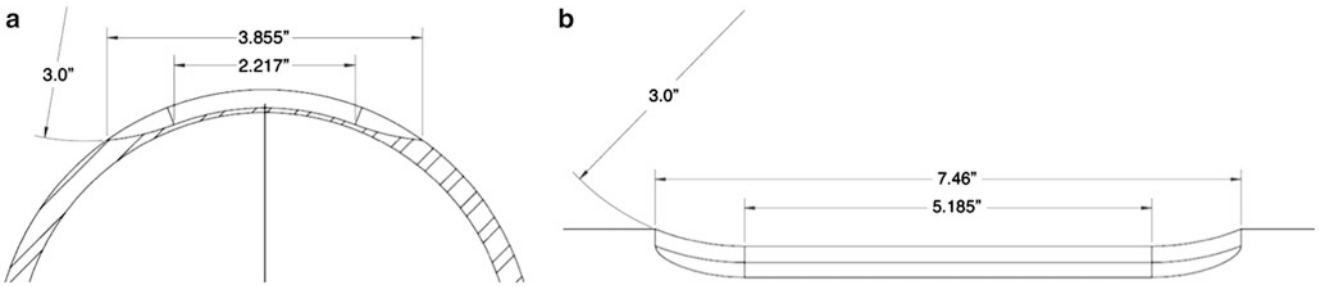

Fig. 39.2 (**a**) Profile view of the machined defect dimensions, (**b**) axial profile of the machined defect dimensions

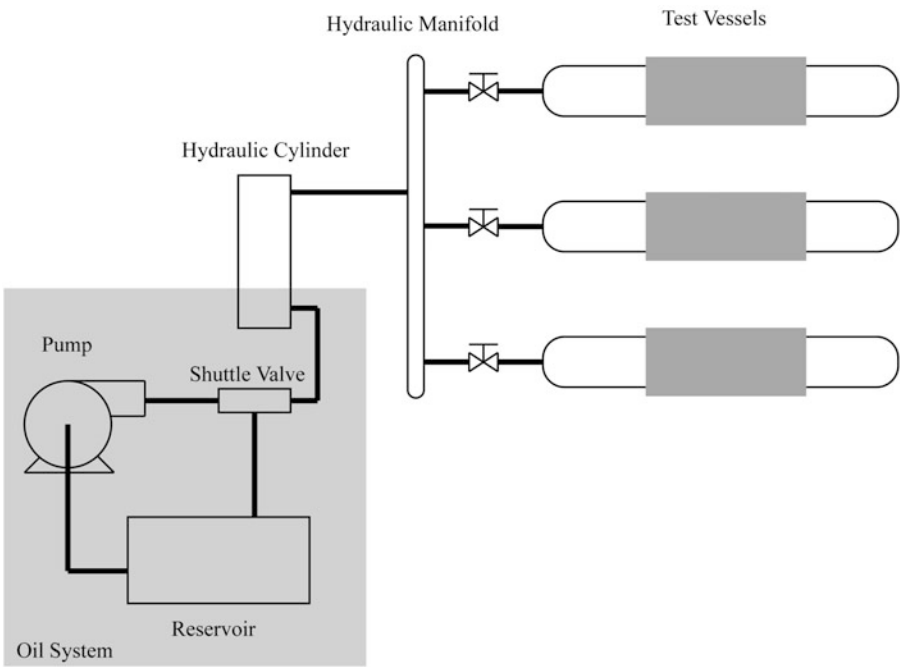

Fig. 39.3 Schematic of the multi-vessel fatigue system

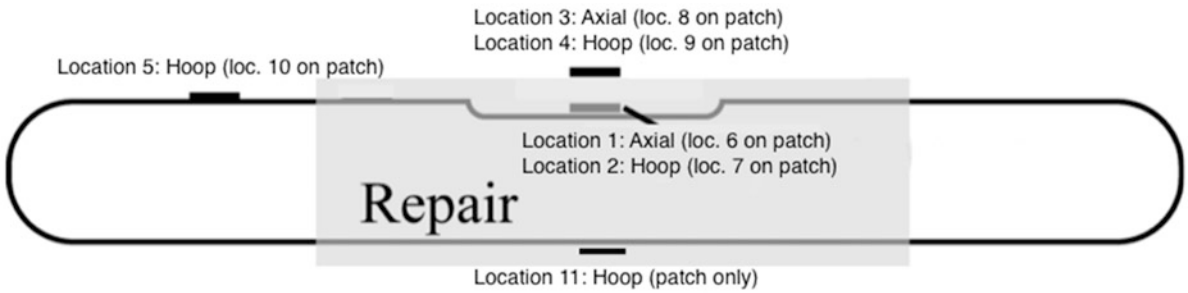

Fig. 39.4 Schematic of strain gage locations

1.1 with additional edge refinements at the edges surrounding the defect at 0.75. Simulations were run using non-reduced integration methods.

39.4 Results and Discussion

39.4.1 Finite Element Results

Figure 39.5a shows strain vs. percent wall loss for the full encircle and patch repairs. As expected, as the wall loss increases, the maximum strain also increases. This trend continues in the repair, as shown in Fig. 39.5b, with the composite repair strain increasing as percent wall loss increases. However, we see that the maximum strain levels in the composite repair and substrate are nearly the same regardless of the repair approach, at least for the lower wall loss values.

Figure 39.6 shows the maximum strain values for a full encirclement repair subjected to a simulated pressure ramp from 0 to 14.6 MPa (2130 psi). From this simulation, the substrate begins to yield at approximately 10.3 MPa (1500 psi). Figure 39.6 also indicates that the substrate yields significantly before the repair begins to respond to the increased strains.

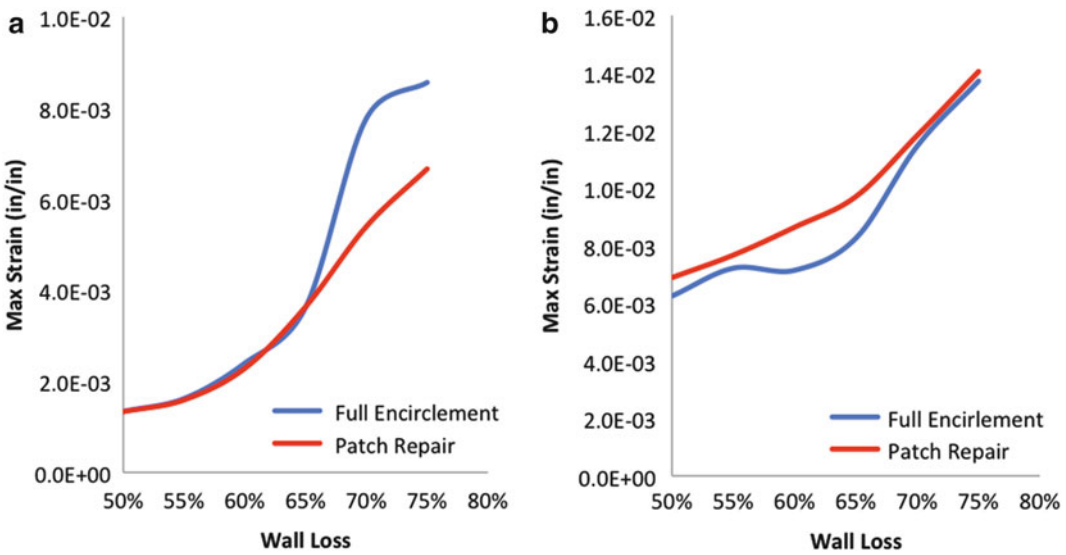

Fig. 39.5 (**a**) Strain vs. wall loss for the substrate only (*left*), (**b**) strain vs. wall loss for composite material (*right*)

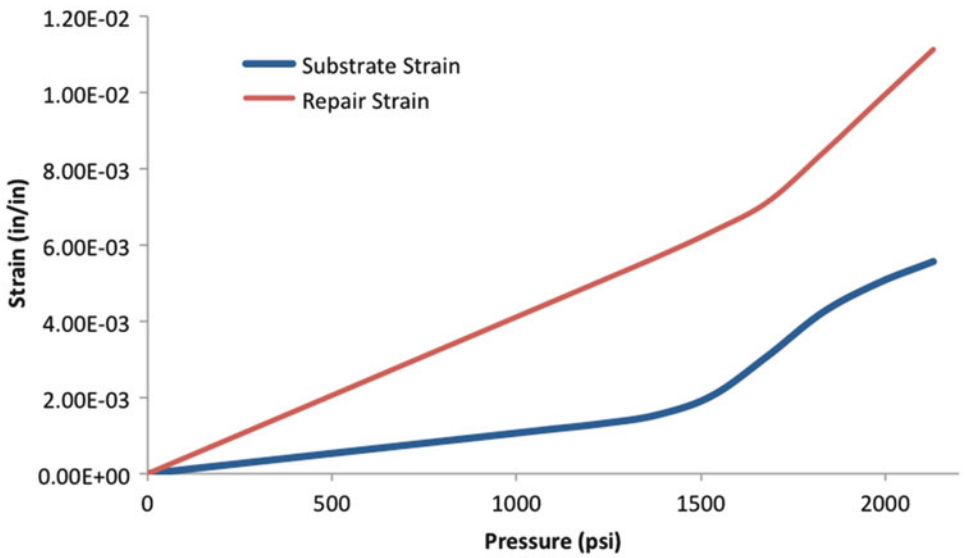

Fig. 39.6 Strain response during pressure loading cycle

This is indicated by the delay between the onset of yielding in the substrate and the slope change in the repair strain response. Factors impacting the efficiency of load transfer between the substrate and repair are still being studied.

Based on the function of the dimensional restoration putty as central to efficient load transfer from the substrate to the repair, a set of simulations were performed to investigate the impact of bulk modulus on repair strain. The hypothesis being that a load transfer material that is nearly incompressible would lead to more efficient load transfer. For these simulations, bulk modulus was varied by fixing the elastic modulus and varying the Poisson ratio from 0.25 to 0.48. As shown in Fig. 39.7, increasing bulk modulus leads to increasing repair strain, however the variation in strain is very small, only 1.26 % from a Poisson ratio of 0.25 to a Poisson ratio of 0.48.

However, a comparison of a pressurization simulation for a system with a Poisson ratio of 0.25 and a system with a Poisson ration of 0.48 indicates that the Poisson ratio has very little impact on the onset of significant load transfer. Studies are ongoing to determine the critical parameter that governs the efficiency of the load transfer (Fig. 39.8).

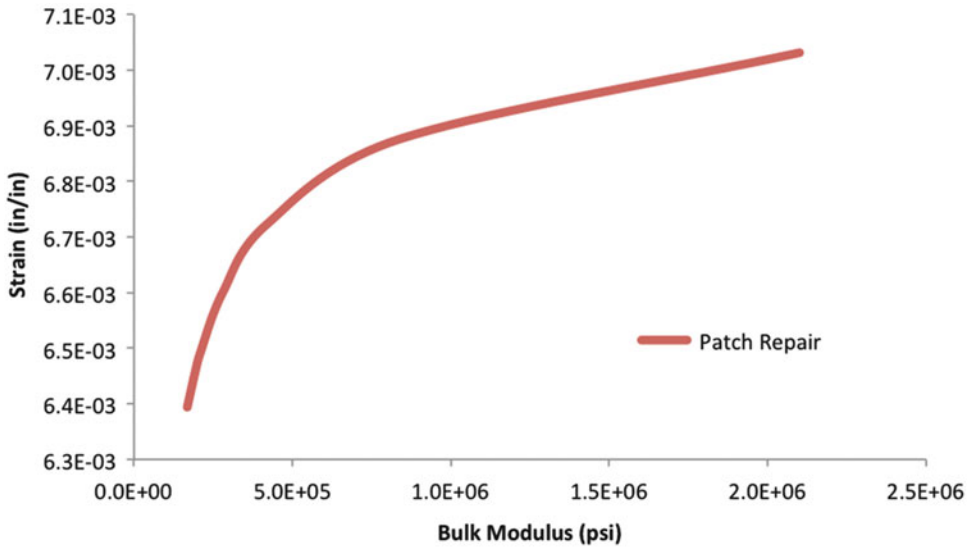

Fig. 39.7 bulk modulus vs. strain plotted for both repair types

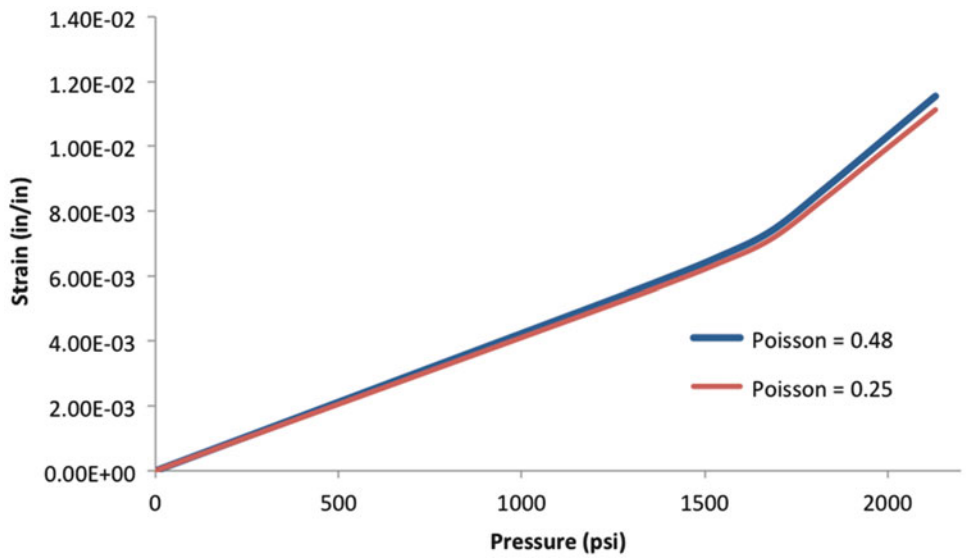

Fig. 39.8 Comparison of Poisson ratio and strain during a pressure cycle

39.4.2 Pressure Fatigue Testing

Figure 39.9 shows one cycle of strain data gathered during testing for both a full encirclement and a patch repair sample. Strain data was collected at of three locations on the full encirclement repairs and four locations on the patch repairs. Table 39.1 shows the comparison of FEA with experimental data. The FEA simulations over predict strain values except for the hoop directions on the defect surface, locations 1 and 2.

Table 39.1 shows a comparison of FEA with experimental results for all of the locations measured in testing. The results generated through FEA are consistently larger in strain predictions for all locations except location 2 (loc. 7 on patch) which were greater in the measured data. We are currently investigating the cause of these large differences, but they may stem from variations in material properties of the repairs or differences between the final thickness of the applied composite repair and the thickness of the modeled repair.

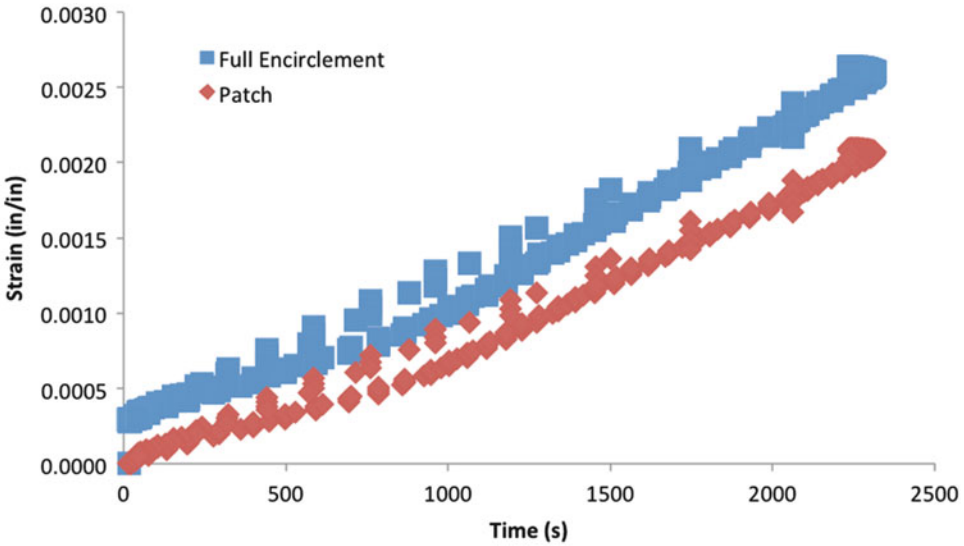

Fig. 39.9 Representative strain data collected in the hoop direction at location 2 (ref. Fig. 39.4) for both patch and full-encirclement repairs

Table 39.1 Comparison of FEA data with gathered experimental data

Strain comparison at 2141 psi					
		Experimental	FEA	Orientation	Percent difference
Full encirclement repair	Strain Gage 1	0.0002650	0.0003552	Axial	29
	Strain Gage 2	0.0023690	0.0017212	Hoop	−32
	Strain Gage 3	0.0003110	0.0005425	Axial	54
	Strain Gage 4	0.0015880	0.0016082	Hoop	1
	Strain Gage 5	0.0005750	0.0006147	Hoop	7
Patch repair	Strain Gage 6	0.0003660	0.0004497	Axial	21
	Strain Gage 7	0.0018550	0.0017002	Hoop	−9
	Strain Gage 8	0.0004670	0.0005415	Axial	15
	Strain Gage 9	0.0014050	0.0016166	Hoop	14
	Strain Gage 10	0.0005500	0.0006203	Hoop	12
	Strain Gage 11	0.0004530	0.0005767	Hoop	24

39.5 Conclusions

Poisson ratio of the dimensional restoration putty has no significant effect on the load transfer between the substrate and the composite. However, increasing Poisson ratio increases the maximum repair strain. Comparison of the FEA model predictions with an initial set of experimental strain data indicates significant over prediction of strains from the FEA analysis. The observed over prediction is likely the result of variations in material properties and variation in the geometry of the installed repair. Research is ongoing to determine the exact cause of these discrepancies.

References

1. Jacobson, G.: Corrosion—a natural but controllable process. AMPTIAC Q. **7**(4),3 (2003)
2. Mableson, R., Patrick, C., Dodds, N., Gibson, G.: Refurbishment of steel tubulars using composite materials. Plast. Rubber Compos. **29**(10), 558–565 (2000)
3. Greenwood, C.: Composite pipe repair method shows versatility, long-lasting. Pipeline Gas J. February 2001
4. Alexander, C., Wilson, F.: Development and testing of the Armor plate pipeline repair system. In: Proceedings of the 1999 ASME energy sources technology conference, Houston, TX, USA. American Society of Mechanical Engineers, Petroleum Division (1999)
5. True, W.: Composite wrap approved for US gas-pipeline repairs. Oil Gas J. **93**(41) (1995)
6. Smith, P., Cuthill, J.: Patching up pipework with carbon–fiber composites. Mater. World **10**(5), 28 (2002)
7. Duell, J.M.: Characterization and FEA of carbon composite overwrap repair system. University of Tulsa (2006)
8. Wilson, J.: Characterization of a carbon fiber reinforced polymer repair system for structurally deficient steel piping. University of Tulsa, 226 (2006)

Chapter 40
Meso-Scale Deformation Behavior of Polymer Bonded Energetic Material Under Quasi-Static Compression

Suraj Ravindran and Addis Kidane

Abstract This paper describes the meso scale deformation behavior of polymer bonded energetic materials under quasi-static compression. Polymer bonded energetic material contains 80–90 % of sugar crystals (as simulant of HMX) and 10–20 % of hydroxyl terminated polybutadiene (HTPB) and plasticizer are cold pressed using a mold made of stainless steel. Meso and macro scale experiments are conducted to understand the multi-scale deformation mechanisms under uniaxial compression. Specimen with different amount of solid loading has been tested under compression and the crack nucleation in the case of high solid volume fraction and low volume fractions are studied. The displacement and strain fields of the specimen in all cases are measured using in-situ high resolution optical microscope and digital image correlation.

Keywords Polymer bonded explosive • Energetic • DIC • Meso-scale • Strain localization

40.1 Introduction

Polymer bonded explosives (PBX) are highly filled particulate composites containing 60–95 % of explosive solid loading and 5–40 % of the polymer binder. The main function of the polymer binder is to hold the explosive particles together and form a rigid material. This formulation also helps in machining the explosive modules to a required shape and size. Furthermore, the polymer binder helps in reducing the sensitivity of PBX to shock loads [1]. Mechanical properties of these materials play a major role in the detonation of the PBX under different loading conditions. Because of the brittle hard particles and soft binder matrix, any of the following mechanism of deformation micro crack nucleation, debonding of the interface, particle fracture and cavitation void failure of the binder can be observed. The volume fraction of the particles and binder also plays an important role in the deformation behavior of PBXs. However, studying the mechanical behavior of these materials is difficult because of the safety problems. To study the mechanical behavior of polymer bonded explosives without any safety issue, usually inert simulants of PBX are used. Mainly, sugar mocks are used in most of the studies of PBX as simulant material. In the present study we have used sugar mocks with polymer binder, to understand the deformation behavior of PBX. Few researchers have studied the quasi static deformation behavior of PBX under tensile loading conditions with the help of Brazilian test geometry; conclusions from these studies were based on the post mortem of the deformed sample [1]. The important conclusion from these studies is that the failure mechanism in the PBX is mainly due to the debonding of the particle-binder interface. This study does not capture the deformation field in connection with the micro structure of the specimen.

Recently, some researchers have used digital image correlation technique to get the full field deformation of the PBX under different loading conditions [2]. They have studied the crack propagation in PBX under quasi-static loading conditions, the result shows the fracture occurred both through the interface and also through the particles. The meso scale deformation behavior of PBX is still not well known due to the complexity of the deformation behavior under different loading conditions. None of these studies consider the effect of solid particle loading on the local deformation behavior of PBXs. In this study we have attempted to obtain the local deformation behavior of the polymer bonded explosives in relation with the micro structure of the specimen at different solid loadings. Two dimensional digital image correlation technique (DIC) [3] was used to obtain the local deformation and local strain field on the specimen.

S. Ravindran (✉) • A. Kidane
University of South Carolina, Columbia, SC, USA
e-mail: muthiram@email.sc.edu

C. Ralph et al. (eds.), *Mechanics of Composite and Multi-functional Materials, Volume 7*,
Conference Proceedings of the Society for Experimental Mechanics Series, DOI 10.1007/978-3-319-21762-8_40

40.2 Materials and Experimental Procedure

40.2.1 Preparation of the Material

In this study polymer bonded explosive simulant contains plasticized hydroxyl terminated polybutadiene (HTPB) as binder and sugar crystals of size vary from 100 to 500 μm is used. HTPB is plasticized with dioctyl sebacate (DOS) and toluene diisocyanate (TDI) is used as curing agent. Steps involved in making raw material for the preparation of simulant specimens involves three steps,

1) Mixing of the plasticized HTPB with sugar crystals,
   First HTPB is mixed with the plasticizer (DOS) with help of a mechanical mixer for 20 min after that curing agent (TDI) has been added and stirred for 10 min, then this blend is mixed thoroughly with the solid loading (sugar crystals). The mixture is then cured at 60 °C for 24 h.
2) Pressing into billets
   The partially cured mixture is then cold pressed in a steel mold at a pressure of 90 MPa to produce billets of size 25 mm in diameter and 25 mm in height. The density of the specimen is shown in the Table 40.1.
3) Curing of the specimen,
   For complete curing of the specimen the pressed billets are then kept at 60 °C for 90 h in oven. Three types of specimens are prepared by varying the amount of solid in the material. The proportions of the constituents, names of each specimen are given in Table. 40.1.

40.2.2 Experimental Procedure

Cubic specimens of dimension 10 × 10 × 10 mm were machined from 25 × 25 mm cylinders. It is then polished using silicon carbide papers of grit size from 300 to 1200, subsequently dry polished with the help of diamond particles of size 3 μm. However, obtaining the microstructure of the specimen was difficult because of the insufficient contrast difference between the polymer binder and the sugar crystals. Therefore the specimen is coated with graphite powder and slightly polished which helps in adhering graphite powder into the polymer binder at the same time clearing away from the sugar crystals. This gives sufficient contrast difference between the sugar crystals and the polymer binder, and the micrograph of the specimen was obtained before loading.

The specimen was loaded under compression using a small loading stage and images were taken using microscope. The complete experimental setup, including the direction of loading and the surface images taken is shown in Fig. 40.1. To facilitate the specimen for digital image correlation technique, specimen is speckled with the help of toner powder of particle sizes 8–12 μm. A thin coat of white paint was first applied on the specimen, and then before it get dried toner powder was blasted on the surface of the specimen, which results in well contrasted, isotropic and random speckle pattern as shown in the Fig. 40.1c. Before starting the experiment images has been captured by translating the specimen with the known distance for correcting the distortion of lenses in the microscope. The complete procedure for the correction for distortion can be found in the reference [4]. Specimen is then attached to the compression module of the small tensile machine, lubricant was applied on the specimen surface to reduce friction at the contact surface of the compression module. Specimen is then loaded at a strain rate of 1.67×10^{-4} s^{-1} and the images were captured at a magnification of 100× with camera of resolution 1600 × 1200 pixels at an interval of 10 s. The field of view of the experiment is 3.4 × 2.5 mm and the resolution of the experiment is 2.12 μm/pixel. For post processing of the images, commercial digital image correlation software Vic2D was

Table. 40.1 Specimen constituents in percentage volume fraction along with the final density

Specimen	Sugar (%)	HTPB (%)	DOS (%)	TDI (%)	Density of specimen (g/cm^3)
PBS-1	80	14.4	3.85	1.75	1.42
PBS-2	85	10.8	2.89	1.31	1.45
PBS-3	90	7.21	1.92	0.87	1.48

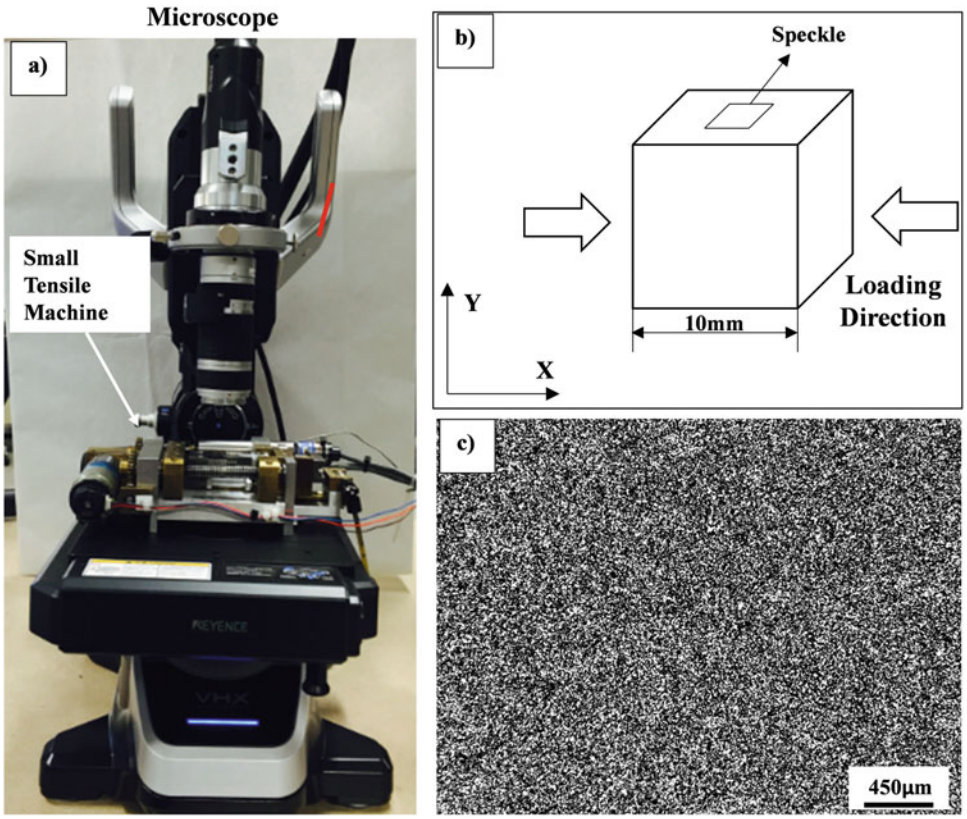

Fig. 40.1 (**a**) Experiment Setup (**b**) Specimen dimensions and loading direction, and (**c**) speckling pattern

used. In post processing a subset size of 30 × 30 μm and step size of 6.12 μm is used, which allows to get at least 1000 points of measurements within the grain (sugar crystal).

40.3 Results and Discussion

Figure 40.2, shows the microstructure of the polymer bonded explosive simulant, showing the interface between the crystals is filled with the polymer binder. The average size of the grains is about 450 μm. Figure 40.3 shows the stress strain curve of the polymer bonded simulant with varying solid loading under compression. PBS-1 is the weakest (least solid loading) it started yielding at a stress of 1.2 MPa whereas PBS-2 started yielding at 2.7 MPa and PBS-3 started yielding at 7 MPa. The strength of the material increases with the increase in solid loading in the material. Young's modulus (E) of PBS-1 is 17.1 MPa, PBS-2 is 90 MPa and PBS-3 is 110 MPa respectively.

40.3.1 Strain Localization in PBS-1, PBS-2 and PBS-3

Figure 40.4 shows the axial local strain at three global strains for the three specimens considered. It is seen that the strain localization is mainly occurred at the interfaces of the crystals (binder). The interfaces between (the polymer binder) undergoes to a large compressive strains (about 10 %), while the solid crystals had small strain in the order of 0.1 %. As

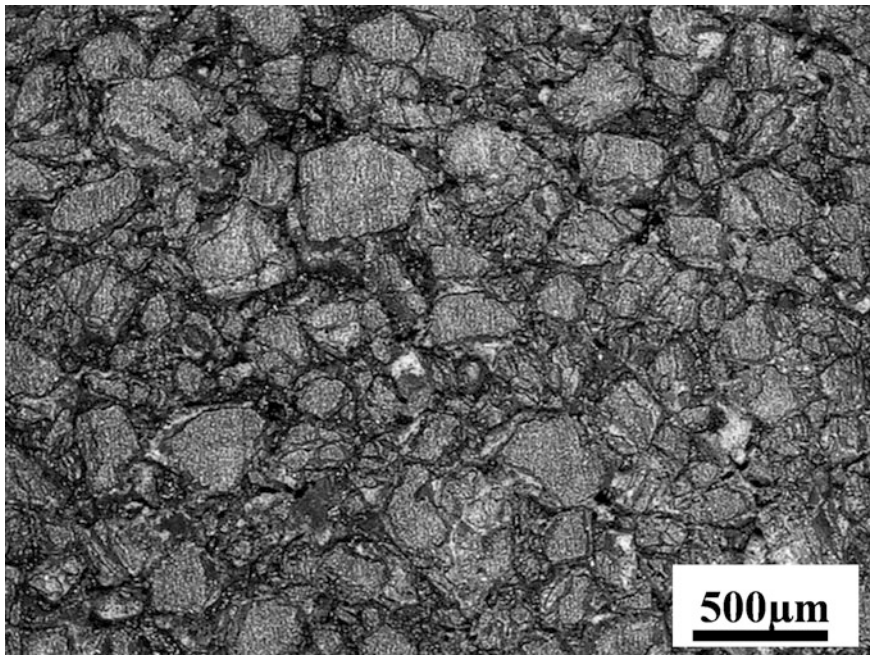

Fig. 40.2 Micrograph of PBS-2

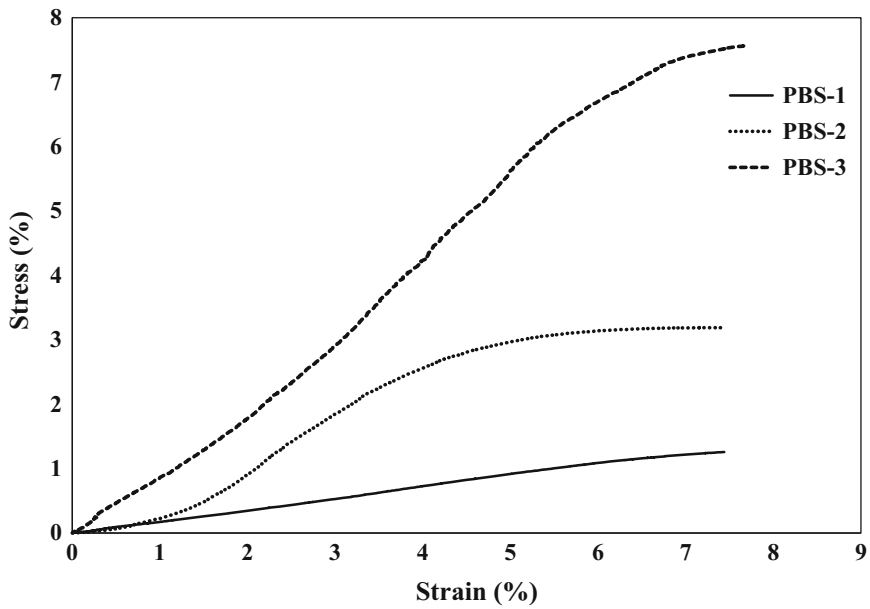

Fig. 40.3 Stress-strain curve of the polymer bonded simulant PBS-1, PBS-2 and PBS-3

strain localization is high at the interface it is expected that the cracks nucleate at the interfaces. In PBS-1 and PBS-2 cracks are formed at the interfaces at lower strain comparing with the high loaded samples PBS-3.

Comparing PBS-3 with PBS-1 and PBS-2 samples, the local strain induced is significantly less in PBS-3, as the thickness of the polymer binder and hence the distance between the boundaries of solid crystals in PBS-3 are less compared to PBS-1 and PBS-2.

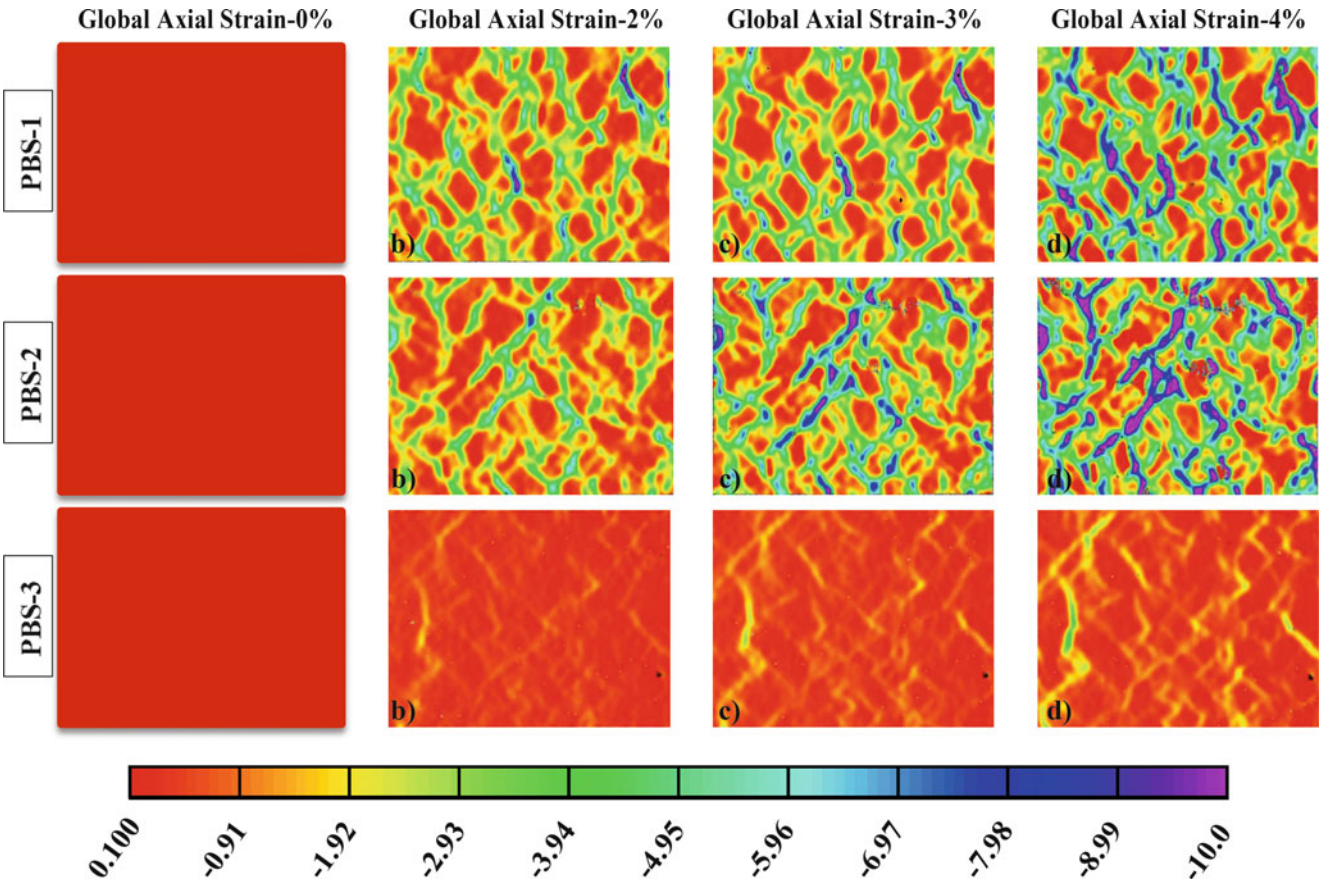

Fig. 40.4 Axial local strain at three global strains for PBS-1, PBS-2 and PBS-3

Figure 40.5 shows the transverse strain induced in PBS-1, PBS-2 and PBS-3 at global axial strain of 2, 3 and 4 %. It is clear that the tensile transverse strain induced in the specimen is significant. For applied strain of 4 % in PBS-1 and PBS-2 the localized strain is as high as 10 %, which causes the debonding of the interfaces. The primary mechanism of failure is debonding of the interfaces. Cracks are initiated at the interfaces and propagate along the weak interfaces. As seen in the case of axial strain the transverse strain is small in the case of PBS-3 compared to PBS-1 and PBS-2.

40.4 Summary

A meso-scale experiment is conducted to understand the deformation and failure mechanisms in PBX. Using digital image correlation, the local deformation and strain localization in three different PBX samples are obtained. The strain localization is predominant in low solid loaded specimen compared to the high solid loading composition. It is also observed that debonding is the primary failure mechanism for all polymer bonded simulant specimens considered.

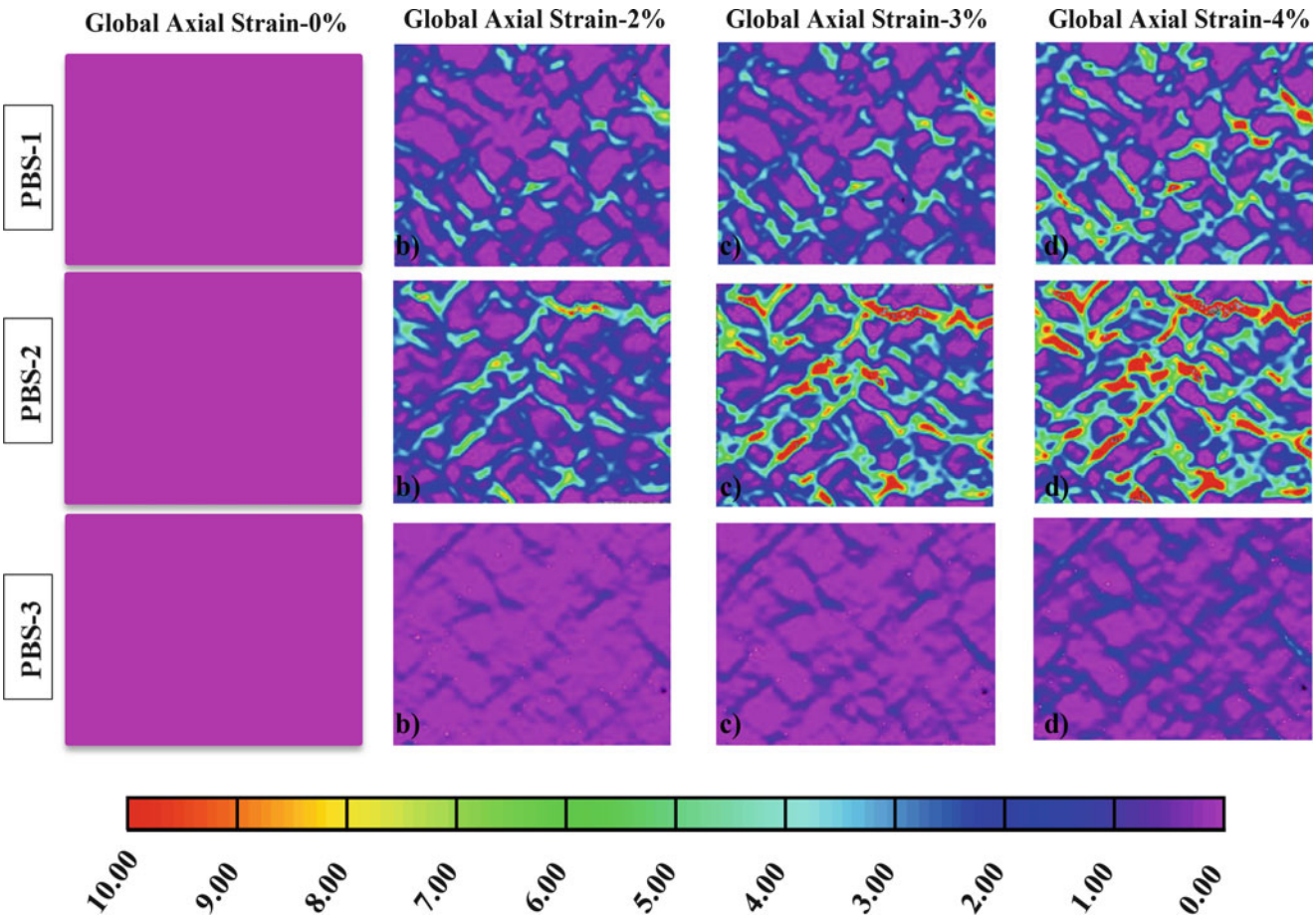

Fig. 40.5 Transverse local strain at three global strains for PBS-1, PBS-2 and PBS-3

Acknowledgement The financial support of Air Force Office of Scientific Research (AFOSR) under Grant No FA9550-14-1-0209 is gratefully acknowledged.

References

1. Rae, P.J., Goldrein, H.T., Palmer, S.J.P., Field, J.E., Lewis, A.L.: Quasi–static studies of the deformation and failure of β–HMX based polymer bonded explosives. Proc. R. Soc. Lond. A Math. Phys. Eng. Sci. **458**(2019), 743–762 (2002)
2. Chen, P., Huang, F., Zhou, Z.: Macro-Micro Mechanical Behavior of a Highly-Particle-Filled Composite Using Digital Image Correlation Method. INTECH Open Access Publisher, Croatia (2011)
3. Chu, T.C., Ranson, W.F., Sutton, M.A.: Applications of digital-image-correlation techniques to experimental mechanics. Exp. Mech. **25**(3), 232–244 (1985)
4. Sutton, M.A., Orteu, J.J., Schreier, H.: Image Correlation for Shape, Motion and Deformation Measurements: Basic Concepts, Theory and Applications. Springer Science & Business Media, New York (2009)

Chapter 41
Subsidence Modeling and Analysis for Sand Shear Strength Parameter Testing

Jiliang Li and Jinyuan Zhai

Abstract A subsidence simulation system using displacement measurement techniques based on opto-electronic displacement measurement sensors has recently been developed based on literature review and introduced in this chapter. Five different cavity making devices at bottom of a sand box type container with a circular/rectangular opening on the bottom, where a plate that fits the opening is placed. The results of subsidence analysis define subsidence parameters including angle draws, angle of break, subsidence factors, etc. Subsidence profiles are determined in mathematical forms. The outcomes are useful for understanding field subsidence mechanism and simulations and teaching the subsidence concepts to undergraduate class. Results also show feasibility of obtaining soil shear strength parameters from the subsidence testing as well.

Keywords Soil Strength Subsidence Testing • Angle of Friction • Angle of Break • Angle of Draw • Laser

41.1 Introduction

Surface subsidence damages surface structures such as foundations, utility lines, infrastructures, ground water regimes, etc. Subsidence is not a far and away issue in other States it also happens in Indiana. As shown in the Fig. 41.1, some southwestern counties of Indiana have some subsidence concerns [1]. In order to avoid or reduce subsidence damages, it is imperative to know the subsidence characteristics of the particular site, and proper design work has to be performed to prevent or minimize subsidence hazards.

There are two types of subsidence [2]: (1) pit, also called sinkhole or pot hole, and (2) trough or sag. Pit subsidence is characterized by an abrupt sinking of the surface, resulting in circular steepsided, crater-like features. Trough subsidence is a gentle, gradual depression of the surface.

Subsidence is controlled by many factors, including width of unsupported cavity, height of cavity, thickness of overburden, strength and fracture system of rock, hydrology, and time [1–3].

In engineering geology class, undergraduate students are exposed to the subsidence geohazards. To help them understand the fundamental subsidence concepts and thus help them prepared to minimize or prevent subsidence damage, it is necessary to understand subsidence phenomena. It is difficult to simulate or predict subsidence development because of the complexity in physical characteristics such as rock failure and yield behavior, dimensional variations and time dependent behavior.

In this chapter a recently developed physical subsidence modeling technique was used to help teach subsidence concepts [3]. The developed method utilizes laser optical triangulation distance measurement devices, which can scan the surface of any material, including granular or viscous materials, and digitally measure vertical distances with an extremely high accuracy and resolution. With this new technique, the effect of cavity shape and size, depth, and material parameters can be analyzed. Using this unique technology and method of analysis, some valuable results were produced. The results of the analysis define the parameters of subsidence including angle draws, angle of break, subsidence factors and width/depth ratios of openings with high accuracy in a systematic manner. Subsidence profiles are determined in mathematical forms. The outcomes are useful for interpreting field subsidence data and simulations and teaching the subsidence concepts to undergraduate class. The subsidence modeling method has been used in the subsidence concepts teaching in engineering geology class. Preliminary survey results indicate that the developed device is effective and helpful in students' understanding of subsidence phenomena.

J. Li (✉)
Purdue University North Central, Westville, IN, USA
e-mail: Li1919@PNC.EDU

J. Zhai
The University of Akron, Akron, OH, USA

C. Ralph et al. (eds.), *Mechanics of Composite and Multi-functional Materials, Volume 7*,
Conference Proceedings of the Society for Experimental Mechanics Series, DOI 10.1007/978-3-319-21762-8_41

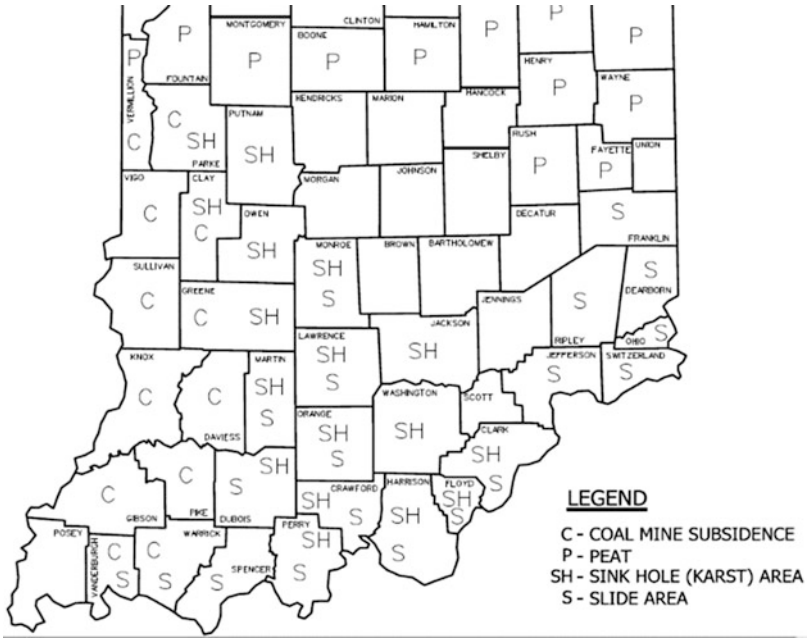

Fig. 41.1 Subsidence concerns in Indiana

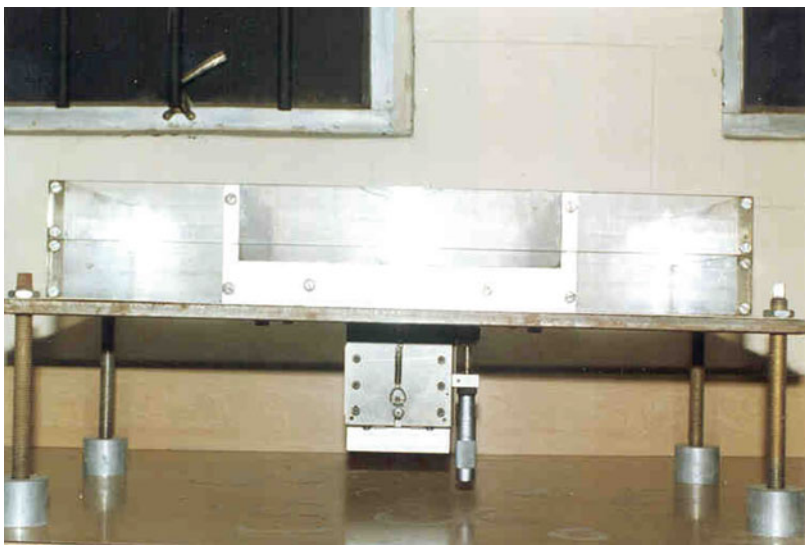

Fig. 41.2 Top view of subsidence simulation system using circular/square plates

41.2 Soil Strength Testing Using Controlled Surface Subsidence

In mining, geological and geotechnical activities, there are many kinds of surface subsidence induced. It is an important issue, some simulation research have been done in the past [4–6]. However, previous subsidence modellings are very sensitive to vibration and not easy and convenient for classroom demonstration and teaching purpose. Therefore, in this chapter the subsidence are generated and controlled for further improvement to model soil subsidence over a small cavity analysis experimentally and theoretically. One of the objectives is to further develop soil testing characterization method utilizing surface subsidence phenomenon. This was also intended to help improve the undergraduate education on subsidence geohazards teaching. Figures 41.2, 41.3, and 41.4 show the subsidence modelling system and example of subsidence laser holographic image captured over the cavity.

In the subsidence phenomenon, the angle of break and angle of draw as shown in Fig. 41.4b are assumed to be related to the soil strength index properties, namely soil cohesion, c, and internal friction angle, φ, based on theoretical analysis.

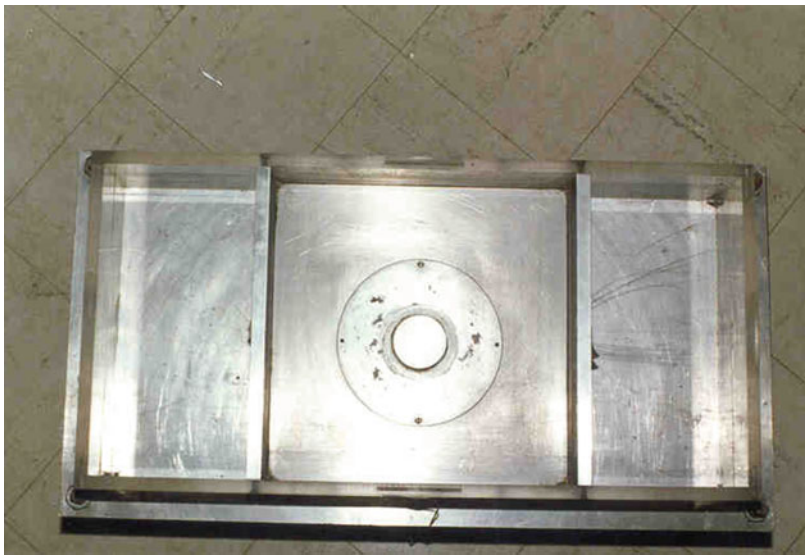

Fig. 41.3 Side view of soil subsidence testing system

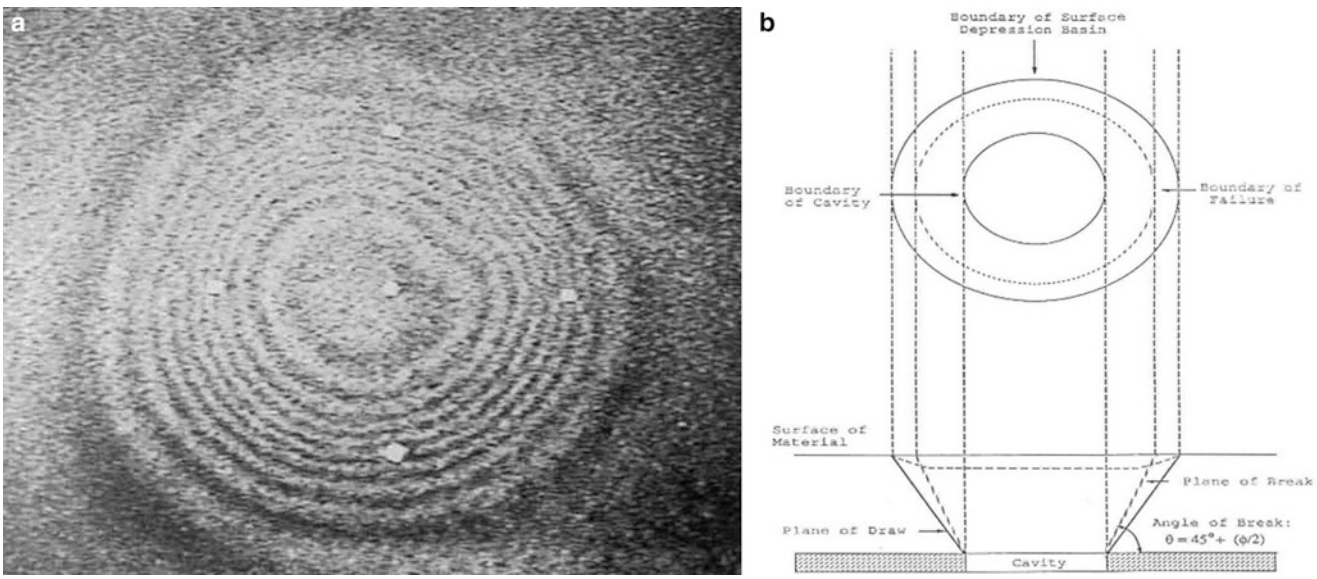

Fig. 41.4 (**a**) Typical fringe pattern for material No. 3 where c = 5.517E–2 MPa, ϕ = 34.0, angle of draw = 62.0 (Cavity Height = 425 μ in, maximum depression = 104 μ in). (**b**) Surface depression basin and simple cavity

The induced surface subsidence can be accurately measured using the deformation measuring device to correlate with angle of break and the soil strength index properties.

To implement those goals, first an approximate theoretical analysis and foundation for measuring soil strength properties are established. In order to implement the theoretical analysis results, a new soil surface deformation monitoring device apparatus has been designed and developed.

This newly designed surface deformation measurement device is of critical importance in the verification and correlations of various kinds of laboratory tests because of its high measurement resolution. This technique could also be of help to the theoretical development of back analysis as it provides a useful and efficient tool to verify the back analysis results. Especially combined with other soil laboratory testing procedures, it could be a great supplement to the development of geomaterial characterization methods.

Other important merit of this surface displacement measurement technique is that it can be used as a benchmark test of various kinds of numerical modelling. This technique should be helpful in checking the credibility and usefulness of numerical modelling and help improve the reliability of numerical simulations.

Finally the experimentally estimated soil strength properties can be used as input parameters for full numerical analysis via ABAQUS to correlate the obtained strength properties with experimental measurements.

41.3 Analysis of Soil Internal Friction Angle and Angle of Break

Figures 41.5 and 41.6 show the field and corresponding laboratory scale of subsidence to recreate and simulate in situ subsidence failure mechanism, respectively.

Figure 41.6 of surface subsidence cross-section view shows an active pressure zone where the middle part of soil is moving downward. It can be reasonably assumed that the soil moves mostly downward with minimum lateral movement in the lateral horizontal direction. Thus the soil moving downward can be idealized as an active retaining wall because the soil to the left of vertical dotted blue line are moving toward it and the soil fails along the idealized slip plane. According to active pressure of Rankine's theory [7–10]:

$$\sigma_3 = \sigma_a = \sigma_h; \quad \sigma_1 = \sigma_v = \gamma h \tag{41.1}$$

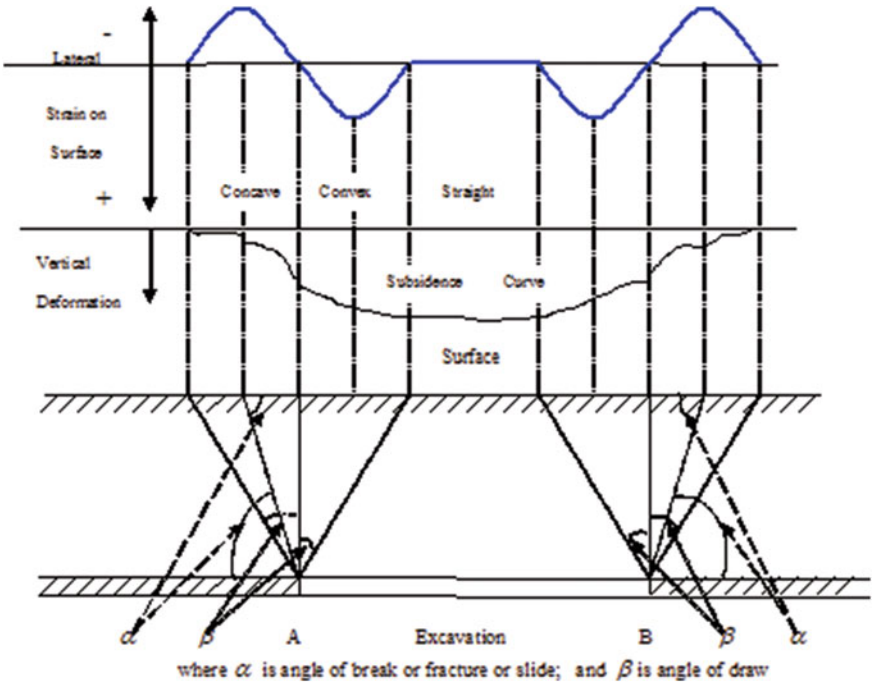

Fig. 41.5 In situ subsidence failure mechanism

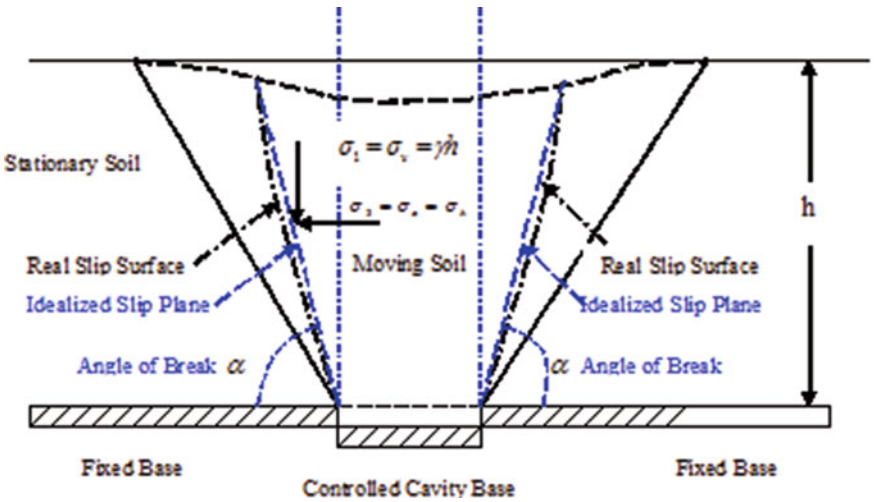

Fig. 41.6 Schematic view of small scale laboratory modeling of subsidence failure mechanism

$$\sigma_3 = \sigma_1 \tan^2\left(45^\circ - \frac{\phi}{2}\right) - 2c \tan\left(45^\circ - \frac{\phi}{2}\right) \tag{41.2}$$

$$p_a = \sigma_a = \sigma_h = \sigma_v \tan^2\left(45^\circ - \frac{\phi}{2}\right) - 2c \tan\left(45^\circ - \frac{\phi}{2}\right) \tag{41.3}$$

Therefore, the angle between the vertical dotted line and the idealized slip failure plane in Fig. 41.6 should be about $45^\circ - \phi/2$. Hence the angle of break, α, is $45^\circ + \phi/2$. Rewritten, the soil strength parameter, angle of internal friction is approximately

$$\phi = 2\alpha - 90^\circ \tag{41.4}$$

41.4 Soil Surface Deformation Measurement Technique

Traditionally classical deformation measurements are usually made using LVDTs (Linear Variable Differential Transducers) and linear potentiometers. Laser holographic interferometry has many applications in science and engineering. In civil/geotechnical and geological investigations, the innovative surface deformation displacements measurement technique was initiated using Laser Holographic Interferometry (LHI) [4–6] to the analysis of ground movement above underground openings. Due to its strict demand on the vibration free environment requirement, it is not that applicable and convenient for the subsidence classroom teaching and demonstration purpose.

In this chapter, a laser-optical measurement with a position sensor supplemented to measure the surface deformation for generating surface deformation profiles is introduced. The non-contact laser transducer shown in Figs. 41.7 and 41.8 is used to scan and measure deformation at the surface. Its measurement accuracy, linearity and quoted resolution are similar to measurements using LVDTs, although its resolution is also dependent on the distance between the transducer and the measurement area (http://www.micro-epison.org). The shorter the distance, the better the portable resolution, which can reach an accuracy of 1 μm for a transducer transmitting to a smooth steel surface. For optoNCDT 1400 50, the measuring

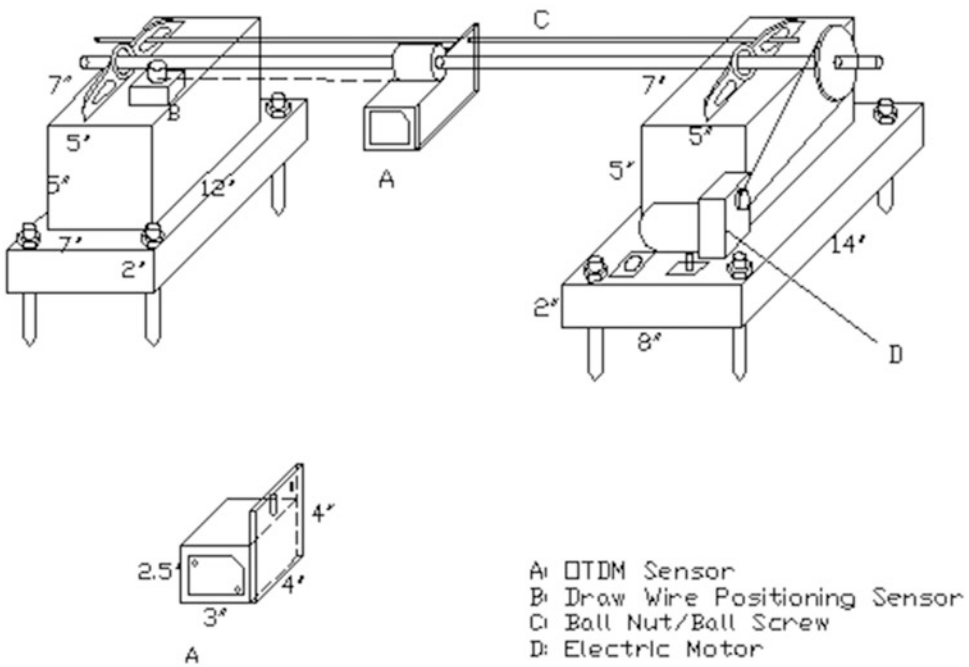

Fig. 41.7 AutoCAD design of surface displacement measurement system

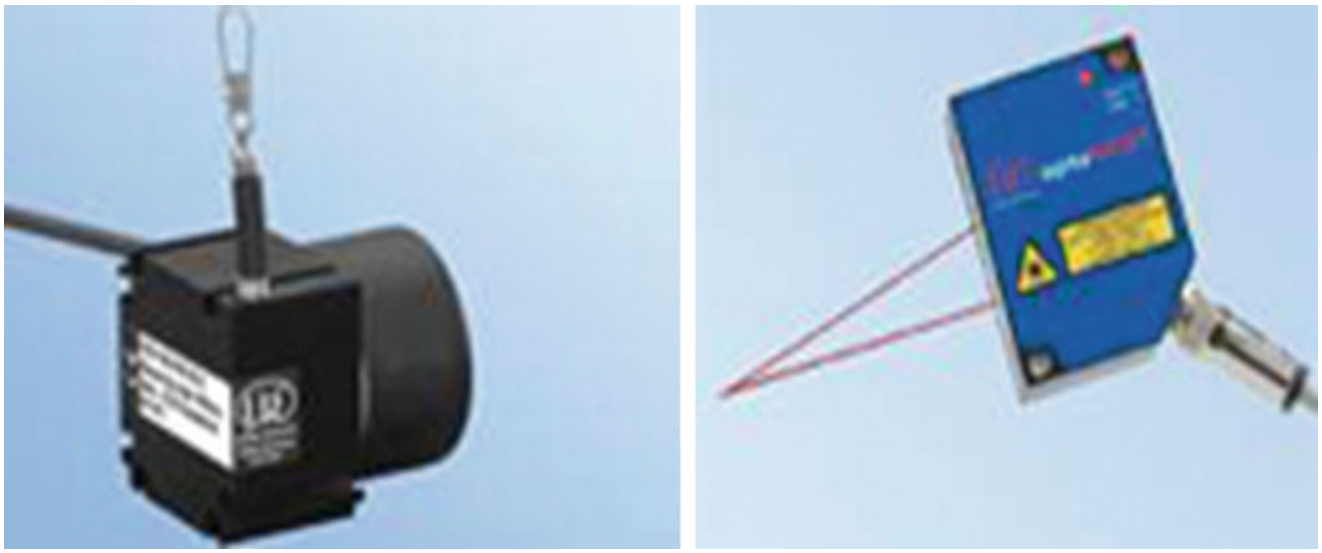

Fig. 41.8 Draw wire position sensor (DWPS) and optical triangulation distance measurement (OTDM) sensor, respectively

Fig. 41.9 (**a**) Subsidence cavity model under the surface displacement measurement system; (**b**) top view; (**c**) side view

range is 50 mm (2.0″) with starting of measuring range 45 mm (1.8″) and end of measuring range 95 mm (3.7″). And its linearity of full scale output is within $p\pm0.2\%$. For optoNCDT 1400 50, its resolution reaches 5 μm when static, and 25 μm with dynamic measurement at 1 KHz. The resolution for granular soils is usually about the size of a grain. The measurement principle is based on triangulation measuring of refraction of a laser beam. The laser transducer is designed to be tracked over an area to measure the soil surface deformation induced under different loading or excavation, subsidence conditions.

With the measured surface deformation, combined with various soil failure criteria models and material constitutive theories, new testing method of subsidence are proposed for characterizing the soil strength parameters. This new soil surface measurement technique can give considerably more accurate quantitative measurement when compared with the LHI measurement which is more of a graphical qualitative measurement by counting the fringes as seen in Fig. 41.4a.

Figure 41.7 shows an AutoCAD design of surface displacement measurement system where a draw wire position sensor (DWPS, as in Fig. 41.8) is used to measure horizontal position and optical triangulation distance measurement (OTDM as in Fig. 41.8) sensor is used to measure vertical surface deformation. Figure 41.9 shows the actually implemented subsidence model under the surface displacement measurement system.

41.5 Physical Model for Subsidence Simulation

A new technique of physical subsidence simulation has been developed using the laser optical triangulation distance measurement (OTDM) technique. This technique can be a proper tool for measuring displacement on a granular model material surface caused by trough type subsidence in a physical simulation.

The physical model was constructed to simulate subsidence by cavity resulted from longwall mining or extensive horizontal underground excavations. A rectangular frame was built on a metal plate to hold the model material (Figs. 41.2–3 and 41.9–10). On the bottom of the metal plate base, a translator with a 50 μm graduation was connected. A small rectangular plate was connected to the tip of the translator and placed in a same size opening at the center of the base. As the micrometer attached to the translator was turned after the model material was filled, the small plate was lowered to create a controlled underground cavity/void.

The cavity size varies depending on the plate size as shown in Fig. 41.10. The sizes of the plate used in this study were 0.5 in. by 5 in. (12.7 mm by 127 mm), 1.0 in. by 5.0 in. (25.4 mm by 127 mm), 1.5 in. by 5.0 in. (38.1 mm by 127 mm), and 2.0 in. by 5.0 in. (50.8 mm by 127 mm). After the plate was moved downward, the displacement monitoring system was activated to measure the subsidence profile. The model material used for the test was well graded sand to simulate highly fractured rock condition [3]. The gradation of the model material is shown in Fig. 41.11.

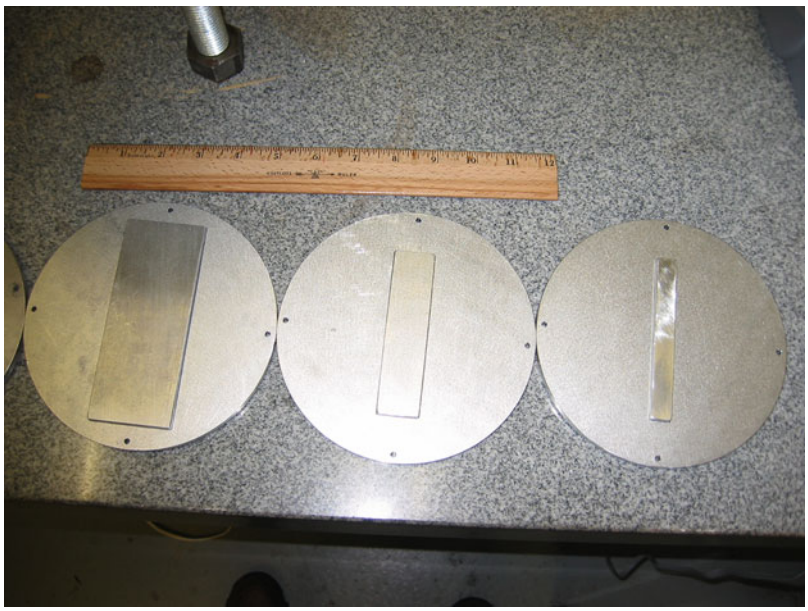

Fig. 41.10 Plates used for creating subsidence cavity (shown here 2.0 in. (50.8 mm) wide, 1.0 in. (25.4 mm) wide, 0.5 in. (12.7 mm) wide)

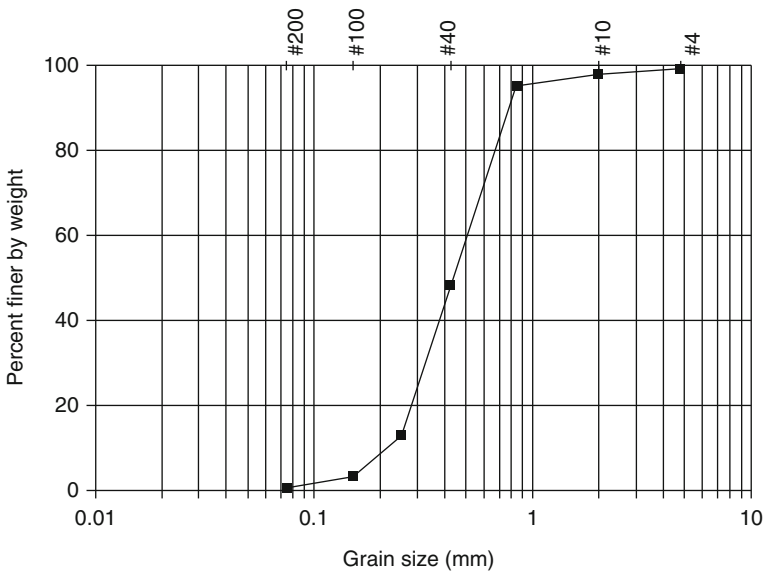

Fig. 41.11 Particle size distribution of model material to be characterized

41.6 Examples of Subsidence Simulation Results and Visualizations

Figure 41.12 shows an actual surface subsidence fracture profile on the sand surface above the controlled underground cavity.

Figure 41.13 is drawn from a series of raw surface subsidence deformation testing data. A subsidence monitoring and analysis program, SMAP, is specifically developed with MATLAB for subsidence visualization and analysis. After exporting the test data to a SMAP system, it can be further visualized for subsidence analysis.

Figure 41.14 shows the pink colored line is the subsidence testing data. The red line is the best fitting curve, in this case. The green line is the first derivative of the fitted curve; the blue line is second derivative of the fitted Gauss curve. While the gray blue dotted line is the third derivative of the mathematically fitted Gaussian curve. The two peaks theoretically correspond to the angle of break. Thus the angle of break can be mathematically determined and visualized.

As the overall large range data fitting has some gaps, so only the right wing of surface subsidence was selected for more accurate curve fitting and analysis as shown in Fig. 41.15.

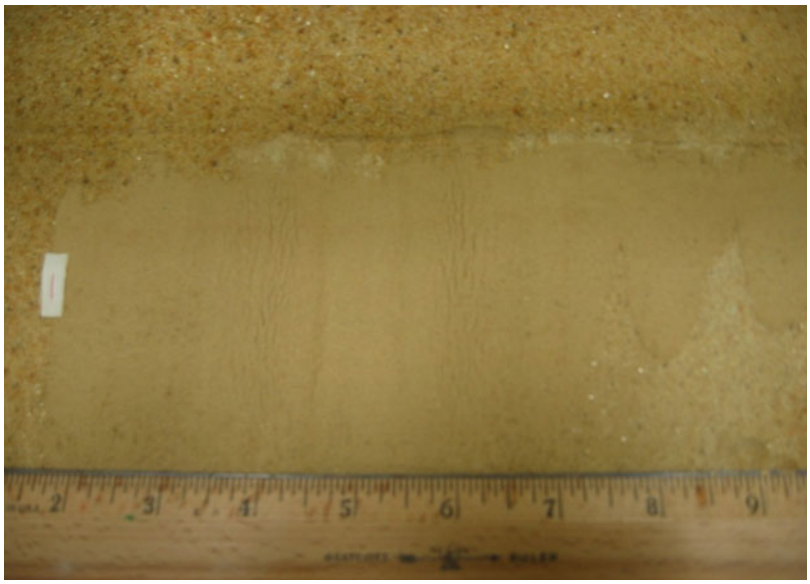

Fig. 41.12 Surface subsidence deformation of 2.0″ (50.8 mm) thick sand subsidence over 2.0″ (50.8 mm) wide 0.30″ (7.62 mm) height cavity

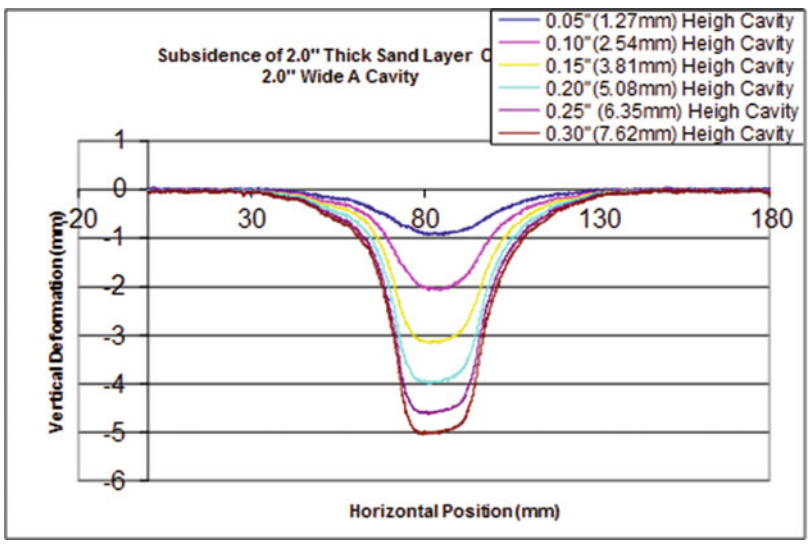

Fig. 41.13 Continuously Increased subsidence cavity and surface deformation profile measured from the newly developed subsidence testing device

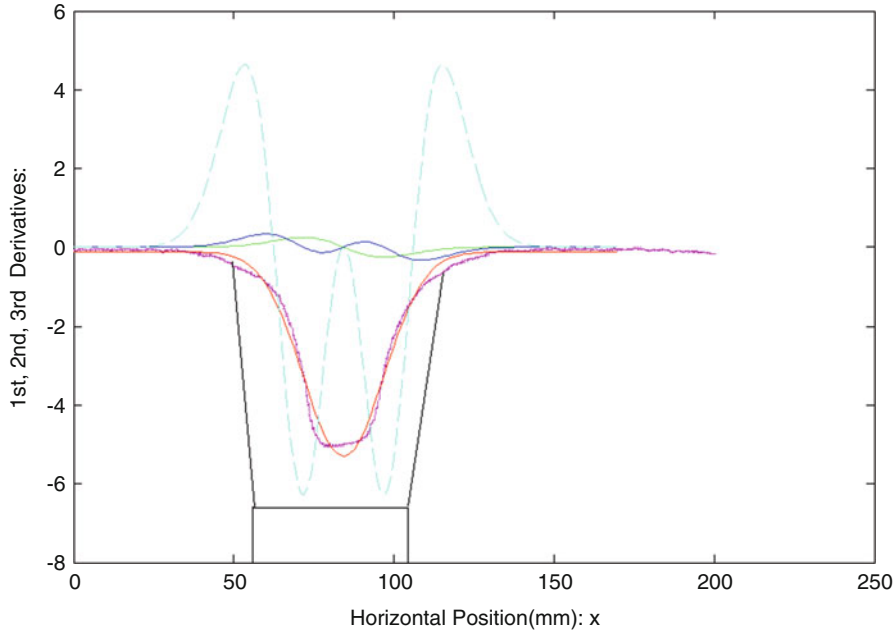

Fig. 41.14 SMAP analysis results and visualization

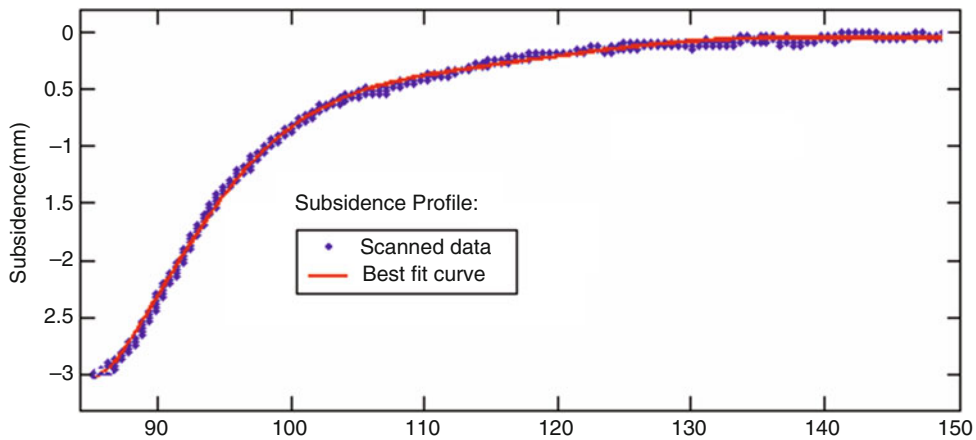

Fig. 41.15 Distance from center of cavity in mm (center of cavity at 85.20 mm) cavity width 1.5 in. (38.1 mm); cavity height 0.3 in. (7.62 mm); overburden 2.0 in. (50.8 mm)

The actually measured surface fracture width is 2.75 in. (69.85 mm) as shown in Fig. 41.12 and the width of the cavity is 2.0 in. (50.8 mm) as schematically shown in Fig. 41.14. Therefore, the angle of break is about:

$$\alpha = \tan^{-1}\left(\frac{50.8}{\frac{69.85-50.8}{2}}\right) = 79.38^{\circ}$$

Equation (41.4) indicates that soil internal friction angle is $\phi = 2\alpha - 90^{\circ} = 2{*}79.38^{\circ} - 90^{\circ} = 68.76^{\circ}$ which seems to be double the actual internal friction angle though. Therefore, $\phi = \alpha - 45^{\circ} = 79.38^{\circ} - 45^{\circ} = 34.38^{\circ}$ may actually better provides the testing of the sand strength friction angle which has a factor of safety of 2 included. Further subsidence testing and research correlations are needed for testing sand strength parameters.

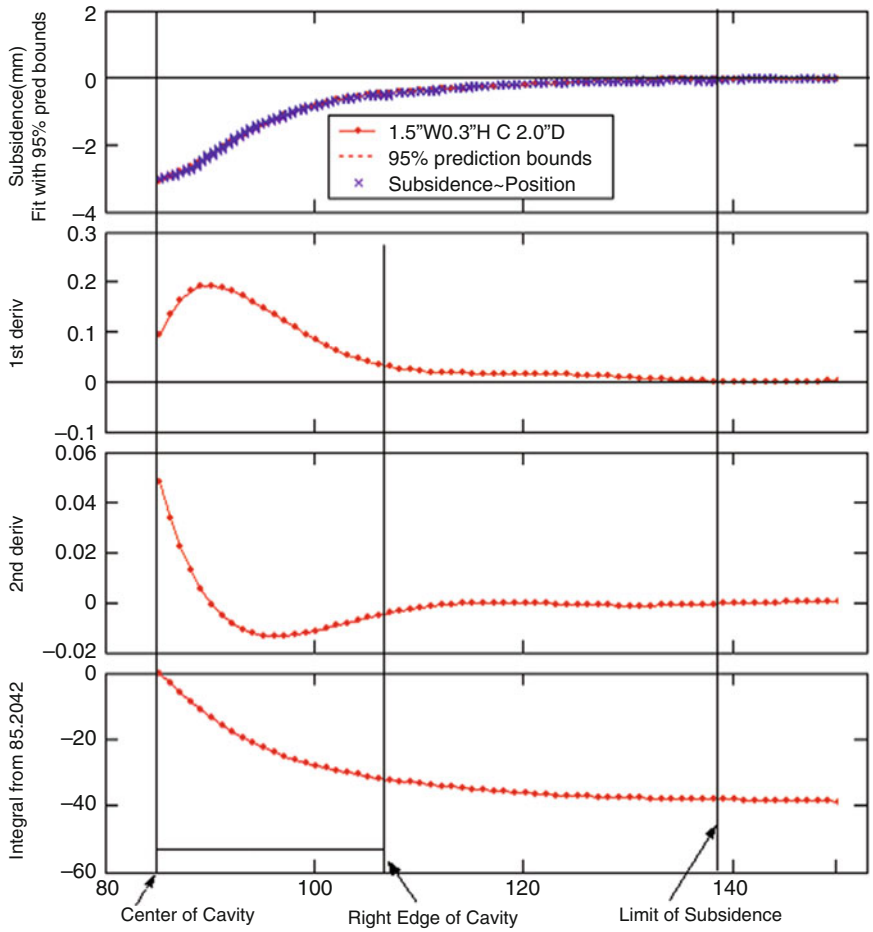

Fig. 41.16 Distance from center of cavity in mm (center of cavity at 85.20 mm)

The surcharge of overburden is 2.0 in. (50.8 mm). From Fig. 41.13, the parameter of Subsidence Factor can be obtained: $\text{SF} = \frac{MaxSubsidence}{CavityHeight} = \frac{5.00}{7.62} = 0.6552$

Test results from the subsidence model were analyzed. The top portion of Fig. 41.16 shows a typical surface subsidence profile. In this case, 1.5 in. (38.1 mm) wide and 5.0 in. (127 mm) long and 0.3 in. (7.6 mm) high cavity created a trough type subsidence. The overburden depth was 2.0 in. (50.8 mm). The width/depth ratio of the cavity was 0.75.

To get the angle of draw the plotted subsidence profile was further analyzed by generating first derivative and second derivative curves as in Fig. 41.16. The first derivative is particularly useful for determining the trough margin. Because the surface subsidence profile reduces very gradually around the trough margin, it is difficult to find the exact point. The first derivative curve shows the trough limit distinctively. The second derivative can be used for analyzing surface strains, and the integral curve shows cumulative subsidence volume along the profile.

41.7 Discussion and Remarks

The relationships between the angle of draws and the width/depth ratios of subsidence causing cavity were obtained and plotted in Fig. 41.17. As the best fit curve indicates, the angle of draw gradually increased from about 33.5° at the cavity width/depth ratio of 0.5 to about 52° at the ratio of 4.0. Subsidence factor is defined as the ratio between maximum subsidence and cavity height. The subsidence factor is an important parameter for predicting subsidence magnitude in the field.

When the cavity width is narrow relative to the overburden depth, the subsidence factor is low. The subsidence factor increases with the width of the cavity until the subsidence fully develops such that the maximum subsidence stops increasing. This stage is the critical subsidence.

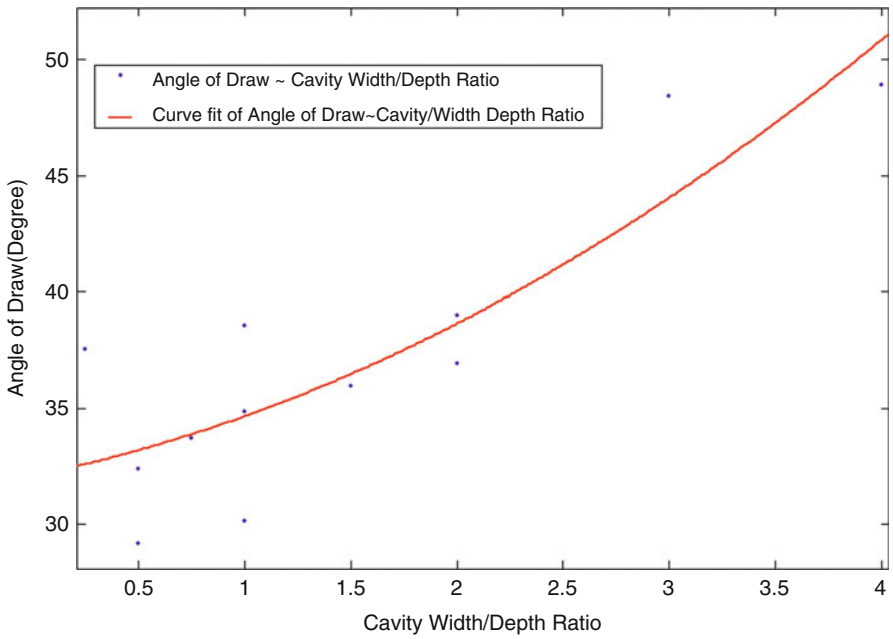

Fig. 41.17 Angle of draw vs. cavity width/depth ratio

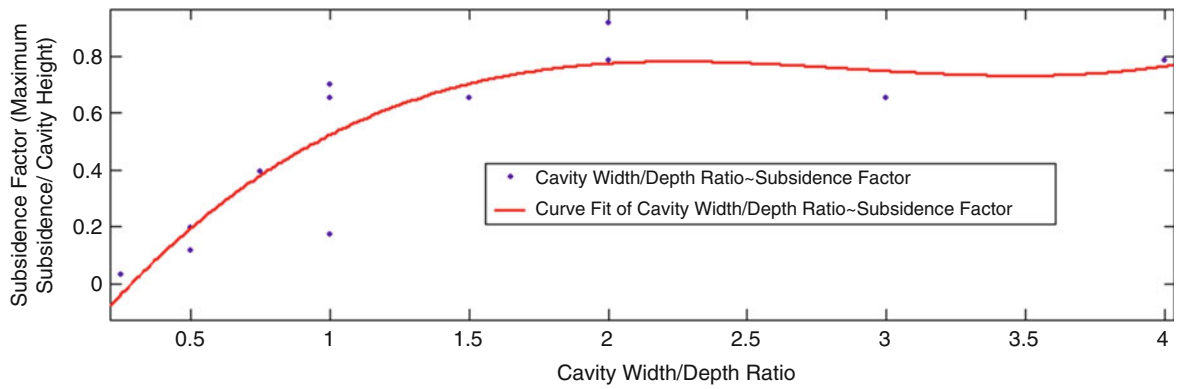

Fig. 41.18 Subsidence factor vs. cavity width/depth ratio

Figure 41.18 shows the relationship between the subsidence factor and the cavity width/depth ratio. The trend is that subsidence factor increases with the increase of cavity width/depth ratio until it reaches between 1.5 and 2.0. This means that the subsidence grows from sub-critical type when the width of cavity is narrow. As the width increases to reach a width/depth ratio of between 1.5 and 2.0, the subsidence becomes fully grown with the maximum possible subsidence at the center point. When the width/depth ratio increases further the maximum subsidence does not increase, but extends to the direction of the side where the width extends, resulting in a super-critical stage.

The subsidence modeling apparatus combined with the laser optical triangulation distance measurement sensors successfully simulated subsidence created by underground cavities. Subsidence profiles obtained by this technique are comparable with field measurements and other theoretical analyses. Other subsidence parameters, such as angle of draws and subsidence factors, were also calculated from the obtained data.

The developed subsidence modeling device has been used in the undergraduate teaching of subsidence geohazard education. Preliminary comparison survey results indicate that students seem to effectively understand the subsidence concepts and mechanism with an intuitive physical understanding of the subsidence testing device. The soil strength and lateral earth pressure concepts could also be reinforced through the subsidence teaching aid.

Acknowledgment The authors appreciate the suggestions and mentoring advice provided by Prof. Duk-Won Park and the research accommodation and support provided at UA and current institute. Students in my engineering geology class are gratefully appreciated for providing an educational survey on the effectiveness of the developed subsidence device as a teaching aid.

References

1. Harper, D.: Mine subsidence in Indiana, Department of Natural Resources Geological Survey Special Report 27 (1982)
2. Larson, G.: Mine Subsidence. GeoFacts, No. 12, Ohio Department of Natural Resources
3. Park, D., Li, J.: Subsidence simulation using laser optical triangulation distance measurement device, ARMA/NARMS 04-548, Gulf Rock, Houston, TX (2004)
4. Park, D.W.: Model studies of subsidence over room and pillar coal mines using holographic interferometry. In: Proceedings, 21st US Symposium on Rock Mechanics, University of Missouri-Rolla, pp. 265–274 (1980)
5. Park, D.W.: Application of laser holographic interferometry to the analysis of ground movement above underground openings. PhD Dissertation, University of Missouri-Rolla, 150 p (1975)
6. Park, D., Summers, D.A., Aughenbaugh, N.B.: Model studies of subsidence and ground movement using laser holographic interferometry. Int. J. Rock Mech. Min. Sci. **14**(6), 235–245 (1977)
7. Rankine, W.J.M.: On the stability of loose earth. Philos. Trans. R. Soc. Lond. **1**, 9–27 (1857)
8. Terzaghi, K., Peck, R.B.: Soil Mechanics in Engineering Practice. Wiley, New York (1967)
9. Das, B.M., Sobhan, K.: Principles of Geotechnical Engineering, 8th edn. Cengage Learning, Stamford, CT (2014)
10. Das, B.M.: Principles of Foundation Engineering, 8th edn. Cengage Learning, Stamford, CT (2016)

Chapter 42
Determining the Shear Relaxation Modulus and Constitutive Models for Polyurea and Polyurea-Based Composite Materials from Dynamic Mechanical Testing Data

Zhanzhan Jia, Alireza V. Amirkhizi, Wiroj Nantasetphong, and Sia Nemat-Nasser

Abstract Polyurea and polyurea-based composite materials are widely used due to their excellent mechanical properties. In order to facilitate large-scale computational studies for this group of materials, a robust and standard method is needed to extract their viscoelastic constitutive parameters. In this study, frequency-domain master curves which cover a wide range of frequencies are developed using the data of dynamic mechanical analysis through time-temperature superposition (TTS). The quality of the master curves is assessed both by Kramers-Kronig relations and by comparing with the ultrasonic wave testing data. Then the time-domain relaxation modulus is obtained by the high-resolution Prony series approximated from the relaxation spectrum. To reduce computational cost, 4 to 8-term Prony series are then fitted from the time-domain relaxation modulus for a limited frequency range of interest. Both the high and low-resolution Prony series are converted back to frequency domain to compare with the master curves developed by TTS and show good agreements. This method is not limited to polyurea and polyurea-based composites and it can be applied to other similar polymer systems as well.

Keywords Polyurea • Master curves • Prony series • Dynamic mechanical analysis • Time-temperature superposition

42.1 Introduction

Polyurea is an elastomeric copolymer synthesized using diisocyanates (e.g. Isonate 143L [1], Dow Chemical) and diaamines (e.g. Versalink P-1000 [2], Air Products). It has a wide range of transition zone between its glassy state and rubbery state, and its storage and loss moduli increase drastically when the frequency or pressure increases. It is an excellent material for protection from blast/impact loadings.

This work focuses on the strain rate effect on the polyurea properties in a wide frequency range. The transition zone of polyurea in the frequency domain spans more than ten decades in the logarithmic scale, and it is extremely challenging to directly measure its mechanical properties directly in such a wide frequency range. Thus alternative methods are necessary to approximate its properties. Time-temperature superposition (TTS) is applied on dynamic mechanical analysis data to get master curves. Care is taken while applying TTS and the quality of the master curves is assessed by Kramers-Kronig relations and by comparing with ultrasonic data. Based on the master curves, time-domain relaxation modulus can be calculated and optimized Prony series with desired number of terms and for the frequency range of interest can be calculated.

This study provides a consistent and convenient method to approximate mechanical properties of polyurea and polyurea composites in a wide frequency range and calculate the Prony series for specific computational applications. The same method can also be applied for some polyurea composites and other similar polymers.

Z. Jia (✉) • W. Nantasetphong • S. Nemat-Nasser
Department of Mechanical and Aerospace Engineering, Center of Excellence for Advanced Materials, University of California, San Diego, 9500 Gilman Drive, La Jolla, CA 92093-0416, USA
e-mail: z1jia@ucsd.edu

A.V. Amirkhizi
Department of Mechanical Engineering, University of Massachusetts, Lowell, MA 01854, USA

C. Ralph et al. (eds.), *Mechanics of Composite and Multi-functional Materials, Volume 7*,
Conference Proceedings of the Society for Experimental Mechanics Series, DOI 10.1007/978-3-319-21762-8_42

42.2 Material Fabrication

Pure polyurea is fabricated by mixing degassed Versalink P-1000 and Isonate 143L together under vacuum. The mixture is transferred into Teflon molds to cure in an environmental chamber for at least 2 weeks before testing. The relative humidity in the environmental chamber is kept at 10 %.

The two composites are polyurea with phenolic microbubbles (PUPMB) and polyurea with milled glass (PUMG). Polyurea with phenolic microbubbles is a synthetic polyurea foam and polyurea with milled glass has both high storage and high loss moduli. The two composites are fabricated by mixing the filler material with Versalink P-1000 before degassing and then mixed under vacuum with the other component Isonate 143L. The composites are cured in the environmental chamber for at least 2 weeks before testing.

Figure 42.1 shows the sample pictures of polyurea and the two polyurea composites. SEM pictures of the two composites are also showed following the sample picture.

42.3 Dynamic Mechanical Analysis and Master Curves Development

Dynamic mechanical analysis (DMA) single-cantilever test is conducted on TA 2980 dynamic mechanical analyzer (as shown in Fig. 42.2), in the temperature range of −80 to ~ 50 °C, with 3 °C increment between temperature points. The test frequencies are 1, 2, 5, 10, 20 Hz. The nominal sample size is 3 mm × 10 mm × 30 mm. Storage and loss Young's moduli are measured at various temperatures and frequencies are collected by the corresponding software of the TA instrument.

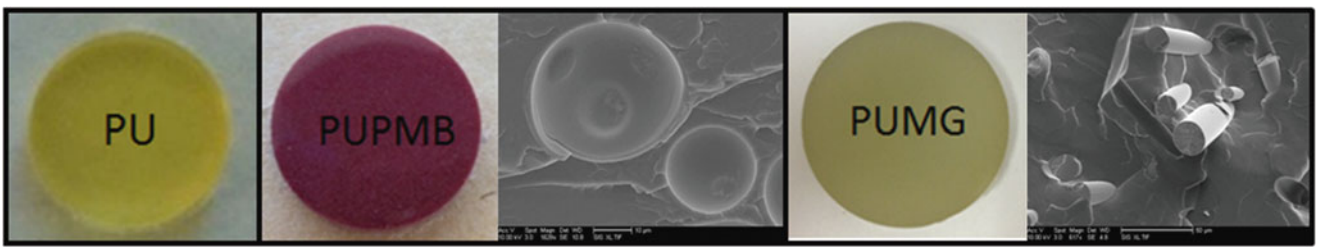

Fig. 42.1 Polyurea (*PU*), polyurea with phenolic microbubbles (*PUPMB*) and polyurea with milled glass (*PUMG*)

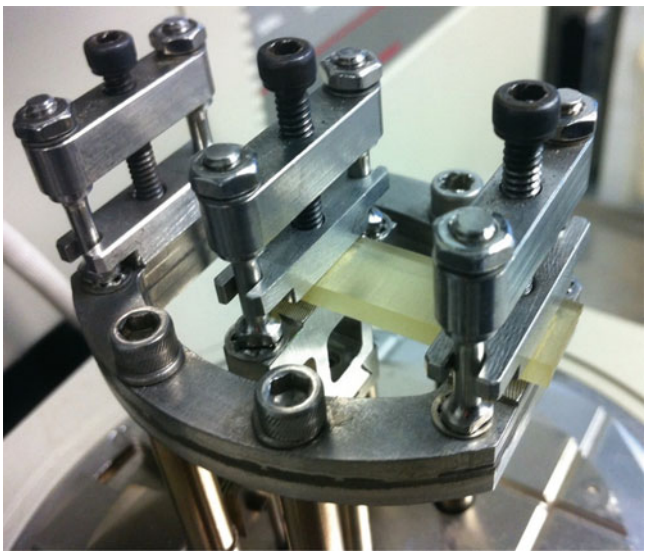

Fig. 42.2 Dynamic mechanical analysis single cantilever bending test

The complex Young's modulus is composed of the storage modulus and loss modulus in the following relation:

$$E^* = E' + iE'' \tag{42.1}$$

Time-temperature superposition is applied on the DMA data to develop master curves at the reference temperature and in a wide frequency range. The classic TTS is shown as follows:

$$E_r^* = b(T, T_0)E^*(\omega, T) \tag{42.2}$$

$$\omega_r = a(T, T_0)\omega \tag{42.3}$$

where T_0 is the reference temperature; E^* and ω are the experimental measurements; E_r^* and ω_r are the reduced modulus and frequencies of the master curve; $a(T, T_0)$ and $b(T, T_0)$ are the horizontal and vertical shift factors. The vertical shift factor is calculated as $\frac{T_o \rho_0}{T \rho}$ [3], where the density of polyurea within the DMA temperature range can be assumed to be constant. The horizontal shift factor $\log(a)$ is the average measurement from both the storage and loss moduli in order for the experimental data measured at various temperatures to connect into smooth master curves, and it can be well represented by the WLF equation [4]:

$$log[a(T, T_0)] = \frac{-C_1(T - T_0)}{C_2 + (T + T_0)} \tag{42.4}$$

where C_1 and C_2 are two constants.

42.4 Master Curves Quality Assessments

If the master curves of storage and loss moduli developed by time-temperature superposition are reliable, they should follow the requirements of causality in any physical system, i.e. the Kramers-Kronig relations [5, 6]. Kramers-Kronig relations show the storage and loss moduli master curves should be interrelated and be able to calculate from each other.

The storage and loss moduli master curves of polyurea and polyurea composites developed by TTS reproduce each other very well except at the two ends where error is introduced during the data extension for calculating the Kramers-Kronig relations.

Another way of assessing the master curve quality is by comparing with the ultrasonic wave measurement. The storage and loss moduli can also be acquired by ultrasonic wave measurements using the following equations [7]:

$$M' = \frac{\rho c^2(1 - r^2)}{(1 + r^2)^2} \tag{42.5}$$

$$M'' = \frac{2\rho c^2 r}{(1 + r^2)^2} \tag{42.6}$$

where c is the measured wave speed, r is the attenuation and M represents longitudinal or shear modulus based on what kind of ultrasonic wave is used for the measurement. The ultrasonic wave test is conducted between -50 °C ~ 30 °C at 1 MHz. Young's modulus is calculated by the measured shear and longitudinal moduli. The ultrasonic Young's modulus can be shifted using the same shifting factors in TTS and compared with the DMA master curves. The storage moduli of DMA master curve and ultrasonic master curve match well with each other.

42.5 Relaxation Modulus and Prony Series

The master curves of polyurea and polyurea composites are first developed in the frequency domain. However, developing Prony series from the frequency domain is more difficult than in the time domain. Thus, master curves are first brought back to the time domain into the relaxation modulus and then Prony series for the frequency range of interest can be fitted from the relaxation modus.

The relaxation spectrum can be calculated from the frequency domain master curves using the second approximation method by William and Ferry [8]. The relation between the relaxation spectrum Φ and relaxation modulus is:

$$E(t) = E_e + \int_0^\infty \Phi e^{-t/\tau} d\ln\tau \tag{42.7}$$

By using Eq. 42.7, the time-domain relaxation modulus which contains the information of the frequency-domain master curves can be calculated. This relaxation modulus can be used to develop 4–8 terms Prony series that insures both accuracy and computational efficiency. The form of Prony series is [3]:

$$E(t) = E_e + \sum_{i=1}^{n} E_i e^{-t/\tau_i} \tag{42.8}$$

42.6 Discussion

This study develops a standard method to obtain master curves and Prony series of polyurea and polyurea-based composites using the experimental data of DMA test. A computational code has been developed and the flow chart of this code is shown in Fig. 42.3. The four inputs are the experimental DMA data, the reference temperature, the frequency range of interest and the number of Prony terms needed for the computation platform. This code automatically develops master curves, assesses their quality and generates optimized Prony series for the frequency range of interest.

With this code, the majority of the time and efforts go into the sample fabrication and DMA testing, which is a comparatively convenient experiments in terms of characterizing the viscoelastic properties of polymers. The same method also applies for some polyurea composites and other similar polymers. Here the two composite examples are PUPMB and PUMG, one with hollow micro inclusions and one with rigid micro inclusions.

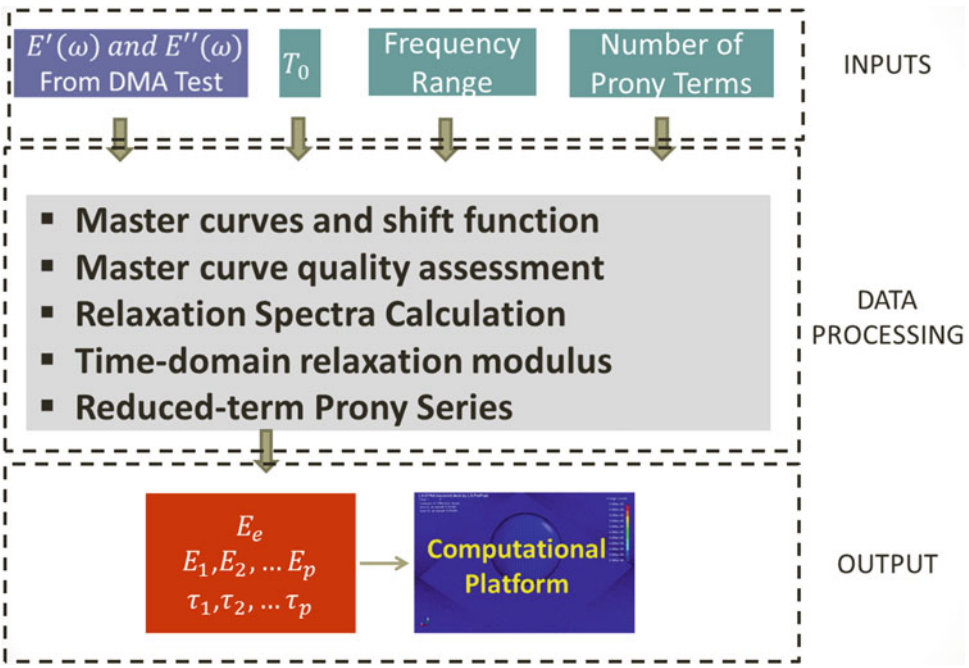

Fig. 42.3 Flow chart of the data processing code for developing Prony series of polyurea and polyurea-based composites

Care needs to be taken for applying TTS on heterogeneous materials. Polyurea has domain separation, and the composites materials have filler materials of different properties. However, when the relaxation mechanism of the major soft domain of polyurea and that of other domains/inclusions differ drastically, for example, when the inclusions can be regard as elastic or rigid, we still regard TTS as a useful method to get meaningful information when direct measurements are not available.

Acknowledgement This work has been supported by the Office of Naval Research (ONR) grant N00014-09-1-1126 to the University of California, San Diego, and also ONR grant N00014-13-1-0392 to the University of Massachusetts, Lowell.

References

1. The Dow Chemical Company: Isonate 143L, Modified MDI. Dow Chemical, Midland, MI (2001)
2. Air Product Chemicals, Inc.: Polyurethane Specialty Products. Air Products and Chemicals, Allentown, PA (2003)
3. Ferry, J.D.: Viscoelastic Properties of Polymers. Wiley, New York (1980)
4. Williams, M.L., Landel, R.F., Ferry, J.D.: The temperature dependence of relaxation mechanisms in amorphous polymers and other glass-forming liquids. J. Am. Chem. Soc. **77**, 3701–3707 (1955)
5. Booij, H.C., Thoone, G.P.J.M.: Generalization of Kramers-Kronig transforms and some approximations of relations between viscoelastic quantities. Rheol. Acta **21**(1), 15–24 (1982)
6. O'Donnell, M., Jaynes, E.T., Miller, J.G.: Kramers-Kronig relationship between ultrasonic attenuation and phase velocity. J. Acoust. Soc. Am. **69**(3), 696–701 (1981)
7. Qiao, J., Amirkhizi, A.V., Schaaf, K., Nemat-Nasser, S., Wu, G.: Dynamic mechanical and ultrasonic properties of polyurea. Mech. Mater. **43**(10), 598–607 (2011)
8. Williams, M.L., Ferry, J.D.: Second approximation calculations of mechanical and electrical relaxation and retardation distributions. J. Polym. Sci. **XI**(2), 169–175 (1952)

Chapter 43
Long Term Stability of UHMWPE Fibers

Amanda L. Forster, Joannie Chin, Jyun-Siang Peng, Kai-li Kang, Kirk Rice, and Mohamad Al-Sheikhly

Abstract The performance of ultra-high molecular weight polyethylene (UHMWPE) fibers for ballistic protection is predicated on the development of a highly aligned molecular structure that allows the polymer to exhibit a superior strength in the axial direction of the fiber. Body armor manufacturers have exploited the inherent strength of these materials to develop body armor that continues to defeat ever-increasing ballistic threats. However, even an ideal molecular structure will be subjected to degradation during use, which can reduce the high strength of these fibers, and impact their ability to protect the wearer. In this work, the long term stability of UHMWPE fibers is investigated by exposing yarns to temperatures of 43, 65, 90, and 115 °C for periods of time up to 81 weeks, and monitoring the tensile strength of the yarns. The activation energy for this aging mechanism was calculated to be approximately 140 kJ/mol. Changes in the oxidation index of this material due to aging were also studied using Fourier Transform Infrared Spectroscopy (FTIR), and these changes are compared with changes in tensile strength. The effect of aging on the morphology of the fibers is also studied using thermal analysis and X-ray diffraction (XRD) methods.

Keywords High strength fibers • Long term stability • Polyethylene • Aging • Body armor

43.1 Introduction

Ultra high molecular weight polyethylene [1–3] (UHMWPE) is one of the two main types of fibers currently used in ballistic-resistant body armor. UHMWPE is a long-chain polyolefin with a molar mass between 3 and 5 million. Its tensile strength is reported to be approximately 40 % greater than PPTA fiber [4] due to its high crystallinity and highly oriented zig-zag sp^3 conformation. Polyethylene has no functional groups, resulting in superior chemical resistance as compared to other materials [5]. A well-publicized field failure in 2003 of a body armor based on the fiber poly(*p*-phenylene-2,6-benzobisoxazole), or PBO, has prompted our work to better understand the long term stability of other classes of fibers used in body armor when exposed to elevated temperatures [6–8].

Degradation of polyolefins initiates from thermal decomposition of hydroperoxides and peroxides produced due to defects, unsaturations, and other impurities introduced during processing [9]. The rate of degradation is dependent upon many factors such as the number of free radicals generated, the presence of scavenger compounds (e.g., antioxidants), the presence of oxygen, and the degree of crystallinity of the polymer. UHMWPE fibers used in soft body armor are protected from photo-oxidation by a protective fabric carrier, and exposure to ionizing radiation is not expected to occur during general use. The likely routes to initiate degradation are thermal exposure (from storage and wear) or mechanically initiated degradation from routine use of the armor. Mechanical degradation initiates free radical formation and can occur at folds [10] due to movement of the armor on the wearer. Once these free radicals are generated they may follow the established free radical reactions such as hydrogen abstraction and hydroperoxide formation resulting in main chain scission, reduction of molecular weight, and oxidation. Each of these short-term exposures results in cumulative damage that may lead to unforeseen performance reductions in the armor over time. In this study, elevated temperature exposure will be used to

A.L. Forster (✉) • K.-l. Kang • K. Rice
National Institute of Standards and Technology, Material Measurement Laboratory, Gaithersburg, MD, USA
e-mail: amanda.forster@nist.gov

J. Chin • J.-S. Peng
National Institute of Standards and Technology, Engineering Laboratory, Gaithersburg, MD, USA

M. Al-Sheikhly
Materials Science and Engineering Department, University of Maryland, College Park, MD, USA

C. Ralph et al. (eds.), *Mechanics of Composite and Multi-functional Materials, Volume 7*,
Conference Proceedings of the Society for Experimental Mechanics Series, DOI 10.1007/978-3-319-21762-8_43

accelerate degradation. Costa and co-authors have discussed thermal, photo, and mechano-oxidation of UHMWPE in detail, and their work includes a reaction scheme of how oxidation occurs in this material [9, 11].

Due to the highly oriented and crystalline microstructure of UHMWPE fibers, it is not immediately clear that accelerating degradation via temperature will follow Arrhenius behavior. The goals of this study are threefold: first to determine whether elevated temperatures follow the constant acceleration assumption, next to determine whether or not mechanical performance shifts to create a master curve, and finally to determine how the calculated activation energy agrees with a previous study to determine the activation energy via elevated temperature exposure [3].

Classically, researchers have extrapolated high temperature behavior to a lower temperature regime using the Arrhenius equation [12–14]. Time-temperature superposition may be used to shift data from different aging temperatures to create a master curve if the increase in temperature increases the rate of degradation by a constant multiplicative factor. When plotted on a logarithmic time graph, all data sets at the various temperatures should have the same overall curve shape. If the data from each elevated temperature can be superposed at a reference temperature by multiplying the aging time by a constant, known as the shift factor, a_t, then the time-temperature superposition is generally regarded as valid. In order to verify the feasibility of time-temperature superposition, a plot of (log a_t versus 1/T) should result in a linear dependence upon temperature [12].

Previous work has focused on understanding the long term stability of bulk UHMWPE typically used in orthopedic joint replacement applications [15]. Chabba and coworkers performed artificial aging experiments on UHMWPE fibers, focusing on oxygen uptake as a marker of degradation and calculating the activation energy of this process as being approximately 120 kJ/mol. In this study, the focus is on tensile strength as an indicator of degradation in the fiber, and not oxygen uptake as in Chabba's study. Tensile strength was selected as a metric for this study because it is generally considered to be an easily-studied parameter that is related to ballistic performance [16]. In order to better represent the aging environment for body armor, aging temperatures of 43 °C and 65 °C were chosen to simulate body temperature and potential storage conditions (e.g., the trunk of a car), and 90 °C and 115 °C were used to accelerate degradation.

43.2 Experimental

Sample Description: Gel spun UHMWPE continuous filament yarns were used in this study. Yarn samples were stored in dark ambient conditions when not being exposed. For the aging experiments, yarns were wound onto perforated spools and placed into ovens at 43 °C, 65 °C, 90 °C, and 115 °C under dry conditions for a predetermined period of time. A series of temperature/relative humidity dataloggers were used to monitor the consistency of the chamber temperature during the exposure period.

Mechanical Properties Measurement: The mechanical properties of the yarns were measured using established methods for measuring the ultimate tensile strength. A universal test machine frame equipped with a 1 kN load cell and pneumatic yarn and cord grips was used for these tests. The experiment was performed in accordance with ISO 2062 [17]. A 58.42 cm (23 in) yarn was given 23 twists (1 twist per 2.54 cm) on a custom designed yarn-twisting device, and the level of twist was maintained while transferring the yarn to the pneumatic grips. The gage length was 25 cm and the crosshead speed was 250 mm/min. The strength at break was recorded and each data point represents the mean of at least seven trials.

Oxidation Measurement: Oxidation of the fiber samples was measured using Fourier Transform Infrared Spectroscopy. A spectrometer (FTIR) equipped with a liquid nitrogen-cooled mercury cadmium telluride (MCT) detector and an attenuated total reflectance (ATR) accessory was used in the oxidation measurement. Consistent pressure on the yarns was applied using the force monitor on the ATR accessory. Final scans represent the average of 128 individual scans with a resolution of 4 cm^{-1} between 650 cm^{-1} and 4000 cm^{-1}, respectively. The spectra were baseline corrected and normalized using the peak at 1472 cm^{-1}, which was attributed to the CH_2 bending mode. Typical standard uncertainties for spectra measurements are 4 cm^{-1} in wavenumber and 1 % in peak intensity. For the purposes of evaluating the degree of oxidation, the overlapping peaks were deconvolved between 1680 and 1740 cm^{-1}. This peak ratio was introduced as the oxidation index [18–20].

Crystallinity Determination: Differential scanning calorimetry (DSC) was carried out after exposure at the specified temperature over a designated time interval. Samples were prepared by coiling the UHMWPE fibers on a rod and sealing them in a hermetic aluminum sample pan. The typical weight of the sample was 3–5 mg. Samples were held at −80 °C for 5 min, then heated at 10 °C/min to 250 °C. The melting points were characterized by the temperature of the maximum endothermic peak, and the heat of fusion was determined by integrating the area under the curve. Three replicates were prepared for each condition. The melting endotherm was deconvolved into multiple Gaussian peaks with post-processing software. Wide angle X-ray scattering (WAXS) measurements were conducted using a laboratory-scale small-angle X-ray scattering instrument in wide angle mode with Mo $K\alpha_1$ radiation of wavelength 0.70926 Å in conventional pinhole

geometry. The incident beam, diffracted beam and sample chamber were under vacuum. An image plate was used to collect the two-dimensional scattering patterns. The fibers were mounted perpendicular to the direction of the beam [21].

43.3 Results and Discussion

Figure 43.1 shows the change in tensile strength as a function of aging at different temperatures. As anticipated, the reduction in tensile strength was lowest at the aging temperature of 43 °C. Only a slight decrease in the tensile strength (2 %) was observed after 1 week of aging, with virtually no change after the first month of aging. A slow, steady deterioration in the tensile strength was observed throughout the long term aging study. The study was ended at 102 weeks of aging, with a final tensile strength loss of 9 %. The reduction in residual tensile strength was more evident at the aging temperature of 65 °C. The decrease in tensile strength after the first week was approximately 3 %, and in the first month it was 8 %. After 94 weeks of aging, the study was ended, with a final tensile strength loss of over 30 %. The reduction in tensile strength was even more apparent at the higher temperatures. The UHMWPE fibers lost 28 % of their initial tensile strength at the aging temperature of 90 °C in the first week, and continuously decreased to 56 % after 17 weeks. Fibers exposed to the aging condition of 115 °C lost 42 % of their original tensile strength after 1 week. The study continued for 17 weeks, after which the fibers had lost 52 % of their original tensile strength. However, given the rapid and catastrophic loss of tensile strength in the fibers aged at 90 and 115 °C, and the fact that the fibers were unconstrained during this experiment, it is possible that these fibers may have undergone a morphological change during elevated temperature exposure. The loss of orientation in the fiber, combined with scissions in the critical tie chains that are important in carrying load in UHMWPE fibers [22] could be partially responsible for the rapid loss in tensile strength (especially at 1 week of aging time) in the fibers aged at 90 and 115 °C, rather than oxidative chain scission. DMTA temperature scans of unaged fibers were previously reported [23] and show reduction in the storage modulus by 30 % and 50 % at 90 °C and 115 °C, respectively, although the material remains 20 °C away from the transition region. Shrinkage of highly drawn and oriented polyethylene has been widely reported [24, 25]. Shrinkage was not directly measured or observed in this study, but remains a potential consequence of small changes in polymer morphology when working with such highly drawn fibers at elevated temperatures. Previous work [23] has shown that the UHMWPE fibers used in this experiment undergo an alpha-relaxation above 80 °C, but degradation may be accelerated at higher temperatures.

In order to assess the long term stability of UHMWPE fibers, the master curve at 43 °C is presented in Fig. 43.1b. The lowest aging temperature represents the base use condition for the fibers (body temperature). A master curve was created by

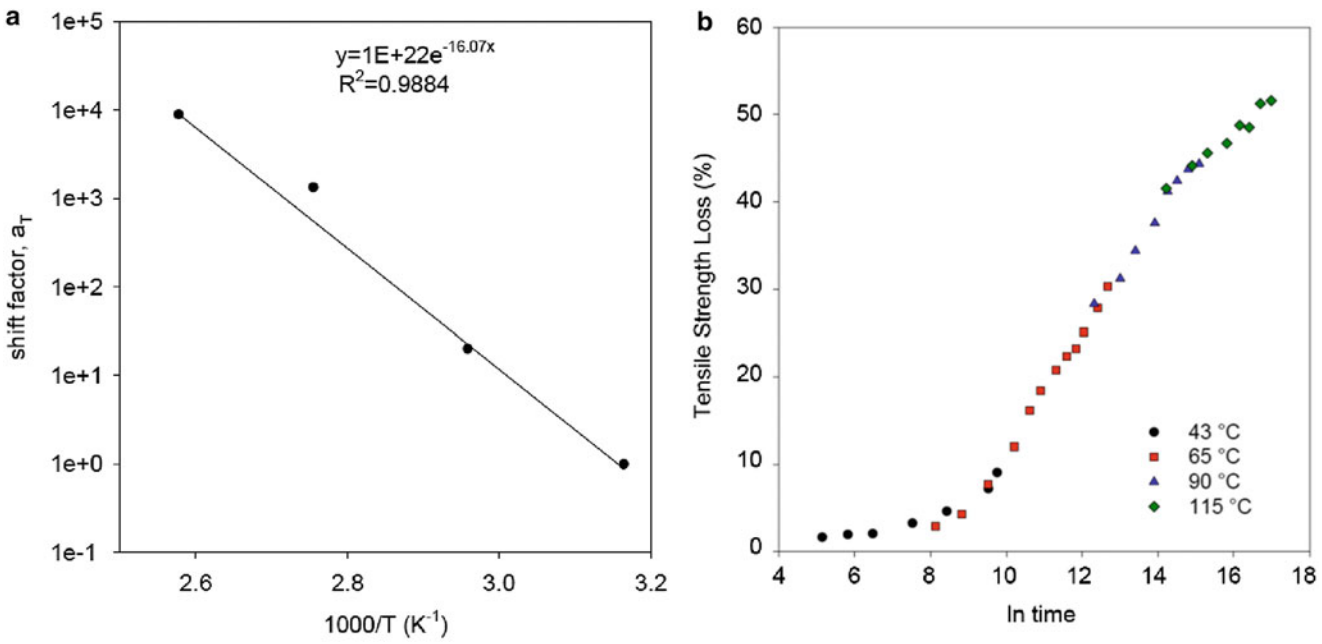

Fig. 43.1 Plot verifying linearity of the shift factors (**a**). Shift factor has no units. Master curve for aging of UHMWPE fibers at the reference temperature of 43 °C. The time axis was in units of hours prior to the natural log being taken. (**b**). *Error bars* are not shown for clarity of presentation in either graph. For both graphs, the standard uncertainty in the data is approximately 5 %

using 43 °C as the reference temperature, and then horizontally shifting the higher temperature aging data until they superimposed smoothly to form a single curve [3, 25, 26]. The amount that each curve must be shifted is called the *shift factor*, a_t, and is used in Eq. 43.1 to determine the activation energy of the aging mechanism.

$$\ln a_t = \ln \frac{t_t}{t_0} = -\frac{E_a}{R}\left(\frac{1}{T_{ref}} - \frac{1}{T}\right) \tag{43.1}$$

Where a_t is the *shift factor*, t_0 is the *aging time of reference temperature*, t_t is *aging time after shifting*, E_a is the *activation energy*, R is the *universal gas constant*, and T_{ref} is the *reference temperature*. The value of the activation energy as calculated by Eq. 43.1 is found to be 140 kJ/mol, with a standard deviation of approximately 15 % (based on the original error in the tensile strength measurements combined with the error in the shift factor calculation), which is approximately 20 kJ/mol higher than previously published results from Chabba [3], which were based on oxygen uptake. This difference is within the error of this measurement. The shift factors are plotted to show linearity in Fig. 43.1a. Assuming that the master curve presented in Fig. 43.1b is valid, one might predict that it will take approximately 36 years for the tensile strength of this UHMWPE yarn to fall by 30 % at 43 °C.

Hydroperoxides were not detected in the ATR-FTIR spectra of the UHMWPE fibers during aging. Gugumus [27–30] has previously shown that FTIR can be used to measure hydroperoxide in LDPE and HDPE films, and that hydroperoxide concentration decreases linearly with film thickness. Temperature has been shown to have a complicated effect on the formation and destruction of free and associated hydroperoxides, which may hinder our ability to resolve any hydroperoxides, even though they are expected to form. The degree of oxidation increases with aging temperature and time, and is identified by the formation of a new peak at 1737 cm^{-1}, which is assigned to an ester. Another shoulder peak is observed at 1713 cm^{-1}, which is identified as a ketone. At least two peaks are superimposed to form a complex FTIR spectrum. The absorption band around 1737 cm^{-1} is not attributed to a single oxidation product. This band is indicative of the presence of oxidation products from the decomposition of peroxides and hydroperoxides. The baseline oxidation level for this material is evident by the presence of a peak at 1737 and 1713 cm^{-1} in the unaged material. It is possible that the peak at 1737 cm^{-1} represents the hindered phenol of an antioxidant. If the antioxidant is present in the baseline material, there are implications for interpreting the oxidation products.

The peak analysis presented for 43 °C in Fig. 43.2 indicates an increasing of the shoulder at 1713 cm^{-1}. The peak at 1737 cm^{-1} appears to shrink with exposure time. This contradicts the production of multiple hydroxyl containing oxidation products that would increase this peak with time. One suggestion is the decrease in the peak at 1737 cm^{-1} is the consumption of an antioxidant ester. The oxidation analysis of 1713 cm^{-1} (discussed later) does not indicate an induction time for the production of the main ketone band that would be expected for the presence of an antioxidant. However, despite the fact that the oxidation products will continue to increase through various oxidation reactions in the amorphous structure, they will

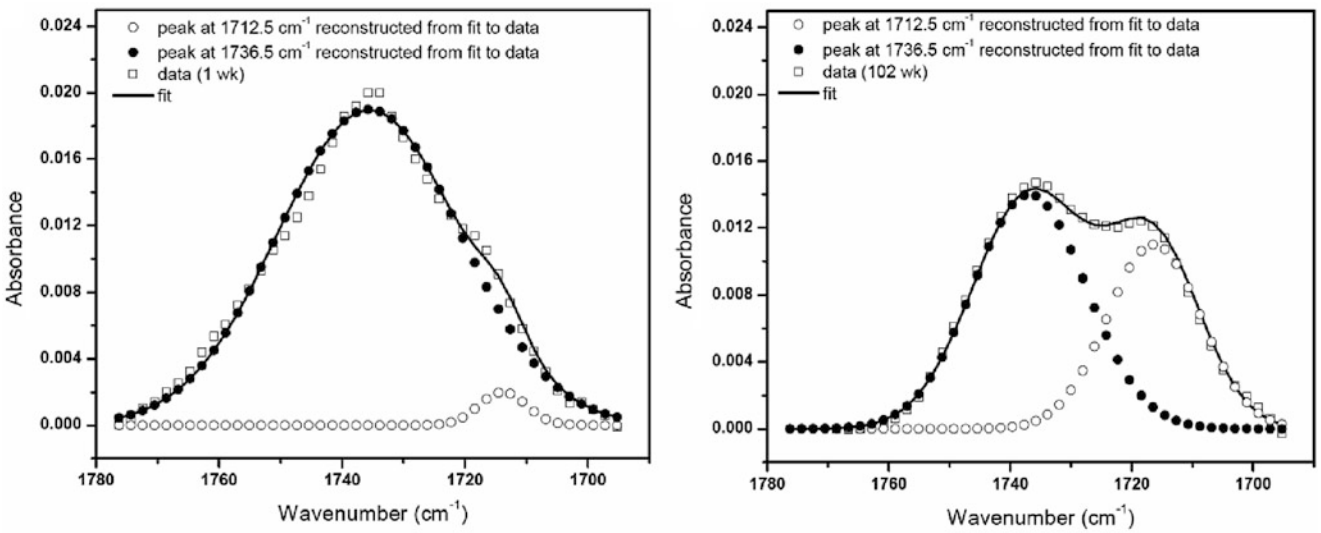

Fig. 43.2 Curve-resolved FTIR spectra of UHMWPE fiber aged at 43 °C for 1 week (*left*) and 102 weeks (*right*), scale enlarged to show the 1680 to 1780 cm^{-1} region, where oxidation appears, more clearly. The units of absorbance are arbitrary. The shoulder of this peak is resolved to elucidate the formation of a new peak around 1713 cm^{-1}. Standard uncertainty in these measurements is approximately 4 cm^{-1}

also decompose continuously to CO_2, CO, and even OH radicals. It should also be mentioned that these reactions take place in the limited amorphous part of the polymer and at the crystalline interfaces. These factors affect the interpretation of the FTIR spectrum in this region. In this material, the available oxygen is limited because the diffusion of oxygen is much lower than the consumption due to the higher crystallinity of this material. Currently, the exact nature of the changes at 1737 cm^{-1} is unknown and remains a convolution of potential degradation or protection mechanisms. The intensity of the ketone group generally increases with increasing aging time at 43 °C. Thus, the degree of oxidation of UHMWPE fibers could potentially be quantified by introducing the oxidation index (OI), as used in other artificial aging applications for bulk UHMWPE [2, 11, 20]. For the purposes of this study, the peak at 1472 cm^{-1} was used as the reference peak, and the OI is the peak area at 1713 cm^{-1} divided by the peak area at 1472 cm^{-1}. The OI increased moderately at the lower aging temperatures of 43 °C and 65 °C. For these aging conditions, the OI increased from 0.0002 to 0.0243 and 0.0249, for 43 °C and 65 °C, respectively. For the higher aging temperatures, the OI increased more rapidly. After 17 weeks of aging at 90 °C, the OI increased from 0.0002 to 0.0385, and for 17 weeks of aging at 115 °C, the OI increased from 0.0002 to 0.0471. Generally these results show that the higher the aging temperature, the faster the drop in tensile strength, regardless of the OI value. This result might be indicative of changes in morphology at these higher aging temperatures, as described previously.

DSC thermograms of UHMWPE fibers aged at all available combinations of temperature and time showed multiple broad melting peaks with overlapping regions between 139 °C and 158 °C. Typically, the calculation of percent crystallinity using a literature value from DSC data (243.4 J/g [3]) is an excellent way to assess relative changes between samples with aging. However, for these UHMWPE fibers, the overall percent crystallinity of the fibers as calculated by this method was nearly unchanged. Figure 43.3 shows that while the overall crystallinity remains about the same between the aged and unaged fibers, there is a change in the shape of the melting endotherm. Therefore, a peak deconvolution method was used to separate the melting endotherm into several discrete peaks which can potentially be assigned to different polyethylene crystal structures. According to previously published results, the monoclinic phase appears at a lower temperature range [31, 32]. It was assumed that monoclinic transformed into orthorhombic phase [33]; therefore, the second peak in the deconvolution plot was assigned to the monoclinic phase. The third peak, which took up over 50 % of total area, was assigned to the main orthorhombic crystal phase. The last peak at 160 °C may represent the phase transition to hexagonal, which only forms when the fibers are heated under constraint. The lamellar likely thickens due to the long duration high temperature exposure of the sample. However, the change in the phase transition region is not well understood. XRD was also performed to better understand how aging affects the morphology of these fibers.

XRD was also performed to further the understanding of the morphological changes in the UHMWPE due to aging. Figure 43.4 shows equatorial wide angle X-ray scattering (WAXS) from UHMWPE fibers in various aging conditions, taken from 2D data . These conditions are unaged samples, samples aged at 43 °C for 21 weeks, samples aged at 65 °C for 102 weeks, samples aged at 65 °C for 73 weeks, samples aged at 90 °C for 17 weeks, and samples aged at 115 °C for 8 weeks.

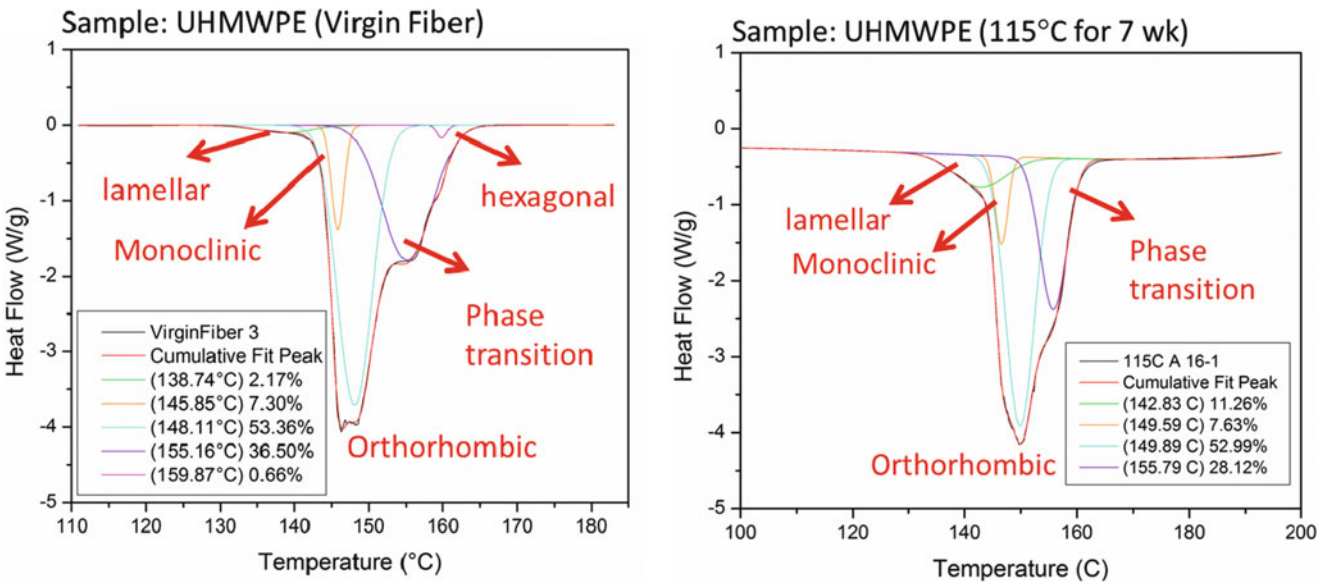

Fig. 43.3 DSC thermograms of unaged UHMWPE fiber (*left*) and aged at 115 °C for 7 weeks (*right*). The melting endotherm was deconvolved and assigned to various phases using literature values. Standard uncertainty in this measurement is approximately 5 %. Aging appears to cause an increase in the lamellar phase, but the mechanism of other changes is unclear

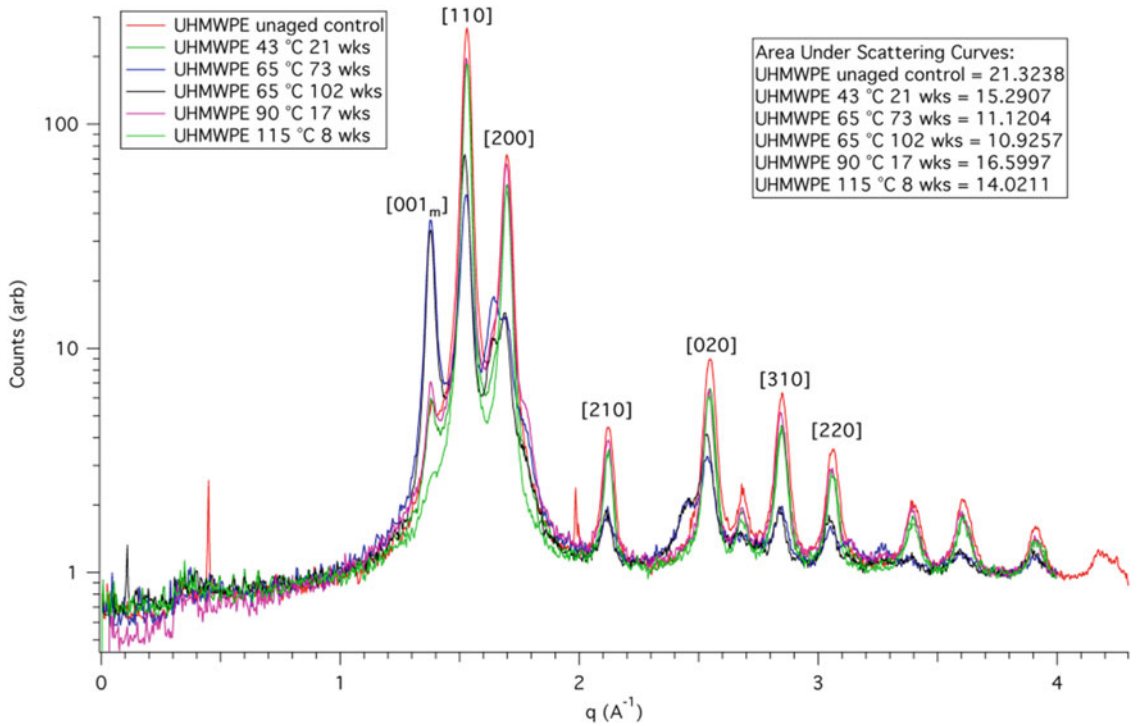

Fig. 43.4 Equatorial wide angle X-ray scattering (*WAXS*) from UHMWPE fibers in various aging conditions, taken from 2D data . These conditions are unaged samples, samples aged at 43 °C for 21 weeks, samples aged at 65 °C for 102 weeks, samples aged at 65 °C for 73 weeks, samples aged at 90 °C for 17 weeks, and samples aged at 115 °C for 8 weeks. Relative standard uncertainty in this measurement is approximately 5 %. Aging at the higher temperatures appears to cause a loss of orientation, and a transition from a mostly orthorhombic structure to monoclinic or hexagonal phase

Increases are seen in the scattering of the [1 0 0] hexagonal peak for fibers aged at 65 °C for 73 and 102 weeks, indicated by the blue and green curves in Fig. 43.4. There are also corresponding decreases in the scattering intensity for the orthorhombic planes at [1 1 0] and [2 0 0], most likely due to the loss of orientation smearing the intensity out azimuthally. Previous work [34] has also shown the formation of a metastable hexagonal phase upon heating of solution-crystallized polyethylene samples, although it is unclear why this result is most pronounced for the fibers heated to 65 °C and not to higher temperatures.

Further examination of WAXS data show the formation of shoulders to the left and right of the [2 0 0] peak. These shoulders may be due to the formation of a second hexagonal peak. The peaks at $[1\ 0\ 0]_h$, [1 1 0], and [2 0 0] are very close together, so it is difficult to discern peak overlap from amorphous (which is typically seen as a broad, ill-defined peak in WAXS). There is likely a contribution from both the amorphous region and the overlap of these peaks that result in broad peaks that do not reach the baseline. The shoulder may also be due to the formation of small crystallites due to recrystallization of the sample after aging at the elevated temperatures, which is akin to annealing of these samples. Overall, the shapes of the peaks appear to broaden and become less intense with increased aging time or temperature. In general, the WAXS results verify that the UHMWPE fibers lose orientation due to aging, and that there is the possible formation of a hexagonal phase. Further experimental work is necessary to fully understand the changes in morphology in UHMWPE fibers due to elevated temperature aging.

43.4 Conclusions

In summary, when exposed to elevated temperatures for long periods of time, UHMWPE fibers lose tensile strength. The inclusion of accelerated aging temperatures that encompass the alpha-relaxation temperature of polyethylene introduced physical effects in addition to oxidative degradation that complicate a simple explanation of the changes in properties. Assuming that the shift factors that were used in this analysis are correct, it would take approximately 36 years for the tensile

strength of this UHMWPE yarn to fall by 30 % at 43 °C. Molecular spectroscopy verified that all samples were oxidized by the elevated temperature exposure, and an analysis of the crystallinity showed that the morphology of these fibers is also changing, although the exact mechanisms have yet to be determined. These factors should all be considered when using these fibers in conditions in which they might be exposed to elevated temperatures for long periods of time.

References

1. Goavert, L., Lemestra, P.: Colloid Polym. Sci. **270**, 455–464 (1992)
2. Karacan, I.: Fibres Text. East. Eur. **13**, 15–21 (2005)
3. Chabba, S., et al.: J. Mater. Sci. **42**, 2891–2893 (2007)
4. Greenwood, J., Rose, P.: J. Mater. Sci. **9**, 1809–1814 (1974)
5. Chin, J., et al.: J. Appl. Polym. Sci. **113**, 567–584 (2009)
6. NIJ: Status Report to the Attorney General of Body Armor Safety Initiative Testing and Activities. NIJ, Washington, DC (2004)
7. NIJ.: Supplement I: Status Report to the Attorney General of Body Armor Safety Initiative Testing and Activities. U.S. Department of Justice, Office of Justice Programs, Washington, DC (2004)
8. NIJ.: Third Status Report to the Attorney General of Body Armor Safety Initiative Testing and Activities. U.S. Department of Justice, Office of Justice Programs, Washington, DC (2005)
9. Costa, L., et al.: Polym. Degrad. Stab. **58**, 41–54 (1997)
10. Holmes, G., et al.: Polym. Compos. **31**, 879–886 (2010)
11. Costa, L., et al.: Polym. Degrad. Stab. **55**, 329–338 (1997)
12. Bernstein, R., et al.: Polym. Degrad. Stab. **88**, 480–488 (2005)
13. Gillen, K.T, et. al.: In: 39th International Symposium of the Society of the Advancement of Material and Process Engineering and Exhibition, Anaheim, CA, USA, 11–14 April 1994
14. Gillen, K.T., Clough, R.I.: Polym. Degrad. Stab. **24**, 137–168 (1989)
15. Taddei, P., et al.: Biomacromolecules **7**, 1912–1920 (2006)
16. Cunniff, P.: In: 18th International Symposium on Ballistics, pp. 1302–1310. San Antonio, TX (1999)
17. ISO Standard 2062: Textiles—Yarns from Packages: Determination of Single-End Breaking Force and Elongation at Break. International Organization for Standardization (ISO), Geneva (1993)
18. Li, S., Burstein, A.: J. Bone Joint Surg. Am. **76**, 1080–1090 (1994)
19. del Prever, E., et al.: Biomaterials **17**, 873–878 (1996)
20. Tashiro, K., et al.: Macromolecules **29**, 7460–7469 (1996)
21. Roe, R.: Methods of X-Ray and Neutron Scattering in Polymer Science. Oxford University Press, Oxford (2000)
22. Dijkstra, D., Pennings, A.: Polym. Bull. **19**, 73–80 (1988)
23. Forster, A. L., Rice, K. D., Riley, M. A., Messin, G., Petit, S. H., Clerici, C., Holmes, G. A., Chin, J. W.: Development of Soft Armor Conditioning Protocols for NIJ 0101.06: Analytical Results. NIST Interagency/Internal Report (NISTIR) – 7627. US Department of Commerce, Washington, DC (2009)
24. Dijkstra, D., Pennings, A.: Polym. Bull. **19**, 65–72 (1988)
25. Menczel, J., Prime, R.: Thermal Analysis of Polymers: Fundamentals and Applications. Wiley, Hoboken, NJ (2009)
26. Cooper, S., Tobolsky, A.: J. Appl. Polym. Sci. **10**, 1837–1844 (1966)
27. Gugumus, F.: Polym. Degrad. Stab. **49**, 29–50 (1995)
28. Gugumus, F.: Polym. Degrad. Stab. **74**, 327–339 (2001)
29. Gugumus, F.: Polym. Degrad. Stab. **76**, 329–340 (2002)
30. Gugumus, F.: Polym. Degrad. Stab. **77**, 147–155 (2002)
31. Kwon, Y.K.: Polymer **41**, 6237 (2000)
32. Pak, J., Wunderlich, B.: Thermochim. Acta **421**, 203–209 (2004)
33. Fu, Y.: J. Macromol. Sci. Part B Phys. **35**, 37 (1996)
34. Rastogi, S., et al.: Macromolecules **31**, 5022–5031 (1998)

Chapter 44
Age Deformation After Stamping of Carbon Fiber Reinforced Polycarbonate Laminates

Masayuki Nakada, Hiroaki Ozaki, and Yasushi Miyano

Abstract This study was concerned with the effect of stamping condition on age deformation after stamping for textile carbon fiber reinforced Polycarbonate (CF/PC) laminates. The textile CF/PC laminates were stamped to hat shape under various stamping temperatures. The specimens were held at several exposure temperatures into the constant temperature chamber after stamping process and the variations of hat angle against exposure time were measured. As results, it is cleared that the age deformation is suppressed with increasing stamping temperature. The variation of hat angle as the long-term dimensional stability can be predicted from the measured data at elevated temperatures based on the time-temperature superposition principle which is held for the viscoelasticity of matrix polycarbonate.

Keywords Carbon fiber reinforced polycarbonate • Stamping • Age deformation • Time-temperature dependence • Viscoelasticity

44.1 Introduction

Carbon fiber reinforced thermoplastics (CFRTP) present important benefits of high recyclability and high productivity in addition to light weight, high strength, and high rigidity, which are demanded for structural materials. Therefore, CFRTP is expected to the applications in the field of automobiles and others because of improvement of fuel efficiency and reduction of forming cost.

CFRTP which consists of textile carbon fiber is useful as structural materials having more high strength and high rigidity. Stamping is generally used for forming the textile CFRTP laminates. The most important technical issue of stamping is to realize structural dimensional accuracy as well as high strength. Numerous reports have described these problems [1–5]. Also, the time dependent age deformation as long-term dimensional stability after stamping is an important issue. However, there are no researches studying the long-term dimensional accuracy and stability.

This study assessed the effects of stamping conditions on dimensional accuracy and age deformation after stamping for textile CFRTP laminates based on the viscoelasticity of matrix resin. The CFRTP laminates which consist of plain-woven carbon fiber and polycarbonate (PC) were employed in this study. The carbon fiber reinforced polycarbonate (CF/PC) laminates were stamped to hat shapes at several stamping temperatures between the glass transition temperature T_g and the melting temperature T_m of PC. After stamping, the hat shaped CF/PC laminates were exposed at several constant temperatures without constraint for acceleration of the age deformation. Then the age deformation which is the hat angle variation was measured. The effect of stamping temperature on age deformation after stamping is discussed based on the viscoelasticity of PC matrix.

44.2 Viscoelastic Model for Spring Back and Age Deformation

The viscoelastic model of thermoplastics is presented by a spring of Hookean elasticity and a dashpot of Newtonian viscosity, as shown in Fig. 44.1, where E_g is the elastic modulus of glassy state, E_r and η_r respectively represent the elastic modulus and the viscosity of the rubbery state, and η_m is the viscosity of the liquid state. In the glassy state, because the

M. Nakada (✉) • Y. Miyano
Materials System Research Laboratory, Kanazawa Institute of Technology, 3-1 Yatsukaho, Hakusan 924-0838, Japan
e-mail: nakada@neptune.Kanazawa-It.aC.jp

H. Ozaki
Composite Machinery Department, Tsudakoma Corporation, 500 Miyanagaichimachi, Hakusan 924-0016, Japan

C. Ralph et al. (eds.), *Mechanics of Composite and Multi-functional Materials, Volume 7*,
Conference Proceedings of the Society for Experimental Mechanics Series, DOI 10.1007/978-3-319-21762-8_44

dashpots η_r and η_m are fixed, the elastic modulus of the model is E_g. In the rubbery state, because the dashpot η_m is fixed and the dashpot η_r is free, the elastic modulus of the model is E_r ($E_r \ll E_g$). In the liquid state, because the dashpots η_r and η_m are free, the elastic modulus of the model is zero. The temperature dependence of elastic modulus of this model is shown on the right side of Fig. 44.1. The variables T_g and T_m, respectively, denote the glass transition temperature and the melting temperature.

Figure 44.2 shows the strain of the specimens during stamping and after stamping. The specimens are suppressed to the strain ε_0 by stamping and those are removed from the mold at $t = s$. The variable T_s shows the stamping temperature. When T_s is higher than T_m, the permanent set occurs as shown by (1) $T_m < T_s$ in Fig. 44.2 because the dashpot η_m moves and the two springs E_g and E_r do not move during the stamping as shown in Fig. 44.1. When T_s is between T_g and T_m, the spring back occurs immediately after stamping. Then the age deformation occurs as shown by (2) $T_g < T_s < T_m$ in Fig. 44.2. The dashpot η_m does not move, but the two springs E_g and E_r move during the stamping. Therefore, the spring back occurs by the spring E_g and the age deformation occurs by the spring E_r and the dashpot η_r. Because the age deformation is explainable by a simple viscoelastic model, it can be expected that the long-term age deformation is predicted from the short-term age deformation measured at elevated temperatures based on the time-temperature superposition principle (TTSP) for the viscoelasticity of matrix resin. When T_s is less than T_g, the spring back only occurs as shown by (3) $T_s < T_m$ in Fig. 44.2. Neither the dashpot η_r nor η_m moves while the spring E_g only moves during stamping.

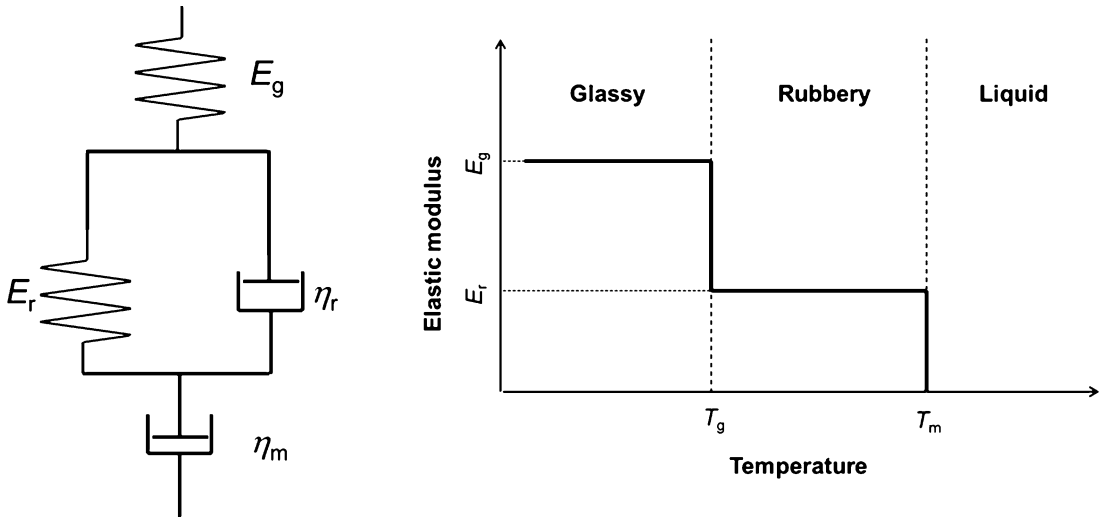

Fig. 44.1 Temperature dependence of elastic modulus of model

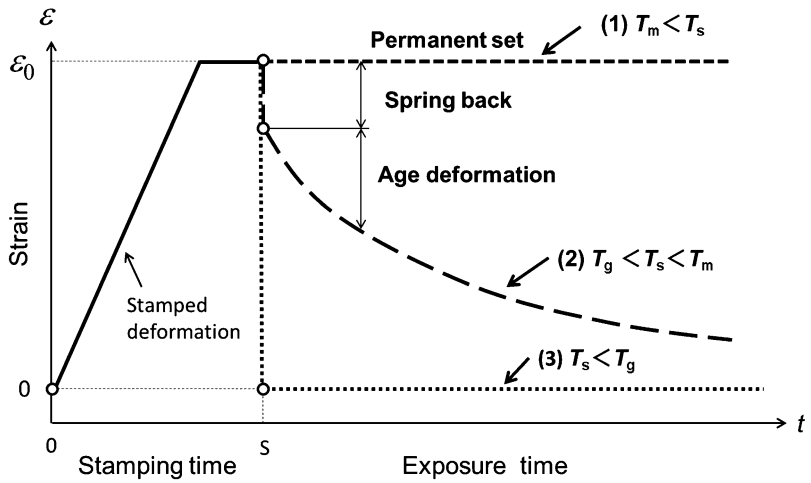

Fig. 44.2 Model for spring back and age deformation after stamping

44.3 Experiments and Results

44.3.1 Preparation of CF/PC Laminates

Carbon fiber (CF) textile sheets and polycarbonate (PC) films were used as CFRTP reinforcements and matrix materials. The CF textile sheet is a plain weave fabric with weft and warp ratio 1:1 produced using PAN-based carbon fibers with fabric areal weight of 200 g/m^2. The PC film thickness is 0.15 mm. The mechanical properties of CF and PC are presented in Table 44.1. Before molding the CF/PC laminates, PC films were dried for 2 h at 120 °C by vacuuming. Eight CF textile sheets and nine PC films were laminated alternately, and then CF/PC laminates were molded by hot press method. The molding temperature, pressure, and time were 280 °C, 3 MPa, and 30 min, respectively.

44.3.2 Determination of Stamping Temperature

To evaluate the viscoelastic behavior of PC, a Dynamic Temperature Ramp Test was conducted using a dual cantilever bending mode with a dynamic mechanical analyzer (DMA) (RSA-III; TA Instruments). Testing conditions of strain, support span, and frequency were, respectively, 0.01 %, 37.5 mm, and 1.0 Hz. The specimen length, width, and thickness were, respectively, 50 mm, 6.7 mm, and 2 mm.

Figure 44.3 presents the temperature dependence of storage modulus *E*' [6]. The *E*' drops drastically at around 140 °C. This result suggests that the glass transition temperature T_g is approximately 150 °C, and that the glassy region is below 140 °C, and that the rubbery region is between 140 and 160 °C. The liquid region is higher than 160 °C. Therefore, stamping temperatures T_s were selected as 140, 160, 180, and 200 °C.

Table 44.1 Mechanical properties of carbon fiber and PC

Materials	Density (g/cm^3)	Tensile modulus (GPa)	Tensile strength (MPa)	Breaking elongation (%)
Carbon fiber	1.80	230	3450	1.5
Polycarbonate	1.20	2.3	60	10

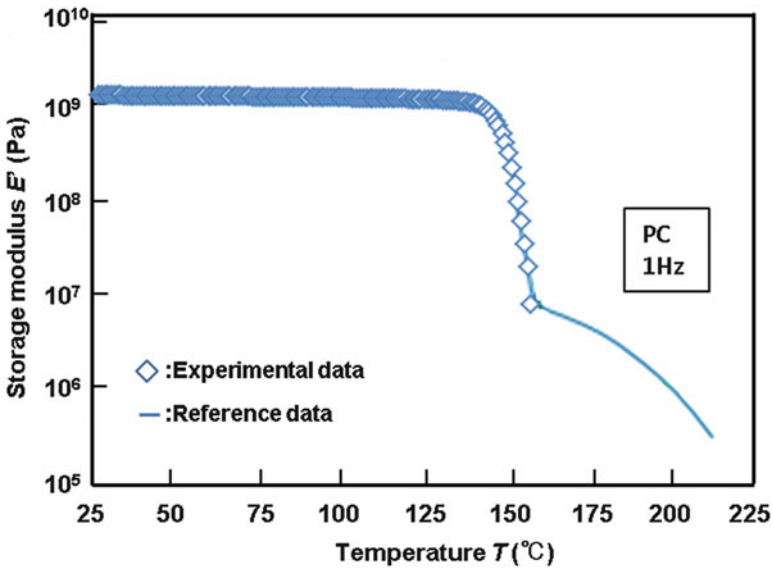

Fig. 44.3 Temperature dependence of storage modulus *E*' [6]

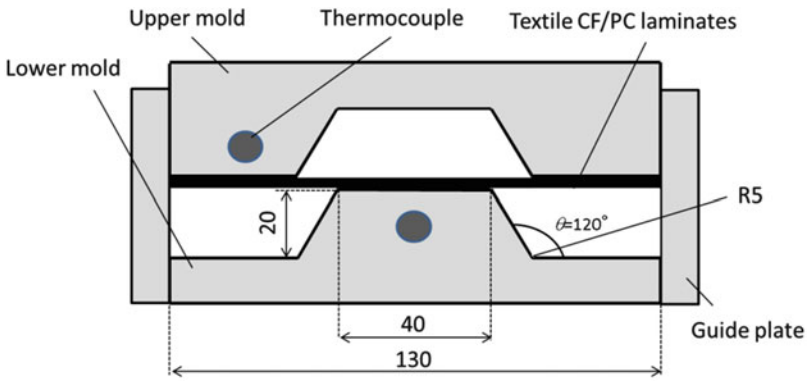

Fig. 44.4 Textile CF/PC laminates stamping system

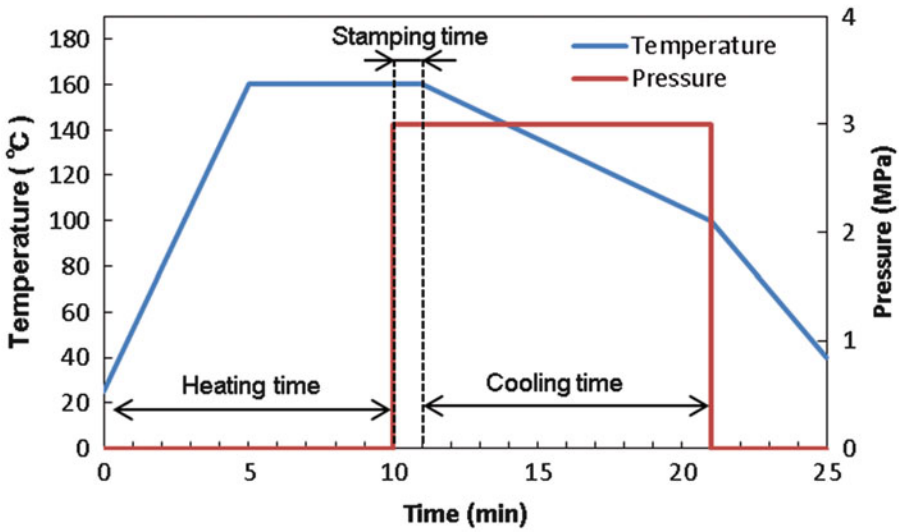

Fig. 44.5 Temperature and pressure histories in the stamping process for the case of $T_s = 160$ °C

44.3.3 Stamping of CF/PC Laminates

The matched mold for stamping is shown in Fig. 44.4. The stamping temperature was monitored by two thermocouples as shown in Fig. 44.4. To heat the mold, we used the hot press with cooling system by water. Before the experiment, the relationships of the mold temperature and the materials temperature were checked by thermocouples. Firstly, the mold was heated to stamping temperature by hot press. And the CF/PC laminates were placed in the mold heated to the stamping temperature as shown in Fig. 44.4. Then the CF/PC laminates were stamped by hot press. Figure 44.5 shows the temperature and pressure histories in the stamping process for the case of $T_s = 160$ °C. The CF/PC laminates were stamped to a hat shape under various temperatures for a single pressure and holding time. The CF/PC laminates were heated in 10 min and pressed in 1 min. Then the mold was cooled to 100 °C in pressing. The product was removed from the mold. Figure 44.6 shows the product stamped at 180 °C.

44.3.4 Observation of Damage of Stamped CF/PC Laminates

Figure 44.7 shows a cross-section of the stamped CF/PC laminates. Delaminations were observed in the specimens stamped at 140 °C, but no delamination or fracture was found in the specimens stamped at temperatures of 160 °C and higher. Furthermore, the resin flow was observed in the edge face of the specimen stamped at 200 °C. The disorder of fiber direction was observed in the specimen stamped at 200 °C.

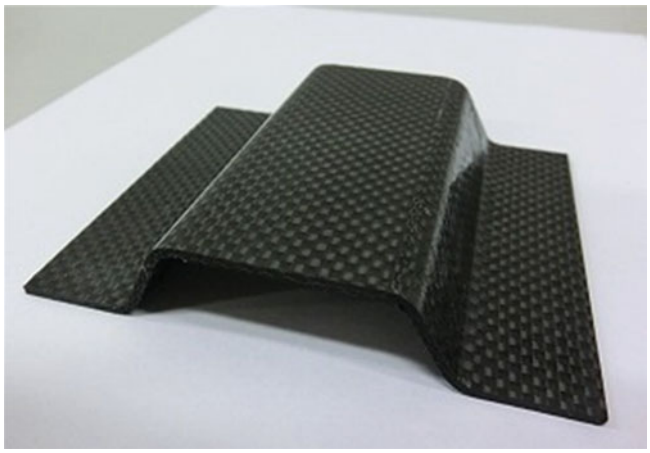

Fig. 44.6 Specimen stamped at 180 °C

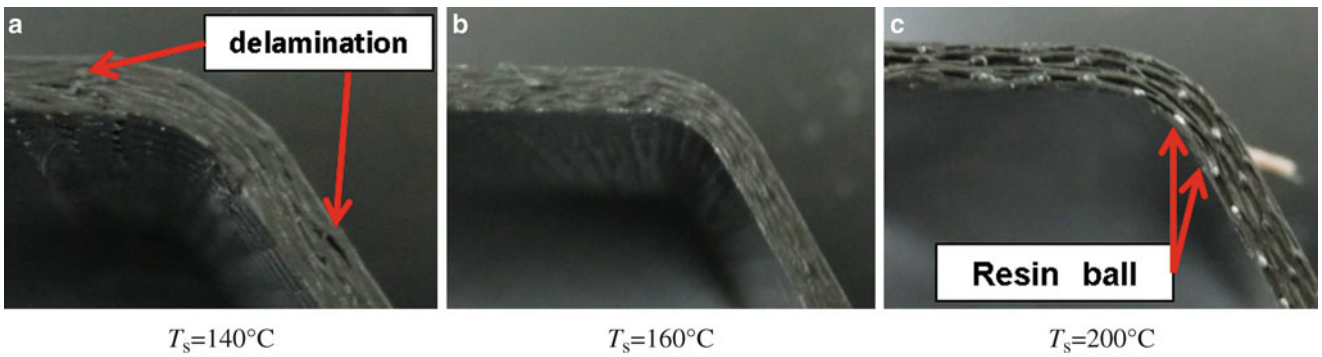

Fig. 44.7 Cross-section of specimens stamped CF/PC laminates

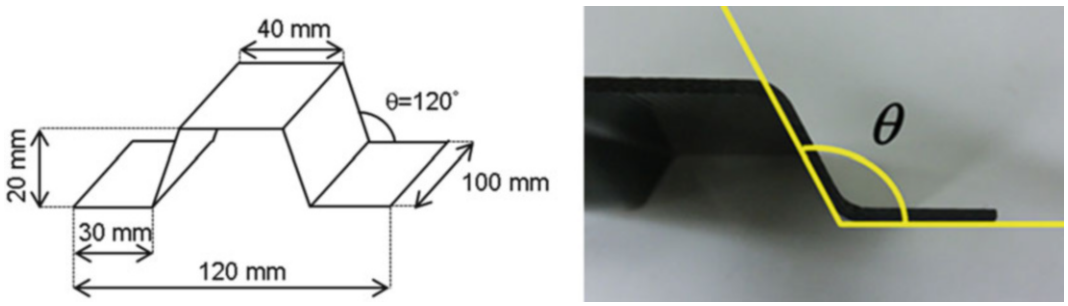

Fig. 44.8 Configuration of specimen and method of measuring angle θ

44.3.5 Spring Back and Age Deformation

As shown in Fig. 44.8, the variation of angle θ with age deformation was measured using image analysis software from photographs of stamping specimen cross-sections. Reference angle θ was 120°. Angle θ was measured using image analysis software with accuracy of ±0.25°. Figure 44.9 shows angle θ measured immediately after stamping at several stamping temperatures T_s. Angle θ of specimens stamped at 140 °C was larger than that of other specimens. Therefore, a spring back occurred in the specimen stamped at 140 °C. The reason is that many spring ingredients remain in the resin, as described in the previous section.

Stamped specimens were exposed at a constant temperature of $T_b = 140$ °C for acceleration of the age deformation. Then the age deformation was measured at room temperature. Figure 44.10 displays the variation of angle θ versus exposure time

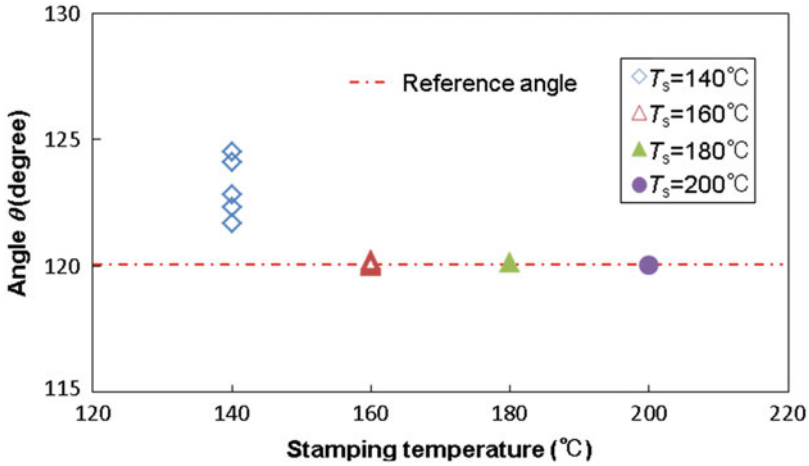

Fig. 44.9 Spring back for angle θ against stamping temperature

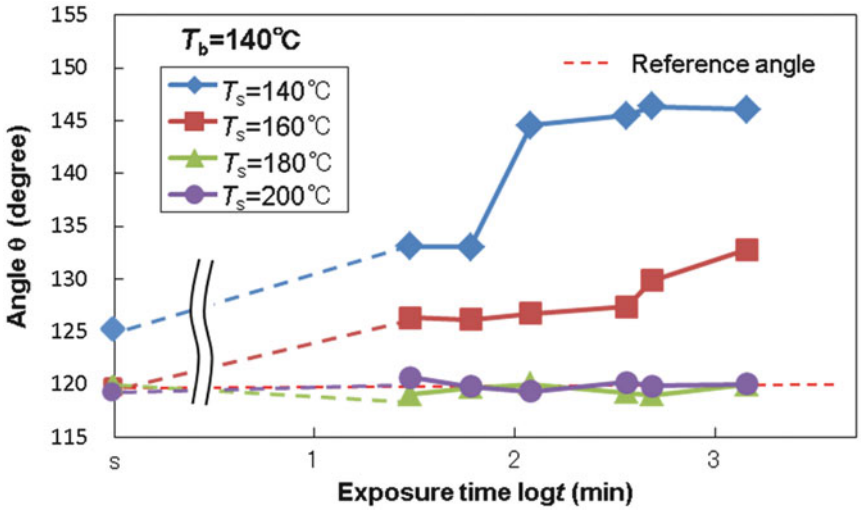

Fig. 44.10 Variation of angle θ against exposure time for various stamping temperature

at $T_b = 140\,^{\circ}C$. In this figure, time point S shows the spring back at room temperature immediately after stamping. From this figure, the angle θ for the specimens stamped at 140 °C and 160 °C is shown to increase with time. The angle θ for the specimens stamped at 180 and 200 °C increases only slightly with time. Therefore, it is cleared that the age deformation is suppressed with increasing stamping temperature.

44.3.6 Long-Term Prediction of Age Deformation

A Frequency/Temperature Sweep Test was conducted using dual cantilever bending mode with DMA. The temperature changed from 25 to 160 °C. The frequency changed from 0.01 to 10 Hz. The left-hand side of Fig. 44.11 shows tan δ versus the inverse of frequency ($1/f$) at various constant temperatures T. The master curve was constructed by shifting tan δ at constant temperatures other than reference temperature $T_0 = 25\,^{\circ}C$ along the log scale of $1/f$. Since the smooth master curve can be obtained, the time-temperature superposition principle is applicable for the viscoelastic behavior of PC.

The time–temperature shift factor a_{T0} (T) is defined by

$$a_{T0}(T) = \frac{t}{t'} \tag{44.1}$$

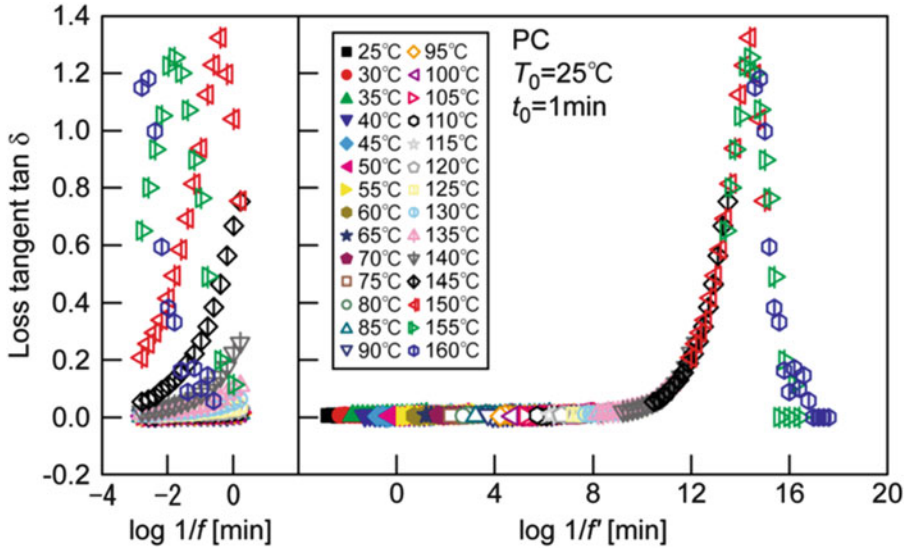

Fig. 44.11 Master curve of tan δ for PC

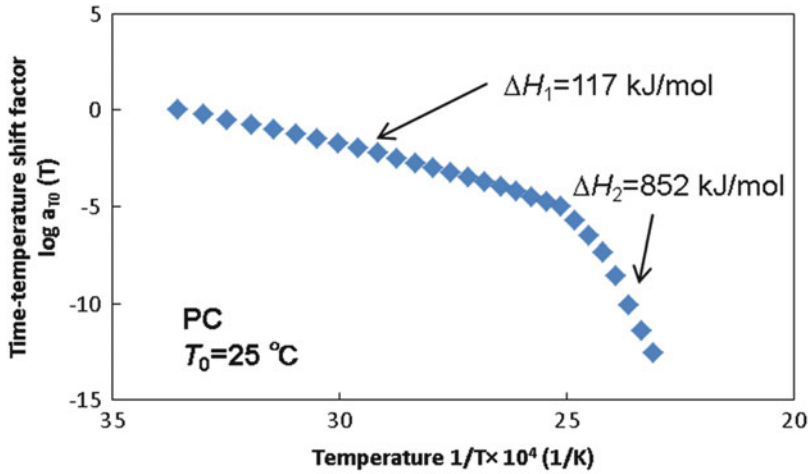

Fig. 44.12 Time-temperature shift factors tan δ for PC

where t' is the corresponding time at $T_0 = 25$ °C, called the reduced time. The shift factors for tan δ obtained experimentally in Fig. 44.11 are presented in Fig. 44.12. All of these shift factors show good quantitative agreement with Arrhenius' equation with different activation energies ΔH_1 and ΔH_2, respectively, as

$$\log a_{T0}(T) = \frac{\Delta H}{2.303G}\left(\frac{1}{T} - \frac{1}{T_0}\right) \tag{44.2}$$

where G is the gas constant 8.314×10^{-3} [kJ/kmol]. In Fig. 44.12, ΔH_1 is 117 [kJ/mol] below 135 °C, and ΔH_2 is 852 [kJ/mol] above 135 °C.

To evaluate long-term dimensional stability, the master curve of angle θ was constructed. The specimens stamped at 160 °C were put into the constant temperature chamber at $T_b = 60$, 100, 120, 130, 135, and 140 °C. Then the angle θ of each was measured, as shown on the left side of Fig. 44.13. The right side of Fig. 44.13 depicts the master curve of angle θ where the reduced time was obtained using the time–temperature shift factors of tan δ for PC shown in Fig. 44.12, when the reference temperature is 80 °C. From Fig. 44.13, the age deformations of angle θ at a reference temperature can be superimposed smoothly each others.

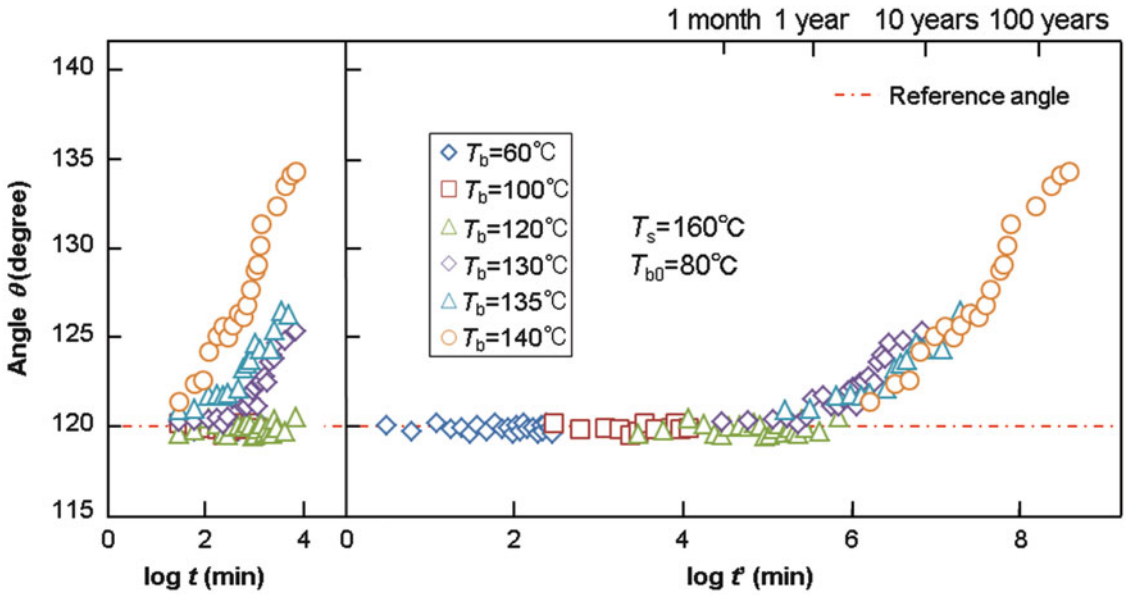

Fig. 44.13 Master curve of angle θ for the specimens stamped at 160 °C

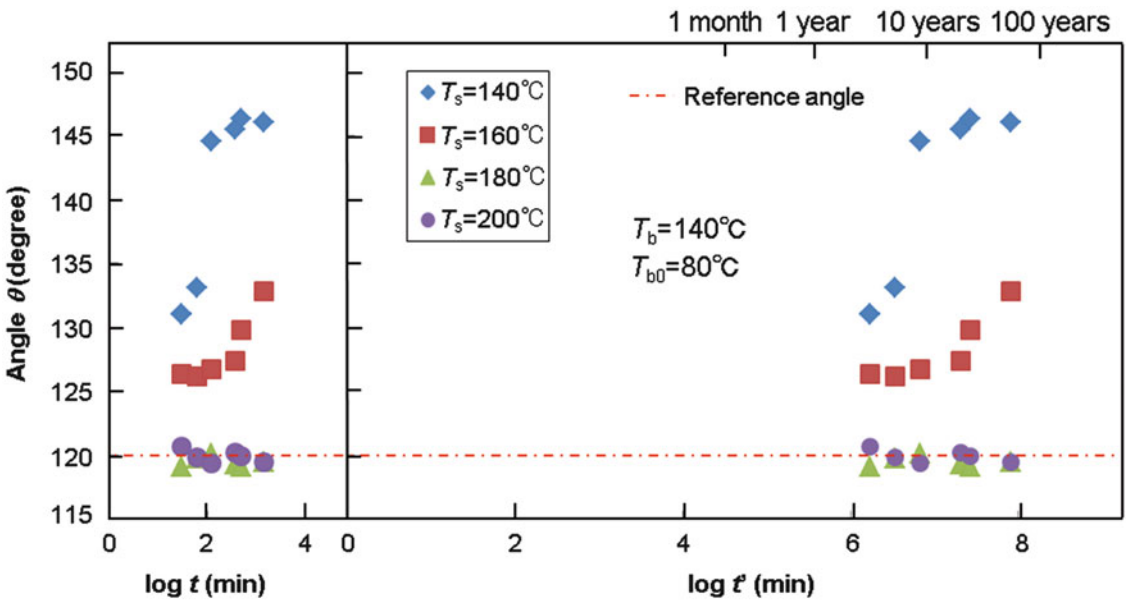

Fig. 44.14 Prediction of long-term age deformation for various stamping temperatures

Figure 44.14 shows the prediction of long-term age deformation for various stamping temperatures. The left side shows the variation of angle θ against exposure time for various stamping temperatures same as data shown in Fig. 44.10. The right side depicts the angle θ against reduced exposure time obtained using the time–temperature shift factors of tan δ for PC shown in Fig. 44.12, when the reference temperature is 80 °C. It can be predicted from this figure that age deformation do not occur for the specimens stamped at 180 and 200 °C.

44.4 Conclusion

The effect of stamping condition on the age deformation after hot stamping for textile CF/PC laminates was assessed based on the viscoelastic behavior of PC matrix. The CF/PC laminates were stamped to a hat shape at various stamping temperatures. Results showed that spring back occurred for the specimens stamped at temperatures below the glass transition temperature in the glassy state. Age deformation occurred for the specimen stamped at a temperature above the glass transition temperature in the rubbery state. The age deformation was suppressed with increasing stamping temperature. Age deformation occurred scarcely for the specimen stamped at the temperature in the liquid state. The long-term age deformation can be predicted from the measured data at elevated temperatures based on the time-temperature superposition principle for the viscoelasticity of PC matrix.

Acknowledgements The authors thank Mr. Makoto Takashima and Mr. Jun Hirai of Tsudakoma Corp., who consulted for this study.

References

1. Hou, M., Friedrich, K.: Appl. Compos. Mater. **1**, 135–153 (1994)
2. Meyer, B.C., Katsiropoulos, C.V., Pantelakis, S.G.: Compos. Struct. **90**, 225–232 (2009)
3. Hwang, S.F., Hwang, K.J.: Compos. Part A **33**, 669–676 (2002)
4. Padovec, Z., Ruzicka, M., Stavrovsky, V.: Appl. Comput. Mech. **6**, 25–34 (2012)
5. Vieille, B., Albouy, W., Taleb, L.: Compos. Part B **45**, 821–834 (2013)
6. TA instruments: RSA-G2 Solid Analyzer Brochure (2011)

Chapter 45
Incremental Formulation for Coupled Viscoelasticity and Hydrolock Effect in Softwood

Sung-Lam Nguyen, Omar Saifouni, and Jean-François Destrebecq

Abstract Specific mechanosorptive tests are first reported for softwood under variable stress and humidity. The test results show the existence of a coupling between the viscoelastic behavior and a "hydrolock" effect, i.e. a temporary locking of the mechanical strain upon drying. Based on thermomechanical considerations, an evolution law is proposed for the hydrolock strain, and a new incremental model for the time dependent hydromechanical behavior of softwood is developed, where the time step is finite, but not necessarily small. This important feature significantly reduces the computational effort while maintaining good accuracy, which can be very beneficial when using the model for numerical simulations of complex wooden structures. Fair agreements with various test results show the efficiency of the model, and its ability to account for the complex behavior of timber structure components when subjected to various loading and humidity conditions.

Keywords Wood • Hydromechanical behavior • Hydrolock strain • Viscoelasticity • Incremental model

45.1 Introduction

Softwood is a lingo-cellulosic material, which is very sensitive to humidity. Its behavior is complicated by the interaction between the mechanical loading and moisture content changes, called mechano-sorptive effect. In the early 60s, Armstrong and Kingston [1] reported a significant increase in the relative creep during the drying phase in relation to that obtaining at constant humidity. Since then, a large number of studies have been devoted to the experimental study and the modeling of this phenomenon. Until now, many works have been performed to find a rational explanation and a satisfactory mathematical solution to describe this complex behavior.

More recently, some approaches to model the mechano-sorptive behavior were based on the assumption of the existence of a "hydrolock effect" [2–6]. This effect was firstly described by Grill [2] who suggested that this phenomenon was resulting from a temporary blocking of the strain in a drying phase under stress. This blocked strain possibly recovered during a wetting phase. Later on, this hydrolock effect was formalized by Dubois *et al.* [3] who used Hooke's law in a wetting phase and a restricted Hooke's law in a drying phase to model this complex behavior. This approach led to synchronized problems that were finally solved by Husson *et al.* [4], where the blocking of strain in the drying phase under stress is ensured by the introduction of a "mechano-sorptive stress". This stress, in addition to the elastic stress, leads to a proportional relationship between the total stress and the stiffness in the drying phase. It may be noted, that this model cannot describe the recoverable phenomenon during the wetting phase in the absence of a mechanical loading. Finally, Colmars *et al.* [5] proposed a discrete model based on stress and strain partition. Although this assumption remains to be justified in the thermodynamic framework, comparing this "box model" with that of Husson showed that the two models are equivalent. It should be noted that the both models assume the existence of a hydrolock effect without clear experimental justification. Additionally, although they are presented in an incremental form, they require retaining the complete history of stress states and moisture content at any location within the body, which makes the calculation process too complex and heavy to be easily applied to real problems.

S.-L. Nguyen (✉) • J.-F. Destrebecq
Clermont Université, Université Blaise Pascal, Institut Pascal, BP 10448, 63000 Clermont-Ferrand, France

CNRS, UMR 6602, Institut Pascal, 63171 Aubière, France
e-mail: sung-lam.nguyen@ifma.fr

O. Saifouni
Clermont Université, Institut Français de Mécanique Avancée (IFMA), Institut Pascal, 63171 Aubière, France

CNRS, UMR 6602, Institut Pascal, 63171 Aubière, France

C. Ralph et al. (eds.), *Mechanics of Composite and Multi-functional Materials, Volume 7*,
Conference Proceedings of the Society for Experimental Mechanics Series, DOI 10.1007/978-3-319-21762-8_45

In this context, a new approach is proposed to take into account the hydrolock effect. The approach is based on a series of tests especially dedicated to evidence the existence of a hydrolock strain causing the blocking effect observed in a drying phase under stress. In the first section, the evolution of the hydrolock strain and its interaction with the viscoelastic strain will be evidenced from test results. In the next section, these observations will be used as a basis for developing an analytical model that takes into account the existence of a hydrolock effect in the hydromechanical behavior of softwood. The introduction of a auxiliary stress justified in the thermodynamic framework, allows solving the recoverable problem of hydrolock strain in the humidification phase. Finally, the analytical model will be turned into an incremental form with finite time step for numerical application. The ability of the model to fairly simulate the hydromechanical behavior of softwood will be discussed in comparison with test results.

45.2 Experimental Evidence of the Hydrolock Effect

An experimental program was carried out in order to evidence the hydrolock effect in silver fir (*Abies alba* Mill.). For this purpose, a mechano-sorptive tensile test was carried out on a small scale specimen (L × R × T: 50 × 3 × 1 mm^3) subjected to cyclic loading and humidity [6]. The stress and the relative humidity were varied stepwise, in such a way as to describe a sinus-like diagram (Fig. 45.1a, b). A 15 min delay was provided between any given stress change and the next relative humidity change, so as to facilitate the identification of their respective effects on the global strain response of the specimen. The elementary contributions of the hydric, the elastic and the viscous effects to the resulting total strain were estimated from a series of preliminary tests. Results from basic creep and relaxation tests showed that the hypothesis of linear viscoelasticity was relevant for the analysis of the rheological effects. Besides, additional tests showed that the creep behavior under varying humidity conditions could be derived from basic creep tests at given levels of steady humidity by means of Boltzmann's superposition principle. By subtracting these elementary contributions from the total resulting strain recorded during the test, it was finally possible to assert the existence of a hydrolock effect as a result of the complex interaction between the mechanical stress and the humidity variations. The resulting evolution of the hydrolock strain is shown on Fig. 45.1c.

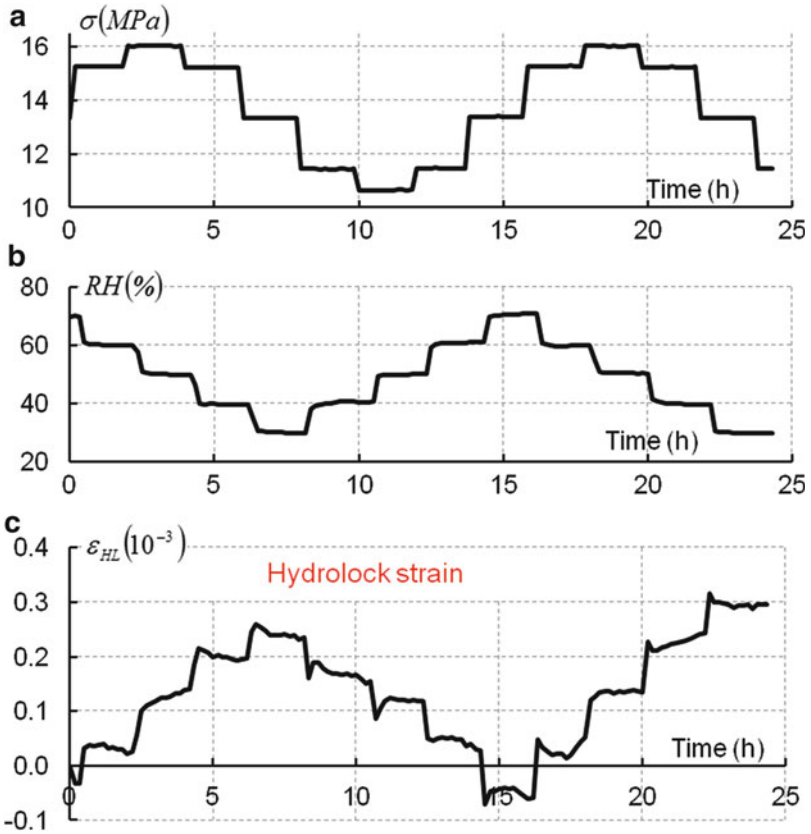

Fig. 45.1 Experimental evidence of the hydrolock effect: (**a**) stepwise cyclic evolution of the applied mechanical stress, (**b**) stepwise cyclic evolution of the applied relative humidity, (**c**) evidenced evolution of the hydrolock strain, as a result of the mechano-sorptive test

The main feature can be summarized as follows. (i) For steady stress state ($\dot{\sigma}$=0), the hydrolock strain arises and develops instantly for each variation of relative humidity in the drying phase ($w < 0$); it evolves stepwise in the course of time. (ii) At a steady moisture content (w=0), the hydrolock strain is not modified by a stress variation ($\dot{\sigma} \neq 0$); in other words, the hydrolock strain can be considered independent of stress and time as far as the moisture content doesn't change. (iii) The hydrolock strain (when it exists) progressively vanishes when the moisture content w returns to its initial value $\overline{w}$ at the beginning of the drying phase under stress. These features are in accordance with the general principles that govern the mechano-sorptive behavior [2–5]. They will serve in later for the construction of the new model.

45.3 Analytical Model

The model bases on the hypothesis of strain partition which was validated from the tests in the previous section:

$$\dot{\varepsilon}_t = \dot{\varepsilon}_e + \dot{\varepsilon}_{HL} + \dot{\varepsilon}_{ve} + \dot{\varepsilon}_w \tag{45.1}$$

where ε_t is the total strain, ε_e is the elastic strain, ε_{HL} is the hydrolock strain, ε_w is a shrinkage-swelling strain which depends on moisture content changes and ε_{ve} is a pure viscoelastic strain which depends on the level and the duration of loading. This hypothesis can be schematized by the analogue model shown in Fig. 45.2. The validity of Eq. (45.1) and the analogue model need be justified in a thermodynamic framework.

45.3.1 Thermodynamic Framework

The justification bases on the choice of a thermodynamic potential, as a function of the state variables. The state variables necessary to describe the hydroelastic behavior at constant temperature (ignoring the viscous effect) are the total strain ε_t and the moisture content w. An additional state variable ε_{HL} is introduced to account for the hydrolock effect. Finally, the free energy is expressed as the sum of two distinct parts, as follows:

$$\psi(\varepsilon, w, \varepsilon_{HL}) = \psi_e(\varepsilon, w) + \psi_{HL}(\varepsilon_{HL}) \tag{45.2}$$

The third state law provides a relationship between the additional state variable ε_{HL} and its associated variable $\tilde{\sigma}$

$$\tilde{\sigma} = \frac{\partial \psi}{\partial \varepsilon_{HL}} = \frac{d\psi_{HL}}{d\varepsilon_{HL}} \quad \Rightarrow \quad \tilde{\sigma} = g(\varepsilon_{HL}) \tag{45.3}$$

In this expression, $\tilde{\sigma}$ appears as a auxiliary stress without special significance. Equation (45.3) shows the existence of a bi-univocal relation between ε_{HL} and $\tilde{\sigma}$, which can also be written

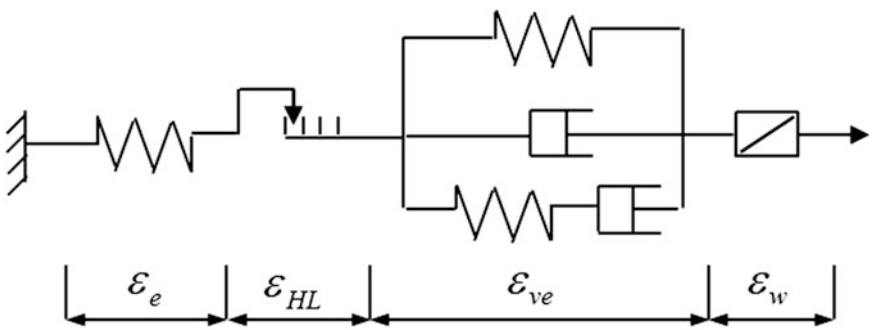

Fig. 45.2 Analogue model: ε_e elastic strain, ε_{HL} hydrolock strain, ε_{ve} pure viscoelastic strain, ε_w hydric strain

$$\varepsilon_{HL} = g^{-1}(\tilde{\sigma}) \tag{45.4}$$

Equation (45.3) need be formulated for drying and wetting phases respectively, which will be done in the following paragraphs.

45.3.2 Hydrolock Strain Formulation in the Drying Phase

In wood, the elasticity modulus $E(w)$ depends on the moisture content. Hence, the sum $\dot{\varepsilon}_e + \dot{\varepsilon}_{HL}$ in Eq. (45.1) writes

$$\dot{\varepsilon}_e + \dot{\varepsilon}_{HL} = \left(\frac{\dot{\sigma}}{E(w)} - \frac{E^{'}(w)}{E^2(w)}\dot{w}\sigma\right) + \dot{\varepsilon}_{HL} \tag{45.5}$$

In Eq. (45.5), $\dot{\varepsilon}_e^{\sigma}=\dot{\sigma}/E(w)$ is the elastic strain variation due to the varying stress $\dot{\sigma}$, and $\dot{\varepsilon}_e^{w}=-E^{'}(w)\dot{w}\sigma/E^2(w)$ is the elastic strain variation due to the varying module caused by a moisture content change $\dot{w}$. Item (i) in Sect. 45.2 mentioned that the hydrolock strain resulted from a blocking of the strain in the drying phase under stress, hence

$$\forall \dot{w} < 0 \quad \left(\dot{\varepsilon}_e^{\sigma} + \dot{\varepsilon}_e^{w} + \dot{\varepsilon}_{HL}\right)_{\dot{\sigma}=0} = 0 \tag{45.6}$$

Therefore, from Eqs. (45.5) and (45.6) in the case of a steady stress state $(\dot{\sigma}=0)$, it follows

$$\dot{\varepsilon}_{HL}|_{\dot{w}<0} = -\dot{\varepsilon}_e^{w} = \frac{E^{'}(w)}{E^2(w)}\dot{w}\sigma \tag{45.7}$$

$\dot{\varepsilon}_{HL}|_{\dot{w}<0}$ expresses the evolution of the hydrolock strain in the drying phase. Equation (45.7) shows that the phenomenon of strain locking during a drying phase is due to the hydrolock strain that arises to compensate the part of elastic strain evolution $\dot{\varepsilon}_e^{w}$ due to the solidifying phase. This equation also shows that the hydrolock strain does not change $(\dot{\varepsilon}_{HL} = 0)$ at constant humidity $(\dot{w}=0)$, regardless of the mechanical stress σ, which agrees with test conclusion in item (ii) in Sect. 45.2.

45.3.3 Hydrolock Strain Formulation in the Wetting Phase

Item (iii) in Sect. 45.2 conclusion stated that the hydrolock strain (if it exists) decreases during the wetting phase until it disappears when the moisture content w returns to its initial value $\overline{w}$ at the beginning of the drying phase under stress. This statement is not sufficient to express the hydrolock strain evolution in the humidification phase. A possibility is to assume that its evolution follows the law given by Eq. (45.7). But it is clear that this equation will not allow to totally recover the hydrolock strain if the stress is not big enough (i.e. close or equal to zero). To overcome this problem, let the mechanical stress σ in Eq. (45.7) be replaced by a auxiliary stress $\tilde{\sigma}$ to determine. This leads to

$$\varepsilon_{HL}|_{w>0} = \frac{E^{'}(w)}{E^2(w)}\, w\, \tilde{\sigma} \tag{45.8}$$

where $\dot{\varepsilon}_{HL}|_{\dot{w}>0}$ represents the evolution of the hydrolock strain in the wetting phase. To satisfy item (iii) in Sect. 45.2, as recalled above, the hydrolock strain must return to zero when $w = \overline{w}$. Therefore, a value of the auxiliary stress $\tilde{\sigma}$ is obtained by integrating Eq. (45.8) on the interval $[w, \overline{w}]$ with the boundary condition $\dot{\varepsilon}_{HL}(\overline{w})=0$, which gives

$$\tilde{\sigma} = \frac{E(w)E(\overline{w})}{E(w) - E(\overline{w})}\varepsilon_{HL} \tag{45.9}$$

It is worth noticing that this expression is the function $g(\varepsilon_{HL})$ predicted by Eq. (45.3).

Finally, all of Eqs. (45.7)–(45.9) establish the evolution law of the hydrolock strain according to thermodynamic principles, in accordance with experimental observations in Sect. 45.2. $\tilde{\sigma}$ is a auxiliary stress which is defined $\forall w \leq \overline{w}$. Its actual value depends on the accumulated amount of hydrolock strain. By introducing this fictitious stress, it is possible to solve the problem of hydrolock strain recovery in a moistening phase, regardless of the loading level. Furthermore, it is noticed that it was not necessary to specify the physical meaning of the fictitious stress to establish the equations above.

45.3.4 Viscoelastic Strain

Item (ii) in Sect. 45.2 stated that the hydrolock strain is time independent. It means that this effect doesn't influence on the viscoelastic part of the behavior. As shown on Fig. 45.2, the analysis of the pure viscoelastic strain is based on a Kelvin's cell, in parallel with a Maxwell's branch. This versatile model is chosen since it can be used easily for both creep and relaxation purposes. Combined with an additional outside spring, this model is equivalent to Maxwell's generalized model with two branches and an isolated spring. Thus, the formulation of elastic and viscoelastic parts are merged in a Boltzmann's equation in the case of relaxation, as follows

$$\sigma(t) = \int_0^t \mathrm{R}(t, \tau, w)\dot{\varepsilon}_{eve}(\tau)d\tau \tag{45.10}$$

where ε_{eve} is the sum of the elastic and viscoelastic strain parts. $R(t, \tau, w)$ is the relaxation function which depends on the actual time t, time of intermediate loading τ and moisture content w. A Dirichlet's series is used for the relaxation function, as follows

$$R(t, \tau, w) \cong E(w)\left(\gamma_0(w) + \sum_{\mu=1}^{r} \gamma_\mu(w)e^{-\beta_\mu(t-\tau)}\right) \tag{45.11}$$

where $E(w)$ and $w = w(t)$ are the Young's modulus and moisture content at time t. β_μ are fixed parameters. The coefficients $\gamma_\mu(w)$ are determined from relaxation tests by the least square method. It should be noted that linear laws for the coefficients $\gamma_\mu(w)$ are sufficiency for good agreement between this function and test results.

45.4 Incremental Model

An incremental model with finite time step is developed to overcome the memory problem arising in a viscoelastic calculation. This is achieved by integrating Eq. (45.1) over a finite interval $[t, t + \Delta t]$. Given the hypothesis of strain partition, it becomes to integrate separately each term of Eq. (45.1), and then summing the all increments as follows

$$\forall t, \Delta t: \quad \Delta\varepsilon_t = \Delta\varepsilon_e + \Delta\varepsilon_{HL} + \Delta\varepsilon_{ve} + \Delta\varepsilon_w = \Delta\varepsilon_{HL} + \Delta\varepsilon_{eve} + \Delta\varepsilon_w \tag{45.12}$$

Each term in this equation is explained below. To simplify the notation, we denote $\sigma = \sigma(t)$ and $E = E(w(t))$, values which are taken by the mechanical stress and the modulus of elasticity at the beginning of the finite time interval $[t, t + \Delta t]$, respectively. We also denote $\Delta\sigma = \sigma(t + \Delta t) - \sigma(t)$, $\Delta E = E(w(t + \Delta t)) - E(w(t))$ and $\Delta w = w(t + \Delta t) - w(t)$ which are respectively the variation of stress, modulus of elasticity and moisture content during a time increment Δt.

45.4.1 Hydric Strain Increment

The incremental free strain depends on incremental moisture content and swelling/shrinkage coefficient, which is assumed constant in this paper. Hence

$$\Delta\varepsilon_w = \alpha\Delta w \tag{45.13}$$

45.4.2 Hydrolock Strain Increment

This area is treated separately for the two phases of drying and moistening.

45.4.2.1 Drying Phase

As mention in Sect. 45.3.2, the varying hydrolock strain in the drying phase compensates the elastic strain variation at constant stress [Eq. (45.7)]. Accordingly, the increment $\Delta\varepsilon_{HL}$ can be obtained by integrating Eq. (45.7) over a finite interval $[t, t+\Delta t]$ under the hypothesis of linear modulus variation over this time interval. It leads

$$\Delta\varepsilon_{HL} = \frac{\Delta E}{2(E+\Delta E)^2}\Delta\sigma + \frac{\sigma\Delta E}{2}\left(\frac{1}{E^2} + \frac{1}{(E+\Delta E)^2}\right) \tag{45.14}$$

45.4.2.2 Wetting Phase

In this case, the hydrolock strain increment is obtained by integrating of $\dot{\varepsilon}_{HL}|_{\dot{w}>0}$ in Eq. (45.8). Replacing Eqs. (45.9) in (45.8) and then resolving the first order differential equation gives

$$\Delta\varepsilon_{HL} = \frac{\Delta E\overline{E}}{(E-\overline{E})(E+\Delta E)}\varepsilon_{HL} \tag{45.15}$$

Finally, the combination of Eqs. (45.14) and (45.15) yields

$$\Delta\varepsilon_{HL} = \eta_{HL}\Delta\sigma + \xi_{HL} \tag{45.16}$$

With

$$\text{if} \quad \dot{w} < 0 \begin{cases} \eta_{HL} = \dfrac{\Delta E}{2(E+\Delta E)^2} \\ \xi_{HL} = \dfrac{\sigma\Delta E}{2}\left(\dfrac{1}{E^2} + \dfrac{1}{(E+\Delta E)^2}\right) \end{cases} \tag{45.17}$$

$$\text{if} \quad \dot{w} > 0 \begin{cases} \eta_{HL} = 0 \\ \xi_{HL} = \dfrac{\Delta E\overline{E}}{(E-\overline{E})(E+\Delta E)}\varepsilon_{HL} \end{cases} \tag{45.18}$$

45.4.3 Viscoelastic Strain Increment

Solving Boltzmann's Eq. (45.10) over a finite time interval yields

$$\Delta\sigma = \sigma(t+\Delta t) - \sigma(t) = \int_0^{t+\Delta t} \mathrm{R}(t+\Delta t, \tau, w+\Delta w)\dot{\varepsilon}_{eve}(\tau)d\tau - \int_0^{t} \mathrm{R}(t,\tau,w)\dot{\varepsilon}_{eve}(\tau)d\tau \tag{45.19}$$

The Eq. (45.19) can be written

$$\Delta\sigma = \int_0^{t} [\mathrm{R}(t+\Delta t,\tau,w+\Delta w) - \mathrm{R}(t,\tau,w)]\dot{\varepsilon}_{eve}(\tau)d\tau + \int_t^{t+\Delta t} \mathrm{R}(t+\Delta t,\tau,w+\Delta w)\dot{\varepsilon}_{eve}(\tau)d\tau \tag{45.20}$$

By replacing Eq. (45.11) in Eq. (45.20), it comes

$$\forall t, \Delta t: \quad \Delta\sigma = \sum_{\mu=0}^{r} \Delta\sigma_\mu \tag{45.21}$$

For $\mu = 0$

$$\Delta\sigma_0 = \int^{t} 0[E(w+\Delta w)\gamma_0(w+\Delta w) - E(w)\gamma_0(w)]\varepsilon_{eve}(\tau)d\tau + \int^{t+\Delta t} tE(w+\Delta w)\gamma_0(w+\Delta w)\varepsilon_{eve}(\tau)d\tau \tag{45.22}$$

Assuming a linear evolution of the strain over the time interval $[t,\, t+\Delta t]$ gives

$$\Delta\sigma_0 = E(w+\Delta w)\gamma_0(w+\Delta w)\Delta\varepsilon_{eve} - [E(w)\gamma_0(w) - E(w+\Delta w)\gamma_0(w+\Delta w)]\varepsilon_{eve}(t) \tag{45.23}$$

Similarly, we obtain for $\mu = 1 \div r$,

$$\Delta\sigma_\mu = \left[E(w+\Delta w)\gamma_\mu(w+\Delta w)\frac{1-e^{-\beta_\mu\Delta t}}{\beta_\mu\Delta t}\right]\Delta\varepsilon_{eve} - \sum_{\mu=1}^{r}\left[1 - \frac{E(w+\Delta w)\gamma_\mu(w+\Delta w)}{E(w)\gamma_\mu(w)}e^{-\beta_\mu\Delta t}\right]\sigma_\mu(t) \tag{45.24}$$

By summing Eqs. (45.23) and (45.24), and inversing the result, we obtain the behavior law expressed in an incremental form as follows

$$\Delta\varepsilon_{eve} = \eta_{eve}\Delta\sigma + \xi_{eve} = \tilde{K}^{-1}\Delta\sigma + \tilde{K}^{-1}\sigma_{hist} \tag{45.25}$$

with

$$\begin{cases} \widetilde{K} = \mathrm{E}(w+\Delta w)\left[\gamma_0(w+\Delta w) + \sum_{\mu=1}^{r}\gamma_\mu(w+\Delta w)\dfrac{1-e^{-\beta_\mu\Delta t}}{\beta_\mu\Delta t}\right] \\ \sigma_{hist} = \left[\mathrm{E}(w)\gamma_0(w) - \mathrm{E}(w+\Delta w)\gamma_0(w+\Delta w)\right]\varepsilon_{eve}(t) + \sum_{\mu=1}^{r}\left[1 - \dfrac{\mathrm{E}(w+\Delta w)\ \gamma_\mu(w+\Delta w)}{\mathrm{E}(w)\ \gamma_\mu(w)}e^{-\beta_\mu\Delta t}\right]\sigma_\mu(t) \end{cases} \tag{45.26}$$

The fictitious modulus $\tilde{K}$ and the term of history σ_{hist} are calculated in the beginning of each time increment. Their values depend on the Dirichlet's series parameters and the time increment Δt, which is finite but not necessarily small. The value of σ_{hist} depends also on intern variables $\sigma_\mu(t)$ attached to the Maxwell's branches. Their values must be updated at the end of each incremental calculation step by using Eq. (45.24).

45.4.4 Global Incremental Formulation

By combining Eqs. (45.13), (45.16) and (45.25), we get the complete model in an incremental form, as follows

$$\Delta\varepsilon = \eta\Delta\sigma + \xi \tag{45.27}$$

with $\eta = \eta_{eve} + \eta_{HL}$ and $\xi = \alpha\Delta w + \xi_{eve} + \xi_{HL}$. The parameters $\eta_{eve}, \eta_{HL}, \xi_{eve}$ and ξ_{HL} are given by Eqs. (45.25) and (45.26) for elastic-viscoelastic parts and Eqs. (45.17) and (45.18) for hydrolock part in a drying or moistening phase, respectively.

The form of Eq. (45.27) is similar to the case of a thermoelastic problem. This property can be used for the numerical implementation of the model, simulating an equivalent linear thermoelastic problem, where η is a fictitious compliance and ξ is an equivalent thermal loading. It should be noted that Eq. (45.27) results from accurate integrals, the only approximation regarding the evolution of $E(w)$ and $\varepsilon(\tau)$ which were considered as linear over the time interval $[t, t + \Delta t]$. It means that the time step Δt in numerical calculation is finite, but not necessarily small. This important property can significantly reduce the computational effort while maintaining good accuracy, which can be very beneficial in the case of application of this model for simulating complex problems.

45.5 Numerical Validation

For the purpose of validation, the model was applied to simulate the mechano-sorptive test presented in Sect. 45.2. The data (material parameters from preliminary tests [6]) are as follows

- specimen size (L × R × T) : 50 × 3 × 1 mm^3
- Young's modulus (GPa): $E = -0.544\,w(\%) + 22.2$
- shrinkage/swelling coefficient: $\alpha = 0.0108$
- stepwise values (repeated cyclically) of the applied stress (MPa): 16.0; 15.2; 13.3; 11.4; 10.7
- stepwise values (repeated cyclically) of the relative humidity: 0.70; 0.60; 0.50; 0.40; 0.29
- average duration of each step (stress or relative humidity): 2 h.
- delay between a stress and moisture increment: about 15 min.
- total duration of the test: 12 steps × 2 h/step (stress or relative humidity) = 24 h.

The numerical simulation was performed in the Matlab® software, based on Eq. (45.27). Given the incremental form of the model, the calculation process is carried out step-by-step for the all duration of the test. The result of the numerical simulation is shown as a dashed line on Fig. 45.3.

The similarity between simulated and experimental values of the total strain shows that the main aspects of the behavior are correctly depicted by the model. The difference between them is greater in the drying phase than in the wetting phase. This difference can be explained by the fact that the hydrolock strain is not sufficient to totally explain the mechano-sorptive effect. Actually, the hydrolock strain represents only the instantaneous reversible part of the mechano-sorptive effect, which must be completed with a mechano-sorptive creep, as it is mentioned in [7] for example.

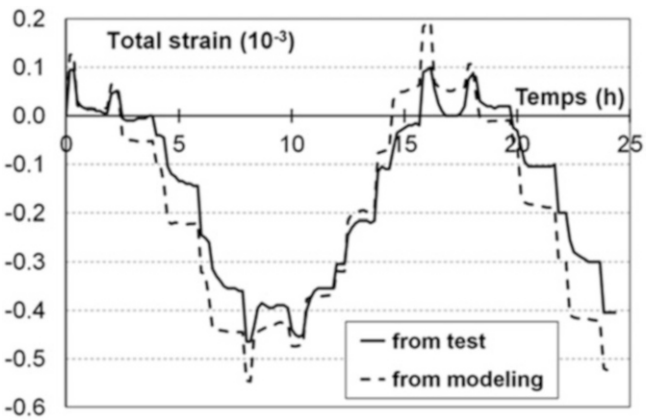

Fig. 45.3 Comparison between simulated values (*dashed line*) and experimental values (*solid line*) of the total strain

45.6 Conclusion

Mechano-sorptive tests were carried out to evidence hydrolock effect, which hasn't been reported yet in literature. The property of time independency of the hydrolock strain allows separating the treatment of the hydrolock part and the viscoelastic part of the strain.

From test results and thermodynamical considerations, an evolution law was proposed for the hydrolock strain. A auxiliary stress was introduced to help recovery of the hydrolock strain in the wetting phase.

An incremental model was established by exact integrals for the hydrolock strain and the viscoelastic strain with variable humidity. It should be noted that the time increment must be finite but not necessarily small. This important feature can significantly reduce the computational effort while maintaining good accuracy.

Good agreement between numerical results and test results confirm the ability of this model for simulating hydromechanical behavior of softwood under complex loading.

Acknowledgment This work has been sponsored by the European Regional Development Fund (ERDF) of the European Union, and by the Region of Auvergne, France.

References

1. Armstrong, L.D., Kingston, R.S.T.: Effect of moisture changes on creep in wood. Nature **185**, 862–863 (1960)
2. Gril, J.: Une modélisation du comportement hygro-rhéologique du bois à partir de sa microstructure. PhD thesis, Paris 6 university, France (1988)
3. Dubois, F., Randriambololona, H., Petit, C.: Creep in wood under variable climate conditions: numerical modeling and experimental validation. Mech. Time-Depend. Mater. **9**, 137–202 (2005)
4. Husson, J.M., Dubois, F., Sauvat, N.: Elastic response in wood under moisture content variations: analytic development. Mech. Time-Depend. Mater. **14**, 203–217 (2010)
5. Colmars, J., Dubois, F., Gril, J.: One-dimensional discrete formulation of a hygrolock model for wood hygromechanics. Mech. Time-Depend. Mater. **18**, 309–328 (2014)
6. Saifouni, O.: Modélisation des effets rhéologiques dans les matériaux: application au comportement mécanosorptif du bois. PhD thesis, Blaise Pascal university, Clermont-Ferrand, France, D.U 2468/EDSPIC 658 (2014)
7. Salin, J.-G.: Numerical prediction of checking during timber drying and a new mechano-sorptive creep model. Holz Roh Werkst. **550**, 195–200 (1992)

Chapter 46
Accelerated Creep Testing of CFRP with the Stepped Isostress Method

J.D. Tanks, K.E. Rader, and S.R. Sharp

Abstract Numerous accelerated methods for testing long-term viscoelastic properties of fiber reinforced polymer (FRP) composites such as creep and relaxation have been developed in order to reduce the time needed to characterize the material behavior. Most of them are based on the time-temperature-stress superposition principle (TTSSP), or some variation thereof, which involves the manipulation of temperature, applied stress, or both as a way to reduce the testing duration. This paper reports the application of a test called the stepped isostress method (SSM) to study tensile creep of CFRP laminates used in rehabilitating prestressed concrete structures, which experience sustained loads above 60 % of ultimate strength for decades. The SSM employs a load-stepping approach, typically with three to five steps for a single specimen resulting in creep rupture. A key feature of this method is the independence of test results on step size or duration. A simple, repeatable SSM protocol is presented and it is shown that this method is also useful for studying creep rupture of CFRP.

Keywords Creep • Creep rupture • Accelerated testing • CFRP • Stepped isostress method

46.1 Introduction

Due to its high strength-to-weight ratio and resistance to galvanic corrosion, carbon fiber reinforced polymers (CFRP) are becoming more common in structural components found in aerospace, automotive, pipeline, wind energy, and civil engineering industries as an alternative to steel, aluminum, and titanium alloys. However, as a polymeric material, CFRP is susceptible to higher levels of time-dependent deformation (creep) and failure (creep rupture) at lower temperatures than most metals, requiring in-depth characterization of long-term behavior. Time is too limited for running creep tests at realistic service-life durations, meaning accelerated tests are necessary [1]. According to the time-temperature-stress-superposition principle (TTSSP), the creep of viscoelastic materials is dependent upon time, temperature, and stress in such a way that a time-equivalence can be determined [2–5]. The following Boltzmann integral represents the TTSSP for variable stress:

$$\varepsilon(t) = C_0\sigma + \int_0^t C_t(t-\tau)\frac{d\sigma(\tau)}{d\tau}d\tau \tag{46.1}$$

where $\varepsilon(t)$ is creep strain, C_0 is instantaneous compliance, σ is applied stress, C_t is creep compliance, and τ is a point in time t when the stress $\sigma(\tau)$ changes. Variable temperature can be incorporated the same way.

From this principle an accelerated creep testing methods has been developed, the stepped isothermal method (SIM), and applied with great success to aramid yarns [6–8]. Unlike many TTSSP approaches that use different specimens for each reference temperature, the SIM uses a single specimen for a given reference temperature and the temperature is stepped up in uniform increments until material failure.

More recently, the stepped isostress method (SSM) was developed and showcased at Cambridge University, first applied to aramid yarns [7–9] and then to semicrystalline thermoplastics (polyamide-6) [1]. The basic principle of the SSM is the same as the SIM, but instead temperature is held constant and stress is stepped up until material failure. This captures the stress history of a single specimen rather than extrapolate across stress levels between different specimens. This paper describes the first application (to the authors' knowledge) of the SSM to study creep deformation and creep rupture of unidirectional CFRP laminates; preliminary results are presented here and much more exhaustive experimentation is

J.D. Tanks (✉) • K.E. Rader • S.R. Sharp
Virginia Center for Transportation Innovation and Research, 530 Edgemont Road, Charlottesville, VA 22903, USA
e-mail: jdt5ca@virginia.edu

C. Ralph et al. (eds.), *Mechanics of Composite and Multi-functional Materials, Volume 7*,
Conference Proceedings of the Society for Experimental Mechanics Series, DOI 10.1007/978-3-319-21762-8_46

ongoing. The purpose of this paper is to describe the test method, the data analysis procedure, and suggest implications of the results of this method as a promising approach to reliable accelerated creep testing for composite materials.

46.2 Test Method

46.2.1 Materials and Specimens

The material studied in this paper was a $[90]_8$ CFRP pultruded laminate with thickness of 1.2 mm and a stock-width of 100 mm. The fully-cured composite contained 0.68 volume fraction PAN carbon fibers in a standard epoxy matrix, which had a nominal glass transition of $T_g = 120\,^{\circ}\text{C}$ (according to the manufacturer). Tensile specimens for measuring quasi-static strength and creep behavior were cut using a carbide blade, after which the edges were sanded smooth and all surfaces were cleaned with soap and water, then dried completely. Gripping tabs measuring 25 × 25 mm were cut from 1.6 mm thick aluminum sheets, and a cyanoacrylate adhesive was cured for 24 h at 22 °C for bonding tabs to the specimens. A specimen just after a completed test is depicted in Fig. 46.1 (inset). All tensile testing was performed on a servohydraulic universal test machine with 5 kN load cell (MTS, 810), and strain was measured with 350 Ω bonded-resistance strain gauges (Omega, KFH-6-350-C1) connected to a datalogger (CS, CR10X).

46.2.2 Preliminary Tensile Tests

Before performing the primary experiment, tensile tests were performed with at least four specimens to find the average ultimate strength of the CFRP. Specimens measuring approximately 12 mm in width by 100 mm in length were prepared, with tabs attached as described in Sect. 46.2.1, leaving a free length of 50 mm. A gripping pressure of 1.72 MPa (250 psi) was used and the samples were pulled at a constant strain-rate of $10^{-4}\ \text{s}^{-1}$ until complete failure occurred. The average ultimate tensile strength was 41.9 MPa (6.08 ksi) with a standard deviation of 5.6 MPa (0.82 ksi). The average elastic modulus, measured in the linear elastic region, was 4.35 GPa (632 ksi).

In an effort to avoid premature failure at the higher creep stress levels, given the 13.5 % COV in strength, the value for average ultimate tensile strength (UTS) used in creep tests for this paper was reduced by one standard deviation, resulting in a value termed the "guaranteed" ultimate tensile strength (GUTS) that was 36.3 MPa (5.27 ksi). This reduces the chances that a specimen will fail

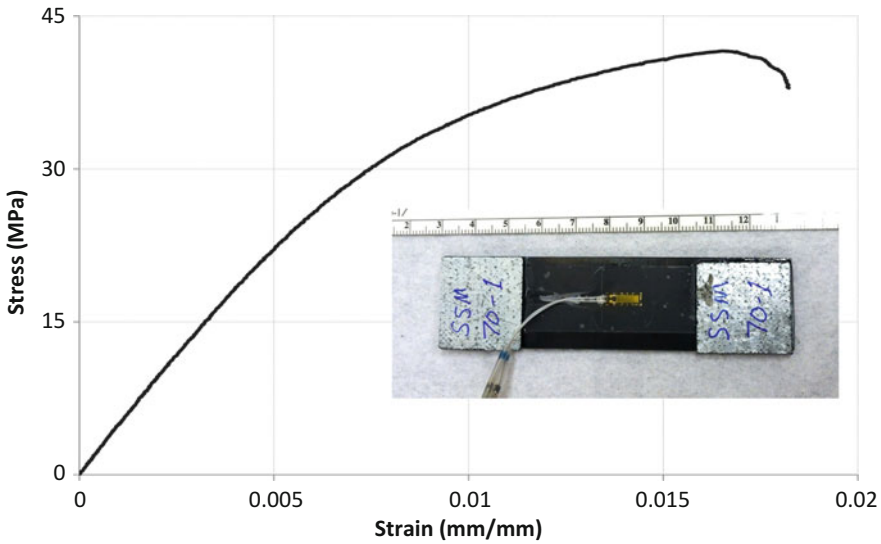

Fig. 46.1 Stress-strain curve for typical tensile test of $[90]_8$ CFRP laminate

Table 46.1 Procedure for creep testing CFRP with the SSM

		Load step			
Reference stress	Step parameters	1	2	3	4
55 % GUTS	Stress level, % GUTS	55	68	81	94
(47.5 % UTS)	Step duration, h (10^3 s)	5 (18)	5 (18)	5 (18)	14.7 (52.9)
70 % GUTS	Stress level, % GUTS	70	78	86	94
(60 % UTS)	Step duration, h (10^3 s)	5 (18)	5 (18)	5 (18)	0 (0.02)

at 100 % GUTS (86.5 % UTS) for the reason of material variability, rather than creep damage. Figure 46.1 illustrates a typical stress-strain curve for the $[90]_8$ laminate, with slight yielding initiating around 27 MPa and over 1.8 % elongation at failure.

46.2.3 SSM Creep Tests

Creep of the CFRP in this paper was studied using SSM at two starting stress levels (reference stress), which would be equivalent to the constant sustained stress level during a conventional (long-term) creep test. The specimen starts at the reference stress in the first load step, then moves to higher ones with each load step until a final step that is held until specimen failure. These stresses are expressed in terms of the GUTS, meaning references stresses of 55 and 70 % GUTS. The stress level for the final load step was chosen to be 94 % GUTS, seeming high enough to avoid a prolonged final step but not high enough to cause immediate failure. The other load steps were simply divided into equal stress increments, each lasting 5 h. Table 46.1 summarizes the test parameters selected for the experiments in this study.

46.3 Results and Discussion

The specimen tested at a reference stress of 70 % GUTS failed during the jump to the final load step, after only about 20 s of increasing stress. Nonetheless, the data analysis method for SSM remains the same as for the 55 % GUTS specimen, which failed after almost 15 h in the final load step. For the purpose of this paper, only one specimen was tested for each reference stress at room temperature to observe overall trends in behavior, rather than minutia from variability; replicate samples are in progress for statistical values. Total strain is defined as the combination of elastic and creep deformation, assuming thermal strains are negligible and reference stresses are in the elastic region with modulus E:

$$\varepsilon_{total} = \varepsilon_{elastic} + \varepsilon_{creep} \tag{46.2}$$

$$\sigma_0 = \varepsilon_{elastic} E \tag{46.3}$$

46.3.1 Procedure for Data Analysis

The stress profiles and raw strain data for the SSM creep tests are shown in Fig. 46.2a, b, respectively. Figure 46.3 contains each step of the data analysis process for 55 % GUTS as an example, with the raw strain data in Fig. 46.3a. There are three major parts of the sequence for analyzing data obtain through the SSM and constructing creep master curves: (1) vertical shifting, (2) rescaling, and (3) horizontal shifting.

1. Vertical shifting is merely the subtraction of elastic strains each load step to create a continuous curve in terms of strain, as in Fig. 46.3b.
2. Rescaling is the second step, and it essentially accounts for stress history—creep and damage from previous steps—and strain equivalence for each load step, as seen in Fig. 46.3c. The creep curve for an individual step must be extrapolated to zero creep strain, then shifted on the time axis by the difference between the real start time of that step and the extrapolated start time. Also, the time axis is converted to logarithm of time.
3. Finally, the rescaled individual creep curves must be placed along the log(time) axis to create the complete master curve, i.e., superposition. This is accomplished through a shift factor for reduced time, $\log(a_\sigma)$, and one must be found for each stress level.

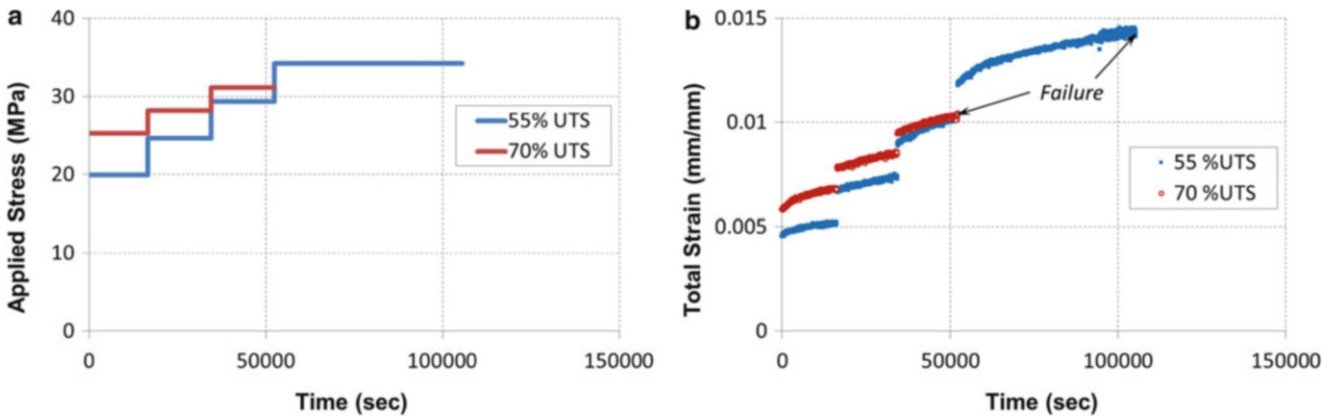

Fig. 46.2 SSM creep test results: (**a**) stress profiles measured by the load cell, and (**b**) raw strain data

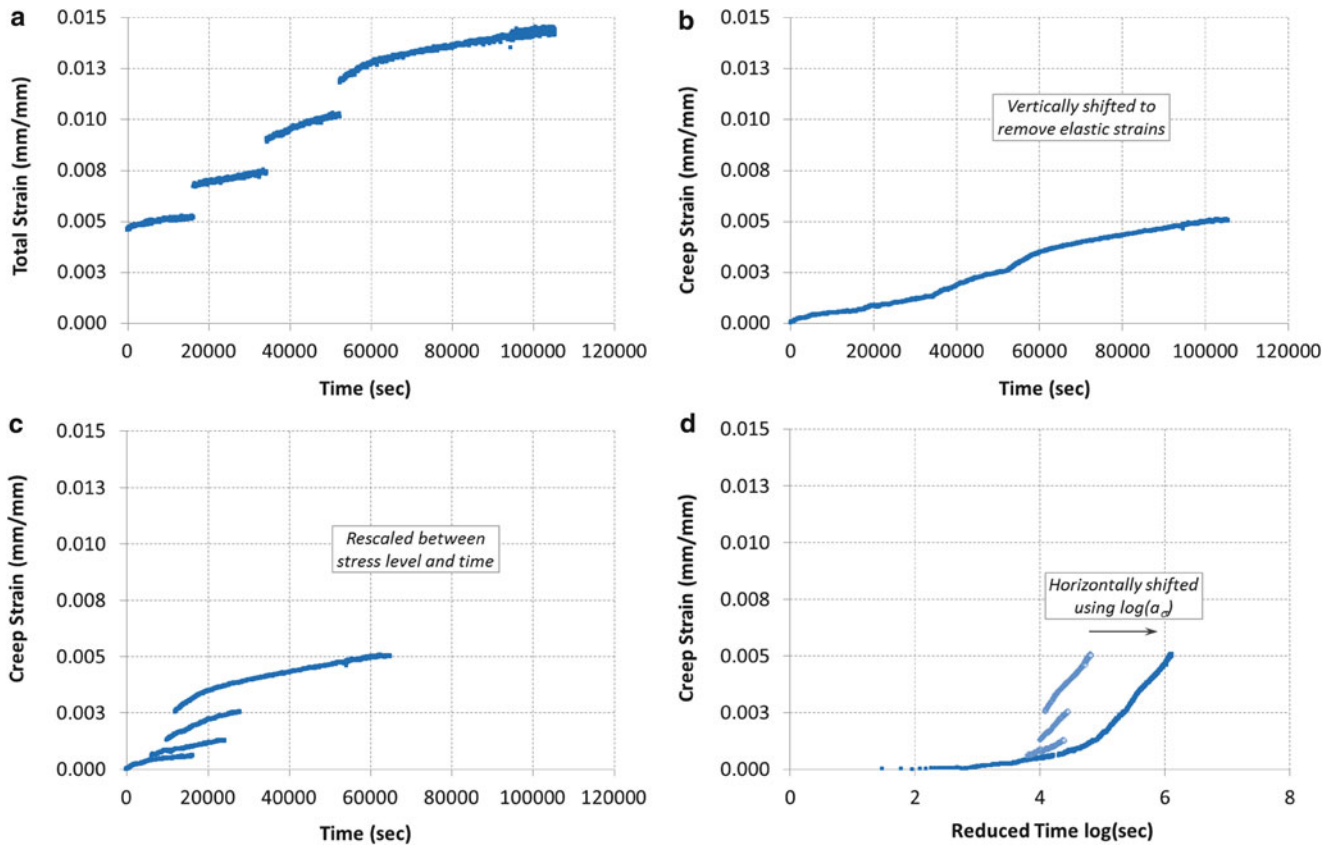

Fig. 46.3 Sequence for SSM data analysis demonstrated with 55 % GUTS: (**a**) raw strain data, (**b**) vertical shifting, (**c**) rescaling, and (**d**) horizontal shifting

46.3.2 Creep Master Curves

Abbreviated master curves for both specimens are included in Fig. 46.4, limited up to 10^5 s (reduced time) for the purpose of comparing common time scales, since rupture occurred at different times for each. The smoothness and shape of each master curve indicates that the analysis procedure adequately manipulates the data from this testing program to create a realistic creep master curve that would result from a conventional long-term test at that reference stress. It is apparent that

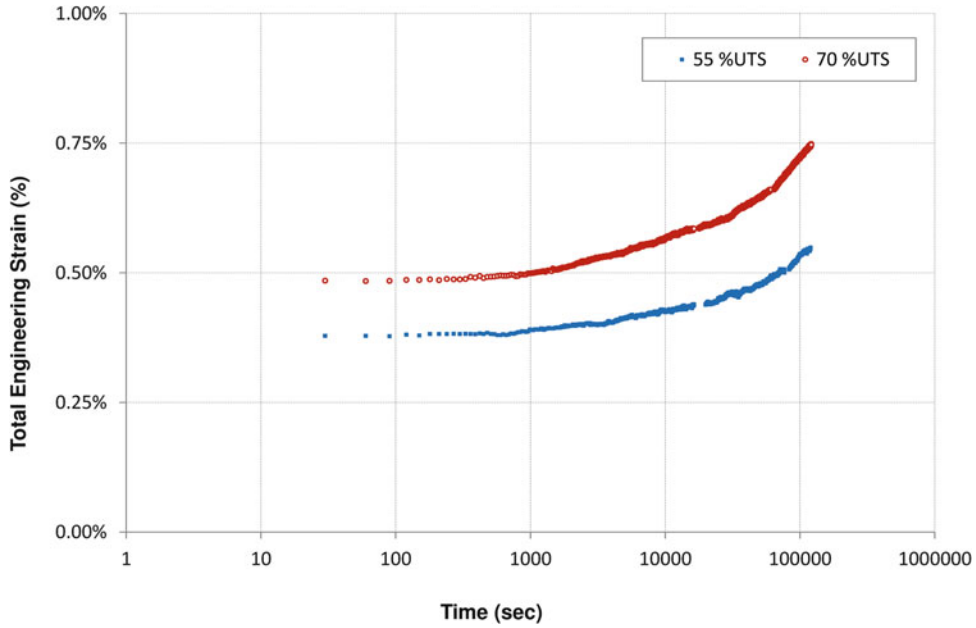

Fig. 46.4 Creep master curves for $[90]_8$ CFRP laminate at 55 and 70 % GUTS

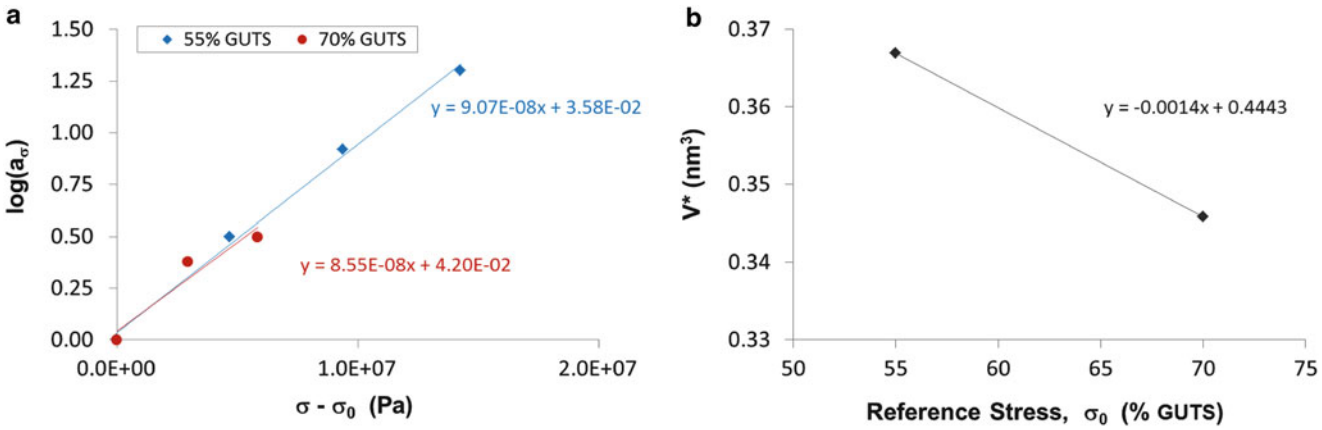

Fig. 46.5 Relationship between (**a**) stress level and time shift factor, and (**b**) reference stress and activation volume

the creep strain-rate for 70 % GUTS is higher than for 55 % GUTS, as expected. Furthermore, the relationship between the shift factor and stress level is illustrated in Fig. 46.5, and from this the activation volume can be described based on the Eyring equation:

$$\log(a_\sigma) = \frac{V^*}{kT}(\sigma - \sigma_0) \tag{46.4}$$

where $\log(a_\sigma)$ is the stress-dependent time shift factor, T is temperature, k is the Boltzmann constant, σ_0 and σ are the reference and accelerating stresses (respectively), and V^* is the activation volume. It seems that activation volume is inversely proportional to reference stress, which matches reports for $[90]_{16}$ AS4/3501-6 in the literature [10]. The linear relationship in Fig. 46.5a indicates that the same creep mechanism is likely dominant for both reference stresses examined here, meaning the superposition method used in the SSM is valid. For this laminate, $V^* = 0.367$ nm^3 for 55 % GUTS and $V^* = 0.346$ nm^3 for 70 % GUTS.

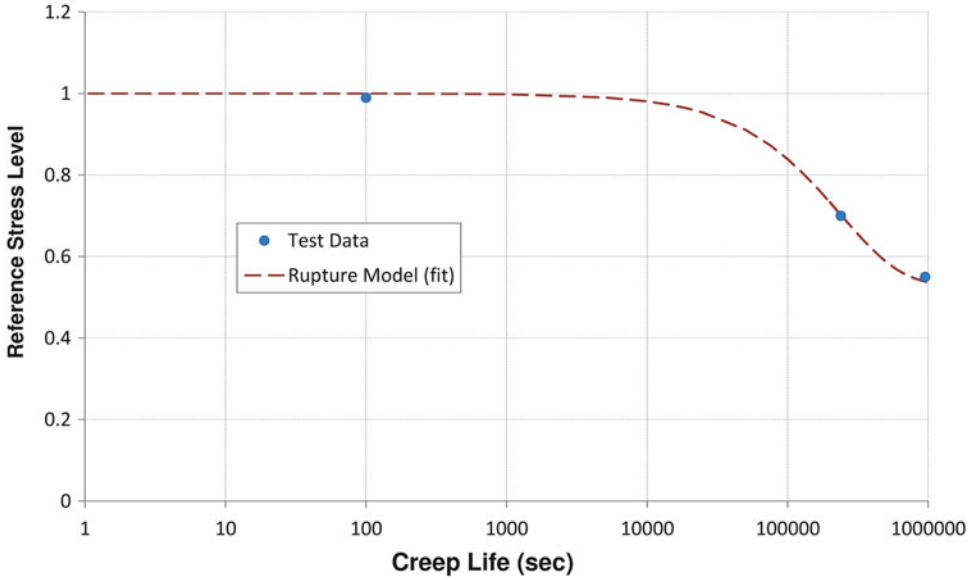

Fig. 46.6 Creep rupture time for reference stresses examined in this study, compared to a curve-fit creep rupture model

Table 46.2 Model parameters for predicting creep rupture of $[90]_8$ CFRP laminates based on the SSM

	a	b	σ_∞	σ_{ult}
Model parameter	s	–	MPa	MPa
Value (curve fit)	238,095	2.128	19.2	36.3

46.3.3 Creep Rupture

In addition to creep deformation, the SSM can be used to study creep rupture behavior of CFRP as well. Two assumptions are made when analyzing these results: (1) a reference stress equal to 99 % of the quasi-static strength corresponds to an extremely short (but non-zero) creep rupture time, arbitrarily set at 100 s, and (2) there is likely some reference stress below which the CFRP will not rupture within a reasonable amount of time, labeled σ_∞ (though not anywhere near infinite). For practical implementation of the SSM in creep rupture testing programs, consider that this "rupture-threshold" stress σ_∞ is the lowest usable design stress that a given CFRP structural component will endure for the design life of that component. For instance, a tie-rod loaded at 30 % GUTS for 50 years, as opposed to a pressurized pipe section loaded at 65 % GUTS for 10 years. Thus, combined with the quasi-static strength, the rupture times from 55 and 70 % GUTS can be plotted against the reference stress (normalized to GUTS) in Fig. 46.6. These experimental results match similar studies on creep rupture of CFRP [11].

Using the concepts described here, a semi-empirical model for the creep life is proposed that fits this set of data very well, expressed in Eq. (46.5):

$$t_r = (-a)\ln\left[b\left(\frac{\sigma_0 - \sigma_\infty}{\sigma_{ult}}\right)\right] = (-a)\ln\left[\left(\frac{\sigma_0 - \sigma_\infty}{\sigma_{ult} - \sigma_\infty}\right)\right] \tag{46.5}$$

where t_r is the time to rupture, σ_{ult} is the ultimate tensile strength, and a is a material constant. Values for these model parameters are given in Table 46.2. It is reasonable to hypothesize that a is stress-independent; it is possible it depends on factors like temperature, activation energy, or activation volume. It could also represent a damage variable, perhaps one sensitive to strain-rate, which would be influenced by loading directionality with respect to the fiber orientation (for unidirectional CFRP). Interestingly, there is a strong correlation between the constant a and the ratio of average activation volume to specimen (material) volume, different by exactly 10^{-27} (exact out to six digits). For convenience, b is defined within Eq. (46.5) so that the reference and rupture-threshold stresses can be written normalized to the ultimate strength (values from 0 to 1). This model is compared to the experimental data in Fig. 46.6, for a valid stress range of 50–100 % GUTS, and the results bear resemblance to other analytical models such as the maximum stress-work criterion [12].

46.4 Summary

A promising accelerated testing method for creep deformation and creep rupture of polymeric composites has been applied to unidirectional CFRP laminates, for what appears to be the first time. The flexibility and validity of the SSM have been demonstrated with aramid yarns and polyamide-6 thermoplastics, but have yet to be thoroughly evaluated for CFRP. However, this preliminary investigation agrees with other studies in terms of capturing a dominant creep mechanism that is understood based on polymer physics, and the creep rupture data appears reliable for the examined stress range. Finally, a simple analytical model was formulated to successfully predict creep rupture based on data collected using the SSM. Since this research is ongoing, there will soon be results for more reference stress levels (40–90 % GUTS) and temperatures as well, to fully compare and validate the SSM to other well-known TTSSP-based accelerated methods.

Acknowledgements The authors would like to thank William Ordel (VCTIR) for his assistance, as well as Glasforms, Inc. for providing the cured CFRP laminates. This research was funded by the Virginia Center for Transportation Innovation and Research.

References

1. Hadid, M., Guerira, B., Bahri, M., Zouani, A.: Assessment of the stepped isostress method in the prediction of long term creep of thermoplastics. Polym. Test. **34**, 113–119 (2014)
2. Luo, W., Wang, C., Zhao, R.: Application of time-temperature-stress superposition principle to nonlinear creep of poly(methyl methylacrylate). Key Eng. Mater. **340–341**, 1091–1096 (2007)
3. Wenbo, L., Ting-Qing, Y., Qunli, A.: Time-temperature-stress equivalence and its application to nonlinear viscoelastic materials. Acta Mech. Solida Sin. **14**, 195–199 (2001)
4. Chang, F.-C., Lam, F., Kadla, J.F.: Application of time-temperature-stress superposition on creep of wood-plastic composites. Mech. Time-Depend. Mater. **17**, 427–437 (2013)
5. Cai, H., Nakada, M., Miyano, Y.: Simplified determination of long-term viscoelastic behavior of amorphous resin. Mech. Time-Depend. Mater. **17**, 137–146 (2013)
6. Giannopoulos, I.P., Burgoyne, C.J.: Accelerated creep testing for aramid fibres using the stepped isothermal method. J. Mater. Sci. **43**, 4789–4800 (2008)
7. Giannopoulos, I.P., Burgoyne, C.J.: Stress limits for aramid fibres. Proc. Inst. Civ. Eng. **162**, 221–232 (2009)
8. Giannopoulos, I.P., Burgoyne, C.J.: Accelerated and real-time creep and creep-rupture results for aramid fibres. J. Appl. Polym. Sci. **125**, 3856–3870 (2012)
9. Giannopoulos, I.P., Burgoyne, C.J.: Prediction of the long-term behavior of high modulus fibres using the stepped isostress method. J. Mater. Sci. **46**, 7660–7671 (2011)
10. Raghavan, J., Meshii, M.: Creep of polymer composites. Compos. Sci. Technol. **57**, 1673–1688 (1998)
11. Raghavan, J., Meshii, M.: Creep rupture of polymer composites. Compos. Sci. Technol. **57**, 375–388 (1997)
12. Guedes, R.M.: Mathematical analysis of energies for viscoelastic materials and energy based failure criteria for creep loading. Mech. Time-Depend. Mater. **8**, 169–192 (2004)

Chapter 47
Coupon-Based Qualification for the Fatigue of Composite Repairs of Pressure Equipment

Ibrahim A. Alnaser and Michael W. Keller

Abstract Corrosion damage is one the critical problems in the maintenance of pressure equipment. This damage can manifest itself in one of two forms, internal and external corrosion. Both forms cause degradation in the pressure carrying capacity and reduce the factor of safety inherent in the design. Several repair techniques are available, but bonded composite repairs have become increasingly popular. Repairs on interior corrosion defects have the added complication of having the potential to become through-wall defects. For quasi-static pressure loadings, these repairs have demonstrated the ability to adequately restore the pressure carrying capacity of pressure equipment. In this paper, we present a study of fatigue performance of bonded composite repairs using a simple coupon-based test of width-tapered double cantilevered beam specimens. The specimens were fatigue cycled in load control to simulate pressure fatigue of through-wall defects.

Keywords Composite repair • Pressure vessel • Fatigue • Adhesive bond, fatigue cycles

47.1 Introduction

Worldwide, steel pipelines are considered to be one of the most economical methods for the long-distance transport of high-pressure fluids and gases. Much of the pipeline infrastructure in the US was installed decades ago and only advances in inspection and repair techniques have prevented the need for large-scale replacements. One of the most common issues found in pipelines is corrosion, which can occur internally or externally. The yearly estimated cost of corroded pipeline for the gas and petroleum industry reaches billions of dollars [1]. There are several ways to repair degraded pipes, such as replacing the defective section or the installation of welded steel sleeves. Both of those techniques are expensive because the pressure equipment must be shut down during the repairs. They can also be unsafe because of the need to weld the repairs into place. Therefore, there has been a focus put on developing rehabilitation approaches that do not require the need to shut down the pipeline [2].

One such repair method is the use of bonded composite to rehabilitate piping with degraded regions. Basically, the bonded composite repair technique uses uncured reinforcement fiber wrapped over a defect section on the pressure equipment in the field that had been wetted out with a liquid resin. The bonded composite repair can be formed to any complex geometry or curves because it can cure in place in the field. Another benefit of bonded composite repair is the cost; it is 24 % cheaper than welded sleeve repair and 75 % cheaper than completely replacing the defect section [3].

In the case of through-wall repair, the interface between the two materials is very important. The strength of the repair and its success depends solely on the adherence of the two materials to each other and the ability of this interface to resist fracture. Thus, there is a critical need to develop techniques to rapidly characterize and understand the fracture behavior of these interfaces.

I.A. Alnaser • M.W. Keller (✉)
Department of Mechanical Engineering, The University of Tulsa, 800 S. Tucker Dr., Tulsa, OK 74104, USA
e-mail: mwkeller@utulsa.edu

C. Ralph et al. (eds.), *Mechanics of Composite and Multi-functional Materials, Volume 7*,
Conference Proceedings of the Society for Experimental Mechanics Series, DOI 10.1007/978-3-319-21762-8_47

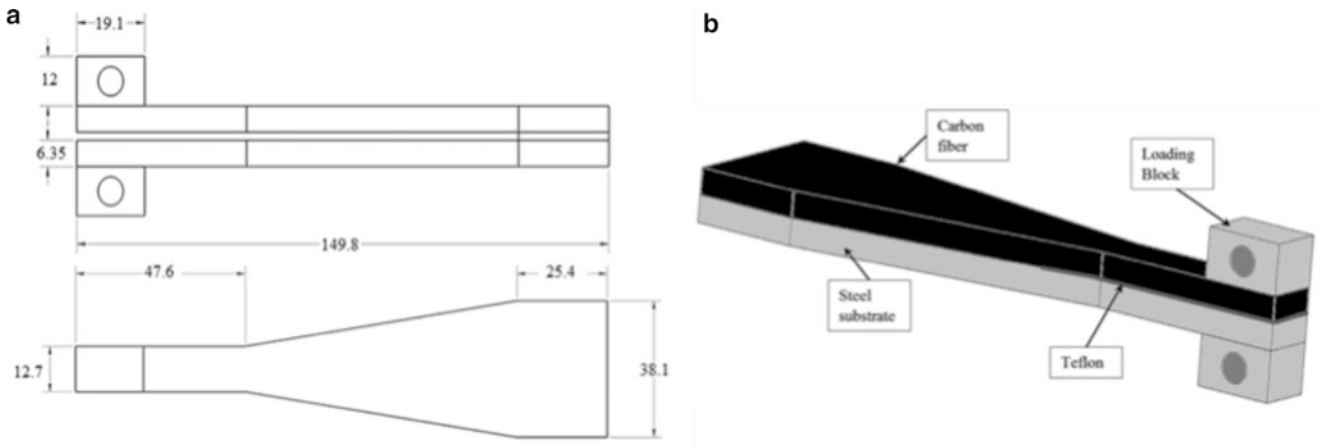

Fig. 47.1 (**a**) WTDCB schematic dimension in mm. (**b**) final shape of WTDCB specimen

47.2 Experimental Methods

47.2.1 Specimen Manufacture

Figure 47.1a shows the basic geometry of the width-tapered double cantilever beam (WTDCB) specimen that was produced following the design of Jin, et al. [4]. To mimic the geometry of the composite repair, the upper adherend was a carbon-fiber composite and the lower adherend was a low-carbon steel similar to pipeline steel. The thickness of the lower adherend was approximately 0.25 in to simulate the pipe wall of 6-in. Schedule 40 pipe. The steel adherend was cut by water-jet with dimensions given in Fig. 47.1a. Then, the steel adherend was grit-blasted to achieve a clean and rough surface. A commercial composite repair system (Citadel Technologies, Tulsa, OK) was used to form the upper adhered. Plain weave carbon fiber was hand laid up to the required thickness on a waxed platen. To fabricate a specimen, multiple steel adherends were then placed on top of the uncured composite. A Teflon film was used to create an initial crack of the specimen. After at least 24 h of curing at room temperature, the specimens were separated using a carbide saw. Then, the steel adherend was used as a guideline to trim the composite using a high-speed router. After this, the loading block was mounted using an adhesive on the composite adherend. A schematic of a completed specimen is given in Fig. 47.1b.

47.2.2 Fatigue Testing

The WTDCB specimens were tested under cyclic load control, using a servohydraulic load frame (MTS). Loads were set at 50 % G_{IC} determined from quasi-static testing and were applied at 1 or 2 Hz depending on the test. Load profile was applied using a sinusoidal wave shape. All tests were performed until complete specimen failure. Crack lengths were determined using the compliance approach based on a series of calibration specimens.

47.3 Results and Discussion

47.3.1 Specimen Calibration

Calibration of the WTDCB specimen had been performed previously. The results of this calibration are shown in Fig. 47.2.

As expected, the WTDCB shows a quadratic dependence on crack length, which is indicative of constant change in compliance with change in crack area. This confirms that the specimen is a crack-length independent measure of fracture energy. The compliance calibration shown in Fig. 47.3 was used to determine the crack lengths presented below.

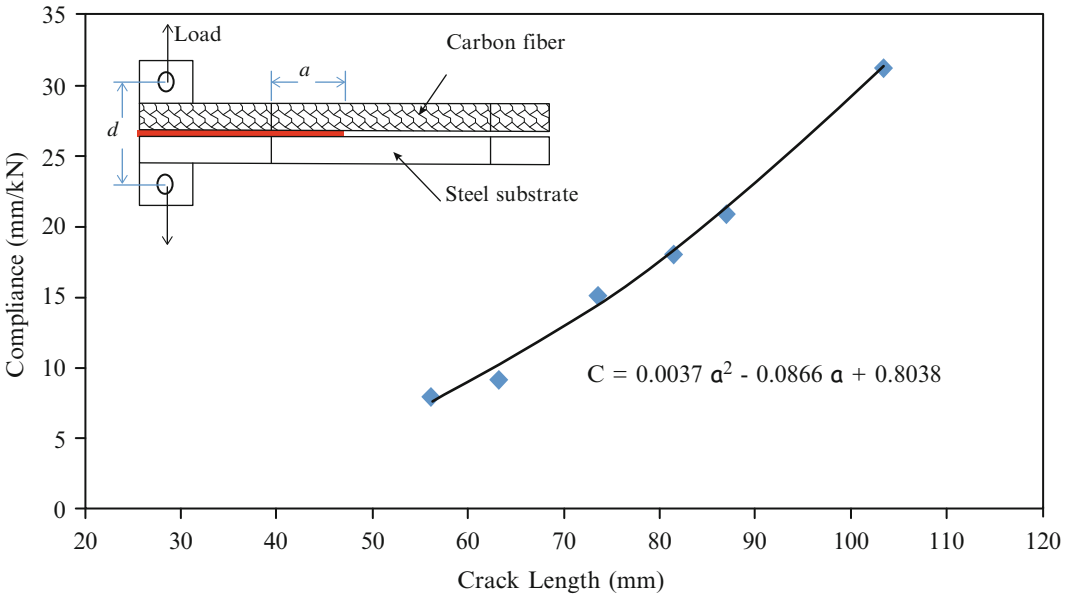

Fig. 47.2 Compliance versus crack length

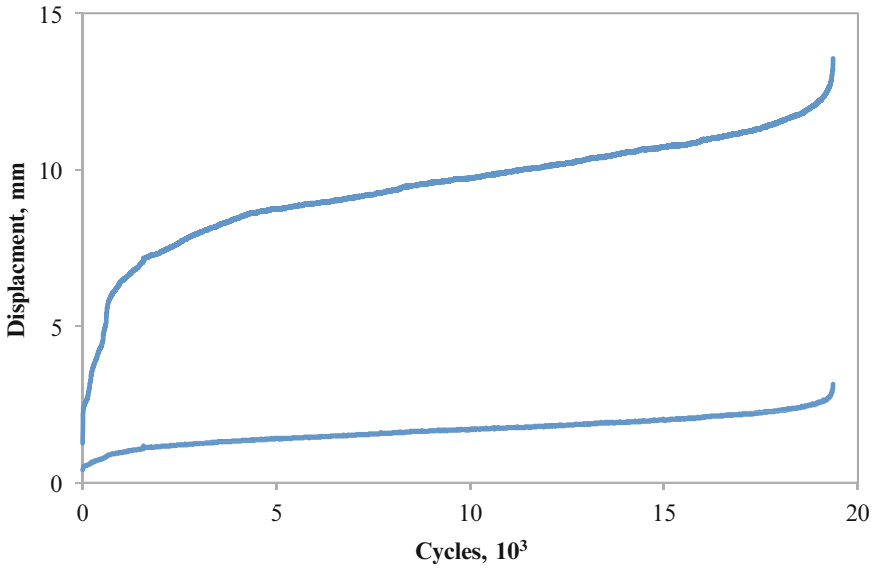

Fig. 47.3 Displacement vs. fatigue cycle for sample cycled at 1 Hz

47.3.2 Fatigue Testing

Both samples were loaded at 50 % of average critical load ($P_C = 203$ N). Coupon samples were tested in a servohydraulic load frame as described above. Load ratio for this test was $\Delta K = K_{max}/K_{min} = 20$, which is quite severe. Testing is ongoing to investigate the influence of loading ratio on the performance of these types of interfaces. However, pressure cycling when investigating fatigue performance of these repairs is usually performed on similar effective load ratios (i.e. unpressurized to full allowable operating pressure). Under this fixes loading ratio, two samples were fatigue tested using 1 Hz and 2 Hz as the frequency of the applied sine wave. Figure 47.3 the peak and valley displacement values for the sample tested at 1 Hz. This plot has two curves, with the upper curve is the maximum displacement and the lower curve is minimum displacement. These displacements representing K_{max} and K_{min}, respectively. We see three regions of behavior in this specimen, a rapid progression of the crack at the beginning of the test for approximate 2000–3000 cycles. After this period, the crack enters a long linear section prior to complete separation.

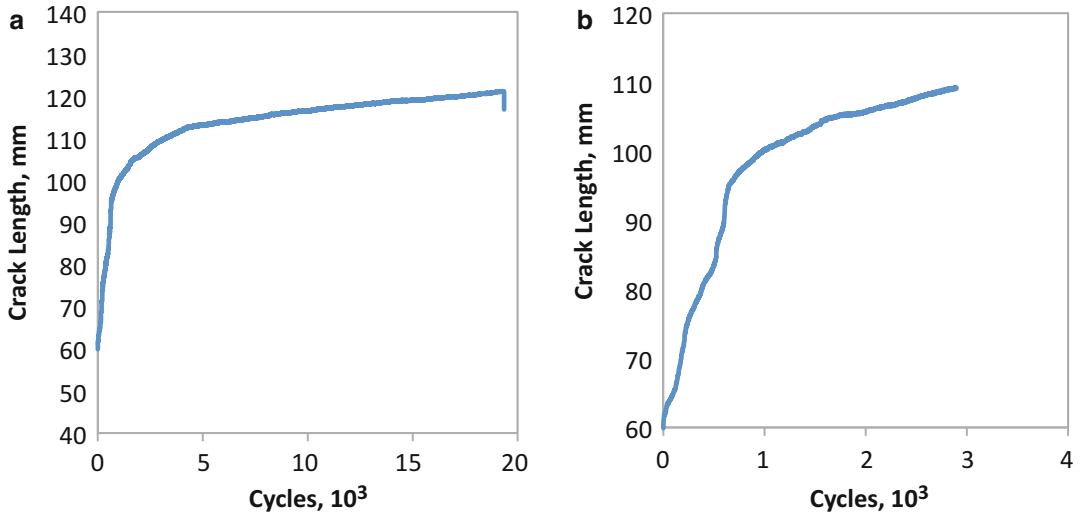

Fig. 47.4 (**a**) Crack length calculated from compliance calibrations for a sample cycled at 1 Hz. (**b**) First 3000 cycles of sample 1

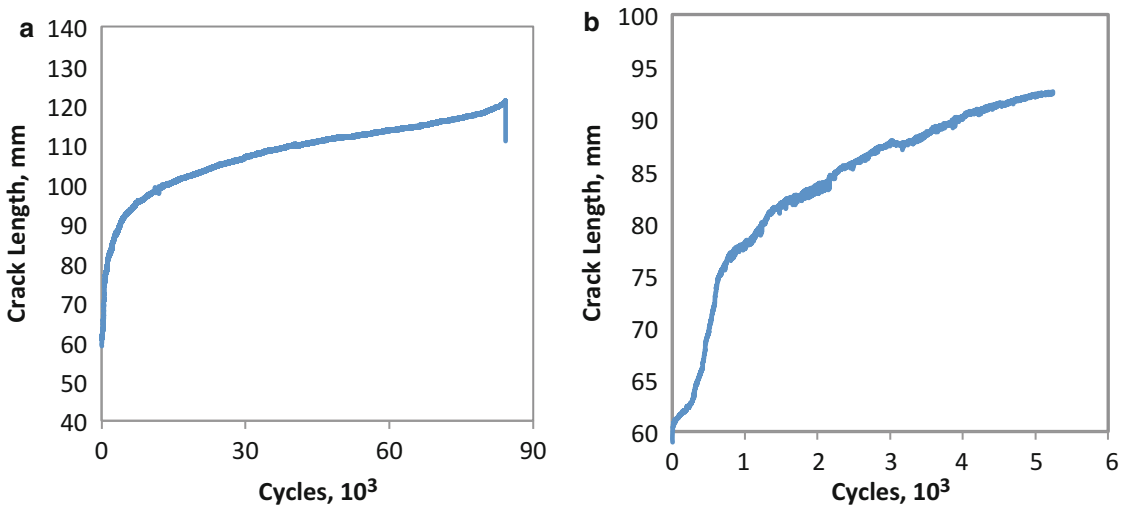

Fig. 47.5 (**a**) Sample number cycled at 2 Hz. (**b**) Zoomed region of cycles vs. crack length of specimen in Fig. 6a

Performing the compliance-based calibration, we recover the crack-length vs. cycles for this specimen, which is shown in Fig. 47.4a. Based on this figure, we can interpret the regions of sample behavior shown in Fig. 47.3. The initial, fast growing region represents crack propagation through the tapered, constant compliance region of the WTDCB specimen shown in Fig. 47.1a. The long plateau region is prorogation through the end region of the specimen and therefore does not represent a valid constant K test region.

We can see a rapid progression of crack growth in Fig. 47.4b, which presents only the first 3000 cycles of the fatigue test. From this we see the rapid crack growth of approximately 0.03 mm/cycle, which leads to 45 mm of crack growth in the first 1500 cycles. An optical calibration of the specimen to verify the compliance calibration is ongoing and is required to confirm the observed behavior of the multi-material interfacial fracture specimen.

Figure 47.5a shows the crack length vs fatigue cycle curve for second specimen that was cycled at 2 Hz. As was the case for the first specimen, there are three general regions of fatigue, with only the initial steep growth representing crack growth in the valid constant K region of the specimen. Aside from the anomalous slow growth at the beginning of the test, shown in Fig. 47.5b, this specimen had a similar 0.03 mm/cycle growth rate until the initiation of slowing crack growth at approximately 1000 cycles. Whether this behavior is an impact of the higher loading rate or due to sample-to-sample variation is still under investigation.

Based on a preliminary test of a full-scale specimen with a through-wall defect repaired using composite materials, coupon specimens appear to have considerably higher crack growth rates than the full-scale tests. A single full-scale specimen sustained 1000 pressure cycles to 50 % of the quasi-static failure pressure, before being halted. If this full-scale specimen had been experiencing similar crack growth rates to the coupon specimen, it is likely failure would have occurred. However, a clear understanding of the stability of interfacial cracks growth in composite repairs is still lacking. Further study is necessary to relate sample performance to full-scale repair performance.

47.4 Conclusions

A preliminary set of coupon-based fatigue tests that simulate pressure fatigue loading of composite repairs were performed. Crack growth rates in the constant K region of the specimen were the same for loading rate at 1 and 2 Hz at approximately 0.03 mm/cycle. A comparison of one full-scale test with the results from the coupon-based fatigue performance indicates that coupon-based specimens likely overstate crack-growth rates.

Acknowledgments This work was supported in part by a Department of Transportation Cooperative Agreement (DTPH56-13-H-CAAP02).

References

1. Mabelson, A.R., Dunn, K.R., Dodds, N., Gibson, A.G.: Refurbishment of steel tubular pipes using composite materials. J. Plast. Rubber Compos. **29**(10), 558–565 (2000)
2. Batisse, R.: Review of gas transmission pipeline repair methods. In: Safety, Reliability and Risks Associated with Water, Oil and Gas Pipelines. NATO Science for Peace and Security Series C: Environmental Security, pp. 335–349. Springer, Netherlands (2008)
3. Koch, G.H., Brongers, M.P., Tompson, N.G., Virmani, Y.P., Payer, J.H.: Corrosion Cost and Preventative Strategies in the United States. Federal Highway Administration, Office of Infrastructure Research and Development, pp. 260–311
4. Jin, H., Miller, G.M., Sottos, N.R., White, S.R.: Fracture and fatigue response of a self-healing epoxy adhesive. Polymer **52**, 1628–1634 (2011)

Chapter 48
Effect of a Composite Coupler on Automotive Windshield Wiper System Chatter

Yaomin Dong

Abstract A composite coupler has been developed to prevent automotive windshield wiper systems from being damaged by excessive loads when the normal wiping pattern is restricted. The coupler is composed of a pultruded composite rod with injection-molded plastic spherical sockets attached at either end. Unlike the traditional steel coupler used in wiper systems, the composite coupler will buckle at a prescribed compressive load threshold and become extremely compliant. As a result, the peak loading of the coupler and the entire wiper system can be greatly reduced. Since the composite coupler is less rigid than its steel counterpart, the dynamic performance of the wiper system is investigated in this work. This chapter details the methodology that was employed to determine the chatter characteristics of the wiper systems under untreated and Rain-X treated windshields under different wiping conditions.

Keywords Composite materials • Buckling • Wiper systems • Durability • Chatter

48.1 Introduction

Automotive windshield wiper systems, in conjunction with washer systems, are used in vehicles to remove contaminants such as rain, sleet, snow, and dirt from the windshield. As shown in Fig. 48.1, a typical wiper system consists of an electric motor, a linkage to transform the rotational motion from the motor to oscillatory motion, and a pair of wiper arms and blades. The areas of the windshield that must be wiped by the wiper system are mandated by the federal motor vehicle safety standards FMVSS 104 [1].

Failures in automotive windshield wiper systems have been caused by over-loading due to snow build-up and icy stack. Realistically, two load cases can happen: the snow pack on the windshield prevents the arms and blades from going in-wipe, or the arms and blades are frozen to the windshield and cannot go to out-wipe. Should any of these extreme situations occur due to a snow or ice storm, and if the wiper system is fairly rigid and the motor is powerful enough to generate very high loads in the system, damage to components of the wiper system may result. As shown in Fig. 48.2, snow and ice often build up on the windshield glass in the winter. The snow/ice stack can literally block the wiper arms/blades, and therefore the wiper system load will significantly increase. Such an excessive load, often referred as snow load, will cause either fatigue or catastrophic system failure. Figure 48.3 shows a broken rocker arm.

If the wiper system is stiff, which is the case today in production, when the arms and blades go to in-wipe position and strike on packed snow, tremendous loads will be generated in the system that may cause breakage and failure of the weakest component in the wiper system. Composite materials are widely used due to their advantages in high strength to weight ratios, high corrosion resistance, high fatigue life in cyclic loading, and great potential in styling design. A composite coupler is a good solution to this problem [2–7]. Under the same conditions, the composite coupler will buckle when the compressive load reaches a critical value, as shown in Fig. 48.4. In other words, the composite coupler acts as a snow clutch, or a force "circuit breaker" that automatically resets. In addition, by using composite materials, the mass of the coupler is reduced by about 60 %. It is possible that this coupler will become a technological breakthrough that allows us to build lighter, stiffer wiper systems. In Fig. 48.4, the hatched area represents snow/ice pack above the cowl screen, which restricts the normal motion of the wiper system. Once the arms have contacted the restriction, the loading in the system increases as the motor torque approaches the motor's stall torque. However, once the critical load is reached in the composite coupler, it

Y. Dong (✉)
Department of Mechanical Engineering, Kettering University, 1700 University Avenue, Flint, MI 48504-4898, USA
e-mail: ydong@kettering.edu

C. Ralph et al. (eds.), *Mechanics of Composite and Multi-functional Materials, Volume 7*,
Conference Proceedings of the Society for Experimental Mechanics Series, DOI 10.1007/978-3-319-21762-8_48

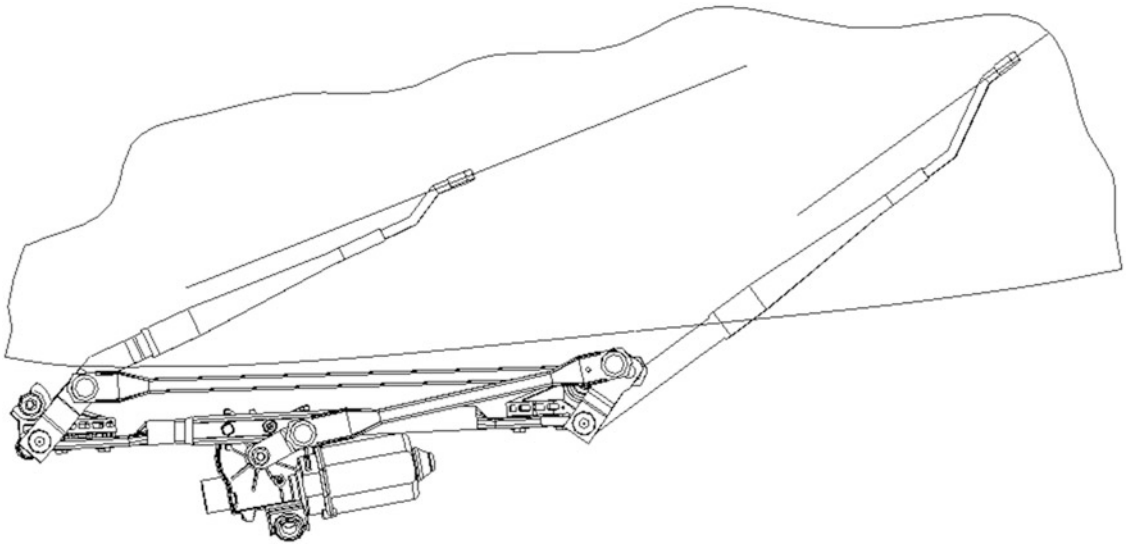

Fig. 48.1 A typical wiper system

Fig. 48.2 Windshield wipers under snow load

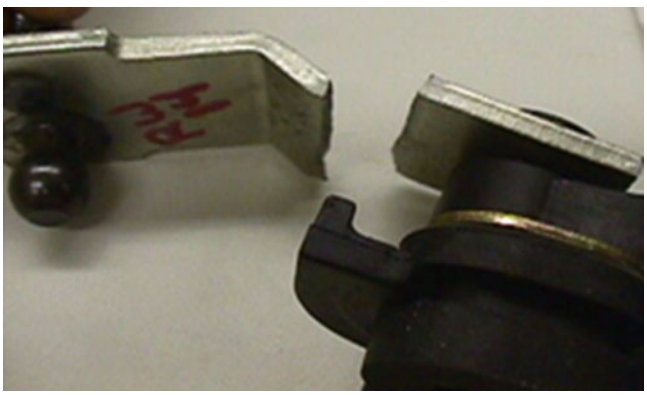

Fig. 48.3 A broken rocker arm due to snow load

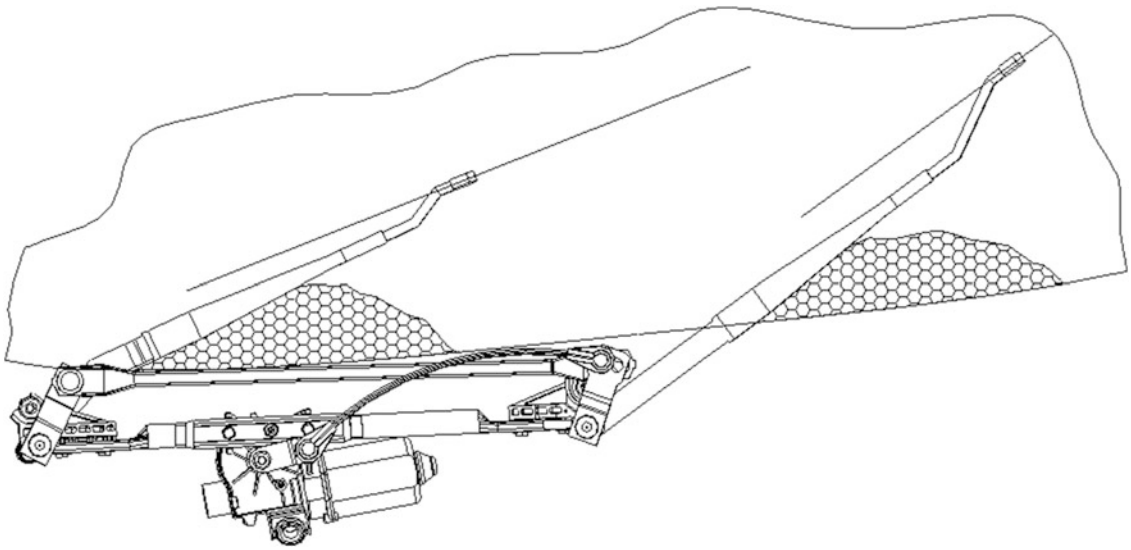

Fig. 48.4 Windshield wipers with a flexible coupler

will buckle limiting any further increase in system loading and allowing the crank arm to rotate through the reversal position. In the illustration, the composite coupler is shown in the post-buckled configuration.

48.2 Design of the Composite Coupler

The buckling load of the composite coupler should be determined such that it will be substantially higher than the maximum normal wiping load so as to avoid inadvertently buckling the coupler. On the other hand, the buckling load needs to be less than the minimum load that will stall the wiper motor. For the given application used in this work, test on production wiper systems was performed to obtain the following data to facilitate the composite coupler design:

- The maximum normal wiping load in the coupler was 560 N
- The maximum load in the coupler under restricted wiping conditions was 2100 N

A buckling load of 850 N was chosen for the composite coupler and experimentally validated to meet the above requirements, as shown in Fig. 48.5. Employing such a composite coupler reduced the load in the coupler from 2100 to 560 N. Therefore, the system peak load due to restricted wiping conditions can be greatly reduced to prevent wiper system failures demonstrated previously. Figure 48.5 also shows the enormous difference in stiffness of the composite coupler before and after buckling. The elastic-perfectly plastic behavior provides the most desirable functionality for the wiper system. Under normal wiping conditions, the composite coupler functions just like a traditional steel coupler. In case of restricted wiping conditions, the composite coupler buckles and keeps nearly constant post buckling load, which enables the wiper system to wipe at a reduced wiping pattern without collapsing. Such a safety device not only protects the wiper system from overload damages, but also provides vehicle operators with a functional wiper system under extreme weather conditions.

Figure 48.6 depicts the coupler with a cord length L, cross sectional area A, and cross sectional moment of inertia I. The elastic modulus of the material is denoted as E. The ends of the coupler are free to rotate due to the socket-ball joints. External compressive load P is applied at the centroid of the cross section.

As the load is increased and assuming that the elastic limit of the material is not reached, a critical point is encountered at which the rod deforms laterally. The applied load at which this transition occurs is referred to as the critical load Pcr. The critical load can be determined for a given cross section, column length, and material from [8]

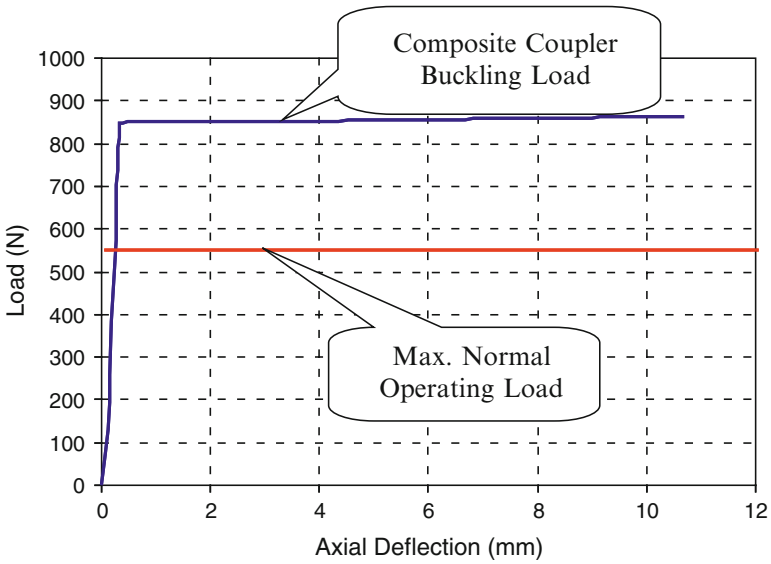

Fig. 48.5 Elastic-perfectly plastic property of the composite coupler

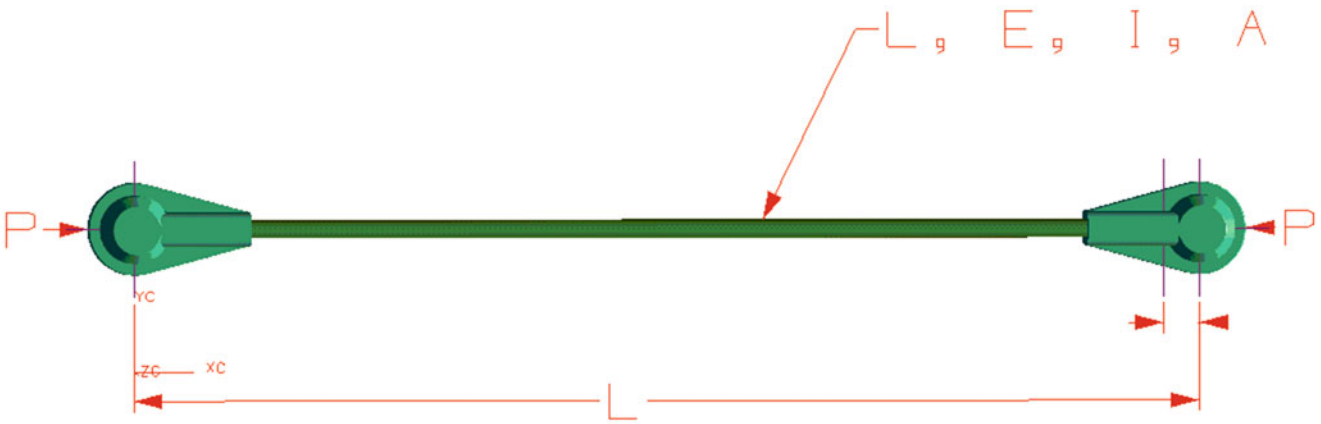

Fig. 48.6 A flexible coupler

$$Fcr = \frac{\pi^2 EI}{L^2} \tag{48.1}$$

The formula for the cross sectional moment of inertia of a rectangular section is given by

$$I = \frac{1}{12}(b-2R)h^3 + \frac{1}{12}(2R)(h-2R)^3 + 2\left\{0.1098R^4 + \frac{\pi}{2}R^2\left[\frac{4R}{3\pi} + \frac{1}{2}(h-2R)\right]^2\right\} \tag{48.2}$$

Where b and h denote the width and height of the rectangular cross section, and R represents the radius of fillets. Note that the pultrusion process requires that the section have filleted corners. The engineering drawing of the composite coupler is depicted in Fig. 48.7.

The composite material is selected per following specification [4]:

Resin Specification: Thermoset Polyester (21 % by weight)
Fiber Specification: 113 Yield E-glass Roving (75 % by weight)
Filler content (4 % by weight)

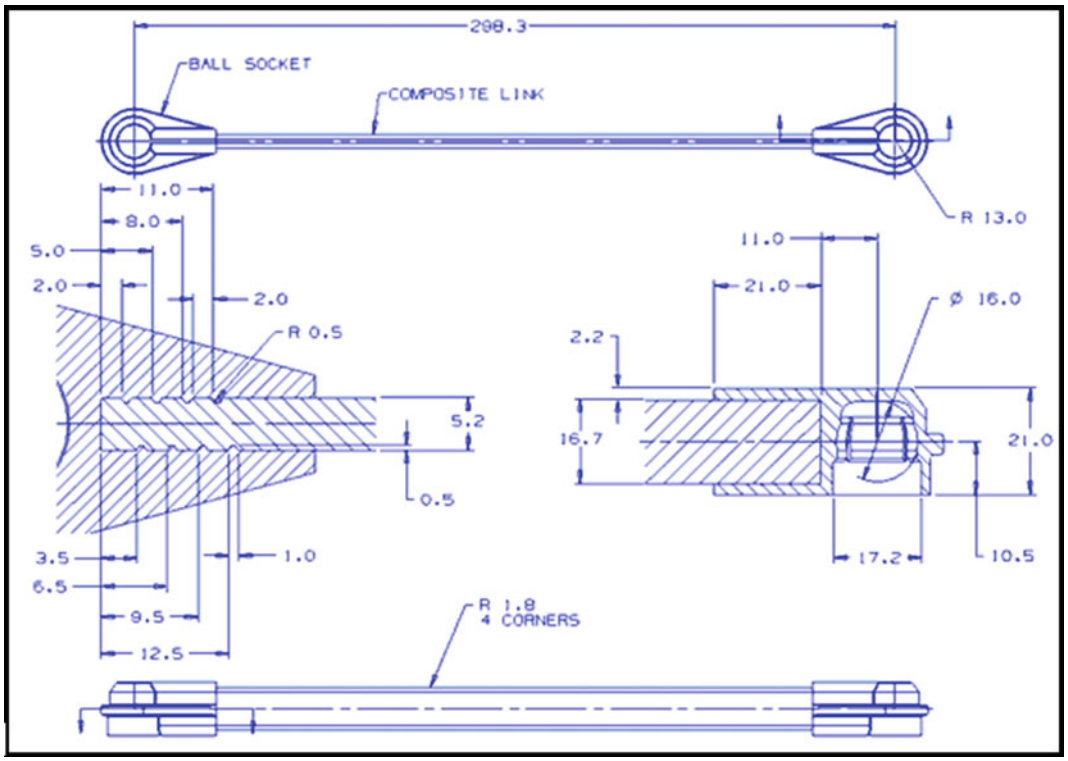

Fig. 48.7 Design of the composite coupler

Monotonic mechanical properties of the materials are:

Elastic Modulus: 43 GPa
Ultimate Strength: 1140 MPa
Strain at Fracture: 2.6 %
Specific Gravity: 1.92

48.3 Validation Test Results and Discussions

48.3.1 Durability Test

A series of tests were performed to characterize the performance of the composite coupler at both the component and system levels. For the cyclic test at the component level, the composite coupler was mounted on the MTS testing machine using fixtures with the ball joints. Figure 48.7 is a semilog plot of the S-N characteristic of the material from cyclic test. Each data point represents a test sample indicating the cycle count when damage (i.e. broken fibers) was visually detected. It was observed that fatigue failure occurred on the outermost glass fibers on the tension side of the pultruded rod. Values on the ordinate axis represent the peak stress in compression occurring during a cycle. Values on the abscissa indicate the cycle count when the failure criterion was met. The higher the peak stress is, the lower the cycle count before failure. The S-N curve shown in Fig. 48.8 provides a design and application guideline of this technology: relationship between the peak stress level and the cyclic life of the material. Note that even the composite coupler experiences first visual damage on the outermost layer, it is not a catastrophic system failure. In this case the composite coupler will continue to work at reduced critical loads [4].

Wiper systems equipped with the composite coupler were tested in order to validate the technology. The performance of the prototypes met or exceeded that of their conventional counterparts in the following system tests:

- Standard Durability Test: 1.5 millions cycles was reached simulating 10 years of normal ambient operation.

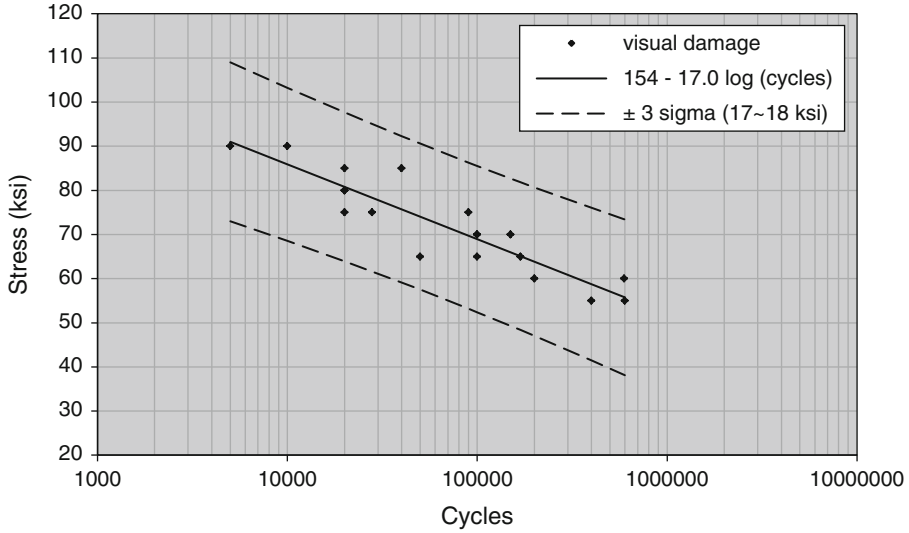

Fig. 48.8 S-N curve for first visual damage

- Cold Test: low temperature at −30 °C restricted wipe test, which simulates snow/ice build up at both the cowl screen and the A-pillar. This test determines the capability of the wiper system to withstand highly abusive loads for an extended period of time. This test was run for 52 h equivalent to 5 years of restricted wiping operation.
- Restricted out of Park Test: it mimics the loading observed when the blades are frozen to the glass and the system is energized. For the application considered, this test simulates the highest expected tension load seen by the connecting rod. This test was run at −30 °C as well.
- Weighted-arm testing that simulates the highest inertial loading the system is expected to see. The arm weighting is designed to simulate the build up of snow and ice on the arms and blades. This test was run exclusively at high speed and at an ambient temperature of −30 °C.

48.3.2 Chatter Test

Due to the fact that the composite coupler has less rigidity and mass comparing to the steel coupler, it is very important to examine the wiping quality in terms of chatter. A wiper system chatter test was designed and performed to confirm that the system operation does not generate additional chatter with the composite coupler. The objectives of chatter test are:

- Simultaneously collect driver-side (DS) and passenger-side (PS) arms chatter data using LabVIEW data acquisition system.
- Compile the data along with the wiper arm positions to locate maximum chatter displacements on the untreated and Rain-X treated windshields.
- Compare chatter data of the prototype and production systems.

The chatter test setup is shown in Fig. 48.9. The wiper system was mounted on the boiler plate test buck with the application specific windshield and mounting points. Three prototype and production wiper systems were tested at both low and high speeds on untreated and Rain-X treated windshields. Figure 48.10 shows the graphical representation of the accelerometer location on the wiper arm. The accelerometers were placed at the arm tip for DS and PS chatter measurements, and the test blades were cleaned with 70 % isopropyl rubbing alcohol. The cleaning was necessary to induce chatter in the system. For each low and high speed measurement, voltage at the motor terminals was maintained to 13.5 VDC. The accelerometer signals were recorded in 6 s with a sampling rate of 512 Hz and analyzed using the LabVIEW Chatter data acquisition and analysis program.

Three wiper systems were used for testing. Chatter performance varies in a certain range for production wiper systems of a given application. In order to directly compare the chatter test results between the composite and steel couplers, a composite coupler prototype and a standard production steel coupler were used on each wiper system and results are compared for the same system. Table 48.1 shows four different chatter test conditions in this work, denoted TC #1–TC #4.

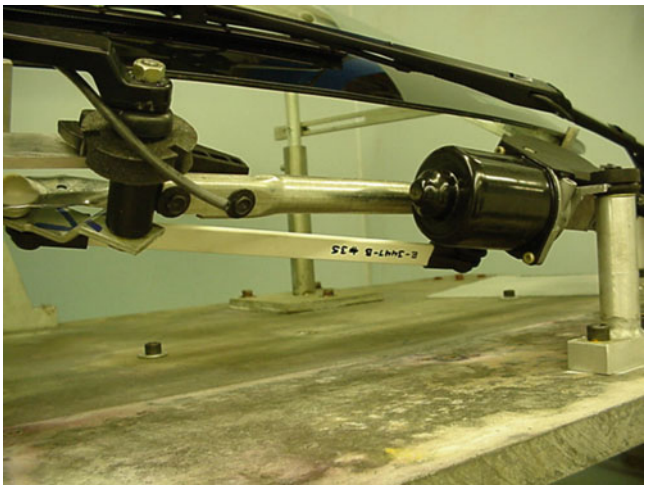

Fig. 48.9 Chatter test setup

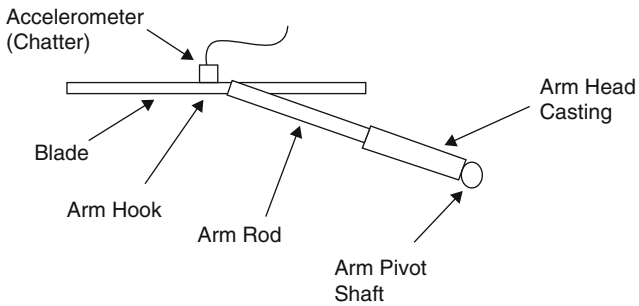

Fig. 48.10 Accelerometer location diagram

Table 48.1 Testing conditions of front wiper system chatter

Testing conditions	System configurations	Glass conditions	Wiping speed
TC #1	Composite 1	Untreated	Low
	Composite 2		
	Composite 3		
	Standard 1		
	Standard 2		
	Standard 3		
TC #2	Composite 1		High
	Composite 2		
	Composite 3		
	Standard 1		
	Standard 2		
	Standard 3		
TC #3	Composite 1	Rain-X Treated	Low
	Composite 2		
	Composite 3		
	Standard 1		
	Standard 2		
	Standard 3		
TC #4	Composite 1		High
	Composite 2		
	Composite 3		
	Standard 1		
	Standard 2		
	Standard 3		

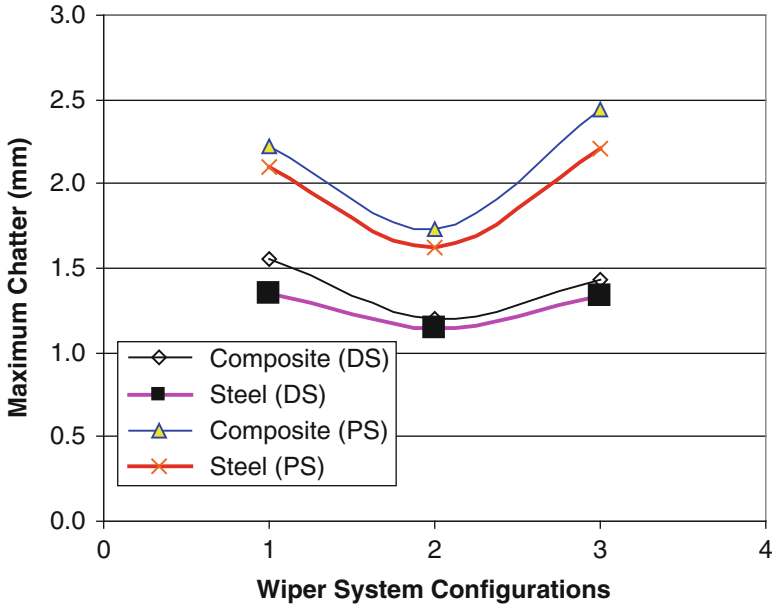

Fig. 48.11 Chatter test result (TC #1)

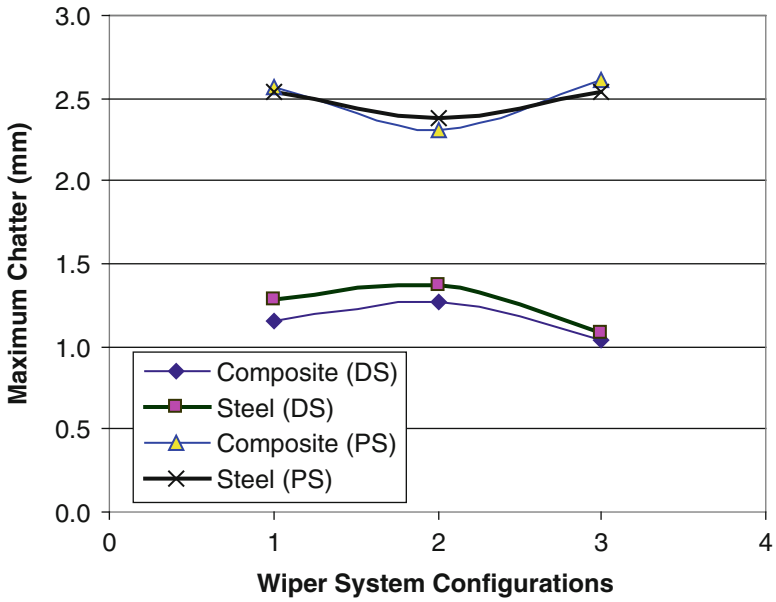

Fig. 48.12 Chatter test result (TC #2)

The windshield has two different conditions, namely, untreated and Rain-X treated. The maximum chatter displacements were measured using wet windshields through rain maker under low (45 rpm) and high (70 rpm) wiping speeds.

Figure 48.11 depicts maximum chatter on the driver side (DS) and passenger side (PS) under testing condition TC #1 (untreated glass, low wiping speed). Note that the maximum chatters with the composite couplers for all three wiper systems, for both DS and PS, are approximately 0.122 mm (8 %) greater that those with the steel couplers. It can also been seen that, under the same testing condition, TC #1 for example, the variation of chatter for the three production systems with standard steel couplers is approximately 0.201 mm, or 15 %. For high speed wiping and untreated glass (TC #2), as shown in Fig. 48.12, chatter in all three wiper systems are very close to that with the production systems. On the untreated windshield, the chatter was not visible for the steel as well as for the composite couplers. As for Rain-X treated windshield, under low speed (TC #3, Fig. 48.13) and high speed (TC #4, Fig. 48.14), the chatter was clearly visible for both the composite and the steel couplers. Both designs exhibited comparable amounts of chatter displacements. Although the difference is slightly higher at low speed (TC #3) compared to the untreated windshield (TC #1 and TC #2), the difference is still not significant.

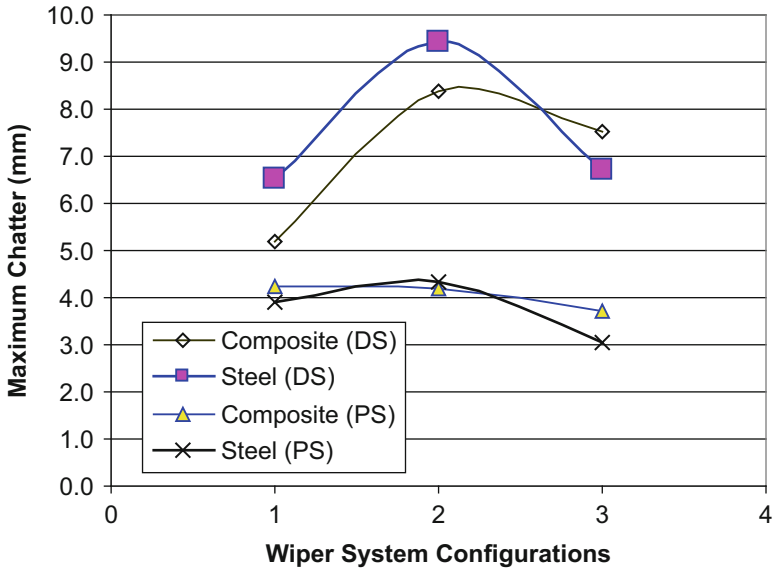

Fig. 48.13 Chatter test result (TC #3)

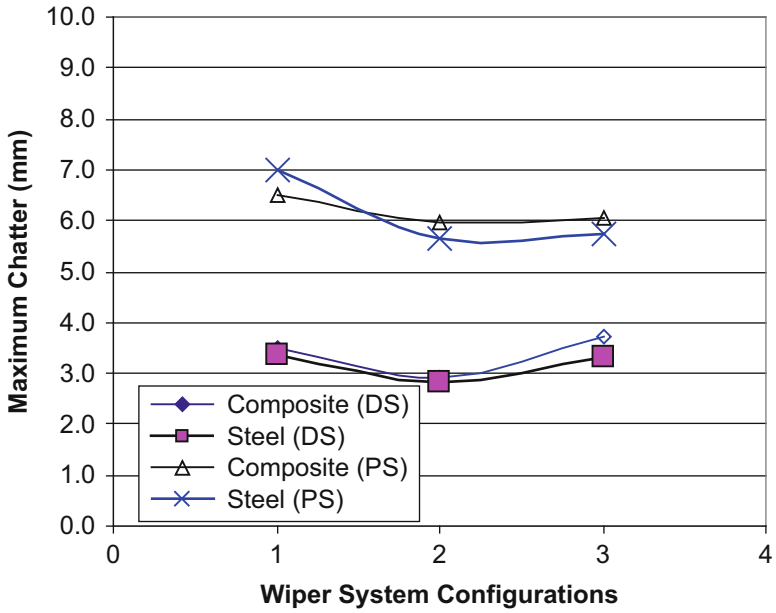

Fig. 48.14 Chatter test result (TC #4)

Table 48.2 Averaged chatter results and comparison

	Composite (DS)	Steel (DS)	Difference δ (%)	Composite (PS)	Steel (PS)	Difference δ (%)
TC #1	1.398	1.276	8.705	2.135	1.973	7.572
TC #2	1.156	1.243	−7.557	2.496	2.485	0.467
TC #3	7.035	7.550	−7.321	4.048	3.766	6.974
TC #4	3.382	3.164	6.465	6.173	6.124	0.783

The chatter test results were averaged for all three systems of each category and tabulated in Table 48.2. The difference in chatter between wiper systems with the steel and composite couplers is defined as

$$\delta = \frac{d_{comp} - d_{steel}}{d_{comp}}$$

where

δ = relative difference in maximum chatter between composite and steel couplers
d_{comp} = maximum chatter using composite couplers (mm)
d_{steel} = maximum chatter using steel couplers (mm)

The composite coupler did not have any noticeable effect on the wiper system performance in terms of the chatter. It did not worsen the chatter compared to the steel link on the untreated as well as Rain-X applied windshields. On the untreated windshield, the chatter was not visible for the steel as well as for the composite link. The difference (average) between the composite and the steel chatters is not significant (Table 48.2).

48.4 Conclusions

The peak loading in the wiper systems under restricted wiping conditions is reduced when a composite coupler is used. For the sample application used in the work, with the protection of the composite coupler, the maximum load in the coupler is reduced from 2100 to 850 N. Because the system is protected from loading extremes, durability of the wiper system is enhanced. Moreover, now the system can be made extremely stiff resulting in excellent pattern control without fear of the extreme loads that normally result from extreme stiffness. The composite coupler is retrofitted in a given application and has passed all the standard wiper validation tests. One of the major concerns, wiper systems chatter, is experimentally proved a non issue. The composite material did not have any noticeable effect on the wiper system performance in terms of the chatter. With the novel use of the composite material, it is possible to eliminate material in some components in the wiper systems, which holds the potential for cost savings. Also, coupling this potential with the fact that composite couplers are only 25 % the mass of their steel counterparts, mass savings are inevitable.

References

1. FMVSS 571-104, 49 CFR, Federal Motor Vehicle Safety Standards; Windshield Wiping and Washing Systems, National Highway Traffic Safety Administration, DOT, USA
2. Buchanan, H.C., Dong, Y.: Windshield wiping system. US Patent 6,148,470, Valeo Electrical Systems, Inc. (2000)
3. Buchanan, H.C., Dong, Y.: Windshield wiping system. US Patent 6,381,800 B1, Valeo Electrical Systems, Inc. (2002)
4. Penrod, J., Dong, Y., Buchanan, H.C. A novel use of a composite material to limit the loads in windshield wiper system. SAE Technical Paper Series, SP-1575, 2001-01-0104 (2001)
5. Penrod, J., Dong, Y.: An application flexible method to limit the loads in windshield wiper system. SAE Technical Paper Series, 2005-01-1835 (2005)
6. Bryson, B.A., Buchanan, H.C., Penrod, J., Dong, Y.: Windshield wiping system manufacturing method. US Patent 06,881,373, Valeo Electrical Systems, Inc. (2005)
7. Dong, Y., Penrod, J.: Use of a designed experiment to determine the optimal method to join injection-molded parts to pultrusions. SAE Technical Paper Series, 2006-01-3575 (2006)
8. Beer, F.P., Johnston, E.R.: Mechanics of Materials. McGraw-Hill, New York (1981)

Chapter 49
Through Process Modeling Approach: Effect of Microstructure on Mechanical Properties of Fiber Reinforced Composites

Mouna Zaidani, Mohammad Atif Omar, and S. Kumar

Abstract In this work, A Through Process Modelling (TPM) methodology suitable for coupling the microstructure and the elastic properties of composites considering plastic injection molding process is presented. The key tasks discussed in this study are: (1) simulation of the whole manufacturing process in order to get the fiber orientation distribution (FOD) at each point of the part, (2) estimation of local effective properties using the orientation tensor obtained by performing a two-step homogenization and (3) Prediction of macroscopic mechanical response as a function of a local anisotropy using a mean-field homogenization technique which is based on assumed relationships between average values of strain and stress fields in each phase. The scheme suggested allows, to analyze the influence of processing conditions on elastic properties of composites. By changing these conditions, for example, the injection mode (central or linear), the cavity thickness, the fiber volume fraction, the microstructure and hence the local elastic properties of the material can be tailored. Thus, for desired structural response of composites, the optimum filling parameters can be chosen even at the stage of design.

Keywords Through process modelling • Plastic injection • Processing conditions • Elastic properties • Fiber orientation

49.1 Introduction and Motivations

In this study, an innovative work about the application of TPM approach on composites manufacturing processes and especially the plastics injection molding process is presented. This work will enable us to highlight the capability of this approach to successfully accelerate materials and component development activities. Fiber reinforced thermoplastics are a cost efficient solution which combines sufficient stiffness for many structural components and a large freedom of shapes provided by injection molding. These materials have long been used for components which do not undergo much loading. They are now increasingly used to make structural parts, which are subjected to complex and repeated mechanical loading. Therefore, the need for a method to predict the mechanical behavior under mechanical loading has become a serious issue during the last decade. For example, De Monte's and Klimkeit's recent fatigue experiments on reinforced thermoplastics give the basis for a comparative study of different fatigue criteria [1, 2]. The use of reinforced thermoplastics for automotive and aeronautic applications for example involves different kinds of difficulties. First, the nonlinear mechanical response of these materials is highly sensitive to both temperature and water content. This topic has been addressed in other works, where complex loading histories under different environmental conditions have been investigated [3, 4]. Another difficulty is due to the injection molding process, which produces a complex fiber orientation distribution over injected structures, and thus in an anisotropic mechanical response. As the fiber orientation distribution also strongly affects the mechanical properties and life time [5, 6], modeling the anisotropic behavior and the knowledge of the local mechanical response of fiber reinforced thermoplastics is mandatory for a reliable design and is the topic of this research work.

It has been pointed out by several researchers that fiber orientation is one of the major factors in determining the mechanical strength as well as the stiffness of a molded part. There Insufficient experimental evidence available that fiber orientation influences the mechanical properties of parts molded by different processes [7, 8] obtained a substantial increase in the tensile modulus of a transfer molded glass-epoxy compound as fibers were aligned more in the direction of the flow. Darlington et al. [9] injection molded edge gated discs of glass reinforced polypropylene over a range of conditions. They found that the Tensile strength and modulus were higher where significant fiber alignment was observed.

M. Zaidani (✉) • M.A. Omar
Engineering Systems and Management, Masdar Institute of Science and Technology, Abu Dhabi, United Arab Emirates
e-mail: mzaidani@masdar.ac.ae

S. Kumar
Mechanical and Materials Engineering, Masdar Institute of Science and Technology, Abu Dhabi, United Arab Emirates

C. Ralph et al. (eds.), *Mechanics of Composite and Multi-functional Materials, Volume 7*,
Conference Proceedings of the Society for Experimental Mechanics Series, DOI 10.1007/978-3-319-21762-8_49

The injection molding of fiber-reinforced thermoplastics is a complicated process. The reinforced composites don't possess isotropic material properties. The thermal and mechanics properties of the composite strongly depend on the fiber orientation pattern. The composite is stronger in the fiber orientation direction and weaker in the transverse direction. The microstructure of a short-fiber-reinforced composite is formed at the stage of filling and remains the same after solidification. As indicated in many studies [10], the inhomogeneity of the material is caused by the flow of the viscous medium during filling. Microphotographic observations of the cross section of moldings [11, 12] show that the orientation pattern of fibers has a layered structure. In the mid layer, the fibers are oriented mainly perpendicularly to the flow direction. However, in the layers close to the mold walls called shear layers, they are mainly parallel with the flow direction. And finally, in the surface layers, a lower concentration and random orientation of the fibers are usually observed (Fig. 49.1).

As mechanical properties of short fiber reinforced thermoplastic injected components depend on flow induced fiber orientation, there is considerable interest in validating and improving models which link the flow field and fiber orientations to mechanical properties. The present paper concerns firstly the numerical modeling of fiber orientation distribution (FOD) in a rectangular plaque 60×30 mm with adjustable thickness 2, 3 and 4 mm and molded with 10, 15, 20, 30, 40, 45 and 50 wt % short fiber reinforced polypropylene for two different injection mode, linear and central (Fig. 49.2). A classical skin (with orientation parallel to the flow)–core (with orientation perpendicular) structure is observed. It is shown that injection mode (linear or central), the cavity thickness and different levels of fiber interactions, due to different fiber concentrations, are responsible for these observations. Secondly, for fiber reinforced parts the consideration of anisotropic material behavior is required to analyze the influence of processing conditions on elastic properties of composites. In the scope of this fact a procedure is described how to consider these effects in terms of process-structure interaction and how to achieve possible benefits on the mechanical performance of reinforced molded parts with different injection mode and part geometry to help designers and technicians with plastic part design optimization.

The aim of the current work is to present a model which allows us to estimate the elastic properties of glass fiber reinforced structures manufactured by injection molding. The starting step is the numerical prediction of the microstructure of a short-fiber-reinforced composite developed during the filling stage of the manufacturing process. For this purpose, the Moldflow Plastic Insight a finite element mesh model, comprised of two-dimensional nodes and triangular shell elements located in a three dimensional (3-D) x, y, z space is used. As a result of simulating the filling process, a second-rank

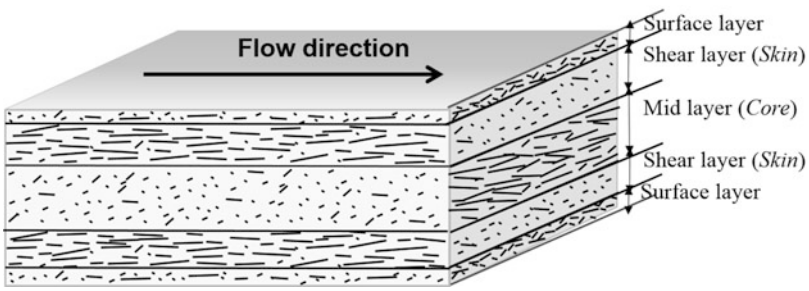

Fig. 49.1 Schematic representation of the skin-core microstructure resulting from the injection molding process of fiber reinforced thermoplastic

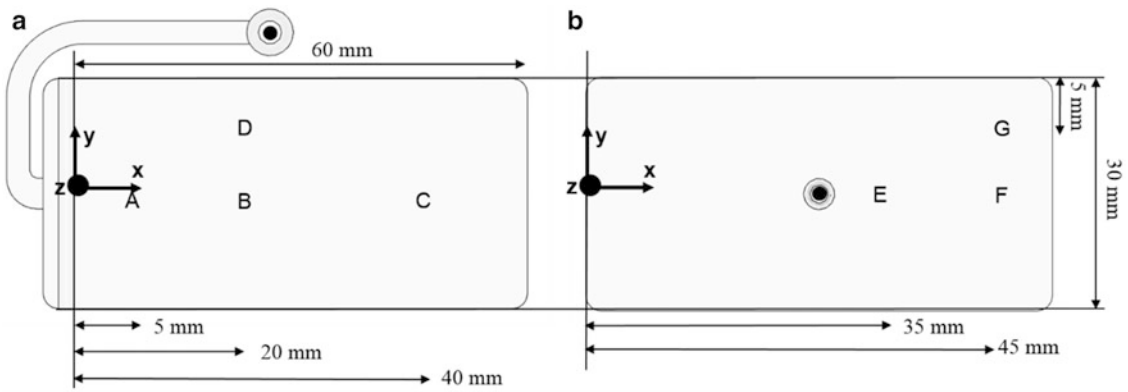

Fig. 49.2 Geometry and dimensions of the cavity, and positions of observation A, B, D and C for linear injection mode (**a**) and E, F and G for central injection (**b**)

orientation tensor characterizing the microstructure of the material is obtained. The elastic properties of the prepared material locally depend on the orientational distribution of fibers. The constitutive equation is formulated by means of orientational averaging for a given orientation tensor. The tensor of elastic material properties is computed and translated into the format for a stress-strain analysis based on the DIGIMAT finite-element code. The numerical procedure and the convergence of results are discussed for a rectangular plate. The influence of manufacturing conditions on the stress-strain state under uniaxial static loading is illustrated.

49.2 Numerical Modeling

49.2.1 Fiber Reinforced Plastic Flow Modeling

During mold filling, the flow field can be modeled as non-isothermal, and Non-Newtonian flow [13, 14], the molten polymer can be assumed to be incompressible. Therefore, with these assumptions, three governing equations, namely the mass conservation, momentum, and energy conservation equations, are solved together with the Fiber Orientation Distribution (FOD) equation and the rheological characteristics of the fiber reinforcement. In addition, the inertia is negligible because of the high viscosity of the polymer melt. As a result, the mass and momentum conservation equations can be written as follows:

The mass conservation leads to the following continuity equation without any time derivative term.

$$\nabla(\rho.u) = 0 \tag{49.1}$$

Where u is the velocity vector. The momentum equation neglecting the body force is of the form

$$\rho\left(\frac{\partial u}{\partial t} + u\nabla.u\right)A = -\nabla p + \nabla.\tau \tag{49.2}$$

Where p is the pressure, τ is the deviatoric stress tensor, which is:

$$\tau = 2\eta D \tag{49.3}$$

Here, η is the viscosity and D is the rate of strain tensor of the form

$$D = \frac{1}{2}(\nabla u + \nabla u^T) \tag{49.4}$$

The energy conservation equation take the following form:

$$\rho C_p\left(\frac{\partial T}{\partial t} + u.\nabla T\right) = \nabla.(k\nabla T) + \eta\dot{\gamma}^2 \tag{49.5}$$

In the above equations, t is the time, u is the velocity vector, p is the hydrostatic pressure, ρ is the density, η is the viscosity, C_p is the specific heat and k is the thermal conductivity. The last term in the right-hand side comes from the viscous dissipation. The shear rate $\dot{\gamma}$ is given as:

$$\dot{\gamma} = \left(2D : D^T\right)^{1/2} \tag{49.6}$$

In most injection molding simulations, the non-isothermal effects would most likely suppress the coupling between the flow and fiber orientation, due to the rapid solidification of the polymer in regions where the coupling is strongest [15]. Therefore, the flow and orientation coupling can be neglected. Thus, the cross-model has been employed to describe the rheological and

the non-Newtonian behavior of the polymer melt and present the temperature and shear rate dependency of the viscosity. Whose expression, in terms of viscosity function, is [16]:

$$\eta(\dot{\gamma}, T) = \frac{\eta_0(T)}{1 + (\eta_0(T)\dot{\gamma}/\tau^*)^{1-n}} \tag{49.7}$$

Where η is the melt viscosity, η_0 is the zero shear viscosity or the 'Newtonian limit' in which the viscosity approaches a constant at very low shear rates, $\dot{\gamma}$ is the shear rate (1/s), τ^* is the critical stress level at the transition to shear thinning and n is the power law index in the high shear rate regime that should be determined from experimental measurement for a specific polymer, This viscosity model is implemented with user function in Moldflow. This viscosity model was incorporated into the finite-element flow modeling software Moldflow.

49.2.2 Fiber Orientation Distribution (FOD) Modeling

In the present investigation, numerical simulation of three-dimensional fiber orientation distribution in injection molding was carried out. Second-order fiber orientation tensor was adopted to describe fiber orientation efficiently similar to the approach proposed by Advani and Tucker [17]. A weakness of this approach is that a fourth-order tensor must be approximated as a known second-order tensor to solve the governing equation. A modified hybrid closure approximation, which can accurately describe random-in-space, random-in-plane, and uniaxial distribution of fiber orientation, is adopted for better predictions.

Calculation of three-dimensional fiber orientation during mold filling can be performed based on the assumptions that the fibers are rigid cylinders, uniform in size and the number of fibers per unit volume is uniform. Therefore, the second and fourth-order orientation tensor of the fibers can be defined as dyadic products of two and four unit vectors, respectively, in the direction of the fibers axes [17]:

Second-order:

$$a_{ij} = \int_p p_i p_j \psi(p) dp \tag{49.8}$$

Fourth-order:

$$a_{ijkl} = \int_p p_i p_j p_k p_l \psi(p) dp \tag{49.9}$$

Where p is a unit vector is parallel to the fiber's axis of symmetry, and $\psi(p)$ is the probability distribution function for fiber orientation at any position in the flow.

The governing equation of the second-order orientation tensor which will be used in this investigation can be expressed as follows [18]:

$$\begin{aligned} \frac{Da_{ij}}{Dt} &= \frac{\partial a_{ij}}{\partial t} + u_k \frac{\partial a_{ij}}{\partial x_k} \\ &= -\frac{1}{2}\left(\omega_{ik}a_{kj} - a_{ik}\omega_{kj}\right) + \frac{1}{2}\lambda\left(\dot{\gamma}_{ik}a_{kj} + a_{ik}\dot{\gamma}_{kj} - 2\dot{\gamma}_{kl}a_{ijkl}\right) + 2D_r\left[\delta_{ij} - 3a_{ij}\right] \end{aligned} \tag{49.10}$$

Where δ_{ij} is a unit tensor, and $\dot{\gamma}_{ij} = \left(\nabla u + (\nabla u)^T\right)$ and $\omega_{ij} = \left(\nabla u - (\nabla u)^T\right)$ are the strain rate and vorticity tensors, respectively. λ is a parameter that depends on fiber aspect ratio, $\lambda = (r_e{}^2 - 1)/(r_e{}^2 + 1)$ with r_e being the equivalent fiber aspect ratio $r_e = L/D$, where L and D are the fiber length and diameter respectively. D_r is the rotary diffusivity term used to model the interaction between fibers suggested by Folgar and Tucker [19].

To solve Eq. (49.10), the fourth-order orientation tensor a_{ijkl} must be approximated as a function of the second-order orientation tensor a_{ij}. The major drawback of the orientation tensor approach is that obtaining a closed-form solution using Eq. (49.10) is impossible due to the presence of the fourth order orientation tensor. To tackle this problem, a_{ijkl} needs to be approximated in terms of the second order one using a closure approximation. Recent progresses has been done in the field of closure approximations [20, 21]. In this work, the standard hybrid closure method is used [17].

49.2.3 Estimation of Elastic Properties

To calculate the mechanical properties, all the theories follow a two-step procedure, the properties of a unidirectional short fiber reinforced material are estimated. These properties are then averaged across the laminates according to the fiber orientation distribution density. Thus, this methodology independently accounts for the influence of fiber aspect ratio and fiber orientation. For this purpose, to model the elastic properties of glass-reinforced thermo-plastic injection molded parts, we use Digimat which is a mean-field homogenization (MFH) based finite element analysis software that aims at predicting the nonlinear constitutive behavior of multi-phase materials based on the constitutive properties of the base materials and the composite morphology (filler content, length and aspect ratio, orientation). In such a case we will take into account the fiber orientation predicted by injection molding simulation and create a micro-mechanical digital material model that is coupled with the output of a Moldflow simulation to give more accurate FEA results.

The homogenization of such composites is carried out in two steps, the first step is the determination of an equivalent unidirectional composite, with for example the Mori–Tanaka scheme. The overall mechanical elastic tensor $\mathbb{C}^{UD}$ is transversely isotropic. $\mathbb{C}^{UD}$ is characterized by five elastic constants K_i. The second step is an orientation average of these elementary UD composites, according to their orientation. A stiffness averaging is often suggested in the literature, the Voigt model is used in this second step to determine the elastic tensor $\mathbb{C}^e$ in the general anisotropic case:

$$\mathbb{C}^e = \int_{\Omega} \mathbb{C}^{UD}\left(\underline{p}\right)\psi\left(\underline{p}\right)d\omega \tag{49.11}$$

49.3 Results and Discussion

During the molding process, fiber orientation at a point is controlled by the fluid motion, the prediction accuracy depends upon the accuracy of the velocity gradient calculated. Like velocity, the representation of the orientation tensor is also coordinate system dependent. All numerical schemes suitable for the calculation of velocity gradients can be used to calculate the orientation gradient. Numerically, the same element system is used to represent the velocity and orientation fields, consequently the same scheme is used to calculate the velocity and orientation gradients and the fiber orientation prediction is coupled with the mold filling simulation. Simulations are carried out for fiber orientation prediction in a three-dimensional rectangular cavity for two different injection mode, linear and central. A schematic diagram which represents the physical system is shown in Fig. 49.2 with dimensions Length = 60 mm, Width = 30 mm, and variable thickness = 2, 3, 4 mm. The flow direction is along the x-axis, while y-axis and z-axis are the width, and thickness directions, respectively. The polymer is polypropylene melt containing 10, 15, 20, 30, 40, 45 and 50 % by weight (5, 8, 11, 17, 24, 28, 32 % by volume) short glass fibers as reinforcement.

For reinforced plastic injection molding, The simulation of the flow and fiber distribution in the flat plates was performed using the program 'Moldflow Plastic Insight (MPI)', which is based on the finite element method (FEM) to solve the flow problem described by Navier Stokes equations for simulations in 3D, or the Hele-Shaw equations for simulation in 2D [18, 22]. For 3D simulations it then uses the computed velocity gradient and volume of fluids method (VOF) [22] to advance the flow front. To calculate the fiber orientation the Folgar Tucker model with a hybrid closure approximation was used [see Eq. (49.10)], A mean fiber aspect ratio L/D of 25 has been used, so that C_I can be calculated. In addition, the viscosity is modeled with the cross-WLF model, which is widely used with temperature dependent zero-shear viscosity. The modelled part had a very fine mesh density and was simulated fully 3D with inertia effects. This approach is quite common for the estimation of the fiber orientation. The program parameters were chosen as follows. The mass and mold temperature were 225 °C and 38 °C, respectively. The flow rate was set to 50 cm^3/s and the maximum injection pressure was 20 MPa. Figure 49.3 present a display of the injection simulation results and the fiber orientation distribution (FOD) for a 3 mm rectangular cavity as a function of the injection mode, linear injection where the flow front is meanly longitudinal and central

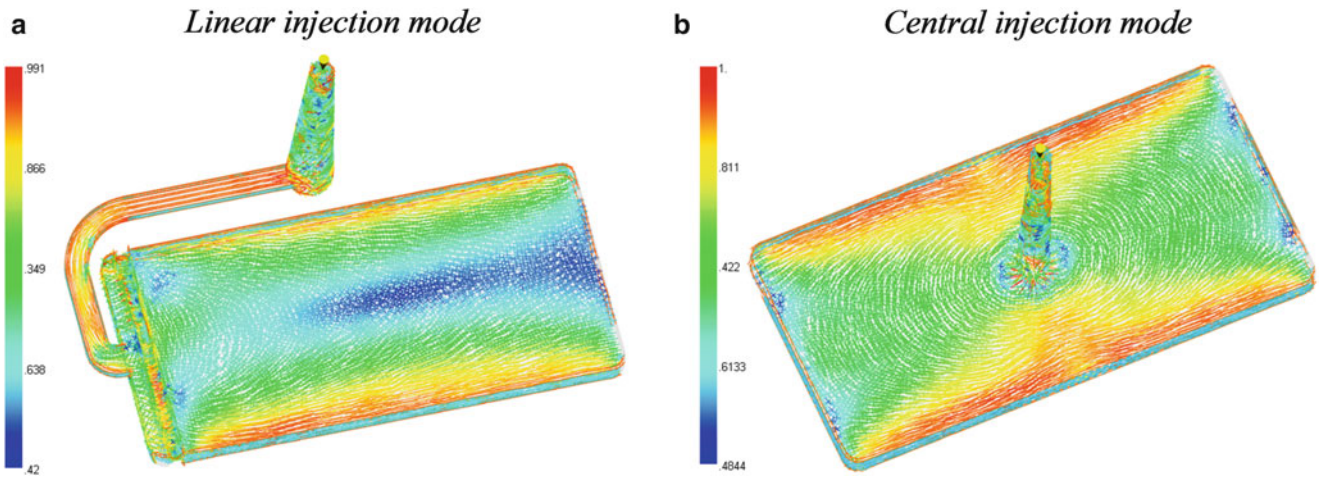

Fig. 49.3 Injection simulation of the rectangular plate, and display of the fiber orientation distribution FOD over the surface. The plate dimension is 60 mm × 30 mm × 3 mm. A 14682 (**a**) and 12142 (**b**) *triangular* shell elements with 21 Gauss points through the thickness are used for the numerical computation, injection location is marked with the *yellow cone*

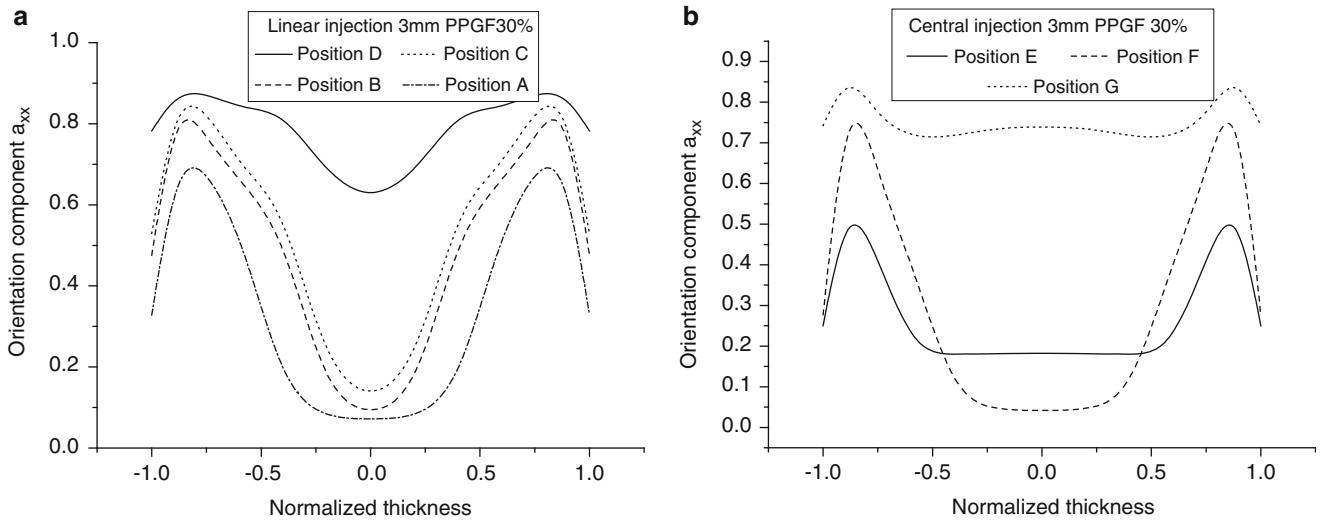

Fig. 49.4 Evolution of a_{xx} in the thickness direction of 3 mm thick plaque for PPGF 30 % at the end of filling, for linear injection mode in positions A, B, C and D (**a**) and the central injection mode E, F and G (**b**)

injection where the flow front is radial. The FOD is highly dependent at a point by the fluid motion, for the same injected part, the properties and the distribution of the fibers is different as a function of the flow front direction and the choice of the injection mode.

Shown from Fig. 49.4a, b are comparisons between the central and linear injection mode of flow directional fiber orientation components a_{xx} across the mold thickness at different positions of the injected part (Fig. 49.2). The physical meaning of these orientation components is related to the direction of the principal axes of the fibers. If the value of a_{xx} is close to unity, then it implies that the axes of the fibers are oriented to the flow direction, 1 indicating perfectly aligned to the flow direction and 0 indicates that the fibers are oriented perpendicular to the flow direction. On the other hand, small values of a_{xx} indicates poor orientation of fibers to the flow direction.

For both linear and injection case, generally, due to the fact that the shear stress decreases at the midplane of the cavity where the flow is extensional flow dominated, the orientation values will not change significantly since they leave the mold gate. Therefore, this behavior and symmetry principle lead to parabolic shaped curves as shown in Fig. 49.4, the simulation results for the flow directional orientation components are in good agreement with published numerical and experimental measurements from [23, 24]. whatever the position along the plaque, close to the mold walls, the values of flow directional orientation tensor component a_{xx}, are important and close to unity, in the core region the values of a_{xx} are smaller because of

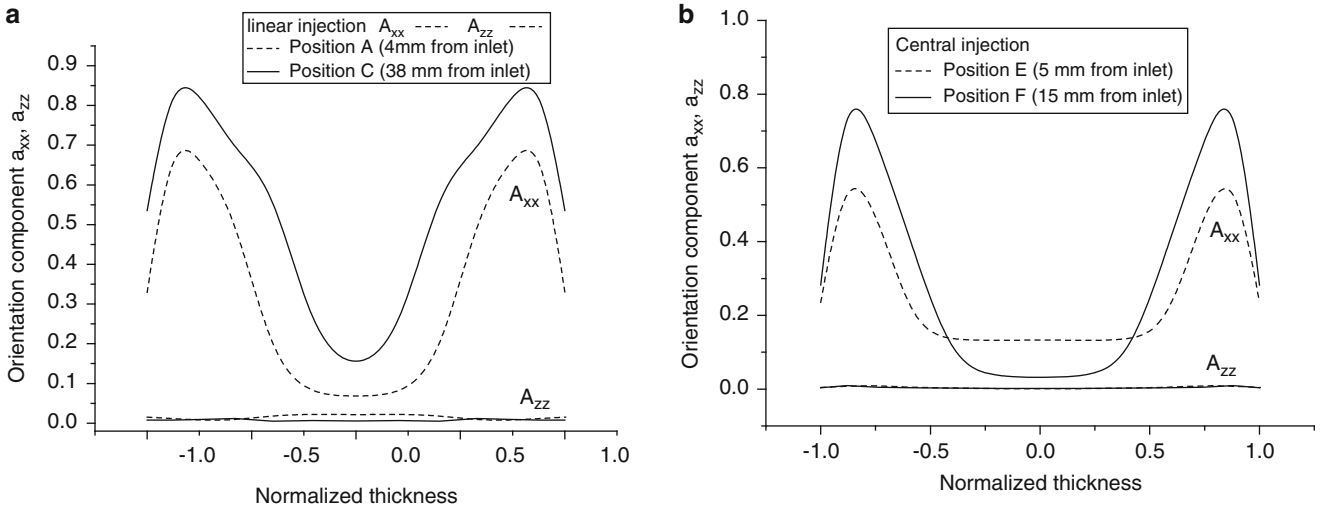

Fig. 49.5 Results of orientation components a_{xx} and a_{zz} 3 mm thick plaque for PPGF 30 % at the end of filling, near and far from the inlet for linear (**a**) and central injection mode (**b**)

Table 49.1 Mechanical properties of the studied glass fiber reinforced polypropylene

Volume fraction	Aspect ratio L/D	Young modulus	Density	Poisson coefficient
Glass fibers				
10, 15, 20, 30, 40, 45, 50 %	25	72000 MPa	2.54 g/cm^3	0.22
Young modulus	Shear modulus	Poisson coefficient	Density	
Polypropylene				
2733 MPa	1624 MPa	0.39	1.24 g/cm^3	

the fibers are meanly oriented in the transverse direction and poorly oriented to the flow direction. These big values of a_{xx} indicate that the fibers are perfectly aligned to the flow direction near the mold walls.

Figure 49.5 shows comparisons of flow and thickness directional orientation components (a_{xx} and a_{zz}) across the mold thickness at different positions from the inlet for linear and central injection. The physical meaning of these orientation components is related to the direction of the principal axes of the fibers.

For both linear and central injection, the value of a_{xx} far from the inlet is more important than near to the injection gate especially near to mold walls, then it implies that far from the inlet the fibers are oriented to the flow direction, 1 indicating perfectly aligned to the flow direction and 0 indicates that the fibers are oriented perpendicular to the flow direction. On the other hand, small values of a_{xx} in the core region indicates poor orientation of fibers to the flow direction. The simulation results predicting very small value of the thickness directional orientation component a_{zz}, small values of a_{zz} show that fibers are aligned more to the flow direction or to the width direction. The values of a_{zz} are always higher at mid plane and they keep decreasing towards the mold walls. Numerical values prediction of a_{zz} are significantly smaller than a_{xx} as can be observed in Fig. 49.5, even in regions near the middle of the flow where fluid stretching should be dominant.

We will show some features of a complete analysis under monotonic tensile test of the structures of short-fiber-reinforced composite materials under different injection molding parameters (injection mode, fiber weight fraction...) and stress analysis. The behavior of the resulting composite thus exhibits the features of the glass fiber reinforced polypropylene induced by the fiber orientation distribution. Table 49.1 shows the microstructural and elastic parameters of both matrix and fiber phases of the studied material.

The numerical prediction of the stress strain state of a 3 mm PPGF rectangular injected plate, a comparison between central and linear injection mode for monotonic tensile tests at 2.5 % min^{-1} as a strain loading rate is displayed in Fig. 49.6 for different fiber weight fraction. Let us remark that the mechanical response of the reinforced plastic injected plate is highly affected by the reinforcement fraction, the injection mode and consequently by the fiber orientation distribution, the effective stiffness of the central injected part is significantly higher than the part linearly injected, In short fiber-reinforced thermosetting polymer composites, it is reasonable to assume that the elastic properties are determined primarily by orientation effects. Moreover, the placement of the injection gate will have a strong influence on the plastic flow direction consequently on the final mechanical properties of the molded part and must be carefully chosen.

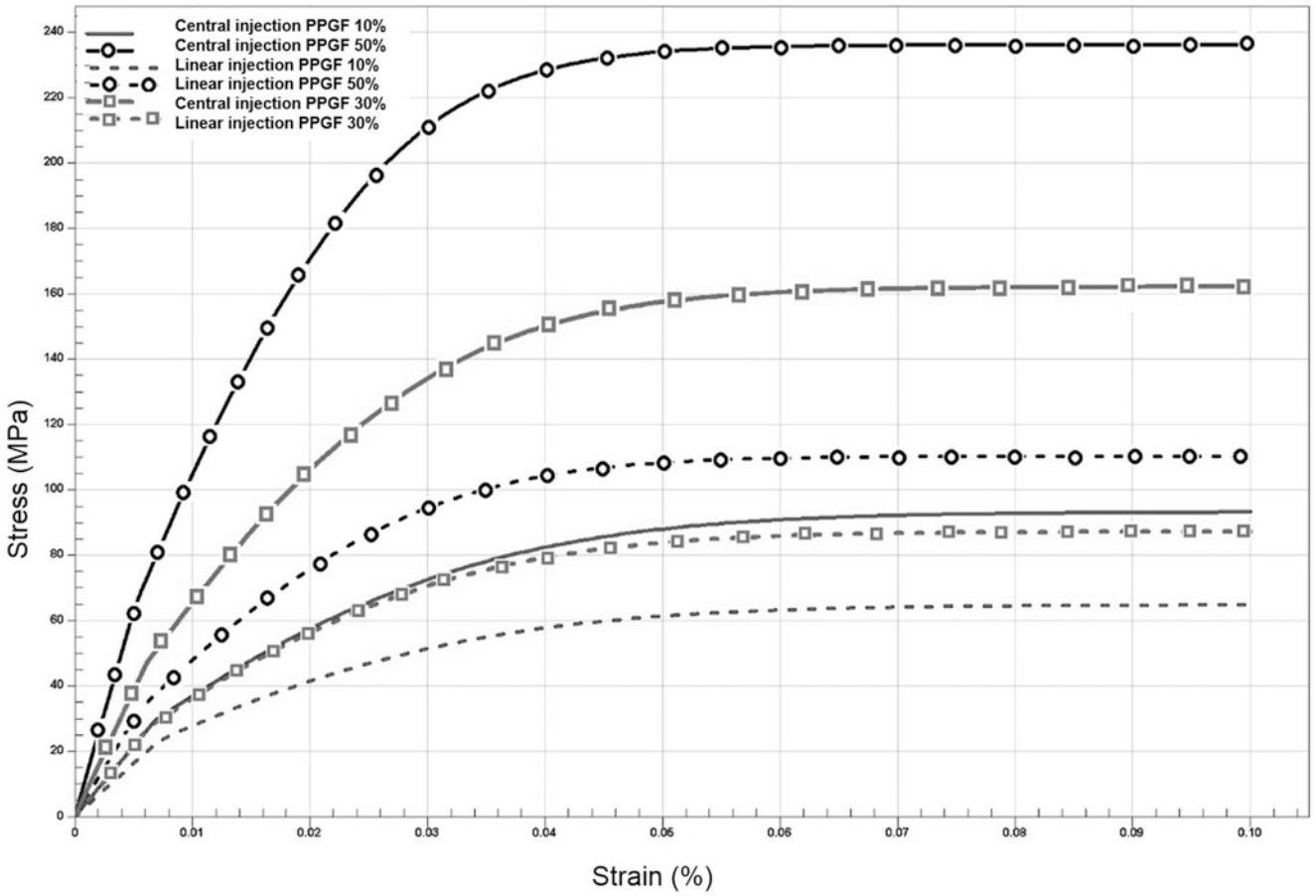

Fig. 49.6 Numerical predictions of the strain-stress state for central injection versus linear injection on 3 mm rectangular injected plate with different fiber weight fraction, for monotonic tensile tests

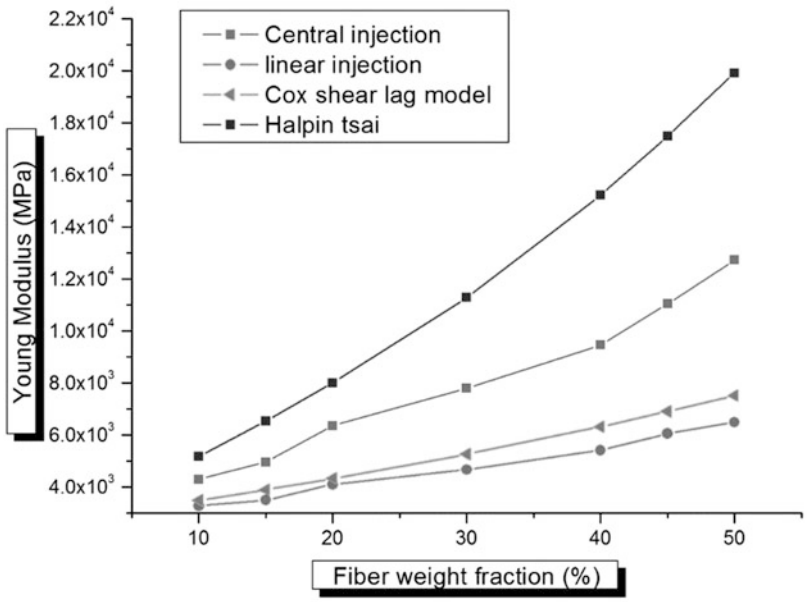

Fig. 49.7 Comparison of Young Modulus numerical prediction (central injection and linear injection) with theoretical models

In order to show the influence of fiber orientation distribution on the estimation of the mechanical properties, Fig. 49.7 shows a comparison between the theoretical and numerical prediction of the Young modulus for different fiber weight fraction. The numerical prediction using the through process modeling approach take into account the injection mode and consider the effect of the induced fiber orientation distribution onto the elastic properties of the reinforced molded part.

Many micromechanical theories and models such as the Halpin-Tsai [25] and the shear lag models [26], have been developed to predict the modulus and strength of random, discontinuous fiber-reinforced composites, without taking into account the FOD induced by the injection process parameters, these models use the mechanical properties of the fiber and the matrix to calculate the properties of the composite. The Young modulus theoretically estimated is consistent with the numerical prediction.

49.4 Conclusion

In this study, the possibility of a successive finite-element analysis of the injection-molding process and the stress–strain state of reinforced plastic articles is demonstrated. The investigation scheme developed allows one to estimate the local elastic properties of the material from the results of fiber orientation. Based on the results obtained, we can conclude the following.

1. The microstructure of fiber orientation caused by the filling process is highly non uniform. The influence of this microstructure must be taken into account in estimating the stress–strain state of the molded articles.
2. In designing articles of short-fiber-reinforced thermoplastics, both the injection-molding process and the stress–strain state of the prepared articles must be analyzed.
3. The investigation scheme suggested allows us, for known loading conditions of a structure, to analyze the influence of processing conditions on its elastic properties. By changing these conditions, for example, the filling mode, the filling rate, and the mold geometry, we can affect the microstructure of fiber orientation and hence the local elastic properties of the material. Thus, for given operating conditions of a structure under loading, the optimum filling parameters can be chosen even at the stage of design.

References

1. De Monte, M., Moosbugger, E., Jasckek, K., Quaresimin, M.: Multiaxial fatigue of a short fibre reinforced polyamide 6.6 – fatigue and fracture behaviour. Int. J. Fat. **32**, 7–28 (2010)
2. Klimkeit, B.: Etude expérimentale et modélisation du comportement en fatigue multiaxiale d'un polymère renforcé pour application automobile. Ph.D. Thesis, École Nationale Supérieure de Mécanique et d'Aérotechnique (2009)
3. Launay, A., Maitournam, M., Marco, Y., Raoult, I., Szmytka, F.: Cyclic behavior of short glass fiber reinforced polyamide: experimental study and constitutive equations. Int. J. Plast. **27**, 1267–1293 (2011)
4. Launay, A., Marco, Y., Maitournam, M., Raoult, I.: Influence of temperature and relative humidity on the cyclic behaviour of a short glass fiber reinforced polyamide. Mech. Mater. (submitted for publication)
5. Bernasconi, A., Davoli, P., Basile, A., Filippi, A.: Effect of fiber orientation on the fatigue behaviour of a short glass fiber reinforced polyamide-6. Int. J. Fat. **29**, 199–208 (2007)
6. De Monte, M., Moosbugger, E., Quaresimin, M.: Influence of temperature and thickness on the off-axis behaviour of short glass fibre reinforced polyamide 66 – quasi-static loading. Compos. Part A **41**, 859–871 (2010)
7. Goettler, L.A.: Flow orientation of short fibers in transfer molding. In: Proceedings of 25th Annual Conference on SPIRP/CDiv., Sect 14-A (1970a)
8. Goettler, L.A.: Controlling flow orientation in molding of short-fiber compounds. Mod. Plast. **47**, 140 (1970b)
9. Darlington, M.W., Gladwell, B.K., Smith, G.R.: Structure and mechanical properties in injection molded discs of glass fiber reinforced polypropylene. Polymer **18**, 1269 (1977)
10. Hegler, R.P.: Faserorientierung beim Verarbeiten kurzfaserverstärkter Thermoplaste. Kunststoffe **74**, 271–277 (1984)
11. Bay, R.S., Tucker, C.L.: Fiber orientation in simple injection moldings. Pt. 2. Experimental results. Polym. Compos. **13**, 332–341 (1992)
12. Saito, M., Kukula, S., Kataoka, Y., Miyata, T.: Practical use of statistically modified laminate model for injection moldings. Mater. Sci. Eng. **A285**, 280–287 (2000)
13. Ding, D., et al.: Finite element simulation of an injection moulding process. Int. J. Numer. Methods Heat Fluid Flow **7**(7), 751–766 (1997)
14. VerWeyst, B.E., et al.: Fiber orientation in 3-D injection molded features: prediction and experiment. Int. Polym. Process **14**, 409–420 (1999)
15. VerWeyst, B.E.: Numerical predictions of flow-induced fiber orientation in three-dimensional geometries. Mechanical Engineering, University of Illinois, Urbana-Champaign (1998)
16. Bay, R.S., Tucker, C.L.: Fiber orientation in simple injection moldings. Part I: theory and numerical methods. J. Polym. Compos. **13**(4), 317–331 (1992)
17. Advani, S.G., Tucker, C.L.: The use of tensors to describe and predict fiber orientation in short fiber composites. J. Rheol. **31**, 751–784 (1987)
18. San Rafael, Learning Autodesk Moldflow Insight Basic – Theory and Concepts 2012; 2011. Autodesk Inc. CA : ASCENT - Center for Technical Knowledge (2011)
19. Folgar, F., Tucker, C.L.: Orientation behavior of fibers in concentrated suspensions. J. Reinf. Plast. Compos. **3**(2), 98–119 (1984)

20. Chung, D.H., Kwon, T.H.: Fiber orientation in the processing of polymer composites. Korea–Aust. Rheol. J. **14**(4), 175–88 (2002)
21. Chung, D.H., Kwon, T.H.: Applications of recently proposed closure approximations to injection molding filling simulation of short-fiber reinforced plastics. Korea–Aust. Rheol. J. **12**(2), 125–33 (2000)
22. Patel, N.: Validation of 3D Moldflow filling analysis for TPV's. Master's thesis, University of Massachusetts, Lowell (2000)
23. Michel, V., Girould, T., Clarke, A., Eberhardt, C.: Description and modeling of fiber orientation in injection molding of fiber reinforced thermoplastics. Polymer **46**, 6719–6725 (2005)
24. Nemet, A., Mamat, O.: A study of fiber orientation in short fiber-reinforced composites with simultaneous mold filling and phase change effects. Compos. Part B **43**, 1087–1094 (2012)
25. Halpin, J.C.: Stiffness and expansion estimates for oriented short fiber composites. J. Compos. Mater. **3**, 732–734 (1969)
26. Cox, H.L.: The elasticity and strength of paper and other fibrous materials. Br. J. Appl. Phys. **3**, 72–79 (1952)

Chapter 50
Molding Strain of Glass Fibers of Model GFRP

Tatsuro Kosaka, Takahiro Horiuchi, and Kazuhiro Kusukawa

Abstract In order to evaluate strain induced by shrinkage of resin during cure process, model specimen of glass optical fiber-reinforced polymers were manufactured. Single FBG sensor was embedded in the specimen for measuring molding process-induced strain. From the experimental results, it was found that cure shrinkage strain as well as thermal strain should be considered for evaluating residual stress in reinforcing fibers. An viscoelastic FEM analysis was conducted to evaluate the molding strain of reinforcements. Mechanical and thermal properties of resin as functions of degree of cure were measured and used for the simulation. It appeared that the calculated results agreed well with experimental results. Therefore, it was found that viscoelastic property, thermal expansion and curing shrinkage of resin play significant roles for cure process-induced strain of reinforcing fibers of FRP. The ratio of cure process-induced strain by curing shrinkage of the resin to whole molding process-induced strain was 17.7 %. This fact indicates that the effect of curing shrinkage of the resin should be taken into account for evaluation of molding process-induced strain of the reinforcements.

Keywords FRP • Process-induced strain • FBG sensor • FEM analysis • Process monitoring

50.1 Introduction

It is well known that residual stress of fiber and matrix of FRP (Fiber Reinforced Plastics) induced by molding process affect the durability and accuracy of dimension [1–3]. Therefore, control of residual stress is a key technology for manufacturing high quality FRP. It is considered that the process-induced residual stress is governed by thermal deformation and cure shrinkage during cure and cooling process. However, it is not enough to evaluate process-induced strain because it is difficult to measure stress or strain during molding process.

Recently, process monitoring methods of FRP using embeddable fiber optic sensors, which have small size, flexibility and high sensitivity, have been developed. There are many kinds of fiber optic sensors which can measure temperature, pressure, cure index or strain. Especially, strain measurement using a fiber optic strain sensor is an only method to measure stain during molding.

In this paper, model specimen of glass optical fiber-reinforced polymers were manufactured and an FBG (Fiber Bragg Grating) optical fiber strain sensor was embedded to measure molding process-induced strain of reinforcement. Degree of cure of the specimen was also measured by embedded Fresnel-based refractive-index sensors. Furthermore, an FE viscoelastic analysis was conducted in order to evaluate the experimental results.

50.2 Material and Experimental Method

50.2.1 Model Specimens

Glass optical fibers were employed for reinforcements. The diameter of optical fiber whose jacket was removed was 125 μm. Aligned 21 optical fibers were fixed to a paper frame and the 7 optical-fiber layers were stacked in a small mold. A bisphenol-A epoxy resin (jER801N, Mitsubishi Chemical, Co. Ltd.) with curing agent (epicure 3080), where the mixture ratio was 100:45 in weight, was used as matrix resin. The resin was poured in the mold after mixture process. The mold was

T. Kosaka (✉) • T. Horiuchi • K. Kusukawa
Kochi University of Technology, School of Systems Engineering, 185 Miyanokuchi, Tosayamada-cho, Kami-city, Kochi 782-8502, Japan
e-mail: kosaka.tatsuro@kochi-tech.ac.jp

C. Ralph et al. (eds.), *Mechanics of Composite and Multi-functional Materials, Volume 7*,
Conference Proceedings of the Society for Experimental Mechanics Series, DOI 10.1007/978-3-319-21762-8_50

set in an oven and heated from 25 to 100 °C in 100 min. The temperature was held at 100 °C for 3 h and then the specimen was naturally cooled to room temperature. Figure 50.1 shows a photograph of specimen. The length is 20 mm, width is 3.3 mm, thickness is 1 mm, and volume fraction of optical fibers is 54.6 %. The FBG sensor whose gage length was 10 mm was embedded in the center position of the specimen.

50.2.2 Measurement of Strain by FBG Sensors

In this experiment, single EBG sensor was embedded in resin. An FBG sensor has a periodical grating of refractive index which reflects narrow-band light when broad-band light is incident. Because a center wavelength of the reflected narrow-band light is a function of a period of the grating, strain ε_3 and temperature shift ΔT can be calculated from the wavelength shift $\Delta\lambda$ using the following equation.

$$\frac{\Delta\lambda}{\lambda_0} = \left[1 - \frac{n_0^2}{2}\{p_{12} - \nu_s(p_{11} + p_{12})\}\right](\varepsilon_3 - \alpha_s \Delta T) + \left(\alpha_s + \frac{1}{n_0}\frac{dn_0}{dT}\right)\Delta T. \tag{50.1}$$

Here, λ_0 is an initial centre wavelength, n_0 is an effective refractive index, p_{12} and p_{11} are Pockel's constants, n_s and α_s are Poisson's ratio and thermal expansion coefficient of an optical fiber. Sensitivities of the sensor were experimentally obtained as Figure 50.2 illustrates an experimental setup for measuring molding strain of an FBG sensor embedded in

$$\left[1 - \frac{n_0^2}{2}\{p_{12} - \nu_s(p_{11} + p_{12})\}\right] = 0.7368, \quad \left(\alpha_s + \frac{1}{n_0}\frac{dn_0}{dT}\right) = 6.138 \times 10^{-6}. \tag{50.2}$$

the model GFRP specimen. The initial wavelength was 1550 nm, the diameter was 125 μm and the gage length was 10 mm. High power SLD light source (the center wavelength is 1550 nm) was used as a light source. The spectrum of narrow-band light reflected from the FBG sensor was measured by an optical spectrum analyzer (OSA). Temperature of the specimen was measured by an embedded thermo-couple. Using the Eq. (50.1), strain of the embedded optical fiber was calculated from measured wavelength shift and temperature shift.

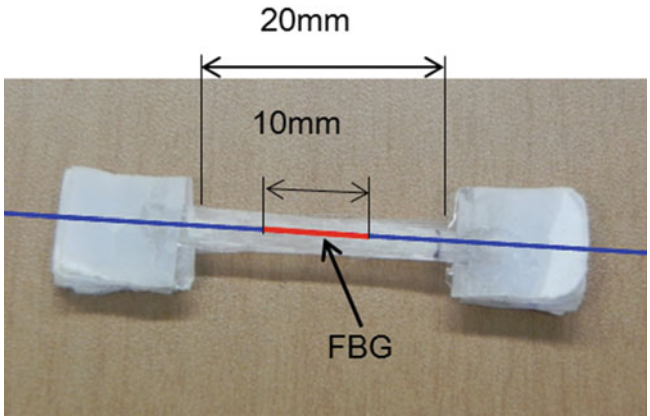

Fig. 50.1 Photograph of model specimen (width is 3.3 mm, thickness is 1 mm, volume fraction of optical fibers is 54.6 %)

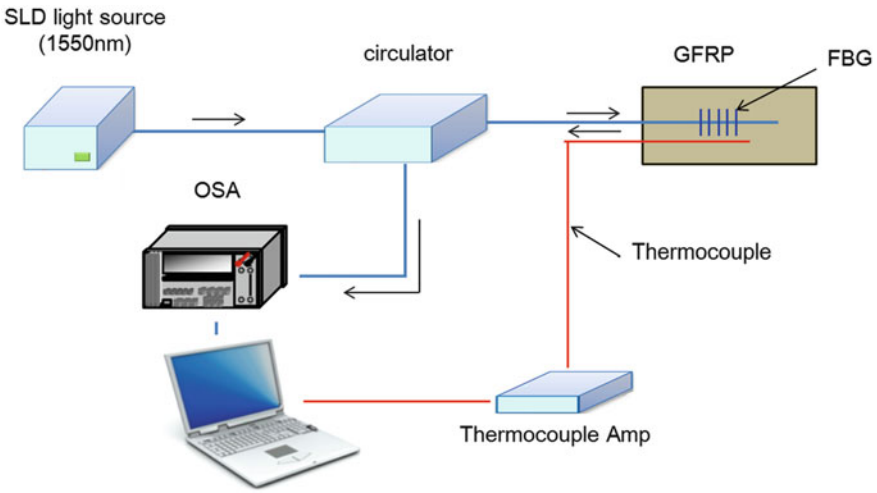

Fig. 50.2 Experimental setup for measuring molding strain of an FBG sensor embedded in the model GFRP

50.3 Fem Analysis

50.3.1 Constitutive Equation

A viscoelastic constitutive equation for general isotropic viscoelastic materials can be represented by

$$\boldsymbol{\sigma}(t) = \int_0^{\tau(t)} 2G\left(\tau - \tau'\right)\dot{\mathbf{e}}d\tau' + \mathbf{I}\int_0^{\tau(t)} K\left(\tau - \tau'\right)\dot{\phi}d\tau', \tag{50.3}$$

$$\phi = \varepsilon_{11} + \varepsilon_{22} + \varepsilon_{33} \quad \text{and} \quad \mathbf{e} = \boldsymbol{\varepsilon} - \frac{1}{3}\phi\mathbf{I} \tag{50.4}$$

where $\boldsymbol{\sigma}$ is a stress tensor, $\boldsymbol{\varepsilon}$ is a mechanical strain tensor, $\mathbf{e}$ is a deviatoric strain tensor, ϕ is a bulk strain, $\mathbf{I}$ is a unit tensor, G is a shear modulus, K is a bulk modulus, t is real time and $\tau(t)$ is reduced time as a function of temperature. The reduced time can be written using a temperature shit factor of resin $A_T(T)$ as

$$\tau(t) = \int_0^t \frac{dt'}{A_T(T(t'))}. \tag{50.5}$$

In the present paper, we supposed that moduli of resin varied during cure process and then the Eq. (50.3) was modified to represent viscoelastic constitutive equation of resin during molding as follows.

$$\boldsymbol{\sigma}(t) = \int_0^{\tau} 2G\left(\alpha, \tau - \tau'\right)\dot{\mathbf{e}}d\tau' + \mathbf{I}\int_0^{\tau} K\left(\alpha, \tau - \tau'\right)\dot{\phi}d\tau' \tag{50.6}$$

where α is degree of cure of resin which varies from 0 to 1 during moulding process. The viscoelastic shear modulus $G(\alpha,t)$ of resin during cure process was defined by Prony series as

$$G(\alpha, t) = G_0 A_\alpha(\alpha)\left\{1 - \sum_{i=1}^{n_G} g_i\left(1 - e^{-t/\tau_i}\right)\right\} \tag{50.7}$$

where G_0 is an instantaneous shear modulus, A_α is a decrease index of shear modulus and g_i and τ_i are Prony parameters. On the other hand, it was supposed that the bulk modulus was constant during cure, that is,

$$K(\alpha, t) = K_0. \tag{50.8}$$

Here K_0 is an instantaneous bulk modulus. From the Eqs. (50.6), (50.7) and (50.8), the following equations were obtained.

$$\boldsymbol{\sigma}(t) = 2G_0\left(\widetilde{\mathbf{e}} - \sum_{i=1}^{n_G} g_i \widetilde{\mathbf{e}}_i\right) + \mathbf{I}K_0\phi, \tag{50.9}$$

$$\widetilde{\mathbf{e}} = \int_0^{\tau(t)} A_\alpha(\alpha)\frac{d\mathbf{e}}{d\tau'}\,d\tau' \quad , \quad \widetilde{\mathbf{e}}_i = \int_0^{\tau(t)} A_\alpha(\alpha)\left(1 - e^{(\tau'-\tau)/\tau_i}\right)\frac{d\mathbf{e}}{d\tau'}\,d\tau' \tag{50.10}$$

where $\widetilde{\mathbf{e}}$ and $\widetilde{\mathbf{e}}_i$ represent deviatoric elastic strain and viscoelastic strain, respectively. In this study, a stress tensor was numerically calculated by discrete equations of (50.9) and (50.10).

50.3.2 Material Characteristics of Resin

Most parameters necessary for calculation of viscoelastic response of resin during cure process were experimentally obtained in the present study. DOC of resin at arbitrary curing condition was calculated by the following Kamal's model [4].

$$\dot{\alpha} = (k_1 + k_2\alpha^m) \times (1 - \alpha)^n, \tag{50.11}$$

$$k_1 = A_1 \exp\left(-\frac{E_1}{RT}\right), \quad k_2 = A_2 \exp\left(-\frac{E_2}{RT}\right), \tag{50.12}$$

where R is gas constant, E_1 and E_2 are activation energies and m, n, A_1 and A_2 are material constants. These parameters were obtained by curve fitting the Eq. (50.11) to the experimental DOC curves as a function of temperature. The experimental curves were measured by DSC. The fitted parameters are listed in Table. 50.1.

Prony parameters of the epoxy resin were experimentally measured. A master curve of shear compliance was obtained from data of creep tests conducted by a DMA (Dynamic Mechanical Analyzer, DMA7e, Perkin Elmer. Inc). Then, a master curve of shear modulus was calculated from the master curve of shear compliance using Laplace transform. The fitted Prony parameters to the master curve of shear modulus were shown in Table 50.1.

Table. 50.1 Materials properties used in FEM analysis

Parameter		n		1.7115	
Glass (optical fiber)		A_1 (s^{-1})		188.15	
G_0(MPa)	72,000	A_2 (s^{-1})		3613.5	
ν	0.25	E_2(kcal/mol)		48,043.9	
α_T	0.5×10^{-6}	E_2(kcal/mol)		44,017.4	
Epoxy resin		$\alpha(0)$		0.69	
G_0(MPa)	978.26	$\varepsilon(\alpha)$		$-0.01769\alpha + 0.01203$	
ν	0.38	$A_\alpha(\alpha)$		$3.179\alpha - 2.179$ ($\alpha > 0.69$)	
α_T($T < 73°C$)	8.3×10^{-5}	g_1	0.0975735	τ_1(s)	0.012501125
α_T($T > 73°C$)	1.8×10^{-4}	g_2	0.1118394	τ_2(s)	0.172643289
		g_3	0.1767384	τ_3(s)	4.596961408
		g_4	0.05560065	τ_4(s)	107.212392
		g_5	0.003347833	τ_5(s)	2609.399055
m	0.35	g_6	0.001034613	τ_6(s)	49,050.86574

In the present paper, A temperature-time shift factor A_T was defined by a simple Arrhenius' formula as follows.

$$A_T = A\exp\left(-\frac{E}{RT}\right), \tag{50.13}$$

The temperature-time shift factor function was obtained from the experimental creep data of the resin as follows.

$$A_T = \exp(210.190418 - 68369.44073/(T + 273.15)), \tag{50.14}$$

The decrease index of shear modulus A_α was measured by a parallel-plate method using a rheometer (Visco Analyzer VAR100, Reologica Instruments, Inc.). The relaxation share modulus was measured as a function of cure cycle at the curing temperature condition of 2.5 °C/min for 30 min and 100 °C for 180 min. The A_α curve was obtained by dividing measured shear modulus by converged shear modulus. The following relationship was used for the FE calculation in this paper.

$$A_\alpha(\alpha) = 3.179\alpha - 2.179 \quad (\alpha > 0.69), \tag{50.15}$$

The curing strain ε_c caused by curing shrinkage experimentally measured by a dilatometer as a function of degree of cure as follows,

$$\varepsilon_c = -0.01769\alpha + 0.01203 \tag{50.16}$$

50.3.3 FEM Model

In order to evaluate strain of matrix resin, stain measured by the embedded FBG sensors was analyzed by a viscoelastic FEM. Figure 50.3 shows the 1/8 FEM model of the specimen. The second-order solid elements were used for meshing. Symmetric boundary condition were set on the three surfaces and the other surfaces were free. The applied time-temperature profiles were the same as the experiment. The calculation started when the degree of cure of resin was over 0.68. Thermal strain $\alpha_T \Delta T$ and curing strain ε_c caused by curing shrinkage was applied to the resin part as follows;

$$\boldsymbol{\varepsilon} = \boldsymbol{\varepsilon}_t - (\alpha_T \Delta T + \varepsilon_c(\alpha))\mathbf{I} \tag{50.17}$$

where $\boldsymbol{\varepsilon}_t$ is a strain tensor at time t.

An FEM analyses were conducted by an FEM software ABAQUS 8.6. The discrete constitutive equation of resin was programmed by FORTRAN and assembled into a user-subroutine UMAT. In order to evaluate strain of matrix resin, average stain along the sensor part of the embedded FBG sensor was calculated.

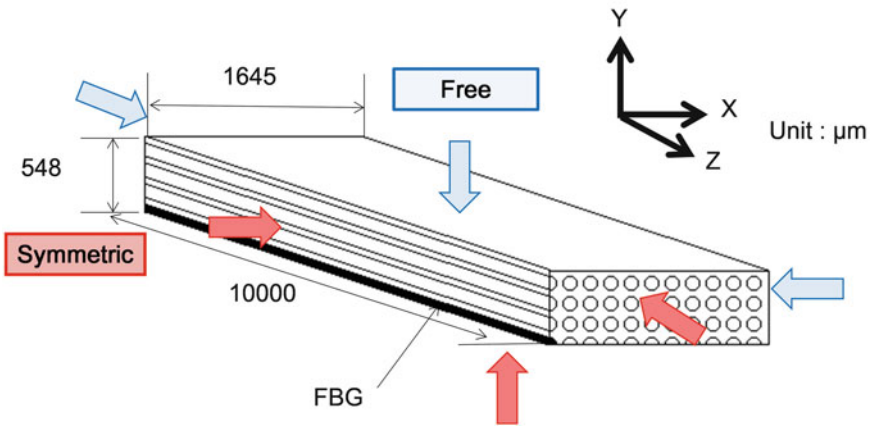

Fig. 50.3 1/8 FEM model of the specimen

50.4 Results and Discussion

The time histories of measured strain by FBG and temperature s were plotted against molding time in Fig. 50.4. At first, strain decreased from the start to the A point because it is considered that pre-tensile strain of optical fiber was relaxed. From the point A to B, strain increased. This reason is thought to be that thermal expansion of the mold tensed optical fiber by a friction force. The decreasing strain behavior from the point B to C is very complicated because it is considered that the three factors of relaxation by release from the friction, thermal expansion of resin and curing shrinkage by cure reaction, exist. From the point C to D, the decreasing strain is caused by curing shrinkage of the resin because the temperature is almost constant. The decrease of strain by curing shrinkage from the point C to D was −63 με. During cooling process from the point D to F, strain decreased due to thermal shrinkage of resin. It appeared that the cooling process-induced strain was −293 με and the molding process-induced strain was −356 με. Therefore, the ratio of curing cure process-induced strain by curing shrinkage of the resin to whole molding process-induced strain was 17.7 %. This fact indicates that the effect of curing shrinkage of the resin should be taken into account for evaluation of molding process-induced strain of the reinforcements.

Strains calculated by the FEM analysis were plotted against temperature with experimental curves in Fig. 50.5. From the figure, it appeared that the FEM analytical strain curve agreed very well with the experimental strain curve. The analytical curve shows that the calculation started between the point B and C because the optical fiber was constrained by resin when the degree of cure exceeded 0.69. The slopes of the analytical and experimental strain-temperature curves were small until the point C because the stiffness of resin was low and the curing shrinkage of resin was canceled by the thermal expansion.

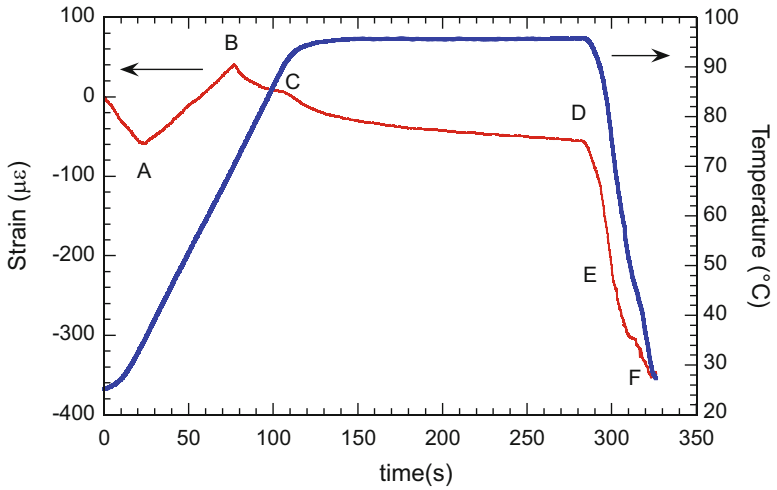

Fig. 50.4 Relationships between strain measured by FBG sensors, temperature and molding time during molding process

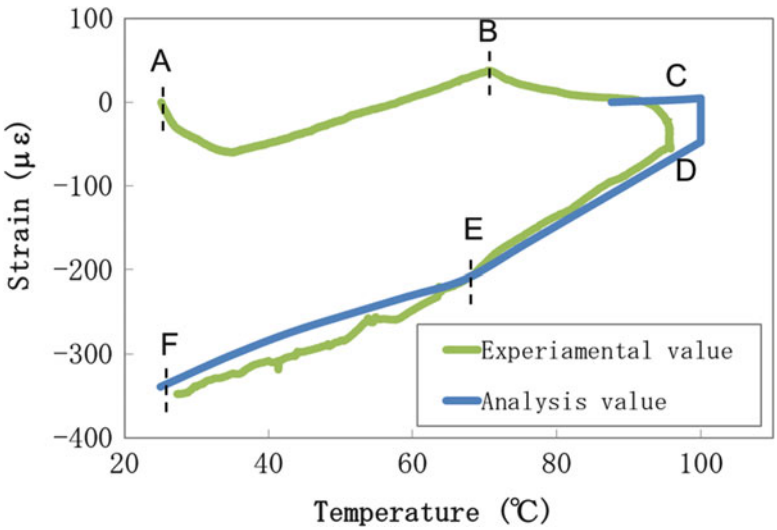

Fig. 50.5 Relationships between strain and temperature for experimental and analytical results during molding process

The compressive strain of the analytical result from the point C to D was −52 με and showed good agreement with the experimental result. In the cooling process from the point D to F, the both strain-temperature curves showed a knee point at the point E because the thermal expansion coefficient and stiffness of resin changed when temperature exceeded the glass transition temperature of resin. The agreement between the both curves shows the viscoelastic model of the resin as a function of degree of cure is suitable for prediction of molding process-induced strain of reinforcing fibers of FRP.

50.5 Conclusion

In the present paper, molding process-induced strain of reinforcing fibers of model GFRP was measured by the embedded FBG sensor. Moreover, the viscoelastic FEM method for calculation of process-induced strain was proposed. Most parameters used for calculation such as viscoelastic properties and a profile of curing shrinkage of resin were experimentally measured. From the experimental and analytical results, it appeared that the calculated results agreed well with experimental results. Therefore, it was found that viscoelastic property, thermal expansion and curing shrinkage of resin play significant roles for cure process-induced strain of reinforcing fibers of FRP. The ratio of curing cure process-induced strain by curing shrinkage of the resin to whole molding process-induced strain was 17.7 %. This fact indicates that the effect of curing shrinkage of the resin should be taken into account for evaluation of molding process-induced strain of the reinforcements.

Acknowledgement This work was supported by Council for Science, Technology and Innovation (CSTI), "Innovative structural materials" of "Cross-ministerial Strategic Innovation Promotion Program (SIP)" (Funding agency: JST).

References

1. Murukeshan, V.M., Chan, P.Y., Ong, L.S., Seah, L.K.: Sensors Actuators A **79**(2), 153–161 (2000)
2. Leng, J., Asundi, A.: Smart Mater. Struct. **11**, 249–255 (2002)
3. Kosaka, T., Kurimoto, H., Osaka, K., Nakai, A., Osada, T., Hamada, H., Fukuda, T.: Adv. Compos. Mater. **13**, 157–170 (2004)
4. Kamal, M.R.: Polym Eng. Sci **14**(3), 231–239 (1974)

Chapter 51
Effect of Molding Conditions on Process-Induced Deformation of Asymmetric FRP Laminates

Taishi Senoh, Tatsuro Kosaka, Takahiro Horiuchi, and Kazuhiro Kusukawa

Abstract It is well known that process-induced deformation of laminates affected dimensional accuracy of FRP components strongly. It is very important for manufacturing of FRP laminates to investigate cure shrinkage and thermal strain during molding process. In the present paper, in order to investigate effect of molding conditions on process-induced deformation of asymmetric GFRP laminates, several molding patterns of temperature and pressure and two types of interfacial conditions between FRP and a mold were employed for manufacturing of the laminates by a hot press molding method. Single-hold pattern or double-hold patterns of temperature were applied to the molding process. The highest molding temperature was 140 °C and the first hold temperature of double-hold patterns were 90 °C, 110 °C and 120 °C. Fiber optic strain sensors and refractive index sensors were used for measurement of strain and degree of cure. It was confirmed that prepreg was cured perfectly at the first holding step. Curvature of the specimen were measured after demolding and drying processes. From the experimental results, it was found that the first holding temperature of double-hold patterns did not affect the curvature of warping deflection after demolding. The results of strain measurements suggested that the strain during cure process was governed mainly by friction between laminates and deformation of molding plates. Moreover, it was found that Interfacial constraint between the laminates and molding plates strongly affected process-induced deformation of asymmetric GFRP laminates.

Keywords FRP • Process-Induced Deformation • Asymmetric Laminates • Process Monitoring

51.1 Introduction

Since FRP (Fiber Reinforced plastics) have high mechanical properties, high durability and low weight, they are applied to many engineering fields such as aircraft, marine and automotive engineering. Recently, large and complex-shaped FRP components such as wings of aircraft or automotive frames have been manufactured. In the manufacturing of large-scale FRP, dimensional errors such as spring-back or spring-in caused by process-induced deformation is considered to be serious problem. Therefore, process simulation of FRP has been developed by many researchers to estimate molding process-induced deformation [1]. However, it is difficult to predict precise deformation for any FRP because the effect of thermal deformation, curing shrinkage, mechanical properties and constraint by a mold which dramatically change as functions of degree of cure and temperature during molding process, is not clear.

On the other hand, recent development of optical fiber sensors technology allows us to measure internal state of FRP materials. Therefore, measurement techniques of degree of cure [2], temperature and strain of FRP by embedding optical fiber sensors are very effective to investigate factors governing molding process-induced strain of FRP.

In the present paper, asymmetric FRP laminates were manufactured to investigate the effect of curing temperature patterns and constraint by a mold on process-induced deformation because large warping deflection occurs by thickness-wise distribution of asymmetric mechanical properties after molding process. Several temperature patterns and two types of constrain condition by a mold are used for the manufacturing. Curvature of the specimen was measured after demolding specimens from a mold. Moreover, degree of cure and strain of the FRP laminates for each condition was measured by embedded optical fiber sensors. The experimental data were used for discussion on the factors governing molding process-induced strain of asymmetric FRP laminates.

T. Senoh (✉) • T. Kosaka • T. Horiuchi • K. Kusukawa
Kochi University of Technology, School of Systems Engineering, 185 Miyanokuchi, Tosayamada-cho, Kami-city, Kochi 782-8502, Japan
e-mail: Mokut22412@gmail.com

C. Ralph et al. (eds.), *Mechanics of Composite and Multi-functional Materials, Volume 7*,
Conference Proceedings of the Society for Experimental Mechanics Series, DOI 10.1007/978-3-319-21762-8_51

51.2 Material and Experimental Method

51.2.1 Materials

GFRP prepreg (Mitsubishi Rayon GE352G135SB) sheets of 120 μm thickness were cut for size of 30 × 120 mm. The prepreg sheets were stacked on an aluminum plate as the stacking sequence was $[0_5/90_5]$ as shown in Fig. 51.1. An aluminium spacer of 1 mm was used to control thickness of the FRP laminates. For manufacturing the Type A group of specimens, the prepregs were sandwiched by teflon sheets to reduce effect of frictional force between the FRP and molding plates. On the other hand, the Type B group of specimens contacted with molding plates treated by unmolding agent in order to investigate effect of constraint by molding plate. The optical fiber sensor and a thermocouple were embedded between the first and second sheets in order to measure degree of cure and temperature, respectively. After vacuuming, the laminates were cured with molding pressure of 0.5 MPa by a hot-press machine.

Figure 51.2 shows the four temperature patterns which prepared for the molding process. Initial temperature was 20 °C and final temperature was 140 °C. The first step temperatures of double-hold patterns were 90 °C, 110 °C and 120 °C and the heating rate was 2 °C/min. The holding time of the first step was 5 h for 90 °C step and 2 h for 110 °C and 120 °C, respectively. FRP was cooled naturally after cure process. The patterns were named as T90, T110, T120 and T140, where the number indicates holding temperature of the first step.

51.2.2 Measurement of Degree of Cure

During the molding process, degree of cure was measured by the Fresnel-based refractive-index optical fiber sensor embedded in the specimen during molding. This sensor uses Fresnel's reflection at the flat-end of a glass optical fiber caused by mismatch of refractive index between resin and glass. Refractive index of resin can be calculated from the reflected optical power because the change in refractive index of glass is very small during molding. Degree of cure can be obtained by eliminating temperature effect on refractive index.

For the specimens of T90 and T140, strain in 90° layers was measured by the embedded optical fiber strain sensors. In this study, the optical distributed sensor interrogation system (ODiSI, Luna technologies, Inc.), which measure distribution of Rayleigh scattering along an optical fiber, was used. The sensor was embedded in the outmost layer.

51.2.3 Measuring Warping Deflection After Demolding

After demolding the laminates from the molding plates, residual warping deformation occurred due to the asymmetric stacking sequence. The warping deflection of the specimens at room temperature and at dry condition was measured by a

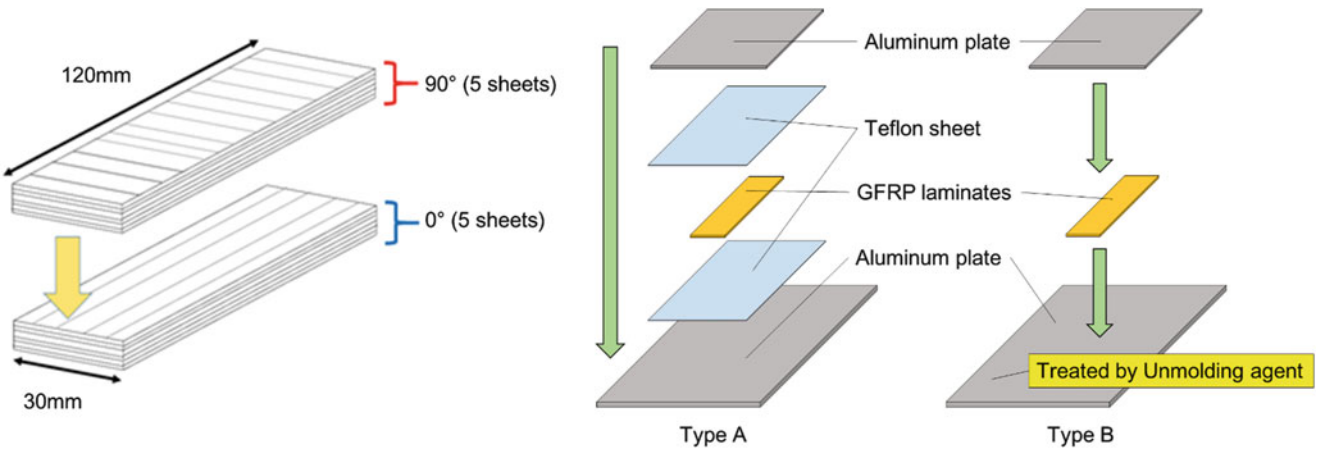

Fig. 51.1 Manufacturing of GFRP laminates

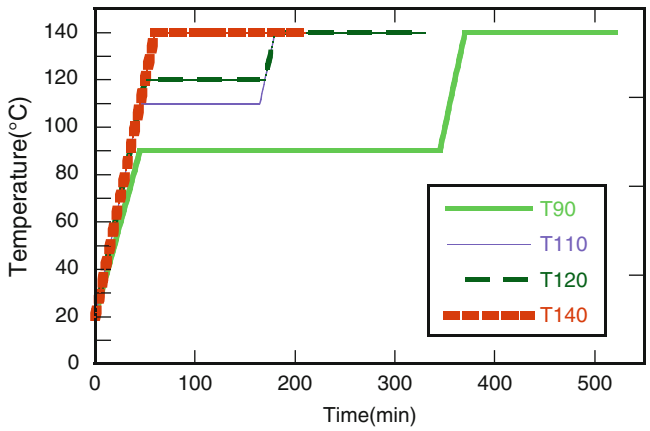

Fig. 51.2 Temperature patterns for FRP molding

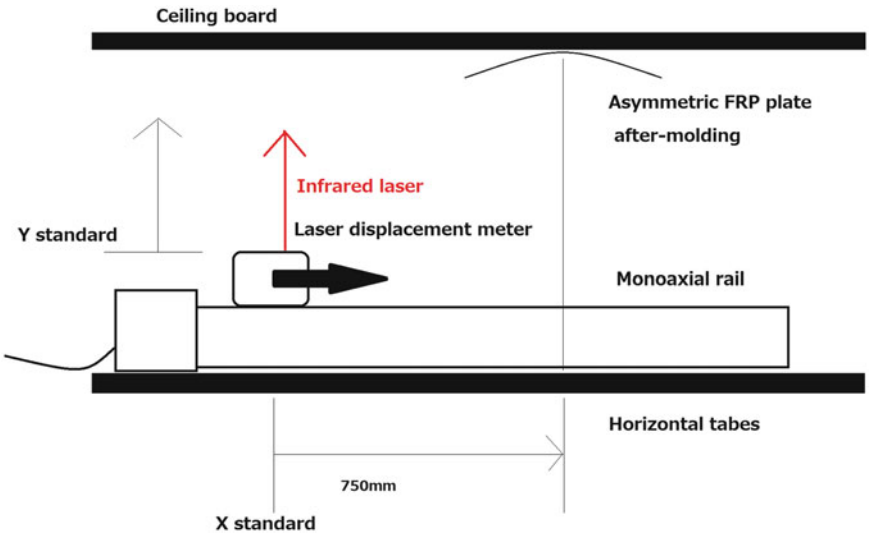

Fig. 51.3 Equipment of measuring deflection of FRP laminates

laser displacementmeter. Figure 51.3 illustrates schematic view of the experimental set-up for measuring warping deflection of the specimens. It consists of a laser displacementmeter and a uniaxial linear stage. The ceiling board is parallel to the linear rail. The specimen was put on the ceiling board so as to set the concave surface down. The measurement devices was covered to maintain dry condition. The warping profile was measured by moving the stage. Curvature was calculated by fitting a circular function to the profile.

51.3 Experimental Results and Discussion

51.3.1 Effect of Temperature Pattern on Process-Induced Deformation

Figure 51.4 shows relationship between the warping deflection of T90, T110, T120 and T140 specimens and x-axis position of the specimens. From the figure, it was found that the all profiles were almost the same as each other. Radius of curvature was calculated by fitting a circular function to the profile data with a least square method. Then, the curvature was determined as reciprocal number of radius of curvature. Average curvatures for the temperature pattern of T90, T110, T120 and T140 specimens are listed in Table 51.1. From the results, it was found that the T140 specimens showed the maximum curvature and the T120, the minimum value. However, the difference between the minimum and maximum was small and there was not clear correlation between curvature and the first stage temperature. Therefore, temperature of the first stage of cure process hardly affected warping deflection of asymmetric FRP laminates.

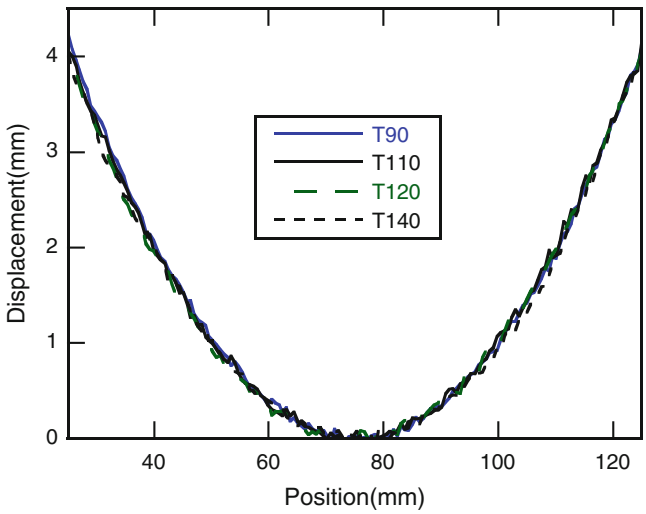

Fig. 51.4 Deflection of FRP laminates for each temperature pattern

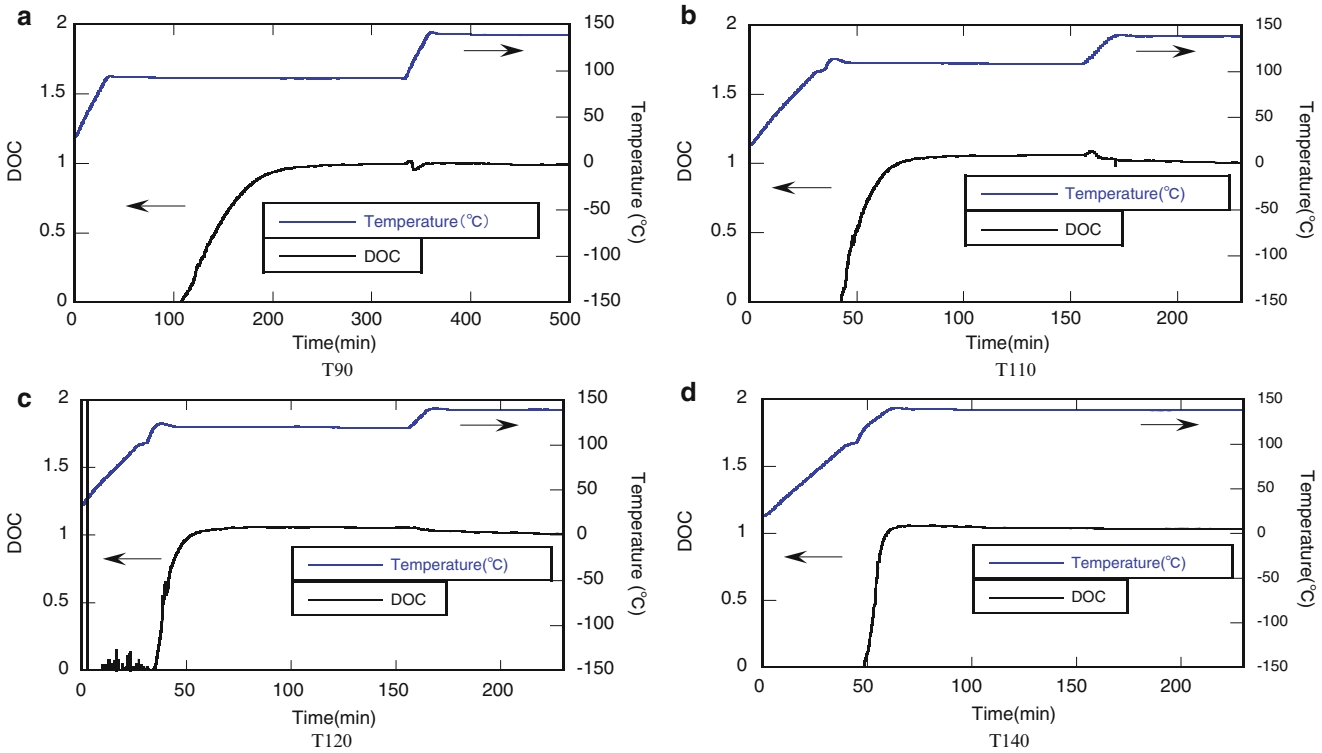

Fig. 51.5 Degree of cure curve with temperature for each temperature pattern

Table 51.1 Curvature of after-molding

Temperature pattern	T90	T110	T120	T140
Curvature[1/m]	3.10	3.07	2.93	3.17

Figure 51.5 shows relationships between degree of cure, temperature and molding time for all temperature patterns. The graph of T90 showed that the cure reaction did not start when temperature reached 90 °C and started at 100 min. For the T110, T120 and T140 specimens, the cure reaction started when the temperature became 100 °C. The time from the start to the end of cure reaction was almost 100 min for the T90 and 20 min for T140. Therefore, it appeared that the curing rate was lower with the lower first stage temperature. From these figures, it was found that the degree of cure reached 100 % for all temperature patterns. These results indicate that the temperature when cure reaction completed is the holding temperature of

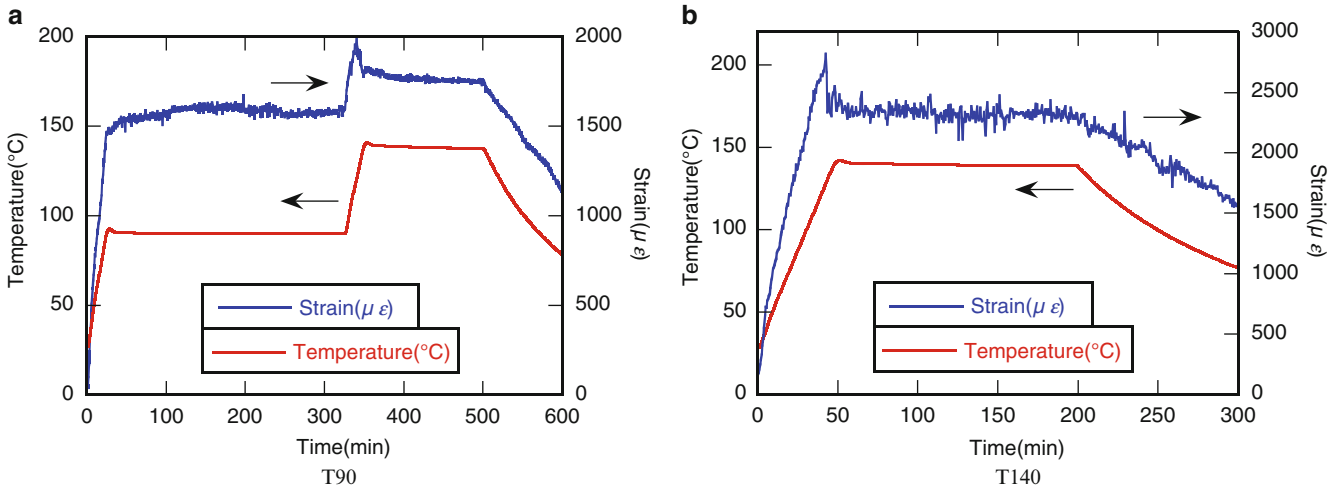

Fig. 51.6 Process-induced strain and temperature in 90° layer of asymmetric GFRP laminates during molding process

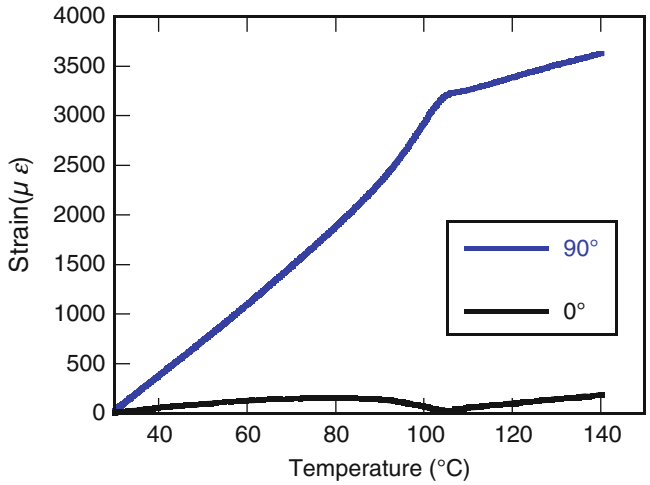

Fig. 51.7 Thermal strain of after-molding asymmetric GFRP plate (T140)

the first stage. Therefore, it can be considered that the effect of curing shrinkage and thermal expansion of resin on process-induced strain during cure process is the largest for the T90 specimen.

The process-induced strain in 90° layer of the T90 and T140 specimens was measured by the embedded optical fiber strain sensors. The process-induced strain and temperature are plotted against molding time during molding process in Fig. 51.6. The figure shows that the strain increased with increase of molding temperature although cure reaction did not start as shown in Fig. 51.5. Therefore, it was considered that the strain grew by friction between the fiber sensor and prepreg until the cure reaction began. In the figure of T90, the compressive strain by curing shrinkage was not observed at the first holding-temperature step at 90 °C. On the other hand, the instant decrease of strain was observed for the both specimens when temperature became 140 °C. This decrease of strain is thought to be caused not by the curing shrinkage but by the slip between the FRP laminates and the molding plates. Therefore, friction between the laminates and molding plates strongly affected the process-induced strain during cure process.

In order to investigate stiffness of the laminates at high temperature, thermal strain measurement was conducted by strain gages adhere to the concave surfaces for the T140 specimen after molding process. Figure 51.7 shows relationship between strain along 0° and 90° directions and temperature. From the figure, it was found that the thermal strain rates along 90° direction was 42.7 με/°C from 30 °C to 105 °C and 11.4 με/°C during 105 °C to 140 °C. Temperature 105 °C is called glass transition temperature. From the results, it was found that the warping deflection of the asymmetric GFRP laminates is very small when temperature is higher than the grass transition temperature. This is considered to be because that stiffness of laminates dramatically decrease when the temperature increase more than glass transition temperature.

Table 51.2 Curvature for die restrain (T140)

Constraint type	Type B	Type A
Curvature[1/m]	4.05	3.17

51.3.2 Effect of Constraint by a Molding Die

Type B specimen was manufactured to investigate effect of constraint by mold plates on process-induced strain of asymmetric laminates. The interfacial friction of Type B between the specimen and mold plates was very strong because the laminates directly contacted to surface of the mold with unmolding agent. Table 51.2 shows average of curvature of the Type A and B specimen after molding process. From the results, it appeared that curvature of the Type B specimen was 28 % larger than that of the Type B. From these results, it is suggested that interfacial condition between FRP and a molding die affected molding process-induced deformation strongly.

51.4 Conclusion

Asymmetric GFRP laminates were manufactured for several molding conditions. Degree of cure and molding strain were measured by embedded fiber-optic sensors. After demolding, warping deflection of the specimen was measured and the curvature was calculated. From the experimental results, it was found that the first holding temperature of double-hold patterns did not affect the curvature of warping deflection after demolding. The results of strain measurements suggested that the strain during cure process was governed mainly by friction between laminates and deformation of molding plates. Moreover, it was found that Interfacial constraint between the laminates and molding plates strongly affected process-induced deformation of asymmetric GFRP laminates.

Acknowledgement This work was supported by Council for Science, Technology and Innovation (CSTI), "Innovative structural materials" of "Cross-ministerial Strategic Innovation Promotion Program (SIP)" (Funding agency: JST).

References

1. Bapanapalli, S.K., Smith, L.V.: A linear finite element model to predict processing-induced distortion in FRP laminates. Compos. Part A **36**(12), 1666–1674 (2005)
2. Kosaka, T., Osaka, K., Sawada, Y.: Cure monitoring of resin by real-time measurement of refractive index using single-mode optical fibers. J. Soc. Mater. Sci., Jpn. **59**(5), 391–397 (2010)

Chapter 52
Simulation of High Rate Failure Mechanisms in Composites During Quasi-static Testing

Mark Pankow and Brandon A. McWilliams

Abstract High Rate testing is often difficult to perform, requires specialized equipment and often had results that are difficult to interpret. Being able to simulate the same failure mechanisms at high rates would enable rapid material selection. In this experimental investigation, the mechanical response is determined of different hybrid composites materials. A modified through-the-thickness tests has been used to force a high order of failure mode that is similar to those seen in high speed impact. Failure is observed in the samples and stresses on the surface are determine to help with failure envelope measurements. The details of a comparison between 2D fabrics vs. 3D woven fabrics has been under taken and a comparison will be presented showing the similarities and differences in response. A discussion of the comparison between the high rate testing and the low-rate testing will be investigated and discussion on the applications of the testing will be examined for failure envelope prediction.

Keywords Composites • Penetration mechanics • Dynamic failure mechanisms • High strain rate behavior

52.1 Introduction

The widespread use of composite materials in impact prone applications drives a need to properly understand their failure mechanism and associated effects of rate dependent loading. High strain rate testing for materials typically involves the used of Hopkinson bar testing to get an idea of elevated rate mechanics. The use of Hopkinson bar testing in various configurations including tension, compression and torsion was used to investigate 2D woven materials and found that their response under high rates resulted in shear band formations under elevated compression through the thickness [1, 2]. Further studies then investigated the use of 3D woven composites to examine the response of these newer materials [3]. These investigations showed similar shear band failures occurred in these materials. A comparison of low rate to high rate tests revealed that these materials have different failure modes at different rates lending to different amounts of energy dissipation [4]. These shear bands that form at high rates have been investigated to determine if these is a link to material properties and possibly a failure envelope [5].

High Strain rate testing is often very difficult to perform and the information that is obtained is often left for interpretation. The punch shear method looks at recreating high-speed impact events with quasi-static rates, however, these tests provided limited information. Interpretation is often difficult to perform due to contact stresses and a circular failure mode [6]. Since composites are not homogeneous material data analysis from the circular failure surface is not an accurate representation of material properties. The major finding from these quasi-static tests is that the additional confinement provides similar failure surface to that observed at elevated rates [7]. The use of a quasi-static procedure to mimic elevated rate type failure can be accomplished through the use of a confined compression experiment. The use of this method offers a powerful prediction for response at elevated rates which could eliminate some of the high sample volume testing that would need to be done at elevated rates.

In this work confined compression experiments were used to try and isolate the failure mechanisms for uni-directional and 2D woven material systems glass fiber composites. Tests were performed with confinement to capture the shear band

M. Pankow (✉)
Department of Mechanical and Aerospace Engineering, North Carolina State University, Raleigh, NC 27695, USA
e-mail: mrpankow@ncsu.edu

B.A. McWilliams
US Army Research Laboratory, Aberdeen Proving Ground, MD 21005, USA

C. Ralph et al. (eds.), *Mechanics of Composite and Multi-functional Materials, Volume 7*,
Conference Proceedings of the Society for Experimental Mechanics Series, DOI 10.1007/978-3-319-21762-8_52

formation that occurs. Additional tests were performed to develop a compression shear failure envelope for both material systems. Results show the ability to accurately capture a through-thickness response that mimics that of high rates, with the addition of failure maps for varying loading conditions.

52.2 Material

The material tested in this paper was S2-Glass fibers with an SC-15 matrix system. Panels were infused with a Vacuum Assisted Resin Transfer Molding system (VARTM). Two configurations were tested. 2D plain-woven material was also created from different amounts of layers of 2D woven fabric. Three different thicknesses were fabricated: 0.25″, 0.50″ and 0.75″ thick materials. Samples were post-cured

52.3 Laterally Constrained Compression Test

Current through thickness testing methods rely on a cube of material tested through the thickness, which allows for large amounts of plasticity in the matrix material that is not observed upon local compression of a smaller area of a panel. A different test must be performed to simulate the confinement from other parts of panel when subjected to localize penetration. In order to simulate this better a sample has been loaded through the thickness in compression. However, additional constraints have been added to prevent Poisson's effect from happening in one of the directions. These tests work well for an-isotropic materials, however isotropic materials typically do not form failure planes.

When the specimen is loaded until failure a sliding plane will form where failure occurs in the material, this will form an angle θ with the surface of the material, see Fig. 52.1. In this case the normal stress S_{FC} can be defined as

$$S_{FC} = \frac{F_{max}}{A}$$

where, F_{max} is the maximum force and A is the cross sectional area. Using these results an the known angle that if formed at the failure surface, Mohr's circle allows us to calculate the normal and shear forces acting on the surface of the failure plane. These stresses are computed as

$$S_N = S_{FC} \cos^2\theta$$

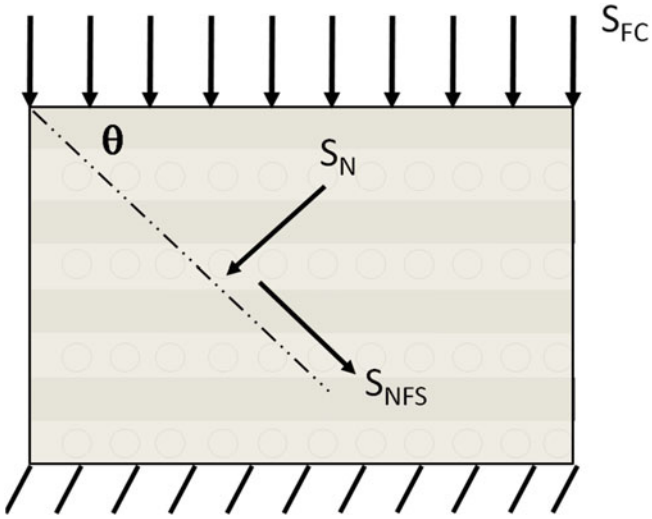

Fig. 52.1 Shear failure plane of the material under confined compression

$$S_{NFS} = 0.5\, S_{FC} \sin 2\theta$$

where S_N and S_{NFS} are the compressive normal stress and shear stress, respectively. These results are dependent upon the fact that the two principal stresses are S_{FC} and 0. The compressive stress in the opposite direction does not affect these results as the failure does not lie in that plane.

52.3.1 Sample Preparation

Samples were ground down to 0.750 in. on a liquid cooled surface grinding machine. Samples were held to within a tolerance of +0.000 and −0.002 to ensure proper confinement in the samples. With a looser tolerance sample will have a wider spread of data due to the variation in confinement of the samples.

Additional samples were created with notches as will be discussed later in the paper. Notches were cut into samples using a diamond coated wet saw run on a linear stage with an angular mounting surface to create consistent notches from sample to sample. Due to the ground surfaces all angles were within ±0.5°. All samples were measured prior to testing including the notched samples, which measured the reduced cross sectional area.

52.3.2 2D Woven Data

2D Woven samples were examined, which are a simple stack up of in-plane woven layers. Samples were made in three different thicknesses to help understand any scaling issues that may arise through the thickness. Samples were cut to 0.75 × 0.75 × thickness where three different thicknesses were used (0.75″, 0.50″ and 0.25″). All specimens had the same cross sectional area and therefore the only difference was overall thickness.

The effective stress and shear angle has been calculated in Table 52.1. This data shows that there is very little variation between all of the thicknesses. The material has almost identical loads, with nearly identical angles that were formed. A scan of the surface for a single sample can be seen in Fig. 52.2. These pictures show that the samples all exhibited similar failure modes as the thickness was increased. Although the thinnest sample had multiple cracks forming the results were nearly identical in terms of failure angle and strength. Therefore the multiple cracks do not seem to affect the overall results obtained.

Table 52.1 Stress and effective shear angle for varying thickness 2D woven composites

	Effective stress ksi	Shear angle deg
0.75	98.88 ± 6 %	43.871 ± 5 %
0.5	100.47 ± 4 %	42.72 ± 11 %
0.25	101.13 ± 6 %	44.84 ± 3 %

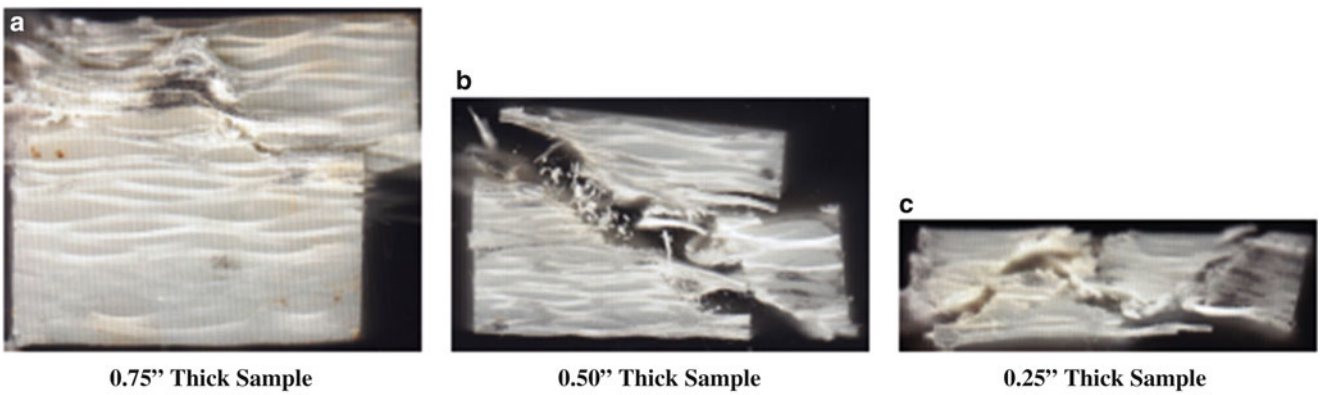

Fig. 52.2 Comparison of failed specimens with various different panel thicknesses. These results show that there is no variation in panel thickness

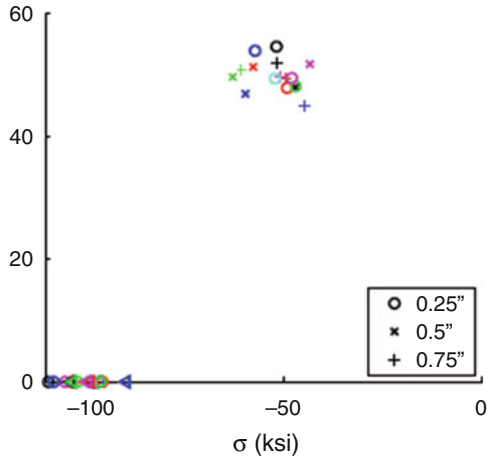

Fig. 52.3 Failure envelope based off the failure

Table 52.2 Physical parameters from LCC test in notched specimens

	Effective stress ksi	Shear angle deg
0.75	82.7 ± 4 %	44
0.5	84.2 ± 5 %	43

Table 52.3 Physical parameters from LCC test in notched specimens

	Effective stress ksi
60	70.8 ± 9 %
45	78.2 ± 4 %
30	72.9 ± 4 %
20	102.3 ± 10 %
10	97.2 ± 8 %

The shear angle allows us to break down the data further to examine the effective stresses acting on the surfaces of the fracture face. These stresses have been broken down in Fig. 52.3. It can be seen here that that data is consistent and has a tight grouping, due to the fact that there was small variation in thickness and shear angle. This information is critical because as we begin to look at thicker structural materials we know that the small coupon level testing applies for these much larger models.

With a good understanding of the thickness scaling effects, we would like to get a better idea of how different combinations of compression and shear create a failure envelope for the 2D woven material. Samples are again notched as discussed previously to provide a source of failure

Specimens were then notched with these similar failure angles found in the first round of experiments 45°. These specimens were then loaded in a similar manner. The results can be seen in Table 52.2. These values compare to those obtained on the notched sample with a value of 1.2 difference, this is the same notch sensitivity that is shown through finite element simulations.

With a good understanding of how the notch will affect the fiber failure data. Samples were notched at various different angles to produce a failure envelope for the combined compression shear against the fibers. Angles of 60°, 45°, 30°, 20°, 10° were chosen as the sampling points to conduct this analysis. The failure data can be seen in Table 52.3 and Fig. 52.4, which shows the various different combinations of failure stress that has occurred in the material.

It should be noted however that the 20° and 10° specimens did not fail as catastrophically as those seeded with higher angles, fiber pull out was also being seen in the samples. This shallow angle is too low to produce proper failure in the specimens. Due to this pull out the data for these angles goes uncorrected because it will be un-affected by the stress concentration since the failure has changed modes. Samples at 60° suffered from small cross sectional areas, due to the high angle and fixed thickness. These samples produced a lower failure load due to localized crushing, and not failure in the notch. Perhaps the V-Notched rail shear test is more appropriate at these higher angles or a simplified punch shear test.

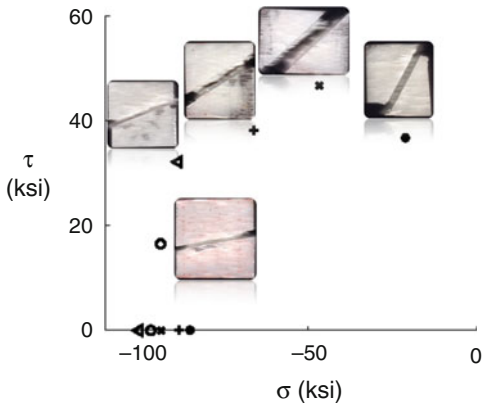

Fig. 52.4 Failure envelope based off the failure for notched specimens

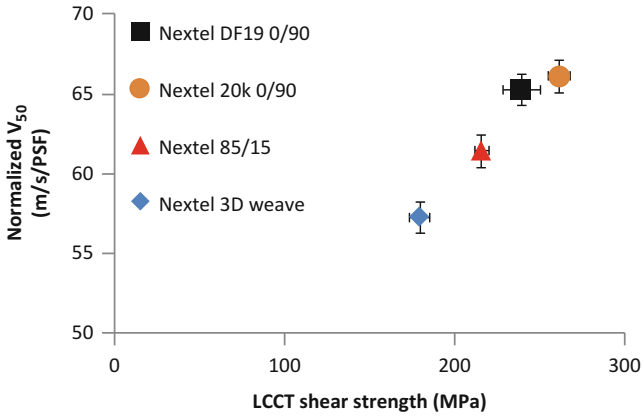

Fig. 52.5 Normalized V_{50}^{BL} versus LCCT shear strength for the four fabric reinforced weave architectures

52.3.3 Comparison to Ballistic Testing

One of the goals of the present work was to determine if a correlation could be found between the resistance to ballistic impact of a material and its through thickness crush strength determined from Laterally Constrained Compression Test (LCCT) testing. LCCT testing was conducted on four MMC materials to quantify the effects of weave architecture on the through thickness crush strength and fiber shearing failure modes of the fabric reinforced MMCs. The $V_{50}{}^{BL}$ of each MMC is plotted versus its LCCT crush strength in Fig. 52.5 and shows a linear correlation. This result supports the hypothesis that the LCCT test emulates the self confinement experienced by the material in the impact zone by the surrounding unaffected material during ballistic impact and that this test is a reasonable indicator of relative ballistic performance for this class of fabric reinforced MMC materials and could be used to evaluate new weave/fabric/composite designs and layups without having to conduct full scale ballistic testing on a large series of candidate materials. As samples are only 0.75 in. square instead of 8 in. square much less material is required for testing.

52.4 Conclusions

The LCC test was investigated to look at its ability to capture the high rate failure mechanisms of composites during impact. Overall the method can be used to determine the compression shear failure envelop for the material. Additionally the thickness for 2D woven material was shown to not play a role in these failure mechanisms. Finally a correlation to experimental V50 Data showed a strong correlation and an easy way to effectively down select material based on smaller sample size.

References

1. Guden, M., Yildirim, U., Hall, I.: Effect of strain rate on the compression behavior of a woven glass fiber/sc-15 composite. Polym. Test. **23**(6), 719–725 (2004)
2. Song, B., Chen, W., Weerasooriya, T.: Quasi-static and dynamic compressive behaviors of a s-2 glass/sc15 composite. J. Compos. Mater. **37** (19), 1723–1743 (2003)
3. Sun, Y., Wang, G.: Compressive response of UHMWPE/vinyl ester 3d orthogonal woven composites at high strain rates. Adv. Mater. Res. **97–101**, 522–525 (2010)
4. Pankow, M., Salvi, A., Waas, A., Yen, C., Ghiorse, S.: Split Hopkinson pressure bar testing of 3d woven composites. Compos. Sci. Technol. **71** (9), 1196–1208 (2011)
5. Gillespie Jr., J., Gama, B., Cichanowski, C., Xiao, J.: Interlaminar shear strength of plain weave s2-glass/sc79 composites subjected to out-of-plane high strain rate compressive loadings. Compos. Sci. Technol. **65**(1112), 1891–1908 (2005)
6. Manzella, A., Gama, B., Gillespie Jr., J.: Effect of punch and specimen dimensions on the confined compression behavior of s-2 glass/epoxy composites. Compos. Struct. **93**(7), 1726–1737 (2011)
7. Yen, C.-F.: A ballistic material model for continuous-fiber reinforced composites. Int. J. Impact Eng. **46**, 11–22 (2012)

Chapter 53
Meso-scale Deformation Mechanisms of Polymer Bonded Energetic Materials Under Dynamic Loading

Suraj Ravindran, Addis Tessema, Addis Kidane, and Michael A. Sutton

Abstract To understand the plastic deformation mechanism of polymer bonded energetic materials, a meso-scale experiment is conducted under dynamic loading. Energetic simulant material with polymer plasticizer are cold pressed using a mold made of stainless steel. An experimental setup is developed to obtain the local strain field at the meso-scale under dynamic loading conditions. The setup consists of a high speed camera with extension tube and microscope objective lens to obtain magnifications ranging from 1× to 50×. A high intensity halogen light source is used for illumination. The field of view for the experiment is 1700 × 690 μm, with a spatial resolution of 4.427 μm/pixel at 100,000 frames/s. Dynamic loading is performed using a split Hopkinson pressure apparatus to obtain a range of strain rates. The strain fields are obtained using digital image correlation technique. To facilitate for the digital image correlation technique, the specimens are speckled using air brush with average speckle size ranging from 12 to 18 μm. Results are presented for the measured strain fields and the associated deformation mechanisms as a function of loading rate.

Keywords Polymer bonded explosive • Dynamic • DIC • Meso-scale • Strain localization

53.1 Introduction

Polymer bonded explosives (PBX) are highly solid filled class of particulate composites that have a wide variety of applications. Though there are different formulations and variety of polymer binder materials, most of the PBX material contains 70–95 % explosive solid particles and 5–30 % binder materials [1, 2]. The main function of the binder is to hold the particles together which also enables for easy machining and casting into required shape and size. Most of these materials are shock sensitive and the sensitivity is a function of material properties. Weak shock initiation of the polymer bonded explosives is not very well understood because of the difficulty in obtaining the deformation fields in the polymer bonded explosive under dynamic loading conditions, its complexity in composition, microstructure and limitations in the experimental techniques.

Characterization of these materials under shock loading conditions is difficult due to safety issues. Therefore most of research work conducted is with the help of mock materials [3]. One of the main mock materials used is sugar. In this study we have used sugar crystals as the mock simulant and hydroxyl terminated polybutadiene (HTPB) as binder.

Most of the shock based experimental research work on PBX was done with the help of Split Hopkinson bar apparatus and Taylor experiments. Some researchers used digital image correlation to get the full field deformation field [4]. However, according to our knowledge, the local deformation occurred in these materials under dynamic loading conditions are not investigated yet. In this study we have developed an experimental setup to study the local deformation behavior of these materials at meso scale under dynamic loading conditions. The experimental technique, specimen preparation and results from the experiments are presented.

S. Ravindran (✉) • A. Tessema • A. Kidane • M.A. Sutton
University of South Carolina, Columbia, SC, USA
e-mail: muthiram@email.sc.edu

C. Ralph et al. (eds.), *Mechanics of Composite and Multi-functional Materials, Volume 7*,
Conference Proceedings of the Society for Experimental Mechanics Series, DOI 10.1007/978-3-319-21762-8_53

Table 53.1 Specimen constituents and final density of the material

Specimen	Sugar (%)	HTPB (%)	DOS (%)	TDI (%)	Density of specimen (g/cm^3)
PBS	85	10.8	2.89	1.31	1.45

53.2 Materials and Experimental Procedure

53.2.1 Preparation of the Material

In this study polymer bonded sugar contains plasticized hydroxyl terminated polybutadiene (HTPB) as binder and sugar crystals of size vary from 100 to 500 μm is used. HTPB is mixed with plasticizer dioctyl sebacate (DOS) and curing agent toluene diisocynate (TDI). Steps involved in making raw material for the preparation of simulant specimens involves following steps,

1) Mixing of the plasticized HTPB with sugar crystals,
   First HTPB is mixed with the plasticizer (DOS) with the help of a mechanical mixer for 20 min. Subsequently, curing agent (TDI) is added and stirred for 10 min. The blended material is mixed thoroughly with the sugar crystals. The mixture is then cured at 60 °C for 24 h.
2) Pressing into billets
   The partially cured mixture is then cold-pressed in a steel mold at a pressure of 90 MPa to produce billets of size 25 mm in diameter and 25 mm in height. The density of the specimen along with the constituents is shown in the Table 53.1.
3) Curing of the specimen,
   For complete curing of the specimen, the pressed billets are kept at 60 °C for 90 h in a vacuum oven. The proportions of the constituents and names of each specimen are given in Table 53.1.

53.2.2 Experimental Methods

Cubic specimens of dimension 12 × 12 × 12 mm were extracted from 25 × 25 mm cylinders. The specimen is polished using silicon carbide papers of grit size from 300 to 1200 and then dry polished with the help of diamond particles of size 3 μm to give the final dimension of 10 × 10 × 10 mm. Due to insufficient contrast between the polymer binder and the sugar crystals, capturing the micrograph of the specimen is difficult. Therefore, graphite was deposited on the specimen. A final polishing step was introduced to remove the graphite from the sugar crystal component. The polishing process resulted in a specimen surface with sufficient contrast difference between the sugar crystals and the polymer binder so that micrographs of the specimen could be obtained before loading.

The complete experimental setup for the meso-dynamic experiments is shown in Fig. 53.1. The setup is comprised of an extension tube (Navitar) for high magnification imaging, high speed camera (Photron SA-X2), high intensity halogen lamps (EKKA), oscilloscope (Not shown), strain amplifier (not shown) and a data acquisition system (not shown). To obtain the images of the deforming specimen, the triggering of the camera is done from the output of the oscilloscope. The magnification of the extension tube is set to be 2X, resulting in a field of view of 1700 × 690 μm^2 at an image capturing speed of 100,000 frames/s. Spatial resolution for the experiment is 4.427 μm/pixel. The distance of the extension tube from the specimen is 86 mm and the depth of field of the system is 550 μm. Loading of the specimen is conducted with the help of a split Hopkinson bar setup. In this experiment the material to be tested is soft due to the presence of polymer in the composition. Therefore, obtaining sufficient transmitted signal is difficult. We have used a low impedance polycarbonate bar to overcome this issue [5, 6]. The split Hopkinson bar setup in this experiment includes an input and output bar of 1830 mm in length and 25.4 mm in diameter. The striker is made of the same material as the incident and output bars. Strain gages are placed at the center of the input and out bar.

The digital image correlation technique [7] was used to obtain the local strain field in this experiment. To facilitate taking high contrast images, the specimens are speckled using spray paint and boron nitride black powder with particle sizes 12–18 μm. A thin coat of white paint was first applied on the specimen, and then just before it dried, boron nitride powder was distributed on the paint, which results in a high contrast and random speckle pattern as shown in the Fig. 53.2c. During testing, the specimen is placed between the incident and transmission bars of the Hopkinson bar setup. Lubricant is applied

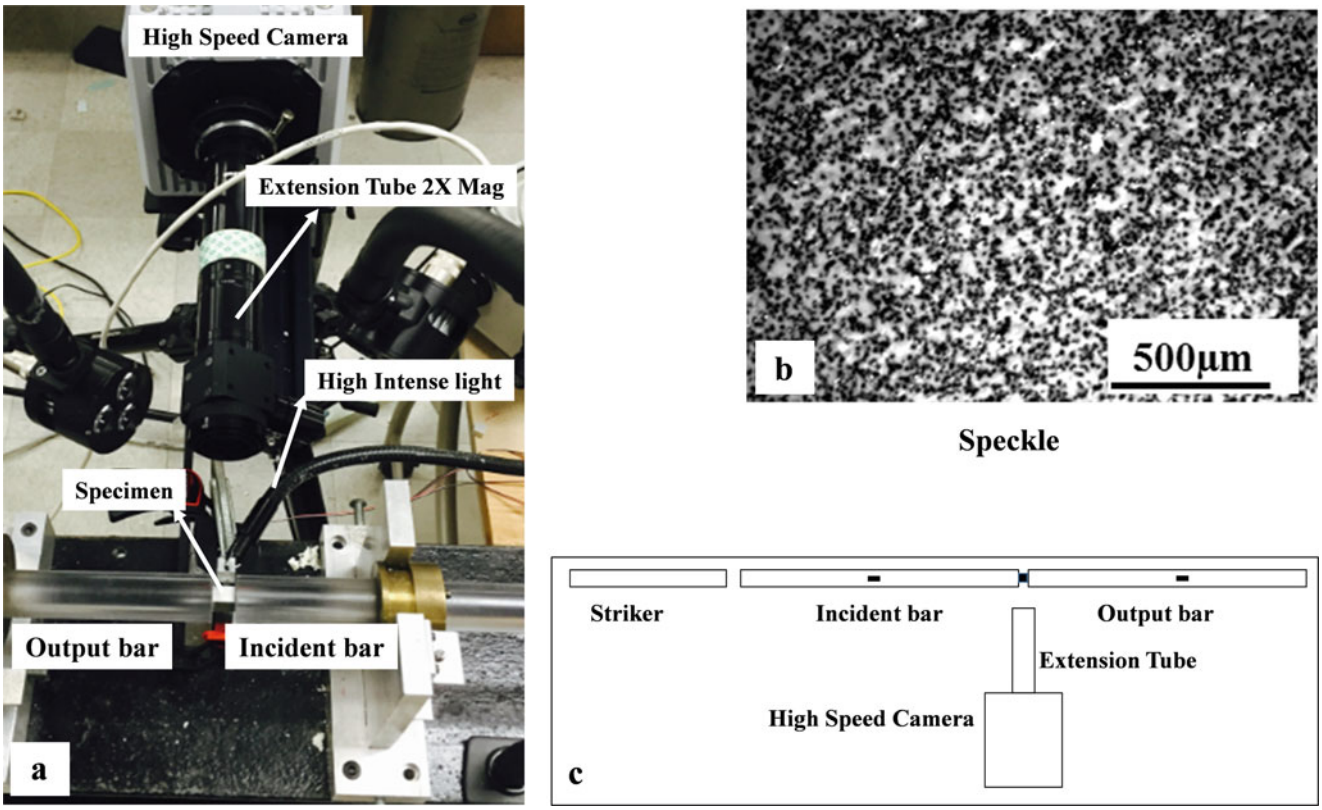

Fig. 53.1 Experiment setup and speckle pattern

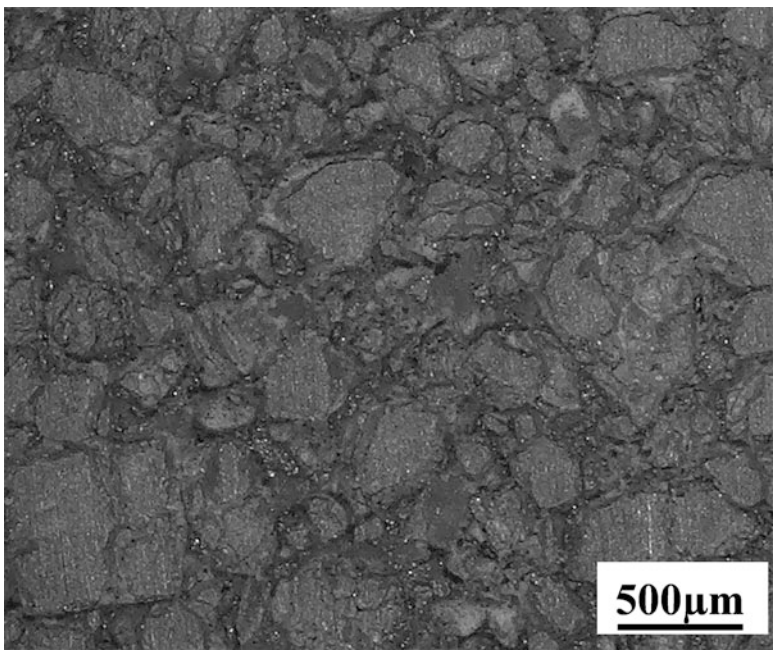

Fig. 53.2 Micro-graph of the specimen

on the specimen surface to reduce friction at the contact surface of the specimen and the bars. The camera is arranged in such a way that the camera lens is perpendicular to the front face of the specimen. For post processing of the images, commercial digital image correlation software Vic2D was used. In post processing a subset size of 21 × 21 pixels (89 × 89 μm^2) and step size of 3 pixels.

53.3 Results and Discussion

The microstructure of the polymer bonded sugar simulant is shown in Fig. 53.2, indicating an average size of the crystals is about 400 μm. Thus, approximately 15 subsets are analyzed within a single sugar crystal.

Figure 53.3 presents a typical stress-strain curve for of PBS specimen under dynamic loading at a strain rate of 1200 s^{-1}. It shows that the yielding starts at about 11.2 MPa and at a strain ~2.7 %.

Local axial strain distributions developed in the PBS specimen under dynamic loading for three different global strains are shown in the Fig. 53.4. It clearly shows that the local strain varies from small tensile strain to compressive strain of 2 %. It is expected that the low strain corresponds to the solid particles in the materials and the higher compressive strain occurs in the polymer bond between the crystals (Fig. 53.4).

Local transverse strain in specimen loaded under compression is tensile in nature which would result in debonding of the crystals from the binder material in the material (Fig. 53.5). It can be seen that localization is along the diagonal close to 45° with the loading axis. Further loading resulted in crack initiation, with failure occurring along the line shown in Fig. 53.6a. It is noted that the crack is curved at the right bottom of the specimen and the strain along both sides of the localized cracks are reduced, suggesting that fracture occurred along the interface of the crystals.

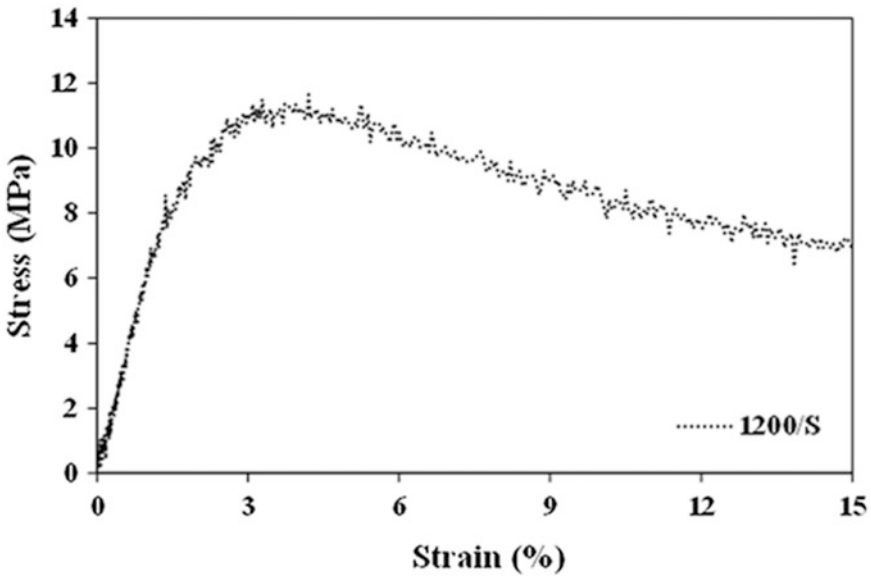

Fig. 53.3 Stress-strain curve for quasistatic and dynamic loading conditions

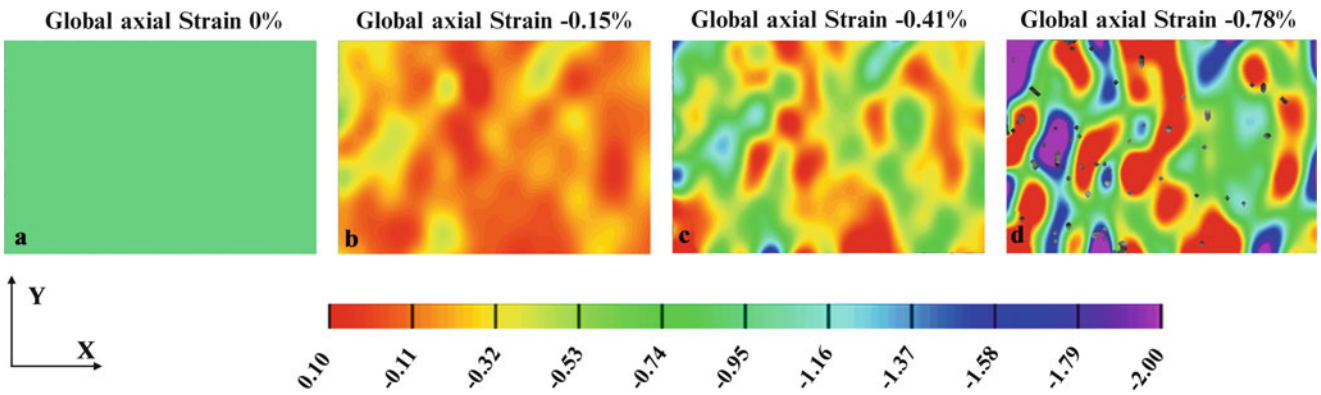

Fig. 53.4 Local axial strain field

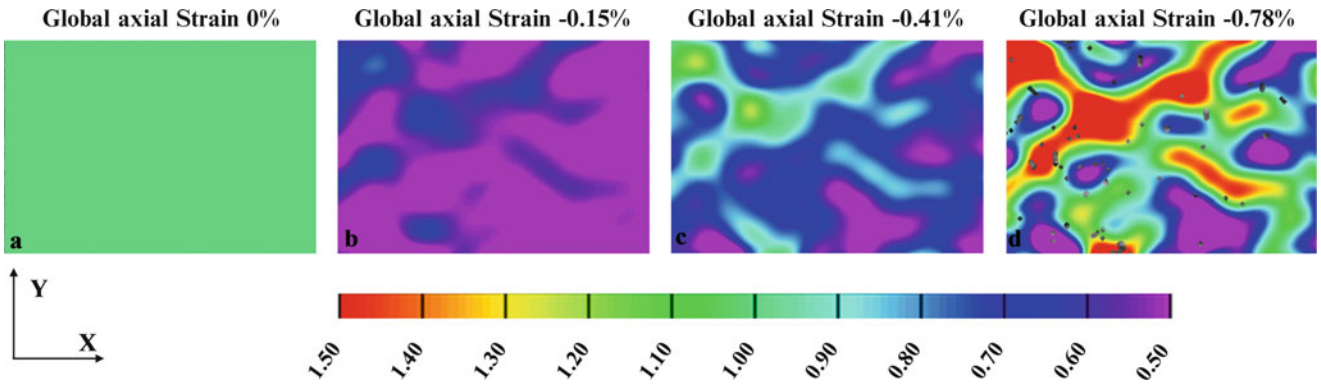

Fig. 53.5 Local transverse strain field

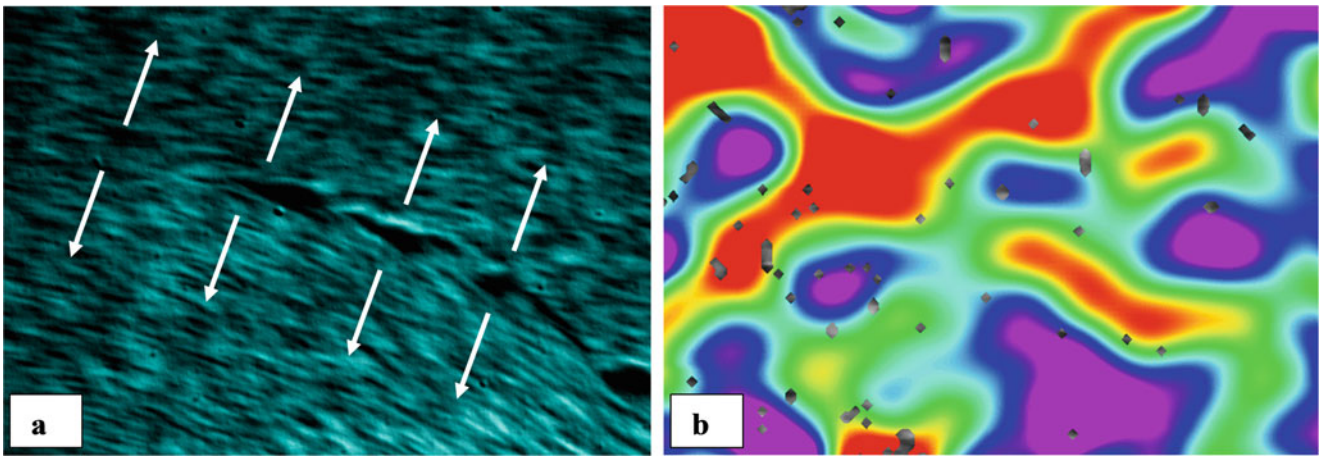

Fig. 53.6 (**a**) Crack formation in the PBS sample, (**b**) Strain field just before crack formation from DIC

53.4 Summary

A DIC based experimental system is developed for meso-scale dynamic characterization of materials. Strain localization is captured up to 0.78 % of the applied compressive strain. In the PBS specimen considered in this work, failure occurred along the weak binder boundary due to debonding caused by transverse tensile strain.

Acknowledgement The financial support of Air Force Office of Scientific Research (AFOSR) under Grant No. FA9550-14-1-0209is gratefully acknowledged.

References

1. Bouma, R.H.B., van der Heijden, A.E.D.M., Sewell, T.D., Thompson, D.L.: Simulations of deformation processes in energetic materials. In: Awrejcewicz J (ed) Numerical simulations of physical and engineering processes. INT. Ope. Acc. Pub. 29–59 (2011)
2. Field, J.E., Walley, S.M., Proud, W.G., et al.: Review of experimental techniques for high rate deformation and shock studies. Int. J. Impact Eng. **30**, 725–775 (2004)
3. Balzer, J.E., Siviour, C.R., Walley, S.M., et al.: Behaviour of ammonium perchlorate-based propellants and a polymer-bonded explosive under impact loading. Proc. R Soc. A Math. Phys. Eng. Sci. **460**, 781–806 (2004)

4. Chen, P., Zhou, Z., Huang, F.: Macro-micro mechanical behavior of a highly-particle-filled composite using digital image correlation method. Int. Ope. Acc. Pub. **437–461** (2011)
5. Zhao, H., Gary, G., Klepaczko, J.R.: On the use of a viscoelastic split Hopkinson pressure bar. Int. J. Impact Eng. **19**, 319–330 (1997)
6. Sharma, A., Shukla, A., Prosser, R.A.: Mechanical characterization of soft materials using high speed photography and split Hopkinson pressure bar technique. J. Mater. Sci. **37**, 1005–1017 (2002)
7. Chu, T.C., Ranson, W.F., Sutton, M.A.: Applications of digital-image-correlation techniques to experimental mechanics. Exp. Mech. **25**, 232–244 (1985)

Chapter 54
High Strain Rate Tensile Behavior of Fiber Metal Laminates

Ankush Sharma and Venkitanarayanan Parameswaran

Abstract Fiber metal laminates (FMLs) consist of thin metallic layers alternately bonded together with layers of fiber reinforced composite. FMLs are reported to possess excellent impact properties, improved damage tolerance and outstanding in-plane fatigue and fracture properties. In the present study, FML based on 2024-T3 aluminum (Al) alloy sheet and composite layer consisting of uni-directional glass fiber reinforced epoxy is prepared using hand layup process. High strain rate response of the FML in tension is measured using split Hopkinson pressure bar. High-speed imaging is used to record real time deformation and failure of the FML during high strain rate experiment. Digital Image Correlation is employed to measure the sample strain directly in quasi-static and high strain rate test. Dynamic and quasi-static stress-strain responses of the FML are compared.

Keywords Impact • Fatigue • Fracture • High-speed imaging • Digital Image Correlation

54.1 Introduction

Fiber metal laminates (FMLs) are hybrid laminates having thin metallic sheets and fiber reinforced composite layers stacked together. FMLs combine the ductility of metals with the high specific strength and stiffness of composite materials [1, 2]. Reports indicate that the use of glass-fiber reinforced aluminum laminates (GLARE) in fuselage skins has shown weight savings of 15–25 % for the Airbus family of aircrafts [3]. FMLs have excellent fatigue resistance, due to crack bridging by intact fibers, which reduces the stress intensity at the crack tip in the aluminum layers. Because of this, FMLs are reported to exhibit crack growth rates 10–100 times slower than their monolithic aluminum constituents [4, 5].

The motivation behind the development of high strain rate test data is to understand the behavior of FMLs in the situation of a crash event of automobile or aircraft [6]. These test results are also used as inputs to computational software to build accurate material models. Santiago and Alves [7] stated that the mechanical strength of FMLs is not studied in detail at high strain rate loading, although its constituents are reported to exhibit rate sensitive behavior. They investigated aluminum-fiber glass material using Split Hopkinson pressure bar (SHPB) and reported various experimental issues related to these tests. Zhou et al. [8] performed an experimental study on the tensile behavior of Kevlar fiber reinforced aluminum laminates (KRALL) at high strain rates using high-speed tensile impact machine. They reported that application of pre-stress on KRALL increased the yield strength, decreased the failure strain, but had no effect on the tensile strength. Vlot [9] studied the influence of strain rate on tensile properties of FMLs. Tensile strength of GLARE increased by more than 20 % over approximately five decades of strain rate whereas aramid fiber reinforced aluminum laminates (ARALL) only exhibited a small increase in strength at highest strain rates.

McCarthy et al. [10] studied rate-sensitive behavior of GLARE having the stacking sequence [A/0^0/90^0/A/90^0/0^0/A] (A stands for aluminum) using SHPB. In their study, samples having fibers aligned at 0^0/90^0 to loading axis showed that an increase in strain rate from quasi-static to 3300/s results in an increase in failure load from 4200 N to approximately 5000 N. For response at medium (nominally 100/s) and quasi-static rates of loading, no difference was observed. However, for samples having fibers aligned at +/−45^0 to loading axis, maximum extension increased significantly with strain rate, but the tensile strength increased by only a small amount. For samples tested at medium and high rates, load-deformation responses were similar. Kim et al. [11] studied tensile behavior of aluminum/carbon fiber reinforced polymer hybrid composites (CFRP) with different CFRP stacking sequences at strain rates between 0.001 and 100/s. In case of FML, as the strain rate was increased, both the tensile strength and failure strain increased. Stacking sequence of CFRP layer was observed to be strongly responsible for the differences in tensile properties and degree of strain rate sensitivity.

A. Sharma (✉) • V. Parameswaran
Department of Mechanical Engineering, Indian Institute of Technology Kanpur, Kanpur 208016, India
e-mail: apsharma@iitk.ac.in

C. Ralph et al. (eds.), *Mechanics of Composite and Multi-functional Materials, Volume 7*,
Conference Proceedings of the Society for Experimental Mechanics Series, DOI 10.1007/978-3-319-21762-8_54

In the present study, FMLs having on 0.4 mm thick Al 2024-T3 sheet and uni-directional glass fiber reinforced epoxy (GFRP) is prepared by hand layup process. Their tensile response at high strain rates is measured using SHPB. High-speed imaging is used to record real time deformation and failure of the FML during the experiment. The sample strain in quasi-static and high strain rate test is directly measured by Digital Image Correlation (DIC). The quasi-static and dynamic stress strain responses of the FML are compared.

54.2 Experimental Details

54.2.1 Specimen Configuration

The FML considered in the present study had three layers of 0.4 mm thick Al 2024-T3 sheets and two composite layers of GFRP, each layer having a $0^0/90^0$ layup. The overall stacking sequence of FML is $[A4/0^0/90^0/A4/90^0/0^0/A4]$ where A4 stands for 0.4 mm thick aluminum layer. The FML was prepared by hand layup process in the form of rectangular sheet having size 230 $\times$ 230 mm^2 and the thickness achieved was 3.7 mm. The composite layers had 50 % fiber volume fraction. For FMLs, the metal thickness fraction is defined as the ratio of total thickness of metallic layers to the total laminate thickness and was 0.33 in the present study. From the prepared sheet, specimens for the static and dynamic tests as were cut using a water-cooled slicing saw. The geometry of the specimen for static and high strain rate tests is shown in Fig. 54.1 [12, 13]. Specially designed specimen grips as shown in Fig. 54.2 were used in high strain rate tensile tests.

54.2.2 Quasi-static Loading

The specimens were loaded using friction grips in a universal testing machine at 1 mm/min. The average strain in the specimen within the gage length was measured using DIC technique.

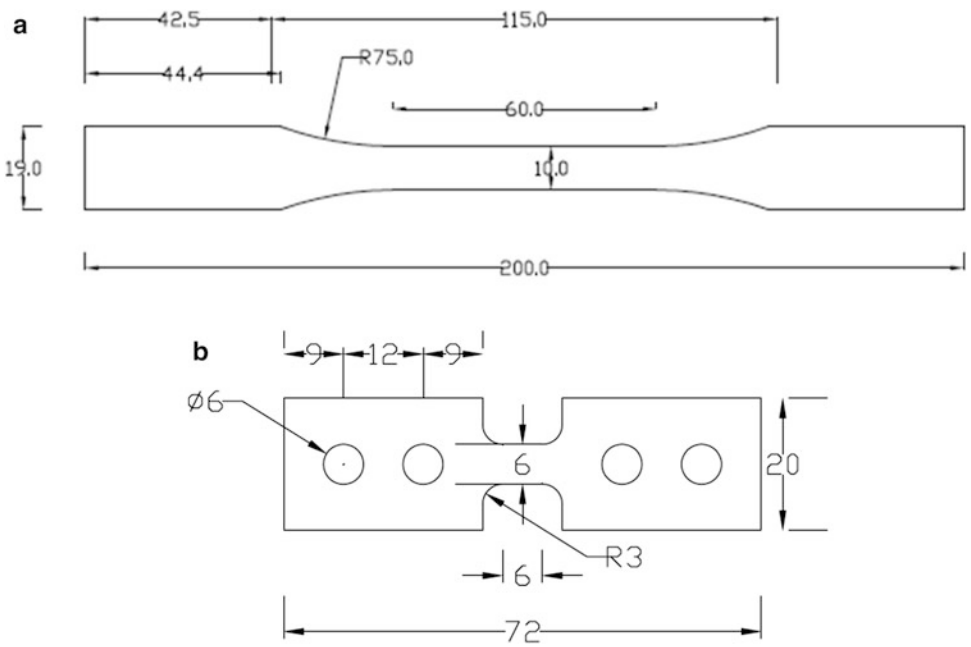

Fig. 54.1 Geometry of (**a**) the static and (**b**) the high strain rate test specimens (All dimensions are in mm)

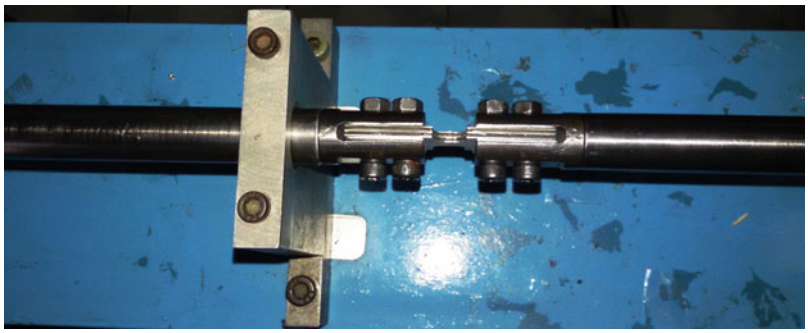

Fig. 54.2 Photograph of specimen grips used in SHPB tests

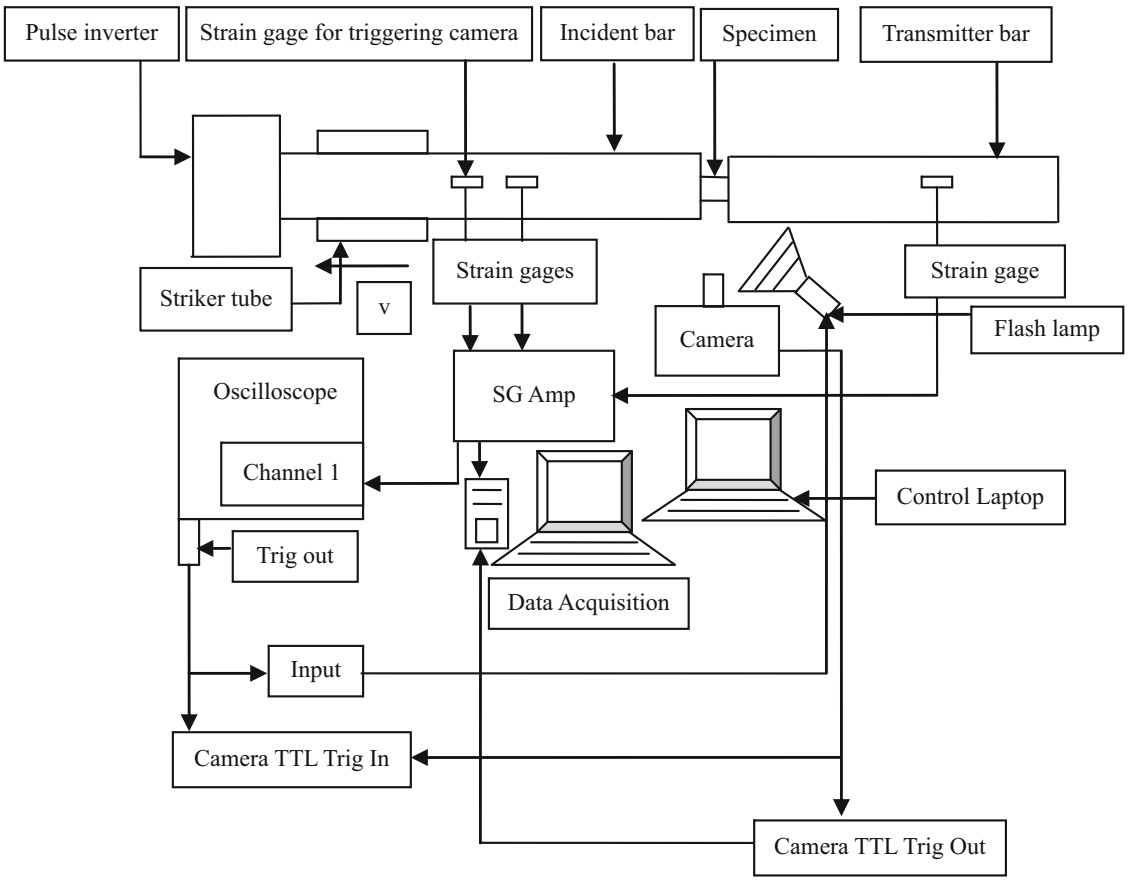

Fig. 54.3 Schematic diagram of the tensile split Hopkinson pressure bar

54.2.3 High Strain Rate Loading

High strain rate tensile tests were carried out using a tensile SHPB apparatus, schematic of which is shown in Fig. 54.3. The incident bar, transmitter bar and the striker were made of Maraging steel (VascoMax 300). A compressed air gun was used to accelerate a 350 mm long striker tube towards the pulse inverter shown in Fig. 54.3. A finite length compressive loading pulse is generated in the pulse inverter by this axial impact. This strain pulse reflects from the inverter's free end as a tensile pulse and propagates along the incident bar towards the specimen. When the tensile stress pulse reaches the specimen, part of it gets transmitted through the specimen into the transmitter bar and the remaining pulse is reflected back into the incident bar due to impedance mismatch. A pair of strain gages, each placed on the incident and transmitter bars was used to record the incident, reflected and transmitted strain signals using a set of Ectron 563H amplifiers and a data Acquisition system (NI PCI-6115) at a sampling rate of 1 MHz. DIC technique was used to measure the specimen strain.

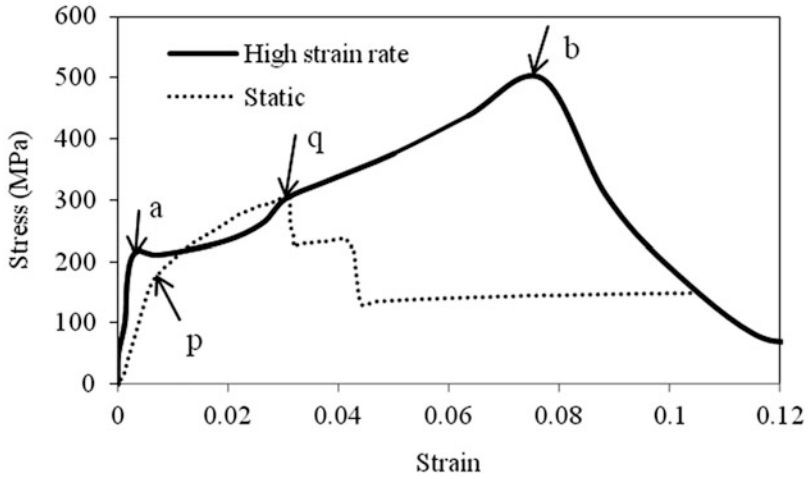

Fig. 54.4 Stress versus strain plot from high strain rate tensile test on SHPB for FML

54.2.4 High Speed Real Time Digital Imaging

During SHPB tests, a Photron SA1.1 camera was used to record the images of the specimen at framing rates of 10^5/s with an exposure time of 1 microsecond. A high intensity flash lamp was used for illumination of the specimen. The signal from a strain gage mounted on the incident bar was used to trigger a Digital Storage Oscilloscope (DSO). The DSO slave triggered the camera, flash lamp and the data acquisition system. In this way, time synchronization between the strain signals and the photographs was achieved.

54.3 Results

The specimen stress as a function of time was calculated from the transmitted signal [14, 15]. Typical dynamic stress-strain response along with the quasi-static response is shown in Fig. 54.4.

The stresses corresponding to points a, b indicated on the stress strain curve for high strain rate loading are respectively 218 and 499 MPa. It is observed that the aluminum layer starts yielding at (a) followed by failure of the composite at (b). Similarly, stress levels corresponding to points p and q indicated on the FML stress strain curve for quasi-static loading are respectively 170 and 308 MPa. Yielding of aluminum sheet takes place at (p) followed by complete failure of the composite at (q). It is observed that the stress at yield of the FML in dynamic tensile test is 1.3 times than that in static test where as the ultimate tensile strength in dynamic test is 1.6 times that measured in static test.

54.4 Conclusions

The present study shows that there is a significant increase in tensile strength at high strain rate loading compared to that at quasi-static loading for the FML investigated. While the increase in yield strength is about 30 %, the increase in ultimate strength is much more at 60 %. Further investigations are in progress to identify the individual contributions of aluminum and composite to increase in strength at high strain rates.

Acknowledgement The authors would like to acknowledge the financial support by Ministry of Human Resource and Development, Government of India for the high speed camera used in this study.

References

1. Vlot, A., Kroon, E., LaRocca, G.: Impact response of fiber metal laminates. Key Eng. Mater. **141–143**, 235–276 (1998)
2. Wu, H.F.: Effect of temperature and strain rate in tensile mechanical properties of ARALL-1 laminates. J. Mater. Sci. **26**, 3721–3729 (1991)
3. Asundi, A., Choi Alta, Y.N.: Fiber metal laminates: an advanced material for future aircraft. J. Mater. Process. Technol. **63**, 384–394 (1997)
4. Vlot, A., Vogelesang, L.B., deVries, T.J.: Towards application of fibre metal laminates in large aircraft. Aircr Eng Aerosp Technol **71**(6), 558–570 (1999)
5. Vogelesang, L.B., Vlot, A.: Development of fibre metal laminates for advanced aerospace structures. J. Mater. Process. Technol. **103**, 1–5 (2000)
6. http://www.sae.org/standardsdev, June 2006.
7. Santiago, R.C., Alves, M.: Dynamic characterization of a fiber metal laminate. Key Eng. Mater. **535–536**, 48–51 (2013)
8. Zhou, Y., Wang, Y., Mallick, P.K.: An experimental study on the tensile behavior of Kevlar fiber reinforced aluminum laminates at high strain rates. Mater. Sci. Eng. A **381**, 355–362 (2004)
9. Vlot, A.: Impact properties of fiber metal laminates. Compos. Eng. **3**, 911–927 (1993)
10. McCarthy, M.A., Xiao, J., Petrinic, N., Kamoulakos, A., Melito, V.: Modelling of bird strike on an aircraft wing leading edge made from fibre metal laminates—part 1: material modelling. Appl. Compos. Mater. **11**, 295–315 (2004)
11. Kim, J.G., Kim, H.C., Kwon, J.B., Shin, D.K., Lee, J.J., Huh, H.: Tensile behavior of aluminum/carbon fiber reinforced polymer hybrid composites at intermediate strain rates. J. Compos. Mater. **49**, 1179–1193 (2014)
12. Villanueva, G.R.: Processing and characterisation of the mechanical properties of novel fibre-metal laminates. PhD thesis, University of Liverpool (2002)
13. Huh, H., Kang, W.J., Han, S.S.: A tension split Hopkinson bar for investigating the dynamic behavior of sheet metals. Exp. Mech. **42**(1), 8–17 (2002)
14. Kuhn, H., Medlinm, D. (eds.): Mechanical testing and evaluation. In: ASM Hand Book, ASM International, Materials Park, OH vol. 8, 427–529 (2000)
15. Ellwood, S., Griffiths, L.J., Parry, D.J.: A tensile technique for materials testing at high strain rates. J. Phys. **15**, 1169–1172 (1982)

Chapter 55
Compressive Response of Cellular Core Filled with Micro-Sphere Embedded Aluminum

Kanti Lal Solanki, Venkitanarayanan Parameswaran, and Jim Sorensen

Abstract In recent years, sandwich structures have received a lot of attention due to their potential application in impact and blast mitigation. Sandwich structures are made of a soft core sandwiched between two strong thin face sheets. The objective of the present work is to understand the compressive stress-strain response of a cellular core used in sandwich structures under quasi-static and dynamic loading conditions. The core considered has a cellular structure with a cell size (3.6×4.7) mm^2 and walls made of 0.5 mm thick titanium sheet. These titanium cells are filled with aluminum having embedded glass micro-spheres. Quasi-static tests were performed using a universal testing machine whereas dynamic tests were performed using a split Hopkinson pressure bar. The compressive response of the core is evaluated by loading the core along the walls of the titanium cell and also perpendicular to the walls of the titanium cell in both quasi-static and dynamic tests. High-speed imaging is used to record the real-time deformation and failure of the samples.

Keywords Aluminum foam • Titanium cellular structure • Glass micro sphere • High strain rate • High speed imaging

55.1 Introduction

In recent years, due to the increased threats to civil and military infrastructure, different materials have been developed and explored for their potential application in impact and blast mitigation. Amongst these advanced materials, lightweight metallic foams and sandwich materials have shown great potential for impact and blast mitigation. This lead to their increased demand, predominantly, in aerospace and naval sectors. Metal matrix foams are composite materials prepared by filling a metallic matrix with hollow particles known as micro-spheres. These foams undergo large strain at a constant stress level, compared to their monolithic counterpart, leading to increased energy absorption prior to densification. Cellular structure in the foam also plays a very important role in energy absorption through deformation of the cells and buckling of the cell walls. Dynamic response of polymeric and metallic foams has been investigated by many researchers in the past [1–4]. Different types of polymer based syntactic foams and metallic syntactic foams have been investigated. Compressive response of aluminum embedded with glass micro-spheres and silicon carbide hollow spheres has been reported in [5–9]. Compressive response of metal matrix foams with honeycomb structure has also been reported in [10, 11]. In the present investigation, a cellular structure filled with hollow glass micro-sphere embedded aluminum is investigated to understand the response of this material under quasi-static and high strain rate loading.

55.2 Experimental Details

55.2.1 Material Description

The material considered in the present investigation has a cellular structure. The walls of the cellular structure are made of titanium and its cells are filled with aluminum embedded with glass micro-spheres. The foam was prepared by CPS Technologies Corporation, MA, USA. SEM images of micro-sphere filled aluminum and titanium cell are shown in Fig. 55.1.

K.L. Solanki (✉) • V. Parameswaran
Department of Mechanical Engineering, Indian Institute of Technology Kanpur, Kanpur 208016, India
e-mail: kanti@iitk.ac.in

J. Sorensen
CPS Technologies Corporation, 111 S. Worcester Street, Norton, MA 02766, USA

C. Ralph et al. (eds.), *Mechanics of Composite and Multi-functional Materials, Volume 7*,
Conference Proceedings of the Society for Experimental Mechanics Series, DOI 10.1007/978-3-319-21762-8_55

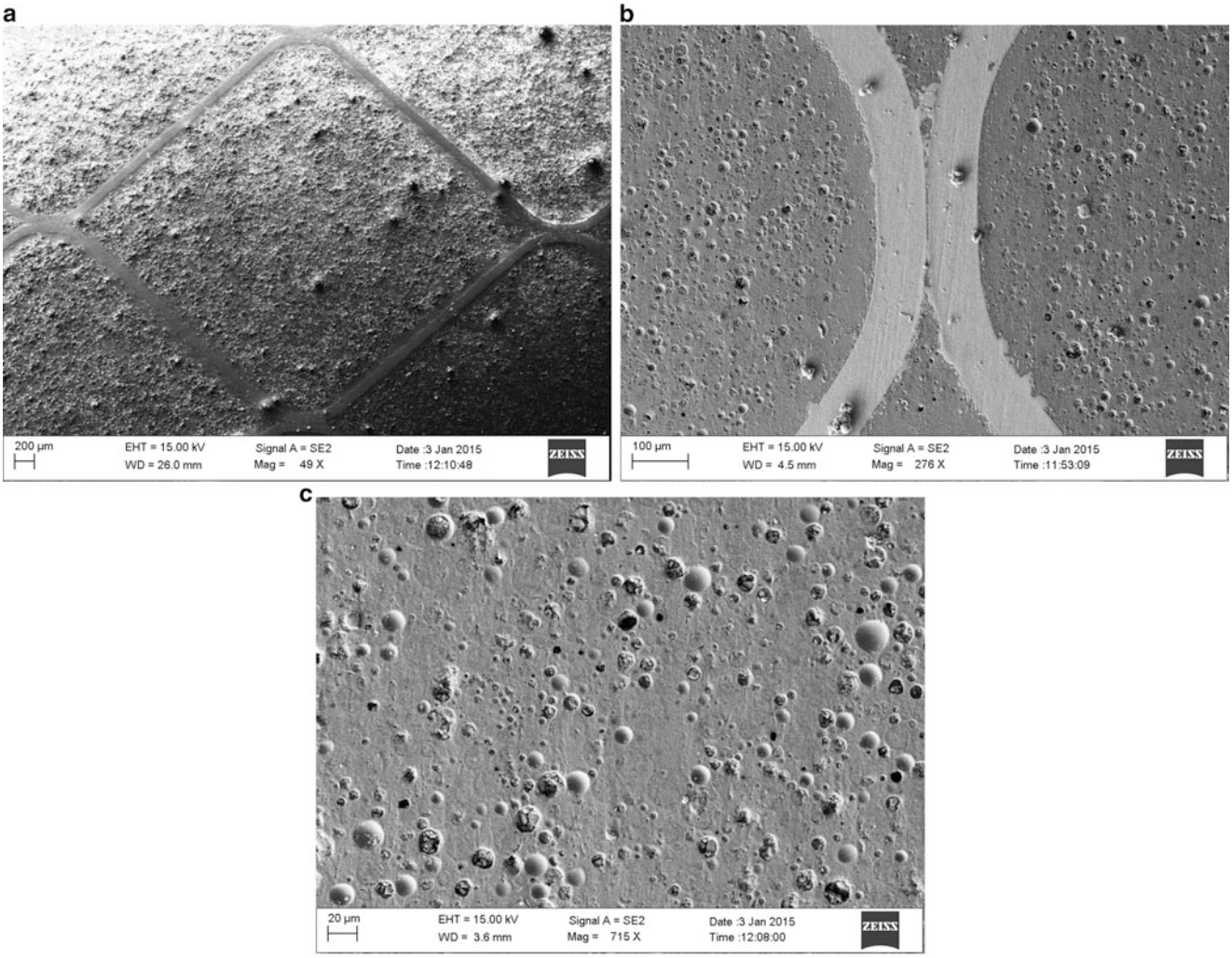

Fig. 55.1 SEM images of cellular core filled with glass micro-sphere embedded aluminum

The micro-spheres shown in the Fig. 55.1 are hollow glass bubbles having diameter in the range of ~20–60 µm. Thickness of the cell wall is about 500 µm. Cubical samples of size 9 mm, were cut from a larger size square plate using a wire electric discharge machine. Before testing, samples were polished with superfine abrasive paper to make the loading faces parallel to each other. Figure 55.2 shows X-Ray CT-scan images of the cellular core filled with micro-sphere embedded aluminum.

To obtain the high strain rate response of the foam sample, a Split Hopkinson Pressure Bar (SHPB) setup was used. As shown in Fig. 55.3, the main components of the setup are incident bar, transmitted bar and striker. The incident bar, transmitted bar and striker were made of stainless steel. The length of the incident bar, transmitted bar and striker were 3000 mm, 2000 mm and 1200 mm respectively. The diameter of all the three bars was 20 mm. Strain gauges having a resistance of $120 \pm 0.3\ \Omega$ and gauge factor of 2.1, were placed diametrically opposite to each other at mid length of the incident bar and transmitted bar. The foam sample was placed between the incident bar and the transmitted bar. An ultra high-speed camera (SIM02-16) was used to take real time images of the deformation of the foam sample. The striker, accelerated by a gas gun, impacts axially one end of the incident bar. This impact generates a compressive stress wave in the incident bar. On reaching the interface between incident bar and foam sample, a part of this wave reflects back into the incident bar whereas the remaining part is transmitted through the specimen into the transmitter bar. These strain signals are recorded using strain gages placed at mid-length of the incident and transmitter bars and further processed to generate the stress-strain response of the sample.

Figure 55.3 shows the schematic of experimental set-up. Upon impact, a make trigger placed on the impact face of the incident bar, triggered the camera which further triggered the data acquisition system. To compare the dynamic stress-strain

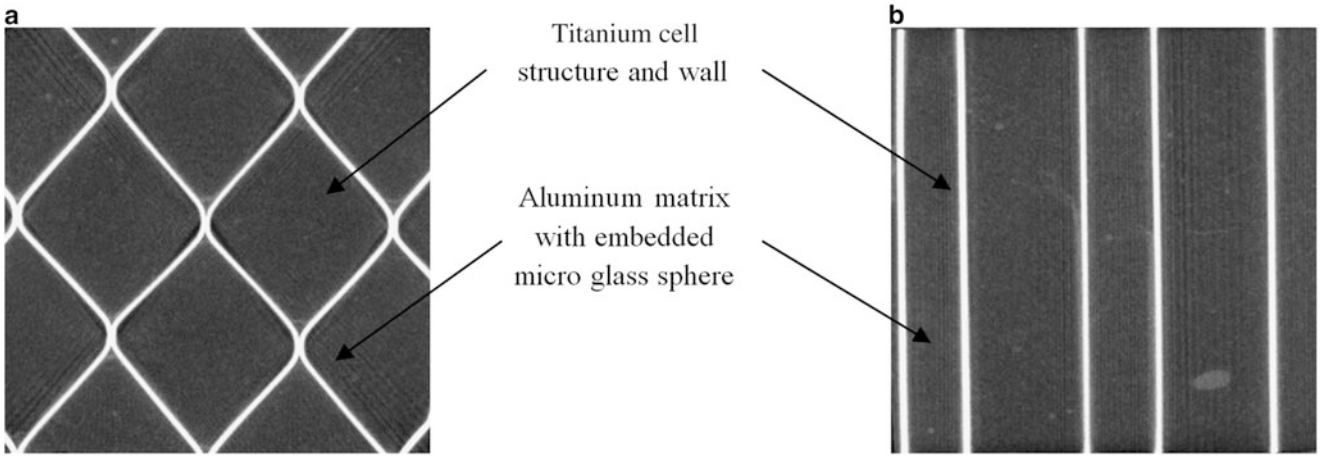

Fig. 55.2 CT scan images of cellular core filled with glass micro-sphere embedded aluminum

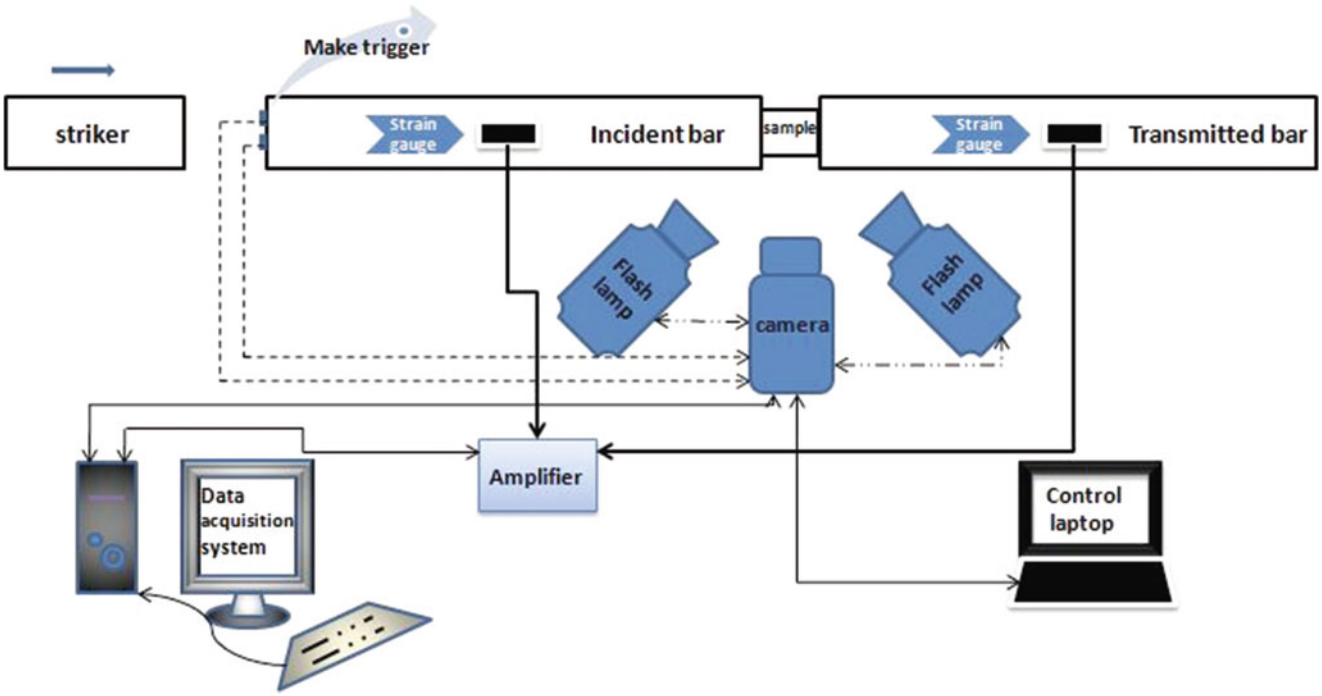

Fig. 55.3 Schematic diagram of experimental setup

behavior with static behavior, quasi-static tests were also performed using a universal testing machine at a strain rate of 0.001/s. Cubic samples of size 9 mm were used for both quasi-static and dynamic tests. In quasi-static compression test, six core samples were tested; three were loaded perpendicular to wall (PTW) and three were loaded along the wall (ATW). Similarly in dynamic test also six samples were tested; three were loaded perpendicular to wall and three were loaded along the wall.

55.3 Results and Discussion

55.3.1 Quasi-Static Compressive Stress-Strain Behaviour

The quasi-static stress-strain behavior of the core, loaded perpendicular to wall and along the wall, is shown in Fig. 55.4. In each case, three samples were tested. It was observed from these tests that the variation in results is less than 2 % and hence

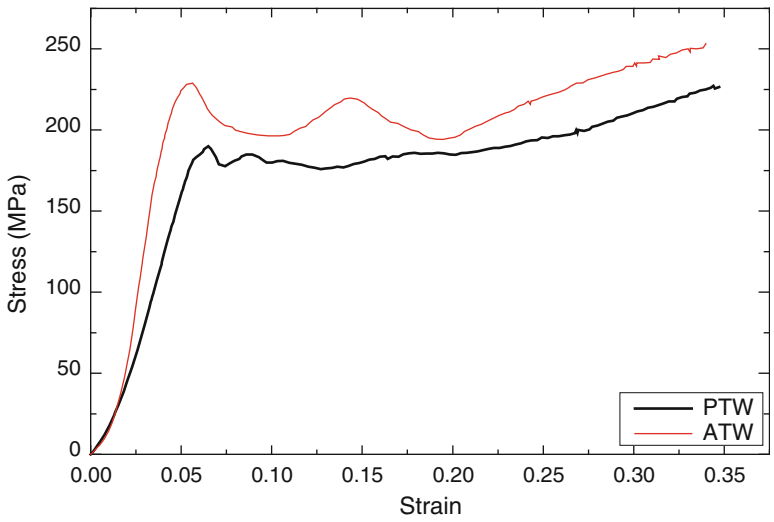

Fig. 55.4 Quasi-static compressive stress-strain behavior of cellular core filled with micro-sphere embedded aluminum

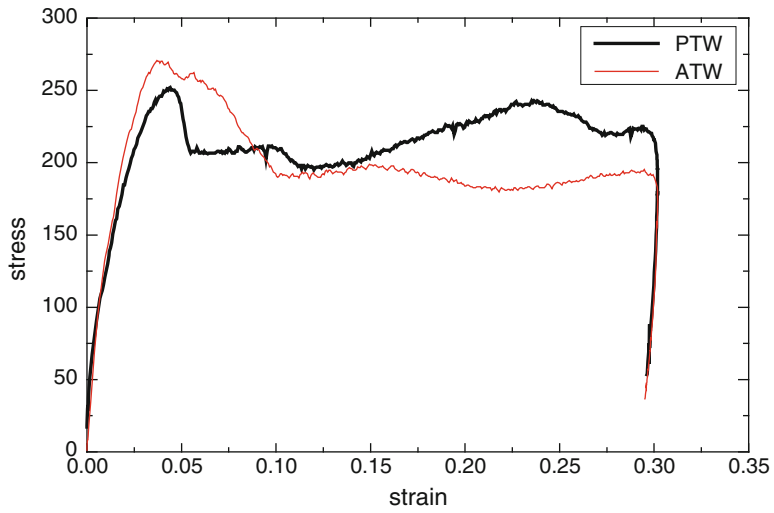

Fig. 55.5 Dynamic compressive stress-strain behavior of cellular core filled with micro-sphere embedded aluminum

only typical response is reported. Figure 55.4 indicates that the stress-strain response under quasi-static loading exhibits an initial linear region till the peak stress after which yielding starts at a strain of about 5 % for samples loaded along the wall, and at a strain of about 6 % for the samples loaded perpendicular to wall. In case of along the wall loading, a second peak is observed at a strain of about 14 % . This is believed to be due to the progressive collapse of the cell walls. Whereas, in the case of loading perpendicular to wall, several small oscillations are observed indicating the compression of each layer of titanium cell and foam material. It can be observed that the samples loaded along the wall have a higher peak stress (about 225 MPa) compared to the samples loaded perpendicular to wall (about 180 MPa). Further, the energy (area under the curve) absorbed by the sample loaded along the wall before compaction is about 25 % higher than that of sample loaded perpendicular to wall.

55.3.2 Dynamic Compressive Stress-Strain Behavior

The dynamic stress-strain behavior of core, loaded perpendicular to wall and along the wall, is shown in Fig. 55.5. In dynamic tests also three samples were tested for each case and only typical response is reported. The stress strain response for both cases, loading perpendicular to wall and loading along the wall, is nearly similar as shown in Fig. 55.5. A slightly higher peak stress (about 275 MPa) is observed in case of the sample loaded along the wall. The reason for such a behavior is attributed to the fact that the cell walls provide more load bearing capacity. After the peak stress, both the samples show a

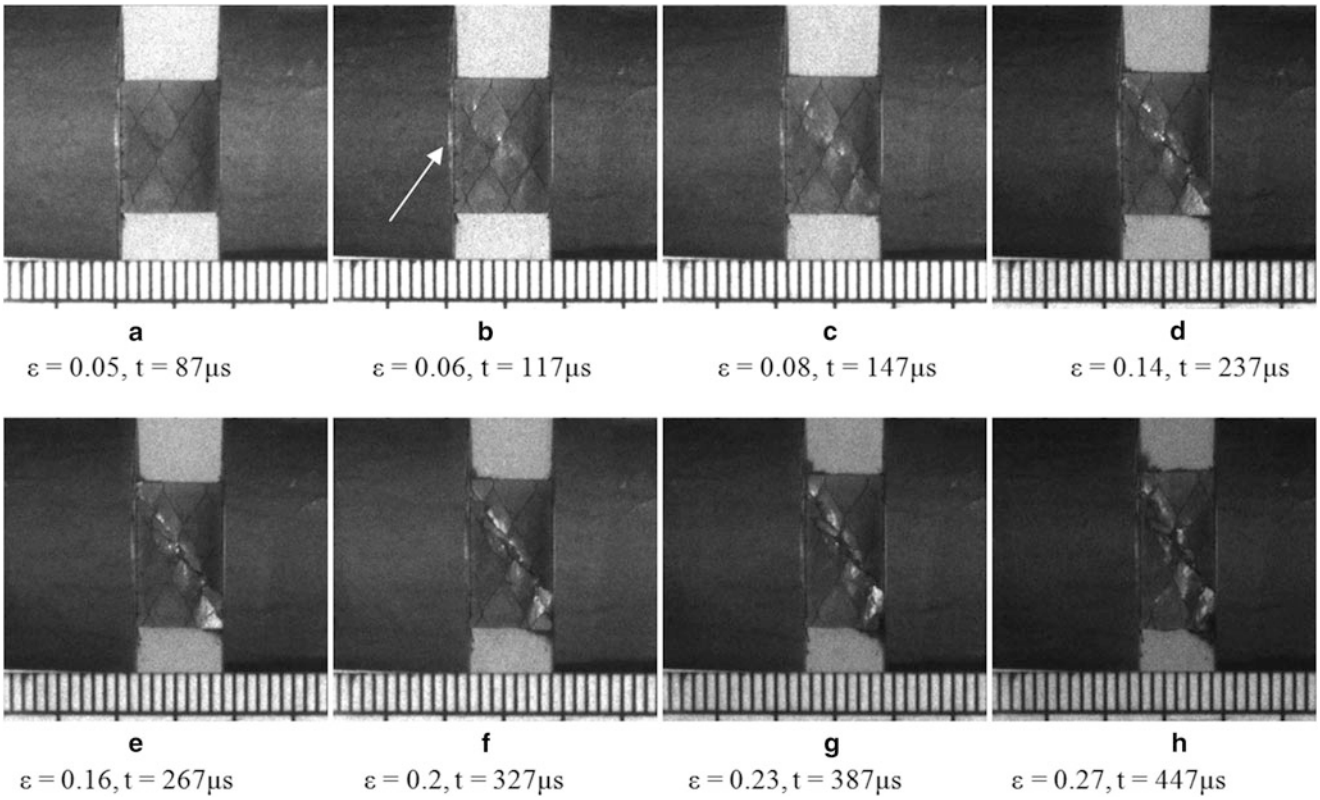

Fig. 55.6 Real time images of failure process of the core tested PTW

nearly constant stress (about 200 MPa up to about 30 % of strain) region. The energy absorbed up to plateau region is about the same in both cases.

Real-time images of failure of the core are shown in Figs. 55.6 and 55.7. The images are synchronized with stress-strain data. The strain and the time corresponding to each image are also reported in Figs. 55.6 and 55.7. It can be observed from Fig. 55.6 that, in the case of the sample loaded perpendicular to wall, there is no visible damage appearing up to a strain 0.05. At a strain 0.06, a crack growing at an angle to the loading direction is clearly observed (shown by white arrow in Fig. 55.6). The sample is sheared along the crack plane as shown in Fig. 55.6. While in the case of the sample loaded along the wall, (Fig. 55.7) there are no visible damages up to a strain 0.07. At a strain 0.09, a crack initiates along the cell wall (shown by white arrow in Fig. 55.7). As the deformation progresses further, more cracks appear in different directions as shown in Fig. 55.7g.

55.4 Conclusion

The stress-strain behavior of core, having a cellular structure filled with glass micro-sphere embedded aluminum, has been investigated at high strain rates using SHPB technique. Real time images have been captured using an ultra high speed camera to gain understanding of the failure process. The core samples were loaded in two different directions; along the wall and perpendicular to wall. In the both case, the peak stress and the plateau stress are higher in dynamic test compared to that in static test. In the case of along the wall loading, it is observed that the dynamic compressive strength at a strain rate of 600/s is about 21 % higher than the quasi-static compressive strength, whereas it is 38 % higher in case of perpendicular to wall loading. Investigations on sandwich samples, having cellular core filled with micro-sphere embedded aluminum is in progress.

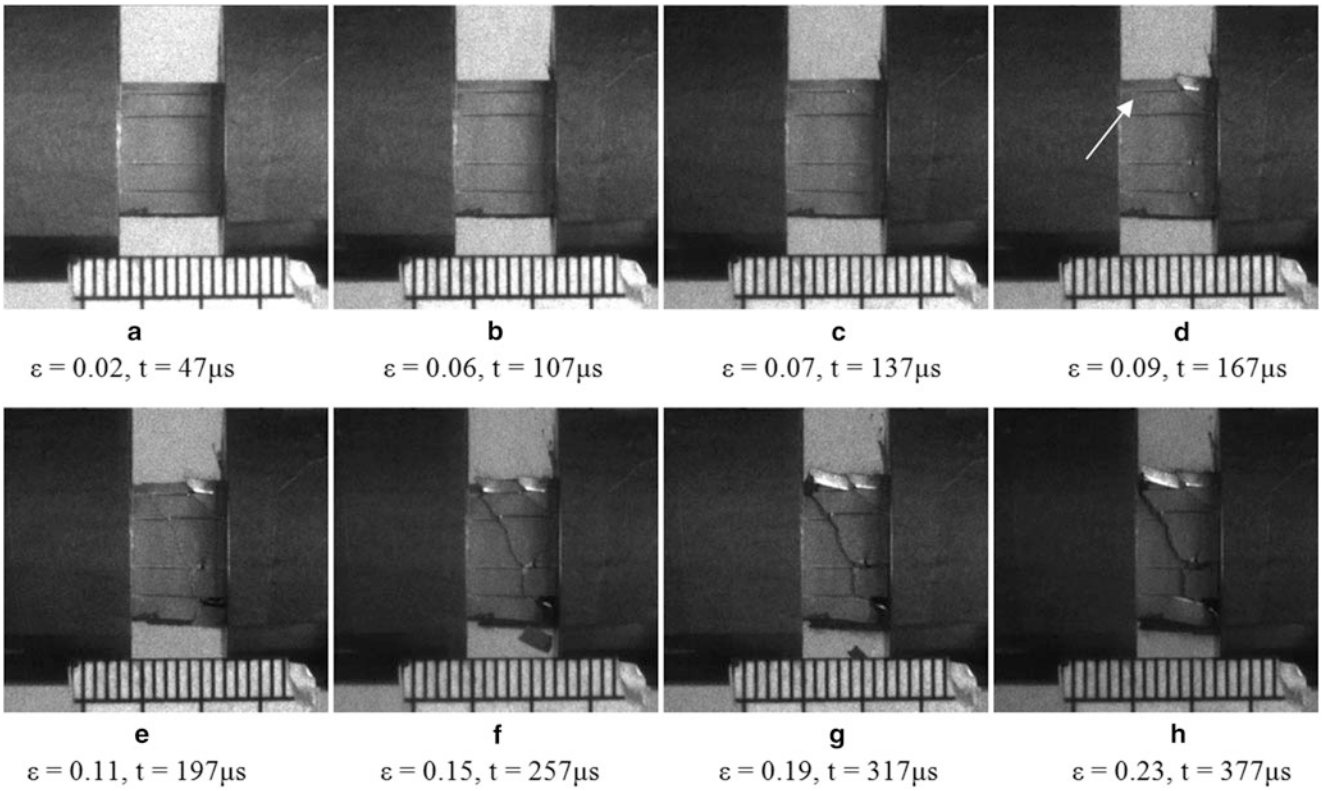

Fig. 55.7 Real time images of failure process of the core tested ATW

Acknowledgments The authors would like to acknowledge the financial support under the FIST program by Department of Science and Technology, Government of India for the Ultra-high speed camera used in this study through grant number SR/FST/ETII-003/2006.

References

1. Ruan, D., Lu, G., Chen, F.L., Siores, E.: Compressive behaviour of aluminium foams at low and medium strain rates. Compos. Struct. **57**(1–4), 331–336 (2002)
2. Edwin Raj, R., Parameswaran, V., Daniel, B.S.S.: Comparison of quasi-static and dynamic compression behavior of closed-cell aluminum foam. Mater. Sci. Eng. A **526**(1–2), 11–15 (2009)
3. Dannemann, K.A., Lankford Jr., J.: High strain rate compression of closed-cell aluminium foams. Mater. Sci. Eng. A **293**(1–2), 157–164 (2000)
4. Subhash, G., Liu, Q., Gao, X.-L.: Quasistatic and high strain rate uniaxial compressive response of polymeric structural foams. Int. J. Impact Eng. **32**(7), 1113–1126 (2006)
5. Santa Maria, J.A., Schultz, B.F., Ferguson, J.B., Rohatgi, P.K.: Al–Al_2O_3 syntactic foams—Part I: Effect of matrix strength and hollow sphere size on the quasi-static properties of Al-A_20_6/Al_2O_3 syntactic foams. Mater. Sci. Eng. A **582**, 415–422 (2013)
6. Dou, Z.Y., Jiang, L.T., Wu, G.H., Zhang, Q., Xiu, Z.Y., Chen, G.Q.: High strain rate compression of cenosphere-pure aluminum syntactic foams. Scr. Mater. **57**(10), 945–948 (2007)
7. Luong, D.D., Gupta, N., Daoud, A., Rohatgi, P.K.: High strain rate compressive characterization of aluminum alloy/fly ash cenosphere composites. JOM **63**(2), 53–56 (2011)
8. Zhang, Q., Lee, P.D., Singh, R., Wu, G., Lindley, T.C.: Micro-CT characterization of structural features and deformation behavior of fly ash/aluminum syntactic foam. Acta Mater. **57**(10), 3003–3011 (2009)
9. Parameswaran V., Sorensen J., and Bajpai M., "High strain rate response of layered micro balloon filled aluminum," In: Song, B., Casem, D., and Kimberley, J. (eds.) Dynamic Behavior of Materials, vol. 1, pp. 237–243. Springer International Publishing (2014).
10. Crupi, V., Epasto, G., Guglielmino, E.: Comparison of aluminium sandwiches for lightweight ship structures: honeycomb vs. foam. Mar. Struct. **30**, 74–96 (2013)
11. Zarei Mahmoudabadi, M., Sadighi, M.: A study on the static and dynamic loading of the foam filled metal hexagonal honeycomb—theoretical and experimental. Mater. Sci. Eng. A **530**, 333–343 (2011)

ERRATUM TO

Mechanics of Composite and Multifunctional Materials, Volume 7

Carter Ralph, Meredith Silberstein, Piyush R. Thakre, and Raman P. Singh

Chapter 19
Advanced Structured Composites as Novel Phononic Crystals and Acoustic Metamaterials

Kathryn H. Matlack, Sebastian Krödel, Anton Bauhofer, and Chiara Daraio

C. Ralph et al. (eds.), *Mechanics of Composite and Multi-functional Materials, Volume 7*,
Conference Proceedings of the Society for Experimental Mechanics Series, DOI 10.1007/978-3-319-21762-8_19

DOI 10.1007/978-3-319-21762-8_56

The following corrections were made in this chapter;

1. The X-axis label in image 19.2b was incorrect. The correct image is as shown below;

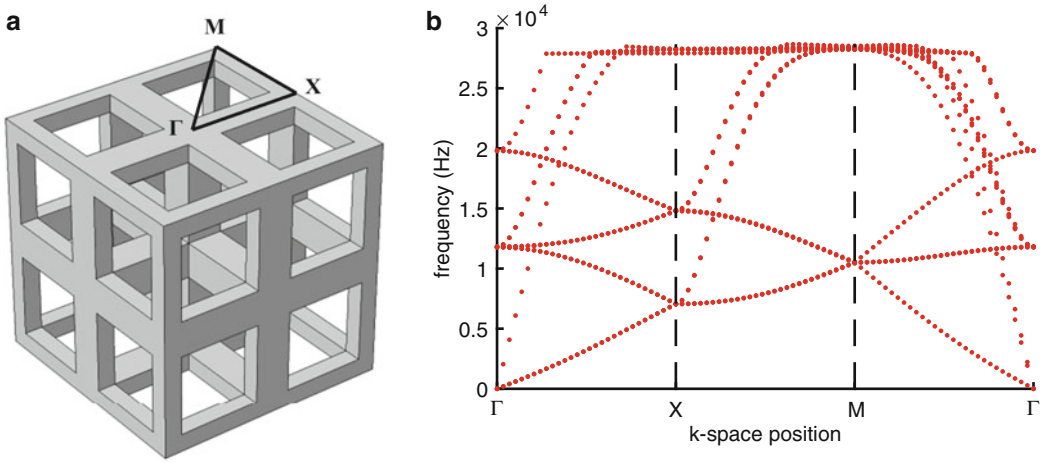

Fig. 19.2 Cubic unit cell (**a**) and corresponding dispersion curves (**b**). The irreducible Brillouin zone for a two-dimensional square lattice is superimposed on the unit cell, showing the Γ, X, and M edge points

The online version of the updated original chapter can be found at
http://dx.doi.org/10.1007/978-3-319-21762-8_19

C. Ralph et al. (eds.), *Mechanics of Composite and Multi-functional Materials, Volume 7*,
Conference Proceedings of the Society for Experimental Mechanics Series, DOI 10.1007/978-3-319-21762-8_56

2. The X-axis label in image 19.3 b was incorrect. The correct image is as shown below;

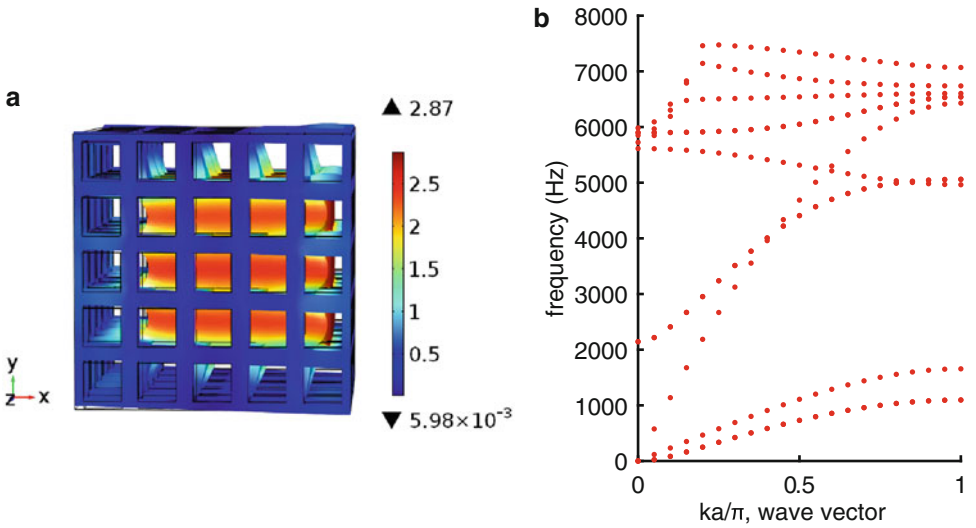

Fig. 19.3 Unit cell showing in-plane resonator mode (**a**) and calculated dispersion curves (**b**) for 1D square lattice-resonator chain, for both periodicity and wave propagation along the *x*-direction. The wave vector *k* is normalized by *a*/π, where *a* is the unit cell length. Note displacements in the unit cell are relative

3. The X-axis label in image 19.4 b was incorrect. The correct image is as shown below;

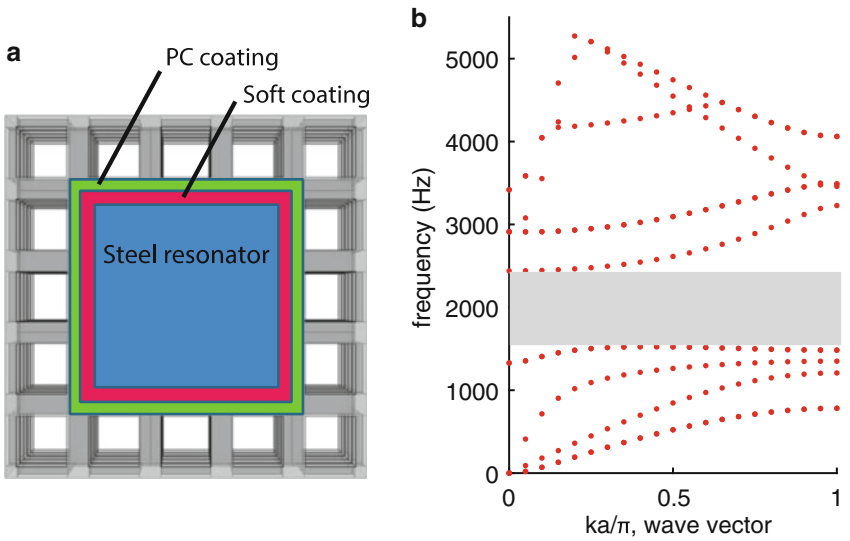

Fig. 19.4 1D chain of lattice-resonator structure with soft coating surrounding the local resonating mass, in pictorial representation (**a**), and resulting dispersion curves (**b**). The soft coating facilities the opening of a band gap centered around 2000 Hz

4. The X-axis label in image 19.5 b was incorrect. The correct image is as shown below;

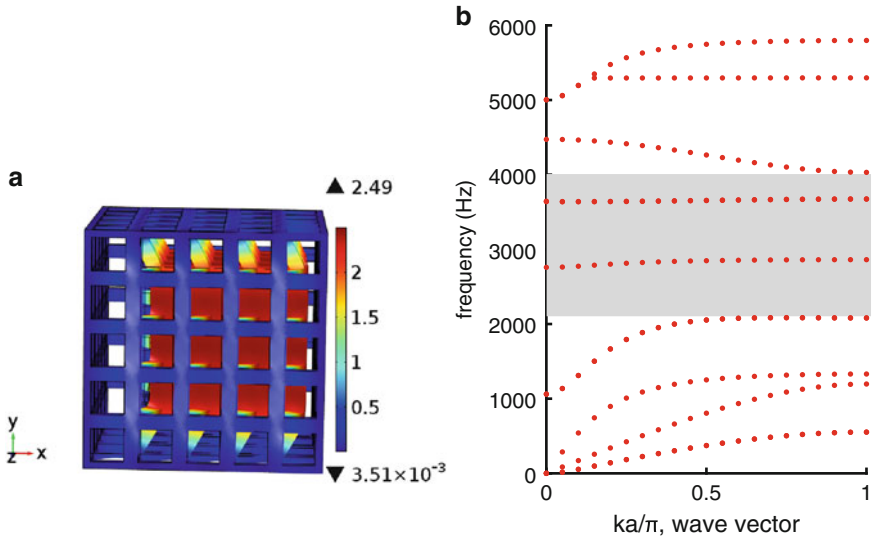

Fig. 19.5 Unit cell of 1D square lattice-resonator chain with beams under axial loading removed (**a**), and resulting band structure calculation (**b**). The removal of axially loaded beams decreases the stiffness of resonator-related modes to open up band gaps in the structure. Periodicity is in the *x*-direction

5. The X-axis label in image 19.6 b was incorrect. The correct image is as shown below;

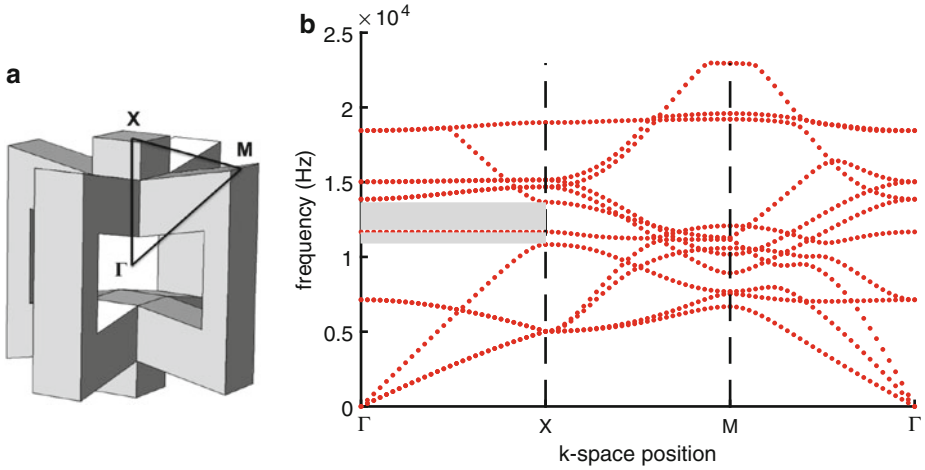

Fig. 19.6 Unit cell (**a**) and dispersion curves (**b**) for auxetic lattice geometry, with periodicity in all dimensions. *Grey boxes* indicate the directional band gaps in the ΓX direction

6. The X-axis label in image 19.7 b was incorrect. The correct image is as shown below;

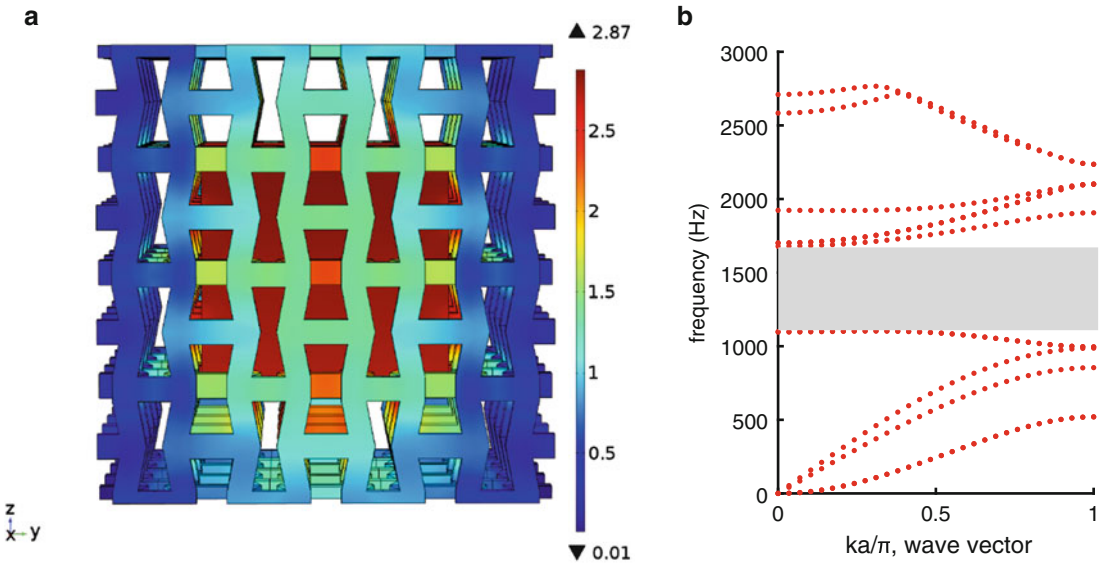

Fig. 19.7 Unit cell for 1D auxetic lattice-resonator chain (**a**), and resulting dispersion relations (**b**). The resulting band gap is centered at 1400 Hz. Periodicity is along the *y*-direction. Note that the mode displacements are not shown on the unit cell to more clearly see the geometry

7. The X-axis label in image 19.9a and 19.9b was incorrect. The correct image is as shown below;

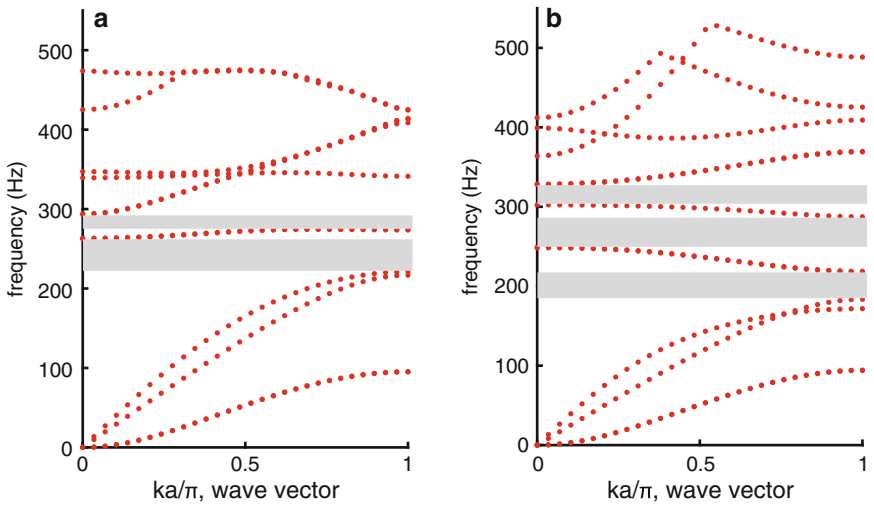

Fig. 19.9 Dispersion curves of 1D auxetic lattice-resonator chains, in the embedded (**a**) and exposed (**b**) configurations

8. In Section 19.2, the last line in the paragraph is as follows;

Thus the wavenumber defined over the space $k \in [-\pi/a, \pi/a]$. Due to symmetry about 0 within the dispersion relations, this space can further be reduced to $k \in [0, \pi/a]$.

9. In Section 19.3, the correct Equation 19.2 is as follows;

$$-\omega^2 \mathbf{Mq} + i\omega \mathbf{Cq} + \mathbf{Kq} = 0 \tag{19.2}$$

10. In Sect. 19.6.1 the number 444 is actually 4×4×4, the numbers 333 is 3×3×3.